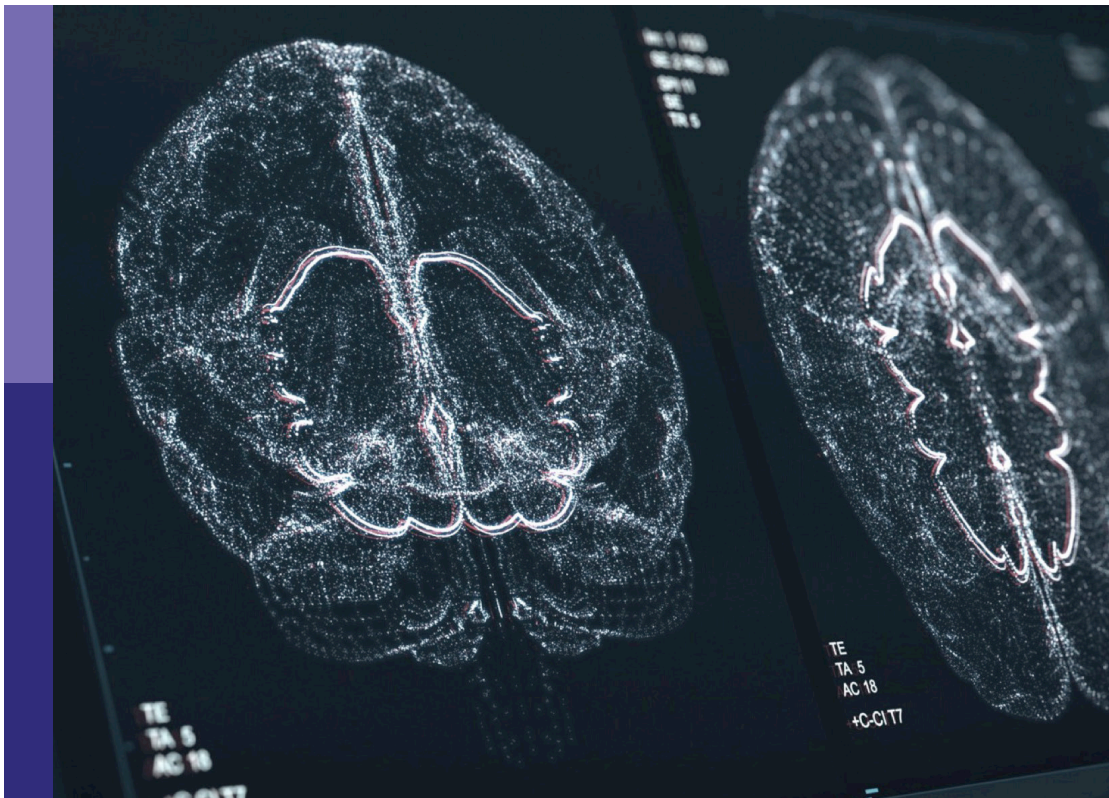
frontiers | Research Topics

Frontiers in neuroinformatics editor's pick 2021

Edited by
Jan G. Bjaalie and Sean L. Hill

Published in
Frontiers in Neuroinformatics



FRONTIERS EBOOK COPYRIGHT STATEMENT

The copyright in the text of individual articles in this ebook is the property of their respective authors or their respective institutions or funders. The copyright in graphics and images within each article may be subject to copyright of other parties. In both cases this is subject to a license granted to Frontiers.

The compilation of articles constituting this ebook is the property of Frontiers.

Each article within this ebook, and the ebook itself, are published under the most recent version of the Creative Commons CC-BY licence. The version current at the date of publication of this ebook is CC-BY 4.0. If the CC-BY licence is updated, the licence granted by Frontiers is automatically updated to the new version.

When exercising any right under the CC-BY licence, Frontiers must be attributed as the original publisher of the article or ebook, as applicable.

Authors have the responsibility of ensuring that any graphics or other materials which are the property of others may be included in the CC-BY licence, but this should be checked before relying on the CC-BY licence to reproduce those materials. Any copyright notices relating to those materials must be complied with.

Copyright and source acknowledgement notices may not be removed and must be displayed in any copy, derivative work or partial copy which includes the elements in question.

All copyright, and all rights therein, are protected by national and international copyright laws. The above represents a summary only. For further information please read Frontiers' Conditions for Website Use and Copyright Statement, and the applicable CC-BY licence.

ISSN 1664-8714
ISBN 978-2-83251-595-2
DOI 10.3389/978-2-83251-595-2

About Frontiers

Frontiers is more than just an open access publisher of scholarly articles: it is a pioneering approach to the world of academia, radically improving the way scholarly research is managed. The grand vision of Frontiers is a world where all people have an equal opportunity to seek, share and generate knowledge. Frontiers provides immediate and permanent online open access to all its publications, but this alone is not enough to realize our grand goals.

Frontiers journal series

The Frontiers journal series is a multi-tier and interdisciplinary set of open-access, online journals, promising a paradigm shift from the current review, selection and dissemination processes in academic publishing. All Frontiers journals are driven by researchers for researchers; therefore, they constitute a service to the scholarly community. At the same time, the *Frontiers journal series* operates on a revolutionary invention, the tiered publishing system, initially addressing specific communities of scholars, and gradually climbing up to broader public understanding, thus serving the interests of the lay society, too.

Dedication to quality

Each Frontiers article is a landmark of the highest quality, thanks to genuinely collaborative interactions between authors and review editors, who include some of the world's best academicians. Research must be certified by peers before entering a stream of knowledge that may eventually reach the public - and shape society; therefore, Frontiers only applies the most rigorous and unbiased reviews. Frontiers revolutionizes research publishing by freely delivering the most outstanding research, evaluated with no bias from both the academic and social point of view. By applying the most advanced information technologies, Frontiers is catapulting scholarly publishing into a new generation.

What are Frontiers Research Topics?

Frontiers Research Topics are very popular trademarks of the *Frontiers journals series*: they are collections of at least ten articles, all centered on a particular subject. With their unique mix of varied contributions from Original Research to Review Articles, Frontiers Research Topics unify the most influential researchers, the latest key findings and historical advances in a hot research area.

Find out more on how to host your own Frontiers Research Topic or contribute to one as an author by contacting the Frontiers editorial office: frontiersin.org/about/contact

Frontiers in neuroinformatics editor's pick 2021

Topic editors

Jan G. Bjaalie — University of Oslo, Norway

Sean L. Hill — Krembil Centre for Neuroinformatics, CAMH, Canada

Citation

Bjaalie, J. G., Hill, S. L., eds. (2023). *Frontiers in neuroinformatics editor's pick 2021.* Lausanne: Frontiers Media SA. doi: 10.3389/978-2-83251-595-2

Table of contents

6 FuNP (Fusion of Neuroimaging Preprocessing) Pipelines: A Fully Automated Preprocessing Software for Functional Magnetic Resonance Imaging
Bo-yong Park, Kyoungseob Byeon and Hyunjin Park

20 Brain Segmentation From Computed Tomography of Healthy Aging and Geriatric Concussion at Variable Spatial Resolutions
Andrei Irimia, Alexander S. Maher, Kenneth A. Rostowsky, Nahian F. Chowdhury, Darryl H. Hwang and E. Meng Law

32 Visbrain: A Multi-Purpose GPU-Accelerated Open-Source Suite for Multimodal Brain Data Visualization
Etienne Combrisson, Raphael Vallat, Christian O'Reilly, Mainak Jas, Annalisa Pascarella, Anne-lise Saive, Thomas Thiery, David Meunier, Dmitrii Altukhov, Tarek Lajnef, Perrine Ruby, Aymeric Guillot and Karim Jerbi

46 PManalyzer: A Software Facilitating the Study of Sensorimotor Control of Whole-Body Movements
Thomas H. Haid, Matteo Zago, Arunee Promsri, Aude-Clémence M. Doix and Peter A. Federolf

59 Spatial Localization of EEG Electrodes in a TOF+CCD Camera System
Shengyong Chen, Yu He, Huili Qiu, Xi Yan and Meng Zhao

70 Dilated Dense U-Net for Infant Hippocampus Subfield Segmentation
Hancan Zhu, Feng Shi, Li Wang, Sheng-Che Hung, Meng-Hsiang Chen, Shuai Wang, Weili Lin and Dinggang Shen

82 A Brief History of Simulation Neuroscience
Xue Fan and Henry Markram

110 Reconstruction and Simulation of a Scaffold Model of the Cerebellar Network
Stefano Casali, Elisa Marenzi, Chaitanya Medini, Claudia Casellato and Egidio D'Angelo

129 Multi-Lag Analysis of Symbolic Entropies on EEG Recordings for Distress Recognition
Arturo Martínez-Rodrigo, Beatriz García-Martínez, Luciano Zunino, Raúl Alcaraz and Antonio Fernández-Caballero

144 Processing Pipeline for Atlas-Based Imaging Data Analysis of Structural and Functional Mouse Brain MRI (AIDAmri)
Niklas Pallast, Michael Diedenhofen, Stefan Blaschke, Frederique Wieters, Dirk Wiedermann, Mathias Hoehn, Gereon R. Fink and Markus Aswendt

158 Novel Technological Solutions for Assessment, Treatment, and Assistance in Mild Cognitive Impairment
Gianmaria Mancioppi, Laura Fiorini, Marco Timpano Sportiello and Filippo Cavallo

181 The LONI QC System: A Semi-Automated, Web-Based and Freely-Available Environment for the Comprehensive Quality Control of Neuroimaging Data
Hosung Kim, Andrei Irimia, Samuel M. Hobel, Mher Pogosyan, Haoteng Tang, Petros Petrosyan, Rita Esquivel Castelo Blanco, Ben A. Duffy, Lu Zhao, Karen L. Crawford, Sook-Lei Liew, Kristi Clark, Meng Law, Pratik Mukherjee, Geoffrey T. Manley, John D. Van Horn and Arthur W. Toga

201 CoreNEURON : An Optimized Compute Engine for the NEURON Simulator
Pramod Kumbhar, Michael Hines, Jeremy Fouriaux, Aleksandr Ovcharenko, James King, Fabien Delalondre and Felix Schürmann

215 Analysis of Decision-Making Process Using Methods of Quantitative Electroencephalography and Machine Learning Tools
Grzegorz M. Wojcik, Jolanta Masiak, Andrzej Kawiak, Lukasz Kwasniewicz, Piotr Schneider, Filip Postepski and Anna Gajos-Balinska

231 ASD-DiagNet: A Hybrid Learning Approach for Detection of Autism Spectrum Disorder Using fMRI Data
Taban Eslami, Vahid Mirjalili, Alvis Fong, Angela R. Laird and Fahad Saeed

242 Magia: Robust Automated Image Processing and Kinetic Modeling Toolbox for PET Neuroinformatics
Tomi Karjalainen, Jouni Tuisku, Severi Santavirta, Tatu Kantonen, Marco Bucci, Lauri Tuominen, Jussi Hirvonen, Jarmo Hietala, Juha O. Rinne and Lauri Nummenmaa

255 Prediction of Pilot's Reaction Time Based on EEG Signals
Bartosz Binias, Dariusz Myszor, Henryk Palus and Krzysztof A. Cyran

268 A Standardized Protocol for Efficient and Reliable Quality Control of Brain Registration in Functional MRI Studies
Yassine Benhajali, AmanPreet Badhwar, Helen Spiers, Sebastian Urchs, Jonathan Armoza, Thomas Ong, Daniel Pérusse and Pierre Bellec

280 Robust Monte-Carlo Simulations in Diffusion-MRI: Effect of the Substrate Complexity and Parameter Choice on the Reproducibility of Results
Jonathan Rafael-Patino, David Romascano, Alonso Ramirez-Manzanares, Erick Jorge Canales-Rodríguez, Gabriel Girard and Jean-Philippe Thiran

296 A Smart Region-Growing Algorithm for Single-Neuron Segmentation From Confocal and 2-Photon Datasets
Alejandro Luis Callara, Chiara Magliaro, Arti Ahluwalia and Nicola Vanello

308 Predicting Body Mass Index From Structural MRI Brain Images Using a Deep Convolutional Neural Network
Pál Vakli, Regina J. Deák-Meszlényi, Tibor Auer and Zoltán Vidnyánszky

320 EEG Signal Reconstruction Using a Generative Adversarial Network With Wasserstein Distance and Temporal-Spatial-Frequency Loss
Tian-jian Luo, Yachao Fan, Lifei Chen, Gongde Guo and Changle Zhou

340 A Quantitative EEG Toolbox for the MNI Neuroinformatics Ecosystem: Normative SPM of EEG Source Spectra
Jorge Bosch-Bayard, Eduardo Aubert-Vazquez, Shawn T. Brown, Christine Rogers, Gregory Kiar, Tristan Glatard, Lalet Scaria, Lidice Galan-Garcia, Maria L. Bringas-Vega, Trinidad Virues-Alba, Armin Taheri, Samir Das, Cecile Madjar, Zia Mohaddes, Leigh MacIntyre, CHBMP , Alan C. Evans and Pedro A. Valdes-Sosa

frontiers in Neuroinformatics

ORIGINAL RESEARCH
published: 11 February 2019
doi: 10.3389/fninf.2019.00005

FuNP (Fusion of Neuroimaging Preprocessing) Pipelines: A Fully Automated Preprocessing Software for Functional Magnetic Resonance Imaging

*Bo-yong Park[1,2], Kyoungseob Byeon[1,2] and Hyunjin Park[2,3]**

[1] Department of Electrical and Computer Engineering, Sungkyunkwan University, Suwon, South Korea, [2] Center for Neuroscience Imaging Research, Institute for Basic Science, Suwon, South Korea, [3] School of Electronic and Electrical Engineering, Sungkyunkwan University, Suwon, South Korea

The preprocessing of functional magnetic resonance imaging (fMRI) data is necessary to remove unwanted artifacts and transform the data into a standard format. There are several neuroimaging data processing tools that are widely used, such as SPM, AFNI, FSL, FreeSurfer, Workbench, and fMRIPrep. Different data preprocessing pipelines yield differing results, which might reduce the reproducibility of neuroimaging studies. Here, we developed a preprocessing pipeline for T1-weighted structural MRI and fMRI data by combining components of well-known software packages to fully incorporate recent developments in MRI preprocessing into a single coherent software package. The developed software, called FuNP (Fusion of Neuroimaging Preprocessing) pipelines, is fully automatic and provides both volume- and surface-based preprocessing pipelines with a user-friendly graphical interface. The reliability of the software was assessed by comparing resting-state networks (RSNs) obtained using FuNP with pre-defined RSNs using open research data (n = 90). The obtained RSNs were well-matched with the pre-defined RSNs, suggesting that the pipelines in FuNP are reliable. In addition, image quality metrics (IQMs) were calculated from the results of three different software packages (i.e., FuNP, FSL, and fMRIPrep) to compare the quality of the preprocessed data. We found that our FuNP outperformed other software in terms of temporal characteristics and artifacts removal. We validated our pipeline with independent local data (n = 28) in terms of IQMs. The IQMs of our local data were similar to those obtained from the open research data. The codes for FuNP are available online to help researchers.

Keywords: functional magnetic resonance imaging, data preprocessing, volume- and surface-based preprocessing, fully automated software, fusion of existing software

OPEN ACCESS

Edited by:
Antonio Fernández-Caballero, University of Castilla–La Mancha, Spain

Reviewed by:
Enrico Glerean, Aalto University, Finland
David Mayerich, University of Houston, United States

****Correspondence:***
Hyunjin Park
hyunjinp@skku.edu

Received: *31 July 2018*
Accepted: *24 January 2019*
Published: *11 February 2019*

Citation:
Park B-y, Byeon K and Park H (2019) FuNP (Fusion of Neuroimaging Preprocessing) Pipelines: A Fully Automated Preprocessing Software for Functional Magnetic Resonance Imaging. Front. Neuroinform. 13:5. doi: 10.3389/fninf.2019.00005

INTRODUCTION

Functional magnetic resonance imaging (fMRI) is a useful tool for exploring brain functions non-invasively. The preprocessing of raw fMRI data is an essential step before performing further analyses because of the following reasons. First, fMRI measures spontaneous fluctuations of blood oxygen-level dependent (BOLD) signals that are related to neuronal activities. However, BOLD

signals contain non-neuronal contributions, such as head motion, physiological contributions, tissues outside the scope of interest, and MRI-induced artifacts, as well as neuronal signals (Murphy et al., 2013; Bright and Murphy, 2015; Caballero-Gaudes and Reynolds, 2017). The non-neuronal components in BOLD signals complicate the interpretation of fMRI signals. Secondly, the quality of fMRI data largely depends on the image acquisition parameters used. Different MRI data might have a different range of intensity values, matrix sizes, and orientations depending on the acquisition parameters used. Thus, preprocessing steps for fMRI data are required to handle these issues.

In previous studies, researchers have developed freely available open-source neuroimaging data preprocessing tools, such as statistical parametric mapping (SPM)[1], analysis of functional neuroimages (AFNI) (Cox, 1996), FMRIB software library (FSL) (Jenkinson et al., 2012), FreeSurfer (Fischl, 2012), Workbench (Marcus et al., 2013), and fMRIPrep (Esteban et al., 2019). These are widely used software tools, but each one of them employs a different strategy for data preprocessing. SPM and FSL provide fully automated graphical user interface (GUI)-based preprocessing pipelines and are suitable for volume data. FreeSurfer is suitable for surface data and provides a fully automated command line-based pipeline. AFNI and Workbench process both volume and surface data, but they do not provide a fully automated pipeline in a user-friendly interface. Users need to rearrange different functions in these disparate software tools if they seek to implement automatic data preprocessing. Different data preprocessing strategies across different software packages might yield differing results, which might reduce the reproducibility of the neuroimaging studies. The fMRIPrep is a recent development incorporating many of the state-of-the-art MRI preprocessing steps.

There are many steps in a given preprocessing pipeline, including field inhomogeneity correction, motion correction, registration, and segmentation steps. Many of these steps are standardized, but some of them are still being actively developed and refined to better preprocess fMRI data. For example, many researchers argue that cortical signals are better handled via surface-based approaches, while sub-cortical signals are better handled via volume-based approaches (Glasser et al., 2013, 2016a,b). Data-driven approaches, such as independent component analysis (ICA), to identify unwanted signals are being increasingly adopted (Salimi-Khorshidi et al., 2014; Pruim et al., 2015a,b). Time-series volume data with large head movements are sometimes removed based on frame-wise displacement (FD) (Power et al., 2012; Damaraju et al., 2014; Yeo et al., 2015). To the best of our knowledge, no single software package has all the recent developments fully incorporated. Thus, neuroimaging researchers are forced to integrate different components of various software packages if they seek to adopt all the recent developments in fMRI preprocessing.

Here, we propose a novel software for fMRI data preprocessing, named FuNP (Fusion of Neuroimaging Processing) pipelines, a wrapper software that combines components of existing software tools (i.e., AFNI, FSL, FreeSurfer, and Workbench) to fully incorporate recent developments in MRI preprocessing. Such wrapper software might be of practical impact for researchers with limited data processing background. Our software consists of preprocessing steps for structural (T1-weighted MRI) and functional (fMRI) data. We assessed the reliability of our software by comparing resting-state networks (RSNs) obtained using FuNP with pre-defined RSNs because it is difficult to obtain the ground truth of the preprocessing results. In addition, the quality of the preprocessed data was assessed using the image quality metrics (IQMs) proposed in the previous paper (Esteban et al., 2017). The major advantages of our software are as follows. FuNP can handle both volume- and surface-based preprocessing. The software is fully automated and has a user-friendly GUI.

[1]http://www.fil.ion.ucl.ac.uk/spm/

MATERIALS AND METHODS

FuNP provides two different types of fMRI preprocessing steps: (1) volume-based and (2) surface-based preprocessing pipelines. Both preprocessing pipelines include steps to process structural (T1-weighted MRI) and functional (fMRI) data. In the volume-based pipeline, data are preprocessed in 3D volume space. Volume-based analysis has been widely adopted in many neuroimaging studies. In the surface-based pipeline, data are preprocessed both in volume and surface spaces. The surface-based pipeline operates in 2D surface space but requires intermediate outcomes from volume analyses. In this pipeline, the cortical regions are represented as a 2D surface, while the sub-cortical regions are represented as a 3D volume. This mixing of surface and volume spaces is a recent development, and some researchers have claimed that it can improve the sensitivity of neuroimaging studies (Glasser et al., 2013, 2016a,b). Our software provides flexibility to perform each of the preprocessing steps. Users can select "Yes" or "No" options for every step in our software to selectively perform the steps as required. Furthermore, users can select user specified parameters for each step. For example, the degrees of freedom (DOF) and cost functions for registration could be specified in the GUI. Details of each preprocessing steps can be found in following sections.

Volume-Based T1-Weighted MRI Data Preprocessing

The volume-based preprocessing steps for T1-weighted structural data are presented in **Figure 1**.

De-Oblique

During data acquisition, the scan angle is sometimes tilted from the horizontal line (i.e., between the anterior and posterior commissure) to cover the whole brain and to avoid MRI-induced artifacts caused by air and water in the eyes and nose (**Figure 2A**). Such a tilted scan is referred to as an oblique scan. Oblique scans enable us to acquire data with less noise, but can make the registration between two different images more difficult. Thus, a de-oblique process needs to be performed. De-oblique is performed using the "3drefit" function in AFNI (Cox, 1996).

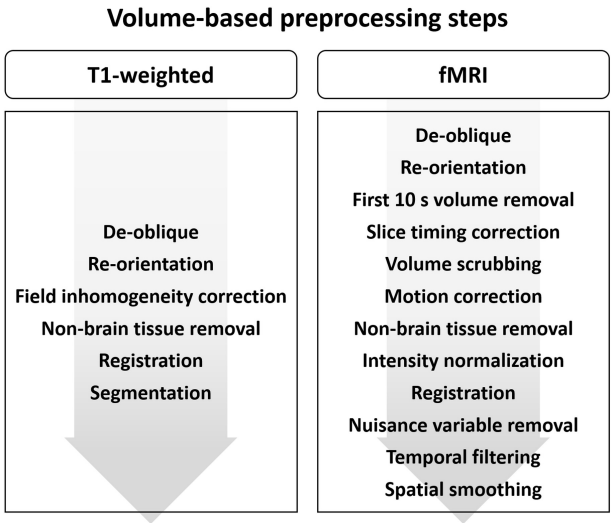


FIGURE 1 | Diagram of the preprocessing steps for volume-based **(A)** T1-weighted structural MRI and **(B)** fMRI data.

Re-orientation

The orientation of data depends on the settings of the data acquisition process (**Figure 2B**). Differences in orientation might lead to mis-registration, and thus all data should be matched to have the same orientation. Orientation is specified with a three-element vector: (1) left or right, (2) anterior or posterior, and (3) superior or inferior. For example, if the right, posterior, and inferior directions are chosen, the orientation of the data is called RPI. Orientation can be defined in any way but should be the same for all data. Re-orientation is performed using the "3dresample" function in AFNI (Cox, 1996).

Magnetic Field Inhomogeneity Correction

The brain consists of different tissues, namely gray matter (GM), white matter (WM), and cerebrospinal fluid (CSF). The magnetic field within the scanner should be constant but, in reality, it decreases when it encounters brain tissue, and the decreasing rate differs across different tissue types (Cheng et al., 2017). This phenomenon is referred to as magnetic field inhomogeneity. These differences in the magnitude of the magnetic field cause abnormally bright and dark areas, which make it difficult to detect tissue boundaries (**Figure 2C**). Thus, magnetic field inhomogeneity correction should be performed before the non-brain tissue removal and tissue segmentation steps. Magnetic field inhomogeneity correction is performed using the "3dUnifize" function in AFNI by making intensity values in WM more homogeneous (Cox, 1996).

Non-brain Tissue Removal

The region of interest (ROI) of neuroimaging studies lies within the brain. Non-brain tissues, such as those of the skull, neck, eyes, nose, and mouth, are thus not important (**Figure 2D**). The non-brain tissue removal step is performed by considering the gradient of the intensity values across different types of tissues.

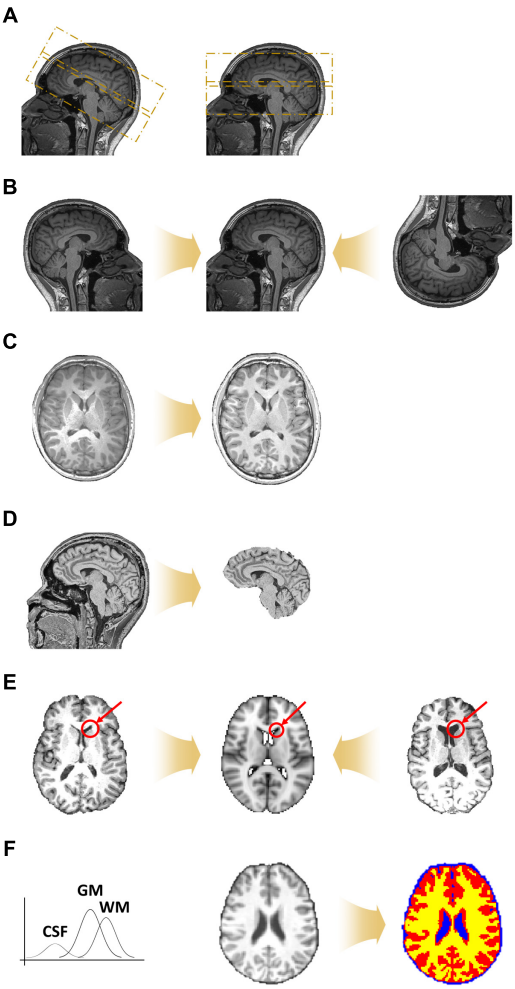


FIGURE 2 | Preprocessing steps for volume-based T1-weighted structural MRI data. **(A)** De-oblique step. Example images of (left) tilted and (right) non-tilted data are shown. **(B)** Matched data with different orientations to the same orientation. **(C)** Magnetic field inhomogeneity correction. **(D)** Non-brain tissue removal. **(E)** Registration onto the standard space. **(F)** Segmentation of brain tissues into gray matter (GM; red), white matter (WM; yellow), and cerebrospinal fluid (CSF) (blue).

Non-brain tissue removal is performed using the "3dSkullStrip" function in AFNI (Cox, 1996).

Registration

Registration is the process of aligning images from different geometric spaces to a common space (**Figure 2E**). There are three main components of registration. First, a spatial geometric transformation needs to be specified. The 3D transformation parameters are translation, rotation, scaling, and shearing in the x-, y-, and z-directions. Rigid-body transformation consists of six DOF, involving three translations and three rotations, while affine transformation consists of 12 DOFs involving three scaling and three shearing factors in addition to the rigid-body parameters, which we adopt in FuNP. Secondly, a cost function that measures the goodness of alignment has to be specified. In FuNP, users can

select either the correlation ratio or mutual information as the cost function. The correlation ratio is useful when registering two images of the same modality, while mutual information is useful for images from different modalities. Finally, an interpolation method has to be specified. In FuNP, the trilinear interpolation technique is used. Registration is performed using the "flirt" function in FSL (Jenkinson et al., 2012).

Segmentation

It has been shown that the fluctuations of time series in GM are associated with neuronal signals, while those in WM and CSF are related to artifacts (Salimi-Khorshidi et al., 2014). Thus, distinguishing between GM, WM, and CSF tissues is important for extracting signals of interest. The Gaussian mixture model distribution is used for discriminating between GM, WM, and CSF tissues (**Figure 2F**). Segmentation is performed using the "fast" function in FSL (Jenkinson et al., 2012).

Volume-Based fMRI Data Preprocessing

The volume-based preprocessing steps for fMRI data are presented in **Figure 1**.

Removal of the First N Volumes

The de-oblique and re-orientation steps are first performed on fMRI data as described in Section "Volume-Based T1-Weighted MRI Data Preprocessing." The next step is to remove the first few volumes. When a magnetic field is applied to the brain, hydrogen molecules are aligned in the direction of the magnetic field. It takes from 5 to 6 s for these molecules to approach to the steady state, and thus the volumes acquired during the first few seconds (typically 10 s) have to be removed (**Figure 3A**) (Bright and Murphy, 2015; Bijsterbosch et al., 2017). This process is performed using the "fslroi" function in FSL (Jenkinson et al., 2012).

Slice Timing Correction

Slice timing correction is performed to correct the time differences at which each slice was acquired. For example, as shown in **Figure 3B**, the time of the signal evoked at slice 8 is shifted toward that of slice 4 to match the starting time. The shifted signal is then interpolated. Because the slice timing correction approach uses interpolation, it causes a temporal smoothing effect, which might cause loss of information. Thus, this step is not recommended if the repetition time (TR) of the fMRI data is short (<1 s) (Bijsterbosch et al., 2017). Slice timing correction is performed using the "slicetimer" function in FSL (Jenkinson et al., 2012).

Motion Correction and Volume Scrubbing

Participants are instructed not to move their heads during an MRI scan. However, there are always unavoidable head movements, and thus the data becomes corrupted with motion-related artifacts. Thus, head motion correction should be performed on all fMRI data. Motion correction is performed by registering all volumes to a reference volume via a rigid-body transformation (**Figure 3C**). The reference volume can be any volume, but typically the first or middle volume of the whole data is selected. The next step is to remove volumes with severe head motion. This approach is referred to as volume scrubbing (Power et al., 2012). As the rigid-body transformation is used, three translation parameters (with their units in millimeters) and three rotation parameters (with their units in degrees) are calculated. These six motion parameters are used to calculate FD, which measures the degree of head motion (Power et al., 2012). Volumes whose FD exceed 0.5 mm are considered to have severe head motions and are thus removed. Volumes with severe head motion are detected using the "fsl_motion_outliers" function and motion correction is performed using the "mcflirt" function in FSL (Jenkinson et al., 2012).

Field Map Correction

After head motion correction, field inhomogeneity correction can be performed. This step requires the collection of a dedicated field map. However, many neuroimaging studies, especially older ones, did not collect field map data and thus we make this step optional. This was intentional so that our software could be applied to many existing neuroimaging studies. If a certain study has a field map-corrected EPI data (e.g., computed using FSL), the user can supply this data as an optional input to our software and the program will proceed with the rest of the pipeline using the field map-corrected data.

Intensity Normalization

Because MRI data does not have a specific unit, different MRI data might have different ranges of intensity values. Intensity normalization is performed to standardize the range of intensity values across all 4D volumes with a specific value (**Figure 3D**). In FuNP, a value of 10,000 is used. Intensity normalization is performed using the "fslmaths" function in FSL (Jenkinson et al., 2012).

Registration

Unlike T1-weighted structural MRI data, the resolution of fMRI data is lower and has lower inter-tissue contrast. Thus, it is difficult to directly register fMRI data to the standard space. In FuNP, two-stage registration is adopted (**Figure 3E**) (Jenkinson et al., 2012; Glasser et al., 2013). Low-resolution fMRI data is registered onto high-resolution preprocessed T1-weighted structural MRI data of the same subject via a rigid-body transformation. The T1-weighted structural MRI data is then registered onto the standard space via an affine transformation. The two transformation matrices are concatenated and then applied to the fMRI data to register them onto the standard space. Registration is performed using the "flirt" function in FSL (Jenkinson et al., 2012).

Nuisance Variable Removal

The fMRI data contains both signal and noise components. The noise components include head motion, WM, CSF, cardiac pulsations, and arterial and large vein-related contributions. The noise components can be removed via ICA-FIX (**Figure 3F**) (Salimi-Khorshidi et al., 2014). ICA is a method for decomposing fMRI signals into a set of spatially independent components (ICs) (Beckmann and Smith, 2004; Beckmann et al., 2005).

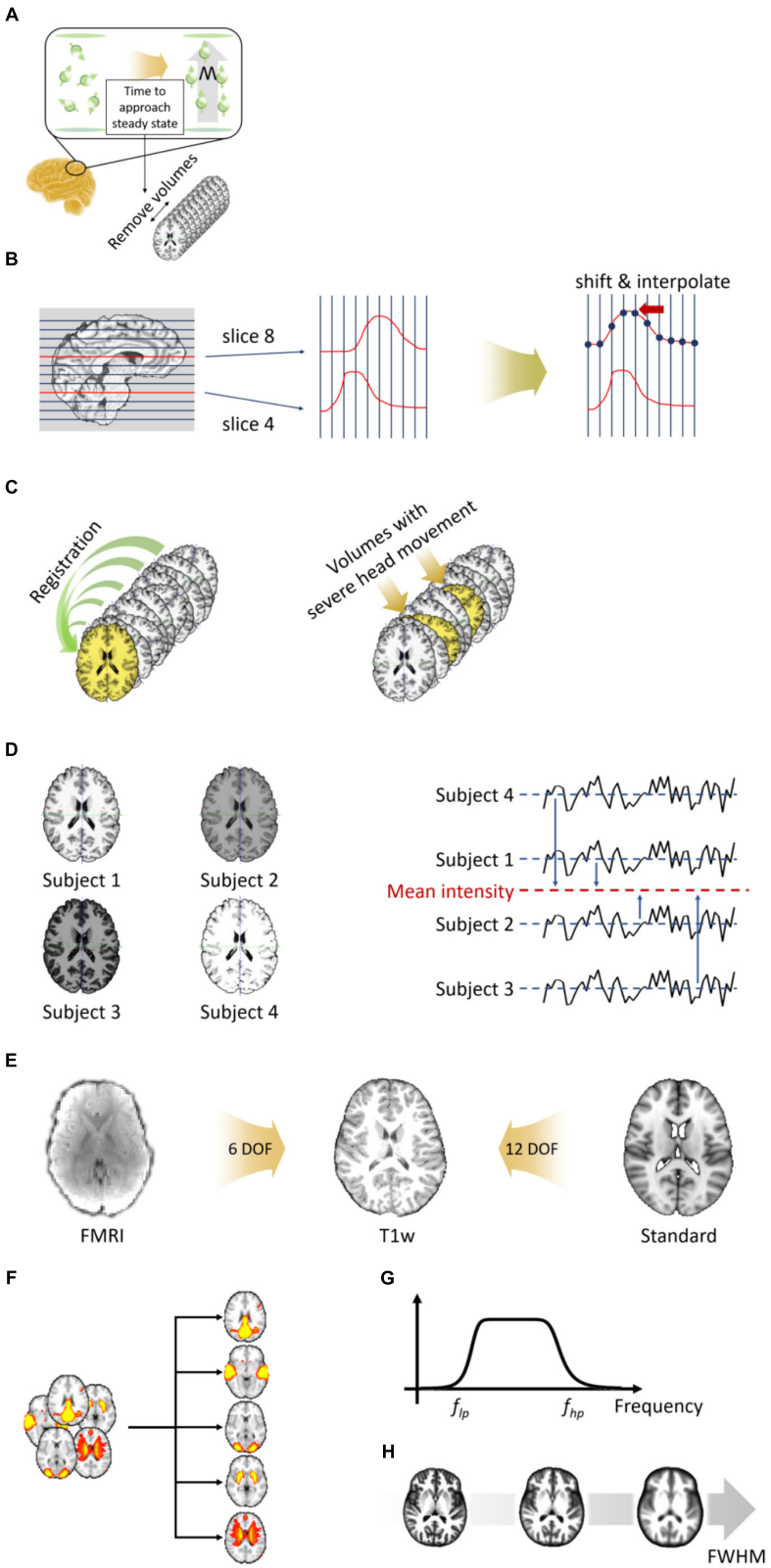


FIGURE 3 | Preprocessing steps for volume-based fMRI data. **(A)** Removal of the first few volumes. **(B)** Slice timing correction. **(C)** Head motion correction (left) and volume scrubbing (right). **(D)** Intensity normalization. **(E)** Two-stage registration. **(F)** Nuisance variable removal via ICA-FIX. **(G)** Temporal filtering. **(H)** Spatial smoothing.

The computed ICs are further classified into signal and noise components considering their temporal and spatial features (Salimi-Khorshidi et al., 2014). This classification procedure is performed using a hierarchical classification model described in a previous study and it successfully removed artifacts (Salimi-Khorshidi et al., 2014). There are automatic methods to classify ICs, but their performance can be unreliable at times (Kelly et al., 2010; Griffanti et al., 2017). Thus, a manual approach to classify ICs is recommended. The following three major aspects have to be considered to distinguish between signal and noise components. First, spatial maps of signal components largely overlap with GM, while those of noise components overlap with WM, CSF, and blood vessels (Kelly et al., 2010; Griffanti et al., 2017). Secondly, the time series of signal components are relatively stable without sudden spikes (Kelly et al., 2010; Griffanti et al., 2017). Components with sudden isolated spikes in their time series are often classified as head motion-related artifacts. Finally, the frequency spectrum of signal components usually occupies the low-frequency range (<0.1 Hz), while that of noise components occupies a variable band (Kelly et al., 2010; Griffanti et al., 2017). Once the noise components are defined, they are regressed out from the original fMRI data. Nuisance variable removal is performed using the "fix" function in FSL (Jenkinson et al., 2012). The FuNP uses the pre-trained datasets that were trained using different image acquisition settings provided by the FSL team[2]. Thus, the users do not need to manually train their data but choose from one of the several choices that best suits the input data.

Temporal Filtering

The signals of interest of fMRI data are known to exist in the low-frequency range (<0.1 Hz) (Biswal et al., 1995; Boubela et al., 2013). However, extremely low-frequency signals (<0.01 Hz) are considered as slow drifts (i.e., non-neuronal signals) (Biswal et al., 1995; Boubela et al., 2013). Thus, band-pass filtering with a frequency range between 0.009 and 0.08 Hz is widely used to capture the signals of interest (**Figure 3G**). The cut-off frequencies are slightly different across studies, but filtering ranges of 0.008–0.09 Hz and 0.01–0.1 Hz are typically considered (Biswal et al., 1995; Margulies et al., 2010; Yeo et al., 2011; Boubela et al., 2013). In FuNP, users can select either low-pass, high-pass, or band-pass filters with user-set cut-off frequencies. Temporal filtering is performed using the "3dFourier" function in AFNI (Cox, 1996).

Spatial Smoothing

Spatial smoothing is achieved by calculating the weighted average over neighboring voxels using a Gaussian kernel and yields blurred data (**Figure 3H**). The full width at half maximum (FWHM) of the kernel is usually set as two times the voxel size (Worsley and Friston, 1995; Mikl et al., 2008). Spatial smoothing offers the advantage of reducing noise, but it also can lower the intensity of the signal. Therefore, researchers need to proceed with caution when applying spatial smoothing. Spatial smoothing is performed using the "3dmerge" function in AFNI (Cox, 1996).

[2]https://fsl.fmrib.ox.ac.uk/fsl/fslwiki/FIX/UserGuide

Surface-Based T1-Weighted MRI Data Preprocessing

The surface-based preprocessing steps of MRI data contain both volume and surface processing steps. This is because the surface processing steps require output from the volume processing steps. The required volume processing steps are largely the same as those described in the previous sections. The surface-based preprocessing steps for T1-weighted structural data is presented in **Figure 4**. Initial surface-based preprocessing is performed using the "recon-all" function in FreeSurfer (Fischl, 2012). For volume processing, magnetic field inhomogeneity correction, non-brain tissue removal, intensity normalization, segmentation, and registration are performed. For surface processing, white and pial surfaces are generated. The white surface is located between WM and GM, while the pial surface is located between GM and CSF. These white and pial surfaces are generated by following the boundaries between different tissues. The surfaces are then inflated to spheres, and spherical registration between the T1-weighted structural data and the standard space is performed. The surfaces constructed using FreeSurfer are adjusted to obtain accurate surfaces using Workbench as follows (Marcus et al., 2013). The T1-weighted volume data preprocessed using FreeSurfer are registered onto the standard space via an affine transformation. Afterward, the transformation matrix is applied to the white and pial surfaces to register them onto the standard space. These surfaces are then averaged to generate a mid-thickness surface, which is in turn used to generate an inflated surface. The spherical surface is finally registered onto a 164k vertex mesh and then down-sampled to a 32k vertex mesh.

Surface-Based fMRI Data Preprocessing

The surface-based preprocessing steps for fMRI data also contain volume and surface processing steps. The volume preprocessing steps are the same as those described in Section "Volume-Based fMRI Data Preprocessing" except for spatial smoothing (**Figure 4**). Spatial smoothing is only performed to subcortical areas and not to cortical areas. The surface-based preprocessing

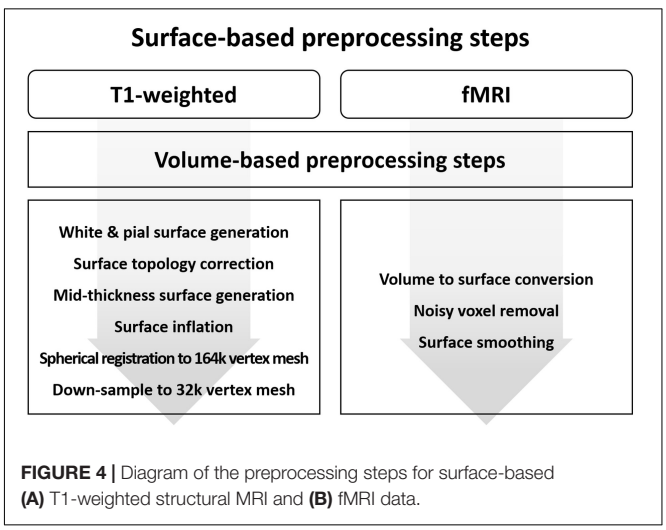


FIGURE 4 | Diagram of the preprocessing steps for surface-based **(A)** T1-weighted structural MRI and **(B)** fMRI data.

steps are performed using Workbench and FSL (Jenkinson et al., 2012; Marcus et al., 2013). The preprocessed fMRI cortical volume data are converted into surface data to define vertices within the GM ribbon using a cortical ribbon-constrained algorithm (Glasser et al., 2013). Voxels with high variation in their time series (>0.5 standard deviation [SD] of the mean variation of other voxels in a 5-mm neighborhood) are not converted into a surface because they usually contain large blood vessels (Glasser et al., 2013). Surface smoothing on the cortical areas is applied with a FWHM value of twice the voxel size (Worsley and Friston, 1995; Mikl et al., 2008).

Experiments

The reliability of the developed software was assessed by constructing RSNs using preprocessed resting-state fMRI (rs-fMRI) data obtained from the Human Connectome Project (HCP) database (Van Essen et al., 2013). We hypothesized that if the data were preprocessed properly, the obtained RSNs should be consistent with existing known RSNs. To compare the quality of the preprocessed data from FuNP and other software, we compared our results with those from volume-based preprocessing pipeline using FSL (Jenkinson et al., 2012) and fMRIPrep (Esteban et al., 2019). The IQMs proposed in the previous paper (Esteban et al., 2017) were calculated from the preprocessed data of three different software packages (i.e., FuNP, FSL, and fMRIPrep).

Participants and Imaging Data

The data used in this study came from two sources. The first dataset was obtained from the HCP database. We used all the data in the Q3 release version which had both T1-weighted and rs-fMRI data, which led to 90 healthy subjects (58% female) (Van Essen et al., 2013). The mean age was 28.74 with an SD of 3.42. The Institutional Review Board (IRB) of Sungkyunkwan University approved this retrospective study, and it was performed in full accordance with local IRB guidelines. All participants provided written informed consent. All imaging data were obtained using a Siemens Skyra 3T scanner at Washington University. The imaging parameters of the T1-weighted structural data were as follows: TR = 2,400 ms; echo time (TE) = 2.14 ms; field of view (FOV) = 224 mm × 224 mm; voxel size = 0.7 mm isotropic; and number of slices = 256. The imaging parameters for rs-fMRI were as follows: TR = 720 ms; TE = 33.1 ms; FOV = 208 mm × 180 mm; voxel size = 2 mm isotropic; number of slices = 72; and number of volumes = 1,200.

An additional 28 T1-weighted structural MRI and rs-fMRI data of healthy subjects (100% female) were recruited from Sungkyunkwan University to assess the reproducibility of our software. The mean age was 23 with an SD of 2.09. All subjects provided written informed consent according to the procedures approved by the IRB of Sungkyunkwan University. The imaging data were obtained using a Siemens Skyra 3T scanner at Sungkyunkwan University. The imaging parameters of the T1-weighted structural data were as follows: TR = 2,400 ms; TE = 2.34 ms; FOV = 224 mm × 224 mm; voxel size = 0.7 mm isotropic; and number of slices = 224. The imaging parameters for rs-fMRI were as follows: TR = 1,000 ms; TE = 39.8 ms; FOV = 224 mm × 224 mm; voxel size = 2 mm isotropic; number of slices = 72; and number of volumes = 360.

RSN Construction

RSNs were defined via an ICA approach (Minka, 2000; Himberg and Hyvärinen, 2003; Beckmann and Smith, 2004; Beckmann et al., 2005; Calhoun et al., 2009). Volume-based preprocessed rs-fMRI data were temporally concatenated across all subjects and fed into the "melodic" function in FSL (Beckmann and Smith, 2004; Beckmann et al., 2005; Jenkinson et al., 2012). The number of dimensions was automatically determined via principal component analysis (PCA) (Minka, 2000; Beckmann and Smith, 2004; Beckmann et al., 2005). The generated volume-based ICs (VICs) were classified as signal and noise components via visual inspection (Kelly et al., 2010; Griffanti et al., 2017). The signal VICs were compared with known RSNs via cross-correlation to see whether the generated VICs were similar to the pre-defined RSNs (Smith et al., 2009).

Surface-based preprocessed rs-fMRI data were handled using the ICASSO approach on the temporally concatenated voxel-wise time series across all subjects[3] (Himberg and Hyvärinen, 2003). This was done because FSL cannot perform ICA on surface-based preprocessed rs-fMRI data. The generated surface-based ICs (SICs) were visually compared with the known RSNs because there are no openly available RSN data in surface format.

Comparison With Other Software

We compared the results of FuNP with those from volume-based preprocessing pipeline using FSL (Jenkinson et al., 2012) and fMRIPrep (Esteban et al., 2019). The comparison was limited to volume-based approaches as FSL did not provide surface-based results. The preprocessing steps of FSL were as follows: the first 10 s volumes were removed and head motion was corrected. The non-brain tissue was removed using the temporally averaged fMRI data. The noise reduction process was performed using a non-linear filtering. The intensity normalization, high-pass filtering, and spatial smoothing were applied. The fMRI data were registered onto the T1-weighted structural data and then consequently onto the MNI standard space. The preprocessing steps of fMRIPrep were as follows: a reference volume and its skull removed data were generated. Head motion and susceptibility distortions were corrected. The distortion corrected data were registered onto the T1-weighted structural data and then consequently onto the MNI standard space. The nuisance variables including head motion, physiological regressors, and global signals of WM, CSF, and the whole brain were removed. The ICA-based Automatic Removal Of Motion Artifacts (ICA-AROMA) was performed to remove the head motion-related artifacts (Pruim et al., 2015b). High-pass filtering was applied and then volumetric resampling configured with Lanczos interpolation was applied to minimize the smoothing effect. The quality of the preprocessed data was assessed using the IQMs proposed in the previous paper (Esteban et al., 2017). The IQMs that assess the temporal information were (1) SD of DVARS (D means temporal derivative of time

[3]https://research.ics.aalto.fi/ica/icasso/

series, VARS means root mean square variance over voxels) that measures the rate of BOLD signal changes and (2) temporal signal-to-noise ratio (tSNR). The IQMs that assess the artifacts were (1) mean FD that measures the amount of displacement of the head motion, (2) percentage of the volumes with large head motion over the whole volumes, (3) ghost-to-signal ratio (GSR) in x- and (4) y-directions, (5) AFNI's outlier ratio (AOR) that calculates number of outliers across the time series, and (6) AFNI's quality index (AQI) that represents mean quality index by measuring whether the intensity values of each volume are not very different from norm of the whole volumes. We also compared the computational performances among the three software packages. The computational performances were measured using running time and peak memory usage over a subset of HCP data ($n = 10$). The software packages were allowed access to a single-thread CPU resource. The size of the input data (format of .nii.gz) was 1.67 GB on average. Our computation node was equipped with Intel Xeon CPU E5-2637 v3 and 256 GB of memory.

RESULTS

Developed Software

We developed a novel data preprocessing software, called FuNP (**Figure 5**), for T1-weighted structural MRI and fMRI data. FuNP consists of volume- and surface-based preprocessing approaches. The volume-based approach requires AFNI and FSL (Cox, 1996; Jenkinson et al., 2012), and the surface-based approach requires AFNI, FSL, FreeSurfer, and Workbench (Cox, 1996; Fischl, 2012; Jenkinson et al., 2012; Marcus et al., 2013). Each approach performs the preprocessing of T1-weighted structural MRI and fMRI data separately. Our software, FuNP, is available at in GitLab[4].

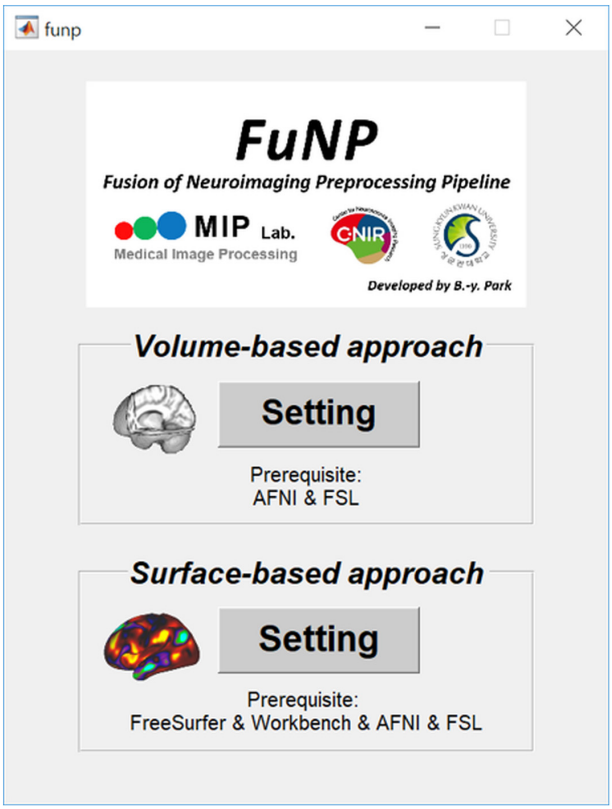


FIGURE 5 | Screenshot of the developed software, called FuNP.

Reliability of the Software

To assess the reliability of the output of FuNP, we constructed volume- and surface-based RSNs using the HCP rs-fMRI data preprocessed by FuNP. A total of 29 VICs were automatically generated and classified as 24 signals and 5 noise components (**Figure 6**). VICs 1–5 were the visual network (VN), consisting of the superior-, middle-, and inferior-occipital gyri, cuneus, and the lingual gyrus. VICs 6 and 7 were the default mode network (DMN), consisting of the superior- and middle-frontal gyri, the medial orbitofrontal gyrus, and the posterior cingulate cortex. VICs 8–10 were the executive control network (ECN), consisting of the middle- and medial-orbitofrontal gyri and anterior cingulate cortex. VICs 11–17 were the frontoparietal network (FPN), consisting of the middle- and inferior-orbitofrontal gyri and the superior- and inferior-parietal lobule. VICs 18–21 were the sensorimotor network (SMN), consisting of the paracentral lobule and the postcentral gyrus. VICs 22 and 23 were the auditory network (AN), consisting of Heschl's gyrus, the superior temporal gyrus, and the supramarginal gyrus. VIC 24 was the cerebellum. These 24 functionally interpretable VICs were compared with pre-defined RSNs by computing cross-correlation (Smith et al., 2009). The mean cross-correlation value was 0.38, with an SD of 0.17. The results obtained with FuNP showed high similarities between the generated VICs and the pre-defined RSNs, indicating that the data were properly preprocessed.

In addition to the VICs, 20 SICs were generated and classified as 16 signal and 4 noise components (**Figure 7**). SICs 1 and 2 were the VN, consisting of the primary visual cortex (V1), the early visual cortices (V2 and V3), and the extrastriate visual cortices [V3A, V6, V6A, middle temporal (MT), and middle superior temporal (MST)]. SICs 3 and 4 were the DMN, consisting of the dorsolateral prefrontal cortex, the medial- and inferior-frontal cortices, the anterior- and posterior-cingulate cortices, and the insula. SICs 5–7 were the ECN, consisting of the dorsolateral prefrontal cortex, the medial orbitofrontal cortex, the inferior frontal cortex, and the anterior cingulate cortex. SICs 8–14 were the FPN, consisting of the dorsolateral prefrontal cortex, the medial- and inferior-frontal cortices, the superior- and inferior-parietal lobules, and the paracentral lobule. SICs 15 and 16 were the SMN, consisting of the somatosensory and motor cortices, the premotor cortex, and the paracentral lobule. Regions of the AN were partly included in the SICs of the FPN (SICs 10, 11, 12, and 14). The SICs showed similar patterns to those of known RSNs, suggesting that the preprocessing pipeline was reliable.

[4]https://gitlab.com/by9433/funp

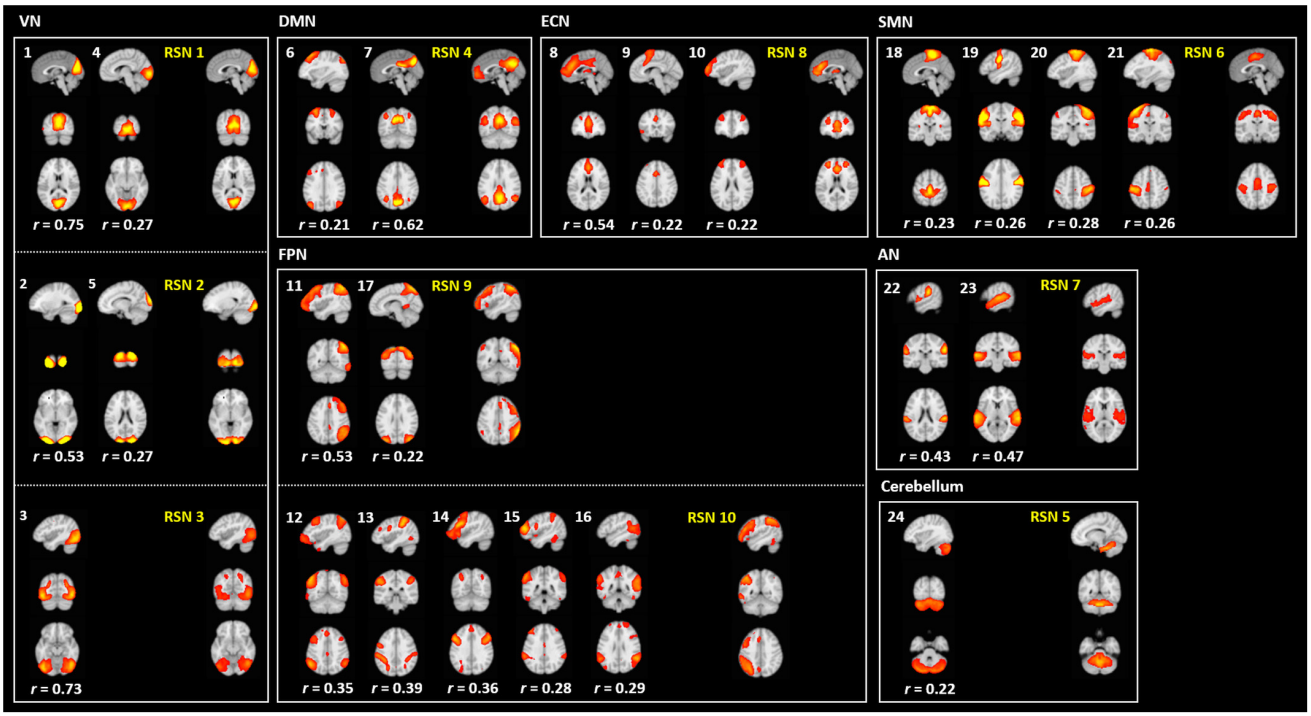


FIGURE 6 | Generated VICs using the HCP data (labeled in a white font) along with pre-defined RSNs (labeled in a yellow font) (Smith et al., 2009). The cross-correlation values of the spatial maps between the generated VICs and RSNs are presented.

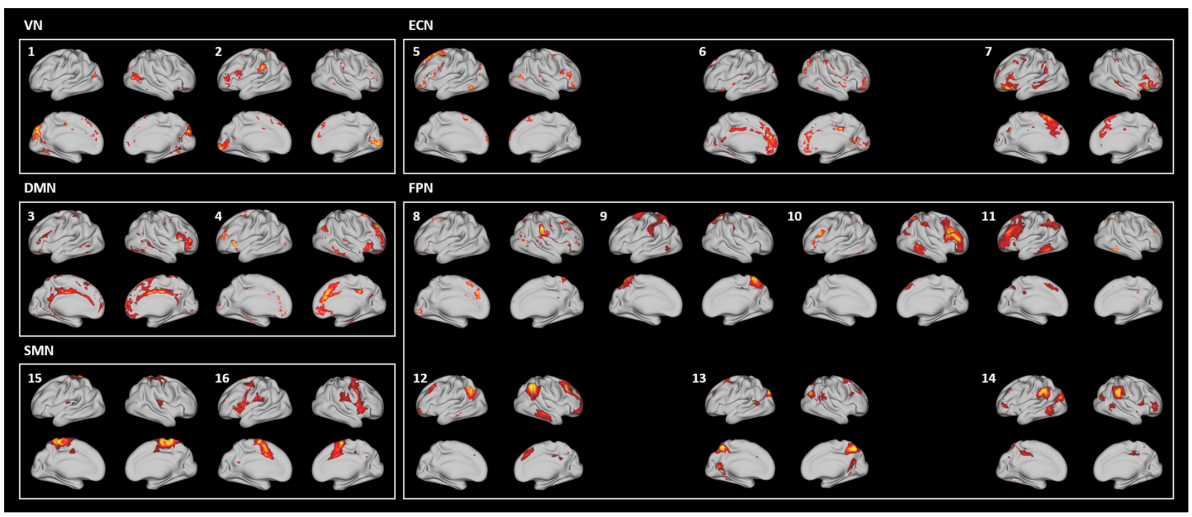


FIGURE 7 | Generated SICs using the HCP data matched with known RSNs.

Comparison With Other Software

The quality of the volume-based preprocessed rs-fMRI data from FuNP, FSL, and fMRIPrep was assessed using the IQMs (Esteban et al., 2017). We found that FuNP yielded lower SD of DVARS compared to other software. The mean FD and percentage of volumes with large head motion of FuNP were comparable to fMRIPrep and lower than FSL. The results suggest the head motion-related artifacts were better removed using FuNP (**Figure 8**). The tSNR and GSR showed higher values in FuNP compared to other software indicating the processed data using FuNP were robust to noise (**Figure 8**). In addition, AOR and AQI showed smaller values for FuNP suggesting there was a smaller number of outliers compared to other software (**Figure 8**). Taken together, our FuNP outperformed other software in terms of temporal characteristics and artifacts removal.

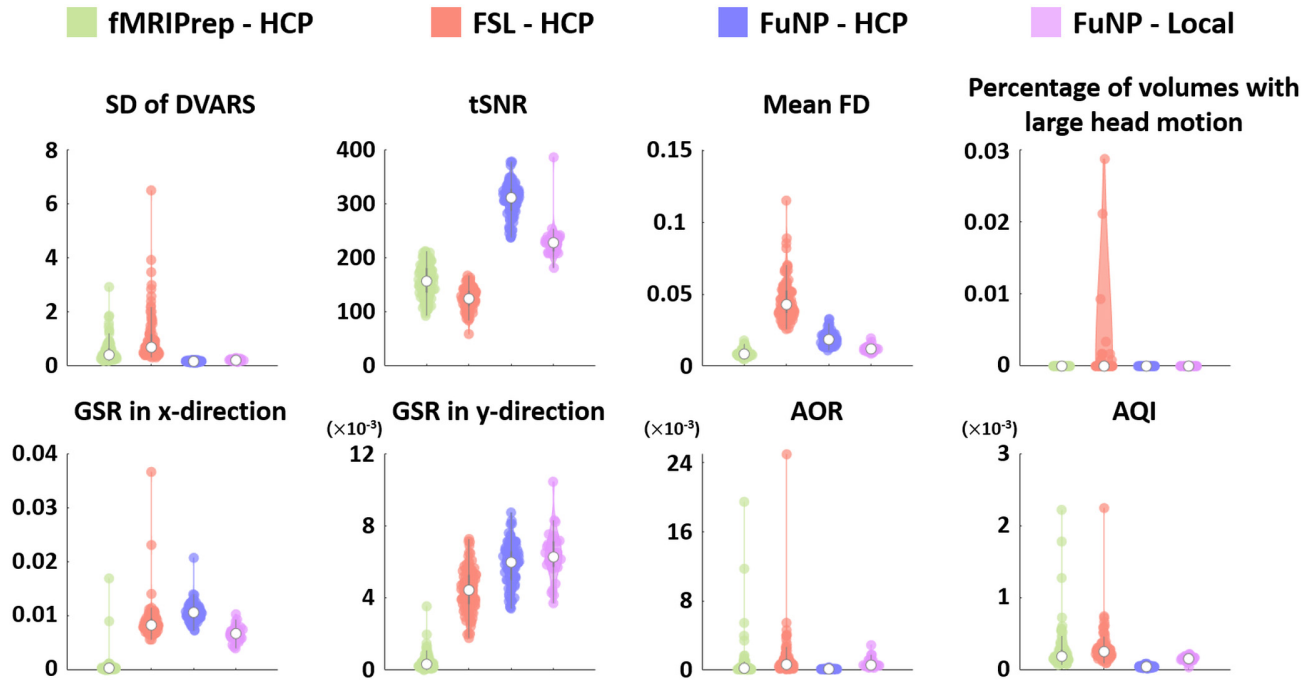


FIGURE 8 | The IQMs of the volume-based preprocessed rs-fMRI data using different software packages. The values were plotted using violin plots. The white circle denotes the median value. The AOR and AQI were very small but the results of some software packages had high variability.

Comparison of Computational Resources

We measured the computational performances among the three software packages using running time and peak memory usage. On average, the running time was approximately 3 h for FuNP, 11 h for fMRIPrep, and 11 h and 30 min for FSL (**Table 1**). Possible reasons behind the longer computation time for fMRIPrep could be different head motion correction and registration methods compared to ours. The FuNP took 6 min, while fMRIPrep took 86 min on average for the motion correction (**Table 1**). The FuNP was faster (12 min) than fMRIprep (4 h and 52 min) for the registration procedure on average (**Table 1**). During the 4D data registration, fMRIPrep splits the 4D data into 3D volumes and performs registration onto the reference space. The results of the registration were stored on a disk for all 3D volumes and later concatenated to form the 4D registered data. The operations involve many disk input/output operations and thus could be slow. Our FuNP performs the entire procedure all within the memory and thus does involve fewer disk input/output operations than fMRIPrep. This could lead to faster computation for FuNP. For both fMRIPrep and FSL, the longer computation time might be due to the use of different noise removal strategies. The FuNP was faster (1 h and 29 min) than the two approaches (fMRIPrep; 9 h and 25 min, FSL; 11 h) (**Table 1**). The fMRIPrep performs nuisance variable removal by calculating various kinds of confounds of mean global signal, mean tissue class signal, PCA-based noise areas defined by anatomy or temporal variance, FD, DVARS, six head motion parameters, respectively (Esteban et al., 2019). In addition, ICA-AROMA for head motion-related artifact removal is performed if the option is set. In contrast, FuNP only uses ICA-FIX that showed good performance of noise removal (Salimi-Khorshidi et al., 2014). In addition, the use of complex non-linear noise filtering algorithm, smallest univalue segment assimilating nucleus (SUSAN), across the whole time series might affect the computation time (Smith and Brady, 1997). In contrast, FuNP only does temporal filtering using a conventional Fourier transform and spatial smoothing for noise removal. Although simple approaches were adopted in FuNP, it exhibited lower outlier ratio compared to other software packages (**Figure 8**). In terms of peak memory usage, FuNP used 12.5 GB on average, fMRIPrep used 33.1 GB, and FSL used 9.5 GB. Note that the peak memory usage was dependent on the size of the input data. In summary, the running time for the whole preprocessing was fastest when the FuNP was adopted compared to fMRIPrep and FSL.

Reproducibility of the Software

To assess the reproducibility of our software, FuNP, we performed additional data preprocessing using local data (n = 28). The quality of the results was assessed using IQMs. **Figure 8** shows that the IQMs of the preprocessed local and HCP data using FuNP were similar. In addition to the IQMs, we performed volume- and surface-based ICA and found results (from local data) that were similar to the main results (HCP data) (**Figures 6**, **7** and **Supplementary Figures S1, S2**). Taken together, we believe our pipeline

TABLE 1 | Computation time of each preprocessing step for three software packages.

	fMRIPrep	FSL	FuNP
First N volumes removal	N/A	7.4 m(0.5 m)	7.4 m(0.5 m)
Slice timing correction	N/A	N/A	N/A
Volume scrubbing	N/A	N/A	26.8 m(0.4 m)
Motion correction	1 h 26.6 m(6.3 m)	2.2 m(0.4 m)	6.2 m(0.8 m)
Non-brain tissue removal	6.4 m(5.0 m)	4.2 m(0.4 m)	4.6 m(0.5 m)
Intensity normalization	N/A	1.2 m(0.4 m)	1.2 m(0.4 m)
Registration	4 h 52.0 m(1 h 3.2 m)	1.1 m(0.3 m)	12.0 m(2.0 m)
Nuisance variable removal	9 h 25.0 m(1 h 45.2 m)	11 h 0.2 m(1 h 8.8 m)	1 h 29.2 m(10.5 m)
Temporal filtering	1.1 m(0.3 m)	3.2 m(0.4 m)	3.2 m(0.4 m)
Spatial smoothing	N/A	1.8 m(0.4 m)	1.8 m(0.4 m)
Total	11 h 6.6 m(12.9 m)	11 h 35.0 m(52.6 m)	2 h 55.0 m(11.2 m)

Means and SDs are reported. SD values are reported in parentheses.
h, hour; m, minute; N/A, not available.

could yield reproducible results based on the analyses of two independent data sets.

DISCUSSION

In this study, we developed a preprocessing pipeline for T1-weighted structural MRI and fMRI data by combining components of well-known software packages, namely AFNI, FSL, FreeSurfer, and Workbench, to fully incorporate recent developments in MRI preprocessing into a single software package (Cox, 1996; Fischl, 2012; Jenkinson et al., 2012; Marcus et al., 2013). The developed software, FuNP, is not the first wrapper software that incorporates recent developments in MRI preprocessing. The fMRIPrep is a notable software package that incorporates many of the state-of-the-art MRI preprocessing steps from existing software tools of AFNI, FSL, FreeSurfer, and ANTs (Esteban et al., 2019). They reported that the pipeline is robust to the acquisition parameters of the input data, easy to use as it requires a minimum number of user specified parameters for each step, and provides a summary in results of segmentation, registration, global signals, and motion-related artifacts (Esteban et al., 2019). Our software, FuNP, has the following advantages. First, FuNP contains both volume- and surface-based preprocessing pipelines. Using the surface-based pipeline, researchers can handle cortical and sub-cortical data better and more consistently with recent developments (Glasser et al., 2013, 2016a,b). Secondly, FuNP provides a fully automated preprocessing framework. Thirdly, FuNP is user-friendly owing to its graphical interface, which is intuitive and easy to manipulate. Fourthly, we designed our software so that the pipeline could be applied to fMRI data without field map data. This might be important because, in old neuroimaging studies, researchers often did not collect field map data. In such cases, modern researchers cannot use up-to-date preprocessing pipelines that require field map data. The reliability of FuNP was assessed by constructing RSNs using rs-fMRI data from the HCP database (Van Essen et al., 2013). Both the volume- and surface-based brain networks were well-defined and were consistent with pre-defined brain networks (**Figures 6**, **7**). In addition to RSNs, the IQMs of temporal characteristics and artifacts were calculated to assess the quality of the preprocessed data. We found that FuNP outperformed FSL and fMRIPrep in terms of the IQMs (**Figure 8**). These results indicate that the developed preprocessing pipelines for T1-weighted structural MRI and fMRI data are of high-quality and reliable. Our software can be used as robust and easy-to-use neuroimaging data preprocessing framework.

There are several options to choose from to perform a given preprocessing step. Following statements are the justifications of the choices we made for each preprocessing step. Some choices (e.g., skull stripping) could be considered as optimal (Iglesias et al., 2011; Puccio et al., 2016), still, some could be suboptimal due to on-going controversies (e.g., nuisance removal) (Ciric et al., 2017). To remove the non-brain tissues, we selected "3dSkullStrip" function in AFNI rather than "bet" function in FSL, "antsBrainExtraction" function in ANTs, and "HWA" function in FreeSurfer. Previous studies reported that the function in AFNI outperformed equivalent functions in FSL and FreeSurfer for non-brain tissue removal (Iglesias et al., 2011; Puccio et al., 2016). A previous study reported ANTs showed better skull stripping results than other conventional approaches by visual inspection suggesting that our choice might be suboptimal (Esteban et al., 2019). For the step of magnetic field inhomogeneity correction, we chose "3dUnifize" function in AFNI out of coincidence. There are alternatives of "N4BiasFieldCorrection" function in ANTs and "fast" function in FSL. When performing registration, we chose "flirt" function in FSL. One study reported that neuroimaging registration could be better performed using "antsRegistration" function in ANTs compared to FSL and SPM (Dadar et al., 2018). Thus, we built two versions of FuNP. The new version adopted "antsRegistration" function and is referred to as FuNP v.2.0. We decided to keep the old version, referred to as FuNP v.1.0, because "flirt" requires fewer computation resources (i.e., runs fasters) compared to ANTs. For fMRI data registration,

the FuNP used the two-stage registration that aligns the fMRI data to the T1-weighted structural data and then subsequently onto the MNI standard space. However, a previous study demonstrated that registration of fMRI data using echo planar imaging template improved the statistical power and reduced variability across subjects compared to the two-stage registration approach (Calhoun et al., 2017). Thus, our strategy for fMRI data registration might be suboptimal. In the tissue segmentation step, "fast" function in FSL was adopted that showed good performance compared to other algorithms (Eggert et al., 2012; Kazemi and Noorizadeh, 2014; Valverde et al., 2015). For slice timing correction, we chose "slicetimer" function in FSL and there are alternatives of "3dTshift" function in AFNI and "spm_slice_timing" function in SPM. For head motion correction, "mcflirt" function in FSL was adopted. It was shown that there was no single package that outperformed others for head motion correction (Oakes et al., 2005). There are many approaches to remove the nuisance variables in fMRI data such as head motion, cardiac, respiratory, WM, and CSF, but there is no single approach that can eliminate the artifacts completely (Ciric et al., 2017). A previous study reported that there were trade-offs among different strategies for nuisance variables removal and thus users need to select appropriate strategies in the context of their scientific goals (Ciric et al., 2017). In FuNP, "fix" function in FSL, the state-of-the-art approach, was adopted to remove nuisance variables of head motion, WM, CSF, cardiac pulsations, and arterial and large vein-related contributions (Salimi-Khorshidi et al., 2014). This approach requires the pre-trained datasets to classify between the signal and noise components (Parkes et al., 2018). The FuNP uses the pre-trained datasets that were trained using different image acquisition settings provided by the FSL team[2]. The users of FuNP need to choose which pre-trained data best suits their data being processed. Thus, the users do not need to manually train their data but choose from one of the several choices. However, if the input data were scanned with a very different image acquisition setting compared to existing choices, then "fix" function of FSL might not work well.

We compared the computational performances among three different software packages. We found that FuNP outperformed other software packages in terms of running time. This computational efficiency might be practical beneficial for preprocessing large-scale data which are likely to become more pervasive. A previous study reported that the total processing speed for registration accelerated two to three times when graphics processing unit (GPU) was adopted (Luo et al., 2015). The processing speed of recon-all, which was used for surface-based T1-weighted MRI data preprocessing in FuNP, could be improved 10 to 150 times with the help of GPU based computations according to the FreeSurfer official website[6]. We plan to update FuNP with GPU capabilities in the future.

[6] https://surfer.nmr.mgh.harvard.edu/fswiki/CUDADevelopersGuide

CONCLUSION

In this study, we incorporated existing software packages of AFNI, FSL, FreeSurfer, and Workbench to build a preprocessing pipeline for T1-weighted structural MRI and fMRI data. The developed software, FuNP, provides a fully automated and user-friendly GUI volume- and surface-based preprocessing pipelines. The FuNP showed good performance in terms of temporal characteristics and artifacts removal. We believe our pipeline might help researchers who need MRI data preprocessing.

DATA AVAILABILITY STATEMENT

The HCP dataset analyzed for this study can be found in the Human Connectome Project (http://www.humanconnectome.org/) upon request (Van Essen et al., 2013). The local dataset analyzed for this study are not publicly available.

AUTHOR CONTRIBUTIONS

B-yP and HP wrote the manuscript. KB aided the experiments. HP was the guarantor of this work, and as such, had full access to all the data in the study and takes responsibility for the integrity of the data and the accuracy of the data analysis.

FUNDING

This work was supported by the Institute for Basic Science (Grant No. IBS-R015-D1), the NRF (National Research Foundation of Korea (Grant Nos. NRF-2016H1A2A1907833 and NRF-2016R1A2B4008545), and the Ministry of Science and ICT of Korea under the ITRC program (Grant No. IITP-2018-2018-0-01798).

ACKNOWLEDGMENTS

Data were provided by the Human Connectome Project, WU-Minn Consortium (principal investigators: David Van Essen and Kamil Ugurbil, 1U54MH091657), funded by the 16 NIH Institutes and Centers that support the NIH Blueprint for Neuroscience Research and by the McDonnel Center for Systems Neuroscience at Washington University.

SUPPLEMENTARY MATERIAL

The Supplementary Material for this article can be found online at: https://www.frontiersin.org/articles/10.3389/fninf.2019.00005/full#supplementary-material

REFERENCES

Beckmann, C. F., DeLuca, M., Devlin, J. T., and Smith, S. M. (2005). Investigations into resting-state connectivity using independent component analysis. *Philos. Trans. R. Soc. B* 360, 1001–1013. doi: 10.1098/rstb.2005.1634

Beckmann, C. F., and Smith, S. M. (2004). Probabilistic independent component analysis for functional magnetic resonance imaging. *IEEE Trans. Med. Imaging* 23, 137–152. doi: 10.1109/TMI.2003.822821

Bijsterbosch, J., Smith, S. M., and Beckmann, C. F. (2017). *Introduction to Resting State fMRI Functional Connectivity*. Oxford: Oxford University Press.

Biswal, B., Yetkin, F. Z., Haughton, V. M., and Hyde, J. S. (1995). Functional connectivity in the motor cortex of resting human brain using echo-planar MRI. *Magn. Reson. Med.* 34, 537–541. doi: 10.1002/mrm.1910340409

Boubela, R. N., Kalcher, K., Huf, W., Kronnerwetter, C., Filzmoser, P., and Moser, E. (2013). Beyond noise: using temporal ICA to extract meaningful information from high-frequency fMRI signal fluctuations during rest. *Front. Hum. Neurosci.* 7:168. doi: 10.3389/fnhum.2013.00168

Bright, M. G., and Murphy, K. (2015). Is fMRI "noise" really noise? Resting state nuisance regressors remove variance with network structure. *Neuroimage* 114, 158–169. doi: 10.1016/j.neuroimage.2015.03.070

Caballero-Gaudes, C., and Reynolds, R. C. (2017). Methods for cleaning the BOLD fMRI signal. *Neuroimage* 154, 128–149. doi: 10.1016/j.neuroimage.2016.12.018

Calhoun, V., Liu, J., and Adalı, T. (2009). A review of group ICA for fMRI data and ICA for joint inference of imaging, genetic, and ERP data. *Neuroimage* 45, S163–S172. doi: 10.1016/j.neuroimage.2008.10.057.A

Calhoun, V. D., Wager, T. D., Krishnan, A., Rosch, K. S., Seymour, K. E., Nebel, M. B., et al. (2017). The impact of T1 versus EPI spatial normalization templates for fMRI data analyses. *Hum. Brain Mapp.* 38, 5331–5342. doi: 10.1002/hbm.23737

Cheng, Y.-H., Lin, Y.-C., and Chang, Y. (2017). "Magnetic field measurement in brain tissue," in *Proceedings of the 2017 10th Biomedical Engineering International Conference (BMEiCON)*, Hokkaido, 1–5. doi: 10.1109/BMEiCON.2017.8229103

Ciric, R., Wolf, D. H., Power, J. D., Roalf, D. R., Baum, G. L., Ruparel, K., et al. (2017). NeuroImage Benchmarking of participant-level confound regression strategies for the control of motion artifact in studies of functional connectivity. *Neuroimage* 154, 174–187. doi: 10.1016/j.neuroimage.2017.03.020

Cox, R. W. (1996). AFNI: software for analysis and visualization of functional magnetic resonance neuroimages. *Comput. Biomed. Res.* 29, 162–173. doi: 10.1006/cbmr.1996.0014

Dadar, M., Fonov, V. S., and Collins, D. L. (2018). A comparison of publicly available linear MRI stereotaxic registration techniques. *Neuroimage* 174, 191–200. doi: 10.1016/j.neuroimage.2018.03.025

Damaraju, E., Allen, E. A., Belger, A., Ford, J. M., McEwen, S., Mathalon, D. H., et al. (2014). Dynamic functional connectivity analysis reveals transient states of dysconnectivity in schizophrenia. *Neuroimage Clin.* 5, 298–308. doi: 10.1016/j.nicl.2014.07.003

Eggert, L. D., Sommer, J., Jansen, A., Kircher, T., and Konrad, C. (2012). Accuracy and reliability of automated gray matter segmentation pathways on real and simulated structural magnetic resonance images of the human brain. *PLoS One* 7:45081. doi: 10.1371/journal.pone.0045081

Esteban, O., Birman, D., Schaer, M., Koyejo, O. O., Poldrack, R. A., and Gorgolewski, K. J. (2017). MRIQC: advancing the automatic prediction of image quality in MRI from unseen sites. *PLoS One* 12:e0184661. doi: 10.1371/journal.pone.0184661

Esteban, O., Markiewicz, C. J., Blair, R. W., Moodie, C. A., Isik, A. I., Erramuzpe, A., et al. (2019). fMRIPrep: a robust preprocessing pipeline for functional MRI. *Nat. Methods* 16, 111–116. doi: 10.1038/s41592-018-0235-4

Fischl, B. (2012). FreeSurfer. *Neuroimage* 62, 774–781. doi: 10.1016/j.neuroimage.2012.01.021

Glasser, M. F., Coalson, T. S., Robinson, E. C., Hacker, C. D., Harwell, J., Yacoub, E., et al. (2016a). A multi-modal parcellation of human cerebral cortex. *Nature* 536, 171–178. doi: 10.1038/nature18933

Glasser, M. F., Smith, S. M., Marcus, D. S., Andersson, J. L. R., Auerbach, E. J., Behrens, T. E. J., et al. (2016b). The human connectome project's neuroimaging approach. *Nat. Neurosci.* 19, 1175–1187. doi: 10.1038/nn.4361

Glasser, M. F., Sotiropoulos, S. N., Wilson, J. A., Coalson, T. S., Fischl, B., Andersson, J. L., et al. (2013). The minimal preprocessing pipelines for the human connectome project. *Neuroimage* 80, 105–124. doi: 10.1016/j.neuroimage.2013.04.127

Griffanti, L., Douaud, G., Bijsterbosch, J., Evangelisti, S., Alfaro-Almagro, F., Glasser, M. F., et al. (2017). Hand classification of fMRI ICA noise components. *Neuroimage* 154, 188–205. doi: 10.1016/j.neuroimage.2016.12.036

Himberg, J., and Hyvärinen, A. (2003). "ICASSO: Software for investigating the reliability of ICA estimates by clustering and visualization," in *Proceedings of the IEEE Workshop Neural Networks for Signal Processing*, (Ermioni: IEEE), 259–268. doi: 10.1109/NNSP.2003.1318025

Iglesias, J. E., Liu, C. Y., Thompson, P. M., and Tu, Z. (2011). Robust brain extraction across datasets and comparison with publicly available methods. *IEEE Trans. Med. Imaging* 30, 1617–1634. doi: 10.1109/TMI.2011.2138152

Jenkinson, M., Beckmann, C. F., Behrens, T. E. J., Woolrich, M. W., and Smith, S. M. (2012). Fsl. *Neuroimage* 62, 782–790. doi: 10.1016/j.neuroimage.2011.09.015

Kazemi, K., and Noorizadeh, N. (2014). Quantitative Comparison of SPM, FSL, and brainsuite for brain MR image segmentation. *J. Biomed. Phys. Eng.* 4, 13–26.

Kelly, R. E. J., Alexopoulos, G. S., Wang, Z., Gunning, F. M., Murphy, C. F., Morimoto, S. S., et al. (2010). Visual inspection of independent components: defining a procedure. *J. Neurosci. Methods* 189, 233–245. doi: 10.1016/j.jneumeth.2010.03.028.Visual

Luo, Y. G., Liu, P., Shi, L., Luo, Y., Yi, L., Li, A., et al. (2015). Accelerating neuroimage registration through parallel computation of similarity metric. *PLoS One* 10:e0136718. doi: 10.1371/journal.pone.0136718

Marcus, D. S., Harms, M. P., Snyder, A. Z., Jenkinson, M., Wilson, J. A., Glasser, M. F., et al. (2013). Human Connectome Project informatics: quality control, database services, and data visualization. *Neuroimage* 80, 202–219. doi: 10.1016/j.neuroimage.2013.05.077

Margulies, D. S., Böttger, J., Long, X., Lv, Y., Kelly, C., Schäfer, A., et al. (2010). Resting developments: a review of fMRI post-processing methodologies for spontaneous brain activity. *Magn. Reson. Mater. Phys. Biol. Med.* 23, 289–307. doi: 10.1007/s10334-010-0228-5

Mikl, M., Mareèek, R., Hluštík, P., Pavlicová, M., Drastich, A., Chlebus, P., et al. (2008). Effects of spatial smoothing on fMRI group inferences. *Magn. Reson. Imaging* 26, 490–503. doi: 10.1016/j.mri.2007.08.006

Minka, T. P. (2000). *Automatic Choice of Dimensionality for PCA*. Cambridge, MA: MIT Media Lab.

Murphy, K., Birn, R. M., and Bandettini, P. A. (2013). Resting-state fMRI confounds and cleanup. *Neuroimage* 80, 349–359. doi: 10.1016/j.neuroimage.2013.04.001

Oakes, T. R., Johnstone, T., Ores Walsh, K. S., Greischar, L. L., Alexander, A. L., Fox, A. S., et al. (2005). Comparison of fMRI motion correction software tools. *Neuroimage* 28, 529–543. doi: 10.1016/j.neuroimage.2005.05.058

Parkes, L., Fulcher, B., Yücel, M., and Fornito, A. (2018). An evaluation of the efficacy, reliability, and sensitivity of motion correction strategies for resting-state functional MRI. *Neuroimage* 171, 415–436. doi: 10.1016/j.neuroimage.2017.12.073

Power, J. D., Barnes, K. A., Snyder, A. Z., Schlaggar, B. L., and Petersen, S. E. (2012). Spurious but systematic correlations in functional connectivity MRI networks arise from subject motion. *Neuroimage* 59, 2142–2154. doi: 10.1016/j.neuroimage.2011.10.018

Pruim, R. H. R., Mennes, M., Buitelaar, J. K., and Beckmann, C. F. (2015a). Evaluation of ICA-AROMA and alternative strategies for motion artifact removal in resting state fMRI. *Neuroimage* 112, 278–287. doi: 10.1016/j.neuroimage.2015.02.063

Pruim, R. H. R., Mennes, M., van Rooij, D., Llera, A., Buitelaar, J. K., and Beckmann, C. F. (2015b). ICA-AROMA: a robust ICA-based strategy for removing motion artifacts from fMRI data. *Neuroimage* 112, 267–277. doi: 10.1016/j.neuroimage.2015.02.064

Puccio, B., Pooley, J. P., Pellman, J. S., Taverna, E. C., and Craddock, R. C. (2016). The preprocessed connectomes project repository of manually corrected skull-stripped t1-weighted anatomical MRI data. *Gigascience* 5:45. doi: 10.1186/s13742-016-0150-5

Salimi-Khorshidi, G., Douaud, G., Beckmann, C. F., Glasser, M. F., Griffanti, L., and Smith, S. M. (2014). Automatic denoising of functional MRI data: combining independent component analysis and hierarchical fusion of classifiers. *Neuroimage* 90, 449–468. doi: 10.1016/j.neuroimage.2013.11.046

Smith, S. M., and Brady, J. M. (1997). SUSAN – A new approach to low level image processing. *Int. J. Comput. Vis.* 23, 45–78. doi: 10.1023/A:1007963824710

Smith, S. M., Fox, P. T., Miller, K. L., Glahn, D. C., Fox, P. M., Mackay, C. E., et al. (2009). Correspondence of the brain's functional architecture during activation and rest. *Proc. Natl. Acad. Sci. U.S.A.* 106, 13040–13045. doi: 10.1073/pnas.0905267106

Valverde, S., Oliver, A., Cabezas, M., Roura, E., and Lladó, X. (2015). Comparison of 10 brain tissue segmentation methods using revisited IBSR annotations. *J. Magn. Reson. Imaging* 41, 93–101. doi: 10.1002/jmri.24517

Van Essen, D. C., Smith, S. M., Barch, D. M., Behrens, T. E. J., Yacoub, E., and Ugurbil, K. (2013). The WU-Minn human connectome project: an overview. *Neuroimage* 80, 62–79. doi: 10.1016/j.neuroimage.2013.05.041

Worsley, K. J., and Friston, K. J. (1995). Analysis of fMRI time-series revisited—again. *Neuroimage* 2, 173–181. doi: 10.1006/nimg.1995.1023

Yeo, B. T. T., Krienen, F. M., Sepulcre, J., Sabuncu, M. R., Lashkari, D., Hollinshead, M., et al. (2011). The organization of the human cerebral cortex estimated by intrinsic functional connectivity. *J. Neurophysiol.* 106, 1125–1165. doi: 10.1152/jn.00338.2011

Yeo, B. T. T., Tandi, J., and Chee, M. W. L. (2015). Functional connectivity during rested wakefulness predicts vulnerability to sleep deprivation. *Neuroimage* 111, 147–158. doi: 10.1016/j.neuroimage.2015.02.018

Conflict of Interest Statement: The authors declare that the research was conducted in the absence of any commercial or financial relationships that could be construed as a potential conflict of interest.

Copyright © 2019 Park, Byeon and Park. This is an open-access article distributed under the terms of the Creative Commons Attribution License (CC BY). The use, distribution or reproduction in other forums is permitted, provided the original author(s) and the copyright owner(s) are credited and that the original publication in this journal is cited, in accordance with accepted academic practice. No use, distribution or reproduction is permitted which does not comply with these terms.

frontiers in Neuroinformatics

METHODS
published: 18 March 2019
doi: 10.3389/fninf.2019.00009

Brain Segmentation From Computed Tomography of Healthy Aging and Geriatric Concussion at Variable Spatial Resolutions

Andrei Irimia[1], Alexander S. Maher[1], Kenneth A. Rostowsky[1], Nahian F. Chowdhury[1], Darryl H. Hwang[2] and E. Meng Law[2,3,4]*

[1] USC Leonard Davis School of Gerontology, Ethel Percy Andrus Gerontology Center, University of Southern California, Los Angeles, CA, United States, [2] Department of Radiology, Keck School of Medicine of USC, University of Southern California, Los Angeles, CA, United States, [3] Department of Biomedical Engineering, Viterbi School of Engineering, University of Southern California, Los Angeles, CA, United States, [4] Faculty of Medicine, Nursing and Health Sciences, Central Clinical School, Monash University, Melbourne, VIC, Australia

When properly implemented and processed, anatomic T_1-weighted magnetic resonance imaging (MRI) can be ideal for the noninvasive quantification of white matter (WM) and gray matter (GM) in the living human brain. Although MRI is more suitable for distinguishing GM from WM than computed tomography (CT), the growing clinical use of the latter technique has renewed interest in head CT segmentation. Such interest is particularly strong in settings where MRI is unavailable, logistically unfeasible or prohibitively expensive. Nevertheless, whereas MRI segmentation is a sophisticated and technically-mature research field, the task of automatically classifying soft brain tissues from CT remains largely unexplored. Furthermore, brain segmentation methods for MRI hold considerable potential for adaptation and application to CT image processing. Here we demonstrate this by combining probabilistic, atlas-based classification with topologically-constrained tissue boundary refinement to delineate WM, GM and cerebrospinal fluid (CSF) from head CT images. The feasibility and utility of this approach are revealed by comparison of MRI-only vs. CT-only segmentations in geriatric concussion victims with both MRI and CT scans. Comparison of the two segmentations yields mean Sørensen-Dice coefficients of 85.5 ± 4.6% (WM), 86.7 ± 5.6% (GM) and 91.3 ± 2.8% (CSF), as well as average Hausdorff distances of 3.76 ± 1.85 mm (WM), 3.43 ± 1.53 mm (GM) and 2.46 ± 1.27 mm (CSF). Bootstrapping results suggest that the segmentation approach is sensitive enough to yield WM, GM and CSF volume estimates within ∼5%, ∼4%, and ∼3% of their MRI-based estimates, respectively. To our knowledge, this is the first 3D segmentation approach for CT to undergo rigorous within-subject comparison with high-resolution MRI. Results suggest that (1) standard-quality CT allows WM/GM/CSF segmentation with reasonable accuracy, and that (2) the task of soft brain tissue classification from CT merits further attention from neuroimaging researchers.

Keywords: segmentation, tissue classification, computed tomography, multimodal imaging, concussion, geriatrics

OPEN ACCESS

Edited by:
Jan G. Bjaalie, University of Oslo, Norway

Reviewed by:
Valerie Cardenas, Neurobehavioral Research, United States
Frithjof Kruggel, University of California, Irvine, United States

****Correspondence:***
Andrei Irimia
irimia@usc.edu

Received: *09 July 2018*
Accepted: *05 February 2019*
Published: *18 March 2019*

Citation:
Irimia A, Maher AS, Rostowsky KA, Chowdhury NF, Hwang DH and Law EM (2019) Brain Segmentation From Computed Tomography of Healthy Aging and Geriatric Concussion at Variable Spatial Resolutions. Front. Neuroinform. 13:9. doi: 10.3389/fninf.2019.00009

INTRODUCTION

The clinical use of computed tomography (CT) for patient diagnosis and treatment has been increasing steadily throughout the past few decades, particularly in relation to stroke and traumatic brain injury (TBI) (Haydel et al., 2000; Pelc, 2014). In developed countries, the number of CT scanners greatly exceeds that of magnetic resonance imaging (MRI) machines, and CT may be preferable to MRI in emergency radiology settings due to the former modality's convenience, wide availability and speed (Seo et al., 2008). Nevertheless, the task of classifying soft brain tissues based on CT images has long been disregarded because white matter (WM) and gray matter (GM) have relatively poor contrast in CT compared to T_1- or T_2-weighted MRI. The primary reason for this is that soft brain tissues have relatively similar radiodensities, which means that conventional CT images acquired at standard radiation doses typically differentiate GM from WM rather poorly. This frequently makes the CT-based delineation of WM/GM boundaries difficult and inaccurate; if hard thresholds of image intensity are used as primary criteria for delineation, poor GM/WM contrast can lead to substantial error during tissue segmentation. For similar reasons, models involving seed-based region-growing techniques can also lead to misleading results.

Whereas the automatic segmentation of brain MRI volumes is relatively routine compared to CT segmentation (Friston, 2007; Jenkinson et al., 2012; Velasco-Annis et al., 2017), there are very few software solutions for CT-based brain tissue classification. Nevertheless, recent progress in CT scanner technology and the accompanying improvement in CT image quality both suggest that the ability to distinguish soft tissue types using CT is becoming increasingly feasible (Li et al., 2014). As of the date of this study, only a handful of automatic methods for CT brain tissue segmentation exist, none of which have been applied to or validated on neurotrauma patients. Gupta et al. (2010), for example, proposed a heuristic segmentation method which leverages intensity thresholding to distinguish WM from GM and from CSF. The efficacy of this method, however, was only postulated based on manually-contoured, high-confidence fiducial brain regions and in the absence of independent confirmation by other imaging techniques. By contrast, Kemmling et al. (2012) introduced a probabilistic atlas based on previously-segmented MRI volumes which was co-registered to CT images to perform tissue classification, but no validation or quantitative evaluation of this approach was implemented in their study. More recently, Manniesing et al. (2017) proposed a method for CT-based segmentation which requires manual corrections using dedicated software and which also relies on the averaging of CT volumes acquired longitudinally from the same subject after the administration of a contrast agent to improve SNR. The accuracy of these authors' approach is unknown in the scenario where no more than one CT scan is available, as in our case. Furthermore, averaging of longitudinally-acquired CT volumes may produce undesirable results in cases where pathology evolution between time points modifies brain shape and structure, such as in TBI or stroke. Additionally, the method of Manniesing et al. involves the segmentation of GM, WM and CSF from *contrast* CT.

The premise of the present study is that brain segmentation methods for MRI hold considerable potential for adaptation to CT image processing. Specifically, our purpose here is to illustrate how two standard MRI analysis methods—namely (A) probabilistic, atlas-based classification and (B) topologically-constrained tissue boundary refinement—can be combined to delineate WM, GM and cerebrospinal fluid (CSF) from head CT images. In MRI analysis, voxel intensities are often modeled using a mixture of Gaussian random variables and tissue classification can be performed within a Bayesian framework. The probability that each voxel belongs to a certain tissue class is then calculated based on anatomic priors, and class membership is assigned based on this probability. In CT, however, where GM/WM contrast is typically quite poorer than in MRI, this approach can frequently result in spurious, anatomically-implausible class membership assignments for voxels near tissue boundaries. We propose to address this shortcoming by applying a standard approach to the neuroanatomy-constrained correction of tissue boundaries based on the local topological properties of the GM/WM interface. Because this method was previously applied only to MRI, part of our study's novelty involves its application to CT.

The feasibility and utility of the segmentation approach illustrated here are revealed by direct comparison of MRI vs. CT segmentations in a group of concussion victims from whom both standard-quality CT and T_1-weighted MRI were acquired. Here and throughout, "standard-quality CT" refers to CT images acquired at radiation dosages which are typical of routine clinical scans in the United States (∼2 mSv). Because radiation dosage is intimately related to CT signal quality and to the signal-to-noise ratio (SNR) of CT images, the utility of contrast-based approaches to brain segmentation is substantially dependent upon radiation dosage. In this context, applying our method to CT scans acquired at a standard radiation dosage is critical for highlighting the broad applicability of the segmentation approach.

To our knowledge, this is the only CT segmentation method to undergo rigorous within-subject comparison with high-fidelity MRI. Furthermore, none of the existing CT methods has been used to segment the brains of older adults or of concussion victims. Both qualitative and quantitative comparison of CT- vs. MRI-based segmentations of WM, GM, and CSF indicate noteworthy agreement between the two, as well as superior segmentation quality compared to the very few other methods currently available. On the other hand, our findings also suggest that—although the reliable CT-based calculation of WM/GM/CSF volumetrics is feasible at standard radiation dosages—the accuracy of CT-derived metrics is unlikely to ever surpass that of MRI-derived ones as the "gold standard" in the field. Scientists who wish to use CT-based volumetrics to make scientific inferences should be mindful that CT-based volumetrics are likely associated with greater error than MRI-based measures. Awareness of this is necessary to prevent future CT-based segmentation studies from conveying an overly

optimistic impression regarding the ability of CT segmentations to furnish reliable estimates of brain volumetrics.

MATERIALS AND METHODS

Participants

This study was carried out in accordance with the recommendations of the Institutional Review Board of the University of Southern California with written informed consent from all subjects. All subjects gave written informed consent in accordance with the Declaration of Helsinki. The protocol was approved by the Institutional Review Board at the University of Southern California. Study participants were selected from two volunteer pools, namely (i) concussion victims who had participated in an unrelated study, and (ii) individuals who had been scanned using MRI/CT for clinical treatment unrelated to this study. To be included, patients had to (A) have had both MRI and CT volumes acquired and available, (B) be 50 years of age or older at the time of their initial brain scan, and (C) exhibit no gross head pathology detectable using CT or MRI at scan time. The exclusion criteria were (A) unavailability of MRI and/or CT data; (B) patient age under 50 years; (C) the existence of substantial, gross head pathology at scan time, as detected via CT and/or MRI and (D) poor CT/MRI data quality (e.g., visually detectable artifacts of any kind). The concussed group included 10 participants (5 males; age: mean $\mu = 65$ years; standard deviation $\sigma = 7$ years; range: 54–75 years). The non-concussed group included 25 participants (12 males; age: $\mu = 61$ years; $\sigma = 9$ years; range: 52–83 years). Volunteers under the age of 50 were excluded because of our desire to test our method on brains with variable degrees of atrophy. The most important difference between the two groups pertains to the spatial resolution of CT/MRI data. Specifically, in the concussed volunteer group, CT slice thickness was 1.25 mm and MRI slice thickness was 1 mm; in the non-concussed volunteer group, slice thickness was 3.75 mm for CT and 5 mm for MRI. This selection of data was intentional, as the difference in spatial resolution allowed us to explore segmentation reliability as a function of slice thickness and to illustrate the necessity of evaluating CT segmentation approaches like ours using MRI of research-grade resolution.

Data Acquisition

All data were deidentified and delinked prior to analysis. CT volumes were acquired using a 16-slice General Electric scanner. In the concussed volunteer group, images were acquired clockwise, in helical mode, with a standard convolution kernel and the following parameters: matrix size = 512 × 512; voxel size = 1.5 mm × 1.5 mm × 1.25 mm; kilovoltage peak (kVp) = 120 kV; data collection diameter = 500 mm; exposure time = 600 ms; X-ray tube current = 100 mA; exposure = 100 mA·s; focal spot = 1.2 mm. MRI volumes were acquired at 3 T using a Prisma MAGNETOM Trio TIM scanner (Siemens Corp., Erlangen, Germany). Images were acquired using a magnetization-prepared rapid acquisition gradient echo (MP-RAGE) sequence with the following parameters: repetition time (T_R) = 1,950 ms; echo time (T_E) = 3 ms; inversion time (T_I) = 900 ms; flip angle (FA) = 9 degrees; percentage sampling = 100; pixel bandwidth (BW) = 240 Hz/pixel; matrix size = 256 × 256; voxel size = 1 mm × 1 mm × 1 mm. In the non-concussed volunteer group, CT volumes were acquired clockwise, in helical mode, with a standard convolution kernel and the following parameters: matrix size = 512 × 512; voxel size = 1.5 mm × 1.5 mm × 3.75 mm; kVp = 120 kV; data collection diameter = 250 mm; exposure time = 750 ms; X-ray tube current = 220 mA; exposure = 130 mA·s; focal spot = 1.2 mm. MRIs were acquired at 3 T using a Signa HDxt scanner (General Electric Corp., Boston, USA). Images were acquired using a fast spin-echo (FSE) sequence with the following parameters: $T_R = 567$ ms; $T_E = 18$ ms; FA = 90 degrees; percentage sampling = 100; pixel BW = 81 Hz/pixel; matrix size = 512 × 512; voxel size = 0.5 mm × 0.5 mm × 5 mm.

MRI Segmentation

MRI volumes were segmented using the widely-utilized FreeSurfer 6.0 software as detailed elsewhere (Dale et al., 1999; Fischl et al., 1999), with default execution parameters. Very briefly, this process includes (1) the removal of non-brain tissue using a hybrid watershed/surface deformation procedure, (2) automated Talairach space transformation, (3) volume intensity normalization, (4) segmentation of cortical and subcortical GM, (5) tessellation of the GM/WM boundary, and (6) automated surface topology correction. The reader is referred to references (Dale et al., 1999; Fischl et al., 1999) for comprehensive details on each of these steps involved in the MRI segmentation procedure.

CT Segmentation

As previously stated, an important goal of this study is to illustrate how MRI-tailored approaches can be combined and adapted for CT. Because of this, our segmentation strategy is inspired by MRI-tailored approaches to template-based tissue classification, including pioneering approaches by Ashburner and Friston (1997, 2000, 2005, 2007) and by Dale et al. (1999) and Fischl et al. (1999). The starting point for our implementation was the probabilistic classification method of Ashburner and Friston (2005), as available in SPM 12.0; this was adapted, modified and augmented in MATLAB to incorporate topology-constrained segmentation (Dale et al., 1999; Fischl et al., 1999). An overview of the entire tissue classification procedure is provided in this section, and details specific to each step are described in subsequent sections. Briefly, to perform tissue classification, voxel intensity values are used to assign their probabilities of belonging to one of several tissue classes by estimating the parameters of the intensity distributions of each class. This is accomplished by first defining an objective function derived from a mixture of Gaussian random variable models, and by then minimizing the value of this function using a parameter optimization process. A set of *a priori* tissue probability maps specified in a standard space (atlas) are used to assist the classification. The objective function can assist this process by weighing the probability maps of the standard space according to Bayesian inference principles and then deforming them so that they match the volumes being segmented. Specifically, the template is warped to each subject's brain volume (Collins et al., 1995), after which the latter can

be segmented and the ensuing spatial classifications can be smoothed (Evans et al., 1994). When combined with *a priori* information specified by the template, Bayesian inference can be used to calculate posterior probabilities, based on each subject's voxel intensity values. The interface between the resulting GM and WM volumes is smoothed according to principles inspired from nonlinear filter theory, subject to topological constraints dictated by the structural neuroanatomy of the human brain (Dale et al., 1999; Fischl et al., 1999).

Gaussian Mixture Model

The distribution of image intensities in a neuroimaging volume is modeled here by a mixture of K clusters, each consisting of Gaussian random variables (Bishop, 1995). Each Gaussian variable is parameterized by its mean μ_k, variance σ_k^2 and mixing coefficient γ_k, subject to the constraint that the sum of all mixing coefficients must be equal to 1. Fitting this Gaussian mixture model to the image intensity data vector $\mathbf{y}$ of length I involves maximizing the probability of observing the data given the model parameterization. The probability that a voxel has intensity y_i given that it belongs to the k-th Gaussian random variable (i.e., given that $c_i = k$) parameterized by μ_k and σ_k^2 is

$$P\left(y_i|c_i = k, \mu_k, \sigma_k^2\right) = \frac{1}{\left(2\pi\sigma_k^2\right)^{1/2}} \exp\left[-\frac{\left(y_i - \mu_k\right)^2}{2\sigma_k^2}\right]. \quad (1)$$

Because the probability that y_i belongs to the k-th Gaussian random variable given the proportion γ_k of voxels which belong to that random variable is $P\left(c_i = k|\gamma_k\right)$, Bayes' rule indicates that

$$P\left(y_i, c_i = k|\mu_k, \sigma_k^2, \gamma_k\right) = P\left(y_i|c_i = k, \mu_k, \sigma_k^2\right) P\left(c_i = k|\gamma_k\right), \quad (2)$$

and the total probability of observing y_i becomes

$$P\left(y_i|\boldsymbol{\mu}, \boldsymbol{\sigma}, \boldsymbol{\gamma}\right) = \sum_{k=1}^{K} P\left(y_i, c_i = k|\mu_k, \sigma_k^2, \gamma_k\right), \quad (3)$$

whilst the probability

$$P\left(\mathbf{y}|\boldsymbol{\mu}, \boldsymbol{\sigma}, \boldsymbol{\gamma}\right) = \prod_{i=1}^{I} P\left(y_i|\boldsymbol{\mu}, \boldsymbol{\sigma}, \boldsymbol{\gamma}\right) \quad (4)$$

that all I intensities in $\mathbf{y}$ are observed given $\boldsymbol{\mu}$, $\boldsymbol{\sigma}$, and $\boldsymbol{\gamma}$ can be maximized by varying the latter parameters in the cost function

$$\mathcal{E} = -\log P\left(\mathbf{y}|\boldsymbol{\mu}, \boldsymbol{\sigma}, \boldsymbol{\gamma}\right). \quad (5)$$

Spatial Priors, Deformation, and Regularization

A probabilistic atlas is used to specify the prior probability that each voxel belongs to any tissue class in the Gaussian mixture model. This is done without assuming that any intensity distribution for each class is Gaussian, such that the prior probability of voxel i being drawn from the k-th Gaussian distribution is

$$P\left(c_i = k|\boldsymbol{\gamma}\right) = \frac{\gamma_k P_{ik}}{\sum_{j=1}^{K} \gamma_j P_{ij}}, \quad (6)$$

where P_{ik} is the tissue probability for class k at voxel i. For voxels located at the boundary between tissues (e.g., the GM/WM boundary), this model accommodates the difficulty of ascertaining the class to which voxel i belongs. The atlas used here is a modified version of the MNI_{152} atlas (Grabner et al., 2006), which is based on an average of T_2-weighted MRI volumes acquired from 152 healthy control subjects. The original atlas has a resolution of 1 mm × 1 mm × 1 mm and its image intensities range from 0 to 90 in increments of 1.3×10^{-3}. For the present study, the atlas in question was modified to reflect the intensity profile of CT brain scans, where CSF is hypointense.

Let $\boldsymbol{\alpha}$ be a vector of diffeomorphic deformation parameters which allow the co-registration of the spatial template and a subject volume. Here, spatial priors are deformed according to $\boldsymbol{\alpha}$, to allow co-registration according to

$$P\left(c_i = k|\boldsymbol{\gamma}, \ \boldsymbol{\alpha}\right) = \frac{\gamma_k P_{ik}(\alpha)}{\sum_{j=1}^{K} \gamma_j P_{ij}(\alpha)}. \quad (7)$$

With this adjustment, one obtains

$$\mathcal{E} = -\sum_{i=1}^{I} \log P\left(\mathbf{y}|\boldsymbol{\mu}, \boldsymbol{\sigma}, \boldsymbol{\gamma}, \alpha\right) \quad (8)$$

or, more explicitly,

$$\mathcal{E} = -\sum_{i=1}^{I} \log \sum_{k=1}^{K} P\left(c_i = k|\boldsymbol{\gamma}, \ \boldsymbol{\alpha}\right) P\left(y_i|c_i = k, \mu_k, \sigma_k^2\right). \quad (9)$$

The parameterization of the deformation is implemented using a linear combination of sinusoidal transform bases (Christensen et al., 1994) subject to spatial regularization by maximizing $P\left(\mathbf{y}, \boldsymbol{\alpha}|\boldsymbol{\mu}, \boldsymbol{\sigma}, \boldsymbol{\gamma}\right)$. Only the lowest frequencies of a discrete sine transform were used, resulting in 392 ($7 \times 3 \times 8$) parameters to describe deformations along each spatial dimension. Three additional parameters were used to model linear scaling and one parameter was used to model linear image intensity inhomogeneities (Ashburner and Friston, 1999). The probability densities of the spatial parameters $\boldsymbol{\alpha}$ are modeled by multivariate Gaussian random variables with mean $\mathbf{0}$ and covariance matrices $\mathbf{C}_{\boldsymbol{\alpha}}$. The spatial regularization involving these covariance matrices and deformations prevents undesirable interactions between parameter estimates (Evans et al., 1994). Initially, parameter value estimates are assigned randomly, and nonlinear deformation coefficients are set to zero. Model parameters are then optimized using an expectation maximization (EM) algorithm (Bishop, 1995), where the Gaussian mixture and deformations are re-calculated by iteratively updating exactly one while the others are held constant. Deformations are optimized using a Gauss-Newton scheme (Wedderburn, 1974).

Topology-Constrained Refinement

After probabilistic assignment of voxels to one of three classes (WM, GM or CSF), the segmentation is refined iteratively using *a priori* information concerning the local properties of the cortex (Dale et al., 1999). Specifically, because the surface defined by the WM/GM interface is smooth and its curvature is both defined and finite everywhere on it, the local topology of the brain can be used to correct the probabilistic tissue classification. This process is analogous to the application of a nonlinear, anisotropic filter whose nonlinearity is high near the WM/GM boundary. As the distance from some given voxel to the WM/GM boundary increases, the filter becomes more linear; because the true boundary is topologically smooth, the filter shape must be planar at this interface. In our approach, the segmentation is corrected in two steps. First, we identify the plane crossing the boundary which is intersected by voxels whose intensity variance is minimal. Once this is done, the voxels within this plane are examined to determine whether (A) a substantial proportion of them have ambiguous classifications based on their intensity or whether (B) they are surrounded by voxels whose class memberships vary greatly. If changing the class assignment of these voxels decreases the in-plane intensity variance, the voxels in question are re-assigned to their more appropriate class (Dale et al., 1999).

Qualitative Segmentation Comparison

CT segmentations were compared to MRI-based segmentations within each participant. Prior to this comparison, the skull-stripped MRI and CT volumes were co-registered using a 12-parameter, affine registration. MRI- and CT-based segmentations were compared by plotting both and inspecting the ability of the CT segmentation to reproduce cortical folding patterns and to identify landmarks of interest, including the thalamus, ventricular system, and various gyri. To visually inspect the effect of slice thickness upon segmentation, the CT volume of a representative concussion victim was first down-sampled using trilinear interpolation to change the voxel size from 1 mm × 1 mm × 1.25 mm to 1 mm × 1 mm × 3.75 mm. The lower-resolution volume was then segmented, and the results were compared.

Quantitative Segmentation Comparison

In addition to comparing the CT- and MRI-based GM, WM and CSF classifications qualitatively, four measures were calculated: (1) the Sørensen-Dice coefficient (which conveys the extent of overlap between CT and MRI tissue label maps), (2) the Hausdorff distance (which measures, in this case, how far the CT- and MR-based boundaries are between two tissues), (3) the intraclass correlation coefficient (a measure of how reproducible measurements are when made using distinct techniques) and (4) the stretching distance (a measure of average spatial prior deformations).

For two tissue classes X and Y, the Sørensen-Dice coefficient C_{SD} is defined as

$$C_{SD} = 2\frac{|X \cap Y|}{|X| + |Y|}. \tag{10}$$

If there is perfect overlap between the two tissue classes, C_{SD} is equal to 1; no overlap results in C_{SD} being equal to 0. The original Hausdorff distance d_H is defined as

$$d_H(X, Y) = \max\left\{\sup_{x\epsilon X}\inf_{y\epsilon Y}\ d(x, y), \sup_{y\epsilon Y}\inf_{x\epsilon X}\ d(x, y)\right\} \tag{11}$$

where X and Y are non-empty sets of a metric space (M, d), sup is the supremum and inf is the infimum. This measure involves the distance between points located along the edges of two surfaces and conveys how well the two surfaces overlap. In the present study, X and Y are MRI- and CT-derived segmentation volume surfaces, respectively, and d is a Euclidian distance. Here, the modified Hausdorff distance is used, as defined formally elsewhere (Dubuisson and Jain, 1994).

The intraclass correlation coefficient r_{IC} is a measure of within-subject measurement variability relative to between-subject variability (Iscan et al., 2015). In the present case, these measurements are volumes of the GM, WM, or CSF computed from either MRI or CT, and their r_{IC} value can be used to quantify the reliability of the CT segmentation. As reported elsewhere, the calculation of r_{IC} is predicated upon experimental design and statistical model assumptions (Shrout and Fleiss, 1979). In cases like ours, the one-way random effect model is appropriate (McGraw and Wong, 1996), such that $r_{IC} \simeq (MS_b - MS_w)/MS_b$, where MS_b and MS_w are between- and within-group mean sums of squared measurements, respectively. These quantities were computed like in an analysis of variance (Shou et al., 2013). Bootstrapping was used to calculate the average amount by which CT volume estimates can be expected to deviate from their MRI-derived values.

To assess the relationship between segmentation quality and the amount of deformation applied to the spatial priors, one can calculate the mean absolute stretching distance d_S between two volumes (Ewert et al., 2019). Intuitively, this distance can be conceptualized as the average amount by which volume elements within a moving volume must move to match the shape of a target volume. The mapping between volume elements in the two volumes (template and subject) is specified by the deformation field of the transformation. In other words, d_S is the average amount by which voxels in the atlas must move to optimize the atlas-subject deformation. The larger the deformation, the greater d_S.

To determine whether outliers as well as any bias existed in favor of any of the segmentation classes, the MRI- and CT-derived volumes of WM, GM, and CSF were plotted against each other. The relationships between d_H and C_{SD}, and between d_H and d_S were explored visually in a similar way, i.e., by plotting one against the other. In this study, all GM and WM measures were calculated based on all neuroanatomical structures in the cranial cavity. By contrast, only ventricular CSF volumes and Sørensen-Dice coefficients were compared because T_1-weighted MRI is insufficiently suited—compared to T_2-weighted MRI—for quantifying water content in the CSF layer around the cerebrum, as well as in locations surrounding the cerebellum, brainstem, etc. However, T_2-weighted MRI scans were unavailable to us; to alleviate this drawback, only ventricular CSF measures were compared across modalities.

In implementations like ours, there is a risk that segmentation results could be dominated by the nonlinear deformation of the template to each individual case. In other words, the radiodensities of distinct tissue classes (e.g., GM, WM) may have relatively little influence upon the segmentation. To test this hypothesis, the following analysis was implemented for each CT volume: (A) The mean μ and standard deviation σ were calculated across all brain CT voxels. (B). All brain voxels were assigned radiodensity values sampled at random from a Gaussian distribution with parameters μ and σ. This operation effectively removed the contrast between GM and WM. (C) The modified brain CT volume was segmented. (D) C_{SD} and d_H values were computed based on the segmentation of the modified brain CT volume and then compared to the values of these metrics as obtained by segmenting the original CT volume. We argue that, if tissue class radiodensities had no effect upon segmentations, there would be no statistically-significant difference between C_{SD} values calculated based on original CT volumes vs. based on modified CT volumes.

RESULTS

Qualitative Assessment

The conclusions of our qualitative assessment are reflected by the results conveyed in **Figure 1**, where both MRI and CT segmentations are displayed for a representative subject. When performing this comparison, the MRI-based segmentation is treated as the gold standard. Overall, the agreement between MRI- and CT-derived classifications is quite reasonable, with our method being able to capture the most prominent features of cerebral neuroanatomy appropriately. In what follows we discuss specific findings, as reflected by the sagittal, coronal and axial views of the brain, respectively.

The sagittal slice of the brain displayed in **Figure 1** is approximately co-planar with the longitudinal fissure. This depiction indicates visually-acceptable agreement between the segmentations, with good coverage of cerebral GM, callosal WM and of the brainstem. Ventricular CSF classifications also appear to be satisfactory. There is even agreement between segmentations pertaining to cerebral areas where only little GM is visible in the selected slice, such as the medial parietal lobe and occipital lobes. The most notable difference in the sagittal view pertains to the frontal lobe, where the CT algorithm appears to have classified more tissue along the longitudinal fissure as GM than the MRI method. This, however, is to be expected due to the relatively low SNR of CT compared to MRI as well as to the excellent ability of FreeSurfer software to delineate the natural boundary between hemispheres.

The coronal slice displays a view of the parietal lobe, with a substantial portion of the cerebellum and lateral ventricles being visible as well. This view is particularly useful because it conveys the substantial similarities in gyrification patterns between the two segmentations. Visual assessment confirms that local structural variations are captured relatively well in the CT segmentation. Though the basal ganglia are poorly delineated by CT, our segmentation appears to be able to capture them well. The axial slice is at the level of the inferior temporal lobe, with some frontal lobe structures—such as the orbital gyri/sulci—being visible as well. As in the coronal slice, the overall local shape of the GM/WM boundary is reflected well in the CT segmentation.

Figure 2 displays MRI- and CT-based three-dimensional reconstructions of the ventricular CSF, brain, bones and skin for the volunteer in **Figure 1**. The second row displays segmentation results based on the original-resolution volume (1 mm × 1 mm × 1.25 mm). Although the MRI-based segmentation is superior in its ability to resolve the gyrification of the cortex, the CT segmentation does reproduce the overall shape of the brain and ventricular system. The reconstruction of the lateral ventricles, third ventricle and inter-thalamic adhesion appears to be within reasonable limits for the purposes of neuroanatomic reference and delineation. Results in the third row are based on the same volume after down-sampling to the resolution of the volumes acquired from non-concussed volunteers (1 mm × 1 mm × 3.75 mm). Here, the method is seen to over-estimate GM volume and to lose some ability to capture cortical folding details; overall, there is some perceived loss of tissue classification fidelity compared to MRI.

Quantitative Assessment of Concussion Group

Across all concussion cases considered, the mean and standard deviation of the Sørensen-Dice coefficient were found to be 86.7 ± 5.6% for WM, 86.0 ± 2.0% for GM, and 92.2 ± 0.7% for ventricular CSF. The means and standard deviations of the coefficient are more similar for WM and GM, presumably because these tissues' similar radiodensities translates into similar abilities to classify them. On the other hand, ventricular CSF has a somewhat greater coefficient presumably because its lower radiodensity compared to GM/WM makes CSF easier to distinguish from soft brain tissue. The average modified Hausdorff distance was found to be 3.4 ± 1.5 mm (WM), 3.7 ± 1.8 mm (GM), and 2.5 ± 1.3 mm (CSF), which confirms that CSF classification is likely best, followed by WM and then GM. This view is recapitulated by the fact that d_S was found to have means of 3.4 ± 2.3 mm (WM), 3.5 ± 1.9 mm (GM), and 1.8 ± 0.6 mm (CSF).

In the concussion sample, the intraclass correlation coefficient was found to be 0.64 for WM, 0.68 for GM, and 0.74 for CSF. Bootstrapping results suggested, based on this sample, that the segmentation method is sensitive enough, to yield WM, GM, and CSF volume estimates within ∼5.4%, ∼4.3%, and ∼3.2% of their MRI-based estimates, respectively. As percentages of the MRI-derived mean volume, the 2σ confidence intervals (CIs) for these error estimates were [2.9, 7.9]% for GM, [2.2, 6.4]% for WM, and [1.4, 5.0]% for CSF. In other words, for a randomly selected volunteer, there was a ∼95% estimated probability that the discrepancy between her/his CT-derived and her/his MRI-derived GM volume was between 2.9% and 7.9% of the latter.

The results of the quantitative assessment for concussion victims are summarized in **Figure 3**. In particular, **Figure 3A** suggests that, in the case of volume measurements, no outlier or bias in favor of any tissue class are present in our cohort of

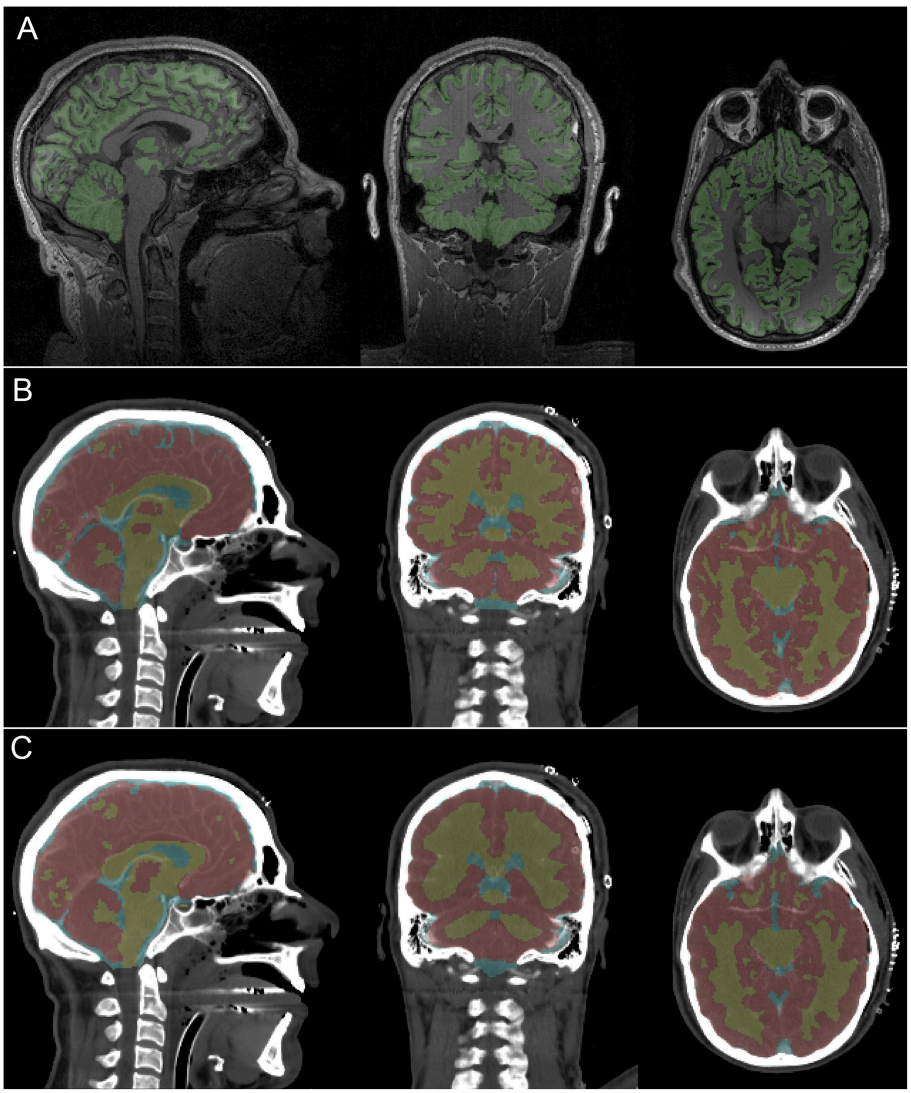


FIGURE 1 | MRI and CT segmentations and their corresponding imaging slices for a representative subject. Colored voxel label maps are translucent to ease inspection of the underlying neuroanatomy. **(A)** T_1-weighted MRI slices show GM (green). The WM is left uncolored to facilitate identifying occasional differences between the true GM/WM boundary and the FreeSurfer-identified boundary. **(B)** CT slices display labeled GM (red), WM (yellow) and CSF (light blue) based on segmentation at the original CT volume resolution (1 × 1 × 1.25 mm). **(C)** Like **(B)**, based on segmentation at a down-sampled CT volume resolution (1 × 1 × 3.75 mm).

concussion victims. **Figure 3B** suggests that, as expected, there is a direct relationship between d_H and C_{SD}. Comparison of the plots for WM, GM and CSF illustrates how both metrics have a smaller range and variance for CSF than for the other two classes. This can be explained by the fact that CSF is easier to segment from both CT and MRI due to the relatively large difference in radiodensity between CSF and either GM or WM. This is confirmed by **Figure 3C**, where the relationship between d_H and d_S is explored. As expected, these quantities are also directly proportional to each other because they both trend higher as the quality of the segmentation decreases.

When testing the hypothesis that tissue class intensities had no effect upon segmentations, the Sørensen-Dice coefficients computed based on CT volumes with modified radiodensities were found to be 64.2 ± 8.9% for WM and 69.4 ± 7.3% for GM across all concussion cases. The average modified Hausdorff distance was found to be 5.21 ± 1.61 mm (WM) and 4.87 ± 1.95 mm (GM) in this group. These values are significantly different ($p < 0.001$) from those obtained based on the original CT volumes, which suggests that tissue class radiodensities do have a significant effect upon segmentations.

Quantitative Assessment of Volunteers Without Concussions

Across non-concussed participants (whose MRI volumes had thicker slices), the mean and standard deviation of the Sørensen-Dice coefficient were found to be 63.7 ± 7.2% for WM, 59.4 ± 8.9% for GM, and 73.5 ± 6.6% for ventricular CSF. In this

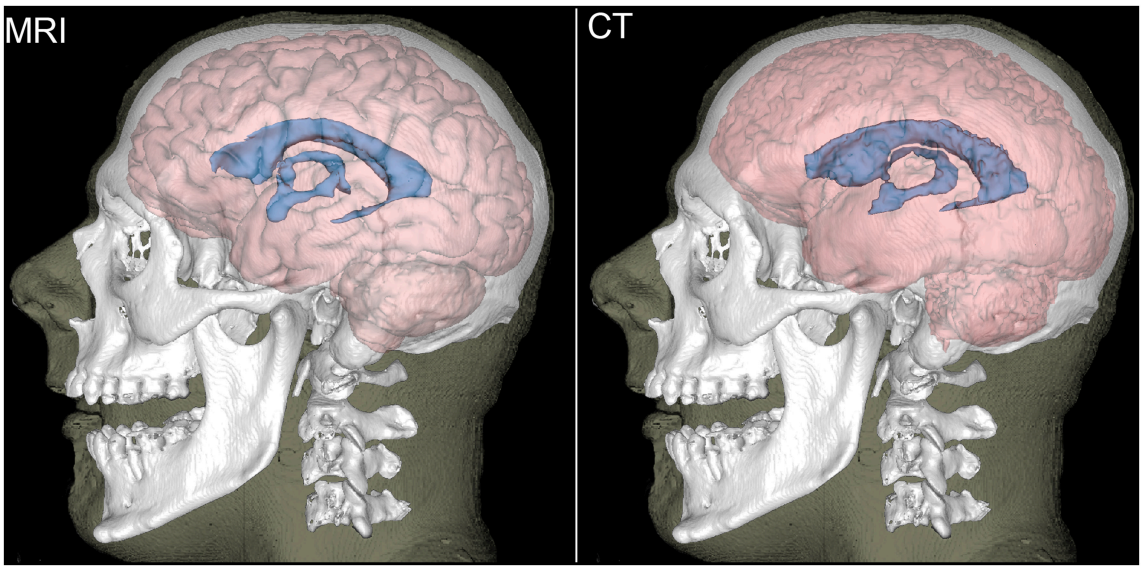


FIGURE 2 | Reconstructions of the brain (light red), ventricular CSF (blue), bones (white), and skin (translucent) for a representative participant. The brain and ventricular CSF are based on MRI **(left)** and on CT **(right)**. Bones and the skin surface were reconstructed from CT.

group, the average modified Hausdorff distance was found to be 6.18 ± 2.34 mm (WM), 6.75 ± 2.87 mm (GM), and 4.89 ± 1.86 mm (CSF). Presumably, the results are substantially inferior to those obtained in the concussed patient sample because the MRI slice thickness in the non-concussed group was 3.75 mm. The intraclass correlation coefficient was found to be 0.51 for WM, 0.56 for GM, and 0.61 for CSF. In this lower-resolution sample, the segmentation method was estimated to be sensitive enough to detect percentage volume differences between MRI and CT which amounted to an average of ∼7.1% (CI: [3.9, 10.3]%) for WM, ∼6.2% (CI: [3.5, 8.9]%) for GM, and ∼5.4% (CI: [3.1, 7.7]%) for CSF. The d_S metric was found to be 7.1 ± 4.12 mm (WM), 6.7 ± 3.9 mm (GM), and 3.4 ± 1.6 mm (CSF). Although the means and standard deviations of these quantities differ from those observed in the concussion group, the relationships between quantities recapitulate the findings illustrated in **Figure 3** to indicate that d_H and d_S are directly proportional. Overall, these results thus confirm the necessity of validating CT-based soft tissue segmentations using MRI of standard, research-grade thickness (e.g., 1 mm) rather than MRI with slices of relatively large thickness (e.g., 3.75 mm).

DISCUSSION

Feasibility

The ability to segment soft brain tissues from CT is largely dependent upon image contrast-to-noise ratio (CNR). In CT, the CNR itself depends on tube settings, iterative reconstruction method, radiation dosage and other factors; at standard dosages, the average radio-densities of GM and WM have been reported as 38.7 ± 2.2 Hounsfield units (HU) and 31.8 ± 2.3 HU, respectively (Craddock et al., 2006), resulting in an average X-ray attenuation of ∼5 HU. Bier et al. (2016) similarly report radio-densities of 40.2 ± 3.3 HU (GM) and 28.48 ± 3.6 HU (WM) in their CT images, with the GM-WM radio-intensity difference being significantly different ($p < 0.0001$). The GM-WM CNR is reported as ∼3 (Rapalino et al., 2012; Bier et al., 2016), but image filtering techniques have been reported to enhance the CNR by a factor as large as ∼10 (Diwakar and Kumar, 2014; Bier et al., 2016). This allows the CT GM-WM CNR to compare favorably with the GM-WM CNR obtained from T_1-weighted MRI at 3 T, where a meta-analysis found that single-slice and multi-slice MR images yield CNRs of ∼18 and ∼9, respectively (Fushimi et al., 2007). Together, these findings suggest that the delineation of the GM/WM boundary from CT is feasible using available CT technology. Nevertheless, it should be reiterated that, when available and of enough quality, MRI is by far preferable to CT for the purpose of brain soft tissue segmentation.

Applications

Despite very limited previous research on CT brain tissue segmentation, there are numerous potential applications for this technology, including (1) the detection of brain pathology, (2) the measurement of brain volumetrics to assist studies of aging in health and disease, and (3) the quantitation of neuroanatomy in settings where MRI is undesirably expensive, unavailable or inaccessible. For example, the US Centers for Disease Control (CDC) report that the number of CT scanners exceeds that of MRI scanners by a factor which ranges between ∼1.5 (developed countries) and ∼5 (developing countries) (CDC, 2010). Furthermore, CT is more affordable than MRI and additionally constitutes the method of choice in certain clinical settings where image acquisition time is of the essence, such as neurocritical care (Williamson et al., 2017). For the latter reason, the availability of CT segmentation tools could be beneficial for TBI studies.

In stroke, TBI and other conditions which frequently involve CT, segmentation of images acquired with this modality could

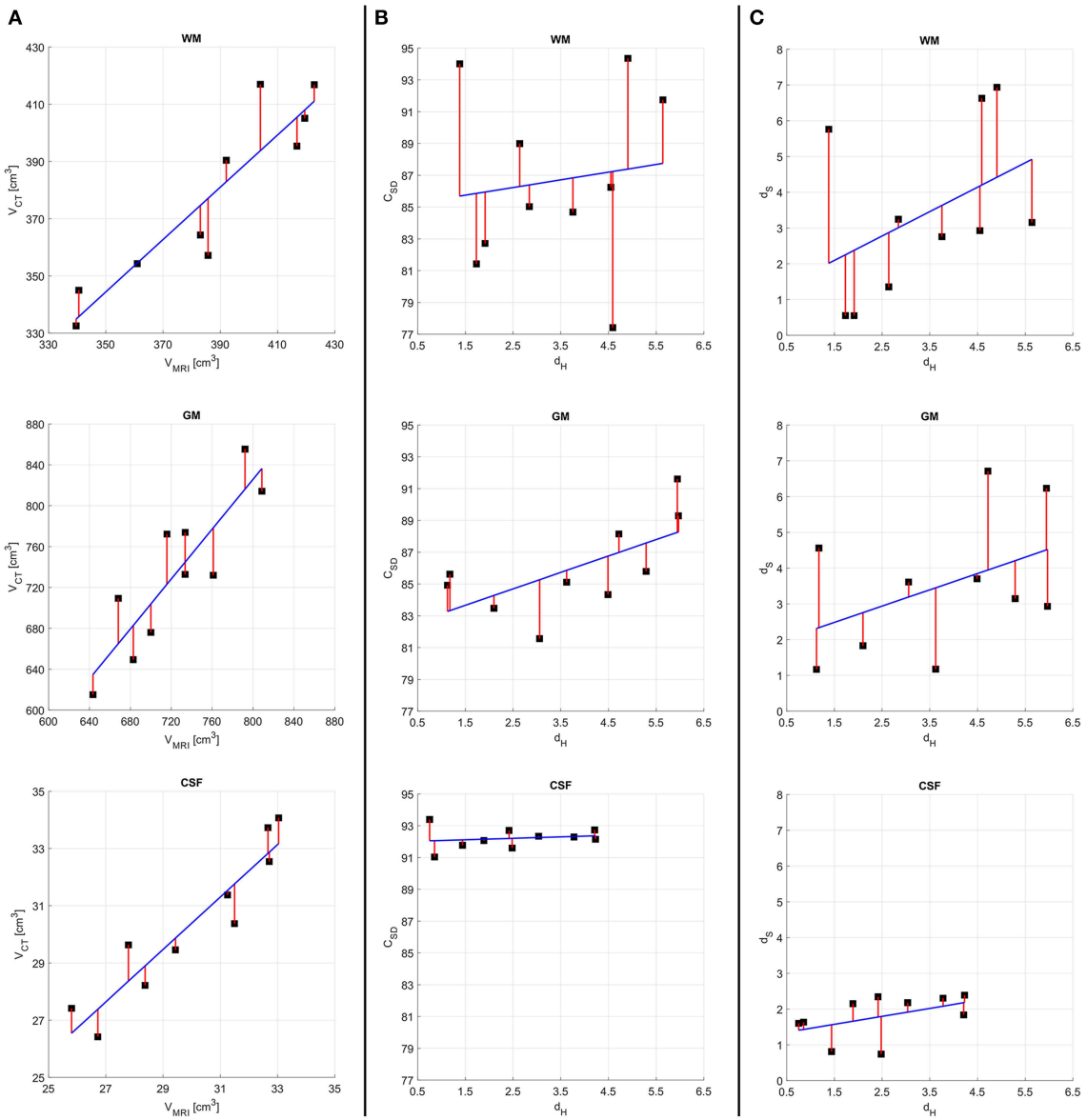


FIGURE 3 | Results of quantitative analysis for concussion victims. For all quantities plotted, the regression line of best fit (blue) and residuals (red) are shown on plots with identical ranges along both *x* and *y*, to facilitate comparison. **(A)** MRI- vs. CT-derived volumes. **(B)** The Hausdorff distance d_H vs. the Sørensen-Dice coefficient C_{SD}. **(C)** The Hausdorff distance d_H vs. the stretching distance d_S. Quantities pertaining to WM, GM, and CSF are displayed in the first, second, and third rows, respectively.

also be used to analyze perfusion imaging to study blood flow in the brain and to distinguish between the cores and penumbrae of cerebral lesions. CT-based volumetrics could also be useful in quantitative studies of brain atrophy associated with healthy aging, TBI or neurodegenerative diseases. Specifically, because the rate of brain atrophy in health differs from that observed in many diseases of the central nervous system, brain volumetrics can be used in conjunction with other anatomic and functional measures to estimate mortality risk and other parameters which are of substantial interest to clinicians, biomedical scientists, demographers, and epidemiologists.

Given that MRI availability in developing countries is relatively limited, software for CT-based brain segmentation could substantially extend the scope of certain large-scale epidemiological studies being carried out there. One such study is the Tsimané Health & Life History Project now underway in a region of rural Bolivia where MRI is logistically unfeasible yet where CT is available (Kaplan et al., 2017). Furthermore, because some patients cannot undergo MRI scanning due to claustrophobia, pacemaker implantation or other contraindications, techniques such as ours could facilitate the enrollment of these individuals in imaging

studies. Given how transformative the research field of brain MRI processing has been over the past 30 years, the potential applicability of CT-based segmentation is thus clear.

Comparison to Other Methods

There are very few other methods to which our approach can be compared quantitatively. One study which reports metrics like ours is that of Manniesing et al. (2017), where averages and standard deviations for C_{SD}, d_H, and d_C are reported for CT-only segmentations of WM and GM. In all cases, our results compare very favorably to theirs; for example, Manniesing et al. report $\langle C_{SD} \rangle = 0.79 \pm 0.05$ and $\langle d_H \rangle = 0.74 \pm 0.26$ mm for WM, where $\langle\rangle$ denotes the mean. In all three cases, our Sorensen-Dice coefficients are greater and the two distances quoted are smaller than theirs, as desirable; this statement also applies to the comparison of GM segmentations. By contrast, as expected, MRI-based segmentations clearly remain preferable. For example, Iscan et al. (2015) report that, for FreeSurfer-segmented GM, $\langle r_{IC} \rangle = 0.88 \pm 0.15$ in a dataset of repeated MRI measurements. Furthermore, whereas our approach can—at its best— yield GM volume measurements which are within an average of ∼5.4% of their MRI-derived values, the latter typically fall within <1% of their true values, on average (Eggert et al., 2012). Similarly, a comparison of the MRI- and CT-derived surfaces in **Figure 1** easily indicates that only MRI-based segmentation can capture fine local variations in cortical shape, such as those due to gyri and sulci. In conclusion, our method could clearly benefit from refinement and from technology improvements to improve CT image SNR and CNR.

LIMITATIONS

For clarity, our study's limitations can be divided into two groups, i.e., extrinsic or intrinsic. Extrinsic limitations involve factors pertaining to the imaging data themselves and which affect the efficacy of the method independently of it; such factors include radiation dose, the number of scans available, and the presence of metal objects inside the head. Since there is a direct—albeit nonlinear—relationship between radiation dose and SNR (Yu et al., 2009), we expect our algorithm to perform better if the data are acquired at higher radiation doses. Similarly, if repeated measurements are obtained, within-subject co-registration and averaging of CT volumes can improve SNR. If, on the other hand, metal objects (e.g., deep brain stimulation electrodes) are present inside the head, resulting artifacts may substantially compromise segmentation efficacy. One intrinsic limitation of our approach is the fact that, as **Figure 1** illustrates, its ability to identify tissue boundaries correctly is suboptimal at brain locations where thin, long slabs of WM protrude into GM. Because the ability of our method to capture the geometric variability of the GM/WM interface is dependent upon GM/WM contrast, it results that the algorithm may not perform well in locations where the structure of the boundary is particularly complex. Improvements in the SNR and CNR between GM and WM can alleviate this drawback. A second limitation of this study involves the fact that T_2-weighted MRI is preferable to T_1-weighted MRI for quantifying water concentration in the brain. For this reason, the validation of CT-based CSF segmentations should be performed, if possible, based on the former MRI technique. Here, to circumvent this problem in the absence of T_2-weighted MRI, we opted to compare ventricular CSF segmentations because brain ventricles are typically much larger than the CSF layer around the brain, especially in older adults. Nevertheless, future studies should strive to include T_2-weighted MRI when undertaking validation of CT segmentations.

CONCLUSION

The ability to segment soft brain tissues accurately from CT can substantially extend the utility of this important and cost-effective neuroimaging technique. Despite the limitations pertaining to the approach proposed here, our preliminary results indicate that reasonable segmentations of WM, GM and CSF can be obtained based on standard CT volumes of the human head. The methodological contributions described in this study can also be used as a foundation for the development of additional, more complex segmentation procedures for tasks such as the automated labeling of brain lobes and/or the identification of smaller structures such as gyri and sulci. Such refinements of our method, if feasible, would likely increase the utility of CT segmentation for brain imaging studies. Nevertheless, the accurate labeling of GM within thin gyri and of CSF within narrow sulci based on CT is likely to remain quite limited without substantial progress on CT technology to allow major improvements of image quality. When undertaking population-based studies of brain volumetrics calculated from CT data, researchers should duly account for the uncertainty of these measurements, especially in their statistical analyses. Such uncertainties are recapitulated by the magnitude of the variance in our Dice coefficients and Hausdorff distances, and this suggests that our ability to further refine our segmentation approach is largely predicated on the availability of CT head volumes with improved CNRs between WM and GM. MRI+CT data acquired from larger human samples are also required to improve the statistical estimates of our CT-based volume measurement errors relative to MRI.

AUTHOR CONTRIBUTIONS

AI conceived, funded and designed the study, implemented the segmentation approach, acquired imaging data, interpreted study results, wrote and coordinated the production of the manuscript. AM, KR, and NC contributed to the design of the study, analyzed imaging data, tabulated results, and contributed to their interpretation. DH contributed to the design of the study, identified eligible study participants, facilitated access to their neuroimaging data, and participated in the interpretation of study results. EL contributed to the design of the study, provided access to clinical data from eligible participants and participated in the interpretation of study results. All contributed approved the final version of the manuscript.

ACKNOWLEDGMENTS

This study was funded by the National Institutes of Health, grants R01 NS 100973 (to AI) and RF1 AG 054442 (subaward to AI). AI wishes to thank Caleb E. Finch, Hillard S. Kaplan, Gregory S. Thomas, M. Linda, and James D. Sutherland, and the other members of the Tsimané Health & Life History Project for useful discussions, suggestions, support and encouragement. The authors also thank study volunteers for their participation.

REFERENCES

Ashburner, J., and Friston, K. (1997). Multimodal image coregistration and partitioning—a unified framework. *Neuroimage* 6, 209–217. doi: 10.1006/nimg.1997.0290

Ashburner, J., and Friston, K. (2007). "Statistical parametric mapping," in *Segmentation. Statistical Parametric Mapping: The Analysis of Functional Brain Images*, eds K. Friston, J. Ashburner, S. Kiebel, T. Nichols, and W. Penny (London, UK: Academic Press), 81–91.

Ashburner, J., and Friston, K. J. (1999). Nonlinear spatial normalization using basis functions. *Hum. Brain Map.* 7, 254–266. doi: 10.1002/(SICI)1097-0193(1999)7:4<254::AID-HBM4>3.0.CO;2-G

Ashburner, J., and Friston, K. J. (2000). Voxel-based morphometry - the methods. *Neuroimage* 11, 805–821. doi: 10.1006/nimg.2000.0582

Ashburner, J., and Friston, K. J. (2005). Unified segmentation. *Neuroimage* 26, 839–851. doi: 10.1016/j.neuroimage.2005.02.018

Bier, G., Bongers, M. N., Ditt, H., Bender, B., Ernemann, U., and Horger, M. (2016). Enhanced gray-white matter differentiation on non-enhanced CT using a frequency selective non-linear blending. *Neuroradiology* 58, 649–655. doi: 10.1007/s00234-016-1674-1

Bishop, C. M. (1995). *Neural Networks for Pattern Recognition.* New York, NY: Oxford University Press.

CDC. (2010). *Number of magnetic resonance imaging (MRI) units and computed tomography (CT) scanners: Selected countries, selected years*, 1990–2007 (https://www.cdc.gov/nchs/data/hus/2010/120.pdf). ed Department of Health and Human Services (Washington, DC: CDC).

Christensen, G. E., Rabbitt, R. D., and Miller, M. I. (1994). 3D Brain mapping using a deformable neuroanatomy. *Phys. Med. Biol.* 39**,** 609–618. doi: 10.1088/0031-9155/39/3/022

Collins, D. L., Evans, A. C., Holmes, C., and Peters, T. M. (1995). Automatic 3D segmentation of neuro-anatomical structures from MRI. *Inform. Proc. Med. Imaging* 3**,** 139–152.

Craddock, C., Chen, M. Y., Dixon, R. L., Schlarb, C. A., and Williams, D. W. 3rd (2006). The effect of skull volume and density on differentiating gray and white matter on routine computed tomography scans of the head. *J. Comput. Assist. Tomogr.* 30**,** 734–738. doi: 10.1097/01.rct.0000216111.16774.d2

Dale, A. M., Fischl, B., and Sereno, M. I. (1999). Cortical surface-based analysis. i. segmentation and surface reconstruction. *Neuroimage* 9**,** 179–194. doi: 10.1006/nimg.1998.0395

Diwakar, M., and Kumar, M. (2014). "CT Image noise reduction based on adaptive wiener filtering with wavelet packet thresholding," in *2014 International Conference on Parallel, Distributed and Grid Computing* (Solan: PDGC), 94–98.

Dubuisson, M.-P., and Jain, A. K. (1994). A modified Hausdorff distance for object matching. *Proc. Intl. Conf. Patt. Recog.* 1**,** 566–568. doi: 10.1109/ICPR.1994.576361

Eggert, L. D., Sommer, J., Jansen, A., Kircher, T., and Konrad, C. (2012). Accuracy and reliability of automated gray matter segmentation pathways on real and simulated structural magnetic resonance images of the human brain. *PLoS ONE* 7**:**e45081. doi: 10.1371/journal.pone.0045081

Evans, A. C., Kamber, M., Collins, D. L., and Macdonald, D. (1994). An MRI-based probabilistic atlas of neuroanatomy. *Mag. Reson. Scan. Epilepsy* 264**,** 263–274. doi: 10.1007/978-1-4615-2546-2_48

Ewert, S., Horn, A., Finkel, F., Li, N., Kuhn, A. A., and Herrington, T. M. (2019). Optimization and comparative evaluation of nonlinear deformation algorithms for atlas-based segmentation of DBS target nuclei. *Neuroimage* 184**,** 586–598. doi: 10.1016/j.neuroimage.2018.09.061

Fischl, B., Sereno, M. I., and Dale, A. M. (1999). Cortical surface-based analysis. II: inflation, flattening, and a surface-based coordinate system. *Neuroimage* 9**,** 195–207. doi: 10.1006/nimg.1998.0396

Friston, K. (2007). "A short history of SPM," in *Statistical Parametric Mapping. The Analysis of Functional Brain Images* (Academic Press), 3–9. doi: 10.1016/B978-012372560-8/50001-2

Fushimi, Y., Miki, Y., Urayama, S., Okada, T., Mori, N., Hanakawa, T., et al. (2007). Gray matter-white matter contrast on spin-echo T1-weighted images at 3 T and 1.5 T: a quantitative comparison study. *Eur. Radiol.* 17**,** 2921–2925. doi: 10.1007/s00330-007-0688-9

Grabner, G., Janke, A. L., Budge, M. M., Smith, D., Pruessner, J., and Collins, D. L. (2006). Symmetric atlasing and model based segmentation: an application to the hippocampus in older adults. *Med. Image Comput. Comput. Assist. Interv.* 9**,** 58–66. doi: 10.1007/11866763_8

Gupta, V., Ambrosius, W., Qian, G., Blazejewska, A., Kazmierski, R., Urbanik, A., et al. (2010). Automatic segmentation of cerebrospinal fluid, white and gray matter in unenhanced computed tomography images. *Acad. Radiol.* 17**,** 1350–1358. doi: 10.1016/j.acra.2010.06.005

Haydel, M. J., Preston, C. A., Mills, T. J., Luber, S., Blaudeau, E., and Deblieux, P. M. (2000). Indications for computed tomography in patients with minor head injury. *N. Engl. J. Med.* 343**,** 100–105. doi: 10.1056/NEJM200007133430204

Iscan, Z., Jin, T. B., Kendrick, A., Szeglin, B., Lu, H., Trivedi, M., et al. (2015). Test-retest reliability of freesurfer measurements within and between sites: effects of visual approval process. *Hum. Brain Map.* 36**,** 3472–3485. doi: 10.1002/hbm.22856

Jenkinson, M., Beckmann, C. F., Behrens, T. E., Woolrich, M. W., and Smith, S. M. (2012). FSL. *Neuroimage* 62**,** 782–790. doi: 10.1016/j.neuroimage.2011.09.015

Kaplan, H., Thompson, R. C., Trumble, B. C., Wann, L. S., Allam, A. H., Beheim, B., et al. (2017). Coronary atherosclerosis in indigenous South American Tsimane: a cross-sectional cohort study. *Lancet* 389**,** 1730–1739. doi: 10.1016/S0140-6736(17)30752-3

Kemmling, A., Wersching, H., Berger, K., Knecht, S., Groden, C., and Nolte, I. (2012). Decomposing the hounsfield unit: probabilistic segmentation of brain tissue in computed tomography. *Clin. Neuroradiol.* 22**,** 79–91. doi: 10.1007/s00062-011-0123-0

Li, Z. L., Li, H., Zhang, K., Li, W. J., Chen, X., Wu, B., et al. (2014). Improvement of image quality and radiation dose of CT perfusion of the brain by means of low-tube voltage (70 kV). *Eur. Radiol.* 24**,** 1906–1913. doi: 10.1007/s00330-014-3247-1

Manniesing, R., Oei, M. T., Oostveen, L. J., Melendez, J., Smit, E. J., Platel, B., et al. (2017). White matter and gray matter segmentation in 4D computed tomography. *Sci. Rep.* 7**:**119. doi: 10.1038/s41598-017-00239-z

McGraw, K. O., and Wong, S. P. (1996). Forming inferences about some intraclass correlation coefficients. *Psychol. Methods* 1, 30–46. doi: 10.1037/1082-989X.1.1.30

Pelc, N. J. (2014). Recent and future directions in CT imaging. *Ann. Biomed. Eng.* 42**,** 260–268. doi: 10.1007/s10439-014-0974-z

Rapalino, O., Kamalian, S., Kamalian, S., Payabvash, S., Souza, L. C., Zhang, D., et al. (2012). Cranial CT with adaptive statistical iterative reconstruction: improved image quality with concomitant radiation dose reduction. *AJNR Am. J. Neuroradiol.* 33**,** 609–615. doi: 10.3174/ajnr.A2826

Seo, Y., Mari, C., and Hasegawa, B. H. (2008). Technological development and advances in single-photon emission computed tomography/computed tomography. *Semin. Nucl. Med.* 38**,** 177–198. doi: 10.1053/j.semnuclmed.2008.01.001

Shou, H., Eloyan, A., Lee, S., Zipunnikov, V., Crainiceanu, A. N., Nebel, N. B., et al. (2013). Quantifying the reliability of image replication studies: the image intraclass correlation coefficient (I2C2). *Cogn. Affect Behav. Neurosci.* 13**,** 714–724. doi: 10.3758/s13415-013-0196-0

Shrout, P. E., and Fleiss, J. L. (1979). Intraclass correlations: uses in assessing rater reliability. *Psychol. Bull.* 86**,** 420–428. doi: 10.1037/0033-2909.86.2.420

Velasco-Annis, C., Akhondi-Asl, A., Stamm, A., and Warfield, S. K. (2017). Reproducibility of brain MRI segmentation algorithms: empirical comparison of local MAP PSTAPLE, FreeSurfer, and FSL-FIRST. *J. Neuroimaging* 28, 162–172. doi: 10.1111/jon.12483

Wedderburn, R. W. M. (1974). Quasi-likelihood functions, generalized linear-models, and Gauss-Newton method. *Biometrika* 61**,** 439–447.

Williamson, C., Morgan, L., and Klein, J. P. (2017). Imaging in neurocritical care practice. *Semin. Respir. Crit. Care Med.* 38**,** 840–852. doi: 10.1055/s-0037-1608770

Yu, L., Liu, X., Leng, S., Kofler, J. M., Ramirez-Giraldo, J. C., Qu, M., et al. (2009). Radiation dose reduction in computed tomography: techniques and future perspective. *Imaging Med.* 1**,** 65–84. doi: 10.2217/iim.09.5

Conflict of Interest Statement: The authors declare that the research was conducted in the absence of any commercial or financial relationships that could be construed as a potential conflict of interest.

Copyright © 2019 Irimia, Maher, Rostowsky, Chowdhury, Hwang and Law. This is an open-access article distributed under the terms of the Creative Commons Attribution License (CC BY). The use, distribution or reproduction in other forums is permitted, provided the original author(s) and the copyright owner(s) are credited and that the original publication in this journal is cited, in accordance with accepted academic practice. No use, distribution or reproduction is permitted which does not comply with these terms.

frontiers in Neuroinformatics

ORIGINAL RESEARCH
published: 22 March 2019
doi: 10.3389/fninf.2019.00014

Visbrain: A Multi-Purpose GPU-Accelerated Open-Source Suite for Multimodal Brain Data Visualization

Etienne Combrisson[1], Raphael Vallat[2], Christian O'Reilly[3], Mainak Jas[1], Annalisa Pascarella[4], Anne-lise Saive[1], Thomas Thiery[1], David Meunier[5], Dmitrii Altukhov[6,7], Tarek Lajnef[1,8], Perrine Ruby[2], Aymeric Guillot[9] and Karim Jerbi[1,10]*

[1] Computational and Cognitive Neuroscience Lab (CoCo Lab), Psychology Department, University of Montreal, Montreal, QC, Canada, [2] Lyon Neuroscience Research Center, Brain Dynamics and Cognition team, INSERM UMRS 1028, CNRS UMR 5292, Université Claude Bernard Lyon 1, Université de Lyon, Lyon, France, [3] Blue Brain Project, École Polytechnique Fédérale de Lausanne, Geneva, Switzerland, [4] Institute for Applied Mathematics Mauro Picone, National Research Council, Rome, Italy, [5] Aix Marseille Univ, CNRS, INT, Inst Neurosci Timone, Marseille, France, [6] National Research University Higher School of Economics, Moscow, Russia, [7] MEG Center, Moscow State University of Pedagogics and Education, Moscow, Russia, [8] Center for Advanced Research in Sleep Medicine, Hôpital du Sacré-Coeur de Montréal, Montreal, QC, Canada, [9] Inter-University Laboratory of Human Movement Biology, University of Lyon, University Claude Bernard Lyon 1, Villeurbanne, France, [10] MEG Unit, University of Montreal, Montreal, QC, Canada

OPEN ACCESS

Edited by:
Sean L. Hill, Krembil Centre for Neuroinformatics, Centre for Addiction and Mental Health, Canada

Reviewed by:
Chaitanya Chintaluri, University of Oxford, United Kingdom
Rembrandt Bakker, Radboud University Nijmegen, Netherlands

***Correspondence:**
Etienne Combrisson
e.combrisson@gmail.com

Received: *27 September 2018*
Accepted: *19 February 2019*
Published: *22 March 2019*

Citation:
Combrisson E, Vallat R, O'Reilly C, Jas M, Pascarella A, Saive A, Thiery T, Meunier D, Altukhov D, Lajnef T, Ruby P, Guillot A and Jerbi K (2019) Visbrain: A Multi-Purpose GPU-Accelerated Open-Source Suite for Multimodal Brain Data Visualization. Front. Neuroinform. 13:14. doi: 10.3389/fninf.2019.00014

We present Visbrain, a Python open-source package that offers a comprehensive visualization suite for neuroimaging and electrophysiological brain data. Visbrain consists of two levels of abstraction: (1) objects which represent highly configurable neuro-oriented visual primitives (3D brain, sources connectivity, etc.) and (2) graphical user interfaces for higher level interactions. The object level offers flexible and modular tools to produce and automate the production of figures using an approach similar to that of Matplotlib with subplots. The second level visually connects these objects by controlling properties and interactions through graphical interfaces. The current release of Visbrain (version 0.4.2) contains 14 different objects and three responsive graphical user interfaces, built with PyQt: *Signal*, for the inspection of time-series and spectral properties, *Brain* for any type of visualization involving a 3D brain and *Sleep* for polysomnographic data visualization and sleep analysis. Each module has been developed in tight collaboration with end-users, i.e., primarily neuroscientists and domain experts, who bring their experience to make Visbrain as transparent as possible to the recording modalities (e.g., intracranial EEG, scalp-EEG, MEG, anatomical and functional MRI). Visbrain is developed on top of VisPy, a Python package providing high-performance 2D and 3D visualization by leveraging the computational power of the graphics card. Visbrain is available on Github and comes with a documentation, examples, and datasets (http://visbrain.org).

Keywords: visualization, neuroscience, python, open-source, brain, OpenGL, EEG, MEG

INTRODUCTION

The aim of scientific visualization is to graphically illustrate datasets—which are can be highly complex- in order to provide a better understanding and facilitate the interpretation of the data. As scientific technologies continue to evolve, it becomes increasingly important to develop up-to-date and comprehensive visualization software capable of handling complex and large datasets. This is especially true in the field of neuroscience, which involves a myriad of neural recording types, and consequently, a wide and diverse range of possible data representations.

To date, Matlab (Mathworks, 2012) is one of the most widely-used commercial programming language for brain data analysis and visualization, thanks to a large number of toolboxes such as SPM (Penny et al., 2011), Brainstorm[1] (Tadel et al., 2011), EEGlab[2] (Delorme and Makeig, 2004) and Fieldtrip[3] (Oostenveld et al., 2011). Alternative visualization solutions that run on non-commercial open-source programming environments, such as Python, are rare. These include high-quality packages such as MNE[4] (Gramfort et al., 2013), PySurfer[5], Nilearn[6] (Abraham et al., 2014) or 3d slicer (Fedorov et al., 2012). Both MNE and Nilearn rely on Matplotlib for visualizations which is not suited for real-time interactions of brain imaging data involving thousands of data points. In addition, MNE also relies on PySurfer for 3D visualizations. PySurfer is built on top of Mayavi which contains a powerful rendering engine and allows smooth interactions. However, some issues have been reported when installing Mayavi, (which uses VTK), which may affect its user-friendliness.

In this context, we propose a Python open-source software called Visbrain, distributed under a Berkeley Software Distribution (BSD) license and dedicated to the visualization of neuroscientific data. Visbrain is built on top of VisPy (Campagnola et al., 2015), a high-performance visualization library that leverages the Graphics Processing Units (GPU). As a result, Visbrain efficiently handles the visualization of large and complex multi-dimensional datasets. The purpose of Visbrain is two-fold: (1) To provide within a common framework several Python-based visualization tools for neuroscientific data, (2) To allow users, including those with little or no programming skills access to high-end visualization functions, through a comprehensive documentation[7] and a user-friendly API.

Many scenarii for the use of Visbrain are possible. For instance, a user with a set of intracranial EEG data could use visbrain to visualize in a first subplot the location of electrodes (e.g., NumPy array) either in individual or standard MNI space. Next, in a second subplot, the user may choose to project the data onto the cortical mesh (e.g., gamma power, *t*-values, decoding accuracies, etc). Additional subplots can be added, for example, to include data from other subjects, or various contrasts across experimental conditions. Because figures are dynamic, subplots can be added on the fly with various visualization objects such as connectivity, region of interest etc. The same procedure could be applied to M/EEG source data. Finally, each subplot can be animated and exported into a video file (e.g., animated GIF) or in a standard high-resolution publication-ready image file (e.g., PNG, JPG, TIFF).

With the release of this package and publication of this paper, we hope to develop a community of users that could facilitate extending and adapting this software to better cover the needs of researchers in neuroscience.

MATERIALS AND METHODS

The philosophy of Visbrain is to provide elementary visualization building blocks which can easily be combined in a modular manner, and to design a flexible and responsive graphical user interface (GUI) which can be used to change the active visualization parameters in real time. Visbrain is not designed to duplicate data analysis functions which are already available in well-established packages such as scipy[8], pandas[9], SciKits[10], or statsmodels[11], except when it serves illustration purposes.

Programming Language and Code Guidelines

Although we initially considered Matlab and Julia (Bezanson et al., 2017) as language for Visbrain given their high level of abstraction, we finally chose Python since this mature and easy-to-learn language benefits from a large range of high-quality packages, a thriving and rapidly growing user community, and thorough documentation. Python software packages are portable, cross-platform, and easily distributed. More importantly, Python is free, open source, open access, and is thereby ideal for open science.

From a programming perspective, we paid particular attention to avoid memory-intensive data copy and to enable loading and processing of large dataset. Visbrain is hosted on GitHub[12], and is documented using NumPyDoc, a Sphinx extension to generate NumPy-like documentation. We also provide illustrative examples and datasets. Code blocks are well-commented and follow PEP8 guidelines for code readability. Finally, package installation and features are tested under Linux and Windows through a continuous integration protocol (current coverage >85%).

Dependencies

As Python 2.7 will not be maintained past 2020, Visbrain is a pure Python package for Python 3 only. Here is the list of Visbrain's dependencies are listed in **Table 1**.

[1]http://neuroimage.usc.edu/brainstorm/
[2]https://sccn.ucsd.edu/eeglab/
[3]http://www.fieldtriptoolbox.org/
[4]https://martinos.org/mne/stable/index.html
[5]https://pysurfer.github.io/
[6]http://nilearn.github.io/
[7]http://visbrain.org
[8]https://www.scipy.org/
[9]https://pandas.pydata.org/
[10]http://scikits.appspot.com/
[11]http://www.statsmodels.org/stable/index.html
[12]https://github.com/EtienneCmb/visbrain

In addition to the above-mentioned packages, the use of some specific functionalities will require a few more dependencies. These include:

- Pandas (McKinney, 2011): for importing and exporting region of interest defined in the brain
- MNE-Python (Gramfort et al., 2013): alternative for loading sleep data files instead of using functions included in Visbrain
- Nibabel: for supporting certain file formats
- Tensorpac[13] for computing phase-amplitude coupling
- Imageio: for Graphics Interchange Format (GIF) export

Finally, the Visbrain package can be downloaded using the python package manager pip[14].

TABLE 1 | List of dependencies and package version.

Package name	Purpose	Version
NumPy	Scientific computing	≥1.13
SciPy	Scientific computing	-
PyQt5	Graphical user interfaces creation	-
VisPy	Graphics rendering	≥0.5.2
Matplotlib	Colors/colormaps related functions	≥1.5.5
Pillow	Screenshots and image file format support	-
PyOpenGL	Python binding to OpenGL	-

GPU-Powered High-Speed Graphics

As the size, dimensionality and complexity of brain data continues to increase, data visualization tools have to be increasingly efficient, in particular if real-time interaction is needed. For example, high-density EEG or full-night sleep recordings can be associated with files of up to tens of gigabytes. Matplotlib, which is one of the most

[13]https://github.com/EtienneCmb/tensorpac
[14]https://pypi.org/project/visbrain/

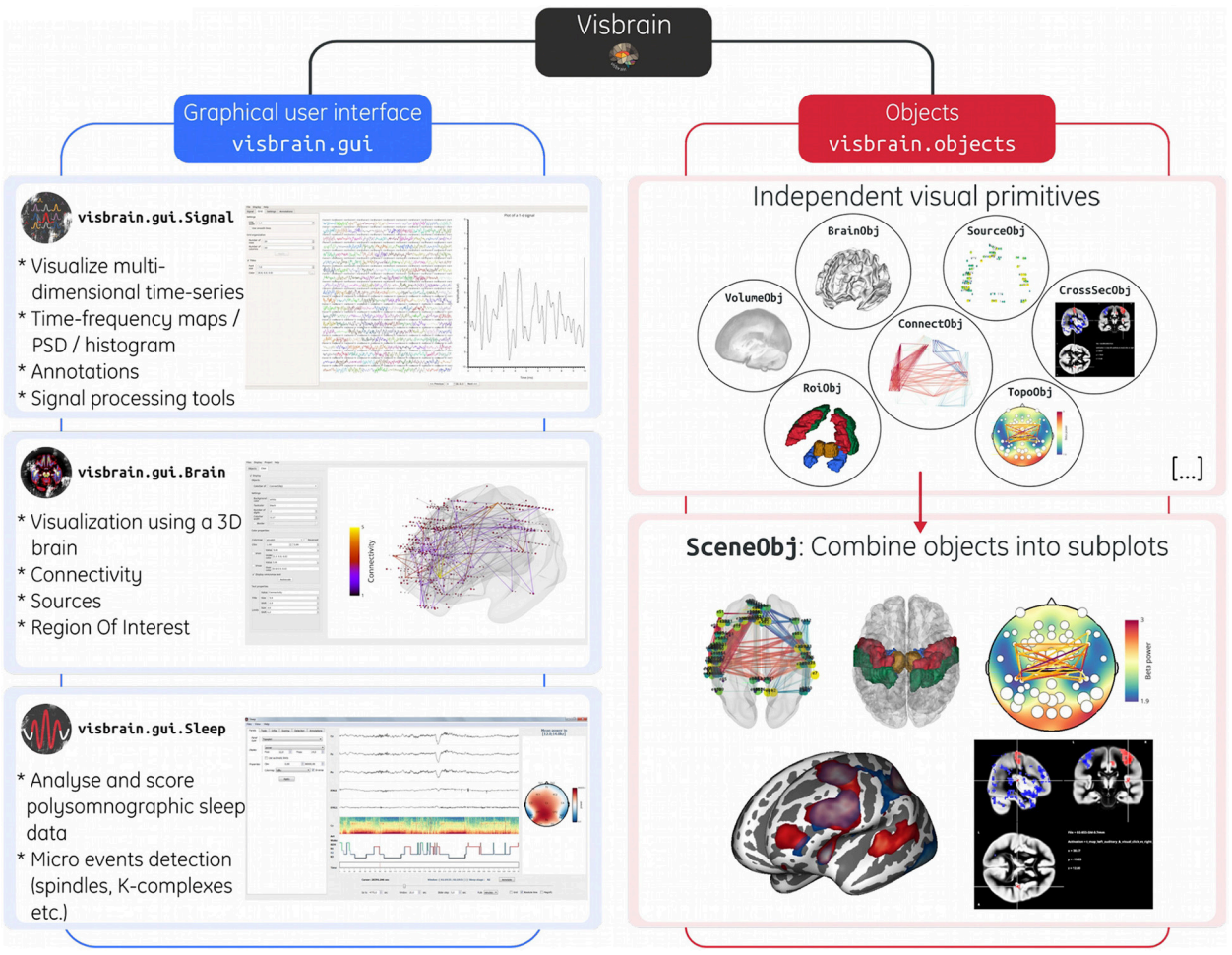


FIGURE 1 | Architecture of the Visbrain software. The left branch in blue illustrates the three included graphical user interfaces (*Signal, Brain,* and *Sleep* and). For advanced users that want to interact programmatically with Visbrain, the right branch in red shows 6 of the 14 implemented objects in Visbrain. These objects are presented in circles to emphasize the fact that each of them is independent. Then, using the scene (*SceneObj*) these objects can be superimposed or juxtaposed into subplots inside a unique figure. The scene offers a finer grain control over the layout. Note that each subplot is interactive, meaning that rotation, translation and zoom can be applied in real time on each subplot.

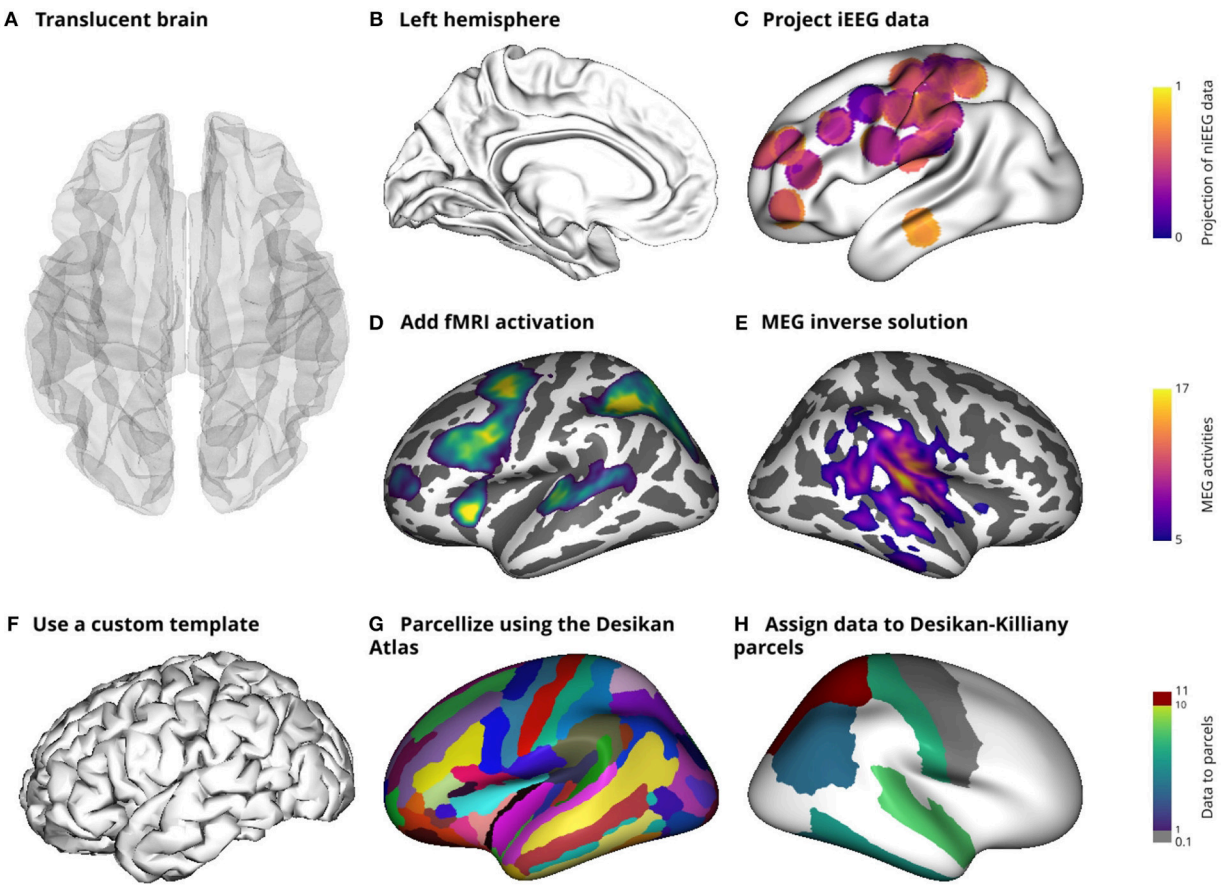


FIGURE 2 | Illustration of the main features of the brain object (*BrainObj*). This object delivers some basic features as the possibility to display a translucent or opaque brain mesh **(A)** or to pick only one hemisphere **(B)**. Intracranial data can also be projected onto the surface **(C)** and other recording modalities can also be displayed [fMRI activation **(D)** and MEG data **(E)**]. In addition, parcels can also be used **(G)** and data can be assigned to those parcels **(H)**. All of those subplots use MNI templates included with Visbrain, but the user can also define and save a custom template by defining subsets of vertices and faces **(F)**.

famous Python plotting libraries (Hunter, 2007), is primarily designed to provide static publication-quality figures and is unfortunately currently not suited for handling large data and user interactions. Seaborn[15], which is built on top of Matplotlib is also not a viable option for the same reasons. Among libraries with mature development and real-time interaction, we also considered PyQtGraph[16] and Glumpy[17] (Rougier, 2015). Both options could certainly have been excellent alternatives. We rather considered the VisPy package (Campagnola et al., 2015), which is a high-performance interactive 2D/3D data visualization library leveraging the computational power of the GPU through OpenGL. The choice of VisPy was made mainly for the ease of installation and also because it is a combined effort by the authors of several visualization libraries (PyQtGraph, VisVis, Galry, and Glumpy)

The use of VisPy library is a critical component of Visbrain. By offloading most of the graphical rendering cost to the GPU, VisPy allows real-time interactivity, even for large datasets, while at the same time minimizing CPU overhead. As a result, Visbrain is able, on any modern-day laptop, to efficiently display large datasets and allows for real-time user interactions.

Graphical Interface and User Interactions

Scientific visualization software often come with easy-to-use GUIs. Although most of the analyses can be performed in the command-line, such interfaces often greatly enhance the user experience. GUIs also allow users with no or little programming knowledge to use the software, making it more accessible to the scientific community.

To embed VisPy graphics in full-featured widgets, we chose to use the cross-platform C++ GUI toolkit Qt[18], for which Python

[15]http://seaborn.pydata.org
[16]http://pyqtgraph.org/
[17]https://glumpy.github.io/

[18]https://www.qt.io/

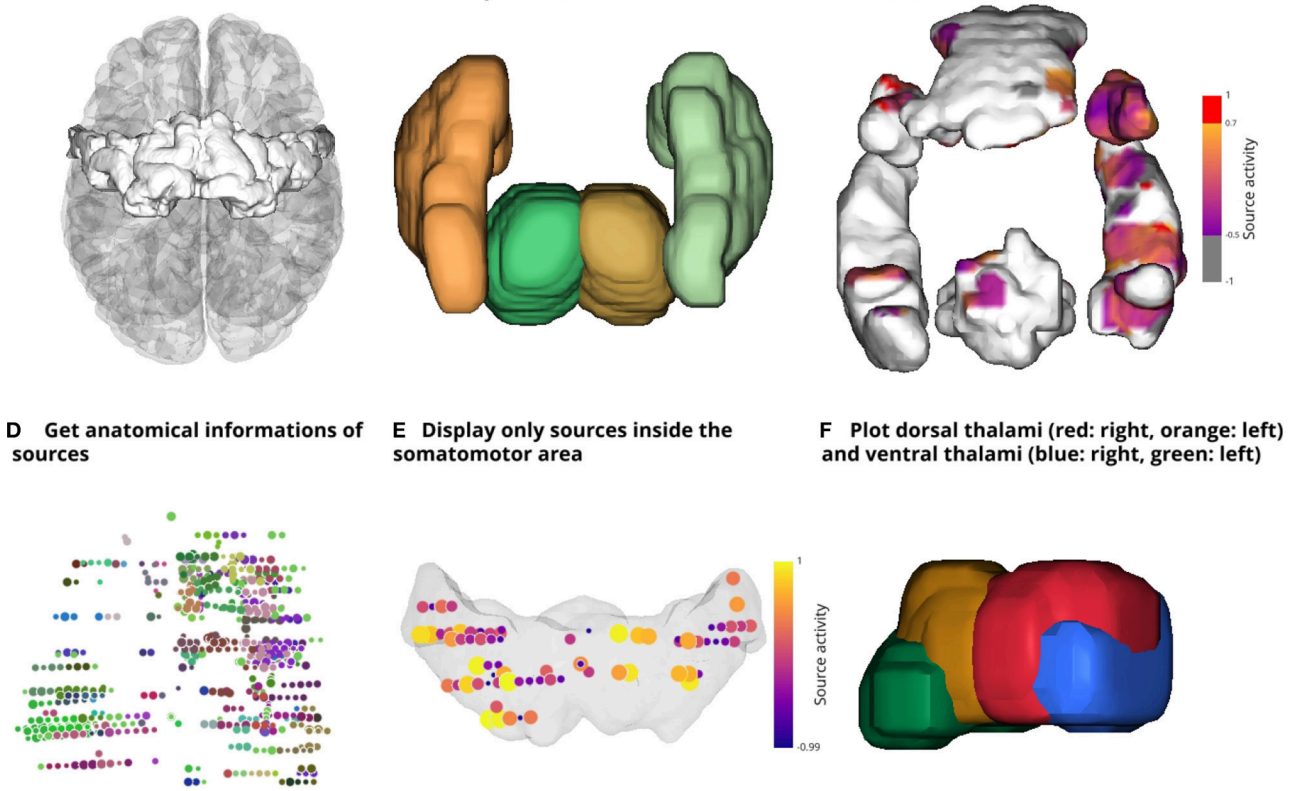


FIGURE 3 | Illustration of the main features of the region of interest (ROI) object (*RoiObj*). Visbrain provides several default atlases that can be used to extract the mesh of specific regions **(A**,**B**,**F)**. In addition, the source object (*SourceObj*) can interact with the ROI object. For example, sources' activity can be projected onto the mesh **(C)**. The *RoiObj* can also be used to identify in which region a source is contained. Here, sources are color-coded according to the MIST **(D)** but a table with all of the anatomical informations can also be exported. Finally, it is also possible to keep only the sources that fall into the volume formed by the mesh **(E)**.

bindings are available (i.e., PyQt & PySide). Specifically, GUIs of the different Visbrain modules were built using the Qt designer tool and were then converted to Python code using PyQt.

Documentation and Examples

Visbrain comes with a detailed step-by-step documentation built with Sphinx[19] and hosted on the Visbrain website[20]. This documentation describes how to install Visbrain and use its modules. We also provide a description of GUI components and inputs for all class modules. Moreover, we provide a description of each graphical element using tooltips that appear when hovering corresponding widgets with the cursor. Lastly, we provide examples[21] and python scripts that can be downloaded from the website. Some examples requires additional data to be fully functionals. Those data are either generated or comes from other open-sources softwares (i.e., MNE-Python, PySurfer, and Nilearn).

[19]http://www.sphinx-doc.org/en/stable/
[20]http://visbrain.org
[21]http://visbrain.org/auto_examples/index.html

RESULTS

From the user's perspective, Visbrain is subdivided into two main levels: *(1) Objects:* independent visual primitives that can be defined and used without the need for a GUI. *(2) Graphical user interface:* a user-friendly interface built on top of Visbrain objects for interactive visualization. The visbrain architecture is summarized in **Figure 1**.

Objects

Objects represent the lowest level of Visbrain and can be considered as neuro-oriented visual primitives. Each object is highly configurable and serves a single visualization purpose. For example, the brain object (*BrainObj*) is used to display 3D brains. The definition of every object is independent, but some of them can interact together. For example, the activity of a source object can be projected onto the surface of the brain (see section Source object for the description of the projection). Those primitives bring modularity to Visbrain.

Those objects can then be superimposed and juxtaposed inside subplot (see section Scene object). It should be noted

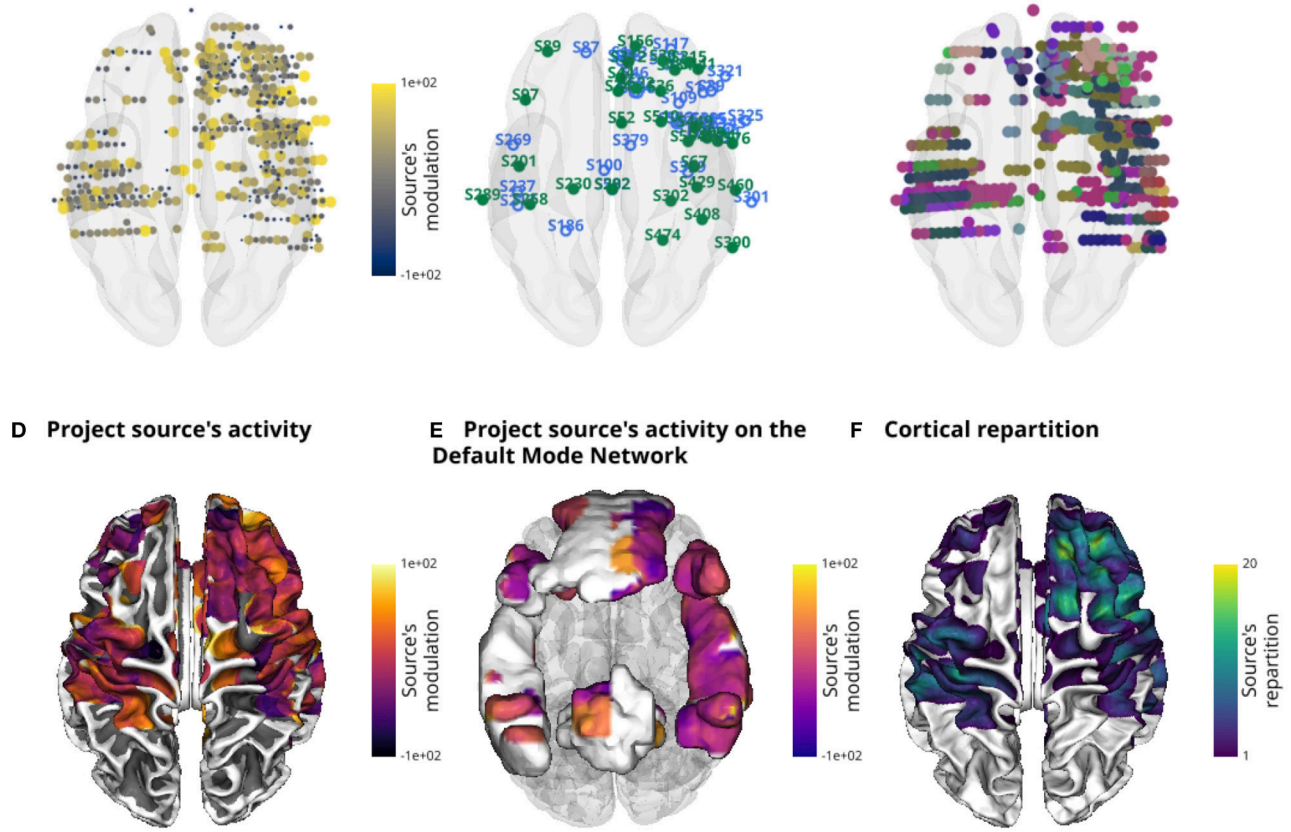


FIGURE 4 | Illustration of the main features of the source object (*SourceObj*) using an intracranial dataset. Additional data can be assigned to sources and the color can either be individually defined or based on a colormap **(A)**. A text can also be attached to sources **(B)**. In a similar way to **Figure 3D**, here, sources are colored according to Brodmann areas **(C)**. The data attached to sources in **(A)** is then projected onto the surface of the brain **(D)** or onto the surface of the default mode network (DMN) **(E)**. Finally, the cortical repartition **(F)** is the number of contributing sources per vertex. It can be an interesting feature to estimate the number of sources that have contributed to each point of the cortical mesh when projecting source's data.

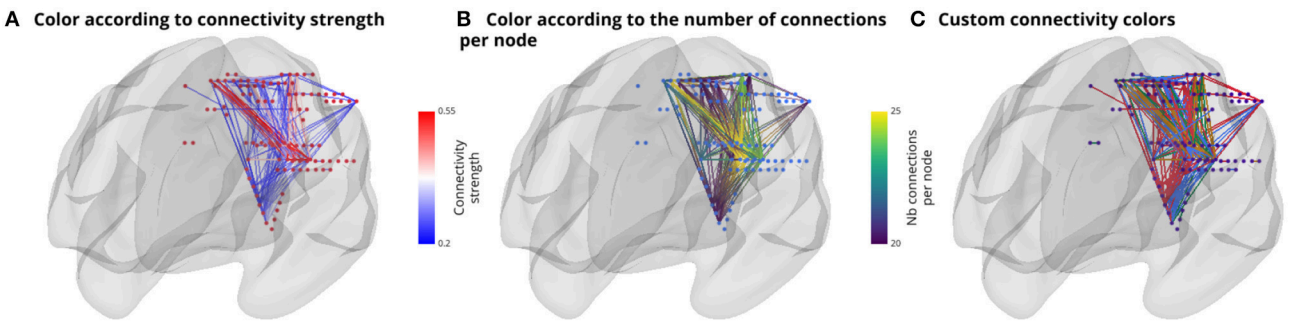


FIGURE 5 | Illustration of the main features of the connectivity object (*ConnectObj*). The three sub-visuals express three coloring methods. The first method **(A)** is simply to color edges by connectivity strength. The second **(B)** color edges according to the number of connections per node and finally, **(C)** use colors that are manually defined.

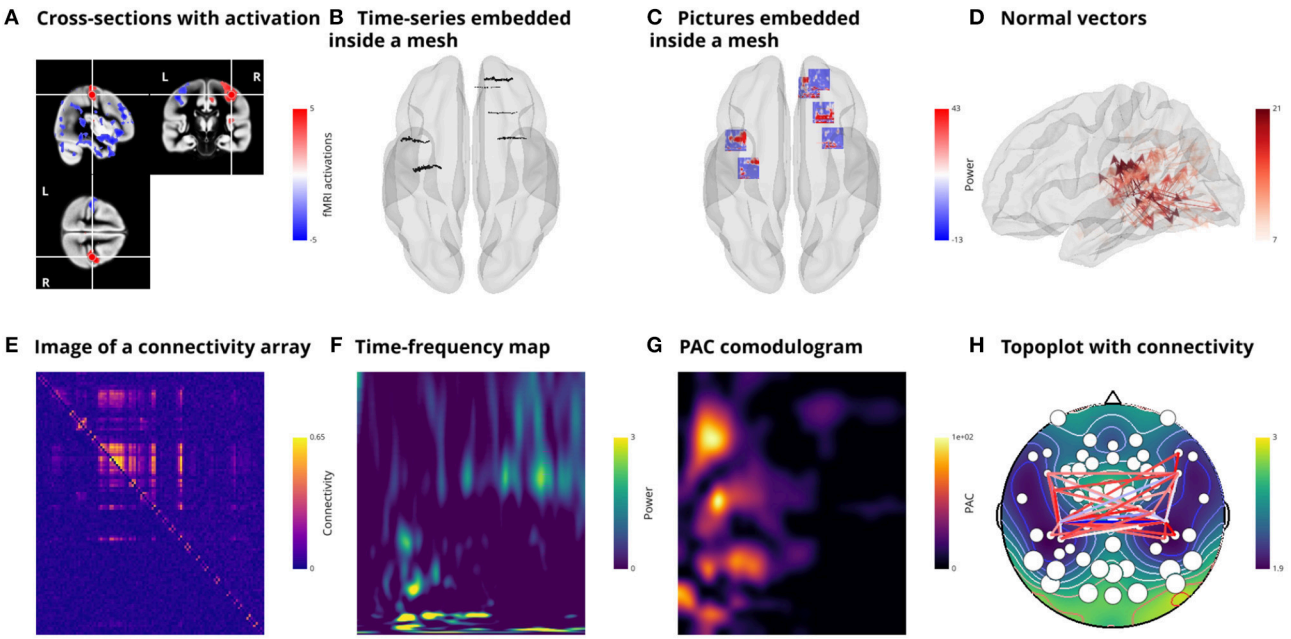


FIGURE 6 | Illustration of additional implemented objects. **(A)** cross-section of fMRI data (*CrossSecObj*). The cross-section can be used to load background anatomical images and superimposed activations. It is also possible to move around the volume by clicking on it (still under development). Subplots **(B, C)** respectively illustrate time-series (*TimeSeries3DObj*) and pictures (*Picture3DObj*) embedded inside the mesh. Here, the pictures are time-frequency maps. **(D)** Plot vector-valued (*VectorObj*) MEG inverse solution. Visbrain also contains objects to plot images (*ImageObj*) as illustrated in **(E)** with a connectivity matrix, time-frequency maps (*TimeFrequencyObj*) **(F)**, phase-amplitude coupling (*PacmapObj*) **(G)**. Finally, the *TopoObj* can be used to plot topographic representations of EEG data, draw levels and connectivity links between EEG sensors **(H)**.

that **Figures 2–6**, that combine these objects, were not post-paginated (i.e., static rendering), but were generated from the scene object as real-time interactive figures. Finally, objects can also be animated, either independently or within subplots. Furthermore, such animations can be exported as a gif file.

Implemented Objects

The current version of Visbrain implement many classes, among them 14 defines visual objects that can be directly imported from *visbrain.objects* and be added to a scene. The API for interacting with those primitives are described inside the documentation[22] (see **Table 2** for a list of the visual objects).

TABLE 2 | List of the 14 visual objects implemented in Visbrain.

Object name	Description
BrainObj	3D brain with vertices colored according to data
ColorbarObj	Colorbar associated with another object
ConnectObj	3D connectivity lines between nodes
CrossSecObj	Interactive fMRI cross-section (axial, sagittal and coronal views)
HypnogramObj	Hypnogram for sleep data
ImageObj	Images or 2D arrays
PacmapObj	Phase-amplitude coupling of a single time-series (PAC)
Picture3DObj	Images distributed in 3D space
RoiObj	Volumetric region of interest
SourceObj	Sources distributed in 3D space (intracranial/MEG/EEG)
TimeFrequencyObj	Time-frequency map of a single time-series
TimeSeries3DObj	Time-series distributed in 3D space
VectorObj	3D vectors
VolumeObj	Volumetric data

Illustrations of the Main Functionalities of the Objects

In this section, we provide a non-exhaustive review of the main features of some of the most used objects.

Scene object

Probably one of the most useful objects of Visbrain is called the scene (*SceneObj*). The scene is not a visual primitive in the sense that it cannot be used to represent any kind of brain data. Instead, it is an equivalent of Matplotlib's subplots meaning that objects can be superimposed inside sub visuals or displayed side by side. While requiring from the user some modest programming skills, the scene presents three major advantages: 1) it is undoubtedly a more flexible way to meet some specific visualization needs, 2) scenes can be integrated inside loops, on a local computer or on a distant server which means that the production of figures can easily be automated,3) the layout of figures for scientific publications can be assessed using this scene and 4) subplots remains interactives which allow the user to continue to interact

[22]http://visbrain.org/api.html#objects

with each object independently. **Figures 2–6** are defined using the *SceneObj* and the **code snippet 1** illustrates a basic example of how to use the scene object to define the layout of a figure.

```
import numpy as np
from visbrain.objects import BrainObj, SourceObj, SceneObj

# Define the scene
sc = SceneObj()
# Define two brain objects with, respectively only the left and right hemisphere
b_left = BrainObj('white', hemisphere='left', translucent=False)
b_right = BrainObj('white', hemisphere='right', translucent=True)
# Define random MNI coordinates for 100 sources / intracranial sites. We
# We then define a source object
xyz = np.random.uniform(0, 50, (100, 3))
s_obj = SourceObj('sources', xyz)
# Add these two brain objects and sources to the scene and to different subplots
sc.add_to_subplot(b_left, row=0, col=0, rotate='right', title='Left hemisphere')
sc.add_to_subplot(b_right, row=0, col=1, rotate='left', title='Right
hemisphere')
sc.add_to_subplot(s_obj, row=0, col=1)
# Finally, display the scene
sc.preview()
```

Code Snippet 1 | Display the left and right hemispheres into two separate subplots along with random MNI sources/contacts/electrodes.

Brain object

The brain object (*BrainObj*) can be used for every scenario where a 3D brain mesh is needed. Left and right hemispheres can be individually displayed on a translucent or opaque mesh. In addition, overlays of data can also be added to the mesh to illustrate fMRI, M/EEG or intracranial activations. The brain object capabilities are summarized in **Figure 2**.

Region of interest object.

Regions of interest (ROI) are labeled volumes, i.e. a 3D array of voxels associated with an anatomical label (e.g., "Somatosensory cortex"). By default, Visbrain supports Brodmann areas, the Automated Anatomical Labeling (AAL; Tzourio-Mazoyer et al., 2002), the Talairach atlas (Talairach and Tournoux, 1993) and the Multiresolution Intrinsic Segmentation Template (MIST; Urchs et al., 2017). New ROIs can also be defined by providing a 3D array for the volume and labels. The *RoiObj* provide the users with an interface to the volume and let them extract the mesh of a specific region and assign different colors to it. The **code snippet 2** shows how to extract the mesh of the thalamus and **Figure 3** demonstrates some core features of this object.

```
from visbrain.objects import RoiObj

# Load the AAL atlas
aal = RoiObj('aal')
# Get all labels included with the volume
labels = aal.get_labels()
print(labels)
# Find the integer index of the thalamus
idx = aal.where_is('Thalamus')
# Extract the mesh of the thalamus
aal.select_roi(idx)
# Display thalamus
 aal.preview()
```

Code Snippet 2 | Display the left and right thalamus

Source object

The source object (*SourceObj*), depending on the recording modality can either represent intracranial recording sites, M/EEG sensors or reconstructed source activity. A text and marker color can also be assigned to each source. In addition, data can be provided to those sources to have marker radius proportional to the data.

Another useful and relatively rare feature among existing software is the ability to use the source object to project intracranial data onto a mesh (e.g the cortical surface of the brain or onto ROI). Usually, the implantation of intracranial electrodes is subject dependent, which then poses a problem to visualize the results across subjects. Cortical projections can solve this limitation and have been previously used (Combrisson et al., 2017a). When projecting the data, each vertex in the mesh can be considered a bin which simply accumulates the data (e.g. beta power) from nearby intracranial sites. The data from all sites that are under a certain radius (10 mm by default) contribute to this bin. It is what gives the circular aspect to this projection (see **Figure 2C**). Instead of projecting data, it is also possible to project the number of sources that contribute to each point of the mesh. In this case, the color indicates how many sources participated. Finally, the last feature that we want to point out is the possibility to get anatomical informations on sources using the ROI object. For example, this can be used to deduce in which Brodmann area a source (e.g., or an electrode) is contained. Those functionalities are presented in **Figure 4**.

Connectivity object

The connectivity object (*ConnectObj*) is used to draw connectivity lines between nodes. We provide three coloring methods: 1) set color to the edges according to connectivity strength, 2) set color to the node according to the number of connections per node or 3) set color of edges manually. **Figure 5** shows an example of those differences in coloring methods. Display of directional connectivity is still an experimental feature and therefore is not presented.

Other objects

Visbrain contains several other objects serving various purposes, such as drawing vectors, displaying images, time-frequency maps, and phase-amplitude coupling comodulograms. For EEG recordings, topographic representations such as cross-sections previously shown for anatomical and functional MRI can also be plotted. **Figure 6** summarizes the use of these objects.

For a list of all supported data types for the various objects we refer the reader to the online API documentation[23]

GUI Based Interfaces

The main objective of GUIs is to connect and centralize the main features of the smaller visualization bricks. At the moment, Visbrain contains three interfaces:

- ***Signal*:** for the inspection of time-series and spectral properties (PSD power and time-frequency map decomposition, phase-amplitude coupling,...)

[23]http://visbrain.org/api.html#module-visbrain.objects

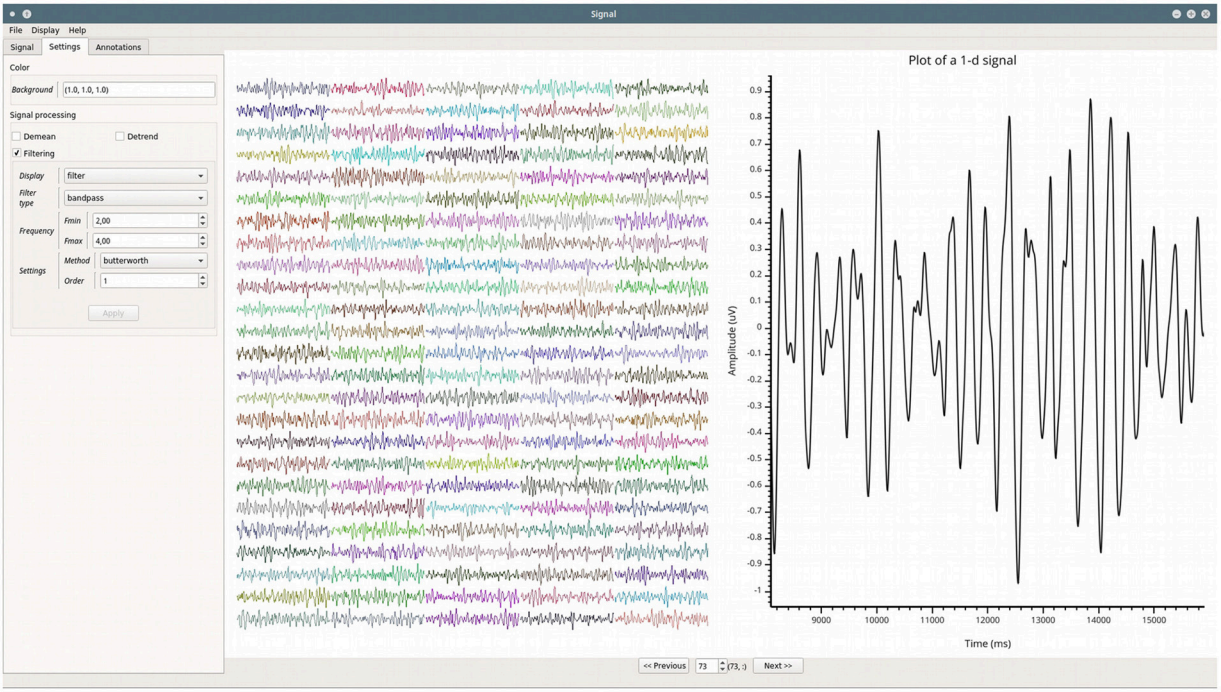


FIGURE 7 | Example of the GUI of the *Signal* module. Leftmost is the setting panel, and side-by-side are all of the time-series re-arranged into a 2D clickable grid and rightmost, an enlarged version of one of those time-series.

- ***Brain*:** for any type of visualization involving a representation containing an opaque or translucent brain
- ***Sleep*:** for plotting, staging, and analyzing sleep data

GUI can be imported from *visbrain.gui*. Those interfaces share the following properties and functionalities:

- A responsive GUI with a common graphical design and structure: a "quick settings" panel disposed on the left (which can be hidden or displayed) and plot on canvases displayed on the rest of the screen. This settings panel contains PyQt widgets to control objects' properties and apply changes in real time.
- The use of VisPy to exploit GPU capabilities.
- A "File" menu to import and export files (such as datasets, annotations, …). From this menu, it is also possible to save and load the GUI state, i.e., the value of each PyQt graphical elements (checkboxes, comboboxes,...). The configuration is saved into a text file with a JavaScript Object Notation (JSON) structure and can later be reloaded to retrieve the session.
- A "Display" menu that controls which elements are displayed or hidden on the screen.
- A "Help" menu to open an informative web page in a browser about the current module and features. This help can also be downloaded in PDF format.
- The support of keyboard shortcuts and mouse events (left and right clicks, double clicks, mouse wheel scrolling,...). The list of supported shortcuts is referenced in a table accessible from the help menu.
- A screenshot window to either export the entire window or select canvas with controllable size, resolution, and printing options. Visbrain supports several standard picture formats (such as PNG, JPG, PDF, EPS, or TIFF). The transparency and background color can also be controlled from this window. An "auto-crop" option can also be checked to automatically crop the exported image to the closest non-background pixel.

Signal: Time-Series Visualization and Spectral Properties

A common first step when exploring electrophysiological data consists of inspecting time-series. This inspection phase is useful to get an idea of the shape of the signals, as well as quickly detecting artifacts, epileptic spikes, eye movement contamination, etc. Spectral properties such as power spectrum density (PSD) or time-frequency maps are complementary tools for such quality control and data exploration. Such data inspection can be complicated for multi-dimensional datasets (e.g., number of trials x tasks x time points). To address this issue, we developed the *Signal*[24] module for the visualization of multidimensional signals. The GUI is divided into two layouts presented in **Figure 7**. On the left, the dataset overview. This consists of a grid where all of the time-series in the dataset are displayed. Multi-dimensional arrays are systematically reshaped into a 2D grid. On the right, the detailed view of a single signal.

[24]http://visbrain.org/signal.html

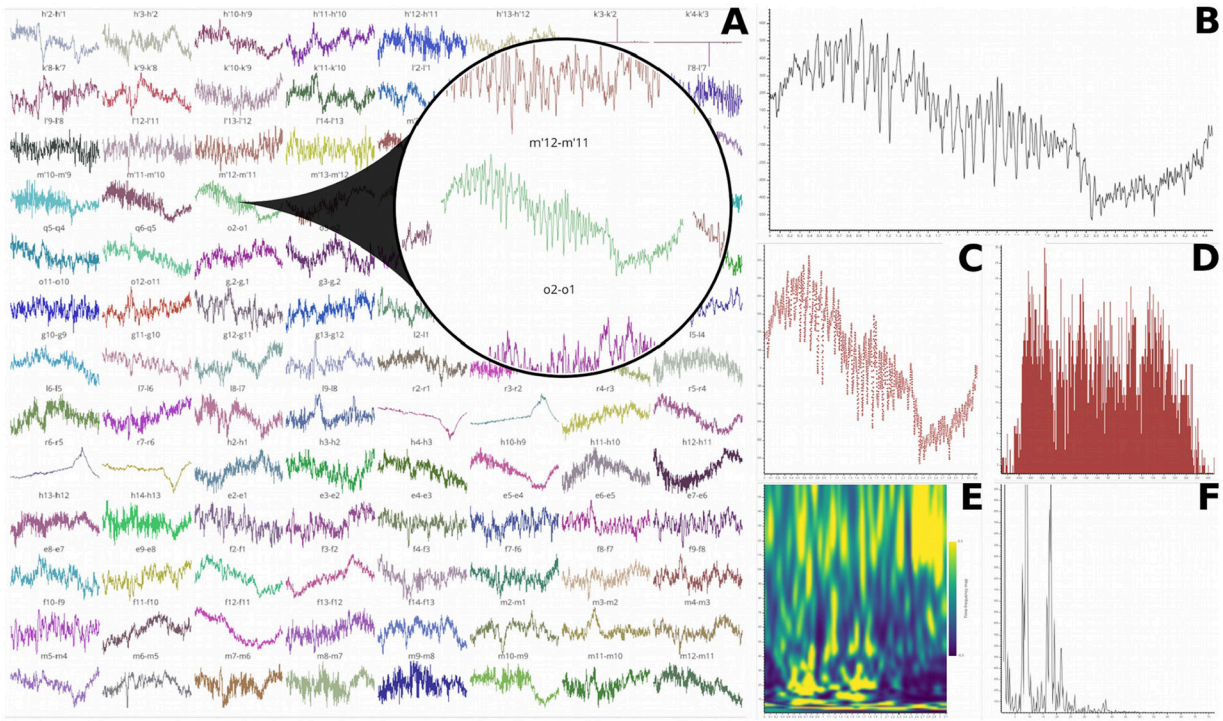


FIGURE 8 | Plotting capabilities of *Signal*. **(A)** 104 intracranial recording sites of 4,000 time points each are rearranged into a clickable 13 rows by 8 columns grid. A double-click on one signal of the grid enlarges it in the second layout. This enlarged time-series can either be displayed as a continuous line **(B)** or a cloud of points **(C)**. A histogram can also be computed **(D)** as well as the time-frequency map using Morlet's wavelets **(E)** or the power spectrum density **(F)**.

This second layout can be used to plot the time-series, the PSD or the time-frequency map.

Grid disposition

The usefulness of this data exploration module is demonstrated by one of the VisPy examples[25], in which thousands of signals, each having thousands of points, can be instantly plotted using the GPU graphics rendering. These signals are presented in a two-dimensional grid and the user can zoom on each of them. Since this grid of signals can be useful for plotting electrophysiological data, this representation has been integrated into the *Signal* module (see **Figure 7**). The aim of this grid is to provide an overview of the entire dataset in a convenient way to visualize all the time-series at once. In order to take advantage of the width and height of the screen, the program tries to determine an optimal number of rows and columns for the grid. A title can also be added on top of each signal of the grid to facilitate the orientation of the user. To better visualize the signal on a specific channel, the user can double-click on it in the grid. This enlarges the selected signal by opening it in the second layout.

Plotting forms

In addition to the grid, a second layout is provided to inspect one time series at a time. The default plotting method is a continuous line but it can be changed to markers for a cloud of points. We also included the possibility to compute the histogram, the PSD or a highly configurable wavelet-based time-frequency map (such as normalization method, baseline bounds, etc.). The grid and those plotting forms are summarized in **Figure 8**.

Annotations, thresholding, and signal processing tools

This module also supports annotations by double-clicking on the canvas that contains the single time-series. All inserted annotations are referenced in a table that can be exported or imported. Selecting a row of this table displays the annotated trial with associated annotations. Then, the *Signal* module also allows the user to define a lower and upper threshold for the identification of time-series extrema. These annotations and thresholding capabilities are summarized in **Figure 9**. We also included some signal processing tools such as filtering, detrending, smoothing, and demeaning.

Brain: Visualization on a 3D Brain

Brain[26] is the second graphical interface that has been developed for all types of visualizations involving a 3D brain. This interface is not intended to provide extra functionality compared to what can be done with the Visbrain objects and scenes. Instead, it provides

[25]https://github.com/vispy/vispy/blob/master/examples/demo/gloo/realtime_signals.py

[26]http://visbrain.org/brain.html

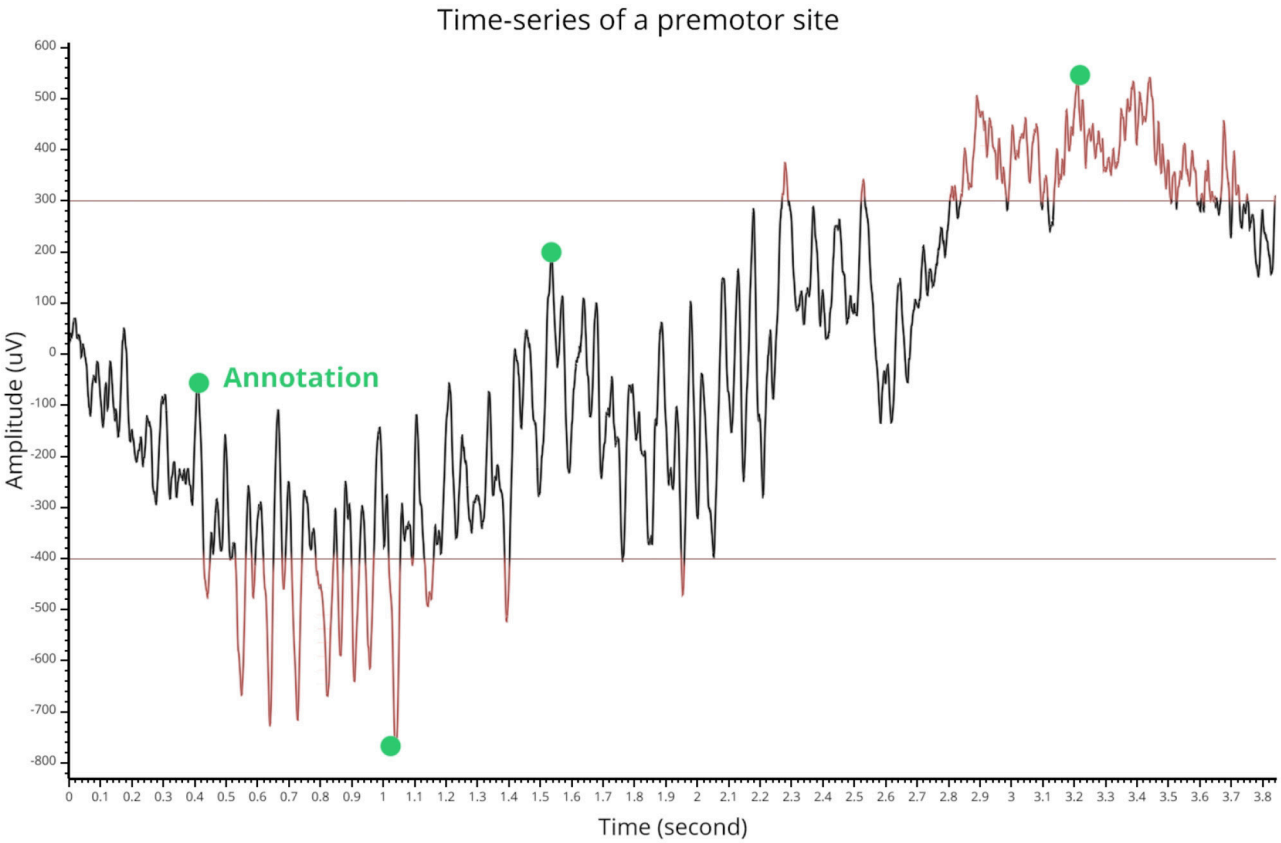


FIGURE 9 | Thresholding and annotation example of an intracranial time-series. The two horizontal lines indicate the threshold values and time points that are either above or under are turned in red. The green markers show inserted annotations that can also be exported.

a GUI to control these objects and the interactions between them.

Object and colorbar control

The *Brain* class can take as input objects or list of objects from the following classes: brain, sources and connectivity (*BrainObj*, *SourceObj* and *ConnectObj*), 3D time-series, pictures, and vectors (*TimeSeries3DObj*, *Picture3DObj*, *VectorObj*) and volume related objects (*VolumeObj*, *CrossSecObj,* and *RoiObj*). Any object passed to the *Brain* class can then be directly controlled from the *Object* tab inside the settings panel (see **Figure 10**). In addition, since each visual object has its own color properties, the colorbar can be controlled individually for each of them from the *Cbar* tab (see **Figure 11**).

Class method for command line interaction

All the functionality and object properties that are accessible from the GUI can also be used and set using *Brain* class methods. The use of methods does not require the graphical interface to be open, even for screenshots. Hence, users can leverage those class methods in custom python scripts to speed up the production of large sets of figures. All of these methods are referenced in the documentation[26].

Sleep: Polysomnographic Data Visualization and Edition

Sleep[27] is the Visbrain module dedicated to the visualization and analysis of sleep data and has been previously described (Combrisson et al., 2017b). It should be noted that new features have been added to the *Sleep* module since the publication of this article, such as the possibility to replace the default event detections with custom external algorithms. This allows different sleep research teams to use the same data visualization platform while still keeping their custom, lab-specific, algorithms for the detection of transient events during sleep.

API and Scripting

As visbrain is subdivided into two main levels (Objects and GUI where GUIs are built on top of objects) we also provide an API for higher level interactions. GUIs are of course ideal when user interaction is needed. That said, GUIs are obviously not intended to be embedded inside loops for scripting. Conversely, the object level offers less options for graphical interactions (except for translations and rotations) but is ideal for scripting, automating and streamlining the production of high-quality figures. This could be implemented either on a local computer or remotely

[27]http://visbrain.org/sleep.html

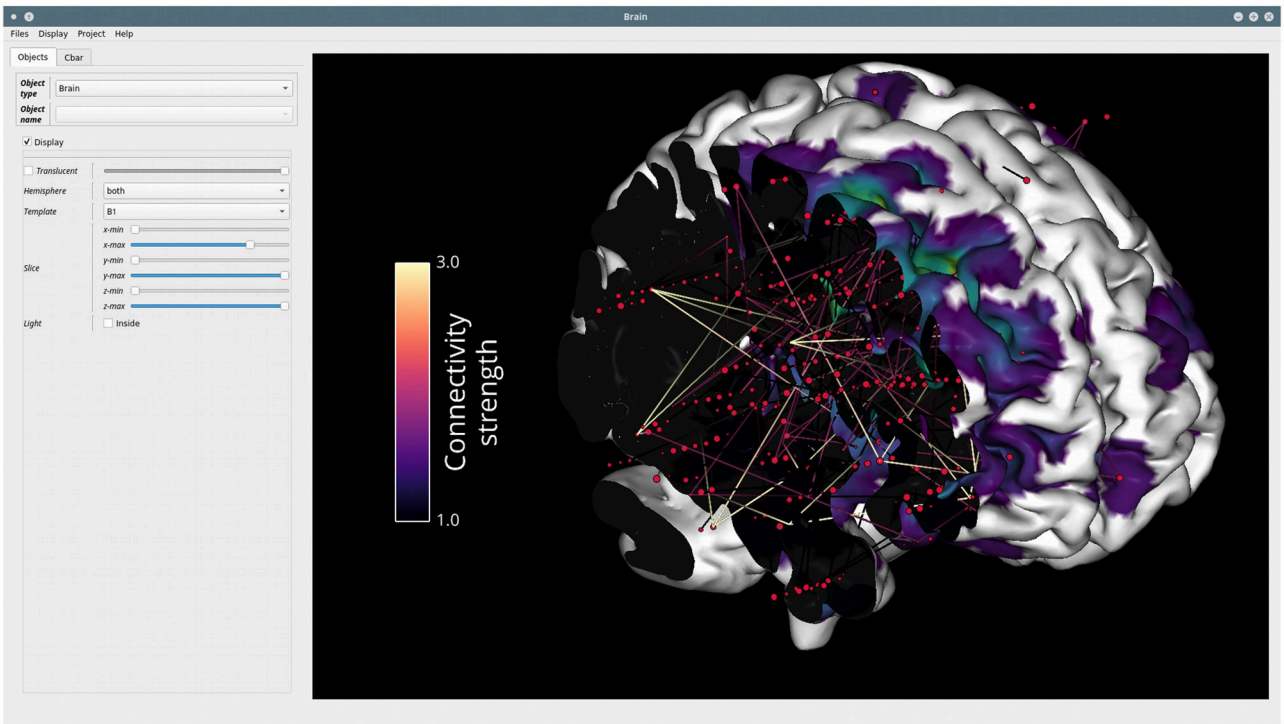


FIGURE 10 | Example of the GUI of the *Brain* module. The settings panel on the left can either be displayed or hidden. This panel contains two tabs: *Objects*, in order to control the properties of each visual class (e.g., *BrainObj*, *SourceObj,* etc.) passed to the interface and *Cbar* for controlling the colorbar and color properties of a selected object. On the right, the main canvas contains the MNI brain with sources and connectivity links between those sources. This canvas allows fluid rotation, zoom and translation, but also mesh slicing along the (x, y, z) axes. Here, the colorbar of connectivity strength is displayed but it can also be hidden.

on a distant server. In addition, the API provision also implies that other toolboxes that have intensive visualization needs (e.g. MNE-Python) can benefit from this API and the modularity of Visbrain objects. The full Visbrain's API can be found in the online documentation[28].

DISCUSSION

Summary

The ever-growing complexity of neuroimaging recording techniques, relying on analyses in higher-dimensional space and on larger datasets, are gradually transforming brain data visualization into a real challenge for the existing body of neuroimaging software. This challenge is further complicated by the difficulty of meeting the specific needs from individual research teams and by license compatibility issues with proprietary software. With these problems in mind, we propose Visbrain, a versatile Python 3 package for multi-modal brain data visualization. As other softwares, Visbrain includes graphical user interfaces for higher level interactions with visual primitives. But the greatest novelty and added-value of Visbrain lies in its structure and especially the object level which, once configured properly, can offer a great modularity for designing figures and layout that reflect brain data results. This package is also configured and tested on continuous integration servers to improve its robustness on different platforms using Travis (Linux) and AppVeyor (Windows). In addition, the documentation is built and deployed automatically using CircleCi. This also implies that Visbrain can be used on a remote server in headless mode.

Limitations and Perspectives

Although much effort has been devoted in providing a software compatible with multi-modal data, it is not equally featured across recording techniques. For example, fMRI cross-section is still a beta feature and electrocorticographic data-specific visualization tools are not implemented so far. Secondly, efforts must now be made to make Visbrain fully compatible with Jupyter in order to have visuals embedded inside notebooks and iPython for interactive shell. We are also considering adding the compatibility with the Brain Imaging Data Structure (BIDS; Gorgolewski et al., 2016; Niso et al., 2018), a set of guidelines for organizing behavioral, MRI and M/EEG data that facilitates data sharing and reproducibility. Finally, Visbrain also contains experimental functions for the compatibility with MNE-Python (Gramfort et al., 2013), but this compatibility will be substantially enhanced in the future.

[28]http://visbrain.org/api.html

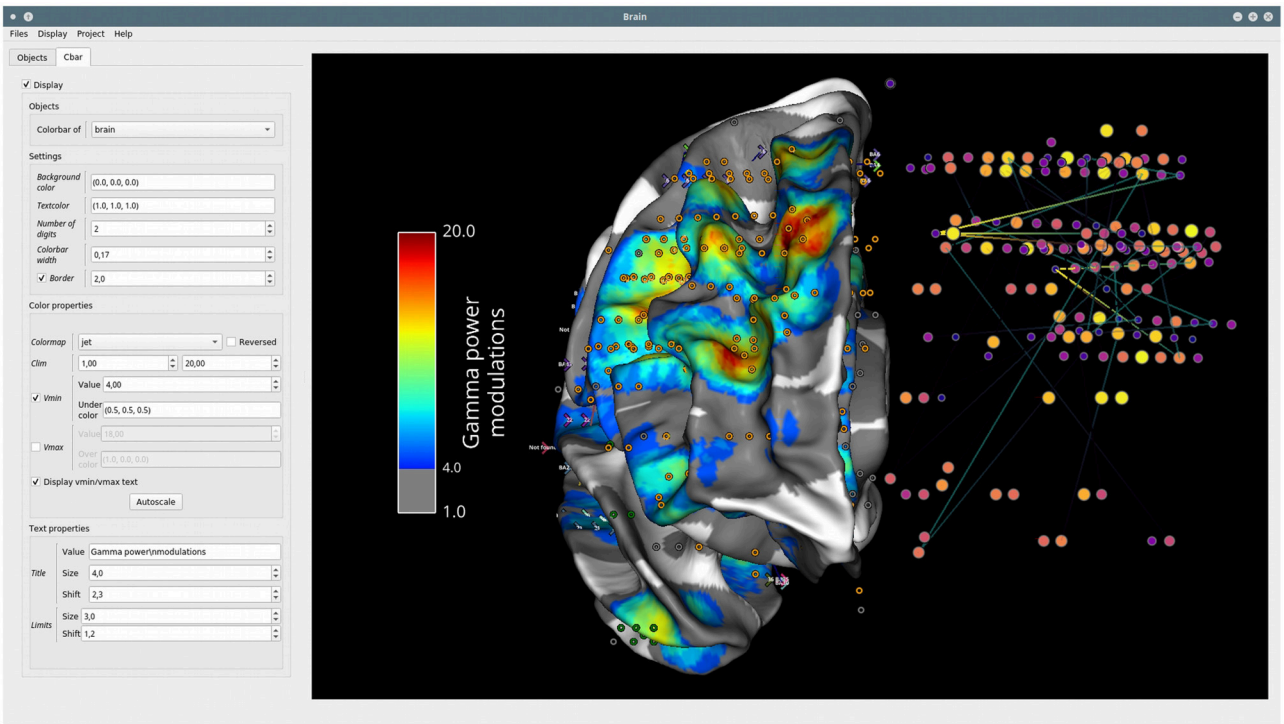


FIGURE 11 | Colorbar control. The *Cbar* tab of the settings panel contains all of the properties to design the colorbar of a specific object (width, colormap, limits, lower and upper thresholds, title, etc.). In addition, these properties can be modified for each object. Here, the widget controls the colorbar for the data projected onto the surface of the brain.

CONCLUSIONS

In summary, Visbrain is a Python open-source and cross-platform software for brain data visualization which provides, among others, the following features: (1) GPU-powered graphical rendering providing efficient data plotting, even for large datasets and real-time interactions. (2) Modularity and flexibility with respect to users' specific needs through neuro-oriented visual primitives that can be juxtaposed or superimposed into subplots, following a Matplotlib-like behavior. (3) Complete control over the aesthetic through highly customizable configuration of color properties, allowing better use of this particularly informative dimension. Visbrain is in its early stages of development, but the present core should hopefully motivate users and programmers to contribute to the project and build a community-driven, powerful, sustainable, and full-featured open-source solution for brain data visualization.

AUTHOR CONTRIBUTIONS

EC is the main developer of this software. RV, CO, MJ, AP, AS, TT, DM, TL, and DA contributed in testing and in the development of this software and writing of the article. PR, AG, and KJ actively helped in the writing process.

FUNDING

EC acknowledges support through a PhD Scholarship awarded by the Ecole Doctorale Inter-Disciplinaire Sciences-Santé (EDISS), Lyon, France, and by funding via a Natural Sciences and Engineering Research Council of Canada (NSERC). KJ is supported by funding from the Canada Research Chairs program and a Discovery Grant (RGPIN-2015-04854) from the Natural Sciences and Engineering Research Council of Canada, a New Investigators Award from the Fonds de Recherche du Québec - Nature et Technologies (2018-NC-206005) and an IVADO-Apogée fundamental research project grant.

REFERENCES

Abraham, A., Pedregosa, F., Eickenberg, M., Gervais, P., Muller, A., Kossaifi, J., et al. (2014). Machine learning for neuroimaging with scikit-learn. *Front. Neuroinform.* 8:14. doi: 10.3389/fninf.2014.00014

Bezanson, J., Edelman, A., Karpinski, S., and Shah, V. B. (2017). Julia: a fresh approach to numerical computing. *SIAM Rev.* 59, 65–98. doi: 10.1137/141000671

Campagnola, L., Klein, A., Larson, E., Rossant, C., and Rougier, N. P. (2015). "VisPy: harnessing the GPU for fast, high-level visualization," *in Proceedings*

of the 14th Python in Science Conference. Available online at: https://hal.inria.fr/hal-01208191/ (Accessed May 23, 2017).

Combrisson, E., Perrone-Bertolotti, M., Soto, J. L., Alamian, G., Kahane, P., Lachaux, J.-P., et al. (2017a). From intentions to actions: neural oscillations encode motor processes through phase, amplitude and phase-amplitude coupling. *NeuroImage* 147, 473–487. doi: 10.1016/j.neuroimage.2016.11.042

Combrisson, E., Vallat, R., Eichenlaub, J.-B., O'Reilly, C., Lajnef, T., Guillot, A., et al. (2017b). Sleep: an open-source python software for visualization, analysis, and staging of sleep data. *Front. Neuroinform*. 11:60. doi: 10.3389/fninf.2017.00060

Delorme, A., and Makeig, S. (2004). EEGLAB: an open source toolbox for analysis of single-trial EEG dynamics including independent component analysis. *J. Neurosci. Methods* 134, 9–21. doi: 10.1016/j.jneumeth.2003.10.009

Fedorov, A., Beichel, R., Kalpathy-Cramer, J., Finet, J., Fillion-Robin, J.-C., Pujol, S., et al. (2012). 3D Slicer as an image computing platform for the quantitative imaging network. *Magn. Reson. Imaging* 30, 1323–1341. doi: 10.1016/j.mri.2012.05.001

Gorgolewski, K. J., Auer, T., Calhoun, V. D., Craddock, R. C., Das, S., Duff, E. P., et al. (2016). The brain imaging data structure, a format for organizing and describing outputs of neuroimaging experiments. *Sci. Data* 3:sdata201644. doi: 10.1038/sdata.2016.44

Gramfort, A., Luessi, M., Larson, E., Engemann, D. A., Strohmeier, D., Brodbeck, C., et al. (2013). MEG and EEG data analysis with MNE-Python. *Front. Neurosci.* 7:267. doi: 10.3389/fnins.2013.00267

Hunter, J. D. (2007). Matplotlib: a 2D graphics environment. *Comput. Sci. Eng.* 9, 90–95. doi: 10.1109/MCSE.2007.55

Mathworks, I. (2012). *MATLAB and Statistics Toolbox Release 2012b*. Natick, MA.

McKinney, W. (2011). "Pandas: a foundational Python library for data analysis and statistics." in *Python for High Performance and Scientific Computing*, 1–9.

Niso, G., Gorgolewski, K. J., Bock, E., Brooks, T. L., Flandin, G., Gramfort, A., et al. (2018). MEG-BIDS, the brain imaging data structure extended to magnetoencephalography. *Sci. Data* 5:180110. doi: 10.1038/sdata.2018.110

Oostenveld, R., Fries, P., Maris, E., and Schoffelen, J.-M. (2011). FieldTrip: open source software for advanced analysis of MEG, EEG, and invasive electrophysiological data. *Comput. Intell. Neurosci.* 2011:1. doi: 10.1155/2011/156869

Penny, W. D., Friston, K. J., Ashburner, J. T., Kiebel, S. J., and Nichols, T. E. (eds.). (2011). *Statistical Parametric Mapping: The Analysis of Functional Brain Images*. London: Academic press.

Rougier, N. P. (2015). "*Glumpy*," in *EuroScipy* (Cambridge).

Tadel, F., Baillet, S., Mosher, J. C., Pantazis, D., and Leahy, R. M. (2011). Brainstorm: a user-friendly application for MEG/EEG analysis. *Comput. Intell. Neurosci.* 2011:8. doi: 10.1155/2011/879716

Talairach, J., and Tournoux, P. (1993). *Referentially Oriented Cerebral MRI Anatomy: An Atlas of Stereotaxic Anatomical Correlations for Gray and White Matter*. Thieme.

Tzourio-Mazoyer, N., Landeau, B., Papathanassiou, D., Crivello, F., Etard, O., Delcroix, N., et al. (2002). Automated anatomical labeling of activations in SPM using a macroscopic anatomical parcellation of the MNI MRI single-subject brain. *Neuroimage* 15, 273–289. doi: 10.1006/nimg.2001.0978

Urchs, S., Armoza, J., Benhajali, Y., St-Aubin, J., Orban, P., and Bellec, P. (2017). MIST: a multi-resolution parcellation of functional brain networks. *MNI Open Res.* 1. doi: 10.12688/mniopenres.12767.1

Conflict of Interest Statement: The authors declare that the research was conducted in the absence of any commercial or financial relationships that could be construed as a potential conflict of interest.

Copyright © 2019 Combrisson, Vallat, O'Reilly, Jas, Pascarella, Saive, Thiery, Meunier, Altukhov, Lajnef, Ruby, Guillot and Jerbi. This is an open-access article distributed under the terms of the Creative Commons Attribution License (CC BY). The use, distribution or reproduction in other forums is permitted, provided the original author(s) and the copyright owner(s) are credited and that the original publication in this journal is cited, in accordance with accepted academic practice. No use, distribution or reproduction is permitted which does not comply with these terms.

frontiers in Neuroinformatics

ORIGINAL RESEARCH
published: 05 April 2019
doi: 10.3389/fninf.2019.00024

PManalyzer: A Software Facilitating the Study of Sensorimotor Control of Whole-Body Movements

Thomas H. Haid[1]*, *Matteo Zago*[2], *Arunee Promsri*[1,3], *Aude-Clémence M. Doix*[1] and *Peter A. Federolf*[1]

[1] Department of Sport Science, University of Innsbruck, Innsbruck, Austria, [2] Department of Electronics, Information and Bioengineering, Politecnico di Milano, Milan, Italy, [3] Department of Physical Therapy, University of Phayao, Mae Ka, Thailand

Motion analysis is used to study the functionality or dysfunctionality of the neuromuscular system, as human movements are the direct outcome of neuromuscular control. However, motion analysis often relies on measures that quantify simplified aspects of a motion, such as specific joint angles, despite the well-known complexity of segment interactions. In contrast, analyzing whole-body movement patterns may offer a new understanding of movement coordination and movement performance. Clinical research and sports technique evaluations suggest that principal component analysis (PCA) provides novel and valuable insights into control aspects of the neuromuscular system and how they relate to coordinative patterns. However, the implementation of PCA computations are time consuming, and require mathematical knowledge and programming skills, drastically limiting its application in current research. Therefore, the aim of this study is to present the Matlab software tool "PManalyzer" to facilitate and encourage the application of state-of-the-art PCA concepts in human movement science. The generalized PCA concepts implemented in the PManalyzer allow users to apply a variety of marker set independent PCA-variables on any kinematic data and to visualize the results with customizable plots. In addition, the extracted movement patterns can be explored with video options that may help testing hypotheses related to the interplay of segments. Furthermore, the software can be easily modified and adapted to any specific application.

Keywords: sensorimotor control, motion analysis, clinical gait analysis, postural control, coordination, principal component analysis PCA

OPEN ACCESS

Edited by:
Antonio Fernández-Caballero, University of Castilla La Mancha, Spain

Reviewed by:
Karen Zentgraf, Goethe-Universität Frankfurt am Main, Germany
Thorsten Stein, Karlsruhe Institute of Technology (KIT), Germany

***Correspondence:**
Thomas H. Haid
thomas.haid@uibk.ac.at

Received: *24 August 2018*
Accepted: *18 March 2019*
Published: *05 April 2019*

Citation:
Haid TH, Zago M, Promsri A, Doix A-CM and Federolf PA (2019) PManalyzer: A Software Facilitating the Study of Sensorimotor Control of Whole-Body Movements. Front. Neuroinform. 13:24. doi: 10.3389/fninf.2019.00024

INTRODUCTION

Sensorimotor control of movements is one of the most important functions of the nervous system. It involves *detecting* the physical state which the biomechanical system is in; *processing* this information to determine which changes to the system are desired or need to be opposed; and *activating* the motor system to generate the forces that produce the required changes to the system. From a biophysical viewpoint, the *state* of the biomechanical system is fully described, when the position and velocity of the body segments are known. Thus, full-body motion analysis offers an approach for studying the function of the nervous system by determining, on the one hand, the state of the system and thus the input to the various sensory systems, and, on the other hand, the accelerations of the body segments and thus the resultant output of the neuromuscular system.

However, multi-segment human movements allow many degrees of freedom DOF and typically allow a large variety of different movement strategies to successfully achieve a goal (Bernstein, 1967), i.e., human movements are mechanically complex. Therefore, conventional movement analyses often look into specific, pre-determined aspects of a motion. Such analyses often neglect important information about segment interactions; and the complex nature of these interactions makes a priori variable determination prone to false identification of important aspects. That is why other approaches quantify whole body kinematics (Honegger et al., 2013; Boström et al., 2018). Nevertheless, most of these approaches still rely on pre-defined aspects of specific movements such as angles, torques, or segment trajectories.

In the past two decades several principal component analysis (PCA) based approaches were developed for various applications in kinematic data analysis (Sadeghi et al., 1997; Troje, 2002; Daffertshofer et al., 2004; Wang et al., 2014), with the aim of determining relevant aspects of a motion in an unbiased and data driven way. One of these approaches identifies whole-body movement components (Troje, 2002; Daffertshofer et al., 2004), later called principal movements PM_k (Federolf et al., 2012), thus reducing data complexity without neglecting segment interactions. In this framework, a PCA yields eigenvectors $\boldsymbol{PC_k}$, eigenvalues EV_k and score time-series called principal positions $\boldsymbol{PP_k}(t)$. Each $\boldsymbol{PC_k}$ defines one type of movement or movement strategy that the respective PM_k describes, while each EV_k determines the amount of total variance in the data explained by the respective PM_k. Furthermore, the scores $\boldsymbol{PP_k}(t)$ determine the evolution of the respective PM_k over time.

Among the first papers applying PCA in this sense were studies on walking patterns and gait forms (Troje, 2002; Daffertshofer et al., 2004; Verrel et al., 2009). In these studies, a separate PCA was conducted for each trial and the individual EV-spectra characterizing the amount of contribution of each individual postural strategy were compared. On the one hand, this approach allowed programming a motion synthesizer that displays gait forms according to different classifiers such as gender, weight, and emotional condition (Troje, 2002). On the other hand, it could be shown that gait regularity is not only affected by cognitive dual-tasking, but that different age groups display different changes in regularity (Verrel et al., 2009).

These results established PCA as a useful tool to analyze human movements. However, only EV-spectra describing the contribution of trial specific movement patterns could be compared, thus the comparison of movements between subjects or trials remained unsolved. Soon after, it was shown that one PCA could be conducted on several trials of various participants simultaneously, if the datasets were normalizing appropriately (Federolf P. et al., 2013). This approach enabled the comparison of the movement executions $\boldsymbol{PP_k}(t)$ between trials. Furthermore, the relative contribution of each PM_k to a trial's overall variance (corresponding to the EV_k) was quantified with the variable $rVAR_k$ computed on the $\boldsymbol{PP_k}(t)$.

Amongst others, the $rVAR_k$ and $\boldsymbol{PP_k}(t)$ have provided new insights into the execution of sports techniques in alpine skiing, cross-country skiing, karate, dancing, cycling and race-walking (Donà et al., 2009; Moore et al., 2011; Masurelle et al., 2013; Federolf et al., 2014; Gløersen et al., 2017; Zago et al., 2017a). Moreover, related variables such as residual variances RV_k or relative standard deviations $rSTD_k$ have been used to quantify the dimensionality of coordinative tasks such as juggling or balancing (Zago et al., 2017b; Haid and Federolf, 2018).

While the studies discussed so far applied the PCA method to compare movements, they have not calculated velocities or accelerations, and thus have not studied the control of movements. Only in 2016 it was suggested to differentiate the $\boldsymbol{PP_k}$-time series to obtain principal velocities $\boldsymbol{PV_k}$ and principal accelerations $\boldsymbol{PA_k}$ (Federolf, 2016). Since then, $\boldsymbol{PA_k}$ and variables based on $\boldsymbol{PA_k}$ have been used to study differences in movement control due to aging (Haid et al., 2018) or leg dominance/laterality (Promsri et al., 2018a). The $\boldsymbol{PP_k}$ and $\boldsymbol{PP_k}$-variables were also applied in postural control research and linked to COP-time-series (Federolf, 2016), which are analyzed in a range of clinical applications that investigate impairments due to aging, overweight, back pain, concussion, multiple sclerosis, autism spectrum disorders, or Parkinson's disease (Fino et al., 2016; Huisinga et al., 2017; Lim et al., 2017; Yamagata et al., 2017; Han et al., 2018; MacRae et al., 2018; Nikaido et al., 2018). A recent study evaluated COP-irregularity by linking it to $\boldsymbol{PP_k}(t)$ irregularity and to the complexity of the movement structure as defined by $rSTD_k$ (Haid et al., 2018).

Variables computed on PM time-series contain information about whole-body positioning, which allows studying the movements of the human body as a system, while preserving or possibly enhancing (Federolf P. A. et al., 2013) the ability to discriminate groups. Therefore, the PCA approach is well-suited for addressing any research questions where coordination or the interplay of segment movements is of importance. However, despite its research potential the implementation of PCA approaches requires a fair amount of programming and mathematical skills, and can be very time consuming. Therefore, the development of new PCA based variables and research output validation comparing different computational options is severely hampered.

The main goal of this paper is to present the PManalyzer-software. It generalizes many of the existing PCA concepts and was designed to motivate the development and validation of kinematic PCA related variables and methods within a user-friendly graphical environment. On the one hand, the software will allow researchers and clinicians without extensive programming or mathematical skills to perform PCA on kinematic data; on the other hand, it will allow users with more advanced knowledge in the area to adapt and further develop the software.

MATERIALS AND METHODS

The software was designed to pre-process the kinematic input data and then compute a PCA on it. Furthermore, the PManalyzer can compute a range of PCA variables. In this section the mathematical background of kinematic feature extraction and some of the most important variables are explained.

General Data Model and Data Pre-processing

Typical kinematic data consists of 3D positions in time obtained by tracking the motion of n anatomical landmarks; either utilizing a motion capture system or video-tracking (Figueroa et al., 2003). The kinematic data is then available in matrix form in which the $N = 3 \cdot n$ columns represent the time-series $s_i(t)$ ($i \in \{1, 2 \ldots, N\}$) of the respective x-y-z-coordinates of each anatomical landmark. Each row contains the measured 3D positions of all markers at one time-point:

$$\boldsymbol{D} = \begin{bmatrix} s_1(t_1) & \cdots & s_N(t_1) \\ \vdots & \ddots & \vdots \\ s_1(t_T) & \cdots & s_N(t_T) \end{bmatrix},$$

Where T equals the number of measured time-points. The application of PCA to human movement is based on the idea of identifying linear whole-body movement patterns that dominate the recorded movements. However, when identifying movement patterns within a group of several subjects, both the mean positioning of a participant and anthropometrical differences distort the results. To reduce such distortions, the data of each subject can be centered, weighted and normalized (Federolf P. et al., 2013; Zago et al., 2017b; Haid et al., 2018).

The data is centered by subtracting the mean $< \boldsymbol{s_i} >$ of each individual time-series $\boldsymbol{s_i}$ (each column) from the respective time-series $\boldsymbol{s_i^c} = \boldsymbol{s_i} - < \boldsymbol{s_i} >$:

$$\boldsymbol{D^c} = \begin{bmatrix} \boldsymbol{s_1^c}(t_1) & \cdots & \boldsymbol{s_N^c}(t_1) \\ \vdots & \ddots & \vdots \\ \boldsymbol{s_1^c}(t_T) & \cdots & \boldsymbol{s_N^c}(t_T) \end{bmatrix},$$

preventing differences in mean marker positioning in space to affect the results. Furthermore, a participant's weight distribution can influence marker movements. As an example, when moving a hand, less mass has to be accelerated and controlled, in comparison to moving a thigh. Therefore, each of the N time-series can be scaled according to the weight w_i ($i \in \{1, 2 \ldots, N\}$), that the respective marker represents:

$$\boldsymbol{D^{c,\,w}} = \boldsymbol{D^c} \cdot \begin{bmatrix} w_1 & \cdots & 0 \\ \vdots & \ddots & \vdots \\ 0 & \cdots & w_N \end{bmatrix},$$

Weighting has been applied in literature (Federolf P. et al., 2013; Gløersen et al., 2017; Haid et al., 2018; Promsri et al., 2018a), often considering gender-specific mass distributions (Defense Technical Information Center, 1988; de Leva, 1996; Gallagher and Heymsfield, 1998).

Another important aspect to be considered when comparing trials is that anthropometric differences can influence the amount of movement produced. Therefore, each data-set should be normalized according to application specific criteria:

$$\boldsymbol{D^{c,\,w,n}} = \boldsymbol{D^{c,w}} \cdot \frac{1}{d_{norm}}$$

Normalization factors d_{norm} such as the mean Euclidean distance (MED) (Federolf P. et al., 2013; Zago et al., 2017b) or the body height (Haid and Federolf, 2018; Haid et al., 2018) have been proposed to reduce anthropometric differences. In detail, the MED ensures that all subjects contribute equally to the overall variance, while the body height normalization scales the data to a trial-independent anthropometric parameter.

Once the data sets of each participant are centered, weighted and normalized[1], one large data matrix $\boldsymbol{D^{all}}$ is formed, containing all data sets of all X trials concatenated vertically (with index 1..X representing different subjects and/or several trials of different subjects):

$$\boldsymbol{D^{all}} = \begin{bmatrix} \boldsymbol{D_1^{c,\,w,n}} \\ \vdots \\ \boldsymbol{D_X^{c,\,w,n}} \end{bmatrix}$$

Feature Extraction—PCA

After pre-processing, the eigenvectors $\boldsymbol{PC_k}$and eigenvalues EV_k of the covariance matrix of $\boldsymbol{D^{all}}$ are computed [implemented as SVD (Shlens, 2014)]. The eigenvectors $\boldsymbol{PC_k}$ form a new orthonormal basis that spans posture space (Federolf P. et al., 2013), a space in which each of the axes determines one specific linear, one-dimensional whole-body movement. Furthermore, scores **S** can be obtained by projecting the data onto the new PC_k basis:

$$\boldsymbol{S} = \boldsymbol{D^{all}} \cdot \boldsymbol{PC_k} \tag{1}$$

The k-th column of the score matrix **S** can be interpreted as time-series $\boldsymbol{PP_k}(t)$ that quantitatively describes the evolution over time of the respective principal movement $\mathrm{PM_k}$, i.e., the manifestation of the one-dimensional $\mathrm{PM_k}$ defined by the corresponding $\boldsymbol{PC_k}$:

$$\boldsymbol{S} = \begin{bmatrix} \boldsymbol{PP_1}(t_1) & \cdots & \boldsymbol{PP_N}(t_1) \\ \vdots & \ddots & \vdots \\ \boldsymbol{PP_1}(t_T) & \cdots & \boldsymbol{PP_N}(t_T) \end{bmatrix}$$

In addition, the eigenvalues EV_k describe the amount of variance (or movement) explained by each $\mathrm{PM_k}$ and are typically presented as percentages or relative eigenvalues rEV_k[2].

To compute one PCA on each trial separately can be done by running the software for each trial separately. However,

[1]The default order in the software is centering, then weighting and finally normalizing the individual data sets. Depending on the pre-processing selection, the order might influence the results.

[2]In literature the "relative eigenvalues" $\mathrm{rEV_k}$ are sometimes referred to as $\mathrm{EV_k}$ out of simplicity. In addition, the term "relative eigenvalues" may refer to the "trial specific relative variances" as described in the following section. In this manuscript we aim at consistency.

this feature is not explicitly supported, because the authors recommend only comparing trials with respect to one PCA basis that describes the group as a whole. The benefit of the current procedure—being able to compare the $\boldsymbol{PP_k}(t)$ of trials—outweighs the benefit of obtaining several, trial-specific PCA-bases that only allow comparisons of rEV_k-spectra, but not of $\boldsymbol{PP_k}(t)$. Moreover, the $\boldsymbol{PP_k}(t)$ can be used to compute variables that describe the subjects specific variance explained by each PM_k and further variables that quantify the additional aspects of a movement or of neuromuscular control.

Interpretation of the Movement Components

As mentioned in the previous section, the $\boldsymbol{PC_k}$ form a basis of the posture space. Moreover, they have the property that they point in the direction of the largest correlated variance expressed in the data. Therefore, they point in the direction of the most common patterns of correlated marker movements. As a consequence, the PM_k are *linear* approximations of the analyzed movements and interpreting them as *real* movements should be done with caution. For example, to explain non-linear movements such as rotations at least two linear components are needed. Nevertheless, for movements with small perturbations such as static balancing tasks (tandem, bipedal, one-legged) past research has found the PM_k to describe the main dynamics of well established, nonlinear movement strategies, e.g., ankle sway or upper body rotation (Haid and Federolf, 2018; Haid et al., 2018; Promsri et al., 2018a). Moreover, also for movements with higher amplitudes the PM_k have been found to reflect the main the dynamics of established movement strategies, such as isolated leg or arm swinging, trunk leaning, or coordinated multi-segment movements (Troje, 2002; Verrel et al., 2009; Eskofier et al., 2013; Gløersen et al., 2017; Zago et al., 2017a,b).

Advantages of analyzing the movement with PMs are that few variables are needed to approximate the movement to great detail and obtaining the PMs is data-driven—not postulated from subjective observations. Moreover, the PMs can be visualized which improves interpretation of results. In the current paper we further propose that movement analysis involving rotational movements of large amplitudes could additionally benefit from non-linear coordinate transformations. To the best of our knowledge, there is no literature to support this assumption, therefore, a motivational example will be presented.

PCA Variables

In the following some of the most common kinematic PCA variables in literature are described. These, amongst others, are pre-implemented in the software.

Trial Specific Movement Structure or Composition

The rEV_k determine the overall variance explained by each PM_k either in the respective trial—if one PCA is computed for one trial—or in the overall variance produced by all trials—if one PCA is computed for the concatenated trials-matrix. In the latter, trial-specific relative variances $rVAR_k$ can be computed that represent the explained variance of each PM_k (Federolf P. et al., 2013), analogously to the rEV_k for applications in which one PCA is computed for each trial. Therefore, the sum of all variances of each trial's individual $\boldsymbol{PP_k}(t) \sim$ time-series

$$totVAR^{trial} := \sum\nolimits_k \mathrm{VAR}_\mathrm{k}^\mathrm{trial} := \sum\nolimits_k \mathrm{VAR}\left(\boldsymbol{PP_k^{trial}}(\mathrm{t})\right),$$

can be computed. The subject specific relative variances are then defined by

$$rVAR_k^{trial} = \frac{\mathrm{VAR}_\mathrm{k}^\mathrm{trial}}{totVAR^{trial}} \cdot 100.$$

To obtain a similar variable that quantifies the movement structure and explains the relative contributions to a movement, but scales as the original movement, the variance in the $rVAR_k$ computation can be replaced by the standard deviation to compute trial-specific relative standard deviations $rSTD_k$ (Haid and Federolf, 2018; Haid et al., 2018).

When the dimensionality of a movement is of interest, it makes sense to define subject specific cumulative relative variances as

$$CUM_rVAR_k := \frac{\Sigma_{1\le n\le k}\mathrm{VAR}_\mathrm{n}^\mathrm{trial}}{totVAR^{trial}} \cdot 100,$$

or analogously CUM_rSTD_k, which explain the cumulative contribution of the respective component order. This can further be used to compute subject specific residual variances

$$RV^3 := 100 - CUM_rVAR_m = \frac{\sum_{k>m}\mathrm{VAR}_\mathrm{k}^\mathrm{trial}}{\sum_k \mathrm{VAR}_\mathrm{k}^\mathrm{trial}} \cdot 100$$

where m is the highest PC-order included (Zago et al., 2017b,c).

Kinematics in Posture Space and Measures of Postural Control

Similarly to conventional kinematics in biomechanics (Federolf, 2016) the $\boldsymbol{PP_k}(t)$ time-series can be utilized to analyze the execution of movements with respect to their PM_k. Different trajectories or performances can therefore be directly compared to another if the $\boldsymbol{PP_k}(t)$ of all trials are coordinates in the same posture space, i.e., if one only one PCA was computed.

Furthermore, the $\boldsymbol{PP_k}(t)$ can be utilized to compute principal velocities $\boldsymbol{PV_k}(t)$ and principal accelerations $\boldsymbol{PA_k}(t)$ by differentiating the $\boldsymbol{PP_k}$ once and twice, respectively. The dynamics of all three PM time-series can be studied using conventional time-series analysis. For example, postural reconfiguration can be ascribed to acting external forces, such as gravity, and internal forces, such as acting muscle forces. Therefore, the $\boldsymbol{PA_k}(t)$ can be used to compute variables that characterize the neuromuscular control of movement, as they represent the acceleration of the postural movements. For example, it has been shown that the $\boldsymbol{PA_k}$ can be used to quantify the amount and the variability of the neuromuscular control, by further defining variables N_k and σ_k (Haid et al., 2018; Promsri et al., 2018a), which represent the number of $\boldsymbol{PA_k}$ -zero-crossings (changes in the direction in which the neuro-muscular control

[3]Residual variances can also be computed for the overall contributions by substituting the rVARk with the rEVk.

system influences the current motion) and the time-variability between the zero-crossings, respectively.

Table 1 contains a summary and a description of these PCA variables. However, any other type of time-series analysis that fits the research question may be applied to the three PM time-series.

PCA Validity Considerations

To quantify which $\boldsymbol{PC_k}$ basis is adequate to describe the group as a whole, a leave-one-out cross-validation can be performed (Diana and Tommasi, 2002; Bro et al., 2008; Camacho and Ferrer, 2012). Therefore, the $\boldsymbol{PC_k}$ are computed several times, while omitting one trial each time. The changes between the used $\boldsymbol{PC_k}$ and the newly obtained $\boldsymbol{PC_k'}$ can be quantified as angles and serve as a PM-inclusion criterion (Federolf, 2016; Haid and Federolf, 2018; Haid et al., 2018).

RESULTS—THE PMANALYZER SOFTWARE

The Interface

As depicted in **Figure 1**, the PMAnalyzer interface is organized into five main panels with red margin and font: 1. "Input data," 2. "Computation and output," 3. "Plots," 4. "Videos" and 5. "Save/Load interface settings." Following the subpanels one by one allows the user to move through the conventional steps for a PCA applied to kinematic data as described in the section Materials and methods. The block scheme in **Figure 2** visualizes the steps of the parameter selection when using the PMAnalyzer.

Once the computational options are selected, the user can save interface settings and reload them later if needed. To improve efficiency when repeating calculation steps, computed data can also be saved, and loaded. The compatibility of the computing vs. loading vs. disabling options is regulated over the interface to avoid the selection of incompatible features.

Note: The interface was created with the "guide" tool in "MATLAB 2015a" in "Windows 10" on a screen with a 1,920 × 1,080 resolution. Both "Units" and "FontUnits" were set to "normalized" with respect to screen size. For other software or hardware configurations (for example on Mac books) some adaptations may be necessary. Also, some of the plotting features may produce errors if the PMAnalyzer is run on earlier versions of MATLAB^{TM}.

TABLE 1 | Summary and description of the variables.

Abbreviation	Variable name	Description
$\boldsymbol{PC_k}$	Principal components/eigenvectors	Contains the information about the marker movements that define the PM_k
EV_k	Eigenvalues	Absolute contribution of PM_k to overall variance
$\boldsymbol{PP_k}(t)$	Principal positions	Time-series that quantifies the evolution of the posture with respect to $\boldsymbol{PC_k}$
$\boldsymbol{PV_k}(t)$	Principal velocities	Time-series that quantifies the velocity of the postural changes defined by PM_k
$\boldsymbol{PA_k}(t)$	Principal accelerations	Time-series that quantifies the acceleration of the postural changes defined by PM_k
rEV_k	Relative eigenvalues	Relative contribution of PM_k to overall variance
$rVAR_k$	Relative variances	Relative contribution of PM_k to variance produced by trial.
$rSTD_k$	Relative standard deviations	Relative contribution of PM_k to movement of trial.
CUM_rEV_k	Cumulative relative eigenvalues	Cumulative relative contribution of PM_k to overall variance.
CUM_rVAR_k	Cumulative relative variances	Cumulative relative contribution of PM_k to variance produced by trial.
CUM_rSTD_k	Cumulative relative standard deviations	Cumulative relative contribution of PM_k to movement in trial.
RV_m	Residual variance	Unexplained variance after setting threshold of PM-order m.
N_k	number of PA zero crossings	Number of interventions of the control system with respect to the movement defined by PM_k
σ_k	Standard deviation of times between zero crossings	Standard deviation of times between the interventions of the control system with respect to the movement defined by PM_k

Code Structure and Computation

The source code is built upon the structure of the user interface and kinematic PCA described in the methods. To monitor the code activity a text describing the current computational step is printed in the output-console. Furthermore, the code is documented by comments to identify the task of each code section and help identifying important computational variables and their respective role in the code. Despite the self-regulating interface, it is possible to select options that do not match the data. The code has implemented fail-safes to identify obvious selection errors and forward them to the user, e.g., when users choose to make video files of data that was not read in.

Functions containing computational options meant for the user to customize (pre-processing, coordinate transformations, normalizations, weighting, variables on PM time-series, video-coloring and creating additional plots) are contained in the PMAnalyzer subfolder "FunctionsToEdit." Users can follow the descriptions and the examples provided inside each function to implement their new options. When starting, the GUI automatically loads all functions contained in subfolders and updates the interface with the available options.

Application Example

In this section, an example computation will be presented to highlight the flexibility of the software. Then, a standard PCA-analysis procedure is outlined. The input is a data subset taken from a previously published tandem stance study that served as template for the PMAnalyzer (Haid et al., 2018).

Computational Parameters and Modifications

For the sample tandem-stance data the first two columns containing time-frames and the headers were deleted. Then gap-filling (Gløersen and Federolf, 2016) was performed on each data set if needed, and a pre-processing option was created that mirrors specific data to make it comparable (unsymmetrical markers were deleted and data with left foot

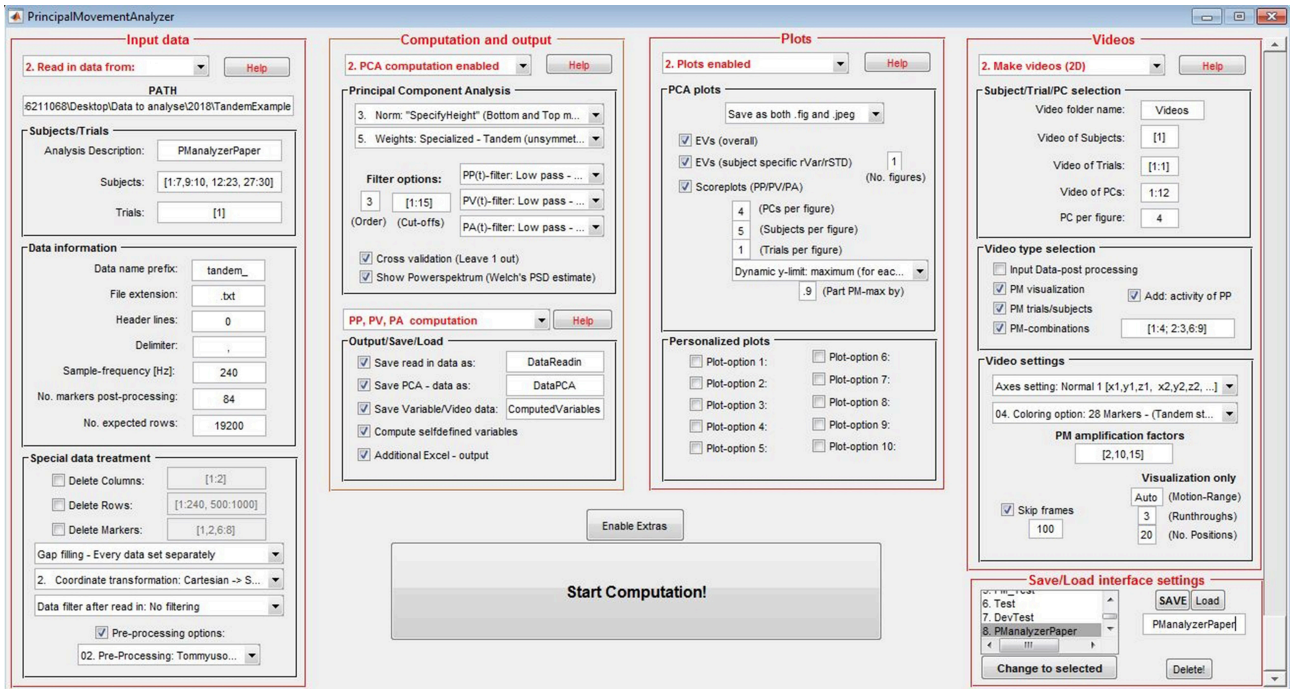


FIGURE 1 | General user interface (GUI) of the PManalyzer. The input settings shown here were used for the computation of the example discussed in the current paper.

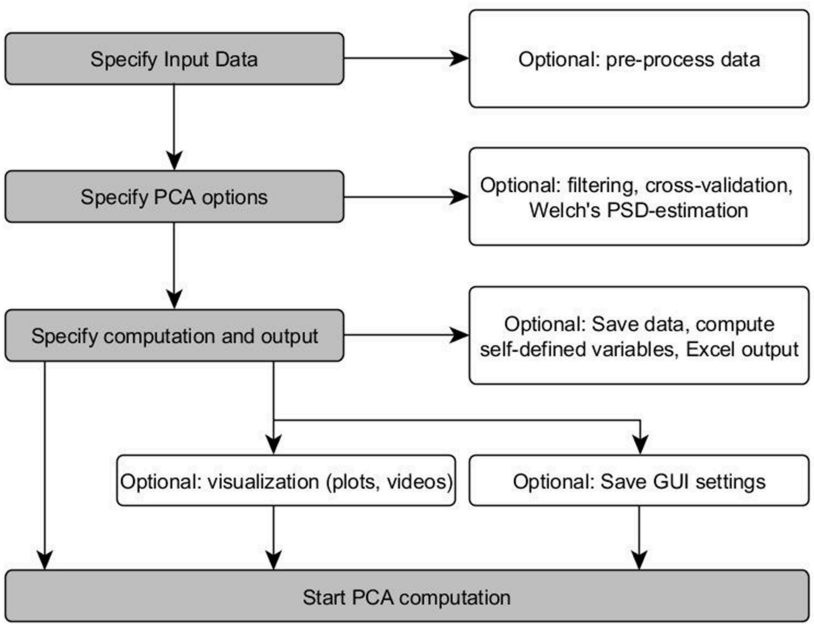


FIGURE 2 | Block-scheme of the PManalyzer computation options. Gray fields describe essential parameter selections. White field represent optional GUI features (Welch's PSD-estimation can be used to estimate the power spectral density of data and to determine a plausible cut-off frequency).

in front was mirrored). The data was then centered, weighted to standard human mass distribution (Defense Technical Information Center, 1988) and normalized with the height of the participants. We also filtered the data with a low-pass filter of 7 Hz, since Fourier analysis suggested signal power up to this frequency. As this example shows, standard pre-processing options can be performed on all of the data by simple parameter selection.

Another interesting pre-processing option that is rarely taken advantage of in kinematic PCA-research is a coordinate transformation. The PManalyzer has two types of coordinate transformations pre-implemented (spherical and cylindrical). Hence, we recomputed the analysis twice using the same parameter selection as described above, but transforming the data either into spherical or cylindrical coordinates, respectively.

Moreover, we selected several of the standard plotting options for the standard PCA variables (rEV_k, $rSTD_k$, $rVAR_k$, ***PP***, ***PV***, ***PA***). Further variables such as N_k or σ_k (Haid et al., 2018; Promsri et al., 2018a) can be computed by selecting "Compute selfdefined variables" and can either be analyzed via Excel output or plotted by defining plots in the function *personalizedPlots.m*. In addition, we selected several video options (2D, 3D, and three different coloring choices. The **Supplementary Files** contain a summary of the important results of these computations, which we will discuss in the following section.

PCA Results

As a common first step, the overall eigenvalues were analyzed to see how much overall variance can be explained by the components (individually or cumulatively). These results (**Figure 3**) show that using spherical or cylindrical coordinate transformations would allow to explain more variance with fewer components. Therefore, we chose to continue the analysis with the results obtained by using spherical coordinates.

As a next step, the PM-movies can be used to describe the movement components to form a better understanding of the extracted movements (compare "ColoringNone_2D_PM1-5_vis.mp4"). It is often helpful to implement specific coloring options (compare "Coloring1_2D_PM1-5_vis.mp4" and "Coloring1_2D_PM1-5_vis.mp4"). For this sample data, the first principal movement resembled an anteroposterior ankle sway. The second PM resembled an upper body retraction accompanied by front knee flexion, etc. The amplification factors displayed in the titles can be adjusted individually for every PM_k. This is helpful when identifying movements of different magnitudes.

Furthermore, PM time-series plots show the execution of the individual trials with respect to the extracted movements (see **Figure 4**) and the PP activity over time can also be displayed in the video option ("Subject1_2D_PM-5.mp4" and "Subject1_3D_PM-5.mp4"). Both can be useful developing hypotheses related to the dynamics of PMs or their interplay. Users may define any sort of variable in the function *optionsVariablesComp.m*. These variables can then be computed on $\boldsymbol{PP_k}$ -, $\boldsymbol{PV_k}$- and $\boldsymbol{PA_k}$-time-series, thus describing specific aspects of movement components that were not a priori defined, but play an important role producing the observed variance. As an example, we plotted the trial specific relative variances $rVAR_k$ and standard deviations $rSTD_k$ that have been very useful when comparing movement structures amongst various groups (Federolf, 2016; Haid et al., 2018; Promsri et al., 2018a). In the current example it can be observed that while the overall movement of subject 2 is dominated by anteroposterior ankle sway, subject 3 has a more balanced movement structure, where several movements contribute effectively (**Figure 5**).

DISCUSSION

Application of PCA-Variables

In human movement analyses, one of the most important steps is the reduction of the numerous degrees of freedom. Several approaches have been proposed in order to reduce the DOF while capturing the most important dynamics of human movements. For example, in static balance research, one of the most common approaches is to quantify the center of pressure movement, reducing the complex whole-body kinematics to the resultant point where the vertical ground reaction forces act. Indeed, COP based variables proved to be effective at distinguishing different pathological groups and different balancing conditions. However, literature findings are inconsistent and some interpretations are controversial. For example, COP-irregularity has been interpreted as a sign of very active and effective postural control (Cavanaugh et al., 2006; Donker et al., 2007; Haran and Keshner, 2008; Stins et al., 2009; De Beaumont et al., 2011), but also as a sign of a disordered and less effective control (Donker et al., 2007; Stins et al., 2009; Borg and Laxåback, 2010; Gao et al., 2011).

Reducing the DOF via PCA has helped to address some of the inconsistencies in COP literature. As a first step it was shown that the information contained in the COP-excursion should also be contained in PCA variables, since the COP-trajectories can be calculated from the $\boldsymbol{PP_k}$ and $\boldsymbol{PA_k}$ time series (Federolf, 2016). Then, follow-up research found that COP-irregularity correlates with both the mechanical complexity of the movement, as quantified by the movement structure $rSTD_k$, and the irregularity of the neuromuscular control as quantified by $\boldsymbol{PP_k}$-irregularity (Haid and Federolf, 2018). Hence, these findings suggest that COP-irregularity depends on more than one interacting phenomenon, possibly explaining some of the controversial results.

As another example, in research areas that involve postural control and motor control theories, e.g., neurosciences, distinguishing movement strategies can be of great importance. For example, the minimal intervention principle MIP, as discussed in the context of the optimal feedback control theory (Todorov and Jordan, 2002), states that postural control focuses on task relevant movements, while allowing variability in redundant ones. Furthermore, evidence suggests that ankle, knee and hip strategies dominate the whole-body kinematics of balancing tasks (Gage et al., 2004; Kuznetsov and Riley, 2012). In addition, coherence analyses of respective joint angles (Kilby et al., 2015; Masumoto and Inui, 2015) and muscle-EMGs (Alfuth and Gomoll, 2018; Pollock et al., 2019) suggest that these strategies are coordinated (Huisinga et al., 2017; Shahvarpour et al., 2018). Nevertheless, further evidence suggests that when modeling the dynamics according to these segment interactions (Oliveira et al., 2017; McNair et al., 2018), the models seem unable to explain the full extent of the movement dynamics (Hume et al., 2019). Hence, since these studies depend on only a few pre-selected muscles and DOF they might be limited when testing hypotheses related to the MIP.

The advantage of the PCA approach is that the extracted principal movement components are inherent in the data. They represent coordinated marker movements that generate

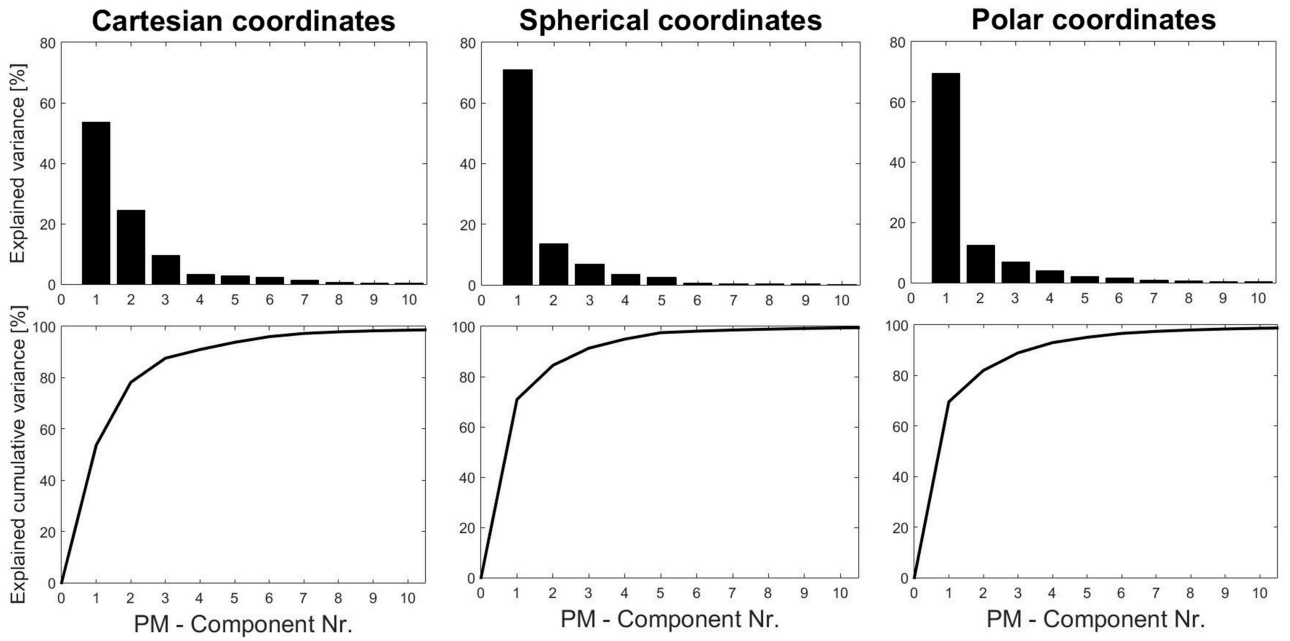


FIGURE 3 | Eigenvalue and cumulative eigenvalue spectra obtained from three coordinate systems (standard kinematic PCA applications use Cartesian-coordinate systems). To explain roughly 98% of the variance it takes 9 PMs using Cartesian, 8 PMs using polar and 6 PMs using spherical coordinates.

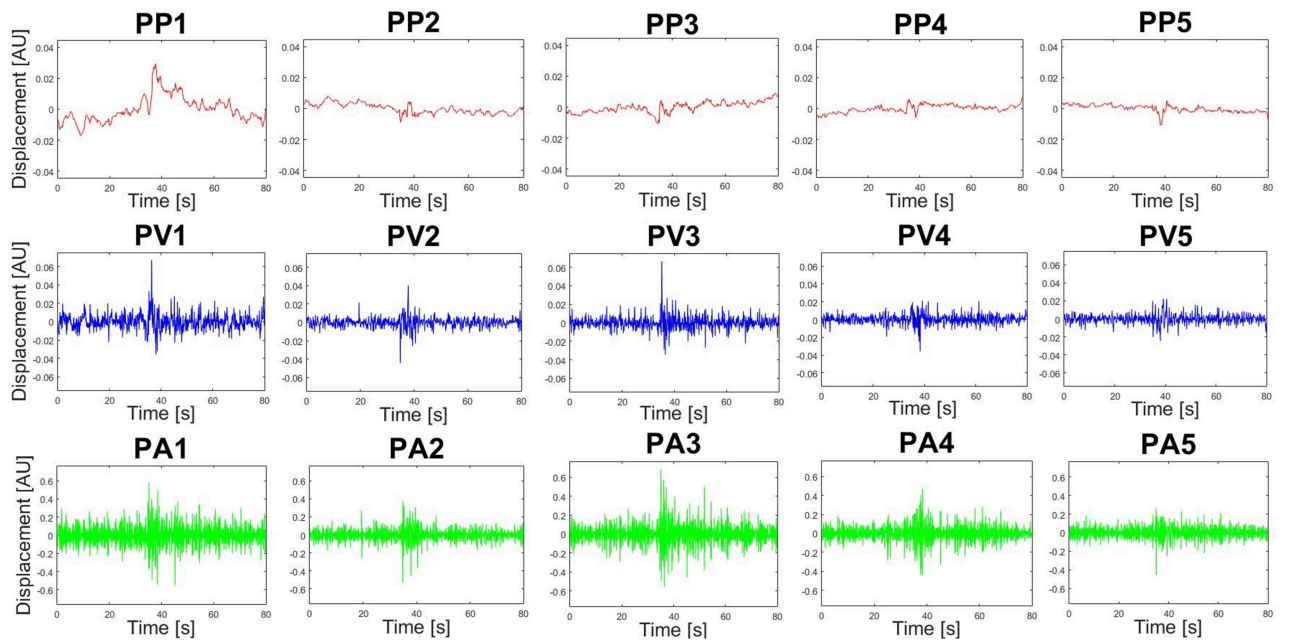


FIGURE 4 | Exemplary PP-, PV- and PA-time-series produced by the PManalyser. This specific data was recorded from a subject performing a tandem stance balance trial. The number of trials, subjects and PMs displayed per figure can be selected in the interface. Units are arbitrary (AU), since they represent a combined motion of all markers and may depend on pre-processing options.

quantifiable amounts of the overall variance produced by the analyzed movement. This allows categorizing them with respect to their relative contribution to the overall movement and to determine a movement's composition of PM, i.e. the movement structure (*rSTD*). Furthermore, the respective PM-time-series can be used to quantify novel aspects of postural control, such

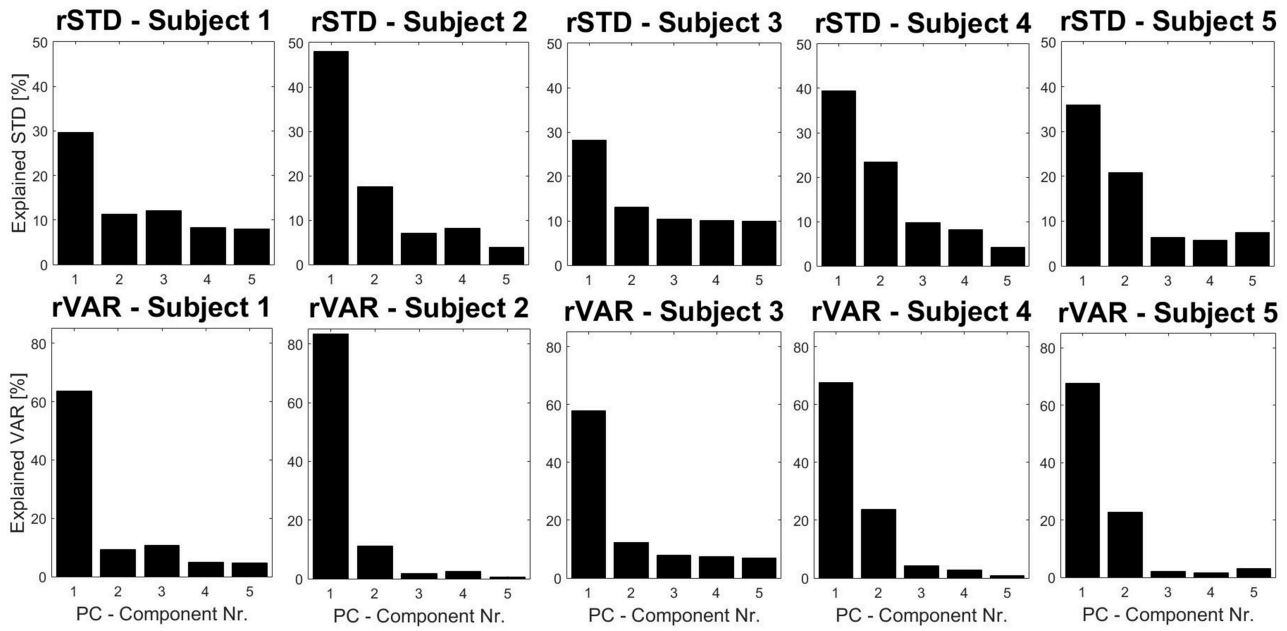


FIGURE 5 | Subject specific relative variances and standard deviations (rSTD and rVAR) for five subjects performing a tandem stance, using spherical coordinates. These eigenvalues are useful to compare the coordinative structure of a movement. In a similar fashion to **Figure 3** the cumulative versions of the variables can also be plotted with the software.

as how tight a movement is controlled (how often the control system intervenes (N_k) and how variable the control (σ_k) of the respective PM_k is). As an example, in accordance with the MIP the tandem stance study mentioned in the results of this paper (Haid et al., 2018) found that aging effects emerged in the movement structure and control of specific, task relevant components, but did not affect other movement components. In detail, the movement component with the least base of support exhibited less relative contribution and tighter control in the younger age group. Also leg dominance was studied in a similar fashion (Promsri et al., 2018b) revealing differing movement control characteristics in different movement components.

In addition, the PCA variables were used in several studies with clinical purposes, or for fundamental research. Specifically, they were helpful to classify gait patterns that are a result of spastic diplegia (Zago et al., 2017c), affect (Karg et al., 2010), gender or age (Troje, 2002; Verrel et al., 2009; Eskofier et al., 2013), or shoe material (Maurer et al., 2012; von Tscharner et al., 2013). Principal movements were also calculated as pre-processing step in research on work-related musculoskeletal disorders that aimed at characterizing the variability and the local dynamic stability of the movements (Longo et al., 2018a,b). The PM calculation allowed distinguishing cycle-to-cycle variability from changes in the overall postural configuration—a prerequisite for the calculation of non-linear variables such as the largest Lyapunov exponent in this context. In sports, coordinative strategies were studied, by identifying and quantifying PCA-eigenvectors, eigenvalues and score time-series, for example in alpine skiing (Federolf et al., 2014), cross-country skiing (Gløersen et al., 2017), Karate (Zago et al., 2017a), dancing (Masurelle et al., 2013), cycling (Moore et al., 2011), diving (Young and Reinkensmeyer, 2014), and race-walking (Donà et al., 2009).

In summary, literature suggests that kinematic PCA can be an effective tool to study pathological conditions or sport performance, and to address unsolved problems of motor control theories such as the minimal intervention principle. The basic code structure of the PManalyzer was originally developed for the tandem stance study (Haid et al., 2018). Later, the code was further developed to be applicable in a wider range of static balancing tasks. However, as discussed in the following section, it is also modifiable to be used in other application areas.

Computational Features and Advantages of the Software

The main purpose of the PManalyzer software was to make PCA computations more easily accessible for users, particularly for users less familiar with programming or with the mathematical background of PCA applications. The PManalyzer offers the broad spectrum of available computational options and the large variety of easily customizable visualization options. It also allows a user to perform pre-processing steps like PCA-based gap-filling (Gløersen and Federolf, 2016), deleting markers, columns or rows, or to integrate any other self-defined data pre-processing steps. Additionally, the PManalyzer can transform data from a Cartesian into a spherical or polar coordinate system. Users with more advanced mathematical knowledge can implement further coordinate transformations. Moreover, a number of pre-defined normalization options are available, of which two have been validated (mean Euclidean distance and height) through

previous research (Federolf P. et al., 2013; Zago et al., 2017b; Haid et al., 2018; Promsri et al., 2018a), while others (such as maximum movement range in x, y, or z direction) have yet to be explored. Also the weighting options for the standard 39 and 37 (no fingers) plug-in gate marker systems are pre-implemented, as well as the specialized 28 marker system (only symmetric markers) used in the tandem stance study of the results (Haid et al., 2018).

Furthermore, new variables can easily be implemented to be computed on all PM-time-series. If selected, they will be saved with the other variables on the ***PP***-, ***PV***- and ***PA***-time-series (*rVAR*, *rSTD*, *N*, σ, RMS, mean, standard deviation, amongst others). For users not familiar with Matlab programming, the results of all computed variables can be exported to an Excel spread sheet. Moreover, users can create customized plots that are directly integrated into the interface. Finally, any video coloring option can be added to the software without extensive Matlab skills, saving programming time and effort.

To validate the obtained basis $\boldsymbol{PC_k}$, a leave one out cross-validation has been implemented that produces a figure displaying the angle-changes as described in section PCA validity considerations. Furthermore, a figure containing a Welch's power spectral density estimate can be created to help determine a suitable filtering frequency. Moreover, specifying a vector of cut-off frequencies will run the selected PCA-computations consecutively with different filtering cut-off frequencies and saving the results in separate folders. This is particularly useful, in order to conduct a frequency analysis to ensure that statistical results are stable for various cut-off frequencies (Haid and Federolf, 2018; Haid et al., 2018; Promsri et al., 2018a).

Limitations and Future Research Potential

When it comes to effectively applying kinematic PCA and to establishing reliable norm values for a clinical and sports related environment, several factors should be considered. First, kinematic PCA is only one of many interesting feature extraction algorithms. For example, independent component analysis (von Tscharner et al., 2013), isometric feature mapping (Blackburn et al., 2003) and linear discriminant analysis (Karg et al., 2010) have been used as kinematic feature extraction tools and shown to outperform PCA in specific situations. Hence, there is tremendous potential for systematic research into the advantages and disadvantages of PCA compared to several other feature extraction techniques (Van Der Maaten et al., 2009).

Second, in order to establish norm values it is essential to define standard procedures. Hence, marker systems, pre-processing options, normalization and weighting, and coordinate transformations must be explored and standardized for different types of movements. Specifically, coordinate transformations are an interesting, yet relatively unexplored feature in kinematic PCA. As an example, the tandem-stance study analyzed nine different ankle, knee, upper body and head strategies, explaining 98% of the overall variance. The results in this study show that only 6 PMs would be necessary to achieve the same accuracy, if spherical coordinates were used. Furthermore, also moving coordinate systems offer unexplored potential. The example of alpine skiing technique analysis (Federolf et al., 2014) shows that body-positioning-dependent coordinate systems can help focus the analysis by neglecting movements with respect to specified planes. A similar, implemented pre-processing feature in the PManalyzer is the pre-processing option that moves the coordinate system into the center of mass, which can be used to avoid body displacements being represented as PMs.

Third, PCA based variables described in this study have been applied successfully to quantify movement coordination and complexity (*rEV*, *rVAR*, *rSTD*, and *RV*), and movement control (*N*, σ, ***PP***-irregularity), amongst others. However, especially the variables of movement control computed on the ***PA***-time-series (*N*, σ) react sensitively to the quality of kinematic data and filtering settings, due to double differentiation of the data. Nevertheless, a frequency analysis of the variables of movement control indicated that the underlying effects are robust to changes in filtering frequency and not random artifacts (Haid and Federolf, 2018; Haid et al., 2018; Promsri et al., 2018a). Hence, it should be possible to use PCA variables to establish objective norm values that describe movement performance. However, follow-up research is needed to further validate existing variables and possible to develop new ones.

Finally, the extracted principal movements must be carefully interpreted. Each PM is defined by one linear movement of each marker. Since real whole-body movements are usually not linear, individual PMs can only approximate real movements, at best. However, some of the PMs obtained from movements with small amplitudes, such bipedal static balancing tasks (Federolf, 2016; Haid et al., 2018), seem to be realistic approximations of movement strategies that were already described in the literature, such as ankle sway and hip-strategies (Gage et al., 2004; Kuznetsov and Riley, 2012; Kilby et al., 2015). Others, such as certain upper body strategies have not been described in literature but seem realistic in the author's eyes. Furthermore, non-linear movements with higher amplitudes would require at least two or more PMs to be approximated in a realistic way. In theory, this limitation could be overcome with specialized non-linear coordinate transformations or other feature extraction techniques. At the moment, evidence suggests that the PMs of higher amplitude movements describe interesting features that allow group classifications, e.g., gait recognition (Troje, 2002; Verrel et al., 2009; Karg et al., 2010) or sport performance (Donà et al., 2009; Federolf et al., 2014; Young and Reinkensmeyer, 2014). However, further research is needed to link specific linear PM-combinations to realistic non-linear movements.

In terms of the PManalyzer, some of the GUI options, for example weighing markers according to the segment masses they represent, depend on the input data (number and distribution of markers) and the type of movement analyzed. A flexible usage requires the user to define these options for non-standardized input data, since, specifically for these options, the software relies on pre-implemented options rather than on software recognition. However, only basic, easily acquirable Matlab knowledge is needed to follow the templates in the editable functions and to perform such changes in the according functions. Furthermore, despite beta testing, bugs can never be excluded. Nevertheless, we are confident that the software works well, as it has been tested on various data sets (Haid and Federolf, 2018; Haid et al., 2018; Longo et al., 2018a,b, 2019; Promsri et al., 2018a,b), yielding the

expected results. We encourage the community to report possible improvements to the authors.

CONCLUSIONS

We presented the PManalyzer, a software tool that is meant as a basis code for applying PCA in the analysis of human movement and its sensorimotor control. We hope this will encourage colleagues to more often apply PCA in their movement control related research. The computational options are not meant to be complete, but rather to enable easy software modifications to assist future users in the development of specialized applications.

ETHICS STATEMENT

The example data in section Discussion was taken from a study that was conducted in agreement with the Declaration of Helsinki, in particular, an institutionalized ethics review board had approved the study design and informed written consent was obtained from all volunteers prior to any measurements.

AUTHOR CONTRIBUTIONS

TH developed and implemented the PManalyzer, and wrote the first draft of the paper, the quick start guide and the user's manual, constantly updating the software and the manuscripts. MZ validated the software's computational steps, by comparing the PCA outputs to previously published results, and repeatedly revised both the paper and the starter guide. AP contributed by challenging several software-updates as they became available and helped eliminating numerous update-bugs. She also gave valuable insights on how to improve the software's usability and revised the starter guide. A-CD tested the functionality and adaptability of the software, improving code-documentation and contributed to the manuscript and the quick start guide. PF contributed as mentor and PCA-teacher, which lead to the PManalyzer software project. For this paper he was also deeply involved in the writing-process, improving its structure, and wording. Moreover, his regular and critical software evaluations drastically improved the PManalyzer.

ACKNOWLEDGMENTS

We would like to thank all students and co-workers involved in testing early versions of the software for their feedback. Particularly, Julian Kiefer, Roman Rethwilm, Inge Werner, Alessia Longo, and Felix Wachholz.

The current study was an internal research project that did not receive external funding. Internal university grants may cover parts of the open access publishing costs after the paper has been published.

SUPPLEMENTARY MATERIAL

The Supplementary Material for this article can be found online at: https://www.frontiersin.org/articles/10.3389/fninf.2019.00024/full#supplementary-material Supplementary materials (the PManalyzer software, documentation, data examples and video files) can be found online at: https://www.uibk.ac.at/isw/forschung/neurophysiologie-bewegungswissenschaft/software.html.

The website contains the most recent, updated versions of the software, a quick start guide "GettingStarted_PManalyzer.docx" and a user's manual ("UsersManual_PManalyzer.pdf").

REFERENCES

Alfuth, M., and Gomoll, M. (2018). Electromyographic analysis of balance exercises in single-leg stance using different instability modalities of the forefoot and rearfoot. *Phys. Ther. Sport Off. J. Assoc. Chart. Physiother. Sports Med.* 31, 75–82. doi: 10.1016/j.ptsp.2018.01.002

Bernstein, N. (1967). *The Co-Ordination and Regulation of Movements*. Oxford: Pergamon-Press.

Blackburn, J. T., Riemann, B. L., Myers, J. B., and Lephart, S. M. (2003). Kinematic analysis of the hip and trunk during bilateral stance on firm, foam, and multiaxial support surfaces. *Clin. Biomech.*18, 655–661. doi: 10.1016/S0268-0033(03)00091-3

Borg, F. G., and Laxåback, G. (2010). Entropy of balance–some recent results. *J. Neuroeng. Rehabil.* 7:38. doi: 10.1186/1743-0003-7-38

Boström, K. J., Dirksen, T., Zentgraf, K., and Wagner, H. (2018). The contribution of upper body movements to dynamic balance regulation during challenged locomotion. *Front. Hum. Neurosci.* 12:8. doi: 10.3389/fnhum.2018.00008

Bro, R., Kjeldahl, K., Smilde, A. K., and Kiers, H. A. L. (2008). Cross-validation of component models: a critical look at current methods. *Anal. Bioanal. Chem.* 390, 1241–1251. doi: 10.1007/s00216-007-1790-1

Camacho, J., and Ferrer, A. (2012). Cross-validation in PCA models with the element-wise k-fold (ekf) algorithm: theoretical aspects. *J. Chemom.* 26, 361–373. doi: 10.1002/cem.2440

Cavanaugh, J. T., Guskiewicz, K. M., Giuliani, C., Marshall, S., Mercer, V. S., and Stergiou, N. (2006). Recovery of postural control after cerebral concussion: new insights using approximate entropy. *J. Athl. Train.* 41, 305–313.

Daffertshofer, A., Lamoth, C. J. C., Meijer, O. G., and Beek, P. J. (2004). PCA in studying coordination and variability: a tutorial. *Clin. Biomech.* 19, 415–428. doi: 10.1016/j.clinbiomech.2004.01.005

De Beaumont, L., Mongeon, D., Tremblay, S., Messier, J., Prince, F., Leclerc, S., et al. (2011). Persistent motor system abnormalities in formerly concussed athletes. *J. Athl. Train.* 46, 234–240. doi: 10.4085/1062-6050-46.3.234

de Leva, P. (1996). Adjustments to Zatsiorsky-Seluyanov's segment inertia parameters. *J. Biomech.* 29, 1223–1230.

Defense Technical Information Center (1988). *DTIC ADA304353: Anthropometry and Mass Distribution for Human Analogues, Volume I. Military Male Aviators.* Available online at: http://archive.org/details/DTIC_ADA304353 (accessed April 25, 2018).

Diana, G., and Tommasi, C. (2002). Cross-validation methods in principal component analysis: a comparison. *Stat. Methods Appl.* 11, 71–82. doi: 10.1007/BF02511446

Donà, G., Preatoni, E., Cobelli, C., Rodano, R., and Harrison, A. J. (2009). Application of functional principal component analysis in race walking: an emerging methodology. *Sports Biomech.* 8, 284–301. doi: 10.1080/14763140903414425

Donker, S. F., Roerdink, M., Greven, A. J., and Beek, P. J. (2007). Regularity of center-of-pressure trajectories depends on the amount of attention invested in postural control. *Exp. Brain Res.* 181, 1–11. doi: 10.1007/s00221-007-0905-4

Eskofier, B. M., Federolf, P., Kugler, P. F., and Nigg, B. M. (2013). Marker-based classification of young-elderly gait pattern differences via direct PCA feature extraction and SVMs. *Comput. Methods Biomech. Biomed. Eng.* 16, 435–442. doi: 10.1080/10255842.2011.624515

Federolf, P., Reid, R., Gilgien, M., Haugen, P., and Smith, G. (2014). The application of principal component analysis to quantify technique in sports. *Scand. J. Med. Sci. Sports* 24, 491–499. doi: 10.1111/j.1600-0838.2012.01455.x

Federolf, P., Roos, L., and Nigg, B. (2012). The effect of footwear on postural control in bipedal quiet stance. *Footwear Sci.* 4, 115–122. doi: 10.1080/19424280.2012.666270

Federolf, P., Roos, L., and Nigg, B. M. (2013). Analysis of the multi-segmental postural movement strategies utilized in bipedal, tandem and one-leg stance as quantified by a principal component decomposition of marker coordinates. *J. Biomech.* 46, 2626–2633. doi: 10.1016/j.jbiomech.2013.08.008

Federolf, P. A. (2016). A novel approach to study human posture control: "Principal movements" obtained from a principal component analysis of kinematic marker data. *J. Biomech.* 49, 364–370. doi: 10.1016/j.jbiomech.2015.12.030

Federolf, P. A., Boyer, K. A., and Andriacchi, T. P. (2013). Application of principal component analysis in clinical gait research: identification of systematic differences between healthy and medial knee-osteoarthritic gait. *J. Biomech.* 46, 2173–2178. doi: 10.1016/j.jbiomech.2013.06.032

Figueroa, P. J., Leite, N. J., and Barros, R. M. L. (2003). A flexible software for tracking of markers used in human motion analysis. *Comput. Methods Programs Biomed.* 72, 155–165. doi: 10.1016/S0169-2607(02)00122-0

Fino, P. C., Nussbaum, M. A., and Brolinson, P. G. (2016). Decreased high-frequency center-of-pressure complexity in recently concussed asymptomatic athletes. *Gait Post.* 50, 69–74. doi: 10.1016/j.gaitpost.2016.08.026

Gage, W. H., Winter, D. A., Frank, J. S., and Adkin, A. L. (2004). Kinematic and kinetic validity of the inverted pendulum model in quiet standing. *Gait Post.* 19, 124–132. doi: 10.1016/S0966-6362(03)00037-7

Gallagher, D., and Heymsfield, S. B. (1998). Muscle distribution: variations with body weight, gender, and age. *Appl. Radiat. Isot.* 49, 733–734.

Gao, J., Hu, J., Buckley, T., White, K., and Hass, C. (2011). Shannon and Renyi entropies to classify effects of Mild Traumatic Brain Injury on postural sway. *PLoS ONE* 6:e24446. doi: 10.1371/journal.pone.0024446

Gløersen, Ø., and Federolf, P. (2016). Predicting missing marker trajectories in human motion data using marker intercorrelations. *PLoS ONE* 11:e0152616. doi: 10.1371/journal.pone.0152616

Gløersen, Ø., Myklebust, H., Hallén, J., and Federolf, P. (2017). Technique analysis in elite athletes using principal component analysis. *J. Sports Sci.* 36, 229–237. doi: 10.1080/02640414.2017.1298826

Haid, T., and Federolf, P. (2018). Human postural control: assessment of two alternative interpretations of center of pressure sample entropy through a principal component factorization of whole-body kinematics. *Entropy* 20:30. doi: 10.3390/e20010030

Haid, T. H., Doix, A.-C. M., Nigg, B. M., and Federolf, P. A. (2018). Age effects in postural control analyzed via a principal component analysis of kinematic data and interpreted in relation to predictions of the optimal feedback control theory. *Front. Aging Neurosci.* 10:22. doi: 10.3389/fnagi.2018.00022

Han, A., Fu, A., Cobley, S., and Sanders, R. H. (2018). Effectiveness of exercise intervention on improving fundamental movement skills and motor coordination in overweight/obese children and adolescents: a systematic review. *J. Sci. Med. Sport* 21, 89–102. doi: 10.1016/j.jsams.2017.07.001

Haran, F. J., and Keshner, E. A. (2008). Sensory reweighting as a method of balance training for labyrinthine loss. *J. Neurol. Phys. Ther.* 32, 186–191. doi: 10.1097/NPT.0b013e31818dee39

Honegger, F., Tielkens, R. J. M., and Allum, J. H. J. (2013). Movement strategies and sensory reweighting in tandem stance: differences between trained tightrope walkers and untrained subjects. *Neuroscience* 254, 285–300. doi: 10.1016/j.neuroscience.2013.09.041

Huisinga, J., Mancini, M., Veys, C., Spain, R., and Horak, F. (2017). Coherence analysis of trunk and leg acceleration reveals altered postural sway strategy during standing in persons with multiple sclerosis. *Hum. Mov. Sci.* 58, 330–336. doi: 10.1016/j.humov.2017.12.009

Hume, D. R., Navacchia, A., Rullkoetter, P. J., and Shelburne, K. B. (2019). A lower extremity model for muscle-driven simulation of activity using explicit finite element modeling. *J. Biomech.* 84, 153–160. doi: 10.1016/j.jbiomech.2018.12.040

Karg, M., Kuhnlenz, K., and Buss, M. (2010). Recognition of Affect Based on Gait Patterns. *IEEE Trans. Syst. Man Cybern. Part B Cybern.* 40, 1050–1061. doi: 10.1109/TSMCB.2010.2044040

Kilby, M. C., Molenaar, P. C. M., and Newell, K. M. (2015). Models of postural control: shared variance in joint and COM motions. *PLoS ONE* 10:e0126379. doi: 10.1371/journal.pone.0126379

Kuznetsov, N. A., and Riley, M. A. (2012). Effects of breathing on multijoint control of center of mass position during upright stance. *J. Mot. Behav.* 44, 241–253. doi: 10.1080/00222895.2012.688894

Lim, Y. H., Partridge, K., Girdler, S., and Morris, S. L. (2017). Standing postural control in individuals with autism spectrum disorder: systematic review and meta-analysis. *J. Autism Dev. Disord.* 47, 2238–2253. doi: 10.1007/s10803-017-3144-y

Longo, A., Federolf, P., Haid, T., and Meulenbroek, R. (2018a). Effects of a cognitive dual task on variability and local dynamic stability in sustained repetitive arm movements using principal component analysis: a pilot study. *Exp. Brain Res.* 236, 1611–1619. doi: 10.1007/s00221-018-5241-3

Longo, A., Haid, T., Meulenbroek, R., and Federolf, P. (2019). Biomechanics in posture space: properties and relevance of principal accelerations for characterizing movement control. *J. Biomech.* 82, 397–403. doi: 10.1016/j.jbiomech.2018.11.031

Longo, A., Meulenbroek, R., Haid, T., and Federolf, P. (2018b). Postural reconfiguration and cycle-to-cycle variability in patients with work-related musculoskeletal disorders compared to healthy controls and in relation to pain emerging during a repetitive movement task. *Clin. Biomech.* 54, 103–110. doi: 10.1016/j.clinbiomech.2018.03.004

MacRae, C. S., Critchley, D., Lewis, J. S., and Shortland, A. (2018). Comparison of standing postural control and gait parameters in people with and without chronic low back pain: a cross-sectional case-control study. *BMJ Open Sport Exerc. Med.* 4:e000286. doi: 10.1136/bmjsem-2017-000286

Masumoto, J., and Inui, N. (2015). Motor control hierarchy in joint action that involves bimanual force production. *J. Neurophysiol.* 113, 3736–3743. doi: 10.1152/jn.00313.2015

Masurelle, A., Essid, S., and Richard, G. (2013). "Multimodal classification of dance movements using body joint trajectories and step sounds," in *2013 14th International Workshop on Image Analysis for Multimedia Interactive Services (WIAMIS)*. Paris, 1–4. doi: 10.1109/WIAMIS.2013.6616151

Maurer, C., Federolf, P., von Tscharner, V., Stirling, L., and Nigg, B. M. (2012). Discrimination of gender-, speed-, and shoe-dependent movement patterns in runners using full-body kinematics. *Gait Post.* 36, 40–45. doi: 10.1016/j.gaitpost.2011.12.023

McNair, P. J., Boocock, M. G., Dominick, N. D., Kelly, R. J., Farrington, B. J., and Young, S. W. (2018). A comparison of walking gait following mechanical and kinematic alignment in total knee joint replacement. *J. Arthroplasty* 33, 560–564. doi: 10.1016/j.arth.2017.09.031

Moore, J. K., Kooijman, J. D. G., Schwab, A. L., and Hubbard, M. (2011). Rider motion identification during normal bicycling by means of principal component analysis. *Multibody Syst. Dyn.* 25, 225–244. doi: 10.1007/s11044-010-9225-8

Nikaido, Y., Akisue, T., Kajimoto, Y., Tucker, A., Kawami, Y., Urakami, H., et al. (2018). Postural instability differences between idiopathic normal pressure hydrocephalus and Parkinson's disease. *Clin. Neurol. Neurosurg.* 165, 103–107. doi: 10.1016/j.clineuro.2018.01.012

Oliveira, A. S., Silva, P. B., Lund, M. E., Farina, D., and Kersting, U. G. (2017). Balance training enhances motor coordination during a perturbed sidestep cutting task. *J. Orthop. Sports Phys. Ther.* 47, 853–862. doi: 10.2519/jospt.2017.6980

Pollock, C. L., Hunt, M. A., Vieira, T. M., Gallina, A., Ivanova, T. D., and Garland, S. J. (2019). Challenging standing balance reduces the asymmetry of motor control of postural sway poststroke. *Motor Control.* 1–17. doi: 10.1123/mc.2017-0098

Promsri, A., Haid, T., and Federolf, A. P. (2018a). How does lower limb dominance influence postural control movements during single leg stance? *Hum. Mov. Sci.* 58, 165–174. doi: 10.1016/j.humov.2018.02.003

Promsri, A., Haid, T., Werner, I., and Federolf, P. (2018b). Influence of lower-limb dominance on coordinative movement structures observed during single-leg balancing on a multiaxial unstable surface. *Gait Posture.* 65, 60–61. doi: 10.1016/j.gaitpost.2018.06.047

Sadeghi, H., Allard, P., and Duhaime, M. (1997). Functional gait asymmetry in able-bodied subjects. *Hum. Mov. Sci.* 16, 243–258. doi: 10.1016/S0167-9457(96)00054-1

Shahvarpour, A., Gagnon, D., Preuss, R., Henry, S. M., and Larivière, C. (2018). Trunk postural balance and low back pain: reliability and relationship with clinical changes following a lumbar stabilization exercise program. *Gait Post.* 61, 375–381. doi: 10.1016/j.gaitpost.2018.02.006

Shlens, J. (2014). A tutorial on principal component analysis. *arXiv [preprint]* arXiv:1404.1100

Stins, J. F., Michielsen, M. E., Roerdink, M., and Beek, P. J. (2009). Sway regularity reflects attentional involvement in postural control: effects of expertise, vision and cognition. *Gait Post.* 30, 106–109. doi: 10.1016/j.gaitpost.2009.04.001

Todorov, E., and Jordan, M. I. (2002). Optimal feedback control as a theory of motor coordination. *Nat. Neurosci.* 5, 1226–1235. doi: 10.1038/nn963

Troje, N. F. (2002). Decomposing biological motion: a framework for analysis and synthesis of human gait patterns. *J. Vis.* 2, 371–387. doi: 10.1167/2.5.2

Van Der Maaten, L., Postma, E., and Van den Herik, J. (2009). Dimensionality reduction: a comparative. *J. Mach. Learn. Res.* 10, 66–71.

Verrel, J., Lövdén, M., Schellenbach, M., Schaefer, S., and Lindenberger, U. (2009). Interacting effects of cognitive load and adult age on the regularity of whole-body motion during treadmill walking. *Psychol. Aging* 24, 75–81. doi: 10.1037/a0014272

von Tscharner, V., Enders, H., and Maurer, C. (2013). Subspace identification and classification of healthy human gait. *PLoS ONE* 8:e65063. doi: 10.1371/journal.pone.0065063

Wang, Z., Molenaar, P. C. M., Challis, J. H., Jordan, K., and Newell, K. M. (2014). Visual information and multi-joint coordination patterns in one-leg stance. *Gait Post.* 39, 909–914. doi: 10.1016/j.gaitpost.2013.11.017

Yamagata, M., Ikezoe, T., Kamiya, M., Masaki, M., and Ichihashi, N. (2017). Correlation between movement complexity during static standing and balance function in institutionalized older adults. *Clin. Interv. Aging* 12, 499–503. doi: 10.2147/CIA.S132425

Young, C., and Reinkensmeyer, D. J. (2014). Judging complex movement performances for excellence: a principal components analysis-based technique applied to competitive diving. *Hum. Mov. Sci.* 36, 107–122. doi: 10.1016/j.humov.2014.05.009

Zago, M., Codari, M., Iaia, F. M., and Sforza, C. (2017a). Multi-segmental movements as a function of experience in karate. *J. Sports Sci.* 35, 1515–1522. doi: 10.1080/02640414.2016.1223332

Zago, M., Pacifici, I., Lovecchio, N., Galli, M., Federolf, P. A., and Sforza, C. (2017b). Multi-segmental movement patterns reflect juggling complexity and skill level. *Hum. Mov. Sci.* 54, 144–153. doi: 10.1016/j.humov.2017.04.013

Zago, M., Sforza, C., Bona, A., Cimolin, V., Costici, P. F., Condoluci, C., et al. (2017c). How multi segmental patterns deviate in spastic diplegia from typical developed. *Clin. Biomech. Bristol Avon* 48, 103–109. doi: 10.1016/j.clinbiomech.2017.07.016

Conflict of Interest Statement: The authors declare that the research was conducted in the absence of any commercial or financial relationships that could be construed as a potential conflict of interest.

Copyright © 2019 Haid, Zago, Promsri, Doix and Federolf. This is an open-access article distributed under the terms of the Creative Commons Attribution License (CC BY). The use, distribution or reproduction in other forums is permitted, provided the original author(s) and the copyright owner(s) are credited and that the original publication in this journal is cited, in accordance with accepted academic practice. No use, distribution or reproduction is permitted which does not comply with these terms.

frontiers in Neuroinformatics

TECHNOLOGY REPORT
published: 09 April 2019
doi: 10.3389/fninf.2019.00021

Spatial Localization of EEG Electrodes in a TOF+CCD Camera System

Shengyong Chen[1,2]*, *Yu He*[1], *Huili Qiu*[2], *Xi Yan*[1,3] *and Meng Zhao*[2]

[1] College of Computer Science, Zhejiang University of Technology, Hangzhou, China, [2] School of Computer Science and Engineering, Tianjin University of Technology, Tianjin, China, [3] College of Business, Missouri State University, Missouri, TX, United States

A crucial link of electroencephalograph (EEG) technology is the accurate estimation of EEG electrode positions on a specific human head, which is very useful for precise analysis of brain functions. Photogrammetry has become an effective method in this field. This study aims to propose a more reliable and efficient method which can acquire 3D information conveniently and locate the source signal accurately in real-time. The main objective is identification and 3D location of EEG electrode positions using a system consisting of CCD cameras and Time-of-Flight (TOF) cameras. To calibrate the camera group accurately, differently to the previous camera calibration approaches, a method is introduced in this report which uses the point cloud directly rather than the depth image. Experimental results indicate that the typical distance error of reconstruction in this study is 3.26 mm for real-time applications, which is much better than the widely used electromagnetic method in clinical medicine. The accuracy can be further improved to a great extent by using a high-resolution camera.

Keywords: EEG, TOF camera, system calibration, point cloud, electrode localization

OPEN ACCESS

Edited by:
Antonio Fernández-Caballero, University of Castilla La Mancha, Spain

Reviewed by:
Aureli Soria-Frisch, Starlab Barcelona Sl, Spain
Stavros I. Dimitriadis, Cardiff University, United Kingdom

***Correspondence:**
Shengyong Chen
sy@ieee.org

Received: *08 April 2018*
Accepted: *13 March 2019*
Published: *09 April 2019*

Citation:
Chen S, He Y, Qiu H, Yan X and Zhao M (2019) Spatial Localization of EEG Electrodes in a TOF+CCD Camera System. Front. Neuroinform. 13:21. doi: 10.3389/fninf.2019.00021

INTRODUCTION

The electroencephalograph (EEG) technology is now widely used in clinical medicine such as epilepsy, coma, brain deaths and so on, due to its use, economy, safety, and non-invasive detection (Jeon et al., 2018). To well-use the EEG technology for analyzing the brain activities, it is important to accurately locate the position of scalp signal in the cerebral cortex (Qian and Sheng, 2011; Reis and Lochmann, 2015; Butler et al., 2016; Saha et al., 2017; Liu et al., 2018). At present, there are several kinds of EEG electrode localization methods, including (1) manual method, (2) digital radio frequency (RF) electromagnetic instrument, (3) magnetic resonance (MR), (4) ultrasonic transmission and reflection, and (5) photogrammetric method (Koessler et al., 2007). The manual method needs a relevant tool to measure the distance according to the preset sensor. This method is low in cost, but it is time-consuming and labor-consuming, and it is easy to cause errors due to manual operation (Russell et al., 2005). Electromagnetic RF digital instrumentation is currently the most widely utilized method. The principle is to locate the position of an EEG electrode through the magnetic field, and its accuracy is up to 4 mm. Of course, it is faster and more convenient than the manual method, but the disadvantage is that single point measurements are prone to mistakes, which means that to obtain accurate results the work needs to be repeated many times. Moreover, this method is strict with the overall

measurement environment, requiring appropriate air humidity and temperature and no metal artifacts. Additional data conversion tools are also necessary. The specific implementation of the MR method requires an additional calibration object, which is not applicable to multi-sensor situations. The ultrasonic method is the same as the digital electromagnetic conversion method, which requires a single point measurement and consumes time and energy. One of the common disadvantages of the above methods is that the electrical signal will interfere with the weak EEG signals, which will affect the final detection results.

Compared with traditional methods, the photogrammetric method is fast, accurate, and easy to operate. From early 2000, Bauer et al. used a method to achieve the EEG electrode localization system with 12 industrial cameras, which did not specify the system settings and operating procedures (Bauer et al., 2000). Russell et al. used 11 sets of industrial cameras to locate the electrode position (Russell et al., 2005). The method is simple in operation, time-saving for operators, and there is no need for additional devices. The experimental process only takes 15–20 min, and patients are not required to participate in the subsequent data processing, which brings great convenience to patients and doctors. The working principle of this method is to calibrate the 11 cameras and obtain the three-dimensional (3D) information of each electrode with the ideas of stereo matching in computer vision. Yet, there are three shortcomings. Firstly, each electrode of the image must be manually marked, which is likely to cause artificial errors. Secondly, the system is only suitable for self-made electrode caps, not applicable to other types of electrode caps, but other traditional methods do not have this limitation. Thirdly, the system can only identify the visible electrode points. For some invisible electrode points which may be hidden in the hair, this method is useless, but electromagnetic digital method and ultrasonic method do not have this limitation (Zhang et al., 2014). The equipment is so complex that it is not easy to operate. Baysal and Sengül (2010) used only one camera to locate the electrode position, hoping to reduce costs. The working process is to move the camera along a pre-set route, taking pictures at every angle (Koessler et al., 2007). Although the cost is reduced, the patient must stay still for a long period of time, increasing the likelihood of human error and prolonging the duration of data acquisition.

Recently, there has been a great deal of interest in the development and applications of time-of-flight (TOF) depth cameras. In 2015, Yao et al. presented the full very large-scale integration (VLSI) implementation of a new high-resolution depth-sensing system on a chip (SoC) based on active infrared structured light, which estimates the 3D scene depth by matching randomized speckle patterns (Yao et al., 2015). At the same year, Golbach et al. presented a computer-vision system for seedling phenotyping that combines best of both approaches by utilizing TOF depth cameras (Golbach et al., 2016). Although TOF has its unique features, the practical applicability of TOF cameras is still limited by low resolution and quality of depth measurements. This has motivated many researchers to combine TOF cameras with other sensors in order to enhance and upsample depth images (Eichhardt et al., 2017). Calibration between depth cameras and other sensors has become a major concern. A modified method about multi-modal camera calibration is proposed in this report.

In summary, methods in previous studies, to some degree, can solve data acquisition and operability, but there are still many limitations. This report proposes a convenient and accurate method, which is also based on the photogrammetry principle (Russell et al., 2005; Clausner et al., 2017). The acquisition system of EEG signals based on RGB-Depth (RGB-D) multi-modal data is constructed by using the high resolution industrial camera and the high precision depth camera to capture the object's distance and color information simultaneously. The system captures images from five perspectives, which contains all the collected electrodes from all the perspectives. Electrode distribution of the electrode cap adopts the international 10–20 standard. The information collecting process can be performed in real-time. All image processing algorithms are achieved off-line, which greatly improves the flexibility and operability of the system.

This article reports the design of such a photogrammetry system both theoretically and experimentally. The remainder of this report is structured as follows. Section Technology and Implementation introduces the implementation technology, including the sensing method, camera calibration, and singular value decomposition (SVD) algorithm. The experimental process for electrode identification and localization will be presented in section Experiments and Results. Finally, the report summarizes the findings and concluding remarks.

TECHNOLOGY AND IMPLEMENTATION

System Setup

The existing photogrammetric methods, whether measured through a monocular, binocular, or multi-camera system, without exception, are to obtain 3D information of the electrode positions by adopting the stereo vision method. Theoretically, each electrode point needs to be captured by two or more cameras. They need to deal with more pictures, and the algorithm is more complex. Therefore, this report proposes the use of a depth camera, MESA-SR-4000, based on TOF technology, which can directly obtain the depth information. The existing depth camera cannot directly identify the position of the EEG electrode because of its low resolution. However, the color camera can get the target color, texture and other 2D information. Hence, this project combines the two cameras to get the distance and color information of the scene. Accordingly, the EEG signal acquisition system based on RGB-D multi modal data is built. As long as all the electrodes are captured by the system, all the 3D information of the electrode can be obtained. This system can avoid the complexity of shooting the same electrode from two or more angles. Compared with the multipurpose camera, the system reduces the cost of materials, decreases the number of cameras, and greatly simplifies the algorithm. Compared with the single-camera, this system simplifies the experimental process and makes the operation simpler. There is no need to have a pre-set line nor to debug the angle of the placed mirror (Qian and Sheng, 2011), while at the same time, it improves efficiency.

The system processes in the following way. Firstly, the image is collected by using both the color camera and the depth camera.



FIGURE 1 | The camera system.



FIGURE 2 | The electrode cap on a head model and on a subjective head.

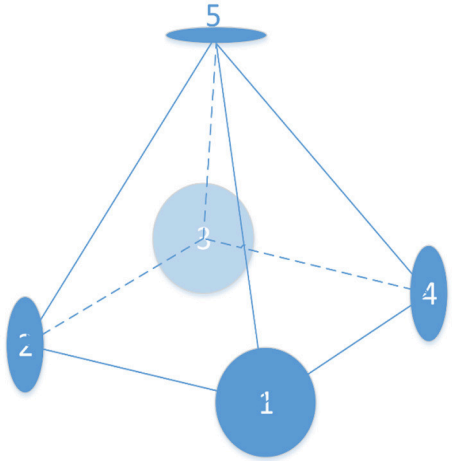


FIGURE 3 | The schematic diagram.

The color camera is responsible for the color picture of the electrode, so that the EEG electrode can be conveniently detected in the image and the 2D information of the electrode can be obtained. The depth camera is responsible for obtaining the point cloud data of the electrode, so that distance information of the electrode can be obtained. The key issue is the calibration of two different cameras. Secondly, this project uses the multi-camera measurement scheme, which can obtain all the electrodes, rather than the distance information. In this project, a five-camera group is applied to photograph the experimental targets in five angles. The five angles are located around the head. Of course, if the experimental equipment is not complete, the same camera group can also be located around the head at five angles, respectively. Ideally all the electrode information can be captured by the camera in five angles. Compared with the color camera based photogrammetry system, the photogrammetric system designed in this project has greatly reduced the number of angles taken and the complexity of the systematic framework.

In this project, the resolution of the color camera CCD is 1,624 × 1,234, and the depth camera TOF (MESA-SR-4000) has a resolution of 176×144. The combined camera system is shown in **Figure 1**. The electrode cap covered on a head model and a subjective head for practical tests are shown in **Figure 2**. The 10–20 electrodes are organized on a cap that is placed on the heads. The different colors on the electrode dot can easily be made, e.g., using some paint coat or sticky paper. In either way it is also easy to change colors. Making the dot colors does not affect the electrode functions or costs.

According to the accuracy of the TOF camera's sensing range, the best shooting distance of the TOF camera is between 0.5 and 8 m. The schematic diagram is shown in **Figure 3**. Five groups of cameras are used in this system to take pictures simultaneously, four (1, 2, 3, and 4 in **Figure 3**) of which are aligned around the head with an angle of 90°, while the last is located overhead. Then all the electrodes will be reconstructed through the color image captured by the CCD camera and depth information is obtained by the TOF camera. The target RGB-D data is obtained from multiple angles. The horizontal distance between the model and the camera is 60 cm and the vertical distance is 40 cm.

The operational flow of the system is shown in **Figure 4**. Firstly, the color images and the 3D point cloud data are obtained by using the color camera and the depth sensor in five angles. Then, electrode coordinates are detected and extracted in color images. Its coordinates in 3D space can be calculated by using the calibration results of color camera and depth sensor. Finally, the correlation algorithm is used to calculate the relationship between the five coordinate systems of the five views (Wang et al., 2017). Therefore, all the electrodes of different angles of view in five different coordinate systems are registered in the same spatial coordinate system.

System Calibration

Traditionally, the calibration method utilizes the depth map obtained by the TOF camera and the color map obtained by the CCD camera to complete calibration (Cheng et al., 2016; Raposo et al., 2016). Nevertheless, the resolution of the depth image is very low, and the results are often unstable. In order to solve this problem, this project uses a new calibration plate and accurate

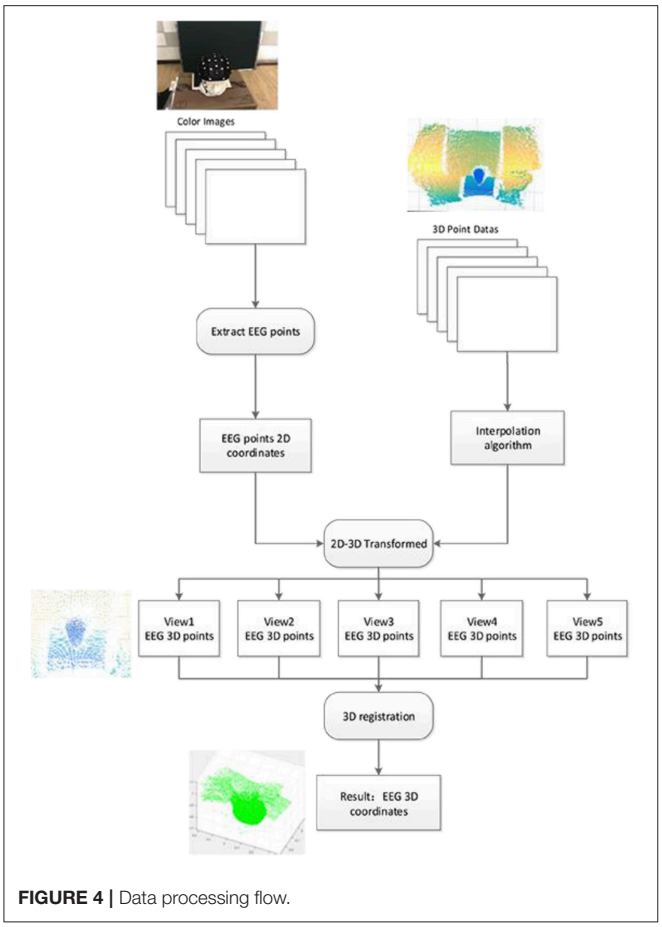


FIGURE 4 | Data processing flow.

point cloud data to perform camera calibration (Jung et al., 2015; Wei and Zhang, 2015). The comparison of the two methods will be described in the next section. The camera calibration model is designed as follows. Assuming that Q is a point in the space, the coordinates of the camera coordinate system are $(x_c, y_c, z_c)^T$. The projection of point Q in the normalized image is $\boldsymbol{X}_{\mathrm{n}}$

$$\boldsymbol{X}_n = \begin{bmatrix} x \\ y \end{bmatrix} = \begin{bmatrix} x_c/z_c \\ y_c/z_c \end{bmatrix} \tag{1}$$

If taking into account the lens distortion, the above coordinates are mapped $\boldsymbol{X}_{\mathrm{d}}$

$$\boldsymbol{X}_d = \begin{bmatrix} x' \\ y' \end{bmatrix} = (1 + k_1 r^2 + k_2 r^4)\boldsymbol{X}_n \tag{2}$$

where $r = \sqrt{x^2 + y^2}$, k_1, k_2 are radial distortion coefficients. $\boldsymbol{X}_{\mathrm{d}}$ is mapped to the image coordinates $\boldsymbol{X}_{\mathrm{q}}$, i.e.,

$$\boldsymbol{X}_q = \begin{bmatrix} x^* \\ y^* \end{bmatrix} = \begin{bmatrix} f_x x' + c_x \\ f_y y' + c_y \end{bmatrix} \tag{3}$$

where f_{x} and f_{y} are focal length in x and y directions, respectively, and c_{x} and c_{y} are the principle point coordinates.

The relationship between the camera groups can be described as the relationship between the coordinates of the point Q in the two camera coordinates. Assuming $\boldsymbol{X}_{\mathrm{cd}}$ is the coordinate vector of the point Q in the TOF camera coordinate system, $\boldsymbol{X}_{\mathrm{cc}}$ is the coordinate vector of the point Q in the CCD camera coordinate system, and their relationship can be described as

$$\boldsymbol{X}_{cc} = R\boldsymbol{X}_{cd} + T \tag{4}$$

The goal of calibration is to solve the rotation matrix R and the translation matrix T.

Decomposition for Data Stitching

With regard to the point cloud stitching problem, many works use an ICP algorithm or improved ICP algorithm (Cheng et al., 2016; Yang et al., 2016). However, here, due to the large deviation of the angle of view, the performance of ICP algorithm is not ideal, thus SVD is adopted to calculate the conversion relationship between the two sets of point clouds (Sorkine, 2009; Jung et al., 2015; Raposo et al., 2016). The principle is described firstly from this transform

$$(R, \boldsymbol{t}) = \operatorname{armgin} \sum_{i=1}^{n} w_i \left\| (R\boldsymbol{m}_i + \boldsymbol{t}) - \boldsymbol{n}_i \right\|^2 \tag{5}$$

where $w_{\mathrm{i}} > 0$ is the weight of each point in the cloud. Calculate the displacement, and the above formula R is set to invariant to derive t, at the same time $F_{(\mathrm{t})} = (R, t)$, which has the derived derivative

$$\begin{aligned} 0 &= \frac{\partial F}{\partial \boldsymbol{t}} = \sum\nolimits_{i=1}^{n} 2w_i \left(R\boldsymbol{m}_i + \boldsymbol{t} - \boldsymbol{n}_i\right) \\ &= 2\boldsymbol{t}\left(\sum\nolimits_{i=1}^{n} w_i\right) + 2R\left(\sum\nolimits_{i=1}^{n} w_i \boldsymbol{m}_i\right) - 2\sum\nolimits_{i=1}^{n} w_i \boldsymbol{n}_i \end{aligned} \tag{6}$$

where

$$\overline{\boldsymbol{m}} = \frac{\sum_{i=1}^{n} w_i \boldsymbol{m}_i}{\sum_{i=1}^{n} w_i}, \quad \overline{\boldsymbol{n}} = \frac{\sum_{i=1}^{n} w_i \boldsymbol{n}_i}{\sum_{i=1}^{n} w_i} \tag{7}$$

$$\mathbf{t} = \overline{\boldsymbol{n}} - R\overline{\boldsymbol{m}} \tag{8}$$

Substitute (6–8) into (5) and we have

$$\begin{aligned} \sum_{i=1}^{n} w_i \left\| (R\boldsymbol{m}_i + \boldsymbol{t}) - \boldsymbol{n}_i \right\|^2 &= \sum_{i=1}^{n} w_i \left\| R\boldsymbol{m}_i + \overline{\boldsymbol{n}} - R\overline{\boldsymbol{m}} - \boldsymbol{n}_i \right\|^2 \\ &= \sum_{i=1}^{n} w_i \left\| R(\boldsymbol{m}_i - \overline{\boldsymbol{m}}) - (\boldsymbol{n}_i - \overline{\boldsymbol{n}}) \right\|^2 \end{aligned} \tag{9}$$

$$\boldsymbol{X}_i := \boldsymbol{m}_i - \overline{\boldsymbol{m}}, \quad \boldsymbol{Y}_i := \boldsymbol{n}_i - \overline{\boldsymbol{n}}. \tag{10}$$

$$\mathrm{R} = \operatorname{armgin} \sum_{i=1}^{n} w_i \left\| R\boldsymbol{X}_i - \boldsymbol{Y}_i \right\|^2 \tag{11}$$

To calculate the amount of rotation (11), is expanded in a matrix representation,

$$\begin{aligned} \left\| R\boldsymbol{X}_i - \boldsymbol{Y}_i \right\|^2 &= \left(R\boldsymbol{X}_i - \boldsymbol{Y}_i\right)^T \left(R\boldsymbol{X}_i - \boldsymbol{Y}_i\right) \\ &= \left(\boldsymbol{X}_i{}^T \mathrm{R}^T - \boldsymbol{Y}_i{}^T\right)\left(R\boldsymbol{X}_i - \boldsymbol{Y}_i\right) \\ &= \boldsymbol{X}_i{}^T \mathrm{R}^T R\boldsymbol{X}_i - \boldsymbol{Y}_i{}^T R\boldsymbol{X}_i - \boldsymbol{X}_i{}^T \mathrm{R}^T \boldsymbol{Y}_i + \boldsymbol{Y}_i{}^T \boldsymbol{Y}_i \\ &= \boldsymbol{X}_i{}^T \boldsymbol{X}_i - \boldsymbol{Y}_i{}^T R\boldsymbol{X}_i - \boldsymbol{X}_i{}^T \mathrm{R}^T \boldsymbol{Y}_i + \boldsymbol{Y}_i{}^T \boldsymbol{Y}_i \end{aligned} \tag{12}$$

Since the rotation matrix R is an orthogonal matrix, there is $R^T R = 1$. ${\boldsymbol{Y}_i}^T R \boldsymbol{X}_i$ and ${\boldsymbol{X}_i}^T \mathrm{R}^T \boldsymbol{Y}_i$ are scalar. The transposition of the scalar is still equal to the scalar itself, i.e.,

$$ {\boldsymbol{X}_i}^T \mathrm{R}^T \boldsymbol{Y}_i = \left({\boldsymbol{X}_i}^T \mathrm{R}^T \boldsymbol{Y}_i\right)^T = {\boldsymbol{Y}_i}^T R \boldsymbol{X}_i. \quad (13) $$

$$ \|R\boldsymbol{X}_i - \boldsymbol{Y}_i\|^2 = {\boldsymbol{X}_i}^T \boldsymbol{X}_i - 2{\boldsymbol{Y}_i}^T R \boldsymbol{X}_i + {\boldsymbol{Y}_i}^T \boldsymbol{Y}_i \quad (14) $$

Only one of them is related to R and transforms it into the minimum of its variable,

$$ \operatorname{armgin}\left(-2\sum_{i=1}^{n} w_i {\boldsymbol{Y}_i}^T R \boldsymbol{X}_i\right) \quad (15) $$

$$ \operatorname{armgin}\left(-2\sum_{i=1}^{n} w_i {\boldsymbol{Y}_i}^T R \boldsymbol{X}_i\right) = \operatorname{armgin}\sum_{i=1}^{n} w_i {\boldsymbol{Y}_i}^T R \boldsymbol{X}_i. \quad (16) $$

$$ \sum_{i=1}^{n} w_i {\boldsymbol{Y}_i}^T R \boldsymbol{X}_i = tr\left(W Y^T R X\right) \quad (17) $$

The conversion of the above formula makes a switch from cumulative to matrix based multiplication. Here, **W** is a diagonal matrix of n × n, and **X** and **Y** are 3 × n matrices. The traces of these matrices are equal to the left-hand side of the equation.

$$ \mathrm{tr}\,(\mathrm{AB}) = \mathrm{tr}\,(\mathrm{BA}) \quad (18) $$

$$ \mathrm{tr}\left(WY^T RX\right) = \mathrm{tr}\left(\left(WY^T\right)(RX)\right) = \mathrm{tr}\left(RXWY^T\right) \quad (19) $$

$$ S = XWY^T, svd\,(S) \rightarrow S = U\sum V^T \quad (20) $$

$$ \mathrm{tr}\left(RXWY^T\right) = \mathrm{tr}\,(\mathrm{RS}) = \mathrm{tr}\left(RU\sum V^T\right) = tr\left(\sum V^T RU\right) \quad (21) $$

The last step of the above transformation also uses the nature of (18). Since U, R, and V are orthogonal matrices, $O = V^T RU$ is also an orthogonal matrix.

$$ I = \mathbf{o}_j^T \mathbf{o}_j = \sum_{i=1}^{d} \mathrm{o}_{ij}^2 \Longrightarrow \mathrm{o}_{ij} \leq 1 \Longrightarrow \left|\mathrm{o}_{ij}\right| < 1 \quad (22) $$

$$ \mathrm{tr}\left(\sum O\right) = \begin{pmatrix} \sigma_1 & \cdots & 0 \\ \vdots & \ddots & \vdots \\ 0 & \cdots & \sigma_d \end{pmatrix} \begin{pmatrix} o_{11} o_{12} & \ldots & o_{1d} \\ o_{21} o_{22} & \ldots & o_{2d} \\ \vdots & \vdots & \vdots \\ o_{d1} & o_{d2} \ldots & o_{dd} \end{pmatrix} $$

$$ = \sum_{i=1}^{d} \sigma_i o_{ii} \leq \sum_{i=1}^{d} \sigma_i \quad (23) $$

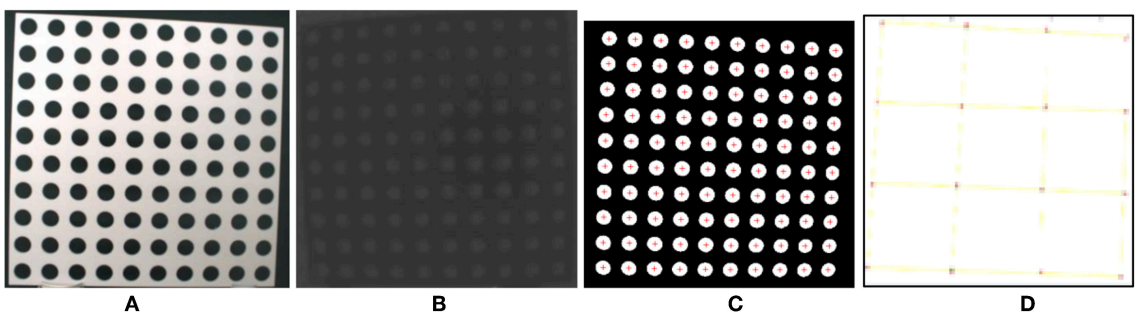


FIGURE 5 | Calibration plate. **(A)** Color image of the target, **(B)** depth image, **(C)** detected points, **(D)** fitted points.

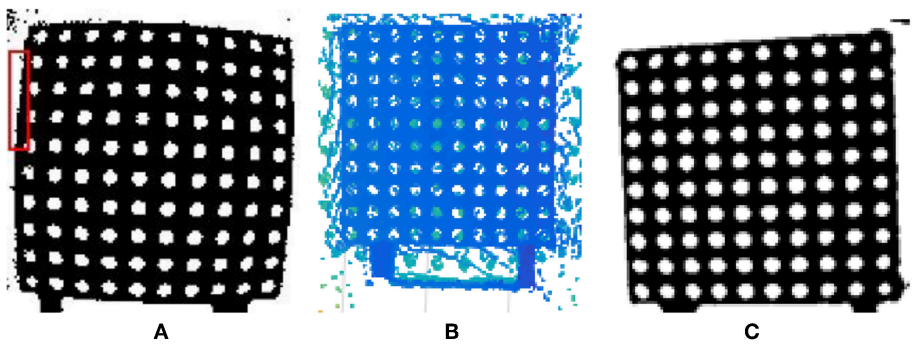


FIGURE 6 | Comparison of the depth map and point cloud. **(A)** Original depth map, **(B)** point cloud, **(C)** projected coordinates without distortion.

From the above two terms, if the maximum trace is required, we must make the value of O_{ii} equal to I, while O is the orthogonal matrix. So, O must be the unit matrix

$$\mathrm{I} = \mathrm{O} = V^T RU \Longrightarrow V = RU \Longrightarrow R = VU^T \tag{24}$$

EXPERIMENTS AND RESULTS

This section contains two parts, i.e., camera calibration and electrode identification and localization. The accuracy of camera calibration plays a very important role in the whole system. In this part, a new calibration method for the depth camera is proposed and compared with the traditional method. The experimental results show that the accuracy of our calibration method is more significant. The experimental procedure of electrode identification and localization is also described in detail in this part.

Calibration

The traditional method to calibrate the TOF camera and the CCD camera (Wei and Zhang, 2015; Bonnabel et al., 2016; Onunwor and Reichel, 2017) produces very unsatisfactory results because the resolution of the TOF camera is quite different from the CCD camera resolution, and the acquired parameters are very unstable. The pixel of the depth image acquired by the depth camera represents the distance from the subject to the camera. In 2012, Li and Zhuo proposed a 2.5D calibration plate that takes full advantage of the depth image characteristics, which improves the accuracy of camera registration, and simplifies the complexity of the algorithm (Li and Zhuo, 2012).

Figure 5 shows the calibration plate designed in this project. **Figure 5A** is the color image of the calibration plate. **Figure 5B** shows the depth image of the calibration plate. The size of the calibration plate is 500 × 500 mm, round hole diameter is 30 mm, and pitch of holes is 50 mm, there are 100 holes. The characteristic point is the center of each circular hole of the calibration plate.

The calibration process has two main steps. The first is to extract calibration points, i.e., to select a region of interest (ROI), to binarize the image by an automatic threshold, to remove image noise, to calculate the connected area, and to determine the center of each connected area, as shown in **Figure 5C**. The center of the connected area is regarded as a feature point. The second step is to fit feature points. The least square method is used to fit the characteristic points of each column and row in order to reduce the position error, as shown in **Figure 5D**.

The above method improves the accuracy of registration, yet the depth map still has radial distortion, as shown in **Figure 6A**. Although the use of fitting feature points can reduce errors, there is still room for improvement. Therefore, this report modifies the process of cameral calibration proposed in Li and Zhuo (2012) by employing accurate point cloud data other than the depth map. The specific process in this report includes two stages. The first is point cloud interpolation. Since the TOF camera has a low resolution, in order to obtain more accurate data, the system uses the bilinear interpolation algorithm to interpolate the point cloud data, so that its resolution is consistent with the color map. The second stage is to convert a point cloud to a 2D image. Since the point cloud represents 3D data, it cannot be directly calibrated with the color image, and thus the point cloud is required to be converted into a 2D image. In this project, the 3D coordinates are projected onto the 2D plane using the pinhole model as the theoretical basis. The result is indicated in **Figures 6B,C**. Compared with **Figures 6A,C**, we may discover that the image distortion is almost resolved.

According to the results obtained by the two methods, we can compare the distance errors of the two sets of points. The abscissa represents 100 data points, and the ordinate represents the distance difference between the two points before and after the calibration. **Figure 7** shows the comparison of errors caused by Li-Zhuo method (Li and Zhuo, 2012) and the proposed method

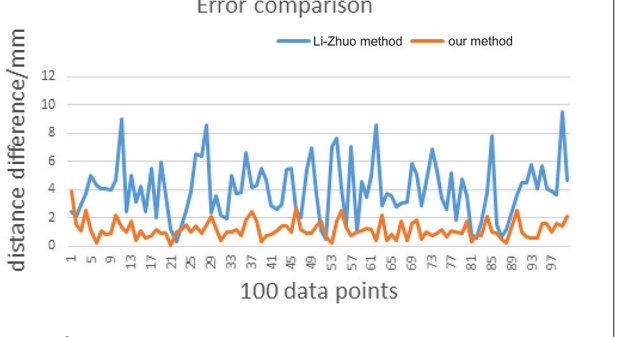


FIGURE 7 | Error comparison.

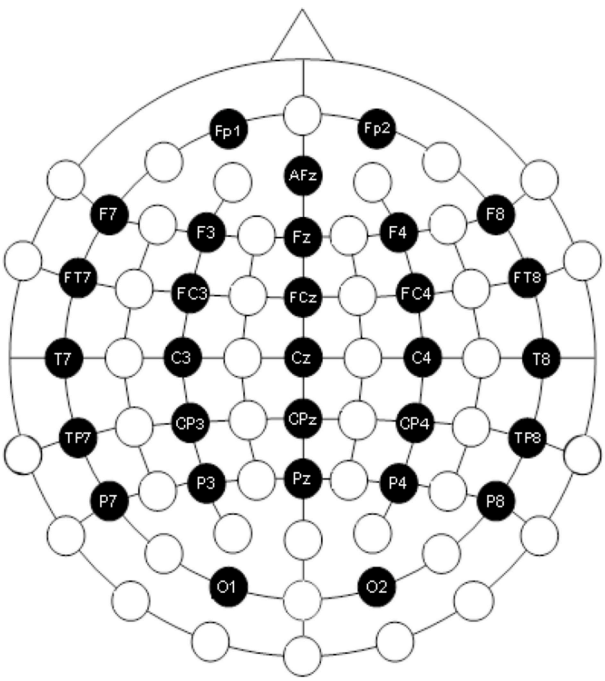


FIGURE 8 | Electrode distribution diagram.

in this study. From the data we can find that the calibration error has dropped from the original average 3.95–1.16 mm.

Electrode Point Identification and Localization

Electrode Identification

Assume that the electrode cap has a 30-channel EEG amplified signal recorder (Trotta et al., 2018). The electrode dot distribution diagram, provided by the electrode cap manufacturers, is typically shown in **Figure 8**. The electrodes here are marked with black color, and those names are shown in the figure.

If the precise position of the EEG electrode in color image is determined, the 3D location of the EEG electrode can be calculated by the transformation presented in section Calibration, using the similar calibration equations. In order to get precise EEG electrodes in the color image, this project adopts a method by detecting the connected region of the color image. When the electrode is detected in the color image, there will be a lot of interference because of the real electrode cap. When the color image is binarized with the appropriate threshold, there are lots of little interference regions, as shown in **Figure 9A**. In order to solve this problem, all connected regions are calculated and labeled, and the area of each connected region is calculated, after selecting the ROI, which contains the electrodes on the head in this picture, as shown in **Figure 9B**. In order to detect the electrode accurately, the algorithm adaptively adjusts the appropriate area threshold to preserve the connected area larger

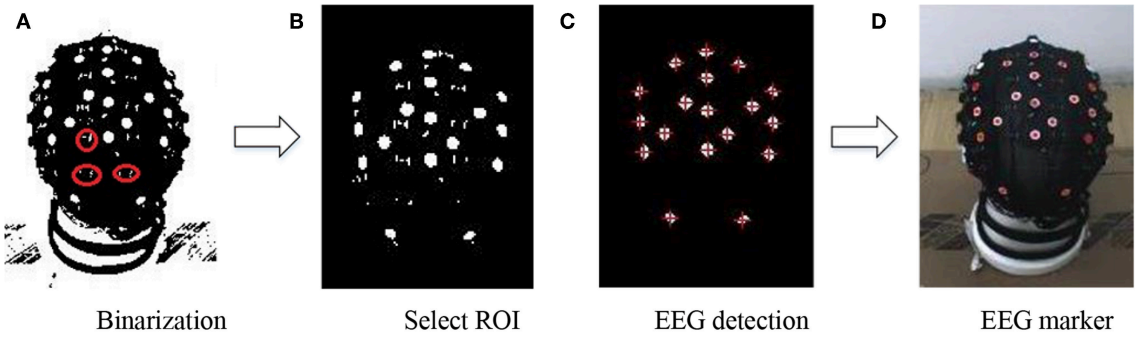


FIGURE 9 | Real electrode detection on the EEG signal cap **(A)** Binarization **(B)** Select ROI **(C)** EEG detection **(D)** EEG marker.

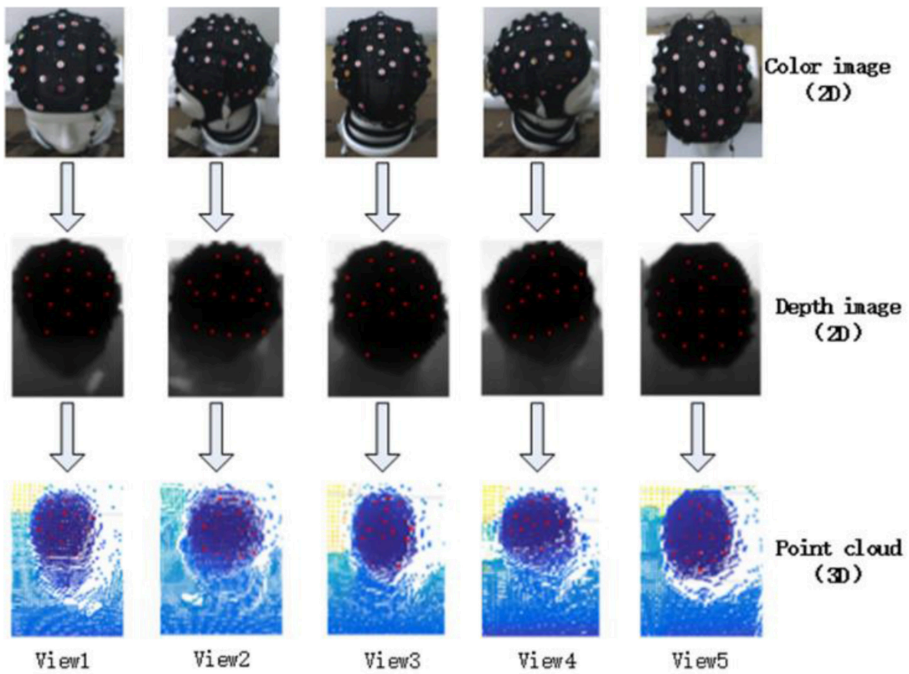


FIGURE 10 | EEG electrode registration.

TABLE 1 | Electrodes, camera views, and quantities.

Electrode	Camera view	N
Fp1	1	1
Fp2	1	1
AFz	1 + 5	2
F8	4	1
F4	1 + 4 + 5	3
Fz	1 + 5	2
F3	1 + 2 + 5	3
F7	2	1
FT7	2	1
FC3	1 + 2 + 5	3
FCz	1 + 2 + 3 + 4 + 5	5
FC4	1 + 4 + 5	3
FT8	4	1
T8	4	1
C4	4 + 5	2
Cz	1 + 2 + 3 + 4 + 5	5
C3	2 + 5	2
T7	2	1
TP7	2	1
CP3	2 + 3	2
CPz	2 + 3 + 5	3
CP4	3 + 4	2
TP8	4	1
P7	2	1
P3	2 + 3	2
Pz	3 + 5	2
P4	3 + 4	2
P8	4	1
O1	3	1
O2	3	1

than the threshold, filter out the connected area less than the threshold, as shown in **Figure 9C**. This method reduces the noise of the electrodes. Then, the center of the connected region is calculated, and that is the center of the electrode. The coordinates of the center point are used as the positions of the electrodes, as shown in **Figure 9D**. Taken as an example, **Figure 9** shows the image of view 3, and other views have the same process. When this step is finished, there are five color images with detected electrodes.

Electrode Localization

Figure 10 shows the five shot images from each direction. The first row is the color image which is obtained by the CCD camera, with the detected electrodes. The second row is the depth image which is obtained by the TOF camera with the transformational electrodes, and the third row is the point cloud data with the 3D electrode positions. The electrodes in the first row are detected by the method described in section Electrode identification. The electrodes in the second and third row are determined by using the transformation between the CCD camera and the TOF camera. Of course, the electrodes in the third row have three dimensions.

3D Registration

We need to rebuild the entire brain model and the position of electrodes. In the process of point cloud stitching, many people use the classic ICP algorithm (Kim, 2015), which is only suitable for small angle stitching, i.e., with a large overlapped area, and so it is not ideal for the situation in this study. Since the angle intervals between five camera groups are relatively large, in order to reduce registration errors, this report takes the surrounding four point cloud points, i.e., view1, view2, view3, and view4, to match the view5 point cloud, respectively. The SVD algorithm described earlier in this report is used to solve the transformation relation. The electrodes, the camera angle, and the number of angles are shown in **Table 1**, which illustrates the situation of how the electrodes are taken. **Figure 11** shows the results of the registration for all electrodes into the same coordinate system. **Figure 11A** is a registration diagram containing only the electrodes. **Figure 11B** shows the distribution of the electrodes on the head model.

The SVD algorithm can obtain stable and reliable results with only two angles of 5–15 sets of matching points, which is much simpler than traditional photography methods. This is mainly because the TOF camera can directly obtain the exact depth of the value. In the traditional photographic methods, for either multi-camera or single-camera with multi-angle, each electrode must be shot from different directions and the depth information can be calculated according to that. The process is not only complex, but also very easy to cause human errors and matching errors. The algorithm of the multi-purpose camera method is too complicated and requires manual participation in the electrode marking process and can only use the matching electrode cap. A single camera method is a brilliant approach, yet the operation requirements are high, which is easy to cause human error. Qian and Sheng (2011) also proved that only six electrodes could reduce error when shot by more cameras, and that the other electrodes did not have this trend.

RESULTS

In the EEG positioning system, the inaccurate location of the electrode may cause an incorrect location of the source, and thus the accuracy of the electrode positioning is very important for research in brain science. The standard positioning error is given by $\Delta = \sqrt{(X_a - X)^2 + (Y_a - Y)^2 + (Z_a - Z)^2}$, where X, Y, Z are estimated 3D coordinates, X_a, Y_a, Z_a are the real coordinate values obtained by a higher precision device, for which in this study we use a portable 3D handheld scanner, the Artec 3Ds Space Spider, with an accuracy of 0.05 mm.

The experimental process is repeated five times, using the electrode cap on the head model. A typical result of the average error of the 30 electrodes is shown in **Table 2**. We also tested the same process with the electrode cap on human heads and got the similar results. Therefore, with the RGB-D multi modal system, the proposed method yields an average of 3.26 mm localization error, much better than other digitizer methods where the typical equipment has a mean error of 6.1 mm. Furthermore, if we use a high-precision CCD camera for calibration and measurement,

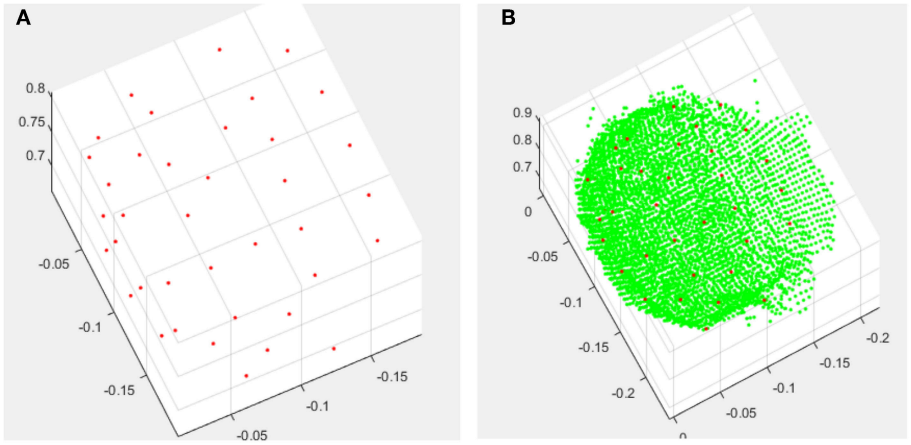


FIGURE 11 | Registration results. **(A)** EEG electrode registration. **(B)** Registration of electrodes on head model.

the accuracy can be easily improved up to 10 times, i.e., the error can be reduced to about 0.3 mm. Since the error is much less than the size of an electrode dot which has a diameter of 10 mm, our result is good enough for practical applications. Anyway, there are two sources of the experimental errors. One of them is the error resulting from the camera calibration, introduced in section Calibration the other is from the point cloud splicing. The points with large errors are mainly located in the edge position of the electrode cap. The error of the point in the middle position is much smaller. In fact, it is normally accepted for users if the error is <5 mm for dense arrays of electrodes. Therefore, the proposed system with this accuracy is rather sufficient for most practical applications. Some technology information and data sets carried out in this project are available on the web, http://www.sychen.com/research/vision/LEEG.htm, where some MATLAB codes are provided to demonstrate the main algorithms.

There is another advantage that the method achieves good performance in terms of flexibility and simplicity of operation, which can be used in EEG source localization applications on the human brain. On the other hand, since the calibration process and brain model building can be done off-line, the on-line process only needs to detect the electrodes and map them to the brain model. This process is performed very fast and can be easily implemented for real-time applications.

TABLE 2 | Electrode positioning error (mm).

Electrode	ΔX	ΔY	ΔZ	Δr
Fp1	1.41	0.21	−0.37	1.47
Fp2	−1.39	−0.20	0.39	1.45
AFz	−0.79	−1.55	−2.94	3.42
F8	−4.75	0.59	−0.31	4.80
F4	−3.27	−0.88	−1.77	3.82
Fz	0.78	−0.80	2.53	2.77
F3	−2.00	2.99	−0.10	3.60
F7	2.60	−1.46	1.84	3.50
FT7	1.55	0.85	−1.27	2.18
FC3	−0.24	0.92	−1.43	1.72
FCz	1.84	−1.17	1.33	2.55
FC4	1.78	2.91	0.11	3.41
FT8	−1.15	−5.22	−0.42	5.36
T8	0.64	2.42	−2.01	3.21
C4	−3.46	−1.78	2.04	4.39
Cz	1.16	2.1	3.12	3.94
C3	−0.54	0.35	−1.32	1.47
T7	0.19	1.10	−4.01	4.16
TP7	−3.14	0.44	−0.76	3.26
CP3	1.48	−2.49	−0.56	2.95
CPz	−1.68	1.40	−1.10	2.45
CP4	3.19	1.49	0.15	3.52
TP8	0.47	2.15	0.67	2.3
P7	−1.20	−0.92	4.19	4.45
P3	1.30	−1.78	3.42	4.07
Pz	−1.31	0.01	−2.95	3.23
P4	1.76	−1.74	−0.53	2.53
P8	4.80	0.05	2.07	5.23
O1	2.89	1.13	−1.56	3.47
O2	−2.78	−1.03	1.22	3.20
AVE				3.26

DISCUSSION

In this study, we combine a TOF depth camera and a CCD color camera to locate the EEG electrode positions in 3D space and yield satisfactory results for practical use. Compared with the existing contributions in the literature (**Table 3**), such 3D positions are normally obtained by a stereo vision system, where a pair of CCD cameras used as two eyes for identification and 3-D reconstruction of electrodes. However, stereo vision is normal useful for robots but it always has its own limitations and it's still used for industrial applications, especially when there is a high requirement on precision and reliability. For example, the work by Schulze et al. (2014) is a typical realization of this technology. There are some comparisons between photogrammetry system

TABLE 3 | Comparison of the typical methods.

Method	Principle	Equip size	Time	Accuracy	Reliability	Typical Ref.
Manual measurement	Coordinate measuring, calipers	Small	Very slow (>10 min)	0.4 mm	Mid	De Munck et al. (1991)
Camera matrix	Stereo vision	Large	Real-time (<0.1 s)	1.27 mm	Bad	Koessler et al. (2007)
Positioning tool	Electromagnetic digitizer	Small	5 min	2–8 mm	Mid	Dalal et al. (2014)
Photogrammetry	Structure-from-motion	Small	Slow (5–10 min)	0.8 mm	Mid	Clausner et al. (2017)
Laser scanner	Laser	Small	Slow	0.05–0.2 mm	Good	Jeon et al. (2018)
Color+depth	Color+TOF	Small	Real-time	0.3–3.3 mm	Good	This report

and manual measurements or electromagnetic digitizers made in Koessler et al. (2007). One main problem of stereo vision is its reliability. The passive vision system is very sensitive to environmental conditions. When anything, like the lighting, the object size in the working space, the vision system structure, the working distance, changes, the vision system will meet a big problem of 3D reconstruction. It even could not obtain a good image for analysis anymore. The calibration of stereo cameras is very tedious because it requires an inconvenient process by an expert in robot vision. Furthermore, such a process has to be redone when either one of the settings, such as the focus, the baseline distance, the camera pose, is changed. That means such an expert has to stay there for making the system use in practical clinical applications.

Regarding the locating accuracy, an error below 5–10 mm can satisfy the current EEG signal research or clinical applications. A manual process with a tool can get the accuracy of 3.6 mm, but it takes about 8 min. Schulze et al. reports their system of camera matrix can achieve a localization error of 0.761 mm. In fact, Koessler et al. (2007) already achieve the position error under 1.27 mm 10 years ago, where they distribute 11 CCD cameras on the dome for imaging. Actually, with the currently new CCD cameras, higher accuracy, e.g., 0.1 mm, can also be theoretically achieved. However, it is hard to produce general systems using such technology of stereo vision for the clinical applications. On the other hand, using laser-based equipment can, of course, get very high accuracy, e.g., the 3D handheld scanner in our laboratory can give us the accuracy of 0.05 mm.

Since there is no complicated computation required to perform the algorithms of this study, the system can be implemented for real-time applications with common personal computers. In the experiments, we mostly use ordinary devices, e.g., TOF camera (MESA-SR-4000) and CCD camera (Manta G-201C 30fps). It is performed in a personal computer with Intel i3-4130 CPU at 3.4 GHz, 4.0 GB RAM, and x64-based Windows 7 OS. A relatively lower configuration of the computer does not much affect the efficiency. Due to the resolution limited by MESA-SR-4000 and MG-201C, the result is got with a precision of 3.26 mm within 30 ms. This is usually adequate for practical real-time applications. Of course, using latest better hardware with higher resolutions, e.g., TOF camera (OPNOUS GC4 NIR) and CCD camera (Kodak KAI-08050 PoE) in our lab, we can get a corresponding higher precision but lower efficiency. Increasing the resolution of the cameras would significantly improve the accuracy, but at the same time it correspondingly decreases the efficiency. On the contrary, the number of EEG sensors has little sense to affect the performance because there are only tens of points in total.

Anyway, we have to concern the aspects of reliability, flexibility, and real-time computation for the positioning system. As we know, due to the corresponding process in stereo vision, it takes several minutes for computing and thus cannot be used for real-time purpose, e.g., when the subject needs to move the heads during a test. One advantage of the technology in this study is that it avoids the complicated computation of correspondence among multiple images, which is unlikely realized in real-time for high-resolution images on a common computer. The data acquisition and registration process is very fast by the method in this report. It means the method can be used for dynamic tests where the patient is free to move its head or body during the acquisition time. Therefore, some other research or test tasks can also be done with a system by this technology. Our method also takes advantage of flexibility. We do not need to setup a large equipment structure or working space, like a dome. The subject will also feel comfortable in the test because both the sensors and the subjects can move freely in the space.

CONCLUSION

In this report, an EEG electrode positioning method using photogrammetry is presented. By combining CCD and TOF cameras, the system can achieve both good accuracy (due to the precise industrial camera) and real-time efficiency (due to the reliable TOF camera). The vision system can reliably get the position and colors of the electrodes at the same time. A depth calibration plate for the TOF camera is designed, according to its distance-sensitive feature. Meanwhile, in order to improve the accuracy we apply the point cloud data to replace the traditional depth map with the calibration. In the experiments, we use a head model and 30-channel EEG electrode cap. The calibration process can be performed off-line, and the on-line acquisition algorithm can be realized in real-time, which can bring great convenience for patients and doctors. Thus, the combination of the TOF camera and the CCD camera can not only ensure the accuracy of positioning, but also simplify the complexity of the algorithm and operation.

AUTHOR CONTRIBUTIONS

SC: idea and conception; YH, HQ, and MZ: development of methods; HQ: experiments; HQ and XY: data analysis and programming; HQ: drafting the manuscript; SC, YH, XY, and MZ: critical revision.

FUNDING

This work was supported by National Key R&D Program of China (grant no: 2018YFB1305200) and National Natural Science Foundation of China (grant no: U1509207 and 61703304).

ACKNOWLEDGMENTS

Thanks to Prof. Xiaoli Li of Beijing Normal University for his useful ideas and helpful discussions, Mr. Yangyang Zhang for his experimental work and data processing, and the students of Tianjin University of Technology for their subjective tests in the research project.

REFERENCES

Bauer, H., Lamm, C., Holzreiter, S., Hollnder, I., Leodolter, U., and Leodolter, M. (2000). Measurement of 3D electrode coordinates by means of a 3D photogrammetric head digitizer. *Neuroimage* 11, S461–S461. doi: 10.1016/S1053-8119(00)91392-2

Baysal, U., Sengül, G. (2010). Single camera photogrammetry system for EEG electrode identification and localization. *Ann. Biomed. Eng.* 38, 1539–1547. doi: 10.1007/s10439-010-9950-4

Bonnabel, S., Barczyk, M., and Goulette, F. (2016). "On the covariance of ICP-based scan-matching techniques," in *American Control Conference* (Boston, MA: IEEE), 5498–5503.

Butler, R., Gilbert, G., Descoteaux, M., Bernier, P. M., and Whittingstall, K. (2016). Application of polymer sensitive MRI sequence to localization of EEG electrodes. *J. Neurosci. Methods* 278, 36–45. doi: 10.1016/j.jneumeth.2016.12.013.

Cheng, K. L., Xuan, R. F., Ju. X., Tang. M., Chang, J., and Zhang. J. J. (2016). A linear approach for depth and colour camera calibration using hybrid parameters. *J. Comput. Sci. Technol.* 31, 479–488. doi: 10.1007/s11390-016-1641-7

Clausner, T., Dalal, S. S., and Crespo-García, M. (2017). Photogrammetry-based head digitization for rapid and accurate localization of EEG electrodes and MEG fiducial markers using a single digital SLR camera. *Front. Neurosci.* 11:264. doi: 10.3389/fnins.2017.00264

Dalal, S. S., Rampp, S., Willomitzer, F., and Ettl, S. (2014). Consequences of EEG electrode position error on ultimate beamformer source reconstruction performance. *Front. Neurosci.* 8:42. doi: 10.3389/fnins.2014.00042

De Munck, J. C., Vijn, P. C., and Spekreijse, H. (1991). A practical method for determining electrode positions on the head. *Electroencephalogr. Clin. Neurophysiol.* 78, 85–87.

Eichhardt, I., Chetverikov, D., and Jank, Z. (2017). Image-guided TOF depth upsampling: a survey. *Mach. Vis. Appl.* 28, 1–16. doi: 10.1007/s00138-017-0831-9

Golbach, F., Kootstra, G., Damjanovic, S., Otten, G., and van de Zedde, R. (2016). Validation of plant part measurements using a 3D reconstruction method suitable for high-throughput seedling phenotyping. *Mach. Vis. Appl.* 27, 663–680. doi: 10.1007/s00138-015-0727-5

Jeon, S., Chien, J., Song, C., Hong J. (2018). A preliminary study on precision image guidance for electrode placement in an EEG study. *Brain Topogr.* 31, 174–185. doi: 10.1007/s10548-017-0610-y

Jung, J., Lee, J. Y., Jeong, Y., and Kweon, I. S. (2015). Time of flight sensor calibration for a color and depth camera pair. *IEEE Trans. Pattern Anal. Mach. Intell.* 37, 1501–1513. doi: 10.1109/TPAMI.2014.2363827

Kim, J. H. (2015). *Apparatus and Method for Calibrating Depth Image Based on Relationship Between Depth Sensor and Color Camera*. Daejeon: Patent USPTO #20140112574.

Koessler, L., Maillard, L., Benhadid, A., Vignal, J. P., Braun, M., and Vespignani, H. (2007). Spatial localization of EEG electrodes. *Clin. Neurophysiol.* 37, 97–102. doi: 10.1016/j.neucli.2007.03.002

Li, S., and Zhuo, Q. (2012). "A new approach to calibrate range image and color image from Kinect," in *4th International Conference on Intelligent Human-Machine Systems and Cybernetics 2*, (Nanchang), 252–255.

Liu, Q., Ganzetti, M., Wenderoth, N., and Mantini, D. (2018). Detecting large-scale brain networks using EEG: impact of electrode density, head modeling and source localization. *Front. Neuroinform.* 12:4. doi: 10.3389/fninf.2018.00004

Onunwor, E., and Reichel, L. (2017). On the computation of a truncated SVD of a large linear discrete ill-posed problem. *Numerical Algorithms* 75:359. doi: 10.1007/s11075-016-0259-8

Qian, S., and Sheng, Y. (2011). A single camera photogrammetry system for multi-angle fast localization of EEG electrodes. *Ann. Biomed. Eng.* 39, 2844–2856. doi: 10.1007/s10439-011-0374-6

Raposo,C., Barreto, J. P., and Nunes, U. (2016). Extrinsic calibration of multi-modal sensor arrangements with non-overlapping field-of-view. *Mach. Vis. Appl.* 27, 1–15. doi: 10.1007/s00138-016-0815-1

Reis, P. M., and Lochmann, M. (2015). Using a motion capture system for spatial localization of EEG electrodes. *Front. Neurosci.* 9:130. doi: 10.3389/fnins.2015.00130

Russell, G. S., Jeffrey Eriksen, K., Poolman, P., Luu, P., and Tucker, D. M. (2005). Geodesic photogrammetry for localizing sensor positions in dense-array EEG. *Clin. Neurophysiol.* 116, 1130–1140. doi: 10.1016/j.clinph.2004.12.022

Saha, S., Nesterets, Y., Rana, R., Tahtali, M., de Hoog, F., and Gureyev, T. (2017). EEG source localization using a sparsity prior based on Brodmann areas. *Int. J. Imaging Syst. Technol.* 27, 333–344. doi: 10.1002/ima.22236

Schulze, W. H., Mackens, P., Potyagaylo, D., Rhode, K., Tülümen, E., Schimpf, R., et al. (2014). Automatic camera-based identification and 3-D reconstruction of electrode positions in electrocardiographic imaging. *Biomed. Eng.* 59, 515–528. doi: 10.1515/bmt-2014-0018

Sorkine, O. (2009). Least-squares rigid motion using SVD. *Tech. Notes* 120:52. doi: 10.1088/1742-6596/298/1/012008

Trotta, M. S., Cocjin, J., Whitehead, E., Damera, S., Wittig, JH., Jr, Saad, Z. S., et al. (2018). Surface based electrode localization and standardized regions of interest for intracranial EEG. *Hum. Brain Mapp.* 39, 709–721. doi: 10.1002/hbm.23876

Wang, B., Li, J., Liu, C., and Yu, J. (2017). Generalized total least squares prediction algorithm for universal 3D similarity transformation. *Adv. Space Res.* 59, 815–823. doi: 10.1016/j.asr.2016.09.018

Wei, S., and Zhang, X. (2015). "Disparity search range estimation based on TOF-stereo fusion," *in Proceedings Volume 9449. The International Conference on Photonics and Optical Engineering* (Xi'an: SPIE).

Yang, J., Li, H., Campbell, D., and Jia, Y. (2016). Go-ICP: a globally optimal solution to 3D ICP point-set registration. *IEEE Trans. Pattern Anal. Mach. Intell.* 38, 2241–2254. doi: 10.1109/TPAMI.2015.2513405

Yao, H., Ge, C., Hua, G., and Zheng, N. (2015). The VLSI implementation of a high-resolution depth-sensing soc based on active structured light. *Mach. Vis. Appl.* 26, 533–548. doi: 10.1007/s00138-015-0680-3

Zhang, J., Chen, S., Xiao, G., and Li, X. (2014). Multimodal spatial calibration for accurately registering EEG sensor positions. *Comput. Mathemat. Methods Med.* 14:26019. doi: 10.1155/2014/826019

Conflict of Interest Statement: The authors declare that the research was conducted in the absence of any commercial or financial relationships that could be construed as a potential conflict of interest.

Copyright © 2019 Chen, He, Qiu, Yan and Zhao. This is an open-access article distributed under the terms of the Creative Commons Attribution License (CC BY). The use, distribution or reproduction in other forums is permitted, provided the original author(s) and the copyright owner(s) are credited and that the original publication in this journal is cited, in accordance with accepted academic practice. No use, distribution or reproduction is permitted which does not comply with these terms.

frontiers in Neuroinformatics

ORIGINAL RESEARCH
published: 24 April 2019
doi: 10.3389/fninf.2019.00030

Dilated Dense U-Net for Infant Hippocampus Subfield Segmentation

Hancan Zhu[1,2], *Feng Shi*[3], *Li Wang*[1], *Sheng-Che Hung*[1], *Meng-Hsiang Chen*[4], *Shuai Wang*[1], *Weili Lin*[1] *and Dinggang Shen*[1,5*]

[1] Department of Radiology and Biomedical Research Imaging Center, University of North Carolina at Chapel Hill, Chapel Hill, NC, United States, [2] School of Mathematics Physics and Information, Shaoxing University, Shaoxing, China, [3] Shanghai United Imaging Intelligence Co., Ltd., Shanghai, China, [4] Department of Diagnostic Radiology, Kaohsiung Chang Gung Memorial Hospital, Chang Gung University College of Medicine, Kaohsiung, Taiwan, [5] Department of Brain and Cognitive Engineering, Korea University, Seoul, South Korea

Accurate and automatic segmentation of infant hippocampal subfields from magnetic resonance (MR) images is an important step for studying memory related infant neurological diseases. However, existing hippocampal subfield segmentation methods were generally designed based on adult subjects, and would compromise performance when applied to infant subjects due to insufficient tissue contrast and fast changing structural patterns of early hippocampal development. In this paper, we propose a new fully convolutional network (FCN) for infant hippocampal subfield segmentation by embedding the dilated dense network in the U-net, namely DUnet. The embedded dilated dense network can generate multi-scale features while keeping high spatial resolution, which is useful in fusing the low-level features in the contracting path with the high-level features in the expanding path. To further improve the performance, we group every pair of convolutional layers with one residual connection in the DUnet, and obtain the Residual DUnet (ResDUnet). Experimental results show that our proposed DUnet and ResDUnet improve the average Dice coefficient by 2.1 and 2.5% for infant hippocampal subfield segmentation, respectively, when compared with the classic 3D U-net. The results also demonstrate that our methods outperform other state-of-the-art methods.

Keywords: fully convolutional network, dilated dense network, deep learning, hippocampal subfield segmentation, infant hippocampus

OPEN ACCESS

Edited by:
Tianzi Jiang,
Institute of Automation (CAS), China

Reviewed by:
Liang Zhan,
University of Pittsburgh, United States
Yalin Wang,
Arizona State University, United States

***Correspondence:**
Dinggang Shen
dgshen@med.unc.edu

Received: *07 February 2019*
Accepted: *02 April 2019*
Published: *24 April 2019*

Citation:
Zhu H, Shi F, Wang L, Hung S-C, Chen M-H, Wang S, Lin W and Shen D (2019) Dilated Dense U-Net for Infant Hippocampus Subfield Segmentation. Front. Neuroinform. 13:30. doi: 10.3389/fninf.2019.00030

INTRODUCTION

Hippocampus plays important roles in memory and spatial navigation, and is closely related to neurological diseases, such as autism, attention deficit hyperactivity disorder, and Alzheimer's Disease (Shi et al., 2009; Bartsch, 2012; Li et al., 2013). Hippocampus consists of several histologically and functionally specialized subfields (Dalton et al., 2017). It has been shown that different pathological conditions affect subfields differently, suggesting that subfields may provide more precise information for earlier disease diagnosis than simply using the whole hippocampus (Small, 2014).

Accurate segmentation of hippocampal subfields from magnetic resonance (MR) brain images is a critical step for studying memory-related neurological diseases. However, it is a challenging task especially in infant subjects, because of the small size of each hippocampal subfield, the blurred boundaries between subfields, and the large inter-subject variations. Manual segmentation is widely adopted, but it suffers high intra- and inter-operator variability, and is also excruciatingly

time-consuming. Therefore, automatic hippocampal subfield segmentation methods are desirable. The existing automatic hippocampal subfield segmentation methods can be mainly categorized into three different types: (1) generative model based method (Van Leemput et al., 2009), (2) multi-atlas based method (Wang et al., 2013; Pipitone et al., 2014; Caldairou et al., 2016; Romero et al., 2017), and (3) multi-modality learning based method (Wu et al., 2018).

In the first category (Van Leemput et al., 2009), a generative model of image around the hippocampal area was produced by using a mesh-based probabilistic atlas learned from a set of ultra-high-resolution training images. The model was used to obtain automated hippocampal subfield segmentations on 10 adult subjects with the age range of 22–89 years.

In the past years, the second category of methods, namely multi-atlas based image segmentation (MAIS) methods, have been widely used in the field of medical image segmentation, including hippocampal subfield segmentation on adult subjects (Wang et al., 2013; Pipitone et al., 2014; Caldairou et al., 2016; Romero et al., 2017). In the MAIS methods, all selected atlas images are first registered to the target image, and the corresponding atlas labels are then warped to the target image space. Afterwards, these warped atlas labels are combined to obtain the final segmentation by label fusion. Note, in the MAIS methods, label fusion plays an important role. For example, a weighed voting label fusion was proposed (called joint label fusion) in a previous work (Wang et al., 2013), in which weights were obtained by minimizing the total expected error between the consensus segmentation and the ground-truth segmentation. This method was later combined with a learning-based error correction method for hippocampal subfield segmentation (Yushkevich et al., 2015). In another work (Romero et al., 2017), a new non-local patch based label fusion method was proposed based on a multi-contrast patch matching process. To further improve the segmentation, authors exploited a neural network-based error correction step for minimizing systematic segmentation errors. MAGeT-Brain (Multiple Automatically Generated Templates) was also proposed for automatic segmentation of the hippocampus and subfields, aiming to minimize the number of atlases needed whilst still achieving similar agreement to the multi-atlas approaches (Pipitone et al., 2014),. Besides, a surface patch-based segmentation method (Caldairou et al., 2016) was proposed for hippocampal subfield segmentation by combining surface-based processing with a patch-based template library and feature matching.

Besides the above two categories of methods, learning-based methods in the third category were also proposed for adult hippocampal subfield segmentation using 3T multi-modality MR images, including structural MRI (T1w, T2w) and resting-state fMRI (rs-fMRI) (Wu et al., 2018). In that paper (Wu et al., 2018), authors extracted both appearance features and relationship features to capture the appearance patterns in structural MR images and the connectivity patterns in rs-fMRI, respectively. These extracted features were then fed into a random forest classifier for voxel-wise classification.

Although several automatic methods have also been proposed for hippocampal subfield segmentation, most of them were evaluated only on the adult subjects, and thus cannot be directly applied to infant subjects due to insufficient tissue contrast and fast changing structural patterns of early hippocampal development.

In the recent years, deep convolutional neural networks (CNN) have been widely applied in the medical image segmentation (de Brébisson and Montana, 2015; Zhang et al., 2015; Moeskops et al., 2016). In CNN based segmentation methods, a patch centered at the target voxel (or pixel for 2D images) is taken as input for networks, and the tissue class of the center voxel is produced as the output of the networks. By learning sets of convolutional kernels, CNNs can capture highly non-linear mappings between inputs and outputs. Compared with MAIS methods and the traditional learning-based methods, CNN based segmentation methods are free of image registration and manual feature extraction.

A drawback of the CNN based segmentation approaches is that the input patches from neighboring voxels have huge overlap and the same convolutions are computed for many times. To address this limitation, fully convolutional networks (FCN) were proposed for voxel-wise dense prediction, by reformatting the fully connected layers as convolutional layers (Long et al., 2015). So far, a number of FCNs have been proposed and successfully used in medical image segmentation, including hippocampal segmentation (Ronneberger et al., 2015; Milletari et al., 2016; Chen Y. et al., 2017; Yu et al., 2017; Cao et al., 2018). For example, in the paper (Ronneberger et al., 2015), a U-net architecture was proposed by comprising a contracting (down-sampling) path, followed by an expanding (up-sampling) path. The features in the contracting path are concatenated to the corresponding features in the expanding path to recover the detailed image information that is lost during the down-sampling process. In the work (Milletari et al., 2016), authors extended U-net to a V-net structure by incorporating residual blocks (He et al., 2016a). In the paper (Yu et al., 2017), authors proposed a new volumetric convolutional neural network with mixed residual connections, where both the short connections between successive layers and the long connections between contracting path and expanding path are implemented with residual connections. In the work (Cao et al., 2018), authors proposed a multi-task CNN for joint hippocampal segmentation and clinical score regression with U-net as a subnet for hippocampal segmentation. In the paper (Chen Y. et al., 2017), authors proposed a multi-view ensemble approach to combine multiple decision maps obtained from several deep neural networks for hippocampal segmentation. Besides these contracting-expanding structures, dilated FCNs were also proposed for image segmentation, which can enlarge the receptive field exponentially without reducing any spatial resolution (Liang-Chieh et al., 2015; Yu and Koltun, 2015;Li et al., 2017; McKinley et al., 2017).

The U-net like structures are particularly successful in the field of medical image segmentation. One of the most important factors in the U-net is the long-skip connections which can concatenate the features in the contracting path to the corresponding features in the expanding path to recover the

lost image information. However, the levels of features in the contracting path are much lower than those in the expanding path. Thus, it may not obtain optimal results when directly concatenating these features.

In this paper, we develop an automatic method to address the challenging infant hippocampal subfield segmentation problem with state-of-the-art deep learning techniques (LeCun et al., 2015; Litjens et al., 2017; Shen et al., 2017). To overcome the limitation of U-net structure, we propose a novel network by embedding a dilated dense network in the U-net, namely DUnet. The embedded dilated dense network can generate multi-scale features while keeping high spatial resolution, which is useful in fusing the low-level features in the contracting path with the high-level features in the expanding path. To further improve the performance, we use residual connections to group every pair of convolutional layers in DUnet, and obtain the Residual DUnet (ResDUnet).

The proposed method was applied for segmenting infant hippocampal subfields based on the Baby Connectome Project (BCP) dataset, containing 10 infant subjects. To the best of our knowledge, this is the first work to propose an automatic method for infant hippocampal subfield segmentation. To further illustrate the effectiveness of our proposed method, we also validated our proposed method for segmenting adult hippocampal subfields on a publicly available dataset. Experimental results show that our proposed DUnet and ResDUnet, respectively, improve the average Dice coefficient by 2.1 and 2.5% for infant hippocampal subfield segmentation, and 0.5 and 0.6% for adult hippocampal subfield segmentation, compared to the classic 3D U-net (Çiçek et al., 2016). Our proposed ResDUnet also outperforms both the state-of-the-art ConvNet (Yu et al., 2017) and hippocampal subfield segmentation method (HIPS) (Romero et al., 2017).

MATERIALS

Two image datasets were used for validating our method. The first dataset is from BCP, which was funded by the National Institutes of Health (NIH) as a component of the Lifespan Human Connectome Project. The BCP aims to provide scientists with unprecedented information about how the human brain develops from birth through early childhood and will uncover factors contributing to healthy brain development. For this project, researchers are acquiring MRI scans (including T1- and T2-weighted structural MRI, DTI, and rs-fMRI) of 500 typically developing children, ages 0–5 years, over the course of 4 years. In our experiment, 10 infant subjects (6 females/4 males) were randomly selected, each with T1w and T2w images acquired at 12 months old with 3T Siemens Prisma MRI scanners at the Biomedical Research Imaging Center (BRIC) at the University of North Carolina at Chapel Hill. **Table 1** lists the imaging protocol for acquiring the T1w and T2w MR images. Five hippocampal subfields were manually labeled for each subject by the consensus of two neuroradiologists, including cornu ammonis sectors 1 (CA1), CA2/3, subiculum (SUB), CA4/dentate gyrus (DG), and Uncus. All T1w and T2w images underwent intensity inhomogeneity correction using the N3 bias field correction, and T2w images were rigidly aligned with corresponding T1w images. All images were aligned to a selected subject with affine registration.

The second dataset is a publicly available dataset (https://www.nitrc.org/projects/mni-hisub25), which contains 25 adult subjects (31 $\pm$ 7 years, 12 males). Each subject consists of an isotropic 3D-MPRAGE T1-weighted image (TR = 3,000 ms; TE = 4.32 ms; TI = 1,500 ms; flip angle = 7°; matrix size = 336 × 384; FOV = 201 × 229 mm^2; 240 axial slices with 0.6 mm slice thickness resulting in 0.6 × 0.6 × 0.6 mm^3 voxels; acquisition time = 16.48 min), an anisotropic 2D T2-weighted TSE image (TR = 10,810 ms; TE = 81 ms; flip angle = 119°; matrix size = 512 × 512; FOV = 203 × 203 mm^2, 60 coronal slices angled perpendicular to the hippocampal long axis, slice thickness of 2 mm, resulting in 0.4 × 0.4 × 2.0 mm^3 voxels; acquisition time = 5.47 min), and a manually labeled image for hippocampal subfields including CA1-3, SUB, and CA4/DG (Kulaga-Yoskovitz et al., 2015). All T1w and T2w images underwent automated correction for intensity non-uniformity and intensity standardization. All images were linearly registered to the MNI152 space and resampled to a resolution of 0.4 × 0.4 × 0.4 mm^3. Following the previous work (Romero et al., 2017), we named this dataset as Kulaga-Yoskovitz dataset. **Figure 1** shows an example of T1w image and manual hippocampal subfield segmentation from the BCP dataset and the Kulaga-Yoskovitz dataset, respectively.

To facilitate the processing, we identified a bounding box that is big enough to cover the hippocampus of unseen target subject (Hao et al., 2014). In particular, for each subject in the BCP dataset and the Kulaga-Yoskovitz dataset, we went through all the training subjects to find the minimum and maximum x, y, z positions of the hippocampus, and empirically add 32 voxels in each direction as a bounding box to cover the hippocampus and its surrounding tissues. This step was done separately for these two datasets given the large hippocampus size differences in infants and adults. Then, we cropped all images with the box and applied a histogram matching method to the cropped images for obtaining similar intensity levels across all training subjects. To leverage the limited data, we *left-right* flipped each training image to double the number of training subjects.

METHODS

We propose a new FCN for hippocampal subfield segmentation. The FCN based segmentation methods can implement dense prediction by estimating the posterior probabilities for each voxel. Given the posterior probability $p_k(x|\theta)$ of voxel x belonging to the kth category, where θ is the FCN model parameters, the hippocampal subfield label of voxel x is determined by

$$L(x) = argmax_{k\in\mathbb{C}}\, p_k\,(x|\theta)\,,$$

where $\mathbb{C} = \{1, 2, \ldots, K\}$, and K is the number of categories. In the remaining part of this section, we will introduce the details of our proposed FCN architectures and its loss function.

TABLE 1 | Imaging protocol for acquiring infant T1w and T2w MR images.

	Matrix	FOV	Resolution mm^3	FA	TE	TR	Slices orientation	AF/MB	Time
T1w	320 × 320	256 × 256	0.8 × 0.8 × 0.8	8	2.24	2,400/1,060	208/Sag	AF = 2	6:38
T2w	320 × 320	256 × 256	0.8 × 0.8 × 0.8	VAR	564	3,200	208/Sag	AF = 2	5:57

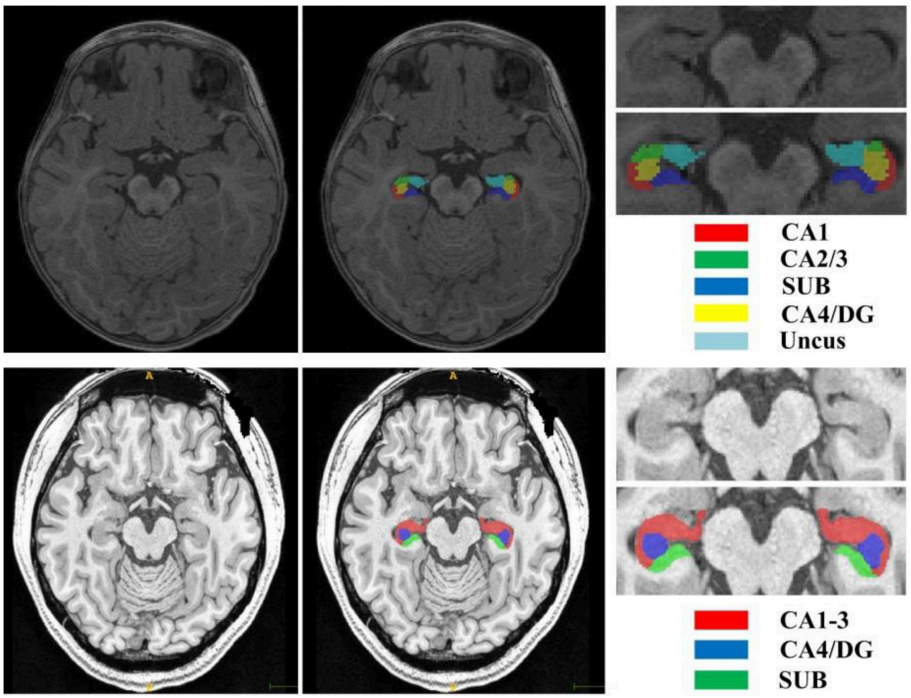


FIGURE 1 | T1w image and manual segmentation of a representative subject from the BCP dataset **(top row)** and Kulaga-Yoskovitz dataset **(bottom row)**, respectively.

Dilated Dense Network

Recent 3D neural networks often use small convolutional kernels with size 3 × 3 × 3 to reduce the number of parameters, and enlarge the receptive field by alternating convolutions and pooling operations to capture large image contexts (Çiçek et al., 2016). This successive down-sampling process will significantly reduce spatial resolution, which will lose detailed image information. Recently, dilated convolutions were proposed for semantic image segmentation (Liang-Chieh et al., 2015; Yu and Koltun, 2015). By using the dilated convolutions, the feature maps can be computed with a high spatial resolution, and the size of the receptive field can be enlarged arbitrarily. **Figure 2** illustrates the dilated convolutional kernels with different dilation rates. Let $F: \mathbb{Z}^3 \rightarrow \mathbb{R}$ be a 3 dimensional discrete function, and $h: \Omega_r \rightarrow \mathbb{R}$ be a discrete filter with a dilation rate l, where $\Omega_r = [-r, r]^3 \bigcap \mathbb{Z}^3$. The dilated convolution $*l$ can be defined as (Yu and Koltun, 2015),

$$\left(F *_l h\right)(\boldsymbol{p}) = \sum_{\boldsymbol{s}+l\boldsymbol{t}=\boldsymbol{p}} F(\boldsymbol{s})\, h(\boldsymbol{t}). \quad (1)$$

Note that, when $l = 1$, the dilated convolution becomes the normal convolution.

With the dilated convolutions, we design a dilated dense network using dense connections (Huang et al., 2016), as shown in **Figure 3**. In the dilated dense network, we use dilated convolutions with different dilation rates to enlarge the receptive field, and use dense connections to concatenate all previous generated features to the current feature maps. To avoid overfitting, dropout operations are used after each 3 × 3 × 3 convolution with dropout rate 0.5 (Srivastava et al., 2014). Thus, the dilated dense network can capture contextual image information while keeping high spatial resolution and generate multi-scale image features. This dilated dense network will be embedded in our proposed DUnet, as introduced in the next subsection.

Dilated Dense U-Net

U-net (Ronneberger et al., 2015) consists of a contracting path to extract abstract features and an expanding path to recover spatial resolution. The features in the contracting path are concatenated to the corresponding features in the expanding path to provide the detailed image information that is lost during the successive

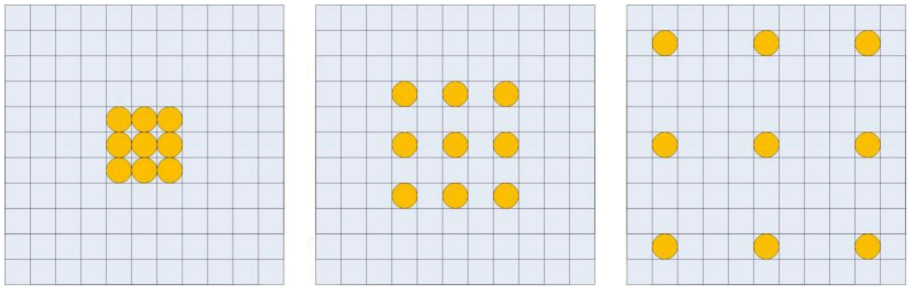


FIGURE 2 | Illustration of dilated convolutional kernels: 1-dilated convolutional kernel **(left)**; 2-dilated convolutional kernel **(middle)**; 4-dilated convolutional kernel **(right)**.

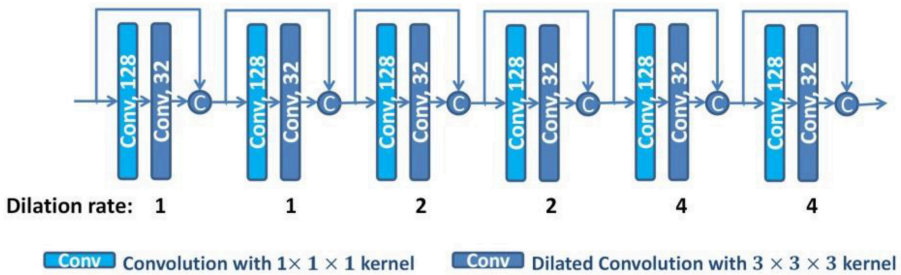


FIGURE 3 | The structure of the dilated dense network. The number in each operation rectangle is the number of kernels. All operations are implemented in a 3D manner, and "c" denotes the concatenation.

down-sampling steps. However, the level of features in the contracting path is much lower than that in the expanding path. It will not obtain the optimal results when directly concatenating these features. To overcome this limitation, we embed the dilated dense network in the U-net to obtain a new network (DUnet). **Figure 4** shows the structure of our proposed DUnet.

Same to U-net, the proposed DUnet consists of a contracting path and an expanding path. The contracting path is built by alternating two $3 \times 3 \times 3$ convolutions and one $2 \times 2 \times 2$ max pooling operation with stride 2. The contracting path is followed by two $3 \times 3 \times 3$ convolutions. Correspondingly, the expanding path is built by alternating one $4 \times 4 \times 4$ deconvolution with stride 2, and two $3 \times 3 \times 3$ convolutions. The expanding path is then followed by a $1 \times 1 \times 1$ convolution, which outputs K feature maps (K is the number of label categories including the background). Each $3 \times 3 \times 3$ convolution is followed by a batch normalization layer and a rectified linear unit (ReLU). Different from the original U-net, some padded convolution layers are also used to maintain the spatial dimension.

The feature maps before the first pooling layer and the last pooling layer are concatenated to the corresponding feature maps in the expanding path. The feature maps before the second pooling layer are first input into the dilated dense network which is introduced in the last subsection of this paper. Then, the output features of the dilated dense network are concatenated to the corresponding feature maps in the expanding path. The dilated dense network can provide multi-scale features while remaining high spatial resolution. Moreover, two different kinds of features provided by the dilated dense network and the contracting-expanding path are fused, providing more abundant image information for dense prediction.

Residual Dilated Dense U-net

To further improve the performance, we use residual connections in DUnet to promote the information flow within the network (He et al., 2016a). Formally, the residual connection can be expressed as:

$$x_l = H_l\left(x_{l-1}\right) + x_{l-1},$$

where x_{l-1} and x_l are the input and output of the lth unit, and $H_l(\cdot)$ is a non-linear function which is used to learn the residual $x_l - x_{l-1}$ of the lth unit. We group every pair of convolutional layers with one residual connection along the contracting path and the expanding path of DUnet, and obtain the Residual DUnet (ResDUnet). **Figure 5** shows the structure of our proposed ResDUnet. The difference between ResDUnet and DUnet is the use of residual connections in ResDUnet, which connects two adjacent convolutions with an identity mapping (or a $1 \times 1 \times 1$ convolution if the number of feature maps is not matched).

Loss Function

We train our models using Softmax loss (Gu et al., 2017):

$$L_{Softmax} = -\sum_{i=1}^{N}\sum_{k=1}^{K} 1\left\{y_i = k\right\} \log \frac{e^{z_{k,i}}}{\sum_{j=1}^{K} e^{z_{j,i}}},$$

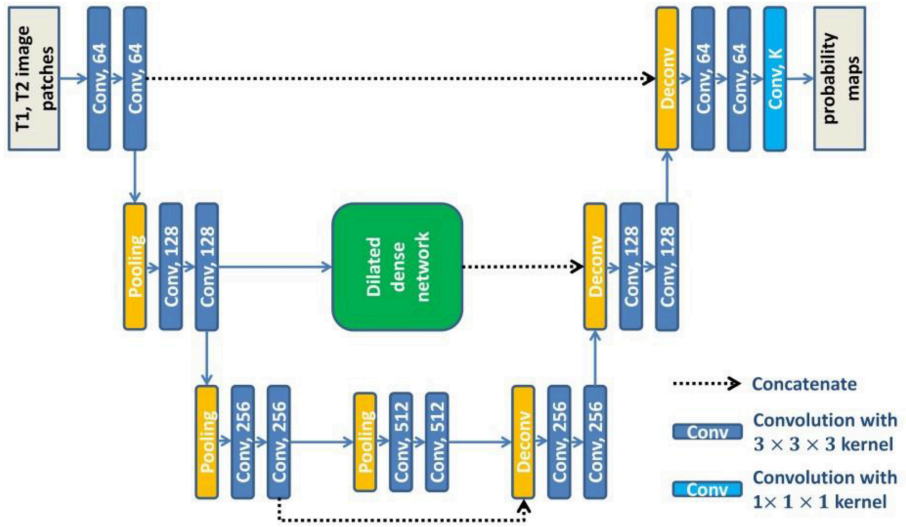


FIGURE 4 | The structure of our proposed DUnet. The number in each operation rectangle is the number of kernels. All operations are implemented in a 3D manner.

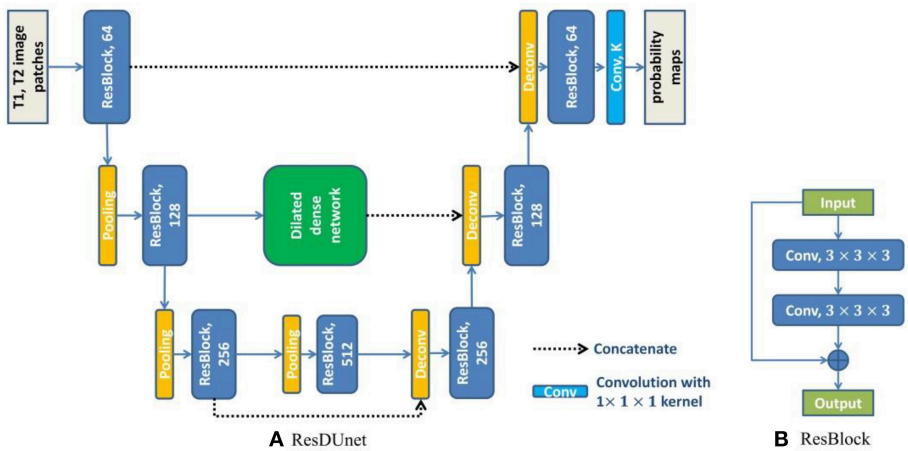


FIGURE 5 | The structure of our proposed ResDUnet. The number in each operation rectangle is the number of kernels. "⊕" denotes the element-wise summation, and all operations are implemented in a 3D manner.

where $z_{k,i}$ represents the kth output of the last network layer for the ith voxel, $y_i \in \{1, 2, \ldots, K\}$ represents the corresponding ground-truth label, K and N are the number of categories and the number of voxels, respectively. The term $\frac{e^{z_{k,i}}}{\sum_{j=1}^{K} e^{z_{j,i}}}$ represents the prediction probability for the kth class of the ith voxel, which is computed by the Softmax function.

Evaluation Metrics

We evaluated the image segmentation results based on two types of segmentation evaluation measures (Jafari-Khouzani et al., 2011): Dice coefficient (Dice) and Average Symmetric Surface Distance (ASSD). Dice is used to measure the relative volumetric overlap between the automated segmentation and the manual segmentation, and ASSD is used to measure the agreement between segmentation boundaries. By denoting A as the manual segmentation, B as the automated segmentation, and $V(X)$ as the volume of segmentation X, the two evaluation measures are defined as:

$$\text{Dice} = 2\frac{\text{V}(\text{A} \cap \text{B})}{V(\text{A}) + \text{V}(\text{B})},$$

$$\text{ASSD} = \left(\text{mean}_{\text{e}\in\partial\text{A}}\left(\min_{\text{f}\in\partial\text{B}} \text{d}\left(\text{e}, \text{f}\right)\right) + \text{mean}_{\text{e}\in\partial\text{B}}\left(\min_{\text{f}\in\partial\text{A}} \text{d}\left(\text{e}, \text{f}\right)\right)\right)/2,$$

where ∂A denotes the boundary voxels of A, and $d(\cdot, \cdot)$ is the Euclidian distance between two points.

EXPERIMENTS AND RESULTS

Experimental Details

Five-fold cross validation was used in the experiment for the BCP dataset. In each fold, we selected 7 subjects for training, 1 subject for validation, and 2 subjects for testing. Experiments were performed using a NVIDIA Titan Xp with 12 GB memory. Because of the restriction of limited training subjects and GPU memory, we randomly extracted patches from each training subject, instead of using the whole images as input for each network. We extracted about 1,300 patches from each subject. These patches were extracted as follows. First, we extracted patches one by one with stride of $2 \times 2 \times 2$. The extracted patches that contain at least one hippocampal voxel were taken, and were numbered as 1, 2,…, n. Then, these numbers were randomly reordered. At last, we took the first half part of the reordered patches as our training patches. The patch size was optimally set to $24 \times 24 \times 24$ by comparing the results obtained by the baseline 3D U-net method with different patch sizes, which is shown in **Table 2**. Since both T1w and T2w images were available, we concatenated the corresponding T1w and T2w image patches as input for each network. The networks were trained by Adam method with a batch size of 5, which were implemented with Caffe (Jia et al., 2014). The learning rates were initially set to 0.0001 and were decreased by a factor of $\gamma = 0.1$ every 10,000 iterations. We used a weight decay of 0.0005 and a momentum of 0.9 in all networks. The training process was stopped after 60,000 iterations. For segmenting a testing image, patches were extracted to feed into the trained models with an overlapped sliding windows strategy. The patch size was set to $24 \times 24 \times 24$ with stride of $8 \times 8 \times 8$. We used a majority voting strategy for the overlap regions to get the whole image prediction. Note that we used the same hyper-parameters during the 5-fold cross-validation.

As the networks are trained based on image patches extracted around the hippocampus, the global spatial information of brain structures may not be perfectly captured. Thus, the obtained network models can well-recognize the hippocampal subfields around the hippocampus, but cannot recognize those far away from hippocampal region. For example, a patch in the caudate (denoted by the pink circle in the left of **Figure 6**) may look similar to the patches in the hippocampus, and will be classified to hippocampal subfields in the testing stage. As a result, there are some isolated false positives outside the hippocampal region, as shown in **Figure 6**. To remove these artifacts automatically, our post-processing steps include searching the voxels of each automated segmentation to find the non-zero neighbors of current voxel, and to obtain several connected regions. Then, we selected two regions with maximum volumes for the final left and right hippocampal subfields.

Five-fold cross validation was also used in the Kulaga-Yoskovitz dataset. In each fold, we selected 15 subjects for training, 5 subjects for validation, and 5 subjects for testing. The same experimental settings were used as the BCP dataset, except that the patch size was set to $32 \times 32 \times 32$ as the resolution of images in this dataset is much higher, and the batch size was set to 3 because of the GPU memory limit. The same post-processing was used to remove isolated tiny blocks outside the hippocampal region.

TABLE 2 | Mean (STD) values of Dice for each subfield segmentation using different patch sizes ($R \times R \times R$) on the BCP dataset by 3D U-net.

	$R = 16$	$R = 24$	$R = 32$
CA1	0.635 (0.066)	**0.648** (0.078)	0.638 (0.107)
CA2/3	0.565 (0.071)	**0.567** (0.082)	0.556 (0.099)
SUB	0.717 (0.038)	**0.719** (0.080)	0.708 (0.123)
CA4/DG	**0.711** (0.063)	0.709 (0.072)	0.706 (0.057)
Uncus	0.710 (0.034)	**0.712** (0.050)	0.704 (0.069)
Average	0.668	**0.671**	0.662

Higher Dice values indicate better segmentation performance. The best results are shown in bold.

The Efficacy of Multi-Modality

In this subsection, we studied the efficacy of multi-modality by comparing the segmentation results obtained using only single modality images (i.e., T1w or T2w) and multi-modality images (T1w+T2w), respectively. All experiments were carried out on the BCP dataset with the same network architecture (ResDUnet) and the same training strategies. **Table 3** lists the Dice coefficients of segmentation results using different image modalities. It shows that training using multi-modality images can obtain better results in the most subfields, compared with those using only either T1w or T2w single-modality images. This demonstrates that the network trained with multi-modality images can generate more discriminative features, which improves the performance of hippocampal subfield segmentation. From the results, we also find that T1w images can provide more useful information than T2w images for hippocampal subfield segmentation on the BCP dataset. In some subfields, training using only T1w images obtains similar or even a little better segmentation results than those using multi-modality images.

Comparison With State-of-the-Art Methods

Our proposed method was also compared with two state-of-the-art networks, namely, 3D U-net (Çiçek et al., 2016) and ConvNet (Yu et al., 2017). The 3D U-net is extended from the previous 2D version (Ronneberger et al., 2015) into a 3D variant for volumetric feature representation. For a fair comparison, the 3D

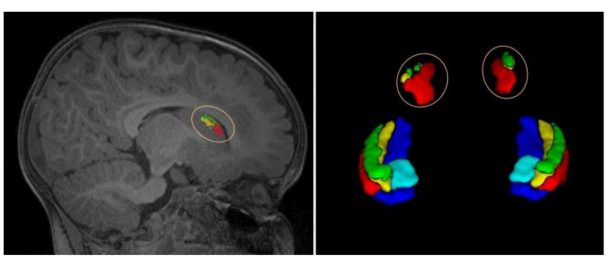


FIGURE 6 | An example of isolated tiny blocks, outside the hippocampal region, appeared in the automated segmentation.

TABLE 3 | Mean (STD) values of Dice for each subfield segmentation using different modalities on the BCP dataset.

	T1w	T2w	T1w+T2w
CA1	**0.674** (0.044)	0.604 (0.142)*#	0.672 (0.050)
CA2/3	0.571 (0.069)*	0.546 (0.104)*	**0.598** (0.041)
SUB	**0.745** (0.032)	0.644 (0.223)*#	0.745 (0.051)
CA4/DG	0.723 (0.027)	0.662 (0.157)*	**0.729** (0.032)
Uncus	0.725 (0.031)	0.645 (0.203)*#	**0.736** (0.035)
Average	0.688	0.620	**0.696**

Higher Dice values indicate better segmentation performance. The best results are shown in bold.
**Indicates that T1w + T2w achieves significant improvement over the corresponding method, and #indicates that T1w achieves significant improvement over the corresponding method in the Wilcoxon signed rank tests with $p < 0.05$.*

U-net used in our experiments consists of three pooling layers and three deconvolutional layers, which are the same as our proposed DUnet. The only difference is that the dilated dense network is used to fuse the middle level features of the contracting path with those of the expanding path in DUnet, instead of directly concatenating them as in 3D U-net. ConvNet (Yu et al., 2017) is a volumetric convolutional neural network with mixed residual connections, which also consists of three pooling layers and three deconvolutional layers. In ConvNet, residual connections are used between the successive convolution layers to form the residual blocks, and also between the feature maps of contracting path and those of expanding path. Besides, ConvNet (Yu et al., 2017) exploits a deep supervision mechanism to accelerate its convergence speed. All these comparative networks use Softmax loss as loss function, and the same post-processing is used to remove the tiny isolated blocks of segmentation results that appear outside of the hippocampal region.

Table 4 reports the Dice coefficients of the segmentation results obtained by different networks on the BCP dataset. It shows that our proposed DUnet outperforms 3D U-net (Çiçek et al., 2016) in segmenting CA1, SUB, CA4/DG and Uncus, and our proposed ResDUnet outperforms 3D U-net (Çiçek et al., 2016) in segmenting CA1, CA2/3, SUB, and Uncus, according to the Wilcoxon signed rank tests with $p < 0.05$. As can be seen in the table, our proposed ResDUnet achieves the highest Dice coefficient for the average of subfields. **Table 5** reports the ASSD coefficients of the segmentation results, which shows that our proposed ResDUnet achieves the best ASSD coefficient for the average of subfields. **Figure 7** shows hippocampal subfield segmentations of a randomly selected subject from the BCP dataset, obtained by manual segmentation and four different networks. It can be seen that our proposed ResDUnet achieves the most accurate results.

Results on a Public Adult Dataset

Tables 6, **7** list the Dice and ASSD coefficients of the segmentation results obtained by five different networks on the Kulaga-Yoskovitz dataset. The results show that our proposed DUnet outperforms 3D U-net (Çiçek et al., 2016) and ConvNet (Yu et al., 2017) in segmenting CA1-3 and SUB, and our proposed ResDUnet outperforms 3D U-net (Çiçek et al., 2016) and ConvNet (Yu et al., 2017) in segmenting all subfields, according to the Wilcoxon signed rank tests with $p < 0.05$. **Table 6** also lists the comparison of our proposed method with the state-of-the-art hippocampal subfield segmentation method (HIPS), which obtained the best segmentation results on the Kulaga-Yoskovitz dataset so far (Romero et al., 2017). Note that, for a fair comparison, we use the published results of HIPS as reported in Romero et al. (2017). It shows that our proposed DUnet and ResDUnet also outperform HIPS method, especially for segmenting the CA4/DG subfield which is the most difficult task (Dalton et al., 2017). **Figure 8** shows hippocampal subfield segmentations of a randomly selected subject from Kulaga-Yoskovitz dataset, obtained by manual segmentation and four different networks. It can be seen that our proposed DUnet and ResDUnet achieve the most accurate results.

DISCUSSION

FCNs have achieved great success in the field of medical image segmentation, which usually consist of a contracting path to extract abstract features, and an expanding path to up-sample the feature maps for dense prediction (Ronneberger et al., 2015; Çiçek et al., 2016; Chen H. et al., 2017; Lian et al., 2018; Nie et al., 2018). The detailed image information may be lost during these contracting and expanding processes. The existing U-net-like FCNs concatenate the feature maps in the contracting path to the corresponding feature maps in the expanding path to recover the lost image information. However, the levels of features in the contracting path are much lower than those in the expanding path. It may not obtain the optimal results when directly concatenating these features. To overcome this limitation and fully exploit multi-level image features, we proposed a new FCN by exploiting a dilated dense network to connect the features of the contracting path and the features of the expanding path. The dilated dense network uses the dilated convolutions to extract contextual features without reducing spatial resolution, and it also employs dense connections to aggregate multi-scale features. Thus, multi-scale features can be generated from the dilated dense network, which are fused with the corresponding features in the expanding path. To avoid overfitting, dropout operations are also used in the dilated dense network (Srivastava et al., 2014).

By using the dilated dense network to connect the feature maps in the contracting path and expanding path, our proposed method provides a way to fuse the finer-grained low-level features in the contracting path and the coarse high-level features in the expanding path. Moreover, the multi-scale features extracted by the dilated dense network are useful for segmenting multi-structures with different shapes and different scales. To further promote information propagation and accelerate the convergence, we introduce residual connections to group every pair of convolutional layers (He et al., 2016a,b).

Different from natural images, many imaging modalities are 3D in the field of medical image analysis. In the past few years, a lot of effort has been dedicated to exploit CNNs to

TABLE 4 | Mean (STD) values of Dice for each subfield segmentation by different networks on the BCP dataset.

	3D U-net (Çiçek et al., 2016)	ConvNet (Yu et al., 2017)	DUnet (proposed)	ResDUnet (proposed)
CA1	0.648 (0.078)*#	0.670 (0.046)	0.665 (0.061)	**0.672** (0.050)
CA2/3	0.567 (0.082)*	0.584 (0.038)*	0.589 (0.045)*	**0.598** (0.041)
SUB	0.719 (0.080)*#	0.737 (0.045)*	0.742 (0.052)	**0.745** (0.051)
CA4/DG	0.709 (0.072)#	0.726 (0.030)	**0.733** (0.028)	0.729 (0.032)
Uncus	0.712 (0.050)*#	0.721 (0.035)	0.733 (0.034)	**0.736** (0.035)
Average	0.671	0.688	0.692	**0.696**

Higher Dice values indicate better segmentation performance. The best results are shown in bold.
**Indicates that ResDUnet achieves significant improvement over the corresponding method, and # indicates that DUnet achieves significant improvement over the corresponding method in the Wilcoxon signed rank tests with $p < 0.05$.*

TABLE 5 | Mean (STD) values of ASSD for each subfield segmentation by different networks on the BCP dataset.

	3D U-net (Çiçek et al., 2016)	ConvNet (Yu et al., 2017)	DUnet (proposed)	ResDUnet (proposed)
CA1	0.175 (0.089)*	**0.146** (0.033)	0.158 (0.048)	0.147 (0.034)
CA2/3	0.211 (0.104)*	0.175 (0.020)	0.178 (0.028)*	**0.170** (0.025)
SUB	0.153 (0.073)*	**0.132** (0.030)	0.136 (0.040)	0.134 (0.039)
CA4/DG	0.157 (0.080)	**0.133** (0.019)	0.134 (0.019)	**0.133** (0.020)
Uncus	0.179 (0.055)*	0.168 (0.038)	0.170 (0.041)	**0.167** (0.044)
Average	0.175	0.151	0.155	**0.150**

Smaller ASSD values indicate better segmentation performance. The best results are shown in bold.
**Indicates that ResDUnet achieves significant improvement over the corresponding method in the Wilcoxon signed rank tests with $p < 0.05$.*

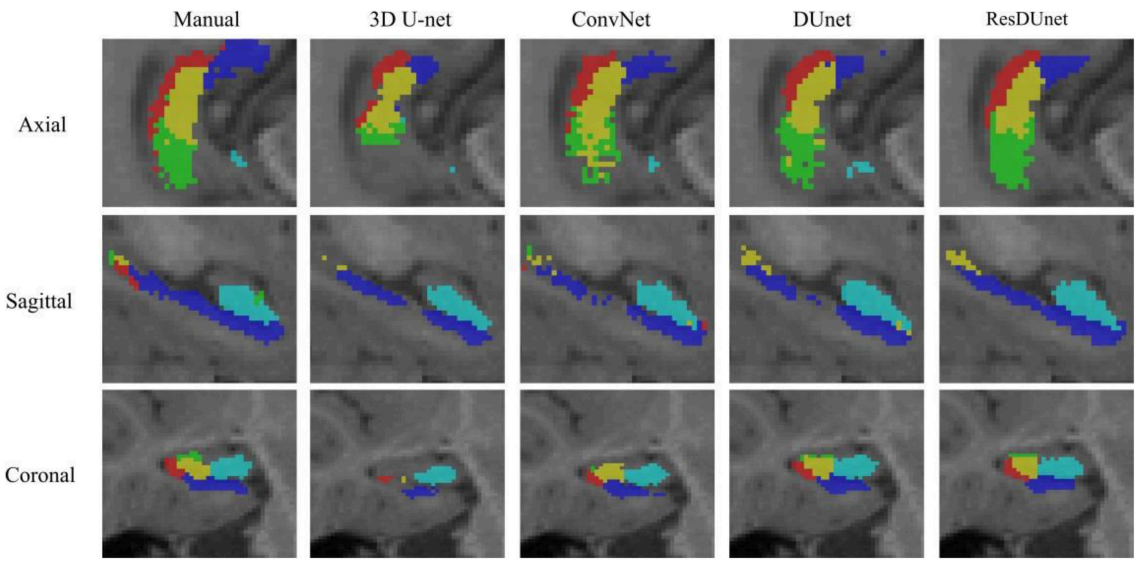


FIGURE 7 | Hippocampal subfield segmentations of a randomly selected subject from the BCP dataset, obtained by manual segmentation, and four different networks.

process volumetric data. Some of them applied 2D CNNs to each slice of volumetric images (Prasoon et al., 2013; Setio et al., 2016; Chen Y. et al., 2017). To effectively make full use of the 3D spatial information, recent studies applied 3D CNNs to deal with volumetric images (Çiçek et al., 2016; Chen H. et al., 2017;Nie et al., 2018; Wachinger et al., 2018). Following these methods, our proposed FCNs were also implemented in a 3D manner. As the number of our training subjects is limited, we randomly extracted patches from each training subject, instead of using the whole image as the input for each network. The patch size was set to $24 \times 24 \times 24$ for the BCP dataset and $32 \times 32 \times 32$ for Kulaga-Yoskovitz

TABLE 6 | Mean (STD) values of Dice for each subfield segmentation by five different methods on the KULAGA-YOSKOVITZ dataset.

	HIPS (Romero et al., 2017)	3D U-net (Çiçek et al., 2016)	ConvNet (Yu et al., 2017)	DUnet (proposed)	ResDUnet (proposed)
CA1-3	0.916 (0.015)	0.916 (0.011)*#	0.918 (0.010)*#	0.919 (0.011)	**0.920** (0.011)
CA4/ DG	0.862 (0.034)	0.871 (0.021)*	0.870 (0.016)*	0.875 (0.020)*	**0.879** (0.020)
SUB	0.886 (0.021)	0.883 (0.016)*#	0.887 (0.018)*#	**0.890** (0.016)	0.888 (0.018)#
Average	0.888	0.890	0.892	0.895	**0.896**

Higher Dice values indicate better segmentation performance. Best results are shown in bold.
**Indicates that ResDUnet achieves significant improvement over the corresponding method, and # indicates that DUnet achieves significant improvement over the corresponding method in the Wilcoxon signed rank tests with $p < 0.05$.*

TABLE 7 | Mean (STD) values of ASSD for each subfield segmentation by four different networks on the KULAGA-YOSKOVITZ dataset.

	3D U-net (Çiçek et al., 2016)	ConvNet (Yu et al., 2017)	DUnet (proposed)	ResDUnet (proposed)
CA1-3	0.065 (0.011)*#	0.064 (0.009)*#	**0.062** (0.009)	**0.062** (0.010)
CA4/DG	0.077 (0.014)*	0.079 (0.015)*	0.075 (0.015)*	**0.072** (0.014)
SUB	0.069 (0.013)*#	0.066 (0.013)*#	**0.064** (0.012)	0.065 (0.013)#
Average	0.070	0.070	0.067	**0.066**

Smaller ASSD values indicate better segmentation performance. The best results are shown in bold.
**Indicates that ResDUnet achieves significant improvement over the corresponding method, and # indicates that DUnet achieves significant improvement over the corresponding method in the Wilcoxon signed rank tests with $p < 0.05$.*

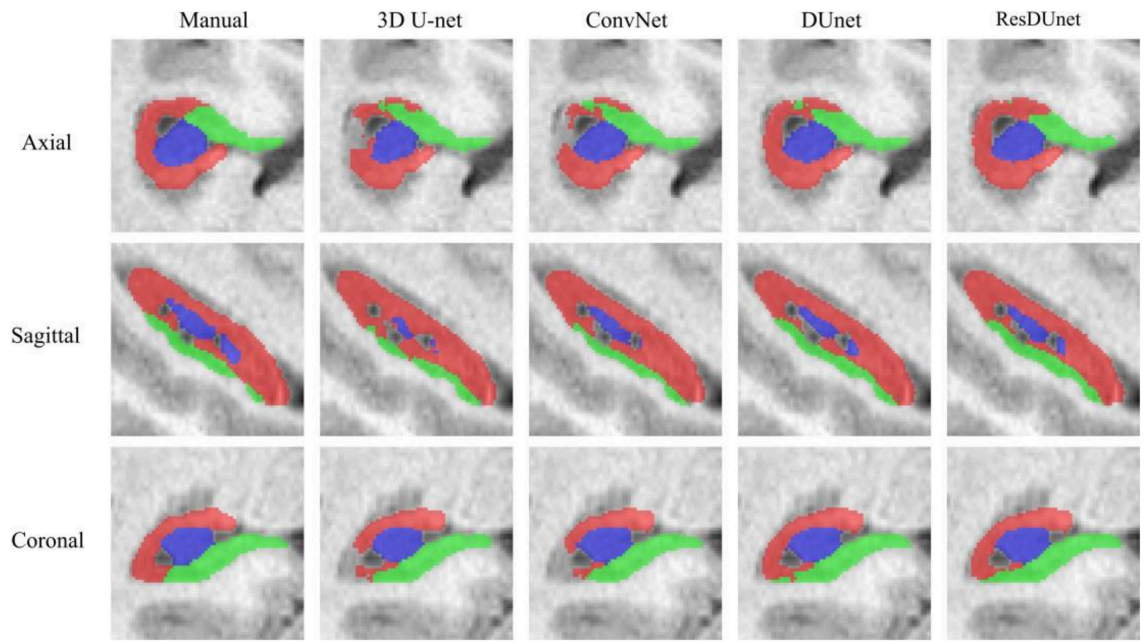


FIGURE 8 | Hippocampal subfield segmentations of a randomly selected subject from the Kulaga-Yoskovitz dataset, obtained by manual segmentation, and four different networks.

dataset, considering different image resolutions in these two datasets.

As both T1w and T2w images were available for each subject, we concatenated the extracted T1w and T2w image patches as input to the networks. Compared with single modality data, multi-modality MR images can provide complementary contextual information, which contributes to better segmentation performance. From our experiments, we find that training using multi-modality images can obtain better results than using only single-modality images, and we also find

that T1w images can provide more discriminative information than T2w images for hippocampal subfield segmentation.

Experimental results on the BCP dataset show that our proposed DUnet and ResDUnet improve the average Dice coefficient by 2.1 and 2.5%, respectively, for infant hippocampal subfield segmentation, compared with the 3D U-net (Çiçek et al., 2016). To further validate the effectiveness, we also applied our proposed method for adult hippocampal subfield segmentation based on a publicly available dataset. The results show that our proposed DUnet and ResDUnet improve the average Dice coefficients of 0.5 and 0.6%, respectively, compared with the 3D U-net (Çiçek et al., 2016). The improvement of our proposed ResDUnet method on both infant dataset and adult dataset comes from (1) multi-scale image features aggregation for distinguishing different hippocampal subfields; (2) utilization of the embedded dilated dense network for effectively fusing the low-level features in the contracting path and the high-level features in the expanding path; and (3) utilization of residual connections for promoting information propagation and accelerating the convergence.

However, the proposed method was mainly designed for infant hippocampal subfield segmentation on the BCP dataset. First, the embedded dilated dense network can provide multi-scale image features, which are especially useful for segmenting infant hippocampal subfields, since tissue contrast between infant hippocampal subfields are much blurrier than in adults. Second, the task of infant hippocampal subfield segmentation on the BCP dataset is to segment hippocampus into five parts (CA1, CA2/3, SUB, CA4/ DG, and Uncus), while there are only three parts (CA1-3, SUB, and CA4/DG) on the Kulaga-Yoskovitz dataset. Therefore, the segmented hippocampal subfields in the infant subjects are much smaller than those of the adult subjects. In our proposed network, the embedded dilated dense network can capture contextual image information without losing detailed image information, which is extremely useful for segmenting small structures.

CONCLUSION

In this paper, we have proposed a new FCN by integrating U-net and dilated dense network for hippocampal subfield segmentation. Our proposed method can avoid losing the detailed image information in the successive down-sampling steps, effectively fuse the low-level features of the contracting path with the coarse high-level features of the expanding path, and generate multi-scale image features. Experimental results show that our proposed method outperforms the state-of-the-art methods.

ETHICS STATEMENT

This study was approved by the Institutional Review Board in School of Medicine, the University of North Carolina (UNC) at Chapel Hill.

AUTHOR CONTRIBUTIONS

HZ, FS, LW, SW, and DS contributed to the method development and the manuscript preparation. WL contributed to providing infant imaging data, and S-CH and M-HC did manual labeling of infant hippocampal subfields. HZ undertook the statistical analysis.

ACKNOWLEDGMENTS

This work utilizes data collected by a NIH grant (1U01MH110274) and the efforts of the UNC/UMN Baby Connectome Project Consortium. HZ was partially supported by National Natural Science Foundation of China (Nos. 61602307, 61877039), and Natural Science Foundation of Zhejiang Province (No. LY19F020013).

REFERENCES

Bartsch, T. (2012). *The Clinical Neurobiology of the Hippocampus: An Integrative View*. Vol. 151. Oxford: Oxford University Press. doi: 10.1093/acprof:oso/9780199592388.001.0001

Caldairou, B., Bernhardt, B. C., Kulaga-Yoskovitz, J., Kim, H., Bernasconi, N., and Bernasconi, A. (2016). "A surface patch-based segmentation method for hippocampal subfields," in *Paper Presented at: International Conference on Medical Image Computing and Computer-Assisted Intervention* (Athens).

Cao, L., Li, L., Zheng, J., Fan, X., Yin, F., Shen, H., et al. (2018). Multi-task neural networks for joint hippocampus segmentation and clinical score regression. *Multimedia Tools Applic.* 77, 29669–29686. doi: 10.1007/s11042-017-5581-1

Chen, H., Dou, Q., Yu, L., Qin, J., and Heng, P.-A. (2017). VoxResNet: Deep voxelwise residual networks for brain segmentation from 3D MR images. *Neuroimage* 170, 446–455. doi: 10.1016/j.neuroimage.2017.04.041

Chen, Y., Shi, B., Wang, Z., Zhang, P., Smith, C. D., and Liu, J. (2017). "Hippocampus segmentation through multi-view ensemble ConvNets," in *2017 IEEE 14th International Symposium on Biomedical Imaging (ISBI 2017)* (Melbourne, VIC) 192–196.

Çiçek, Ö., Abdulkadir, A., Lienkamp, S. S., Brox, T., and Ronneberger, O. (2016). "3D U-Net: learning dense volumetric segmentation from sparse annotation," in *Paper presented at: International Conference on Medical Image Computing and Computer-Assisted Intervention* (Athens).

Dalton, M. A., Zeidman, P., Barry, D. N., Williams, E., and Maguire, E. A. (2017). Segmenting subregions of the human hippocampus on structural magnetic resonance image scans: an illustrated tutorial. *Brain Neurosci. Adv.* 1:2398212817701448. doi: 10.1177/2398212817701448

de Brébisson, A., and Montana, G. (2015). "Deep neural networks for anatomical brain segmentation," in *Proceedings of the IEEE Conference on Computer Vision and Pattern Recognition Workshops* (Boston, MA), 20–28.

Gu, J., Wang, Z., Kuen, J., Ma, L., Shahroudy, A., Shuai, B., et al. (2017). Recent advances in convolutional neural networks. *Pattern Recogn.* 77, 354–377. doi: 10.1016/j.patcog.2017.10.013

Hao, Y., Wang, T., Zhang, X., Duan, Y., Yu, C., Jiang, T., et al. (2014). Local label learning (LLL) for subcortical structure segmentation: Application to hippocampus segmentation. *Hum. Brain Mapp.* 35, 2674–2697. doi: 10.1002/hbm.22359

He, K., Zhang, X., Ren, S., and Sun, J. (2016a). "Deep residual learning for image recognition," in *Proceedings of the IEEE Conference on Computer Vision and Pattern Recognition* (Las Vegas, NV), 770–778.

He, K., Zhang, X., Ren, S., and Sun, J. (2016b). "Identity mappings in deep residual networks," in *European Conference on Computer Vision* (Amsterdam: Springer), 630–645.

Huang, G., Liu, Z., van der Maaten, L., and Weinberger, K. Q. (2016). "Densely connected convolutional networks," in *Proceedings of the IEEE Conference on Computer Vision and Pattern Recognition* (Honolulu, HI), 4700–4708.

Jafari-Khouzani, K., Elisevich, K. V., Patel, S., and Soltanian-Zadeh, H. (2011). Dataset of magnetic resonance images of nonepileptic subjects and temporal lobe epilepsy patients for validation of hippocampal segmentation techniques. *Neuroinformatics* 9, 335–346. doi: 10.1007/s12021-010-9096-4

Jia, Y., Shelhamer, E., Donahue, J., Karayev, S., Long, J., Girshick, S., et al. (2014). "Caffe: convolutional architecture for fast feature embedding," *Proceedings of the 22nd ACM International Conference on Multimedia* (Orlando, FL: ACM), 675–678.

Kulaga-Yoskovitz, J., Bernhardt, B. C., Hong, S. J., Mansi, T., Liang, K. E., van der Kouwe, A. J., et al. (2015). Multi-contrast submillimetric 3 Tesla hippocampal subfield segmentation protocol and dataset. *Sci. Data* 2:150059. doi: 10.1038/sdata.2015.59

LeCun, Y., Bengio, Y., and Hinton, G. (2015). Deep learning. *Nature* 521, 436–444. doi: 10.1038/nature14539

Li, J., Jin, Y., Shi, Y., Dinov, I. D., Wang, D. J., Toga, A. W., et al. (2013). "Voxelwise spectral diffusional connectivity and its applications to Alzheimer's disease and intelligence prediction," in *Paper Presented at: International Conference on Medical Image Computing and Computer-Assisted Intervention* (Nagoya).

Li, W., Wang, G., Fidon, L., Ourselin, S., Cardoso, M. J., and Vercauteren, T. (2017). "On the compactness, efficiency, and representation of 3D convolutional networks: brain parcellation as a pretext task," in *International Conference on Information Processing in Medical Imaging* (Boone, NC), 348–360.

Lian, C., Zhang, J., Liu, M., Zong, X., Hung, S. C., Lin, W., et al. (2018). Multi-channel multi-scale fully convolutional network for 3D perivascular spaces segmentation in 7T MR images. *Med. Image Anal.* 46, 106–117. doi: 10.1016/j.media.2018.02.009

Liang-Chieh, C., Papandreou, G., Kokkinos, I., Murphy, K., and Yuille, A. (2015). "Semantic image segmentation with deep convolutional nets and fully connected crfs," in *International Conference on Learning Representations* (San Diego, CA).

Litjens, G., Kooi, T., Bejnordi, B. E., Setio, A. A. A., Ciompi, F., Ghafoorian, M., et al. (2017). A survey on deep learning in medical image analysis. *Med. Image Anal.* 42, 60–88. doi: 10.1016/j.media.2017.07.005

Long, J., Shelhamer, E., and Darrell, T. (2015). "Fully convolutional networks for semantic segmentation," in *Proceedings of the IEEE Conference on Computer Vision and Pattern Recognition* (Boston, MA), 3431–3440.

McKinley, R., Jungo, A., Wiest, R., and Reyes, M. (2017). "Pooling-free fully convolutional networks with dense skip connections for semantic segmentation, with application to brain tumor segmentation," in *International MICCAI Brainlesion Workshop* (Quebec, QC), 169–177.

Milletari, F., Navab, N., and Ahmadi, S-A. (2016). "V-net: fully convolutional neural networks for volumetric medical image segmentation," in *2016 Fourth International Conference on 3D Vision (3DV)* (Stanford, CA), 565–571.

Moeskops, P., Viergever, M. A., Mendrik, A. M., de Vries, L. S., Benders, M. J., and Išgum, I. (2016). Automatic segmentation of MR brain images with a convolutional neural network. *IEEE Trans. Med. Imaging* 35, 1252–1261. doi: 10.1109/TMI.2016.2548501

Nie, D., Wang, L., Adeli, E., Lao, C., Lin, W., and Shen, D. (2018). 3-D fully convolutional networks for multimodal isointense infant brain image segmentation. *IEEE Trans. Cybernet.* 99, 1–14. doi: 10.1109/TCYB.2018.2797905

Pipitone, J., Park, M. T. M., Winterburn, J., Lett, T. A., Lerch, J. P., Pruessner, J. C., et al. (2014). Multi-atlas segmentation of the whole hippocampus and subfields using multiple automatically generated templates. *Neuroimage* 101, 494–512. doi: 10.1016/j.neuroimage.2014.04.054

Prasoon, A., Petersen, K., Igel, C., Lauze, F., Dam, E., and Nielsen, M. (2013). "Deep feature learning for knee cartilage segmentation using a triplanar convolutional neural network," in *International Conference on Medical Image Computing and Computer-Assisted Intervention* (Nagoya), 246–253.

Romero, J. E., Coupé, P., and Manjón, J. V. (2017). HIPS: a new hippocampus subfield segmentation method. *Neuroimage* 163, 286–295. doi: 10.1016/j.neuroimage.2017.09.049

Ronneberger, O., Fischer, P., and Brox, T. (2015). "U-net: convolutional networks for biomedical image segmentation," in *International Conference on Medical Image Computing and Computer-Assisted Intervention* (Munich), 234–241.

Setio, A. A. A., Ciompi, F., Litjens, G., Gerke, P., Jacobs, C., van Riel, S. J., et al. (2016). Pulmonary nodule detection in CT images: false positive reduction using multi-view convolutional networks. *IEEE Trans. Med. Imag.* 35, 1160–1169. doi: 10.1109/TMI.2016.2536809

Shen, D., Wu, G., and Suk, H-I. (2017). Deep learning in medical image analysis. *Annu. Rev. Biomed. Eng.* 19, 221–248. doi: 10.1146/annurev-bioeng-071516-044442

Shi, F., Liu, B., Zhou, Y., Yu, C., and Jiang, T. (2009). Hippocampal volume and asymmetry in mild cognitive impairment and Alzheimer's disease: meta-analyses of MRI studies. *Hippocampus* 19, 1055–1064. doi: 10.1002/hipo.20573

Small, S. A. (2014). Isolating pathogenic mechanisms embedded within the hippocampal circuit through regional vulnerability. *Neuron.* 84, 32–39. doi: 10.1016/j.neuron.2014.08.030

Srivastava, N., Hinton, G., Krizhevsky, A., Sutskever, I., and Salakhutdinov, R. (2014). Dropout: a simple way to prevent neural networks from overfitting. *J. Mach. Learn. Res.* 15, 1929–1958.

Van Leemput, K., Bakkour, A., Benner, T., Wiggins, G., Wald, L. L., Augustinack, J., et al. (2009). Automated segmentation of hippocampal subfields from ultra-high resolution *in vivo* MRI. *Hippocampus* 19, 549–557. doi: 10.1002/hipo.20615

Wachinger, C., Reuter, M., and Klein, T. (2018). DeepNAT: Deep convolutional neural network for segmenting neuroanatomy. *Neuroimage* 170, 434–445. doi: 10.1016/j.neuroimage.2017.02.035

Wang, H., Suh, J. W., Das, S. R., Pluta, J. B., Craige, C., and Yushkevich, P. A. (2013). Multi-atlas segmentation with joint label fusion. *Pattern Anal. Mach. Intell. IEEE Trans.* 35, 611–623. doi: 10.1109/TPAMI.2012.143

Wu, Z., Gao, Y., Shi, F., Ma, G., Jewells, V., and Shen, D. (2018). Segmenting hippocampal subfields from 3T MRI with multi-modality images. *Med. Image Anal.* 43, 10–22. doi: 10.1016/j.media.2017.09.006

Yu, F., and Koltun, V. (2015). Multi-scale context aggregation by dilated convolutions. *arXiv [preprint] arXiv:1511.07122.*

Yu, L., Yang, X., Chen, H., Qin, J., and Heng, P-A. (2017). "Volumetric ConvNets with mixed residual connections for automated prostate segmentation from 3D MR images," in *AAAI'17 Proceedings of the Thirty-First AAAI Conference on Artificial Intelligence* (San Francisco, CA), 66–72.

Yushkevich, P. A., Pluta, J. B., Wang, H., Xie, L., Ding, S. L., Gertje, E. C., et al. (2015). Automated volumetry and regional thickness analysis of hippocampal subfields and medial temporal cortical structures in mild cognitive impairment. *Hum. Brain Mapp.* 36, 258–287. doi: 10.1002/hbm.22627

Zhang, W., Li, R., Deng, H., Wang, L., Lin, W., Ji, S., et al. (2015). Deep convolutional neural networks for multi-modality isointense infant brain image segmentation. *Neuroimage.* 108:214–224. doi: 10.1016/j.neuroimage.2014.12.061

Conflict of Interest Statement: FS was employed by company Shanghai United Imaging Intelligence Co., Ltd., China.

The remaining authors declare that the research was conducted in the absence of any commercial or financial relationships that could be construed as a potential conflict of interest.

Copyright © 2019 Zhu, Shi, Wang, Hung, Chen, Wang, Lin and Shen. This is an open-access article distributed under the terms of the Creative Commons Attribution License (CC BY). The use, distribution or reproduction in other forums is permitted, provided the original author(s) and the copyright owner(s) are credited and that the original publication in this journal is cited, in accordance with accepted academic practice. No use, distribution or reproduction is permitted which does not comply with these terms.

frontiers in Neuroinformatics

REVIEW
published: 07 May 2019
doi: 10.3389/fninf.2019.00032

A Brief History of Simulation Neuroscience

Xue Fan and Henry Markram*

Blue Brain Project, École Polytechnique Fédérale de Lausanne (EPFL), Geneva, Switzerland

Our knowledge of the brain has evolved over millennia in philosophical, experimental and theoretical phases. We suggest that the next phase is simulation neuroscience. The main drivers of simulation neuroscience are big data generated at multiple levels of brain organization and the need to integrate these data to trace the causal chain of interactions within and across all these levels. Simulation neuroscience is currently the only methodology for systematically approaching the multiscale brain. In this review, we attempt to reconstruct the deep historical paths leading to simulation neuroscience, from the first observations of the nerve cell to modern efforts to digitally reconstruct and simulate the brain. Neuroscience began with the identification of the neuron as the fundamental unit of brain structure and function and has evolved towards understanding the role of each cell type in the brain, how brain cells are connected to each other, and how the seemingly infinite networks they form give rise to the vast diversity of brain functions. Neuronal mapping is evolving from subjective descriptions of cell types towards objective classes, subclasses and types. Connectivity mapping is evolving from loose topographic maps between brain regions towards dense anatomical and physiological maps of connections between individual genetically distinct neurons. Functional mapping is evolving from psychological and behavioral stereotypes towards a map of behaviors emerging from structural and functional connectomes. We show how industrialization of neuroscience and the resulting large disconnected datasets are generating demand for integrative neuroscience, how the scale of neuronal and connectivity maps is driving digital atlasing and digital reconstruction to piece together the multiple levels of brain organization, and how the complexity of the interactions between molecules, neurons, microcircuits and brain regions is driving brain simulation to understand the interactions in the multiscale brain.

Keywords: simulation neuroscience, digital reconstruction, brain modeling, neuronal types, connectome, brain structure and function, history

OPEN ACCESS

Edited by:
Qingming Luo,
Hainan University, China

Reviewed by:
Thomas Marston Morse,
Yale University, United States
Richard C. Gerkin,
Arizona State University,
United States

****Correspondence:***
Xue Fan
xue.fan@epfl.ch

Received: *12 February 2019*
Accepted: *12 April 2019*
Published: *07 May 2019*

Citation:
Fan X and Markram H (2019) A Brief History of Simulation Neuroscience. Front. Neuroinform. 13:32. doi: 10.3389/fninf.2019.00032

THE NEXT PHASE OF BRAIN RESEARCH

Over past millennia, brain research evolved through a series of fundamental transformations of human thinking to approach the mind and the brain. At the dawn of human civilization, mainly based on intuitive and analogical thinking, the deeply philosophical phase relied on subjective experience and "pure reason" (Lamb, 1925), without any empirical method for proving suggested ideas. To gain empirical evidence, mainly based on reductionist thinking, brain research evolved into an experimental phase, by means of observation, measurement and experimentation,

which led to the hyper-specialization we see in modern neuroscience. During this phase, huge amounts of disconnected datasets were produced, each limited to a certain level of brain structure and function (Frackowiak and Markram, 2015). To deal with the daunting forests of data, abstraction and simplification methods from physics, mathematics and computer science gave rise to the theoretical phase of neuroscience. This kind of abstractive thinking follows the logic that "if one squeezes out all the complexity from a system, one eventually reaches its essence and then, and then only, does one truly understand the brain." Theoretical neuroscience tries to interpret experimental data and to gain analytical tractability by simplifying experimental observations, generating concepts and building minimal mathematical models (Gerstner et al., 2012). This phase also gave rise to artificial intelligence and its evolution to its current form today.

Experimental and theoretical phases have developed through three main paths: neuronal mapping that tries to classify and catalog different types of cells in the brain; connectivity mapping that aims to map connectivity between individual neurons (neighboring neurons, neurons in neighboring groups, neurons in distant brain regions), between groups of neurons (layers, columns, nuclei, etc.) and between brain regions (visual area, auditory area, etc.); functional mapping that tries to relate brain function and behavior to the structure of the brain (e.g., role of partial connectomes or the whole connectome).

Neuronal mapping is evolving from subjective descriptions towards objective classifications of cell types, from morphological types (Berlin, 1858; Meynert, 1867; Golgi, 1883; Ramón y Cajal, 1909) to genetic types (Monyer and Markram, 2004; Toledo-Rodriguez et al., 2004; Urban and Rossier, 2012; Wagner et al., 2016) and multidimensional types (e.g., according to a combination of morphological, electrical, afferent, efferent, molecular and genetic types; Markram et al., 2004, 2015; Zeng and Sanes, 2017).

Connectivity mapping is evolving from loose topographic maps of major nerve tracts between brain regions (Vicq-d'Azyr, 1786; Gall and Spurzheim, 1810; Meynert, 1871) towards dense anatomical and physiological maps of connections between individual genetically distinct neurons (Oh et al., 2014; Swanson and Lichtman, 2016). The nomenclature of the types of connections formed in the brain evolves at the pace of the development of the nomenclature of cell types and is set on a path towards a nomenclature for a large addressing system indicating each cell type in the brain.

Functional mapping is evolving from psychological and behavioral stereotypes towards a map of behaviors emerging from structural and functional connectomes (Gall and Spurzheim, 1810; Vogt and Vogt, 1903; Brodmann, 1908; Sporns, 2016), from observing and characterizing brain responses to stimulation (Hitzig and Fritsch, 1870; Penfield and Boldrey, 1937) towards understanding the causal relationship between neural connectivity and brain function (Bassett and Sporns, 2017; Reimann et al., 2017a). Today, at the cellular level, neuroscientists are still surprised to find that different neurons respond to different inputs in a different manner and are still composing an endless spectrum of stimulus preference maps for neurons, while we are moving from considering only how the type of neurons is responsible for their different responses towards identifying the contribution of the underlying networks. At the whole-brain level, studies are beginning to reveal how the underlying connectome shapes, for example, functional magnetic resonance imaging (fMRI) image patterns. At the behavioral level, attempts to map signatures of specific cognitive functions to the underlying structures are still limited to networks of brain regions. As the number of brain regions found to be involved in any cognitive task grows, functional mapping will likely evolve from statistical subgraphs of the brain towards dynamic full graphs.

However, in these three paths, experimental and theoretical approaches are hindered by the barriers of scale and complexity. How can we scale up cellular phenotyping and deal with the dynamics of cellular properties to achieve a comprehensive census of cell types in mammalian brains? How can we rise to the challenge of volume, time and dynamics in full connectome mapping potentially even down to the nanoscale? How can we trace all the molecular and cellular mechanisms that give rise to brain function and behavior?

To transcend these barriers, simulation neuroscience was born. It is arguably the next phase of brain research, after its philosophical, experimental and theoretical phases. Simulation neuroscience combines experimental and theoretical approaches to achieve a dense digital reconstruction of the brain consistent with experimental data, which in itself forms a unifying theory of brain structure and function and which can be used to test and evolve new theories (**Figure 1**). The goal of simulation neuroscience is to build a digital copy of the brain instead of an arbitrary model, even if that model could imitate certain brain functions (Markram, 2006; Markram et al., 2015). Since neither a comprehensive repertory of data nor a complete map of the brain exists or will likely be obtained purely from experiments, we obviously cannot do this blindly. It requires building the digital copy by formulating principles of cellular structure to synthesize all the neurons and glial cells, principles of molecular organization and interaction, principles of how ion channels and receptors are formed and distributed in neurons, principles of synaptic connectivity, principles of how brain regions are connected, and ultimately, principles of how the brain is coupled to the body. It is through formulating and exercising these principles that simulation neuroscience makes progress systematic and understanding tractable. If correct, these principles allow predicting vast gaps in data and drive a new question: what is the minimal, not maximal, data we need to reconstruct the brain? Indeed, experimental neuroscience should be asking what can be predicted and what must be measured.

Reconstructing the brain recapitulates the history of neuroscience by evolving and accelerating its major steps, from early morphological descriptions of the nerve cell to later electrophysiological and biochemical studies of neural connectivity: synthesize and evolve available knowledge, methods and technologies into a new science, and take a quantum leap onto a path that, in the end, can lead to understanding the multiscale brain. Industrialization of

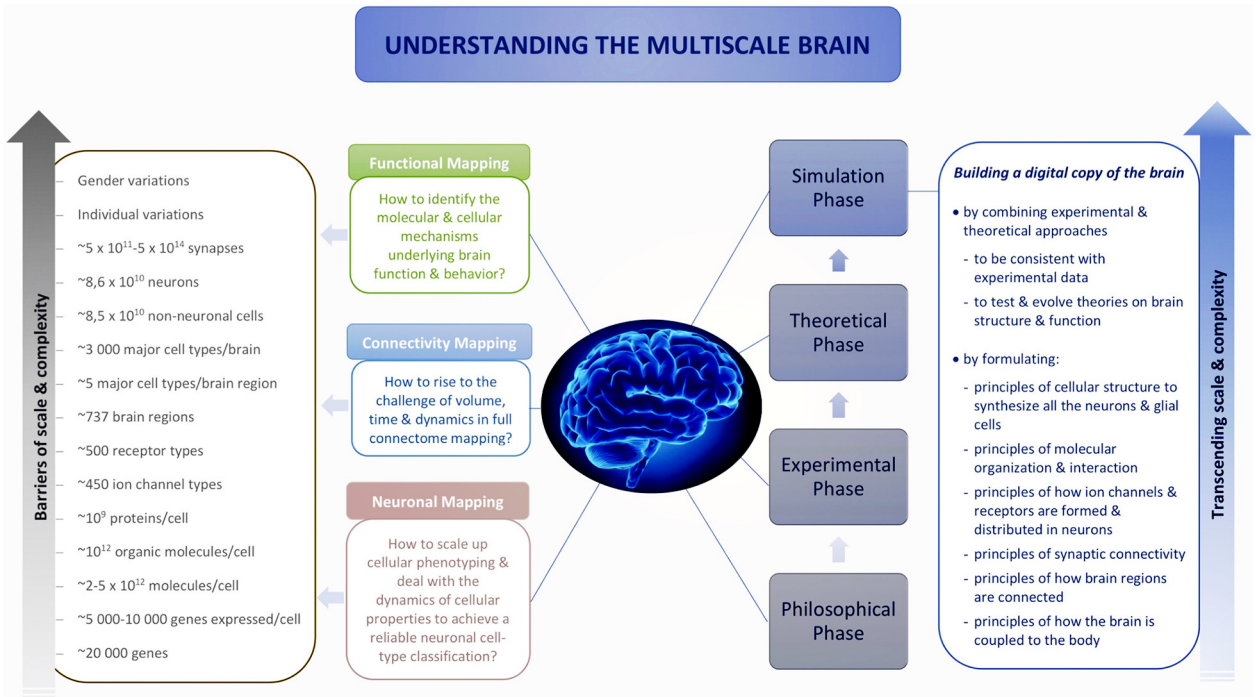


FIGURE 1 | Understanding the multiscale brain.

neuroscience and the resulting large disconnected datasets are generating demand for integrative neuroscience; the scale of neuronal and connectivity maps is driving digital atlasing and reconstruction to piece together the multiple levels of brain organization, and the complexity of the interactions between molecules, neurons, microcircuits and brain regions is driving simulation neuroscience to understand the multiscale brain. To explore the origin and making of this paradigm shift, we reconstruct the deep historical paths leading to simulation neuroscience through the philosophical, experimental and theoretical phases of brain research, in particular, from the first observations of the nerve cell to modern attempts to digitally reconstruct and simulate the brain, by identifying the major scientific, technological and conceptual breakthroughs that have guided this passionate quest of humans to understand the brain and their own condition.

FROM THE WEIGHT OF THE HEART TO BRAIN SIMULATION

Humans see and feel, live and die, conscious of their own existence. They think and desire to understand themselves.

About 3,000 years ago, in ancient Egypt, almost 200,000 years after the birth of *Homo sapiens* and 9,000 years after the Agricultural Revolution (Harari, 2014), the heart was still considered to be the seat of emotions and thoughts, weighed after death by gods against a feather representing truth and order to determine the destiny of the deceased: to go to heaven or to be devoured by a monster ("Book of the Dead," Papyrus of Ani, 1250 BC). The brain, considered trivial, was the first organ to be thrown away during embalming: part of it was drawn out through the nostrils with a crooked piece of iron, and the rest was rinsed with drugs (Herodotus, 1875).

About 2,500 years ago, in Ancient Greece, Alcmaeon of Croton (~460 BC), a great philosopher and pioneer of anatomical dissection, traced the nerves of the sense organs until their terminations in the brain and inferred that the brain was the seat of sensation and thought (Tannery, 1887). Thus were laid the foundations of brain science. One century later, influenced by Alcmaeon of Croton, Plato (~360 BC) located the immortal soul, the *logos* (thinking and reasoning), in the head, since it is in the form of a globe, at the top of the body, close to the heaven, reflecting the perfect image of God and the Universe (Lamb, 1925). The *logos* is a *dæmon* inside each of us, a genius given by God to guide humans to communicate with the divine soul of the Universe. Plato located in the thorax the mortal soul—the *thymos* and the *eros*—our fearful but ineluctable passions and desires. However, in Aristotle's view (~350 BC), the intellectual soul (*nous*), imperishable and self-existing, which bestowed on humans the ability to understand and which distinguished them from plants and animals, did not operate through any specific bodily organ (Hicks, 1907). Relating sensation to the blood, relying on the idea that the brain was bloodless and cold, Aristotle thought that the heart was the seat of sensation, while the brain was just an organ for cooling the heat produced by the heart (Ogle, 1911).

About 500 years ago, what has become known as the "Scientific Revolution" began (Burtt and Edwin, 1923;

Butterfield, 1959). We acknowledged our ignorance (Harari, 2014) and embarked on an exploration of the unknown. Modern science was born. The view of the universe and the nature of human life was transformed through the transition from mainly relying on the internal mind to external observation. To survive and evolve, to increase their capacities and to produce new resources, humans gained knowledge and invented technologies both transmittable to others to accelerate scientific discoveries—therefrom arose the powerful collective scientific process. We explored the world and our own body, including the brain. Brain science accelerated.

About 475 years ago, Vesalius (1543) dissected human corpses, described the anatomy of the brain and first distinguished between gray matter and white matter. About 300 years ago, "fine vessels" were observed within a nerve under a self-made one-lens microscope (van Leeuwenhoek, 1719). More than 100 years later, "large, colorless and free globules" and "granules connected in rows by delicate filaments" were described in leech nervous tissue through an achromatic microscope (Ehrenberg, 1833). About 30 years later, "protoplasmic processes" were identified through carmine staining (Deiters, 1865). In about 150 years, "vessels," "globules" and "protoplasmic processes" were finally connected together in the human mind to form a single cellular unit, the nerve cell, named later the "neuron" (von Waldeyer-Hartz, 1891).

Where are we now? Our quest to understand the brain has advanced in scale and complexity through the experimental and theoretical phases of brain research. We are beginning to understand the structural and functional diversity of neurons, how they are connected, and how a specific network of neurons gives rise to emergent functions.

However, since Alcmaeon of Croton dissected brains and suggested that the brain was the seat of sensation and thought, almost 2,500 years have elapsed (Tannery, 1887). We still do not understand the basic neural mechanisms underlying brain function, which give rise to our emotions, thoughts and memories (Koch et al., 2016; Südhof, 2017). We remain "strangers to ourselves" (address by Shimon Peres when the Human Brain Project was awarded, the European Parliament, March 12, 2013).

Modern philosophers continue to reason about the mind and the brain in diverse forms. Dualists argue for the irreducibility of conscious experience and sensory qualia—surviving forms of Plato's and Descartes' substance dualism. In their view, we will probably never obtain a complete explanation of consciousness based on neural mechanisms—What is it like to be a bat or a zombie (Nagel, 1974; Chalmers, 1996)? Relying on the concept of multiple realizability and the computational theory of mind, functionalists pay little attention to neuroscientific details, presuming that a given mental state can be realized through diverse physical mediums, either a brain or a computer (Fodor, 1975; Putnam, 1965). The rise of neurophilosophy fosters the co-evolutionary research methodology, in particular the co-evolution of philosophy with cognitive and computational neuroscience (Churchland, 1986), with the aim of applying neuroscientific findings to classical philosophical concepts such as morality (Prinz, 2007; Churchland, 2011). On the basis of eliminative materialism, neurophilosophers try to replace the categories of "folk psychology" with neuroscientific ontology (Churchland, 1986). Contrary to dualists, they search for a neurobiological explanation of consciousness, a unified theory of how the mind-brain works (Searle, 1992; Dennett, 1993; Churchland and Churchland, 1997). However, today, this goal still remains vague.

In parallel with these philosophical pursuits, methodologies in neuroscience also evolved by crossing the boundaries between different doctrines and disciplines. Against rationalist Descartes' "*Cogito ergo sum*" (Descartes, 1905), empiricists argued a half-century later for "*tabula rasa*" and thought that instead of *a priori* reasoning, the nature of the world and the mind could only be understood through empirical research with observations and experimental reasoning (Locke, 1689). This view prepared the philosophical ground for the rise of experimental neuroscience. Influenced by modern mathematical logic developed in the late 19th century (Frege, 1879, 1960), early empiricism further evolved into logical empiricism (Carnap, 1928; Neurath, 1932), which led to the idea of the mind as a logic machine and the computational theory of mind (McCulloch and Pitts, 1943; Putnam, 1965; Fodor, 1975). This gave rise to another phase in brain research—theoretical neuroscience.

Reduction is the major form of reasoning in both experimental and theoretical neuroscience, although it varies from intertheoretic reduction to "reductionism-in-practice" (Hooker, 1981a,b,c; Bickle, 2003). This kind of reasoning has been challenged by several theories of neuroscientific explanations. Causal-mechanistic reasoning aims to capture the unity of neuroscience by producing a mosaic of explanations at different levels, instead of reductive, unifying or model-based forms of scientific explanations (Craver, 2009). However, to the philosophers of neuroscience in search for a unified theory of brain function and behavior, understanding the brain will require both neurobiology and large-scale theoretical frameworks. In this view, a major methodological theme consists in the co-evolution of macrotheory and microtheory, an interanimation of philosophy, psychology, computer science and neuroscience, of top-down and bottom-up research (Churchland, 1986). This endeavor aims to combine multiple disciplines, in particular philosophy and neuroscience, into a unified science, to obtain a unified theory of the mind-brain. However, since the birth of neurophilosophy, more than 30 years have passed, this goal still remains remote. Why cannot we understand the mind-brain?

Brain research over past millennia is like solving a strange jigsaw puzzle that is devoid of a predetermined picture—various pieces have been accumulated semi-randomly in the hope that all the data and knowledge will self-organize. The mind does not have a shape, but the brain does. Instead of imposing arbitrary forms on the mind, can we reconstruct a brain from its basic molecular and cellular units, find out the principles that connect them together and test our theories in a systematic manner? This quest gave rise to simulation neuroscience. What is the philosophy of this new science?

For thousands of years, seeking truth, philosophers have been addressing fundamental questions about the mind and ourselves,

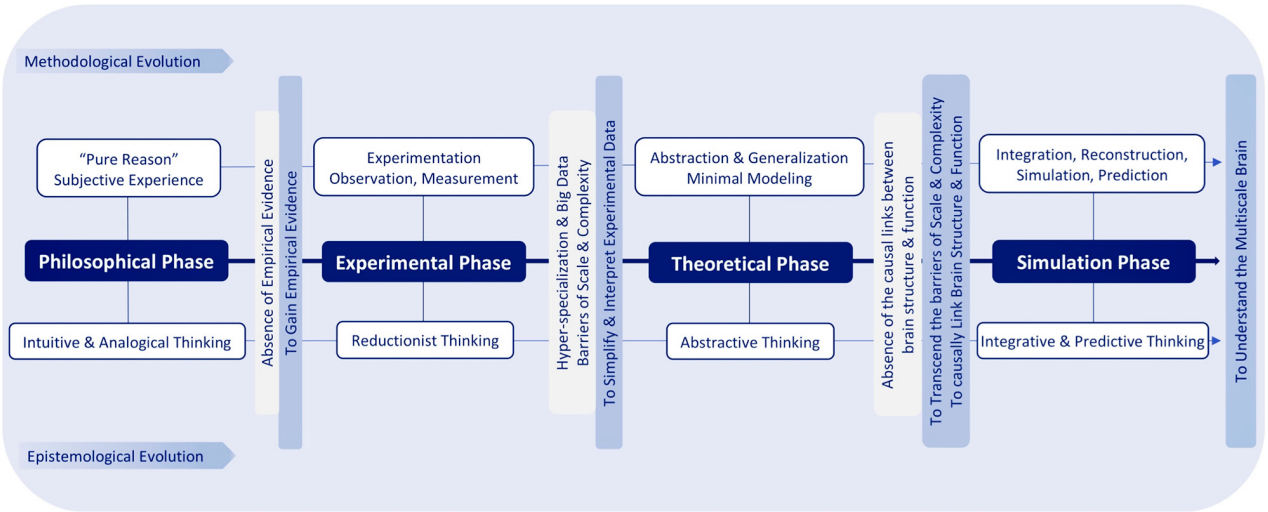


FIGURE 2 | Epistemological and methodological evolution of brain research.

yet without producing empirical evidence; their reasoning wanders in the silence of the desert. For hundreds of years, seeking completeness, experimental neuroscientists have been trying to understand every single part of the brain by breaking it into its basic components and have built forests of datasets, but how much more elements are there still to map, are we lost? For nearly a century, seeking a single unified theory, theoretical neuroscientists have been trying to walk out of these forests by cutting down trees; the complexity indeed decreases but also the structural and functional richness of the ecosystem. Finally, have not the models simply become data fitting functions? If several models can fit the data, does it mean that they all explain brain function? To transcend the barriers to these endeavors, can we get an overview of all the forests of datasets, reorganize and integrate them in the context of the whole brain, while filling the gaps that experiments will never be able to fill and finding ways through the forests by considering the ecosystem of the brain? The deep meaning of simulation neuroscience consists in reconstructing and simulating the brain from the most fundamental principles we can isolate to understand and link the multiple layers that form ourselves, from molecules and cells to brain function and behavior, to give meaning and life to data and theories.

Due to reductionist thinking, experimental neuroscience is hindered by huge amounts of disconnected datasets and seemingly infinite scale and complexity. Based on abstractive thinking, theoretical neuroscience tries to address these problems through simplification but abstracts away detailed brain structures and their emergent functional properties. To reconcile and transcend these two extremes, by leveraging high performance computing, simulation neuroscience approaches the brain through integrative and predictive thinking: integration of experimental and theoretical approaches, integration of disconnected datasets and knowledge and integration of the multiple scales of brain structure and function, in association with predictive methods for filling the gaps (**Figure 2**).

The brain is a multidimensional network of networks of genes, proteins, cells, synapses and brain regions, all interacting inside a dynamically changing environment of neurochemicals. Brain functions emerge as electrical, chemical and mechanical chain interactions through these networks. Since there is no scientific evidence that we can ignore any kind of these interactions, the only way to understand all aspects of the multiscale brain is to reconstruct and simulate all these types of interactions.

The philosophy of simulation neuroscience originates from the will to transcend the barriers of scale and complexity during the evolution of neuronal mapping, connectivity mapping and functional mapping in the experimental and theoretical phases of brain research. The present review will trace the historical evolution of this pursuit by identifying the major milestones that are the most related to it and that are capable of characterizing it in a concise way, instead of conducting an exhaustive survey of all the investigators whose important work has contributed to the evolution of brain research.

NEURONAL MAPPING: FROM THE BIRTH OF THE NEURON TOWARDS A COMPREHENSIVE CENSUS OF BRAIN CELL TYPES

Neurons and glial cells constitute the two major cellular populations in the human brain (∼86 billion neurons vs. ∼85 billion non-neuronal cells; von Bartheld et al., 2016). Although they were probably first described at the same time (Dutrochet, 1824), neurons have been more studied because their electrical excitability correlates well with higher brain functions and are therefore considered essential to brain function and behavior (Galvani, 1791; du Bois-Reymond, 1843). Neurons are

divided into diverse types characterized by their morphological, physiological or molecular properties. Just in the retina, the number of neuronal types is estimated to be 100–150, and 2,500–5,000 in the adult mammalian nervous system (Bota et al., 2003; Zeng and Sanes, 2017). Although efforts are underway to try to achieve a comprehensive census of neuronal cell types over the next decade (Zeng and Sanes, 2017), neuronal cell-type classification is controversial and extremely challenging for the future of neuroscience. Even so, then we will still need to ask: "What does each cell type do?"

To better visualize the trajectory of neuronal mapping in the future, we need to understand its origin. What is the history of the neuron, from its first descriptions to modern neuronal classification? First of all, how did humans discover the neuron?

In fact, humans did not discover the neuron; they reconstructed it.

All Began With a Nerve

About 300 years ago, "fine vessels" were observed within a nerve under a self-made one-lens microscope (van Leeuwenhoek, 1719), clearly identified as axons only more than 60 years later (Fontana, 1781). After about 50 years, "large, colorless and free globules" and "granules connected in rows by delicate filaments" were described in leech nervous tissue through an achromatic microscope, considered yet to be the "excreted nuclei" of red blood cells (Ehrenberg, 1833). Three years later, appeared the first microscopic image of the nerve cell body with the nucleus and nucleolus, but the "primitive fiber" (axon) and the "globule" (soma) were still considered to be separated elements (Valentin, 1836). Nevertheless, in the same year, the anatomical continuity between the nerve fiber and the nerve cell body was observed (Remak, 1836). However, "protoplasmic processes" (dendrites) were only described more than 80 years after the identification of the axon, owing to chromic acid fixation and carmine staining (Deiters, 1865). Only then did humans succeed to reconstruct together the "vessel," "globule" and "protoplasmic processes" into a single nerve cell, which took almost 150 years.

However, at that time, the soma and fiber of the nerve cell were still considered functionally separated. The nerve cell body, often taken for a trophic center, was thought unnecessary to nerve conduction because most anatomists believed that the nerve fiber ran straight through the cell body (Bernard, 1858; Lorente de Nó, 1935). Therefore, electrophysiology was only based on the study of nerves. Nevertheless, recordings of spinal cord antidromic evoked potentials showed that the polarization of conduction in the spinal cord was not a property of nerve fibers, but rather localized in the soma (Sherrington, 1897). However, it was not until the development of intracellular recording (Hodgkin and Huxley, 1939; Ling and Gerard, 1949), making it possible to characterize local potentials in different parts of a neuron, that the soma and fiber of the neuron were functionally reconstructed together by humans, almost 90 years after the morphological reconstruction of the nerve cell (Eccles, 1952).

Even so, at this stage, humans still did not succeed to completely reconstruct the neuron, hindered by the fierce controversy over the mode of connection between nerve cells. On the one hand, nerve cell anastomotic networks connected by axons and/or by dendrites were observed through ammoniated carmine and gold chloride staining or Camillo Golgi's "black reaction" (silver nitrate impregnation after fixation with potassium dichromate and osmic acid), which established the reticular theory (von Gerlach, 1872; Golgi, 1875). On the other hand, ontogenetic method and retrograde degeneration method revealed that each nerve fiber originated from a single cell and that the degeneration of the fibers and somas of nerve cells was limited to the units directly affected (Forel, 1887; His, 1887). These observations were later supported by direct histological evidence obtained with improved Golgi's method, which showed the individuality of each nerve cell and founded the neuron doctrine (Ramón y Cajal, 1888; von Waldeyer-Hartz, 1891).

And yet, neuroscientists at that time were still confronted with another question: how do nerve cells communicate between them? Camillo Golgi thought that the communication between nerve cells and the unified functioning of the nervous system could only be achieved through a continuous network, while Santiago Ramón y Cajal suggested that neural transmission could occur through a kind of "granular cement" or a "particular conductive substance" connecting the surfaces of nerve cells in contact. Ramón y Cajal's idea announced the concept of the synapse (Foster and Sherrington, 1897), demonstrated later through Loewi's famous experiment during which a substance collected from a stimulated heart stimulated another heart in the same way as the action of a nerve (Loewi, 1921).

However, it was not until the mid-20th century that the individuality of each nerve cell and the existence of the synaptic cleft were finally confirmed, owing to electron microscopy (EM) observations (Palade and Palay, 1954; De Robertis and Bennett, 1955). Since the first observation of nerve fibers (van Leeuwenhoek, 1719), the human reconstruction of the neuron as an independent cellular unit had taken almost 240 years. How much time would take the classification of different types of neurons?

A Way Through the "Butterflies of the Soul"

What is the path through the labyrinth of billions of the "butterflies of the soul" (Ramón y Cajal, 1917)? Early researchers first noticed different shapes of nerve cells and named them either by their morphological features or after their discoverers. With the development of histological techniques in the mid-19th century, nerve cells were first classified into pyramidal cells, small and irregular or granular cells and spindle-shaped cells, which founded cytoarchitectonics (Berlin, 1858). Then this morphological classification was further elaborated in association with cortical layers and cell function (Meynert, 1867). About 16 years later, using the "black reaction," Golgi distinguished two basic types of nerve cells in the cerebral cortex and suggested their functions: Type I cell with a long axon giving off a small number of lateral filaments was motor cell; Type II cell with a short axon divided into many complex lateral branches was sensory cell (Golgi, 1883). However, this functional definition of the two cell types was later refuted by

Ramón y Cajal (1894), who observed that Type I cells were abundant in sensory organs and Type II cells were distributed in all nerve centers. This revealed the complex relationship between nerve cell morphology and function. Ramón y Cajal (1909) also attempted to classify neurons by their shapes. However, were these morphological descriptions a reliable way to classify neurons?

Confronted with the subjectivity of these morphological classifications determined by single investigators, some researchers tried to establish objective criteria to classify nerve cells by their electrophysiological or biochemical features. Nissl (1894), using basic aniline dyes, classified nerve cells according to which parts of the cell content were stained and which parts were not and the relationships between the stained and unstained parts. Neurons were also classified by the velocity of their action potentials measured with the cathode ray oscilloscope (Gasser and Erlanger, 1922). Due to a better understanding of the chemical transmission of nerve impulses, neurons were divided into two types: cholinergic and adrenergic cells (Dale, 1933).

However, electrophysiological and biochemical states are limited by their sensitive condition-dependence. Faced with this problem, researchers attempted to characterize neurons with more stable features. With the development of immunohistochemistry in the 1940s and that of RNA and DNA sequencing in the 1970s (Coons et al., 1941; Min Jou et al., 1972; Wu, 1972), molecular classification methods were introduced to classify neurons according to their molecular properties, in particular protein composition and mRNA composition, with the assumption that some molecular features stay permanent to maintain cell identity (Fishell and Heintz, 2013; Deneris and Hobert, 2014). Single-cell transcriptomics, developed in the early 1990s, is considered to have the potential to provide a "complete" census of neuronal types (Toledo-Rodriguez et al., 2004; Poulin et al., 2016; Zeng and Sanes, 2017). High-throughput, multiplexed methods, such as multiplexed fluorescence *in situ* hybridization (FISH) and *in situ* sequencing methods, are being developed to scale up the enterprise of neuronal cell-type classification (Ke et al., 2013; Lee et al., 2014; Chen et al., 2015, 2016).

In 160 years, neuronal classification has evolved from subjective, morphological description to objective, multi-criteria identification; from monothetic approach to polythetic clustering (Berlin, 1858; Ramón y Cajal, 1909; Markram et al., 2004; Migliore and Shepherd, 2005; Armañanzas and Ascoli, 2015). However, a comprehensive census of neuronal cell types is still out of reach. What are the major challenges?

Towards a Comprehensive Census of Brain Cell Types

Neuroscience aims to achieve a comprehensive census of neurons and glial cells in the brain, with molecular annotation at subcellular resolution, such as mRNA expression, ion channels and synaptic proteins. However, there are ∼86 billion neurons in the human brain, and every neuron appears unique; single-cell transcriptome analysis represents only a snapshot due to cyclic and stochastic fluctuations in RNA content (Raj and van Oudenaarden, 2008; Shapiro et al., 2013); gene expression and phenotypic properties of cells can dynamically change in response to internal and external cues (Cohen and Greenberg, 2008; West and Greenberg, 2011). Due to these factors, all neuronal classifications are provisional and hypothetical.

Faced with these challenges, how can we build a way through billions of the "butterflies of the soul"? It is true that there are ∼86 billion neurons in the human brain, but it is possible to define a minimum sample size able to reliably reveal distinct types. It is true that every neuron appears unique, but we have to reduce dimensionality by defining a relevant level of granularity to identify neuronal types. It is true that gene expression in cells is dynamic, but we have to find out their molecular ground states that maintain cell identity. So, the question is: how can we overcome the barriers of scale and complexity to achieve a reliable neuronal cell-type classification?

CONNECTIVITY MAPPING: FROM WHITE MATTER TRACTS TOWARDS A FULL CONNECTOME

Leaves of a Cabbage

Arising from a stem, dispersed into leaves spreading out in a circular shape to form cavities, in the eyes of a 17th-century anatomist, the extending nerve tracts in the brain formed loose nets and ventricles like the leaves of a cabbage (Malpighi and Fracassati, 1669). Since Ancient Greece, nerve tracts had been considered related to brain function (Tannery, 1887). A question then arose: how to trace these tracts?

About 330 years ago, white matter was observed to be composed of fibrils arranged in bundles through the scraping method of dissection (Vieussens, 1684). A century later, nerve tracts were divided into inter- and intra-hemispherical pathways (callosal and association systems; Vicq-d'Azyr, 1786). The first category connected the two hemispheres, including the corpus callosum, the corpora quadrigemina, the anterior and posterior commissures, the cerebral peduncles, the pons, the anterior medullary velum, the interthalamic adhesion and the trigeminal tubercle. The second category was supposed to assure the communication between the base and other parts of the brain, including the arcuate fasciculus, the pillars of the fornix, the peduncles of the pineal gland, the tracts connecting the mammillary tubercles and the anterior thalamic tubercles. More than 20 years later, the projection system was identified through blunt dissection, including afferent and efferent fiber pathways linking the cortex with the subcortical regions, the brain stem and the spinal cord (Gall and Spurzheim, 1810).

However, dissection techniques could not determine the precise trajectory and arrangement of nerve tracts. Detailed tract tracing only became possible with the development of histological methods. Using a Zeiss-microscope and carmine or gold chloride staining, Theodor Meynert identified clearly the three main types of white matter tracts: the association systems—the short arcuate fibers and long association fibers connecting the various parts of the cerebral cortex; the

commissural pathways connecting the two hemispheres; the afferent and efferent projection systems linking the cortex to the subcortical structures (Meynert, 1871).

Early tracing studies, relying on physical diffusion of dyes in fixed material, were limited to large fiber tracts between brain regions. The studies of neurocircuitry required more refined methods applicable to living tissue. Degeneration methods inferred neuronal connectivity from pathological changes following experimental lesions to the nervous system (Türck, 1849; Waller, 1850; von Gudden, 1870; von Monakow, 1897). However, lesions were usually nonspecific, degeneration altered the normal morphology of neurons, and pathological changes were extremely variable (Cowan et al., 1972).

To remedy this, tracing methods exploiting axonal transport in living neurons were developed in the 1970s. Retrograde tracing techniques introduced an enzyme or fluorescent tracer in a downstream location relative to the targeted neurons, capable of labeling the somas of the neurons projecting to the injection site, but unable to visualize the fiber pathways linking them (Kristensson, 1970; Kristensson and Olsson, 1971; LaVail and LaVail, 1972). This problem was resolved by anterograde tracing techniques, based on macromolecule transport from the soma to the axon terminals, such as autoradiographic tracing method (Cowan et al., 1972).

Nevertheless, injections of tracers usually resulted in indiscriminate labeling of different types of neurons, and the surgical procedure to introduce an exogenous tracer was complex. To deal with this, tracing techniques exploiting genetic engineering were developed more than 20 years ago (Prasher et al., 1992; Chalfie et al., 1994), which use intrinsic fluorescence to label exclusively the projections of neurons that express a specific molecular phenotype (Feng et al., 2000; Livet et al., 2007; Kuhlman and Huang, 2008). These techniques were even adapted for live imaging of intact animals such as *Drosophila* (Boulina et al., 2013). The leaves of a cabbage have become a forest of rainbow trees.

However, these tracing methods are limited to anatomical connectivity, which alone is not sufficient to account for brain function, because the synapse is dynamic (Tsodyks and Markram, 1997). Therefore, physiological methods were invented. Owing to intracellular recording techniques, synaptic plasticity was better understood, such as the quantal release of neurotransmitters (Fatt and Katz, 1952), central synaptic inhibition (Coombs et al., 1953), short-term synaptic plasticity (Curtis and Eccles, 1960) and spike-timing-dependent plasticity (STDP; Markram and Sakmann, 1995). Neural plasticity also inspired theoretical studies, such as Hebbian cell assembly and learning rule (Hebb, 1949) and the theoretical study of STDP (Abbott and Blum, 1996; Gerstner et al., 1996). Theoretical approach abstracts away detailed biological mechanisms to loosely model neural connectivity by building artificial neural networks. About 75 years ago, the first mathematical model of a simplified neural network appeared (McCulloch and Pitts, 1943), which led to the computational theory of mind and machine learning. This model then evolved into more sophisticated ones, in particular, multilayer perceptrons (Rosenblatt, 1957), recurrent neural networks (Hopfield, 1982) and convolutional neural networks (Cireşan et al., 2011). However, to get deep insights into the detailed neural structures and mechanisms underlying brain function, we still need biologically realistic models.

Although the aforementioned experimental methods are able to trace neuronal connections on the cellular or even molecular scale, these invasive techniques are limited to postmortem brain tissue and experimental animals. To better understand our own brain, would it be possible to trace the neural connections in the living human brain? In the early 1970s, the development of noninvasive neuroimaging techniques, in particular MRI, made it possible to study the structural and functional connectivity of the human brain *in vivo* (Damadian, 1971; Lauterbur, 1973). Nowadays, human brain atlasing combines MRI with gene expression studies, such as the Allen Human Brain Atlas that comprises a comprehensive "all genes–all structures" array-based dataset (Shen et al., 2012). Nevertheless, generally, MRI methods can only trace neural connections between brain regions usually with millimeter resolution.

Over the past 300 years, connectivity mapping has evolved from gross tracing of major tracts in fixed brains to mapping neuronal projections with cellular and molecular resolution in living tissue, from mapping static neural connectivity to dynamic synaptic plasticity, from postmortem studies to *in vivo* large-scale mapping of human brain connectivity including structure, function and gene expression. Is it possible to experimentally map all the neural connections of the brain—the "connectome"?

Towards Completeness

Science dreams of completeness. Since the emergence of the term "genome" in 1920 (Winkler, 1920), fostered by technological advances in large-scale, high-throughput research, the "ome" has become a doctrine, aiming to capture all the parts of biological systems and their interactions (Sporns, 2013b). Inspired by the "genome," the term "connectome" was introduced in 2005, initially referring to a comprehensive structural description of the network of brain elements and connections (Sporns et al., 2005) or the set of all neuronal connections of the brain (Hagmann, 2005). "Connectomics" aims to map the connectome on the macro-, meso-, micro- and nano-scales and to explain its relation to brain functions (Hagmann, 2005; Sporns, 2013a; Swanson and Lichtman, 2016).

The concept of the connectome originated from the long-held belief that neural connections are related to brain functions, as illustrated by tract tracing since the 17th century. This relationship has been further revealed by recent research: at the microscale, synaptic connectivity is linked to neuronal network dynamics (Chambers and MacLean, 2016); at the macroscale, the anatomical connectivity of the brain is related to its functional connectivity and different states (Hermundstad et al., 2014), and the "connectivity fingerprint" of brain regions may predict their specific functional properties (Saygin et al., 2016; Tavor et al., 2016).

Since the function of neural circuits and systems cannot be explained only through wiring diagrams, we also need information such as the types of neurons and synapses,

the dynamics of neuronal synchronization, and the role of different types of glial cells and neuromodulators (Sporns, 2013b; Fields et al., 2015). Therefore, the concept of the "connectome" is evolving to include all the structural and functional relationships between different types of neurons, as well as all their connections with their cellular partners in a defined neural region or the whole brain (Marc et al., 2013; Sporns, 2016; Swanson and Lichtman, 2016). Nevertheless, this concept owes its origins to MRI methods, which enable *in vivo* rapid-throughput mapping of human brain connectivity at the macroscale.

Mapping Long-Range Neural Connections Between Gray Matter Regions

Macroconnectomics aims to map all the neural connections between gray matter regions at millimeter resolution. It is best suited to *in vivo* human studies with neuroimaging methods, where few of fine-scale methods used in laboratory animals are applicable (Sporns, 2013b; Van Essen, 2013). MRI, the major noninvasive neuroimaging technique for *in vivo* human connectome mapping, was developed in the early 1970s, first used to diagnose cancer (Damadian, 1971; Weisman et al., 1972; Lauterbur, 1973). Described as "*in vivo* Brodmann mapping" (Brodmann, 1908; Turner and Geyer, 2014), MRI cerebral cartography has inherited the long tradition of connectivity mapping, established since the 18th century (Vicq-d'Azyr, 1786).

Diffusion MRI (dMRI) is the main MRI method of mapping structural connections of the brain (Glasser and Van Essen, 2011; Craddock et al., 2013). Invented in the 1980s, dMRI uses water diffusion anisotropy along myelinated axons to map large white matter fiber bundles, combined with probabilistic tractography to estimate fiber trajectories (Le Bihan and Breton, 1985; Margulies et al., 2013; Le Bihan and Iima, 2015). About 30 years ago, the first dMRI images of the human brain were obtained at 0.5T, with an in-plane spatial resolution of 1.09 × 1.09 mm (Le Bihan et al., 1986). Since then, the sensitivity to diffusion has augmented about 100 times (McNab et al., 2013). To improve spatial resolution of white matter fiber tracking, ultrahigh field magnetic resonance engineering is a basic solution. MRI for clinical use is usually at 1.5T or 3T, and more recently at 7T. The first human 8T MRI was installed in 1999 (Robitaille et al., 1999), and 18 years later, a human whole-body 11.7T MRI (Quettier et al., 2017). Efforts are underway for human 14–20T MRI (Ekosi 20 Tesla Project, 2018). Human brain *in vivo* imaging was already performed at 9.4T (Vaughan et al., 2006); rodent brain and human postmortem tissue imaging at 21.1T (Qian et al., 2012). The final resolution also depends on the acquisition and reconstruction of diffusion images. For example, reconstructing nerve fiber orientations, especially in brain regions where fibers of multiple orientations intersect, involves a trade-off between the accuracy of the peak orientation and the sensitivity to crossing fibers and minor fiber bundles (Van Essen et al., 2012; Lowe et al., 2016). Hitherto, the highest resolution for the human brain achieved at 7T is 0.2 mm, owing to motion correction methods (Stucht et al., 2015). However, even this rare performance is not sufficient to study the connections between individual neurons.

Functional MRI (fMRI) is the main MRI method for studying functional connections in the human brain. Developed in the early 1990s, fMRI first used contrast agents administrated intravenously (Belliveau et al., 1991), then exploited correlations in blood oxygen level dependent (BOLD) signals, based on different magnetic susceptibilities of oxygenated and deoxygenated hemoglobin to detect functional correlations between brain regions (Ogawa et al., 1990, 1992; Bandettini et al., 1992; Kwong et al., 1992). Functional MRI includes two main methods: resting-state fMRI (rsfMRI), measuring correlations in spontaneous activity between brain regions in resting subjects, and task-evoked fMRI (tfMRI), trying to detect functionally distinct brain regions during various tasks such as visuomotor or cognitive processes (Glasser et al., 2016). Almost 30 years ago, human fMRI studies were mostly performed at 1.5T with a spatial resolution of 3–4 mm (Bandettini et al., 1992; Kwong et al., 1992). Since then, the spatial resolution of fMRI has been largely improved, such as the achievement of 0.65-mm resolution in the human brain at 7T (Heidemann et al., 2012), but this is still not sufficient to study how individual neurons are connected to generate brain functions. Furthermore, the temporal resolution of fMRI is fundamentally limited by the nature of BOLD signals, which only indirectly reflect neuronal activity. Due to the temporal dynamics of neurovascular coupling, the peak of BOLD response to a neural stimulus occurs with 5–6 s delay (Glover, 2011). Finally, as a result of artifacts and noises, neurobiologically relevant signals represent only ∼4% of primary data (Glasser et al., 2013).

Although MRI is a useful tool for studying human brain connectivity *in vivo*, it offers little data on the connectivity between neurocircuits and between individual neurons that is essential for understanding the mechanisms underlying brain function. Hence the need for meso-, micro- and nano-connectomics.

Mapping Connections Between Neuronal Groups and Between Individual Neurons

Meso- and micro-connectomics aim to map all the connections between different neuronal groups defined by cell types or connectivity patterns and between individual neurons at the micrometer scale. Such studies, using invasive techniques, are limited to experimental animals and postmortem human brain tissue. The first mesoconnectome, capturing cell type-specific connections as well as short- and long-range interregional axonal projections, was achieved in the mouse in 2014, through enhanced green fluorescent protein (EGFP)-expressing adeno-associated viral vectors and high-throughput serial two-photon tomography (Oh et al., 2014).

Single-cell staining is the first and most influential method for studying neural circuits at microscale, established by Golgi and Ramón y Cajal in the late 19th century (Golgi, 1875; Ramón y Cajal, 1888). However, dyes could only be applied to small blocks of tissue, making this method unsuitable for tracing long-distance connections. To resolve this problem, chemical markers were injected into circumscribed neural areas, which, however, could not label selectively different types of neurons (Kristensson, 1970; Kristensson and Olsson, 1971;

Cowan et al., 1972; LaVail and LaVail, 1972). This was later remedied by transgenic multicolor labeling strategies such as "Brainbow" (Livet et al., 2007). More recently, non-optical, high-throughput methods were invented, such as Barcoding of Individual Neuronal Connections (BOINC), which barcodes individual neurons and introduces transsynaptic viruses to map synaptic connections, based on high-throughput DNA sequencing (Zador et al., 2012). Nevertheless, due to several factors, connectivity reconstructed by this method is difficult to interpret as neuronal connectivity with single-synapse precision (Oyibo et al., 2018).

Light microscopy was, at the origin of the history of neuroscience, the major tool for elucidating the problem of intra-/inter-neuronal and interregional connectivity in the brain. However, conventional light microscopes cannot resolve neural structures smaller than ∼0.25 μm, due to the diffraction barrier identified almost 150 years ago (Abbe, 1873). This barrier was finally broken by super-resolution microscopy developed in the late 20th century, which can routinely resolve a few tens of nanometers, such as stimulated emission-depletion (STED) microscope (Hell and Wichmann, 1994), structured illumination microscopy (SIM; Gustafsson, 2000) and photoactivated localization microscopy (PALM; Betzig et al., 2006). Yet, even so, major challenges still lie ahead, in particular, mapping connections in small neural areas where many cells are targeted at the same time and where the connection density is high (Lichtman et al., 2008). This may require a resolution of a few nanometers (Huang et al., 2010). How to map neuronal connections at this scale?

Mapping Neural Connections at Individual Synapses and Gap Junctions

Nanoconnectomics uses EM, the only method capable of identifying unequivocally synapses and gap junctions at nanometer or even sub-nanometer resolution. EM provides high-resolution validation of macro-, meso- and micro-connectomes.

The first electron microscope, a transmission electron microscope (TEM), was built in 1931, only capable of 14.4× magnification (Ruska, 1993). However, 2 years later, the resolving power of the TEM (12,000×) surpassed already the resolution limit of light microscopy at that time (Ruska, 1993). Another major type of EM is scanning electron microscopy (SEM), introduced in 1937 (von Ardenne, 1937), capable of sub-nanometer resolution (Masters et al., 2015). TEM remains to date the highest resolution technology able to validate specific gap junctions and small synapses requiring, for example, 0.3 nm resolution (Marc et al., 2013). Recently, using the aberration correction technique, scanning TEM (STEM) has even achieved a sub-ångström resolution of 45 pm (Sawada et al., 2015).

However, EM methods are extremely time-consuming and labor-intensive, so currently limited to very small postmortem specimens. The first and the only almost complete nanoconnectome, that of *Caenorhabditis elegans* hermaphrodite, whose nervous system has in total 302 neurons, was achieved in 1986 with serial-section TEM, containing about 5,000 chemical synapses, 2,000 neuromuscular junctions and 600 gap junctions (White et al., 1986). Today, studies continue to fill the gaps in this original connectome and to address further questions such as the nature of individuality and how genetic and environmental factors regulate connectivity (Mulcahy et al., 2018).

The goal of connectomics is to experimentally map a full connectome of the mammalian brain, and ultimately the human brain. Is this achievable?

Metaphor and Myth

What About Biological Reality?

Although MRI methods are capable of large-scale, rapid-throughput mapping of human brain connectivity at macroscale, MRI-derived macroconnectomes result from data reduction, simplification and assumptions, and they do not necessarily reflect the actual structure and function of the brain. They are even described as "metaphors" or "caricatures" (Catani et al., 2013; Margulies et al., 2013).

MRI methods suffer from low spatial resolution. The isotropic voxel size often used is 2 mm (dMRI) or 3 mm (rsfMRI) at 3T and 1–2 mm at 7T. However, the human cerebral cortex contains on average 40,000 neurons and 3×10^8 synapses/mm, and the white matter contains ∼300,000 axons/mm^2 (Van Essen et al., 2012).

The fundamental concept of dMRI consists in using water molecules to probe neural tissue structure (Le Bihan and Johansen-Berg, 2012). However, the basic mechanism underlying water diffusion in neural tissue, especially the role of cell membranes in modulating water diffusion, remains to be clarified, hence the fundamental limitation of the sensitivity of dMRI resides in the complexity of water diffusion in the microenvironment of the brain (Van Essen et al., 2014; Le Bihan and Iima, 2015). MRI tractography is indirect and probabilistic: it reconstructs neuronal connections by estimating the "most likely" fiber orientations at every voxel, which may contain tens of thousands of diverging axons; it produces more invalid than valid bundles (Margulies et al., 2013; Maier-Hein et al., 2017). MRI tractography is also biased towards some brain regions, such as the famous "gyral bias," induced by current fiber tracking algorithms which tend to track towards gyral crowns rather than the walls of sulci or the sulcal fundi (Van Essen et al., 2014; Schilling et al., 2018). The signal-to-noise ratio (SNR) in subcortical regions is usually weaker than in cortical regions, mainly due to their buried location relative to the head coil (Uğurbil et al., 2013). Data processing introduces artifacts and distortions that are difficult to distinguish from actual neural connections (Jones et al., 2013).

The sensitivity of fMRI is affected by the fundamental problem of neurovascular coupling. BOLD signals reflect a complex combination of vascular system dynamics as well as the activity of neurons, astrocytes (Iadecola and Nedergaard, 2007), interneurons (Cauli et al., 2004), pericytes (Hall et al., 2014), vascular endothelium (Hillman, 2014) and smooth muscle cells (Cipolla, 2009). However, the way all these elements contribute to fMRI signals still remains to be clarified. Furthermore, fMRI detects only functional correlations between brain regions, and most functional connections show significant

temporal fluctuations depending on measurement and analysis methods—they do not necessarily reflect the causal relationships between neural connections (Friston, 2011). This means that the interpretation of results is often doubtful.

From this point of view, current macroconnectome maps do not offer an actual image of the brain. Reproducibility is also a major concern for MRI studies (Zuo et al., 2014).

Volume, Time and Dynamics

The major challenge for micro- and nano-connectomics is the huge number of neurons in the human brain: ∼86 billion (Herculano-Houzel, 2012). With current techniques, it would take ∼10 million years to map all the synapses in a single human brain (Morgan and Lichtman, 2013). Moreover, the reconstruction of a complete nanoconnectome would only be possible in some invertebrates or simple nervous systems, because the magnification required to visualize synapses produces very small images of tens of μm^2 (DeFelipe, 2015).

The storage and processing of gigantic volumes of data are problematic (Schreiner et al., 2017). The first fairly complete reconstruction of the *C. elegans* nanoconnectome required ∼10,000 EM images (White et al., 1986). Recent local circuit mapping by EM has high data output rates of gigabytes per minute (Helmstaedter and Mitra, 2012). At synaptic resolution, a human brain may require ∼2 million petabytes (Swanson and Lichtman, 2016). And this is just for the anatomical data, but what if we include the electrophysiological, biophysical and biochemical counterparts?

Although section preparation automation techniques such as SBF (serial block-face) SEM (Denk and Horstmann, 2004) and ATUM (automated tape ultramicrotomy) SEM (Schalek et al., 2011) were invented and data acquisition has been accelerated through parallel image processing (Eberle et al., 2015), the automation of large-scale image segmentation and reconstruction remains the fundamental bottleneck for EM. Methods such as machine learning and crowdsourcing are gradually reducing the problem (Kim et al., 2014; Greene et al., 2016; Staffler et al., 2017), but no existing computational segmentation algorithm is accurate enough to completely replace human annotators. A recent reconstruction of the nanoconnectome of 950 neurons in the mouse retina took ∼30,000 h (Helmstaedter et al., 2013). At current speeds, the complete reconstruction of the nanoconnectome of the human brain may require ∼14G person-years (Plaza et al., 2014).

Therefore, it seems impossible that we will ever resolve the full micro- or nano-connectome of any mammal by only relying on experimental methods (Schröter et al., 2017), which in the opinion of many researchers, is nothing more than a myth (Catani et al., 2013). Moreover, the very concept of "full" connectome mapping is problematic: (1) due to connectivity deduction from primary experimental data, individual variability and the parallel application of multiple imaging, reconstruction and analysis methods, any unified map would be based on probabilistic representations of connectivity data (Sporns, 2013b); (2) all the molecular and cellular components of the nervous system are constantly resynthesized or replaced; development involves changes in myelination and the number of neurons; synaptic connections are subject to continuous rewiring and changes in strength and dynamics driven by experiences (Markram and Tsodyks, 1996; Holtmaat and Svoboda, 2009; Bennett et al., 2018; Roelfsema and Holtmaat, 2018). Therefore, any connectome map represents only a snapshot of the dynamic brain; and (3) neurons can rapidly change their functional roles in response to chemical signals such as peptides, hormones or neuromodulators, all with no visible modification to the connectivity diagram, and each wiring diagram can encode many possible circuit outcomes (Bargmann and Marder, 2013).

However, if we want to understand the neural mechanisms underlying brain function, we have to identify their constituent neural connections from the molecular and cellular levels to the whole brain. Facing the "metaphor" of macro-connectomics and the "myth" of micro- and nano-connectomics, how can we overcome the barriers of scale and complexity to reconstruct the neural connections that give rise to brain function?

FUNCTIONAL MAPPING: FROM CRANIAL BUMPS TOWARDS NEURAL MECHANISMS

Feeling the Bumps of the Skull

What is the link between verbal memory and bulging eyes, the cerebellum and sexuality? About 200 years ago, early attempts to localize brain functions and behaviors in cerebral structures began with Franz Gall's phrenology (Gall and Spurzheim, 1810). The brain was considered to be composed of different "organs," each with its own function, and the size of cortical organs depended on the development of mental faculties, reflected through cranial bumps. Gall noticed that individuals with a retentive verbal memory had bulging eyes and that several cases of aphasia were caused by the damage to the frontal lobe. Therefore, he localized verbal memory in the frontal lobes, assuming that the super development of these lobes pushed out the eyes. Feeling the burning nape of a nymphomaniac widow, he considered the cerebellum to be the organ of the sexual instinct (Gall et al., 1838). Although phrenology was based on such false assumptions, it drove the functional mapping of the brain. After all, Gall was not completely wrong with the relation between brain structure and function, which has been partly supported by some modern studies, in particular, the famous MRI study showing that London taxi drivers have larger posterior hippocampi (Maguire et al., 2000).

To surpass the simplistic correlation between cranial bumps and mental faculties, functional mapping further developed in cytoarchitectonics and myeloarchitectonics to build maps of cerebral regions according to their structure and inferred function. Motor function was one of the first functions to be located in the brain, owing to the identification of the giant pyramidal cells (Meynert, 1867; Betz, 1874; Lewis, 1878; Campbell, 1903). Cécile and Oskar Vogt mapped 200 structural and functional areas in the monkey cortex, using myelin-

stained histological sections (Vogt and Vogt, 1903). Five years later, Brodmann (1908) distinguished 43 cytoarchitectonic areas in the human cortex, using cell body-stained histological sections, and assigned to each of them a function. Although today Brodmann's map is still largely used to localize neuroimaging data (Turner and Geyer, 2014), it does not match recent anatomical and functional data in many brain regions, and the mosaic-like segregation of the cerebral cortex is far from reflecting its heterogeneous structure (Amunts and Zilles, 2015).

Methods in cytoarchitectonics and myeloarchitectonics mapped brain functions to brain areas mainly by inference. To relate directly behaviors to brain regions, clinicopathological correlation was one of the first methods developed in the history of functional mapping. The faculty of speech was located in the anterior lobes, the lesions to which led frequently to the loss of speech (Bouillaud, 1825; Broca, 1861). Motor centers were located in the region of the middle cerebral artery through the observation of "Jacksonian seizures" with unilateral convulsions (Jackson, 1870). These early studies suggested that the brain consisted of specific, circumscribed, yet interconnected functional areas, the disconnection of which caused neurological disorders. This led to the concept of disconnection syndromes, caused by the destruction of either the centers of convergence where crucial associations were formed or the conduction pathways transmitting information between these centers (Wernicke, 1874; Dejerine, 1892). The concept of disconnection syndromes was further developed in the 1960s: the studies of split-brain patients revealed the topographic organization and functional specificity of the corpus callosum (Gazzaniga et al., 1962), and neo-associationism reinterpreted apraxia, amnesia, agnosia and hemispatial neglect (Geschwind, 1965a,b). However, the phenomenon of "diaschisis" questioned localization of brain functions: the destruction of a cortical area could produce transient symptoms in other distant areas, which showed that immediate symptoms were not a reliable guide to the function of a destroyed cortical area (von Monakow, 1914). This was one strong argument held by holists. They considered that brain functions were distributed continuously throughout the brain: stimulation of a single point in the nervous system stimulated the whole system; a weakened point weakened the whole system (Flourens, 1842). In the late 20th century, brain functions and dysfunctions were further investigated *in vivo* in human subjects with neuroimaging techniques, in particular positron emission tomography (PET) and fMRI (Frackowiak, 1986, 1994). Today, the relationship between segregation and integration, localized and distributed aspects of brain functions still poses a major challenge to neuroscience (Cauda et al., 2014; Sporns, 2014), and new approaches are mandatory (Frackowiak and Markram, 2015).

To directly test the function of brain regions, experimental methods, in particular, electrical stimulation and ablation techniques were developed. Through electrical stimulation that induced motor responses, the motor centers were first mapped in the dog cerebral cortex (Hitzig and Fritsch, 1870), then in a patient with a cranial malformation exposing parts of both cerebral hemispheres (Bartholow, 1874). These results were demonstrated by destructing the motor centers in the monkey brain, which caused motor paralysis totally dissociated from sensory paralysis (Ferrier, 1875). However, the localization of the motor centers was questioned by the "functional instability" of the motor cortex, revealed by stimulating repetitively the same point in the motor cortex (Brown et al., 1912), which suggested that the motor cortex was a changing organ. The famous "sensory and motor homunculi" were built through electrical stimulation of the cerebral cortex in conscious patients undergoing surgery for epilepsy (Penfield and Boldrey, 1937). Owing to ablation techniques, vision was located in the occipital lobe and auditory function in the temporal lobe (Panizza, 1855; Munk, 1890). And ablation of the frontal lobe in monkey was found to disintegrate the personality and to destroy the ability to classify and synthesize groups of representations (Bianchi, 1920). However, these experimental methods suffered from low resolution and lacked specificity.

With the development of single-cell recording techniques, in particular tungsten microelectrodes invented in the 1950s (Hubel, 1957), specific brain functions were localized in certain populations of cells, such as "complex cells" in the visual cortex with specific oriented receptive fields (Hubel and Wiesel, 1962), "place cells" in the hippocampus that respond to stimuli in specific spatial locations (O'Keefe and Dostrovsky, 1971), "face cells" in the superior temporal sulcus that respond selectively to faces (Desimone et al., 1984), and "mirror neurons" in the rostral part of the inferior premotor cortex that become active not only during the execution but also during the observation of specific movements (di Pellegrino et al., 1992). During the same period, theoretical neuroscience explored brain functions through mathematical modeling, such as Marr's famous models of visual processing widely adopted in computer vision (Marr, 1982). Nevertheless, both of these approaches could not resolve how different types of brain cells and circuits interact together to generate the full array of diverse brain functions.

Over the past 200 years, functional mapping has developed from correlation-based methods to experimental perturbation of brain activity; from observing correlations between cranial bumps and behavioral stereotypes, cyto-/myelo-architectures and brain functions, brain lesions and behavioral deficits, to relating brain regions to behavioral outputs through electrical stimulation or ablation techniques; from localization of brain functions in brain regions to those in specific populations of cells. Functional mapping is evolving towards causally linking brain structure to function with high resolution and specificity. How does modern neuroscience face this major challenge?

Recording and Manipulating Neural Activity

Current correlation-based methods are particularly represented by fMRI studies that detect the similarity of regional activation profiles reflected indirectly in BOLD signals to extract patterns of correlation or covariance and to infer functional connectivity between brain regions. Trying to correlate neural connections and brain regions to pre-defined behavioral categories, this approach is described by some researchers as "neophrenology" (Miller, 2008). The biophysics of how BOLD signals relate to

underlying neural activity remains an unsolved question and represents a fundamental limitation of fMRI studies (Hillman, 2014; Gao et al., 2017). Since correlation-based methods deliver non-causal similarity-based metrics of statistical dependence (Bassett and Sporns, 2017), other methods are used to unravel the causal relationship between neural activity and brain function, in particular recording and manipulating neural activity and observing the behavioral outputs.

About 150 years ago, resting and action potentials were first recorded from frog sciatic nerves with a differential rheotome (Bernstein, 1868). Almost 80 years ago, the first intracellular recording of individual neurons was achieved in the squid giant axon with glass microelectrodes (Hodgkin and Huxley, 1939). Ten years later, voltage clamp was developed, and patch clamp in the 1970s (Cole, 1949; Marmont, 1949; Neher and Sakmann, 1976). About 60 years ago, implantable microelectrodes were developed to record from single neurons in a freely behaving ground squirrel during 4 days (Strumwasser, 1958). Nowadays, penetrating multi-electrode arrays (MEAs) can record from individual neurons simultaneously at multiple sites to study distributed neural circuits (Gehring et al., 2015; Maccione et al., 2015), and mesh nanoelectronics, which are tissue-like electronics consisting of a macroporous mesh structure with addressable electronic devices, have achieved stable single-neuron level chronic recording and stimulation in freely behaving animals for at least 8 months (Fu et al., 2016). Yet, even so, the huge number of neurons and the complexity of neural interactions preclude the high-density parallel recordings of the whole mammalian brain.

Almost 230 years ago, experimental manipulation of neural activity began with electrical stimulation of nerves. The first electrophysiological experiments were achieved in frog neuromuscular preparations through electrical stimulation of sciatic nerves by using electric machine or atmospheric electricity during lightening (Galvani, 1791). Electrical stimulation provides high temporal resolution and can be used in humans to modulate neural activity, such as deep brain stimulation, introduced in clinical practice in the 1950s to treat psychiatric disorders such as schizophrenia (Delgado et al., 1952) and neurological disorders such as Parkinson's disease (Benabid et al., 1987). Multi-electrode arrays were developed in the 1950s to record and manipulate neural activity in living laboratory animals (Strumwasser, 1958) and are evolving towards chronic, large-scale recording and stimulation at the single-neuron level in freely behaving animals (Fu et al., 2016). Optogenetics, developed in the early 21st century, has been generalized during the last decade to test and generate hypotheses on brain function in non-human neuroscience, using genetically encoded light-activated proteins to manipulate cell activity with cell type-specific and high temporal resolution (Zemelman et al., 2002; Boyden et al., 2005; Lima and Miesenböck, 2005). Nevertheless, it is extremely challenging to control separately all of the cells in the mammalian brain with high spatiotemporal resolution during behavior, particularly due to light scattering and power deposition requirements (Deisseroth, 2015).

Noninvasive approaches such as EEG and MEG are suitable for human studies and long-term monitoring of brain activity, but their low spatial resolution precludes studies at the cellular level (Babiloni et al., 2009; Wendel et al., 2009). Efforts are underway to measure at the cellular level brain activity in persons carrying recording or stimulation electrodes or neurotechnological devices for therapeutic applications or experimental studies, such as deep brain stimulation and brain-machine interface (Moran, 2010; Lozano and Lipsman, 2013). However, these studies are not scalable to large-scale monitoring. Noninvasive stimulation techniques for human studies usually activate brain areas on a centimeter scale, such as transcranial magnetic stimulation, introduced in 1985 to stimulate the human motor cortex for neurological examination (Barker et al., 1985). These techniques lack accuracy and specificity.

Over the past 200 years, experimental studies trying to unravel the causal relationship between neural activity and behavior have evolved from recording and stimulating nerves in frog neuromuscular preparations to chronic monitoring and manipulation of individual neurons in freely behaving animals, from electrical stimulation and ablation techniques to optogenetic manipulation with cell type-specific and high temporal resolution, from univariate correlation between brain regions and behavioral stereotypes to large-scale multivariate monitoring and manipulation of neural circuits, with the ultimate goal of producing a dense functional map of the dynamic brain (Insel et al., 2013).

However, to demonstrate the causal relationship between neural activity and brain function, dense functional mapping requires in principle a comprehensive map of the connectome and the parallel recording from the interacting molecules, cells, circuits and areas throughout the brain. Even with technological advances, dense functional mapping of the whole brain is extremely challenging and thus considered by many researchers to be science fiction (Shen, 2013). How can we overcome this challenge to identify all the molecular and cellular mechanisms underlying brain function and behavior?

Identifying the Molecular and Cellular Mechanisms Underlying Brain Function and Behavior

Quantifying behavior is a major challenge to studies that aim to identify the neural correlates of pre-defined classes of behavioral stereotypes, from the movement of a limb to decision making and emotions (Blakemore and Robbins, 2012; Koelsch, 2014; Uhlmann et al., 2017), based on psychological taxonomy or descriptive representations of observable behavioral outputs which are individual- and context-dependent. In these kinds of studies, behaviors are classified into schemes that are either coarse-grained or intuitively defined and biased by human observers' assumptions (Berman, 2018). Such behavior classifications do not necessarily correspond to inherent behavior structure constrained by biophysics and neural activity, and they preclude the identification of intrinsic neural mechanisms that give rise to behavior—the output of the functioning brain as an integrated system.

Automated behavior quantification and classification using techniques such as machine vision and learning to extract

representations of stereotyped behaviors are the first steps towards objectivity and consistency in behavior classification and have the potential to reveal behavioral patterns overlooked by human observers, although these approaches are still based on assumptions and biased (Hong et al., 2015; Robie et al., 2017; Todd et al., 2017; Berman, 2018).

Dense functional mapping is producing huge amounts of data, ranging from molecular and cellular interactions to the connectivity between brain regions and behavioral outputs. Network-based approaches propose to analyze these big, complex data and to model brain networks with theoretical and computational methods such as graph theory and algebraic topology, through statistical inference and dimensionality reduction (Bassett and Sporns, 2017). Although these approaches have the potential to uncover structural and functional features of brain activity, they are subject to methodological and interpretational limitations that result from uncertainties in data acquisition and network definition, thus requiring sophisticated, neurobiologically based brain models down to the molecular scale to reveal the mechanisms underlying brain function and behavior (Sporns, 2014; Medaglia et al., 2015; Bassett and Sporns, 2017).

Organism-level behavior emerges from the interaction of structural connectivity and signaling processes at the molecular, cellular and circuit levels, involving the dynamic activity of huge numbers of molecules and cells as well as multiple physiological and biochemical systems. It is the output of the functioning brain as an integrated system. How can we avoid assumptions in behavior classification that bias our research on the causal relationship between brain structure and function? How can we overcome the barriers of scale and complexity to trace the causal chains of events leading from molecular and cellular mechanisms to brain function and behavior?

SIMULATION NEUROSCIENCE: FROM THE SQUID GIANT AXON TO THE HUMAN BRAIN

Over past millennia, brain research has evolved through philosophical, experimental and theoretical phases, all of which have contributed to the development of modern neuroscience. Great achievements have been realized in neuronal mapping, connectivity mapping and functional mapping, but these endeavors are hindered by the barriers of scale and complexity. How can we scale up cellular phenotyping and deal with the dynamics of cellular properties to achieve a reliable neuronal cell-type classification? How can we rise to the challenge of volume, time and dynamics in full connectome mapping? How can we identify the molecular and cellular mechanisms that give rise to brain function and behavior? To overcome these fundamental barriers, brain research has to shift to a new phase.

Simulation neuroscience aims to fill the gaps in our knowledge of brain structure and function through building a digital copy of the brain with predictive methods, by combining experimental and theoretical approaches (Markram, 2006; Markram et al., 2015; **Figure 3**). It has the potential to overcome the challenge of scale and complexity. The following pages are aimed at exploring the historical roots of this endeavor by identifying the major milestones that are the most related to it and that are capable of characterizing it in a concise way, instead of conducting an exhaustive survey of all the investigators whose important work has contributed to the evolution of modeling and simulation in neuroscience.

All Began With an Axon

Neuroscience originated in a nerve, while detailed simulation in neuroscience began with an axon.

Action potentials were already measured in frog nerve-muscle preparations more than 170 years ago (du Bois-Reymond, 1843), but how is the action potential generated? Although a mathematical model of nerve excitability, the "integrate and fire" model, was built in the early 20th century, based on data obtained from frog nerve stimulation, it was a simple capacitor circuit model (Lapicque, 1907). Since the first measurement of action potentials, the molecular mechanisms of action potential generation had remained an open question over the following 100 years.

More than 60 years ago, two neuroscientists managed to insert voltage clamp electrodes into a squid giant axon and measured the flow of electric current through its surface membrane (Hodgkin and Huxley, 1952). On the basis of their experimental data and inspired by cable theory rooted in the 19th-century model of signaling through submarine telegraph cables (Thomson, 1857), they built a mathematical model of ionic currents to quantitatively account for conduction and excitation and simulated the action potential on the Cambridge University computer. Simulations showed how potassium and sodium ion channels could generate the action potential and predicted the electrical behavior of the axon consistent with experimental data. This was the first detailed digital simulation of a physiological property of a neuron.

Cable theory was further developed to take account of dendritic branching that largely affects neuronal processing. This endeavor gave birth to the first multicompartment dendritic neuron model, based on anatomical and electrophysiological data and simulated on an IBM 650 computer (Rall, 1959, 1962; Segev and Rall, 1998), which was further developed in the following years to unravel the role of dendrites in information transmission (Segev and London, 2000). Single neuron models then evolved into neurocircuit models to study the activity of neuronal populations and synaptic connectivity. The pioneering studies consisted in reconstructions of field potentials and dendrodendritic synaptic circuits in the olfactory bulb for interpreting their underlying mechanisms, based on known anatomical organization and nerve membrane properties and simulated on Honeywell 800 and IBM 370/168 computers (Rall and Shepherd, 1968; Shepherd and Brayton, 1979).

The development of supercomputers in the 1980s drove large-scale simulation of detailed neuron networks, which made it possible to study collective neuronal activities and the neural mechanisms underlying certain brain functions. In 1982, a network model of 100 multicompartment hippocampal

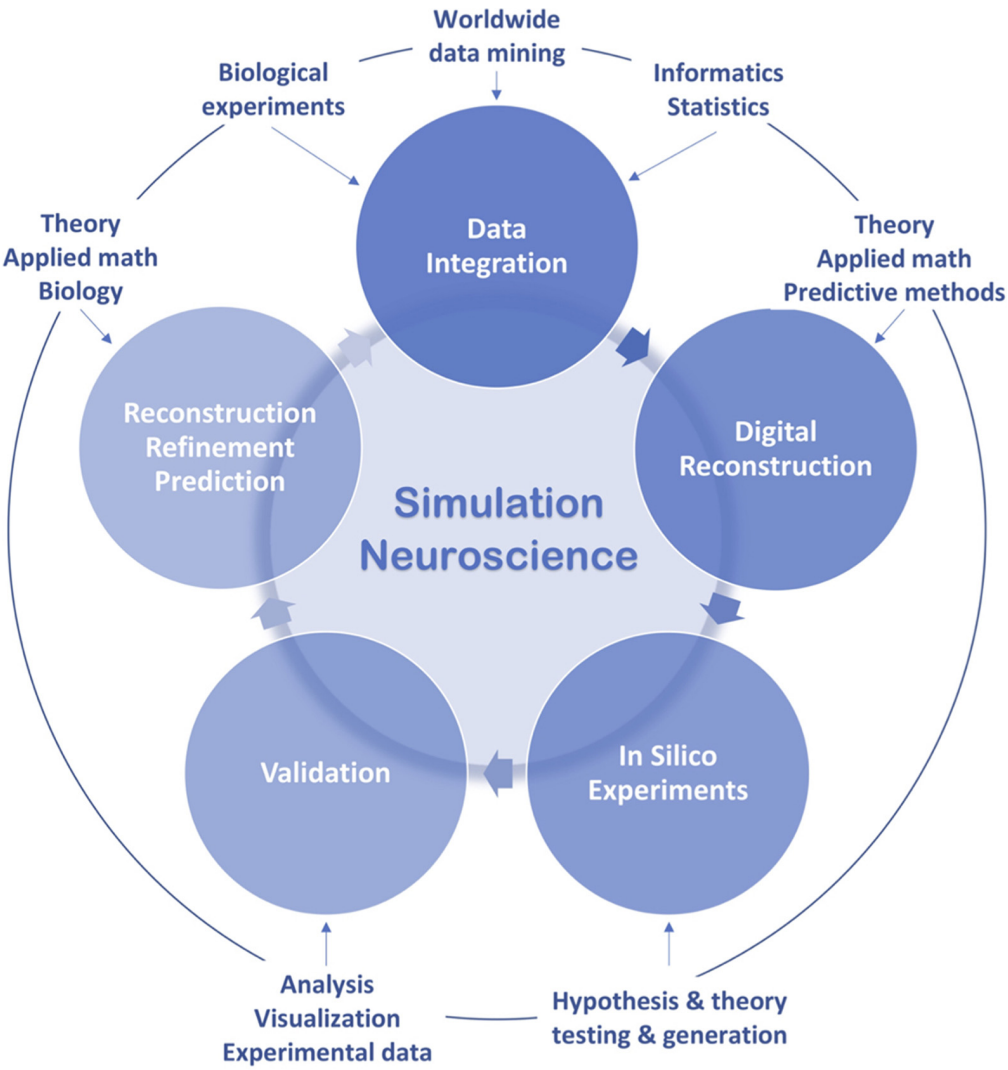


FIGURE 3 | Simulation neuroscience workflow.

neurons, each capable of intrinsic bursting and interconnected by excitatory chemical synapses, was simulated on an IBM 370/168 to reproduce field potentials and intracellular recordings during interictal spikes in epilepsy and to identify the mechanisms underlying this form of neuronal synchronization (Traub and Wong, 1982; IBM Archives, 2003). Six years later, a network of 990 multicompartment hippocampal neurons with different types of cellular interactions was simulated on an IBM 3090 to analyze in particular the mechanisms regulating neuronal synchronization in epilepsy (Traub et al., 1988). At the same time, began the early efforts to simulate neurocircuitry underlying vertebrate behavior, in particular simulation of a segmental network of inhibitory and excitatory interneurons underlying locomotor behavior in lamprey, using Rall neuron models with one soma and a three-compartment dendritic tree, which unraveled the cellular bases of segmental pattern generation, including central and sensory mechanisms and the immediate supraspinal mechanisms initiating locomotion (Grillner et al., 1988, 1991).

In the early 1990s, the simulator "NEURON" was developed for empirically based simulations of single and networks of neurons with complex anatomical and biophysical properties, such as complex branching morphology, multiple channel types, inhomogeneous channel distribution, ionic diffusion and the effects of second messengers (Hines, 1989, 1993). During the same period, was released the GEneral NEural SImulation System (GENESIS), a simulation environment for constructing realistic models of neurobiological systems from subcellular processes and individual neurons to networks of neurons and neuronal systems (Wilson et al., 1989; Bower et al., 2013). In the following years, simulators such as MCell and STEPS were developed to simulate biochemical signaling pathways at the molecular scale (Stiles et al., 1996; Hepburn et al., 2012). As detailed models of neural systems have become more and more sophisticated, efforts

are underway to develop a language that provides a common data format for defining and exchanging descriptions of these detailed models, such as the NeuroML project which aims to develop an eXtensible Markup Language (XML) based description language (Goddard et al., 2001).

In parallel with the development of simulators, large-scale simulations continued to grow. A single-column thalamocortical network model with 3,560 multicompartment neurons, including seven cell types characterized by different types of morphology, connectivity and electrical behavior, was simulated on a Linux cluster (IBM e1350) to particularly address the physiology of network oscillations and epileptogenesis (Traub et al., 2005). Although the model exhibited gamma oscillations, sleep spindles and epileptogenic bursts, it was insufficient to describe other neuronal network behaviors, particularly due to the omission of many cell types, many unknown structural details, the absence of synaptic plasticity and the restriction of the model to a single column. In the modelers' view, their work represented an extremely preliminary step towards understanding subtle aspects of brain function, such as learning or information processing, and they hoped for more detailed models to study a broader range of network phenomena. They considered that detailed modeling of extensive brain circuits was necessary for understanding brain function and for making important experimental predictions that would not have been made without the model.

These previous endeavors mainly aimed to build models to reproduce certain brain functions or dysfunctions, such as action potential generation or neuronal synchronization in epilepsy. However, to trace the causal chains of events leading from molecular and cellular mechanisms to diverse brain functions and behaviors, biologically realistic dense reconstructions of the brain realized without the goal of fitting the model to any specific function (if reconstructions are correct, functions should arise naturally) are demanded. This need led to the birth of simulation neuroscience in the early 21st century (Markram, 2006). Since then, digital reconstructions have increased in size and biological accuracy to unravel deeper mechanisms underlying brain function. To date, the most detailed reconstruction concerns the microcircuitry of rat somatosensory cortex, containing ∼31,000 multicompartmental conductance-based neuron models, including 55 layer-specific morphological and 207 morphoelectrical subtypes, and simulated on supercomputers such as the Blue Brain IV, ranked the 100th most powerful supercomputing system (Top500, June 2015). This digital reconstruction is able to generate emergent network activity and to reproduce an array of *in vitro* and *in vivo* experiments without parameter tuning, and it enables experiments so far impossible either *in vitro* or *in vivo* (Markram et al., 2015).

Since its origin, detailed simulation in neuroscience has evolved from a single cell type to more than 200 cell types characterized by morphological and physiological features, from one type of synaptic connectivity to the predicted anatomical and physiological properties of all the intrinsic synapses formed onto and by any neuron, from specific models aimed at reproducing certain forms of neuronal activity to generic dense reconstructions of brain regions with various neuronal activity patterns and emergent network behaviors, from an action potential generated through a squid giant axon to diverse network behaviors of rat neocortical microcircuitry with 31,000 neurons connected through 36 million synapses. A large body of disconnected experimental datasets and knowledge accumulated since the origin of neuroscience have been integrated into a unified digital copy of neocortical microcircuitry, allowing deeper insights into the neural mechanisms underlying brain function. Efforts are underway to reconstruct more electrophysiological and biochemical mechanisms and to simulate the human brain.

Transcending Scale and Complexity

Simulation neuroscience identifies strategic data and formulates principles of brain structure and function to accelerate our understanding of the brain, instead of experimentally mapping all the elements and activities in the brain, which is impossible to achieve due to their scale and complexity (Markram, 2006; Markram et al., 2015; **Figure 4**).

Neuronal Reconstruction and Simulation

Reconstructions of single neurons are the building blocks of the digital brain. In the early years of simulation in neuroscience, some researchers were aware of the importance of describing the detailed structure of neurons to simulate the voltage response to inputs impinging on the cell in different locations and interactions between cells generated by extracellular current flows. They were also aware of the importance of reconstructing the diverse types of electrical behavior of neurons. Therefore, they argued against using point neuron models (Traub et al., 1988). Nevertheless, at this stage, the endeavor to digitally reconstruct the morphological and physiological types of neurons was limited in scale and accuracy, so new approaches were to be developed.

Historically, neuronal morphologies were first qualitatively described through visual inspection, then quantitatively described based on morphometric parameters. Since these methods are not standardized to objectively describe complex branching patterns of neuronal trees, topological methods have been developed in simulation neuroscience to rigorously quantify the structural differences of neuronal trees and to classify neurons into distinct morphological types by encoding the spatial structure of each neuronal tree with a unique topological signature (Kanari et al., 2018). Then cloning each morphological type with statistical variations allows scaling up the reconstruction of neurons belonging to each morphological type while respecting biological variability.

Automated statistical analysis can reveal distinctive electrical types; computational multi-parametric approach can extract combinatorial expression rules of ion channel genes underlying electrical phenotypes; ion channels can be automatically inserted by simulators combined with an automated fitting algorithm. These methods developed in simulation neuroscience allow objective and high-throughput reconstruction of electrical types (Khazen et al., 2012; Druckmann et al., 2013; Markram et al., 2015).

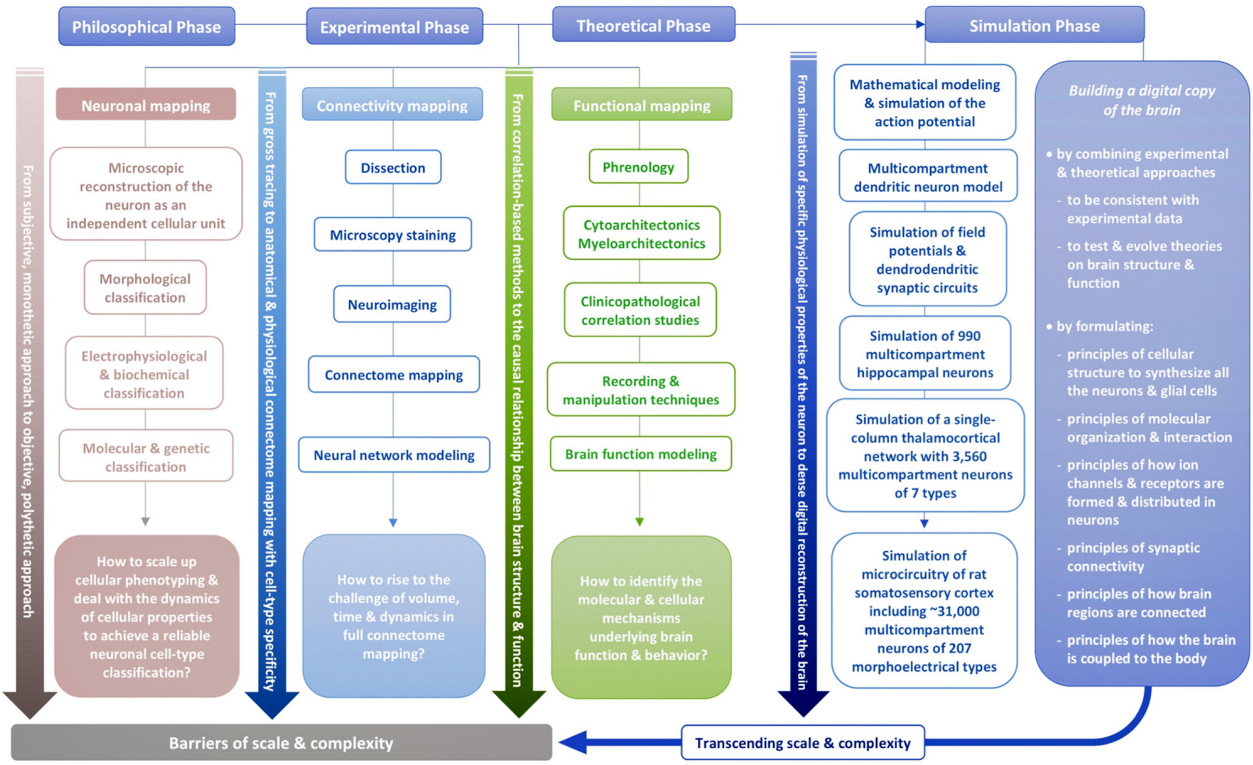


FIGURE 4 | Transcending scale and complexity.

The high-throughput digital reconstruction of different types of neurons can be extended from morphological and electrophysiological features to other dimensions such as projection and molecular features when sufficient data that allow quantifying these features become available. Furthermore, the structure and function of brain cells vary according to their position in the brain; this should be considered while reconstructing different classes of brain cells. To support this endeavor, whole-brain cell atlases are being built, providing insights into cellular organization only possible at the whole-brain scale. The first dynamic 3D cell atlas for the whole mouse brain has recently been achieved, showing cell positions constructed algorithmically from whole brain Nissl and gene expression stains, and providing the densities and positions of all excitatory and inhibitory neurons, astrocytes, oligodendrocytes and microglia in each of the 737 brain regions defined in the Allen Mouse Brain Atlas (Erö et al., 2018).

During the evolution of simulation neuroscience, the digital reconstruction of different types of neurons has become more and more multi-constrained, realistic and high-throughput, and it allows evolving current neuronal classifications (Deitcher et al., 2017). Today, we have objective classification of morphologies which is helping define morphological types; we have more or less agreed electrical protocols that can be used to describe electrical types; we have tracing studies that are helping define the projection types, and we have single cell transcriptome data that are beginning to describe the genetically different types of cells. Efforts are underway to define a minimum sample size capable of reliably revealing distinct types of brain cells, to reduce dimensionality by defining a relevant level of granularity and to identify permanent molecular features that maintain cell identity—a step forward towards an objective and comprehensive classification of neuronal types.

Connectivity Reconstruction and Simulation

More than 100 years ago, Santiago Ramón y Cajal initiated predictive reconstruction by inferring neuronal connectivity from morphological features of neuronal arbors (Ramón y Cajal, 1894). About 80 years later, trying to digitally reconstruct neuronal circuits, some researchers considered pointless to explicitly specify all the neuronal connections, which is unattainable experimentally (Traub et al., 1988). They chose to reconstruct neuronal connections by a series of random choices, based on the statistical properties of the network topology, such as the average number of inputs or outputs per cell and the probability of connection between pairs of cells.

New approaches based on statistical modeling and synaptic rules have been developed in simulation neuroscience to accurately predict synaptic connectivity (Perin et al., 2011; Hill et al., 2012; Ramaswamy et al., 2012), in particular data-driven algorithmic approaches based on established principles of synaptic connectivity and constrained by interdependencies between microcircuit properties such as the number of synapses and bouton densities. With these approaches, it is possible to

predict the number and location of all synaptic connection types shown experimentally and connection properties impossible to measure experimentally such as the number of source and target cells and synapses (Markram et al., 2015; Reimann et al., 2015). The physiology of synapses can be predicted by formulating rules of synaptic types based on experimental data to generate a relatively complete map of synaptic dynamics (Markram et al., 2015). Synaptic plasticity rules can also be formulated (Kalisman et al., 2005; Loebel et al., 2013). In this way, it is possible to predict the anatomical and physiological properties of all the intrinsic synapses formed onto and by any neuron. These predictions combined with future experiments could be used to further refine connectivity reconstruction and simulation.

Functional Reconstruction and Simulation

More than 60 years ago, Hodgkin and Huxley's reconstruction and simulation of the action potential predicted the properties of the gating structures of ion channels (Hodgkin and Huxley, 1952), showing the power of simulation in neuroscience to unravel biological mechanisms long before their experimental observations. Since the birth of simulation neuroscience, digital reconstructions and simulations have been used to fill the vast gaps in our data, to interpret experimental observations and identify the underlying mechanisms, and to test and generate theories about brain function and dysfunction (Markram, 2006; D'Angelo, 2014; Frackowiak and Markram, 2015).

To identify neural mechanisms that give rise to emergent complex behavior, reconstructing and simulating neurons embedded in microcircuits, microcircuits embedded in brain regions and brain regions embedded in the whole brain is an approach consistent with the biological reality that organism-level behavior is the output of the functioning brain as an integrated system, from molecular and cellular interactions to connections between neurocircuits and between brain regions. Neurorobotics, combined with digital reconstructions, creates new possibilities for studying neural mechanisms leading to emergent behavior across different spatiotemporal scales (Falotico et al., 2017).

The deep relationship between structure and function that guided the first investigators at the origin of neuroscience is the foundation of simulation neuroscience. Recent digital reconstructions and simulations of rat neocortical microcircuitry could reproduce the spatial mode and the temporal dynamics of empirically observed functional networks without parameter tuning and showed emergent network states modulated by physiological mechanisms (Markram et al., 2015). In the same reconstructions, a new algebraic topology approach revealed that synaptic networks contain an abundance of cliques of neurons bound into cavities that guide the emergence of correlated activity, showing a formal link between neural network structure and function (Reimann et al., 2017b). Our understanding of brain structure and function is being deepened through building a digital copy of the brain.

Perspectives and Challenges

The dense digital reconstruction of the brain from sparse, complementary datasets by predicting biological parameters that are not available experimentally involves dealing with the relationships between known and unknown parameters, deriving principles from experimental data, and reducing biological complexity while preserving the principles of brain structure and function.

Initial digital reconstructions need to integrate more types of neural mechanisms and signaling systems, such as neuro-glio-vascular unit and neuromodulation (Jolivet et al., 2015; Ramaswamy and Markram, 2018). They will be challenged and refined by new experimental observations. As more types of datasets and parameters are to be integrated, more relevant biological principles have to be derived, and programming complexity will largely increase. Efficient computational methods have to be developed to satisfy the requirements of this nascent science in rapid evolution. Simulation neuroscience is rising to these challenges and constitutes an essential phase of brain research towards transcending scale and complexity to causally link molecules, genes and cells to brain function and behavior.

The Next Phase of Brain Research

Simulation neuroscience is an efficient approach to integrating disconnected datasets and knowledge in neuroscience that have been accumulated over hundreds of years. The extraction of the rules of the relationships between datasets that concern different levels of brain organization helps to build an integrated view of brain structure and function (Tiesinga et al., 2015). Through digital reconstructions and simulations, researchers can conduct in silico experiments, improve experimental methods, test and generate hypotheses and theories, make predictions and suggest new experiments (Druckmann et al., 2011; Reimann et al., 2013; Abdellah et al., 2015; Hay and Segev, 2015).

Neuromorphic computing uses very-large-scale integration (VLSI) systems containing electronic analog circuits to mimic neuroarchitectures of the nervous system (Mead, 1990). This approach has the potential to overcome the major limitations of traditional computing, such as energy consumption, software complexity and component reliability. Current neuromorphic computing consists in large-scale simulations of neuronal connectivity with few biological details (Furber et al., 2014; The FACETS Project, 2018). This research field would benefit from simulation neuroscience, which has the potential to provide the blueprints of neurocircuits.

Without deeper insights into the fundamental mechanisms underlying brain function, we cannot effectively treat neurological disorders, which result from dysfunctions of neural systems down to the molecular scale. The widely known neurodegenerative disease, Alzheimer's disease, was described more than 110 years ago (Alzheimer, 1906). Today, there is still no effective treatment (The Lancet, 2016). In fact, this "disease" is poorly defined, referring to an array of various symptoms ranging from memory loss to diverse cognitive impairments, caused by multiple distinct brain dysfunctions (Scheltens et al., 2016; Frisoni et al., 2017). How can we treat a brain disease if we cannot identify its underlying mechanisms and clearly define it? How can we restore brain dysfunctions if we do not even understand the neural mechanisms underlying normal brain function? Deep understanding of brain structure

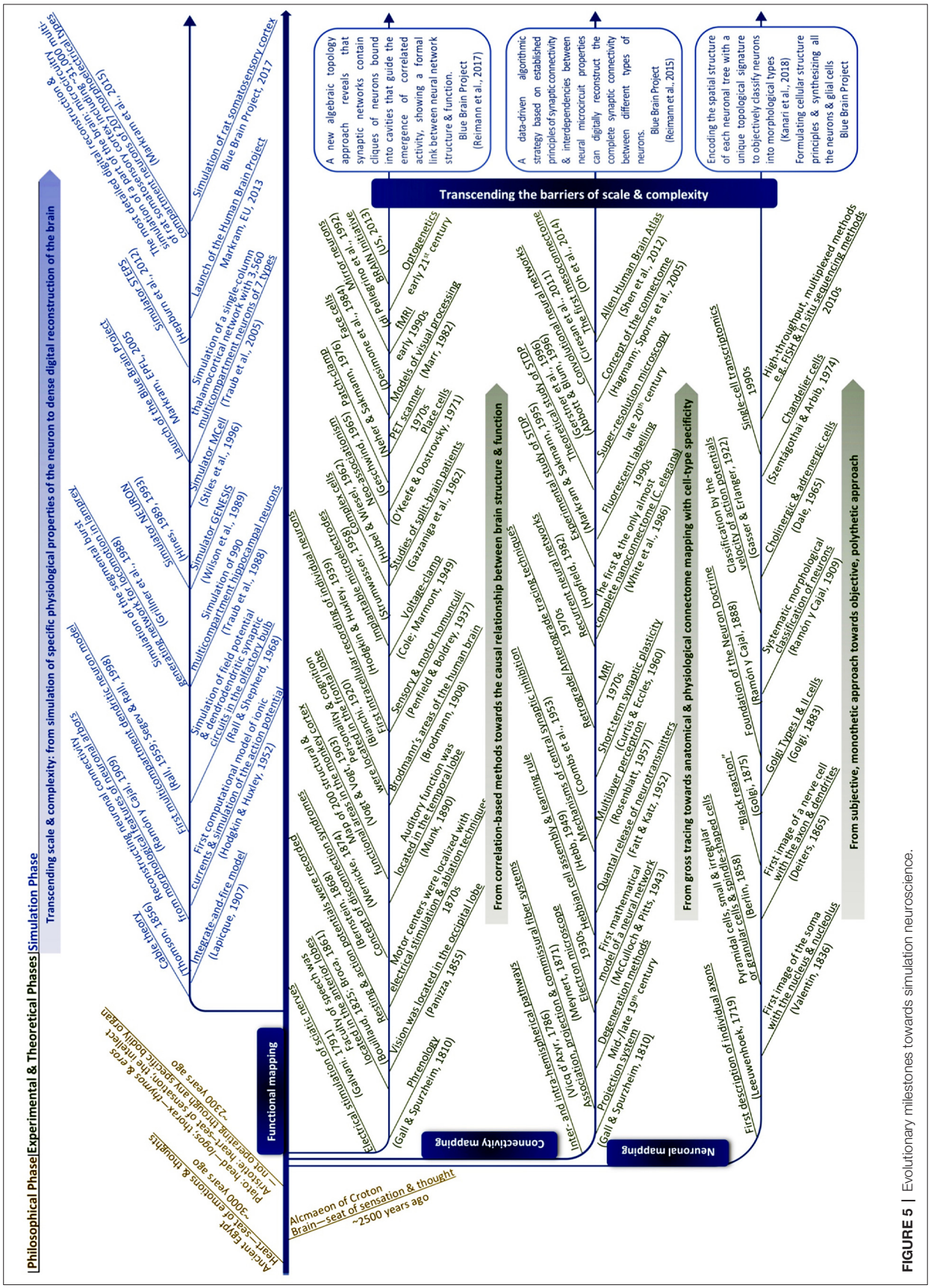


FIGURE 5 | Evolutionary milestones towards simulation neuroscience.

and function is fundamental to clinical research, which will make it possible to identify the "biological signature" of each brain dysfunction instead of simple syndromic descriptions (Frackowiak and Markram, 2015). This is why biologically realistic digital reconstructions of the brain can be a valuable tool for modeling and simulating brain dysfunctions and for developing and validating treatments (D'Angelo, 2014; Frackowiak and Markram, 2015).

Our understanding of brain structure and function is being deepened as we build and refine a digital copy of the brain. Each step unravels new aspects of brain structure and function in a systematic manner. Even though an accurate and complete reconstruction and simulation of the human brain will require at least yottaflop (10^{24} flops) computing or even more[1], we are getting closer to a comprehensive understanding of the brain by developing multiscale simulations. According to the nature of the studied question, some parts of the brain can be simulated at low resolution, and others at high resolution. This allows accelerating our understanding of the brain even before enough computing power becomes available. Finally, it would be possible to trace the neural mechanisms leading to the emergence of biological intelligence and to challenge the foundations of our understanding of consciousness through building a digital copy of the brain.

UNDERSTANDING THE MULTISCALE BRAIN

Since the dawn of neuroscience, hundreds of years ago, this human endeavor has fundamentally been a series of reconstructions: reconstruction of the neuron as a single cellular unit; reconstruction of neurons into distinct types according to their morphological, electrophysiological, biochemical and molecular properties; reconstruction of neural connectivity between brain regions, neuronal groups, individual neurons; reconstruction of the neural mechanisms underlying brain function and behavior. In attempting to complete the reconstruction of brain structure and function, experimental and theoretical approaches are hindered by the fundamental barriers of scale and complexity.

To overcome these barriers, the tools for reconstructing neurons and the brain have dramatically evolved, from Leeuwenhoek's self-made one-lens microscope to compound achromatic microscope and Ramón y Cajal's pencil until today's supercomputers. Leveraging high performance computing, data analysis and statistical inference methods as well as algorithmic approaches, simulation neuroscience quantifies, integrates, scales up and accelerates all the previous reconstruction processes and evolves them into a unified digital copy of the brain—a quantitative and qualitative shift through the dense digital reconstruction and simulation of the brain from sparse experimental data, with the aim of causally linking molecular, cellular and synaptic interactions to brain function and behavior (**Figure 5**).

Since the introduction of the first supercomputers in the mid-20th century, in 70 years, processing power has increased from $\sim 10^3$ to $\sim 143.5 \times 10^{15}$ flops (Dongarra, 2006; November, 2018 | TOP500 Supercomputer Sites). Since the first observation of nerve fibers, the microscopic and physiological reconstruction of the neuron as an independent cellular unit had taken almost 240 years, while the evolution from the first digital reconstruction of the action potential to the dense digital reconstruction of neocortical microcircuitry took about 60 years. What will the future hold for the reconstruction and simulation of the entire brain?

From the dawn of human civilization, the advances in brain research have been generated through a series of fundamental shifts in the types of human thinking to understand the mind and the brain. Relying on intuitive and analogical thinking, ancient philosophers tried to address fundamental questions but were unable to provide empirical evidence. Seeking evidence, reductionist thinkers in experimental neuroscience have gained a deep understanding of many components of the brain but have also produced a huge number of disconnected datasets and knowledge. Theoretical neuroscience applies abstractive thinking to be free from the details in the brain, which may advance artificial intelligence but leaves open the question whether it will advance our understanding of the causal links between brain structure and function. To transcend these barriers, brain research needs a new way of thinking and a new approach. This new phase is proposed to be simulation neuroscience, which is based on integrative and predictive thinking.

Will simulation neuroscience be able to go deep enough through multiple different layers to finally understand the multiscale brain, to answer the probably ultimate question for us, humans, of understanding ourselves, which has haunted us since the dawn of time?

Atoms are combined into molecules; DNA molecules are bound into sequences to produce genes; genes produce proteins; different combinations of proteins produce various types of cells, which are combined into different brain regions to finally form the unique human brain. How do these complex mechanisms interact, leading from single atoms and molecules to brain function and behavior? How does the brain create our small world immersed in the universe? How does the brain incorporate our experiences that define our existence? Still so many unsolved questions.

After thousands of years of brain research, hundreds of years of neuroscience, we remain strangers to ourselves. From the Temple of Apollo, traveling through millennia, the Delphic maxim is still resonating: "Know thyself (Pausanias, 1918)." What will the future hold for us, in 10 years, 100 years, 1,000 years? To understand the multiscale brain, neuroscience now has to shift to a new phase.

[1]High-resolution real-time molecular simulation of the human brain would need $\sim 4 \times 10^{29}$ flops*:

- ~90 billion neurons, ~1,000 trillion synapses
- ~90 billion glial cells, ~450 billion vascular end feet, supporting ~450 trillion synapses
- ~1 trillion molecules/cell, ~1,000 reactions/molecule/s, ~20 diffusion jumps/s
- ~10,000 time steps/s

*Henry Markram. "Will Computers Become as Capable as the Brain?" presented at the conference "What Makes Us Human: From Genes to Machines," The Hebrew University, Jerusalem, June 4–6, 2018.

AUTHOR CONTRIBUTIONS

XF and HM conceived the research and wrote the text. XF wrote most of the text and made all the figures.

FUNDING

This work was supported by the EPFL Blue Brain Project Fund and the ETH Board Funding to the Blue Brain Project.

REFERENCES

Abbe, E. (1873). Beiträge zur theorie des mikroskops und der mikroskopischen wahrnehmung. *Arch. Mikrosk. Anatomie* 9, 413–418. doi: 10.1007/BF02956173

Abbott, L. F., and Blum, K. I. (1996). Functional significance of long-term potentiation for sequence learning and prediction. *Cereb. Cortex* 6, 406–416. doi: 10.1093/cercor/6.3.406

Abdellah, M., Bilgili, A., Eilemann, S., Markram, H., and Schürmann, F. (2015). Physically-based in silico light sheet microscopy for visualizing fluorescent brain models. *BMC Bioinformatics* 16:S8. doi: 10.1186/1471-2105-16-s11-s8

Alzheimer, A. (1906). Über einen eigenartigen schweren erkrankungsprozeβ der hirnrinde. *Neurol. Central.* 23, 1129–1136.

Amunts, K., and Zilles, K. (2015). Architectonic mapping of the human brain beyond brodmann. *Neuron* 88, 1086–1107. doi: 10.1016/j.neuron.2015.12.001

Armañanzas, R., and Ascoli, G. A. (2015). Towards the automatic classification of neurons. *Trends Neurosci.* 38, 307–318. doi: 10.1016/j.tins.2015.02.004

Babiloni, C., Pizzella, V., Gratta, C. D., Ferretti, A., and Romani, G. L. (2009). Fundamentals of electroencefalography, magnetoencefalography, and functional magnetic resonance imaging. *Int. Rev. Neurobiol.* 86, 67–80. doi: 10.1016/s0074-7742(09)86005-4

Bandettini, P. A., Wong, E. C., Hinks, R. S., Tikofsky, R. S., and Hyde, J. S. (1992). Time course EPI of human brain function during task activation. *Magn. Reson. Med.* 25, 390–397. doi: 10.1002/mrm.1910250220

Bargmann, C. I., and Marder, E. (2013). From the connectome to brain function. *Nat. Methods* 10, 483–490. doi: 10.1038/nmeth.2451

Barker, A. T., Jalinous, R., and Freeston, I. L. (1985). Non-invasive magnetic stimulation of human motor cortex. *Lancet* 1, 1106–1107. doi: 10.1016/s0140-6736(85)92413-4

Bartholow, R. (1874). Experimental investigations into the functions of the human brain. *Am. J. Med. Sci.* 66, 305–313. doi: 10.1097/00000441-187404000-00001

Bassett, D. S., and Sporns, O. (2017). Network neuroscience. *Nat. Neurosci.* 20, 353–364. doi: 10.1038/nn.4502

Belliveau, J. W., Kennedy, D. N. Jr., McKinstry, R. C., Buchbinder, B. R., Weisskoff, R. M., Cohen, M. S., et al. (1991). Functional mapping of the human visual cortex by magnetic resonance imaging. *Science* 254, 716–719. doi: 10.1126/science.1948051

Benabid, A. L., Pollak, P., Louveau, A., Henry, S., and de Rougemont, J. (1987). Combined (thalamotomy and stimulation) stereotactic surgery of the VIM thalamic nucleus for bilateral Parkinson disease. *Appl. Neurophysiol.* 50, 344–346. doi: 10.1159/000100803

Bennett, S. H., Kirby, A. J., and Finnerty, G. T. (2018). Rewiring the connectome: evidence and effects. *Neurosci. Biobehav. Rev.* 88, 51–62. doi: 10.1016/j.neubiorev.2018.03.001

Berlin, R. (1858). *Beiträge zur Strukturlehre der Grosshirnwindungen.* Erlangen: Junge.

Berman, G. J. (2018). Measuring behavior across scales. *BMC Biol.* 16:23. doi: 10.1186/s12915-018-0494-7

Bernard, C. (1858). *Leçons sur la Physiologie et la Pathologie du Système Nerveux.* Paris: J.-B. Baillière et fils.

Bernstein, J. (1868). Uber den zeitlichen verlauf der negativen schwankung des nervenströms. *Pflügers Arch.* 1, 173–207. doi: 10.1007/bf01640316

Betz, V. (1874). Anatomischer nachweis zweier gehirncentra. *Zbl. Med. Wiss.* 12, 578–599.

Betzig, E., Patterson, G. H., Sougrat, R., Lindwasser, O. W., Olenych, S., Bonifacino, J. S., et al. (2006). Imaging intracellular fluorescent proteins at nanometer resolution. *Science* 313, 1642–1645. doi: 10.1126/science.1127344

Bianchi, L. (1920). *La Meccanica del Cervello e la Funzione dei Lobi Frontali.* Melano: Bocca.

Bickle, J. (2003). *Philosophy and Neuroscience: A Ruthlessly Reductive Account.* Netherlands: Springer.

Blakemore, S.-J., and Robbins, T. W. (2012). Decision-making in the adolescent brain. *Nat. Neurosci.* 15, 1184–1191. doi: 10.1038/nn.3177

Bota, M., Dong, H.-W., and Swanson, L. W. (2003). From gene networks to brain networks. *Nat. Neurosci.* 6, 795–799. doi: 10.1038/nn1096

Bouillaud, J. B. (1825). Recherches cliniques propres à démontrer que la perte de la parole correspond à la lésion des lobules antérieurs du cerveau, et à confirmer l'opinion de M. Gall, sur le siège de l'organe du langage articulé. *Archs. gén. Méd.* 8, 25–45.

Boulina, M., Samarajeewa, H., Baker, J. D., Kim, M. D., and Chiba, A. (2013). Live imaging of multicolor-labeled cells in *Drosophila*. *Development* 140, 1605–1613. doi: 10.1242/dev.088930

Bower, J. M., Cornelis, H., and Beeman, D. (2013). "GENESIS, the general neural simulation system," in *Encyclopedia of Computational Neuroscience*, eds D. Jaeger and R. Jung (New York, NY: Springer New York), 1–8.

Boyden, E. S., Zhang, F., Bamberg, E., Nagel, G., and Deisseroth, K. (2005). Millisecond-timescale, genetically targeted optical control of neural activity. *Nat. Neurosci.* 8, 1263–1268. doi: 10.1038/nn1525

Broca, P. (1861). Nouvelle observation d'aphémie produite par une lésion de la moitié postérieure des deuxième et troisième circonvolutions frontales gauches. *Bull. Soc. Anat.* 36, 398–407.

Brodmann, K. (1908). Beiträge zur histologischen lokalisation der grosshirnrinde. VI. Mitteilung: die cortexgliederung des menschen. *J. Psychol. Neurol.* 10, 231–246.

Brown, T. G., Sherrington, C. S., and S, F. R. (1912). On the instability of a cortical point. *Proc. R. Soc. Biol. Sci.* 85, 250–277. doi: 10.1098/rspb.1912.0050

Burtt, E. A., and Edwin, A. (1923). *The Metaphysical Foundations of Modern Physical Science; A Historical and Critical Essay.* London: K. Paul, Trench, Trübner.

Butterfield, H. (1959). *The Origins of Modern Science 1300–1800.* New York, NY: The Macmillan Company.

Campbell, A. W. (1903). Histological studies on cerebral localisation. *Proc. R. Soc.* 72, 488–492. doi: 10.1098/rspl.1903.0077

Carnap, R. (1928). *Der logische Aufbau der Welt.* Berlin, Allemagne: Weltkreis.

Catani, M., Thiebaut de Schotten, M., Slater, D., and Dell'Acqua, F. (2013). Connectomic approaches before the connectome. *Neuroimage* 80, 2–13. doi: 10.1016/j.neuroimage.2013.05.109

Cauda, F., Costa, T., and Tamietto, M. (2014). Beyond localized and distributed accounts of brain functions. Comment on "Understanding brain networks and brain organization" by Pessoa. *Phys. Life Rev.* 11, 442–443. doi: 10.1016/j.plrev.2014.06.018

Cauli, B., Tong, X.-K., Rancillac, A., Serluca, N., Lambolez, B., Rossier, J., et al. (2004). Cortical GABA interneurons in neurovascular coupling: relays for subcortical vasoactive pathways. *J. Neurosci.* 24, 8940–8949. doi: 10.1523/JNEUROSCI.3065-04.2004

Chalfie, M., Tu, Y., Euskirchen, G., Ward, W. W., and Prasher, D. C. (1994). Green fluorescent protein as a marker for gene expression. *Science* 263, 802–805. doi: 10.1126/science.8303295

Chalmers, D. J. (1996). *The Conscious Mind: In Search of a Fundamental Theory.* New York, NY: Oxford University Press.

Chambers, B., and MacLean, J. N. (2016). Higher-order synaptic interactions coordinate dynamics in recurrent networks. *PLoS Comput. Biol.* 12:e1005078. doi: 10.1371/journal.pcbi.1005078

Chen, K. H., Boettiger, A. N., Moffitt, J. R., Wang, S., and Zhuang, X. (2015). RNA imaging. Spatially resolved, highly multiplexed RNA profiling in single cells. *Science* 348:aaa6090. doi: 10.1126/science.aaa6090

Chen, F., Wassie, A. T., Cote, A. J., Sinha, A., Alon, S., Asano, S., et al. (2016). Nanoscale imaging of RNA with expansion microscopy. *Nat. Methods* 13, 679–684. doi: 10.1038/nmeth.3899

Churchland, P. S. (1986). *Neurophilosophy: Toward a Unified Science of the Mind-Brain.* Cambridge, MA: MIT Press.

Churchland, P. S. (2011). *Braintrust: What Neuroscience Tells us about Morality.* Princeton, NJ: Princeton University Press.

Churchland, P. M., and Churchland, P. S. (1997). Recent work on consciousness: philosophical, theoretical, and empirical. *Semin. Neurol.* 17, 179–186. doi: 10.1055/s-2008-1040928

Cipolla, M. J. (2009). *The Cerebral Circulation.* San Rafael, CA: Morgan and Claypool Life Sciences.

Cireş an, D. C., Meier, U., Masci, J., Gambardella, L. M., and Schmidhuber, J. (2011). "Flexible, high performance convolutional neural networks for image classification," in *Proceedings of the Twenty-Second International Joint Conference on Artificial Intelligence—Volume Two IJCAI'11* (Barcelona, Catalonia, Spain: AAAI Press), 1237–1242.

Cohen, S., and Greenberg, M. E. (2008). Communication between the synapse and the nucleus in neuronal development, plasticity, and disease. *Annu. Rev. Cell Dev. Biol.* 24, 183–209. doi: 10.1146/annurev.cellbio.24.110707.175235

Cole, K. (1949). Dynamic electrical characteristics of the squid axon membrane. *Arch. Sci. Physiol.* 3, 253–258.

Coombs, J., Eccles, J., and Fatt, P. (1953). The action of the inhibitory synaptic transmitter. *Aust. J. Sci.* 16, 1–5.

Coons, A. H., Creech, H. J., and Jones, R. N. (1941). Immunological properties of an antibody containing a fluorescent group. *Proc. Soc. Exp. Biol. Med.* 47, 200–202. doi: 10.3181/00379727-47-13084P

Cowan, W. M., Gottlieb, D. I., Hendrickson, A. E., Price, J. L., and Woolsey, T. A. (1972). The autoradiographic demonstration of axonal connections in the central nervous system. *Brain Res.* 37, 21–51. doi: 10.1016/0006-8993(72)90344-7

Craddock, R. C., Jbabdi, S., Yan, C.-G., Vogelstein, J. T., Castellanos, F. X., Di Martino, A., et al. (2013). Imaging human connectomes at the macroscale. *Nat. Methods* 10, 524–539. doi: 10.1038/nmeth.2482

Craver, C. F. (2009). *Explaining the Brain: Mechanisms and the Mosaic Unity of Neuroscience.* Oxford: Oxford University Press.

Curtis, D. R., and Eccles, J. C. (1960). Synaptic action during and after repetitive stimulation. *J. Physiol.* 150, 374–398. doi: 10.1113/jphysiol.1960.sp006393

D'Angelo, E. (2014). The urgent need for a systems biology approach to neurology. *Funct. Neurol.* 29:221. doi: 10.11138/FNeur/2014.29.4.221

Dale, H. H. (1933). Nomenclature of fibers in the autonomic system and their effects. *J. Physiol.* 80, 10–11.

Damadian, R. (1971). Tumor detection by nuclear magnetic resonance. *Science* 171, 1151–1153. doi: 10.1126/science.171.3976.1151

De Robertis, E. D. P., and Bennett, H. S. (1955). Some features of the submicroscopic morphology of synapses in frog and earthworm. *J. Biophys. Biochem. Cytol.* 1, 47–58. doi: 10.1083/jcb.1.1.47

DeFelipe, J. (2015). The anatomical problem posed by brain complexity and size: a potential solution. *Front. Neuroanat.* 9:104. doi: 10.3389/fnana.2015.00104

Deisseroth, K. (2015). Optogenetics: 10 years of microbial opsins in neuroscience. *Nat. Neurosci.* 18, 1213–1225. doi: 10.1038/nn.4091

Deitcher, Y., Eyal, G., Kanari, L., Verhoog, M. B., Atenekeng Kahou, G. A., Mansvelder, H. D., et al. (2017). Comprehensive morpho-electrotonic analysis shows 2 distinct classes of L2 and L3 pyramidal neurons in human temporal cortex. *Cereb. Cortex* 27, 5398–5414. doi: 10.1093/cercor/bhx226

Deiters, O. (1865). *Untersuchungen über Gehirn und Rückenmark des Menschen und der Säugethiere.* Braunschweig: Vieweg.

Dejerine, J. J. (1892). Contribution a l'étude anatomo-pathologique et clinique des différentes variétés de cécité verbale. *Mém. Soc. Biol.* 4, 61–90.

Delgado, J. M. R., Hamlin, H., and Chapman, W. P. (1952). Technique of intracranial electrode implacement for recording and stimulation and its possible therapeutic value in psychotic patients. *Confin. Neurol.* 12, 315–319. doi: 10.1159/000105792

Deneris, E. S., and Hobert, O. (2014). Maintenance of postmitotic neuronal cell identity. *Nat. Neurosci.* 17, 899–907. doi: 10.1038/nn.3731

Denk, W., and Horstmann, H. (2004). Serial block-face scanning electron microscopy to reconstruct three-dimensional tissue nanostructure. *PLOS Biol.* 2:e329. doi: 10.1371/journal.pbio.0020329

Dennett, D. C. (1993). *Consciousness Explained.* London: Penguin.

Descartes, R. (1905). *Discours de la Méthode : 1637.* Strasbourg: J.H.E. Heitz.

Desimone, R., Albright, T. D., Gross, C. G., and Bruce, C. (1984). Stimulus-selective properties of inferior temporal neurons in the macaque. *J. Neurosci.* 4, 2051–2062. doi: 10.1523/JNEUROSCI.04-08-02051.1984

di Pellegrino, G., Fadiga, L., Fogassi, L., Gallese, V., and Rizzolatti, G. (1992). Understanding motor events: a neurophysiological study. *Exp. Brain Res.* 91, 176–180. doi: 10.1007/bf00230027

Dongarra, J. (2006). Trends in high performance computing: a historical overview and examination of future developments. *IEEE Circ. Dev. Maga.* 22, 22–27. doi: 10.1109/MCD.2006.1598076

Druckmann, S., Berger, T. K., Schürmann, F., Hill, S., Markram, H., and Segev, I. (2011). Effective stimuli for constructing reliable neuron models. *PLoS Comput. Biol.* 7:e1002133. doi: 10.1371/journal.pcbi.1002133

Druckmann, S., Hill, S., Schürmann, F., Markram, H., and Segev, I. (2013). A hierarchical structure of cortical interneuron electrical diversity revealed by automated statistical analysis. *Cereb. Cortex* 23, 2994–3006. doi: 10.1093/cercor/bhs290

du Bois-Reymond, E. (1843). Vorlaufiger abriss einer untersuchung über den sigenannten froschstrom und umber die elektromotorischen fische. *Annl. Phys.* 58, 1–30. doi: 10.1002/andp.18431340102

Dutrochet, H. (1824). *Recherches Anatomiques et Physiologiques sur la Structure Intime des Animaux et des Végétaux, et Sur Leur motilité.* Paris: J.B. Baillière, Libraire.

Eberle, A. L., Mikula, S., Schalek, R., Lichtman, J., Knothe Tate, M. L., and Zeidler, D. (2015). High-resolution, high-throughput imaging with a multibeam scanning electron microscope. *J. Microsc.* 259, 114–120. doi: 10.1111/jmi.12224

Eccles, J. C. (1952). The electrophysiological properties of the motoneurone. *Cold Spring Harb. Symp. Quant. Biol.* 17, 175–183. doi: 10.1101/sqb.1952.017.01.017

Ehrenberg, C. G. (1833). Nothwendigkeit einer feineren mechanischen zerlegung des gehirns und der nerven vor der chemischen, dargestellt aus beobachtungen. *Annalen der Physik* 104, 449–473. doi: 10.1002/andp.18331040702

Ekosi 20 Tesla Project. (2018). Design of a 20 tesla MRI magnet for improved medical imaging. Available online at: http://ekosi.lbl.gov/ [Accessed February 19, 2018].

Erö, C., Gewaltig, M.-O., Keller, D., and Markram, H. (2018). A cell atlas for the mouse brain. *Front. Neuroinform.* 12:84. doi: 10.3389/fninf.2018.00084

Falotico, E., Vannucci, L., Ambrosano, A., Albanese, U., Ulbrich, S., Vasquez Tieck, J. C., et al. (2017). Connecting artificial brains to robots in a comprehensive simulation framework: the neurorobotics platform. *Front. Neurorobot.* 11:2. doi: 10.3389/fnbot.2017.00002

Fatt, P., and Katz, B. (1952). Spontaneous subthreshold activity at motor nerve endings. *J. Physiol.* 117, 109–128.

Feng, G., Mellor, R. H., Bernstein, M., Keller-Peck, C., Nguyen, Q. T., Wallace, M., et al. (2000). Imaging neuronal subsets in transgenic mice expressing multiple spectral variants of GFP. *Neuron* 28, 41–51. doi: 10.1016/s0896-6273(00)00084-2

Ferrier, D. (1875). Experiments on the brain of monkeys—No. I. *Proc. R. Soc. Lond.* 23, 409–430. doi: 10.1098/rspl.1874.0058

Fields, R. D., Woo, D. H., and Basser, P. J. (2015). Glial regulation of the neuronal connectome through local and long-distant communication. *Neuron* 86, 374–386. doi: 10.1016/j.neuron.2015.01.014

Fishell, G., and Heintz, N. (2013). The neuron identity problem: form meets function. *Neuron* 80, 602–612. doi: 10.1016/j.neuron.2013.10.035

Flourens, P. (1842). *Recherches Expérimentales sur les Propriétés et les Fonctions du Système Nerveux Dans les Animaux Vertébrés.* Paris: J.-B. Ballière.

Fodor, J. A. (1975). *The Language of Thought.* Cambridge, Mass: Harvard University Press.

Fontana, F. (1781). *Traité sur le Venin de la Vipère, sur les Poisons Américains, sur le Laurier-Cerise et sur Quelque Autres Poisons Végétaux. . .* Florence, Paris: Nyon l'aîné.

Forel, A.-H. (1887). Einige hirnanatomische betrachtungen und ergebnisse. *Arch. Psychiat. Nervkrankh.* 18, 162–198. doi: 10.1007/bf02034012

Foster, M., and Sherrington, C. S. (1897). *A Text Book of Physiology.* London; New York, NY: MacMillan.

Frackowiak, R. S. (1986). Measurement and imaging of cerebral function in ageing and dementia. *Prog. Brain Res.* 70, 69–85. doi: 10.1016/s0079-6123(08)64298-3

Frackowiak, R. S. (1994). Functional mapping of verbal memory and language. *Trends Neurosci.* 17, 109–115. doi: 10.1016/0166-2236(94)90119-8

Frackowiak, R., and Markram, H. (2015). The future of human cerebral cartography: a novel approach. *Philos. Trans. R. Soc. Lond. B Biol. Sci.* 370:20140171. doi: 10.1098/rstb.2014.0171

Frege, G. (1960). *The foundations of Arithmetic; A Logico-Mathematical Enquiry into the Concept of Number.* New York, NY: Harper.

Frege, G. (1879). *Begriffsschrift: Eine Der Arithmetische Nachgebildete Formelsprache des Reinen Denkens.* Halle: L. Nebert.

Frisoni, G. B., Boccardi, M., Barkhof, F., Blennow, K., Cappa, S., Chiotis, K., et al. (2017). Strategic roadmap for an early diagnosis of Alzheimer's disease based on biomarkers. *Lancet Neurol.* 16, 661–676. doi: 10.1016/S1474-4422(17)30159-X

Friston, K. J. (2011). Functional and effective connectivity: a review. *Brain Connect.* 1, 13–36. doi: 10.1089/brain.2011.0008

Fu, T.-M., Hong, G., Zhou, T., Schuhmann, T. G., Viveros, R. D., and Lieber, C. M. (2016). Stable long-term chronic brain mapping at the single-neuron level. *Nat. Methods* 13, 875–882. doi: 10.1038/nmeth.3969

Furber, S. B., Galluppi, F., Temple, S., and Plana, L. A. (2014). The SpiNNaker project. *Proc. IEEE* 102, 652–665. doi: 10.1109/JPROC.2014.2304638

Gall, F. J., Combe, A., Vimont, J., and Broussais, F. J. V. (1838). *On the Functions of the Cerebellum.* Edinburgh: Maclachlan and Stewart.

Gall, F., and Spurzheim, G. (1810). *Anatomie et Physiologie du Système Nerveux en Général et sur Celui du Cerveau en Particulier.* Paris: Schoell.

Galvani, L. (1791). *De Viribus Electricitatis in Motu Musculari Commentarius.* Bologna: Ex Typographia Instituti Scientiarum.

Gao, Y.-R., Ma, Y., Zhang, Q., Winder, A. T., Liang, Z., Antinori, L., et al. (2017). Time to wake up: studying neurovascular coupling and brain-wide circuit function in the un-anesthetized animal. *Neuroimage* 153, 382–398. doi: 10.1016/j.neuroimage.2016.11.069

Gasser, H. S., and Erlanger, J. (1922). A study of the action currents of nerve with the cathode ray oscillograph. *Am. J. Physiol. Legacy Content* 62, 496–524. doi: 10.1152/ajplegacy.1922.62.3.496

Gazzaniga, M. S., Bogen, J. E., and Sperry, R. W. (1962). Some functional effects of sectioning the cerebral commissures in man. *Proc. Natl. Acad. Sci. U S A* 48, 1765–1769. doi: 10.1073/pnas.48.10.1765

Gehring, T. V., Vasilaki, E., and Giugliano, M. (2015). Highly scalable parallel processing of extracellular recordings of multielectrode arrays. *Conf. Proc. IEEE Eng. Med. Biol. Soc.* 2015, 4178–4181. doi: 10.1109/embc.2015.7319315

Gerstner, W., Kempter, R., van Hemmen, J. L., and Wagner, H. (1996). A neuronal learning rule for sub-millisecond temporal coding. *Nature* 383, 76–81. doi: 10.1038/383076a0

Gerstner, W., Sprekeler, H., and Deco, G. (2012). Theory and simulation in neuroscience. *Science* 338, 60–65. doi: 10.1126/science.1227356

Geschwind, N. (1965a). Disconnexion syndromes in animals and man. I. *Brain* 88, 237–294. doi: 10.1093/brain/88.2.237

Geschwind, N. (1965b). Disconnexion syndromes in animals and man. II. *Brain* 88, 585–644. doi: 10.1093/brain/88.3.585

Glasser, M. F., Smith, S. M., Marcus, D. S., Andersson, J. L. R., Auerbach, E. J., Behrens, T. E. J., et al. (2016). The human connectome project's neuroimaging approach. *Nat. Neurosci.* 19, 1175–1187. doi: 10.1038/nn.4361

Glasser, M. F., Sotiropoulos, S. N., Wilson, J. A., Coalson, T. S., Fischl, B., Andersson, J. L., et al. (2013). The minimal preprocessing pipelines for the human connectome project. *Neuroimage* 80, 105–124. doi: 10.1016/j.neuroimage.2013.04.127

Glasser, M. F., and Van Essen, D. C. (2011). Mapping human cortical areas *in vivo* based on myelin content as revealed by T1- and T2-weighted MRI. *J. Neurosci.* 31, 11597–11616. doi: 10.1523/JNEUROSCI.2180-11.2011

Glover, G. H. (2011). Overview of functional magnetic resonance imaging. *Neurosurg. Clin. N. Am.* 22, 133–139. doi: 10.1016/j.nec.2010.11.001

Goddard, N. H., Hucka, M., Howell, F., Cornelis, H., Shankar, K., and Beeman, D. (2001). Towards NeuroML: model description methods for collaborative modelling in neuroscience. *Philos. Trans. R. Soc. Lond. B Biol. Sci.* 356, 1209–1228. doi: 10.1098/rstb.2001.0910

Golgi, C. (1875). Sulla fina struttura dei bulbiolfattorii. *Riv. Sper. Freniat. Med. Legal.* 1, 66–78.

Golgi, C. (1883). Recherches sur l'histologie des centres nerveux. *Arch. Ital. Biol.* 3, 285–317.

Greene, M. J., Kim, J. S., Seung, H. S., and EyeWirers. (2016). Analogous convergence of sustained and transient inputs in parallel on and off pathways for retinal motion computation. *Cell Rep.* 14, 1892–1900. doi: 10.1016/j.celrep.2016.02.001

Grillner, S., Buchanan, J. T., and Lansner, A. (1988). Simulation of the segmental burst generating network for locomotion in lamprey. *Neurosci. Lett.* 89, 31–35. doi: 10.1016/0304-3940(88)90476-4

Grillner, S., Wallén, P., Brodin, L., and Lansner, A. (1991). Neuronal network generating locomotor behavior in lamprey: circuitry, transmitters, membrane properties, and simulation. *Annu. Rev. Neurosci.* 14, 169–199. doi: 10.1146/annurev.ne.14.030191.001125

Gustafsson, M. G. (2000). Surpassing the lateral resolution limit by a factor of two using structured illumination microscopy. *J. Microsc.* 198, 82–87. doi: 10.1046/j.1365-2818.2000.00710.x

Hagmann, P. (2005). From diffusion MRI to brain connectomics. Available online at: https://infoscience.epfl.ch/record/33696 [Accessed February 27, 2018].

Hall, C. N., Reynell, C., Gesslein, B., Hamilton, N. B., Mishra, A., Sutherland, B. A., et al. (2014). Capillary pericytes regulate cerebral blood flow in health and disease. *Nature* 508, 55–60. doi: 10.1038/nature13165

Harari, Y. N. (2014). *Sapiens: A Brief History of Humankind.* London: Harvill Secker.

Hay, E., and Segev, I. (2015). Dendritic excitability and gain control in recurrent cortical microcircuits. *Cereb. Cortex* 25, 3561–3571. doi: 10.1093/cercor/bhu200

Hebb, D. O. (1949). *The Organization of Behavior: A Neuropsychological Theory.* New York, NY: Wiley.

Heidemann, R. M., Ivanov, D., Trampel, R., Fasano, F., Meyer, H., Pfeuffer, J., et al. (2012). Isotropic submillimeter fMRI in the human brain at 7 T: combining reduced field-of-view imaging and partially parallel acquisitions. *Magn. Reson. Med.* 68, 1506–1516. doi: 10.1002/mrm.24156

Hell, S. W., and Wichmann, J. (1994). Breaking the diffraction resolution limit by stimulated emission: stimulated-emission-depletion fluorescence microscopy. *Opt. Lett.* 19, 780–782. doi: 10.1364/ol.19.000780

Helmstaedter, M., Briggman, K. L., Turaga, S. C., Jain, V., Seung, H. S., and Denk, W. (2013). Connectomic reconstruction of the inner plexiform layer in the mouse retina. *Nature* 500, 168–174. doi: 10.1038/nature12346

Helmstaedter, M., and Mitra, P. (2012). Computational methods and challenges for large-scale circuit mapping. *Curr. Opin. Neurobiol.* 22, 162–169. doi: 10.1016/j.conb.2011.11.010

Hepburn, I., Chen, W., Wils, S., and De Schutter, E. (2012). STEPS: efficient simulation of stochastic reaction-diffusion models in realistic morphologies. *BMC Syst. Biol.* 6:36. doi: 10.1186/1752-0509-6-36

Herculano-Houzel, S. (2012). The remarkable, yet not extraordinary, human brain as a scaled-up primate brain and its associated cost. *Proc. Natl. Acad. Sci. U S A* 109, 10661–10668. doi: 10.1073/pnas.1201895109

Hermundstad, A. M., Brown, K. S., Bassett, D. S., Aminoff, E. M., Frithsen, A., Johnson, A., et al. (2014). Structurally-constrained relationships between cognitive states in the human brain. *PLoS Comput. Biol.* 10:e1003591. doi: 10.1371/journal.pcbi.1003591

Herodotus. (1875). *History of Herodotus.* New York, NY: Scribner.

Hicks, R. D. (1907). *Aristotle De Anima.* Cambridge: Cambridge University Press.

Hill, S. L., Wang, Y., Riachi, I., Schürmann, F., and Markram, H. (2012). Statistical connectivity provides a sufficient foundation for specific functional connectivity in neocortical neural microcircuits. *Proc. Natl. Acad. Sci. U S A* 109, E2885–E2894. doi: 10.1073/pnas.1202128109

Hillman, E. M. C. (2014). Coupling mechanism and significance of the BOLD signal: a status report. *Annu. Rev. Neurosci.* 37, 161–181. doi: 10.1146/annurev-neuro-071013-014111

Hines, M. (1989). A program for simulation of nerve equations with branching geometries. *Int. J. Biomed. Comput.* 24, 55–68. doi: 10.1016/0020-7101(89)90007-x

Hines, M. (1993). "NEURON—a program for simulation of nerve equations," in *Neural Systems: Analysis and Modeling*, ed. F. H. Eeckman (Boston, MA: Springer US), 127–136.

His, W. (1887). Zur Geschichte des menschlichen Rückenmarkes und der Nervenwurzeln. *Abh. K. Sächs. Ges. Wiss. Math-Phys. Classe* 13, 477–514.

Hitzig, E., and Fritsch, G. (1870). Über die elecktrische Erregbarkeit des Grosshirns. *Arch. Anat. Physiol.* 37, 300–332.

Hodgkin, A. L., and Huxley, A. F. (1939). Action potentials recorded from inside a nerve fibre. *Nature* 144, 710–711. doi: 10.1038/144710a0

Hodgkin, A. L., and Huxley, A. F. (1952). A quantitative description of membrane current and its application to conduction and excitation in nerve. *J. Physiol.* 117, 500–544. doi: 10.1113/jphysiol.1952.sp004764

Holtmaat, A., and Svoboda, K. (2009). Experience-dependent structural synaptic plasticity in the mammalian brain. *Nat. Rev. Neurosci.* 10, 647–658. doi: 10.1038/nrn2721

Hong, W., Kennedy, A., Burgos-Artizzu, X. P., Zelikowsky, M., Navonne, S. G., Perona, P., et al. (2015). Automated measurement of mouse social behaviors using depth sensing, video tracking and machine learning. *Proc. Natl. Acad. Sci. U S A* 112, E5351–E5360. doi: 10.1073/pnas.1515982112

Hooker, C. A. (1981a). Towards a general theory of reduction. Part I: historical and scientific setting. *Dialogue* 20, 38–59. doi: 10.1017/s0012217300023088

Hooker, C. A. (1981b). Towards a general theory of reduction. Part II: identity in reduction. *Dialoguephilosophie* 20, 201–236. doi: 10.1017/s0012217300023301

Hooker, C. A. (1981c). Towards a general theory of reduction. Part III: cross-categorical reduction. *Dialogue* 20, 496–529. doi: 10.1017/s0012217300023593

Hopfield, J. J. (1982). Neural networks and physical systems with emergent collective computational abilities. *Proc. Natl. Acad. Sci. U S A* 79, 2554–2558. doi: 10.1073/pnas.79.8.2554

Huang, B., Babcock, H., and Zhuang, X. (2010). Breaking the diffraction barrier: super-resolution imaging of cells. *Cell* 143, 1047–1058. doi: 10.1016/j.cell.2010.12.002

Hubel, D. H. (1957). Tungsten microelectrode for recording from single units. *Science* 125, 549–550. doi: 10.1126/science.125.3247.549

Hubel, D. H., and Wiesel, T. N. (1962). Receptive fields, binocular interaction and functional architecture in the cat's visual cortex. *J. Physiol.* 160, 106–154. doi: 10.1113/jphysiol.1962.sp006837

Iadecola, C., and Nedergaard, M. (2007). Glial regulation of the cerebral microvasculature. *Nat. Neurosci.* 10, 1369–1376. doi: 10.1038/nn2003

IBM Archives. (2003). System/370 Model 168. Available online at: http://www-03.ibm.com/ibm/history/exhibits/mainframe/mainframe_PP3168.html [Accessed March 10, 2018].

Insel, T. R., Landis, S. C., and Collins, F. S. (2013). Research priorities. The NIH BRAIN initiative. *Science* 340, 687–688. doi: 10.1126/science.1239276

Jackson, J. H. (1870). A study of convulsions. *Trans. St. Andrew's Med. Grad. Assoc.* 3, 162–204.

Jolivet, R., Coggan, J. S., Allaman, I., and Magistretti, P. J. (2015). Multi-timescale modeling of activity-dependent metabolic coupling in the neuron-glia-vasculature ensemble. *PLoS Comput. Biol.* 11:e1004036. doi: 10.1371/journal.pcbi.1004036

Jones, D. K., Knösche, T. R., and Turner, R. (2013). White matter integrity, fiber count and other fallacies: the do's and don'ts of diffusion MRI. *Neuroimage* 73, 239–254. doi: 10.1016/j.neuroimage.2012.06.081

Kalisman, N., Silberberg, G., and Markram, H. (2005). The neocortical microcircuit as a tabula rasa. *Proc. Natl. Acad. Sci. U S A* 102, 880–885. doi: 10.1073/pnas.0407088102

Kanari, L., Dotko, P., Scolamiero, M., Levi, R., Shillcock, J., Hess, K., et al. (2018). A topological representation of branching neuronal morphologies. *Neuroinformatics* 16, 3–13. doi: 10.1007/s12021-017-9341-1

Ke, R., Mignardi, M., Pacureanu, A., Svedlund, J., Botling, J., Wählby, C., et al. (2013). *In situ* sequencing for RNA analysis in preserved tissue and cells. *Nat. Methods* 10, 857–860. doi: 10.1038/nmeth.2563

Khazen, G., Hill, S. L., Schürmann, F., and Markram, H. (2012). Combinatorial expression rules of ion channel genes in juvenile rat (Rattus norvegicus) neocortical neurons. *PLoS One* 7:e34786. doi: 10.1371/journal.pone.0034786

Kim, J. S., Greene, M. J., Zlateski, A., Lee, K., Richardson, M., Turaga, S. C., et al. (2014). Space-time wiring specificity supports direction selectivity in the retina. *Nature* 509, 331–336. doi: 10.1038/nature13240

Koch, C., Massimini, M., Boly, M., and Tononi, G. (2016). Neural correlates of consciousness: progress and problems. *Nat. Rev. Neurosci.* 17, 307–321. doi: 10.1038/nrn.2016.22

Koelsch, S. (2014). Brain correlates of music-evoked emotions. *Nat. Rev. Neurosci.* 15, 170–180. doi: 10.1038/nrn3666

Kristensson, K. (1970). Transport of fluorescent protein tracer in peripheral nerves. *Acta Neuropathol.* 16, 293–300. doi: 10.1007/bf00686894

Kristensson, K., and Olsson, Y. (1971). Uptake and retrograde axonal transport of peroxidase in hypoglossal neurones. *Acta Neuropathol.* 19, 1–9. doi: 10.1007/bf00690948

Kuhlman, S. J., and Huang, Z. J. (2008). High-resolution labeling and functional manipulation of specific neuron types in mouse brain by Cre-activated viral gene expression. *PLoS One* 3:e2005. doi: 10.1371/journal.pone.0002005

Kwong, K. K., Belliveau, J. W., Chesler, D. A., Goldberg, I. E., Weisskoff, R. M., Poncelet, B. P., et al. (1992). Dynamic magnetic resonance imaging of human brain activity during primary sensory stimulation. *Proc. Natl. Acad. Sci. U S A* 89, 5675–5679. doi: 10.1073/pnas.89.12.5675

Lamb, W. R. M. (1925). "Timaeus," in *Plato in Twelve Volumes*, (Cambridge, MA: Harvard University Press), 81e6–82b1.

Lapicque, L. (1907). Recherches quantitatives sur l'excitation électrique des nerfs traitée comme une polarization. *J. Physiol. Pathol. Générale* 620–635.

Lauterbur, P. C. (1973). Image formation by induced local interactions: examples employing nuclear magnetic resonance. *Nature* 242, 190–191. doi: 10.1038/242190a0

LaVail, J. H., and LaVail, M. M. (1972). Retrograde axonal transport in the central nervous system. *Science* 176, 1416–1417. doi: 10.1126/science.176.4042.1416

Le Bihan, D., and Breton, E. (1985). Imagerie de diffusion *in vivo* par résonance magnétique nucléaire. *C. R. Académie Sci.* 93, 27–34.

Le Bihan, D., Breton, E., Lallemand, D., Grenier, P., Cabanis, E., and Laval-Jeantet, M. (1986). MR imaging of intravoxel incoherent motions: application to diffusion and perfusion in neurologic disorders. *Radiology* 161, 401–407. doi: 10.1148/radiology.161.2.3763909

Le Bihan, D., and Iima, M. (2015). Diffusion magnetic resonance imaging: what water tells us about biological tissues. *PLoS Biol.* 13:e1002203. doi: 10.1371/journal.pbio.1002203

Le Bihan, D., and Johansen-Berg, H. (2012). Diffusion MRI at 25: exploring brain tissue structure and function. *Neuroimage* 61, 324–341. doi: 10.1016/j.neuroimage.2011.11.006

Lee, J. H., Daugharthy, E. R., Scheiman, J., Kalhor, R., Yang, J. L., Ferrante, T. C., et al. (2014). Highly multiplexed subcellular RNA sequencing *in situ*. *Science* 343, 1360–1363. doi: 10.1126/science.1250212

Lewis, W. B. (1878). On the comparative structure of the cortex cerebri. *Brain* 1, 79–96. doi: 10.1093/brain/1.1.79

Lichtman, J. W., Livet, J., and Sanes, J. R. (2008). A technicolour approach to the connectome. *Nat. Rev. Neurosci.* 9, 417–422. doi: 10.1038/nrn2391

Lima, S. Q., and Miesenböck, G. (2005). Remote control of behavior through genetically targeted photostimulation of neurons. *Cell* 121, 141–152. doi: 10.1016/j.cell.2005.02.004

Ling, G., and Gerard, R. W. (1949). The normal membrane potential of frog sartorius fibers. *J. Cell. Comp. Physiol.* 34, 383–396. doi: 10.1002/jcp.1030340304

Livet, J., Weissman, T. A., Kang, H., Draft, R. W., Lu, J., Bennis, R. A., et al. (2007). Transgenic strategies for combinatorial expression of fluorescent proteins in the nervous system. *Nature* 450, 56–62. doi: 10.1038/nature06293

Locke, J. (1689). *An Essay Concerning Human Understanding*. Oxford: Oxford University Press.

Loebel, A., Le Bé, J.-V., Richardson, M. J. E., Markram, H., and Herz, A. V. M. (2013). Matched pre- and post-synaptic changes underlie synaptic plasticity over long time scales. *J. Neurosci.* 33, 6257–6266. doi: 10.1523/jneurosci.3740-12.2013

Loewi, O. (1921). Über humorale Übertragbarkeit der Herznervenwirkung. *Pflügers Arch.* 189, 239–242.

Lorente de Nó, R. (1935). The electrical excitability of the motoneurones. *J. Cell. Comp. Physiol.* 7, 47–71. doi: 10.1002/jcp.1030070104

Lowe, M. J., Sakaie, K. E., Beall, E. B., Calhoun, V. D., Bridwell, D. A., Rubinov, M., et al. (2016). Modern methods for interrogating the human connectome. *J. Int. Neuropsychol. Soc.* 22, 105–119. doi: 10.1017/s1355617716000060

Lozano, A. M., and Lipsman, N. (2013). Probing and regulating dysfunctional circuits using deep brain stimulation. *Neuron* 77, 406–424. doi: 10.1016/j.neuron.2013.01.020

Maccione, A., Gandolfo, M., Zordan, S., Amin, H., Di Marco, S., Nieus, T., et al. (2015). Microelectronics, bioinformatics and neurocomputation for massive

neuronal recordings in brain circuits with large scale multielectrode array probes. *Brain Res. Bull.* 119, 118–126. doi: 10.1016/j.brainresbull.2015.07.008

Maguire, E. A., Gadian, D. G., Johnsrude, I. S., Good, C. D., Ashburner, J., Frackowiak, R. S. J., et al. (2000). Navigation-related structural change in the hippocampi of taxi drivers. *Proc. Natl. Acad. Sci. U S A* 97, 4398–4403. doi: 10.1073/pnas.070039597

Maier-Hein, K. H., Neher, P. F., Houde, J.-C., Côté, M.-A., Garyfallidis, E., Zhong, J., et al. (2017). The challenge of mapping the human connectome based on diffusion tractography. *Nat. Commun.* 8:1349. doi: 10.1038/s41467-017-01285-x

Malpighi, M., and Fracassati, C. (1669). *Epistolæ Anatomicæ Virorum Clarissimorum.* Amsterdam: Casparum Commelinum.

Marc, R. E., Jones, B. W., Watt, C. B., Anderson, J. R., Sigulinsky, C., and Lauritzen, S. (2013). Retinal connectomics: towards complete, accurate networks. *Prog. Retin. Eye Res.* 37, 141–162. doi: 10.1016/j.preteyeres.2013.08.002

Margulies, D. S., Böttger, J., Watanabe, A., and Gorgolewski, K. J. (2013). Visualizing the human connectome. *Neuroimage* 80, 445–461. doi: 10.1016/j.neuroimage.2013.04.111

Markram, H. (2006). The blue brain project. *Nat. Rev. Neurosci.* 7, 153–160. doi: 10.1038/nrn1848

Markram, H., Muller, E., Ramaswamy, S., Reimann, M. W., Abdellah, M., Sanchez, C. A., et al. (2015). Reconstruction and simulation of neocortical microcircuitry. *Cell* 163, 456–492. doi: 10.1016/j.cell.2015.09.029

Markram, H., and Sakmann, B. (1995). Action potentials propogating back into dendrites triggers changes in efficacy of single-axon synapses between layer V pyramidal cells. *Soc. Neurosci. Abstr.* 21:2007.

Markram, H., Toledo-Rodriguez, M., Wang, Y., Gupta, A., Silberberg, G., and Wu, C. (2004). Interneurons of the neocortical inhibitory system. *Nat. Rev. Neurosci.* 5, 793–807. doi: 10.1038/nrn1519

Markram, H., and Tsodyks, M. (1996). Redistribution of synaptic efficacy between neocortical pyramidal neurons. *Nature* 382, 807–810. doi: 10.1038/382807a0

Marmont, G. (1949). Studies on the axon membrane. I. A new method. *J. Cell. Comp. Physiol.* 34, 351–382. doi: 10.1002/jcp.1030340303

Marr, D. (1982). *Vision: A Computational Investigation into the Human Representation and Processing of Visual Information.* San Francisco, CA: W.H. Freeman.

Masters, R. C., Pearson, A. J., Glen, T. S., Sasam, F.-C., Li, L., Dapor, M., et al. (2015). Sub-nanometre resolution imaging of polymer-fullerene photovoltaic blends using energy-filtered scanning electron microscopy. *Nat. Commun.* 6:6928. doi: 10.1038/ncomms7928

McCulloch, W. S., and Pitts, W. (1943). A logical calculus of the ideas immanent in nervous activity. *Bull. Math. Biol.* 5, 115–133. doi: 10.1007/BF02478259

McNab, J. A., Edlow, B. L., Witzel, T., Huang, S. Y., Bhat, H., Heberlein, K., et al. (2013). The human connectome project and beyond: initial applications of 300 mT/m gradients. *Neuroimage* 80, 234–245. doi: 10.1016/j.neuroimage.2013.05.074

Mead, C. (1990). Neuromorphic electronic systems. *Proc. IEEE* 78, 1629–1636. doi: 10.1109/5.58356

Medaglia, J. D., Lynall, M.-E., and Bassett, D. S. (2015). Cognitive network neuroscience. *J. Cogn. Neurosci.* 27, 1471–1491. doi: 10.1162/jocn_a_00810

Meynert, T. (1867). Der Bau der Gross- Hirnrinde und seine örtlichen Ver- schiedenheiten, nebst einem patholo- gisch-anatomischen Corollarium. *Vierteljahresschr Psychiatr* 1, 77–93, 1, 198–217, 2, 88–113.

Meynert, T. (1871). *Vom Gerhirne der Säugethiere. In: Stricker S, ed, Handbuch der Lehre von den Geweben des Menschen und der Thiere.* Leipzig: Englemann.

Migliore, M., and Shepherd, G. M. (2005). Opinion: an integrated approach to classifying neuronal phenotypes. *Nat. Rev. Neurosci.* 6, 810–818. doi: 10.1038/nrn1769

Miller, G. (2008). Neuroimaging. Growing pains for fMRI. *Science* 320, 1412–1414. doi: 10.1126/science.320.5882.1412

Min Jou, W., Haegeman, G., Ysebaert, M., and Fiers, W. (1972). Nucleotide sequence of the gene coding for the bacteriophage MS2 coat protein. *Nature* 237, 82–88. doi: 10.1038/237082a0

Monyer, H., and Markram, H. (2004). Interneuron diversity series: molecular and genetic tools to study GABAergic interneuron diversity and function. *Trends Neurosci.* 27, 90–97. doi: 10.1016/j.tins.2003.12.008

Moran, D. (2010). Evolution of brain-computer interface: action potentials, local field potentials and electrocorticograms. *Curr. Opin. Neurobiol.* 20, 741–745. doi: 10.1016/j.conb.2010.09.010

Morgan, J. L., and Lichtman, J. W. (2013). Why not connectomics? *Nat. Methods* 10, 494–500. doi: 10.1038/nmeth.2480

Mulcahy, B., Witvliet, D., Holmyard, D., Mitchell, J., Chisholm, A. D., Meirovitch, Y., et al. (2018). A pipeline for volume electron microscopy of the *Caenorhabditis elegans* nervous system. *Front. Neural Circuits* 12:94. doi: 10.3389/fncir.2018.00094

Munk, H. (1890). Of the visual area of the cerebral cortex and its relation to eye movements. *Brain* 13, 45–67. doi: 10.1093/brain/13.1.45

Nagel, T. (1974). What Is It Like to Be a Bat? *Philos. Rev.* 83, 435–450. doi: 10.2307/2183914

Neher, E., and Sakmann, B. (1976). Single-channel currents recorded from membrane of denervated frog muscle fibres. *Nature* 260, 799–802. doi: 10.1038/260799a0

Neurath, O. (1932). Protokollsätze. *Erkenntnis* 3, 204–214. doi: 10.1007/BF01886420

Nissl, F. (1894). Über die sogenannten Granula der Nervenzellen. *Neurol. Centrbl.* 13, 676–683, 781–789, 810–814.

November. (2018). TOP500 supercomputer sites. Available online at: https://www.top500.org/lists/2018/11/ [Accessed January 8, 2019].

O'Keefe, J., and Dostrovsky, J. (1971). The hippocampus as a spatial map. Preliminary evidence from unit activity in the freely-moving rat. *Brain Res.* 34, 171–175. doi: 10.1016/0006-8993(71)90358-1

Ogawa, S., Lee, T. M., Kay, A. R., and Tank, D. W. (1990). Brain magnetic resonance imaging with contrast dependent on blood oxygenation. *Proc. Natl. Acad. Sci. U S A* 87, 9868–9872. doi: 10.1073/pnas.87.24.9868

Ogawa, S., Tank, D. W., Menon, R., Ellermann, J. M., Kim, S. G., Merkle, H., et al. (1992). Intrinsic signal changes accompanying sensory stimulation: functional brain mapping with magnetic resonance imaging. *Proc. Natl. Acad. Sci. U S A* 89, 5951–5955. doi: 10.1073/pnas.89.13.5951

Ogle, W. (1911). *Aristotle De Partibus Animalium.* Oxford: Clarendon Press.

Oh, S. W., Harris, J. A., Ng, L., Winslow, B., Cain, N., Mihalas, S., et al. (2014). A mesoscale connectome of the mouse brain. *Nature* 508, 207–214. doi: 10.1038/nature13186

Oyibo, H., Cao, C., Ferrante, D. D., Zhan, H., Koulakov, A., Enquist, L., et al. (2018). A computational framework for converting high-throughput DNA sequencing data into neural circuit connectivity. *bioRxiv* [Preprint]. doi: 10.1101/244079

Palade, G. E., and Palay, S. L. (1954). Electron microscope observations of interneuronal and neuromuscular synapses. *Anat. Rec.* 118, 335–336.

Panizza, B. (1855). Osservazioni sul nervo ottico. *Gior. I. R. Ist Lomb. Sci. Lett. Arti.* 7, 237–252.

Papyrus of Ani. (1250 BC). Book of the dead. Available online at: https://www.britishmuseum.org/research/collection_online/collection_object_details.aspx?objectId=113335andpartId=1 [Accessed April 20, 2018].

Pausanias. (1918). *Description of Greece.* Cambridge, MA: Harvard University Press.

Penfield, W., and Boldrey, E. (1937). Somatic motor and sensory representation in the cerebral cortex of man as studied by electrical stimulation. *Brain* 60, 389–443. doi: 10.1093/brain/60.4.389

Perin, R., Berger, T. K., and Markram, H. (2011). A synaptic organizing principle for cortical neuronal groups. *Proc. Natl. Acad. Sci. U S A* 108, 5419–5424. doi: 10.1073/pnas.1016051108

Plaza, S. M., Scheffer, L. K., and Chklovskii, D. B. (2014). Toward large-scale connectome reconstructions. *Curr. Opin. Neurobiol.* 25, 201–210. doi: 10.1016/j.conb.2014.01.019

Poulin, J.-F., Tasic, B., Hjerling-Leffler, J., Trimarchi, J. M., and Awatramani, R. (2016). Disentangling neural cell diversity using single-cell transcriptomics. *Nat. Neurosci.* 19, 1131–1141. doi: 10.1038/nn.4366

Prasher, D. C., Eckenrode, V. K., Ward, W. W., Prendergast, F. G., and Cormier, M. J. (1992). Primary structure of the Aequorea victoria green-fluorescent protein. *Gene* 111, 229–233. doi: 10.1016/0378-1119(92)90691-H

Prinz, J. (2007). *The Emotional Construction of Morals.* Oxford: Oxford University Press.

Putnam, H. (1965). "Brains and behavior," in *Analytical Philosophy* ed. R. J. Butler (Oxford: Blackwell) 1–20.

Qian, C., Masad, I. S., Rosenberg, J. T., Elumalai, M., Brey, W. W., Grant, S. C., et al. (2012). A volume birdcage coil with an adjustable sliding tuner ring for neuroimaging in high field vertical magnets: *ex* and *in vivo* applications at 21.1T. *J. Magn. Reson.* 221, 110–116. doi: 10.1016/j.jmr.2012.05.016

Quettier, L., Aubert, G., Belorgey, J., Berriaud, C., Bourquard, A., Bredy, P., et al. (2017). Iseult/INUMAC whole body 11.7 T MRI magnet. *IEEE Trans. Appl. Supercond.* 27, 1–4. doi: 10.1109/TASC.2016.2627501

Raj, A., and van Oudenaarden, A. (2008). Nature, nurture, or chance: stochastic gene expression and its consequences. *Cell* 135, 216–226. doi: 10.1016/j.cell.2008.09.050

Rall, W. (1959). Branching dendritic trees and motoneuron membrane resistivity. *Exp. Neurol.* 1, 491–527. doi: 10.1016/0014-4886(59)90046-9

Rall, W. (1962). Electrophysiology of a dendritic neuron model. *Biophys. J.* 2, 145–167. doi: 10.1016/s0006-3495(62)86953-7

Rall, W., and Shepherd, G. M. (1968). Theoretical reconstruction of field potentials and dendrodendritic synaptic interactions in olfactory bulb. *J. Neurophysiol.* 31, 884–915. doi: 10.1152/jn.1968.31.6.884

Ramaswamy, S., Hill, S. L., King, J. G., Schürmann, F., Wang, Y., and Markram, H. (2012). Intrinsic morphological diversity of thick-tufted layer 5 pyramidal neurons ensures robust and invariant properties of in silico synaptic connections. *J. Physiol.* 590, 737–752. doi: 10.1113/jphysiol.2011.219576

Ramaswamy, S., and Markram, H. (2018). Data-driven modeling of cholinergic modulation of neural microcircuits: bridging neurons, synapses and network states. *bioRxiv [Preprint]*.323865. doi: 10.1101/323865

Ramón y Cajal, S. (1888). Estructura de los centros nerviosos de las aves. *Rev. trimest. Histol. Norm. Patol.* 1, 305–315.

Ramón y Cajal, S. (1894). The Croonian lecture.—La fine structure des centres nerveux . *Proc. R. Soc. Lond.* 55, 444–468. doi: 10.1098/rspl.1894.0063

Ramón y Cajal, S. (1909). *Histologie du Système Nerveux de l'homme et des Vertébrés.* Paris: Maloine.

Ramón y Cajal, S. (1917). *Recuerdos de mi vida.* Madrid: Madrid Imprenta y Librería de N. Moya.

Reimann, M. W., Anastassiou, C. A., Perin, R., Hill, S. L., Markram, H., and Koch, C. (2013). A biophysically detailed model of neocortical local field potentials predicts the critical role of active membrane currents. *Neuron* 79, 375–390. doi: 10.1016/j.neuron.2013.05.023

Reimann, M. W., Horlemann, A.-L., Ramaswamy, S., Muller, E. B., and Markram, H. (2017a). Morphological diversity strongly constrains synaptic connectivity and plasticity. *Cereb. Cortex* 27, 4570–4585. doi: 10.1093/cercor/bhx150

Reimann, M. W., Nolte, M., Scolamiero, M., Turner, K., Perin, R., Chindemi, G., et al. (2017b). Cliques of neurons bound into cavities provide a missing link between structure and function. *Front. Comput. Neurosci.* 11:48. doi: 10.3389/fncom.2017.00048

Reimann, M. W., King, J. G., Muller, E. B., Ramaswamy, S., and Markram, H. (2015). An algorithm to predict the connectome of neural microcircuits. *Front. Comput. Neurosci.* 9:120. doi: 10.3389/fncom.2015.00120

Remak, R. (1836). Vorläufige Mittheilung microscopischer Beobachtungen über den innern Bau der Cerebrospinalnerven und über die Entwicklung ihrer Formelemente. *Müllers Arch. Anat. Physiol. wiss. Med.* 145–161.

Robie, A. A., Seagraves, K. M., Egnor, S. E. R., and Branson, K. (2017). Machine vision methods for analyzing social interactions. *J. Exp. Biol.* 220, 25–34. doi: 10.1242/jeb.142281

Robitaille, P. M., Warner, R., Jagadeesh, J., Abduljalil, A. M., Kangarlu, A., Burgess, R. E., et al. (1999). Design and assembly of an 8 tesla whole-body MR scanner. *J. Comput. Assist. Tomogr.* 23, 808–820. doi: 10.1097/00004728-199911000-00002

Roelfsema, P. R., and Holtmaat, A. (2018). Control of synaptic plasticity in deep cortical networks. *Nat. Rev. Neurosci.* 19, 166–180. doi: 10.1038/nrn.2018.6

Rosenblatt, F. (1957). *The Perceptron, a Perceiving and Recognizing Automaton Project Para.* New York, NY: Cornell Aeronautical Laboratory.

Ruska, E. (1993). "The development of the electron microscope and of electron microscopy," in *Nobel Lectures, Physics 1981–1990*, eds T. Frängsmyr and G. Ekspong (Singapore: World Scientific Publishing Co.), 355–380.

Sawada, H., Shimura, N., Hosokawa, F., Shibata, N., and Ikuhara, Y. (2015). Resolving 45-pm-separated Si-Si atomic columns with an aberration-corrected STEM. *Microscopy* 64, 213–217. doi: 10.1093/jmicro/dfv014

Saygin, Z. M., Osher, D. E., Norton, E. S., Youssoufian, D. A., Beach, S. D., Feather, J., et al. (2016). Connectivity precedes function in the development of the visual word form area. *Nat. Neurosci.* 19, 1250–1255. doi: 10.1038/nn.4354

Schalek, R., Kasthuri, N., Hayworth, K., Berger, D., Tapia, J., Morgan, J., et al. (2011). Development of high-throughput, high-resolution 3d reconstruction of large-volume biological tissue using automated tape collection ultramicrotomy and scanning electron microscopy. *Microsc. Microanal.* 17, 966–967. doi: 10.1017/s1431927611005708

Scheltens, P., Blennow, K., Breteler, M. M. B., de Strooper, B., Frisoni, G. B., Salloway, S., et al. (2016). Alzheimer's disease. *Lancet* 388, 505–517. doi: 10.1016/S0140-6736(15)01124-1

Schilling, K., Gao, Y., Janve, V., Stepniewska, I., Landman, B. A., and Anderson, A. W. (2018). Confirmation of a gyral bias in diffusion MRI fiber tractography. *Hum. Brain Mapp.* 39, 1449–1466. doi: 10.1002/hbm.23936

Schreiner, D., Savas, J. N., Herzog, E., Brose, N., and de Wit, J. (2017). Synapse biology in the "circuit-age"—paths towards molecular connectomics. *Curr. Opin. Neurobiol.* 42, 102–110. doi: 10.1016/j.conb.2016.12.004

Schröter, M., Paulsen, O., and Bullmore, E. T. (2017). Micro-connectomics: probing the organization of neuronal networks at the cellular scale. *Nat. Rev. Neurosci.* 18, 131–146. doi: 10.1038/nrn.2016.182

Searle, J. R. (1992). *The Rediscovery of the Mind.* Cambridge, MA: MIT Press.

Segev, I., and London, M. (2000). Untangling dendrites with quantitative models. *Science* 290, 744–750. doi: 10.1126/science.290.5492.744

Segev, I., and Rall, W. (1998). Excitable dendrites and spines: earlier theoretical insights elucidate recent direct observations. *Trends Neurosci.* 21, 453–460. doi: 10.1016/s0166-2236(98)01327-7

Shapiro, E., Biezuner, T., and Linnarsson, S. (2013). Single-cell sequencing-based technologies will revolutionize whole-organism science. *Nat. Rev. Genet.* 14, 618–630. doi: 10.1038/nrg3542

Shen, H. (2013). Neurotechnology: BRAIN storm. *Nature* 503, 26–28. doi: 10.1038/503026a

Shen, E. H., Overly, C. C., and Jones, A. R. (2012). The allen human brain atlas: comprehensive gene expression mapping of the human brain. *Trends Neurosci.* 35, 711–714. doi: 10.1016/j.tins.2012.09.005

Shepherd, G. M., and Brayton, R. K. (1979). Computer simulation of a dendrodendritic synaptic circuit for self- and lateral-inhibition in the olfactory bulb. *Brain Res.* 175, 377–382. doi: 10.1016/0006-8993(79)91020-5

Sherrington, C. S. (1897). Double (antidrome) conduction in the central nervous system. *Proc. R. Soc. Lond.* 61, 243–246. doi: 10.1098/rspl.1897.0031

Sporns, O. (2013a). Making sense of brain network data. *Nat. Methods* 10, 491–493. doi: 10.1038/nmeth.2485

Sporns, O. (2013b). The human connectome: origins and challenges. *Neuroimage* 80, 53–61. doi: 10.1016/j.neuroimage.2013.03.023

Sporns, O. (2014). Contributions and challenges for network models in cognitive neuroscience. *Nat. Neurosci.* 17, 652–660. doi: 10.1038/nn.3690

Sporns, O. (2016). "Connectome Networks: from Cells to Systems," in *Micro-, Meso- and Macro-Connectomics of the Brain*, eds H. Kennedy, D. C. Van Essen and Y. Christen (Cham, CH: Springer), 107–127.

Sporns, O., Tononi, G., and Kötter, R. (2005). The human connectome: a structural description of the human brain. *PLoS Comput. Biol.* 1:e42. doi: 10.1371/journal.pcbi.0010042

Staffler, B., Berning, M., Boergens, K. M., Gour, A., Smagt, P., and Helmstaedter, M. (2017). SynEM, automated synapse detection for connectomics. *Elife* 6:e26414. doi: 10.7554/elife.26414

Stiles, J. R., Van Helden, D., Bartol, T. M., Salpeter, E. E., and Salpeter, M. M. (1996). Miniature endplate current rise times less than 100 microseconds from improved dual recordings can be modeled with passive acetylcholine diffusion from a synaptic vesicle. *Proc. Natl. Acad. Sci. U S A* 93, 5747–5752. doi: 10.1073/pnas.93.12.5747

Strumwasser, F. (1958). Long-term recording from single neurons in brain of unrestrained mammals. *Science* 127, 469–470. doi: 10.1126/science.127.3296.469

Stucht, D., Danishad, K. A., Schulze, P., Godenschweger, F., Zaitsev, M., and Speck, O. (2015). Highest resolution *in vivo* human brain MRI using

prospective motion correction. *PLoS One* 10:e0133921. doi: 10.1371/journal.pone.0133921

Südhof, T. C. (2017). Molecular neuroscience in the 21stcentury: a personal perspective. *Neuron* 96, 536–541. doi: 10.1016/j.neuron.2017.10.005

Swanson, L. W., and Lichtman, J. W. (2016). From cajal to connectome and beyond. *Annu. Rev. Neurosci.* 39, 197–216. doi: 10.1146/annurev-neuro-071714-033954

Tannery, P. (1887). "Théophraste, sur les sensations," in *Pour L'histoire de la Science Hellène*, (Paris: Felix Alcan), 341–368.

Tavor, I., Parker Jones, O., Mars, R. B., Smith, S. M., Behrens, T. E., and Jbabdi, S. (2016). Task-free MRI predicts individual differences in brain activity during task performance. *Science* 352, 216–220. doi: 10.1126/science.aad8127

The FACETS Project. (2018). Available online at: https://facets.kip.uni-heidelberg.de/ [Accessed March 10, 2018].

The Lancet. (2016). Alzheimer's disease: expedition into the unknown. *Lancet* 388:2713. doi: 10.1016/S0140-6736(16)32457-6

Thomson, W. (1857). On peristaltic induction of electric currents. *Proc. R. Soc. Lond.* 8, 121–132. doi: 10.1098/rspl.1856.0038

Tiesinga, P., Bakker, R., Hill, S., and Bjaalie, J. G. (2015). Feeding the human brain model. *Curr. Opin. Neurobiol.* 32, 107–114. doi: 10.1016/j.conb.2015.02.003

Todd, J. G., Kain, J. S., and de Bivort, B. L. (2017). Systematic exploration of unsupervised methods for mapping behavior. *Phys. Biol.* 14:015002. doi: 10.1088/1478-3975/14/1/015002

Toledo-Rodriguez, M., Blumenfeld, B., Wu, C., Luo, J., Attali, B., Goodman, P., et al. (2004). Correlation maps allow neuronal electrical properties to be predicted from single-cell gene expression profiles in rat neocortex. *Cereb. Cortex* 14, 1310–1327. doi: 10.1093/cercor/bhh092

Traub, R. D., Contreras, D., Cunningham, M. O., Murray, H., LeBeau, F. E. N., Roopun, A., et al. (2005). Single-column thalamocortical network model exhibiting gamma oscillations, sleep spindles and epileptogenic bursts. *J. Neurophysiol.* 93, 2194–2232. doi: 10.1152/jn.00983.2004

Traub, R. D., Miles, R., and Wong, R. K. S. (1988). Large scale simulations of the hippocampus. *IEEE Eng. Med. Biol. Mag.* 7, 31–38. doi: 10.1109/51.20378

Traub, R. D., and Wong, R. K. (1982). Cellular mechanism of neuronal synchronization in epilepsy. *Science* 216, 745–747. doi: 10.1126/science.7079735

Tsodyks, M. V., and Markram, H. (1997). The neural code between neocortical pyramidal neurons depends on neurotransmitter release probability. *Proc. Natl. Acad. Sci. U S A* 94, 719–723. doi: 10.1073/pnas.94.2.719

Türck, L. (1849). Mikroskopischer befund des Rückenmarkes eines paraplegischen weibes. *Z. für die Gesellschaft der Arzte zu Wien* 5, 173–176.

Turner, R., and Geyer, S. (2014). Introduction to the NeuroImage special issue: "*in vivo* Brodmann mapping of the human brain". *Neuroimage* 93, 155–156. doi: 10.1016/j.neuroimage.2014.01.018

Uğurbil, K., Xu, J., Auerbach, E. J., Moeller, S., Vu, A., Duarte-Carvajalino, J. M., et al. (2013). Pushing spatial and temporal resolution for functional and diffusion MRI in the human connectome project. *Neuroimage* 80, 80–104. doi: 10.1016/j.neuroimage.2013.05.012

Uhlmann, V., Ramdya, P., Delgado-Gonzalo, R., Benton, R., and Unser, M. (2017). FlyLimbTracker: an active contour based approach for leg segment tracking in unmarked, freely behaving *Drosophila*. *PLoS One* 12:e0173433. doi: 10.1371/journal.pone.0173433

Urban, A., and Rossier, J. (2012). Genetic targeting of specific neuronal cell types in the cerebral cortex. *Prog. Brain Res.* 196, 163–192. doi: 10.1016/B978-0-444-59426-6.00009-4

Valentin, G. (1836). Über den Verlauf und die letzten Enden der Nerven. *Nova Acta Phys-Med. Acad. Leopoldina, Breslau* 18, 51–240.

Van Essen, D. C. (2013). Cartography and Connectomes. *Neuron* 80, 775–790. doi: 10.1016/j.neuron.2013.10.027

Van Essen, D. C., Jbabdi, S., Sotiropoulos, S. N., Chen, C., Dikranian, K., Coalson, T., et al. (2014). "Mapping connections in humans and non-human primates: aspirations and challenges for diffusion imaging," in *Diffusion MRI*, eds H. Johansen-Berg and T. E. J. Behrens (San Diego, CA: Academic Press), 337–358.

Van Essen, D. C., Ugurbil, K., Auerbach, E., Barch, D., Behrens, T. E. J., Bucholz, R., et al. (2012). The human connectome project: a data acquisition perspective. *Neuroimage* 62, 2222–2231. doi: 10.1016/j.neuroimage.2012.02.018

van Leeuwenhoek, A. (1719). *Epistolae Physiologicae Super Compluribus Naturae Arcanis.* Delphis: Adrianum Beman.

Vaughan, T., DelaBarre, L., Snyder, C., Tian, J., Akgun, C., Shrivastava, D., et al. (2006). 9.4T human MRI: preliminary results. *Magn. Reson. Med.* 56, 1274–1282. doi: 10.1002/mrm.21073

Vesalius, A. (1543). *Andreae Vesalii Bruxellensis, Scholae Medicorum Patavinae Professoris De Humani Corporis Fabrica Libri Septem.* Basileae: Ex officina Joannis Oporini

Vicq-d'Azyr, F. (1786). *Traité d'anatomie et de physiologie: avec des planches coloriées représentant au naturel les divers organes de l'homme et des animaux.* Paris, France: Impr. de F. A. Didot l'ainé.

Vieussens, R. (1684). *Neurographia Universalis.* Lugduni Lyons, France: Apud Joannem Certe.

Vogt, O., and Vogt, C. (1903). Zur anatomischen Gliederung des Cortex cerebri. *J. Psychol. Neurol.* 2, 160–180.

von Ardenne, M. (1937). Improvements in electron microscopes. British Patent No. 511204, convention date (Germany), 18 Feb 1937.

von Bartheld, C. S., Bahney, J., and Herculano-Houzel, S. (2016). The search for true numbers of neurons and glial cells in the human brain: a review of 150 years of cell counting. *J. Comp. Neurol.* 524, 3865–3895. doi: 10.1002/cne.24040

von Gerlach, J. (1872). Über die structur der granuern substanz des menschlichen grosshirns. Vorläufige mittheilung. *Zbl. Med. Wiss.* 10, 273–275.

von Gudden, B. (1870). Experimentaluntersuchungen über das peripherische und centrale Nervensystem. *Arch. Psychiat. Nervenkr.* 2, 693–723. doi: 10.1007/bf02046772

von Monakow, C. (1897). *Gehirnpathologie.* Vienna: A. Hölder.

von Monakow, C. (1914). *Die Localisation im Grosshirn und der Abbau der Funktion Durch Kortikale Herde.* Wiesbaden: Bergman.

von Waldeyer-Hartz, H. (1891). Über einige neuere forschungen im gebiete der anatomie des centralnervensystems. *Deutsch. Med. Wochenschr.* 17, 1213–1356. doi: 10.1055/s-0029-1206824

Wagner, A., Regev, A., and Yosef, N. (2016). Revealing the vectors of cellular identity with single-cell genomics. *Nat. Biotechnol.* 34, 1145–1160. doi: 10.1038/nbt.3711

Waller, A. (1850). Experiments on the section of the glossopharyngeal and hypoglossal nerves of the frog and observations of the alterations produced thereby in the structure of their primitive fibres. *Philos. Trans. R. Soc. Lond.* 140, 423–429. doi: 10.1098/rstl.1850.0021

Weisman, I. D., Bennett, L. H., Maxwell, L. R., Woods, M. W., and Burk, D. (1972). Recognition of cancer *in vivo* by nuclear magnetic resonance. *Science* 178, 1288–1290. doi: 10.1126/science.178.4067.1288

Wendel, K., Väisänen, O., Malmivuo, J., Gencer, N. G., Vanrumste, B., Durka, P., et al. (2009). EEG/MEG source imaging: methods, challenges and open issues. *Comput. Intell. Neurosci.* 2009:656092. doi: 10.1155/2009/656092

Wernicke, C. (1874). *Der Aphasische Symptomencomplex; eine Psychologische Studie auf Anatomischer Basis.* Breslau: Cohn and Weigert.

West, A. E., and Greenberg, M. E. (2011). Neuronal activity-regulated gene transcription in synapse development and cognitive function. *Cold Spring Harb. Perspect. Biol.* 3:a005744. doi: 10.1101/cshperspect.a005744

White, J. G., Southgate, E., Thomson, J. N., and Brenner, S. (1986). The structure of the nervous system of the nematode *Caenorhabditis elegans*. *Philos. Trans. R. Soc. Lond. B Biol. Sci.* 314, 1–340. doi: 10.1098/rstb.1986.0056

Wilson, M. A., Bhalla, U. S., Uhley, J. D., and Bower, J. M. (1989). "Genesis: a system for simulating neural networks," in *Advances in Neural Information Processing Systems 1*, ed. D. S. Touretzky (San Francisco, California: Morgan-Kaufmann), 485–492.

Winkler, H. (1920). *Verbreitung und Ursache der Parthenogenesis im Pflanzen- und Tierreiche.* Jena: G. Fischer.

Wu, R. (1972). Nucleotide sequence analysis of DNA. *Nature New. Biol.* 236, 198–200. doi: 10.1038/newbio236198a0

Zador, A. M., Dubnau, J., Oyibo, H. K., Zhan, H., Cao, G., and Peikon, I. D. (2012). Sequencing the connectome. *PLoS Biol.* 10:e1001411. doi: 10.1371/journal.pbio.1001411

Zemelman, B. V., Lee, G. A., Ng, M., and Miesenböck, G. (2002). Selective photostimulation of genetically chARGed neurons. *Neuron* 33, 15–22. doi: 10.1016/s0896-6273(01)00574-8

Zeng, H., and Sanes, J. R. (2017). Neuronal cell-type classification: challenges, opportunities and the path forward. *Nat. Rev. Neurosci.* 18, 530–546. doi: 10.1038/nrn.2017.85

Zuo, X.-N., Anderson, J. S., Bellec, P., Birn, R. M., Biswal, B. B., Blautzik, J., et al. (2014). An open science resource for establishing reliability and reproducibility in functional connectomics. *Sci. Data* 1:140049. doi: 10.1038/sdata.2014.49

Conflict of Interest Statement: The authors declare that the research was conducted in the absence of any commercial or financial relationships that could be construed as a potential conflict of interest.

Copyright © 2019 Fan and Markram. This is an open-access article distributed under the terms of the Creative Commons Attribution License (CC BY). The use, distribution or reproduction in other forums is permitted, provided the original author(s) and the copyright owner(s) are credited and that the original publication in this journal is cited, in accordance with accepted academic practice. No use, distribution or reproduction is permitted which does not comply with these terms.

frontiers in Neuroinformatics

ORIGINAL RESEARCH
published: 15 May 2019
doi: 10.3389/fninf.2019.00037

Reconstruction and Simulation of a Scaffold Model of the Cerebellar Network

Stefano Casali[1], *Elisa Marenzi*[1], *Chaitanya Medini*[1], *Claudia Casellato*[1*†] and *Egidio D'Angelo*[1,2*†]

[1] Neurophysiology Unit, Neurocomputational Laboratory, Department of Brain and Behavioral Sciences, University of Pavia, Pavia, Italy, [2] IRCCS Mondino Foundation, Pavia, Italy

Reconstructing neuronal microcircuits through computational models is fundamental to simulate local neuronal dynamics. Here a *scaffold model* of the cerebellum has been developed in order to flexibly place neurons in space, connect them synaptically, and endow neurons and synapses with biologically-grounded mechanisms. The scaffold model can keep neuronal morphology separated from network connectivity, which can in turn be obtained from convergence/divergence ratios and axonal/dendritic field 3D geometries. We first tested the scaffold on the cerebellar microcircuit, which presents a challenging 3D organization, at the same time providing appropriate datasets to validate emerging network behaviors. The scaffold was designed to integrate the cerebellar cortex with deep cerebellar nuclei (DCN), including different neuronal types: Golgi cells, granule cells, Purkinje cells, stellate cells, basket cells, and DCN principal cells. Mossy fiber inputs were conveyed through the glomeruli. An anisotropic volume (0.077 mm^3) of mouse cerebellum was reconstructed, in which point-neuron models were tuned toward the specific discharge properties of neurons and were connected by exponentially decaying excitatory and inhibitory synapses. Simulations using both pyNEST and pyNEURON showed the emergence of organized spatio-temporal patterns of neuronal activity similar to those revealed experimentally in response to background noise and burst stimulation of mossy fiber bundles. Different configurations of granular and molecular layer connectivity consistently modified neuronal activation patterns, revealing the importance of structural constraints for cerebellar network functioning. The scaffold provided thus an effective workflow accounting for the complex architecture of the cerebellar network. In principle, the scaffold can incorporate cellular mechanisms at multiple levels of detail and be tuned to test different structural and functional hypotheses. A future implementation using detailed 3D multi-compartment neuron models and dynamic synapses will be needed to investigate the impact of single neuron properties on network computation.

Keywords: cerebellum, computational spiking models, Python, pyNEST, pyNEURON, connectome

OPEN ACCESS

Edited by:
Gaute T. Einevoll, Norwegian University of Life Sciences, Norway

Reviewed by:
Michele Giugliano, University of Antwerp, Belgium
Tadashi Yamazaki, University of Electro-Communications, Japan

***Correspondence:**
Claudia Casellato
claudia.casellato@unipv.it
Egidio D'Angelo
egidio.dangelo@unipv.it

† These authors have contributed equally to this work as co-last authors

Received: *21 December 2018*
Accepted: *29 April 2019*
Published: *15 May 2019*

Citation:
Casali S, Marenzi E, Medini C, Casellato C and D'Angelo E (2019) Reconstruction and Simulation of a Scaffold Model of the Cerebellar Network. Front. Neuroinform. 13:37. doi: 10.3389/fninf.2019.00037

INTRODUCTION

The causal relationship between components of the nervous system at different spatio-temporal scales, from subcellular mechanisms to behavior, still needs to be disclosed, and this represents one of the main challenges of modern neuroscience. The issue can be faced using *bottom-up* modeling, which allows propagating microscopic phenomena into large-scale networks (Markram, 2012; Markram et al., 2015; D'Angelo and Wheeler-Kingshott, 2017).This *reverse engineering* approach integrates available details about neuronal properties and synaptic connectivity into *realistic* computational models and allows to monitor the impact of microscopic variables on the integrated system. Realistic modeling can predict emerging collective behaviors producing testable hypotheses for experimental and theoretical investigations (Llinas, 2014) and might also play a critical role in understanding neurological disorders (Soltesz and Staley, 2018). In practice, realistic modeling of microcircuit dynamics and causal relationships among multi-scale mechanisms poses complex computational problems. First, the modeling strategy needs to be flexible accounting for a variety of neuronal features and network architectures, to be easy to update as new anatomical, or neurophysiological data become available, and to be easy to modify in order to test different structural and functional hypotheses. Secondly, the modeling tools need to be scalable to the dimension of the network and to the nature of the scientific question (Destexhe et al., 1996), to be suitable for available simulation platforms, e.g., pyNEST and pyNEURON (Brette et al., 2007; Eppler et al., 2008; Hines et al., 2009), and to efficiently exploit High-Performance Computing (HPC) resources.

Markram et al. recently carried out a digital reconstruction of the neocortical microcolumn by integrating experimental measurements of neuronal morphologies, layer heights, neuronal densities, ratios of excitatory to inhibitory neurons, morphological and electro-morphological composition, electrophysiological properties of neurons, and synapses (Markram et al., 2015). Neuron parameters were derived from databases specifically addressing cerebro-cortical neuron properties (e.g., Blue Brain Project and Allen Brain Atlas; Markram, 2006; Sunkin et al., 2013). Microscopic network wiring was then estimated computationally through a touch detection algorithm, that is based on a probability/proximity rule (i.e., the probability that morphologically defined dendrites and axons make a synaptic connection depends on their spatial proximity). This approach, in which the reconstruction of microcircuit connectivity depends on the 3D morphology of the axonal and dendritic processes of individual cells, may apply to brain structures for which datasets comparable to neocortex are available. However, such specific datasets are not available in general for all brain regions and it seems convenient in principle to keep separated neuronal morphology from network connectivity, which is reported as convergence/divergence ratios and axonal/dendritic field geometries in the literature in many cases.

The cerebellum hosts the second largest cortical structure of the brain and contains about half of all brain neurons. Modeling the cerebellum brings about specific issues reflecting the peculiar properties of this circuit, which shows a quasi-crystalline geometrical organization well-defined by convergence/divergence ratios of neuronal connections and by the anisotropic 3D orientation of dendritic and axonal processes (**Figure 1**) (D'Angelo et al., 2016). Moreover, the morphological reconstruction of axonal and dendritic processes of cerebellar neurons is not as developed as for other brain microcircuits, like cerebral cortex, and hippocampus (e.g., see the NeuroMorpho.org repository —https://www.re3data.org/repository/r3d100010107; Akram et al., 2018). Therefore modeling the cerebellum relies on a knowledge base that differs from that available for the cerebral cortex and thus requires a more general approach than in the Markram's modeling workflow (Markram et al., 2015).

Some recent models were purposefully designed to reproduce a limited section of the cerebellar cortex, the granular layer (Maex and De Schutter, 1998; Solinas et al., 2010; Sudhakar et al., 2017), in great detail and incorporated Hodgkin-Huxley-style mechanisms and neurotransmission dynamics (D'Angelo et al., 2001; Solinas et al., 2007a,b; Nieus et al., 2014; Masoli et al., 2015, 2017; Masoli and D'Angelo, 2017). Other models were designed to simulate, in a simplified form, large-scale computationally efficient networks of the olivo-cerebellar system

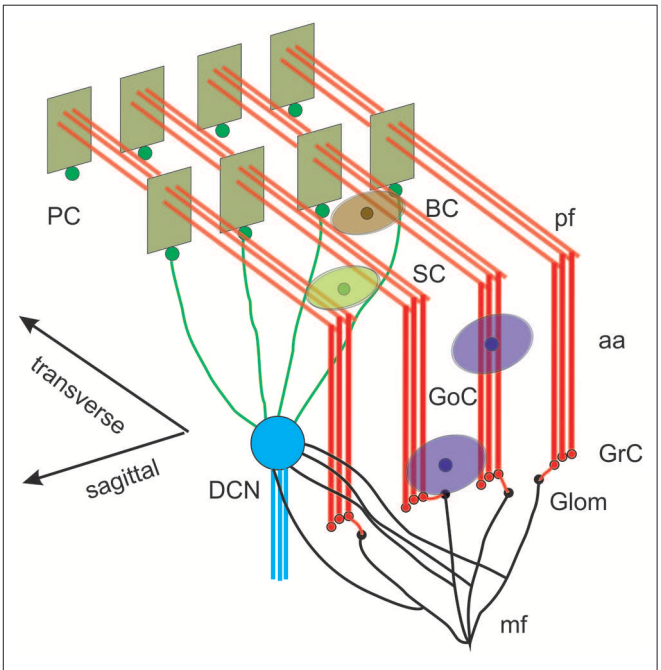


FIGURE 1 | Reconstruction of a scaffold model of the cerebellar network. Schematic representation of the cerebellar network (from D'Angelo et al., 2016). Glomeruli (Glom); mossy fiber (mf); Granule cells (GrC); ascending axon (aa); parallel fiber (pf); Golgi cells (GoC); stellate cell (SC); basket cell (BC); Purkinje cell (PC); Deep Cerebellar Nuclei cell (DCNC). Gloms transmit mf inputs to GrCs, which emit aa and pf, which in turn activate GoCs, PCs, SCs, and BCs. GoCs inhibit GrCs, SCs and BCs inhibit PCs. DCN cells are inhibited by PCs and activated by mf. Note the precise organization of PC dendrites, SC/BC dendrites and GoC dendritic arborization mainly on the parasagittal plane. The same abbreviations are used also in the following figures.

(Medina and Mauk, 2000; Yamazaki and Nagao, 2012). In this work, a new cerebellum *scaffold model* has been developed and tested, allowing to incorporate axonal/dendritic field geometries specifically oriented in a 3D space and to reconnect neurons according to convergence/divergence ratios typically well-defined for the cerebellum (D'Angelo et al., 2016). The cerebellum scaffold model maintains scalability and can be flexibly handled to incorporate neuronal properties on multiple scales of complexity and to change its connectivity rules. For the sake of simplicity, here we used first simplified neuron and synaptic models to evaluate the impact of construction rules. The cerebellum scaffold model was validated by testing its ability to reproduce the structural properties anticipated experimentally and the emergence of complex spatiotemporal patterns in network activity. The model was run on the pyNEST and pyNEURON simulators (Brette et al., 2007; Eppler et al., 2008; Hines et al., 2009) and a test workflow was integrated into a large-scale neuroinformatics infrastructure, the Brain Simulation Platform (https://collab.humanbrainproject.eu/).

MATERIALS AND METHODS

This paper reports the design and implementation of a *scaffold* model of the cerebellum microcircuit. The model architecture is scalable and is designed to host different types of neuronal models and to determine their synaptic connectivity from convergence/divergence ratios and axonal/dendritic field geometries reported in literature. The workflow encompasses two main modules in cascade: cell placement into a user-defined volume; connectivity among neurons. The scaffold can then be used for functional simulations of network dynamics (**Figure 1**).The scaffold is designed to be embedded into different simulators, e.g., pyNEST and pyNEURON. This workflow, by allowing a flexible reconstruction of the cerebellar network, will eventually allow to evaluate physiological, and pathological hypotheses about circuit functioning.

Cell Placement Module

The *Cell Placement Module* placed the cells in a virtual network volume divided in layers based on morphological definitions. The process took into consideration the different cerebellar neuron types: the Golgi Cell (GoC), Granule Cell (GrC), Purkinje Cell (PC), Stellate Cell (SC), Basket Cell (BC), Deep Cerebellar Nuclei glutamatergic GAD-positive Cell (DCNC), and glomerulus (Glom). Glom is actually a mossy fiber terminal and is represented as a neuronal element at the input stage, while DCNCs are placed at the output stage of the circuit. For each neuron type, the density value in a specific layer was derived from literature, and geometric features (including soma radius and 3D-oriented dendritic and axonal fields) were defined according to experimental data. Through *ad hoc* algorithms (*Bounded Self-Avoiding Random Walk Algorithm* and *Purkinje Cells placement algorithm*, see below; and details in **Supplementary Material** *Placement workflow*), the cells were positioned in the 3D volume of each layer, according to their density, soma radius, and anisotropic extension, ensuring that their somata did not overlap. The module was implemented in Python, and its output was saved in an *.hdf5* file containing the unique identification number (ID) of each cell, its corresponding type (an integer value between 1 and 7, as in **Table 1**), and the three spatial coordinates of the soma center (x, y, z). To evaluate the effectiveness of the cell positioning algorithms, we derived a continuous distribution of pair-wise distances using *kernel density estimation* (KDE), in which the Gaussian kernel had fixed bandwidth for each cell population. KDE yielded a single maximum when pair-wise distances were distributed homogeneously (GrC, GoC, SC, BC, DCNC) and multiple local maxima when distances were placed according to different geometric rules (PC). A reconstructed network volume and pair-wise soma distances yielded by this module are illustrated in **Figure 2**.

GrCs, GoCs, SCs, BCs, and DCNCs were placed in thin sublayers (with height = 1.5x soma diameter) using a bounded self-avoiding random walk algorithm. In each sublayer, the cells were initially distributed in 2D and then sublayers were piled one on top of the others. The first cell was placed randomly and each subsequent one was positioned nearby along a random angular direction. The overlap among somata was avoided since, along the selected direction, the minimum distance to place the next cell was equal to the soma diameter. A term was added to the minimum distance to scatter the somata. In details, a potential volume for each cell was computed from density values, then deriving the difference between this compound sphere radius and the soma radius (ε); a value was randomly sampled from as a normal distribution around ε (minimum 0.75· ε, maximum 1.25· ε). This guarantees natural randomness but at the same time a good exploitation of the whole available volume, avoiding undesired clusters or not uniform occupancy. If the surrounding space was completely occupied, i.e., there was insufficient space to place a further cell, a new starting point was selected resetting the random walk process for the remaining neurons in that sub-layer. Once completed, the 2D sub-layer was piled on top of the underlying one. Then, a vertical coordinate was assigned to each cell, from a random uniform distribution within the sublayer height (Korbo et al., 1993). This approach maintained randomness achieving a realistic quasi-Gaussian distribution of pair-wise inter-neuron distances (see **Figure 2C**) and proved computationally efficient.

TABLE 1 | Neuron types, size, and density.

Type	Soma radius (μm)	Density (neurons/ μm^3) *(/ μm^2)
Golgi cell (GoC)	8	9×10^{-6}
Glomerulus (Glom)	1.5	3×10^{-4}
Granule cell (GrC)	2.5	3.9×10^{-3}
Purkinje cell (PC)	7.5	$0.45 \times 10^{-3*}$
Basket cell (BC)	6	0.5×10^{-4}
Stellate cell (SC)	4	0.5×10^{-4}
DCN glutamatergic cell (DCNC)	10	5×10^{-7}

*The table reports the density of neurons in the layer volume (neurons/μm^3), *except for PCs for which the planar density is used (neurons/μm^2). Data for Glom, GrC, GoC, PC, SC, BC from Korbo et al. (1993). The density of DCNC was estimated from the ratio of PCs to DCNCs (Person and Raman, 2012).*

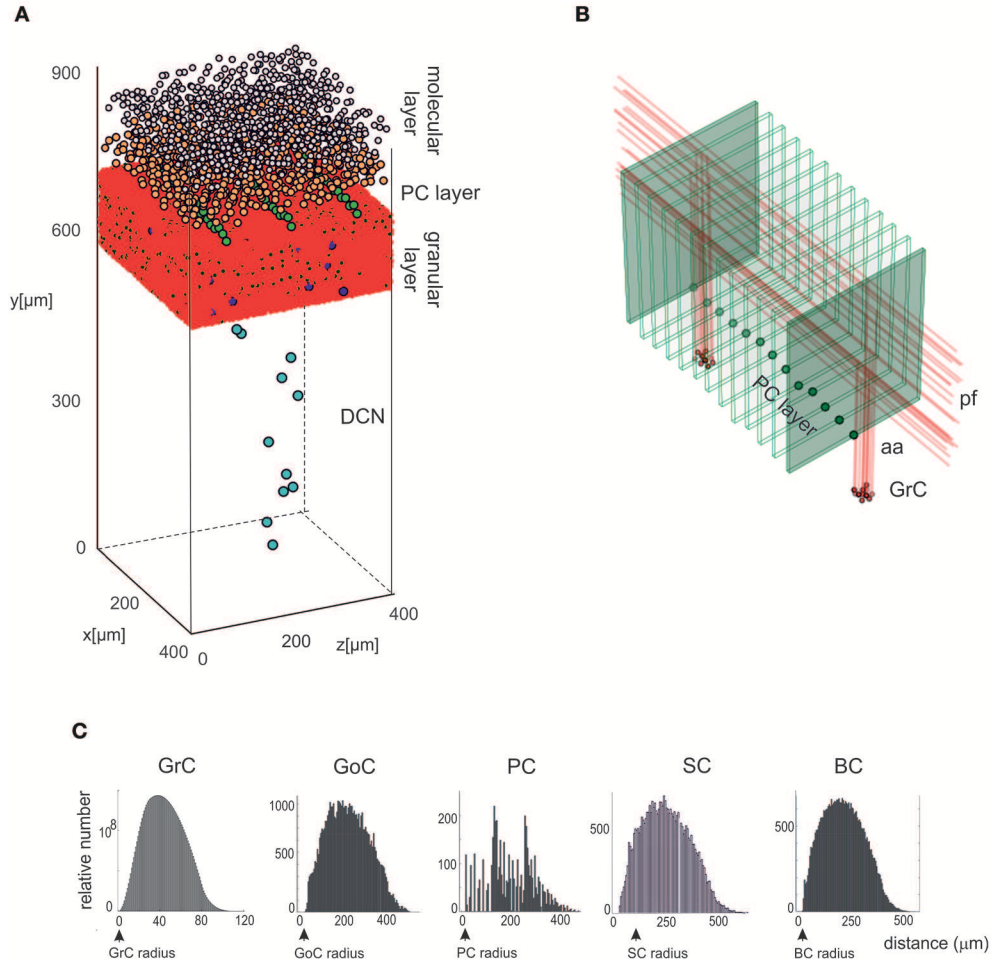


FIGURE 2 | Cell placement and network architecture. **(A)** The cells are placed in the network 3D space using a Bounded Self-Avoiding Random Walk Algorithm. The figure shows the volume of 400 × 400 × 900 μm^3 containing 96,737 neurons and 4,220,752 synapses used for simulations. **(B)** Projection of GrC axons to the molecular layer hosting the PCs (green dots in the PC layer are the somata, the thin green parallelepipeds above are the corresponding dendritic trees occupying the molecular layer). The figure shows two clusters of GrCs and the corresponding aa and pf, illustrating that the cerebellar network connectivity respects the 3D architecture shown in **Figure 1**. **(C)** Distributions of 3D pair-wise inter-soma distances within each neuronal population: GrCs, SCs, GoCs, BCs, and PCs. Note that the distributions are nearly normal, except for the PCs.

The PCs were distributed in a single sub-layer forming an almost planar grid between the granular and molecular layers. The PC inter-soma distances over this plane were constrained by the dendritic trees, which are flat and expand vertically on the parasagittal plane (about 150 µm radius × 30 µm width) without overlapping (Masoli et al., 2015). Since PC somata do not arrange in parallel arrays but are somehow scattered, a noisy offset was introduced creating an average angular shift of about 5° between adjacent PCs. As for the other neuron types, a small random noise was also imposed on the vertical coordinate (Korbo et al., 1993).

The data required for cell positioning in the cerebellar cortex were obtained from literature (Eccles et al., 1967; Magyar et al., 1972; Mezey et al., 1977; Hamori and Somogyi, 1983; Jakab and Hamori, 1988; Korbo et al., 1993; Sultan, 2001; Santamaria et al., 2007; Barmack and Yakhnitsa, 2008; Solinas et al., 2010) and are summarized in **Table 1**. GoCs, GrCs, and Gloms were placed into the granular layer; BCs and SCs in the lower and upper half of the molecular layer, respectively. A certain number of DCNCs was randomly distributed in DCN volume according to the PC/DCNC ratio, since more specific parameters are still missing (Gauck and Jaeger, 2000; Aizenman et al., 2003; Person and Raman, 2012). Special care was given to the GrC ascending axon (aa) that, starting directly from the soma, makes its way up vertically toward the molecular layer. The height of each ascending axon was chosen from a Gaussian distribution in the range of 181 ± 66 µm (Huang et al., 2006). This value represents also the vertical coordinate of the corresponding parallel fiber (pf), running transversally and parallel to the cerebellar surface.

Connectivity Module

The connectivity module created structural connections between pairs of neurons belonging to specific types. Each neuron type

formed input and output connections with other neurons of the same or different types. Therefore, once the placement was completed, it was possible to reconstruct the connectome applying *intersection-connectivity* rules based on proximity of neuronal processes and on *statistical ratios* of convergence and divergence. When available, morphological and statistical literature data were used, otherwise plausible physiological constraints were applied. In our scaffold, 16 connection types were generated (the most important are shown in **Figure 3**), from the volume covered by pre-synaptic axonal processes to that covered by post-synaptic dendritic trees of specific neuron types:

1. From glomeruli to granule cells (Glom-GrC);
2. From glomeruli to basolateral dendrites of Golgi cells (Glom-GoC);
3. From Golgi cells to Gloms (GoC-Glom): this is fused together with Glom-GrC to generate directly GoC-GrC connections;
4. Among Golgi cells (GoC-GoC);
5. From ascending axons of granule cells to Golgi cells (aa-GoC);
6. From parallel fibers of granule cells to apical dendrites of Golgi cells (pf-GoC);
7. Among stellate cells (SC-SC);
8. Among basket cells (BC-BC);
9. From parallel fibers of granule cells to stellate cells (pf-SC);
10. From parallel fibers of granule cells to basket cells (pf-BC);
11. From stellate cells to Purkinje cells (SC-PC);
12. From basket cells to Purkinje cells (BC-PC);
13. From ascending axons of granule cells to Purkinje cells (aa-PC);
14. From parallel fibers of granule cells to Purkinje cells (pf-PC);
15. From Purkinje cells to DCN cells (PC-DCNC);
16. From glomeruli to DCN cells (Glom-DCNC).

Given a connection type, for each pre-synaptic neuron, the potential post-synaptic cells were identified as those that met geometric neuron-specific constraints. Then, given the convergence and divergence ratios, post-synaptic neurons were selected among the potential ones, through a pruning process using distance-based probability functions specific for each volume direction (details and examples in **Figure S1**). The module was implemented in Python, and its output saved in an *.hdf5* file containing a matrix for each connection type, in which each row was defined by three values: the unique ID of the pre-synaptic neuron, the unique ID of the post-synaptic neuron and the inter-soma 3D distance between that pair (see **Figure 4A**).The plots in **Figures 4B,C** compare, for each connection type, the divergence and convergence ratios reported by literature to the values obtained after scaffold reconstruction in a sample volume. The cell placement and connections rules yielded indeed a very good approximation of the anatomical and physiological parameters reported in literature.

Functional Simulations

In order to test the functionality of the scaffold, single neuron models were placed in the corresponding positions of the connectome matrix. In this first version of the cerebellar microcircuit, spiking point-neuron models based on Integrate&Fire (I&F) dynamics with conductance-based exponential synapses (i.e., synaptic inputs cause an exponential-shaped change in synaptic conductances) were used. The output files of these simulations contained all the spike events (neuron IDs and relative spike times). Glomeruli were represented as "parrot neurons" just able to pass the imposed stimulation patterns unaltered. Each other neuron type was characterized by specific values, directly related to neurophysiological quantities (C_m, τ_m, E_L, Δt_{ref}, I_e, V_r, V_{th}), corresponding to biological values taken from literature available from animal experiments or databases (https://neuroelectro.org/) (Tripathy et al., 2014; **Table 2**). In order to account for the neuron-specific dynamics of GABA and AMPA receptor currents, also the decay times of the excitatory and inhibitory synaptic exponential functions (τ_{exc}, τ_{inh}) were set differently for each neuron type (**Table 2**). Each synaptic connection type was characterized by specific values of weight and delay (**Table 3**). These estimates approximated literature data values so that, for example, the synaptic delay was shorter when fibers impinging on PCs came from aa than pf synapse.

The input stimulus was set by defining the volume where Gloms were activated, the onset time, the duration and the frequency of spikes. A background activity was generated by a Poisson process of stochastic neuronal firing at 1 Hz on all the glomeruli. Superimposed on it, a burst at 150 Hz lasting 50 ms (Rancz et al., 2007) was activated 300 ms after the beginning of simulation. Indeed, mossy fibers have a low basal activity, but in response to sensorimotor stimuli, can fire at rates beyond 100 Hz. The stimulated volume had a radius of 140 μm; the simulation lasted 1 sec, including 300 ms pre-stimulus, 50 ms stimulus, and 650 ms post-stimulus.

In a specific set of simulations (see **Figure 8**), we tested the partial contribution of SCs and BCs to the spatiotemporal diffusion of activity among PCs. BCs axonal plexus is preferentially oriented along the parasagittal axis (see Eccles et al., 1967). In these simulations, we oriented the SC and BC axonal plexus orthogonally one to each other and concentrated the stimulation burst in a sphere of 30 μm radius.

Network Data Analysis

For each neuron population, mean frequency rates were extracted in three time windows: baseline pre-stimulus, during stimulus, and steady-state after-stimulus. We then generated peri-stimulus time histograms (PSTH) for each neuronal population with time bins of 3 ms. For each neuron population, we also separated excited from inhibited sub-groups, responding with an increased, or decreased firing rate during the stimulus. To do so, we compared the number of spikes during stimulus vs. pre-stimulus normalized by the time-window durations. If the pre-stimulus firing frequency (i.e., baseline) was at least doubled during stimulation, then the cell was classified as excited. Conversely, to classify the inhibited cells. For GrCs, we added a second constraint: to be labeled as excited, a GrC should fire more than 1 spike during stimulation, allowing to exclude spikes determined by the background noise. For DCNC, all cells stopped firing during the stimulation time-window. For each PC, a further *ad-hoc* analysis allowed to identify burst–pause responses. The cells showing a significant stimulus-induced pause (Cao et al., 2012;

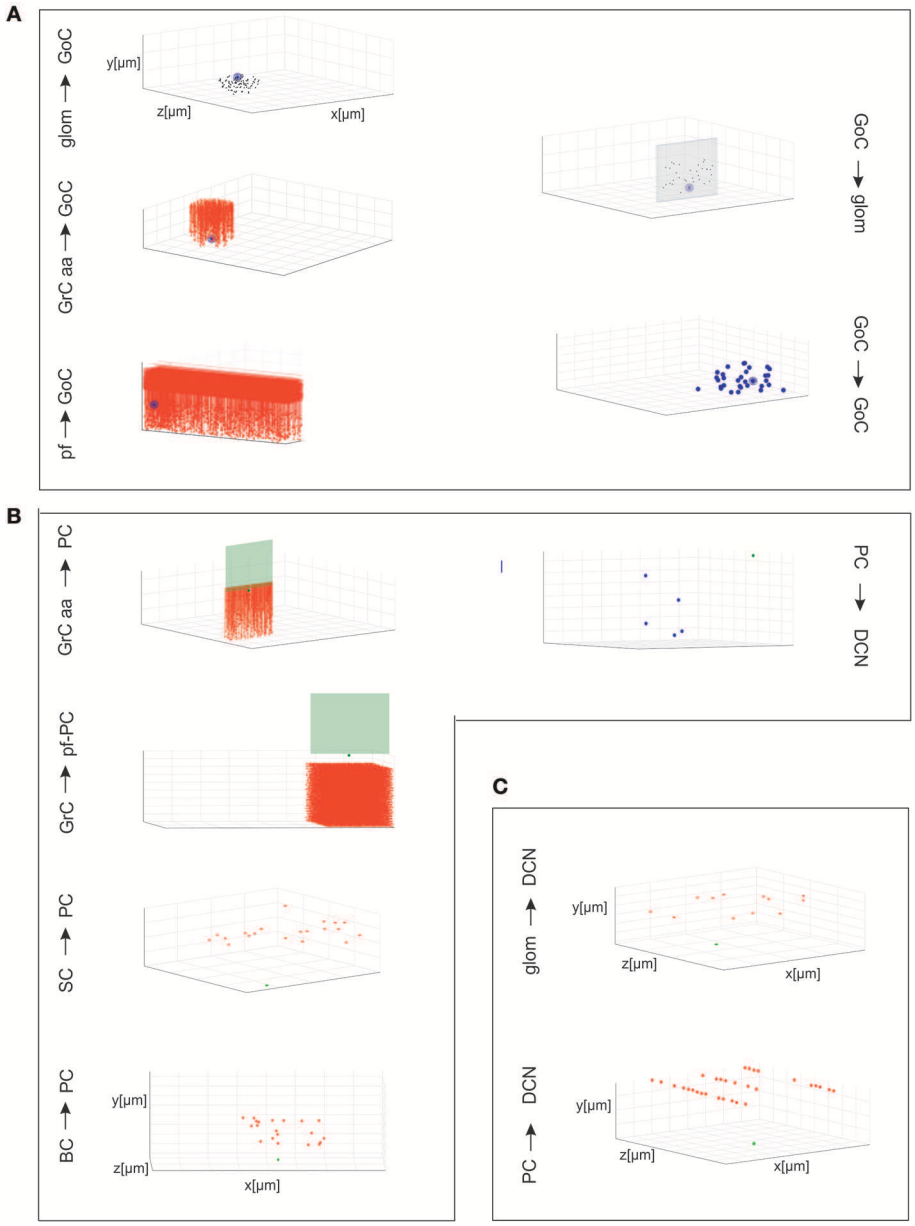


FIGURE 3 | Cell connectivity: examples for specific connections. Examples of divergence and convergence at different connections in the cerebellar network space. The plots have base area (400 × 400 μm^2) and thickness specific for each layer. The plots show a randomly selected pre-synaptic cell together with its connected post-synaptic neurons (divergence) or viceversa (convergence). **(A)** Connections of GrCs and GoCs. **(B)** Connections of PCs, SCs, and BCs. **(C)** Connections of DCNCs.

Herzfeld et al., 2015) were recognized as those in which the first Inter-Spike-Interval (ISI) after the end of the stimulus was >2 standard deviation (sd) of the pre-stimulus ISIs. This comparison was computed within-cell, i.e., for each PC individually.

Center-Surround Analysis

The Excitatory-Inhibitory balance (*EI*) and Center-Surround (*CS*) were calculated from firing rates (*FR*) according to Mapelli and D'Angelo (2007) and Solinas et al. (2010) by considering that inhibition occurs only after a delay following the beginning of stimulation. GrC firing rate was then measured 0–20 ms (*T1*) and 20–40 ms (*T2*) after the beginning of stimulation in response to 50 ms at 150 Hz bursts, both in control (*con*)and with GoC-GrC inhibition switched off (*in_off*). The *CS* and *EI* were calculated as follows:

$$EI = FRcon_{T2} - FRin_off_{T2}$$
$$CS = FRcon_{T1} - EI$$

The *CS* values were normalized between 1 and −1. The extension of the center and surround was calculated by including zones

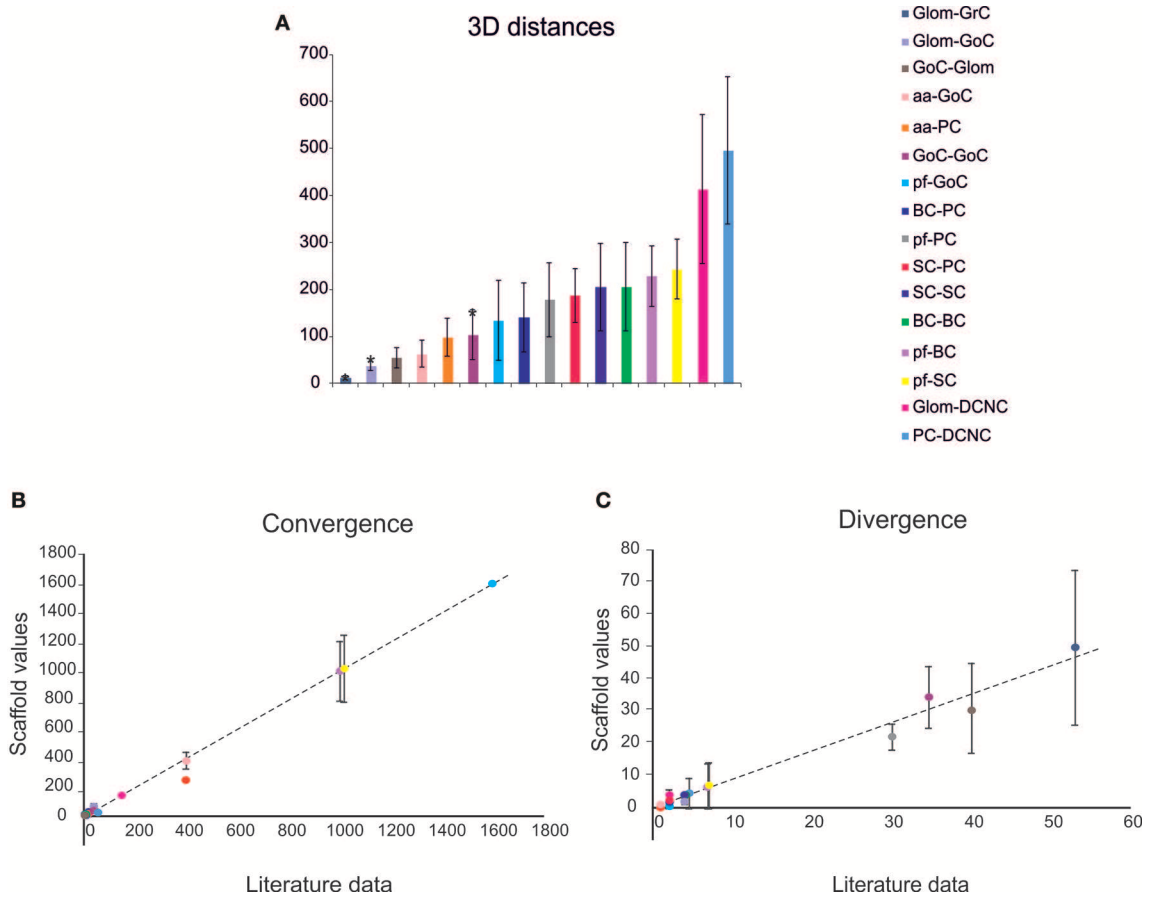


FIGURE 4 | Cell connectivity: pair-wise distance prediction and convergence/divergence validation. **(A)** Pair-wise distance prediction deriving from the placement and subsequent cell-to-cell connectivity. The data that find correspondence in literature are indicated as asterisks. For each connection type, the pair-wise distances between connected cells (inter-soma distance) are reported. Data from: (1) (D'Angelo et al., 2013), (2) (Barmack and Yakhnitsa, 2008), (3) (Rieubland et al., 2014). **(B,C)** The plots compare divergence and convergence for the different connections of the scaffold with those anticipated experimentally. The regression lines show a very close correspondence of the model to experimental results. Linear regression lines are fitted to the data (divergence: $r^2 = 0.98$, slope = 0.88; convergence: $r^2 = 0.99$, slope = 0.99). Data from: (1) (Nieus et al., 2006), (2) (Dieudonne, 1998), (3) (D'Angelo et al., 2013), (4) (Solinas et al., 2010), (5) (Kanichay and Silver, 2008), (6) (Cesana et al., 2013), (7) (Hull and Regehr, 2012), (8) (Lennon et al., 2014), (9) (Huang et al., 2006), (10) (Jorntell et al., 2010), (11) (Sultan and Heck, 2003), (12) (Person and Raman, 2012), (13) (Boele et al., 2013).

with $CS > 0.5$ in the center, and zones with $CS < -0.5$ in the surround. The center and surround relative areas could then be calculated by counting the respective number of pixels and normalizing by the total number of pixels (see **Figure 7C**).

Oscillation Analysis

In order to determine the presence and properties of coherent oscillations in granular layer activity, the activity in a subset of GoCs with overlapping incoming parallel fibers and the related GrCs was analyzed (Maex et al., 2000) during a 5 s at 5 Hz noisy background mossy fiber activity. The autocorrelations of GoCs and GrCs spike trains and the cross correlation between GrCs and GoCs spike trains were calculated using the equation

$$C = \frac{\sum_{n=0}^{len(A)} \left(abs(A_n)\right)}{len(A)}$$

Where C is the index of coherence, A is the array of autocorrelation values, and len(A) is the size of the spike train data array. The same calculus was executed also for the crosscorrelation.

Simulations in pyNEST, pyNEURON, and Implementation on the Brain Simulation Platform

The microcircuit was implemented and simulated both in pyNEST version 2.14 (Eppler et al., 2008) and in pyNEURON (Hines et al., 2009). These neural simulators are commonly used for applications starting from realistic neuron models and up to more abstract representations. These tests were run using external HPC and local resources, maximizing available parallel computing. The time resolution for both simulators was 0.1 ms. As internal validation tests, some exemplificative *ad-hoc* structural and functional alternatives (see **Figure 5**) were made

TABLE 2 | Neuron-specific parameters.

Cell type	C_m[pF]	τ_m(= C_m*R_{in}) [ms]	E_L[mV]	Δt_{ref}(spike width)[ms]	I_e[pA]	V_r[mV]	V_{th}[mV]	τ_{exc}[ms]	τ_{inh}[ms]
GoC	76	21	−65	2	36.8	−75	−55	0.5	10
GrC	3	2	−74	1.5	0	−84	−42	0.5	10
PC	620	88	−62	0.8	600	−72	−47	0.5	1.6
BC	14.6	14.6	−68	1.6	15.6	−78	−53	0.64	2
SC	14.6	14.6	−68	1.6	15.6	−78	−53	0.64	2
DCNC	89	57	−59	3.7	55.8	−69	−48	7.1	13.6

The table shows the parameters used to define specific neuronal properties in the model. Cm, membrane capacitance; τm, membrane time constant; Rin, input membrane resistance; EL, leakage resting potential; Δtref, refractory period; Ie, endogenous current; Vr, reset potential; Vth, threshold potential; τexc, τinh, excitatory and inhibitory synaptic exponential time constants). Data are obtained from NeuroElectro (https://neuroelectro.org/) (Tripathy et al., 2014).

TABLE 3 | Synaptic parameters for each connection type.

Connection types	Weight [nS]	Delay[ms]
Glom-GrC	9.0	4.0
Glom-GoC	2.0	4.0
GoC-GrC (GoC-Glom-GrC)	−5.0	2.0
GoC-GoC	−8.0	1.0
aa-GoC	20.0	2.0
pf-GoC	0.4	5.0
SC-SC	−2.0	1.0
BC-BC	−2.5	1.0
pf-SC	0.2	5.0
pf-BC	0.2	5.0
SC-PC	−8.5	5.0
BC-PC	−9.0	4.0
aa-PC	75.0	2.0
pf-PC	0.02	5.0
PC-DCNC	−0.0075	4.0
Glom-DCNC	0.006	4.0

The parameters result from a tuning procedure based on data reported in different papers and summarized in Maex and De Schutter (1998), Solinas et al. (2010), and Sudhakar et al. (2017). A main additional constraint is that the connection weight is larger from aa then pf connections, both for GoCs and PCs (Sims and Hartell, 2005; Cesana et al., 2013).

in the network and then the same simulations were run (in pyNEST). The firing rates of each cell population and their subgroups affected by stimulus are reported in **Table 4** and **Figure 5** to illustrate the spiking network behaviors.

The entire scaffold can be built and run as a Jupyter Notebook in the Brain Simulation Platform (BSP), one of the platforms of Human Brain Project (Markram, 2012). The BSP is an internet-accessible collaborative platform that comprises a suite of software tools and workflows to reconstruct and simulate multi-level models of the brain at different levels of description, from abstract to highly detailed. Here, cells, network, and volume configuration parameters can be easily read and modified, since they are stored in a single Python script. Such flexible parametric approach allows to continuously include and tune relevant neurophysiological information and to operate at different simplification levels. A test version of the scaffold model is running on the Brain Simulation Platform at https://www.humanbrainproject.eu/en/brain-simulation/brain-simulation-platform/.

RESULTS

The cerebellar network is unique for its precise geometrical organization (**Figure 1**), which was reconstructed generating a *scaffold model* capable of handling neuronal placement, connectivity, and simulations. The neurons were represented as single-point leaky integrate-and-fire (LIF) models (Maas, 1997), tuned to match the input resistance and capacitance, basal discharge, and input-output relationship of the specific cerebellar neuron types. The choice of LIF neuron models was motivated by the need to focus first onto the two main construction operations of the scaffold, cell placement and connectivity, and on the role of these latter in determining network properties.

The scaffold is demonstrated here through the exemplar reconstruction and testing of a cerebellar volume of 0.077 mm^3. The cerebellar cortex volume had 400 × 400 μm^2 base and 330 μm height subdivided into different layers: molecular layer (150 μm), Purkinje cell layer (30 μm), granular layer (150 μm). The DCN layer had 200 × 200μm^2 base (1/4 of cortex) and 600 μm height. As a whole, the model contained 96,734 cells. It should be noted that these parameters were all user-defined and may be modified depending on the needs, as the model is scalable.

Cell Placement

The *Bounded Self-Avoiding Random Walk* algorithm (see section Materials and Methods) successfully placed the neurons into all cerebellar regions with the only exception of PCs, which were positioned using a specific algorithm designed to respect their regular spatial organization (**Figure 2A**). **Figure 2B** shows a row of almost equally distanced PCs connected to incoming parallel fibers, faithfully reproducing the typical PCs geometrical organization. These examples show that the placement algorithms can be flexibly configured to account for complex and variable rules of cellular positioning.

As an internal validation, the distribution of pair-wise distances for each cell type was calculated (**Figure 2C**). For all cell types (except PCs), pair-wise distances were distributed almost normally and the minimum inter-soma distance equated twice the soma radius. As expected, KDE for GrC, GoC, SC, and BC pair-wise distances returned a single maximum (at 180.1, 191.0,

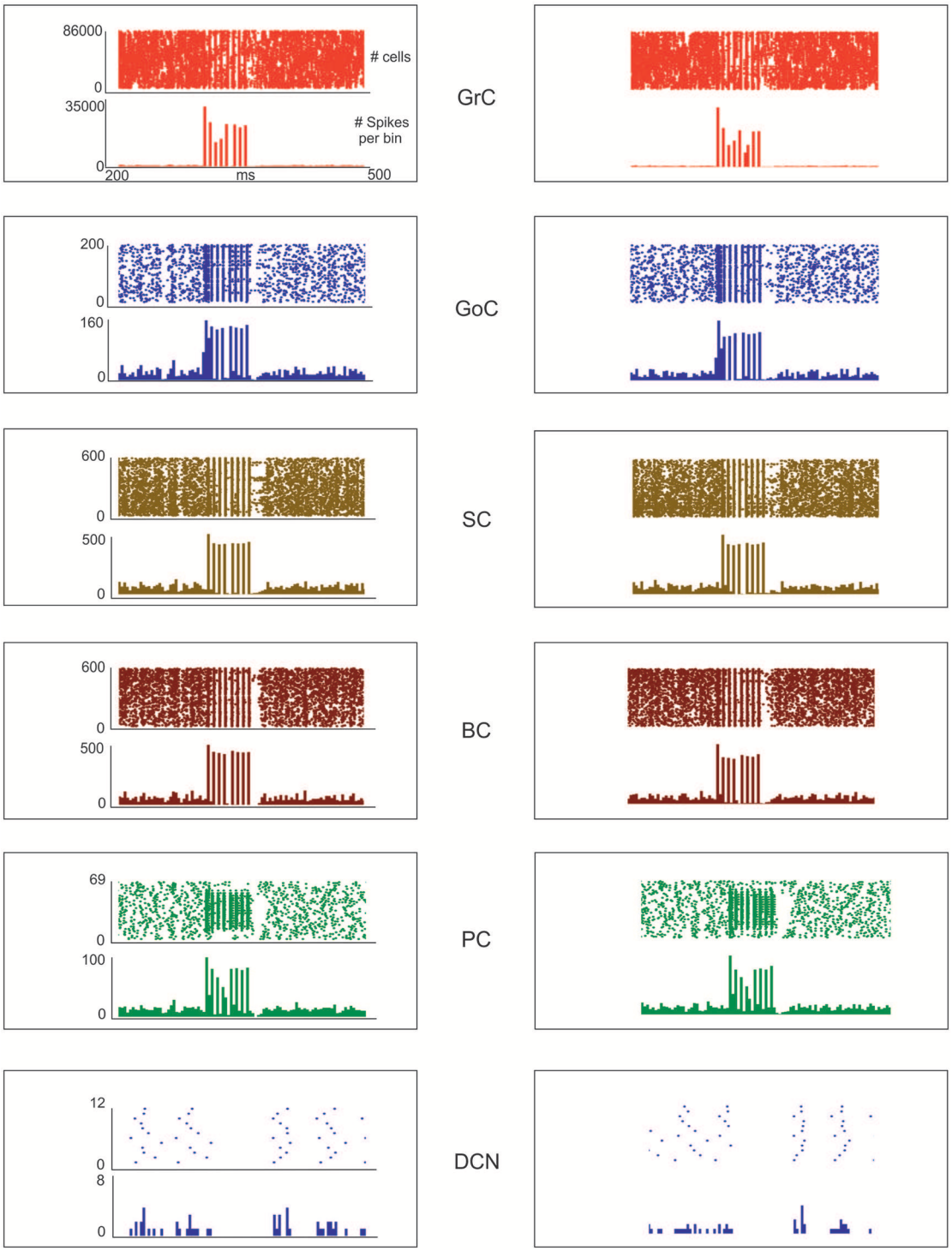


FIGURE 5 | Neuronal discharge. Raster plot and PSTH of the different neuron populations of the cerebellar network model in response to a mossy fiber burst (50 ms at 150 Hz on 2,932 gloms) superimposed on a 1 Hz random background. The two simulations used the same cerebellar scaffold and neurons, which were translated from pyNEST into pyNEURON. The basal activity of the different cell populations is visible before and after the stimulus. The Glom patterns at the input are imposed, so they are identical for both simulations. The mean population firing rates for GrCs are similar between the two simulations, probably due to the very high number of GrCs. Minor differences are detectable for the other neuron types.

TABLE 4 | Firing rates.

Neuron type	N.cells	N. Excited (or inhibited) cells (%)	Before (300 ms) [Hz]	During (50 ms) [Hz]	After (300 ms) [Hz]
Gloms	7,070	E_{NEST}: 2,932 (41%)	1.0 ± 1.8	140.8 ± 4.2	0.9 ± 1.8
		E_{NEURON}: 2,932 (41%)	1.0 ± 1.8	140.8 ± 4.2	0.9 ± 1.8
GrCs	88,158	E_{NEST}: 26,195 (29%)	2.0 ± 2.6	114.0 ± 32.2	1.8 ± 2.5
		E_{NEURON}: 25,240 (28%)	2.0 ± 2.6	114.8 ± 32.8	1.8 ± 2.5
GoCs	219	E_{NEST}: 146 (66%)	22.7 ± 13.1	157.1 ± 37.2	23.5 ± 11.3
		E_{NEURON}: 153 (69%)	22.1 ± 12.4	154.2 ± 28.9	24.9 ± 12.0
SCs	603	E_{NEST}: 445 (73%)	33.9 ± 15.7	126.2 ± 17.4	37.0 ± 14.3
		E_{NEURON}: 452 (74%)	34.2 ± 15.9	131.8 ± 19.6	36.9 ± 15.0
BCs	603	E_{NEST}: 429 (71%)	30.1 ± 15.1	124.1 ± 18.4	33.6 ± 14.0
		E_{NEURON}: 447 (74%)	29.1 ± 15.3	123.3 ± 24.9	33.8 ± 14.4
PCs	69	E_{NEST}: 45 (65%)	58.5 ± 8.5	255.5 ± 63.0	62.8 ± 8.3
		E_{NEURON}: 47 (68%)	60.0 ± 9.3	256.5 ± 63.8	63.0 ± 11.6
DCNCs	12	I_{NEST}: 12 (100%)	16.1 ± 1.2	0.0 ± 0.0	16.3 ± 0.9
		I_{NEURON}: 12 (100%)	16.6 ± 0.0	0.0 ± 0.0	16.6 ± 0.0

For each neuronal population, the firing rates (mean ± sd) are reported before, during and after stimulation. Excited (inhibited) cells are defined as those increasing (decreasing) the number of spikes during the stimulus (see Methods). Simulation results are shown for pyNEST (white rows) and for pyNEURON (gray rows). In the column "During stim," the values indicate the firing rates only averaged on the sub-group "Excited (Inhibited) cells."

184.6, and 188.5 μm, respectively), while for PCs three local maxima occurred (at 48.6, 142.1, and 267.0 μm) (for DCNC, KDE analysis was meaningless, given the low number of cells).

Cell Connectivity

The connection rules adopted in this work were designed to account for the rich and specific information available from literature (Eccles et al., 1967; Palay and Chan-Palay, 1974; Korbo et al., 1993), which accounts for convergence/divergence ratios, number of synapses, and spatial distribution of axons and dendrites (**Figure 3**). The connecting algorithm imposed these geometrical constraints allowing to wire the different neuronal types for a whole of 16 connection types. Five connection types did not require other than these geometric constraints, while pruning was needed in the other 11 cases (either for convergence or divergence or both). The resulting connectome was then compared to the experimental one for validation. **Figure 4** shows that the connection ratios of the scaffold were indeed correctly scaling to the physiological ones. Some specific cases are considered below.

Concerning Glom-GrC connectivity, experimental data demonstrated that granule cell dendrites have a maximum length of 40 μm, with a mean value of ∼13 μm (Solinas et al., 2010). By imposing a convergence value of 4 (each GrC received one Glom on each of its 4–5 dendrites), a mean dendrite length of about ∼12 μm was found, therefore matching experimental and theoretical determinations (Hamori and Somogyi, 1983; Billings et al., 2014).

Concerning connectivity between the aa and PC dendrites (aa-PC), connections were possible only when the aa-segment was very close to the PC dendritic plane. By analyzing the placement of GrCs in the x-z plane and the vertical extension of the aa, it is estimated that only ∼20% of GrCs developed an aa that is sufficiently close to a PC dendrite tree to form a synaptic contact (Bower and Woolston, 1983; Gundappa-Sulur et al., 1999). This estimate was indeed closely matched by the scaffold reconstruction.

Concerning connectivity of parallel fibers with receiving neurons (pf-GoC, pf-SC, pf-BC, pf-PC synapses), the literature is incomplete and shows variable estimates. This most likely reflects difficulties in estimating exact numbers, since the pf can be several millimeters long and they are often cut on the parasagittal plane in histological preparations. In the scaffold reconstruction, the maximum pf length (along z-direction) was bounded to 400 μm (Barbour, 1993; Huang et al., 2006) and pf from GrCs beyond this length were not taken into account.

The statistical distribution of distances between connected cells (**Table 4**) shows a good matching with anatomical values. This validation of the connectome supports the appropriateness of cell placement and connecting rules. Biological randomness in the 3D placement with uniform occupancy of appropriate layers ensures that the resulting connectivity (based on geometrical proximity) has plausible biological values and variability for statistical convergence/divergence ratios, and for distances among connected neurons.

Neuronal Activations in the Cerebellar Network Following Mossy Fiber Stimulation

The aim of these simulations was to assess the emergence of typical spatio-temporal patterns of cerebellar network activity as a consequence of mossy fiber inputs. Simulations were carried out both in pyNEST and pyNEURON. For simplicity, the following data and figures are taken from pyNEST simulations, except for a comparison of the two in **Figure 5** and **Table 4**. As expected, the two simulators yielded similar firing rates in each cell population. The Glom patterns at the input were imposed,

so they were identical for both simulation platforms, while very small differences were detectable for the other neuron types.

Evoked activity simulating the effect of natural sensory stimulation (Chadderton et al., 2004; Roggeri et al., 2008; Ramakrishnan et al., 2016)was elicited over a noisy background (see above) by a 150 Hz−50 ms mossy fiber burst. The mossy fiber activity spread over about 0.012 μm^3 of the granular layer involving 2,932 glomeruli out of the 7,070 placed in the reconstructed volume. Glomeruli had mean firing rate of ∼1 Hz before the burst, 140 Hz during the burst, and ∼1 Hz after the burst. The burst induced transient activity changes, specific for each neuronal population, which reverted back to baseline after the end of the stimulus (**Figure 5**). The sequence of neuronal activations depended on synaptic delays that were set according to physiological data (Eccles et al., 1967; **Figure 6**). The response of the individual neuronal populations was as follows (**Figures 5**, **6**, and **Table 4**):

- The GrCs discharged at 1.8 Hz at rest and at 114 Hz during burst stimulation, consistent with *in-vivo* data showing that GrCs had sparse activity characterized by low background firing rates (partly due to the presence of tonic GABAergic inhibition) and high-frequency bursts in response to evoked sensory stimulation (Chadderton et al., 2004).
- GoCs discharged above 22 Hz at rest and above 150 Hz during burst stimulation, consistent with *in-vivo* data (Heine et al., 2010). The basal GoCs firing rate was raised by the noisy background over the autorhythmic frequency and showed a high variability among cells.
- Molecular layer interneurons, SCs and BCs ($N = 603$ for each cell type), discharged at ∼30 Hz at rest and above 120 Hz during burst stimulation, consistent with the observation of high-frequency activity during sensory stimulation (Chu et al., 2012).
- PCs discharged at ∼58–60 Hz at rest and at ∼255 Hz during burst stimulation consistent with *in-vivo* data (Heine et al., 2010). Interestingly, PCs showed either bursts, or pauses, or burst-pause responses as observed *in vivo* (Herzfeld et al., 2015): out of 69 PCs, the burst was observed in 48 PCs and the pause in 41 PCs. Of the PCs that showed a pause, in 17 PCs it occurred after a burst, while in the other 24 PCs it happened alone.
- DCNCs discharged at ∼16 Hz at rest and were completely silenced during burst stimulation. This behavior was expected from the convergent inhibition coming from PCs, supporting the hypothesis that cortico-nuclear synapses act as simplified inverters (Person and Raman, 2012).

Center-Surround Organization of Granular Layer Responses

A relevant aspect of network activation that emerged in electrophysiological and imaging experiments is the center-surround organization (Mapelli and D'Angelo, 2007; Diwakar et al., 2011; Gandolfi et al., 2014). In the scaffold, the neuronal response of the granular layer to mossy fiber stimulation showed a typical center-surround organization (**Figure 6**). This reflected the excitatory/inhibitory ratio (see section Materials and Methods) with the center more excited than the surround due to lateral inhibition provided by GoCs. The center-surround had a diameter of about 50 μm and GrCs inside the core discharged up to 3–4 spikes organized in a short burst, reflecting previous experimental estimates (Gandolfi et al., 2014). Therefore, the scaffold correctly predicts the consequences of activity in bundles of mossy fibers.

Recently the connectivity of GoCs and GrCs has been extended by the demonstration of new synapses, in particular those between the GrC ascending axon and GoCs (aa-GoC, excitatory) (Cesana et al., 2013) and between GoCs (GoC-GoC, inhibitory) (Hull and Regehr, 2012). The selective switch-off of aa-GoC connections enhanced the center and reduced the surround, the switch-off of GoC-GoC connections reduced the center and increased the surround, while smaller effects followed the switch-off of pf-GoC or mf-GoC synapses (**Figure 9C**).

The Impact of Molecular Layer Interneurons on PC Activation

The molecular layer is critical to regulate PC activity in a way that is still debated (e.g., see Rokni et al., 2007; Santamaria et al., 2007). The first assumption is a differential orientation of SC cell axons (mostly transversal or "on-beam") vs. BC axons (mostly sagittal or "off-beam") (Eccles et al., 1967). Moreover, both aa and pf are used to activate PCs, as reported in literature (Jaeger and Bower, 1994; Canepari et al., 2001; **Figure 8**). Consistently, in the scaffold model, PC responses were circumscribed into a central spot overlaying the center/surround generated in the granular layer with little diffusion along either transversal or sagittal axis. On both axes, in turn, some PCs were clearly inhibited by the molecular layer interneuron inhibitory network.

Then, the effect of disconnecting different network elements was tested. Following the switch-off of both SC and BC inhibition, the responsiveness of PCs increased, as expected from SC and BC inhibitory action on PCs. As expected from anatomy, when only BCs were present (i.e., selective switch-off of SCs), excitation extended more effectively along the transverse axis, while when only SCs were present (i.e., selective switch-off of BCs) excitation extended more effectively along the sagittal axis. However, in both cases there was a diffused (though slight) increase of excitation, due to the reduced background inhibition exerted by intrinsic SC and BC discharge. It should also be noted that the activation of PCs in the central spot remained poorly altered, suggesting that these PCs were already nearly maximally activated in control. The selective switch-off of aa synapses caused a diffuse reduction of PC activation, while the selective switch-off of pf synapses had a much smaller effect. Therefore, changes in molecular layer connectivity consistently modified the PC discharge patterns both on-beam and off-beam and extended to a distance that reflects the propagation of activity through the pfs and the molecular layer interneuron network.

Synchronous Oscillations Caused by Noisy Background Activity in Mossy Fibers

Recordings from the granular layer *in vivo* have revealed low-frequency local field potential oscillations that occur

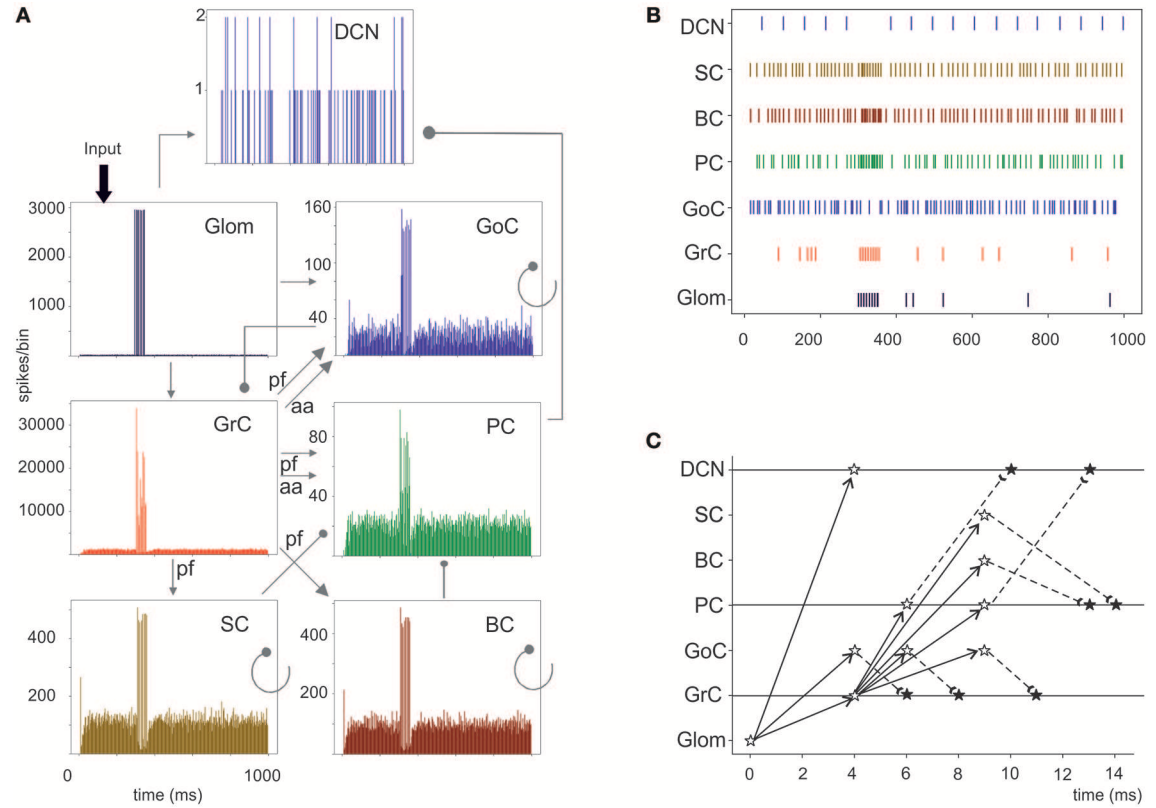


FIGURE 6 | Cerebellar network response to a mossy fiber burst. **(A)** Spikegrams of all cerebellar neurons in the model. A burst in gloms causes a burst-to-burst propagation in GrCs and PCs. GoCs, SCs, and BCs also generate bursts that, by being inhibitory, contribute to terminate the GrC, and PC bursts and to generate the burst-pause PC response. The DCN cells show a pause during stimulation. **(B)** Raster plot of one cerebellar neuron for each population in the model. Note the spread of the mf bursts inside the cerebellar cortical networks and the corresponding pause in the DCN. **(C)** Spike-time response plot showing the temporal sequence of neuronal activation and inhibition. The arrows represent the connectivity (solid lines show excitatory connections, dashed lines inhibitory connections). The stars represent the post-synaptic neuron response: white stars are excited neurons, black stars are inhibited neurons.

synchronously over distances of several hinders of micrometers (Pellerin and Lamarre, 1997; Hartmann and Bower, 1998). Similar properties were observed also in previous granular layer models (Maex and De Schutter, 1998; Solinas et al., 2010; Sudhakar et al., 2017). In the scaffold model, spontaneous circuit activity clearly emerged due to background firing in the mossy fibers, provided that the frequency of the background mossy fiber discharge was increased from 1 to 5 Hz and pfs-GoCs connection weight was increased from 0.4 to 30.4, supporting the concept that oscillations require a specific synaptic balance to emerge (Maex and De Schutter, 1998; Solinas et al., 2010; Sudhakar et al., 2017; **Figure 9**). In response to the input, GrCs sparsely discharged at low frequencies (GrCs do not show intrinsic spontaneous activity), while the intrinsic activity of all the other neurons was modulated (GoC, PC, MLI, and DCNC are autorhythmic) (see I_e values in **Table 3**). Interestingly, the neurons of the granular layer (GrCs and GoCs) showed a pattern of low-frequency oscillations (mean frequency of 1.8 Hz) that was evident across the whole network. The oscillation frequency is the same in autocorrelograms of both GrCs and GoCs, and in the cross-correlogram between Golgi and granule cells. This ensemble behavior is probably due to the inhibitory feedback from GoCs to GrCs in the following way: (1) GrCs activity sums up in several GoCs, (2) GoCs, which are synchronized through parallel fibers and reciprocal inhibitory synapses, discharge almost synchronously, (3) a large population of GrCs is phasically inhibited, (4) inhibition terminates and GrCs recover responsiveness to the background mossy fiber input, then restarting the cycle.

DISCUSSION

In this paper a new scaffold modeling strategy is presented, that is used to simulate fundamental functional properties of the cerebellar microcircuit. The cerebellar scaffold includes the canonical neuron types (GrCs, GoCs, PCs, SCs, BCs, DCNCs), each one with specific geometry of dendritic and axonal fields and with specific convergence/divergence ratios for connectivity. The neurons were purposefully simplified into single point models in order to focus on network connectivity before involving more complex neuronal geometries and properties. The circuit functionality was then tested by applying background activity and burst stimuli and evaluating the network responses. In

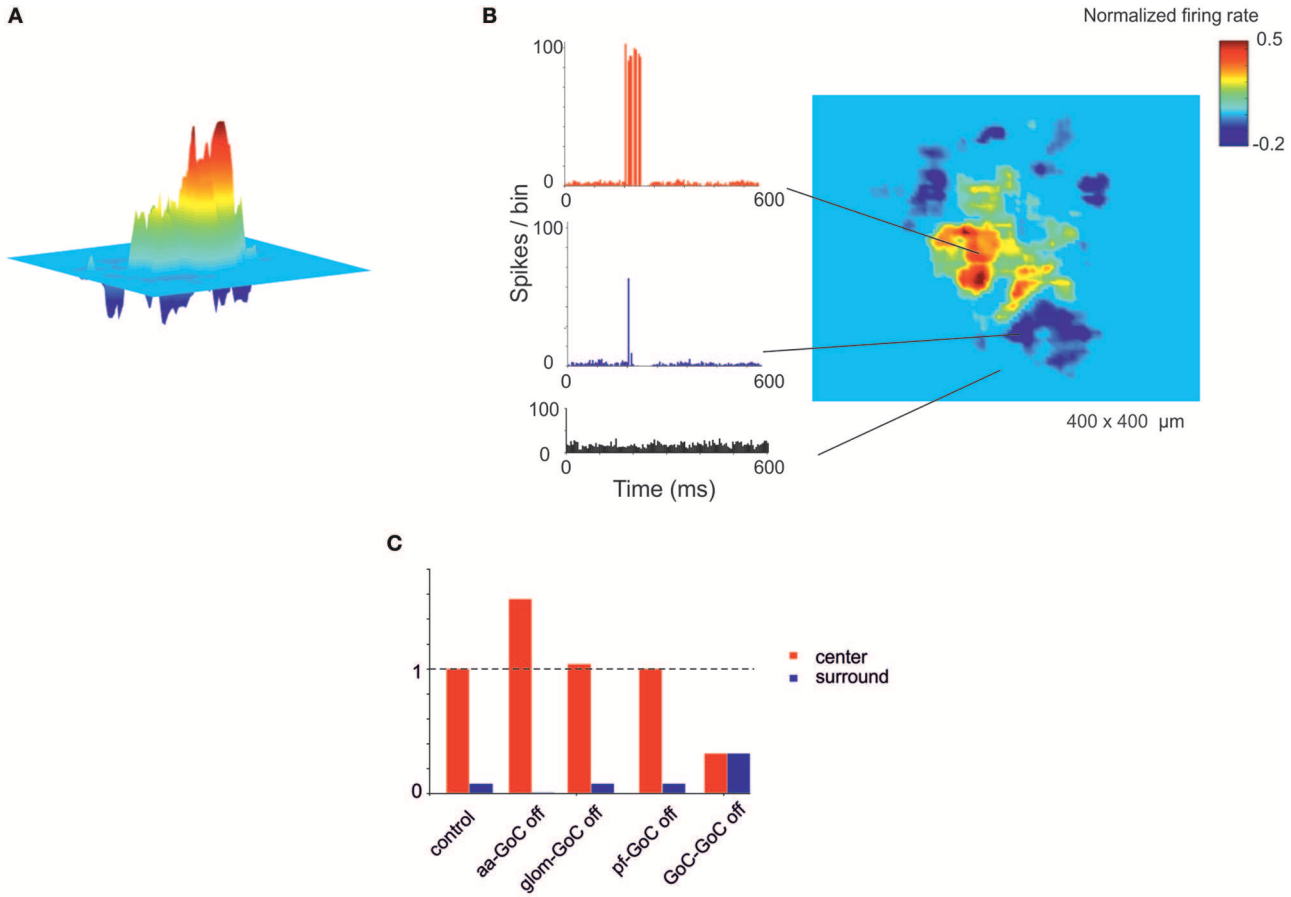


FIGURE 7 | Center-surround organization of activity in the granular layer. **(A)** In response to a mossy fiber burst (40 gloms at 150 Hz for 50 ms), the granular layer responds with a core (red area) of activity surrounded by inhibition (blue area). **(B)** PSTH of GrCs in the center-surround. The activity in the core is characterized by robust spike bursts, while just sporadic spikes are generated in the surround. No activity changes are observed outside the center-surround structure. **(C)** The histogram shows the changes in center-surround extension that occur following selective switch-off of synapses impinging on GoCs. Note the prominent role of aa-GoC synapses and GoC-GoC synapses (bars are values normalized to control).

addition to faithfully reproduce a broad range of experimental observations, the cerebellar scaffold shows the emergence of complex spatiotemporal patterns of activity similar to those observed *in vivo* and eventually predicts the critical role of local connectome for network functionality.

The Scaffold Design

The scaffold includes two modules: cell placement and connectivity. The first module placed neurons in their corresponding layers according to density values derived from literature. Cell placement exploited a bounded self-avoiding random walk algorithm, except for PCs, which required a placement rule accounting for their regular disposition and quasi-planar non-intersecting dendritic trees. The second module generated microcircuit connectivity by defining the pre- and post-synaptic neurons among those intersecting their dendritic and axonal fields and then establishing the corresponding number of synapses through specific connection probabilities. Geometrical constraints and divergence/convergence ratios derived from literature played a critical role to implement the microcircuit connectome. The distributions of soma distances, both for cell positioning and connectivity, were assessed and provided an internal validation for the network construction processes. The cerebellar scaffold was then implemented using LIF neuron models, whose parameters were tuned to approximate the basal firing and input-output relationships of cerebellar neurons. Finally, functional simulations required the scaffold to be uploaded into a neuro-simulator, either pyNEST or pyNEURON, that worked equivalently well for this purpose.

The scaffold modeling strategy used for the cerebellum microcircuit differs from that used for the cortical microcolumn mostly because here the connectivity rules are based on available statistical and geometrical information rather than on single neuron morphologies and touch-detection (Markram et al., 2015). This allows the scaffold to fully exploit the experimental data available in the cerebellar literature despite incomplete availability of detailed morphological reconstructions of cerebellar neurons. By considering that neuron models based on detailed morphological reconstructions are still unavailable

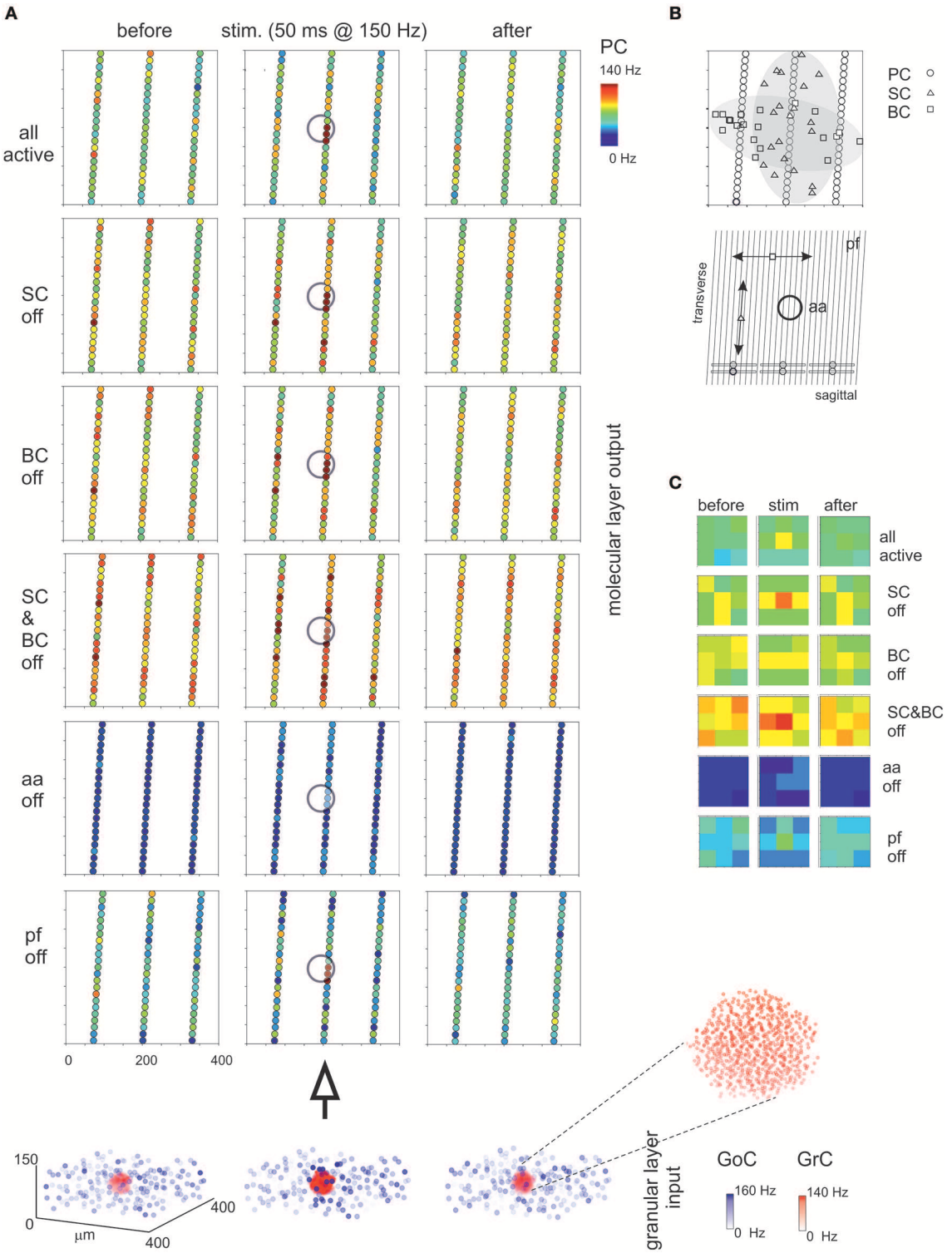


FIGURE 8 | Maps of PC activation and sensitivity to molecular layer connectivity. **(A)** The maps show the activity change of PCs in response to a mossy fiber burst (40 glom at 150 Hz for 50 ms). The pattern of activity is determined by various connection properties that are tested in turn. (all active) PC inhibition is achieved through a differential orientation of SC axons (mostly transversal or "on-beam") vs. BC axons (mostly sagittal or "off-beam") and that PC excitation depends on both aa and pf synapses with specific origin from GrCs. Alternative patterns are generated by (SC off) the specific switch-off of SC, (BC off) the specific switch-off of BC, or (SC&BC off) the complete switch-off of both SC and BC, (aa off) the specific switch-off of aa synapses, (pf off) the specific switch-off of pf synapses. It should be

(Continued)

FIGURE 8 | noted that these changes in network connectivity modify the PC discharge patterns both on-beam and off-beam and extend to a distance that reflects the propagation of activity through the molecular layer interneuron network. The circles indicate the location of the underlying active spots of activity in the granular layer. The bottom plot represents the activity of GoCs (blue) and GrCs (red) before, during and after the stimulus burst. This activity occurs in a spot (enlarged in the inset) corresponding to the center-surround shown in **Figure 7**. **(B)** The schematic diagrams show the orientation of fibers and connections in the network. **(C)** The PC activity was averaged into 3 × 3 matrices in order to better appreciate where activity changes take place. Note the emergence of the central spot in several cases.

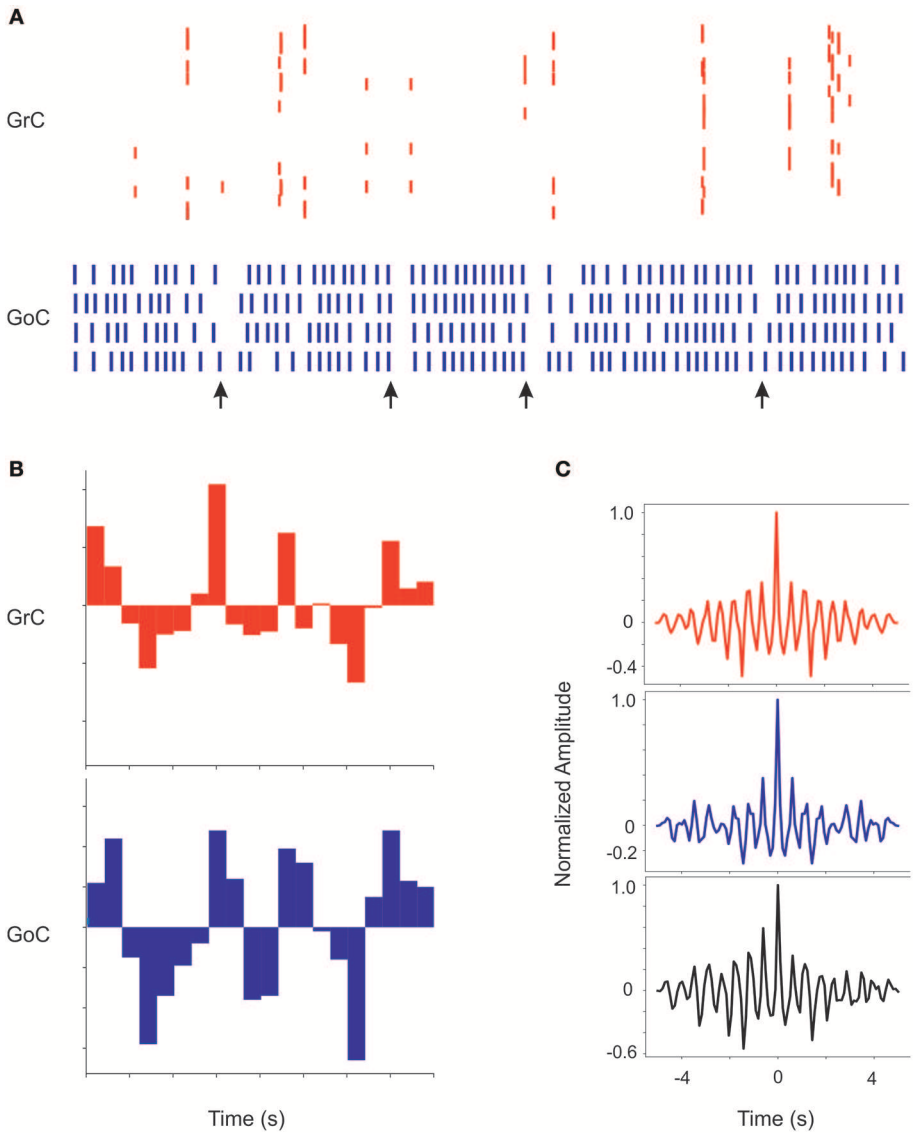


FIGURE 9 | Coherent low-frequency oscillations in granular layer neurons. Activity of GrCs (red) and GoCs (blue) during sustained 5 Hz random mf input. **(A)** Raster plots from exemplar GrCs and GoCs. Note that synchronous patterns are visible in the neuronal response (arrows). In this regimen, GoC activity is more intense than GrC activity due to the autorhytmic discharge of GoC neurons. The neurons are not necessarily part of a center-surround and therefore not all activities appear correlated. **(B)** Cumulative PSTH of the whole GrC and GoC populations of the model along a 5 s period. Note that the two PSTH show marked low-frequency oscillations (average 1.8 Hz) around their average level of activity. **(C)** Autocorrelograms of activity in the GrC and GoC populations and crosscorrelogram of the GrC and GoC populations (in this example the inhibition among GoCs is switched off). Note the high level of correlation in all the three cases on the same main frequency of 1.8 Hz.

in most neuronal circuits, the strategy adopted here for the cerebellum has a large potential for applicability in a variety of different brain microcircuits. It should be noted that our "intersection-connection" rule is formally similar to the "proximity-connection" rule used for touch-detection in Markram et al. (2015). Eventually, the touch detection strategy could be implemented in the scaffold providing a construction alternative, in which connectivity is directly constrained by neuronal morphology. The advantage would be to specifically connect synapses on specific positions of the dendritic tree,

fully exploiting non-linear dendritic computations. Also the data positioning rules could be changed, for example by importing cell positions from the Allen Brain Atlas directly (available at https://portal.bluebrain.epfl.ch/) or using network growing algorithms (Setty et al., 2011; Nguyen et al., 2016).

Simulation and Validation of Cerebellar Network Properties

Following background random inputs and punctuate sensory stimulation, the scaffold model predicted a set of relevant network response properties that matched experimental observations. In the granular layer, the GrC and GoC activity in response to random mossy fiber inputs showed loose synchronicity, as observed *in vivo* (Pellerin and Lamarre, 1997; Hartmann and Bower, 1998). The GrC and GoC activity in response to bursts in mossy fiber bundles revealed a center-surround organization, as reported *in vitro* (Mapelli and D'Angelo, 2007; Diwakar et al., 2011; Gandolfi et al., 2014), which was enhanced by aa synapses (Cesana et al., 2013). At the level of molecular layer, the spatial PC discharge patterns depended on the geometry of SC and BC inhibition (Santamaria et al., 2007), and PC burst-pause discharges were generated (Herzfeld et al., 2015). The local PC response was enhanced by granule cell aa, as anticipated by Bower and Woolston (1983), Walter et al. (2009), and Cesana et al. (2013), supporting the vertical organization of GrC-PC transmission (Rokni et al., 2007).

Interestingly, despite the use of simplified LIF neuron models, the observation of these activity patterns suggests that structural constraints play a critical role in determining local neuronal dynamics. In particular, connectivity allows the emergence of center-surrounds in the granular layer and spots of PC activity in the molecular layer. There are several aspects that remain to be assessed and will be easily incorporated into more advanced versions of the cerebellar scaffold.

First of all, assessing the role of non-linear neuronal properties, like intrinsic oscillations, resonance bursting and rebounds, requires to incorporate into the scaffold realistic ionic-channel based neuronal models. Along with this, dendritic computation needs morphologically detailed neuron models that are currently under construction and testing. These include the PCs model (e.g., De Schutter and Bower, 1994; Masoli et al., 2015; Masoli and D'Angelo, 2017), the GrC model (Masoli et al., 2017), the GoC model (Solinas et al., 2007a,b; Kanichay and Silver, 2008), the SC and BC model (currently under construction), the DCN model (Steuber and Jaeger, 2013). Dynamic synapses (Tsodyks and Markram, 1997; Nieus et al., 2006; Migliore et al., 2015) will likewise be incorporated to introduce synaptic strength modulation mechanisms.

Secondly, the scaffold could be used to evaluate the trade-off between computational efficiency and precision. Therefore, the present LIF single point neurons could be substituted by others (extended generalized LIF, E-GLIF) embedding non-linear firing properties (e.g., Brette and Gerstner, 2005; Geminiani et al., 2018) and accounting for synaptic dendritic location by modifying the transmission weight depending on the distance of synapses from the soma (Rössert et al., 2016) or based on experimental data when available.

Thirdly, fully implementing cerebellar connectivity requires the introduction of models of the inferior cerebellar olive (IO) (Libster and Yarom, 2013; De Gruijl et al., 2014). This will complete the DCN-PC-IO cerebellar circuit, allowing the model to simulate oscillations in the olivo-cerebellar circuit, their impact on PC dendritic calcium signaling and computation, and eventually climbing fiber control of plasticity at parallel fiber synapses (Coesmans et al., 2004).

Finally, the addition of novel connections and cells, like the PC to GrC inhibition (Guo et al., 2016) in the anterior cerebellum, the unipolar-brush cell subcircuit in the flocculo-nodular lobe (Mugnaini and Floris, 1994; Subramaniyam et al., 2014), or the DCN to granular layer connections (Gao et al., 2016) will allow to further expand the simulation of cerebellar processing in different cerebellar modules.

CONCLUSIONS

The scaffold model was able to reconstruct the complex geometry and neuronal interactions of the cerebellar microcircuit based on *intersection-connection* rules. Given its architectural design, that puts in series interchangeable programming modules, the scaffold could now be used to plug-in different network configurations into neuronal simulators like e.g., pyNEST and pyNEURON. Both the cell placement algorithm, the neuron model types and the connectivity rules could be substituted to assess different construction strategies and adapted to available data to probe specific functional hypotheses. For example, the connectivity could be recalculated using realistic neuronal morphologies and touch-detection algorithms (*proximity-connection* rule), as in the cortical microcolumn model (Markram et al., 2015). We envisage that this scaffold modeling strategy, given its versatility, will also be able to host microcircuits different from cerebellum, thus providing a new tool for neurocomputational investigations. It should be noted that the reconstruction procedure is python-based and can be imported in many different simulation frameworks. For example, translation of the scaffold model into PyNN would facilitate neurorobotic and neuromorphic hardware applications (Davison et al., 2008).

AUTHOR CONTRIBUTIONS

SC, EM, CM, and CC have written the code and run the simulations and taken part to the production of text and figures. CC has coordinated the modeling and simulation activity. ED has directed the work and edited the manuscript.

FUNDING

This research was supported by the HBP Brain Simulation Platform funded from the European Union's Horizon 2020 Framework Programme for Research and Innovation under the Specific Grant Agreement No. 720270 (Human Brain Project SGA1) and under the Specific Grant Agreement No. 785907 (Human Brain Project SGA2).

SUPPLEMENTARY MATERIAL

The Supplementary Material for this article can be found online at: https://www.frontiersin.org/articles/10.3389/fninf.2019.00037/full#supplementary-material

Video S1 | The movie displays the sequential placement of Stellate cells in the volume following the bounded self-avoiding random-walk algorithm.

REFERENCES

Aizenman, C. D., Huang, E. J., and Linden, D. J. (2003). Morphological correlates of intrinsic electrical excitability in neurons of the deep cerebellar nuclei. *J. Neurophysiol.* 89, 1738–1747. doi: 10.1152/jn.01043.2002

Akram, M. A., Nanda, S., Maraver, P., Armananzas, R., and Ascoli, G. A. (2018). An open repository for single-cell reconstructions of the brain forest. *Sci. Data* 5:180006. doi: 10.1038/sdata.2018.6

Barbour, B. (1993). Synaptic currents evoked in Purkinje cells by stimulating individual granule cells. *Neuron* 11, 759–769. doi: 10.1016/0896-6273(93)90085-6

Barmack, N. H., and Yakhnitsa, V. (2008). Functions of interneurons in mouse cerebellum. *J. Neurosci.* 28, 1140–1152. doi: 10.1523/JNEUROSCI.3942-07.2008

Billings, G., Piasini, E., Lorincz, A., Nusser, Z., and Silver, R. A. (2014). Network structure within the cerebellar input layer enables lossless sparse encoding. *Neuron* 83, 960–974. doi: 10.1016/j.neuron.2014.07.020

Boele, H. J., Koekkoek, S. K., De Zeeuw, C. I., and Ruigrok, T. J. (2013). Axonal sprouting and formation of terminals in the adult cerebellum during associative motor learning. *J. Neurosci.* 33, 17897–17907. doi: 10.1523/JNEUROSCI.0511-13.2013

Bower, J. M., and Woolston, D. C. (1983). Congruence of spatial organization of tactile projections to granule cell and Purkinje cell layers of cerebellar hemispheres of the albino rat: vertical organization of cerebellar cortex. *J. Neurophysiol.* 49, 745–766. doi: 10.1152/jn.1983.49.3.745

Brette, R., and Gerstner, W. (2005). Adaptive exponential integrate-and-fire model as an effective description of neuronal activity. *J. Neurophysiol.* 94, 3637–3642. doi: 10.1152/jn.00686.2005

Brette, R., Rudolph, M., Carnevale, T., Hines, M., Beeman, D., Bower, J. M., et al. (2007). Simulation of networks of spiking neurons: a review of tools and strategies. *J. Comput. Neurosci.* 23, 349–398. doi: 10.1007/s10827-007-0038-6

Canepari, M., Papageorgiou, G., Corrie, J. E., Watkins, C., and Ogden, D. (2001). The conductance underlying the parallel fibre slow EPSP in rat cerebellar Purkinje neurones studied with photolytic release of L-glutamate. *J. Physiol.* 533, 765–772. doi: 10.1111/j.1469-7793.2001.00765.x

Cao, Y., Maran, S. K., Dhamala, M., Jaeger, D., and Heck, D. H. (2012). Behavior-related pauses in simple-spike activity of mouse Purkinje cells are linked to spike rate modulation. *J. Neurosci.* 32, 8678–8685. doi: 10.1523/JNEUROSCI.4969-11.2012

Cesana, E., Pietrajtis, K., Bidoret, C., Isope, P., D'Angelo, E., Dieudonne, S., et al. (2013). Granule cell ascending axon excitatory synapses onto Golgi cells implement a potent feedback circuit in the cerebellar granular layer. *J. Neurosci.* 33, 12430–12446. doi: 10.1523/JNEUROSCI.4897-11.2013

Chadderton, P., Margrie, T. W., and Hausser, M. (2004). Integration of quanta in cerebellar granule cells during sensory processing. *Nature* 428, 856–860. doi: 10.1038/nature02442

Chu, C. P., Bing, Y. H., Liu, H., and Qiu, D. L. (2012). Roles of molecular layer interneurons in sensory information processing in mouse cerebellar cortex Crus II *in vivo*. *PLoS ONE* 7:e37031. doi: 10.1371/journal.pone.0037031

Coesmans, M., Weber, J. T., De Zeeuw, C. I., and Hansel, C. (2004). Bidirectional parallel fiber plasticity in the cerebellum under climbing fiber control. *Neuron* 44, 691–700. doi: 10.1016/j.neuron.2004.10.031

D'Angelo, E., Antonietti, A., Casali, S., Casellato, C., Garrido, J. A., Luque, N. R., et al. (2016). Modeling the cerebellar microcircuit: new strategies for a long-standing issue. *Front. Cell. Neurosci.* 10:176. doi: 10.3389/fncel.2016.00176

D'Angelo, E., Nieus, T., Maffei, A., Armano, S., Rossi, P., Taglietti, V., et al. (2001). Theta-frequency bursting and resonance in cerebellar granule cells: experimental evidence and modeling of a slow k+-dependent mechanism. *J. Neurosci.* 21, 759–770. doi: 10.1523/JNEUROSCI.21-03-00759.2001

D'Angelo, E., Solinas, S., Mapelli, J., Gandolfi, D., Mapelli, L., and Prestori, F. (2013). The cerebellar Golgi cell and spatiotemporal organization of granular layer activity. *Front. Neural Circuits* 7:93. doi: 10.3389/fncir.2013.00093

D'Angelo, E., and Wheeler-Kingshott, C. (2017). "Modelling the brain: elementary components to explain ensemble functions," in *Rivista Del Nuovo Cimento*, ed L. Cifarelli (Bologna: Società Italiana di Fisica, Italian Physical Society), 36.

Davison, A. P., Bruderle, D., Eppler, J., Kremkow, J., Muller, E., Pecevski, D., et al. (2008). PyNN: a common interface for neuronal network simulators. *Front. Neuroinform.* 2:11. doi: 10.3389/neuro.11.011.2008

De Gruijl, J. R., Sokol, P. A., Negrello, M., and De Zeeuw, C. I. (2014). Modulation of electrotonic coupling in the inferior olive by inhibitory and excitatory inputs: integration in the glomerulus. *Neuron* 81, 1215–1217. doi: 10.1016/j.neuron.2014.03.009

De Schutter, E., and Bower, J. M. (1994). An active membrane model of the cerebellar Purkinje cell. I. Simulation of current clamps in slice. *J. Neurophysiol.* 71, 375–400. doi: 10.1152/jn.1994.71.1.375

Destexhe, A., Bal, T., McCormick, D. A., and Sejnowski, T. J. (1996). Ionic mechanisms underlying synchronized oscillations and propagating waves in a model of ferret thalamic *slices*. 76, 2049–2070. doi: 10.1152/jn.1996.76.3.2049

Dieudonne, S. (1998). Submillisecond kinetics and low efficacy of parallel fibre-Golgi cell synaptic currents in the rat cerebellum. *J. Physiol.* 510(Pt. 3), 845–866. doi: 10.1111/j.1469-7793.1998.845bj.x

Diwakar, S., Lombardo, P., Solinas, S., Naldi, G., and D'Angelo, E. (2011). Local field potential modeling predicts dense activation in cerebellar granule cells clusters under LTP and LTD control. *PLoS ONE* 6:e21928. doi: 10.1371/journal.pone.0021928

Eccles, J. C., Ito, M., and Szentagothai, J. (1967). *The Cerebellum as a Neuronal Machine*. Heidelberg, NY: Springer-Verlag.

Eppler, J. M., Helias, M., Muller, E., Diesmann, M., and Gewaltig, M. O. (2008). PyNEST: a convenient interface to the NEST Simulator. *Front. Neuroinform.* 2:12. doi: 10.3389/neuro.11.012.2008

Gandolfi, D., Pozzi, P., Tognolina, M., Chirico, G., Mapelli, J., and D'Angelo, E. (2014). The spatiotemporal organization of cerebellar network activity resolved by two-photon imaging of multiple single neurons. *Front. Cell. Neurosci.* 8:92. doi: 10.3389/fncel.2014.00092

Gao, Z., Proietti-Onori, M., Lin, Z., Ten Brinke, M. M., Boele, H. J., Potters, J. W., et al. (2016). Excitatory cerebellar nucleocortical circuit provides internal amplification during associative conditioning. *Neuron* 89, 645–657. doi: 10.1016/j.neuron.2016.01.008

Gauck, V., and Jaeger, D. (2000). The control of rate and timing of spikes in the deep cerebellar nuclei by inhibition. *J. Neurosci.* 20, 3006–3016. doi: 10.1523/JNEUROSCI.20-08-03006.2000

Geminiani, A., Casellato, C., Locatelli, F., Prestori, F., Pedrocchi, A., and D'Angelo, E. (2018). Complex dynamics in simplified neuronal models: reproducing golgi cell electroresponsiveness. *Front. Neuroinform.* 12:88. doi: 10.3389/fninf.2018.00088

Gundappa-Sulur, G., De Schutter, E., and Bower, J. M. (1999). Ascending granule cell axon: an important component of cerebellar cortical circuitry. *J. Comp. Neurol.* 408, 580–596. doi: 10.1002/(SICI)1096-9861(19990614)408:4<580::AID-CNE11>3.0.CO;2-O

Guo, C., Witter, L., Rudolph, S., Elliott, H. L., Ennis, K. A., and Regehr, W. G. (2016). Purkinje cells directly inhibit granule cells in specialized regions of the cerebellar cortex. *Neuron* 91, 1330–1341. doi: 10.1016/j.neuron.2016.08.011

Hamori, J., and Somogyi, J. (1983). Differentiation of cerebellar mossy fiber synapses in the rat: a quantitative electron microscope study. *J. Comp. Neurol.* 220, 365–377. doi: 10.1002/cne.902200402

Hartmann, M. J., and Bower, J. M. (1998). Oscillatory activity in the cerebellar hemispheres of unrestrained rats. *J. Neurophysiol.* 80, 1598–1604. doi: 10.1152/jn.1998.80.3.1598

Heine, S. A., Highstein, S. M., and Blazquez, P. M. (2010). Golgi cells operate as state-specific temporal filters at the input stage of the cerebellar cortex. *J. Neurosci.* 30, 17004–17014. doi: 10.1523/JNEUROSCI.3513-10.2010

Herzfeld, D. J., Kojima, Y., Soetedjo, R., and Shadmehr, R. (2015). Encoding of action by the Purkinje cells of the cerebellum. *Nature* 526, 439–442. doi: 10.1038/nature15693

Hines, M. L., Davison, A. P., and Muller, E. (2009). NEURON and Python. *Front. Neuroinform.* 3:1. doi: 10.3389/neuro.11.001.2009

Huang, C. M., Wang, L., and Huang, R. H. (2006). Cerebellar granule cell: ascending axon and parallel fiber. *Eur. J. Neurosci.* 23, 1731–1737. doi: 10.1111/j.1460-9568.2006.04690.x

Hull, C., and Regehr, W. G. (2012). Identification of an inhibitory circuit that regulates cerebellar Golgi cell activity. *Neuron* 73, 149–158. doi: 10.1016/j.neuron.2011.10.030

Jaeger, D., and Bower, J. M. (1994). Prolonged responses in rat cerebellar Purkinje cells following activation of the granule cell layer: an intracellular *in vitro* and *in vivo* investigation. *Exp. Brain Res.* 100, 200–214. doi: 10.1007/BF00227191

Jakab, R. L., and Hamori, J. (1988). Quantitative morphology and synaptology of cerebellar glomeruli in the rat. *Anat. Embryol.* 179, 81–88. doi: 10.1007/BF00305102

Jorntell, H., Bengtsson, F., Schonewille, M., and De Zeeuw, C. I. (2010). Cerebellar molecular layer interneurons—computational properties and roles in learning. *Trends Neurosci.* 33, 524–532. doi: 10.1016/j.tins.2010.08.004

Kanichay, R. T., and Silver, R. A. (2008). Synaptic and cellular properties of the feedforward inhibitory circuit within the input layer of the cerebellar cortex. *J. Neurosci.* 28, 8955–8967. doi: 10.1523/JNEUROSCI.5469-07.2008

Korbo, L., Andersen, B. B., Ladefoged, O., and Møller, A. (1993). Total numbers of various cell types in rat cerebellar cortex estimated using an unbiased stereological method. *Brain Res.* 609, 262–268. doi: 10.1016/0006-8993(93)90881-M

Lennon, W., Hecht-Nielsen, R., and Yamazaki, T. (2014). A spiking network model of cerebellar Purkinje cells and molecular layer interneurons exhibiting irregular firing. *Front. Comput. Neurosci.* 8:157. doi: 10.3389/fncom.2014.00157

Libster, A. M., and Yarom, Y. (2013). In and out of the loop: external and internal modulation of the olivo-cerebellar loop. *Front. Neural Circuits* 7:73. doi: 10.3389/fncir.2013.00073

Llinas, R. R. (2014). Intrinsic electrical properties of mammalian neurons and CNS function: a historical perspective. *Front. Cell. Neurosci.* 8:320. doi: 10.3389/fncel.2014.00320

Maas, W. (1997). Networks of spiking neurons: the third generation of neural network models. *Neural. Networks* 10, 1659–1671. doi: 10.1016/S0893-6080(97)00011-7

Maex, R., and De Schutter, E. (1998). Synchronization of golgi and granule cell firing in a detailed network model of the cerebellar granule cell layer. *J. Neurophysiol.* 80, 2521–2537. doi: 10.1152/jn.1998.80.5.2521

Maex, R., Vos, B. P., and De Schutter, E. (2000). Weak common parallel fibre synapses explain the loose synchrony observed between rat cerebellar golgi cells. *J. Physiol.* 523(Pt. 1), 175–192. doi: 10.1111/j.1469-7793.2000.t01-1-00175.x

Magyar, P., Szechenyi, B., and Palkovits, M. (1972). A quantitative study of the olivocerebellar connections. *Acta Morphol. Acad. Sci. Hung.* 20, 71–75.

Mapelli, J., and D'Angelo, E. (2007). The spatial organization of long-term synaptic plasticity at the input stage of cerebellum. *J. Neurosci.* 27, 1285–1296. doi: 10.1523/JNEUROSCI.4873-06.2007

Markram, H. (2006). The blue brain project. *Nat. Rev. Neurosci.* 7, 153–160. doi: 10.1038/nrn1848

Markram, H. (2012). The human brain project. *Sci. Am.* 306, 50–55. doi: 10.1038/scientificamerican0612-50

Markram, H., Muller, E., Ramaswamy, S., Hill, S. L., Segev, I., Schürmann, F., et al. (2015). Reconstruction and simulation of neocortical microcircuitry. *Cell* 163, 456–492. doi: 10.1016/j.cell.2015.09.029

Masoli, S., and D'Angelo, E. (2017). Synaptic activation of a detailed purkinje cell model predicts voltage-dependent control of burst-pause responses in active dendrites. *Front. Cell. Neurosci.* 11:278. doi: 10.3389/fncel.2017.00278

Masoli, S., Rizza, M. F., Sgritta, M., Van Geit, W., Schurmann, F., and D'Angelo, E. (2017). Single neuron optimization as a basis for accurate biophysical modeling: the case of cerebellar granule cells. *Front. Cell. Neurosci.* 11:71. doi: 10.3389/fncel.2017.00071

Masoli, S., Solinas, S., and D'Angelo, E. (2015). Action potential processing in a detailed Purkinje cell model reveals a critical role for axonal compartmentalization. *Front. Cell. Neurosci.* 9:47. doi: 10.3389/fncel.2015.00047

Medina, J. F., and Mauk, M. D. (2000). Computer simulation of cerebellar information processing. *Nat. Neurosci.* 3(Suppl), 1205–1211. doi: 10.1038/81486

Mezey, E., Palkovits, M., Hamori, J., and Szentagothal, J. (1977). Quantiative cytology and electron microscopy of the cerebellar nuclei in the cat. *Verh. Anat. Ges.* 171–176.

Migliore, M., Cavarretta, F., Marasco, A., Tulumello, E., Hines, M. L., and Shepherd, G. M. (2015). Synaptic clusters function as odor operators in the olfactory bulb. *Proc. Natl. Acad. Sci. U.S.A.* 112, 8499–8504. doi: 10.1073/pnas.1502513112

Mugnaini, E., and Floris, A. (1994). The unipolar brush cell: a neglected neuron of the mammalian cerebellar cortex. *J. Comp. Neurol.* 339, 174–180. doi: 10.1002/cne.903390203

Nguyen, H., Dayan, P., Pujic, Z., Cooper-White, J., and Goodhill, G. J. (2016). A mathematical model explains saturating axon guidance responses to molecular gradients. *Elife* 5:e12248. doi: 10.7554/eLife.12248

Nieus, T., Sola, E., Mapelli, J., Saftenku, E., Rossi, P., and D'Angelo, E. (2006). LTP regulates burst initiation and frequency at mossy fiber-granule cell synapses of rat cerebellum: experimental observations and theoretical predictions. *J. Neurophysiol.* 95, 686–699. doi: 10.1152/jn.00696.2005

Nieus, T. R., Mapelli, L., and D'Angelo, E. (2014). Regulation of output spike patterns by phasic inhibition in cerebellar granule cells. *Front. Cell. Neurosci.* 8:246. doi: 10.3389/fncel.2014.00246

Palay, S. L., and Chan-Palay, V. (1974). *Cerebellar Cortex: Cytology and Organization*. New York, NY: Springer-Verlag. doi: 10.1007/978-3-642-65581-4

Pellerin, J. P., and Lamarre, Y. (1997). Local field potential oscillations in primate cerebellar cortex during voluntary movement. *J. Neurophysiol.* 78, 3502–3507. doi: 10.1152/jn.1997.78.6.3502

Person, A. L., and Raman, I. M. (2012). Synchrony and neural coding in cerebellar circuits. *Front. Neural Circuits* 6:97. doi: 10.3389/fncir.2012.00097

Ramakrishnan, K. B., Voges, K., De Propris, L., De Zeeuw, C. I., and D'Angelo, E. (2016). Tactile stimulation evokes long-lasting potentiation of purkinje cell discharge in vivo. *Front. Cell. Neurosci.* 10:36. doi: 10.3389/fncel.2016.00036

Rancz, E. A., Ishikawa, T., Duguid, I., Chadderton, P., Mahon, S., and Hausser, M. (2007). High-fidelity transmission of sensory information by single cerebellar mossy fibre boutons. *Nature* 450, 1245–1248. doi: 10.1038/nature05995

Rieubland, S., Roth, A., and Hausser, M. (2014). Structured connectivity in cerebellar inhibitory networks. *Neuron* 81, 913–929. doi: 10.1016/j.neuron.2013.12.029

Roggeri, L., Rivieccio, B., Rossi, P., and D'Angelo, E. (2008). Tactile stimulation evokes long-term synaptic plasticity in the granular layer of cerebellum. *J. Neurosci.* 28, 6354–6359. doi: 10.1523/JNEUROSCI.5709-07.2008

Rokni, D., Llinas, R., and Yarom, Y. (2007). Stars and stripes in the cerebellar cortex: a voltage sensitive dye study. *Front. Syst. Neurosci.* 1:1. doi: 10.3389/neuro.06.001.2007

Rössert, C., Pozzorini, C., Chindemi, G., Davison, A. P., Eroe, C., King, J., et al. (2016). Automated point-neuron simplification of data-driven microcircuit models. *arXiv*. arXiv:1604.00087

Santamaria, F., Tripp, P. G., and Bower, J. M. (2007). Feedforward inhibition controls the spread of granule cell-induced Purkinje cell activity in the cerebellar cortex. *J. Neurophysiol.* 97, 248–263. doi: 10.1152/jn.01098.2005

Setty, Y., Chen, C. C., Secrier, M., Skoblov, N., Kalamatianos, D., and Emmott, S. (2011). How neurons migrate: a dynamic *in-silico* model of neuronal migration in the developing cortex. *BMC Syst. Biol.* 5:154. doi: 10.1186/1752-0509-5-154

Sims, R. E., and Hartell, N. A. (2005). Differences in transmission properties and susceptibility to long-term depression reveal functional specialization of ascending axon and parallel fiber synapses to Purkinje cells. *J. Neurosci.* 25, 3246–3257. doi: 10.1523/JNEUROSCI.0073-05.2005

Solinas, S., Forti, L., Cesana, E., Mapelli, J., De Schutter, E., and D'Angelo, E. (2007a). Fast-reset of pacemaking and theta-frequency resonance patterns in cerebellar golgi cells: simulations of their impact *in vivo*. *Front. Cell. Neurosci.* 1:4. doi: 10.3389/neuro.03.004.2007

Solinas, S., Forti, L., Cesana, E., Mapelli, J., De Schutter, E., and D'Angelo, E. (2007b). Computational reconstruction of pacemaking and intrinsic electroresponsiveness in cerebellar Golgi cells. *Front. Cell. Neurosci.* 1:2. doi: 10.3389/neuro.03.002.2007

Solinas, S., Nieus, T., and D'Angelo, E. (2010). A realistic large-scale model of the cerebellum granular layer predicts circuit spatio-temporal filtering properties. *Front. Cell. Neurosci.* 4:12. doi: 10.3389/fncel.2010.00012

Soltesz, I., and Staley, K. (2018). *Computational Neuroscience in Epilepsy, 1st edn*. Cambridge, MA: Academic Press.

Steuber, V., and Jaeger, D. (2013). Modeling the generation of output by the cerebellar nuclei. *Neural Netw.* 47, 112–119. doi: 10.1016/j.neunet.2012.11.006

Subramaniyam, S., Solinas, S., Perin, P., Locatelli, F., Masetto, S., and D'Angelo, E. (2014). Computational modeling predicts the ionic mechanism of late-onset responses in unipolar brush cells. *Front. Cell. Neurosci.* 8:237. doi: 10.3389/fncel.2014.00237

Sudhakar, S. K., Hong, S., Raikov, I., Publio, R., Lang, C., Close, T., et al. (2017). Spatiotemporal network coding of physiological mossy fiber inputs by the cerebellar granular layer. *PLoS Comput. Biol.* 13:e1005754. doi: 10.1371/journal.pcbi.1005754

Sultan, F. (2001). Distribution of mossy fibre rosettes in the cerebellum of cat and mice: evidence for a parasagittal organization at the single fibre level. *Eur. J. Neurosci.* 13, 2123–2130. doi: 10.1046/j.0953-816x.2001.01593.x

Sultan, F., and Heck, D. (2003). Detection of sequences in the cerebellar cortex: numerical estimate of the possible number of tidal-wave inducing sequences represented. *J. Physiol. Paris* 97, 591–600. doi: 10.1016/j.jphysparis.2004.01.016

Sunkin, S. M., Ng, L., Lau, C., Dolbeare, T., Gilbert, T. L., Thompson, C. L., et al. (2013). Allen Brain Atlas: an integrated spatio-temporal portal for exploring the central nervous system. *Nucleic Acids Res.* 41, D996–D1008. doi: 10.1093/nar/gks1042

Tripathy, S. J., Savitskaya, J., Burton, S. D., Urban, N. N., and Gerkin, R. C. (2014). NeuroElectro: a window to the world's neuron electrophysiology data. *Front. Neuroinform.* 8:40. doi: 10.3389/fninf.2014.00040

Tsodyks, M. V., and Markram, H. (1997). The neural code between neocortical pyramidal neurons depends on neurotransmitter release probability. *Proc. Natl. Acad. Sci. U.S.A.* 94, 719–723. doi: 10.1073/pnas.94.2.719

Walter, J. T., Dizon, M. J., and Khodakhah, K. (2009). The functional equivalence of ascending and parallel fiber inputs in cerebellar computation. *J. Neurosci.* 29, 8462–8473. doi: 10.1523/JNEUROSCI.5718-08.2009

Yamazaki, T., and Nagao, S. (2012). A computational mechanism for unified gain and timing control in the cerebellum. *PLoS ONE* 7:e33319. doi: 10.1371/journal.pone.0033319

Conflict of Interest Statement: The authors declare that the research was conducted in the absence of any commercial or financial relationships that could be construed as a potential conflict of interest.

Copyright © 2019 Casali, Marenzi, Medini, Casellato and D'Angelo. This is an open-access article distributed under the terms of the Creative Commons Attribution License (CC BY). The use, distribution or reproduction in other forums is permitted, provided the original author(s) and the copyright owner(s) are credited and that the original publication in this journal is cited, in accordance with accepted academic practice. No use, distribution or reproduction is permitted which does not comply with these terms.

frontiers in Neuroinformatics

ORIGINAL RESEARCH
published: 04 June 2019
doi: 10.3389/fninf.2019.00040

Multi-Lag Analysis of Symbolic Entropies on EEG Recordings for Distress Recognition

Arturo Martínez-Rodrigo[1,2], *Beatriz García-Martínez*[3,4], *Luciano Zunino*[5,6], *Raúl Alcaraz*[7] *and Antonio Fernández-Caballero*[1,4,8]*

[1] Departamento de Sistemas Informáticos, Escuela Politécnica de Cuenca, Universidad de Castilla-La Mancha, Cuenca, Spain, [2] Instituto de Tecnologías Audiovisuales de Castilla-La Mancha, Universidad de Castilla-La Mancha, Cuenca, Spain, [3] Departamento de Sistemas Informáticos, Escuela Técnica Superior de Ingenieros Industriales, Universidad de Castilla-La Mancha, Albacete, Spain, [4] Instituto de Investigación en Informática de Albacete, Universidad de Castilla-La Mancha, Albacete, Spain, [5] Centro de Investigaciones Ópticas (CONICET La Plata–CIC), C.C. 3, Gonnet, Argentina, [6] Departamento de Ciencias Básicas, Facultad de Ingeniería, Universidad Nacional de La Plata, La Plata, Argentina, [7] Research Group in Electronic, Biomedical and Telecommunication Engineering, Escuela Politécnica de Cuenca, Universidad de Castilla-La Mancha, Cuenca, Spain, [8] CIBERSAM (Biomedical Research Networking Centre in Mental Health), Madrid, Spain

Distress is a critical problem in developed societies given its long-term negative effects on physical and mental health. The interest in studying this emotion has notably increased during last years, being electroencephalography (EEG) signals preferred over other physiological variables in this research field. In addition, the non-stationary nature of brain dynamics has impulsed the use of non-linear metrics, such as symbolic entropies in brain signal analysis. Thus, the influence of time-lag on brain patterns assessment has not been tested. Hence, in the present study two permutation entropies denominated Delayed Permutation Entropy and Permutation Min-Entropy have been computed for the first time at different time-lags to discern between emotional states of calmness and distress from EEG signals. Moreover, a number of curve-related features were also calculated to assess brain dynamics across different temporal intervals. Complementary information among these variables was studied through sequential forward selection and 10-fold cross-validation approaches. According to the results obtained, the multi-lag entropy analysis has been able to reveal new significant insights so far undiscovered, thus notably improving the process of distress recognition from EEG recordings.

Keywords: electroencephalography, distress, non-linear metrics, delayed permutation entropy, permutation min-entropy

OPEN ACCESS

Edited by:
Jan G. Bjaalie,
University of Oslo, Norway

Reviewed by:
Stavros I. Dimitriadis,
Cardiff University School of Medicine, United Kingdom
Young-Seok Choi,
Kwangwoon University, South Korea
Karsten Keller,
Universität zu Lübeck, Germany

***Correspondence:**
Antonio Fernández-Caballero
antonio.fdez@uclm.es

Received: *09 June 2018*
Accepted: *16 May 2019*
Published: *04 June 2019*

Citation:
Martínez-Rodrigo A, García-Martínez B, Zunino L, Alcaraz R and Fernández-Caballero A (2019) Multi-Lag Analysis of Symbolic Entropies on EEG Recordings for Distress Recognition. Front. Neuroinform. 13:40. doi: 10.3389/fninf.2019.00040

1. INTRODUCTION

Emotions are essential in human communication and interaction, and considerably influence on daily tasks related to cognition, perception and rational decision-making processes (Coan and Allen, 2007). Traditional techniques for emotion recognition are mainly focused on the analysis of physical aspects like facial expressions and speech characteristics (Calvo and D'Mello, 2010). However, given that emotional responses are initiated in the brain and then spread to other biological systems (Gao et al., 2015), interest in electroencephalogram (EEG) signals for emotion recognition has notably increased during the last years (Martínez-Rodrigo et al., 2017; Fernández-Sotos et al., 2018; Ramirez et al., 2018).

Existing affect models include from a few basic emotions (Ekman, 1992) to a wide variety of emotional states derived from the combination of basic ones (Schröder and Cowie, 2011). Russell's circumplex affect model is one of the approaches most widely used for emotion classification (Russell, 1980). In this bidimensional approach, emotions are distributed according to their level of valence (ranging from negative to positive) and arousal (from deactivated to activated). A relevant emotion that is receiving growing attention is negative stress, also called distress, because it presents a high prevalence in developed countries (Bong et al., 2013; Alberdi et al., 2016). Although today short-term distress is not considered a risk factor for health, a chronic condition of this emotion often causes or aggravates physical and mental disorders (Bender and Alloy, 2011; Mozos et al., 2017). In this regard, automatic distress identification from EEG signals would help prevent health problems and improve people's quality of life.

Since neural processes are non-linear and non-stationary, both at cellular and global level (Cao et al., 2015), non-linear metrics applied to EEG signal analysis should provide more relevant findings than linear indices traditionally used (Valenza et al., 2012). But, few studies have applied non-linearity to automatic detection of negative stress through EEG recordings (García-Martínez et al., 2019a). This is the case of symbolic entropies, such as Permutation Entropy (PE) (Bandt and Pompe, 2002) and Amplitude-Aware Permutation Entropy (AAPE) (Azami and Escudero, 2016), having demonstrated their efficiency in discriminating between calmness and distress (Hosseini and Naghibi-Sistani, 2011; García-Martínez et al., 2017; Martínez-Rodrigo et al., 2019). Here, the quantification of similar patterns is typically obtained through consecutive samples, or their averaging, within a complete time series.

No lag or time delay between patterns is necessary in those cases where the autocorrelation function of the signal presents a steep decay. However, a time series with long-range linear correlations shows a slow decay in its autocorrelation function. Not applying a lag may hinder entropy metrics from properly quantifying the complexity and non-linear dynamics of the signal. Indeed, it has already been demonstrated that time-delayed entropy tests are helpful to diminish the influence of autocorrelation for better evaluation of the non-linearity of time series (Kaffashi et al., 2008). Hence, a multi-lag approach has been applied to localization of epileptogenic areas through EEG recordings (Zhu et al., 2015).

Let us highlight that an improvement of PE called Permutation Min-Entropy (PME) has been recently introduced (Zunino et al., 2015). PME consists of an improved time-delayed symbolic alternative for identifying the existence of hidden temporal correlations in time series. This allows a better discrimination of time series with similar temporal correlations. Moreover, PME has been very recently applied to emotion recognition by using heart rate variability (Xia et al., 2018). The promising outcomes open a door to the hypothesis that time-delayed analysis may uncover existing information in physiological systems, not revealed before through non-delayed or basic multiscale entropy (MSE) analyses. Furthermore, to the best of our knowledge, no previous research has focused on the study of multi-lag approaches for emotion recognition from EEG signals.

For this reason, in the present manuscript a time-delayed version of AAPE—called Delayed Permutation Entropy (DPE)—and PME metrics are applied for the first time with several time delays for the sake of checking the influence of the lag on discrimination between calmness and distress from EEG recordings. The remainder of this paper is structured as follows. Section 2 details the analyzed database, the DPE and PME metrics computed from the EEG recordings and the statistical analysis. Section 3 summarizes the results, which are then discussed in section 4. Finally, section 5 concludes the most remarkable findings related to this study.

2. MATERIALS AND METHODS

2.1. Database

EEG signals were extracted from the publicly available Database for Emotion Analysis using Physiological Signals (DEAP) (Koelstra et al., 2012) to guarantee the reproducibility of this study as well as its fair comparison with previous or future works. This dataset contains a total of 1,280 EEG recordings and other peripheral variables from 32 healthy participants with ages ranging 19–37 (mean age of 26.9; 50% male) under different affective conditions. Forty one-minute length video clips with emotional content were used as stimuli in the experiment leading to the dataset. After each visualization, the participants described their emotional state by means of self-assessment manikins (SAM), two graphical scales representing nine intensity levels of valence and arousal (Morris, 1995).

Although the trials contained within the dataset cover the whole valence-arousal space, only two subsets corresponding to distress and calmness emotional states were studied in the present study, as shown in **Figure 1**. Indeed, calmness and distress groups were selected according to previous works dealing with the same problem (Bastos Filho et al., 2012; Pomer-Escher et al., 2014; García-Martínez et al., 2016; García-Martínez et al., 2017). Hence, distress trials were selected from arousal and valence levels higher than 5 and lower than 3, respectively. On the other hand, the calmness group contained trials with arousal and valence values lower than 4 and between 4 and 6, respectively. Therefore, a total number of 122 and 137 trials of distress and calmness, respectively, were finally analyzed in this work. Moreover, it is important to highlight that only the last 30 s of each trial were selected for further analysis.

2.2. EEG Signal Preprocessing

EEG signals were recorded at a sampling rate of 512 Hz with 32 electrodes placed according to the 10–20 standard system of electrode location (Klem et al., 1999). Before starting any kind of analysis, the recordings were preprocessed to eliminate noise and artifacts, thus preserving only the information related to brain activity. To this respect, the signals were initially down-sampled to 128 Hz and all EEG channels were re-referenced to the average potential of all electrodes. Next, a forward/backward high-pass filter at 3 Hz and a low-pass filter at 45 Hz cutoff

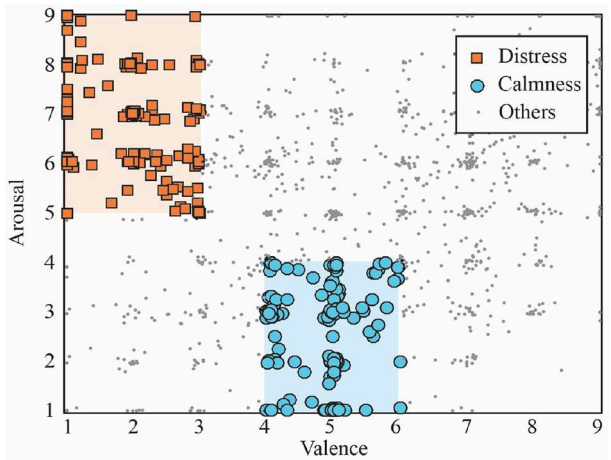


FIGURE 1 | Trials distribution included in DEAP database in the arousal–valence space. Selected groups of distress and calmness trials are highlighted.

frequency were applied to remove baseline and power line interferences, maintaining the frequency bands of interest in EEG recordings (Koelstra et al., 2012). After that, artifacts derived from physical activity (e.g., facial movements, eye blinks, heart bumping, etc.) and technical sources, such as electrode-pops were eliminated by means of independent component analysis (ICA) (Goh et al., 2017).

A well-known method with ability to automatically identify noisy independent components (ICs) was used (Nolan et al., 2010). Briefly, the algorithm firstly computed correlation between all ICs and electrooculography channels, as well as spatial kurtosis, power spectrum slope, Hurst exponent and median gradient for all ICs. Those components presenting at least an index with a value three times higher than standard deviation for all ICs were then removed. As a final step, the denoised EEG signal was reconstructed from the remaining ICs. It is worth noting that 1.05 ± 0.60 ICs were removed in average for each trial. More precisely, any artifactual IC was identified in 38 trials (14.67%), only one was removed in 168 trials (64.86%) and two were rejected in the remaining 53 trials (20.47%).

The EEG channels presenting high-amplitude noise were also detected and replaced by interpolation from adjacent electrodes (Reis et al., 2014). Although these signals were identified before ICA-based denoising of artifacts, their interpolation was developed after that preprocessing. This approach has been previously used by other authors (Forscher et al., 2016; Pincham et al., 2016; Bennett et al., 2018) and its main goal is to avoid mixing any non-linearity introduced by interpolation into the ICA decomposition (Nolan et al., 2010). Nonetheless, noisy EEG channels did not contribute to the rejection of artifacts (Nolan et al., 2010). As a result, the number of interpolated EEG channels was zero for 162 trials (62.55%), one for 83 trials (32.05%), two for 13 trials (5.02%) and three for the remaining trial (0.39%). Additionally, the most frequently interpolated channels were CP1 (in 21 trials, 21.65%), T8 (in 11 trials, 11.34%), CP5 (in 9 trial, 9.28%), AF4 (in 8 trial, 8.25%), T7 (in 6 trials, 6.19%), and FC2 (in 5 trials, 5.15%). The remaining channels were interpolated in <4% of trials.

2.3. Time-Delayed Version of Amplitude-Aware Permutation Entropy

Amplitude-Aware Permutation Entropy (AAPE) is an improvement of Permutation Entropy (PE) to consider amplitude information from analyzed time series (Fadlallah et al., 2013). Although this index has been mainly used in single-lag analyses, it can be adapted to deal with different time scales by changing the embedding delay τ (Azami and Escudero, 2016). Thus, for delayed-time PE computation, a time series $x(n) = \{x(1), x(2), \ldots, x(N)\}$ of length N is converted into $N - (m-1) \cdot \tau$ vectors of m samples, such that $\mathbf{X}_{i,m}^{\tau} = \{X_{i,m}^{\tau}(1), X_{i,m}^{\tau}(2), \ldots, X_{i,m}^{\tau}(m)\} = \{x(i), x(i+\tau) \ldots, x(i+(m-1)\cdot\tau)\}$, for $1 \leq i \leq N-(m-1)\cdot\tau$. Each vector $\mathbf{X}_{i,m}^{\tau}$ is associated with an ordinal pattern, described as permutation $\kappa_i = \{r_0, r_1, \ldots, r_{m-1}\}$ of $\{0, 1, \ldots, m-1\}$, such that its single components fulfill $X_{i,m}^{\tau}(r_0) \leq X_{i,m}^{\tau}(r_1) \leq \ldots \leq X_{i,m}^{\tau}(r_{m-2}) \leq X_{i,m}^{\tau}(r_{m-1})$. Hence, a total number of $m!$ ordinal sequences π_k are obtained from patterns $\mathbf{X}_m^{\tau}$. Then, the relative frequency of each sequence π_k is used to estimate its probability of appearance such that

$$p^{\tau}(\pi_k) = \frac{\sum_{i=1}^{N-(m-1)\cdot\tau} \delta(\pi_k, \kappa_i)}{N-(m-1)\cdot\tau}, \tag{1}$$

being $\delta(u, v)$ the Kronecker delta function modified specifically to work with sequences, i.e.,

$$\delta(u, v) = \begin{cases} 1, & \text{if } u(i) = v(i), \text{ for every } i = 1, 2, \ldots, m; \\ 0, & \text{for otherwise.} \end{cases} \tag{2}$$

Then, delayed-time PE is finally obtained by computing the Shannon entropy from the probability distribution of all symbols, such that

$$\mathrm{PE}(x, m, \tau) = -\frac{1}{\ln(m!)} \sum_{k=1}^{m!} p^{\tau}(\pi_k) \cdot \ln\left(p^{\tau}(\pi_k)\right). \tag{3}$$

The index is normalized by term $ln(m!)$ to obtain values ranging between 0 and 1. In the case of a completely predictable signal, only a pattern π_k is found and PE reports a 0 value. On the contrary, symbols π_k in unpredictable time series present the same probability of occurrence. Thus, PE provides the highest value 1. Hence, predictability information reported by PE is easily interpretable (Zanin et al., 2012). Nevertheless, only the ordinal structure of patterns is considered by this index, thus discarding the information related to the amplitude of each sample.

As amplitude differences could play a key role to determine the predictability of a time series, AAPE was introduced to overcome this limitation (Azami and Escudero, 2016). AAPE computation is based on calculating the probability of repetition of each pattern π_k by considering its relative frequency, and also the average absolute (AA) and relative amplitudes (RA) of vectors

$\mathbf{X}^{\tau}_{i,m}$. Amplitudes AA and RA are obtained, respectively, for a specific vector $\mathbf{X}^{\tau}_{i,m}$ as

$$AA^{\tau}_{i} = \frac{1}{m}\sum_{l=1}^{m}|X^{\tau}_{i,m}(l)| \tag{4}$$

and

$$RA^{\tau}_{i} = \frac{1}{m-1}\sum_{l=2}^{m}|X^{\tau}_{i,m}(l) - X^{\tau}_{i,m}(l-1)| \tag{5}$$

Then, the relative frequency of π_k is computed as

$$p^{\tau *}(\pi_k) = \frac{\sum_{i=1}^{N-(m-1)\cdot\tau}\delta(\pi_k,\kappa_i)\cdot\left(K\cdot AA^{\tau}_{i} + (1-K)\cdot RA^{\tau}_{i}\right)}{\sum_{i=1}^{N-(m-1)\cdot\tau} K\cdot AA^{\tau}_{i} + (1-K)\cdot RA^{\tau}_{i}}, \tag{6}$$

being K an adjusting coefficient of terms AA and RA, ranging from 0 to 1. As recommended by the authors, a value $K = 0.5$ was considered here. Finally, delayed-time AAPE, referred to as Delayed Permutation Entropy (DPE), is computed by means of Shannon entropy, such that

$$\mathrm{DPE}(x,m,\tau) = -\frac{1}{\ln(m!)}\sum_{k=1}^{m!}p^{\tau *}(\pi_k)\cdot\ln\left(p^{\tau *}(\pi_k)\right). \tag{7}$$

2.4. Permutation Min-Entropy

Recently, PE has also been generalized by replacing Shannon entropy with Rényi one, reaching a better characterization of some rare and frequent ordinal patterns (Zhao et al., 2013). More precisely, Rényi Permutation Entropy (RPE) is defined as

$$\mathrm{RPE}(x,m,\tau,q) = \frac{1}{\ln(m!)}\cdot\frac{1}{1-q}\cdot\ln\left(\sum_{k=1}^{m!}p^{\tau}(\pi_k)^{q}\right), \tag{8}$$

where order q ($q \geq 0$ and $q \neq 1$) is a bias parameter. Indeed, $q < 1$ benefits rare events and, contrarily, $q > 1$ privileges salient ones. It is mandatory to note that Shannon entropy is an instance of Rényi entropy for $q = 1$ and, hence, RPE is a more flexible tool than PE. In this respect, RPE has reported a more complete characterization of a variety of complex dynamics, including physiological processes (Mammone et al., 2015). In addition, RPE is featured to converge to a minimum entropy in the limit $q \to \infty$, thus providing Permutation Min-Entropy (PME) (Zunino et al., 2015). This new entropy-based metric is quickly and simply computed as

$$\mathrm{PME}(x,m,\tau) = -\frac{1}{\ln(m!)}\ln\left(\max_{k=1,2,\ldots,m!}\left[p^{\tau}(\pi_k)\right]\right), \tag{9}$$

still retaining the main advantages of PE, such as its simplicity, low computational cost, noise robustness, and invariance with respect to non-linear monotonous transformations. This index has also proven a greater ability than PE to detect the existence of subtle temporal structures in EEG channels (Zunino et al., 2015).

2.5. Feature Selection

Firstly, single DPE and PME values from lag $\tau = 1$ to lag $\tau = 10$ were computed for each subject by using a pattern length $m = 6$. Entropies computed for each time-lag are a measure of predictability of the time series and assess the effect of time dynamics from an inter-lag perspective. Indeed, larger entropy values represent more unpredictable dynamics of the EEG signals, showing an increase of autocorrelated patterns in a long-term fashion.

On the other hand, multi-lag entropy curves were parameterized by means of slopes, areas under curves and arc lengths. Indeed, some studies have previously reported that features extracted from parameterized curves may reveal important information related to the dynamics of the signals across different temporal intervals (Escudero et al., 2006). In this regard, to estimate the trend evolution of each time-lag curve, slopes between delay $\tau = 1$ and $\tau = 2$, 4, 6, 8, and 10 were calculated from all EEG channels of each trial and denoted as $Slp1-\tau$. The slope is estimated as the straight line connecting the multi-lag entropy values under study. Higher slope values suggest larger entropy increases between the original signal ($\tau = 1$) and higher versions in consecutive multi-lag time delays ($\tau = 2$–10).

Furthermore, areas enclosed under the multi-lag curve between lag $\tau = 1$ and lags $\tau = 2$, $\tau = 4$, $\tau = 6$, $\tau = 8$, and $\tau = 10$ were computed and denoted as $Ar1-\tau$. In this sense, a higher area is achieved when DPE and PME entropy values are higher for the majority of time delays, suggesting that time series are less predictable. Finally, the arc length (AL) for each time-delayed curve was computed between lags $\tau = 2$ and $\tau = 10$. An arc length value shows the morphological alterations of the curve across different lags, and may show significant differences among lags from different groups of study. The arc length of each multi-lag curve was computed as

$$AL = \sum_{\tau=2}^{\tau=10}\sqrt{1 + (E[\tau] - E[\tau-1])^2} \tag{10}$$

referring E to the values of DPE and PME for the corresponding time-lag τ in each case.

Hence, a total of 21 features were computed for symbolic-based entropies DPE and PME on each EEG channel. More precisely, 10 single entropy values (one for each of the 10 time-lags computed), 5 tendency parameters related to time-lag curves (slopes $Slp1-2$, $Slp1-4$, $Slp1-6$, $Slp1-8$, $Slp1-10$), and 6 shape-related features (areas under curves $Ar1-2$, $Ar1-4$, $Ar1-6$, $Ar1-8$, $Ar1-10$, and arc length AL) were obtained for each EEG channel.

2.6. Statistical Analysis

Once the features were computed for each metric under study, Shapiro-Wilks and Levene tests corroborated the normality and

homoscedasticity of the data, such that the results are expressed as mean and standard deviation. Then, statistical differences between features obtained for emotional states of calmness and distress were assessed for each time lag τ using a one-way analysis of variance (ANOVA). A value of statistical significance $\rho < 0.05$ was considered as significant.

Furthermore, the discriminatory power of each feature to distinguish between both groups of emotions was tested by using a stratified 10-fold cross-validation scheme. This methodology prevents over-fitting as well as other biases when performing the training/test operation on classifiers (Jung and Hu, 2015). Thus, the database selection containing 259 recordings was sliced into ten equally-sized folds with a balanced number of trials from both groups. Next, ten iterations were performed, such that in each one 9 out of 10-folds were used as a training subset, and 1 out of 10-folds was used as the test subset. To perform the classification, a receiver operating characteristic (ROC) approach was computed using the training trials to obtain an optimal threshold, which was then used to classify the trials in the test subset. It is worth noting that the threshold was selected as the cut-off point that maximizes accuracy (Acc). Values of sensitivity (Se), specificity (Sp), and Acc, obtained from the 10 iterations, were finally averaged to provide global and robust estimates.

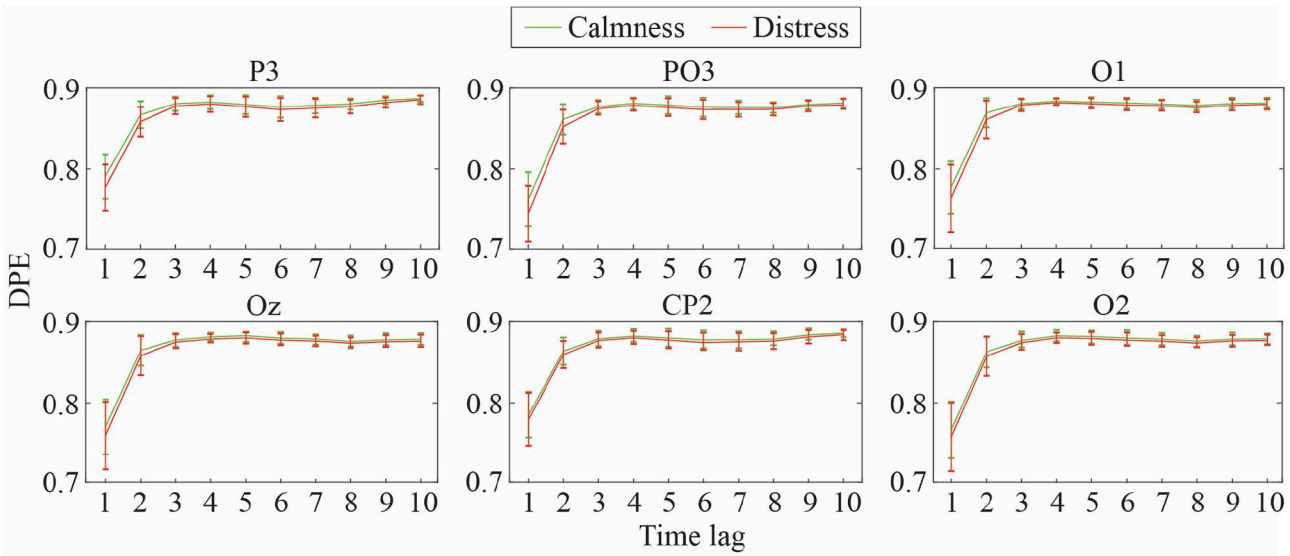


FIGURE 2 | Mean and standard deviation values of DPE at different time-lags for calmness and distress at the most significant EEG channels.

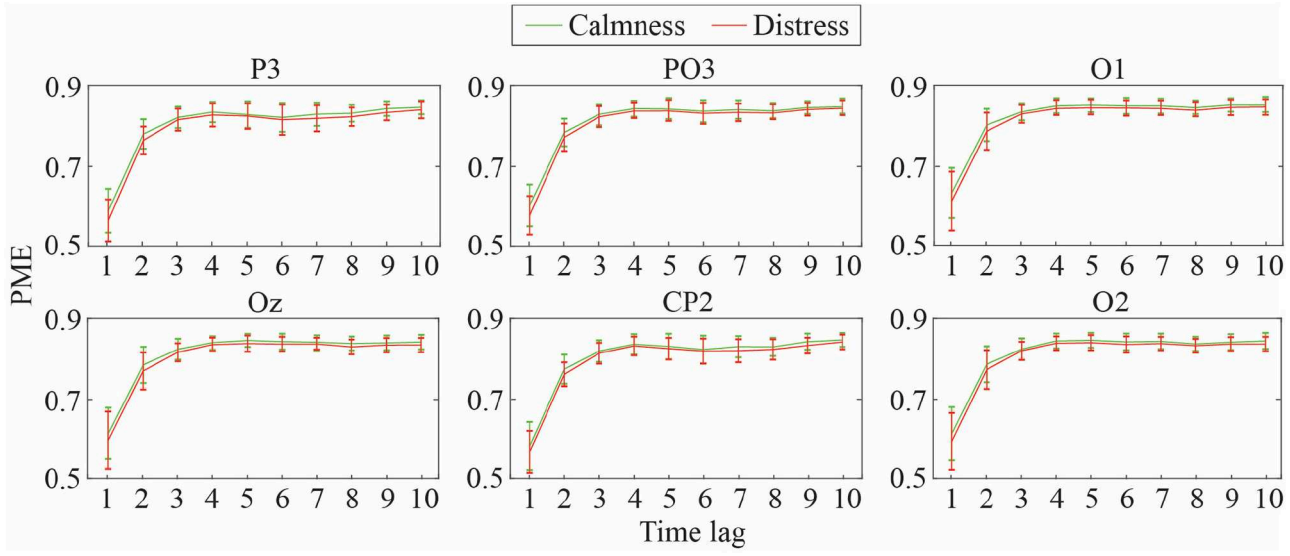


FIGURE 3 | Mean and standard deviation values of PME at different time-lags for calmness and distress at the most significant EEG channels.

Keeping in mind the objective of assessing possible relationships and complementary information among features, several advanced classifiers were used. Thus, a decision tree classifier (DTC), a support vector machine (SVM), a quadratic discriminant analysis (QDA) and a k-nearest neighbor (KNN) classifier were used. Regarding DTC, the nodes' growth was stopped when each node solely contained either fragments from only one group or a number of trials <20% of the entire dataset. Moreover, every node was split by using an impurity-based Gini index. Furthermore, the SVM classifier was run with a cubic kernel function and kernel scale of 1. Finally, the KNN classifier used an Euclidean distance metric with 10 neighbors, where the weight of the distance was computed to perform the classification by means of squared inverse. Nonetheless, given the high amount of analyzed features (21 features × 2 metrics × 32 channels), the subset providing most information was selected in first place for each classifier. Thus, a sequential forward selection (SFS) approach was used to select the subset of features minimizing misclassification rate for each classifier. A stratified 10-fold cross-validation scheme was also used to reduce overfitting in this analysis.

TABLE 1 | Results of ρ and Acc of the most relevant EEG channels for DPE and PME at different time-lags.

DPE		P3	PO3	O1	Oz	CP2	O2
$\tau = 1$	ρ	0.00261	8.85×10^{-5}	0.0044	0.0235	0.132	0.0696
	Acc (%)	62.20	62.90	58.00	58.70	54.00	56.40
$\tau = 2$	ρ	1.88×10^{-4}	0.0049	0.0012	0.0139	0.0455	0.0436
	Acc (%)	63.70	60.89	60.62	61.78	61.00	61.39
$\tau = 3$	ρ	3.23×10^{-5}	0.913	0.0440	0.3023	0.3045	0.0436
	Acc (%)	62.50	56.00	58.80	57.10	54.40	53.30
$\tau = 4$	ρ	6.08×10^{-5}	0.4390	0.2140	0.6010	0.4710	0.6320
	Acc (%)	61.80	55.60	55.60	52.50	57.10	53.70
$\tau = 5$	ρ	6.99×10^{-6}	0.7310	0.0866	0.5114	0.2740	0.7310
	Acc (%)	61.40	59.85	61.00	64.09	61.00	62.16
$\tau = 6$	ρ	2.69×10^{-5}	0.1210	0.0312	0.341	0.697	0.45
	Acc (%)	62.20	59.80	57.60	56.80	55.40	53.30
$\tau = 7$	ρ	3.76×10^{-5}	0.0136	0.0278	0.28	0.185	0.4514
	Acc (%)	62.90	60.60	61.00	53.70	57.50	54.40
$\tau = 8$	ρ	6.55×10^{-5}	0.3520	0.0197	0.1130	0.1630	0.205
	Acc (%)	62.90	58.70	56.40	56.00	55.20	53.70
$\tau = 9$	ρ	1.14×10^{-4}	0.0932	0.0543	0.3210	0.0148	0.5670
	Acc (%)	61.00	57.10	55.00	55.60	60.20	54.80
PME		**P3**	**PO3**	**O1**	**Oz**	**CP2**	**O2**
$\tau = 1$	ρ	3.33×10^{-4}	8.85×10^{-4}	0.017	0.128	0.0824	0.109
	Acc (%)	61.00	59.10	59.10	56.80	54.80	55.60
$\tau = 2$	ρ	4.34×10^{-4}	0.0049	0.0044	0.0637	0.0089	0.1610
	Acc (%)	61.40	59.10	61.00	56.80	56.50	56.40
$\tau = 3$	ρ	0.0905	0.913	0.0532	0.362	0.342	0.633
	Acc (%)	59.80	60.50	59.80	58.30	57.10	53.70
$\tau = 4$	ρ	0.034	0.439	0.865	0.169	0.476	0.764
	Acc (%)	59.20	56.00	56.80	57.80	59.80	61.70
$\tau = 5$	ρ	0.379	0.731	0.181	0.166	0.346	0.749
	Acc (%)	57.50	58.70	64.50	61.00	62.50	60.20
$\tau = 6$	ρ	0.216	0.121	0.0334	0.472	0.674	0.593
	Acc (%)	56.80	62.20	62.20	62.50	56.40	61.40
$\tau = 7$	ρ	6.85×10^{-4}	0.0136	0.194	0.974	0.0173	0.941
	Acc (%)	61.00	64.10	62.20	60.20	62.60	58.2
$\tau = 8$	ρ	1.44×10^{-4}	0.352	0.0786	0.0857	0.145	0.734
	Acc (%)	65.60	62.50	66.40	65.10	60.20	55.20
$\tau = 9$	ρ	5.38×10^{-5}	0.0932	0.0621	0.675	0.0026	0.798
	Acc (%)	68.30	62.90	60.20	59.10	68.70	58.70

3. RESULTS

3.1. Results for Delayed Permutation Entropy and Permutation Min-Entropy

Mean and standard deviation of DPE and PME values for the most relevant EEG channels at different time-lags ($1 \leq \tau \leq 10$) are shown in **Figures 2**, **3**, respectively. As can be observed, both metrics obtained a similar trend throughout the increasing time-lags. DPE and PME values for calmness are higher than for distress trials, especially at lower lags. However, as time-lag increases the average differences between groups become smaller, such that at higher time-lags the mean entropy differences between groups become imperceptible. Furthermore, a certain degree of stabilization at time-lags $>$ 3 for both metrics can also be noticed, where the standard deviation decreases as the analyzed time-lag increases.

TABLE 2 | Results of ρ and Acc of the DPE curve-related parameters.

DPE		P3	PO3	O1	Oz	CP2	O2
$Slp1-2$	ρ	0.0152	3.30×10^{-4}	0.049	0.0970	0.5606	0.2044
	Acc (%)	57.92	61.78	57.14	57.92	54.05	58.69
$Slp1-4$	ρ	2.94×10^{-4}	4.71×10^{-5}	0.0048	0.0160	0.1783	0.0504
	Acc (%)	58.69	61.39	57.53	60.23	54.44	59.46
$Slp1-6$	ρ	4.60×10^{-4}	6.92×10^{-5}	0.0056	0.0189	0.1475	0.0576
	Acc (%)	58.30	60.62	59.46	61.12	53.28	58.30
$Slp1-8$	ρ	0.0011	1.78×10^{-4}	0.0087	0.0350	0.3408	0.0909
	Acc (%)	58.69	62.16	58.30	58.69	53.67	58.42
$Slp1-10$	ρ	5.65×10^{-4}	1.22×10^{-4}	0.0089	0.0456	0.3002	0.0933
	Acc (%)	59.85	62.23	59.07	57.14	53.67	57.53
$Ar1-2$	ρ	4.30×10^{-5}	5.48×10^{-5}	0.0024	0.0174	0.0713	0.0542
	Acc (%)	61.67	62.16	59.07	57.45	55.09	56.76
$Ar1-4$	ρ	1.33×10^{-4}	2.84×10^{-4}	0.0025	0.0279	0.0717	0.0976
	Acc (%)	61.00	59.07	57.92	57.53	55.73	54.05
$Ar1-6$	ρ	1.14×10^{-5}	0.0010	0.0031	0.0457	0.1075	0.1443
	Acc (%)	60.62	59.46	58.87	56.51	56.76	54.44
$Ar1-8$	ρ	0.0016	0.0015	0.0034	0.0543	0.0929	0.1609
	Acc (%)	60.23	60.62	58.30	58.69	55.98	53.28
$Ar1-10$	ρ	6.42×10^{-4}	9.30×10^{-4}	0.0027	0.0488	0.0516	0.1559
	Acc (%)	60.87	59.85	55.20	54.83	57.14	53.02
AL	ρ	0.0021	1.04×10^{-4}	0.0136	0.0351	0.1672	0.0808
	Acc (%)	56.37	63.47	57.53	57.92	55.21	54.95

Table 1 shows the statistical significance and global classification performance, that is accuracy (Acc), for time-lags ($1 \leq \tau \leq 10$) in DPE and PME metrics, respectively. Although there are similarities among mean entropy curves, the performance achieved for each metric differs considerably throughout the time-lags. In general terms, DPE shows a poorer performance discriminating between emotional states of calmness and distress than PME. As can be observed in **Table 1**, only lower time-lag entropies show a relevant statistical significance. Moreover, the overall discriminatory power for all cases is around 60%, decreasing even more when higher time-lags are analyzed. This effect is clearly seen at parieto-occipital and occipital channels PO3, O1, O2, and Oz. For instance, PO3 channel achieved a global performance of 62.9% at time-lag $\tau = 1$, while accuracy decreased down to 57.10% at time-lag $\tau = 9$. Only parietal channel P3 showed a regular statistical significance throughout every single time-lag, reaching a maximum global classification performance at time-lag $\tau = 2$ with 63.7% of subjects classified correctly.

On the contrary, PME showed better global classification performance for certain channels, especially at higher time-lags. For instance, parietal channel P3, classified correctly 68.3% of trials between calmness and distress at time-lag $\tau = 9$. Similarly, centro-parietal channel CP2 showed a poor performance when no lag was applied ($\tau = 1$), but it raised at higher time-lags, achieving the best single global performance at time-lag $\tau = 9$, classifying correctly the 68.7% of the subjects. This improvement supposes an increase of more than 13% regarding PME at no lag $\tau = 1$ and more than 8% compared with DPE metric at time-lag $\tau = 9$. Moreover, there seems to be a certain degree of complementarity between DPE and PME at different time-lags, because the same EEG channels measured with each metric show relevant information at different time-lags. This contrast is well-noticed at parietal channel P3. No relevant differences between several time-lags were found when DPE was computed for P3, i.e., all time-lags presented a similar discriminatory power. On the contrary, the same channel showed an important increasing performance when it was analyzed by means of PME metric at higher time-lags; hence relevant information was noticed when time-delay was performed.

3.2. Results From Curve-Related Parameters

Table 2 summarizes diagnostic accuracy of every curve-based parameter derived from DPE analysis for the most relevant channels. As can be seen, almost all features achieved statistically significant differences between groups ($\rho < 0.05$). Features obtained from parietal channel P3 achieved a notable statistical significance, especially in the area under the time-lag curve ($Ar1 - 2$ to $Ar1 - 6$), thus stating the differences between curves at lower and their convergence at higher time-lags. It is also remarkable that parieto-occipital channel PO3 achieved a good performance for all features. With respect to slope-based parameters, global accuracy ranged from 60.62 to 62.23%, $Slp1 - 10$ being the feature with maximum performance for this channel. Similarly, accuracy of area-based lag parameters ranged from 59.07 to 62.16%, where $Ar1 - 2$ reported the maximal performance. It is also worth noting that arc-length reached the maximum global accuracy, classifying correctly 63.47% of trials, and thus overcoming the best performance obtained by single DPE entropy at the same channel at lag $\tau = 1$. Finally, the rest of the parameters computed from occipital channels O1, O2, and Oz and centro-parietal channel CP2 obtained a more limited performance, their global accuracy ranging from 53.28 to 61.12%.

TABLE 3 | Results of ρ and Acc of the PME curve-related parameters.

PME		P3	PO3	O1	Oz	CP2	O2
$Slp1 - 2$	ρ	0.0324	0.0012	0.2999	0.5982	0.7753	0.2025
	Acc (%)	57.92	59.70	54.83	54.83	52.90	54.05
$Slp1 - 4$	ρ	0.0057	2.94×10^{-4}	0.0148	0.05	0.1168	0.1127
	Acc (%)	58.38	59.07	58.69	59.07	56.37	55.98
$Slp1 - 6$	ρ	0.0013	4.28×10^{-4}	0.0447	0.1396	0.0939	0.1025
	Acc (%)	60.62	58.69	58.42	54.83	55.21	55.60
$Slp1 - 8$	ρ	0.0116	1.89×10^{-4}	0.0344	0.2420	0.1974	0.0688
	Acc (%)	58.69	57.92	53.53	54.05	52.51	55.64
$Slp1 - 10$	ρ	0.0063	2.85×10^{-4}	0.0516	0.1980	0.1914	0.1682
	Acc (%)	60.68	61.39	58.30	56.37	55.21	54.83
$Ar1 - 2$	ρ	2.06×10^{-4}	2.55×10^{-4}	0.0081	0.0878	0.0292	0.1169
	Acc (%)	58.69	59.61	59.07	54.05	51.74	52.90
$Ar1 - 4$	ρ	8.10×10^{-4}	0.009	0.0085	0.1381	0.0447	0.2704
	Acc (%)	58.87	59.46	59.85	54.33	52.90	55.41
$Ar1 - 6$	ρ	0.0060	0.0276	0.0089	0.1538	0.0930	0.3011
	Acc (%)	59.07	57.63	58.78	55.60	54.44	54.44
$Ar1 - 8$	ρ	0.0051	0.0204	0.0094	0.1734	0.0748	0.3732
	Acc (%)	57.92	58.30	59.85	55.21	55.48	53.00
$Ar1 - 10$	ρ	0.0016	0.0193	0.0072	0.1666	0.0440	0.4302
	Acc (%)	60.05	57.92	59.15	55.73	55.21	54.44
AL	ρ	0.0097	5.00×10^{-4}	0.0950	0.1582	0.5373	0.0987
	Acc (%)	59.82	58.69	56.16	53.67	54.44	58.69

Similarly, **Table 3** summarizes discriminant ability of all curve-based parameters derived from PME analysis for the most relevant channels. In this case, both statistical significance and global accuracy are more limited than for DPE curve-related parameters. All features computed on parietal channel P3 and parieto-occipital channel PO3 resulted to be statistical significant. The global accuracy obtained for these channels ranged from 57 to 61%, thus achieving a worse performance than before. Moreover, only a few curve-related parameters from occipital channels O1, O2, and Oz showed statistical significance, and the global accuracy was below 60% for all the parameters. Finally, CP2 achieved the worst performance, where global accuracy was around 55%.

3.3. Multi-Parametric Analysis and Advanced Classification

For each classifier, the optimal number of features minimizing its misclassification rate through an SFS scheme ranged from 5 to 8 in each iteration of a 10-fold cross-validation approach. The occurrence of the most relevant variables are displayed in **Figure 4**. As can be seen, entropy-based metrics were mainly

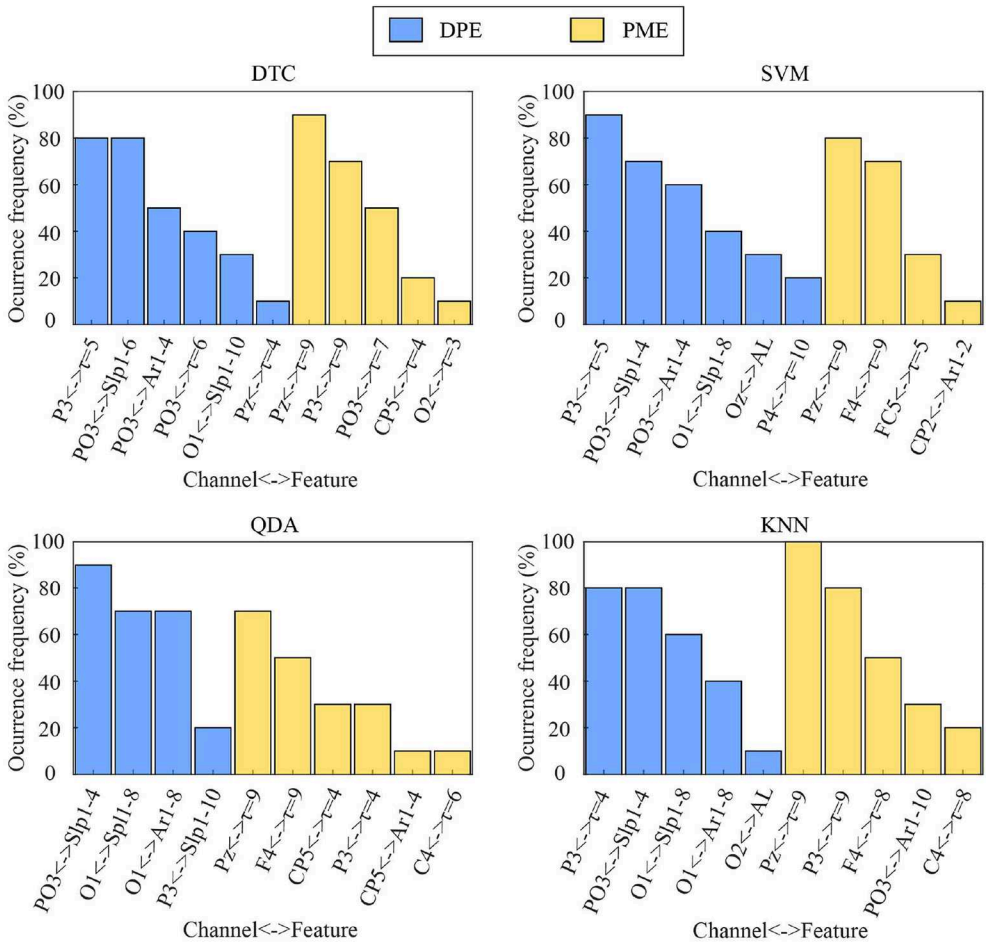


FIGURE 4 | Occurrence of the most selected features through an SFS scheme within a 10-fold cross-validation approach for each classifier.

TABLE 4 | Values of sensitivity, specificity, and accuracy obtained for each classifier once the feature selection process had finished.

	DTC	SVM	QDA	KNN
Sensitivity (%)	75.41	91.97	82.21	93.72
Specificity (%)	83.94	90.16	61.56	90.66
Accuracy (%)	79.92	91.12	75.66	92.32

chosen for time-lags longer than 1 and curve-related variables both from DPE and PME. Moreover, it should be noted that most of these features were selected in nearly all folds, thus only changing the less relevant ones for the resulting classification models. More precisely, for all classifiers, most DPE-based parameters were chosen from EEG channels P3 and PO3 and most PME-based features from channels P3, Pz, FC5, C4, and CP5.

Once the feature selection process finished for each classifier, the obtained classification results are displayed in **Table 4** in terms of sensitivity, specificity and accuracy. Note that global discriminant ability for all approaches ranged from 75.66% (for QDA) to 92.32% (for KNN). Furthermore, the SVM classifier achieved a comparable performance to KNN, classifying correctly 91.12% trials. Finally, it should also be highlighted that both SVM and KNN classifiers reported the largest diagnostic accuracies with well-balanced values of sensitivity and specificity.

4. DISCUSSION

During the last years automatic emotion recognition has received special attention due to its importance in areas, such as medicine and education. Among the different types of emotions, continued distress is one of the most studied because it is often harmful for health. Considering its relevance, distress has been assessed in a wide variety of scenarios, including driving tasks (Healey and Picard, 2005), military exercises (Skinner and Simpson, 2002), surgical procedures (Marrelli et al., 2014), and on-line exams (Gomes et al., 2014), among others. An interesting study recently published shows a methodology to redirect stress episodes toward positive moods (Fernández-Caballero et al., 2016).

Taking into consideration this preamble, several works have been published in the literature. Their research is focused on

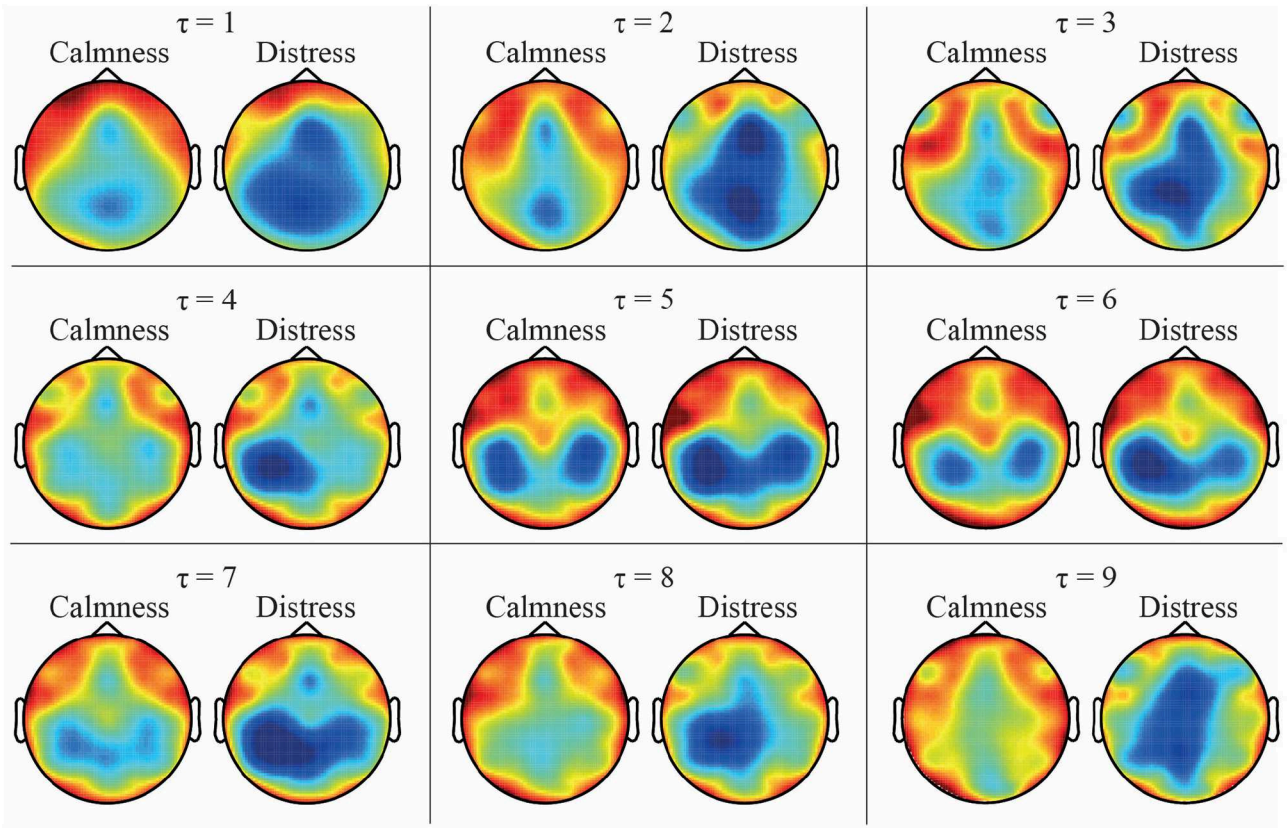


FIGURE 5 | Topological EEG representation of average calmness and distress values for time-lags from τ = 1 to τ = 9 using PME metric.

automatic distress recognition using EEG recordings (Hosseini et al., 2010; Khosrowabadi et al., 2011; Peng et al., 2013; Minguillon et al., 2016; Al-Nafjan et al., 2017; Al-Shargie et al., 2018; Jebelli et al., 2018; García-Martínez et al., 2019b). However, only a few of them have analyzed this phenomena from a non-linear point of view (García-Martínez et al., 2016). Recently, another approach reported that symbolic analysis of brain dynamics was able to detect distress (García-Martínez et al., 2017). In that study, PE and its extension called AAPE were used to assess brain dynamics for each EEG channel. However, the analysis was carried out without considering the possibility of exploring hidden non-linear information at time-lags higher than one. This was the starting point that motivated the present study.

To the best of our knowledge, this is the first work addressing the effects of multi-lag for distress recognition from EEG recordings. For this purpose, a modified version of AAPE was used to analyze EEG signals with distinct time-lags. Additionally, PME was also considered in this study, since it is an improved symbolic alternative for identifying the existence of hidden temporal dynamics in time series and it allows a better discrimination of signals with similar temporal correlations (Zunino et al., 2015). Indeed, it has been recently applied in the study of emotion recognition using heart rate variability with promising results (Xia et al., 2018).

As expected, both DPE and PME metrics reported the same trends when calculating the mean entropy values across the different time-lags, as was observed in **Figures 2**, **3**. Calmness emotional state reported higher entropy values than distress for all EEG channels, especially at lower time-lags. However, this difference became smaller as the time-lag increased. Furthermore, the time-lag analysis revealed additional entropy information not observed at time-lag τ = 1, especially at centro-parietal and occipital channels. This effect can also be well-noticed in **Figure 5**, which shows a topological representation of mean entropy values for each channel at the first nine time-lags using PME. Although the general trend is maintained across time-lags, the imprint patterns change, thus revealing information at certain channels not seen before.

These results enhance the presence of a larger diversity of ordinal patterns in some local time series in calmness trials in comparison to distressed ones, thus suggesting the existence of more complex brain dynamics in calmness state. Such loss of complexity under distress might be associated to a lower brain's ability of adaptation to external stimuli and environmental changes. Indeed, decomplexification of physiological systems has been traditionally identified with a lower ability to manage information, and therefore with a higher probability of suffering a pathological condition (Goldberger et al., 2002; Lipsitz, 2004). Interestingly, these findings are in agreement with other studies

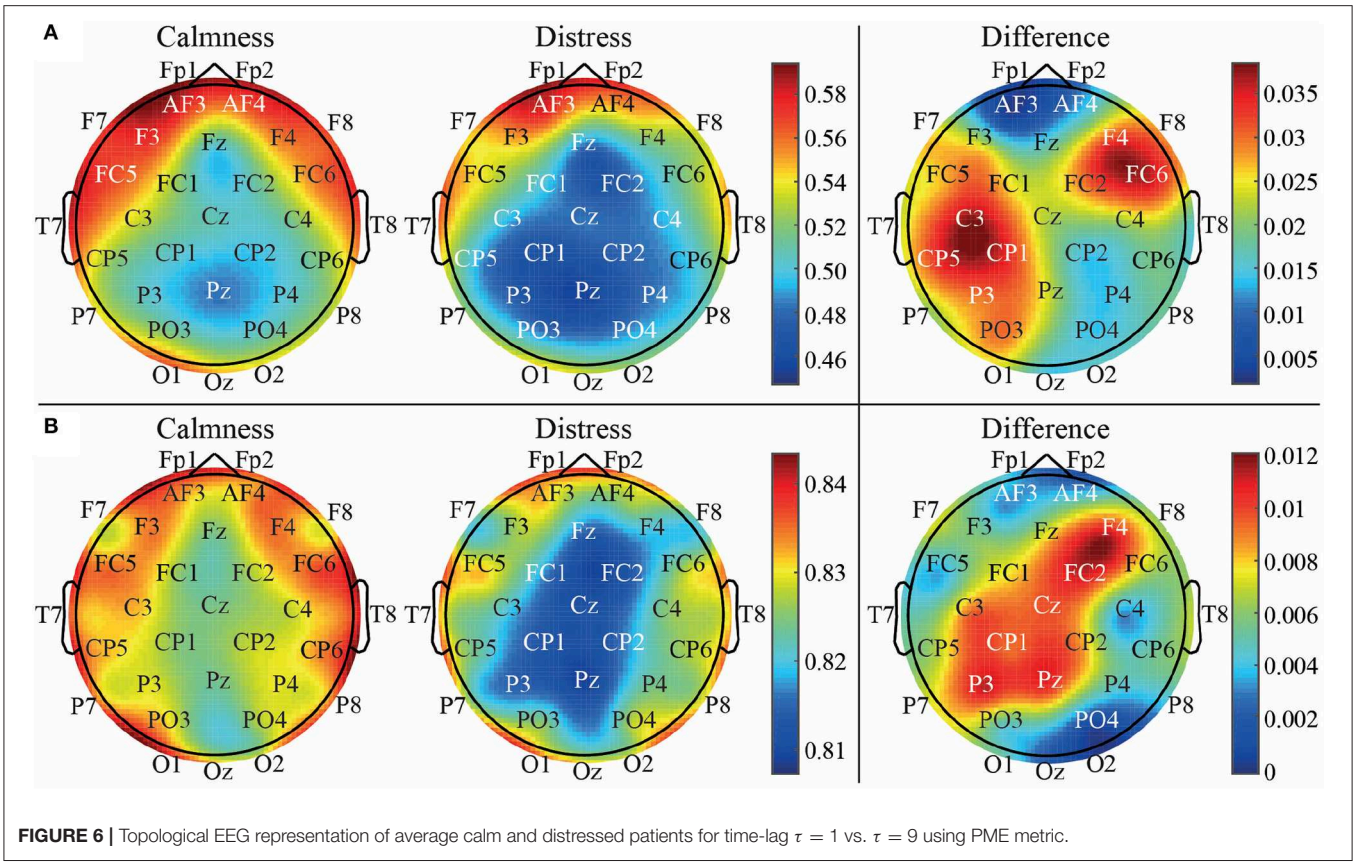


FIGURE 6 | Topological EEG representation of average calm and distressed patients for time-lag $\tau = 1$ vs. $\tau = 9$ using PME metric.

published during the past years. In this sense, increased values of correlation dimension in calm participants with respect to distressed subjects have been reported so far (Hosseini et al., 2015). In another work, a decrease of relative power in subjects facing a series of distressful stimuli was also described (Bastos Filho et al., 2012). Finally, the fact that this trend is maintained throughout the different time-lags reinforces a previous study where no lag was applied (García-Martínez et al., 2017).

Another relevant finding is that single discriminatory power in multi-lag analysis has notably improved with respect to other previous studies dealing with singe-lag (García-Martínez et al., 2017) and MSE (Martínez-Rodrigo et al., 2019) analysis, especially in some specific channels. Thus, left parietal channel P3 is still a very relevant channel for distress detection using symbolic analysis. This finding was already reported in our recent previous work where AAPE was applied to the data (García-Martínez et al., 2017). Nevertheless, other studies have already corroborated this association with the left parietal area. Thus, a higher activation has been observed during normal non-depressed and reasonably positive moods in the left parietal area than in the right one (Davidson, 1988). In the same line, meditation has also been characterized by an increasing activity of the left parietal region (Manna et al., 2010). In the present study, P3 showed robustness and consistency across different time-lags when discriminating between emotional states of calmness and distress. Nevertheless, the global classification performance was improved notably for time-lags higher than one, especially when data was analyzed by means of PME metric, increasing from 61% when no lag was applied up to 68.30% when time-lag $\tau = 9$ was computed.

These findings may indicate the existence of long-range correlations in the data, which have only been sufficiently highlighted by considering a multi-lag entropy-based analysis. Indeed, these observations can be visually corroborated in the topological representation of brain areas depicted in **Figure 6**. It represents average PME values computed from emotional states of calmness and distress for time-lags $\tau = 1$ (a) and $\tau = 9$ (b). As can be seen, entropy values obtained at time-lag $\tau = 9$ are quite different compared to the analysis with no lag, showing a more balanced pattern between left and right hemispheres throughout frontal, parietal and occipital areas. In addition, the entropy differences between calmness and distress are also shown in this figure (on the right column). Thus, the higher differences are found in left central region for $\tau = 1$, whereas a higher activation of left parietal region is obtained for $\tau = 9$.

The right frontal channel F4 also presents a considerable difference of activation between calmness and distress states both in $\tau = 1$ and $\tau = 9$ cases. Interestingly, the relevance of the mentioned areas and the possible relation between frontal and parietal areas of opposite hemispheres has already been depicted in our previous studies. In fact, 30 years ago it was verified that a relative left parietal brain activation is balanced by a relative right parietal brain activation and vice-versa (Davidson, 1988). A similar outcome has also been observed in another study

where patients with different mental disorders were conducted to practice meditation (Rubia, 2009).

Moreover, the right brain hemisphere deserves especial attention in this work. Considering our previous findings, the right centro-parietal channel CP2 showed no relevance when analyzing emotional states with symbolic entropies (García-Martínez et al., 2017). This outcome has been corroborated again in this work, where neither DPE nor PME showed statistical significance at $\tau = 1$ (no lag), and the global classification was below 55% in both cases (see **Table 1**). However, when analyzing the same brain area at higher time-lags, a notable increase of statistical significance and discriminatory power was observed. It is especially the case for CP2 with PME at time-lag $\tau = 9$ ($\rho = 0.0026$ and Acc = 68.70%), thus achieving the highest global classification in this study. The relevance of the channel CP2 can also be observed in **Figure 6**, where the difference is not notable for $\tau = 1$, but it is for $\tau = 9$.

These findings, together with the relevance of the results reported by the left parietal channel P3, reveal the possible existence of complementary information among the parietal lobes of both brain hemispheres. Indeed, a number of previous works reported a certain degree of complementarity between right and left posterior areas under stimulation of distress and calmness. For instance, interesting information about parietal and occipital asymmetry at different frequency bands during distressful tasks has been described (Park et al., 2011). Furthermore, an intensive parietal lobe activation under anxiety and distress conditions has also been reported (Nitschke, 1998).

Recently, occipital electrodes O1 and O2 have also been explored to evaluate variations in complexity provoked by visual elicitation (Tonoyan et al., 2016). In a similar line, the posterior brain area has been related to the arousal component of emotions, thus being their processing essential for the recognition of emotions (Dolcos and Cabeza, 2002). Interestingly, in our previous study the combination of the left parietal channel P3 and the right parietal channel P4 achieved a notable performance discriminating between emotional states of calmness and distress, thus demonstrating the inter-correlation of these brain regions (García-Martínez et al., 2017). However, in that study, brain dynamics were assessed by means of different computation approaches, where each methodology highlighted one of the hemispheres in isolation. In the present work, both areas have resulted to be significant when analyzed with PME metric at higher time-lags, obtaining results comparable to those reported individually by other metrics used in our previous works.

The obtained multi-lag curves were also parameterized and studied to compare the relative complexity of normalized time series. The use of curve profiles for characterization of biological signals has been already proposed by other authors (Costa et al.,

TABLE 5 | Comparison of the most relevant works dealing with automatic identification of negative stress from the recordings.

Work	Experiment	Features	Statistics/ Classifier	Results
Hosseini et al., 2010	15 subjects 5 EEG channels IAPS[a]	FD[b], CD[c], and WEn[d]	LDA[e] and SVM	LDA: 80.1% SVM: 84.9%
Bastos Filho et al., 2012	32 subjects 4 EEG channels Videoclips	Statistical features, PSD[f], and HOC[g]	KNN	Stat.: 66.25% PSD: 70.1% HOC: 69.6%
Peng et al., 2013	13 subjects 3 EEG channels Eyes closed, no stimuli	CD, LZC[h], LLE[i], PSD	ANOVA	Higher complexity in stress
García-Martínez et al., 2016	32 subjects 32 EEG channels Videoclips	SE[j], QSE[k], and DE[l]	Decision tree	75.29%
García-Martínez et al., 2017	32 subjects 32 EEG channels Videoclips	QSE, PE, and AAPE	SVM	81.31%
García-Martínez et al., 2019b	32 subjects 32 EEG channels Videoclips	QSE, CE[m], and CCE[n]	SVM	80.31%
This work	32 subjects 32 EEG channels Videoclips	DPE and MPE	KNN	92.32%

[a] IAPS, International Affective Picture System. [b] FD, Fractal dimension. [c] CD, Correlation dimension. [d] WEn, Wavelet entropy. [e] LDA, Linear discriminant analysis. [f] PSD, Power spectral density. [g] HOC, High-order crossings. [h] LZC, Lempel-Ziv complexity. [i] LLE, Largest Lyapunov exponent. [j] SE, Sample entropy. [k] QSE, Quadratic sample entropy. [l] DE, Distribution entropy. [m] CE, Conditional entropy. [n] CCE, Corrected conditional entropy.

2005). Accordingly, $Slp1-4$ and $Slp1-6$ reflect that the degree of change in the complexity of some EEG channels is more relevant in smaller time-lags. These outcomes were observed in **Figures 2**, **3**, where changes in the slopes could be seen until the curves stabilized around time-lag $\tau = 5$. In this regard, parietal and occipital channels showed statistical relevance at these slopes for DPE metric, but only parietal channels resulted relevant when curved-related parameters were calculated for PME metric. It is worth noting that the same outcomes were also obtained for the area under curve parameters.

On the other hand, the developed multivariate analysis has shown that putting all the data together led to a notably overall performance increase, which demonstrated that multi-lag analysis is able to provide additional, as well as complementary information, to single-lag one. To this respect, an SFS scheme was applied under a 10-fold cross-validation approach to choose the optimal subset of features maximizing the classification rate for each classifier. Interestingly, the most relevant features selected for each classifier were mainly computed from EEG channels showing the largest differences between emotional states of calmness and distress. Indeed, DPE computed from channels PO3 and P3 reported high statistically significant differences between the two groups of trials, as shown in **Tables 1**, **2**. Similarly, PME obtained from channels P3, Pz, FC5, C4, and CP5 provided high visual differences, as shown in **Figures 5**, **6**. Moreover, let us highlight that all selected features were computed from time-lag longer than 1 or from τ-based curves, as shown in **Figure 4**.

Another relevant aspect is that the results obtained in the present study outperformed notably other similar works that have analyzed non-linear metrics from the same database with no lag, such as summarized in **Table 5**. Indeed, a global accuracy of 69.6% has only been reported by applying a high-order crossing approach to four EEG channels (Bastos Filho et al., 2012). In addition, different non-linear metrics have reported a higher level of complexity in stressed subjects (Peng et al., 2013). In other work, combining quadratic sample entropy values from several EEG channels through a DTC classifier, a discriminant ability around 75% has been provided (García-Martínez et al., 2016). On the other hand, a discriminant model based on SVM and using irregularity and symbolic metrics reached a diagnostic accuracy >80% (García-Martínez et al., 2019b). Similarly, variants of PE have already been applied to distress recognition, with a classification performance of 81.31% (García-Martínez et al., 2017). However, in the present study an improvement of about 10% has been reported by making use of the same kind of SVM classifier.

Likewise, the classification results obtained in the present study also significantly improved the sole recent work conducting a MSE analysis on EEG signals for distress identification (Martínez-Rodrigo et al., 2019). In fact, making use of the same SVM-based approach, here a classification rate between distress and calmness emotional states has been obtained about 6% higher than for MSE. It should be noted that both MSE and multi-lag entropy analyses pursue the same goal of quantifying complexity at different time scales. For this purpose, MSE uses a rescaling procedure based on filtering out the shorter oscillations and keeping the longer ones (Humeau-Heurtier, 2015). This approach unavoidably removes some frequency content, specially from rescaled time series presenting very fast oscillations (Humeau-Heurtier, 2015). Such loss of frequency information could explain the aforementioned poorer outcome reached by MSE, because entropy computation from time-lagged samples does not alter time and frequency information from original data (Govindan et al., 2007; Kaffashi et al., 2008). Moreover, this finding could also justify the fact that, whereas no changes were noticed across all time scales in MSE analysis in brain areas activating and supporting distress (Martínez-Rodrigo et al., 2019), large differences have been observed for different time-lags, as extensively described in previous paragraphs.

Finally, there are some limitations in this study that deserve our attention. Firstly, the studied DEAP database is not exclusively designed for recognition of calmness and distress emotions. In fact, many other emotional states were also recorded during the experiment (Koelstra et al., 2012). Moreover, the number of trials eliciting calmness and distress is notably unbalanced for each healthy volunteer, thus making the use of a subject-based classification impossible. Secondly, further analyses on other similar databases like ASCERTAIN (Subramanian et al., 2018), AMIGOS (Miranda Correa et al., 2018), and DREAMER (Katsigiannis and Ramzan, 2018) are required to corroborate and generalize the obtained results. However, the impact of some potential confounding aspects on the results provided by several databases will have to be carefully analyzed for this purpose. Thus, it should be thoughtfully scrutinized how different experimental setups, population distributions in terms of age and gender, and technical aspects related to the acquisition of EEG signals mask changes in brain dynamics under distress. Thirdly, the video clips used as stimuli have a duration of 1 min, which may be too much time to just elicit a single emotional state. Thus, participants may present different emotions for the same stimulus, making it difficult to properly rate their level of valence and arousal. Finally, only EEG signals were assessed in this work, thus discarding the information reported by other physiological variables. However, peripheral recordings also contained in DEAP and other databases, in combination with brain dynamics, will be explored in further studies for the sake of detecting distress episodes.

5. CONCLUSIONS

In this study, two permutation entropies, adapted to work in a multi-lag context, have been analyzed for the first time to automatically identify negative stress. This multi-lag analysis has revealed new insights never seen before, thus notably improving the performance of distress identification. Considering the relevant results that permutation entropy has previously reported in non-lag and multiscale contexts for human emotion detection, it becomes highly interesting to analyze brain dynamics from a time delay viewpoint. For this reason, we hypothesized that there might exist relevant and complementary information at higher time-lags among different brain areas. The results obtained after performing the analyses have confirmed our initial ideas, reporting an improved classification between emotional states of calmness and distress.

Moreover, left parietal and right centro-parietal channels showed remarkable activation at higher time lags, suggesting that removing long-range linear correlations may help to better evaluate the non-linear information of the data. Finally, several discriminant models obtained from advanced classifiers were used to study the complementarity of the features computed at different time-lags for each EEG channel. The resulting functions have combined single entropy values from different channels calculated at lags higher than one with curve-related parameters, thus corroborating that there are more relevant information when time-lags are applied to the time series than when data are analyzed without any time delay or averaging consecutive samples.

AUTHOR CONTRIBUTIONS

AM-R and BG-M conceived and designed the study, programmed the experiments and drafted the manuscript. LZ and RA helped to interpret the results and reviewed the manuscript. Finally, AF-C supervised the experiments, reviewed the manuscript and contributed to the final version. All authors have read and approved the final version of the manuscript.

FUNDING

This work was partially supported by Spanish Ministerio de Ciencia, Innovación y Universidades, Agencia Estatal de Investigación (AEI)/European Regional Development Fund (FEDER, UE) under DPI2016-440 80894-R, TIN2015-72931-EXP, and 2018/11744 grants, by Castilla-La Mancha Regional Government/FEDER, UE under SBPLY/17/180501/000192 grant, and by Biomedical Research Networking Centre in Mental Health (CIBERSAM) of the Instituto de Salud Carlos III. BG-M holds FPU16/03740 scholarship from Spanish Ministerio de Educación y Formación Profesional. LZ acknowledges the financial support from Consejo Nacional de Investigaciones Científicas y Técnicas (CONICET), Argentina.

REFERENCES

Alberdi, A., Aztiria, A., and Basarab, A. (2016). Towards an automatic early stress recognition system for office environments based on multimodal measurements: a review. *J. Biomed. Informatics* 59, 49–75. doi: 10.1016/j.jbi.2015.11.007

Al-Nafjan, A., Hosny, M., Al-Ohali, Y., and Al-Wabil, A. (2017). Review and classification of emotion recognition based on EEG brain-computer interface system research: a systematic review. *Appl. Sci.* 7:1239. doi: 10.3390/app7121239

Al-Shargie, F., Tang, T. B., Badruddin, N., and Kiguchi, M. (2018). Towards multilevel mental stress assessment using SVM with ECOC: an EEG approach. *Med. Biol. Eng. Comput.* 56, 125–136. doi: 10.1007/s11517-017-1733-8

Azami, H., and Escudero, J. (2016). Amplitude-aware permutation entropy: illustration in spike detection and signal segmentation. *Comput. Methods Programs Biomed.* 128, 40–51. doi: 10.1016/j.cmpb.2016.02.008

Bandt, C., and Pompe, B. (2002). Permutation entropy: a natural complexity measure for time series. *Phys. Rev. Lett.* 88:174102. doi: 10.1103/PhysRevLett.88.174102

Bastos Filho, T. F., Ferreira, A., Atencio, A. C., Arjunan, S. P., and Kumar, D. (2012). "Evaluation of feature extraction techniques in emotional state recognition," in *IEEE Proceedings of 4th International Conference on Intelligent Human Computer Interaction* (Kharagpur), 1–6.

Bender, R. E., and Alloy, L. B. (2011). Life stress and kindling in bipolar disorder: review of the evidence and integration with emerging biopsychosocial theories. *Clin. Psychol. Rev.* 31, 383–398. doi: 10.1016/j.cpr.2011.01.004

Bennett, S., Larkin, H., Pincham, H., Carman, S., and Fearon, P. (2018). Neural correlates of children's emotion understanding. *Dev. Neuropsychol.* 43, 329–344. doi: 10.1080/87565641.2018.1432055

Bong, S. Z., Murugappan, M., and Yaacob, S. (2013). Methods and approaches on inferring human emotional stress changes through physiological signals: a review. *Int. J. Med. Eng. Informatics* 5, 152–162. doi: 10.1504/IJMEI.2013.053332

Calvo, R. A., and D'Mello, S. K. (2010). Affect detection: an interdisciplinary review of models, methods, and their applications. *IEEE Trans. Affect. Comput.* 1, 18–37. doi: 10.1109/T-AFFC.2010.1

Cao, Y., Cai, L., Wang, J., Wang, R., Yu, H., Cao, Y., et al. (2015). Characterization of complexity in the electroencephalograph activity of Alzheimer's disease based on fuzzy entropy. *Chaos* 25:083116. doi: 10.1063/1.4929148

Coan, J. A., and Allen, J. J. B. (2007). *Handbook of Emotion Elicitation and Assessment*. Oxford: Oxford University Press.

Costa, M., Goldberger, A. L., and Peng, C. K. (2005). Multiscale entropy analysis of biological signals. *Phys. Rev. E Stat. Nonlinear Soft Matter Phys.* 71:021906. doi: 10.1103/PhysRevE.71.021906

Davidson, R. J. (1988). "Affect, cognition, and hemispheric specialization," in *Emotion, Cognition, and Behavior*, eds C. Izard, J. Kagan, and R. Zajonc (New York, NY: Cambridge University Press), 320–365.

Dolcos, F., and Cabeza, R. (2002). Event-related potentials of emotional memory: encoding pleasant, unpleasant, and neutral pictures. *Cogn. Affect. Behav. Neurosci.* 2, 252–263. doi: 10.3758/CABN.2.3.252

Ekman, P. (1992). An argument for basic emotions. *Cogn. Emot.* 6, 169–200. doi: 10.1080/02699939208411068

Escudero, J., Abásolo, D., Hornero, R., Espino, P., and López, M. (2006). Analysis of electroencephalograms in Alzheimer's disease patients with multiscale entropy. *Physiol. Meas.* 27, 1091–1106. doi: 10.1088/0967-3334/27/11/004

Fadlallah, B., Chen, B., Keil, A., and Príncipe, J. (2013). Weighted-permutation entropy: a complexity measure for time series incorporating amplitude information. *Phys. Rev. E* 87:022911. doi: 10.1103/PhysRevE.87.022911

Fernández-Caballero, A., Martínez-Rodrigo, A., Pastor, J. M., Castillo, J. C., Lozano-Monasor, E., López, M. T., et al. (2016). Smart environment architecture for emotion detection and regulation. *J. Biomed. Informatics* 64, 55–73. doi: 10.1016/j.jbi.2016.09.015

Fernández-Sotos, A., Martínez-Rodrigo, A., Moncho-Bogani, J., Latorre, J. M., and Fernández-Caballero, A. (2018). Neural correlates of phrase quadrature perception in harmonic rhythm: an EEG study using a brain–computer interface. *Int. J. Neural Syst.* 28:1750054. doi: 10.1142/S012906571750054X

Forscher, E. C., Zheng, Y., Ke, Z., Folstein, J., and Li, W. (2016). Decomposing fear perception: a combination of psychophysics and neurometric modeling of fear perception. *Neuropsychologia* 91, 254–261. doi: 10.1016/j.neuropsychologia.2016.08.018

Gao, J., Hu, J., Liu, F., and Cao, Y. (2015). Multiscale entropy analysis of biological signals: a fundamental bi-scaling law. *Front. Comput. Neurosci.* 9:64. doi: 10.3389/fncom.2015.00064

García-Martínez, B., Martínez-Rodrigo, A., Alcaraz, R., and Fernández-Caballero, A. (2019a). A review on nonlinear methods using electroencephalographic recordings for emotion recognition. *IEEE Trans. Affect. Comput.* doi: 10.1109/TAFFC.2018.2890636. [Epub ahead of print].

García-Martínez, B., Martínez-Rodrigo, A., Fernández-Caballero, A., Moncho-Bogani, J., and Alcaraz, R. (2019b). Nonlinear predictability analysis of brain dynamics for automatic recognition of negative stress. *Neural Comput. Appl.* doi: 10.1007/s00521-018-3620-0. [Epub ahead of print].

García-Martínez, B., Martínez-Rodrigo, A., Zangróniz, R., Pastor, J., and Alcaraz, R. (2016). Application of entropy-based metrics to identify emotional distress from electroencephalographic recordings. *Entropy* 18:221. doi: 10.3390/e18060221

García-Martínez, B., Martínez-Rodrigo, A., Zangróniz, R., Pastor, J., and Alcaraz, R. (2017). Symbolic analysis of brain dynamics detects negative stress. *Entropy* 19:196. doi: 10.3390/e19050196

Goh, S., Abbass, H., Tan, K., Al-Mamun, A., Wang, C., and Guan, C. (2017). Automatic EEG artifact removal techniques by detected influential independet components. *IEEE Trans. Emerg. Top. Comput. Intell.* 1, 270–279. doi: 10.1109/TETCI.2017.2690913

Goldberger, A. L., Peng, C. K., and Lipsitz, L. A. (2002). What is physiologic complexity and how does it change with aging and disease? *Neurobiol. Aging* 23, 23–26. doi: 10.1016/S0197-4580(01)00266-4

Gomes, M., Oliveira, T., Silva, F., Carneiro, D., and Novais, P. (2014). "Establishing the relationship between personality traits and stress in an intelligent environment," in *27th International Conference on Industrial Engineering and Other Applications of Applied Intelligent Systems, IEA/AIE 2014* (Kaohsiung: Springer), 378–387.

Govindan, R., Wilson, J., Eswaran, H., Lowery, C., and Preißl, H. (2007). Revisiting sample entropy analysis. *Phys. A Stat. Mech. Appl.* 376, 158–164. doi: 10.1016/j.physa.2006.10.077

Healey, J., and Picard, R. W. (2005). Detecting stress during real-world driving tasks using physiological sensors. *IEEE Trans. Intell. Transport. Syst.* 6, 156–166. doi: 10.1109/TITS.2005.848368

Hosseini, S. A., Khalilzadeh, M. A., and Changiz, S. (2010). Emotional stress recognition system for affective computing based on bio-signals. *J. Biol. Syst.* 18, 101–114. doi: 10.1142/S0218339010003640

Hosseini, S. A., Khalilzadeh, M. A., Naghibi-Sistani, M. B., and Homam, S. M. (2015). Emotional stress recognition using a new fusion link between electroencephalogram and peripheral signals. *Iran. J. Neurol.* 14, 142–151.

Hosseini, S. A., and Naghibi-Sistani, M. B. (2011). Emotion recognition method using entropy analysis of EEG signals. *Int. J. Image Graph. Signal Process.* 3:30. doi: 10.5815/ijigsp.2011.05.05

Humeau-Heurtier, A. (2015). The multiscale entropy algorithm and its variants: a review. *Entropy* 17, 3110–3123. doi: 10.3390/e17053110

Jebelli, H., Khalili, M. M., and Lee, S. (2018). A continuously updated, computationally efficient stress recognition framework using electroencephalogram (EEG) by applying online multi-task learning algorithms (OMTL). *IEEE J. Biomed. Health Informatics*. doi: 10.1109/JBHI.2018.2870963. [Epub ahead of print].

Jung, Y., and Hu, J. (2015). A K-fold averaging cross-validation procedure. *J. Nonparametr. Statistics.* 27, 167–179. doi: 10.1080/10485252.2015.1010532

Kaffashi, F., Foglyano, R., Wilson, C. G., and Loparo, K. A. (2008). The effect of time delay on approximate & sample entropy calculations. *Phys. D* 237, 3069–3074. doi: 10.1016/j.physd.2008.06.005

Katsigiannis, S., and Ramzan, N. (2018). Dreamer: a database for emotion recognition through eeg and ecg signals from wireless low-cost off-the-shelf devices. *IEEE J. Biomed. Health Informatics* 22, 98–107. doi: 10.1109/JBHI.2017.2688239

Khosrowabadi, R., Quek, C., Ang, K. K., Tung, S. W., and Heijnen, M. (2011). "A brain-computer interface for classifying eeg correlates of chronic mental stress," in *The 2011 International Joint Conference on Neural Networks* (San Jose, CA: IEEE), 757–762.

Klem, G. H., Lüders, H. O., Jasper, H., Elger, C. (1999). The ten-twenty electrode system of the International Federation. *Electroencephalogr. Clin. Neurophysiol.* 52, 3–6.

Koelstra, S., Mühl, C., Soleymani, M., Lee, J., Yazdani, A., Ebrahimi, T., et al. (2012). DEAP: a database for emotion analysis using physiological signals. *IEEE Trans. Affect. Comput.* 3, 18–31. doi: 10.1109/T-AFFC.2011.15

Lipsitz, L. A. (2004). Physiological complexity, aging, and the path to frailty. *Sci. Aging Knowl. Environ.* 2004:pe16. doi: 10.1126/sageke.2004.16.pe16

Mammone, N., Duun-Henriksen, J., Kjaer, T. W., and Morabito, F. C. (2015). Differentiating interictal and ictal states in childhood absence epilepsy through permutation Rényi entropy. *Entropy* 17, 4627–4643. doi: 10.3390/e17074627

Manna, A., Raffone, A., Perrucci, M. G., Nardo, D., Ferretti, A., Tartaro, A., et al. (2010). Neural correlates of focused attention and cognitive monitoring in meditation. *Brain Res. Bull.* 82, 46–56. doi: 10.1016/j.brainresbull.2010.03.001

Marrelli, M., Gentile, S., Palmieri, F., Paduano, F., and Tatullo, M. (2014). Correlation between surgeon's experience, surgery complexity and the alteration of stress related physiological parameters. *PLoS ONE* 9:e112444. doi: 10.1371/journal.pone.0112444

Martínez-Rodrigo, A., Fernández-Sotos, A., Latorre, J. M., Moncho-Bogani, J., and Fernández-Caballero, A. (2017). Neural correlates of phrase rhythm: an EEG study of bipartite vs. rondo sonata form. *Front. Neuroinformatics* 11:29. doi: 10.3389/fninf.2017.00029

Martínez-Rodrigo, A., García-Martínez, B., Alcaraz, R., González, P., and Fernández-Caballero, A. (2019). Multiscale entropy analysis for recognition of visually elicited negative stress from EEG recordings. *Int. J. Neural Syst.* 29:1850038. doi: 10.1142/S0129065718500387

Minguillon, J., Lopez-Gordo, M. A., and Pelayo, F. (2016). Stress assessment by prefrontal relative gamma. *Front. Comput. Neurosci.* 10:101. doi: 10.3389/fncom.2016.00101

Miranda Correa, J. A., Abadi, M. K., Sebe, N., and Patras, I. (2018). Amigos: a dataset for affect, personality and mood research on individuals and groups. *IEEE Trans. Affect. Comput.* doi: 10.1109/TAFFC.2018.2884461. [Epub ahead of print].

Morris, J. D. (1995). Observations SAM: The Self-Assessment Manikin—an efficient cross-cultural measurement of emotional response. *J. Advertis. Res.* 35, 63–68.

Mozos, O. M., Sandulescu, V., Andrews, S., Ellis, D., Bellotto, N., Dobrescu, R., et al. (2017). Stress detection using wearable physiological and sociometric sensors. *Int. J. Neural Syst.* 27:1650041. doi: 10.1142/S0129065716500416

Nitschke, W. H. J. B. (1998). The puzzle of regional brain activity in and anxiety: the importance of subtypes and comorbidity. *Cogn. Emot.* 12, 421–447. doi: 10.1080/026999398379664

Nolan, H., Whelan, R., and Reilly, R. (2010). FASTER: fully automated statistical thresholding for EEG artifact rejection. *J. Neurosci. Methods* 192, 152–162. doi: 10.1016/j.jneumeth.2010.07.015

Park, K. S., Choi, H., Lee, K. J., Lee, J. Y., An, K. O., and Kim, E. J. (2011). Patterns of electroencephalography (EEG) change against stress through noise and memorization test. *Int. J. Med. Med. Sci.* 3, 381–389. doi: 10.5897/IJMMS11.001

Peng, H., Hu, B., Zheng, F., Fan, D., Zhao, W., Chen, X., et al. (2013). A method of identifying chronic stress by EEG. *Pers. Ubiquit. Comput.* 17, 1341–1347. doi: 10.1007/s00779-012-0593-3

Pincham, H. L., Bryce, D., Kokorikou, D., Fonagy, P., and Fearon, R. M. P. (2016). Psychosocial intervention is associated with altered emotion processing: an event-related potential study in at-risk adolescents. *PLoS ONE* 11:e0147357. doi: 10.1371/journal.pone.0147357

Pomer-Escher, A. G., de Souza, M. D. P., and Filho, T. F. B. (2014). "Methology for analysis of stress level based on asymmetry patterns of alpha rhythms in EEG signals," in *5th ISSNIP-IEEE Biosignals and Biorobotics Conference (2014): Biosignals and Robotics for Better and Safer Living (BRC)* (Salvador: IEEE), 1–5.

Ramirez, R., Planas, J., Escude, N., Mercade, J., and Farriols, C. (2018). EEG-based analysis of the emotional effect of music therapy on palliative care cancer patients. *Front. Psychol.* 9:254. doi: 10.3389/fpsyg.2018.00254

Reis, P. M., Hebenstreit, F., Gabsteiger, F., von Tscharner, V., and Lochmann, M. (2014). Methodological aspects of EEG and body dynamics measurements during motion. *Front. Human Neurosci.* 8:156. doi: 10.3389/fnhum.2014.00156

Rubia, K. (2009). The neurobiology of meditation and its clinical effectiveness in psychiatric disorders. *Biol. Psychol.* 82, 1–11. doi: 10.1016/j.biopsycho.2009.04.003

Russell, J. A. (1980). A circumplex model of affect. *J. Pers. Soc. Psychol.* 39, 1161–1178. doi: 10.1037/h0077714

Schröder, M., and Cowie, R. (2011). *Toward Emotion-Sensitive Multimodal Interfaces: The Challenge of the European Network of Excellence HUMAINE.* Available online at: http://www.cs.pitt.edu/litman/courses/ads/readings/schroeder_cowie.pdf

Skinner, M. J., and Simpson, P. A. (2002). Workload issues in military tactical airlift. *Int. J. Aviat. Psychol.* 12, 79–93. doi: 10.1207/S15327108IJAP1201_7

Subramanian, R., Wache, J., Abadi, M. K., Vieriu, R. L., Winkler, S., and Sebe, N. (2018). Ascertain: emotion and personality recognition using commercial sensors. *IEEE Trans. Affect. Comput.* 9, 147–160. doi: 10.1109/TAFFC.2016.2625250

Tonoyan, Y., Looney, D., Mandic, D. P., and Van Hulle, M. M. (2016). Discriminating multiple emotional states from EEG using a data-adaptive, multiscale information-theoretic approach. *Int. J. Neural Syst.* 26:1650005. doi: 10.1142/S0129065716500052

Valenza, G., Lanata, A., and Scilingo, E. P. (2012). The role of nonlinear dynamics in affective valence and arousal recognition. *IEEE Trans. Affect. Comput.* 3, 237–249. doi: 10.1109/T-AFFC.2011.30

Xia, Y., Yang, L., Zunino, L., Shi, H., Zhuang, Y., and Liu, C. (2018). Application of permutation entropy and permutation min-entropy in multiple emotional states analysis of RRI time series. *Entropy* 20:148. doi: 10.3390/e20030148

Zanin, M., Zunino, L., Rosso, O., and Papo, D. (2012). Permutation entropy and its main biomedical and econophysics applications: a review. *Entropy* 14, 1553–1577. doi: 10.3390/e14081553

Zhao, X., Shang, P., and Huang, J. (2013). Permutation complexity and dependence measures of time series. *Europhys. Lett.* 102:40005. doi: 10.1209/0295-5075/102/40005

Zhu, G., Li, Y., Wen, P. P., and Wang, S. (2015). "Classifying epileptic EEG signals with delay permutation entropy and multi-scale K-means," in *Signal and Image Analysis for Biomedical and Life Sciences* (Cham: Springer), 143–157.

Zunino, L., Olivares, F., and Rosso, O. A. (2015). Permutation min-entropy: an improved quantifier for unveiling subtle temporal correlations. *Europhys. Lett.* 109:10005. doi: 10.1209/0295-5075/109/10005

Conflict of Interest Statement: The authors declare that the research was conducted in the absence of any commercial or financial relationships that could be construed as a potential conflict of interest.

Copyright © 2019 Martínez-Rodrigo, García-Martínez, Zunino, Alcaraz and Fernández-Caballero. This is an open-access article distributed under the terms of the Creative Commons Attribution License (CC BY). The use, distribution or reproduction in other forums is permitted, provided the original author(s) and the copyright owner(s) are credited and that the original publication in this journal is cited, in accordance with accepted academic practice. No use, distribution or reproduction is permitted which does not comply with these terms.

frontiers in Neuroinformatics

ORIGINAL RESEARCH
published: 04 June 2019
doi: 10.3389/fninf.2019.00042

Processing Pipeline for Atlas-Based Imaging Data Analysis of Structural and Functional Mouse Brain MRI (AIDAmri)

*Niklas Pallast[1], Michael Diedenhofen[2], Stefan Blaschke[1], Frederique Wieters[1], Dirk Wiedermann[2], Mathias Hoehn[2,3], Gereon R. Fink[1,3] and Markus Aswendt[1]**

[1]*Department of Neurology, Faculty of Medicine and University Hospital Cologne, University of Cologne, Cologne, Germany,* [2]*In-vivo-NMR Laboratory, Max Planck Institute for Metabolism Research, Cologne, Germany,* [3]*Cognitive Neuroscience, Institute of Neuroscience and Medicine (INM-3), Research Center Juelich, Juelich, Germany*

Magnetic resonance imaging (MRI) is a key technology in multimodal animal studies of brain connectivity and disease pathology. *In vivo* MRI provides non-invasive, whole brain macroscopic images containing structural and functional information, thereby complementing invasive *in vivo* high-resolution microscopy and *ex vivo* molecular techniques. Brain mapping, the correlation of corresponding regions between multiple brains in a standard brain atlas system, is widely used in human MRI. For small animal MRI, however, there is no scientific consensus on pre-processing strategies and atlas-based neuroinformatics. Thus, it remains difficult to compare and validate results from different pre-clinical studies which were processed using custom-made code or individual adjustments of clinical MRI software and without a standard brain reference atlas. Here, we describe AIDAmri, a novel Atlas-based Imaging Data Analysis pipeline to process structural and functional mouse brain data including anatomical MRI, fiber tracking using diffusion tensor imaging (DTI) and functional connectivity analysis using resting-state functional MRI (rs-fMRI). The AIDAmri pipeline includes automated pre-processing steps, such as raw data conversion, skull-stripping and bias-field correction as well as image registration with the Allen Mouse Brain Reference Atlas (ARA). Following a modular structure developed in Python scripting language, the pipeline integrates established and newly developed algorithms. Each processing step was optimized for efficient data processing requiring minimal user-input and user programming skills. The raw data is analyzed and results transferred to the ARA coordinate system in order to allow an efficient and highly-accurate region-based analysis. AIDAmri is intended to fill the gap of a missing open-access and cross-platform toolbox for the most relevant mouse brain MRI sequences thereby facilitating data processing in large cohorts and multi-center studies.

Keywords: processing pipeline, MRI, atlas registration, stroke, preclinical neuroimaging

OPEN ACCESS

Edited by:
Trygve B. Leergaard, University of Oslo, Norway

Reviewed by:
Sunghyon Kyeong, Yonsei University College of Medicine, South Korea
Nianming Zuo, Institute of Automation (CAS), China
Eszter Agnes Papp, University of Oslo, Norway

****Correspondence:***
Markus Aswendt
markus.aswendt@uk-koeln.de

Received: *23 December 2018*
Accepted: *21 May 2019*
Published: *04 June 2019*

Citation:
Pallast N, Diedenhofen M, Blaschke S, Wieters F, Wiedermann D, Hoehn M, Fink GR and Aswendt M (2019) Processing Pipeline for Atlas-Based Imaging Data Analysis of Structural and Functional Mouse Brain MRI (AIDAmri). Front. Neuroinform. 13:42. doi: 10.3389/fninf.2019.00042

INTRODUCTION

Understanding brain function in health and disease at different hierarchical levels requires collaborative interdisciplinary efforts using multiple experimental methods. Neuroimaging, especially magnetic resonance imaging (MRI), is a critical element of that approach since the use of MRI preserves the anatomical morphology of the brain tissue almost perfectly. Conscious of the high data integrity, large-scale human MRI initiatives are currently underway to provide standardized sharing repositories (Hodge et al., 2016; Gorgolewski et al., 2017) and processing tools (Rex et al., 2003; Jenkinson et al., 2012). In order to be able to compare information derived from different studies, images are spatially normalized to a common coordinate system such as the brain atlas with defined coordinates and assigned structures from Talairach and Tournoux (Fang et al., 1995) or the Montreal Neurological Institute/International Consortium of Brain Mapping (MNI/ICBM; Mazziotta et al., 1995). In order to achieve similar routine atlas-based neuroinformatics of mouse brain MRI, several challenges need to be overcome: (1) the image signal-to-noise ratio (SNR) is dramatically reduced due to image voxels in mice which are 10–15-fold smaller in all dimensions (Nieman et al., 2005); (2) scanner hardware consisting of gradients, coils as well as the animal fixation and anesthesia need to be miniaturized and adapted to the mouse body and physiology (Driehuys et al., 2008); (3) human MRI processing tools usually do not work with mouse brain data due to the striking differences in voxel size; and (4) a common 3D MRI-compatible brain atlas with a detailed segmentation is needed to facilitate atlas-based neuroinformatics at different scales. Recent developments in scanner hardware, e.g., ultra-high-field MRI scanner (>7T) and dedicated ultra-sensitive coils, enabled *in vivo* mouse brain MRI with structural anatomical details at 100 μm in-plane resolution as well as brain-wide network analysis at the functional and structural level (Hoehn and Aswendt, 2013). However, there is currently no standardization or consensus on MRI acquisition, processing, and atlas-based neuroinformatics. Although several mouse brain atlases have been developed and applied (Hess et al., 2018), not all of them are continuously updated and maintained to be accessible online. The most detailed 3D mouse brain atlas, the Allen Brain Reference Atlas (ARA), provides more than 1,000 brain structures (Lein et al., 2007; Dong, 2008). However, the ARA was generated from two-photon microscopy images with a very low image correlation to MRI (e.g., ventricles appear black and not white as in T2-weighted MRI). Most labs rely on custom-made code or adapt their data to the processing requirements of human imaging toolboxes (van Meer et al., 2010; Hübner et al., 2017; Green et al., 2018), often with lack of validation. Existing software pipelines (**Supplementary Table S1**) require commercial software, use different MRI atlases or do not incorporate algorithms for both, structural and functional MRI (Budin et al., 2013; Koch et al., 2019). The associated lack of reproducibility and comparability represents a key drawback for reliable multi-center and translational animal studies. Therefore, we developed a novel the Atlas-based Imaging Data Analysis Pipeline, AIDAmri, for structural and functional MRI of the mouse brain using the ARA coordinate system. AIDAmri provides an automated, efficient and highly accurate region-based analysis of multi-parametric MRI, such as anatomical T2-weighted MRI, diffusion tensor imaging (DTI) and resting-state functional MRI (rs-fMRI). The modular and open-source concept was developed in Python 3.6 for cross-platform use. That allows the critical comparison of different imaging methods and studies. Each processing step of the pipeline was validated with qualitative and quantitative measures on mouse brain MRI data acquired at 7.0, 9.4 and 11.7T using different mouse strains and experimental stroke models. Stroke was chosen as an example, as lesions result in dynamic brain deformations due to tissue swelling and atrophy, which presents a major challenge for all automated processing and atlas registration algorithms.

MATERIALS AND METHODS

Pipeline Overview

The AIDAmri pipeline enables the processing and analysis of both structural and functional mouse brain MRI through distinct modules which can also be used separately. In the following, we provide a detailed explanation of the processing steps (**Figure 1**). The software pipeline is freely available on Github[1]. For a detailed how-to and installation instructions see the manual (**Supplementary Material, Manual**). The AIDAmri interface (GUI) is available for executing the main functions.

A reference adult mouse T2-weighted (T2-w), DTI and rs-fMRI data set acquired at 9.4T is available for testing purposes[2]. Image processing is performed in the Allen Mouse Common Coordinate Framework (CCF v3) using the Allen Mouse Brain Reference Atlas, ARA[3]. It is possible to use manually drawn regions-of-interest (ROIs) or other brain atlases as well. Here, the ARA was implemented as it is the most advanced brain atlas to-date (**Supplementary Figure S1** and **Supplementary Table S2**). To describe the following complex morphological operators (e.g., the image registration), we chose the commonly used mathematical model to describe the image with the given image function $I(x)$ where x describes all voxel positions with $x = \{\vec{x}, \vec{y}, \vec{z}\}$. Based on that model, the given functions transfer voxels of one subset X into another subset Y with $f(x) = \{x \in X \mid f(x) \in Y\}$ in the three-dimensional image space.

We have included algorithms for the most widely used and most relevant MRI sequences assessing structural and functional connectivity changes using MRI which are not available in other pipelines (see **Supplementary Table S1**, for a selection of other mouse brain imaging pipelines):

(1) T2-weighted MRI (acquired with Turbo spin echo (TSE) or Rapid Acquisition with Refocused Echoes (RARE) sequences) for high-contrast and high spatial resolution imaging of brain

[1]https://github.com/maswendt/AIDAmri
[2]https://doi.org/10.12751/g-node.70e11f
[3]http://mouse.brain-map.org/static/atlas

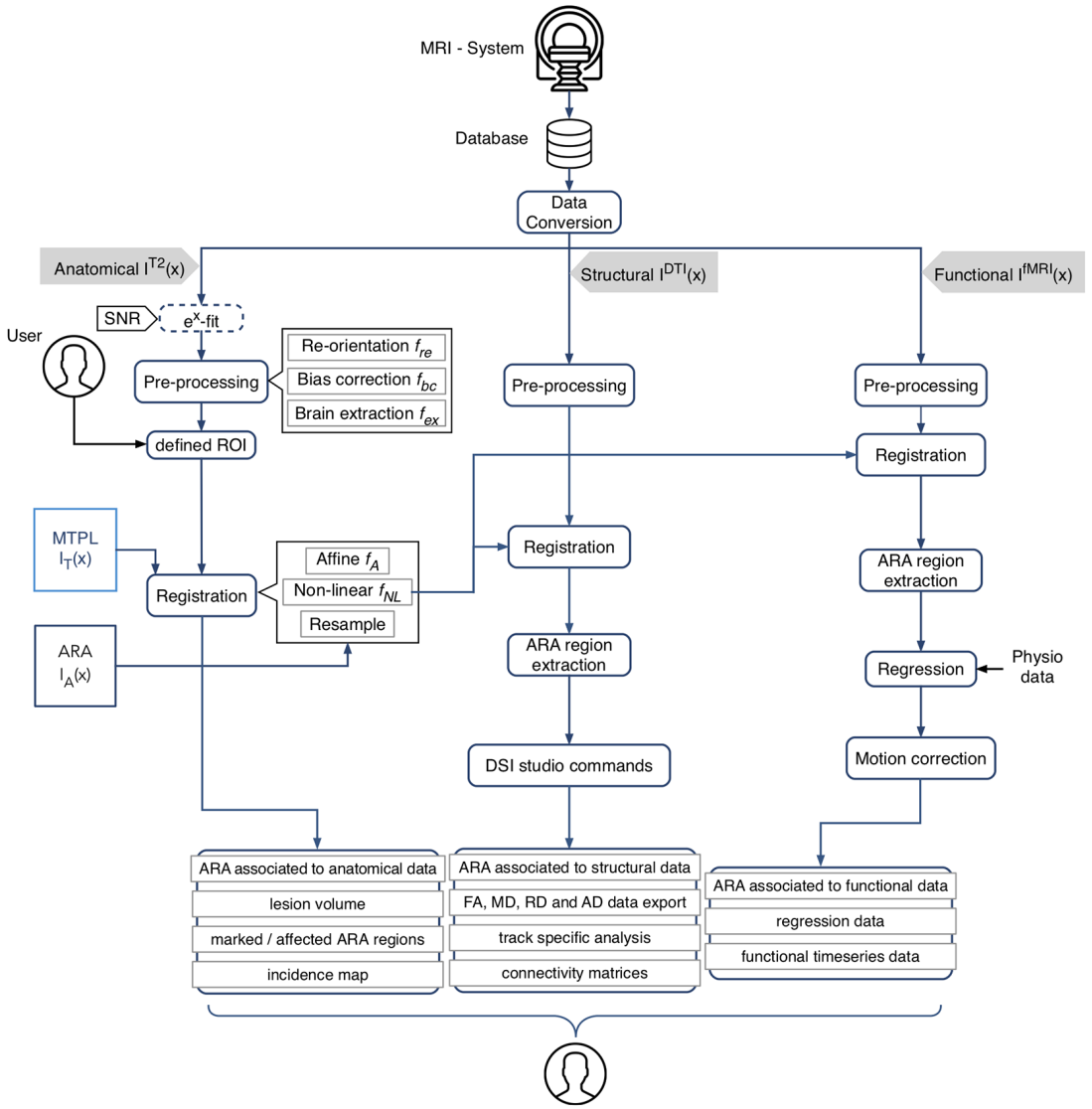


FIGURE 1 | Schematic overview of AIDAmri processing modules and subsequent computational steps for anatomical data (T2-weighted and T2 map), structural (diffusion tensor imaging, DTI) and functional data (resting-state functional magnetic resonance imaging, rs-fMRI). The given image function $I(x)$ represents the 3D MRI image space and describes all intensities at the position $x = \{\vec{x}, \vec{y}, \vec{z}\}$. All data types are pre-processed using a re-orientation $f_{re}(x)$, bias correction $f_{bc}(x)$ and brain extraction $f_{ex}(x)$. The user has the opportunity to define individual regions of interest (ROIs), e.g., a lesion mask, to compare particular areas over different measurements by generating an incidence map. The combined transformation f of the affine f_A and non-linear transformation f_{NL} is applied to MRI template MTPL $I_T(x)$ and subsequently the ARA $I_A(x)$ with the pre-processed data set $I^{T2}(x)$. DTI $I^{DTI}(x)$ and rs-fMRI $I^{fMRI}(x)$ processing steps were implemented based on established protocols (Budde and Song, 2010; Kim et al., 2012; Gorges et al., 2017). AIDAmri generates a variety of outputs such as the connectivity matrices which can be used for further atlas-based connectivity analysis. Icons designed by Smashicons from www.flaticon.com.

anatomy and pathophysiology (e.g., hyperintense signal for segmentation of stroke lesions),

(2) Quantitative T2-mapping (measured for example by multi slice multi echo, MSME, sequences), e.g., for longitudinal monitoring of contrast agent accumulation or lesion development,

(3) DTI, which maps the diffusion process of the water molecules in biological tissues (acquired with diffusion-sensitized sequences such as echoplanar imaging, EPI, along at least 6 directions). DTI is used to derive quantitative measures such as Fractional Anisotropy (FA), Mean Diffusivity (MD), Radial Diffusivity (RD), and Axial Diffusivity (AD). These measures relate to biological differences and are used for clinical diagnosis (Bihan et al., 2001). Furthermore, MRI-based tractography using DTI, provides non-destructive, 3D, brain-wide connectivity maps, which are used in animal and human studies too (Budde and Song, 2010),

(4) Resting state functional MRI (rs-fMRI), which provides functional data on temporal correlation of spontaneous blood-oxygenation level-dependent (BOLD) changes at rest that

reflect regional interactions between two particular brain regions in task-negative state. Functional connectivity derived from rs-fMRI is used in preclinical and clinical studies (Grefkes and Fink, 2014; Gorges et al., 2017).

MRI Data Acquisition

The MRI data was acquired at the Max Planck Institute for Metabolism Research, Cologne, using a 94/20USR BioSpec Bruker system (Bruker, BioSpin, Ettlingen, Germany) equipped with a cryo-coil and operated with ParaVision (v6.0.1). The mice were anesthetized initially with Isoflurane (2%–3% in 70/30 N_2/O_2) and head-fixed in an animal carrier using tooth and ear bars. Fixation and anesthesia are necessary to minimize movement artifacts. Respiration, and body temperature were noninvasively monitored using an MR-compatible monitoring system (Small Animal Instruments Inc., New York, NY, USA) and displayed and recorded using a custom-made data acquisition system based on DASYLab (measX, Mönchengladbach, Germany). To maintain body temperature at 37°C, a feedback-controlled water circulation system (medres, Cologne, Germany) was used. T2-weighted, rs-fMRI and DTI scans (**Table 1**) were sequentially acquired using n = 22 C57BL6/J mice which received photothrombotic stroke in contrast to sham surgery as described previously (Toda et al., 2014). The animal experimental data were collected and managed using a custom-made and cloud-based relational animal database[4] described in detail elsewhere (Pallast et al., 2018). Also, N_T = 40 test data sets linked to previously published (Aswendt et al., 2012; Green et al., 2018) or unpublished (provided by Mathias Hoehn) projects. The data sets were acquired at different field strengths and with animals of different strains.

The pipeline AIDAmri processes DTI and rs-fMRI data independently, but it is necessary to acquire an anatomical reference image in the same measurement, such as a T2-weighted image.

Step 1–Data Conversion and Signal-to-Noise Calculation

In the first step, Bruker raw data are converted to the commonly used format of the Neuroimaging Informatics Technology Initiative (NIfTI; Cox et al., 2004). Other imaging formats, such as DICOM, need to be converted including all header information (e.g., using the software MRIcron[5] or the Python package dicom2nifti[6]). The AIDAmri converter algorithm automatically detects the type of performed measurement and applies conversion in the correct order by reading the respective image header. According to that information, the converted NIfTI-files are sorted in related folders. The anatomical dataset is used to calculate the nonlinear registration which is later applied to the structural and functional data. AIDAmri not only transforms T2-weighted images from the raw data but also calculates the exponential decay over the echo time from multi-echo sequences to calculate quantitative T2 maps.

Automated quality control is included based on SNR calculations based on the automatic noise variance estimation which was chosen proven to be more precise in human MRI (Brummer et al., 1993). Furthermore, that method is less error-prone as the common approach to calculate the SNR (Henkelman, 1985), by placing a ROI inside anatomical regions and another ROI in the noise, and calculate the ratio of the mean signal and the standard-deviation as SNR (Levenberg, 1944).

Step 2–Pre-processing

Image Re-orientation

All subsequent steps, especially the atlas registration, depend on a defined image orientation of the input data. According to the common three-dimensional coordinate system with three planes, we decided to implement the right-hand "neurological" RAS system. In our setting, the mouse lies prone and is inserted with the head-first into the scanner. Images were acquired selecting "head-supine" in ParaVision. Hence, a transformation $f_{re}(x)$ is necessary to re-orientate the images in standard space. This results in images viewed from feet-to-head direction and the right side of the mouse is on the right side of the image.

Bias-Field Correction and Brain Extraction

In case of surface coils, there is a strong bias field on the MR image (**Figure 2A**). AIDAmri contains an automated bias-field correction $f_{bc}(x)$. We implemented the multiplicative intrinsic component optimization (MICO) which was previously used only in human MRI (Li et al., 2014). We compared MICO to the widely-used N4 bias-field correction (Tustison et al., 2010). A total of n = 22 T2-weighted (T2-w) data sets and 10 DTI data sets were compared using the coefficient of variations (CV) metric (see "Results" section) leading to full integration of MICO. The corrected images (**Figure 2B**) are used to apply the brain extraction (skull stripping). AIDAmri runs the FMRIB Software Library (FSL) tool BET with the options -r set to the brain radius in mm and -R for an "robust" iterative estimation of the brain center. Thus, MR images with variable center-of-gravity from animals positioned slightly different between scans will not affect the skull stripping accuracy (**Figure 2C**; Smith, 2002). To allow FSL to process the data, the data dimension of need to be scaled by a factor of 10 to simulate human-similar voxel sizes. In order to avoid image interpolation, up- and downscaling is carried out automatically only for the related NIfTI header file, whereas the voxel size of the raw image remains the same.

Region-of-Interest Segmentation

The user then has the option to define ROIs. We use that option to delineate the ischemic stroke lesion on T2-weighted images using the 3D snake evolution tool of ITK-SNAP[7] (Yushkevich et al., 2006). The resulting segmentation is used to evaluate specific areas separately by generating a list of regions that are overlaid with the segmented area of the brain, e.g., to proof the position of an electrode. If several segmented ROIs are provided, a color-coded incidence map can be created, e.g., to

[4]https://github.com/maswendt/AIDAdb
[5]https://www.nitrc.org/projects/mricron
[6]https://pypi.org/project/dicom2nifti/
[7]www.itksnap.org

TABLE 1 | Characteristics of the performed 9.4 T MRT measurements.

Scan type	T_R[4] (ms)	T_E[5] (ms)	Acq. time (s)	Matrix size	Resolution (mm)	FOV[6] (mm)	Flip angle
T2w[1]	5,500	32.5	352	256 × 256 × 48	0.068 × 0.068 × 0.3	17.5 × 17.5	90°
rs-fMRI[2]	1,420	18	149	128 × 128 × 20	0.141 × 0.141 × 0.4	18.0 × 18.0	90°
DTI[3]	3,000	17.5	840	128 × 128 × 20	0.141 × 0.141 × 0.4	18.0 × 18.0	90°

Over 100 data sets with the given properties were used to test AIDAmri. Abbreviations: [1]T2-weighted MRI, [2]resting-state functional MRI, [3]Diffusion Tensor Imaging, [4]repetition time, [5]echo time, [6]field of view.

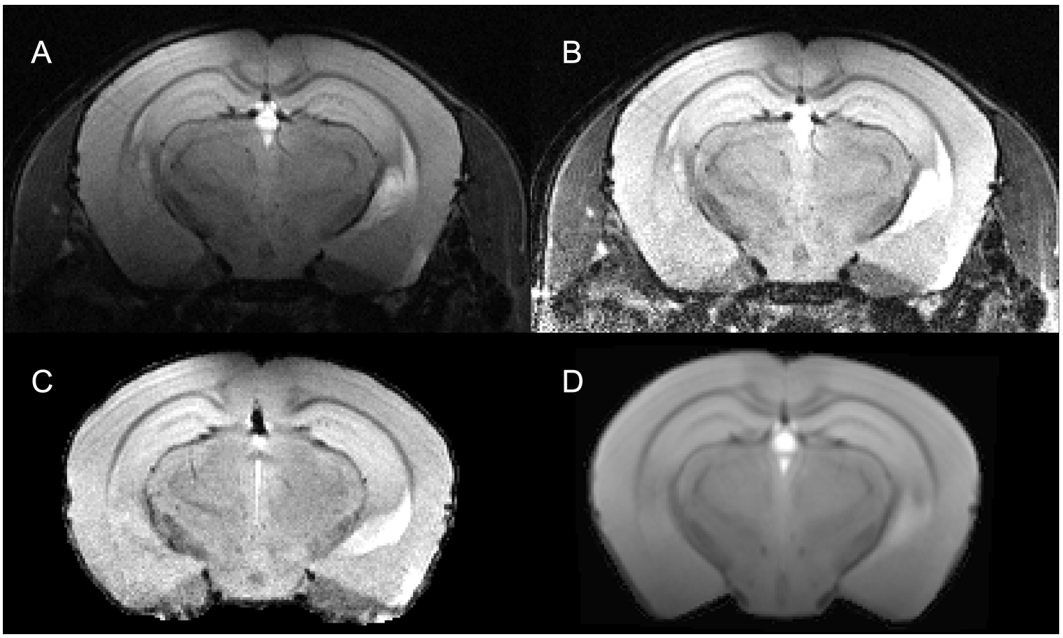


FIGURE 2 | Visualization of step 2—pre-processing for a representative T2-weighted data set. The raw data set $I^{T2}(x)$ **(A)** underwent a re-orientation $f_{re}(x)$ and bias field correction using multiplicative intrinsic component optimization (MICO) $f_{bc}(x)$ to reduce inhomogeneities **(B)**. The subsequent registration is done on a brain extracted volume $I^{T2}_{ex}(x)$ **(C)** by deforming the MTPL $I_T(x)$ **(D)** with affine $f_A(x)$ and non-linear $f_{NL}(x)$ transformation.

highlight how many mice had a certain brain area affected by the stroke.

Mouse Brain Atlas and MRI Template

We developed an in-house MRI template (MTPL) $I_T(x)$ with strong correlation to the T2 raw images I^{T2} (see **Supplementary Figure S2**) by using N = 30 randomly chosen data sets of healthy C57BL6 mice of similar age. The mean of all voxels described in the gray matter (GM), white matter (WM) and cerebrospinal fluid (CSF) were calculated over all N, and the resulting template was associated with the original ARA (Allen Brain Reference Atlas, CCF v3, 50 μm isotropic resolution; **Figures 3A,B**). To obtain a complete overview of the ARA label IDs, we transferred the available information about label IDs, acronyms and names to a custom-made relational database (https://github.com/maswendt/AIDAdb; to access the file, a www.ninoxdb.de account is required). The database lists all brain regions according to the atlas ontology and provides simple access to associated parent and child labels. Using that database, we selected hierarchical lower regions of interest and defined the related parent labels (**Figure 3C**) to build a parental atlas $I_{A\uparrow}(x)$. This results in a reduction from >1,000 regions in $I_A(x)$ to 49 regions in $I_{A\uparrow}(x)$. In order to compare regions of the left vs. right hemisphere, the original ARA and the custom parental ARA were we splitted along the sagittal plane (**Figure 3D**).

Registration

We decided to use a specific multi-step registration scheme (**Figure 4**). The initial assumption of AIDAmri is that all given information of the ARA $I_A(x)$ is represented in the reference image space X. The assignment of this information to the individual MRI measurements $I^{T2}(x)$, $I^{DTI}(x)$ and $I^{fMRI}(x)$ is achieved by a suitable transformation f which transforms X in the acquisition image space Y, such that

$$f : X \rightarrow Y$$

Each individual transformation f is a combination of an affine $f_A(x)$ and non-linear $f_{NL}(x)$ transformation computed using NiftyReg (Centre of Medical Image Computing, University College London, UK). NiftyReg was chosen based on a direct comparison (see **Figure 2D** and **Supplementary Figure S2**) of

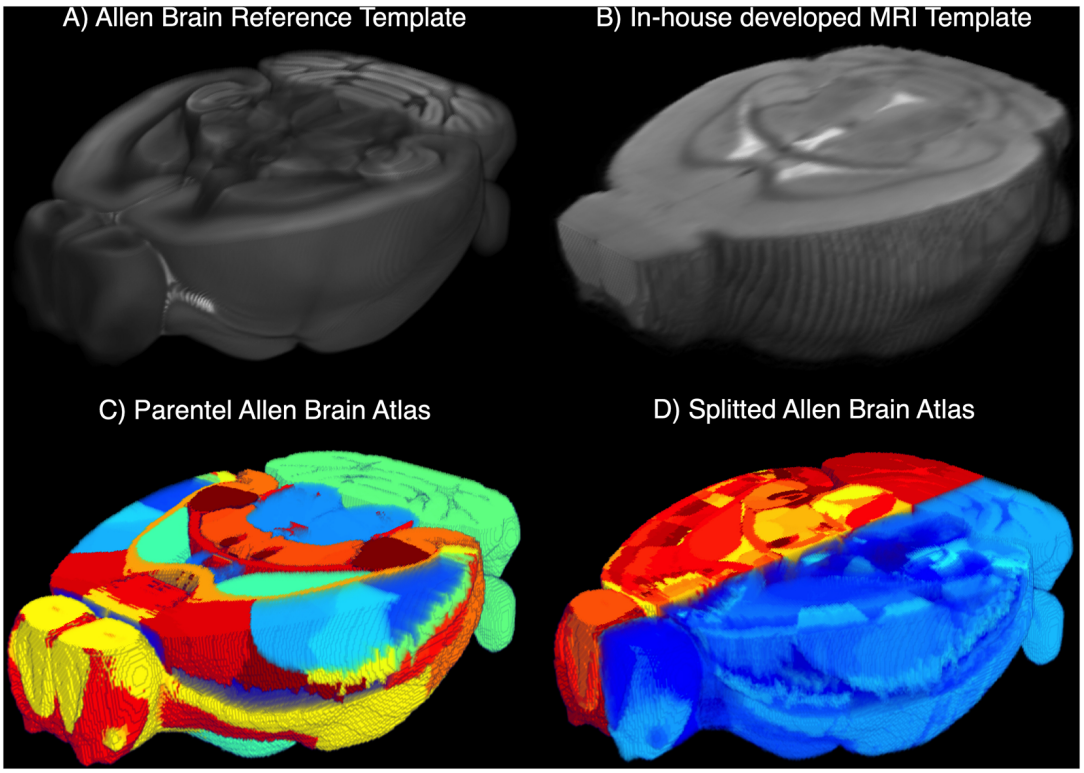


FIGURE 3 | 3D cut-outs of the **(A)** Allen Brain Reference Atlas (ARA) and **(B)** the in-house developed MRI template (MTPL). The annotations of the ARA $I_A(x)$ and the related ARA template **(A)** are overlaid with the MTPL $I_T(x)$ consisting of $N = 30$ T2w. Parental ARA labels $I_{A\uparrow}(x)$ **(C)** and detailed ARA labels with hemisphere split **(D)**.

registration accuracy with the developed MTPL $I_T(x)$ to FSL (Jenkinson et al., 2012), Advanced Normalization Tools (ANTs; Avants et al., 2008) and elastiX (Klein et al., 2010). Consequently, for linear affine registration the symmetric global block matching approach was implemented [NiftyReg, reg_aladin (Modat et al., 2014) with 6 degrees-of-freedom (DOF)]. To describe non-linear deformations, landmark points are placed on the reference image and iteratively deformed [NiftyReg, reg_f3d (Modat et al., 2010), with 12 DOF]. The non-linear transformation $f_{NL}(x)$ describes subcortical brain changes, such as a baseline shift. The multi-step registration requires the different scans to be orientated the same, which can be achieved by copying the orientation from the first to the subsequent scan(s). In that scenario, the non-linear deformations do not change significantly over different scans of one imaging session. Hence, the quantification of $f_{NL}(x)$ is only necessary once and the relative change can be applied to all data sets that are acquired in one session (**Figure 4**). The differences between each data set in one section can be adequately described by an affine $f_A(x)$ transformation which includes scaling, rotation, translation, compression and shearing. The registration procedure exclusively serves the purpose to transfer data of ARA to the related MRI data sets and to correlate functional and structural data. The processing steps to extract the connectivity information from DTI and activity information from rs-fMRI are conducted with the unmodified raw-data.

The deformation f between $I^{T2}(x)$ and $I_T(x)$ is quantified minimizing the Kullback–Leibler divergence (**Figure 4**; Kullback and Leibler, 1951). The combined transformation f of the affine $f_A(x)$ and non-linear transformation $f_{NL}(x)$ are applied to the MTPL $I_T(x)$ and subsequently the ARA $I_A(x)$ with the pre-processed data set $I^{T2}(x)$. Both, the affine transformation $f_A(x)$ and the non-linear transformation $f_{NL}(x)$ are stored for each processed data set separately. As an important factor influencing registration precision, we set the Jacobian determinate penalty to 0.3 where the user can increase the minimum deformation field from 1 mm to 5 mm depending on the strength of the required deformation. The affine transformation $f_A(x)$ is quantified by minimizing the Kullback–Leibler divergence between the current DTI or fMRI measurement and the related T2 measurement $I^{T2}(x)$. At this processing step, we have an ARA for all assumed data sets $I^{T2}(x)$, $I^{DTI}(x)$ and $I^{fMRI}(x)$, which lies in the same image space and is completely superimposed with the respective data. All subsequent fully automatic analysis steps of functional and structural data are based on a quantification that are provided by the anatomical regions of the associated ARA.

In order to validate the performance of the automated registration, we compared the automatically transformed ARA template of $N_T = 40$ test data sets (**Table 2**) with an ARA template that was semi-automatically registered by two independent observers O1 and O2 using a previously described landmark-

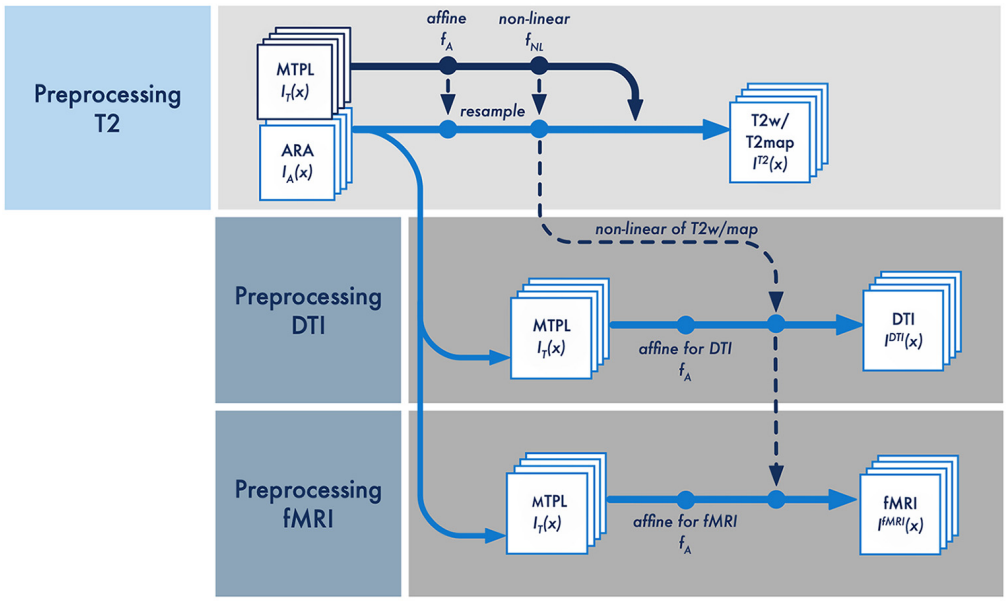


FIGURE 4 | Schematic overview of the multi-step registration procedure for the T2-weighted, DTI and rs-fMRI data [$I^{T2}(x)$, $I^{DTI}(x)$ and $I^{fMRI}(x)$]. The affine f_A and non-linear transformation f_{NL} is applied to MRI template (MTPL) $I_T(x)$ and subsequently the ARA $I_A(x)$ with the pre-processed data set $I^{T2}(x)$. The non-linear deformation f_{NL} between MTPL and the T2w/T2m is calculated only once and then linked to the respective affine transformation to pre-processed data of DTI $I^{DTI}(x)$ and rs-fMRI $I^{fMRI}(x)$.

TABLE 2 | Data overview of N_T = 40 data used to validate the registration.

Name	Scanner (T)	Scans (Σ)	Type	Matrix size	Resolution (mm)	Animals	
Data set 1	11.7	14	T2m	256 × 256 × 16	0.068 × 0.068 × 0.6	Nu/Nu	Adult nude mice
Data set 2	11.7	5	T2m	256 × 256 × 12	0.068 × 0.068 × 0.6	DCX-Luc	Adult transgenic DCX-Luc mice
Data set 3	9.4	10	T2w	256 × 256 × 48	0.068 × 0.068 × 0.6	C57BL6/N	Adult wildtype mice
Data set 4	7.0	11	T2w	128 × 128 × 30	0.109 × 0.109 × 0.5	C57BL6/N	Adult wildtype mice with stroke

All data were acquired on scanners with different characteristics or different image geometries. The registration of the listed data was compared with a manually slice-wise registration performed by two independent observers.

based registration approach with the help of the software 3DSlicer[8] (Kikinis et al., 2014; Ito et al., 2018). The error range between the transformations of both observers was set as a reference. We calculated the distance between $I_A(x)$ and the ARA templates of both approaches to find out where a high agreement exists. The Euclidian distance or L^2-Norm were used as one of the most common mathematical quantity of the distance between two-dimensional image functions. However, a slight shift or a rotation would hardly change the appearance of the image and possibly not be detectable by the human viewer at all. To avoid any dependency on changes in intensity the normalized cross-correlation (CrC) has been established (Avants et al., 2008). Since, the correlation between image fidelity and image quality is in some cases insufficient (Silverstein and Farrell, 1996), we also applied the Structural Similarity Index (SSIM; Wang et al., 2004) to end up with a satisfactory quality description. The idea of structural information is that pixels have strong interdependencies especially if they are spatially close. With these three metrices, we quantified the overall characteristic of the human perception to detect distortion between two images.

Step 3–DTI and rs-fMRI Processing

Pre-processing and Registration

To correlate all given information of the anatomical information of the $I^{T2}(x)$ to its related DTI $I^{DTI}(x,t)$ or fMRI $I^{fMRI}(x,t)$ measurements, some additional pre-processing steps are necessary. First, the dimension of the data must be reduced from 4D to 3D from $I(x,t)$ to $I(x)$. For this purpose and to minimize the noise and reduce artifacts, a minimum filter is applied over time and then the resulting three-dimensional data set is filtered with a Gaussian kernel. These filters preserve structures necessary for a sufficient registration whereas image noise is suppressed. Based on the previously mentioned assumption, for the registration of $I^{DTI}(x)$ or fMRI $I^{fMRI}(x)$ only an affine transformation $f_A(x)$ is performed and the non-linear transformation $f_{NL}(x)$ is applied from the previous T2 calculation (**Figure 4**). Subsequent DTI and rs-fMRI processing steps were implemented based on established protocols, which led to valid results in

[8]https://www.slicer.org/

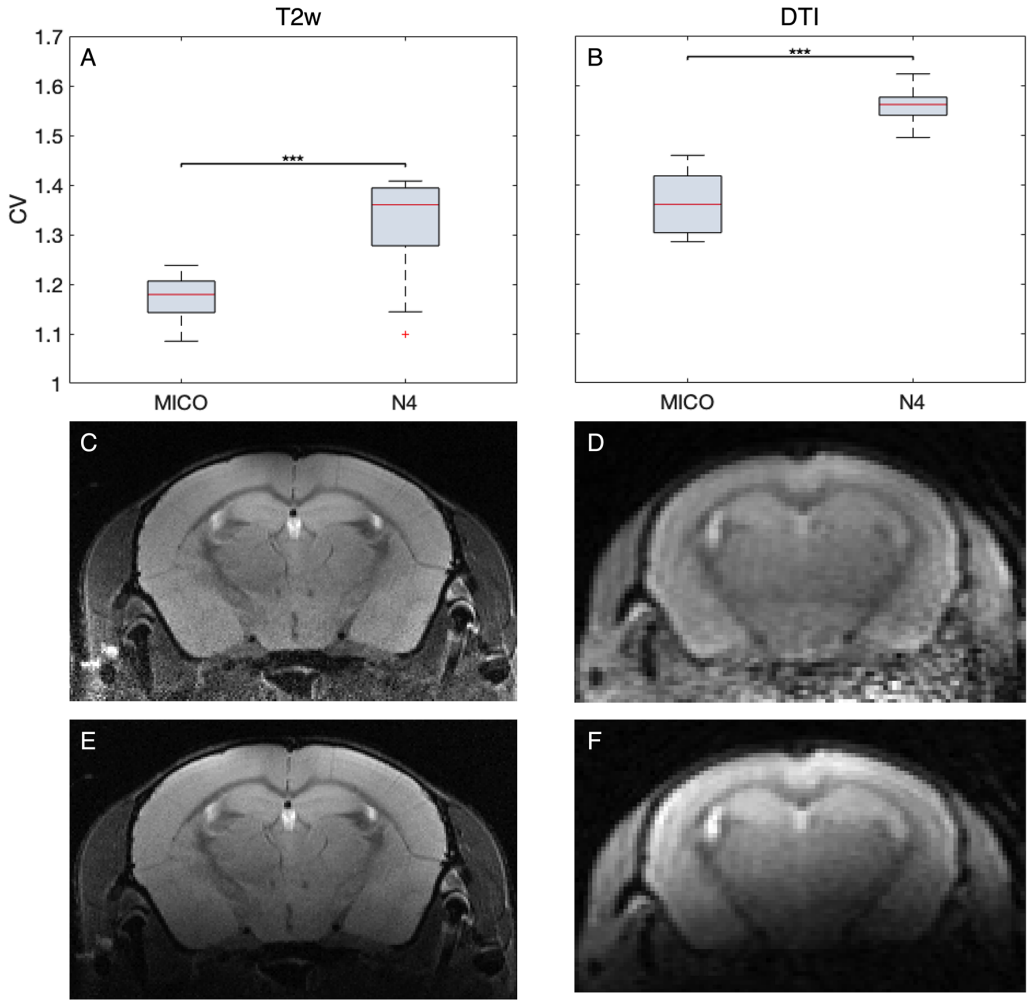


FIGURE 5 | Quantitative and qualitative comparison of MICO and N4 bias-field correction. The calculation of the degree of homogeneity revealed lower coefficient of variations (CV) for MICO compared to N4 for 22 T2w and 10 DTI measurements **(A,B)**. Representative MR images comparing MICO **(C,D)** and N4 **(E,F)** bias-field corrected images for T2w and DTI, respectively.

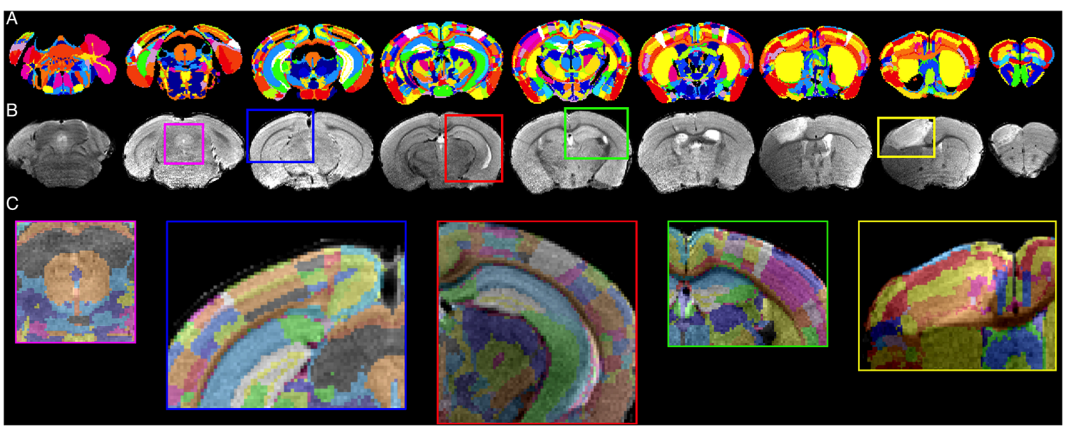


FIGURE 6 | Registration results. Representative transformed ARA annotations **(A)** that are registered on an T2w data set **(B)** with detailed views shown as overlay **(C)**.

previous studies (Budde and Song, 2010; Kim et al., 2012; Gorges et al., 2017).

DTI—Structural Connectivity

Motion artifacts in diffusion imaging mostly origin from subtle head movements due to the fast breathing rhythm, which results in repetitive voxel displacements in the x-y plane. To quantify and spatially correct anatomical dissimilarities with 6 degrees of freedom (DOF), we apply a slice-wise motion correction using FSL MCFLIRT (Jenkinson et al., 2002). Unfortunately, MCFLIRT co-registers every volume in a time series to the one volume in the midst of the series to detect slow physical movement. By adapting the correction from a volume based to a slice-based mode of operation, AIDAmri splits each data set into slices, correcting them separately and merging the motion corrected slice series back into one 4D data set. The motion-corrected data are then fed into DSI-Studio (Yeh et al., 2013). The non-brain tissue was discarded by applying a binary mask of the brain extraction to the original DTI data set $I^{DTI}(x, t)$. The data are reconstructed within DSI-Studio, based on an electrostatically optimized protocol of Jones30 (Skare et al., 2000) with 30 gradient directions. The reconstructed diffusion images are used to perform fiber tracking and analyze the data with respect to the associated regions of the ARA. All reconstructed data sets, AD, radial (RD), MD and the fraction anisotropy (FA) are being exported separately.

The whole brain tractography is conducted with the deterministic streamline propagation using Euler's methods (Basser et al., 2000) and terminates if a total fiber number of one million fibers is reached. The tracking starts from a random voxel position and propagated with a step size of 0.5 mm. All fibers shorter than 0.5 mm or longer than 12 mm were discarded, whereas the tracking is terminated if the angle between two consecutive directions exceeds 55°. The fiber termination criteria were previously tested on several data sets with healthy animals for best parameter settings, concerning true and false fiber generation. The analysis provides connectivity matrices, in which the rows and columns of the matrices represent a region of the ARA and the entries display the connectivity strength between two particular regions.

rs-fMRI—Functional Connectivity

Before the regional characteristics can be evaluated by means of rs-fMRI, some optimizations need to be implemented. The mouse in our setup is fixed with ear bars and a tooth bar minimizing head movements during acquisition. Nevertheless, spontaneous excitement due to fluctuations in anesthesia phases and respiratory motion may affect image stability. Therefore, we recorded the breathing during the measurement to identify regressors describing respiratory artifacts. The physiological data were sampled during EPI data acquisition, indicated by overlaid trigger pulses. The pre-processing of the breathing signal included the detection of inspiration peaks and baseline correction using the median values. Additionally, slice-wise motion correction is applied to the raw rs-fMRI $I^{\mathrm{fMRI}}(x,t)$ by the same approach as for DTI. This additional correction is necessary to detect additional displacement between slices or fast respiratory rhythms. Since for many scientific applications, such as event-triggered fMRI, a slice time correction is essential, it is possible to switch on that function in AIDAmri and perform a correction with FSL SliceTimer (Jenkinson et al., 2002).

Completed by the pre-processed physiological recording, all of this data has been merged into a single multichannel file. The following processing steps were implemented based on the processing steps in FSL FEAT (Woolrich et al., 2001) with some modifications. For example, the smoothing was adapted with a spatial filter. Due to anisotropy of the voxels in z-direction, the spatial filter is applied in the x- and y-plane and not over the whole volume as in FSL FEAT. In our case, the spatial filter smooths the data with FWHM of 3.0 mm and a high-pass filter with a cut-off frequency of 0.01 Hz that reduces additional noise sources. The registered ARA is used to extract the regions in the functional domain generating a 4D file (x, y, slices, region masks) in NIfTI format. That file includes all transformed ARA regions, whereas each three-dimensional region is defined by a binary mask. Among all repetitions of the resting state fMRI data, the mean of the intensities of the voxels of a region is calculated and this average constitutes the averaged time series of the specific region.

RESULTS

Bias-Field Correction

Magnetic field inhomogeneities induced by insufficient shimming, imperfect coil placement and susceptibility artifacts at tissue borders directly relate to image quality. To measure the bias-field, we tested the N4 against the MICO algorithm (**Figure 5**). MICO has so far only been tested for human MRI. The comparison was conducted on 22 T2w data sets and 10 DTI data sets with the CV as metric. For both data sets, MICO-based bias-field correction resulted in lower CV values compared to the N4 algorithms ($p < 0.001$) and better corrections of the bias-field.

Registration

The results of the multi-step registration for a representative mouse brain with large stroke-related deformations are shown in **Figure 6**. The stroke lesion is distinguishable in the anterior slides of T2w data set as the hyperintense regions. Even strong deformations of the anatomical structure are realistically contoured by the algorithm, such that the ARA is precisely overlaid with the T2w data set. In addition to the qualitative assessment, we applied a quantitative quality control (**Figure 7**) using a slice-wise comparison of $N_{\mathrm{T}} = 40$ MR images selected from four different MRI datasets (**Table 2**). Two experienced observers used a semi-manually landmark-based approach to overlay the atlas.

For each data set the error range between the transformations made by observer 1 and 2 I_{01}/I_{02} was used as reference. Due to the different imaging properties and the subjective landmark placing there was a large variability in the median between both observers. In comparison to the automatic registration of AIDAmri the deviation to the ground truth defined by both observers, minimal and not statistically significantly differences for all quantitative measurements (L2, SSMI, CrC). For example, for data set 3 in **Figure 7**, the median of the SSMI between both

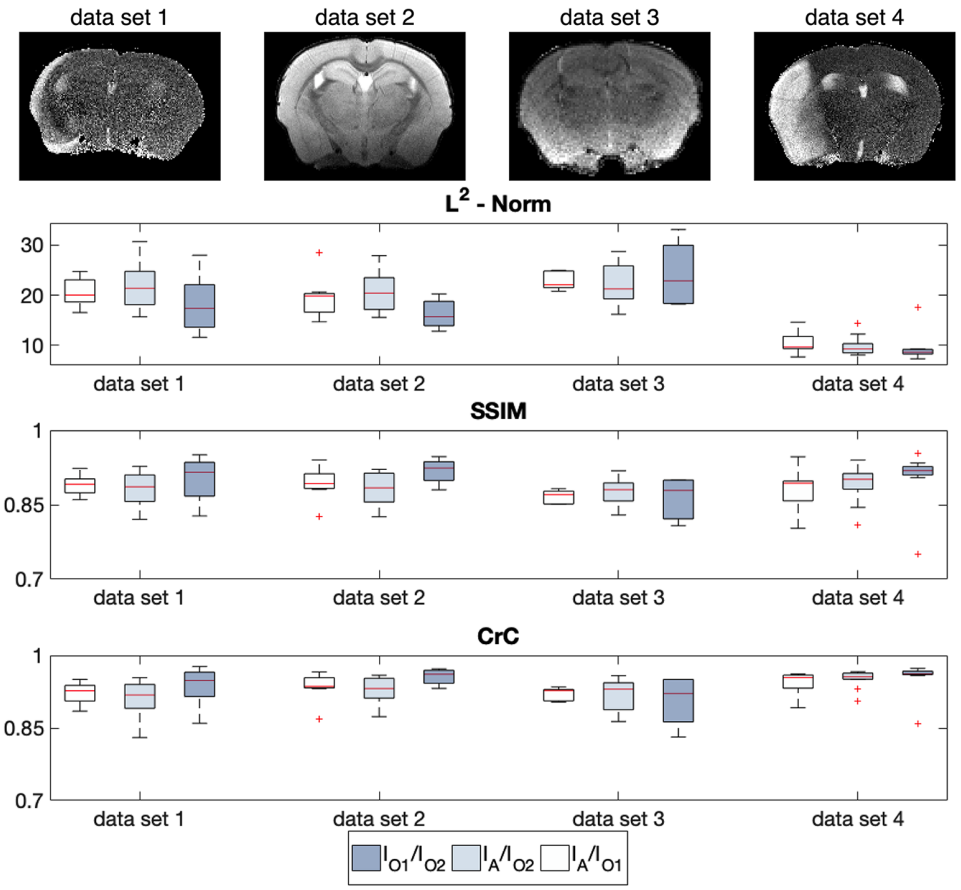


FIGURE 7 | Quantitative registration quality control using a slice-wise comparison of N_T = 40 imaging data grouped in four sets with three metrics [L2-Norm, Structural Similarity Index (SSIM), Cross-Correlation (CrC)] between AIDAmri I_A and two observers I_{01} and I_{02}. The different properties of each data sets are listed in **Table 2** and one example slice is shown above each evaluation. Whereas, the ground-truth was determined with the error range of I_{01}/I_{02}, the average error between the automated approach of AIDAmri and the observer-dependent approach I_A/I_{01} and I_A/I_{02} showed no significant differences in all three metrices.

observers I_{01}/I_{02} is 0.878. Compared to that reference value the median of AIDAmri to both Observes is 0.870 for I_A/I_{01} and 0.880 for I_A/I_{02}. In conclusion, the deviation varies only between 0.81 and 0.92 in the SSIM for all evaluated data sets and shows comparable error values for the CrC.

After successful processing with AIDAmri, the results offer various possibilities for further data analysis (**Figure 8**). Depending on the field of research, users have the opportunity to evaluate their data quantitatively and qualitatively. AIDAmri includes plot functions to visualize structural and functional information of DTI (**Figure 8A**) and rs-fMRI (**Figure 8B**) as adjacency matrices. To achieve a more detailed quantitative evaluation a variety of possibilities are freely available and can be used regardless of the processing pipeline. For example, predefined regions can be examined in regard of their structural and functional properties[9]. Relationships between the ARA regions can also be visualized in a circular Graph[10]. The Brain Connectivity Toolbox (Rubinov and Sporns, 2010) can be used for a quantitative evaluation of the DTI data based on graph theory. Likewise, rs-fMRI data can be evaluated with FSLNETS[11]. In each case, no further pre-processing steps are necessary and the output of AIDAmri can be directly fed into the established tools.

DISCUSSION

Currently, a variety of tools are available for human imaging studies, offering either a full evaluation (Cui et al., 2013) and/or step-by-step workflow (Rubinov and Sporns, 2010). In the pre-clinical environment, standardization of MRI acquisition, processing and sharing standards still need major development. Therefore, the unique translational advantage of MRI, e.g., to directly probe novel scan protocols and biomarker findings from bench to bedside awaits exploitation (Jaiswal, 2015). Here, we present a novel Atlas-based Imaging Data Analysis Pipeline (AIDAmri) for structural and functional MRI of the mouse brain. AIDAmri represents the first region-based

[9]https://de.mathworks.com/matlabcentral/fileexchange/27983-slicer
[10]https://github.com/paul-kassebaum-mathworks/circularGraph
[11]www.fmrib.ox.ac.uk/fsl

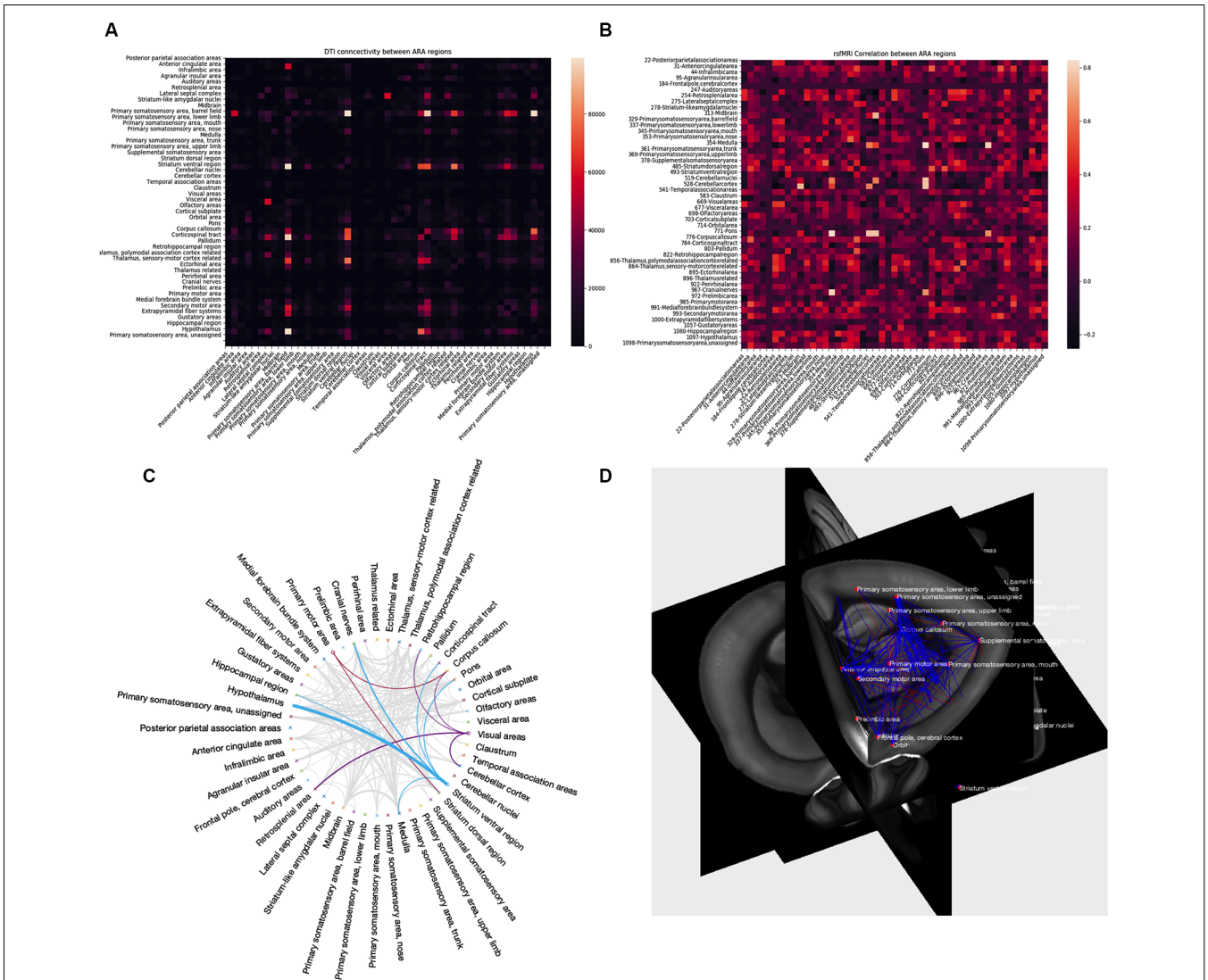


FIGURE 8 | AIDAmri output. Structural and functional information of DTI **(A)** and fMRI **(B)** can be represented as adjacency matrices by using the plot function. The entries in the matrices represent the number of tracks passing or ending in the ARA regions of the DTI and activity pattern of rs-fMRI among all ARA regions to evaluate the results using graph theoretical approaches. Other ways to visualize connectivity patterns (plot function not included in AIDAmri): the circular representation of a row or column vector **(C)** where thicker lines relate to higher matrix values **(C)** and 3D visualization of connectivity in the anatomical context, here the registered atlas **(D)**.

processing pipeline, that extracts the structural and functional information from T2w, DTI and rs-fMRI data, and which enables a region-by-region analysis of preclinical MRI data based on the Allen Brain Reference Atlas (ARA). Importantly, the developed MRI template facilitates co-registration of MRI data with the ARA, which would be impossible by a direct registration. Since the template is co-registered with the ARA in the original image space, research groups of other labs can customize the ARA in higher hierarchical levels to map their individual regions-of-interest without the need to downscale the information. For example, we provide both a (hemisphere-splitted) detailed as well as custom-made parental atlas. The parental atlas is particularly useful for the analysis of DTI and rs-fMRI with have intrinsically lower image resolution and are stronger affected by susceptibility artifacts. Although we carefully validated the registration, the striking differences in original image size and resolution between the atlas and the DTI/rs-fMRI can result in pixel interpolations and region-mismatches, e.g for small thalamic nuclei or single cortical layers. In that case, we recommend the parental atlas, with larger brain regions, where interpolations have negligible effects. In comparison to other atlases, the ARA provides not only the most-detailed structural 3D atlas but also access to the Allen Institute cell type, transcriptomics and brain connectivity database (Lein et al., 2007; Oh et al., 2014). AIDAmri was written in Python 3.6 using freely available algorithm

tools. The modular structure enables efficient processing and the possibility to modify or add modules. To enhance the comparability to other fields of research and to ensure its applicability to a variety of neurological questions, AIDAmri has been comprehensively tested and optimized by following steps. First, we implemented a novel SNR measurement, which has been shown to outperform manual or other semi-automatic measurements (Sijbers et al., 2007). Second, to prepare the data for registration with the ARA, pre-processing steps including re-orientation, bias-field correction, and brain extraction were implemented. We successfully implemented the MICO bias-field correction, which was applied before only on human data (Li et al., 2014). We could show, that MICO generates significantly better data even in the pre-clinical environment than the well-known N4 algorithm. Finally, we applied a quantitative quality control to verify that the developed multi-step registration process works robustly. In a statistical analysis, the results achieved by two-independent and trained observers were found to be not different from the automated registration for various mouse strains. Registration accuracy was also valid for pathologies such as stroke with significant brain deformation due to, e.g., oedema or necrosis. The AIDAmri output contains functional and structural connectivity matrices for all (selected) ARA regions. These matrices can be used to analyze differences in the brain network between health and disease. For the first time, AIDAmri provides in one common processing pipeline and one common atlas system quantitative structure-function relationships, which are known to be crucial to understand the structural underpinnings of brain function and brain plasticity (Straathof et al., 2019). Future studies may focus on the integration of other imaging modalities, e.g., single photon emission computed tomography (SPECT) or positron emission tomography (PET), to the ARA. AIDAmri contributes to the awareness-raising effort of the scientific community to standardize diverse datatypes and analyses across species (Sejnowski et al., 2014) and will facilitate data processing in large cohorts and multi-center studies.

ETHICS STATEMENT

This study was carried out in accordance with the recommendations of ARRIVE and IMPROVE guidelines (Kilkenny et al., 2010; Percie du Sert et al., 2017). The protocol was approved by the Landesamt für Natur, Umwelt und Verbraucherschutz North Rhine-Westphalia (reference number 84-02.04.2016.A461, 84-02.04.2014.A226 and 84-02.04.2012.A190).

AUTHOR CONTRIBUTIONS

NP designed and implemented the pipeline, wrote the manuscript. MD contributed to the code, provided algorithms and processing steps. SB contributed to the code, performed trouble-shooting and testing. FW performed manual atlas registration. DW and MH provided MRI data, contributed to the structure of the pipeline and wrote the manuscript. GF contributed to the design of the pipeline and wrote the manuscript. MA supervised the project, performed atlas registration and wrote the manuscript.

FUNDING

This work was financially supported by the Friebe Foundation (T0498/28960/16).

SUPPLEMENTARY MATERIAL

The Supplementary Material for this article can be found online at: https://www.frontiersin.org/articles/10.3389/fninf.2019.00042/full#supplementary-material

REFERENCES

Aswendt, M., Gianolio, E., Pariani, G., Napolitano, R., Fedeli, F., Himmelreich, U., et al. (2012). *In vivo* imaging of inhibitory, GABAergic neurons by MRI. *Neuroimage* 62, 1685–1693. doi: 10.1016/j.neuroimage.2012.05.029

Avants, B. B., Epstein, C. L., Grossman, M., and Gee, J. C. (2008). Symmetric diffeomorphic image registration with cross-correlation: evaluating automated labeling of elderly and neurodegenerative brain. *Med. Image Anal.* 12, 26–41. doi: 10.1016/j.media.2007.06.004

Basser, P. J., Pajevic, S., Pierpaoli, C., Duda, J., and Aldroubi, A. (2000). *In vivo* fiber tractography using DT-MRI data. *Magnet. Reson. Med.* 44, 625–632. doi: 10.1002/1522-2594(200010)44:4<625::aid-mrm17>3.0.co;2-o

Bihan, D., Mangin, J., Poupon, C., Clark, C. A., Pappata, S., Molko, N., et al. (2001). Diffusion tensor imaging: concepts and applications. *J. Magn. Reson. Imaging* 13, 534–546. doi: 10.1002/jmri.1076

Brummer, M. E., Mersereau, R. M., Eisner, R. L., and Lewine, R. R. J. (1993). Automatic detection of brain contours in MRI data sets. *IEEE Trans. Med. Imaging* 12, 153–166. doi: 10.1109/42.232244

Budde, M. D., and Song, S.-K. (2010). "Insights into diffusion tensor imaging from animal models of white matter pathology," in *Diffusion MRI*, ed. D. K. Jones (Oxford: Oxford University Press), 690–702. doi: 10.1093/med/9780195369779.003.0042

Budin, F., Hoogstoel, M., Reynolds, P., Grauer, M., O'Leary-Moore, S. K., and Oguz, I. (2013). Fully automated rodent brain MR image processing pipeline on a Midas server: from acquired images to region-based statistics. *Front. Neuroinform.* 7:15. doi: 10.3389/fninf.2013.00015

Cox, R. W., Ashburner, J., Breman, H., Fissell, K., Haselgrove, C., Holmes, C. J., et al. (2004). A (sort of) new image data format standard: Nifti-1: we 150. *Neuroimage* 22:e1440.

Cui, Z., Zhong, S., Xu, P., He, Y., and Gong, G. (2013). PANDA: a pipeline toolbox for analyzing brain diffusion images. *Front. Hum. Neurosci.* 7:42. doi: 10.3389/fnhum.2013.00042

Dong, H. (2008). *The Allen Reference Atlas: A Digital Color Brain Atlas of the C57Bl/6J Male Mouse.* Hoboken, NJ: John Wiley & Sons Inc.

Driehuys, B., Nouls, J., Badea, A., Bucholz, E., Ghaghada, K., Petiet, A., et al. (2008). Small animal imaging with magnetic resonance microscopy. *ILAR J.* 49, 35–53. doi: 10.1093/ilar.49.1.35

Fang, A., Nowinski, W. L., Nguyen, B. T., and Bryan, N. R. (1995). "Three-dimensional Talairach-Tournoux brain atlas," in *Proceedings of the SPIE—The International Society for Optical Engineering* (San Diego, CA), 583–592.

Gorges, M., Roselli, F., Müller, H.-P., Ludolph, A. C., Rasche, V., and Kassubek, J. (2017). Functional connectivity mapping in the animal model: principles and applications of resting-state fMRI. *Front. Neurol.* 8:200. doi: 10.3389/fneur.2017.00200

Gorgolewski, K. J., Esteban, O., Schaefer, G., Wandell1, B. A., and Poldrack, R. A. (2017). *OpenNeuro—A Free Online Platform for Sharing and Analysis of Neuroimaging Data.* Vancouver, BC: Organization for Human Brain Mapping, 1677.

Green, C., Minassian, A., Vogel, S., Diedenhofen, M., Beyrau, A., Wiedermann, D., et al. (2018). Sensorimotor functional and structural networks after intracerebral stem cell grafts in the ischemic mouse brain. *J. Neurosci.* 38, 1648–1661. doi: 10.1523/JNEUROSCI.2715-17.2018

Grefkes, C., and Fink, G. R. (2014). Connectivity-based approaches in stroke and recovery of function. *Lancet Neurol.* 13, 206–216. doi: 10.1016/S1474-4422(13)70264-3

Henkelman, M. R. (1985). Measurement of signal intensities in the presence of noise in MR images. *Med. Phys.* 12, 232–233. doi: 10.1118/1.595711

Hess, A., Hinz, R., Keliris, G. A., and Boehm-Sturm, P. (2018). On the usage of brain atlases in neuroimaging research. *Mol. Imaging Biol.* 20, 742–749. doi: 10.1007/s11307-018-1259-y

Hodge, M. R., Horton, W., Brown, T., Herrick, R., Olsen, T., Hileman, M. E., et al. (2016). ConnectomeDB—sharing human brain connectivity data. *Neuroimage* 124, 1102–1107. doi: 10.1016/j.neuroimage.2015.04.046

Hoehn, M., and Aswendt, M. (2013). Structure-function relationship of cerebral networks in experimental neuroscience: contribution of magnetic resonance imaging. *Exp. Neurol.* 242, 65–73. doi: 10.1016/j.expneurol.2012.04.014

Hübner, N., Mechling, A. E., Lee, H.-L., Reisert, M., Bienert, T., Hennig, J., et al. (2017). The connectomics of brain demyelination: functional and structural patterns in the cuprizone mouse model. *Neuroimage* 146, 1–18. doi: 10.1016/j.neuroimage.2016.11.008

Ito, M., Aswendt, M., Lee, A. G., Ishizaka, S., Cao, Z., Wang, E. H., et al. (2018). RNA-sequencing analysis revealed a distinct motor cortex transcriptome in spontaneously recovered mice after stroke. *Stroke* 49, 2191–2199. doi: 10.1161/strokeaha.118.021508

Jaiswal, M. (2015). Toward a high-resolution neuroimaging biomarker for mild traumatic brain injury: from bench to bedside. *Front. Neurol.* 6:148. doi: 10.3389/fneur.2015.00148

Jenkinson, M., Bannister, P., Brady, M., and Smith, S. (2002). Improved optimization for the robust and accurate linear registration and motion correction of brain images. *Neuroimage* 17, 825–841. doi: 10.1016/s1053-8119(02)91132-8

Jenkinson, M., Beckmann, C. F., Behrens, T., Woolrich, M. W., and Smith, S. M. (2012). FSL. *Neuroimage* 62, 782–790. doi: 10.1016/j.neuroimage.2011.09.015

Kikinis, R., Pieper, S. D., and Vosburgh, K. G. (2014). "3D Slicer: a platform for subject-specific image analysis, visualization, and clinical support," in *Intraoperative Imaging and Image-Guided Therapy*, ed. F. Jolesz (New York, NY: Springer), 277–289.

Kilkenny, C., Browne, W., Cuthill, I. C., Emerson, M., Altman, D. G., and NC3Rs Reporting Guidelines Working Group. (2010). Animal research: reporting *in vivo* experiments: the ARRIVE guidelines. *J. Gene Med.* 12, 561–563. doi: 10.1002/jgm.1473

Kim, Y. B., Kalthoff, D., Po, C., Wiedermann, D., and Hoehn, D. G. (2012). Connectivity of thalamo-cortical pathway in rat brain: combined diffusion spectrum imaging and functional MRI at 11.7T. *NMR Biomed.* 25, 943–952. doi: 10.1002/nbm.1815

Klein, S., Staring, M., Murphy, K., Viergever, M. A., and Pluim, J. P. (2010). elastix: a toolbox for intensity-based medical image registration. *IEEE Trans. Med. Imaging* 29, 196–205. doi: 10.1109/tmi.2009.2035616

Koch, S., Mueller, S., Foddis, M., Bienert, T., von Elverfeldt, D., Knab, F., et al. (2019). Atlas registration for edema-corrected MRI lesion volume in mouse stroke models. *J. Cereb. Blood Flow Metab.* 39, 313–323. doi: 10.1177/0271678X17726635

Kullback, S., and Leibler, R. (1951). On information and sufficiency. *Ann. Math. Statistics* 22, 79–86. doi: 10.1214/aoms/1177729694

Lein, E. S., Hawrylycz, M. J., Ao, N., Ayres, M., Bensinger, A., Bernard, A., et al. (2007). Genome-wide atlas of gene expression in the adult mouse brain. *Nature* 445, 168–176. doi: 10.1038/nature05453

Levenberg, K. (1944). A Method for the solution of certain non-linear problems in least squares. *Q. Appl. Math.* 2, 164–168. doi: 10.1090/qam/10666

Li, C., Gore, J. C., and Davatzikos, C. (2014). Multiplicative intrinsic component optimization (MICO) for MRI bias field estimation and tissue segmentation. *Magn. Reson. Imaging* 32, 913–923. doi: 10.1016/j.mri.2014.03.010

Mazziotta, J. C., Toga, A. W., Evans, A., Fox, P., and Lancaster, J. (1995). A probabilistic atlas of the human brain: theory and rationale for its development the international consortium for brain mapping (ICBM). *Neuroimage* 2, 89–101. doi: 10.1006/nimg.1995.1012

Modat, M., Cash, D. M., Daga, P., Winston, G. P., Duncan, J. S., and Ourselin, S. (2014). Global image registration using a symmetric block-matching approach. *J. Med. Imaging* 1:024003. doi: 10.1117/1.jmi.1.2.024003

Modat, M., Ridgway, G. R., Taylor, Z. A., Lehmann, M., Barnes, J., Hawkes, D. J., et al. (2010). Fast free-form deformation using graphics processing units. *Comput. Meth. Prog. Biol.* 98, 278–284. doi: 10.1016/j.cmpb.2009.09.002

Nieman, B. J., Bock, N. A., Bishop, J., Chen, J. X., Sled, J. G., Rossant, J., et al. (2005). Magnetic resonance imaging for detection and analysis of mouse phenotypes. *NMR Biomed.* 18, 447–468. doi: 10.1002/nbm.981

Oh, S. W., Harris, J. A., Ng, L., Winslow, B., Cain, N., Mihalas, S., et al. (2014). A mesoscale connectome of the mouse brain. *Nature* 508, 207–214. doi: 10.1038/nature13186

Pallast, N., Wieters, F., Nill, M., Fink, G. R., and Aswendt, M. (2018). Cloud-based relational database for multimodal animal data. *Database* 2018: bay124. doi: 10.1093/database/bay124

Percie du Sert, N., Alfieri, A., Allan, S. M., Carswell, H. V., Deuchar, G. A., Farr, T. D., et al. (2017). The IMPROVE guidelines (ischaemia models: procedural refinements of *in vivo* experiments). *J. Cereb. Blood Flow Metab.* 37, 3488–3517. doi: 10.1177/0271678x17709185

Straathof, M., Sinke, M. R., Dijkhuizen, R. M., and Otte, W. M. (2019). A systematic review on the quantitative relationship between structural and functional network connectivity strength in mammalian brains. *J. Cereb. Blood Flow Metab.* 39, 189–209. doi: 10.1177/0271678X18809547

Rex, D. E., Ma, J. Q., and Toga, A. W. (2003). The LONI pipeline processing environment. *Neuroimage* 19, 1033–1048. doi: 10.1016/s1053-8119(03)00185-x

Rubinov, M., and Sporns, O. (2010). Complex network measures of brain connectivity: uses and interpretations. *Neuroimage* 52, 1059–1069. doi: 10.1016/j.neuroimage.2009.10.003

Sejnowski, T. J., Churchland, P. S., and Movshon, A. J. (2014). Putting big data to good use in neuroscience. *Nat. Neurosci.* 17, 1440–1441. doi: 10.1038/nn.3839

Sijbers, J., Poot, D., den Dekker, A. J., and Pintjens, W. (2007). Automatic estimation of the noise variance from the histogram of a magnetic resonance image. *Phys. Med. Biol.* 52, 1335–1348. doi: 10.1088/0031-9155/52/5/009

Silverstein, D. A., and Farrell, J. E. (1996). "The relationship between image fidelity and image quality," in *Proceedings of the 3rd IEEE International Conference on Image Processing* (Lausanne: IEEE), 881–884

Skare, S., Hedehus, M., Moseley, M. E., and Li, T.-Q. (2000). Condition number as a measure of noise performance of diffusion tensor data acquisition schemes with MRI. *J. Magn. Reson.* 147, 340–352. doi: 10.1006/jmre.2000.2209

Smith, S. M. (2002). Fast robust automated brain extraction. *Hum. Brain Mapp.* 17, 143–155. doi: 10.1002/hbm.10062

Toda, T., Ishida, K., Kiyama, H., Yamashita, T., and Lee, S. (2014). Down-regulation of KCC2 expression and phosphorylation in motoneurons and increases the number of in primary afferent projections to motoneurons in mice with post-stroke spasticity. *PLoS One* 9:e114328. doi: 10.1371/journal.pone.0114328

Tustison, N. J., Avants, B. B., Cook, P. A., Zheng, Y., Egan, A., Yushkevich, P. A., et al. (2010). N4ITK: improved N3 bias correction. *IEEE Trans. Med. Imaging* 29, 1310–1320. doi: 10.1109/TMI.2010.2046908

van Meer, M. P., van der Marel, K., Wang, K., Otte, W. M., El Bouazati, S., Roeling, T. A., et al. (2010). Recovery of sensorimotor function after experimental stroke correlates with restoration of resting-state interhemispheric functional connectivity. *J. Neurosci.* 30, 3964–3972. doi: 10.1523/JNEUROSCI.5709-09.2010

Wang, Z., Bovik, A., Sheikh, H., and Simoncelli, E. P. (2004). Image quality assessment: from error visibility to structural similarity. *IEEE Trans. Image Process.* 13, 600–612. doi: 10.1109/tip.2003.819861

Woolrich, M. W., Ripley, B. D., Brady, M., and Smith, S. M. (2001). Temporal autocorrelation in univariate linear modeling of fMRI data. *Neuroimage* 14, 1370–1386. doi: 10.1006/nimg.2001.0931

Yeh, F.-C., Verstynen, T. D., Wang, Y., Fernández-Miranda, J. C., and Tseng, W.-Y. (2013). Deterministic diffusion fiber tracking improved by quantitative anisotropy. *PLoS One* 8:e80713. doi: 10.1371/journal.pone.0080713

Yushkevich, P. A., Piven, J., Hazlett, H., Smith, R., Ho, S., Gee, J. C., et al. (2006). User-guided 3D active contour segmentation of anatomical structures: significantly improved efficiency and reliability. *Neuroimage* 31, 1116–1128. doi: 10.1016/j.neuroimage.2006.01.015

Conflict of Interest Statement: The authors declare that the research was conducted in the absence of any commercial or financial relationships that could be construed as a potential conflict of interest.

Copyright © 2019 Pallast, Diedenhofen, Blaschke, Wieters, Wiedermann, Hoehn, Fink and Aswendt. This is an open-access article distributed under the terms of the Creative Commons Attribution License (CC BY). The use, distribution or reproduction in other forums is permitted, provided the original author(s) and the copyright owner(s) are credited and that the original publication in this journal is cited, in accordance with accepted academic practice. No use, distribution or reproduction is permitted which does not comply with these terms.

frontiers in Neuroinformatics

SYSTEMATIC REVIEW
published: 13 August 2019
doi: 10.3389/fninf.2019.00058

Novel Technological Solutions for Assessment, Treatment, and Assistance in Mild Cognitive Impairment

Gianmaria Mancioppi[1], *Laura Fiorini*[1], *Marco Timpano Sportiello*[2] *and Filippo Cavallo*[1]*

[1] *The BioRobotics Institute, Scuola Superiore Sant'Anna, Pisa, Italy,* [2] *Laboratory of Neuropsychology, USL Nordovest Toscana, Pisa, Italy*

Alzheimer's disease, and dementia, represent a common cause of disability and one of the most relevant challenges in the health world. In addition, these conditions do not have, at moment, a pharmacological treatment that can stop the pathological progress. Mild cognitive impairment (MCI), defined as the borderline between normal aging and early dementia, represents a meaningful field of study because, in the transition to dementia, clinicians have defined a useful therapeutic window. Additionally, due to the lack of effective pharmacological interventions, recent years have seen an increase in research into new technological solutions to assess, stimulate, and assist patients afflicted with Alzheimer's disease. This review aims to outline the use of information and communication technologies in the field studying MCI. Particularly, the goal is to depict the framework and describe the most worthwhile research efforts, in order to display the current technologies available, describe the research objectives, and delineate prospective future researches. Regarding data sources, the research was conducted within three databases, PubMed Central, Web of Science, and Scopus, between January 2009 and December 2017. A total of 646 articles were found in the initial search. Accurate definition of the exclusion criteria and selection strategy allowed identification of the most relevant papers to use for the study. Finally, 56 papers were fully evaluated and included in this review. Three major clinical application areas have been portrayed, namely "Cognitive Assessment," "Treatment," and "Assistance." These have been combined with three main technological solutions, specifically "Sensors," "Personal Devices," and "Robots." Furthermore, the study of the publications time series illustrates a steadily increasing trend, characterized by the enrollment of small groups of subjects, and particularly oriented to the subjects assistance using robots companion. In conclusion, despite the new technological solutions for people with MCI have received much interest, particularly regarding robots for assistance, nowadays it still owns vast room for improvement.

Keywords: mild cognitive impairment, ICT, cognitive stimulation, neuropsychological measures, cognitive support technologies, social robotics/HRI, dementia-Alzheimer disease, assistive technologies

OPEN ACCESS

Edited by:
Antonio Fernández-Caballero, University of Castilla La Mancha, Spain

Reviewed by:
Roger C. Ho, National University of Singapore, Singapore
Valeria Manera, University of Nice Sophia Antipolis, France

***Correspondence:**
Filippo Cavallo
filippo.cavallo@santannapisa.it

Received: *22 January 2019*
Accepted: *15 July 2019*
Published: *13 August 2019*

Citation:
Mancioppi G, Fiorini L, Timpano Sportiello M and Cavallo F (2019) Novel Technological Solutions for Assessment, Treatment, and Assistance in Mild Cognitive Impairment. Front. Neuroinform. 13:58. doi: 10.3389/fninf.2019.00058

1. INTRODUCTION

Worldwide, dementia represents one of the most important causes of disability and reduced autonomy in the elderly population. It is defined, in fact, as a syndrome, generally of a chronic or progressive nature, in which is observed deterioration in cognitive function. Alzheimer's Disease (AD) is the most common type of dementia, with a prevalence of 60–65% of the cases (Alzheimer Association, 2017). According to the statistics and the forecasts about AD, today people afflicted by this condition number approximately 46.8 million. This number is expected to steadily increase over the next few years, reaching 74.7 million by 2030 and 100 million by 2050 (Prince et al., 2016). The growth in dementia cases is resulting in an increase in the associated global costs. Particularly, between 2010 and 2015, the expenditure is expected to increase by 35.5%. Furthermore, projections indicate that the expense will reach $1 trillion by the end of 2018 (Prince et al., 2016). Due to the increase in the elderly population, with an increase in the associated costs, the social impacts, and the apparent lack of effective pharmacological treatments, AD and the others types of dementia constitute a dramatic challenge for the public health services. Furthermore, caregivers of patients with dementia have a higher prevalence of mental health disorders, particularly depression and anxiety (Sallim et al., 2015). For this reason, a strong commitment has been made to find ways to exploit and maximize the remaining cognitive resources of patients with initial symptoms of dementia. These patients, in fact, maintain the ability to learn new skills and strategies, and moreover preserve a good awareness (Olazarán et al., 2004; Belleville et al., 2016). Among all the medical labels developed to describe the pre-dementia stage, Mild Cognitive Impairment (MCI) has been recognized as one of the most useful clinical classifications, and it is one that can represent a therapeutic window for early treatment. This nosographic category defines those who are showing the cognitive depletion which is the manifestation of an intermediate stage between healthy aging with slight cognitive changes and dementia, but able to perform the activities of the daily living, and be essentially autonomous (Petersen et al., 2009). For these reasons, in the last decade, a notable amount of research has committed to the identification of signs and symptoms that could be used as reliable predictive markers of the disease. The MCI early identification, and afterward, dementia identification, would allow the implementation of non-pharmacological interventions that may change the natural history of the disorder, slowing down its development (Petersen et al., 2014).

1.1. Traditional Intervention on MCI

Cognitive training (CT) is the most widespread and effective type of cognitive stimulation, among those commonly used in MCI treatment. Particularly, CT protocols take into account bottom-up, and modular tasks aimed at the stimulation of selective cognitive functions, such as memory, language, or, for example, attention (Belleville et al., 2016). Due to their flexibility, CTs are reported as one of the most appropriated technique in the field of MCI. In fact, thanks to their adaptability CTs are particularly recommended with such variegate condition as MCI. On the other hand, more modern stimulation protocols refer to a more complex and holistic model of health that considers physical, emotional, and cognitive aspects. That is due to the high prevalence of Behavioral and Psychological Symptoms of Dementia, namely: agitation, aberrant motor behavior, anxiety, depression, irritability, and apathy, in subjects with dementia (90%) and even in subject with MCI (35–80%) (Monastero et al., 2009; Cerejeira et al., 2012). Particularly, in these cases, apart from the use of CT, are generally adopted, among the others, the music therapy, the multi-sensory behavioral therapy, and the occupational activities (de Oliveira et al., 2015; Massimo et al., 2018). Recently, the relationship between physical practice and other health spheres has become a popular topic. It was demonstrated, indeed, that exercise has a positive influence on hippocampal functions. This effect might facilitate the regulation of long-range cortical networks with a good effect on memory and executive functions (Voss et al., 2010; Chirles et al., 2017). On the other hand, a recent research branch is interested in characterizing the effect of cognitive health on physical activity. It seems that preserved cognitive abilities could allow MCI subjects to perform physical tasks better (Montero-Odasso et al., 2012). According to advanced guidelines, non-pharmacological treatment should possess certain characteristics: they should be performed with high frequency and high intensity; they should provide for a combination of cognitive stimulation and physical exercise; the training should be customized according to the bio-psycho-social characteristics of each participant; and the protocols should be designed in a more ecological fashion and be more generalizable (Belleville et al., 2016).

1.2. The Role of ICT With MCI Subjects

In this framework, information and communication technologies (ICT) are accumulating much interest, particularly concerning the applications of these devices in the neuropsychological field. ICTs have been used as assessment tools (Charchat-Fichman et al., 2014; García-Casal et al., 2017) and also as instruments for cognitive intervention (Charchat-Fichman et al., 2014; Ballesteros et al., 2015; García-Betances et al., 2017), enhancing, or, at least, maintaining AD patients' cognitive skills. Although ICTs are more related to patients with a severe grade of impairment, they are now playing an important role as assistive technologies and are serving to promote the independence and the autonomy of individuals with MCI as well as healthy elderly people (Eghdam et al., 2012; Teipel et al., 2016). In light of the information presented in the previous paragraph, technology should play a crucial role in assessment, treatment, and monitoring of MCI patients, allowing the combination of cognitive and physical treatments and melding of the stimulation protocols with subjects' daily activities (Maselli et al., 2018; Fiorini et al., 2019). Moreover, these technologies should be able to aid in gathering data about the changes in the subjects' autonomy and in their physical and cognitive abilities, and give feedback to patients themselves and to the stakeholders (Rebok et al., 2007; Belleville et al., 2016). There remains a paucity of technological interventions for caregivers who are living with people with dementia (Zhang et al., 2016). In this perspective,

the need to develop technologies that can be used in the patient's home, without the physical presence of the therapist, is crucial. Moreover, these technologies should be embedded in the user daily life and generate a coupled system with the user him/herself, so to produce an enriched environment (Turchetti et al., 2011).

Although this field is rapidly increasing, ICT applications are generally related to dementia. This study aims to review the literature concerning the use of ICT for assessment, cognitive intervention, and assistance of people who are suffering from MCI, provide a comprehensive view of the current state of the art, and highlight current limitations and future perspectives.

2. METHODS

2.1. Search Strategy

An electronic database search was performed for the period from November 2017 until December 2017 using the U.S. National Library of Medicine (PubMed®), Web of Science (ISI®), and Scopus® databases to identify and select articles concerning the clinical applications of ICTs in the neuropsychological field of MCI. Specifically, the search queries included the following terms: [(Information and Communication Technology OR ICT) OR (Internet of Things) OR (Assistive Technology) OR (Cognitive Support Technology OR CST) OR (Robot)] combined with terms to determine outcomes of interest: (Mild Cognitive Impairment OR MCI) AND [(Cognitive Stimulation) OR (Neuropsychological Assessment)].

The terms research was performed regarding titles and/or abstracts. Only original, full-text articles published in English, which addressed the clinical applications of ICTs on MCI, were included in this review. The reference lists of included papers were examined to identify relevant studies which the electronic search might have missed. Duplicated documents were eliminated; thereafter, the abstracts of the papers, retrieved by the electronic search, were examined to identify which deserved a full evaluation. Finally, similar studies published by the same authors were compared to select the most suitable for our purpose. Obtained in the research were 226 references from PubMedCentral®, 285 references from Web of Science®, and 135 references from Scopus®.

During the process, the identified papers were screened and evaluated from three independent reviewers (i.e., the authors). Meetings and discussions were held to resolve disagreements and find solutions.

2.2. Selection Criteria

First, duplicated references were excluded. Then, during the screening procedure, items were excluded if they (i) were an abstract, a short communication, a review article, or a chapter from a book; (ii) were not written in the English language; (iii) were from years prior to 2009. One hundred and seventy-eight references were fully assessed during the evaluation procedure, and papers were excluded if (1) they did not use any type of ICTs; (2) they did not appear appropriate for this review after the reading of title and abstract; (3) they did not address the mild cognitive impairment issue; and (4) they were not full access. In addition, if multiple papers written by the same author had similar content, papers published in journals were selected instead of papers presented at conferences. Furthermore, if multiple papers written by the same author with similar content were presented at conferences, the most recent paper was selected. Finally, 56 papers were fully evaluated and are included in this review (**Figure 1**).

3. RESULTS

Fifty-six papers were selected according to the aforementioned methods and classified on the basis of three major clinical application areas: "Cognitive Assessment," "Treatment," "Assistance."

Among these applications, the majority of the papers (58%) concern the "Assistance" of subjects with MCI (see **Figure 2B**). In particular, these articles address the functional assessment, monitoring, and assistance during the daily activities of MCI subjects, in a prosthetic manner. Conversely, the studies labeled as "Treatment" refer to the specific and unspecific cognitive stimulation of MCI subjects, which results in a overall activation, according to Engel's bio-psycho-social model (Engel, 1978). In conclusion, the articles encompassed in the "Cognitive Assessment" category address the use of new technological solutions for the evaluation and the measurement of subjects cognitive performance. They represent, respectively, the 30.4% (Treatment) and the 11.6% (Cognitive Assessment) of the studies reviewed. Note that a certain percentage of the papers reviewed (18.9%) deal with multiple topics (i.e., assistance and evaluation or treatment and assistance) at the same time.

Regarding the technologies used in these works, most of the studies (54.1%) display a scenario in which service robots, both standalone and cloud networked, interact and support people with MCI. The second most represented technologies are sensors, both environmental and wearable, followed by personal devices, including personal computers, smartphones, tablets, and televisions (see **Figure 2C**). Regarding the sample size of these studies, an ample amount of the research (35.7%) does not include any subject with MCI, but rather healthy controls (HC), caregivers, experts, or no subject at all. This outcome and the general trend represented in **Figure 2D** can be explained by the theoretical nature of the majority of these studies, or, in a smaller portion, by the primary interest in the technical side. Nevertheless, the growing interest and the technical advances achieved seem to be able to reverse this trend, and lead the scientific community toward more practical implementations, although, nowadays, the clinical validation of the proposed solutions is still a matter of debate. Of the 56 fully evaluated papers, 14 (25%) were published in 2017, while 31 (55.4%) were published over the past 3 years. This result confirms the increasing interest for the ICTs application in subjects with MCI (see **Figure 2A**).

Analyzing the journals for the fields of interest of published articles, it can be observed that the leading research sector is the clinical field–17 articles were published in pure clinical journals, indeed. In contrast, only six articles were published in pure technological journals. It is worth mentioning that 4

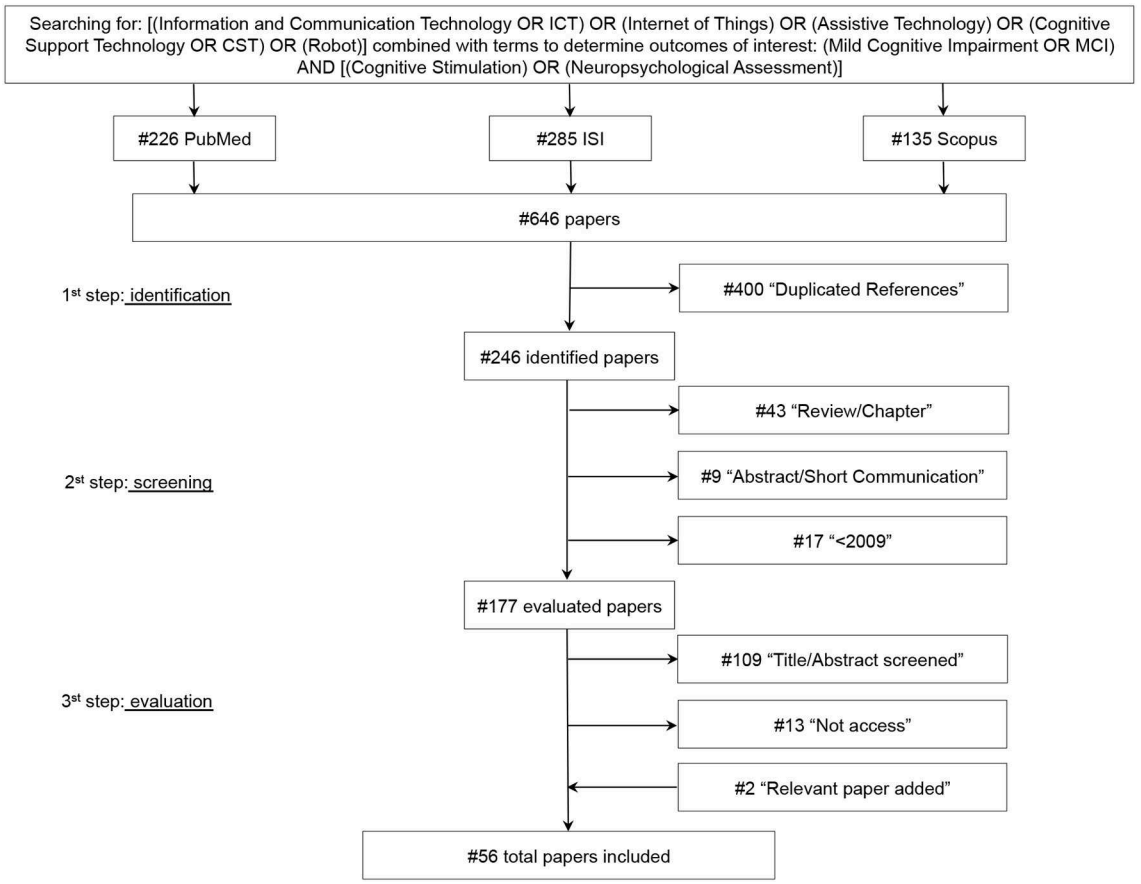


FIGURE 1 | Research methodology for review process.

papers were published in mixed clinical-technological journals. Regarding the clinical side, as summarized in **Figure 2A**, it can be seen that the leading topic is represented by "Medicine," particularly concerning general medicine and geriatrics and gerontology topics (see layer 3, **Figure 3**). The second most sizable category present is, by far, "Neuroscience." On the other hand, regarding technological journals, it can be seen that "Computer Science" is the technological leading area, followed by the engineering field, equally represented by biomedical and electronic, **Figure 4**. This analysis suggests a prominent interest coming from the clinician side, with a wider arrangement of objectives, models, and requirements. This interest seems to be not completely matched with the technical community. It could be explained by a high grade of complexity examined by the clinicians, compared with the level of technological advancement. Notwithstanding, the technological community is approaching the topic in a shorter time frame. The average of the publication year for technological journals, in fact, is about 2016. In contrast, the average is about 2014 for clinical journals as well as for mixed clinical-technological journals.

In addition, **Table 2** summarizes the data gathered from the reviewed papers. This table reports some facts, among which are the technology used in the different works, technology service and domain, subjects' clinical profiles, experimental design, and research goal. All 56 papers are illustrated in detail in **Table 2**. In addition, a brief summary of the data included in this paragraph is included in **Figure 2** and **Table 1**.

4. APPLICATION 1: COGNITIVE ASSESSMENT

The category "Assessment" represents the smallest group of papers among all the applications, with only 8 articles reviewed. This category gather articles that aim at the appraisal of cognitive state using both robotic platform, sensors, and personal devices. More specifically, the articles that consider robots are 2, Kintsakis et al. (2015) and Demetriadis et al. (2016); papers that regard sensors and personal devices (in this case PCs) are 6, equally distributed, Dougherty et al. (2010), Zuchella et al. (2014), Manera et al. (2017) use PC, while (König et al., 2015b; Fiorini et al., 2017; Maselli et al., 2017) study the use of sensors.

Below are described the purposes that have pushed the works and the results obtained. A summary of the characteristics of these studies is included in **Table 2**.

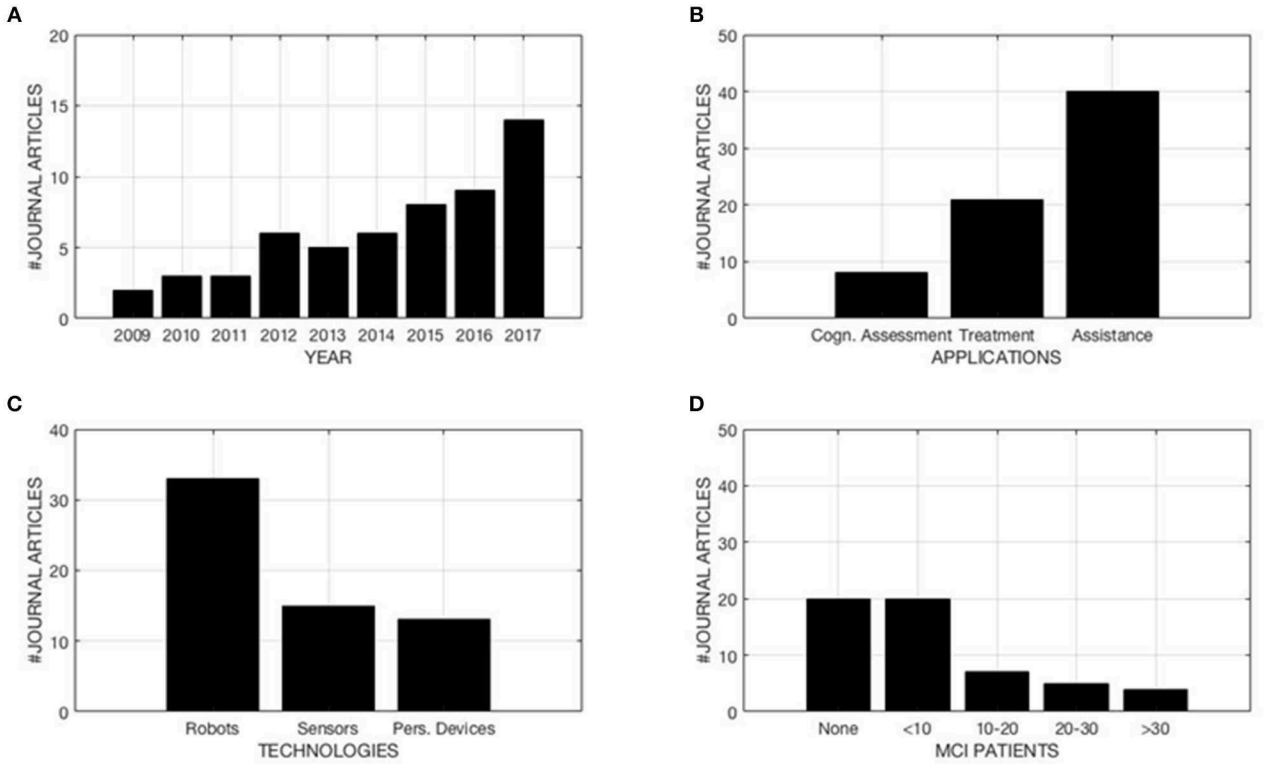


FIGURE 2 | (A) Publication trend per year. **(B)** Paper distribution per service. **(C)** Paper distribution per technologies used; Robot (both stand alone and cloud robots), Sensors (both environmental and wearable), Personal Devices (Personal Computer, Smart phones, and TV). **(D)** MCI patients involved in the studies.

4.1. PC Based Cognitive Assessment

One of the first contributions to the use of PC-based tests for MCI cognitive assessment is the work of Dougherty et al. The authors calculated correlations between subjects' performance in traditional cognitive tests (MMSE and Mini-Cong) and a new PC-based neuropsychological battery called CST. The study results indicate that the CST is a valid and sensitive instrument for evaluating cognitive deficits; in fact, its accuracy in distinguishing between controls and MCI subjects achieved 96%, while the Mini-Mental Status Examination (MMSE) accurately classified 71% and the Mini-Cog 69%. The authors state that PC-based cognitive screening tools may aid in MCI early detection in the primary care setting, and, moreover, due to their ease of use and interpretation, may provide an accurate baseline from which to monitor cognitive changes over time (Dougherty et al., 2010).

Another article about computer-based assessment for people with MCI is the work by Zucchella et al. In this paper, the development and the usability test of a 3D Serious Game (SG), using a virtual environment-based platform for the early identification and characterization of MCI, is described. This SG can record various parameters related to the subjects' cognitive status, including number of correct actions, number of errors, number of false recognitions, number of omissions, and time needed to complete the task. Although the authors claim that SGs could be used in the health domain, in particular in the assessment and rehabilitation of psychiatric and neuropsychological conditions, this usability test underlines problems related to the high complexity of some tasks. For this reason, especially with older people who have limited familiarity with technologies, will need some assistance in the beginning phase. Notwithstanding, SGs have the potential to be new and effective tools in the management and treatment of cognitive impairments (Zuchella et al., 2014).

According to Zucchella et al., a recent work by Manera et al. proposes recommendations for the use of SGs with patients with MCI. Results obtained report that SGs were rated between very adapted and completely adapted for people with MCI. Moreover, SGs are considered as more adapted to people with initial cognitive decline than to people who are already losing autonomy in the activities of daily living. Concerning the use of SGs, participants reported that they found them to range between very adapted and completely adapted for cognitive assessment, as well as to train for physical and cognitive functions, improve well-being, and teach contents. Moreover, concerning the possibility to improve autonomy and social exchanges, they were considered between adapted and very adapted. Importantly, in this paper, the authors stress that the target of SGs, their frequency of use, and the context in which they are played depend on the typology of the SGs (e.g., Exergame, cognitive game), and should be personalized with the help of a clinician (Manera et al., 2017).

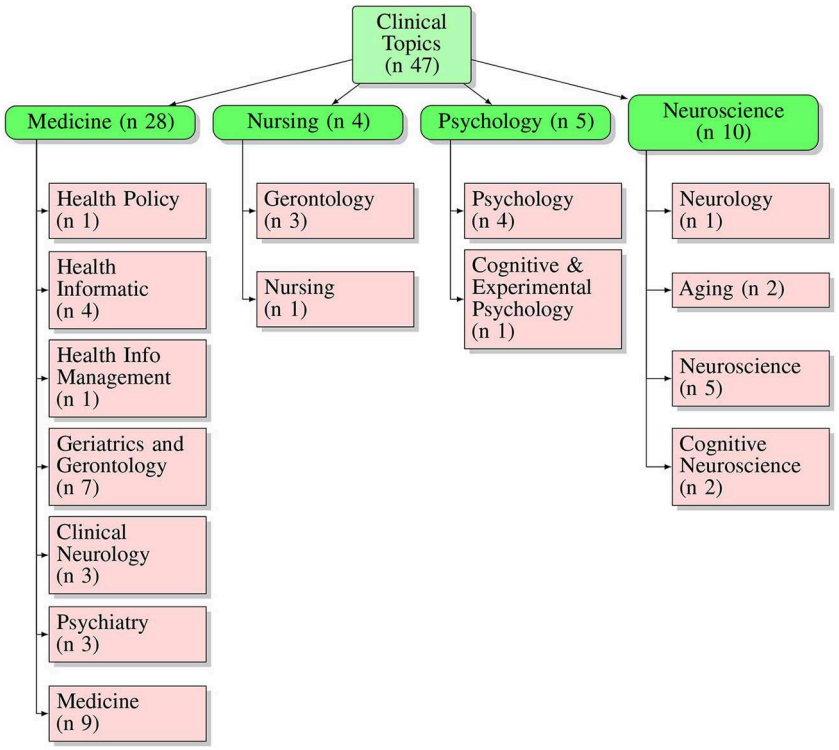


FIGURE 3 | Graphical description of topics touched by articles published in clinical journals. Layer 1, number of general clinical topics; layer 2, main topic categories; layer 3, subcategories of topics.

4.2. Sensors Based Cognitive Assessment

Different types of sensors have been used for MCI cognitive assessment. One example is the work by König et al., in which the authors aim to identify vocal markers correlated to subjects' cognitive status. The classifier developed by the authors showed an accuracy of 79% in discerning between HCs and people with MCI, of 87% in discerning between HCs and people with AD, and of 80% in discerning between people with MCI and people with AD, demonstrating its assessment utility (König et al., 2015b).

Another work was presented by Fiorini et al. The authors designed, and developed, a new tool called SmartWalk System, which aims to assess the sustained auditory attention while the subject walks and simultaneously stimulate the sustained attention domain. The authors compared a traditional test for auditory sustained attention with their SmartWalk system, and the results suggest a good correlation between the two approaches. The results, in fact, show a high significant ($p < 0.05$) correlation for the "correct" and "omitted" scores of the two protocols ($r = 0.73$ and $r = 0.59$, respectively). Also, the "mean" and the "median" response times are significant correlated ($r = 0.59$ and $r = 0.70$, respectively). The authors state that a future research should be focused to increase the number of participants to corroborate the study. Furthermore, a usability study should be planned to estimate whether the SmartWalk system could be used in a daily cognitive training at users' homes (Fiorini et al., 2017).

Similarly, Maselli et al. evaluated the sensitivity of their SmartTapestry System to assess the episodic verbal memory.

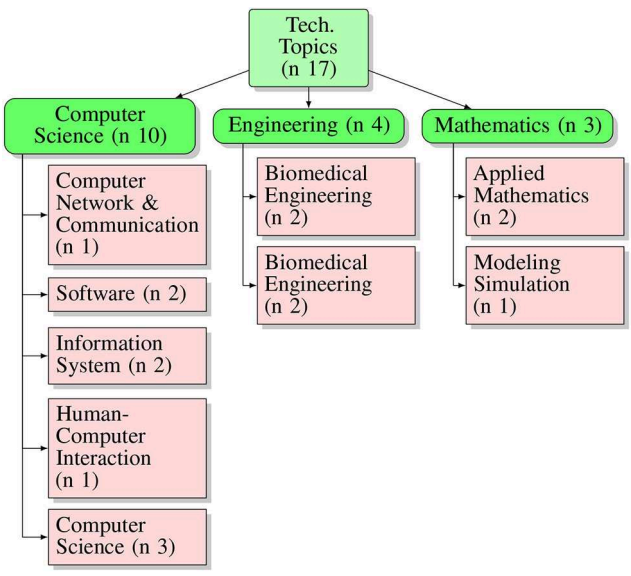


FIGURE 4 | Graphical description of topic touched by articles published in technological journals. Layer 1, number of general technological topics; layer 2, main topics categories; layer 3, subcategories of topics.

The results reported by the authors suggest a good correlation between the two approaches. Such findings indicated that the new system was substantially equivalent to the traditional test

for the assessment of episodic memory. Furthermore, the results showed a better performance in the consolidation-retrieval process when assessed using SmartTapestry rather than the traditional test. These results suggest that a facilitation in the memory performance may be due to the multiple nature of the mnemonic trace; in fact, the SmartTapestry task involves auditory (the auditory track repeating the list of words), visual-spatial (the position of the letters in the tapestry), and kinesthetic information (the movements of the arms needed to press the letters in the tapestry) that may help the consolidation-retrieval process (Maselli et al., 2017).

4.3. Robot Based Cognitive Assessment

Concerning the use of robots in MCI cognitive assessment, it may seem that the development of a robotic assistant, able to assess patients autonomously, would be just a prospect for the future. Nevertheless, Kintsakis et al. proposed the design of a cloud-based NAO robot that aims to engage subjects suffering from MCI during the cognitive test administration. The authors state that use of the robot would increase the compliance and arouse the interest of the subjects during the administration of tests to work memory, arithmetic skills, reasoning, recall, and awareness. Notwithstanding, in this paper, the robotic platform only was presented; the system, in fact, has not yet been evaluated in a real-world scenario (Kintsakis et al., 2015).

4.4. Recommendations and Trends

The research for technological solutions able to address the cognitive assessment of subjects with MCI is a fast-growing niche, as demonstrated by the high number of papers (62.5%) in the field that have been published in the past two years. Although the number of articles encompassed in this section does not permit drawing of precise trends, it is possible to observe that some tendencies are emerging in the three different groups of papers. For example, among the articles that examined PC-based technology, it can be seen that the last articles focused their attention more on SGs and virtual reality (VR) than on self-administered batteries of tests, perhaps because they assessed the subjects' performances in a more ecological way (Zuchella et al., 2014; Manera et al., 2017). In a similar way, the use of sensors aims at the detection of parameters that can provide the clinicians with more direct information about subjects' cognitive status, using these parameters as a window on brain activity and functioning. Through the use of a smart environment, it could be possible to detect information about the patients while they perform their activities of daily living (König et al., 2015b; Fiorini et al., 2017; Maselli et al., 2017). In contrast, the introduction of a robotic therapist, able to conduct a cognitive assessment autonomously, which can increase subjects' compliance and arouse their interest, compared to PC-based technology, has, until now, seemed only to be a future prospect and a target to hit (Kintsakis et al., 2015).

5. APPLICATION 2: TREATMENT

This category, with 21 articles, is the second most sizable category in this review. Robots represent the technology used most heavily for MCI treatment, with 13 out of 21 articles (Tapus et al., 2009; Chan and Nejat, 2010; Wu et al., 2011, 2013, 2016; Tiberio et al., 2012; Granata et al., 2013; Yamaguchi et al., 2014; Kintsakis et al., 2015; Demetriadis et al., 2016; Reppou et al., 2016; Garcia-Sanjuan et al., 2017; Korchut et al., 2017). On the other hand, papers that consider personal devices and smart environment-based treatment make up 8 out 21: (Zaccarelli et al., 2013; Zuchella et al., 2014; Muscio et al., 2015; Segkouli et al., 2015; Fiorini et al., 2017; Kyriazakos et al., 2017; Manera et al., 2017; Maselli et al., 2017).The articles, organized on the basis of different types of technologies, are presented in the following sections.

TABLE 1 | Numbers of paper regarding different technologies and their scopes.

	Cognitive assessment	Treatment	Assistance	Total
Robots	2	13	26	41
Sensors	3	2	11	16
Personal Devices	3	7	9	19
Total	8	22	46	76

5.1. Robot Based Treatment

Although robots represent the most commonly used technology in MCI non-pharmacological treatment, generally the purpose of this technology is mixed. Only 5 papers, in fact, address selectively this topic, the others (8 papers) concern also the assistance (6 out 8 papers) and the assessment (2 out 8 papers) of MCI subjects.

The first work related to the use of robots and cognitive stimulation is an interesting paper by Tapus et al., which aims to assess differences in preferences between the use of a robot therapist, instead of an avatar therapist. Basically, with this study they tried to quantify the "embodiment effect" related to the submission of cognitive games through a robot therapist, involving subjects in an 8 month-long stimulation trial. The authors state that the service robot was able to improve or maintain the cognitive attention of the patients with dementia and/or cognitive impairments through its encouragements in a specific music-based cognitive game. Moreover, the robot's ability to adapt maximized the positive effect of the intervention (Tapus et al., 2009).

Chan and Nejat, similarly, proposed a work that aimed at the possibility to develop a robotic therapist that could stimulate and encourage MCI subjects during memory stimulation games. The authors reported a success rate in identifying and recognizing memory game cards between 96%. Moreover, the robot was successful at selecting and executing appropriate emotion-based behaviors throughout the interactions with the participants. Success rate in providing correct behavioral feedback was about 74%. Concerning the participants feedback, 83% of them stated that the robot helped them stay engaged and interested in the memory game (Chan and Nejat, 2010).

As mentioned, emotion recognition and, more generally, the effective channel could provide the robot with useful information

TABLE 2 | Papers about evaluation.

Reference	Technology	Tech. domains	Tech. services	Research method	Subjects	Research goal
Agrigoroaie and Tapus (2016)	Generic Robot	Assistance	Autonomy	Proof of Concept	None	Present preliminary results from a focus group
Agrigoroaie and Tapus (2017)	Meka M1 Robot Kompaï Robot	Assistance	Emotion	Experimental trial in a HRI scenario	9 HC	Propose a method for extracting and analyzing physiological data
Batista et al. (2015)	Smarphone	Assistance	Social Sphere	Pilot Test in real life	16 MCI	Describe the architecture of the SIMPATIC system as well as its functionality
Bellotto et al. (2017)	Kompaï Robot	Assistance	Autonomy	Lab set test	1 HC	Describe a distributed architecture for AAL services; probabilistic solution for objects localization based on RFID; vision-based approach for estimating the level of activity of a person; entropy-based system for detecting anomalous motion patterns
Broughton et al. (2016)	ENRICHME robot (Kompaï platform)	Assistance	Autonomy	Lab set test	None	Provide the implementation of an library application to detect RFID tags for performing object localization with a mobile robot
Bruno et al. (2013)	Customized Robot Prototype	Assistance	Autonomy Social Sphere Global Cognition	Proof of Concept	None	Define principles and requirements for a wearable SAR aimed at assisting MCI subjects in the execution of everyday activities
Chan and Nejat (2010)	SAR Brian 2.0	Treatment	Memory (LTM; STM) Social Sphere	Proof of Concept laboratory experiments	6 HC	Develop new therapeutic protocols to manage individuals suffering from cognitive impairment by stimulating social and cognitive functioning with a SAR
Darragh et al. (2017)	Generic SAR	Assistance	Autonomy	Questionnaire	7 MCI 2 MD (mild dementia) 8 Caregivers 16 Experts	Gather information about how a robot in the home could assist MCI subjects
Demetriadis et al. (2016)	PROTEAS Tangible Interface for Lego NXT Robot	Cognitive Assessment Treatment	Memory Language Attention Emotion	Test/re-test experiment	25 MCI	Study the usability of a tangible programming interface as a tool for cognitive assessment and evaluate the impact of this type of cognitive training on the patient condition
Diaz-Orueta et al. (2014)	TV Avatar	Assistance	Autonomy Social Sphere	Experimental traial	10 MCI 10 AD	Evaluate what cognitive functions may be involved in the correct interaction with the avatar

(Continued)

TABLE 2 | Continued

Reference	Technology	Tech. domains	Tech. services	Research method	Subjects	Research goal
Dougherty et al. (2010)	PC-based test battery	Cognitive Assessment	Working Memory Visual spatial Executive processing Verbal Fluency Attention Orientation Processing Speed	Experimental trial	27 MCI 84 AD 104 HC	Compare the accuracy in screening between healthy and cognitive impaired subjects between CST and paper and pencil test
Fiorini et al. (2017)	Inertial Sensor	Cognitive Assessment Treatment	Auditory Sustained Attention	Feasibility Study	4 MCI 11 HC	Present a sensorized approach which combines aerobic exercise and traditional cognitive tools for daily training
Foukarakis et al. (2017)	RAMCIP Robot V1	Assistance	Autonomy	Pilot Study	8 MCI 10 HC	Describe the UI framework, its application in RAMCIP and the initial experiences regarding the use of the framework gathered from the preliminary pilot trials of the project with actual patients
Garcia-Sanjuan et al. (2017)	Customized Tangible-Mediated Robot	Treatment	Working Memory Prespective Memory Episodic Memory Attention Executive Functions	Usability study	12 MCI 12 PWD 16 HC	Present a customized tangible-mediated robot enabling more intuitive and appealing interactions for MCI
Granata et al. (2010)	Robot Kompaï	Assistance	Autonomy	Usability test	5 MCI 6 HC	Study the concomitant use of voice and graphical support to increase the usability of a SAR for MCI support
Granata et al. (2013)	Robot Kompaï	Assistance Treatment	Autonomy	Usability test	11 MCI 11 HC	Present the results from usability testing of grocery shopping list services and an agenda application provided by a SAR for MCI subjects
Gross et al. (2011)	Customized Robot Prototype	Assistance	Autonomy Social Sphere	Proof of Concept	None	
Gross et al. (2012)	Customized Robot Prototype	Assistance	Autonomy Social Sphere	Usability Study Acceptance Study	4 MCI 4 CG	Describes the final implementation of the companion robot and presents results of functional user tests
Kintsakis et al. (2015)	NAO supported by a Cloud System	Cognitive Assessment Treatment	Memory Working Memory Reasoning Awareness	Proof of Concept	None	Present a novel system for performing personalized, robot assisted cognitive exercise and tracking the performance of patients

(Continued)

TABLE 2 | Continued

Reference	Technology	Tech. domains	Tech. services	Research method	Subjects	Research goal
König et al. (2015a)	RGBD cameras	Assistance	ADL	Lab based test	23 MCI 12 AD 14 HC	Investigate the use of video analyses assessment of IADL
König et al. (2015b)	Audio Technica AT2020 Condenser Microphone Sensors	Cognitive Assessment	Backward Counting Repeating Sentence Describing images Verbal Fluency Task	Experimental trial	23 MCI 26 AD 15HC	Determine the value of automatic analyses of voice recordings during vocal tasks for the early diagnosis of AD
Korchut et al. (2017)	Generic SAR	Assistance Treatment	Global Cognition ADL Emotion Social Sphere	Focus group Surveys	83 MCI 81 CG 100 Experts	Find MCI's needs and preferences toward SAR
Kyriazakos et al. (2017)	Tablet PC Smart-phone Kinect Fitbit Philips Hue Plugwise Pulse Oxi Meter Omron ThinkLabs	Assistance Treatment	Memory ADL	Exploratory study in home environment	48 MCI	Present an opens-source e-Health platform for MCI
Lazarou et al. (2016)	Jawbone UP24 Withings Aura Wireless Tags Plugwise Circles	Assistance	Memory Social Sphere Emotion	Case study	2 MCI 2 AD	Propose a system for continuous and objective remote monitoring of problematic daily living activity areas and design personalized interventions
Mainetti et al. (2016)	Smartphone BLE Beacon GPS Smart Plugs	Assistance	ADL	Proof of Concept	None	Describe the goal of City4Age project
Mainetti et al. (2017)	Accelerometers Gyroscopes Inertial Modules GPS Smartphone BLE Beacon, Smart Appliance (TV)	Assistance	ADL	Proof of Concept	None	Describe the goal of City4Age project
Manera et al. (2017)	Serious Game Virtual Reality	Cognitive Assessment Treatment	Global Cognition	Web-Surveys Workshop	23 Experts	Present recommendations for the use of SGs in assessment and stimulation of MCI subjects

(Continued)

TABLE 2 | Continued

Reference	Technology	Tech. domains	Tech. services	Research method	Subjects	Research goal
Martínez et al. (2011)	Reed Switch Pressure Sensors Power Plug Sensor Temperature Sensor Smoke Sensor Phone Sensors	Assistance	ADL	Questionnaires Focus group	13 CG 10 Experts	Define MCI behavioral markers
Maselli et al. (2017)	Smart Tissue	Cognitive Assessment Treatment	Episodic Verbal Memory	Feasibility Study	4 MCI 11 HC	Understand system technical viability and its level of sensitivity in measuring memory
Meiland et al. (2014)	Movement Sensors Cameras	Assistance	Memory Social Sphere	Workshops Interviews Expert Consultation	3 MCI 11 PWD 26 CG	Summarize the end users' needs and wishes regarding the development and design of the Rosetta system
Mighali et al. (2017)	Wearable devices Smartphone BLE devices MPU-92509 9-axis MotionTracking device Digital Motion Processor (DMP) ARM Cortex M3 Microcontroller	Assistance	ADL	Lab based test	10 HC	Define a reliable system for controlling the position and the body motility of the elderly in unobtrusive, low-cost and low-power way
Mitseva et al. (2009)	Domestic Sensors Mobile Computer Personal Digital Assistants	Assistance	Autonomy	Proof of concept	None	Describe the initial phases of initiative of offering an intelligent and personalized system for independent living and self-care of seniors with MCI or mild dementia
Muscio et al. (2015)	Serious Game	Treatment	Global Cognition	Proof of concept	None	Define harmonized SGs parameters, and to propose the implementation of biomarkers as enrichment strategy and outcome measures in SGs trial design for MCI
Nakahara et al. (2016)	Customized Robot Prototype	Assistance	ADL	Preliminary study	3HC	Propose a method for logging micro-motion of daily activity based on the skeleton recognition
Nishiura et al. (2014)	PaPeRo Robot	Assistance	Autonomy	Report Case	1 MCI	Reveal how the robot should talk to an older woman with dementia to convince her to perform daily activities
Pahl and Varadarajan (2015)	SCITOS G5 Robot	Assistance	Social Sphere	Proof of Concept	None	Study the use of acoustic sensors utilized for detecting affective haptic inputs
Pino et al. (2012)	Kompaï equipped with a tablet PC	Assistance	ADL	Usability test	11 MCI 11 HC	GUI test

(Continued)

TABLE 2 | Continued

Reference	Technology	Tech. domains	Tech. services	Research method	Subjects	Research goal
Pino et al. (2015)	RobuLAB10 equipped with a tablet PC	Assistance	ADL Social Sphere	Questionnaire Focus Groups	10 MCI 8 HC 7CG	Investigate SAR acceptance
Reppou et al. (2016)	NAO supported by a smart environment	Assistance Treatment	Attention Memory Awareness Social Sphere	Focus Groups Interviews	6 HC 10 Experts	Describe an architecture system
Sacco et al. (2012)	Cameras	Assistance	ADL	Observational study	19 MCI 16 AD 29 HC	Propose DAS score that detects functional impairment using ICTs in AD and MCI compared with healthy subjects
Schroeter et al. (2013)	SCITOS G3 Robot	Assistance	Autonomy	Interview Questionnaire Observation Robots testing	2 MCI 4 PWD 5 CG	Analyze the added value of a mobile robot companion in a smart home environment, and to evaluate users experience, proving that the robot can act autonomously to provide useful and enjoyable services
Seelye et al. (2012)	VGo Robot System	Assistance	Autonomy Social Sphere	Pilot Study	1 MCI 7 HC	Test the feasibility of use and acceptance of the VGo Robot system
Segkouli et al. (2015)	PC Smart-phone PDA Tablet	Treatment	Memory Attention Judgment Communication Ability	Simulation trial	10 MCI 26 HC	Introduce novel virtual user models with enhanced predictive validity in mental processes that will be utilized for accurate simulation results in interface design
Stavropoulos et al. (2017)	RGB-D Cameras	Assistance	Autonomy	Preliminary study	15 HC	Propose a novel computer vision-based automatic action recognition to increase robustness in realistic assistive robot applications
Tapus et al. (2009)	Custom-designed humanoid torso mounted on a ActivMedia Pioneer 2DX	Treatment	Attention	Pilot Study	2 MCI 7 AD	Develop methods toward SAR therapist for individuals suffering from cognitive impairments through the use of music-based cognitive games
Tiberio et al. (2012)	Giraff Robot	Treatment	Memory Language Emotion	Wizard of Oz experiment	8 MCI 9 HC	Describes a study related to the use of such robots in the interaction with elderly people affected by MCI
Tsardoulias et al. (2017)	NAO robot	Assistance	Attention Memory Autonomy	Focus Group	8 MCI	Propose a novel integrated robotics architecture targeting the needs of individual with MCI at risk for social exclusion

(Continued)

TABLE 2 | Continued

Reference	Technology	Tech. domains	Tech. services	Research method	Subjects	Research goal
Vasileiadis et al. (2016)	PIR Sensors, RGB-D cameras	Assistance	ADL	Pilot Study	4 MCI	Evaluate a proposed infrastructure for investigating activity monitoring needs
Wu et al. (2011)	Generic SAR	Assistance Treatment	Memory ADL	Interview Questionnaire	30 MCI	Find MCI's needs and preferences toward SAR
Wu et al. (2012)	Generic SAR	Assistance	Autonomy Social Sphere	Focus group	7 MCI 8 HC	Give recommendations about the design of the robot appearance.
Wu et al. (2013)	Nabaztag Robot PC Virtual Agent	Assistance Treatment	Global Cognition Autonomy Social Sphere	Mixed-method: qualitative and experimental	15 MCI 43 HC	Examine the perception of the robot's expression and the role of agent embodiment
Wu et al. (2014)	Kompai Robot	Assistance	Autonomy Social Sphere	Acceptance study	6 MCI 5 HC	Investigate acceptance of a SAR and the effect of direct experience with it over a 1-month period on its acceptance
Wu et al. (2016)	Kompai Robot	Assistance Treatment	Global Cognition Autonomy Social Sphere	Acceptance Usability study	20 MCI	Explore perceived difficulties and needs of older adults with mild cognitive impairment (MCI) and their attitudes toward a SAR to develop appropriate robot functionality
Yamaguchi et al. (2014)	Bono-01 Robot	Treatment	Social Sphere	Experimental trial	10 HC	Propose a robot that warms up group conversations in which have been used conversation technique called "coimagination", for preventing mild cognitive impairments
Zaccarelli et al. (2013)	SOCIABLE computer battery	Treatment	Reasoning Memory Praxis Executive Functions Attention Social sphere	Efficacy study	106 MCI 118 AD 124 HC	Evaluate the effects of SOCIABLE on the cognition and social sphere, and the affection and the functional abilities of cognitively intact elderly, patients with MCI and patients with mild AD
Zuchella et al. (2014)	Serious Game Virtual Reality	Cognitive Assessment Treatment	Working Memory Prospective Memory LTM Spatial Orientation Selective Attention Executive Functions	Usability test	50 HC	Describe the process used to create the Smart Aging platform for the early identification and characterization of MCI

for it to model its behavior. A work proposed by Tiberio et al. describes the assessment of tolerance indicators, heath rate (HR), and hearth rate variability (HRV) in subjects who were collaborating with a robot therapist during a cognitive stimulation task. The authors did not find differences between sympathetic activation during the tasks conducted by human or robot. These results emphasize the sample tendency to tolerate the presence of the robot (Tiberio et al., 2012).

Similarly, Yamaguchi et al. presented a robot designed to warm up group conversations of older adults by a cognitive stimulation technique called the "coimagination" method, which is used to prevent the development of MCI and dementia. The authors state that the robot successfully elicited more laughter, which is seen as an enjoyment parameter, than did the human participants (Yamaguchi et al., 2014).

Among the articles about robotic therapists, two, more recent papers, propose an alternative way to administer cognitive stimulation through the robots. Demetriadis et al. and Garcia-Sanjuan et al., in fact, presented two works in which the robot is not an agent that leads people in the cognitive stimulation task performance, but, instead, the robot is the tool for the cognitive stimulation process. In the first case, in fact, the stimulation protocol provides for the use of a programmable tangible interface. So, the stimulation program is made possible through the use of the robot and not the robot assistance (Demetriadis et al., 2016).

In the second example, instead, each participant was involved in the therapeutic use of the robot. Particularly, each participant was asked to perform three different tasks using a tangible-mediated robot: control the orientation of the robot, move the Tangibot from one location to another, and perform a combination of the first two (Garcia-Sanjuan et al., 2017). Contrary to the use of therapeutic robots, the use of a tangible robotic interface is recommended more for people with no or mild cognitive impairments. It seems to be too demanding for those with severe cognitive impairments, but up to now this research field has remained mostly unexplored.

5.2. Personal Devices and Smart Environment-Based Treatment

Papers regarding the use of personal devices and smart environment for cognitive non-pharmacological treatment are numerically less represented compared with robotic articles. Despite this, their level of development is, in most cases, higher and better defined compared to the idea of robot therapists or a *fortiori* the use of robots as assistance in the activities of daily iliving.

The first article, here reviewed, about a computer-based cognitive battery, is the work conducted by Zaccarelli et al. In this paper, the authors aim to evaluate the impact of the three-month-long SOCIABLE program on the different cognitive skills. The analysis conducted at the end of the program revealed that MCI patients experienced a positive effect in terms of global cognition, memory, and executive functions. A follow-up examination was conducted to establish the duration of the aftereffects. Examination of follow-up results revealed that healthy elderly individuals showed an increase in memory and language abilities after the use of the program. However, subjects' moods showed an opposite trend and became worse after training, probably due to the increase of self consciousness related to the improvement of cognitive functioning. In conclusion, the authors state that SOCIABLE is an effective intervention suitable for patients suffering from MCI and mild AD (Zaccarelli et al., 2013).

On the other hand, Muscio et al. addressed the topic of SGs for cognitive and social stimulation of MCI subjects. The authors claim that, due to the popularity of video games among the baby-boomers, and a *fortiori* among millennials, video games could be easily turned into enjoyable intervention for cognitive stimulation. In their opinion paper, the authors highlighted the importance of defining harmonized SG parameters and proposed the implementation of bio-markers as enrichment strategy and outcome measures in SG trial design (Muscio et al., 2015).

Another work concerning the use of PC-based technologies is the study by Segkouli et al. The authors developed and tested, a virtual user model (VUM) that simulated the performance of a subject with MCI performing a cognitive task. The purpose of the VUM was to identify and deal with common interface accessibility issues that might occur when people with MCI use PC-based tools for cognitive stimulation. The authors proposed a four-step trial. During the first phase, MCIs and controls were assessed using standard neuropsychological tests and a computer-based battery. Then, during the second phase, the VUM proposed was trained using real users' performances. In the third phase, the authors optimized the VUM and the virtual user interface (VUI). In the last phase, the authors assessed again differences between real and virtual MCIs using the optimized VUI. The authors' new system was able to deal with over 90% of all common interface accessibility issues (Segkouli et al., 2015).

The last, and perhaps, more complete work about the MCI cognitive stimulation, through the use of personal devices, is the research conducted by Kyriazakos et al., also mentioned in section 6. The authors presented the e-Health platform for MCI, in which several personal devices and both environmental and wearable sensors are connected together, via a cloud environment. Among their applications, the e-Health system provides for cognitive games, among which are memory games and tests, attention games, and games using executive functions. This system aims at the preservation of cognitive functions in healthy subjects and especially in MCI subjects. Beyond the good effect on cognition, this type of intervention should help MCI subjects to maintain a good quality of life. This research is still in the design phase, and no results have been reported to date (Kyriazakos et al., 2017).

5.3. Recommendations and Trends

The literature about robots and cognitive stimulation is growing faster, and it is becoming recognized by the academic world. For example, about 66% of the papers presented during some conferences address the topic. In this context, it is possible to observe how the majority of the literature concerns the development of a robotic therapist (Tapus et al., 2009; Chan and Nejat, 2010; Tiberio et al., 2012; Yamaguchi et al., 2014). Meanwhile, a small niche of papers concerns the use of robots

as tools for cognitive stimulation, instead of as instruments that administer and assist the patients during tasks. A couple of articles reviewed here propose programming or steering a robot to use it for stimulation protocols (Demetriadis et al., 2016; Garcia-Sanjuan et al., 2017). Although the purpose, shared by all the articles in this section, is the stimulation, just the work by Tapus et al. provided for a long-lasting intervention. On the other hand, other articles concern a preliminary study about usability and acceptance. Notwithstanding this lack of experimental data, the literature reviewed here confirms that, generally, elderly people and subjects with MCI prefer robot therapists over virtual therapists. However, generally, they prefer the use of a PC instead of a robot. Despite this, research into the topic has not found differences in perceived stress between the use of PC or robot, neither from physiological signals nor questionnaires. Moreover, research has shown that for robot therapists, along with the ability to administer cognitive stimulation tasks, considering also the emotional and the social spheres is crucial. The positive aspects of using a robot therapist, in fact, is largely related to the embodiment effect, but also to the perception of interacting with a smart agent. For this reason, the ability to empathize with the user cannot be ignored.

However, concerning the use of personal devices and smart environments in cognitive stimulation, it can be observed that this field is less addressed with respect to robotic solutions. Nonetheless, as mentioned, their level of development is higher and better defined compared to that for robot therapists. This fact is also pointed out by the substantial presence of literature published in scientific journals. In fact, just one research effort was presented in a conference and is reported as a proceeding. Generally, the studies of such systems, most of which are PC-based battery, are quite sizable, such as in the case of Zaccarelli et al. (2013). In addition, the time span in which the experiments were conducted was more adequate. In fact, the trials, generally, were scheduled over several weeks. Among the different papers reviewed, as noted previously, the use of PC-based batteries for cognitive stimulation represent the central bulk of contributions. Particularly, different aspects of memory, attention and executive functions were addressed. Moreover, mood and self-awareness were also investigated. A significant aspect of these studies provided for the use of serious games and virtual reality environments to exploit the level of engagement and the ecology of the treatments.

6. APPLICATION 3: ASSISTANCE

The category "Assistance" represent the largest group of articles encompassed in this systematic literature review. This category comprises 40 papers, gathering research from 2010 to 2017, and also in this case the overwhelming majority of the study took into consideration robots as the technology used: 26 out 40 papers (Granata et al., 2010, 2013; Gross et al., 2011, 2012; Wu et al., 2011, 2012, 2013, 2014, 2016; Pino et al., 2012, 2015; Seelye et al., 2012; Bruno et al., 2013; Schroeter et al., 2013; Nishiura et al., 2014; Pahl and Varadarajan, 2015; Agrigoroaie and Tapus, 2016, 2017; Broughton et al., 2016; Nakahara et al., 2016; Reppou et al., 2016; Bellotto et al., 2017; Darragh et al., 2017; Foukarakis et al., 2017; Korchut et al., 2017; Tsardoulias et al., 2017). The remaining papers are shared between two types of technology: namely, personal devices and wearable sensors, making up 14 out 40 papers (Mitseva et al., 2009; Martínez et al., 2011; Sacco et al., 2012; Diaz-Orueta et al., 2014; Meiland et al., 2014; Batista et al., 2015; König et al., 2015a; Lazarou et al., 2016; Mainetti et al., 2016, 2017; Vasileiadis et al., 2016; Kyriazakos et al., 2017; Mighali et al., 2017; Stavropoulos et al., 2017).

The papers are summarized in the following sections.

6.1. Robot Based Assistance

The robotic application in the assistance of people with MCI represent the majority of the papers reviewed. As already stated, this is a complex research field because people with Alzheimer's disease require care throughout the day, in different environments, and for varied needs. For these reasons, a significant number of the articles about service robots for assistance are completely theoretical, such as a study by Gross et al., in which they tried to identify the most important functionality for a service robot (Gross et al., 2011), or the work by Agrigoroaie and Tapus, in which the authors suggest that providing further information such as personality attributes, cognitive disability level, emotional internal states, and subjects' preferences would be useful for the process of robot behavior modeling (Agrigoroaie and Tapus, 2016). In an article by Pahl and Varadarajan, the authors suggest the use of unconventional channels to convey meaningful information to the robot, such as haptic inputs for a socially/emotionally based interaction between human and robots (Pahl and Varadarajan, 2015). Concerning theoretical study, an atypical work is the research by Bruno et al., in which the authors proposed the design of a wearable context-aware robot able to share information with a person via speech recognition and production (Bruno et al., 2013).

Another sizable group of papers report that the results came from the clinical and technical experience after focus groups, or were gained through the use of questionnaires and interviews. The work of Wu et al. is an example of that. These authors studied MCI subject's preferences toward robot functionality (Wu et al., 2011) and appearance (Wu et al., 2012). Through their studies they extrapolated seminal insight concerning the embodiment effect, and the interaction aspects between human and robot. The authors state that a robot might offer opportunities for interaction among all members of the elder community, and allow the elders to experience the same power, control, and agency as others.

Similarly, Pino et al. confirmed that learning to perform basic actions using a graphical user interface (GUI) is possible for elderly individuals, either cognitively healthy or impaired (Pino et al., 2012), even though the interfaces should be customized on the basis of the subject's preference, cognitive status, and way of thinking, according to Granata et al. (2010) and (Granata et al., 2013) also investigated the assistive robot acceptance among different groups of older adults living in a community. They evaluated robot and user characteristics, potential applications, feelings about technology, ethical issues, and barriers and

facilitators for robot adoption. According to Wu et al. (2012), subjects with MCI preferred robots with animal-like designs instead of the machine-like robots that were preferred by HCs. This study showed that participants with MCI and caregivers had more positive perceptions of the usefulness of the robot than HCs. Furthermore, they recognized the potential of robots for supporting health and social care at home (Pino et al., 2015).

Differently, Schroeter et al. studied the acceptance of robots after participants lived in a smart home for two days, continuously. During this period, the subjects had the chance to interact with the robotia and perform activities such as video calls with short interviews, interviews on site, and also free robot usage. At the end of the trial, information was gathered via interviews and questionnaires. As observed also by Gross et al. (2012), at the beginning of several trial sessions, participants were a bit skeptic about the robot and had stereotypical ideas about robots. After being introduced to the robotic system, all of them expressed interest and appreciation and actually started to think about ways in which the robot could better meet their needs. Most of the users described the trials as an enjoyable experience. Moreover, results also showed that robots were perceived more as a pet (with personality) than as a passive device like a PC or TV, increasing subjects' acceptance (Schroeter et al., 2013).

Recently, Reppou et al. described a novel architectural design for robotic platforms and reported that older adults did not worry about robots and found them useful. Moreover, the authors stated that new technologies and service robots could assist older adults with cognitive impairment by informing them, ensuring their safety with hazard detection, and practicing their cognitive skills with games that stimulate attention and memory. According to Pino et al. (2015), robots should also show emotion and feelings. Reppou et al. (2016) also found that the ability to show emotions is a key feature for a successful robot.

These findings are consistent with more recent studies by Wu et al., who compared cognitive stimulation protocols conducted by computer-based tools in one case a virtual therapist in another case, and a robot in a third case. Although statistical analysis did not show a significant difference among the different methodologies, qualitative analysis revealed the participants' preference for the laptop PC, followed by the robot, and then the virtual agent. The authors stated that individuals with MCI preferred the laptop PC condition mainly because it provided less distracting interfaces compared with the task proposed by the other conditions. Furthermore, the robot was preferred to the virtual agent because of its physical presence, according to some studies (Tapus et al., 2009; Wu et al., 2013). In another study, Wu et al. invited people with MCI and HCs to their living lab to interact with a Kompaï robot once a week for 4 weeks. The study results suggest that both groups could learn and remember how to use the robot, but MCI participants might encounter more difficulties. Moreover, the subjects with MCI did not perceive the robot as useful. However, they found it easy to use, amusing, and unthreatening (Wu et al., 2014, 2016).

The most recent works about theoretical design of service robots define more precisely the users' needs and the robot's functionalities. They found that robots should be able to track physical and psychological well-being, and deliver therapeutic intervention, specifically for individuals with MCI. Two key recommendations for developing a robot for robotic daily assistance were identified. First, subjects with MCI need particular help with daily challenges related to memory issues, including confusion or uncertainty, and help filling the time. Second, the robot should monitor different health indices, such as cognitive skills, movement, and mood (Darragh et al., 2017). Today, researchers studying technological solutions for people with MCI take into account not only the assistance side, but also the chance to stimulate these subjects' cognitive repertoire. The idea behind the latest works is that people with MCI should be helped to communicate with friends and family, keeping themselves informed about regional and international news and weather conditions, but also practicing their cognitive skills with games that exercise attention and memory and supporting them in the rehabilitation process following, for example, a hip fracture (Tsardoulias et al., 2017). The social acceptance of robotic assistants was studied by Korchut et al., who saw robots as a novel tool to improve cognitive functions and prevent cognitive decline, and stressed that the socio-emotional interaction represents a key requirements to create sustainable relationships between elderly individuals and robots. This type of interaction will enhance the users' acceptance and encourage the adoption of the assistive robotic system. For this reason, the robots should be able to understand the psychological state of the user and then provide for positive impact (Korchut et al., 2017).

Even though researchers try to find more and more channels to exploit the communication between humans and robots (e.g., GUI, social/emotional-based communication, and so on), human communication is based on spoken language. The importance to address this topic properly is seminal, taking into account older people affected by cognitive impairment. An example is offered by the work of Nishura et al. The authors presented results from a report case study, in which a PaPeRo robot asked the participants to perform some daily activities, including taking medicines, measuring blood pressure, and cleaning up the room in three different ways for each task. Study results showed that the talking pattern changed the subjects' performances of daily activities (Nishiura et al., 2014). Another example is the study by Foukarakis et al. in which the authors reported that, regarding the robot speech synthesis system, the users had difficulties understanding some phrases. This could be attributed to the quality of the voice used, or maybe to the fact that some of the users had hearing impairments or were old enough to have lower than average hearing, but also the speaking rate setting of the voice could be higher than the optimal setting, considering the target user group (Foukarakis et al., 2017). Introducing new technologies to those who have MCI could be problematic under several aspects, both related with the subjects' cognitive condition, and with general old age issues. The authors found that people with MCI had more difficulty with technology than healthy older adults, and they were confused about the robot's purpose and function. For this reason, technology should be introduced to them as early as possible to give them time to become familiar with it, and to increase acceptance and long-term use (Seelye et al., 2012).

While the aforementioned group of papers comprises studies focusing on the subjects' attitudes toward the robots, another branch of research is more interested in the ability of the robot itself to understand and interact with the subjects, as well as with the environment. Nakahara et al., in fact, did not work on a robot's service, but on the robot's functionality. The authors believed that, to enable the robot to help subjects in their daily lives and to identify risky situations, the robot should be able to recognize humans' activities. The results showed that the developed system was able to recognize correctly the action performed with the following accuracy levels: eating 46%; drinking 59%, calling 26%, walking 89%, writing 25%, reading 40%, cleaning 42%, cooking 43%. This type of technology could be useful for the collection of micro-motion data, which can be used to monitor subjects, but also for the early detection of MCI (Nakahara et al., 2016). Another similar work is the paper by Agrigoroaie and Tapus, in which the authors presented an algorithm that should enable the robot to extract and analyze physiological parameters such as respiration rate, blinking rate, and temperature variation across different regions of the face, to monitor and evaluate the users' emotional states. Particularly, among all the signals analyzed, during this experiment, the authors affirmed that the thermal data represent the most precise indicator of the subject's internal state. In fact, an increased temperature in the periorbital region is related to the growth of anxiety level (Agrigoroaie and Tapus, 2017). Works by both Korchut et al. and Agrigoroaie and Tapus address an important topic: namely, the Human-Robot Interaction (HRI). In this field, as mentioned in previous works, it is becoming crucial to study several interaction channels, even the emotional channel, to ensure a natural interaction between the robot and the users (Agrigoroaie and Tapus, 2017; Korchut et al., 2017).

A last sub-field of research, which takes into account the use of a robotic platform for MCI assistance, addresses the topic of how a service robot should interact with the surroundings to exploit its capability to assist older adults with MCI. A couple of articles concerning this argument are reported below.

As reported by Darragh et al., subjects with MCI need help particularly with daily challenges related to memory issues. For this reason, Broughton et al. and Bellotto et al. focused their attention on how the assistive robot could help the user in practical problems, such as finding objects in the patient's house. At the moment, one of the main problems with robots is that they still have difficulty in perceiving and making sense of the world around them. For this reason, the authors proposed an RFID-based technology that can localize objects (Broughton et al., 2016; Bellotto et al., 2017).

6.2. Sensors and Personal Device-Based Assistance

This section encompasses articles concerning assistance through the use of new technological solutions. The independent living of older adults is one of the main challenges linked to the aging population, especially those living with MCI and the consequent frailty. This type of patient needs more support in everyday life and needs to be frequently monitored by formal and informal caregivers. The new ICT solutions, among which are sensors and personal devices, are providing a crucial step forward in the assessment and treatment of these subjects.

One of the first works about the assistance of MCI subjects is the study presented by Mitseva et al., in which the authors evaluated the initial phases of the development of an intelligent system for independent living and self-care of MCI subjects. The authors stated that the starting point is represented by the definition of users' needs, and the proposition of smart solutions for them. They contemplated a three-bundle environment in which users themselves, relatives, and caregivers are immersed together (Mitseva et al., 2009). Similarly, Mainetti et al. discussed the use of wearable and environmental sensors to monitor elderly people with MCI. In their first work, the authors described an unobtrusive system that enables clinicians and caregivers, to monitor the MCI subjects by tracking them during indoor and outdoor activities (Mainetti et al., 2016). In addition, after the authors compared their architecture system with others, they concluded that the key point of their system is its ability to automatically recognize behavioral changes in elderly people with an unobtrusive, low-cost, and low-power technique (Mainetti et al., 2017).

Following the Mitseva et al. instructions, Martinez et al. tried to define MCI needs to develop a smart assistance system. The authors opted for focus group work and *ad hoc* questionnaires to define typical symptoms and behaviors or people with MCI. According to focus group results, the authors determined that the main problems correlated with cognitive decline are forgetfulness, reduction of attention, losing items, forgetting medical appointments, repetitive behavior, difficulty in coordination and organization, use of *paspartout* words, lack of interest in things, and changes in personal hygiene (Martínez et al., 2011). In contrast, Meiland et al. asked MCI subjects, people with dementia, and caregivers to rank the proposed functionality of a smart system in relation to their needs. Consistent with the literature, the functionality most often mentioned as relevant and useful by persons with MCI was "help in cases of emergencies." However, the functionalities most often preferred by caregivers were support with navigation outdoors and the calendar function. However, some functionalities proposed were not considered useful, such as providing an overview of activities that were performed during the day (Meiland et al., 2014).

As for the other services analyzed, also in this case, the use of sensors and personal device applications is greater than the robot applications. Although the overwhelming majority of papers regarding robots and assistance is relegated to discussing designing and development steps, in contrast, a notable part of this paper encompasses concerns about the system testing step. An example is the work of Sacco et al., which, following the target set by Martinez et al., aims at the usability demonstration of a video monitoring system to obtain a quantifiable assessment of instrumental activities of daily living (IADLs) in subjects suffering from MCI. Experimental protocol provides for specific tasks concerning a daily activity scenario (DAS), performed by subjects while they are recorded with cameras. The authors report that a receiver operating characteristic (ROC) analysis,

conducted on the results of the DAS score, showed 89% sensitivity and 73% specificity for discriminating MCI from HC participants. These authors developed an algorithm able to recognize and assess the performance of subjects. Moreover, the DAS score provided a pragmatic, ecological, and objective measurement that might improve the prediction of future dementia and help the clinician to lead an early intervention (Sacco et al., 2012).

Similarly, a more recent paper by König et al. examines the use of fixed cameras in the functional assessment of people suffering from MCI. The authors conducted a two-step experiment in which subjects, both controls and MCI, had to perform a set of physical tasks before, and a set of typical IADLs after, the assessment. All the experiment were recorded u a set of sensors. Koönig et al. reported that the activities were correctly and automatically detected, using an algorithm developed by the authors themselves, with a sensitivity of 85.31% and a precision of 75.90%. The authors noted that the proposed method for monitoring and assessing ADL permits the gathering of objective and accurate information about the functional decline of MCI patients. Moreover, the use of such systems could facilitate and support aging-in-place and improve medical care in general for these patients (König et al., 2015a).

The use of cameras represents a mainstream solution for monitoring of MCI at home Vasileiadis et al. used RGB-D cameras to monitor the subjects' performance in ADL. The authors used cameras and infrared sensors in an eight-day-long test. Then, using the SVM technique, the authors were able to recognize the subjects' activities with a precision and recall rate above 80% using only sensor or tracking data, while the precision rate was over 90% through the combination of both data. Additionally, to test the activity detection potential of a sensor-less infrastructure design, an HCRF-based approach was employed, using only the vision-based features described with data sequences extracted from the occupant's movement, body posture, and upper-body geometry, leading to a precision rate of 90.5%. The authors assessed also the acceptance of the infrastructure, and although participants were hesitant to have guests during the experimental protocol, they showed a positive attitude toward the installations of the sensors in their residences (Vasileiadis et al., 2016).

A last, more recent, work that considers action recognition through cameras is the work of Stavropoulos et al. The authors concluded that a key prerequisite for the development of a service robot, which aims to monitor and support MCI patients at home, is the ability to assess the user's behavior during their daily activities. The authors, starting from the EigenJoints descriptor, developed their own action recognition method. More specifically, they proposed novel features that take into account further descriptive information of the user's actions, such as the traveled distance of the joints and how the user's pose evolves in subsequent frames from the reference frame. The obtained results show that the authors' proposed features improve action recognition performance compared to the original EigenJoints method (Stavropoulos et al., 2017).

The assistance of people with MCI goes beyond the use of cameras—other studies address, in fact, different types of technologies, such as smart phones, as in the case of the paper of Battista et al., but also more complex systems, which combine several wearable and environmental sensors with personal devices.

Some examples of that are represented by the work of Lazarou et al., Mighali et al., and Kyriazakos et al. The first paper is the less complex work on the topic. It provides for a set of sensors and personal devices, which encompass bracelets to evaluate movement, cameras, and devices for sleep monitoring, which provide all the necessary tools to clinicians for efficient monitoring of the participants and promote their quality of life via ICTs by focusing on practical aspects of everyday activities (Lazarou et al., 2016).

The papers by Mighali et al. and Kyriazakos et al. propose a similar concept. Both display a two-block structure, a cloud one and a local one (Kyriazakos et al., 2017; Mighali et al., 2017). Particularly, the first structure takes into account the need to recognize and classify typical elderly activities, such as sitting, standing still, lying down, or walking fast/normal. The authors developed a classifier that showed the capacity to correctly recognize the user's body state with an accuracy level equal to 97% (Mighali et al., 2017).

In conclusion, it is worth mentioning also the study by Diaz et al., which aimed to clarify how some cognitive functions might determine the interaction of MCI with technology. The authors found that, first, some functional measures, such as the Barthel ADL index, are related to the expected number of trials needed by a person for the interaction—for example, with an avatar on TV. Second, cognitive measures, especially those related to attention, processing speed, and discrimination between relevant and irrelevant information, can relate to the latency of response that the subjects show when they respond to the avatar. The authors concluded that cognitive and functional measures may help to predict users' expected response to the avatar. Also, these measures may explain how much time that the interaction will take. For these reasons, the authors noted that cognitive and functional measures should be used for guidance to result in a better adaptation of ICTs to elderly people with MCI (Diaz-Orueta et al., 2014).

6.3. Recommendations and Trends

The literature concerning the research in service robots for people with MCI is quite large. This fact can be explained by the fact that, in the overwhelming majority of the cases, the final aim of robots developed for elderly people and/or subjects with MCI are the same they both encompass the design and development of robotic companions for the activities of daily life. For that reason, this section encompasses almost all of the papers about robots, here reviewed. Despite this strong interest in the design and development of robots able to help people with MCI during their daily activities, the technological progress is still in the study of individualization of needs, and in developing usability or acceptability tests. Generally speaking, the sample size of this study is limited, and, moreover, the experimental trial period is a brief and not long enough to draw complete conclusions. Notwithstanding, some results can be presented and some recommendation can be offered. For instance, one of the

possible future fields of interest should be the attempt to make the robots more flexible and suitable, to better address subjects' needs. Particularly, concerning MCI, also the stakeholders must be considered. In fact, due to the subjects' conditions, they are not aware of some of their needs, and for this reason they do not find it useful that the robot would be able to remember them of their appointments or when to take their medicines (Korchut et al., 2017).

Concerning the aspects of robots, generally elderly people find that small size, in comparison to human-size, is more tolerated. Furthermore, anthropomorphic or life-like features should be carefully designed with the aim to make the interaction with the robot more intuitive, pleasant, and easy (Wu et al., 2011). Research specifically focused on individuals with MCI reveal that they prefer animal-like shapes and that they like the possibility to interact with the robot, not only via speaking, but also in a more socially and emotionally based way (Pino et al., 2015). In addition, elderly people seem to prefer a robot that looks like a familiar object in a home setting. For this reason, robots might offer opportunities for interaction among all members of the elder community, and they should allow the older people with MCI to experience the same power, control, and agency as others (Wu et al., 2012).

A last thought goes to the tendency of people with MCI to be unwilling to accept an assistive robot for use at home. This observation seems to be a sort of watershed between healthy elderly and people with cognitive impairment. Even if neither the first nor the second are totally enthusiastic to the idea of living with a companion robot, healthy subjects seems to have a more positive attitude toward this kind of robots. For this reason, and thinking to maximize the residual ability to learn how to use robots, it is recommended to introduce elderly people, even those with MCI, to the robots as early as possible (Pino et al., 2012; Seelye et al., 2012). A last comment concerning the attitude of elderly people and this type of technology is drawn to the fact that in coming years we will begin to meet elderly individuals who are increasingly confident and more expert with technologies. This expected change in the way that older will behave should not be neglected.

Concerning the use of personal devices and/or sensors, and their differences with robot-based solutions, this branch of research is not as advanced as in the other fields. This perhaps explains why assistance represents the last step that can be achieved concerning elderly people in general and subjects with MCI, specifically. When comparing the act of assisting people with the act of assessing or stimulating them, assistance is a more complex task. Assistance should provide for monitoring of the subjects, giving them practical assistance, and also giving them social assistance; it requires a higher level of development both in terms of knowledge about pathological condition and in terms of level of technological progress. Overall, when comparing robotic assistance with the idea of assisting people using personal devices, we note that the sample size of the recent is slightly wider, and its trial duration is more appropriate. Moreover, generally, people seem to be more inclined to use assistive technology during their daily activities (Batista et al., 2015). Furthermore, the use of sensors, personal devices, and avatar displayed on TV seem to be less obtrusive (especially regarding cameras), but low-cost and low-power modes are crucial for all of the solutions mentioned (Mainetti et al., 2017). Also, with the use of personal devices, the act of gathering data seems to be simpler. Notwithstanding, the research field appears less appealing and less studied.

7. DISCUSSION AND CONCLUSIONS

Dementia, and particularly AD, is one of the principal causes of disability and reduced autonomy among the elderly population (Alzheimer Association, 2017). It represents one of the most crucial challenging issues that the "health world" will face in coming years, in terms of economic and social costs (Prince et al., 2015, 2016). As mentioned previously, this disease could evolve over as long as twenty years before subjects meet the dementia criteria (Belleville et al., 2016). Due to the minor level of impairment presented by subjects with MCI, it constitutes a valuable therapeutic window for cognitive stimulation (Olazarán et al., 2004; Belleville et al., 2016). From this literature review, despite the limitation of having a research window confined until 2017, it is possible to identify some key points, such as the importance of frequent and intensive sessions of training, the positive influence of a tailored treatment, and furthermore, the value of using an interpretative model that embraces biological, psychological, and social aspects together, to maximize the treatment effect-size. The development of new ICT solutions, usable at the patient's home, without the need for the physical presence of a therapist, allows us to combine cognitive treatments with exercise and social activity (Belleville et al., 2016; Chirles et al., 2017). Although the interest in applying ICT in assessment, treatment, and assistance of people with MCI is steadily increasing, its study is generally related to more severe forms of impairment, such as dementia. However, through a careful literature review, we can recognize several types of ICT applications concerning MCI: "Evaluation," "Treatment," and "Assistance." It is relevant to observe that of the different studies reviewed, most of them encompassed more than application field. In fact, even though the different research works focused their attention on a different, related topic, such as monitoring, for instance, rather than cognitive stimulation, the idea underlying the overwhelming majority of the literature *corpus* generally referred to a complex way to think about the final aim of the technology: namely, the assistance of MCI subjects. In fact, even though the specific papers debated on single topics, the final purpose was to develop a modular, redundant, and synergistic system to take care of the subjects' needs and assist them. Having said that, we encourage the reader to imagine the use of these technologies as spread in a sort of *continuum* among early diagnosis, stimulation, assistance, and monitoring. Even though this field of research has been growing faster in recent years (see **Figure 2**), some substantial limitations are experienced because of the low number of participants in the different studies. Another index, concerning the novelty of the field, is related to the number of contributors that presented during conferences almost half of the total number of papers. Nonetheless, it

is possible to report some considerations and to draw some recommendation for future works.

Concerning the "Assessment," section, it was not possible to find a dominant type of ICT used. However, SGs and VR will likely be used in increasingly greater numbers. Interesting insights can be drawn from the use of wearable sensors, which would allow clinicians to assess patients during their activities of daily life, increasing the ecology of the measurements. Moreover, thanks to the flexibility of these technologies, they could potentially be combined for assessment and stimulation, both physical and cognitive. The development of robotic therapists just for assessment has been, up to now, minimally studied and used. This kind of solution seems that it will provide a better fit for the stimulation of these patients. The literature regarding stimulation, on the other hand, is more sizable. As just noted, for this application, the development of a robotic therapist is more common, and is one of the driving topics covered in research papers. Notwithstanding the interest gathered by this topic, the literature is lacking experimental data; several works reviewed report usability and acceptance tests. However, some steps forward have been taken. One research study on the topic concluded that a robotic therapist should take into account not only the administration of cognitive stimulation tasks, but also be able to interact with the users in a more emotionally/socially manner. Alternatively, regarding the use of personal devices and smart environments in cognitive stimulation, it is possible to observe a more mature field of research, with wider samples and longer-lasting trials. As aforementioned, regarding the Assessment section, SGs and the use of the VR environment are growing faster and gathering significant interest. Finally, concerning the Assistance section, it represents the widest group of papers, and it is mainly composed of work that examines the use of robots for assistance (Cavallo et al., 2011). Apart from the impressive interest that this field is attracting, it seems to be more a target for future development than a feasible reality, at least for now. That is likely due to a couple of limitations: one, the current state of development for companion robots that assist people, compared to the actual amount of help, in terms of quantity and quality, that the people need, and, two, the massive difficulties in gathering reasonable data. These limitations are primarily related to the complex nature of the service that we need to deliver: assistance. In fact, the gap, present in the other two sections, between the use of robots instead of other technological solutions, is reduced here or, even partially erased. That testifies to the inherent difficulty in assisting properly a human-being, especially one with cognitive impairment.

In conclusion, in our opinion, the challenge should be to address, in a systematical way, the act of steadily stepping up the level of intervention, starting from assessment until complete assistance is provided. Now that users' needs are precisely outlined, and the helpful technologies are identified, a modular, suitable system should be developed that addresses the subjects' strengths and weaknesses; features a smart environment and a cloud architecture; and includes more powerful and intelligent robots. The complexity of the intervention reflects, in fact, the complexity of human beings.

AUTHOR CONTRIBUTIONS

GM and LF were responsible for paper structure and writing, and synthesizing the information from the papers into text and tables. MTS was the clinical supervisor, responsible for clinical aspects, and contributed to the introduction, methodology definition and search strategies. FC was the scientific supervisor, guarantor for the review, and contributed in methodology definition, paper writing, discussion and conclusion. All authors were involved in papers screening, selection and reading, providing feedback, and approving the final manuscript.

FUNDING

The publication was carried out with the co-financing of the European Union—FESR o FSE, PON Ricerca e Innovazione 2014–2020 Progetto ARS01_01120, SI-ROBOTICS—Invecchiamento sano e attivo attraverso SocIal ROBOTICS.

REFERENCES

Agrigoroaie, R., and Tapus, A. (2017). "Contactless physiological data analysis for user quality of life improving by using a humanoid social robot," in *International Conference on Image Analysis and Processing* (Christchurch: Springer), 696–706.

Agrigoroaie, R. M., and Tapus, A. (2016). "Developing a healthcare robot with personalized behaviors and social skills for the elderly," in *Human-Robot Interaction (HRI), 2016 11th ACM/IEEE International Conference on* (Catania: IEEE), 589–590. doi: 10.1109/HRI.2016.7451870

Alzheimer Association (2017). 2017 Alzheimer's disease facts and figures. *Alzheimer. Dement.* 13, 325–373. doi: 10.1016/j.jalz.2017.02.001

Ballesteros, S., Kraft, E., Santana, S., and Tziraki, C. (2015). Maintaining older brain functionality: a targeted review. *Neurosci. Biobehav. Rev.* 55, 453–477. doi: 10.1016/j.neubiorev.2015.06.008

Batista, E., Borràs, F., and Martínez-Ballesté, A. (2015). "Monitoring people with MCI: deployment in a real scenario for low-budget smartphones," in *Information, Intelligence, Systems and Applications (IISA), 2015 6th International Conference on* (Corfu: IEEE), 1–6.

Belleville, S., Boller, B., and del Val, L. P. (2016). "Cognitive training in mild cognitive impairment," in *Cognitive Training* (Springer International Publishing), 187–197. Available online at: https://link.springer.com/chapter/10.1007/978-3-319-42662-4_18#citeas

Bellotto, N., Fernandez-Carmona, M., and Cosar, S. (2017). *Enrichme Integration of Ambient Intelligence and Robotics for AAL*. Standford, CA: AAAI.

Broughton, G., Krajník, T., Fernández-Carmona, M., Cielniak, G., and Bellotto, N. (2016). "Rfid-based object localisation with a mobile robot to assist the elderly with mild cognitive impairments," in *Intelligent Environments (Workshops)* (London: UK), 366–375.

Bruno, B., Mastrogiovanni, F., and Sgorbissa, A. (2013). "Functional requirements and design issues for a socially assistive robot for elderly people with mild cognitive impairments," in *RO-MAN, 2013 IEEE* (Gyeongju: IEEE), 768–773.

Cavallo, F., Aquilano, M., Bonaccorsi, M., Mannari, I., Carrozza, M. C., and Dario, P. (2011). "Multidisciplinary approach for developing a new robotic system for domiciliary assistance to elderly people," in *2011 Annual International Conference of the IEEE Engineering in Medicine and Biology Society* (Boston, MA: IEEE), 5327–5330.

Cerejeira, J., Lagarto, L., and Mukaetova-Ladinska, E. (2012). Behavioral and psychological symptoms of dementia. *Front. Neurol.* 3:73. doi: 10.3389/fneur.2012.00073

Chan, J., and Nejat, G. (2010). "The design of an intelligent socially assistive robot for person-centered cognitive interventions," in *ASME 2010 International Design Engineering Technical Conferences and Computers and Information in Engineering Conference* (Montreal, QC: American Society of Mechanical Engineers), 91–99.

Charchat-Fichman, H., Uehara, E., and Santos, C. F. (2014). New technologies in assessment and neuropsychological rehabilitation. *Temas Psicol.* 22, 539–553. doi: 10.9788/TP2014.3-01

Chirles, T. J., Reiter, K., Weiss, L. R., Alfini, A. J., Nielson, K. A., and Smith, J. C. (2017). Exercise training and functional connectivity changes in mild cognitive impairment and healthy elders. *J. Alzheimer. Dis.* 57, 845–856. doi: 10.3233/JAD-161151

Darragh, M., Ahn, H. S., MacDonald, B., Liang, A., Peri, K., Kerse, N., et al. (2017). Homecare robots to improve health and well-being in mild cognitive impairment and early stage dementia: results from a scoping study. *J. Am. Med. Direct. Assoc.* 18, 1099–e1. doi: 10.1016/j.jamda.2017.08.019

de Oliveira, A. M., Radanovic, M., de Mello, P. C., Buchain, P. C., Vizzotto, A. D., Celestino, D. L., et al. (2015). Nonpharmacological interventions to reduce behavioral and psychological symptoms of dementia: a systematic review. *BioMed Res. Int.* 2015:218980. doi: 10.1155/2015/218980

Demetriadis, S., Tsiatsos, T., Sapounidis, T., Tsolaki, M., and Gerontidis, A. (2016). "Exploring the potential of programming tasks to benefit patients with mild cognitive impairment," in *Proceedings of the 9th ACM International Conference on PErvasive Technologies Related to Assistive Environments* (Rhodes: ACM), 59.

Diaz-Orueta, U., Etxaniz, A., Gonzalez, M. F., Buiza, C., Urdaneta, E., and Yanguas, J. (2014). Role of cognitive and functional performance in the interactions between elderly people with cognitive decline and an avatar on tv. *Univ. Access Inform. Soc.* 13, 89–97. doi: 10.1007/s10209-013-0288-1

Dougherty, J. H. Jr., Cannon, R. L., Nicholas, C. R., Hall, L., Hare, F., Carr, E., et al. (2010). The computerized self test (cst): an interactive, internet accessible cognitive screening test for dementia. *J. Alzheimer. Dis.* 20, 185–195. doi: 10.3233/JAD-2010-1354

Eghdam, A., Scholl, J., Bartfai, A., and Koch, S. (2012). Information and communication technology to support self-management of patients with mild acquired cognitive impairments: systematic review. *J. Med. Int. Res.* 14:e159. doi: 10.2196/jmir.2275

Engel, G. L. (1978). The biopsychosocial model and the education of health professionals†. *Ann. N. Y. Acad. Sci.* 310, 169–181. doi: 10.1111/j.1749-6632.1978.tb22070.x

Fiorini, L., Maselli, M., Castro, E., Tocchini, S., Sportiello, M. T., Laschi, C., et al. (2017). "Feasibility study on the assessment of auditory sustained attention through walking motor parameters in mild cognitive impairments and healthy subjects," in *2017 39th Annual International Conference of the IEEE Engineering in Medicine and Biology Society (EMBC)* (Jeju: IEEE), 897–900.

Fiorini, L., Maselli, M., Esposito, R., Castro, E., Mancioppi, G., Cecchi, F., et al. (2019). Foot inertial sensing for combined cognitive-motor exercise of the sustained attention domain. *IEEE Trans. Biomed. Eng.* 66, 2413–2420. doi: 10.1109/TBME.2019.2906758.

Foukarakis, M., Antona, M., and Stephanidis, C. (2017). "Applying a multimodal user interface development framework on a domestic service robot," in *Proceedings of the 10th International Conference on PErvasive Technologies Related to Assistive Environments* (Rhodes: ACM), 378–384.

García-Betances, R. I., Cabrera-Umpiérrez, M. F., and Arredondo, M. T. (2017). Computerized neurocognitive interventions in the context of the brain training controversy. *Rev. Neurosci.* 29, 55–69. doi: 10.1515/revneuro-2017-0031

García-Casal, J. A., Franco-Martín, M., Perea-Bartolomé, M. V., Toribio-Guzmán, J. M., García-Moja, C., Goñi-Imizcoz, M., et al. (2017). Electronic devices for cognitive impairment screening: a systematic literature review. *Int. J. Technol. Assess. Health Care.* 33, 654–673. doi: 10.1017/S0266462317000800

Garcia-Sanjuan, F., Jaen, J., and Nacher, V. (2017). Tangibot: a tangible-mediated robot to support cognitive games for ageing people–a usability study. *Pervas. Mobile Comput.* 34, 91–105. doi: 10.1016/j.pmcj.2016.08.007

Granata, C., Chetouani, M., Tapus, A., Bidaud, P., and Dupourqué, V. (2010). "Voice and graphical-based interfaces for interaction with a robot dedicated to elderly and people with cognitive disorders," in *RO-MAN, 2010 IEEE* (Viareggio: IEEE), 785–790.

Granata, C., Pino, M., Legouverneur, G., Vidal, J.-S., Bidaud, P., and Rigaud, A.-S. (2013). Robot services for elderly with cognitive impairment: testing usability of graphical user interfaces. *Technol. Health Care* 21, 217–231. doi: 10.3233/THC-130718

Gross, H.-M., Schroeter, C., Mueller, S., Volkhardt, M., Einhorn, E., Bley, A., et al. (2011). "I'll keep an eye on you: home robot companion for elderly people with cognitive impairment," in *Systems, Man, and Cybernetics (SMC), 2011 IEEE International Conference on* (Anchorage, AK: IEEE), 2481–2488.

Gross, H.-M., Schroeter, C., Mueller, S., Volkhardt, M., Einhorn, E., Bley, A., et al. (2012). "Further progress towards a home robot companion for people with mild cognitive impairment," in *Systems, Man, and Cybernetics (SMC), 2012 IEEE International Conference on* (Seoul: IEEE), 637–644.

Kintsakis, A. M., Reppou, S. E., Karagiannis, G. T., and Mitkas, P. A. (2015). "Robot-assisted cognitive exercise in mild cognitive impairment patients: the rapp approach," in *E-Health and Bioengineering Conference (EHB), 2015* (Iasi: IEEE), 1–4.

König, A., Crispim-Junior, C. F., Covella, A. G., Bremond, F., Derreumaux, A., Bensadoun, G., et al. (2015a). Ecological assessment of autonomy in instrumental activities of daily living in dementia patients by the means of an automatic video monitoring system. *Front. Aging Neurosci.* 7:98. doi: 10.3389/fnagi.2015.00098

König, A., Satt, A., Sorin, A., Hoory, R., Toledo-Ronen, O., Derreumaux, A., et al. (2015b). Automatic speech analysis for the assessment of patients with predementia and alzheimer's disease. *Alzheimer's Dement.* 1, 112–124. doi: 10.1016/j.dadm.2014.11.012

Korchut, A., Szklener, S., Abdelnour, C., Tantinya, N., Hernández-Farigola, J., Ribes, J. C., et al. (2017). challenges for service robots–requirements of elderly adults with cognitive impairments. *Front. Neurol.* 8:228. doi: 10.3389/fneur.2017.00228

Kyriazakos, S., Prasad, R., Mihovska, A., Pnevmatikakis, A., op den Akker, H., Hermens, H., et al. (2017). ewall: an open-source cloud-based ehealth platform for creating home caring environments for older adults living with chronic diseases or frailty. *Wirel. Pers. Commun.* 97, 1835–1875. doi: 10.1007/s11277-017-4656-7

Lazarou, I., Karakostas, A., Stavropoulos, T. G., Tsompanidis, T., Meditskos, G., Kompatsiaris, I., et al. (2016). A novel and intelligent home monitoring system for care support of elders with cognitive impairment. *J. Alzheimer. Dis.* 54, 1561–1591. doi: 10.3233/JAD-160348

Mainetti, L., Patrono, L., and Rametta, P. (2016). "Capturing behavioral changes of elderly people through unobtruisive sensing technologies," in *Software, Telecommunications and Computer Networks (SoftCOM), 2016 24th International Conference on* (Split: IEEE), 1–3.

Mainetti, L., Patrono, L., Secco, A., and Sergi, I. (2017). An iot-aware aal system to capture behavioral changes of elderly people. *J. Commun. Softw. Syst.* 13, 68–76. doi: 10.24138/jcomss.v13i2.374

Manera, V., Ben-Sadoun, G., Aalbers, T., Agopyan, H., Askenazy, F., Benoit, M., et al. (2017). Recommendations for the use of serious games in neurodegenerative disorders: 2016 delphi panel. *Front. Psychol.* 8:1243. doi: 10.3389/fpsyg.2017.01243

Martínez, A., Etxeberria, I., Aldaz, E., Roedl, L., Hochgatterer, A., Wöckl, B., et al. (2011). "Supporting diagnostic decision for early detection of a neurodegenerative disease on a behavioural altered pattern basis," in *Proceedings of the IADIS International Conference on e-Health* (Rome), 81–88.

Maselli, M., Fiorini, L., Castro, E., Baldoli, I., Tocchini, S., Sportiello, M. T., et al. (2017). "Development and testing of a new cognitive technological tool for episodic memory: a feasibility study," in *2017 39th Annual International Conference of the IEEE Engineering in Medicine and Biology Society (EMBC)* (Jeju: IEEE), 893–896.

Maselli, M., Fiorini, L., Cecchi, F., Castro, E., Esposito, R., Cavallo, F., et al. (2018). Can physical and cognitive training based on episodic memory be combined in a new protocol for daily training? *Aging Clin. Exp. Res.* 1–9. doi: 10.1007/s40520-018-1107-6

Massimo, L., Kales, H. C., and Kolanowski, A. (2018). State of the science: apathy as a model for investigating behavioral and psychological symptoms in dementia. *J. Am. Geriatr. Soc.* 66, S4–S12. doi: 10.1111/jgs.15343

Meiland, F. J., Hattink, B. J., Overmars-Marx, T., De Boer, M E., Jedlitschka, A., Ebben, P. W., et al. (2014). Participation of end users in the design of assistive technology for people with mild to severe cognitive problems; the european rosetta project. *Int. Psychogeriatr.* 26, 769–779. doi: 10.1017/S1041610214000088

Mighali, V., Patrono, L., Stefanizzi, M. L., Rodrigues, J. J., and Solic, P. (2017). "A smart remote elderly monitoring system based on iot technologies," in *Ubiquitous and Future Networks (ICUFN), 2017 Ninth International Conference on* (Milan: IEEE), 43–48.

Mitseva, A., Kyriazakos, S., Litke, A., Papadakis, N., and Prasad, N. (2009). Isisemd: intelligent system for independent living and self-care of seniors with mild cognitive impairment or mild dementia. *J. Inform. Technol. Healthcare* 7, 383–399.

Monastero, R., Mangialasche, F., Camarda, C., Ercolani, S., and Camarda, R. (2009). A systematic review of neuropsychiatric symptoms in mild cognitive impairment. *J. Alzheimer. Dis.* 18, 11–30. doi: 10.3233/JAD-2009-1120

Montero-Odasso, M., Verghese, J., Beauchet, O., and Hausdorff, J. M. (2012). Gait and cognition: a complementary approach to understanding brain function and the risk of falling. *J. Am. Geriatr. Soc.* 60, 2127–2136. doi: 10.1111/j.1532-5415.2012.04209.x

Muscio, C., Tiraboschi, P., Guerra, U. P., Defanti, C. A., and Frisoni, G. B. (2015). Clinical trial design of serious gaming in mild cognitive impairment. *Front. Aging Neurosci.* 7:26. doi: 10.3389/fnagi.2015.00026

Nakahara, K., Yamaguchi, H., and Higashino, T. (2016). "In-home activity and micro-motion logging using mobile robot with kinect," in *Adjunct Proceedings of the 13th International Conference on Mobile and Ubiquitous Systems: Computing Networking and Services* (Hiroshima: ACM), 106–111.

Nishiura, Y., Inoue, T., and Nihei, M. (2014). Appropriate talking pattern of an information support robot for people living with dementia: a case study. *J. Assist. Technol.* 8, 177–187. doi: 10.1108/JAT-12-2013-0035

Olazarán, J., Muñiz, R., Reisberg, B., Peña-Casanova, J., del Ser, T., Cruz-Jentoft, A. J., et al. (2004). Benefits of cognitive-motor intervention in MCI and mild to moderate Alzheimer disease. *Neurology* 63, 2348 LP–2353. doi: 10.1212/01.WNL.0000147478.03911.28

Pahl, C., and Varadarajan, K. M. (2015). "Emotional feedback for service robots using hapto-acoustic interface," in *Pattern Recognition Association of South Africa and Robotics and Mechatronics International Conference (PRASA-RobMech), 2015* (Port Elizabeth: IEEE), 219–224.

Petersen, R. C., Caracciolo, B., Brayne, C., Gauthier, S., Jelic, V., and Fratiglioni, L. (2014). Mild cognitive impairment: a concept in evolution. *J. Int. Med.* 275, 214–228. doi: 10.1111/joim.12190

Petersen, R. C., Roberts, R. O., Knopman, D. S., Boeve, B. F., Geda, Y. E., Ivnik, R. J., et al. (2009). Mild cognitive impairment: ten years later. *Arch. Neurol.* 66, 1447–1455. doi: 10.1001/archneurol.2009.266

Pino, M., Boulay, M., Jouen, F., and Rigaud, A. S. (2015). "are we ready for robots that care for us?" attitudes and opinions of older adults toward socially assistive robots. *Front. Aging Neurosci.* 7:141. doi: 10.3389/fnagi.2015.00141

Pino, M., Granata, C., Legouverneur, G., and Rigaud, A. S. (2012). "Assessing design features of a graphical user interface for a social assistive robot for older adults with cognitive impairment," in *ISARC Proceedings of the International Symposium on Automation and Robotics in Construction*, Vol. 29 (Taipei: Vilnius Gediminas Technical University, Department of Construction Economics & Property), 1.

Prince, M., Comas-Herrera, A., Knapp, M., Guerchet, M., and Karagiannidou, M. (2016). World Alzheimer report 2016 improving healthcare for people living with dementia. Coverage, Quality and costs now and in the future. *Alzheimer's Dis. Int.* 1–140.

Prince, M., Wimo, A., Guerchet, M., Ali, G., Wu, Y., and Prina, M. (2015). *World Alzheimer Report 2015. The Global Impact of Dementia. Alzheimer's Disease International*. London: Alzheimer's Disease International (ADI).

Rebok, G. W., Carlson, M. C., and Langbaum, J. B. (2007). Training and maintaining memory abilities in healthy older adults: traditional and novel approaches. *J. Gerontol. Ser. B* 62, 53–61. doi: 10.1093/geronb/62.special_issue_1.53

Reppou, S. E., Tsardoulias, E. G., Kintsakis, A. M., Symeonidis, A. L., Mitkas, P. A., Psomopoulos, F. E., et al. (2016). Rapp: a robotic-oriented ecosystem for delivering smart user empowering applications for older people. *Int. J. Soc. Robot.* 8, 539–552. doi: 10.1007/s12369-016-0361-z

Sacco, G., Joumier, V., Darmon, N., Dechamps, A., Derreumaux, A., Lee, J.-H., et al. (2012). Detection of activities of daily living impairment in Alzheimer's disease and mild cognitive impairment using information and communication technology. *Clin. Intervent. Aging* 7:539. doi: 10.2147/CIA.S36297

Sallim, A. B., Sayampanathan, A. A., Cuttilan, A., and Ho, R. (2015). Prevalence of mental health disorders among caregivers of patients with alzheimer disease. *J. Am. Med. Direct. Assoc.* 16, 1034–1041. doi: 10.1016/j.jamda.2015.09.007

Schroeter, C., Mueller, S., Volkhardt, M., Einhorn, E., Huijnen, C., van den Heuvel, H., et al. (2013). "Realization and user evaluation of a companion robot for people with mild cognitive impairments," in *Robotics and Automation (ICRA), 2013 IEEE International Conference on* (Karlsruhe: IEEE), 1153–1159.

Seelye, A. M., Wild, K. V., Larimer, N., Maxwell, S., Kearns, P., and Kaye, J. A. (2012). Reactions to a remote-controlled video-communication robot in seniors' homes: a pilot study of feasibility and acceptance. *Telemed. E-Health* 18, 755–759. doi: 10.1089/tmj.2012.0026

Segkouli, S., Paliokas, I., Tzovaras, D., Tsakiris, T., Tsolaki, M., and Karagiannidis, C. (2015). Novel virtual user models of mild cognitive impairment for simulating dementia. *Comput. Math. Methods Med.* 2015:358638. doi: 10.1155/2015/358638

Stavropoulos, G., Giakoumis, D., Moustakas, K., and Tzovaras, D. (2017). "Automatic action recognition for assistive robots to support mci patients at home," in *Proceedings of the 10th International Conference on PErvasive Technologies Related to Assistive Environments* (Island of Rhodes: ACM), 366–371.

Tapus, A., Tapus, C., and Mataric, M. (2009). "The role of physical embodiment of a therapist robot for individuals with cognitive impairments," in *Robot and Human Interactive Communication, 2009. RO-MAN 2009. The 18th IEEE International Symposium on* (Toyama: IEEE), 103–107.

Teipel, S., Babiloni, C., Hoey, J., Kaye, J., Kirste, T., and Burmeister, O. K. (2016). Information and communication technology solutions for outdoor navigation in dementia. *Alzheimer's Dementia* 12, 695–707. doi: 10.1016/j.jalz.2015.11.003

Tiberio, L., Cesta, A., Cortellessa, G., Padua, L., and Pellegrino, A. R. (2012). "Assessing affective response of older users to a telepresence robot using a combination of psychophysiological measures," in *RO-MAN, 2012 IEEE* (Paris: IEEE), 833–838.

Tsardoulias, E. G., Kintsakis, A. M., Panayiotou, K., Thallas, A. G., Reppou, S. E., Karagiannis, G. G., et al. (2017). Towards an integrated robotics architecture for social inclusion–the rapp paradigm. *Cogn. Syst. Res.* 43, 157–173. doi: 10.1016/j.cogsys.2016.08.004

Turchetti, G., Micera, S., Cavallo, F., Odetti, L., and Dario, P. (2011). Technology and innovative services. *IEEE Pulse* 2, 27–35. doi: 10.1109/MPUL.2011.940428

Vasileiadis, M., Giakoumis, D., Votis, K., and Tzovaras, D. (2016). "A living lab infrastructure for investigating activity monitoring needs in service robot applications," in *Proceedings of the 9th ACM International Conference on PErvasive Technologies Related to Assistive Environments* (Corfu: ACM), 72.

Voss, M. W., Prakash, R. S., Erickson, K. I., Basak, C., Chaddock, L., Kim, J. S., et al. (2010). Plasticity of brain networks in a randomized intervention trial of exercise training in older adults. *Front. Aging Neurosci.* 2:32. doi: 10.3389/fnagi.2010.00032

Wu, Y.-H., Cristancho-Lacroix, V., Fassert, C., Faucounau, V., de Rotrou, J., and Rigaud, A.-S. (2016). The attitudes and perceptions of older adults with mild cognitive impairment toward an assistive robot. *J. Appl. Gerontol.* 35, 3–17. doi: 10.1177/0733464813515092

Wu, Y.-H., Fassert, C., and Rigaud, A.-S. (2012). Designing robots for the elderly: appearance issue and beyond. *Arch. Gerontol. Geriatr.* 54, 121–126. doi: 10.1016/j.archger.2011.02.003

Wu, Y.-H., Faucounau, V., Boulay, M., Maestrutti, M., and Rigaud, A.-S. (2011). Robotic agents for supporting community-dwelling elderly people with memory complaints: perceived needs and preferences. *Health Inform. J.* 17, 33–40. doi: 10.1177/1460458210380517

Wu, Y.-H., Wrobel, J., Cornuet, M., Kerhervé, H., Damnée, S., and Rigaud, A.-S. (2014). Acceptance of an assistive robot in older adults: a mixed-method study

of human–robot interaction over a 1-month period in the living lab setting. *Clin. Intervent. Aging* 9:801. doi: 10.2147/CIA.S56435

Wu, Y.-H., Wrobel, J., Cristancho-Lacroix, V., Kamali, L., Chetouani, M., Duhaut, D., et al. (2013). Designing an assistive robot for older adults: the robadom project. *Irbm* 34, 119–123. doi: 10.1016/j.irbm.2013.01.003

Yamaguchi, K., Nergui, M., and Otake, M. (2014). "A robot presenting reproduced stories among older adults in group conversation," in *Applied Mechanics and Materials*, Vol. 541 (Penang: Trans Tech Publ.), 1120–1126. doi: 10.4028/www.scientific.net/AMM.541-542

Zaccarelli, C., Cirillo, G., Passuti, S., Annicchiarico, R., and Barban, F. (2013). "Computer-based cognitive intervention for dementia: sociable: motivating platform for elderly networking, mental reinforcement and social interaction," in *Proceedings of the 7th International Conference on Pervasive Computing Technologies for Healthcare* (Trento: Institute for Computer Sciences, Social-Informatics and Telecommunications Engineering), 430–435.

Zhang, M. W., Chan, S., Wynne, O., Jeong, S., Hunter, S., Wilson, A., et al. (2016). Conceptualization of an evidence-based smartphone innovation for caregivers and persons living with dementia. *Technol. Health Care* 24, 769–773. doi: 10.3233/THC-161165

Zuchella, C., Sinforiani, E., Tassorelli, C., Cavallini, E., Tost-Pardell, D., Grau, S., et al. (2014). Serious games for screening pre-dementia conditions: from virtuality to reality? A pilot project. *Funct. Neurol.* 29, 153–8. doi: 10.11138/FNeur/2014.29.3.153

Conflict of Interest Statement: The authors declare that the research was conducted in the absence of any commercial or financial relationships that could be construed as a potential conflict of interest.

Copyright © 2019 Mancioppi, Fiorini, Timpano Sportiello and Cavallo. This is an open-access article distributed under the terms of the Creative Commons Attribution License (CC BY). The use, distribution or reproduction in other forums is permitted, provided the original author(s) and the copyright owner(s) are credited and that the original publication in this journal is cited, in accordance with accepted academic practice. No use, distribution or reproduction is permitted which does not comply with these terms.

frontiers in Neuroinformatics

ORIGINAL RESEARCH
published: 28 August 2019
doi: 10.3389/fninf.2019.00060

The LONI QC System: A Semi-Automated, Web-Based and Freely-Available Environment for the Comprehensive Quality Control of Neuroimaging Data

Hosung Kim[1], Andrei Irimia[1,2]*, Samuel M. Hobel[1], Mher Pogosyan[1], Haoteng Tang[1], Petros Petrosyan[1], Rita Esquivel Castelo Blanco[1], Ben A. Duffy[1], Lu Zhao[1], Karen L. Crawford[1], Sook-Lei Liew[1], Kristi Clark[1], Meng Law[1], Pratik Mukherjee[3], Geoffrey T. Manley[3], John D. Van Horn[1] and Arthur W. Toga[1]*

[1] *Laboratory of Neuro Imaging, USC Mark and Mary Stevens Neuroimaging and Informatics Institute, University of Southern California, Los Angeles, CA, United States,* [2] *Department of Gerontology, University of Southern California, Los Angeles, CA, United States,* [3] *Department of Radiology & Biomedical Imaging, University of California, San Francisco, San Francisco, CA, United States*

OPEN ACCESS

Edited by:
Antonio Fernández-Caballero, University of Castilla-La Mancha, Spain

Reviewed by:
Stephen C. Strother, Baycrest Hospital, Canada
Siyuan Liu, The University of North Carolina at Chapel Hill, United States

***Correspondence:**
Hosung Kim
hosung.kim@loni.usc.edu
Andrei Irimia
Andrei.irimia@loni.usc.edu

Received: *22 January 2019*
Accepted: *12 August 2019*
Published: *28 August 2019*

Citation:
Kim H, Irimia A, Hobel SM, Pogosyan M, Tang H, Petrosyan P, Esquivel Castelo Blanco R, Duffy BA, Zhao L, Crawford KL, Liew S-L, Clark K, Law M, Mukherjee P, Manley GT, Van Horn JD and Toga AW (2019) The LONI QC System: A Semi-Automated, Web-Based and Freely-Available Environment for the Comprehensive Quality Control of Neuroimaging Data. Front. Neuroinform. 13:60. doi: 10.3389/fninf.2019.00060

Quantifying, controlling, and monitoring image quality is an essential prerequisite for ensuring the validity and reproducibility of many types of neuroimaging data analyses. Implementation of quality control (QC) procedures is the key to ensuring that neuroimaging data are of high-quality and their validity in the subsequent analyses. We introduce the QC system of the Laboratory of Neuro Imaging (LONI): a web-based system featuring a workflow for the assessment of various modality and contrast brain imaging data. The design allows users to anonymously upload imaging data to the LONI-QC system. It then computes an exhaustive set of QC metrics which aids users to perform a standardized QC by generating a range of scalar and vector statistics. These procedures are performed in parallel using a large compute cluster. Finally, the system offers an automated QC procedure for structural MRI, which can flag each QC metric as being 'good' or 'bad.' Validation using various sets of data acquired from a single scanner and from multiple sites demonstrated the reproducibility of our QC metrics, and the sensitivity and specificity of the proposed Auto QC to 'bad' quality images in comparison to visual inspection. To the best of our knowledge, LONI-QC is the first online QC system that uniquely supports the variety of functionality where we compute numerous QC metrics and perform visual/automated image QC of multi-contrast and multi-modal brain imaging data. The LONI-QC system has been used to assess the quality of large neuroimaging datasets acquired as part of various multi-site studies such as the Transforming Research and Clinical Knowledge in Traumatic Brain Injury (TRACK-TBI) Study and the Alzheimer's Disease Neuroimaging

Initiative (ADNI). LONI-QC's functionality is freely available to users worldwide and its adoption by imaging researchers is likely to contribute substantially to upholding high standards of brain image data quality and to implementing these standards across the neuroimaging community.

Keywords: quality control, magnetic resonance imaging, diffusion tensor imaging, functional magnetic resonance imaging, LONI Pipeline

INTRODUCTION

To ensure the highest standards of research quality, reliability, validity, and reproducibility in brain imaging studies, investigators who acquire and/or analyze neuroimaging data are required to test and monitor all facets of image acquisition. For this reason, image quality control (QC) is a prerequisite to most single and multisite projects. Acquisition protocols with relatively long scanning times, such as diffusion tensor imaging (DTI) and functional magnetic resonance imaging (fMRI), may be sensitive to substantial noise or artifacts during scanning – for instance, artifacts related to subject motion during relatively long duration acquisitions. Adherence to standardized protocol compliance may be inconsistent. Such neuroimaging challenges become more germane in imaging studies of children (Yoshida et al., 2013) and adolescents (Satterthwaite et al., 2012); the confounding influence of head motion on resting-state functional connectivity and DTI structural connectivity (Lauzon et al., 2013; Yoshida et al., 2013) have received substantial attention (Power et al., 2012; Satterthwaite et al., 2012; Van Dijk et al., 2012). Similar effects (Reuter et al., 2015) are evident in 3D acquisitions of structural MRI (sMRI).

In addition to head motion-induced artifacts, the common classes of artifacts found in MRI include ringing artifacts driven by aliasing, EPI distortions due to gradient effects, intensity inhomogeneity across regions due to MR strength attenuation and use of multiple channel coils, zero fill artifact, zipper artifact related to blood flow, impulse noise that likely drops the signal-to-noise ratio (SNR), magnetic susceptibility creating image geometric distortion (Bastin et al., 1998; Skare et al., 2000; Anderson, 2001), chemical shift due to the differences between resonance frequencies of fat and water (Reiser et al., 2008), and aliasing artifacts resulting from a field of view that is smaller than the object (Heim et al., 2004; Owens et al., 2012; Jones et al., 2013; Pizarro et al., 2016). Beyond the aforementioned artifacts, the quality of DTI measurement is also susceptible to eddy currents. These confounds likely contribute to inaccuracies in segmentation of anatomical MRI images (Pizarro et al., 2016; Keshavan et al., 2017), assessment of inter-regional correlation of blood-oxygen-level dependent (BOLD) time courses on resting state-fMRI (Power et al., 2012, 2014), and the tensor fitting of DTI data (Le Bihan et al., 2006). Poorly inspected data has the potential to obscure the presence of actual biological changes and/or produce spurious associations with study phenotypes. However, most neuroscientific and clinical studies do not describe whether or not image QC was performed in their research publications. Others rely solely upon a visual inspection method of image QC and follow in-house QC protocols, which may not be well documented. The use of visual inspection methods which often rely on subjective interpretation to identify 'bad' quality data are mainly due to the absence of an existing standardized procedure for QC. Furthermore, variations in QC approaches make data aggregation across datasets even more difficult.

Development of quantitative QC metrics is imperative for addressing the subjectivity in visual assessment and would serve to facilitate an automated QC system of brain image data so that methods of assessment can be reproduced across multisite datasets. A survey of the literature (**Supplementary Data 1**) presents studies performing systematic assessment of image quality of MRI data using quantitative QC for typical MRI modalities (sMRI: n = 9; fMRI: 5; DTI: 3). The types of QC (i.e., manual or fully automated annotation of 'bad' images), the number of QC metrics (n = 1–190) and the type of datasets (i.e., inclusion of patients or healthy subjects only, age range, sample size, use of publicly open data or their own data) used in these studies vary considerably. In particular, inclusion of pathologic brains or inclusion of pediatric or elderly groups in some studies may result in a different distribution of the QC metrics – suggesting different interpretations of their relative image quality since these are factors likely changing the degree of artifacts or degrading the image preprocessing for the computation of QC metrics. This may ultimately present confounds for the users during their interpretation of the QC results. Recent work shows more promising results and provides more advanced features that improve the accessibility and reliability of the QC system: The nine studies shown in **Supplementary Data 1** focused on developing a QC system for structural MRI (sMRI). Similarly, these studies derived a number of QC metrics that characterize different aspects of imaging artifacts on sMRI and used supervised classifiers to determine a decision boundary by which the best agreement with visual inspection results was obtained. One of these frameworks is not publicly available (Pizarro et al., 2016). Roalf et al. (2016) recently developed a publicly open script which calculates several QC metrics to assess the image quality of DTI data. They performed a systematic evaluation on a large DTI dataset showing sensitivity and specificity of their proposed QC metrics to bad quality data. Oguz et al. (2014) have also developed the DTIPrep tool, open-source software featuring a graphical user interface (GUI), which can perform QC on DTI images. This tool has two separate modules including an automatic QC and artifact correction/removal as well as a module enabling visual assessment. One fMRI study using a QC metric of temporal variation in signal changes showed that this metric is sensitive to motion artifacts and also related to reductions in functional connectivity (Power et al., 2012). In their

follow-up study, they expanded their findings by investigating methods to remove the censored motion artifact (Power et al., 2014). There have also been efforts made for the quality assurance of post-image processing such as in the studies evaluating brain structural segmentation on sMRI (Keshavan et al., 2017) and fiber tractography extracted from DTI data (Sommer et al., 2017). However, this type of QC processing may tend to be computationally costly, requiring numerous stages of image processing prior to the image quality evaluation.

Despite these recent efforts in various MRI modalities, several challenges exist which potentially limit neuroimaging researchers' and clinicians' access to or familiarity with currently available QC tools: First, There are no other comprehensive QC tools covering sMRI, fMRI, computed tomography (CT) and DTI simultaneously, even though there are other QC tools covering part of these image modalities[1,2] (Marcus et al., 2013; Esteban et al., 2017). Second, most of the QC tools do not provide a user-friendly GUI which can increase the accessibility of novice-level users to these tools. Most tools also require preinstalled software libraries such as FSL, SPM or AFNI in order to enable their functionality on a local host computer. Furthermore, the facility for automated QC is not routinely included in many neuroimaging software packages, which potentially implies a dependence on human efforts in the QC process. Lastly, running a given QC tool on a personal computer or small size compute clusters may limit QC efforts in large-scale data collections.

Here, we describe the LONI QC system (version 1.0) which features a detailed scientific workflow for the objective review and assessment of various modality and contrast imaging data including sMRI, fMRI, DTI, and CT data. The current QC system has two options to perform its functionality: (1) a completely online system supported by various commonly-used web-browsers and which requires no preinstalled software; (2) a downloadable framework which runs on the user's local computing environment but does necessitate prerequisite software. In the online system, the design allows users to anonymously upload imaging data to the LONI QC system, either through LONI Integrated Data Archive (IDA) or using a direct uploading interface. It computes a comprehensive set of standard QC metrics that have been described in the literature and performs a standardized QC via an automated pre-processing system specifically designed to generate a range of scalar and vector statistics along with derived images. LONI QC data processing workflows are implemented using the LONI Pipeline[3] that facilitates designing, modifying, and maintaining the system, whilst the QC data processing is performed on the LONI processing grid in the Mark and Mary Stevens Neuroimaging and Informatics Institute at the University of Southern California (USC) – a cluster of thousands of central processing units (CPUs). LONI QC system also features a user-friendly web GUI that is designed for those whose level of expertise can range from novice to expert. Upon completion of the QC process, the system provides the users a detailed report containing a range of quantitative metrics which can be used to assess neuroimaging data quality. Finally, the LONI QC system enables image evaluation based on flagging each QC metric as 'good,' 'questionable,' or 'bad' based on a statistical distribution of prior results.

To provide an illustration of the LONI QC system, we evaluate various datasets including imaging data scanned with different imaging modalities (sMRI, fMRI, DTI), sequences (T1-weighted, T2-weighed, FLAIR) and different acquisition parameters (e.g., repetition time, echo time, voxel size). We also evaluate the QC metrics' reproducibility (for a dataset collected from the same scanner and collected from multiple scanners with different acquisition parameters) as well as sensitivity and specificity to the identification of 'bad' quality images in comparison to visual inspection to assess the utility of the automated QC rating process.

MATERIALS AND METHODS

The online LONI QC system consists of the following three stages (**Figure 1**): (1) Initialization, including online account creation and uploading data; (2) Computation of QC metrics for various modality images; and (3) Image QC reporting including automated QC rating and user's visual inspection. The automated QC feature provides a way for users to be informed about whether the assessed image data is of good quality or needs further careful inspection by a human expert. In the following sections, the workflow and technical specifications of the system are described. More details that explain how the GUI of the current system interacts with the workflow and the proposed features are provided in **Figure 2** and **Supplementary Data 2**.

The offline version of the LONI QC framework may be downloaded at http://qc.loni.usc.edu. This package includes the related LONI pipeline workflow file, the scripts required by the workflow, and a document instructing the installation and the list of the packages to be preinstalled, such as FSL, AFNI, FreeSurfer, and SPM.

Initialization (Figure 1-1)

Once users create their account on the LONI QC system and login, they can submit image data from the existing data collection to the QC processing workflow. To enable the submission of image data by a user, the LONI QC system either interacts with the LONI-Image Data Archive (IDA)[4] or uses a separate module that allows the user to directly upload their data to the QC system. The IDA is a user-friendly environment for archiving, searching, sharing, curating and disseminating neuroimaging and related clinical data (Crawford et al., 2016). It has been employed in a large number of neuroimaging research projects across the globe and accommodates MRI, MR angiography (MRA), magnetic resonance spectroscopy (MRS), DTI, CT, positron emission tomography (PET) and other imaging modalities. An engine for flexible data de-identification and encrypted file transmission are then used to

[1] http://preprocessed-connectomes-project.org/quality-assessment-protocol/

[2] https://mriqc.readthedocs.io/en/stable/

[3] http://pipeline.loni.usc.edu

[4] http://ida.loni.usc.edu

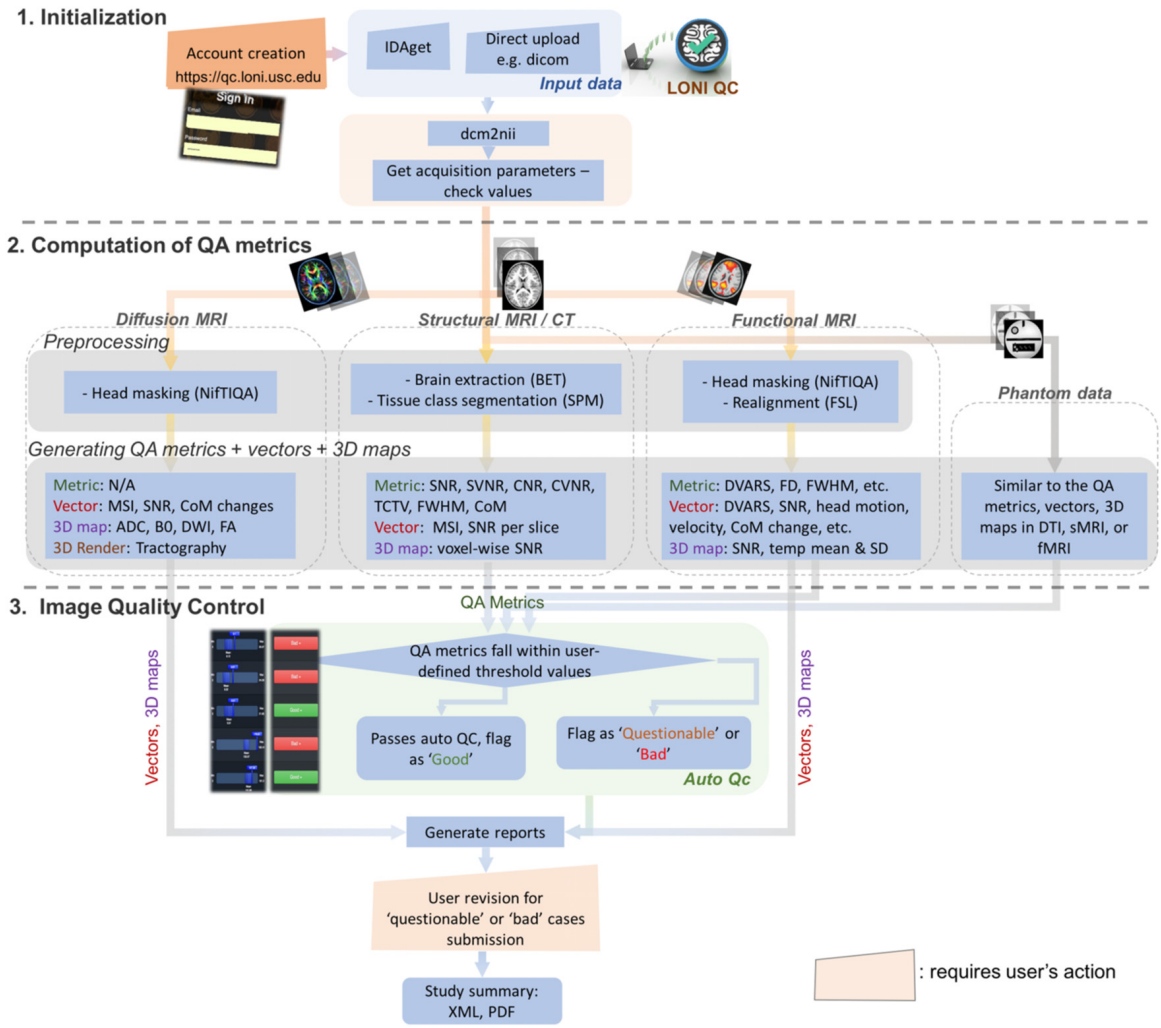


FIGURE 1 | Overall workflow for the LONI QC system. The LONI QC system consists of the three main stages: **(1)** Initialization including the creation of an online account and uploading data; **(2)** Computation of QC metrics for different image modalities. The system computes and generates various QC metrics, vectors and 3D maps and renderings for user's comprehensive evaluation of image quality; and **(3)** Image QC including automated QC and user's visual evaluation. The automated QC feature provides a way for users to be informed about whether the assessed image data is of good quality or needs further careful inspection by a human expert. IDA, Integrated Data Archive; QC, quality assessment; QC, quality control; MSI, mean slice intensity; SNR, signal-to-noise ratio; CoM, Center of Mass; ADC, apparent diffusion coefficient; DWI, diffusion-weighted imaging; FA, fractional anisotropy; SVNR, signal variance-to-noise variance ratio; TCTV, tissue contrast-to-tissue variance ratio; DVARS, the root-mean-squared change in blood oxygenation level-dependent signal across time; FWHM, full width half maximum; FD, frame-wise displacement; SD, standard deviation.

ensure compliance with patient-privacy regulations. Uploading data through the IDA automatically archives the data in the IDA securely, which requires no specialized hardware, software or personnel. The IDA and the direct upload module automatically extract relevant metadata from all de-identified image files. The direct upload method implemented in the current system version (v1.0) permits DICOM and Nifti formats as well as uploading multiple files at a time (up to 2 gigabytes or up to 30 files).

Computation of QC Metrics for Various Modality Images (Figure 1-2)

The users can initiate the system for computation of the QC metrics by selecting data included in the existing data collection. The LONI QC system uses a LONI Pipeline workflow (Rex et al., 2003) to pre-process image data prior to the calculation of QC metrics including correction for intensity inhomogeneity (Sled et al., 1998) and eddy current correction for the geometric distortion on DTI (Jezzard et al., 1998). Once the preprocessing is done, the system then inspects all XML header information and verifies that the data are suitable for analysis: e.g., whether the modality of the image is within the category of sMRI, fMRI, DTI or CT, and whether there is missing information about the imaging parameters. The results of this inspection are used as input to a module which either instructs the system to proceed with the calculation of metrics or transmits information to an error reporting module. We describe in the following

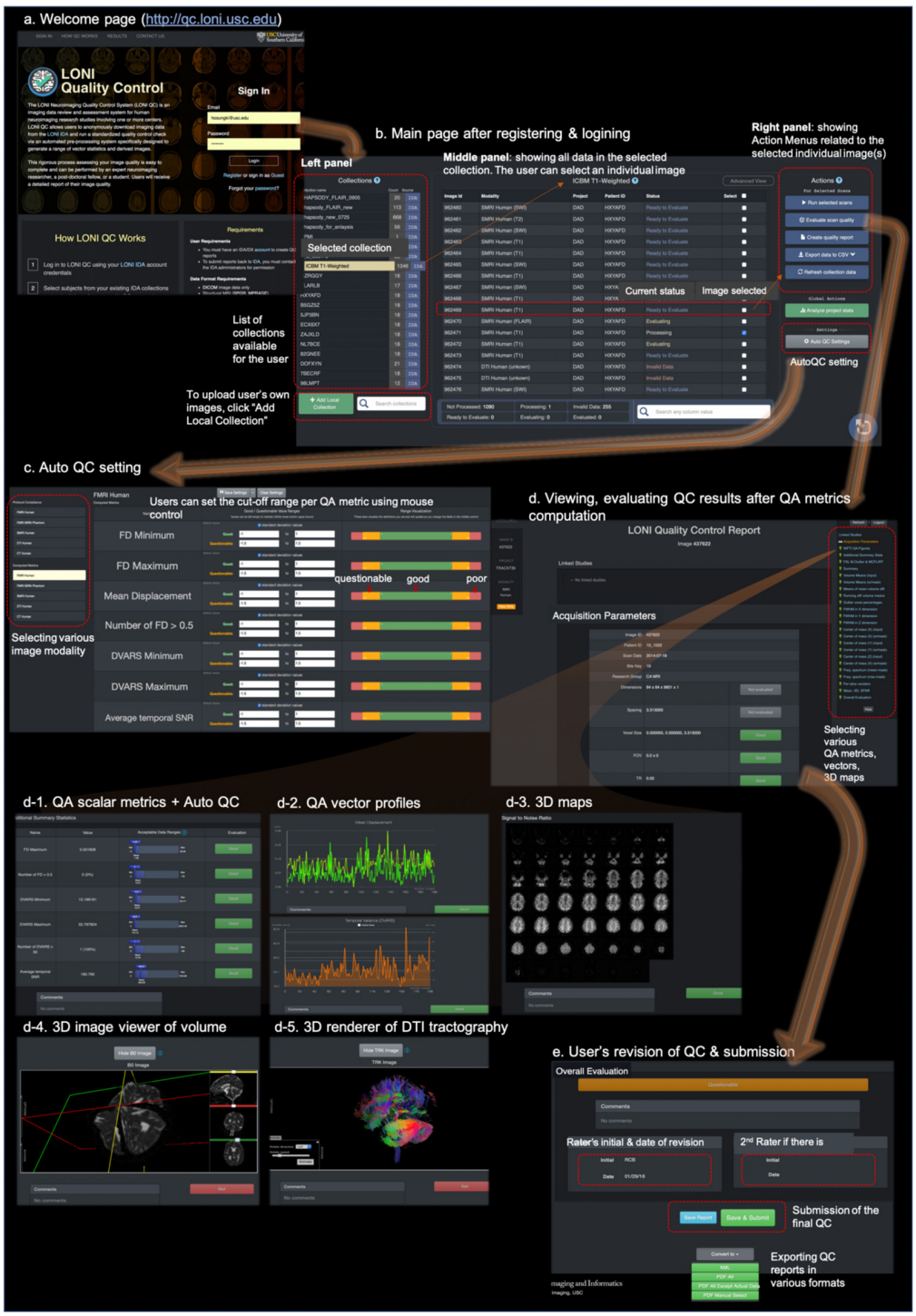


FIGURE 2 | The web-based user-friendly GUI for LONI QC system. **(a)** Entering to http://qc.loni.usc.edu using any web-browser, users can register their accounts and log in to LONI QC system. **(b)** After sign-in, users enter into the main page. In the left panel the user can first select a data collection. The user can select image(s) in the selected collection in the middle panel. Finally, in the left panel, the user can select an Action related to the selected image(s): either run new QC, evaluate QC result, create QC report, export QC data to a CSV file or refresh collection data. **(c)** The user can set or change the cutoff values/ranges in 'auto QC setting.' The cutoff ranges are set per image modality by selecting it on the left-bottom panel. The ranges can be compared to the mean and SD of the previously processed datasets. **(d)** Once QC metrics computation were completed and the user clicked "Evaluate scan quality" in the left panel of the main page, the user can appreciate and evaluate the calculated QC metrics **(d-1)**, vectors **(d-2)**, and 3D maps and renderings **(d-3,4,5)** per image. If the auto QC was performed, they can find the 'good,' 'questionable' or 'bad' flags and can revise the results if they do not agree. After the evaluation and revision of QC, users can submit the final evaluation to the system and request to export the QC reports in various formats such as XML or PDF **(e)**.

sections how and what QC metrics are computed in each imaging modality.

Workflow and QC Metrics for sMRI and CT

The following QC metrics are computed: (1) mean slice intensity (MSI): AFNI software is used to calculate MSI, a vector representing the mean intensities for all the slices. A quick change in mean intensity at a slice compared to its previous one may indicate a quality issue; (2) SNR: The lower 10% of the intensity distribution is used to separate the image background from the head. The SNR is, then, computed as mean signal intensity of the head divided by the standard deviation (SD) of the intensity in the background. The range of possible values is between zero and infinity. Lower SNR indicates poorer image quality; (3) signal variance-to-noise variance ratio (SVNR): Signal intensity variance of the head is divided by the signal intensity variance of the background. Here, the range of possible values is between zero and infinity. Higher SVNR indicates bad image quality; (4) contrast-to-noise ratio (CNR): Image is skull stripped to label the brain using FSL-BET[5]. The FSL-BET is subject to the generation of a poorly fitting brain mask. However, we intend for the LONI QC system to use simple and minimum image pre-processing steps rather than employing learning-based approaches, *per se*, which often perform better or worse depending on the training-set. Furthermore, the LONI QC system has the functionality for users to visually check the quality of the BET-generated mask, allowing for the finalization of the QC more comprehensively. Segmentation of gray matter (GM), white matter (WM), and cerebrospinal fluid (CSF) is performed on the skull-stripped brain using SPM8[6] package. The means of GM and WM signal intensities are subtracted from one another. Their absolute value is divided by the SD of the background signal intensity. Possible values range from zero to infinity. Lower CNR indicates poorer image quality; (5) Contrast of Variance-to-Noise Ratio (CVNR): Instead of the means of GM and WM intensities, their SDs are used; (6) brain tissue contrast-to-tissue intensity variation (TCTV): The means of GM and WM signal intensities are subtracted from one another. Their absolute value is divided by the pooled SD of the GM and WM as $\sqrt{\sigma_{GM}^2 + \sigma_{WM}^2}$ where σ is SD of the signal intensities for a given tissue type. Range of values is zero to infinity. Smaller TCTV indicates poorer image quality. This metric was used in a recent study (Pizarro et al., 2016) and we observed this is sensitive to the motion artifact more than SNR or CNR; (7) full-width-at-half-maximum (FWHM): This metric that characterizes the smoothness of the image is determined using the variance of derivatives method of Worsley et al. (1992): The FWHM was computed within the brain area and calculated separately for each axis in the image volume. Also, the number of 'resolvable elements' is calculated by dividing the number of voxels in the brain by the geometric mean of the FWHM of each axis; (8) center of mass (CoM) of the volume in each dimension (X, Y, and Z). The CoM is computed by dividing the sum of each coordinate X, Y, or Z for the voxels inside the brain by the number of these voxels (Fesl et al., 2008).

[5]https://fsl.fmrib.ox.ac.uk/fsl/fslwiki/BET

[6]http://www.fil.ion.ucl.ac.uk/spm/

Workflow and Metrics for DTI

The module first ensures whether data for all gradient directions are available or not by extracting B_0 values and the diffusion gradient direction matrix from DICOM headers. If this is not the case, the workflow generates error messages to the user. The following QC vectors are computed: (1) the SNR; (2) CoM computed for each gradient direction volume; (3) histogram of image intensities and its related descriptive statistics for each volume are generated within the head mask; (4) the mean signal intensity (MSI) and SNR for volumes associated with each gradient direction; and (5) the displacement from the mean of the CoM in each of the X, Y, and Z directions is calculated for each gradient direction. Using TrackVis[7], the following features as volume maps are computed and visualized for users to examine: B_0, fractional anisotropy (FA), mean diffusivity (MD) and apparent diffusion coefficient (ADC) volumes. The 3D rendering of WM fibers is generated using streamline tractography methods (Mori et al., 1999; Lazar et al., 2003). A detailed report containing information about the number of voxels, mean intensity, standard deviation, and minimum and maximum intensities for each slice is also generated.

Workflow and Metrics for fMRI

For each point in an fMRI time series, capabilities are provided to calculate the following scalar metrics: (1) MSI per volume; (2) the average temporal SNR; (3) the frame-wise displacement (FD): the mean displacement of the head for each frame from the first frame volume using the algorithm of Power et al. (2012). The maximum FD and the number of the volume frames with FD $>$ 0.5 are also computed; and (4) DVARS: The algorithm of Power et al. (2012) is also used to compute the root-mean-squared change in blood oxygenation level-dependent (BOLD) signal across time, which is known as the DVARS measure. We used FSL tools called fsl_motion_outliers to compute FD and DVARS. We further compute the maximum DVARS, the number of frames with DVARS $>$ 50. Plots across time (i.e., across the volume frames) are also provided for the following quantities: (1) FD; (2) DVARS; (3) the volume mean of SNR; (4) estimated head translations and rotations in each dimension; (5) the volume mean of the signal intensity; (6) the volume mean of the running difference ('velocity'); (7) percentage of outlier voxels [using the 3dToutcount function in the AFNI software package (Cox, 1996)]; (8) the FWHM in each dimension; (9) the CoM change in each dimension; (10) the mean and maximum of the fMRI signal's frequency spectrum over the brain-masked volume; and (11) the image intensity variation per slice and the signal-to-fluctuation noise ratio (SFNR) computed as described by Friedman and Glover (2006). In the processes where the alignment was required, we used FSL-FLIRT and MCFLIRT tools with the cost function of the normalized correlation.

Workflow and Metrics for Phantoms

The LONI QC system accommodates data collected from MRI phantoms as a separate category and all the metrics described above for human data can be computed automatically for MRI

[7]http://www.trackvis.org

phantoms as well. This process can be essential for helping the user to decide on acceptable values and ranges for metrics computed from human data. The QC protocol for phantoms is similar to that for each type of imaging (sMRI/CT, DTI or fMRI), with minor differences. The QC metrics reported for phantoms are the MSI, odd-even slice intensity differences, the SFNR, the CoM in each dimension, and to obtain plots of the raw fMRI signal and Fourier spectrum magnitude.

Image QC (Figure 1-3)

User's Qualitative and Quantitative QC of Image Data

Once the image data were processed and QC metrics have been computed, the system awaits the users' evaluation. The graphical user interface (GUI) of LONI QC system then is provided for users' visual inspection of the quality of images as well as their quantitative evaluation of QC metrics (**Figure 2**):

- Visual inspection: The GUI is fully integrated with the LONI Viewer based on a web-enabled neuroimage viewing engine. For sMRI volumes, the LONI viewer allows users to inspect neuroimaging slices in the axial, sagittal and coronal planes. For DTI volumes, a magnetic field gradient direction table is provided in addition to FA, MD and ADC images. DTI tractography files can be inspected using the LONI Viewer with an online 3D visualization module.
- Quantitative evaluation: Using the GUI of the system, the users can view and examine the resulting QC metrics as in value for the following metrics [sMRI: SNR, CNR, SVNR, CVNR, TCTV, COV, FHWM [x,y,z], CoM [x,y,z]; fMRI: average temporal SNR, maximum FD, number of frames with FD $>$ 0.5, minimum DVARS, maximum DVARS, number of frames with DVARS $>$ 50; DTI: N/A], as in graph plotting the vector of image arrays (sMRI), gradient volume series (DTI), and time series profiles (fMRI) for the following metrics: [sMRI: MSI; DTI: MSI per gradient volume, SNR changes, CoM change in each dimension; fMRI: FD, DVARS, volume mean of SNR, head translations, and rotations in each dimension, volume mean of signal intensity, volume mean of running difference ('velocity'), percentage of outlier voxels, FWHM in each dimension, CoM change in each dimension, mean and maximum of the fMRI signal's frequency spectrum over the brain-masked volume, image intensity variation per slice and signal-to-fluctuation noise ratio], and as in voxel-wise volume map (sMRI: SNR; DTI: SNR, B_0, FA, MD, ADC; FMRI: SNR, temporal mean, temporal SD).

Automated QC and User's Revision

It is almost impossible for users to perform image QC for all the data in instances of the analysis of large or multisite datasets. Even analyzing a smaller dataset, image QC for every single subject is time-consuming. To facilitate, the LONI QC system provides a user-friendly automated QC system that flags each scan with 'good,' 'questionable' or 'bad' and suggests the user to carry out an additional visual QC on those with 'questionable' or 'bad' flags. This feature is currently available for the sMRI and fMRI data where we have single-value QC metrics whereas the QC metrics for DTI are in a vector format. The system's GUI provides the users a way to set a range for each QC metric, with which they can classify the resulting metric to the 'good,' or 'bad' category (note: 'questionable' is merged into either 'good' or 'bad' in autoQC, see Evaluation section). This is performed by comparing the location of each metric value with a user-defined cut-off range. Metrics whose values fall outside this interval are then labeled automatically as 'bad.' In the current study, the criteria for the classification of 'good' or 'bad' were determined compared to the visual QC as the gold standard. More specifically, the criteria were defined based on the cut-off values which we determined at the best performance in terms of (sensitivity + specificity)/2. More details and the best cut-off values used for the current version of autoQC are found in the Evaluation section. Finally, if more than a user-specified number (system default: 3) of computed metrics are flagged as 'bad,' the system flags the assessed case as 'bad' and suggests it to be more closely checked.

To finalize a QC report review and submission, the user provides an overall evaluation of the volume on the basis of the result of the auto QC as well as that of their own qualitative QC. The users can either accept the auto QC result or submit their revised annotation. Once reviewed, the report can be saved only, or saved and submitted to the QC database. If the report is only saved, additional changes can still be made until its final submission to the QC database. In each case, the users can convert the report into either PDF or CSV format for further download, distribution, or offline analysis. The entire QC process can be completed within less than a minute for each scan by an expert neuroimaging researcher who has been trained on how to use the system.

QC Study Summaries

One feature being provided by the QC system is the ability is to compile summaries of volume quality over a study or multiple studies with hundreds to thousands of participants, over particular acquisition types (sMRI, DTI, fMRI, etc.), over distinct project sites and over user-defined date ranges when the data were acquired.

Evaluation of the QC Metrics and the Auto QC

To aid in a better understanding of the QC metrics used by the system and provide a guideline to set up the cutoff ranges for the auto QC, we performed the following evaluations with various datasets:

Distribution of QC Metrics in Data Collected Using a Single MRI Sequence

We computed the QC metrics on sMRI data (n = 642; age = 74 $\pm$ 8 years, 25–75% = 68–78 years) that have been collected in the Alzheimer's Disease Neuroimaging Initiative (ADNI) using the same imaging parameter setting (T1-weighted Sagittal MP-RAGE; details found in **Table 1**). In the following analyses, we used the magnitude of each CoM and FWHM by computing $\sqrt{a_x^2 + a_y^2 + a_z^z}$, where a is either CoM or FWHM, instead of analyzing each of x, y, z directional metrics separately.

TABLE 1 | Acquisition parameters for structural MRI of the ADNI dataset.

	Alzheimer's Disease Neuroimaging Initiative (ADNI)
Sequence	Sagittal MP-RAGE/IR-SPGR
TR [ms]	7
TE [ms]	3
TI [ms]	400
Flip angle [degrees]	11
Matrix	256 × 256
Voxel size [mm^3]	1 × 1 × 1
FOV [mm]	(260 – 270) × (252 – 262)
Number of axial slices	176 – 196
Number of scans	642

TR, repetition time; TE, echo time; TI, inversion time; FOV, field of view; MP-RAGE, magnetization-prepared rapid acquisition gradient echo; SPGR, spoiled gradient recalled echo.

To assess the distribution of the QC metrics, we plotted the histogram for each of them. The distributions characterized using the histogram were used as the reference in the following analysis of the data using the multi-sites multi-sequences. For fMRI, we analyzed 657 scans that were selected also from the ADNI project (age = 74 ± 7, 25–75% = 69–78), which were acquired using a single set of imaging parameters (ADNI Axial resting state fMRI protocol) shown in **Table 2**.

Reproducibility of QC Metrics on Data Collected From Multi-Sites, From Different Scanners and Using Multi-MRI Sequences

For sMRI, we used multisite datasets including data from Parkinson's Progression Markers Initiative (PPMI) (Kang et al., 2016) and Transforming Research and Clinical Knowledge in Traumatic Brain Injury (TRACK-TBI) projects while using the ADNI data as the reference of the single sequence imaging data. For TRACK-TBI data, we included only those with non-visible injury on images in the analysis. As a result, we analyzed 1196 T1-weighted imaging data from PPMI (age = 62 ± 10, 25–75% = 56–69) and 1569 from TRACK-TBI projects (age = 37 ± 17, 25–75% = 24–52). For fMRI, we analyzed 1555 from TRACK-TBI (age = 37 ± 16, 25–75% = 24–52). The information of MRI acquisition parameters used in these sMRI and fMRI datasets are presented in **Tables 2**, **3**.

TABLE 2 | Acquisition parameters for the two different resting state-fMRI dataset: ADNI represents data acquired using a single set of imaging parameters whereas Track-TBI represents dataset acquired using various parameters from multi-sites for the cross-validation.

	ADNI	Track-TBI
Sequence	ADNI2 Axial resting-state fMRI	Axial Resting State fMRI
TR [ms]	3000	3000 – 3671
TE [ms]	30	30
TI [ms]	N/A	N/A
Flip angle [degrees]	80	80
Matrix	64 × 64	(60 – 480) × (64 – 512)
Voxel size [mm^3]	3.3 × 3.3 × 3.3	(2.8 – 3.4) × (2.75 – 3.4) × (1 – 3.4)
FOV [mm]	212 × 206	(64 - 512) × (62 – 497)
Number of axial slices	48	39 – 52
Number of frames	140	140, 200
Number of scans	657	1555

TR, repetition time; TE, echo time; TI, inversion time; FOV, field of view.

To assess the distribution of the QC metrics, we plotted the histogram for each of them. For each modality of sMRI or fMRI, we created the histogram separately for each of the two datasets and compared the distribution of each metric between the two datasets. To this end, we first computed the z-score per QC metric using the pooled datasets of the two datasets. Then, the histogram in each dataset was normalized using the same number of the bins and by dividing the height of each bin by the area of the histogram, resulting in an empirical probability density map. Finally, to evaluate whether the manufacturer of the scanner affect the distribution of the QC metrics, we compare the histogram of the QC metrics measured in the subjects scanned on the Siemens scanner which comprised the major portion (n = 655; 42%; more information in **Table 3**) of the TRACK-TBI dataset with those measured in the whole TRACK-TBI dataset.

More subject motion is presumed to be involved in pediatric samples. Furthermore, more CSF volume, less cortical GM volume and smaller GM/WM tissue intensity contrast are expected in elderly (Steen et al., 1995; Salat et al., 2009) and dementia populations (Westlye et al., 2009; Salat et al., 2011). These factors possibly influence the measurement of the QC metrics. Thus, we correlated the age at scanning and each QC metrics. Visual inspection of the shape for each dataset's probability density map and computing the Dice overlap index between them assessed their similarity.

Finally, a user may expect one or a combination of QC metrics to characterize a different aspect of the image artifacts. To evaluate the independency of a given QC metric to others for each modal image data, we constructed a matrix, each component of which computed a Pearson's correlation efficient between the given metric and one of the rest of the metrics.

Reproducibility of QC Metrics for the Cases Scanned on the Same Scanner With the Same MRI Protocol

Four healthy volunteers, as well as a BIRN MRI phantom (Friedman and Glover, 2006), were scanned at 1-week intervals for a month (four scans) using the ADNI3 (Weiner and Veitch, 2015) neuroimaging protocol. This consisted of (A) structural MRI scans, including (i) a magnetization-prepared rapid acquisition gradient echo (MP-RAGE) T_1-weighted scan, (ii) a spoiled gradient-echo (SPGR) T_2*-weighted scan and (iii) a fluid-attenuated inversion recovery (FLAIR) scan, (B) a 126-direction DTI scan, and (C) an fMRI scan. The acquisition parameters for each of these are listed in **Table 4**. These volumes were acquired using the 3 T Siemens Prisma MRI scanner at the Mark and Mary Stevens Neuroimaging and Informatics Institute. All volunteers scanned in the single MRI machine provided written informed consent and the study was undertaken with the approval of the Institutional Review Board at the Keck School of

TABLE 3 | Acquisition parameters for the multi-site datasets used for the cross-validation: structural MRI.

	Track-TBI		PPMI	
Sequence	**Sagittal 3D T1 MPRAGE / 3D T1 IR-SPGR**		**Sagittal 3D T1 MPRAGE or 3D T1 IR-SPGR**	
TR [ms]	4 – 35	1160 – 2530	5 – 11	1650 – 2400
TE [ms]	1 – 8	2 – 20	2 – 6	2 – 20
TI [ms]	400 – 750	500 – 1300	400 – 500	844 – 1100
Flip angle [degrees]	8 – 30	7 – 160	8 – 30	8 – 160
Matrix	(224 – 512) × (256 – 512)	(204 – 512) × (245 – 512)	(256 – 512) × (160 – 512)	(192 – 560) × (192 – 560)
Voxel size [mm^3]	(0.4 – 1.4) × (0.4 – 1.4) × (0.5 – 3)	(0.4 – 1) × (0.4 – 1) × (0.5 – 3)	(0.4 – 1.2) × (0.4 – 1) × (0.7 – 2)	(0.4 – 1.3) × (0.4 – 1.3) × (0.5 – 3)
FOV [mm]	(220 – 350) × (2134 – 340)	(220 – 260) × (214 – 252)	(160 – 266) × (155 – 258)	(220 – 270) × (214 – 262)
Number of axial slices	60 – 336	64 – 208	72 – 256	72 – 240
Number of scans	800	769	286	910
Scanner name (*n*)	Simens Triotrim (655) Simems Skyra (145)	Philips Achiava (531) GE Signa-HDXT (238)	N/A	N/A

TR, repetition time; TE, echo time; TI, inversion time; FOV, field of view; MP-RAGE, magnetization-prepared rapid acquisition gradient echo; SPGR, spoiled gradient recalled echo; N/A, not available.

Medicine of USC and according to the Declaration of Helsinki. The ages of the volunteers were 24, 25, 25, and 35; all were right-handed and healthy, with no history of a neurologic or psychiatric disease. We expected a very small variability in the QC metrics across these images which were acquired in the same scanner relative to data collected from different scanners with different image sequences. We thus performed an *F*-test of Variance on a ratio as $SD_multi_scanner^2/SD_single_scanner^2$, by comparing the variance of each metric for these four individual images with the variance for the multi-site datasets mentioned above. This sample was created by consisting of only subjects in the same range of age as the four volunteers. The smaller the ratio SD_within_scanner/SD_multi_scanner was, the more reproducible the QC metrics were within a scanner.

Performance of Auto QC

We assessed the performance of the auto QC in comparison to the result of the visual inspection. To find the best cutoff values as well as compare these values with the human visual QC results, we used the sMRI data of the TRACK-TBI dataset and tested various cutoff values to identify the QC labels ('good' vs. 'bad') that best agreed with the labels created by systematically performed expert's visual inspection. Here, we tested only sMRI data as visual inspection of sMRI was performed solely using the evaluation of the original images without checking QC metrics. Visual inspection of fMRI normally entails the examination of the QC metrics as well, which could bias the inspection result. Furthermore, no scalar QC metrics were calculated for DTI data and thus the auto QC of DTI was not included in the current system. For visual inspection, we used the following categories of the artifact to identify 'questionable (or moderate)' and 'bad' quality images: ringing artifacts due to motion or aliasing, zipper artifact related to blood flow, impulse noise that likely drops the SNR, magnetic susceptibility creating image geometric distortion, wrap around artifacts happening when the size of the imaged object is larger than the field of view and

TABLE 4 | Acquisition parameters for the four healthy volunteers and 1 phantom scanned using the 3T Siemens Prisma MRI scanner at the Mark and Mary Stevens Neuroimaging and Informatics Institute.

		sMRI		**DTI**	**fMRI**
Weighting	T_1	T_2*	FLAIR	T_2*	N/A
Sequence	MP-RAGE	SPGR	SE	EPI	FSE EPI
TR [ms]	2300.00	650.00	4800.00	3400.00	607.00
TE [ms]	2.95	20.00	441.00	71.00	32.00
TI [ms]	900.00	N/A	1650.00	N/A	N/A
Flip angle [degrees]	9	20	120	90	50
ETL	1	1	243	87	88
Acquisition type	3D	2D	3D	2D	2D
Matrix size	256 × 240	256 × 192	256 × 256	116 × 116	88 × 88
In-plain voxel size [mm]	1.05 × 1.05	0.86 × 0.86	1.00 × 1.00	1.00 × 1.00	2.50 × 2.50
Slice thickness [mm]	1.2	4.0	1.2	2.0	2.5
Phase FOV [%]	93.75	100.00	100	100	100
Bandwidth [Hz/pixel]	240	200	850	2270	2365

The imaging parameters used in this acquisition were chosen in accordance with ADNI3 protocol. sMRI, structural magnetic resonance imaging; DTI, diffusion tensor imaging; fMRI, functional MRI; MP-RAGE, magnetization-prepared rapid acquisition gradient echo; SPGR, spoiled gradient recalled echo; SE, spin echo; EPI, echo planar imaging; FSE, fast SE; TR, repetition time; TE, echo time; TI, inversion time; ETL, echo train length; FOV, field of view; 2D, two-dimensional; 3D, three-dimensional.

small head coverage. The details of the visual inspection are provided in **Supplementary Data 3**. Using this protocol and being independent of the auto QC results, one rater (HT) labeled 1,569 individual t1-weighted sMRI data in the TRACK-TBI set and another rater (RECB) did this for a randomly subsampled 100 cases to test their reproducibility. The 'questionable' quality data in the visual assessment were either merged to 'good' or 'bad.'

To assess the binary classification accuracy of each QC metric with respect to various cutoff values, we first changed the cutoff values per QC metric from z-score = −5 to z-score = 5 with a very small step size (z-score = 0.05). To compute sensitivity and specificity compared to expert labeling, we calculated the receiver operating characteristics (ROCs) and the related area under the curve (AUC). The logistic ROC analysis used a threefold cross-validation approach to estimate AUC and optimal cutoff score that resulted in the greatest accuracy as '(sensitivity + specificity)/2'. Larger AUC values indicated the more accurate classification of participants.

In the Auto QC, more than a user-specified number of computed metrics were flagged as 'bad' and the system flagged the assessed case as 'bad.' Therefore, we assessed how many 'bad' flagged QC metrics should be used to best agree with the labels in the visual inspection. Using the optimal cutoff values that were determined previously, we flagged all the 7 QC metrics either into 'good' or 'bad' and counted the number of the 'bad' labeled metrics per image. At each threshold from 1 to 7, we computed the specificity, sensitivity, and accuracy compared to the visual inspection results.

All p-values were corrected using Bonferroni adjustment.

RESULTS

Processing Time

The processing times for the preprocessing (e.g., brain masking) and calculation of QC metrics (mean ± SD) were approximately 7 min for sMRI, 6 min for CT, 8 min for fMRI and 4 min for DTI on a single Intel i7 CPU. Including the queuing process and possible network traffics, the average computational times were 22.8 ± 6.6 min for sMRI, 18.5 ± 5.9 min for CT, 16.0 ± 4.2 min for fMRI and 7.6 ± 2.2 min for DTI.

Distribution of QC Metrics in Data Collected Using a Single MRI Sequence

For sMRI, the histogram of each QC metric is shown in **Figure 3**. Their mean and SD were: SNR = 21.4 ± 3.0; SVNR = 233 ± 56; CNR = 7.45 ± 3.33; CVNR = 788 ± 1680; TCTV = 1.00 ± 0.58; FWHM = 5.30 ± 0.3; CoM = 17.4 ± 3.8. A visual evaluation found that the distribution of SNR, SVNR, CNR, and FWHM was left-right symmetric and similar to the shape of a Gaussian function whereas that of CVNR and CoM was skewed and close to the shape of an F-distribution function. The distribution of TCTV displayed with two modes and was like the function of a bimodal Gaussian mixture function.

For fMRI, the histograms are shown in **Figure 4**. The mean and SD of each QC metic were: maximum FD (maxFD) = 1.60 ± 8.80; the number of frames with FD > 0.5 (FD > 0.5) = 17.4 ± 24.3; average temporal signal-to-noise ratio (avgTSNR) = 126 ± 31; maximum DVARS (maxDVARS = 83.4 ± 37.4; minimum DVARS (minDVARS) = 23.0 ± 6.1; the number of frames with DVARS > 50 (DVARS > 50) = 21.9 ± 28.4. The distribution of avgTSNR, and minDVARS tended to be left-right symmetric and similar to the shape of Gaussian function whereas that of maxDVARS, maxFD, FD > 0.5 and DVARS > 50 was skewed. The estimated FWHM along each of the x, y, and z axes for fMRI was included in the system. However, because the resultant measurement is not a scalar but a time series vector, we did not include this in the result because of the complexity of the time-series vector metric.

Reproducibility of QC Metrics for Data Acquired on a Scanner Using a Single Imaging Sequence

sMRI

All the individual QC metrics computed for the four volunteers' longitudinal scans are provided in **Tables 5–7**. The means of all the QC metrics for the T1w MRI data were similar to those computed using the ADNI dataset and the multi-site PPMI and TRACK-TBI datasets whereas the variations for these single-scanner-acquired data were significantly smaller than those acquired from the multiple sites (F-test; $F > 19$; $p < 0.00001$). The distribution of each metric did not differ among the four individuals (ANOVA; $F < 2.0$; $p > 0.3$). The computation of the QC metrics in T2* and FLAIR imaging data showed different characteristics of their means and SDs compared to T1-weighted data (paired t-tests; $t > 3.7$; $p < 0.05$), advising the choice of different cutoff values in the auto QC setting depending on the used acquisition sequence. As expected, the mean SNR for the phantom was approximately 3–5 times higher for all three sequences. Similar differences between human subjects and the phantom were observed for the SVNR and FWHM.

fMRI

The computed QC metrics are shown in **Table 8**. As in sMRI, their means were similar to those computed using TRACK-TBI and ADNI datasets except minimum DVARS and maximum DVARS ($t > 4.2$; $p < 0.005$). The variations for all the metrics were significantly smaller (F-test; $F > 15$; $p < 0.00001$). Results illustrated that, as expected, the temporal SNR was four times higher in the phantom whereas the FD and DVARS values were many times larger in human subjects ($t > 21$; $p < 0.00001$). This was because both FD and DVARS reflect greater subject motion, such that larger values are associated with more motion during the scan.

Reproducibility of QC Metrics for Multi-Site and Multi-Scanner Data

sMRI

All the distributions of the sMRI QC metrics are shown in **Figure 3**. The overall shapes of the histogram for all the metrics were similar between the PPMI and ADNI single sequence datasets. The distributions in all the QA metrics of PPMI data were well overlapped with those in the ADNI data, whereas the

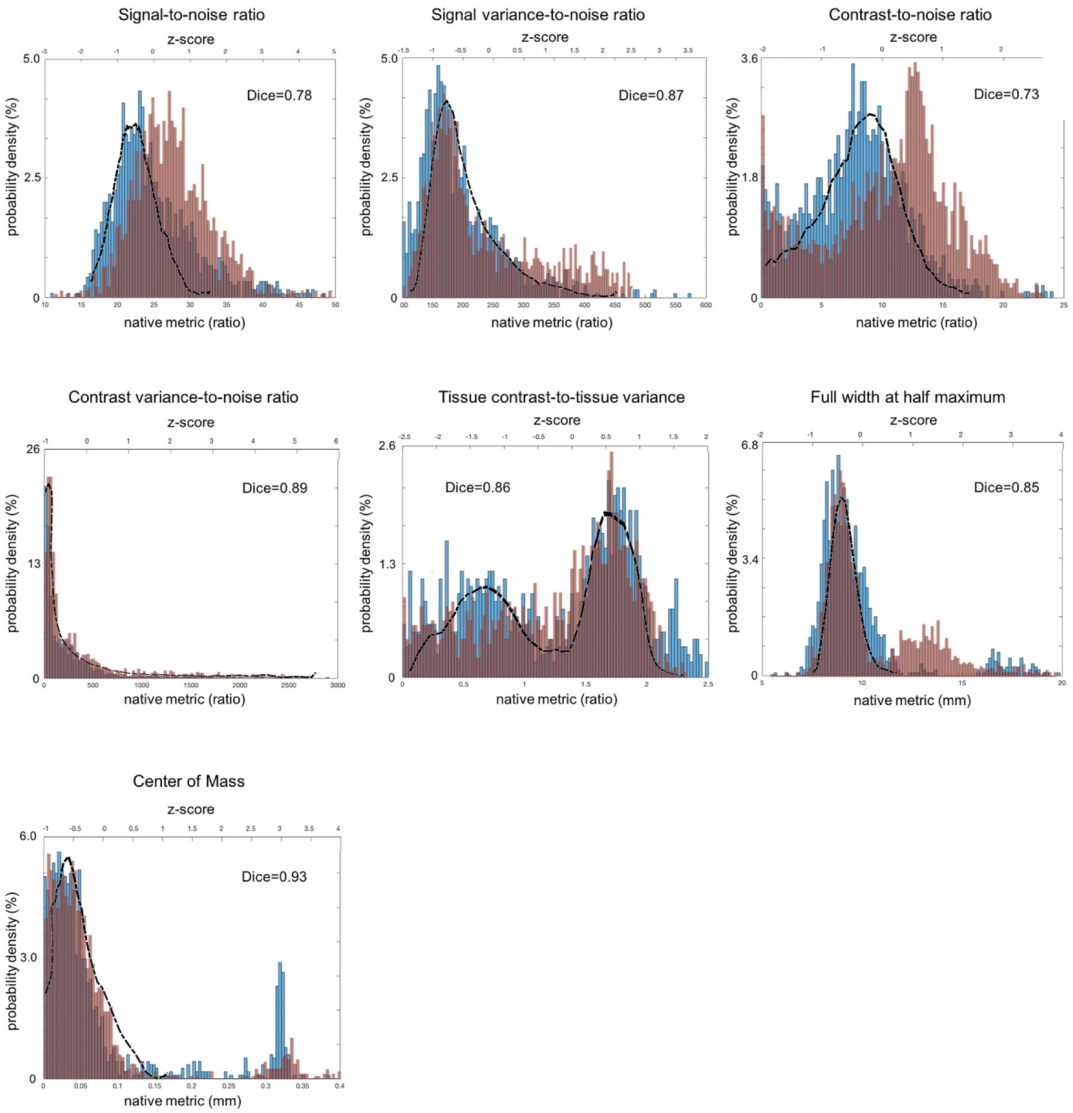


FIGURE 3 | Distribution of sMRI QC metrics for two different datasets that were acquired with multiple imaging parameter settings and collected from multi-sites. The PPMI dataset is colored in blue and the TRACK-TBI in red while the ADNI dataset that was acquired using a single imaging parameter setting is used a reference and shown with the black outline. All the images included in this analysis were based on T1-weighted acquisition (The image sequence parameters are described in **Table 3**). The Dice similarity index was computed for each QC metric to evaluate the overlap between the distributions from the two multi-sites datasets. This was used as a measure of reproducibility of the metrics. Dice index: 0.6–0.8 – good; 0.8–1.00 – excellent (Altman, 1999).

distributions of SNR and CNR in TRACK-TBI data displayed a shift of the whole shape from the PPMI and ADNI data, driven by their higher mean (SNR: +3.1; CNR = +4.2). Indeed, TRACK-TBI data displayed significantly higher mean SNR (26.6 ± 6.0 vs. 27.8 ± 5.8; $t = 4.6$; $p < 0.001$), and higher mean CNR (27 ± 0.1 vs. 27 ± 0.1; $t = 4.8$; $p < 0.001$) than PPMI data. No other QC metrics differed in their means ($p > 0.2$).

The overlap between PPMI and TRACK-TBI datasets was generally very high across metrics (Dice index: $\mu \pm \sigma = 0.88 \pm 0.03$, range: 0.85–0.93) except SNR and CNR (0.76 ± 0.04) that displayed relatively smaller overlap. The largest overlap was observed in CoM (Dice index = 0.93), followed by CVNR (0.89), FWHM (0.87), TCTV (0.86), SVNR (0.85), SNR (0.78) and CNR (0.73), respectively. Despite the high overlap of the main distribution between TRACK-TBI and PPMI datasets, the FWHM displayed significant smaller peaks unequally located in the right-hand tail for both data sets. We found this was driven by a number of cases with artifacts.

The overlap between Siemens data of the TRACK-TBI and the whole TRACK-TBI data was also high across all the metrics (Dice index: $\mu \pm \sigma = 0.90 \pm 0.05$, range: 0.73–0.93) except CoM (0.73) that displayed relatively smaller overlap. The largest overlap was observed in CVNR (Dice index = 0.95), followed by SVNR (0.89), CNR (0.87), TCTV (0.86), SNR (0.85), FWHM (0.82) and CoM (0.73), respectively (**Supplementary Data 4**).

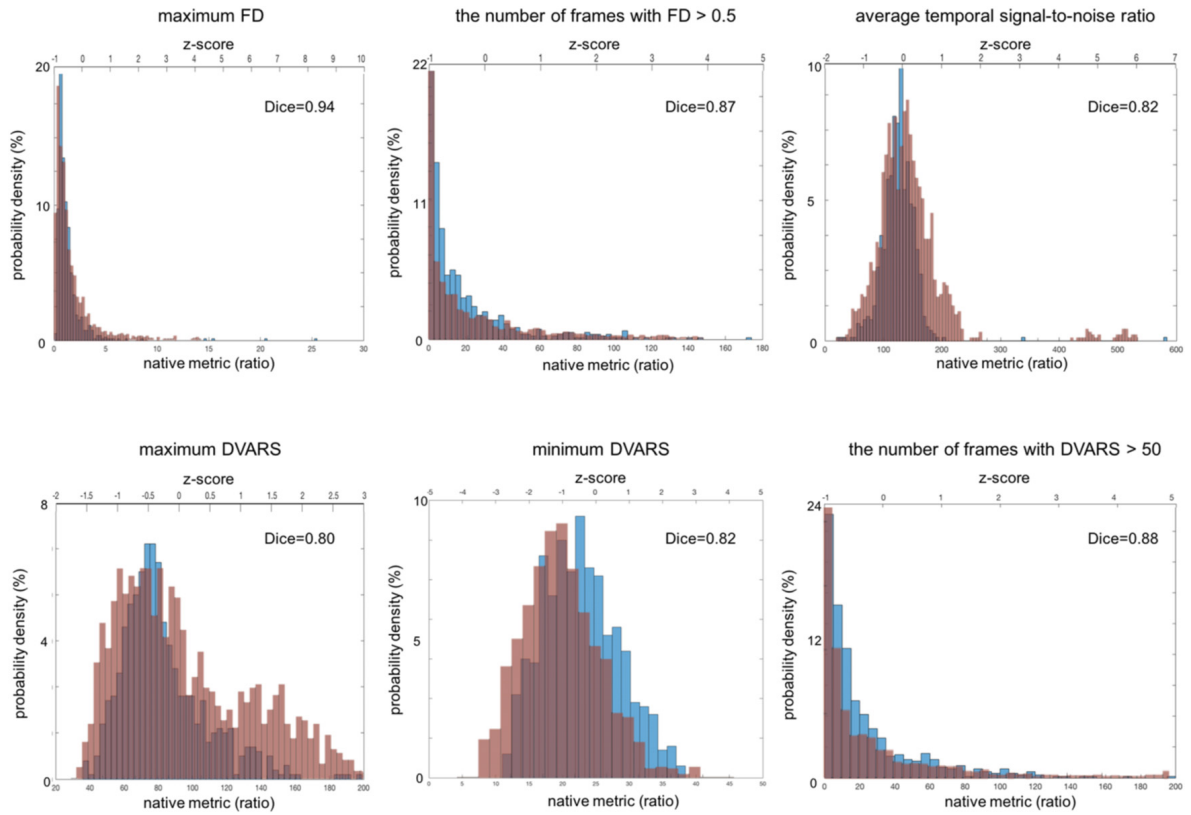


FIGURE 4 | Distribution of fMRI QC metrics for two different multi-site data. The ADNI set that was acquired using a single imaging parameter setting is colored in blue while the TRACK-TBI set that was acquired using multiple imaging parameter settings is in red. All the images included in this analysis were based on Axial Resting State fMRI sequence (details in **Table 3**). The Dice similarity index was computed for each QC metric to evaluate the overlap between the distributions from the two datasets. This was used as a measure of reproducibility of the metrics.

TABLE 5 | QC metrics for T_1-weighted sMRI scans.

	SNR	SVNR	CNR	CVNR	TCTV	FWHM	CoM
S1	29.3 ± 0.5	251 ± 60	12.5 ± 0.1	83 ± 61	1.99 ± 0.34	10.7 ± 0.1	0.16 ± 0.00
S2	31.8 ± 3.4	316 ± 52	10.3 ± 6.0	148 ± 111	1.44 ± 0.55	11.0 ± 0.2	0.18 ± 0.01
S3	30.6 ± 0.8	260 ± 17	15.9 ± 6.8	374 ± 52	1.44 ± 1.06	10.4 ± 0.1	0.17 ± 0.01
S4	30.9 ± 1.8	259 ± 28	14.4 ± 0.6	140 ± 112	1.93 ± 0.91	11.2 ± 0.2	0.15 ± 0.01
All	30.7 ± 1.7	272 ± 26	13.3 ± 3.4	184 ± 83	1.70 ± 0.78	10.8 ± 0.1	0.17 ± 0.01
P	125.9 ± 2.5	569 ± 30	–	–	–	27.8 ± 0.4	0.13 ± 0.01

Shown are the mean μ and standard deviation σ for each subject (S1, S2, S3, and S4) as well as for the phantom (P). CNR, CVNR and TCTV for the phantom were not computed as GM/WM tissue contrast is not defined.

TABLE 6 | QC metrics for T_2* sMRI scans.

	SNR	SVNR	CNR	CVNR	TCTV	FWHM	CoM
S1	26.1 ± 0.3	214 ± 4	2.2 ± 0.9	343 ± 32	0.21 ± 0.09	21.3 ± 0.3	0.19 ± 0.01
S2	30.5 ± 0.2	285 ± 5	1.1 ± 0.9	335 ± 56	0.09 ± 0.08	21.2 ± 0.5	0.20 ± 0.00
S3	28.7 ± 1.5	252 ± 18	1.3 ± 0.6	235 ± 34	0.11 ± 0.05	22.7 ± 0.2	0.19 ± 0.01
S4	25.9 ± 0.7	243 ± 10	1.0 ± 0.5	475 ± 80	0.08 ± 0.04	20.9 ± 0.3	0.18 ± 0.01
All	27.8 ± 0.7	248 ± 9	1.4 ± 0.7	347 ± 51	0.12 ± 0.07	21.5 ± 0.3	0.19 ± 0.01
P	107.5 ± 2.1	582 ± 17	–	–	–	35.9 ± 0.5	0.19 ± 0.01

Shown are the mean μ and standard deviation σ for each subject (S1, S2, S3, and S4) as well as for the phantom (P). CNR, CVNR and TCTV for the phantom were not computed as GM/WM tissue contrast is not defined.

TABLE 7 | QC metrics for FLAIR sMRI scans.

	SNR	SVNR	CNR	CVNR	TCTV	FWHM	CoM
S1	21.4 ± 0.5	154 ± 12	8.6 ± 2.2	43.5 ± 17.7	1.31 ± 0.40	8.81 ± 0.27	0.14 ± 0.01
S2	25.7 ± 0.9	212 ± 14	13.2 ± 0.3	34.1 ± 2.1	1.81 ± 0.04	9.59 ± 0.29	0.16 ± 0.01
S3	25.0 ± 0.8	199 ± 16	11.0 ± 0.4	19.4 ± 4.1	1.66 ± 0.08	9.81 ± 0.20	0.15 ± 0.00
S4	23.2 ± 1.2	196 ± 19	11.7 ± 0.9	34.3 ± 3.4	1.61 ± 0.20	9.73 ± 0.22	0.14 ± 0.01
All	23.8 ± 0.8	190 ± 15	11.1 ± 0.9	32.8 ± 6.8	1.60 ± 0.18	9.49 ± 0.24	0.15 ± 0.01
P	67.0 ± 3.9	186 ± 36	–	–	–	18.3 ± 0.6	0.13 ± 0.01

Shown are the mean μ and standard deviation σ for each subject (S1, S2, S3, and S4) as well as for the phantom (P). CNR, CVNR and TCTV for the phantom were not computed as GM/WM tissue contrast is not defined.

TABLE 8 | QC metrics for fMRI.

	max (FD)	No. FD > 0.5	max (DVARS)	min (DVARS)	No. DVARS > 50	Temporal SNR
S1	0.868 ± 0.591	11.4 ± 14.0	104.2 ± 18.9	30.7 ± 0.8	20.2 ± 10.1	101.8 ± 7.6
S2	0.57 ± 0.318	6.2 ± 7.7	106.9 ± 64.3	29.4 ± 4.9	16.0 ± 11.3	128.9 ± 13.8
S3	0.505 ± 0.118	7.7 ± 7.2	76.7 ± 11.2	36.1 ± 1.7	11.3 ± 15.6	112.4 ± 5.9
S4	2.38 ± 0.648	14.0 ± 12.3	160.8 ± 31.2	33.9 ± 1.6	15.6 ± 17.6	88.5 ± 11.7
All	1.08 ± 0.419	11.1 ± 13.5	112.2 ± 31.4	32.6 ± 2.3	20.1 ± 18.5	108.0 ± 9.8
P	0.047 ± 0.011	0.05 ± 0.01	13.7 ± 0.9	13.1 ± 0.9	0.05 ± 0.01	438.5 ± 40.1

Shown are the mean μ and standard deviation σ for each subject (S1, S2, S3, and S4) as well as for the phantom (P). SNR averages are computed across time. FD values are multiplied by 100 to facilitate comparison.

Analysis of the age at scanning showed no correlation of any QC metric with aging in any dataset (Pearson's correlation coefficient: $r < 0.2$; $p > 0.1$). Subgrouping the TRACK-TBI data into the pediatric (<20 years, $n = 220$) and adult (>20 years, $n = 1349$) groups did not display a difference in any QC metric ($t < 1.0$; $p > 0.4$) between these two groups. However, subgrouping the TRACK-TBI data into the elderly (>60 years, $n = 260$) and non-elderly (<60 years, $n = 1309$) showed a significant drop-down in SNR and CNR in the elderly group relative to the non-elderly ($t > 4.7$; $p < 0.001$). The mean of SNR and CNR in the elderly group of TRACK-TBI did not differ from those computed in PPMI or ADNI dataset ($t < 1.3$; $p > 0.3$). A subsequent investigation found that the lower SNR in the elderly than in the non-elderly group was driven by a significantly lower mean signal intensity within the head (the numerator of SNR; $t = 6.1$; $p < 0.0001$) while a variance of intensity in the background (the denominator of SNR) did not differ between the two age groups ($F = 1.4$; $p > 0.1$). The lower CNR in the elderly was due to a lower mean tissue contrast (the numerator of CNR; $t = 10$; $p < 0.00001$) while the variance of brain intensity (the denominator) was not different between the elderly and non-elderly group.

fMRI

All the distributions of the fMRI QC metrics are shown in **Figure 4**. The overall shapes of the histogram for all the metrics were also very similar between the TRACK-TBI dataset with multiple settings of imaging parameters and ADNI dataset with a single setting of imaging parameters. The overlaps between these two datasets were very high (Dice index: $\mu \pm \sigma = 0.86 \pm 0.05$, range: 0.80–0.94). The largest overlap was observed in maxFD (Dice index = 0.94), followed by DVARS > 50 (0.88), FD > 0.5 (0.87), avgTSNR (0.82), minDVARS (0.82), and maxDVARS (0.80), respectively. The mean and the variance of each metric did not significantly differ between ADNI data than TRACK-TBI ($p > 0.1$). There was no correlation between any QC metric and the age in either of the two groups ($r < 0.2$; $p > 0.1$).

Association of a Given QC Metric With Other Metrics

sMRI (Figure 5A)

Analysis of the correlations between a given QC metric and others in the pooled dataset of TRACK-TBI and PPMI sets showed that most of metrics were not significantly associated ($r < 0.5$; $p > 0.1$) whereas the following pairs were highly correlated: SNR-SVNR, CNR-TCTV, and CoM-FWHM ($r > 0.5$; $p < 0.05$). The reason for their significant correlation was likely due to that SNR and SVNR used the same denominator; CNR and TCTV used the same numerator and; CoM and FWHM characterized similarly about the head shape: i.e., the position and the blurriness.

fMRI (Figure 5B)

Analysis of the correlations between a given QC metric and others in the pooled dataset of TRACK-TBI and ADNI sets showed that the following pairs were highly correlated: maxFD-FD > 0.5, maxFD-maxDVARS, FD > 0.5-maxDVARS, FD > 0.5-minDVARS, DVARS > 50-FD > 50, DVARS > 50-maxDVARS, and DVARS > 50-minDVARS, ($r > 0.3$; $p < 0.05$). The avgTSNR did not correlate with any other metrics ($r < 0.12$; $p > 0.2$).

Evaluation of the Auto QC System

In the visual inspection of 1569 sMRI data in the TRACK-TBI project, 1345 images (85.7%) were classified into 'good,'

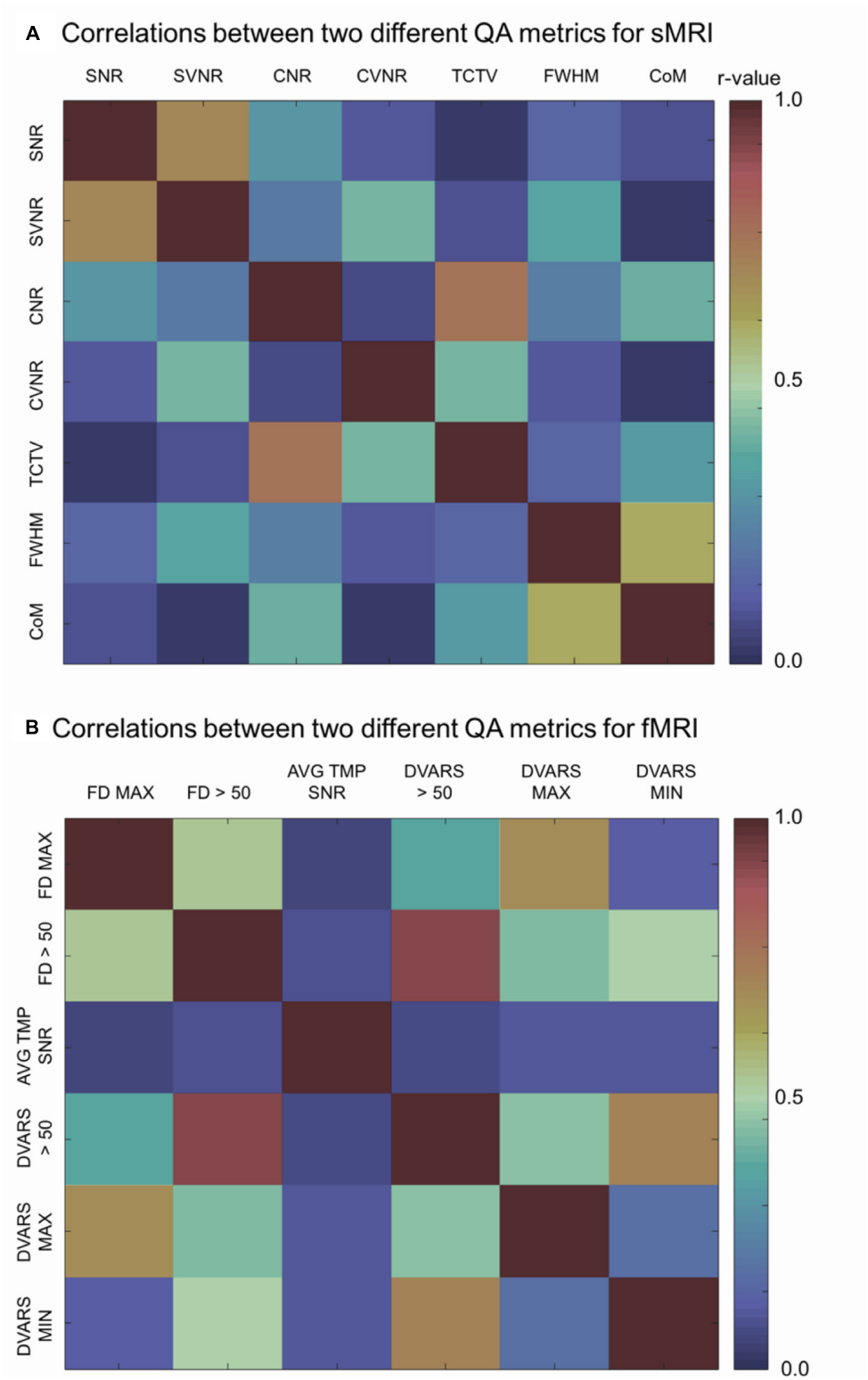


FIGURE 5 | Correlation matrices. Each cell indicates the Pearson's correlation coefficient computed between two indicated QC metrics. SNR, signal-to-noise ratio; SVNR, signal variance-to-noise ratio; CNR, contrast-to-noise ratio; CVNR, Contrast variance-to-noise ratio; TCTV, tissue contrast-to-tissue (intensity) variance; FWHM, full width-at-half maximum; CoM, center of mass; FD MAX, maximum Frame-wise displacement (FD); FD > 0.5, the number of frames with FD is larger than 0.5 mm; AVG TMP SNR, average temporal SNR; DVARS, the root-mean-squared change in blood oxygenation level-dependent signal across time; DVARS > 50, the number of frames with DVARS > 50; DVARS MAX, maximum DVARS; DVARS MIN, minimum DVARS.

TABLE 9 | ROC analysis QC metrics for fMRI.

		Bad vs. Good and Questionable	Bad and Questionable vs. Good
SNR	AUC	0.7235	0.6732
	Sensitivity/Specificity	0.7090/0.7500	0.6465/0.6547
	Cutoff (*Z*-score)	13.0972 (−2.5500)	14.2491 (−2.3500)
SVNR	AUC	0.7369	0.5596
	Sensitivity/Specificity	0.6870/0.7083	0.5685/0.4798
	Cutoff (*Z*-score)	57.0564 (−1.6500)	77.4662 (−1.5000)
CNR	AUC	0.9189	0.728
	Sensitivity/Specificity	0.8171/0.8696	0.6744/0.6528
	Cutoff (*Z*-score)	5.6558 (−0.9500)	9.5552 (−0.2000)
CVNR	AUC	0.6169	0.5131
	Sensitivity/Specificity	0.6047/0.5652	0.4465/0.5648
	Cutoff (*Z*-score)	106.2423 (−0.400)	228.6781 (−0.300)
TCTV	AUC	0.8689	0.696
	Sensitivity/Specificity	0.7999/0.8261	0.5444/0.7963
	Cutoff (*Z*-score)	0.4680 (−1.1000)	1.3580 (0.2500)
FWHM	AUC	0.8447	0.5346
	Sensitivity/Specificity	0.8935/0.8261	0.5667/0.4861
	Cutoff (*Z*-score)	14.3189 (1.3000)	9.9080 (−0.3500)
CoM	AUC	0.8774	0.5559
	Sensitivity/Specificity	0.9446/0.7391	0.7428/0.3843
	Cutoff (*Z*-score)	0.2877 (2.8500)	0.0615 (0)

For each QC metric, the area under the ROC curve (AUC), as well as the sensitivity, specificity and cutoff value at the best performance are displayed. For an easier choice of the cutoff values, we provide the readers the cutoff values in the original metric and z-score. We tested two different classifications: (1) Bad vs. Good and Questionable categories; (2) Bad and Questionable vs. Good. We found that the classification of (1) is overall more accurate using the QC metrics used in our system.

199 (12.8%) into 'questionable' and 25 (1.5%) into 'bad' quality. The kappa statistic of the two raters (HT, RECB) was 92%, indicating excellent agreements between the raters using the protocol described in **Supplementary Data 3**. When merging the 'questionable' cases to the 'good' group, the auto QC for all QC metrics showed higher agreements with the visual inspection results compared to when merging the 'questionable' cases to the 'bad' group (0.61–0.91 vs. 0.51–0.73). The QC metric yielding the largest AUC was CNR (0.91 for good + questionable, 0.73 for bad + questionable), followed by CoM (0.88, 0.56), TCTV (0.87, 0.70), FWHM (0.85, 0.54), SVNR (0.74, 0.56), and CVNR (0.62, 0.51), respectively. At the best cutoff values, the auto QC of FWHM showed the highest classification accuracy, which was 0.86, followed by the analyses of CNR (0.84), CoM (0.84), TCTV (0.81), SNR (0.73), SVNR (0.70), and CVNR (0.58). The results including the cutoff values used for the best performance of the auto QC are summarized in **Table 9** and **Figure 6**. We found that 3 or more QC metrics with 'bad' flags could be used to identify an image as 'bad' and result in the best agreement with the visual inspection (sensitivity = 85%, specificity = 87%, accuracy = 89%; overall AUC = 0.93). This was 3, 0, and 2% higher in sensitivity, specificity, and accuracy compared to the results using the CNR only that yielded the best result among all the QC metrics.

DISCUSSION

Here, we have introduced the LONI QC system, a web-based and expandable system which features a rigorous workflow for the review and assessment of multimodal MRI including sMRI, fMRI, and DTI as well as CT. We also detailed the features of the user-friendly GUI that facilitates user's execution of data uploading, initiating new QC, executing Auto QC, setting parameters for QC, visualizing the resulting QC metrics, vectors and 3D maps, evaluating and revising the QC results, and submitting the final QC. All these functionalities are found in the LONI QC website[8] through the GUI that interacts with the various menus, or panels that were explained in the previous sections. A newly added tutorial helps the users follow the testing with demo data[9] (yellow 'tutorial' button on the top-left corner), which will potentially increase the accessibility of the current functionalities in the system.

In a thorough evaluation of the system using various sets of data acquired from a single scanner and multiple sites and we found a strong degree of similarity among the datasets as well as distinguishing the characteristics specific to each dataset. The QA metrics are generally reproducible both within as well as consistent across subjects. In addition, we found that some data specific properties would be useful to be added as potential covariates in the automated QC method. Notably, anatomical changes due to normal patterns of aging may need to be considered in the user's analyses, especially for SNR and CNR metrics.

Here, we extensively evaluated the utility of the auto QC by analyzing sensitivity and specificity of the cutoff value per sMRI QC metric to the identification of 'bad' quality images in comparison to visual inspection. Our results can be used as a guideline for the proper settings for the QC process and as users' interpretation on the QC in their own data. To the best of our knowledge, the LONI QC is the first online QC system that uniquely supports to perform the image QC of multi-contrast and multimodal brain imaging data. The LONI QC system provides users a various level of image QC from the first aid of the user's own image quality assessment to the high-end QC that automatically flags bad quality images based on the user's setting of cutoff values. This service provides various options of MRI QC (i.e., computation of QC metrics, auto QC, user's own evaluation on QC metrics and visual QC), depending what type of the QC the users prefer to perform. LONI QC differs from the previously developed tools that push the QC to correction of bad quality images by de-noising or removing the voxels or volume frames affected with artifacts (Zhou et al., 2011; Li et al., 2013; Liu et al., 2015). These correction processes are computationally costly.

Pros and Cons of LONI QC Compared to Other Extant QC Systems

Compared to previously developed QC tools, the current QC system has the following new features: It is the first completely online system which is supported by various web-browsers and

[8]http://qc.loni.usc.edu

[9]https://qc.loni.usc.edu/dashboard

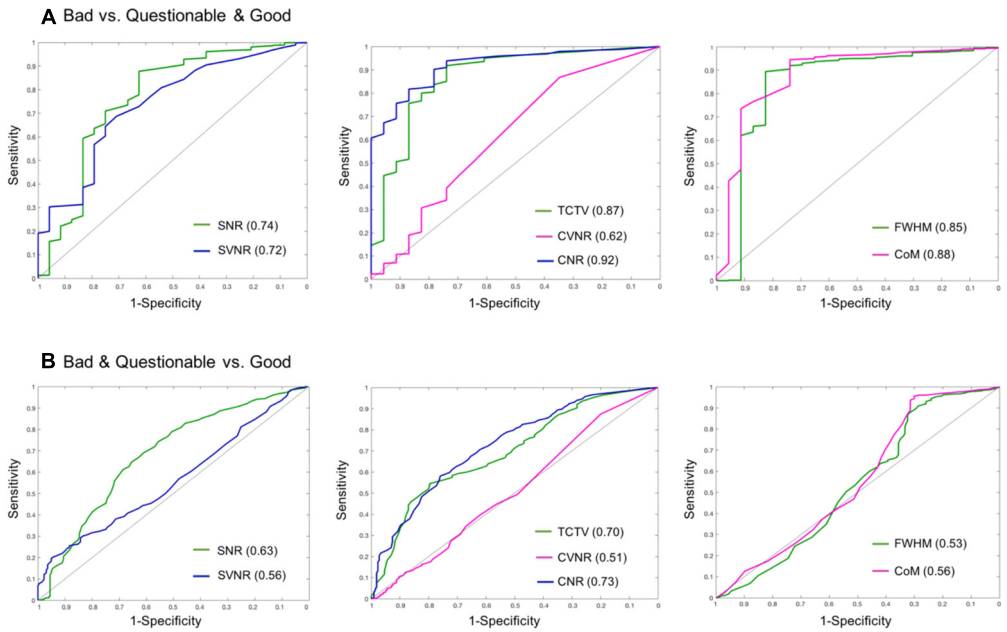


FIGURE 6 | Receiver–operator characteristic (ROC) curves based on using sMRI QC metrics for classification. **(A)** ROCs for differentiating bad data from acceptable data (questionable and good). CNR best differentiated bad data from the acceptable data as it yielded the largest area under the curve (AUC = 0.92). **(B)** ROCs for differentiating poor (bad + questionable) data from good data. CNR and TCTV showed the best performance with AUC = 0.7–0.73. SNR, signal-to-noise ratio; SVNR, signal variance-to-noise ratio; CNR, contrast-to-noise ratio; CVNR, Contrast variance-to-noise ratio; TCTV, tissue contrast-to-tissue (intensity) variance; FWHM, full width-at-half maximum; CoM, center of mass.

requires no preinstalled software. The online system allows users to anonymously upload imaging data to the LONI QC system, either through LONI Integrated Data Archive (IDA) or using a direct uploading interface, thus having no issue of identity theft in the processed data. The automated QC has been set with the default parameters using those determined as in **Table 9**, which can be adapted to the user's data. It computes a standard set of QC metrics that have been described in the literature and performs a standardized QC via an automated pre-processing system which is specifically designed to generate a range of scalar and vector statistics along with derived images. The QC data processing is performed on the LONI processing grid in the USC Mark and Mary Stevens Neuroimaging and Informatics Institute making possible parallel computing using a cluster of thousands of central processing units (CPUs) whereas the previously developed approaches were designed to work on a single-core of the personal computer where the source code was downloaded. LONI QC system also features a user-friendly web-based GUI and a tutorial with demo data that help particularly novice users get familiar with the QC system.

There are several important considerations that potentially improve the LONI QC approach compared to the current limitations of other approaches: First, it is freely accessible through the Internet so that it is impossible to process offline data while also provided as a downloadable framework which runs on the user's local computing environment – but which does necessitate the independent installation of prerequisite software. The LONI QC system is partly dependent on the data archiving capacity of the IDA. Large size image datasets are preferably collected and archived in the IDA prior to the QC execution. The direct data uploading module has been tested with a small set of data ($n < 30$ at one uploading) with a small number of simultaneous network connections (number of users < 5). This eventually prevents the users from keeping their image data in our online storage after QC reports are generated. The capacity of the network traffic and the data storage in our computing cluster when using the direct uploading module is currently being expanded and tested by our developer team, allowing the affordability of more users who have difficulty or are reluctant to access LONI QC system through the IDA. Second, the current system has yet to support the auto QC of DTI data as no scalar QC metrics for DTI are computed. Roalf and his colleagues in their recent work (Roalf et al., 2016) devised a number of DTI QC metrics and showed a high degree of sensitivity and specificity. Indeed, it is particularly challenging for a human rater to assess the quality of the time series volumes of fMRI and the multidirectional volumes of DTI data. Therefore, we plan to include the quantitative metrics discussed by Roalf et al. (2016) or equivalent ones, to support the auto QC of DTI data in future releases of LONI QC. Third, the optimal setting of cutoff values for auto QC may vary depending on the image sequence and weighting methods, as also shown in the current study. In pediatric imaging data, a greater degree of motion artifact can be involved compared to adult data. This may require an adaptive setting regarding such confounding effects. The current version of the system provides the default setting with

the parameters achieved in our evaluation (see **Table 9**) with a flexibility of scaling cutoff values by the users. Furthermore, the current system only analyzes each QC metric separately using a univariate fashion. A machine learning approach using multivariate modeling of the QC metric's distribution can classify the quality of each image data with a higher accuracy as found in Pizarro et al. (2016), Esteban et al. (2017), and Fonov et al. (2018). Fourth, recent studies (Li et al., 2013; Oguz et al., 2014; Power et al., 2014) developed and evaluated methods to reduce, correct or remove some types of artifacts existing on DTI and fMRI images. Such image reconstruction or enhancement, albeit with the possibility of inducing a bias, may help to decrease the chance of permanent exclusions of the cases with a bad image quality from the subsequent biological or clinical analyses. Fifth, a previous study (Mortamet et al., 2009) designed QC metrics that are sensitive to the identification of machine-inherent noises (e.g., Gaussian noise, aliasing, zipper pattern) by masking out the head area in measurement whereas we included a more variety of QC metrics that can capture the types of noise occurring inside (e.g., head motion) and outside the brain region. Finally, a future improvement of the study is to evaluate the effects of running LONI-QC on the performance in subsequent image analysis. This can be hinted by the attempts made for the quality assurance of post-image processing such as in the studies evaluating brain structural segmentation on sMRI (Keshavan et al., 2017) and fiber tractography extracted from DTI data (Sommer et al., 2017).

Reproducibility of the QC Metrics Adopted in LONI QC System

The choice of metrics when evaluating the quality of a neuroimaging dataset has substantial implications for how data processing steps are carried out subsequent to image acquisition. In the current system, we included a broad range of QC metrics modeling various aspects of the image artifacts possibly occurring during image acquisition. Many of these metrics were also chosen or developed by other studies in the literature (Friedman and Glover, 2006; Power et al., 2012; Li et al., 2013; Marcus et al., 2013; Pizarro et al., 2016). The histogram analysis of these metrics showed their reproducibility in multiple datasets including those acquired with a single setting of imaging acquisition parameters or with multiple settings of imaging parameters used in multiple scanners. The distributions of these metrics were not significantly influenced by different parameter settings if the analyzed images were acquired using the same sequence (e.g., T1-weighted) and the same modality (sMRI, fMRI, DTI). On the other hand, results in the analysis of T1-weighted sMRI suggest that the means of SNR and CNR can differ when imaging elderly or a dementia patient populations. In the analysis of the possible introduction of larger motion artifacts in younger subjects, we did not observe the influence of the age variation on the QC metrics measured in the data tested here. While this finding shows the age would not be a confounding factor in younger adult cohorts of TRACK-TBI, it does not necessarily imply that the severity of motion artifacts in pediatric data is as same as that in adult data. Previous studies indeed showed that some obvious bad quality images displayed a significant correlation between QC metrics and age (Roalf et al., 2016) and prospective motion correction improved diagnostic sensitivity in pediatric data (Kuperman et al., 2011).

When data are collected in a single machine with uniform imaging parameters, the variance of the QC metrics becomes significantly smaller, suggesting that the variance in the multi-site data partly explains the machine characteristics and the difference in imaging parameters. On the other hand, differences in the image sequence (e.g., T1-weighted, T2-weighted, FLAIR), even acquiring a same modality image appear to create a significant difference in their distribution, suggesting that the direct comparison of the QC metrics resulting from two datasets acquired using different image sequences may not be suitable. The users may need to consider the aforementioned factors in setting the proper cutoff values in the auto QC to identify bad quality images.

Correlational analyses illustrated that the major proportion of the QC metrics in sMRI were not associated each other whereas many in fMRI showed significant correlations each other. The main reason why the many fMRI QC metrics were correlated is likely that these metrics characterize temporal signal changes or head displacements that can be driven by head motion. The LONI QC system was designed with this in mind, and one of its strengths is that it calculates for the users not only standard—and occasionally correlated—metrics such as the CNR and CVNR, but also more information-rich evaluations. In doing so, the LONI QC system provides a platform for evaluating the relationships between a wide variety of QC metrics and allows the users to choose those metrics which may be more relevant in their studies. Generating QC vectors and 3D maps, a greater variety of choices is given for the users to perform image quality assurance and control in depth. This idea is not different from those adopted in the previously published works (Oguz et al., 2014; Esteban et al., 2017). Eventually feature reconstruction approaches such as principal component analysis (Tenenbaum et al., 2000) or independent component analysis (Cao et al., 2003) may reduce the number of QC metrics while keeping their QC performance by projecting them on to the axes that explain larger variations of the data or better explain the information implied in the data.

Auto QC: Comparison to Visual Inspection

Recent studies have made an unprecedented effort to acquire an enormous size of MRI dataset in line with the emergence of the new generation of the analysis in 'BIG' data. Nearly every week, more than 1000 new scans of sMRI, fMRI or DTI data are archived in the repository of the LONI-IDA. The tedious and time-consuming visual inspection in the quality of such massive datasets is not practical. Automated QC that quantifies image QC metrics, and labels the degree of image quality is of major interest and there have been recent attempts to substitute the manual QC procedure. In the current paper, we introduced such an automated procedure that used various QC metrics and their cutoff values to flag bad quality images. The strength of LONI QC and other similar methods that were proposed recently (Oguz et al., 2014; Pizarro et al., 2016; Roalf et al., 2016;

Esteban et al., 2017) lies on the use of multiple QC metrics that characterize various aspects of image artifacts involved in the brain image acquisition. Furthermore, these metrics have an ability to differentiate the degree of the artifact severity as they are continuous and not categorical or dichotomous (i.e., good or bad).

However, the results from automated QC and similarly those previously published (Pizarro et al., 2016; Roalf et al., 2016; Esteban et al., 2017) do not always fully agree with the visual inspection results. This is because the univariate analysis of each metric may be able to detect one type of the image artifact whereas the visual assessment performs a comprehensive evaluation where the deterioration in image quality is multifaceted with simultaneously occurring multiple noise types. The use of thresholds along with the number of simultaneously occurring 'bad' QC metrics further improved the classification accuracy. Another study (Pizarro et al., 2016) used a multivariate analysis by employing a support-vector machine-based classifier and showed the potential improvement against univariate analyses. Interestingly, the QC metrics utilized in LONI QC were more sensitive to the classification when merging the 'questionable' or 'moderate' quality images to 'good' images. We separately performed the 3-class classification, but this showed a worse result (AUC = 0.5–0.6) than 2 class classification. This suggests that questionable cases would not be clustered as an independent "moderate" group, but their characteristics would be closer to that of the "good" group. However, it is not clear whether or not the questionable quality images are potentially problematic in the post-image processing or the subsequent biological/clinical analyses. Further examination of quality clustering will form the basis of ongoing activities for the LONI QC framework.

CONCLUSION

Quality control of neuroimaging data is an essential, though a complex and challenging component of image processing and analysis. Although many previous studies have aimed to identify an ideal set of measures which can distinguish between images of good and bad quality, it remains the case that different researchers have different intuitive, qualitative and quantitative standards of what image quality should be, and of how that quality ought to be quantified. The LONI QC system was specifically designed with these considerations in mind, and is the first both web-based and freely-available QC system which provides users with the ability to specify their own standard of image quality, automatically apply that standard to their data, and then download the results of their QC analysis in CSV and/or PDF format for further post-processing using the tools and methods of their choice. Because it accommodates a wide variety of imaging modalities, the LONI QC system can appeal to a substantial cross-section of researchers in the neuroimaging community who are interested in applying and maintaining the highest standards of image quality to their image analyses and, by extension, to their research efforts. The streamlined integration of the LONI QC system with the LONI IDA and with the LONI Pipeline—both of which are widely used by neuroimaging researchers—throws additional weight behind the argument that this novel, state-of-the-art system can be easily adopted by a large number of neuroimaging researchers worldwide, thereby potentially leading to the formulation and adoption of a much-needed standardized protocol for neuroimaging QC and analysis.

AUTHOR CONTRIBUTIONS

HK: study design, evaluation, statistical analysis, and manuscript drafting. AI: study design, evaluation, and manuscript drafting. SH, PP, and MP: implementation and system maintenance. HT: assisted in evaluation. RE: manual/visual quality control. BD, S-LL, KC, and ML: statistical analysis and manuscript editing. LZ: data acquisition, statistical analysis, and manuscript editing. KLC: data accessing and implementation. PM and GM: data acquisition and sharing. JVH: study design, manuscript editing, and revising. AT: study design, primary funding, and manuscript editing.

FUNDING

This study was supported by the National Institutes of Health grants (P41EB015922, U54EB020406, K01HD091283, U19AG024904, U01NS086090, and 003585-00001).

ACKNOWLEDGMENTS

The authors would like to thank the donors of the Alzheimer's Disease Research, a program of BrightFocus Foundation, for supporting this research. The authors would also like to thank the Alzheimer's Disease Neuroimaging Initiative (ADNI) and the Parkinson's Progression Markers Initiative (PPMI).

SUPPLEMENTARY MATERIAL

The Supplementary Material for this article can be found online at: https://www.frontiersin.org/articles/10.3389/fninf.2019.00060/full#supplementary-material

REFERENCES

Altman, D. G. (1999). *Practical Statistics for Medical Research*. Boca Raton, FL: CRC Press.

Anderson, A. W. (2001). Theoretical analysis of the effects of noise on diffusion tensor imaging. *Magn. Reson. Med.* 46, 1174–1188. doi: 10.1002/mrm.1315

Bastin, M. E., Armitage, P. A., and Marshall, I. (1998). A theoretical study of the effect of experimental noise on the measurement of anisotropy in diffusion imaging. *Magn. Reson. Imaging* 16, 773–785. doi: 10.1016/S0730-725x(98)00098-98

Cao, L. J., Chua, K. S., Chong, W. K., Lee, H. P., and Gu, Q. M. (2003). A comparison of PCA, KPCA and ICA for dimensionality reduction in support

vector machine. *Neurocomputing* 55, 321–336. doi: 10.1016/S0925-2312(03)00433-438

Cox, R. W. (1996). AFNI: software for analysis and visualization of functional magnetic resonance neuroimages. *Comput. Biomed. Res.* 29, 162–173. doi: 10.1006/cbmr.1996.0014

Crawford, K. L., Neu, S. C., and Toga, A. W. (2016). The image and data archive at the laboratory of neuro imaging. *Neuroimage* 124(Pt B), 1080–1083. doi: 10.1016/j.neuroimage.2015.04.067

Esteban, O., Birman, D., Schaer, M., Koyejo, O. O., Poldrack, R. A., and Gorgolewski, K. J. (2017). MRIQC: predicting quality in manual MRI assessment protocols using no-reference image quality measures. *bioRxiv*

Fesl, G., Braun, B., Rau, S., Wiesmann, M., Ruge, M., Bruhns, P., et al. (2008). Is the center of mass (COM) a reliable parameter for the localization of brain function in fMRI? *Eur. Radiol.* 18, 1031–1037. doi: 10.1007/s00330-008-0850-z

Fonov, V., Dadar, M., and Collins, D. L. (2018). Deep learning of quality control for stereotaxic registration of human brain MRI. *bioRxiv*

Friedman, L., and Glover, G. H. (2006). Report on a multicenter fMRI quality assurance protocol. *J. Magn. Reson. Imaging* 23, 827–839. doi: 10.1002/jmri.20583

Heim, S., Hahn, K., Samann, P. G., Fahrmeir, L., and Auer, D. P. (2004). Assessing DTI data quality using bootstrap analysis. *Magn. Reson. Med.* 52, 582–589. doi: 10.1002/mrm.20169

Jezzard, P., Barnett, A. S., and Pierpaoli, C. (1998). Characterization of and correction for eddy current artifacts in echo planar diffusion imaging. *Magn. Reson. Med.* 39, 801–812. doi: 10.1002/mrm.1910390518

Jones, D. K., Knosche, T. R., and Turner, R. (2013). White matter integrity, fiber count, and other fallacies: the do's and don'ts of diffusion MRI. *Neuroimage* 73, 239–254. doi: 10.1016/j.neuroimage.2012.06.081

Kang, J. H., Mollenhauer, B., Coffey, C. S., Toledo, J. B., Weintraub, D., Galasko, D. R., et al. (2016). CSF biomarkers associated with disease heterogeneity in early Parkinson's disease: the Parkinson's progression markers initiative study. *Acta Neuropathol.* 131, 935–949. doi: 10.1007/s00401-016-1552-1552

Keshavan, A., Datta, E., Mcdonough, I. M., Madan, C. R., Jordan, K., and Henry, R. G. (2017). Mindcontrol: a web application for brain segmentation quality control. *Neuroimage* 170, 365–372. doi: 10.1016/j.neuroimage.2017.03.055

Kuperman, J. M., Brown, T. T., Ahmadi, M. E., Erhart, M. J., White, N. S., Roddey, J. C., et al. (2011). Prospective motion correction improves diagnostic utility of pediatric MRI scans. *Pediatr. Radiol.* 41, 1578–1582. doi: 10.1007/s00247-011-2205-2201

Lauzon, C. B., Asman, A. J., Esparza, M. L., Burns, S. S., Fan, Q., Gao, Y., et al. (2013). Simultaneous analysis and quality assurance for diffusion tensor imaging. *PLoS One* 8:e61737. doi: 10.1371/journal.pone.0061737

Lazar, M., Weinstein, D. M., Tsuruda, J. S., Hasan, K. M., Arfanakis, K., Meyerand, M. E., et al. (2003). White matter tractography using diffusion tensor deflection. *Hum. Brain Mapp.* 18, 306–321. doi: 10.1002/hbm.10102

Le Bihan, D., Poupon, C., Amadon, A., and Lethimonnier, F. (2006). Artifacts and pitfalls in diffusion MRI. *J. Magn. Reson. Imaging* 24, 478–488. doi: 10.1002/jmri.20683

Li, Y., Shea, S. M., Lorenz, C. H., Jiang, H., Chou, M. C., and Mori, S. (2013). Image corruption detection in diffusion tensor imaging for post-processing and real-time monitoring. *PLoS One* 8:e49764. doi: 10.1371/journal.pone.0049764

Liu, B., Zhu, T., and Zhong, J. (2015). Comparison of quality control software tools for diffusion tensor imaging. *Magn. Reson. Imaging* 33, 276–285. doi: 10.1016/j.mri.2014.10.011

Marcus, D. S., Harms, M. P., Snyder, A. Z., Jenkinson, M., Wilson, J. A., Glasser, M. F., et al. (2013). Human connectome project informatics: quality control, database services, and data visualization. *Neuroimage* 80, 202–219. doi: 10.1016/j.neuroimage.2013.05.077

Mori, S., Crain, B. J., Chacko, V. P., and van Zijl, P. C. (1999). Three-dimensional tracking of axonal projections in the brain by magnetic resonance imaging. *Ann. Neurol.* 45, 265–269. doi: 10.1002/1531-8249(199902)45:2<265::aid-ana21>3.0.co;2-3

Mortamet, B., Bernstein, M. A., Jack, C. R. Jr., Gunter, J. L., Ward, C., Britson, P. J., et al. (2009). Automatic quality assessment in structural brain magnetic resonance imaging. *Magn. Reson. Med.* 62, 365–372. doi: 10.1002/mrm.21992

Oguz, I., Farzinfar, M., Matsui, J., Budin, F., Liu, Z., Gerig, G., et al. (2014). DTIPrep: quality control of diffusion-weighted images. *Front. Neuroinform.* 8:4. doi: 10.3389/fninf.2014.00004

Owens, S. F., Picchioni, M. M., Ettinger, U., McDonald, C., Walshe, M., Schmechtig, A., et al. (2012). Prefrontal deviations in function but not volume are putative endophenotypes for schizophrenia. *Brain* 135(Pt 7), 2231–2244. doi: 10.1093/brain/aws138

Pizarro, R. A., Cheng, X., Barnett, A., Lemaitre, H., Verchinski, B. A., Goldman, A. L., et al. (2016). Automated quality assessment of structural magnetic resonance brain images based on a supervised machine learning algorithm. *Front. Neuroinform.* 10:52. doi: 10.3389/fninf.2016.00052

Power, J. D., Barnes, K. A., Snyder, A. Z., Schlaggar, B. L., and Petersen, S. E. (2012). Spurious but systematic correlations in functional connectivity MRI networks arise from subject motion. *Neuroimage* 59, 2142–2154. doi: 10.1016/j.neuroimage.2011.10.018

Power, J. D., Mitra, A., Laumann, T. O., Snyder, A. Z., Schlaggar, B. L., and Petersen, S. E. (2014). Methods to detect, characterize, and remove motion artifact in resting state fMRI. *Neuroimage* 84, 320–341. doi: 10.1016/j.neuroimage.2013.08.048

Reiser, M., Semmler, W., and Hricak, H. (2008). *Magnetic Resonance Tomography*. Berlin: Springer.

Reuter, M., Tisdall, M. D., Qureshi, A., Buckner, R. L., van der Kouwe, A. J. W., and Fischl, B. (2015). Head motion during MRI acquisition reduces gray matter volume and thickness estimates. *Neuroimage* 107, 107–115. doi: 10.1016/j.neuroimage.2014.12.006

Rex, D. E., Ma, J. Q., and Toga, A. W. (2003). The LONI pipeline processing environment. *Neuroimage* 19, 1033–1048. doi: 10.1016/s1053-8119(03)00185-x

Roalf, D. R., Quarmley, M., Elliott, M. A., Satterthwaite, T. D., Vandekar, S. N., Ruparel, K., et al. (2016). The impact of quality assurance assessment on diffusion tensor imaging outcomes in a large-scale population-based cohort. *Neuroimage* 125, 903–919. doi: 10.1016/j.neuroimage.2015.10.068

Salat, D. H., Chen, J. J., van der Kouwe, A. J., Greve, D. N., Fischl, B., and Rosas, H. D. (2011). Hippocampal degeneration is associated with temporal and limbic gray matter/white matter tissue contrast in Alzheimer's disease. *Neuroimage* 54, 1795–1802. doi: 10.1016/j.neuroimage.2010.10.034

Salat, D. H., Lee, S. Y., van der Kouwe, A. J., Greve, D. N., Fischl, B., and Rosas, H. D. (2009). Age-associated alterations in cortical gray and white matter signal intensity and gray to white matter contrast. *Neuroimage* 48, 21–28. doi: 10.1016/j.neuroimage.2009.06.074

Satterthwaite, T. D., Wolf, D. H., Loughead, J., Ruparel, K., Elliott, M. A., Hakonarson, H., et al. (2012). Impact of in-scanner head motion on multiple measures of functional connectivity: relevance for studies of neurodevelopment in youth. *Neuroimage* 60, 623–632. doi: 10.1016/j.neuroimage.2011.12.063

Skare, S., Hedehus, M., Moseley, M. E., and Li, T. Q. (2000). Condition number as a measure of noise performance of diffusion tensor data acquisition schemes with MRI. *J. Magn. Reson.* 147, 340–352. doi: 10.1006/jmre.2000.2209

Sled, J. G., Zijdenbos, A. P., and Evans, A. C. (1998). A nonparametric method for automatic correction of intensity nonuniformity in MRI data. *IEEE Trans. Med. Imaging* 17, 87–97. doi: 10.1109/42.668698

Sommer, S., Kozerke, S., Seifritz, E., and Staempfli, P. (2017). Fiber up-sampling and quality assessment of tractograms - towards quantitative brain connectivity. *Brain Behav.* 7:e00588. doi: 10.1002/brb3.588

Steen, R. G., Gronemeyer, S. A., and Taylor, J. S. (1995). Age-related changes in proton T1 values of normal human brain. *J. Magn. Reson. Imaging* 5, 43–48. doi: 10.1002/jmri.1880050111

Tenenbaum, J. B., de Silva, V., and Langford, J. C. (2000). A global geometric framework for nonlinear dimensionality reduction. *Science* 290, 2319–2323. doi: 10.1126/science.290.5500.2319

Van Dijk, K. R., Sabuncu, M. R., and Buckner, R. L. (2012). The influence of head motion on intrinsic functional connectivity MRI. *Neuroimage* 59, 431–438. doi: 10.1016/j.neuroimage.2011.07.044

Weiner, M. W., and Veitch, D. P. (2015). Introduction to special issue: overview of Alzheimer's disease neuroimaging initiative. *Alzheimers Dement.* 11, 730–733. doi: 10.1016/j.jalz.2015.05.007

Westlye, L. T., Walhovd, K. B., Dale, A. M., Espeseth, T., Reinvang, I., Raz, N., et al. (2009). Increased sensitivity to effects of normal aging and Alzheimer's disease on cortical thickness by adjustment for local variability in gray/white contrast: a multi-sample MRI study. *Neuroimage* 47, 1545–1557. doi: 10.1016/j.neuroimage.2009.05.084

Worsley, K. J., Evans, A. C., Marrett, S., and Neelin, P. (1992). A three-dimensional statistical analysis for CBF activation studies in human brain. *J. Cereb. Blood Flow Metab.* 12, 900–918. doi: 10.1038/jcbfm.1992.127

Yoshida, S., Oishi, K., Faria, A. V., and Mori, S. (2013). Diffusion tensor imaging of normal brain development. *Pediatr. Radiol.* 43, 15–27. doi: 10.1007/s00247-012-2496-x

Zhou, Z., Liu, W., Cui, J., Wang, X., Arias, D., Wen, Y., et al. (2011). Automated artifact detection and removal for improved tensor estimation in motion-corrupted DTI data sets using the combination of local binary patterns and 2D partial least squares. *Magn. Reson. Imaging* 29, 230–242. doi: 10.1016/j.mri.2010.06.022

Conflict of Interest Statement: The authors declare that the research was conducted in the absence of any commercial or financial relationships that could be construed as a potential conflict of interest.

Copyright © 2019 Kim, Irimia, Hobel, Pogosyan, Tang, Petrosyan, Esquivel Castelo Blanco, Duffy, Zhao, Crawford, Liew, Clark, Law, Mukherjee, Manley, Van Horn and Toga. This is an open-access article distributed under the terms of the Creative Commons Attribution License (CC BY). The use, distribution or reproduction in other forums is permitted, provided the original author(s) and the copyright owner(s) are credited and that the original publication in this journal is cited, in accordance with accepted academic practice. No use, distribution or reproduction is permitted which does not comply with these terms.

frontiers in Neuroinformatics

TECHNOLOGY REPORT
published: 19 September 2019
doi: 10.3389/fninf.2019.00063

CoreNEURON : An Optimized Compute Engine for the NEURON Simulator

Pramod Kumbhar[1], *Michael Hines*[2], *Jeremy Fouriaux*[1], *Aleksandr Ovcharenko*[1], *James King*[1], *Fabien Delalondre*[1] *and Felix Schürmann*[1]*

[1] *Blue Brain Project, École Polytechnique Fédérale de Lausanne (EPFL), Geneva, Switzerland,* [2] *Department of Neuroscience, Yale University, New Haven, CT, United States*

The NEURON simulator has been developed over the past three decades and is widely used by neuroscientists to model the electrical activity of neuronal networks. Large network simulation projects using NEURON have supercomputer allocations that individually measure in the millions of core hours. Supercomputer centers are transitioning to next generation architectures and the work accomplished per core hour for these simulations could be improved by an order of magnitude if NEURON was able to better utilize those new hardware capabilities. In order to adapt NEURON to evolving computer architectures, the compute engine of the NEURON simulator has been extracted and has been optimized as a library called CoreNEURON. This paper presents the design, implementation, and optimizations of CoreNEURON. We describe how CoreNEURON can be used as a library with NEURON and then compare performance of different network models on multiple architectures including IBM BlueGene/Q, Intel Skylake, Intel MIC and NVIDIA GPU. We show how CoreNEURON can simulate existing NEURON network models with 4–7x less memory usage and 2–7x less execution time while maintaining binary result compatibility with NEURON.

Keywords: NEURON, simulation, neuronal networks, supercomputing, performance optimization

OPEN ACCESS

Edited by:
Arjen van Ooyen,
VU University Amsterdam, Netherlands

Reviewed by:
Anders Lansner,
Stockholm University, Sweden
Thomas Nowotny,
University of Sussex, United Kingdom

***Correspondence:**
Felix Schürmann
felix.schuermann@epfl.ch

Received: *01 June 2019*
Accepted: *04 September 2019*
Published: *19 September 2019*

Citation:
Kumbhar P, Hines M, Fouriaux J, Ovcharenko A, King J, Delalondre F and Schürmann F (2019) CoreNEURON : An Optimized Compute Engine for the NEURON Simulator. Front. Neuroinform. 13:63. doi: 10.3389/fninf.2019.00063

1. INTRODUCTION

Simulation in modern neuroscientific research has become a third pillar of the scientific method, complementing the traditional pillars of experimentation and theory. Studying models of brain components, brain tissue or even whole brains provides new ways to integrate anatomical and physiological data and allow insights into causal mechanisms crossing scales and linking structure to function. Early studies covered for example the levels from channels to cell behavior accounting for detailed morphology (e.g., De Schutter and Bower, 1994; Mainen and Sejnowski, 1996) and integrating this detail into models of networks (e.g., Davies, 1992). More recently, studies have been accounting for increased electrophysiological detail and diversity in the tissue model (e.g., Markram et al., 2015; Arkhipov et al., 2018), giving a glimpse at functional importance of the underlying connectome (e.g., Gal et al., 2017; Reimann et al., 2017) allowing for example the reinterpretation of aggregate brain signals such as LFP (e.g., Anastassiou et al., 2015). At the same time, computational studies have strived to look even deeper into the biochemical workings of the cell, studying the role of intracellular cascades in neuromodulation (e.g., Lindroos et al., 2018) or metabolism (e.g., Jolivet et al., 2015), and to abstract some of the detail while maintaining cell type diversity (e.g.,

Izhikevich and Edelman, 2008; Potjans and Diesmann, 2012; Dahmen et al., 2016), or to move the integrated and modeled data all the way to fMRI (Deco et al., 2008).

As the biochemical and biophysical processes of the brain span many orders of magnitudes in space and time, different simulator engines have been established over time incorporating the appropriate idioms, computational representations and numerical methods (e.g., at the biochemical level—STEPS Wils and De Schutter, 2009, at the detailed cellular level - NEURON Migliore et al., 2006, using simplified neuron representations—NEST Gewaltig and Diesmann, 2007, or even more abstract—TVB Sanz-Leon et al., 2015 to name a few).

The more detail is included in these models and the larger the models become, the larger are the computational requirements of these simulation engines, making it necessary to embrace advanced computational concepts and faster computers (Hines et al., 2011; Hepburn et al., 2016; Ippen et al., 2017). **Table 1** shows exemplarily five different network models used in this paper for benchmarking and indicates their size and complexity.

A single-column thalamocortical network model (Traub et al., 2005) is used to better understand population phenomena in thalamocortical neuronal ensembles. It has 3,560 multi-compartment neurons with soma, branching dendrites and a portion of axon. It consists of 14 different neuron types, 3,500 gap junctions and 1.1 million connections. The neurons were connected together by chemical synapses (using AMPA and NMDA receptors) and gap junctions that were non-rectifying and voltage-independent. This model uses standard repertoire of 11 active conductances in all of the cells. A scaled-down variant of the full-scale dentate gyrus model (Dyhrfjeld-Johnsen et al., 2007) developed in the (Soltesz Lab, 2019) is used to understand hippocampal spatial information processing and field potential oscillations. It consists of 5,143 multi-compartment neurons and 4,121 Poisson spike sources, and includes 6 different cell types, 1.2 million connections and about 600 gap junctions. This model uses 9 classes of active conductance mechanisms such as sodium, potassium, calcium channels, and calcium-dependent potassium channels. A synthetic model with specific computational characteristics is often needed to evaluate target hardware based on number of cells, branching patterns, compartments per branch etc. For this purpose, a multiple ring network model of branching neurons and minimal spike overhead is used (Hines, 2017a). The Blue Brain Project has published a first-draft digital reconstruction of the microcircuitry of somatosensory cortex in 2015 (Markram et al., 2015). This model contains about 219,000 neurons, with 55 layer-specific morphological and 207 morpho-electrical neuron subtypes. The neurons in this model employ up to 13 different Hodgkin-Huxley conductance classes, with up to 8 of those classes used in the dendrites. Together with other partners in the European Human Brain Project, this group is also working on a full-scale model of a rat hippocampus CA1 (Human Brain project, 2018). A first draft of this model contains about 789,000 neurons with 13 morphological types and 17 morpho-electrical types. The neurons in this model employ up to 11 active conductance classes, with up to 9 of those classes used in the dendrites.

The number of neurons and synapses, however, is not always the best indicator of the computational complexity of a model. In the model of Markram et al. (2015) each neuron averages to about 20,000 differential equations to represent its electrophysiology and connectivity. To simulate the microcircuit of 31,000 neurons, it is necessary to solve over 600 million equations every 25 ms of biological time–a requirement far beyond the capabilities of any standard workstation. It is necessary to utilize massively parallel systems for such simulations but fully exploiting the capabilities these systems is a challenging task for a large number of scientific codes, including NEURON. Significant efforts are necessary to prepare scientific applications to fully exploit the massive amount of parallelism and hardware capabilities offered by these new systems (Ábrahám et al., 2015).

In this paper we present our efforts to re-engineer the internal computational engine of the NEURON simulator, CoreNEURON, to adapt to emerging architectures while maintaining compatibility with existing NEURON models developed by the neuroscience community. Our work was guided by the goal to leverage the largest available supercomputers for neuroscientific exploration by scaling the simulator engine to run on millions of threads. A key design goal was to reduce the memory footprint compared to NEURON as total memory and memory bandwidth are scarce and costly resources when running at scale. Lastly, for this capability to be easily usable by the normal NEURON community, we endeavored to tightly integrate CoreNEURON with NEURON.

2. NEURON SIMULATION ENVIRONMENT

NEURON is a simulation environment developed over the last 35 years for modeling networks of neurons with complex branched anatomy and biophysical membrane properties. This includes extracellular potential near membranes, multiple channel types, inhomogeneous channel distribution and ionic accumulation. It can handle diffusion-reaction models and integrating diffusion

TABLE 1 | Summary of network models.

Model name	Summary	#Neurons	#Compartments	#Synapses
Traub	A single column thalamocortical network model	3,560	465,740	1,099,820
Dentate	Dentate Gyrus model including Granule cells with dendritic compartments	5,137	175,719	1,199,988
Ring	Ring network of branching cells	32,768	9,535,488	33,280
Cortex + Plasticity	Somatosensory cortex model with synaptic plasticity	219,422	99,581,138	872,922,040
Hippocampus	Rat Hippocampus CA1 model	789,595	565,495,731	361,937,388

functions into models of synapses and cellular networks. Morphologically detailed models simulated using NEURON are able to represent the spatial diversity of electrical and biophysical properties of neurons.

Individual neurons are treated as a tree of unbranched cables called *sections*. Each section can have its own set of biophysical parameters, independently from other sections, and is discretized as a set of adjacent *compartments* (see e.g., Hines, 1993). Compartmental models of neurons take into account not only the connectivity between neurons but also the individual morphologies and inhomogeneities of each neuron. The electrical activity of neurons is modeled using the cable equation (see e.g., Tuckwell, 2005) applied to each section, where the quantity representing the state of a neuron at a given point in space and instant in time is the *membrane potential*. The general form of the cable equation for a section, in the case of constant parameters and conductance based synapse modeling, is given by:

$$\frac{d}{4R_a}\frac{\partial^2 v}{\partial x^2} = c_m\frac{\partial v}{\partial t} + I_{pas} + I_{ion} + I_{syn} \tag{1}$$

where

- $d\,[\mu m]\,, R_a\,[\Omega cm]\,, c_m\left[\frac{\mu F}{cm^2}\right], I_{pas}\left[\frac{mA}{cm^2}\right]$ are biophysical parameters contributing to the passive component of the cable equation (unit conversion factors are not shown but each term has the units of mA/cm^2).
- $I_{ion}\left[\frac{mA}{cm^2}\right]$ is the active contribution arising from ion channels along the section, whose conductances g_i and resting potentials e_i might depend in a non-linear fashion upon a set of state variables representing those channels.
- $I_{syn}\left[\frac{mA}{cm^2}\right]$ is the contribution from the synapses placed at positions x_j, whose conductances g_j and resting potentials e_j might depend in a non-linear fashion upon a set of state variables and which take effect in a strongly localized manner. Individual synapses have units of nA and conversion to mA/cm^2 involves a Dirac delta function, $\delta(x-x_j)$, with units $1/\mu m$, and the diameter; i.e., conversion of absolute current to current per unit area implies division by the compartment area where the synapse is located.

One needs to couple (1) to a set of additional differential equations that describe the evolution of the states of ion channels and synapses, thus giving rise to a system of PDEs/ODEs as the final problem. Spatial discretization of the PDEs results in a tree topology set of stiff coupled equations which is most effectively solved by implicit integration methods. In particular, direct Gaussian elimination with minimum degree ordering is computationally optimum in the sense that the number of arithmetic operations is identical to direct Gaussian elimination of a non-branching cable with the same number of nodes (Hines and Carnevale, 1997; Hines et al., 2008). The general structure of a *hybrid clock-event driven algorithm* (Hines, 1993) in NEURON can be divided into a set of operations that are performed at every integration time step and an interprocess spike exchange operation where a list of spike generation times and identifiers are synchronized across all processors every minimum spike delay interval. The per integration step operations are:

- Event-driven spike delivery step where the callback function of each synapse activated by a spike at a given timestep is executed.
- Matrix assembly step where the I_{ion} and I_{syn} contributions are computed and included in the matrix.
- Matrix resolution step where the membrane potential for the current step is obtained by solving a linear system.
- State variables update step where the evolution equations for the states of ion channels and synapses are solved to advance to the current timestep.
- Threshold detection step where each neuron is scanned to see if it has met a particular firing condition, and if so a particular list of events is updated.

Although the simulator has demonstrated scaling up to 64,000 cores on the IBM Blue Gene/P system (Hines et al., 2011), with the emerging computing architectures (like GPUs, many-core architectures) the key challenges are numerical efficiency and scalability. The simulator needs to : (1) expose fine grain parallelism to utilize the massive number of hardware cores, (2) be optimized for memory hierarchies and (3) fully utilize processor capabilities such as vector units. To simulate models with billions of neurons on a given computing resource, memory capacity is another major challenge. In order to address these challenges, the compute algorithm of the NEURON simulator was extracted and optimized into a standalone library called CoreNEURON.

3. CORENEURON DESIGN AND IMPLEMENTATION

The integration interval operations (listed in section 2) consume most of the simulation time (Kumbhar et al., 2016). The goal of CoreNEURON is to efficiently implement these operations considering different hardware architectures. This section describes the integration of CoreNEURON with the NEURON execution workflows, major data structure changes to reduce memory footprint, memory transfer between NEURON-CoreNEURON and a checkpoint-restore implementation to facilitate long running simulations.

3.1. NEURON to CoreNEURON Workflow

One of the key design goal of CoreNEURON is to be compatible with the existing NEURON models and user workflows. With the integration of CoreNEURON library, the NEURON simulator supports three different workflows depicted in **Figure 1**.

- NEURON mode
- CoreNEURON Online mode
- CoreNEURON Offline mode

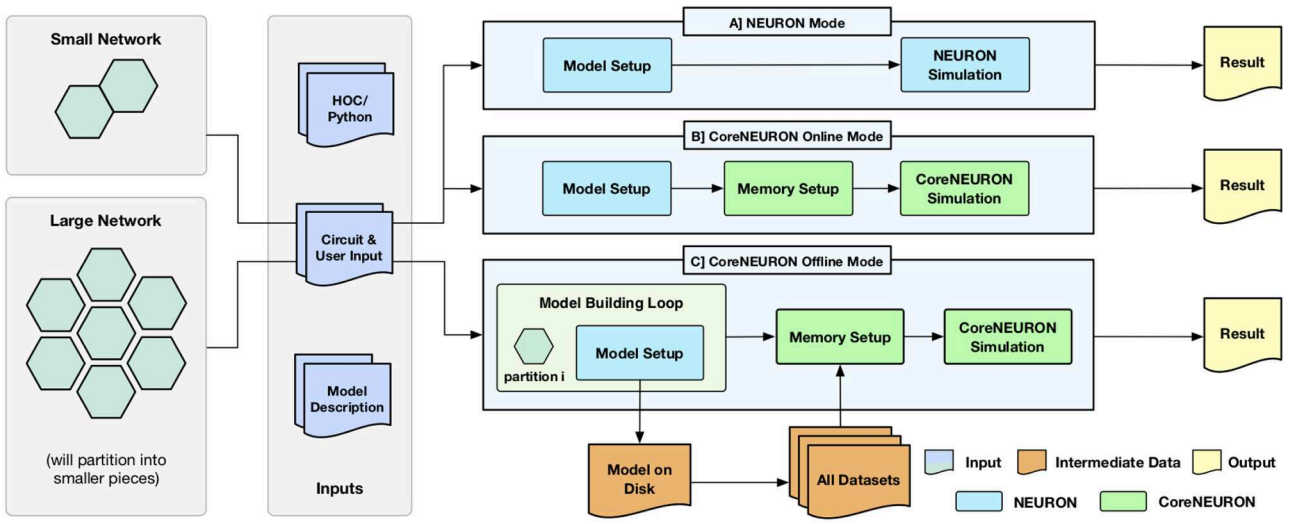


FIGURE 1 | Different execution workflows supported by NEURON simulator with CoreNEURON : (A) shows the existing simulation workflow where HOC/Python interface is used for building a model which is then simulated by NEURON; (B) shows the new CoreNEURON based workflow where the in-memory model constructed by NEURON is transferred using direct memory access and then simulated by CoreNEURON; (C) shows new CoreNEURON based workflow where NEURON partitions a large network model into smaller chunks, iteratively instantiates each model piece in memory, and copies that subset of model information to disk. CoreNEURON then loads the whole model in memory and simulates it.

Existing users are familiar with the default *NEURON mode*. The model descriptions written in NMODL (Hines and Carnevale, 2000) are used to build a dynamically loadable shared library. The HOC/Python scripting interface is used to build a network model in memory (*Model Setup phase*). This in-memory model is then simulated using the *hybrid clock-event driven algorithm* described in section 2 (*Simulation phase*). Users have full control over model structure and can introspect or record all events, states, and model parameters using the scripting or graphical user interface (*Result phase*).

CoreNEURON Online Mode allows users to run their models efficiently with minimal changes. After the *Model Setup phase*, the in-memory representation is copied into CoreNEURON's memory space. CoreNEURON then re-organizes the memory during *Memory Setup phase* for efficient execution (see section 4.2). The *Simulation phase* is executed in CoreNEURON and spike results are written to disk. Note that the same NMODL model descriptions are used both in NEURON as well as CoreNEURON.

CoreNEURON Offline mode is intended for large network models that cannot be simulated with NEURON due to memory capacity constraints. In this mode, instead of loading the entire model at once, the *Model Setup phase* builds a subset of the model that fits into available memory. That subset is written to disk, the memory used by the subset is freed, and the *Model Setup phase* constructs another subset. After all subsets are written by NEURON, CoreNEURON reads the entire model from the disk and begins the *Simulation phase*. Because CoreNEURON's cell and network connection representations are much lighter weight than NEURON's, 4-7x larger models than NEURON can be simulated with CoreNEURON (see section 5).

Users can adapt existing models to the *CoreNEURON Online Mode* workflow with the trivial replacement of the *psolve* function call with *nrncore_run* of the (ParallelContext, 2019) class.

3.2. Data Structure Changes

NEURON is used as a general framework for designing and experimenting with neural models of varying anatomical detail and membrane complexity. Users can interactively create cells with branches of varying diameters and lengths, insert ionic channels, create synapses, and visualize different properties using a GUI. In order to provide this introspection capability, NEURON maintains a large number of complex data structures. Typically, once the users are satisfied with the behavior of the model, they run larger/longer simulations on workstations or clusters where those interactivity or detailed introspection capabilities are often no longer required. In this type of batch execution, memory overhead from many large, complex data structures with many mutual pointers can be significantly reduced by replacing them with fixed arrays of data structures in which the few necessary pointers are replaced by integers. For example, the network connection object (*Netcon*) and the common synapse base class (*Point_process*), which are responsible for a significant portion of memory usage in NEURON, were reduced from 56 to 40 and 56 to 8 bytes respectively in CoreNEURON. **Table 2** lists the important data structures and their memory usage comparison between NEURON and CoreNEURON. CoreNEURON eliminates the Python/HOC interpreter and so, datastructures like *Node*, *Section*, *Object* are no longer needed. The memory usagemprovements from these optimizations for different network models are discussed in section 5.

TABLE 2 | Memory footprint comparison for different data structures (in bytes).

Data structure	Purpose	NEURON	CoreNEURON
Node	Compartment of the neuron	128	–
Section	Unbranched cable of the neuron	96	–
Object	High level HOC object	64	–
Presyn	Synapse object at origin	208	64
InputPresyn	Similar to Presyn	–	24
Point_process	Synapse overhead	56	8
Prop	Property object in compartment	48	–
Netcon	Connection between neuron	56	40
Pointer	Memory address	8	4
Memb_list	List of mechanisms or channels	56	64
NrnThreadMembList	Mechanism list for group of neurons	34	40
PreSynHelper	Helper object for PreSyn	–	4
Symbol	Token parsed by HOC interpreter	56	–

3.3. Pointer Semantics

NEURON users can define their own data structures and allocate memory through the use of *POINTER* and *VERBATIM* constructs of NMODL (Hines, 2019). Many internal data structures of NEURON use pointer variables to manage various dynamic properties, connections, event queues etc. As a model is built incrementally using the scripting interface, various memory pools are allocated during the *Model Setup phase*. As data structures between NEURON and CoreNEURON are different, serializing memory pools becomes one of the major memory management challenges of the CoreNEURON implementation. With serialization, pointer variables need to be augmented with meta information to allow proper decoding by CoreNEURON. This meta information indicates the *pointer semantics*. All data variables which potentially are the target pointers are grouped into a contiguous memory pool and pointer variables are converted to an integer offset into the memory pool. When the NEURON pointers are copied to CoreNEURON's memory space, the semantic type associated with the pointer variable is used to compute the corresponding integer offset. Different semantic types with their purpose are listed in Supplementary Material (see **Table S1**).

3.4. Checkpoint-Restart Support

The network simulations for studying synaptic plasticity can run from a week to a month. Enabling such simulations of long biological time-scales is one of the important use cases for CoreNEURON. Most of the cluster and supercomputing resources have a maximum wall clock time limit for a single job (e.g., up to 24 h). The checkpoint-restart (Schulz et al., 2004) is commonly used technique to enable long running simulations and has been implemented in CoreNEURON. Since the checkpoint operation could take place at anytime with varying degrees of cell firing activity, it was necessary to account for generated yet undelivered synaptic events in addition to saving the in-memory state of the simulator. When a cell fires, it may have many connections to other cells with different delivery delays. During the checkpoint operation, any undelivered messages are collapsed back into the original event of the firing cell so that a single event can be saved. Once the network simulation is checkpointed, users have flexibility to launch multiple simulations with different stimuli or random number streams in order to explore network stability and robustness. The execution workflow of such simulations is shown in **Figure 2**.

3.5. Spike Communication

In CoreNEURON, the MPI communication and event queue handling for spike delivery is inherited from NEURON and remains on the CPU. Performance of those components is discussed in Kumar et al. (2010), Hines et al. (2011). However, when GPUs are in use, all the spikes within a time step that are destined for a specific synapse type are copied to the GPU to a type specific buffer and thereafter all NET_RECEIVE block computations take place on the GPU. Conversely, threshold detection takes place on the GPU as well and spike generation is buffered until the end of the time step at which point the buffer spikes are copied to the CPU for MPI transfer and enqueueing onto the priority queue. The exception to this strategy is that ARTIFICIAL_CELL instances, which compute and generate spikes solely by their NET_RECEIVE block response to delivered events, exist only on the CPU.

3.6. Portability Considerations

CoreNEURON can transparently handle all spiking network simulations including gap junction coupling with the fixed time step method. The model descriptions written in NMODL need to be (THREADSAFE, 2019) to exploit vector units of modern CPUs and GPUs. A model can be non thread-safe if a MOD file contains GLOBAL variables which are used for temporary storage by getting assigned a value in one procedure and evaluated in another. Such variables need to be converted from GLOBAL to RANGE. This can be achieved with the help of NEURON's *mkthreadsafe* tool or the user can manually make the minor change to such MOD files. New keywords like *COREPOINTER* and *CONDUCTANCE* have been added to NMODL to facilitate serialization and improve performance optimization respectively. These keywords are also backported to NEURON so that the models remain compatible for either NEURON or CoreNEURON execution. For scalability and portability of random numbers on platforms like GPUs, CoreNEURON supports the Random123 pseudo-random generator (Salmon et al., 2011).

4. OPTIMIZATIONS

In order to improve the performance of CoreNEURON on different architectures, different optimization schemes are implemented for multi-threading, memory layout, vectorization,

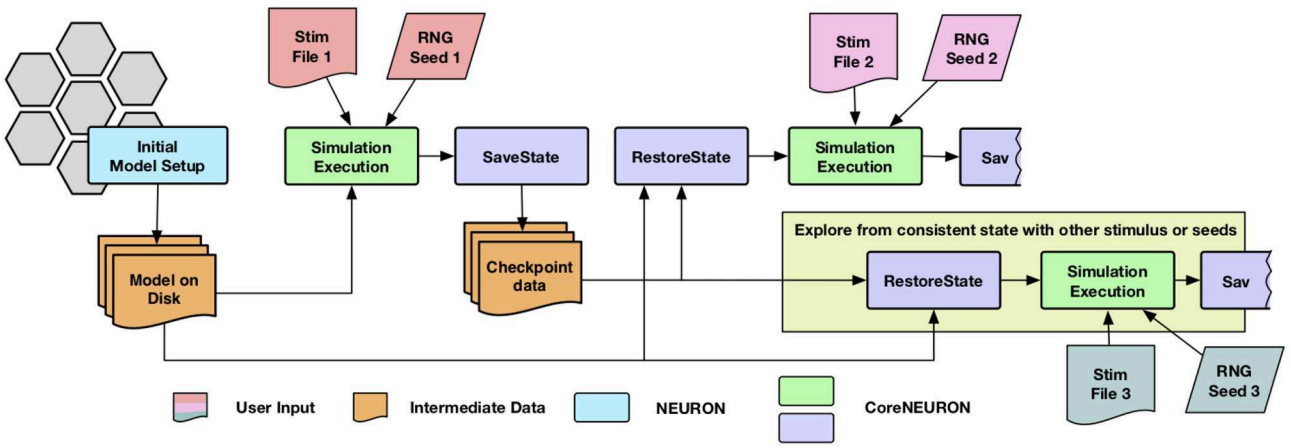


FIGURE 2 | Simulation workflow with the checkpoint-restart feature : CoreNEURON loads the model from disk, simulate it and dumps in-memory state back to disk (*SaveState* step). CoreNEURON can load checkpoint data (*RestoreState* step) and continue the simulation on a different machine using the checkpoint data. The user has flexibility to launch multiple simulations with different stimuli or random number streams (*Stim* or *RNG*) in order to explore network stability and robustness.

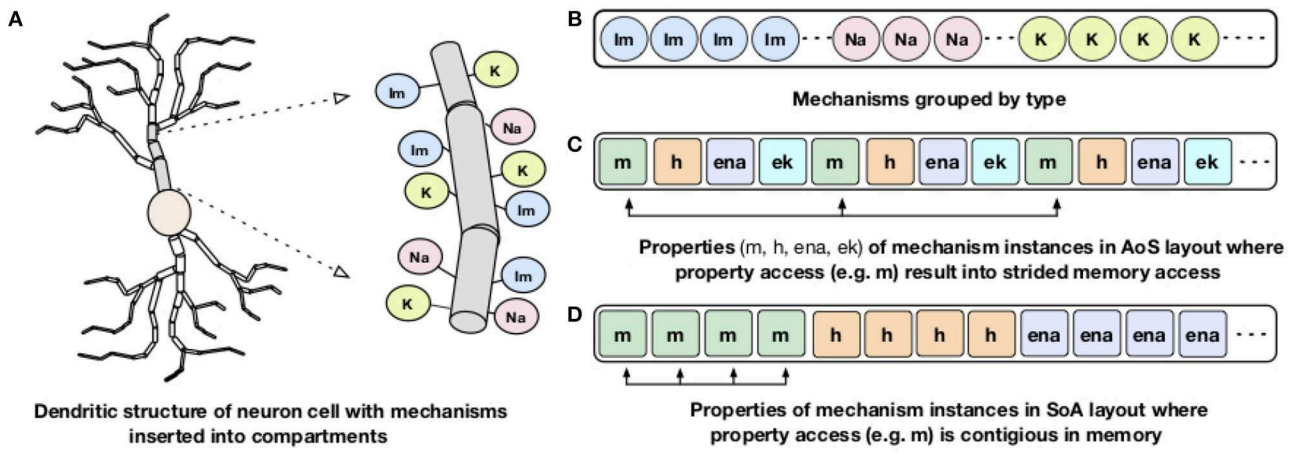


FIGURE 3 | Dendritic structure and memory layout representation of a neuron: A schematic representation of dendritic structure of a neuron with different mechanisms inserted into the compartment is shown on the left **(A)**. On the right: **(B)** shows how NEURON and CoreNEURON groups the mechanism instances of the same type; **(C)** shows how NEURON stores properties of individual mechanism in the *AoS* layout; **(D)** shows the new *SoA* layout in CoreNEURON for storing mechanism properties.

and code generation. These optimizations are described in this section.

4.1. Parallelism

Both NEURON and CoreNEURON use the *Message Passing Interface* (MPI) to implement distributed memory parallelism. Although NEURON supports multi-threading based on Pthread (Nichols et al., 1996), users commonly use pure MPI execution due to better scaling behavior. But, pure MPI execution will affect scalability due to MPI communication and memory overhead of internal MPI buffers when executing at scale (Lange et al., 2013). To address this scalability and parallelism challenge, CoreNEURON relies on three distinct levels of parallelism. First, at the highest level, a set of neurons that have equivalent computational cost are grouped together and assigned to each MPI rank on the compute node. Second, within a node, an individual neuron group is assigned to an OpenMP (Dagum and Menon, 1998) thread executing on a core. This thread simulates the given neuron group for the entire simulation ensuring data locality. Finally, vector units of the core are utilized for executing groups of channels in parallel. With respect to MPI and OpenMP, simulations may benefit from fewer MPI processes per compute node (down to a single process per node). Based on target architecture, users can choose a number of MPI ranks and corresponding OpenMP threads per rank to reduce communication overhead.

4.2. Memory Layout and Vectorization

Processor memory bandwidth is one of the scarce resources and often the major impediment to improve the performance

of many applications including NEURON. The compute kernels of channels and synapses are bandwidth limited and can reach close-to-peak memory bandwidth (Kumbhar et al., 2016). The dendritic structures of a neuron are divided into small compartments and different membrane channels or mechanisms are inserted into different compartments (**Figure 3A**). For memory locality, both NEURON and CoreNEURON groups the channels by their type as shown in **Figure 3B**. But, NEURON organizes properties of individual mechanisms (like *m*, *h*, *ena*) in the *Array of Structs (AoS)* memory layout (**Figure 3C**). When a specific property is accessed, for example, *m*, it results in strided memory accesses with inefficient memory bandwidth utilization and hence poor performance. To address this issue, CoreNEURON organizes channel properties into the *Structure of Arrays (SoA)* memory layout (**Figure 3D**). This allows efficient vectorization and efficient memory bandwidth utilization for all channel and synapse computations. For code vectorization, CoreNEURON is dependent on the compiler's auto-vectorization capabilities. To assist the compiler in auto-vectorization, hints like *#pragma ivdep* are used. The performance improvements from this optimization is discussed in Kumbhar et al. (2016).

4.3. NMODL Source-to-Source Translator

NEURON has had support for code generation through the model description language, NMODL, since version 2 released in 1989 (Blundell et al., 2018). The code generation program of NEURON has been modified into a standalone tool called *MOD2C* (MOD2C GitHub Repository, 2019). This tool is used by CoreNEURON to support all NEURON models written in NMODL. **Figure 4** shows the high level workflow of MOD2C. The first step of source-to-source translator is *lexical analysis* where lexical patterns in the NMODL code are detected and tokens are generated. The *syntax analysis* step uses those tokens and determine if the series of tokens are appropriate in the language. The *semantic analysis* step make sure if syntactically valid sentences are meaningful as part of the model description. *Code generation* is the step in which a C++ file is created with compiler hints for auto-vectorization (e.g., *#pragma ivdep*) and GPU parallelization with the OpenACC programming model (Wikipedia, 2012). MOD2C also takes care of code generation for *AoS* and *SoA* memory layouts. MOD2C uses open source flex and bison tools (Levine and John, 2009) for this implementation. More information about the NMODL code generation pipeline can be found in Blundell et al. (2018).

4.4. GPU Porting

Prior to the CoreNEURON project, a substantial effort was made to port NEURON to the GPU architecture using the CUDA programming model (Wikipedia, 2006; NVIDIA Corporation, 2006–2017). One of the two major components of this implementation was the extension of the NMODL source-to-source compiler to emit CUDA code. The other major component managed an internal memory transformation from NEURON's thread efficient *AoS* memory layout to a more GPU memory efficient *SoA* layout. For generating CUDA code, there was a separate version of the NMODL source-to-source compiler. NEURON maintains complex data structures of section, segment for interactive use. The memory management of these *non-POD type* (Plain Old Data) data structures between CPU and GPU was quite complex as memory allocations were not contiguous. This experimental NEURON version (Hines, 2014) was quite efficient for matrix setup and channel state integration for cellular simulations but did not reach network simulation capability. The project foundered on software administration difficulties of maintaining two completely separate codebases, the difficulty of understanding the data structure changes involved for memory layout transformation from *AoS* to *SoA*, and the difficulty of managing pointer updates in the absence of pointer semantics information. It became clear that a more general view was required that could not only alleviate these problems for the GPU but had a chance of evolving to work on future architectures. This view is embodied in CoreNEURON development. As discussed in section 4.2, CoreNEURON data structures and memory layout have been optimized for efficient memory access. MOD2C supports code generation with the OpenACC programming model that helps to target different accelerator platforms. Users need to compile the CoreNEURON library with a compiler that supports OpenACC. **Figure 5** shows GPU enabled execution workflow where different stages of the CoreNEURON simulator running on CPU and GPU are described.

One of the performance challenges for a GPU implementation is irregular memory accesses due to the non-homogeneous tree structure of neurons. For example, **Figure 6A** shows three different morphological types and their compartmental tree connection topology in the simulator is shown in **Figure 6B**. The GPU delivers better performance when consecutive threads (in groups of 16 or 32) perform the same computations and load the data from consecutive memory addresses. When there are a large number of cells per morphological type, it is straightforward to achieve optimal performance by interleaving the compartments of identical cells. But, with few cells per morphological type, Gaussian elimination suffers from non-contiguous layout of parents relative to a group of nodes. This results in irregular, strided memory accesses and hence poor performance (Valero-Lara et al., 2017). To address this, two alternative node orderings schemes, *Interleaved* layout and *Constant Depth* layout, are implemented as illustrated in **Figures 6D,E**. All cells have the same number of compartments but each has a different branching pattern (**Figure 6C**). Nodes (representing compartments) within a cell are numbered with successive integers. In the case of *Interleaved* layout, a compartment from each of N cells forms an adjacent group of N compartments. The groups are in any root to leaf order but corresponding compartments in identical cells are adjacent. As an example, for a group of three threads the vertical square braces highlight parent indices that have the same order as the nodes. This results in either contiguous memory loads (*CL*) or strided memory load (*SL*). For each Gaussian elimination operation the number of threads that can compute in parallel is equal to the number of cells and hence this scheme is referred as *one cell per thread layout*. For *Constant Depth* layout, all nodes at the same depth from the root are adjacent. For a given depth, corresponding nodes of identical cells are adjacent. Children of branch nodes

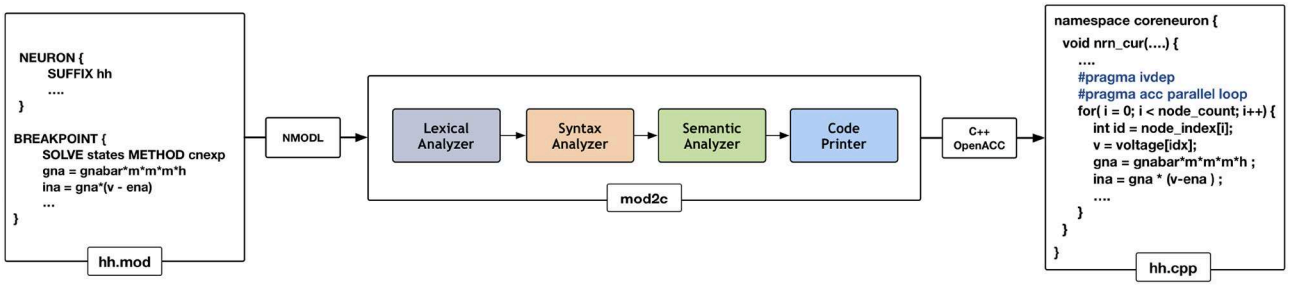


FIGURE 4 | Code generation workflow for CoreNEURON : different phases of the source-to-source compiler are shown in the middle that translates the input model description file (hh.mod) to C++ code (hh.cpp). Compiler hints like *ivdep* and *acc parallel loop* are inserted to enable CPU vectorization/GPU parallelization.

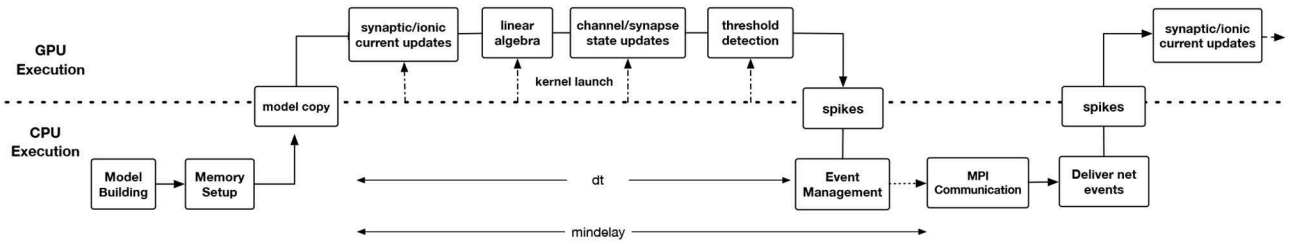


FIGURE 5 | Timeline showing the workflow of GPU-enabled CoreNEURON execution. The *Model Building* and *Memory Setup* phases are executed on CPU by NEURON and CoreNEURON respectively. The latter performs an in-place memory AoS to SoA transformation and node permutation to optimize Gaussian elimination. The CoreNEURON in-memory model is then copied to GPU memory using *OpenACC* APIs. All time step integration phases including threshold detection for event generation and event delivery to synapse models take place on the GPU. At the end of each timestep (*dt*), the generated spike events are transferred to the CPU. Conversely, all the spike events to be delivered during a step are placed in a per-synapse type buffer and transferred at the beginning of each timestep to the GPU. At the end of *mindelay* interval all spikes destined to other processes are transferred using MPI Communication.

in the same cell are kept as far apart as possible to minimize contention while updating the same node from different threads.

To analyse the impact of node ordering schemes on the execution time, we used a multiple Ring network model of cells with random tree topology (Hines, 2017a). This test allows to evaluate performance impact when parents of a contiguous group of 32 nodes are not contiguous and executed in chunks of 32 threads (a so-called *warp*). We used a multiple Ring model with a total of 131,072 cells comprising 10,878,976 nodes running for 10 ms on NVIDIA K20X GPU (NVIDIA Corporation, 2012). Every cell has the same number (83) of nodes but different cell types have a different random branching pattern of the 40 dendrites. The number of identical cells per type ranges from 1 (131,072 distinct branching patterns) to 32 (4096 distinct branching patterns). Note that regardless of the branching pattern, Gaussian elimination takes exactly the same number of arithmetic operations. **Figure 6D** shows performance of Interleaved Layout and Constant Depth Layout. For both node ordering schemes, performance is optimal with regard to parent ordering when there are at least 32 cells of each type corresponding to the 32 threads operating in *Single Instruction Multiple Data (SIMD)* mode. With fewer cells per type, parent node ordering becomes less than optimal and the performance of Interleaved layout suffers by up to a factor of two. Note that the total runtime deteriorates more rapidly than Gaussian elimination time due to the fact that the parent contiguity also affects the performance of tree matrix setup during evaluation of a node's current balance equation. The execution time of *Constant Depth* layout shows that it is possible to permute node ordering so that parent nodes are more likely to be in significant conti guous order relative to their children. The constant ratio between total runtime and Gaussian elimination is due to negligible time contribution of passive dendrites to matrix setup in combination with the significant role of parent ordering in computing the effect of topologically adjacent nodes on matrix setup of the current balance equations.

5. BENCHMARKS AND PERFORMANCE

Not all network models are compute intensive or benefit equally from CoreNEURON optimizations. In order to evaluate the performance improvements with the optimizations discussed in the previous section we ran several published network models listed in **Table 1** on different computing architectures. This section describes the benchmarking platforms and compares performance between NEURON and CoreNEURON.

The benchmarking systems with hardware details, compiler toolchains and network fabrics are summarized in **Table 3**. The Blue Brain IV (BB4) and Blue Brain V (BB5) systems are based on IBM BlueGene/Q (Haring et al., 2012) and HPE SGI 8600 (Hewlett Packard Enterprise, 2019) platforms

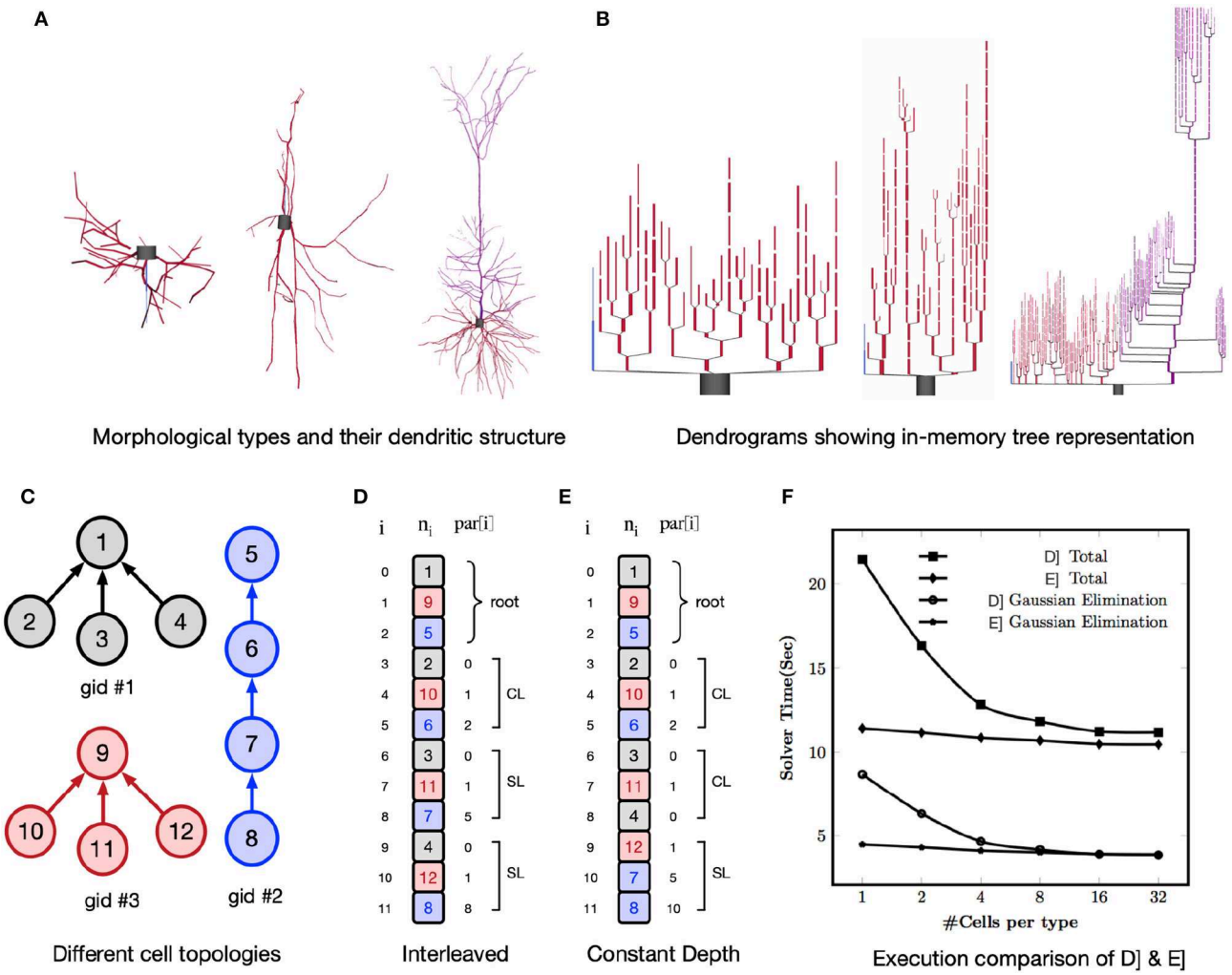


FIGURE 6 | The top row shows three different morphological types with their dendritic tree structure in **(A)** and dendrograms showing in-memory tree representation of these types in CoreNEURON in **(B)**. The bottom row shows different node ordering schemes to improve the memory access locality on GPUs : **(C)** Example topologies of three cells with the same number of compartments; **(D)** Interleaved Layout where a compartment from each of N cells forms an adjacent group of N compartments. For *i*th node, n_i is node index and *par[i]* is its parent index. With three executor threads, square brace highlight parent indices that result into contiguous memory load (CL) and strided memory load (SL); **(E)** Constant Depth Layout where all nodes at same depth from root are adjacent; **(F)** Comparison of two node ordering schemes for Ring network model showing execution time of whole simulation and Gaussian Elimination step.

respectively, hosted at the Swiss National Computing Center (CSCS) in Lugano, Switzerland. The BB4 system has 4,096 nodes comprising 65,536 PowerPC A2 cores. The BB5 system has three different compute nodes: Intel KNLs with low clock rate but high bandwidth MCDRAM, Intel Skylakes with high clock rate, and NVIDIA Volta GPUs. Vendor provided compilers and MPI libraries are used on both systems. The BB4 system is used for strong scaling benchmarks (see **Figure 8**) as it has a large core count compared to the BB5 system. All benchmarks were executed in pure MPI mode by pinning one MPI rank per core. During the model building phase, NEURON divides model into *n* equal chunks where *n* is total number of MPI ranks. CoreNEURON continues execution with the same number of MPI ranks as NEURON. For GPU executions we used one MPI rank per GPU node.

We compared the memory footprint of different network models listed in **Table 1**. **Figure 7** on the left shows memory usage reduction with CoreNEURON simulation compared to NEURON simulation. The memory reduction factor depends on various model properties (e.g., number of compartments, sections, synapses, etc.) but one can expect 4-7x reduction with the use of CoreNEURON. Note that *CoreNEURON Online mode* will need $\frac{1}{7}$x to $\frac{1}{4}$x more memory during the *Memory Setup phase*. But once the model is transferred to CoreNEURON for simulation, NEURON can free allocated memory.

Figure 7 on the right shows the speedup achieved on a single node for different models with CoreNEURON compared to

NEURON. Note that the Cortex and Hippocampus models are very large in terms of memory capacity requirement. For single node performance analysis we used a smaller subset of these two models.

The memory layout and code vectorization optimization described in section 4.2 shows greatest improvement when most of the computation time is spent in channel and synapse computations. The Cortex, Cortex+Plasticity and Hippocampus models have cells with 200 to 800 compartments and 20 different channel types. This makes these models compute intensive and lets them benefit most by CoreNEURON. The Ring network model has computations only from passive dendrites and active soma.

Intel KNL has 512-bit SIMD vectors and high bandwidth memory (MCDRAM). One needs to efficiently utilize these hardware features to achieve best performance. In the case of CoreNEURON, NMODL generated code is auto-vectorized by the compiler and has *SoA* memory layout to provide uniform, contiguous memory access. NEURON uses *AoS* memory layout which results in strided memory accesses. Due to the lower clock frequency of KNL cores, the performance impact of non-vectorized code and strided memory accesses is high compared to other architectures. Hence CoreNEURON delivers better performance on KNL compared to NEURON. Note that the Cortex+Plasticity and Hippocampus models have relatively less improvement (2-4x) compared to the Cortex model (3-7x). This is because some of the channel and synapse descriptions explicitly request integration methods that present compilers cannot efficiently vectorize. Alternative code generation for these methods is being considered.

On the BlueGene/Q platform the speedup with most of the models is limited to 2x. This is because the IBM XL compiler is not able to vectorize most of the channel and synapse kernels. Observed performance improvement on this platform is due to more efficient memory accesses from the *SoA* layout discussed in the section 4.2.

TABLE 3 | Details of benchmarking systems.

BlueGene/Q (BB4)	Processor	IBM PowerPC A2, 16 cores @ 1.6 GHz, 16 GB DRAM
	Compiler toolchain	IBM XL 12.1 and IBM MPI
	Network	Integrated 5-D torus
Intel Skylake (BB5)	Processor	2 Xeon 6140, 36 cores @ 2.3 GHz, 384 GB DRAM
	Compiler toolchain	Intel 2018.1 and HPE-MPI (MPT)
	Network	InfiniBand EDR
Intel KNL (BB5)	Processor	Xeon Phi (7230), 64 cores @ 1.3 GHz, 96 GB DRAM
	Compiler toolchain	Intel 2018.1 and HPE-MPI (MPT)
	Network,	InfiniBand EDR
NVIDIA GPU (BB5)	Processor	NVIDIA GPU V100 SXM2, 2 Xeon 6140, 36 cores @ 2.3 GHz
	Compiler toolchain	PGI 18.10, OpenMPI 2.0
	Network	InfiniBand EDR

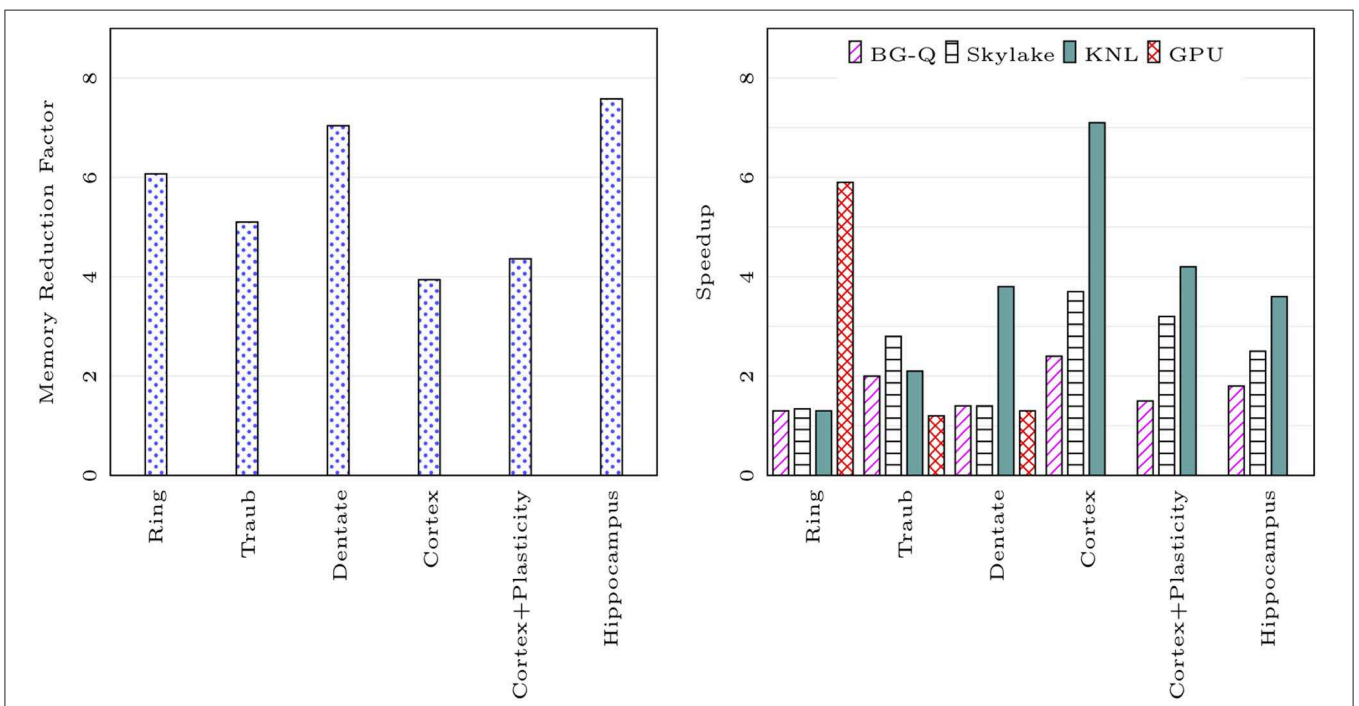


FIGURE 7 | Memory usage reduction and speedup using CoreNEURON : ratios of memory usage between NEURON and CoreNEURON for different models in **Table 1** are shown on the left (measured on BB4 system). Speedups of CoreNEURON simulations compared to NEURON on various architectures (using single node) for the same models are shown on the right.

GPU support has been recently added to CoreNEURON. Two models used in this benchmark, Cortex+Plasticity and Hippocampus, use legacy HOC based stimulus implementations which are not adapted for GPU yet. The Ring network model has large number of identical cells which suits SIMD computations on GPU and hence shows significant performance improvement compared to other architectures. The Traub model has a small number of cells exposing limited parallelism and the Dentate model has gap junctions which require copying of voltages between CPU and GPU every timestep. This limits the performance improvement on GPU.

The reduction in the memory footprint of models translates directly into benefits for users of large-scale models. For example, while models of the size of Cortex + Plasticity and Hippocampus models had a memory requirement when using NEURON that necessitated a minimum of 2,048 nodes on an IBM BlueGene/Q system, can now run on the same system requiring only 128 or 256 nodes for the Cortex+Plasticity and Hippocampus model respectively when using the *CoreNEURON Offline Mode*. This is a significant usability improvement and translates directly into a better use of a user's compute allocation.

Finally, **Figure 8** shows that CoreNEURON maintains good strong scaling properties for large models, as illustrated on the example of the Cortex+Plasticity and Hippocampus models simulating one second of biological time on an IBM BlueGene/Q system. As these models are compute intensive and a small fraction of execution time is spent in spike communication, the scaling behavior depends on how well a given number of cells can be distributed across the available number of ranks to yield good load balance. Both models show excellent strong scaling behavior up to 2,048 nodes. Due to the large size range of morpho-electrical neuron types, at least 7–10 cells per MPI process are required to achieve good load balance. With 32,000 MPI processes (16 ranks per node) and about 219,000 cells of Cortex+Plasticity, the load balance is not as good as with the Hippocampus model of about 789,000 cells. Hence, the Cortex+Plasticity model exhibits poorer scaling behavior compared to the Hippocampus model.

6. DISCUSSION

Modern compute architectures can significantly boost application performance and the study of the brain *in silico* is in dire need to embrace this capability and trend. Accordingly, the widely used NEURON simulator that supports a large variety of models has been over the years successfully adapted to embrace massively parallel architectures, but its primary design goals were to allow for a flexible definition of models and interactive introspection thereof. It was neither designed for ultimate memory efficiency nor maximal performance. However, the larger and more detailed the models get, the larger are the resource requirements to simulate those models. Eventually, the costs of a system required for an un-optimized simulator should be weighed against the effort of reworking the simulator to make more efficient use of resources. In the context of the Blue Brain Project we took the decision to contribute to making the NEURON simulator more efficient for large models, effectively leading to reduced resource requirements, faster time-to-solution, or simply the capability to run bigger models on a given resource.

6.1. Compatibility With Existing NEURON Models

As the neuroscience community has developed and shared thousands of models with NEURON, compatibility and reproducibility has been one of the primary design goals. To maintain maximal compatibility, we chose the path of extracting the computational relevant parts of NEURON into a library called CoreNEURON and adapting it to exploit the computational features of modern compute architectures. This is a different path as for example taken by the Arbor (Akar et al., 2019) which started its developments from scratch. While such a fresh start has its benefits in terms of designing for future architectures from the start, we can show that the transformation approach we took immediately gives compatibility with a large number of existing NEURON models with minimal modification. Currently, CoreNEURON does not handle non thread-safe models and requires NMODL modifications if constructs like POINTER are used. We are working on handling such models transparently.

6.2. Flexibility for Model Building and Efficiency for Model Simulation

Many modeling workflows related to detailed brain models require flexibility for quickly inspecting and changing the models. By extracting the compute engine from the NEURON simulator environment and providing different methods of how it can interact with the NEURON simulator, one maintains the flexibility of NEURON for the construction of the models and can more easily apply optimizations to the compute engine for the costly simulation phase. The *Offline* execution mode of CoreNEURON provides flexibility to build and simulate large network models that cannot be simulated with NEURON. Thanks to the use of MPI, and the OpenMP and OpenACC programming models to achieve portability across different architectures such as multi-core, many-core CPUs, and GPUs.

6.3. Reduced Memory and Faster Time-to-Solution

The data structure changes allow CoreNEURON to use significantly less memory compared to NEURON. The *SoA* memory layout and code vectorization allow CoreNEURON to simulate modelsí efficiently. We benchmarked five different network models on different architectures showing 4-7x memory usage reduction and 2-7x execution time improvement.

6.4. Future Work

We discussed the implementation of the most significant changes and optimizations in NEURON and CoreNEURON. Although CoreNEURON can be used transparently within NEURON, users cannot currently access or modify model properties during integration. Work is ongoing in regard to bidirectional data copy routines activated by normal NEURON variable name evaluation and assignment syntax ranging in granularity from the entire model, to specific named arrays, down to individual variables. On the numerical side, CoreNEURON today supports network

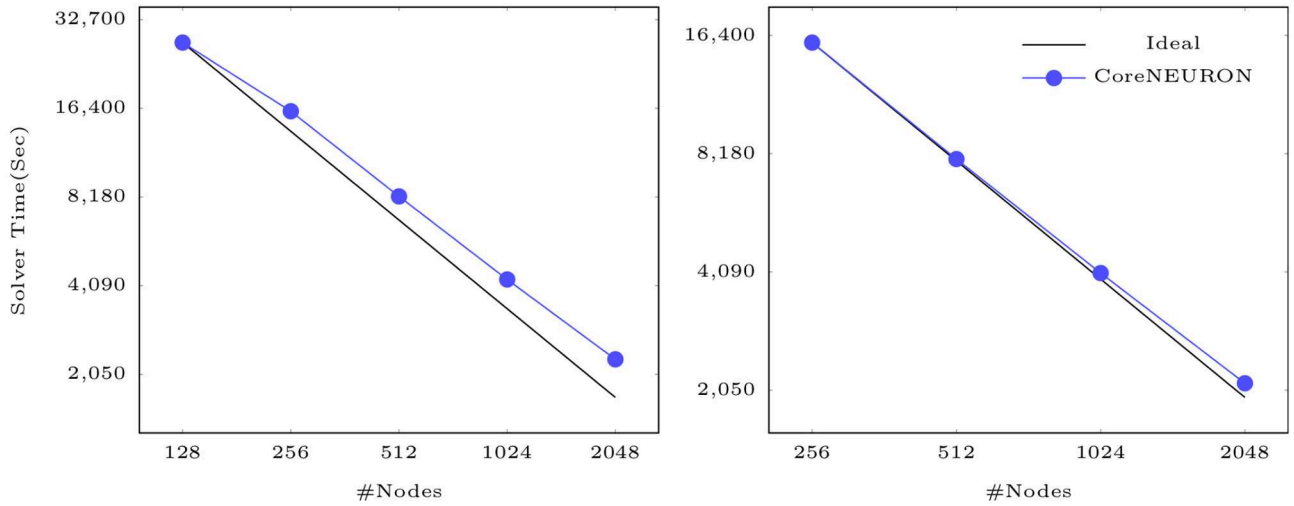


FIGURE 8 | Strong scaling of CoreNEURON on the BB4 system for two large scale models listed in **Table 1**: the Cortex+Plasticity model with 219 k neurons (on the left) and the Hippocampus CA1 model with 789 k neurons (on the right).

simulations using the fixed time step method but not the variable time step integration method (CVODE) (Cohen and Hindmarsh, 1996). The latter is rarely used in network simulations because state or parameter discontinuities in response to synaptic events demand continuous re-initialization of variable step integrators. Research is ongoing on how to improve the applicability of variable time step schemes in network simulation and can be considered for inclusion at a later stage. Currently, mapping of multiple MPI ranks to GPUs is not optimal and this will be addressed in future releases. Lastly, the NMODL source-to-source translator will be improved to generate efficient code for stiff, coupled, non-linear gating state complexes that require the *derivimplicit* integration method as well as the generation of optimal code for GPUs.

6.5. Availability

CoreNEURON and code generation program MOD2C are open sourced and available on GitHub (CoreNEURON GitHub Repository, 2019; MOD2C GitHub Repository, 2019).

DATA AVAILABILITY STATEMENT

The datasets relevant for the main conclusions of this study (i.e,. Ring model, Traub model, and Dentate gyrus model) can be accessed on GitHub (Raikov and Hines, 2016; Hines, 2017a,b). The remaining supplementary datasets that further support the generalization were granted by the respective research groups prior to their publication.

AUTHOR CONTRIBUTIONS

MH was creator of NEURON simulator and developing CoreNEURON library with PK. JF and AO contributed to the development of core features in CoreNEURON. JK has integrated CoreNEURON with NEURON using HOC and Python scripting interface and helped in the validation of simulations. FD and FS has guided overall development and scientific roadmap of CoreNEURON. The final version of the article is written and edited jointly by all authors.

FUNDING

This work has been funded by the EPFL Blue Brain Project (funded by the Swiss ETH board), NIH grant number R01NS11613 (Yale University), the European Union Seventh Framework Program (FP7/2007-2013) under grant agreement n° 604102 (HBP) and the European Union's Horizon 2020 Framework Programme for Research and Innovation under Grant Agreement n° 720270 (Human Brain Project SGA1) and Grant Agreement n° 785907 (Human Brain Project SGA2).

ACKNOWLEDGMENTS

The authors would like to thank Bruno Magalhaes, Francesco Cremonesi, Sam Yates, and Timothee Ewart for contributions to the CoreNEURON development. This manuscript has been released as a Pre-Print at https://arxiv.org/abs/1901.10975 (Kumbhar et al., 2019).

SUPPLEMENTARY MATERIAL

The Supplementary Material for this article can be found online at: https://www.frontiersin.org/articles/10.3389/fninf.2019.00063/full#supplementary-material

REFERENCES

Ábrahám, E., Bekas, C., Brandic, I., Genaim, S., Johnsen, E. B., Kondov, I., et al. (2015). "Preparing hpc applications for exascale: challenges and recommendations," in *2015 18th International Conference on Network-Based Information Systems* (Taipei), 401–406.

Akar, N. A., Cumming, B., Karakasis, V., Küsters, A., Klijn, W., Peyser, A., et al. (2019). "Arbor — a morphologically-detailed neural network simulation library for contemporary high-performance computing architectures," in *2019 27th Euromicro International Conference on Parallel, Distributed and Network-Based Processing (PDP)* (Pavia), 274–282.

Anastassiou, C. A., Perin, R., BuzsÃiki, G., Markram, H., and Koch, C. (2015). Cell type- and activity-dependent extracellular correlates of intracellular spiking. *J. Neurophysiol.* 114, 608–623. doi: 10.1152/jn.00628.2014

Arkhipov, A., Gouwens, N. W., Billeh, Y. N., Gratiy, S., Iyer, R., Wei, Z., et al. (2018). Visual physiology of the layer 4 cortical circuit *in silico*. *PLOS Comput. Biol.* 14, 1–47. doi: 10.1371/journal.pcbi.1006535

Blundell, I., Brette, R., Cleland, T. A., Close, T. G., Coca, D., Davison, A. P., et al. (2018). Code generation in computational neuroscience: a review of tools and techniques. *Front. Neuroinform.* 12:68. doi: 10.3389/fninf.2018.00068

Cohen, S. D., and Hindmarsh, A. C. (1996). Cvode, a stiff/nonstiff ode solver in c. *Comput. Phys.* 10, 138–143.

CoreNEURON GitHub Repository (2019). *CoreNEURON - Simulator Optimized for Large Scale Neural Network Simulations*. Available online at: https://github.com/BlueBrain/CoreNeuron (accessed May 1, 2019).

Dagum, L., and Menon, R. (1998). OpenMP: an industry standard API for shared-memory programming. *IEEE Comput. Sci. Eng.* 5, 46–55.

Dahmen, D., van Albada, S. J., Tetzlaff, T., Hagen, E., Grün, S., Diesmann, M., et al. (2016). Hybrid scheme for modeling local field potentials from point-neuron networks. *Cereb. Cortex* 26, 4461–4496. doi: 10.1093/cercor/bhw237

Davies, S. N. (1992). Neural networks of the hippocampus. by Roger D. Traub and Richard Miles. pp. 281. Cambridge university press, 1991. isbn 0 521 36481 7. *Exp. Physiol.* 77, 238–238.

De Schutter, E., and Bower, J. (1994). An active membrane model of the cerebellar purkinje cell i. simulation of current clamps in slice. *J. Neurophysiol.* 71, 375–400.

Deco, G., Jirsa, V. K., Robinson, P. A., Breakspear, M., and Friston, K. (2008). The dynamic brain: from spiking neurons to neural masses and cortical fields. *PLOS Comput. Biol.* 4, 1–35. doi: 10.1371/journal.pcbi.1000092

Dyhrfjeld-Johnsen, J., Santhakumar, V., Morgan, R. J., Huerta, R., Tsimring, L., and Soltesz, I. (2007). Topological determinants of epileptogenesis in large-scale structural and functional models of the dentate gyrus derived from experimental data. *J. Neurophysiol.* 97, 1566–1587. doi: 10.1152/jn.00950.2006

Gal, E., London, M., Globerson, A., Ramaswamy, S., Reimann, M., Muller, E., et al. (2017). Rich cell-type-specific network topology in neocortical microcircuitry. *Nat. Neurosci.* 20, 1004–13. doi: 10.1038/nn.4576

Gewaltig, M.-O., and Diesmann, M. (2007). NEST (NEural simulation tool). *Scholarpedia* 2:1430. doi: 10.4249/scholarpedia.1430

Haring, R., Ohmacht, M., Fox, T., Gschwind, M., Satterfield, D., Sugavanam, K., et al. (2012). The IBM blue gene/Q compute chip. *IEEE Micro* 32, 48–60. doi: 10.1109/MM.2011.108

Hepburn, I., Chen, W., and Schutter, E. D. (2016). Accurate reaction-diffusion operator splitting on tetrahedral meshes for parallel stochastic molecular simulations. *J. Chem. Phys.* 145:054118.

Hewlett Packard Enterprise (2019). *HPE SGI 8600 System*. Available online at: https://h20195.www2.hpe.com/V2/getpdf.aspx/A00016640ENW.pdf (accessed May 1, 2019).

Hines, M. (1993). "NEURON—a program for simulation of nerve equations," in *Neural Systems: Analysis and Modeling*, ed F. Eeckman (Norwell, MA: Kluwer), 127–136.

Hines, M. (2014). *NEURON GPU Implementation*. Available online at: https://bitbucket.org/nrnhines/nrngpu (accessed May 1, 2019).

Hines, M. (2017a). *Ring Network Model of Ball-and-Stick neurons*. Available online at: https://github.com/nrnhines/ringtest (accessed May 1, 2019).

Hines, M. (2017b). *Traub 2005 model for CoreNEURON*. Available online at: https://github.com/nrnhines/nrntraub (accessed May 1, 2019).

Hines, M. (2019). *NMODL User Guide*. Available online at: https://www.neuron.yale.edu/neuron/static/py_doc/modelspec/programmatic/mechanisms/nmodl.html (accessed May 1, 2019).

Hines, M., Kumar, S., and Schurmann, F. (2011). Comparison of neuronal spike exchange methods on a blue gene/p supercomputer. *Front. Comput. Neurosci.* 5:49. doi: 10.3389/fncom.2011.00049

Hines, M. L., and Carnevale, N. T. (1997). The neuron simulation environment. *Neural Comput.* 9, 1179–1209.

Hines, M. L., and Carnevale, N. T. (2000). Expanding neuron's repertoire of mechanisms with nmodl. *Neural Comput.* 12, 995–1007. doi: 10.1162/089976600300015475

Hines, M. L., Markram, H., and Schürmann, F. (2008). Fully implicit parallel simulation of single neurons. *J. Comput. Neurosci.* 25, 439–448. doi: 10.1007/s10827-008-0087-5

Human Brain project (2018). *Community Models of Hippocampus*. Available online at: https://www.humanbrainproject.eu/en/brain-simulation/hippocampus/ (accessed January 11, 2018).

Ippen, T., Eppler, J. M., Plesser, H. E., and Diesmann, M. (2017). Constructing neuronal network models in massively parallel environments. *Front. Neuroinform.* 11:30. doi: 10.3389/fninf.2017.00030

Izhikevich, E. M., and Edelman, G. M. (2008). Large-scale model of mammalian thalamocortical systems. *Proc. Natl. Acad. Sci. U.S.A* 105, 3593–3598. doi: 10.1073/pnas.0712231105

Jolivet, R., Coggan, J. S., Allaman, I., and Magistretti, P. J. (2015). Multi-timescale modeling of activity-dependent metabolic coupling in the neuron-glia-vasculature ensemble. *PLOS Comput. Biol.* 11, 1–23. doi: 10.1371/journal.pcbi.1004036

Kumar, S., Heidelberger, P., Chen, D., and Hines, M. (2010). Optimization of applications with non-blocking neighborhood collectives via multisends on the blue gene/p supercomputer. *IPDPS* 2010, 1–11. doi: 10.1109/IPDPS.2010.5470407

Kumbhar, P., Hines, M., Fouriaux, J., Ovcharenko, A., King, J., Delalondre, F., et al. (2019). CoreNEURON : an optimized compute engine for the NEURON Simulator. *arXiv:1901.10975*.

Kumbhar, P., Hines, M., Ovcharenko, A., Mallon, D. A., King, J., Sainz, F., et al. (2016). *Leveraging a Cluster-Booster Architecture for Brain-Scale Simulations* (Frankfurt: Springer International Publishing), 363–380.

Lange, M., Gorman, G., Weiland, M., Mitchell, L., and Southern, J. (2013). Achieving efficient strong scaling with petsc using hybrid mpi/openmp optimisation. in *Supercomputing* eds J. M. Kunkel, T. Ludwig, and H. W. Meuer (Berlin; Heidelberg: Springer), 97–108.

Levine, J., and John, L. (2009). *Flex & Bison, 1st Edn*. O'Reilly Media, Inc. Available online at: http://shop.oreilly.com/product/9780596155988.do

Lindroos, R., Dorst, M. C., Du, K., FilipoviÄ, M., Keller, D., Ketzef, M., et al. (2018). Basal ganglia neuromodulation over multiple temporal and structural scales simulations of direct pathway msns investigate the fast onset of dopaminergic effects and predict the role of kv4.2. *Front. Neural Circ.* 12:3. doi: 10.3389/fncir.2018.00003

Mainen, Z. F., and Sejnowski, T. J. (1996). Influence of dendritic structure on firing pattern in model neocortical neurons. *Nature* 382, 363–366.

Markram, H., Muller, E., Ramaswamy, S., Reimann, M. W., Abdellah, M., Sanchez, C. A., et al. (2015). Reconstruction and simulation of neocortical microcircuitry. *Cell* 163, 456–492. doi: 10.1016/j.cell.2015.09.029

Migliore, M., Cannia, C., Lytton, W. W., Markram, H., and Hines, M. L. (2006). Parallel network simulations with nEURON. *J. Comput. Neurosci.* 21, 119–129. doi: 10.1007/s10827-006-7949-5

MOD2C GitHub Repository (2019). *MOD2C - Converter for Mod Files to C Code*. Available online at: http://github.com/BlueBrain/mod2c (accessed May 1, 2019).

Nichols, B., Buttlar, D., and Farrell, J. (1996). *Pthreads Programming: A POSIX Standard for Better Multiprocessing*. O'Reilly Media, Inc. Available online at: http://shop.oreilly.com/product/9781565921153.do

NVIDIA Corporation (2006–2017). *CUDA*. Available online at: https://developer.nvidia.com/about-cuda (accessed January 24, 2019).

NVIDIA Corporation (2012). *TESLA K20X GPU Accelerator*. Available online at: https://www.nvidia.com/content/pdf/kepler/tesla-k20x-bd-06397-001-v07.pdf (accessed April 4, 2019).

ParallelContext (2019). *NEURON User Guide*. Available online at: https://www.neuron.yale.edu/neuron/static/docs/help/neuron/neuron/classes/parcon.html#psolve (accessed May 1, 2019).

POINTER (2019). *NMODL User Guide*. Available online at: https://www.neuron.yale.edu/neuron/static/py_doc/modelspec/programmatic/mechanisms/nmodl.html#pointer (accessed May 1, 2019).

Potjans, T. C., and Diesmann, M. (2012). The cell-type specific cortical microcircuit: Relating structure and activity in a full-scale spiking network model. *Cereb. Cortex* 24, 785–806. doi: 10.1093/cercor/bhs358

Raikov, I., and Hines, M. (2016). *Model of a Dentate Granule Cells Adapted for CoreNEURON*. Available online at: https://github.com/pramodk/reduced_dentate (accessed May 1, 2019).

Reimann, M. W., Nolte, M., Scolamiero, M., Turner, K., Perin, R., Chindemi, G., et al. (2017). Cliques of neurons bound into cavities provide a missing link between structure and function. *Front. Comput. Neurosci.* 11:48. doi: 10.3389/fncom.2017.00048

Salmon, J. K., Moraes, M. A., Dror, R. O., and Shaw, D. E. (2011). "Parallel random numbers: as easy as 1, 2, 3," in *Proceedings of 2011 International Conference for High Performance Computing, Networking, Storage and Analysis*, SC '11 (New York, NY:ACM), 16:1–16:12.

Sanz-Leon, P., Knock, S. A., Spiegler, A., and Jirsa, V. K. (2015). Mathematical framework for large-scale brain network modeling in the virtual brain. *NeuroImage* 111, 385–430. doi: 10.1016/j.neuroimage.2015.01.002

Schulz, M., Bronevetsky, G., Fernandes, R., Marques, D., Pingali, K., and Stodghill, P. (2004). "Implementation and evaluation of a scalable application-level checkpoint-recovery scheme for MPI programs," in SC '04: *Proceedings of the 2004 ACM/IEEE Conference on Supercomputing* (Pittsburgh, PA: IEEE), 38–38. doi: 10.1109/SC.2004.29

Soltesz Lab (2019). Available online at: http://med.stanford.edu/ivansolteszlab/front-page.html (accessed May 1, 2019).

THREADSAFE (2019). *NEURON User Guide*. Available online at: https://www.neuron.yale.edu/neuron/static/py_doc/modelspec/programmatic/network/parcon.html#ParallelContext.Threads (accessed May 1, 2019).

Traub, R. D., Contreras, D., Cunningham, M. O., Murray, H., LeBeau, F. E. N., Roopun, A., et al. (2005). Single-column thalamocortical network model exhibiting gamma oscillations, sleep spindles, and epileptogenic bursts. *J. Neurophysiol.* 93, 2194–2232. doi: 10.1152/jn.00983.2004

Tuckwell, H. C. (2005). *Introduction to Theoretical Neurobiology: Volume 2, Nonlinear and Stochastic Theories*, Volume 8. Cambridge University Press. Available online at: https://www.cambridge.org/fr/academic/subjects/mathematics/mathematical-biology/introduction-theoretical-neurobiology-volume-2?format=PB&isbn=9780521019323

Valero-Lara, P., Martínez-Perez, I., Peña, A. J., Martorell, X., Sirvent, R., and Labarta, J. (2017). cuHinesBatch: Solving multiple hines systems on GPUs human brain project. *Proc. Comput. Sci.* 108, 566–575. doi: 10.1016/j.procs.2017.05.145

Wikipedia (2006). *NVIDIA CUDA*. Available online at: https://en.wikipedia.org/wiki/CUDA (accessed April 20, 2019).

Wikipedia (2012). *OpenACC*. Available online at: https://en.wikipedia.org/wiki/OpenACC (accessed April 20, 2019).

Wils, S., and De Schutter, E. (2009). Steps: modeling and simulating complex reaction-diffusion systems with python. *Front. Neuroinform.* 3:15. doi: 10.3389/neuro.11.015.2009

Conflict of Interest: The authors declare that the research was conducted in the absence of any commercial or financial relationships that could be construed as a potential conflict of interest.

Copyright © 2019 Kumbhar, Hines, Fouriaux, Ovcharenko, King, Delalondre and Schürmann. This is an open-access article distributed under the terms of the Creative Commons Attribution License (CC BY). The use, distribution or reproduction in other forums is permitted, provided the original author(s) and the copyright owner(s) are credited and that the original publication in this journal is cited, in accordance with accepted academic practice. No use, distribution or reproduction is permitted which does not comply with these terms.

frontiers in Neuroinformatics

ORIGINAL RESEARCH
published: 27 November 2019
doi: 10.3389/fninf.2019.00073

Analysis of Decision-Making Process Using Methods of Quantitative Electroencephalography and Machine Learning Tools

Grzegorz M. Wojcik[1], Jolanta Masiak[2], Andrzej Kawiak[1], Lukasz Kwasniewicz[1], Piotr Schneider[1], Filip Postepski[1] and Anna Gajos-Balinska[1]*

[1] Chair of Neuroinformatics and Biomedical Engineering, Faculty of Mathematics, Physics and Computer Science, Institute of Computer Science, Maria Curie-Sklodowska University, Lublin, Poland, [2] Neurophysiological Independent Unit of the Department of Psychiatry, Medical University of Lublin, Lublin, Poland

The electroencephalographic activity of particular brain areas during the decision making process is still little known. This paper presents results of experiments on the group of 30 patients with a wide range of psychiatric disorders and 41 members of the control group. All subjects were performing the Iowa Gambling Task that is often used for decision process investigations. The electroencephalographical activity of participants was recorded using the dense array amplifier. The most frequently active Brodmann Areas were estimated by means of the photogrammetry techniques and source localization algorithms. The analysis was conducted in the full frequency as well as in alpha, beta, gamma, delta, and theta bands. Next the mean electric charge flowing through each of the most frequently active areas and for each frequency band was calculated. The comparison of the results obtained for the subjects and the control groups is presented. The difference in activity of the selected Brodmann Areas can be observed in all variants of the task. The hyperactivity of amygdala is found in both the patients and the control group. It is noted that the somatosensory association cortex, dorsolateral prefrontal cortex, and primary visual cortex play an important role in the decision-making process as well. Some of our results confirm the previous findings in the fMRI experiments. In addition, the results of the electroencephalographic analysis in the broadband as well as in specific frequency bands were used as inputs to several machine learning classifiers built in Azure Machine Learning environment. Comparison of classifiers' efficiency is presented to some extent and finding the most effective classifier may be important for planning research strategy toward finding decision-making biomarkers in cortical activity for both healthy people and those suffering from psychiatric disorders.

Keywords: electroencephalography, sLORETA, psychiatric disorders, frequency band analysis, machine learning, Iowa Gambling Task, decision-making

OPEN ACCESS

Edited by:
Ludovico Minati,
Tokyo Institute of Technology, Japan

Reviewed by:
Stavros I. Dimitriadis,
Cardiff University, United Kingdom
Ryszard Tadeusiewicz,
AGH University of Science and Technology, Poland

****Correspondence:***
Grzegorz M. Wojcik
gmwojcik@live.umcs.edu.pl

Received: *25 April 2019*
Accepted: *14 November 2019*
Published: *27 November 2019*

Citation:
Wojcik GM, Masiak J, Kawiak A, Kwasniewicz L, Schneider P, Postepski F and Gajos-Balinska A (2019) Analysis of Decision-Making Process Using Methods of Quantitative Electroencephalography and Machine Learning Tools. Front. Neuroinform. 13:73. doi: 10.3389/fninf.2019.00073

INTRODUCTION

Decision-making is an essential skill in everyday life but currently there is little systematic knowledge about how decision-making is affected in people with a diagnosis of psychiatric disorders. Decision-making is a process in which many cognitive functions are engaged. Probably that is why the IGT was often chosen as a task for investigating the behavior of the people with psychiatric disorders, however, there is relatively not much known about the cortical activity of individuals while making decisions in both healthy people and those with psychiatric disorders diagnosis. Some research has been done on the patients with major depressive disorder (Cella et al., 2010; Brevers et al., 2013). Similarly, the cohort of subjects with borderline personality disorder was investigated using IGT (Haaland and Landrø, 2007) as well as bipolar disorder (Paulus, 2007). IGT applications for a variety of research and different disorders are presented to some extent in a review by Brevers et al. (2013) and originally in Bechara (2007). With many applications in psychiatry, we decided to choose the IGT out of many other tasks for this stage of our research.

Quantitative electroencephalography is at its Renaissance stage in last decades (Sand et al., 2013) and has developed toward some forms of research in modern psychiatry (Kamarajan and Porjesz, 2015; Martínez-Rodrigo et al., 2017).

The rapid increase in the number of publications concerning Brain-Computer Interfaces (BCI) is observed (Mikołajewska and Mikołajewski, 2012, 2013, 2014; Teruel et al., 2017; Ozga et al., 2018; Wierzgała et al., 2018) and the EEG activity can be recognized as one of possible solutions in BCI engineering (Kotyra and Wojcik, 2017a,b). In addition, any ideas for finding biomarkers of psychiatric disorders (Chapman and Bragdon, 1964; Sutton et al., 1965; Campanella, 2013; Golonka et al., 2017) are in demand as the interview is still the most often used tool in psychiatry to make the diagnosis.

The expansion of computational modeling techniques applied to neuroscience makes it possible to simulate selected parts of the brain tissues which we are familiar with (Wojcik et al., 2007; Wojcik and Kaminski, 2008; Wojcik and Garcia-Lazaro, 2010) or even investigate the influence of electrophysiological parameters of single cells on the dynamics of the whole simulated system (Wojcik and Kaminski, 2007; Wojcik, 2012). However, we are still very far from explaining complex phenomena like psychiatric disorders or syndromes e.g., burn-out (Chow et al., 2018). Higher cognitive functions are sometimes a source of inspiration in biomedical engineering (Kaminski and Wojcik, 2004; Ważny and Wojcik, 2014; Wojcik and Ważny, 2015; Kufel and Wojcik, 2018) and artificial intelligence (Ogiela et al., 2008; Szaleniec et al., 2008, 2013) mixed with cognitive science methodology provides some explanation or leads to the construction of classification tools. Nevertheless, we are still in demand for verification theory in the experiment.

There are different electroencephalographic methods that allow visualization of recorded activity on the brain model. One of them is the standardized low-resolution brain electromagnetic tomography algorithm (sLORETA) (Pascual-Marqui et al., 1994, 1999; Pascual-Marqui, 2002). This method advantages come from the high temporal resolution of modern electroencephalographs (Tohka and Ruotsalainen, 2012) and makes possible to compute the subjects brain activity distributed in time and put it on brain topography with the tomography-like quality of detail. Applications of sLORETA were reported e.g., for the attention-deficit-hyperactivity disorder (ADHD) (Mann et al., 1992) and neurodegenerative diseases (Wu et al., 2014). The sLORETA can be also applied in the frequency band analysis (Moretti et al., 2004; Saletu et al., 2010).

Using EEG based source localization techniques for the measurement of subcortical activity can be controversial. We are aware of the fact that for example in Krishnaswamy et al. (2017) authors state that subcortical structures produce smaller scalp EEG signals. This happens because they are farther from the head surface than cortical structures. To make matters worse, subcortical neurons can have a closed-field geometry that further weakens the observed distant fields and subcortical structures are surrounded by the cortical mantle. So measurements of activity in deep brain structures can potentially be explained by a surrogate distribution of currents on the cortex. That is why it can be very difficult to measure subcortical activity when cortical activity is occurring at the same time (Krishnaswamy et al., 2017). However, there are various mathematical models (Grech et al., 2008) that allow us to make some estimation of such kind of activity. Our lab is equipped with the very sophisticated and developed for 25 years GeoSource software[1], where such models are implemented and based on the results given by it, having access to the photogrammetry station which generates the head model with high accuracy, we are able to draw some conclusions that are some extrapolated indicators for subcortical areas increased activity. The GeoSource is not the only software with subcortical areas activity algorithmic detectors. We have done some comparative analysis with BESA and its: ERP analysis and averaging[2] and source analysis and imaging[3] packages getting the same quality of results.

The investigations of Event-Related Potentials are often chosen by experimental psychologists as well as clinicians and biomedical engineers. One of the best-recognized ERP experiments in which decision-making is investigated was proposed by Bechara et al. (1994). It is known as the Iowa Gambling Task (IGT) and is described in detail in the Materials and Methods section of this contribution.

IGT was used in many clinical experiments (Cui et al., 2013; Mapelli et al., 2014; Tamburin et al., 2014). In Tamburin et al. (2014) the patients with chronic low back pain were investigated and the authors tried to find correlations between the ERP responses and the cognitive measures taken on them. On the other hand, in Cui et al. (2013) the students were investigated during IGT and the amplitudes of P3 potential were observed and discussed. Similar research is reported (Mapelli et al., 2014)

[1]GeoSource 3 electrical source imaging packages: https://www.egi.com/research-division/electrical-source-imaging/geosource

[2]BESA: ERP analysis and averaging, http://www.besa.de/products/besa-research/features/erp-analysis-and-averaging/

[3]BESA: Source analysis and imaging, http://www.besa.de/products/besa-research/features/source-analysis-and-imaging/

but in this case it was focused on the people with Parkinson's disease making decisions and after that their ERP potentials were analyzed. The research mentioned above is concentrated on the analysis of the shape of statistically averaged potential and there are no source localization procedures applied to the analysis.

The aim of the research presented herein was to apply the methodology proposed in Wojcik et al. (2018a) and Wojcik et al. (2018b) to the quantitative electroencephalographic analysis of cortical activity from the patients in different frequency bands as well as in the full spectrum of the EEG signal. We used source localization techniques and having measured the average amperage in time for particular Brodmann Areas (BA) the mean electric charge flowing through them during the experiment was conducted for each patient and member of the control group. For this contribution, the brain activity of a group of patients with selected psychiatric disorders was measured using dense array EEG. These results were compared with those obtained from the participants of the control group. Both groups performed IGT.

Additionally, the results gathered for both healthy and disordered people in the broad and particular frequency EEG bands were taken as inputs to seven different machine learning classifiers in order to distinguish two types of responses in IGT, basing only on BA activity. The efficiency of these classifiers was compared and is presented to some extent.

MATERIALS AND METHODS

The Department of Neuroinformatics is equipped with the dense array amplifier recording the cortical activity with up to 500 Hz frequency through 256 channels HydroCel GSN 130 Geodesic Sensor Nets provided by EGI[4]. In addition, in the EEG Laboratory the Geodesic Photogrammetry System (GPS) was used. Eleven cameras placed in the corners of GPS take a set of subject's photos and then it is possible to make a model of the particular subject brain based on its calculated size, proportion and shape. Next the software imposes all computed activity results on this model with a very good accuracy. The amplifier operates on the Net Station 4.5.4 software, GPS is under control of the Net Local 1.00.00 and GeoSource 2.0. The eye blinks and saccades elimination as well as gaze calibration are obtained owing to the application of dedicated eye-tracker operated by SmartEye 5.9.7. The Event-Related Potentials (ERP) experiments are conducted in the PST e-Prime 2.0.8.90 environment[5].

We investigated 30 patients, 9 females and 21 males (avg. age 28.1, s.d. 12.4). They have been diagnosed with a wide range of psychiatric disorders. The disorders are classified in ICD-10 as: 12 × F41 (Panic disorder), 5 × F32.1 (Major depressive episode), 5 × F84.5 (Asperger syndrome), 3 × F40 (Social anxiety disorders), 2 × F31 (Bipolar affective disorder), 2 × F42 (Obsessive-compulsive disorder co-occurrent with the patients with F84.5), 2 × F51.1 (Non-organic hypersomnia), and 1× F20 (Schizophrenia). The control group of 30 healthy volunteers were also examined. The control group were only males (avg. age 22.4, s.d. 1.7). It is worth noting that about 30% more subjects were investigated from both control and patients' groups as the signal of all those for whom the recordings were too noisy or incomplete had to be eliminated. All participants were right-handed and measured by a handedness questionnaire (Chapman and Chapman, 1987).

The IGT was introduced by Bechara et al. (1994) and since then it has become one of the favorite tasks given to the subjects participating in a wide range of experimental psychology experiments. Originating from the research first carried out at the University of Iowa the IGT was intended to get hold of mechanisms of decision-making process during the reward-punishment oriented card game. The aim of the task is to choose one card deck symbol out of four in each of 100 trials. The participants are told to earn as much of virtual money as possible starting with 0 dollars. In each set of four cards (or symbols) there is a couple of so-called good cards for which there is a reward and a couple of so-called bad cards for which there is a punishment. The participants do not know which card is good and which is bad but they can conclude it from the game behavior. However, at the beginning all cards seem to be good, but for two of them they make impression to be better as the reward for choosing them is remarkably higher than for choosing the others. After several choices of the better cards, the punishments for choosing the next are extremely high. On the other hand the punishment for choosing cards after the initial selection of those worse at the beginning is very low which finally gives the better financial results when compared to the other case. The typical screens shown on the computer on which our participants make decisions is shown in **Figure 1**.

The electroencephalographic signal was recorded. After the test the photo of each participant was taken using the GPS. Such a technique allows obtaining spatial resolutions comparable to 1.5 T MRI without the necessity of MRI brain scanning for each participant. Thus, the anatomical models of participants' brains are generated using the GeoSource software and GPS photogrammetry which allows us to estimate the activity of particular BAs with satisfactory precision. Note, that in our approach we do not use the default model of the head, which is also possible. We make use of GPS to achieve the best possible accuracy of source localization.

Such methodology allowed us to apply the source localization algorithm with a satisfactory accuracy and estimate the most active Brodmann Areas in each participant during the decision-making process. The Net Station software along with the GeoSource tool has implemented the most popular version of the sLORETA algorithm which is described in the chapter titled Brain Source Localization Using EEG Signals in Nidal and Malik (2014). It is based on standardization of the current density assumption. That means that both the variance of the noise in the signal and the biological variance in the actual signal are taken into account (Goldenholz et al., 2009; Nidal and Malik, 2014). Independent and uniform distribution of the biological signal variance across the brain cortex is taken into consideration and this results in a linear imaging localization technique having exact, zero-localization error (Goldenholz et al., 2009; Nidal and

[4]Electrical Geodesic Systems, Inc., 500 East 4th Ave. Suite 200, Eugene, OR, 97401, USA.

[5]Psychology Software Tools, Inc. PST, Sharpsburg Business Park, 311 23rd Street Ext., Suite 200, Sharpsburg, PA, 15215-2821, USA.

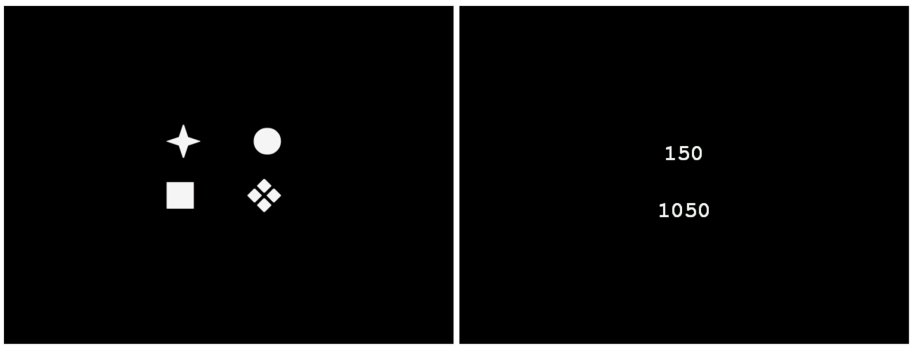


FIGURE 1 | Typical screens shown to participants during the IGT experiment. Card decks—in the left and reward/punishment with account state in the right. The screens are generated by the PST e-Prime 2.0.8.90 which is synchronized with Net Station 4.5.4 recordings.

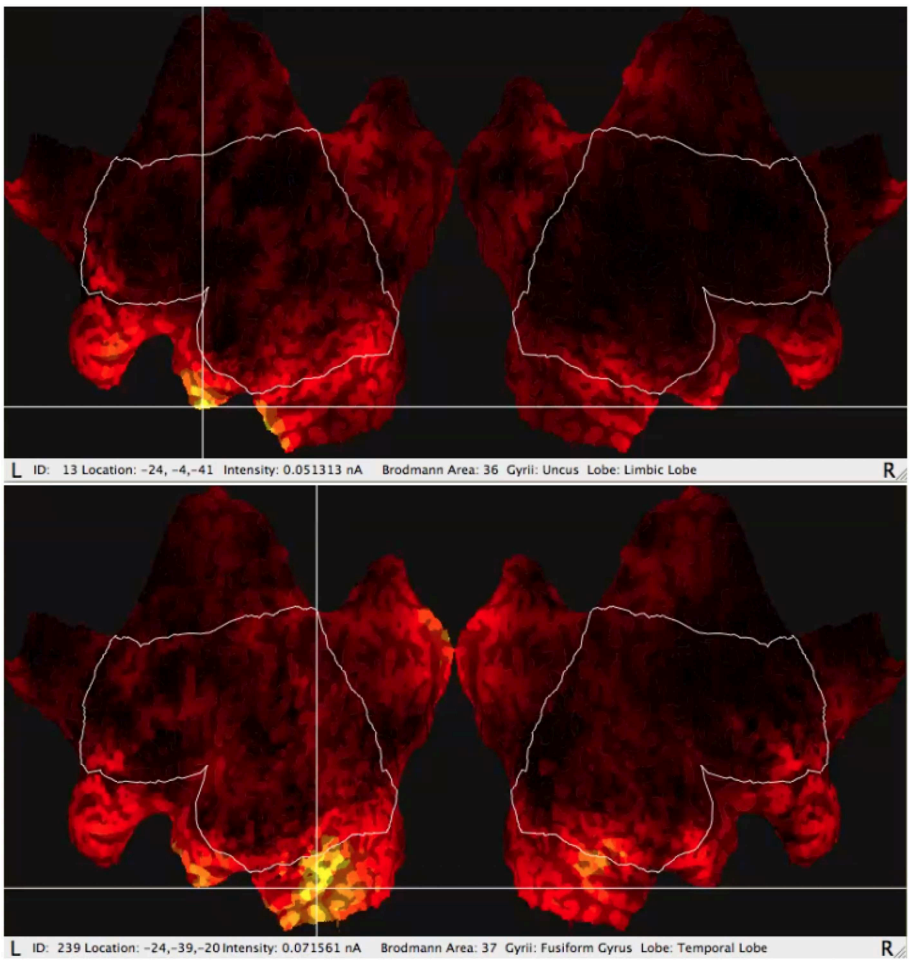


FIGURE 2 | Typical results of GeoSource BA activity visualization on the brain cortex so-called Flat Map. The increase of activity in BA36 (Uncus Lobe, Limbic Lobe) for good choice and BA37 (Fusiform Gyrus, Temporal Lobe) for bad choice are indicated.

Malik, 2014). For more details see the comparison of different types of LORETA in Nidal and Malik (2014).

The literature reports a few bands that cover typical rhythmical activity of the brain (Niedermeyer and da Silva, 2005) described as follows: δ—delta band (<4 Hz), θ—theta (4–7 Hz), α—alpha (8–15 Hz), β—beta (16–31 Hz), γ—gamma (more than 31 Hz), and sometimes μ—mu (8–12 Hz) bands. Sometimes the frequency ranges that define each band are slightly different. In

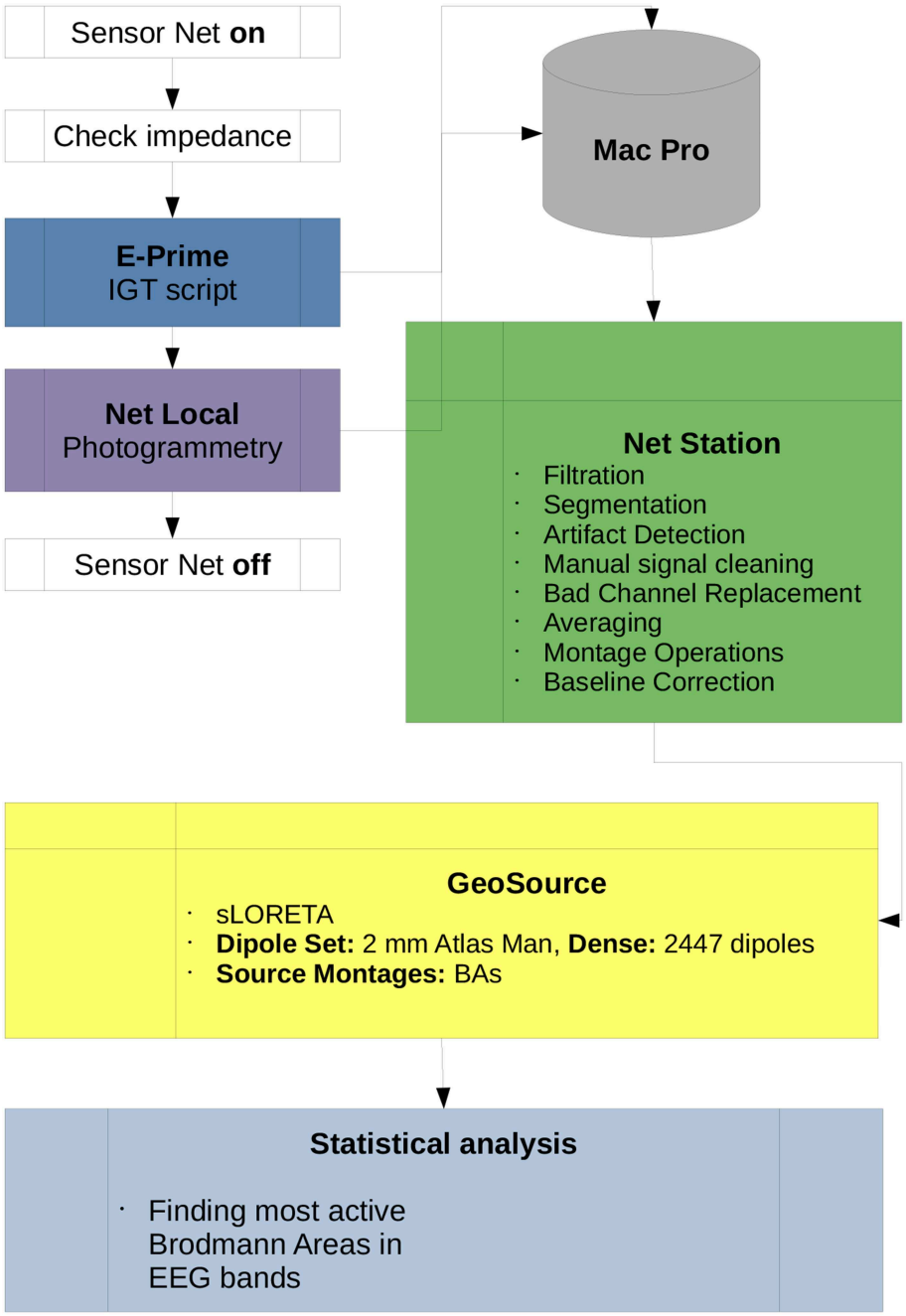


FIGURE 3 | Diagram of the IGT research protocol used in this paper. All scripts used for the preprocessing data in Net Station and post-processing in GeoSource are listed. Participation of the subject in the experiment begins when the Sensor Net is put on and ends when it is taken off. All data is collected by the Mac Pro workstation which is the central computational unit of the lab. Statistical analysis, finding the most active BAs in full or each of α, β, γ, δ, and θ frequency bands as well as ι estimations can be conducted on other machines.

our lab by default the frequency bands are set as follow: δ—delta band (0.1–3 Hz), θ—theta (4–7 Hz), α—alpha (7–12 Hz), β—beta (12–30 Hz), γ—gamma (more than 32 Hz).

One of the most useful functions of the GeoSource software is the possibility of estimation of the amperage of the most active areas (**Figure 2**) varying in time using source localization. The most active BA is indicated by the GeoSource as the BA with the highest electric current flowing through it in time. The activity of a particular BA could last at its maximum value for a longer or shorter period and it could appear more than once during each epoch. The signal was divided into epochs, as usual in ERP, in this case, IGT experiments, then averaged giving amperage in

TABLE 1 | Most active BA in particular subjects of the patients' group while receiving a reward during the IGT experiment in the full and in the alpha, beta, gamma, delta, and theta EEG bands.

No.	Diag.	Full band	α	β	γ	δ	θ
1	F20	BA05	BA29	BA29	BA05	BA34	BA29
2	F31	BA09	Amygd.	Amygd.	BA09	Amygd.	BA09
3	F31	BA05	Hipp.	Amygd.	BA17	Amygd.	Amygd.
4	F32.1	BA36	BA17	Amygd.	BA17	Amygd.	Amygd.
5	F32.1	BA17	BA05	Amygd.	BA17	Amygd.	BA05
6	F32.1	BA05	Amygd.	BA36	BA05	BA36	BA17
7	F32.1	BA17	Amygd.	Amygd.	BA17	BA36	Amygd.
8	F32.1	BA17	Amygd.	BA09	BA09	BA34	BA09
9	F40	Amygd.	Amygd.	Amygd.	Amygd.	BA05	BA04
10	F40	BA09	BA29	BA29	BA09	BA08	BA34
11	F40	BA46	BA24	BA36	Amygd.	BA05	BA46
12	F41	BA09	BA09	BA05	BA09	Amygd.	BA09
13	F41	Amygd.	Amygd.	BA29	Amygd.	BA29	Amygd.
14	F41	Amygd.	Amygd.	Amygd.	Amygd.	Amygd.	BA17
15	F41	BA09	Amygd.	Amygd.	BA09	Amygd.	BA04
16	F41	BA05	BA05	BA05	BA05	Amygd.	BA09
17	F41	Amygd.	Amygd.	Amygd.	Amygd.	Amygd.	BA17
18	F41	Amygd.	BA45	BA45	BA17	BA45	BA45
19	F41	BA09	Amygd.	Amygd.	BA04	Amygd.	BA09
20	F41	BA27	Amygd.	Amygd.	BA34	Amygd.	Amygd.
21	F41	Amygd.	Amygd.	Amygd.	Amygd.	Amygd.	BA04
22	F41	BA04	Amygd.	Amygd.	BA09	Amygd.	BA09
23	F41	BA05	BA36	BA27	BA05	BA27	BA05
24	F51.1	Amygd.	Amygd.	Amygd.	BA05	BA05	Amygd.
25	F51.1	BA17	BA05	BA36	BA17	BA36	BA17
26	F84.5	Amygd.	Amygd.	Amygd.	BA04	Amygd.	Amygd.
27	F84.5	BA09	BA17	BA17	BA09	BA17	BA09
28	F84.5	BA45	Hipp.	Hipp.	BA45	BA45	BA45
29	F84.5, F42	BA04	BA05	BA05	Amygd.	Amygd.	Amygd.
30	F84.5, F42	BA45	BA45	BA05	BA09	BA05	BA45

"Amygd." indicates Amygdala, "Hipp." for Hippocampus areas. For detail see Discussion section in text.

TABLE 2 | Most active BA in particular subjects of the patients' group while receiving a punishment during the IGT experiment in the full and in the alpha, beta, gamma, delta, and theta EEG bands.

No.	Diag.	Full band	α	β	γ	δ	θ
1	F20	BA05	BA34	BA29	BA05	BA34	BA29
2	F31	BA09	Amygd.	Amygd.	BA09	Amygd.	Amygd.
3	F31	Amygd.	Amygd.	Amygd.	BA17	Amygd.	Amygd.
4	F32.1	BA17	BA05	Amygd.	Amygd.	Amygd.	BA17
5	F32.1	BA05	Amygd.	BA05	BA17	BA05	Amygd.
6	F32.1	BA36	Amygd.	Amygd.	BA17	BA36	BA17
7	F32.1	Amygd.	Amygd.	Amygd.	Amygd.	Amygd.	Amygd.
8	F32.1	BA17	BA09	BA09	BA09	BA34	BA09
9	F40	Amygd.	BA05	BA04	Amygd.	BA05	BA17
10	F40	BA09	BA29	BA29	BA09	BA29	BA17
11	F40	BA05	Amygd.	BA36	Amygd.	Amygd.	BA17
12	F41	Amygd.	Amygd.	BA05	BA09	Amygd.	BA05
13	F41	BA04	Amygd.	BA29	BA05	BA29	Amygd.
14	F41	BA43	BA17	BA05	Amygd.	BA36	BA17
15	F41	Amygd.	BA05	Amygd.	Amygd.	Amygd.	Amygd.
16	F41	Amygd.	BA05	BA05	BA05	Amygd.	BA09
17	F41	Amygd.	Amygd.	Amygd.	Amygd.	Amygd.	Amygd.
18	F41	Amygd.	BA45	BA45	Amygd.	BA45	BA45
19	F41	Amygd.	Amygd.	Amygd.	Amygd.	Amygd.	Amygd.
20	F41	BA27	Amygd.	Amygd.	BA23	Amygd.	BA17
21	F41	BA04	Amygd.	Amygd.	BA09	Amygd.	BA04
22	F41	BA04	Amygd.	Amygd.	Amygd.	Amygd.	Amygd.
23	F41	BA05	BA05	BA27	Amygd.	BA41	BA05
24	F51.1	BA05	Amygd.	Amygd.	Amygd.	Amygd.	Amygd.
25	F51.1	BA05	BA05	BA34	BA17	Amygd.	BA17
26	F84.5	Amygd.	Amygd.	Amygd.	BA05	Amygd.	BA05
27	F84.5	BA09	Amygd.	BA17	BA09	BA17	BA09
28	F84.5	BA41	Hipp.	Hipp.	BA45	BA31	BA45
29	F84.5, F42	Amygd.	BA05	Amygd.	Amygd.	Amygd.	BA05
30	F84.5, F42	BA05	BA05	BA05	BA05	BA05	BA05

"Amygd." indicates Amygdala, "Hipp." for Hippocampus areas. For detail see Discussion section in text.

the function of time. Based on the electrical current measured by the EEG amplifier, most active BAs precisely indicated by the photogrammetry station and having precisely estimated time intervals owing to the perfect EEG time resolution, one of many numerical methods for integration can be applied to calculate the mean electric charge ι with good precision (Wojcik et al., 2018a) by integrating the electrical current in time. The details of mean electric charge estimation are described in detail in Wojcik et al. (2018a).

The sLORETA can be run for the full EEG frequency band above 0.1 Hz including the γ spectrum and for the selected frequency band analysis. Besides the full band there were taken into consideration each of the following: alpha, beta, gamma, delta, and theta. For each band including the full band, the varying in time value of amperage of particular BAs was obtained from the GeoSource. Having the amperage in the function of time one can calculate the mean electric charge ι flowing through the given BA as described in Wojcik et al. (2018a). The typical visualization of the GeoSource application to the signal is shown in the flat maps in **Figure 2**.

The time interval in which the BA activity was calculated was set to 5 ms and there was chosen the 800 ms segmentation (each segment starting with the stimuli) for signal averaging.

The BA1, BA2, and BA3 were eliminated from our analysis as they are part of Primary Somatosensory Cortex (S1) which was hyperactive owing to the subject's fingertips contact with the response pad during the experiment.

The scheme of the methodology and research protocol are presented in **Figure 3**. The full band analysis protocol in the case of P300 experiments was presented in Wojcik et al. (2018a) and the frequency band analysis protocol was described in detail in DIGITS related paper in Wojcik et al. (2018b). For this contribution the mixture of both methods proposed in Wojcik et al. (2018a,b) is applied.

TABLE 3 | The ι for the most active BA in particular patients receiving a reward during the IGT experiment obtained from the sLORETA quantitative analysis.

No.	Diag.	Full band ι [μC]	α ι [μC]	β ι [μC]	γ ι [μC]	δ ι [μC]	θ ι [μC]
1	F20	25.45	8.60	7.49	30.96	9.47	7.12
2	F31	45.10	3.99	5.59	43.32	6.03	17.82
3	F31	11.77	2.82	3.54	14.82	5.55	5.60
4	F32.1	37.92	3.40	33.19	38.90	11.31	6.01
5	F32.1	77.11	20.28	7.56	38.91	9.94	15.80
6	F32.1	200.70	15.17	19.93	56.61	17.39	20.45
7	F32.1	55.50	11.87	12.61	30.02	13.26	6.03
8	F32.1	24.65	4.58	9.10	69.61	8.19	8.05
9	F40	19.24	18.92	14.47	23.05	9.04	6.61
10	F40	46.20	5.35	5.60	20.27	2.67	7.69
11	F40	20.49	2.88	3.81	16.15	3.55	6.82
12	F41	67.16	6.03	10.13	20.88	14.89	6.40
13	F41	48.25	6.29	25.76	45.79	22.14	6.50
14	F41	118.70	5.40	6.24	50.14	9.89	20.32
15	F41	55.71	4.41	3.95	32.42	4.74	6.36
16	F41	68.59	11.27	11.07	44.56	8.43	16.58
17	F41	81.21	14.93	20.20	53.17	19.26	14.13
18	F41	45.66	8.50	15.83	39.21	14.15	15.55
19	F41	40.30	3.68	3.75	44.72	4.55	11.12
20	F41	91.03	9.34	11.66	93.58	16.13	7.46
21	F41	67.74	5.46	8.14	45.63	8.99	10.91
22	F41	26.20	6.75	10.53	61.26	14.79	9.62
23	F41	29.25	4.96	8.02	20.15	11.23	6.23
24	F51.1	34.89	2.46	3.56	17.63	3.06	5.62
25	F51.1	28.82	2.14	3.22	20.67	3.49	4.06
26	F84.5	27.53	4.15	5.82	8.55	7.11	6.88
27	F84.5	44.27	2.05	6.32	28.75	7.86	5.04
28	F84.5	20.34	6.18	5.89	37.28	2.03	14.97
29	F84.5, F42	15.99	5.19	6.85	16.47	4.32	5.52
30	F84.5, F42	27.07	5.95	33.39	34.75	26.89	10.16

For detail see the Discussion section in the text.

TABLE 4 | The ι for the most active BA in particular patients receiving a punishment during the IGT experiment obtained from the sLORETA quantitative analysis.

No.	Diag.	Full band ι [μC]	α ι [μC]	β ι [μC]	γ ι [μC]	δ ι [μC]	θ ι [μC]
1	F20	58.78	8.41	11.80	19.74	14.19	13.74
2	F31	36.15	5.56	9.09	62.91	9.05	11.46
3	F31	19.13	3.33	10.09	16.76	10.48	5.27
4	F32.1	70.61	9.02	29.37	35.87	28.28	19.50
5	F32.1	44.21	39.90	13.93	44.60	20.02	25.72
6	F32.1	86.34	29.29	40.46	62.67	31.10	33.35
7	F32.1	70.96	14.87	17.38	39.71	19.95	25.57
8	F32.1	88.81	13.66	15.96	54.23	21.21	22.31
9	F40	33.17	26.94	25.38	22.23	20.06	6.64
10	F40	117.98	9.74	8.07	68.39	6.65	11.47
11	F40	30.50	5.26	7.00	22.34	8.58	8.03
12	F41	99.30	9.41	17.07	49.72	28.45	9.55
13	F41	49.64	6.88	43.05	37.35	46.80	12.43
14	F41	231.56	11.06	11.79	87.43	18.20	15.64
15	F41	103.02	8.47	8.90	91.82	12.95	15.18
16	F41	100.32	15.01	19.75	54.24	15.90	22.40
17	F41	84.65	20.36	26.41	64.05	37.07	47.20
18	F41	148.46	19.03	32.64	74.02	28.62	28.91
19	F41	57.55	6.54	5.95	39.59	9.03	18.25
20	F41	134.75	13.39	16.48	77.11	24.33	16.96
21	F41	117.67	9.80	12.43	87.12	18.07	10.34
22	F41	69.91	12.87	17.81	83.47	25.76	23.91
23	F41	77.93	10.15	12.17	48.43	18.50	15.37
24	F51.1	28.63	6.77	5.90	25.05	5.29	10.72
25	F51.1	22.51	4.22	6.80	25.58	8.54	7.28
26	F84.5	21.58	6.90	8.32	9.72	9.31	5.00
27	F84.5	76.76	5.10	12.97	92.33	16.31	21.26
28	F84.5	35.00	9.39	8.56	49.69	3.91	22.36
29	F84.5, F42	56.93	6.52	11.55	1.37	8.46	9.62
30	F84.5, F42	121.72	11.22	55.63	39.35	51.99	12.92

For detail see the Discussion section in the text.

The so-called Waveform Tools package from the Net Station ecosystem was used and all scripts shown in **Figure 3** originate from it. The description of algorithms used in the preprocessing and post-processing stages of the research is given in Electrical Geodesics (2003) and the procedures used in the photogrammetry Net Local are described in the EGI Lab documentation (Electrical Geodesics, 2009, 2011). There were 100 trials for each participant, duration of the experiment was around 12 min. For the preprocessing we used the following and suggested by EGI engineers rules: As an average reference the average of all electrodes was taken. The artifact correction parameters were set as follow: bad channels filtering—Max-Min $>$ 200 μV; eye-blinks—Max-Min $>$ 140 μV, eye movements—Max-Min $>$ 140 μV—all performed in moving average of 80 ms. Filtration settings were set to passband gain 99%, stopband gain 1% and rollof 2 Hz, The segmentation was performed from 100 ms before stimulus to 700 after stimulus with offset 13 ms. The baseline correction was set to 100 ms from portion of segment. The rejection of trials took place when there were more than 10 bad channels.

The Holy Grail for the quantitative EEG based psychiatry is finding the biomarkers of particular psychiatric disorders based on the measured electrical activity of the brain. We proposed some idea to find such biomarkers in Wojcik et al. (2018b) by using the frequency band analysis and estimating the most active BAs in an above-mentioned way. Some research was also reported in Zolubak et al. (2019) where authors were investigating low frequency markers in neurofeedback therapy. But indicating the most active BAs can be not enough. In the last decades, we can, however, observe the rapid growth of data science methods applied to big datasets. One of the most important of them are machine learning tools and our idea was to check whether applying different classifiers to our results, both in broadband and specific frequency band analysis, could shed

TABLE 5 | The most active BA in particular subjects of the control group while receiving a reward during the IGT experiment in the full and in the alpha, beta, gamma, delta, and theta EEG bands.

No.	Full band	α	β	γ	δ	θ
1	Amygd.	BA05	BA05	Amygd.	BA05	BA05
2	Amygd.	Amygd.	Amygd.	Amygd.	Amygd.	Amygd.
3	BA17	BA05	BA17	BA09	Hipp.	BA09
4	BA17	Amygd.	BA36	BA17	BA36	BA17
5	BA09	BA05	BA05	BA09	BA27	BA09
6	BA17	Amygd.	Amygd.	BA17	Amygd.	BA17
7	BA17	Amygd.	Amygd.	BA09	Amygd.	BA09
8	BA05	Amygd.	BA05	BA05	BA05	BA09
9	BA09	BA18	BA24	BA17	BA18	BA17
10	BA28	BA34	BA34	BA09	BA34	Amygd.
11	BA05	Amygd.	BA05	BA05	BA05	BA05
12	BA09	BA46	BA05	BA09	Amygd.	BA09
13	BA17	BA17	BA17	BA17	BA17	BA17
14	BA09	Amygd.	Amygd.	BA09	Amygd.	BA17
15	BA09	Amygd.	BA27	BA09	BA27	BA17
16	BA09	BA05	Amygd.	BA09	Amygd.	BA05
17	BA09	BA29	BA29	BA17	BA28	BA17
18	BA05	Amygd.	BA34	BA09	Amygd.	BA09
19	Amygd.	BA04	BA04	Amygd.	BA04	Amygd.
20	BA09	Amygd.	Amygd.	BA09	Amygd.	Amygd.
21	BA17	Amygd.	BA36	BA17	BA36	BA17
22	Amygd.	Amygd.	Amygd.	Amygd.	BA28	Amygd.
23	Hipp.	BA17	BA27	BA17	BA27	BA17
24	BA41	Amygd.	Amygd.	BA17	BA05	Amygd.
25	BA17	BA42	BA42	BA17	BA27	BA17
26	BA09	BA09	Amygd.	BA09	Amygd.	BA17
27	BA05	BA09	Amygd.	Amygd.	Amygd.	BA09
28	BA46	Amygd.	Amygd.	Amygd.	BA05	BA46
29	Amygd.	BA45	BA27	BA17	BA27	BA45
30	BA17	BA05	BA05	BA17	BA36	Amygd.

"Amygd." indicates Amygdala, "Hipp." the Hippocampus areas.

TABLE 6 | The most active BA in particular subjects of the control group while receiving a punishment during the IGT experiment in the full and alpha, beta, gamma, delta, and theta EEG bands.

No.	Full band	α	β	γ	δ	θ
1	Amygd.	BA05	BA05	Amygd.	BA05	BA05
2	BA05	Amygd.	Amygd.	Amygd.	Amygd.	Amygd.
3	BA45	BA09	BA41	BA17	BA17	BA09
4	BA05	BA45	Amygd.	BA17	BA36	BA17
5	BA05	BA05	BA05	Amygd.	BA27	BA09
6	BA09	BA17	Amygd.	BA09	Amygd.	BA17
7	BA09	Amygd.	Amygd.	Amygd.	Amygd.	BA09
8	Amygd.	Amygd.	Amygd.	Amygd.	Amygd.	Amygd.
9	BA17	BA07	BA18	BA17	BA18	BA17
10	BA29	BA17	BA34	Amygd.	BA34	BA17
11	BA05	Amygd.	BA05	BA05	BA05	Amygd.
12	BA04	Amygd.	BA05	BA09	Amygd.	BA09
13	BA17	BA17	BA17	BA17	BA41	BA17
14	BA05	Amygd.	BA27	BA05	BA41	Amygd.
15	BA09	Amygd.	Amygd.	BA17	BA28	BA09
16	Amygd.	BA05	Amygd.	BA09	Amygd.	BA05
17	BA09	BA29	BA29	BA09	BA28	BA05
18	BA09	BA04	Amygd.	BA09	BA34	BA09
19	BA05	BA04	BA29	Amygd.	BA04	Amygd.
20	Amygd.	Amygd.	Amygd.	BA17	Amygd.	Amygd.
21	BA17	BA17	BA36	BA17	BA36	BA17
22	BA17	Amygd.	BA28	BA17	BA28	BA17
23	BA17	BA17	BA05	BA17	BA27	BA17
24	BA41	Amygd.	Amygd.	BA17	Amygd.	Amygd.
25	BA17	BA42	BA42	BA17	BA27	BA05
26	BA09	Amygd.	BA09	BA09	Amygd.	Amygd.
27	BA05	Amygd.	BA05	Amygd.	BA05	Amygd.
28	BA05	Amygd.	Amygd.	BA05	Amygd.	BA05
29	BA09	BA05	BA27	BA09	Amygd.	BA17
30	Amygd.	BA05	BA05	BA17	BA36	Amygd.

"Amygd." indicates Amygdala, "Hipp." the Hippocampus areas.

some light on solving diagnoses problems. If there is a secret code of particular disorders to be found in EEG activity—the application of machine learning tools, like classifiers, seems to be the best way to decode this. As the input to classifiers, the activity of BAs in the spectrum of the mean electric charge flowing through them should be considered. Because our patients' group consisted of only 30 subjects and with a wide range of disorders it was impossible to design classifiers that could distinguish the particular disorder from the another. However, the possibility of distinguishing the reward cortical states from the punishment activity was investigated and the efficiency of selected classifiers will be discussed in the following sections to some extent.

RESULTS

For each participant from both the patient and control groups, we estimated the most active BAs in each EEG frequency band during the reward and punishment phases of the IGT experiment.

Thus the most active BAs for the reward variant in the patient group are presented in **Table 1** and for the punishment in **Table 2**. The mean electric charge ι flowing through particular BA when receiving a reward by a patient is shown in **Table 3** and for punishment in **Table 4**.

In analogy for the control group the reward associated most active BAs are presented in **Table 5** and the punishment responses in **Table 6**. **Tables 7**, **8** present the values of ι calculated for each member of the control group in the reward and punishment variants of response, respectively.

As follows from **Tables 1**–**8** in all cases the Amygdala is hyperactive and the order of the value of ι tends to be similar for reward and punishment in both the subject and control groups in each frequency band.

TABLE 7 | The ι for the most active BA in particular subjects of the control group receiving a reward during the IGT experiment obtained from the sLORETA quantitative analysis.

No.	Full band ι [μC]	α ι [μC]	β ι [μC]	γ ι [μC]	δ ι [μC]	θ ι [μC]
1	35.13	4.97	6.25	21.43	8.76	5.09
2	123.05	20.57	11.64	157.64	5.93	42.89
3	18.50	2.29	3.12	30.77	3.75	6.08
4	28.76	3.10	2.37	49.85	3.44	6.78
5	34.17	4.95	6.11	45.50	3.89	13.49
6	35.07	2.95	4.85	56.67	3.46	11.16
7	44.39	4.44	4.68	41.99	4.94	9.71
8	44.52	2.57	2.82	27.37	3.55	5.54
9	22.01	2.59	3.50	44.04	5.46	4.52
10	29.10	3.58	5.32	36.85	6.92	4.49
11	74.89	2.90	8.60	43.62	7.82	3.83
12	16.20	2.82	2.76	42.64	2.88	6.58
13	91.48	4.22	4.35	93.37	1.06	7.83
14	26.73	6.71	7.43	17.22	1.06	6.80
15	31.23	3.03	5.06	69.70	6.23	11.95
16	40.49	2.96	2.81	25.40	2.68	5.86
17	19.58	5.02	9.06	9.08	4.37	5.10
18	29.44	5.69	7.51	20.83	3.24	6.22
19	20.94	12.05	10.69	27.52	4.98	17.75
20	36.71	2.56	4.77	26.71	2.23	5.51
21	36.85	4.48	3.62	40.97	6.17	9.02
22	22.35	2.60	4.17	11.91	4.64	4.07
23	25.54	9.62	6.41	60.50	6.38	16.57
24	93.76	4.25	5.60	13.82	5.45	6.00
25	28.75	9.77	18.81	27.34	6.59	6.99
26	41.20	6.59	8.00	89.68	8.19	14.10
27	77.02	5.40	10.27	95.49	6.93	13.58
28	16.18	2.64	3.44	18.24	3.72	4.03
29	19.45	2.88	2.76	26.82	2.98	4.51
30	22.57	16.39	20.27	30.82	7.50	7.19

For detail see the Discussion section in the text.

TABLE 8 | The ι for the most active BA in particular subjects of the control group receiving a punishment during the IGT experiment obtained from the sLORETA quantitative analysis.

No.	Full band ι [μC]	α ι [μC]	β ι [μC]	γ ι [μC]	δ ι [μC]	θ ι [μC]
1	47.89	8.94	11.78	63.56	15.64	8.99
2	203.19	27.55	22.29	277.38	10.28	75.45
3	34.32	4.23	19.78	21.88	5.85	5.68
4	34.02	3.95	4.14	24.11	4.80	12.66
5	41.10	8.24	12.84	54.96	6.38	15.80
6	80.51	7.69	8.61	47.67	9.31	18.62
7	55.34	7.10	8.21	29.96	9.99	15.50
8	125.22	4.56	5.83	63.70	7.58	8.83
9	29.85	5.90	6.48	37.00	9.27	11.87
10	89.41	8.66	10.62	82.42	12.51	7.70
11	132.74	6.12	11.68	109.95	13.24	6.27
12	34.78	5.58	4.91	40.29	4.90	6.63
13	203.37	6.69	6.21	89.38	0.99	31.37
14	37.34	14.02	11.15	34.81	1.80	14.62
15	51.69	10.40	13.26	35.51	17.34	11.14
16	31.28	4.35	4.32	17.42	6.62	8.93
17	46.04	6.65	13.57	14.03	6.91	5.08
18	50.01	7.94	11.22	78.38	6.83	12.96
19	39.11	11.51	14.88	40.65	8.03	16.86
20	45.93	2.76	3.95	34.68	4.67	6.29
21	68.19	10.09	7.55	73.64	10.18	15.74
22	34.54	4.33	7.62	29.19	10.21	6.92
23	58.34	18.68	12.75	75.45	9.00	18.49
24	118.22	9.63	11.49	64.50	11.44	14.56
25	70.20	17.48	19.10	55.03	10.83	9.88
26	54.22	9.57	13.28	103.73	13.20	23.43
27	158.88	8.50	11.97	71.10	10.81	16.73
28	26.53	4.51	5.84	15.03	5.85	5.23
29	32.70	3.66	4.68	34.81	5.66	7.71
30	45.49	24.36	30.51	34.31	13.03	14.36

For detail see the Discussion section in the text.

However, the comparison shown in **Figure 4** for the rewards and in **Figure 5** for the punishment can shed some light on the main differences in cortical responses of people with psychiatric disorders and members of the control group.

As far as the frequency of BA appearances in the IGT reward cortical responses are concerned (**Figure 4**) one can note that:

- The one of the amygdala is significantly higher in the patients compared to the control group when observed in the full, beta and delta frequency bands.
- The one of BA17 is significantly higher in the control group than in the patients when observed in the gamma and theta bands.
- The one of BA09 is higher in the control compared to the patients' group in the full and gamma frequency bands.

When considering the frequency of BA appearance in the IGT punishment responses one can observe that:

- The one of the amygdala is significantly higher in the patients than in the control group members in the full, alpha, beta, delta and gamma frequency bands.
- The one of BA17 is significantly higher in the control than in the patients' group in the full and gamma bands.
- The BA09 is significantly higher in the control group members than in patients when looking at the full and theta frequency bands.
- The BA05 in the control group is higher than in the patients in the full and beta frequency bands while in the alpha band it is lower.

The role of the amygdala during the decision-making process was discussed before even by the authors of IGT (Bechara et al., 2003). It is known that both the amygdala and orbitofrontal cortex are parts of a neural circuit critical for judgement and decision-making being under influence of "primary inducers"

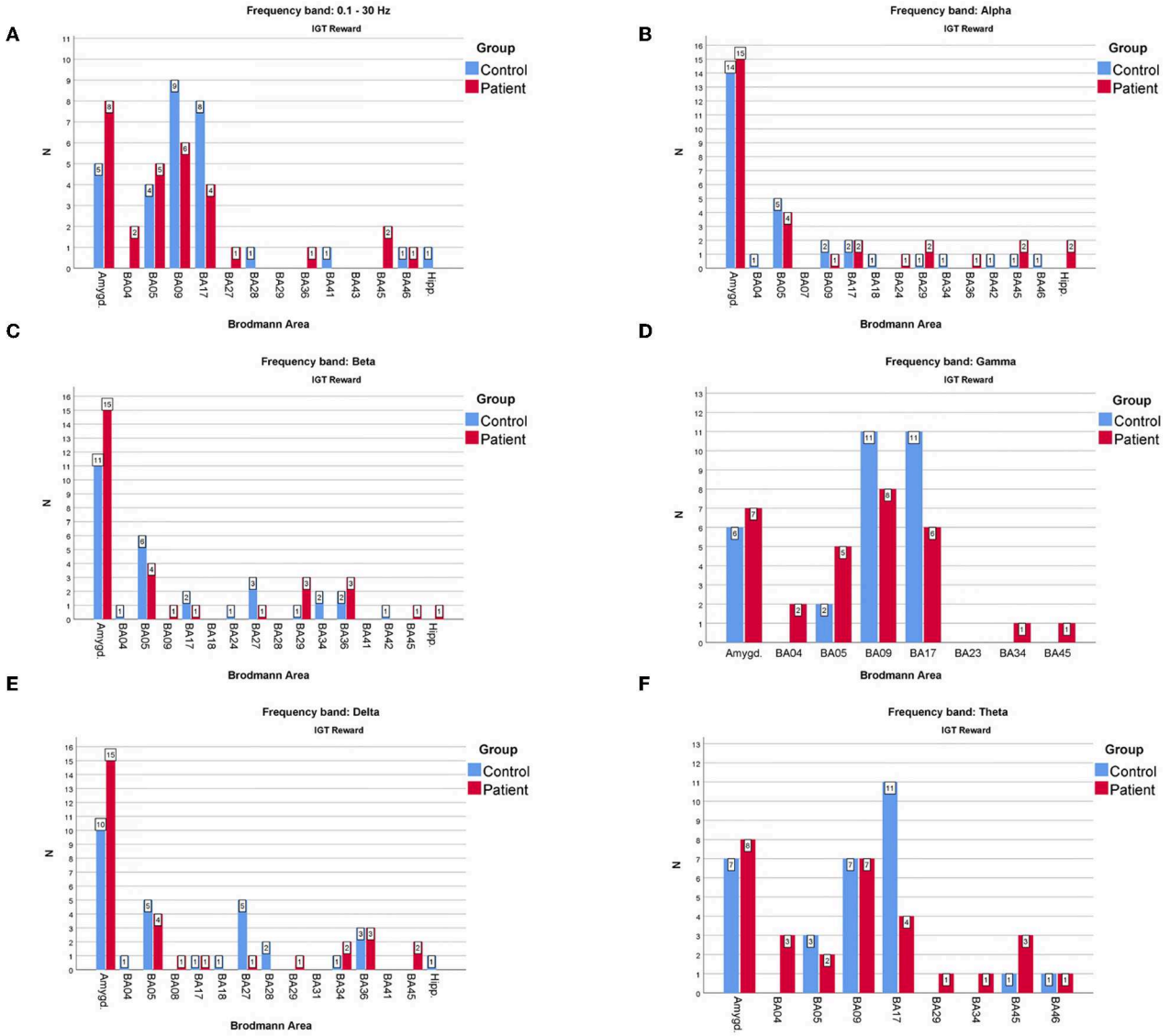


FIGURE 4 | The comparison of the most frequently active BAs in the patients and the control groups in the "reward" variant of IGT response for **(A)**—full, **(B)**—alpha, **(C)**—beta, **(D)**—gamma, **(E)**—delta, **(F)**—theta frequency bands. The y-axis refers to the N—number of subjects with particular BA maximum activity noted.

defined as stimuli that unconditionally, or through learning (e.g., conditioning and semantic knowledge), can (perceptually or subliminally) produce states that are pleasurable or aversive (Bechara et al., 2003).

In order to verify the somatic marker hypothesis which proposes that decision-making is a process depending on emotion, some research of the destroyed amygdala was carried out (Bechara et al., 1999; Gupta et al., 2011). During some fMRI studies it was shown that amygdala influences the decision-making process in the risk-taking experiments involving information ambiguity (Hsu et al., 2005).

Our experiments show that the people with psychiatric disorders have the amygdala more frequently hyperactive when compared to healthy participants from the control group.

The Azure Machine Learning Studio was used to construct seven different classifiers and next to compare their efficiency in the reward/punishment characteristic cortical activity detection and classification tasks. Our classifiers were designed in order to separate two classes (reward/punishment) and were as follow: logistic regression, decision jungle, support vector machine, boosted decision tree, averaged perceptron, Bayes point machine, classic neural network and locally-deep support vector algorithms. Each classifier had its own characteristics which are shown in **Table 10**. The registered activity of particular BAs manifesting itself by the mean electric charge ι in all discussed EEG frequency bands, including the broadband was taken as inputs to the classifier.

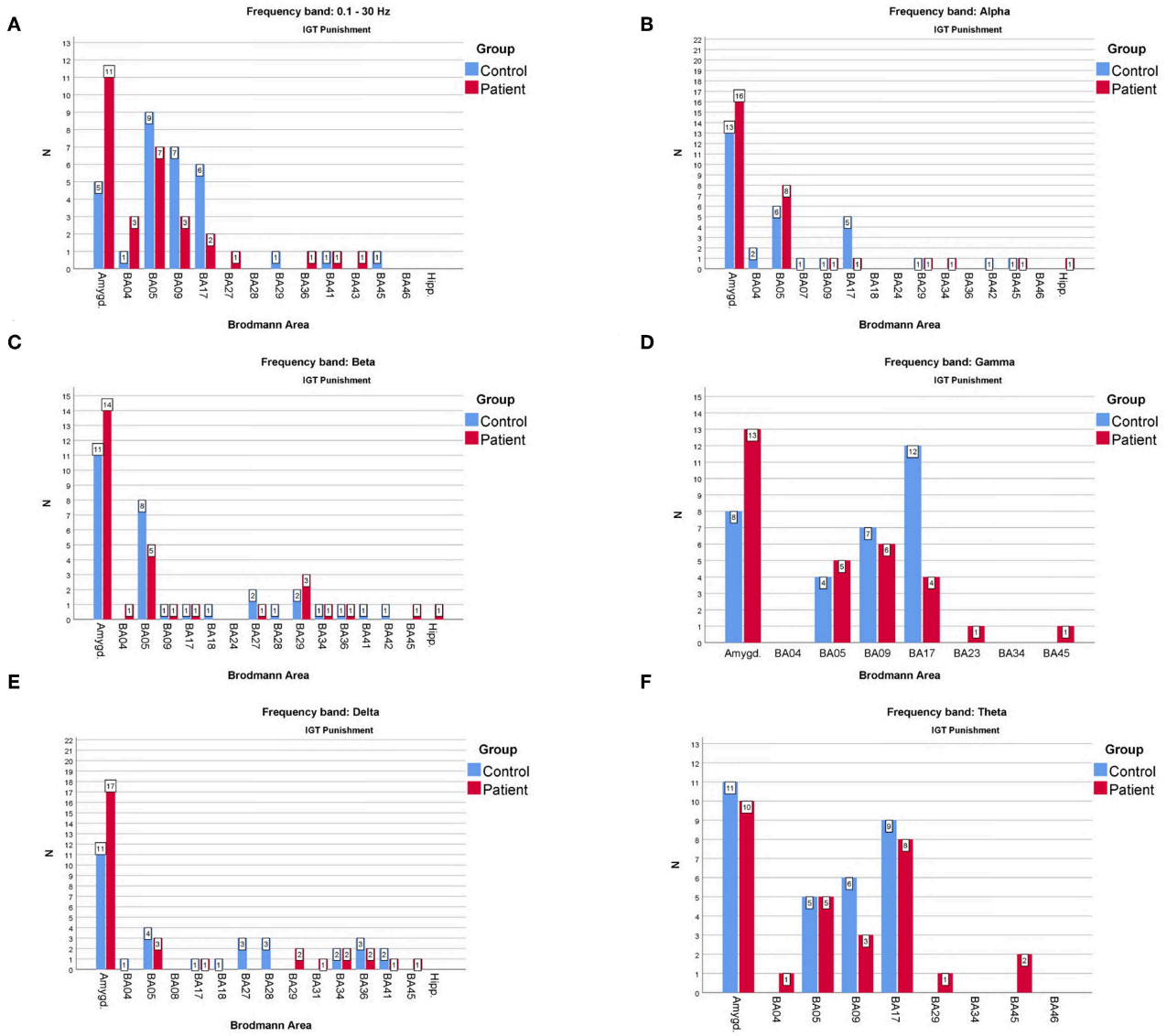


FIGURE 5 | The comparison of the most frequently active BAs in the patients and the control groups in the "punishment" variant of IGT response for **(A)**—full, **(B)**—alpha, **(C)**—beta, **(D)**—gamma, **(E)**—delta, **(F)**—theta frequency bands. The y-axis refers to the N—number of subjects with particular BA maximum activity noted.

Under ideal conditions, it would be expected to construct effective classifiers for particular psychiatric disorders, but having only 30 diagnosed subjects in our cohort with so many different diagnoses is far from being enough to perform any statistics. For the machine learning tasks, the control group was extended by an additional 11 healthy males finally reaching 41 subjects. Thus, the joined cohort consisted of 41 healthy males and 30 males with some disorders, in a total of 71 participants. Note that in typical ERP experiments there are standard (STD) and target (TGT) stimuli. In the case of IGT, the punishment is treated as STD and the reward is TGT as practically everyone dares to win. For each participant registered the reward and punishment states, finally giving $2 \times 71 = 142$ averaged responses to the investigated set.

The 5-fold Cross-Validation method was used to validate the efficiency of all classifiers.

Then the values of classification accuracy, recall and precision were calculated and results are presented in **Table 9**.

As one can see in **Table 9** there is no ideal classifier that could be applied to all of the EEG frequency bands, including the broadband.

For the broadband, the best results were achieved by the Locally-Deep Support Vector (acc. 0.698) and the Average Perceptron Classifier (acc. 0.684) methods.

In the α band the Logistic Regression (acc. 0.690) and Neural Network (acc. 0.669) turned out to be the best classifiers

TABLE 9 | Comparison of the discussed classifiers efficiency for all frequency bands, including the broadband in the STD (punishment) and TGT (reward) classification tasks.

Broad-band	Corr. TGT	Inc. TGT	Corr. STD	Inc.STD	Acc.	Recall	Prec.
Logistic regression	55	32	39	16	0.662	0.549	0.709
Decision jungle	42	31	40	29	0.577	0.563	0.580
Support vector machine	35	25	46	36	0.561	0.521	0.698
Avg. perceptron classifier	53	32	39	18	0.684	0.549	0.684
Bayes point machine	33	15	56	38	0.627	0.789	0.596
Neural network	55	41	30	16	0.652	0.423	0.652
Locally-deep support vector	55	34	37	16	0.698	0.648	0.561
α							
Logistic regression	54	27	44	17	0.690	0.620	0.721
Decision jungle	48	27	44	23	0.648	0.620	0.657
Support vector machine	41	29	42	30	0.585	0.577	0.683
Avg. perceptron classifier	51	28	43	20	0.662	0.606	0.683
Bayes point machine	46	28	43	25	0.627	0.606	0.632
Neural network	61	37	34	10	0.669	0.479	0.773
Locally-deep support vector	41	29	42	30	0.585	0.592	0.583
β							
Logistic regression	51	23	48	20	0.697	0.676	0.706
Decision jungle	51	24	47	20	0.690	0.662	0.701
Support vector machine	53	26	45	18	0.690	0.634	0.714
Avg. perceptron classifier	49	24	47	22	0.676	0.662	0.681
Bayes point machine	35	13	58	36	0.655	0.817	0.617
Neural network	58	36	35	13	0.655	0.493	0.729
Locally-deep support vector	46	29	42	25	0.620	0.592	0.627
γ							
Logistic regression	52	33	38	19	0.634	0.535	0.667
Decision jungle	42	30	41	29	0.585	0.577	0.586
Support vector machine	52	29	42	19	0.662	0.592	0.689
Avg. perceptron classifier	49	32	39	22	0.620	0.549	0.639
Bayes point machine	34	17	54	37	0.620	0.761	0.593
Neural network	50	33	38	21	0.620	0.535	0.644
Locally-deep support vector	41	31	40	30	0.570	0.563	0.571
δ							
Logistic regression	56	28	43	15	0.697	0.606	0.741
Decision jungle	49	23	48	22	0.683	0.775	0.743
Support vector machine	56	27	44	15	0.704	0.620	0.746
Avg. perceptron classifier	56	27	44	15	0.704	0.620	0.746
Bayes point machine	39	14	57	32	0.676	0.803	0.640
Neural network	62	37	34	9	0.676	0.479	0.791
Locally-deep support vector	50	28	43	21	0.655	0.606	0.672
θ							
Logistic regression	53	24	47	18	0.704	0.662	0.723
Decision jungle	51	31	40	20	0.641	0.563	0.667
Support vector machine	50	26	45	21	0.669	0.521	0.569
Avg. perceptron classifier	45	27	44	26	0.627	0.620	0.629
Bayes point machine	29	14	57	42	0.606	0.803	0.576
Neural network	61	41	30	10	0.641	0.423	0.750
Locally-deep support vector	50	26	45	21	0.669	0.521	0.569

Note, that numbers in rows sum to 142—for detail see text.

TABLE 10 | Characteristics of the Two-Class classifiers used in IGT analysis.

Two-class logistic regression	
Optimization tolerance	0.0001
L1 weight	0.1
L2 weight	0.1
Memory size	11
Quiet	True
Use threads	True
Allow unknown levels	True
Two-class decision jungle	
Ensemble element count	8
Max. depth	32
Max. width	128
Optimization step count	2
Resampling method	Bagging
Random number seed	5
Allow unknown levels	True
Two-class support vector machine	
Number of iterations	101
Lambda	1.0
Normalize features	True
Perform projection	False
Allow unknown levels	True
Two-class average perceptron classifier	
Batch size	256
Initial learning rate	0.1
Learning rate decay exponent	0.5
Averaging weight	0.5
Tolerance	1E-05
Maximum number of iterations	101
Allow unknown levels	True
Two-class bayes point machine	
Allow unknown levels	True
Random number seed	2,342
Training iteration count	30
Add bias	True
Two-class neural network	
Loss function	CrossEntropy
Is initialized from string	False
Is classification	False
Initial weights diameter	0.1
Learning rate	0.1
Momentum	0
Data normalizer type	MinMax
Number of input features	88
Number of hidden nodes	100
Number of iterations	51
Shuffle	True
Allow unknown levels	True
Two-class locally-deep support vector	
Tree depth	2
Lambda W	0.1
Lambda theta	0.1
Lambda theta prime	0.1
Sigma	1
Number of iterations	14,500
Normalizer type	MinMax
Allow unknown levels	True

When one looks at classifiers' results in the β band he notes the Logistic Regression (acc. 0.697), Decision Jungle (acc. 0.690) and Support Vector Machine (0.690) as the best, however the Logistic Regression has the highest recall value of 0.676, while the highest precision of 0.714 is achieved by Support Vector Machine.

If one studies the activity in the γ band he finds the highest efficiency for the Support Vector Machine (acc. 0.662) and again Logistic Regression (acc. 0.634).

For the δ band the highest accuracy 0.704 was achieved by the Support Vector Machine and Average Perceptron Classifier.

In case of the θ band, the best three ones were Logistic Regression (acc. 0.704), Support Vector Machine (0.669), and Locally Deep Support Vector (0.669), the Logistic Regression with the highest precision 0.723.

Note that the Bayes Point Machine did not perform well in any of EEG frequency bands.

DISCUSSION

In our experiment the relations between the decision-making process and the emotional responses given by the soma under such experimental conditions are also visible. Somatosensory association cortex (SAC) is mentioned in some papers on decisions making where it is even stated that somatosensory pattern marks the scenario as good or bad (Bechara et al., 2000; Donner et al., 2009). Our results also show that BA05 is one of the few most frequently active BAs in the patients and the control groups members., Moreover, the activity is qualitatively different in different frequency bands.

As well the dorsolateral prefrontal cortex (BA09) is often reported as engaged in decision-making processes. It was even found that damage of this structure results in poor performance in IGT (Fellows and Farah, 2004) and the fMRI studies have shown that the dorsolateral prefrontal cortex plays a role of negotiator establishing the link among sensory evidence, decision, and action during the decision making (Heekeren et al., 2006). Hyperactive BA09 is also reported to be found in other cognitive processes (Elliott, 2003), like working memory (Barbey et al., 2013), cognitive flexibility (Monsell, 2003), and planning (Chan et al., 2008). In our experiments the BA09 seems to be much more active in the control group when compared to the patients.

The visual processing areas provide the sensory evidence for a decision (Heekeren et al., 2004) and our results confirmed that the primary visual cortex is one of the most engaged areas in such processes, much more active in the control than in the patients' group. Some experiments involve the visual motion detection in the decision-making process among macaques (Huk and Shadlen, 2005) and this can be an inspiration for our future research.

The research protocol has been proposed to record the electroencephalographical cortical activity of the human brain during the decision making process. We chose

the IGT as one of the tasks that are most often used to investigate people making decisions. The sLORETA was then applied to find the most frequently active BA in the brain cortex both in the patients and the control group.

Some attempts to find biomarkers in the quantitative EEG signals were made for example by John et al. (1988). The frequency band analysis is often used in real-time computing of the engagement index (Lubar et al., 1995; Pope et al., 1995; Chaouachi et al., 2010). Moreover, some cognitive functions in patients with psychiatric disorders are different from those in healthy members of control groups (Trivedi, 2006).

Even though the cohorts were not large we could prove some findings reported after performing such experiments by means of much more sophisticated techniques including fMRI. We had 30 subjects with several different diagnoses. That is why it is hard to apply any more sophisticated statistical analysis. Collecting neurophysiological data is a real challenge for neuroinformatics (Bigdely-Shamlo et al., 2016; Cavanagh et al., 2017). In future it would require building separate cohorts for each particular disorder, for all genders and age ranges. Then it would be possible to make quantitative comparisons of cortical activity which hopefully could even lead to building psychiatric disorders classifiers.

The additional aim of this paper was to check whether it is possible to assess without looking into logs the subject's response in the IGT experiments using only the brain cortical electric activity as the input to the algorithm. The effectiveness of seven different tools from the Azure Machine Learning environment was investigated. The summary of the results is presented in **Table 9**.

It was shown that there is no universal classifier for each frequency band. However, for the future analysis the Logistic Regression in the α, β, and θ bands should be considered as well as the Support Vector Machine in the β, γ, and δ. Very interesting behavior can be observed for the Averaged Perceptron Classifier in the δ band which together with the Support Vector Machine has one the best recall and precision characteristics in the discussed research.

It is expected that for the larger dataset the efficiency would be much higher. This is the initial stage of our research but one can take it for granted that tuning-up the parameters would also improve the method performance. Now it is hard to predict which methods would be best for additional improving such classifiers. Probably the applications of sophisticated tools offered by applied mathematics (Kakiashvili et al., 2012; Koczkodaj and Szybowski, 2015) or even solutions found for engineering applications in computer science (Bolanowski and Paszkiewicz, 2015; Grabowski et al., 2015) along with big data analysis in such case could add some value.

At this stage, we had access to a limited number of patients. In our methodology, we decided to choose only those who had not taken any psychotropic medicines before. The aim of the research presented in this paper was to show the way in which the biomarkers can be searched. Putting the representatives of several disorders into one group by some readers can be recognized as controversial. On the other hand, we did not intend to give the final answer and to satisfy the definition of a biomarker in the full range of its properties. This would require at least 30 cases for each disorder and if one takes into consideration males and females, different age ranges, handedness—we get the number of about 400 patients for one problem, not saying about the control group. Consideration only the one disorder based on several patients does not make much sense as it would be hard to do the serious statistical analysis. But our results show that there can be quantitative methods to start the hunt for psychiatric disorders biomarkers.

Remembering that the interview is still the most important tool used in current psychiatry we are aware of the fact that developing tools and methods able to support the psychiatrist in the process of diagnosing are in a great demand and would improve the comfort of patients' life in the future.

DATA AVAILABILITY STATEMENT

The raw data supporting the conclusions of this manuscript will be made available by the authors, without undue reservation, to any qualified researcher.

ETHICS STATEMENT

This study was carried out in accordance with the recommendations of Guidelines for Good Clinical Practice (GCP). The protocol was approved by the Medical University of Lublin Bioethical Commission. All subjects gave written informed consent in accordance with the GCP. Permission No. KE-0254/138/2015 and No. KE-0254/140/2015 given by the Medical University of Lublin Bioethical Commission on May 28th, 2015.

AUTHOR CONTRIBUTIONS

GW: project idea and coordination, experiment design, subjects' recruitment, interpretation of results. JM: project idea, experiment design, subjects' recruitment, psychiatric diagnosis, interpretation of results. AK: work in laboratory, cleaning signal, computations, statistical analysis. PS, FP, and LK: statistical analysis, writing scripts, work in laboratory, cleaning signal. AG-B: work in laboratory.

ACKNOWLEDGMENTS

Special thanks to Mr. Slawomir Kotyra, M.Sc. from the Institute of Computer Science, Maria Curie-Sklodowska University in Lublin for solving the problem of electromagnetic noise in our laboratory.

REFERENCES

Barbey, A. K., Koenigs, M., and Grafman, J. (2013). Dorsolateral prefrontal contributions to human working memory. *Cortex* 49, 1195–1205. doi: 10.1016/j.cortex.2012.05.022

Bechara, A. (2007). *Iowa Gambling Task*. Lutz, FL: Psychological Assessment Resources.

Bechara, A., Damasio, A. R., Damasio, H., and Anderson, S. W. (1994). Insensitivity to future consequences following damage to human prefrontal cortex. *Cognition* 50, 7–15.

Bechara, A., Damasio, H., and Damasio, A. R. (2000). Emotion, decision making and the orbitofrontal cortex. *Cereb. Cortex* 10, 295–307. doi: 10.1093/cercor/10.3.295

Bechara, A., Damasio, H., and Damasio, A. R. (2003). Role of the amygdala in decision-making. *Ann. N. Y. Acad. Sci.* 985, 356–369. doi: 10.1111/j.1749-6632.2003.tb07094.x

Bechara, A., Damasio, H., Damasio, A. R., and Lee, G. P. (1999). Different contributions of the human amygdala and ventromedial prefrontal cortex to decision-making. *J. Neurosci.* 19, 5473–5481.

Bigdely-Shamlo, N., Makeig, S., and Robbins, K. A. (2016). Preparing laboratory and real-world EEG data for large-scale analysis: a containerized approach. *Front. Neuroinform.* 10:7. doi: 10.3389/fninf.2016.00007

Bolanowski, M., and Paszkiewicz, A. (2015). "The use of statistical signatures to detect anomalies in computer network," in L. Gołębiowski and M. Mazur (eds.) *Analysis and Simulation of Electrical and Computer Systems* (Springer International), 251–260.

Brevers, D., Bechara, A., Cleeremans, A., and Noël, X. (2013). Iowa gambling task (IGT): twenty years after–gambling disorder and igt. *Front. Psychol.* 4:665. doi: 10.3389/fpsyg.2013.00665

Campanella, S. (2013). Why it is time to develop the use of cognitive event-related potentials in the treatment of psychiatric diseases. *Neuropsychiatr. Dis. Treat.* 9:1835. doi: 10.2147/NDT.S53687

Cavanagh, J. F., Napolitano, A., Wu, C., and Mueen, A. (2017). The patient repository for EEG data+ computational tools (PRED+CT). *Front. Neuroinform.* 11:67. doi: 10.3389/fninf.2017.00067

Cella, M., Dymond, S., and Cooper, A. (2010). Impaired flexible decision-making in major depressive disorder. *J. Affect. Disord.* 124, 207–210. doi: 10.1016/j.jad.2009.11.013

Chan, R. C., Shum, D., Toulopoulou, T., and Chen, E. Y. (2008). Assessment of executive functions: review of instruments and identification of critical issues. *Archiv. Clin. Neuropsychol.* 23, 201–216. doi: 10.1016/j.acn.2007.08.010

Chaouachi, M., Chalfoun, P., Jraidi, I., and Frasson, C. (2010). "Affect and mental engagement: towards adaptability for intelligent systems," in *Proceedings of the 23rd International FLAIRS Conference* (Daytona Beach, FL: Citeseer).

Chapman, L. J., and Chapman, J. P. (1987). The measurement of handedness. *Brain Cogn.* 6, 175–183.

Chapman, R. M., and Bragdon, H. R. (1964). Evoked responses to numerical and non-numerical visual stimuli while problem solving. *Nature* 203:1155.

Chow, Y., Masiak, J., Mikołajewska, E., Mikołajewski, D., Wójcik, G. M., Wallace, B., et al. (2018). Limbic brain structures and burnout–a systematic review. *Adv. Med. Sci.* 63, 192–198. doi: 10.1016/j.advms.2017.11.004

Cui, J.-F., Chen, Y.-h., Wang, Y., Shum, D. H., and Chan, R. C. (2013). Neural correlates of uncertain decision making: ERP evidence from the iowa gambling task. *Front. Hum. Neurosci.* 7:776. doi: 10.3389/fnhum.2013.00776

Donner, T. H., Siegel, M., Fries, P., and Engel, A. K. (2009). Buildup of choice-predictive activity in human motor cortex during perceptual decision making. *Curr. Biol.* 19, 1581–1585. doi: 10.1016/j.cub.2009.07.066

Electrical Geodesics, I. (2003). *Net Station Waveform Tools Technical Manual*. Eugene, OR: EGI.

Electrical Geodesics, I. (2009). *Geodesic Photogrammetry System Technical Manual*. Eugene, OR: EGI.

Electrical Geodesics, I. (2011). *GeoSource 2.0 Technical Manual*. Eugene, OR: EGI.

Elliott, R. (2003). Executive functions and their disorders: imaging in clinical neuroscience. *Br. Med. Bull.* 65, 49–59. doi: 10.1093/bmb/65.1.49

Fellows, L. K., and Farah, M. J. (2004). Different underlying impairments in decision-making following ventromedial and dorsolateral frontal lobe damage in humans. *Cereb. Cortex* 15, 58–63. doi: 10.1093/cercor/bhh108

Goldenholz, D. M., Ahlfors, S. P., Hämäläinen, M. S., Sharon, D., Ishitobi, M., Vaina, L. M., et al. (2009). Mapping the signal-to-noise-ratios of cortical sources in magnetoencephalography and electroencephalography. *Hum. Brain Mapp.* 30, 1077–1086. doi: 10.1002/hbm.20571

Golonka, K., Mojsa-Kaja, J., Popiel, K., Marek, T., and Gawlowska, M. (2017). Neurophysiological markers of emotion processing in burnout syndrome. *Front. Psychol.* 8:2155. doi: 10.3389/fpsyg.2017.02155

Grabowski, F., Paszkiewicz, A., and Bolanowski, M. (2015). "Wireless networks environment and complex networks," in *Analysis and Simulation of Electrical and Computer Systems* (Springer International Publishing), 261–270.

Grech, R., Cassar, T., Muscat, J., Camilleri, K. P., Fabri, S. G., Zervakis, M., et al. (2008). Review on solving the inverse problem in EEG source analysis. *J. Neuroeng. Rehabil.* 5:25. doi: 10.1186/1743-0003-5-25

Gupta, R., Koscik, T. R., Bechara, A., and Tranel, D. (2011). The amygdala and decision-making. *Neuropsychologia* 49, 760–766. doi: 10.1016/j.neuropsychologia.2010.09.029

Haaland, V. Ø., and Landrø, N. I. (2007). Decision making as measured with the iowa gambling task in patients with borderline personality disorder. *J. Int. Neuropsychol. Soc.* 13, 699–703. doi: 10.1017/S1355617707070890

Heekeren, H. R., Marrett, S., Bandettini, P. A., and Ungerleider, L. G. (2004). A general mechanism for perceptual decision-making in the human brain. *Nature* 431:859. doi: 10.1038/nature02966

Heekeren, H. R., Marrett, S., Ruff, D. A., Bandettini, P., and Ungerleider, L. G. (2006). Involvement of human left dorsolateral prefrontal cortex in perceptual decision making is independent of response modality. *Proc. Natl. Acad. Sci. U.S.A.* 103, 10023–10028. doi: 10.1073/pnas.0603949103

Hsu, M., Bhatt, M., Adolphs, R., Tranel, D., and Camerer, C. F. (2005). Neural systems responding to degrees of uncertainty in human decision-making. *Science* 310, 1680–1683. doi: 10.1126/science.1115327

Huk, A. C., and Shadlen, M. N. (2005). Neural activity in macaque parietal cortex reflects temporal integration of visual motion signals during perceptual decision making. *J. Neurosci.* 25, 10420–10436. doi: 10.1523/JNEUROSCI.4684-04.2005

John, E. R., Prichep, L., Fridman, J., and Easton, P. (1988). Neurometrics: computer-assisted differential diagnosis of brain dysfunctions. *Science* 239, 162–169.

Kakiashvili, T., Koczkodaj, W. W., and Woodbury-Smith, M. (2012). Improving the medical scale predictability by the pairwise comparisons method: evidence from a clinical data study. *Comput. Methods Prog. Biomed.* 105, 210–216. doi: 10.1016/j.cmpb.2011.09.011

Kamarajan, C., and Porjesz, B. (2015). Advances in electrophysiological research. *Alcohol Res. Curr. Rev.* 37:53.

Kaminski, W. A., and Wojcik, G. M. (2004). Liquid state machine built of Hodgkin–Huxley neurons. *Informatica* 15, 39–44. Available online at: https://content.iospress.com/articles/informatica/inf15-1-03

Koczkodaj, W. W., and Szybowski, J. (2015). Pairwise comparisons simplified. *Appl. Math. Comput.* 253, 387–394. doi: 10.1016/j.amc.2014.12.069

Kotyra, S., and Wojcik, G. M. (2017a). "The station for neurofeedback phenomenon research," in *Polish Conference on Biocybernetics and Biomedical Engineering* (Cham: Springer), 32–43.

Kotyra, S., and Wojcik, G. M. (2017b). "Steady state visually evoked potentials and their analysis with graphical and acoustic transformation," in *Polish Conference on Biocybernetics and Biomedical Engineering* (Cham: Springer), 22–31.

Krishnaswamy, P., Obregon-Henao, G., Ahveninen, J., Khan, S., Babadi, B., Iglesias, J. E., et al. (2017). Sparsity enables estimation of both subcortical and cortical activity from MEG and EEG. *Proc. Natl. Acad. Sci. U.S.A.* 114, E10465–E10474. doi: 10.1073/pnas.1705414114

Kufel, D. S., and Wojcik, G. M. (2018). Analytical modelling of temperature effects on an ampa-type synapse. *J. Comput. Neurosci.* 44, 379–391. doi: 10.1007/s10827-018-0684-x

Lubar, J. F., Swartwood, M. O., Swartwood, J. N., and O'Donnell, P. H. (1995). Evaluation of the effectiveness of eeg neurofeedback training for adhd in a clinical setting as measured by changes in tova scores, behavioral ratings, and WISC-R performance. *Biofeedback Selfregul.* 20, 83–99. doi: 10.1007/BF01712768

Mann, C. A., Lubar, J. F., Zimmerman, A. W., Miller, C. A., and Muenchen, R. A. (1992). Quantitative analysis of eeg in boys with attention-deficit-hyperactivity disorder: controlled study with clinical implications. *Pediatr. Neurol.* 8, 30–36.

Mapelli, D., Di Rosa, E., Cavalletti, M., Schiff, S., and Tamburin, S. (2014). Decision and dopaminergic system: an ERPS study of Iowa gambling task in Parkinson's disease. *Front. Psychol.* 5:684. doi: 10.3389/fpsyg.2014.00684

Martínez-Rodrigo, A., Fernández-Sotos, A., Latorre, J. M., Moncho-Bogani, J., and Fernández-Caballero, A. (2017). Neural correlates of phrase rhythm: an EEG study of bipartite vs. rondo sonata form. *Front. Neuroinform.* 11:29. doi: 10.3389/fninf.2017.00029

Mikołajewska, E., and Mikołajewski, D. (2012). Neuroprostheses for increasing disabled patients' mobility and control. *Adv. Clin. Exp. Med.* 21, 263–272. Available online at: http://www.advances.umed.wroc.pl/pdf/2012/1410.pdf

Mikołajewska, E., and Mikołajewski, D. (2013). Ethical considerations in the use of brain-computer interfaces. *Central Eur. J. Med.* 8, 720–724. doi: 10.2478/s11536-013-0210-5

Mikołajewska, E., and Mikołajewski, D. (2014). The prospects of brain computer interface applications in children. *Open Med.* 9, 74–79. doi: 10.2478/s11536-013-0249-3

Monsell, S. (2003). Task switching. *Trends Cogn. Sci.* 7, 134–140. doi: 10.1016/S1364-6613(03)00028-7

Moretti, D. V., Babiloni, C., Binetti, G., Cassetta, E., Dal Forno, G., Ferreric, F., et al. (2004). Individual analysis of eeg frequency and band power in mild Alzheimer's disease. *Clin. Neurophysiol.* 115, 299–308. doi: 10.1016/S1388-2457(03)00345-6

Nidal, K., and Malik, A. S. (2014). *EEG/ERP Analysis: Methods and Applications*. Boca Raton, FL; London; New York, NY: CRC Press.

Niedermeyer, E., and da Silva, F. L. (2005). *Electroencephalography: Basic Principles, Clinical Applications, and Related Fields*. New York, NY: Lippincott Williams & Wilkins.

Ogiela, L., Tadeusiewicz, R., and Ogiela, M. R. (2008). Cognitive techniques in medical information systems. *Comput. Biol. Med.* 38, 501–507. doi: 10.1016/j.compbiomed.2008.01.017

Ozga, W. K., Zapała, D., Wierzgała, P., Augustynowicz, P., Porzak, R., and Wójcik, G. M. (2018). Acoustic neurofeedback increases beta ERD during mental rotation task. *Appl. Psychophysiol. Biofeedback* 44, 103–115. doi: 10.1007/s10484-018-9426-0

Pascual-Marqui, R. D. (2002). Standardized low-resolution brain electromagnetic tomography (sLORETA): technical details. *Methods Find Exp. Clin. Pharmacol.* 24, 5–12. Available online at: http://www.institutpsychoneuro.com/wp-content/uploads/2015/10/sLORETA2002.pdf

Pascual-Marqui, R. D., Lehmann, D., Koenig, T., Kochi, K., Merlo, M. C., Hell, D., et al. (1999). Low resolution brain electromagnetic tomography (LORETA) functional imaging in acute, neuroleptic-naive, first-episode, productive schizophrenia. *Psychiatry Res. Neuroimaging* 90, 169–179.

Pascual-Marqui, R. D., Michel, C. M., and Lehmann, D. (1994). Low resolution electromagnetic tomography: a new method for localizing electrical activity in the brain. *Int. J. Psychophysiol.* 18, 49–65.

Paulus, M. P. (2007). Decision-making dysfunctions in psychiatry altered homeostatic processing? *Science* 318, 602–606. doi: 10.1126/science.1142997

Pope, A. T., Bogart, E. H., and Bartolome, D. S. (1995). Biocybernetic system evaluates indices of operator engagement in automated task. *Biol. Psychol.* 40, 187–195.

Saletu, B., Anderer, P., and Saletu-Zyhlarz, G. (2010). EEG topography and tomography (LORETA) in diagnosis and pharmacotherapy of depression. *Clin. EEG Neurosci.* 41, 203–210. doi: 10.1177/155005941004100407

Sand, T., Bjørk, M., and Vaaler, A. (2013). Is EEG a useful test in adult psychiatry? *Tidsskr. Norske Laegeforen.* 133, 1200–1204. doi: 10.4045/tidsskr.12.1253

Sutton, S., Braren, M., Zubin, J., and John, E. (1965). Evoked-potential correlates of stimulus uncertainty. *Science* 150, 1187–1188.

Szaleniec, J., Wiatr, M., Szaleniec, M., SkłAdzień, J., Tomik, J., Oleś, K., et al. (2013). Artificial neural network modelling of the results of tympanoplasty in chronic suppurative otitis media patients. *Comput. Biol. Med.* 43, 16–22. doi: 10.1016/j.compbiomed.2012.10.003

Szaleniec, M., Tadeusiewicz, R., and Witko, M. (2008). How to select an optimal neural model of chemical reactivity? *Neurocomputing* 72, 241–256. doi: 10.1016/j.neucom.2008.01.003

Tamburin, S., Maier, A., Schiff, S., Lauriola, M. F., Di Rosa, E., Zanette, G., et al. (2014). Cognition and emotional decision-making in chronic low back pain: an erps study during iowa gambling task. *Front. Psychol.* 5:1350. doi: 10.3389/fpsyg.2014.01350

Teruel, M. A., Navarro, E., Romero, D., García, M., Fernández-Caballero, A., and González, P. (2017). "An innovative tool to create neurofeedback games for ADHD treatment," in *International Work-Conference on the Interplay Between Natural and Artificial Computation* (Cham: Springer), 183–192.

Tohka, J., and Ruotsalainen, U. (2012). Imaging brain change across different time scales. *Front. Neuroinform.* 6:29. doi: 10.3389/fninf.2012.00029

Trivedi, J. (2006). Cognitive deficits in psychiatric disorders: current status. *Indian J. Psychiatry* 48:10. doi: 10.4103/0019-5545.31613

Ważny, M., and Wojcik, G. M. (2014). Shifting spatial attention numerical model of posner experiment. *Neurocomputing* 135, 139–144. doi: 10.1016/j.neucom.2013.12.043

Wierzgała, P., Zapala, D., Wójcik, G. M., and Masiak, J. (2018). Most popular signal processing methods in motor-imagery bci: a review and meta-analysis. *Front. Neuroinform.* 12:78. doi: 10.3389/fninf.2018.00078

Wojcik, G. M. (2012). Electrical parameters influence on the dynamics of the Hodgkin–Huxley liquid state machine. *Neurocomputing* 79, 68–74. doi: 10.1016/j.neucom.2011.10.007

Wojcik, G. M., and Garcia-Lazaro, J. A. (2010). Analysis of the neural hypercolumn in parallel pcsim simulations. *Proc. Comput. Sci.* 1, 845–854. doi: 10.1016/j.procs.2010.04.092

Wojcik, G. M., and Kaminski, W. A. (2007). Liquid state machine and its separation ability as function of electrical parameters of cell. *Neurocomputing* 70, 2593–2597. doi: 10.1016/j.neucom.2006.12.015

Wojcik, G. M., and Kaminski, W. A. (2008). "Self-organised criticality as a function of connections' number in the model of the rat somatosensory cortex," in *International Conference on Computational Science* (Berlin; Heidelberg: Springer), 620–629.

Wojcik, G. M., Kaminski, W. A., and Matejanka, P. (2007). "Self-organised criticality in a model of the rat somatosensory cortex," in *International Conference on Parallel Computing Technologies* (Berlin; Heidelberg: Springer), 468–476.

Wojcik, G. M., Masiak, J., Kawiak, A., Kwasniewicz, L., Schneider, P., Polak, N., et al. (2018b). Mapping the human brain in frequency band analysis of brain cortex electroencephalographic activity for selected psychiatric disorders. *Front. Neuroinform.* 12:73. doi: 10.3389/fninf.2018.00073

Wojcik, G. M., Masiak, J., Kawiak, A., Schneider, P., Kwasniewicz, L., Polak, N., et al. (2018a). New protocol for quantitative analysis of brain cortex electroencephalographic activity in patients with psychiatric disorders. *Front. Neuroinform* 12:27. doi: 10.3389/fninf.2018.00027

Wojcik, G. M., and Ważny, M. (2015). Bray-curtis metrics as measure of liquid state machine separation ability in function of connections density: [Procs 51C (2015) 2948–2951]. *Proc. Comput. Sci.* 51:2978. doi: 10.1016/j.procs.2015.07.446

Wu, L., Wu, L., Chen, Y., and Zhou, J. (2014). A promising method to distinguish vascular dementia from Alzheimer's disease with standardized low-resolution brain electromagnetic tomography and quantitative EEG. *Clin. EEG Neurosci.* 45, 152–157. doi: 10.1177/1550059413496779

Zolubak, M., Pelc, M., Siui, D., Macek-Kaminska, K., Kolanska-Pluska, J., Ozana, S., et al. (2019). "Application of low frequency wave markers for diagnostic tests and neurofeedback therapy," in *2019 Progress in Applied Electrical Engineering (PAEE)* (IEEE), 1–5.

Conflict of Interest: The authors declare that the research was conducted in the absence of any commercial or financial relationships that could be construed as a potential conflict of interest.

Copyright © 2019 Wojcik, Masiak, Kawiak, Kwasniewicz, Schneider, Postepski and Gajos-Balinska. This is an open-access article distributed under the terms of the Creative Commons Attribution License (CC BY). The use, distribution or reproduction in other forums is permitted, provided the original author(s) and the copyright owner(s) are credited and that the original publication in this journal is cited, in accordance with accepted academic practice. No use, distribution or reproduction is permitted which does not comply with these terms.

frontiers in Neuroinformatics

ORIGINAL RESEARCH
published: 27 November 2019
doi: 10.3389/fninf.2019.00070

ASD-DiagNet: A Hybrid Learning Approach for Detection of Autism Spectrum Disorder Using fMRI Data

Taban Eslami[1,2], *Vahid Mirjalili*[3], *Alvis Fong*[1], *Angela R. Laird*[4] *and Fahad Saeed*[2]*

[1] *Department of Computer Science, Western Michigan University, Kalamazoo, MI, United States,* [2] *School of Computing and Information Science, Florida International University, Miami, FL, United States,* [3] *Department of Computer Science and Engineering, Michigan State University, East Lansing, MI, United States,* [4] *Department of Physics, Florida International University, Miami, FL, United States*

Heterogeneous mental disorders such as Autism Spectrum Disorder (ASD) are notoriously difficult to diagnose, especially in children. The current psychiatric diagnostic process is based purely on the behavioral observation of symptomology (DSM-5/ICD-10) and may be prone to misdiagnosis. In order to move the field toward more quantitative diagnosis, we need advanced and scalable machine learning infrastructure that will allow us to identify reliable biomarkers of mental health disorders. In this paper, we propose a framework called ASD-DiagNet for classifying subjects with ASD from healthy subjects by using *only* fMRI data. We designed and implemented a joint learning procedure using an autoencoder and a single layer perceptron (SLP) which results in improved quality of extracted features and optimized parameters for the model. Further, we designed and implemented a data augmentation strategy, based on linear interpolation on available feature vectors, that allows us to produce synthetic datasets needed for training of machine learning models. The proposed approach is evaluated on a public dataset provided by Autism Brain Imaging Data Exchange including 1,035 subjects coming from 17 different brain imaging centers. Our machine learning model outperforms other state of the art methods from 10 imaging centers with increase in classification accuracy up to 28% with maximum accuracy of 82%. The machine learning technique presented in this paper, in addition to yielding better quality, gives enormous advantages in terms of execution time (40 min vs. 7 h on other methods). The implemented code is available as GPL license on GitHub portal of our lab (https://github.com/pcdslab/ASD-DiagNet).

Keywords: fMRI, ASD, SLP, autoencoder, ABIDE, classification, data augmentation

OPEN ACCESS

Edited by:
Pierre Bellec,
Université de Montréal, Canada

Reviewed by:
Nianming Zuo,
Institute of Automation (CAS), China
Desiree Lussier-Levesque,
Université de Montréal, Canada

***Correspondence:**
Fahad Saeed
fsaeed@fiu.edu

Received: *31 July 2019*
Accepted: *12 November 2019*
Published: *27 November 2019*

Citation:
Eslami T, Mirjalili V, Fong A, Laird AR and Saeed F (2019) ASD-DiagNet: A Hybrid Learning Approach for Detection of Autism Spectrum Disorder Using fMRI Data. Front. Neuroinform. 13:70. doi: 10.3389/fninf.2019.00070

1. INTRODUCTION

Mental disorders such as Autism Spectrum Disorder (ASD) are heterogeneous disorders that are notoriously difficult to diagnose, especially in children. The current psychiatric diagnostic process is based purely on behavioral observation of symptomology (DSM-5/ICD-10) and may be prone to misdiagnosis (Nickel and Huang-Storms, 2017). There is no quantitative test that can be prescribed to patients that may lead to definite diagnosis of a person. Such quantitative and definitive tests are a regular practice for other diseases such as diabetes, HIV, and hepatitis-C.

It is widely known that defining and diagnosing mental health disorders is a difficult process due to overlapping nature of symptoms, and lack of a biological test that can serve as a definite and quantified gold standard (National Collaborating Centre for Mental Health (UK), 2018). ASD is a lifelong neuro-developmental brain disorder which causes social impairments like repetitive behavior and communication problems in children. More than 1% of children suffer from this disorder and detecting it at early ages can be beneficial. Studies show that some demographic attributes like gender and race vary among ASD and healthy individuals such that males are four times more prone to ASD than females (Baio et al., 2018). Diagnosing ASD has been explored from different aspects, like monitoring behavior, extracting discriminatory patterns from the demographic information and analyzing the brain data. Behavioral data such as eye movement and facial expression are studied in Liu et al. (2016), Jaiswal et al. (2017), Zunino et al. (2018). For instance, Zunino et al. classified ASD from healthy subjects by applying recurrent neural network to the video clips recorded from them (Zunino et al., 2018).

Quantitative analysis of brain imaging data can provide valuable biomarkers that result in more accurate diagnosis of brain diseases. Machine learning techniques using brain imaging data [e.g., Magnetic Resonance Imaging (MRI) and functional Magnetic Resonance Imaging (fMRI)] have been extensively used by researchers for diagnosing brain disorders like Alzheimer's, ADHD, MCI, and Autism (Colby et al., 2012; Peng et al., 2013; Yang et al., 2014; Deshpande et al., 2015; Hosseini-Asl et al., 2016; Khazaee et al., 2017; Eslami and Saeed, 2018b, 2019).

In this paper, we focus on classifying subjects suffering from ASD from healthy control subjects using fMRI data. We propose a method called *ASD-DiagNet* which consists of an autoencoder and a SLP. These networks are used for extracting lower dimensional features in a hybrid manner and the trained perceptron is used for the final round of classification. In order to enlarge the size of the training set, we designed a data augmentation technique which generates new data in feature space by using available data in the training set.

Detecting ASD using fMRI data has recently gained a lot of attention, thanks to Autism Brain Imaging Data Exchange (ABIDE) initiative for providing functional and structural brain imaging datasets collected from several brain imaging centers around the world (Craddock et al., 2013). Many studies and methods have been developed based on ABIDE data (Iidaka, 2015; Chen et al., 2016; Abraham et al., 2017; Heinsfeld et al., 2018; Itani and Thanou, 2019). Some studies included a subset of this dataset based on specific demographic information to analyze their proposed method. For example, Iidaka (2015) used probabilistic neural network for classifying resting state fMRI (rs-fMRI) data of subjects under 20 years old. In another work, Plitt et al. (2015) used two sets of rs-fMRI data, one containing 118 male individuals (59 ASD; 59 TD) and the other containing 178 age and IQ matched individuals (89 ASD; 89 TD) from ABIDE dataset and achieved 76.67% accuracy. Besides using fMRI data, some studies also included structural and demographic information of subjects for diagnosing ASD. For example, Parisot et al. (2018) proposed a framework based on Graph Convolutional Networks that achieved 70.4% accuracy. In their work, they represented the population as a graph in which nodes are defined based on imaging features and phenotypic information describe the edge weights. In another study, Sen et al. (2018) proposed a new algorithm which combines structural and functional features from MRI and fMRI data and got 64.3% accuracy by using 1111 total healthy and ASD subjects. Nielsen et al. (2013) obtained 60% accuracy on a group of 964 healthy and ASD subjects using the functional connectivity between 7266 regions and demographic information like age, gender, and handedness attributes. In another study, Parikh et al. (2019) tested the performance of different machine learning methods on demographic information provided by ABIDE dataset including age, gender, handedness, and three individual measures of IQ.

Machine learning techniques such as Support Vector Machines (SVM) and random forests are explored in multiple studies (Abraham et al., 2017; Subbaraju et al., 2017; Bi et al., 2018b; Fredo et al., 2018). For instance, Chen et al. (2016) investigated the effect of different frequency bands for constructing brain functional network, and obtained 79.17% accuracy using SVM technique applied to 112 ASD and 128 healthy control subjects.

Recently, using neural networks and deep learning methods such as autoencoders, Deep Neural Network (DNN), Long Short Term Memory (LSTM), and Convolutional Neural Network (CNN) have also become very popular for diagnosing ASD (Dvornek et al., 2017; Guo et al., 2017; Bi et al., 2018a; Brown et al., 2018; Khosla et al., 2018; Li et al., 2018). Brown et al. (2018) obtained 68.7% classification accuracy on 1,013 subjects composed of 539 healthy control and 474 with ASD, by proposing an element-wise layer for DNNs which incorporated the data-driven structural priors.

Most recently, Heinsfeld et al. (2018) used a deep learning based approach and achieved 70% accuracy for classifying 1,035 subjects (505 ASD and 530 controls). They claimed this approach improved the state of the art technique. In their technique, distinct pairwise Pearson's correlation coefficients were considered as features. Two stacked denoising autoencoders were first pre-trained in order to extract lower dimensional data. After training autoencoders, their weights were applied to a multi-layer perceptron classifier (fine-tuning process) which was used for the final classification. However, they also performed classification for each of the 17 sites included in ABIDE dataset separately, and the average accuracy is reported as 52%. The low performance on individual sites was justified to be due to the lack of enough training samples for intra-site training.

Generally, most related studies for ASD diagnosis using machine learning techniques have only considered a subset of ABIDE dataset, or they have incorporated other information besides fMRI data in their model. There are few studies such as Heinsfeld et al. (2018), which only used fMRI data without any assumption on demographic information and analyzed *all* the 1,035 subjects in ABIDE dataset. To the best of our knowledge (Heinsfeld et al., 2018) is currently state of the art technique for ASD diagnosis on whole ABIDE dataset, which we use as the baseline for evaluating our proposed method.

Although employing other types of information like anatomical features and demographic attributes of subjects could provide more knowledge to the model and may increase its accuracy, the goal of our study is to merely design a quantitative model for ASD diagnosis based on the functional data of the brain. This model can be used in conjunction with other tools assisting clinicians to diagnose ASD with more precision. Another aspect that we targeted in this study is the running time of the model. Unfortunately, the running time required for training the model or analyzing the data is not discussed in most of research papers mentioned above. Achieving high diagnosis accuracy in a shorter amount of time would be more desirable in clinical studies. Deep learning models are time consuming techniques due to the huge number of parameters that should be optimized. Although utilizing GPUs has reduced the running time needed for training the models tremendously, it still depends on the architecture of the model and size of the data. We considered the running time of the model as a factor while designing the architecture of our model. Using our hybrid learning strategy the model needs fewer number of iterations for training, which reduces the running time of the model. We also decreased the number of features by keeping anti-correlated and highly correlated functional connections and removing the rest, which reduces the size of the network significantly.

The structure of this paper is as follows: First, in section 2 we provide a brief introduction to fMRI data, the dataset we used in this study and explain ASD-DiagNet method in detail. In section 3, we describe the experiment setting and discuss the results of ASD-DiagNet. Finally, in section 4, we conclude the paper and discuss the future direction.

2. MATERIALS AND METHODS

2.1. Functional Magnetic Resonance Imaging and ABIDE Dataset

Functional Magnetic Resonance Imaging (fMRI) is a brain imaging technique that is used for studying brain activities (Lindquist et al., 2008; Eslami and Saeed, 2018a). In fMRI data, the brain volume is represented by a group of small cubic elements called voxels. A time series is extracted from each voxel by keeping track of its activity over time. Scanning the brain using fMRI technology while the subject is resting is called resting state fMRI (rs-fMRI), which is widely used for analyzing brain disorders. In this study, we used preprocessed ABIDE-I dataset that is provided by the ABIDE initiative. This dataset consists of 1112 rs-fMRI data including ASD and healthy subjects collected from 17 different sites. We used fMRI data of the same group of subjects which was used in Heinsfeld et al. (2018). This set consists of 505 subjects with ASD and 530 healthy control from all the 17 sites. **Table 1** shows the class membership information for each site. ABIDE-I provided the average time series extracted from seven sets of regions of interest (ROIs) based on seven different atlases which are preprocessed using four different pipelines. The data used in our experiments is preprocessed using C-PAC pipeline (Craddock et al., 2013) and is parcellated into 200 functionally homogeneous regions generated using spatially constrained spectral clustering algorithm (Craddock et al., 2012) (CC-200). The preprocessing steps include slice time correction, motion correction, nuisance signal removal, low frequency drifts, and voxel intensity normalization. It is worth mentioning that each site used different parameters and protocols for scanning the data. Parameters like repetition time (TR), echo time (TE), number of voxels, number of volumes, openness or closeness of the eyes while scanning are different among sites.

2.2. ASD-DiagNet: Feature Extraction and Classification

Functional connectivity between brain regions is an important concept in fMRI analysis and is shown to contain discriminatory patterns for fMRI classification. Among correlation measures, Pearson's correlation is mostly used for approximating the functional connectivity in fMRI data (Liang et al., 2012; Baggio et al., 2014; Zhang et al., 2017). It shows the linear relationship between the time series of two different regions. Given two times series, u and v, each of length T, the Pearson's correlation can be computed using the following equation:

$$\rho_{uv} = \frac{\sum_{t=1}^{T}(u_t - \bar{u})(v_t - \bar{v})}{\sqrt{\sum_{t=1}^{T}(u_t - \bar{u})^2}\sqrt{\sum_{t=1}^{T}(v_t - \bar{v})^2}} \quad (1)$$

where $\bar{u}$ and $\bar{v}$ are the mean of times series u and v, respectively. Computing all pairwise correlations results in a correlation matrix $C_{m\times m}$ where m is the number of time series (or regions). Due to the symmetric property of Pearson's correlation, we only considered the strictly upper triangle part of the correlation matrix. Since we used CC-200 atlas in which the brain is parcellated into $m = 200$ regions, there are $m \times (m-1)/2 = 19,900$ distinct pairwise Pearson's correlations. In this regard, we selected half of the correlations comprising 1/4 largest and 1/4 smallest values and eliminated the rest. To do so, we first compute the average of correlations among all subjects in

TABLE 1 | Class membership information of ABIDE-I dataset for each individual site.

Site	Caltech	CMU	KKI	Leuven	MaxMun	NYU	OHSU	OLIN	PITT	SBL	SDSU	Stanford	Trinity	UCLA	UM	USM	Yale
ASD	19	14	20	29	24	75	12	19	29	15	14	19	22	54	66	46	28
Healthy control	18	13	28	34	28	100	14	15	27	15	22	20	25	44	74	25	28
Male count	29	21	36	55	48	139	26	29	48	30	29	31	47	86	113	71	40
Female count	8	6	12	8	4	36	0	5	8	0	7	8	0	12	27	0	16
Average age	27	26	10	18	25	15	10	16	18	34	14	9	16	13	14	22	12

training set and then pick the indices of the largest positive and negative values from averaged correlation array. We then pick the correlations at those indices from each sample as our feature vector. Keeping half of the correlations and eliminating the rest reduces the size of input features by a factor of 2. There is no limitation of the number of high- and anti-correlations that should be kept. Removing more features results in higher computational efficiency as well as reducing the chance of overfitting, however removing too many features can also cause losing important patterns.

In order to further reduce the size of features, we used an autoencoder to extract a lower dimensional feature representation. An autoencoder is a type of feed-forward neural network model, which first encodes its input x to a lower dimensional representation,

$$h_{enc} = \phi_{enc}(x) = \tau\left(W_{enc}x + b_{enc}\right) \tag{2}$$

where τ is the hyperbolic tangent activation function (*Tanh*), and W_{enc} and b_{enc} represent the weight matrix and the bias for the encoder. Then, the decoder reconstructs the original input data

$$x' = \phi_{dec}(h_{enc}) = W_{dec}h_{enc} + b_{dec} \tag{3}$$

where W_{dec} and b_{dec} are the weight matrix and bias for the decoder. In this work, we have designed an autoencoder with tied weights, which means $W_{dec} = W_{enc}^{\top}$. An autoencoder can be trained to minimize its reconstruction error, computed as the Mean Squared Error (MSE) between x and its reconstruction, x'. The choice of using autoencoder instead of other feature extraction techniques like PCA is its ability to reduce the dimensionality of features in a non-linear way. The structure of an autoencoder is shown in **Figure 1**.

The lower dimensional data generated during the encoding process contains useful patterns from the original input data with smaller size, and can be used as new features for classification. For the classification task, we used a single layer perceptron (SLP) which uses the bottleneck layer of the autoencoder, h_{enc}, as input, and computes the probability of a sample belonging to the ASD patient class using a sigmoid activation function, σ,

$$\begin{aligned} f(x) &= \sigma\left(W_{slp}h_{enc} + b_{slp}\right) \\ &= \sigma\left(W_{slp}\tau(W_{enc}x + b_{enc}) + b_{slp}\right) \end{aligned} \tag{4}$$

where W_{slp} and b_{slp} are the weight matrix and the bias for the SLP network. The SLP network can be trained by minimizing the Binary Cross Entropy loss, $\mathcal{H}$, using the ground-truth class label, y, and the estimated ASD probability for each sample, $f(x)$:

$$\mathcal{H}(y, f(x)) = -\left(y \times f(x) + (1-y) \times (1-f(x))\right) \tag{5}$$

Finally, the predicted class label is determined by thresholding the estimated probability

$$\hat{y} = \begin{cases} 1, & \text{if } f(x) \geq 0.5, \\ 0, & \text{otherwise.} \end{cases} \tag{6}$$

Typically, an autoencoder is fully trained such that its reconstruction error is minimized, then, the features from bottleneck layer, h_{enc}, are used as input for training the SLP classifier, separately. In contrast, here, we train the autoencoder and the SLP classifier simultaneously. This can potentially result in obtaining low dimensional features that have two properties

1. Useful for reconstructing the original data,
2. Contain discriminatory information for the classification task.

This is accomplished by adding the two loss functions, i.e., MSE loss for reconstruction, and Binary Cross Entropy for the classification task, and training both networks jointly. After the joint training process is completed, we further fine-tune the SLP network for a few additional epochs.

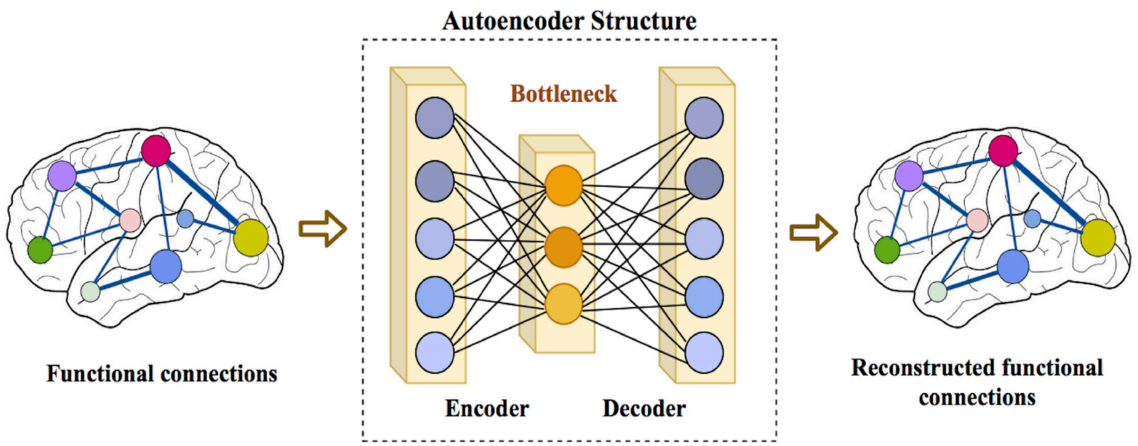


FIGURE 1 | Structure of an autoencoder consisting of an encoder that receives the input data and encodes it into a lower dimensional representation at the bottleneck layer, and a decoder that reconstructs the original input from the bottleneck layer.

2.3. Data Augmentation Using Linear Interpolation

Machine learning and especially deep learning techniques can be advantageous if they are provided with enough training data. Insufficient data causes overfitting and non-generalizability of the model (Raschka and Mirjalili, 2017). Large training sets are not always available and collecting new data might be costly like in medical imaging field. In these situations, data augmentation techniques can be used for generating synthetic data using the available training set (Karpathy et al., 2014; Eitel et al., 2015; Wong et al., 2016; Xu et al., 2016; Perez and Wang, 2017). There are a few data augmentation methods proposed for different applications, such as random translation/rotation/cropping (for image data), adding random noise to the features (for general type of data), extracting overlapping windows from the original time series (for time series data), as well as more sophisticated methods such as Generative Adversarial Networks. However, these methods are not either applicable to our data due to the structure of our features, not interpretable, or they may be computationally more intensive than our proposed method.

The data augmentation technique that we propose in this study is inspired by Synthetic Minority Over-sampling Technique (SMOTE) (Chawla et al., 2002). SMOTE is an effective model which is used for oversampling the data in minority class of imbalanced datasets. SMOTE generates synthetic data in feature space by using the nearest neighbors of a sample. After k-nearest neighbors of sample p are found ($\{q_1, q_2, ..., q_k\}$), a random neighbor is selected (q_r) and the synthetic feature vector is computed using the following equation:

$$p' = \alpha \times p + (1 - \alpha) \times q_r \tag{7}$$

In this equation, α is a random number selected uniformly in the range $[0, 1]$. Finding the nearest neighbors of a sample is based on a distance or similarity metric. In our work, the samples have feature vectors of size 9,950 (half of the correlations). One idea for computing nearest neighbors is to use Euclidean distance, however, computing the pairwise Euclidean distances with 9,950 features is not efficient. In order to compute the similarity between samples and finding the nearest neighbors, we used a measure called Extended Frobenius Norm (EROS). This measure computes the similarity between two multivariate time series (MTS) (Yang and Shahabi, 2004). fMRI data consists of several regions each having a time series so we can consider it as a multivariate time series. Our previous study on ADHD disorder has shown that EROS is an effective similarity measure for fMRI data and using it along with k-Nearest-Neighbor achieves high classification accuracy (Eslami and Saeed, 2018b). This motivated us to utilize it as part of the data augmentation process. EROS computes the similarity between two MTS items A and B based on eigenvalues and eigenvectors of their covariance matrices using the following equation:

$$\begin{aligned} EROS(A, B, w) &= \sum_{i=1}^{n} w_i \left| \langle a_i, b_i \rangle \right| \\ &= \sum_{i=1}^{n} w_i \left| cos\theta_i \right| \end{aligned} \tag{8}$$

where, θ_i is the cosine of the angle between i_{th} corresponding eigenvectors of covariance matrices of multivariate time series A and B. Furthermore, w is the weight vector which is computed based on eigenvalues of all MTS items using Algorithm 1. This algorithm computes the weight vector w by normalizing eigenvalues of each MTS item followed by applying an aggregate function f (here, we used mean) to all eigenvalues over the entire training dataset and finally normalizing them so that $\sum_{i=1}^{n} w_i = 1$.

Algorithm 1: Computing weight vector for EROS (Yang and Shahabi, 2004)

Input: An $n \times N$ matrix S, where n is the number of variables for the dataset and N is the number of MTS items in the dataset. Each column vector s_i in S represents all the eigenvalues for i_{th} MTS item in the dataset. s_{ij} is a value at column i and row j in S. s_{*i} is i_{th} row in S. s_{i*} is i_{th} column

1: **for** $i = 1$ to N **do**
2: $\quad s_i \leftarrow s_i / \sum_{j=1}^{n} s_{ij}$
3: **end for**
4: **for** $i = 1$ to n **do**
5: $\quad w_i \leftarrow f(s_{*i})$
6: **end for**
7: **for** $i = 1$ to n **do**
8: $\quad w_i \leftarrow w_i / \sum_{j=1}^{n} w_j$
9: **end for**

Algorithm 2: Data augmentation using EROS similarity measure

Input: Training dataset of size N

1: **for** $i = 1$ to N **do**
2: $\quad$ Find 5 nearest neighbors to i using EROS
3: $\quad j \leftarrow$ A random sample among nearest neighbors
4: $\quad r \leftarrow$ Random number in the range $[0, 1]$
5: $\quad x^*_{i+N} \leftarrow \alpha \times x_i + (1 - \alpha) \times x_j$
6: **end for**

The dimension of each sample's covariance matrix is $m \times m$, where m is the number of brain regions. The covariance matrix of each subject is pre-computed in the beginning and is re-used when the sample is selected as a candidate. In order to further reduce the time needed for computing the pairwise similarities, we considered using the first two eigenvectors of each sample. Our experiments showed that this simplification does not affect the results while reducing the running time significantly compared to using all eigenvectors and eigenvalues.

Now, using EROS as the similarity measure, our data augmentation process is shown in Algorithm 2. After finding $k = 5$ nearest neighbors of each sample i in the training set, one of them is randomly selected, a new sample is generated using linear interpolation between the selected neighbor and sample i. Choosing $k = 5$ was based on the original implementation of SMOTE algorithm (Chawla et al., 2002). Our experiments did not show a significant change in the results when using different

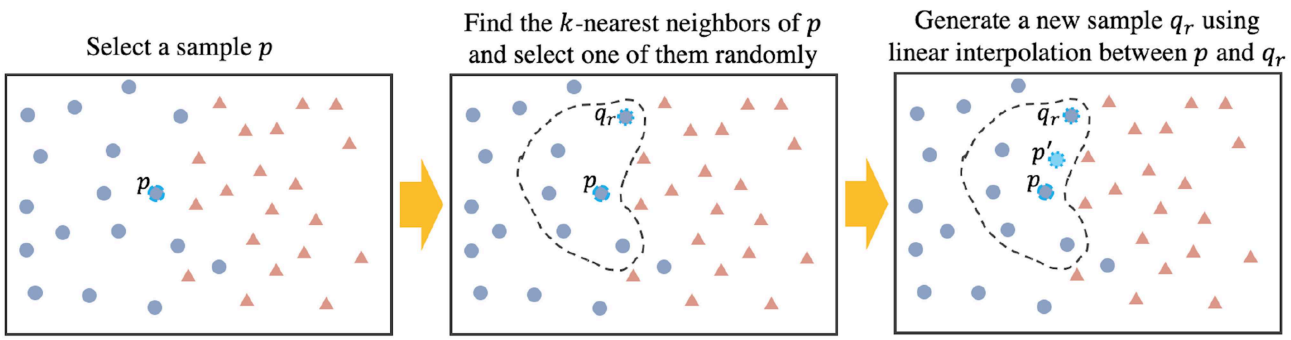


FIGURE 2 | Generating new artificial data: Step (1) Selecting a sample (p). Step (2) Find k-nearest neighbors of p from the same class, and pick one random neighbor (q_r). Step (3) Generate new sample p' using p and q_r by linear interpolation.

values of k. Using this approach, one synthetic sample is created for each training point which results in doubling the size of the training set. **Figure 2** shows the data augmentation process and **Figure 3** shows the overall process of ASD-DiagNet method.

3. EXPERIMENTS AND RESULTS

For all the experiments reported in this section, we used a Linux server running Ubuntu Operating System. The server contains two Intel Xeon E5-2620 Processors at 2.40 GHz with a total 48 GBs of RAM. The system contains an NVIDIA Tesla K-40c GPU with 2,880 CUDA cores and 12 GBs of RAM. CUDA version 8 and PyTorch library were used for conducting the experiments.

We evaluated ASD-DiagNet model in two phases by performing k-fold cross validation. In the first phase, the model was evaluated using the whole 1,035 subjects from all sites and in the second phase, the model was evaluated for each site separately. As stated earlier, data centers may have used different experimental parameters for scanning fMRI images, so considering all of them in the same pool determines how our model generalizes to data with heterogeneous scanning parameters. On the other hand, by considering each data center separately, fewer subjects are available for training the model and the results indicate how it performs on small datasets. In each of these experiments, the effect of data augmentation is evaluated.

The value of k in k-fold cross validation must be chosen such that train/test partitions are representative of the whole dataset. Since the whole dataset contains a lot more samples than each individual site, using a large value of k like 10 in k-fold cross validation provides more samples in the training process. This helps the model to capture more information from the data while leaving enough test samples to measure the ability of the model in classifying unseen data. On the other hand, we are dealing with a small number of samples in some of the sites, for example, CMU which only contains 27 samples. Hence performing k-fold cross validation with large values of k like 10 results in only 2–3 samples in test set and increases the variance of cross-validation estimation, so we chose $k = 5$ when analyzing each site separately. Other studies such as Heinsfeld et al. (2018) used the same values of k for performing k-fold cross validation.

We report accuracy, sensitivity, and specificity of different methods for evaluating their classification performance. Accuracy measures the proportion of correctly classified subjects (actual ASD classified as ASD and actual healthy classified as healthy). Sensitivity represents the proportion of actual ASD subjects which are correctly classified as ASD and specificity measures the proportion of actual healthy subjects which are classified as healthy. We also compared the performance of each model's diagnostic test by their Receiver Operating Characteristic (ROC) curves. The area under ROC curves (AUC) shows the capability of the model for distinguishing between ASD and healthy subjects based on different thresholds. The higher AUC value indicates that the model is better in distinguishing between ASD and healthy subjects. We compared the performance of ASD-DiagNet with three other baselines: SVM, random forest and the method proposed by Heinsfeld et al. (2018). Hyperparameter tuning for SVM and random forest classifiers are performed by grid search technique. Hyperparameters such as kernel type, regularization constant (C), kernel coefficient (γ) for SVM, and the number of trees as well as the function to measure the quality of a split for random forest are tuned using grid search. SVM and random forest were trained using 19,900 pairwise Pearson's correlations for each subject. The implementations of the grid search, SVM, and random forest are carried out using the built-in functions provided by scikit-learn library. In order to speed up the grid search, it is parallelized on 10 cores.

The following subsections explain each experiment in more details.

3.1. Phase 1: Experiments Using the Whole Dataset

In this phase, we performed 10-fold cross-validation on the whole 1,035 subjects using CC-200 atlas. **Table 2** compares accuracy, sensitivity, and specificity of our approach with Heinsfeld et al. (2018), random forest, and SVM. As the results show, ASD-DiagNet achieves 70.3% which outperforms other methods.[1] The proposed data augmentation helps to improve the results by around 1%. Based on **Figure 4**, ASD-DiagNet (with and without

[1]We like to mention that Heinsfeld et al. (2018) reported 70% accuracy in their paper, however, the accuracy we reported here is the result of running their method on our system using their default parameters and the code they provided online. The different results observed here could be due to some missing details in the implementation.

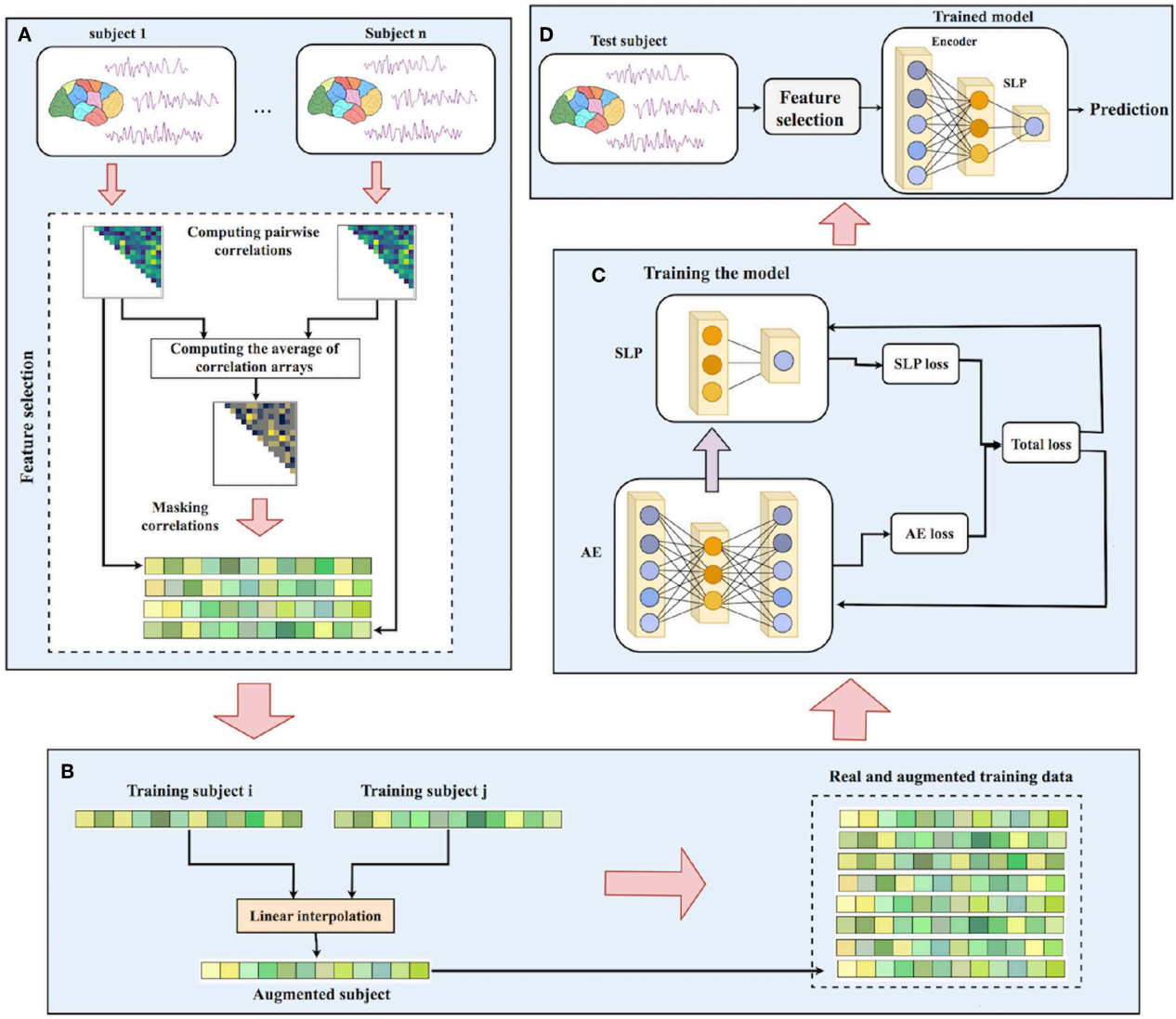


FIGURE 3 | Workflow of ASD-DiagNet: **(A)** Pairwise Pearson's correlations for each subject in the training set is computed. The average of all correlation arrays is computed and the position of 1/4 largest and 1/4 smallest values in the average array is considered as a mask. Masked correlation array of each sample is considered as its feature vectors. **(B)** A set of artificial samples is generated using the feature vectors of training samples. **(C)** Autoencoder and SLP are jointly trained by adding up their training loss in each iteration. **(D)** For a test subject, the features are extracted using the mask generated in part A, followed by passing the features through the encoder part of the autoencoder, and finally predicting its label using the trained SLP.

TABLE 2 | Classification performance using 10-fold cross-validation on the whole dataset; Note that our proposed approach, ASD-DiagNet (with data augmentation) achieves the highest accuracy among other methods.

Method	Accuracy	Sensitivity	Specificity
ASD-DiagNet	**70.3**	68.3	72.2
ASD-DiagNet (no aug.)	69.4	69.6	69.2
SVM	68.3	64.4	72
Random forest	66.3	60.8	71.4
Heinsfeld et al., 2018	65.4	61	69.3

Bold values show the highest accuracy among all methods.

data augmentation) achieved higher area under comparing to other methods.

3.2. Phase 2: Intra-Site Evaluation

In this phase, we performed 5-fold cross-validation on each site separately using CC-200 atlas. The accuracy of each method is provided in **Table 3**. Based on these results, our method achieves the highest accuracy in most cases (10 out of 17 sites) and outperforms other methods on average. In addition, note that the proposed data augmentation helps improving the result around 3% overall. Especially, for OHSU, the data augmentation improves the accuracy significantly (10% increase). However, in

a couple of datasets no improvement is observed (e.g., MaxMun). These datasets have shown low prediction accuracy by other methods as well. In these cases, the artificial data generated by data augmentation does not improve the results since the functional connectivity of the original data does not carry enough discriminatory information that can be used by the classifiers.

3.3. Running Time

We measured the running time of performing 10-fold cross validation by different approaches. The training and evaluation for all methods are performed on the same Linux system (described in section 3). The running time needed by each method is as follows: 41 min by ASD-DiagNet, 20 min by ASD-DiagNet (no aug.), 7 h and 48 min by SVM, 17 min by random forest and 6 h by Heinsfeld et al. (2018). As can be observed, ASD-DiagNet performs significantly faster than SVM and Heinsfeld et al. (2018). The data augmentation doubles the size of the training set by generating one artificial sample per subject in the training set. As a result, the data augmentation increases the computation time by a factor of 2.

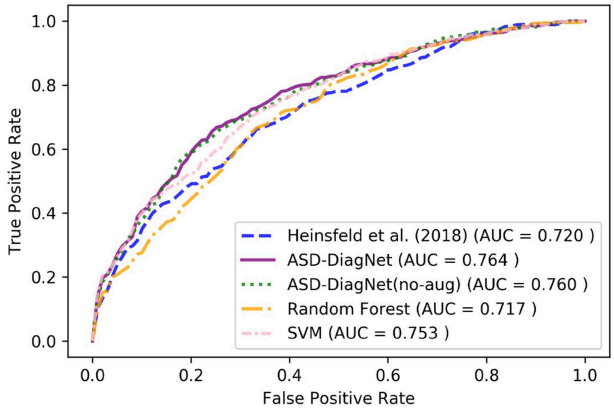


FIGURE 4 | ROC curves of different methods for classification of whole dataset using CC-200 parcellation.

TABLE 3 | Classification accuracy using 5-fold cross-validation on individual data centers using our proposed method, ASD-DiagNet (with and without data augmentation), compared with other methods.

Site	ASD-DiagNet	ASD-DiagNet (no aug.)	Heinsfeld et al., 2018	SVM	Random-Forest
Caltech	52.8	49.9	52.3	46.9	**54.2**
CMU	**68.5**	67.4	45.3	66.6	62.4
KKI	**69.5**	68.6	58.2	66.4	66.6
Leuven	**61.3**	57	51.8	59.8	59.8
MaxMun	48.6	51.4	**54.3**	53.8	49.2
NYU	68	65.1	64.5	**71.4**	61.8
OHSU	**82**	71.9	74	79.4	54.3
Olin	**65.1**	58.8	44	59.5	52.2
Pitt	**67.8**	65.9	59.8	66.3	59.9
SBL	51.6	47.5	46.6	**60**	48.3
SDSU	63	61.3	**63.6**	58.7	62.7
Stanford	**64.2**	53	48.5	51.4	62.1
Trinity	54.1	51.2	**61**	53.1	54.5
UCLA	**73.2**	70.3	57.7	72.1	69.3
USM	68.2	65.1	62	**73.2**	58
UM	63.8	**65.7**	57.6	64.2	64.8
Yale	**63.6**	61.7	53	61.6	55.3
Average	**63.8**	60.7	56.1	62.6	58.6

Bold and color values corresponds to highest accuracy achieved among all datasets.

3.4. Experiment on Other Parcellations

We tested ASD-DiagNet on two other ROI atlases besides CC-200: Automated Anatomical Labeling (AAL) and Talaraich and Tournoux (TT) which parcellate the brain into 116 and 97 regions respectively. The data for these parcellations is provided by ABIDE-I consortium. Similar to CC-200 atlas, for each parcellation, half of the correlations (keeping the 1/4 largest and 1/4 smallest values, and removing the rest intermediate values) are selected as input features to the model. The resulting average accuracy, sensitivity, and specificity of performing 10-fold cross-validation on the whole dataset using different approaches for AAL and TT are shown in **Tables 4**, **5**.

For AAL parcellation, ASD-DiagNet and SVM outperform other techniques with the classification accuracy of 67.5% and achieve competitive result for TT atlas. Note that the classification accuracy obtained using these parcellations are below the accuracy obtained using CC-200 atlas, which implies that the pairwise correlations among CC-200 regions contain more discriminatory patterns than AAL and TT atlases. Based on **Figures 5**, **6**, SVM and ASD-DiagNet achieved higher AUC than other methods.

TABLE 4 | Classification accuracy using 10-fold cross-validation on the whole dataset based on AAL atlas.

Method	Accuracy	Sensitivity	Specificity
ASD-DiagNet	**67.5**	63.4	71.5
ASD-DiagNet (no aug.)	64.5	60.9	68
SVM	**67.5**	63.9	70.9
Random forest	65	56.8	72.7
Heinsfeld et al., 2018	63.3	58.6	67.8

Bold values show the highest accuracy among all methods.

TABLE 5 | Classification accuracy using 10-fold cross-validation on the whole dataset based on TT atlas.

Method	Accuracy	Sensitivity	Specificity
ASD-DiagNet	65.3	63.4	66.9
ASD-DiagNet (no aug.)	65.2	61.1	69
SVM	**66.4**	61.6	71
Random forest	65.1	60.3	69.7
Heinsfeld et al., 2018	63.2	59.8	66.4

Bold values show the highest accuracy among all methods.

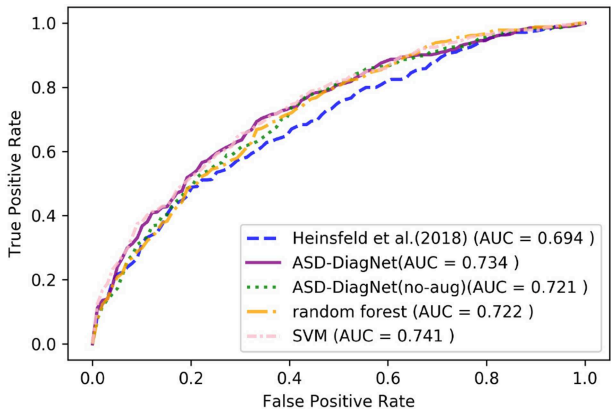


FIGURE 5 | ROC curves of different methods for classification of whole dataset using AAL parcellation.

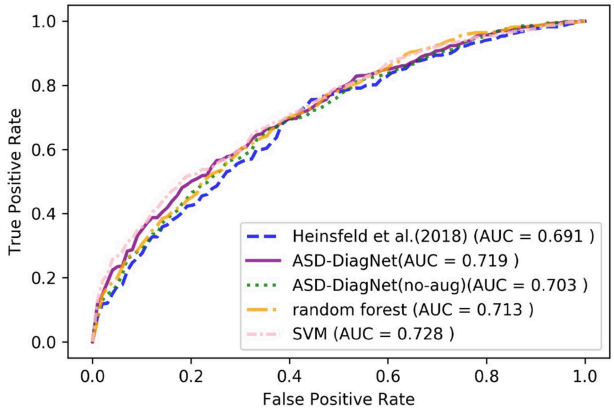


FIGURE 6 | ROC curves of different methods for classification of whole dataset using TT parcellation.

3.5. Experiments on Young Age Group

Diagnosing ASD at early ages and starting medical treatment can have a positive effect on the patient's life. In this experiment, we evaluated our proposed method as well as other baselines on subjects below the age of 15 (550 subjects in ABIDE dataset containing 448 males and 102 females) using CC-200 atlas. Considering this subset of subjects, the classification performance, as well as ROC curves of performing 10-fold cross-validation of different methods are provided in **Table 6** and **Figure 7**.

As can be observed from the results, ASD-DiagNet achieves higher accuracy as well as higher AUC value compared to other methods. The overall accuracy is around 2% below the accuracy achieved for classification of the whole dataset, which we believe is due to the smaller training set.

TABLE 6 | Classification accuracy using 10-fold cross-validation on the subjects below the age of 15.

Method	Accuracy	Sensitivity	Specificity
ASD-DiagNet	**68.2**	66.7	69.4
ASD-DiagNet (no aug.)	66.9	59.2	74.3
SVM	66.9	64.5	69.2
Random forest	64.3	57.4	70.8
Heinsfeld et al., 2018	65.2	62.1	68.3

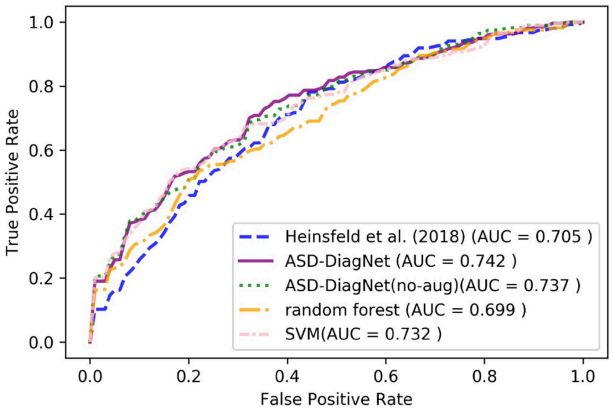


FIGURE 7 | ROC curves of different methods for classification of subjects below the age of 15 using CC-200 parcellation.

4. CONCLUSION AND FUTURE WORK

In this paper, we targeted the problem of classifying subjects with ASD disorder from healthy subjects. We used fMRI data provided by ABIDE consortium, which has been collected from different brain imaging centers. Our approach, called *ASD-DiagNet*, is based on using the most correlated and anti-correlated connections of the brain as feature vectors and using an autoencoder to extract lower dimensional patterns from them. The autoencoder and a SLP are trained in a joint approach for performing feature selection and classification. We also proposed a data augmentation method in order to increase the number of samples using the available training set. We tested this method by performing 10-fold cross-validation on the whole dataset and achieved 70.3% accuracy in 40 min. The running time of our approach is significantly shorter than 6 h needed by the state of the art method while achieving higher classification accuracy. In another experiment, we evaluated our method by performing 5-fold cross-validation on each data center, separately. The average result shows significant improvement in accuracy compared to the state of the art method. In this case, data augmentation helps to improve the accuracy by around 3%. A different range of accuracies can be observed among sites, from low accuracies in sites such as Caltech and MaxMun to higher accuracies for OHSU and UCLA. The variable accuracy among different sites can also be observed in other studies (Nielsen et al., 2013; Heinsfeld et al., 2018). It should be noted that the protocols and parameters used for scanning the subjects are heterogeneous among sites, which can cause variability in the functional patterns among different subjects. Also, the difference in demographic information among the datasets, such as age, IQ, and gender, makes the data distribution different among them. These differences could be

the reason for variable accuracies. We will consider this issue in our future works by involving the demographic information of the samples in data augmentation and the learning process. This will help the classifier to learn associations between functional connectivity patterns and demographic features which decreases the disparity among accuracies of different sites. We will also analyze other parcellations such as Power-264 by Power et al. (2011). The functional network constructed using this parcellation has shown promising results in diagnosing brain disorders (Greene et al., 2016; Khazaee et al., 2016).

Overall, experiments on different parcellations as well as subjects below the age of 15 show higher accuracy and AUC value for ASD-DiagNet comparing to other methods. These results demonstrate that our approach can be used for both intra-site brain imaging data, which are usually small sets generated in research centers, and bigger multi-site datasets like ABIDE in a reasonable amount of time.

While our model has shown promising results for diagnosing ASD disorder, there is still room for improvement by fusing structural and phenotypic information of the subjects to the functional patterns and creating hybrid features. Combination of discriminatory information provided by these three sources could increase the prediction accuracy of ASD. We consider this feature fusion as one of the future directions of our study. Another direction that we will pursue is improving the data augmentation strategy. Overall, the proposed data augmentation has improved the accuracy by generating synthetic data, but in a couple of cases low or no improvement is observed. Optimizing the current data augmentation method and considering the structural and phenotypic data for generating new samples could potentially improve the data augmentation process, and as a result, may lead to increase the diagnosis accuracy.

DATA AVAILABILITY STATEMENT

The datasets analyzed for this study can be found in the ABIDE-I repository (Craddock et al., 2013).

AUTHOR CONTRIBUTIONS

TE, VM, and FS conceived the study. TE pursued the implementation of the method, conducted the experiments and generated the results. TE and FS wrote the manuscript. AL and AF provided critical feedback and suggestions for performing the experiments. FS, AF, and VM provided valuable suggestions in writing the manuscript.

FUNDING

This research was supported by National Institute of General Medical Sciences (NIGMS), NIH Award Number R15GM120820, and National Science Foundations (NSF) under Award Numbers NSF OAC 1925960. The content is solely the responsibility of the authors and does not necessarily represent the official views of governmental agencies.

ACKNOWLEDGMENTS

This manuscript has been released as a Pre-Print at Eslami et al. (2019).

REFERENCES

Abraham, A., Milham, M. P., Di Martino, A., Craddock, R. C., Samaras, D., Thirion, B., et al. (2017). Deriving reproducible biomarkers from multi-site resting-state data: An autism-based example. *Neuroimage* 147, 736–745. doi: 10.1016/j.neuroimage.2016.10.045

Baggio, H.-C., Sala-Llonch, R., Segura, B., Marti, M.-J., Valldeoriola, F., Compta, Y., et al. (2014). Functional brain networks and cognitive deficits in parkinson's disease. *Human Brain Mapp.* 35, 4620–4634. doi: 10.1002/hbm.22499

Baio, J., Wiggins, L., Christensen, D. L., Maenner, M. J., Daniels, J., Warren, Z., et al. (2018). Prevalence of autism spectrum disorder among children aged 8 years—autism and developmental disabilities monitoring network, 11 sites, united states, 2014. *MMWR Surveill. Summar.* 67:1. doi: 10.15585/mmwr.ss6706a1

Bi, X.-A., Liu, Y., Jiang, Q., Shu, Q., Sun, Q., and Dai, J. (2018a). The diagnosis of autism spectrum disorder based on the random neural network cluster. *Front. Human Neurosci.* 12:257. doi: 10.3389/fnhum.2018.00257

Bi, X.-A., Wang, Y., Shu, Q., Sun, Q., and Xu, Q. (2018b). Classification of autism spectrum disorder using random support vector machine cluster. *Front. Genet.* 9:18. doi: 10.3389/fgene.2018.00018

Brown, C. J., Kawahara, J., and Hamarneh, G. (2018). "Connectome priors in deep neural networks to predict autism," in *2018 IEEE 15th International Symposium on Biomedical Imaging (ISBI 2018)* (Washington, DC: IEEE), 110–113. doi: 10.1109/ISBI.2018.8363534

Chawla, N. V., Bowyer, K. W., Hall, L. O., and Kegelmeyer, W. P. (2002). SMOTE: synthetic minority over-sampling technique. *J. Artif. Intell. Research* 16, 321–357. doi: 10.1613/jair.953

Chen, H., Duan, X., Liu, F., Lu, F., Ma, X., Zhang, Y., et al. (2016). Multivariate classification of autism spectrum disorder using frequency-specific resting-state functional connectivity—a multi-center study. *Prog. Neuro Psychopharmacol. Biol. Psychiatry* 64, 1–9. doi: 10.1016/j.pnpbp.2015.06.014

Colby, J. B., Rudie, J. D., Brown, J. A., Douglas, P. K., Cohen, M. S., and Shehzad, Z. (2012). Insights into multimodal imaging classification of ADHD. *Front. Syst. Neurosci.* 6:59. doi: 10.3389/fnsys.2012.00059

Craddock, C., Benhajali, Y., Chu, C., Chouinard, F., Evans, A., Jakab, A., et al. (2013). The neuro bureau preprocessing initiative: open sharing of preprocessed neuroimaging data and derivatives. *Neuroinformatics*. doi: 10.3389/conf.fninf.2013.09.00041

Craddock, R. C., James, G. A., Holtzheimer, P. E. III, Hu, X. P., and Mayberg, H. S. (2012). A whole brain fMRI atlas generated via spatially constrained spectral clustering. *Human Brain Mapp.* 33, 1914–1928. doi: 10.1002/hbm.21333

Deshpande, G., Wang, P., Rangaprakash, D., and Wilamowski, B. (2015). Fully connected cascade artificial neural network architecture for attention deficit hyperactivity disorder classification from functional magnetic resonance imaging data. *IEEE Trans. Cybernet.* 45, 2668–2679. doi: 10.1109/TCYB.2014.2379621

Dvornek, N. C., Ventola, P., Pelphrey, K. A., and Duncan, J. S. (2017). "Identifying autism from resting-state fMRI using long short-term memory networks," in *International Workshop on Machine Learning in Medical Imaging* (Quebec, QC: Springer), 362–370. doi: 10.1007/978-3-319-67389-9_42

Eitel, A., Springenberg, J. T., Spinello, L., Riedmiller, M., and Burgard, W. (2015). "Multimodal deep learning for robust RGB-D object recognition," in *2015 IEEE/RSJ International Conference on Intelligent Robots and Systems (IROS)* (Hamburg: IEEE), 681–687. doi: 10.1109/IROS.2015.7353446

Eslami, T., Mirjalili, V., Fong, A., Laird, A., and Saeed, F. (2019). ASD-diagnet: a hybrid learning approach for detection of autism spectrum disorder using fMRI data. *arXiv [preprint]. arXiv:1904.07577*.

Eslami, T., and Saeed, F. (2018a). Fast-GPU-PCC: a GPU-based technique to compute pairwise pearson's correlation coefficients for time series data–fMRI study. *High Throughput* 7:11. doi: 10.3390/ht7020011

Eslami, T., and Saeed, F. (2018b). "Similarity based classification of ADHD using singular value decomposition," in *Proceedings of the ACM International Conference on Computing Frontiers 2018* (ACM), 19–25.

Eslami, T., and Saeed, F. (2019). "Auto-ASD-network: a technique based on deep learning and support vector machines for diagnosing autism spectrum disorder using fMRI data," in *Proceedings of ACM Conference on Bioinformatics, Computational Biology, and Health Informatics* (Niagara Falls, NY: ACM).

Fredo, A. J., Jahedi, A., Reiter, M., and Müller, R.-A. (2018). Diagnostic classification of autism using resting-state fMRI data and conditional random forest. *Age* 12, 6–41.

Greene, D. J., Church, J. A., Dosenbach, N. U., Nielsen, A. N., Adeyemo, B., Nardos, B., et al. (2016). Multivariate pattern classification of pediatric tourette syndrome using functional connectivity MRI. *Dev. Sci.* 19, 581–598. doi: 10.1111/desc.12407

Guo, X., Dominick, K. C., Minai, A. A., Li, H., Erickson, C. A., and Lu, L. J. (2017). Diagnosing autism spectrum disorder from brain resting-state functional connectivity patterns using a deep neural network with a novel feature selection method. *Front. Neurosci.* 11:460. doi: 10.3389/fnins.2017.00460

Heinsfeld, A. S., Franco, A. R., Craddock, R. C., Buchweitz, A., and Meneguzzi, F. (2018). Identification of autism spectrum disorder using deep learning and the abide dataset. *Neuroimage Clin.* 17, 16–23. doi: 10.1016/j.nicl.2017.08.017

Hosseini-Asl, E., Gimel'farb, G., and El-Baz, A. (2016). Alzheimer's disease diagnostics by a deeply supervised adaptable 3D convolutional network. *arXiv [preprint]. arXiv:1607.00556*.

Iidaka, T. (2015). Resting state functional magnetic resonance imaging and neural network classified autism and control. *Cortex* 63, 55–67. doi: 10.1016/j.cortex.2014.08.011

Itani, S., and Thanou, D. (2019). Combining anatomical and functional networks for neuropathology identification: a case study on autism spectrum disorder. *arXiv [preprint]. arXiv:1904.11296*.

Jaiswal, S., Valstar, M. F., Gillott, A., and Daley, D. (2017). "Automatic detection of ADHD and ASD from expressive behaviour in RGBD data," in *2017 12th IEEE International Conference on Automatic Face & Gesture Recognition (FG 2017)* (Washington, DC: IEEE), 762–769.

Karpathy, A., Toderici, G., Shetty, S., Leung, T., Sukthankar, R., and Fei-Fei, L. (2014). "Large-scale video classification with convolutional neural networks," in *Proceedings of the IEEE Conference on Computer Vision and Pattern Recognition* (Columbus, OH), 1725–1732.

Khazaee, A., Ebrahimzadeh, A., and Babajani-Feremi, A. (2016). Application of advanced machine learning methods on resting-state fMRI network for identification of mild cognitive impairment and alzheimer's disease. *Brain Imaging Behav.* 10, 799–817. doi: 10.1007/s11682-015-9448-7

Khazaee, A., Ebrahimzadeh, A., Babajani-Feremi, A., Initiative, A. D. N., et al. (2017). Classification of patients with MCI and AD from healthy controls using directed graph measures of resting-state fMRI. *Behav. Brain Res.* 322, 339–350. doi: 10.1016/j.bbr.2016.06.043

Khosla, M., Jamison, K., Kuceyeski, A., and Sabuncu, M. (2018). "3D convolutional neural networks for classification of functional connectomes," in *Deep Learning in Medical Image Analysis and Multimodal Learning for Clinical Decision Support* (Granada: Springer), 137–145. doi: 10.1007/978-3-030-00889-5_16

Li, H., Parikh, N. A., and He, L. (2018). A novel transfer learning approach to enhance deep neural network classification of brain functional connectomes. *Front. Neurosci.* 12:491. doi: 10.3389/fnins.2018.00491

Liang, X., Wang, J., Yan, C., Shu, N., Xu, K., Gong, G., and He, Y. (2012). Effects of different correlation metrics and preprocessing factors on small-world brain functional networks: a resting-state functional MRI study. *PLoS ONE* 7:e32766. doi: 10.1371/journal.pone.0032766

Lindquist, M. A. (2008). The statistical analysis of fMRI data. *Stat. Sci.* 23, 439–464. doi: 10.1214/09-STS282

Liu, W., Li, M., and Yi, L. (2016). Identifying children with autism spectrum disorder based on their face processing abnormality: a machine learning framework. *Autism Res.* 9, 888–898. doi: 10.1002/aur.1615

National Collaborating Centre for Mental Health (UK) (2018). *Attention Deficit Hyperactivity Disorder: Diagnosis and Management of ADHD in Children, Young People and Adults*. Leicester: British Psychological Society.

Nickel, R. E., and Huang-Storms, L. (2017). Early identification of young children with autism spectrum disorder. *Indian J. Pediatr.* 84, 53–60. doi: 10.1007/s12098-015-1894-0

Nielsen, J. A., Zielinski, B. A., Fletcher, P. T., Alexander, A. L., Lange, N., Bigler, E. D., et al. (2013). Multisite functional connectivity MRI classification of autism: Abide results. *Front. Human Neurosci.* 7:599. doi: 10.3389/fnhum.2013.00599

Parikh, M. N., Li, H., and He, L. (2019). Enhancing diagnosis of autism with optimized machine learning models and personal characteristic data. *Front. Comput. Neurosci.* 13:9. doi: 10.3389/fncom.2019.00009

Parisot, S., Ktena, S. I., Ferrante, E., Lee, M., Guerrero, R., Glocker, B., and Rueckert, D. (2018). Disease prediction using graph convolutional networks: application to autism spectrum disorder and Alzheimer's disease. *Med. Image Anal.* 48, 117–130. doi: 10.1016/j.media.2018.06.001

Peng, X., Lin, P., Zhang, T., and Wang, J. (2013). Extreme learning machine-based classification of ADHD using brain structural MRI data. *PLoS ONE* 8:e79476. doi: 10.1371/journal.pone.0079476

Perez, L., and Wang, J. (2017). The effectiveness of data augmentation in image classification using deep learning. *arXiv [preprint]. arXiv:1712.04621*.

Plitt, M., Barnes, K. A., and Martin, A. (2015). Functional connectivity classification of autism identifies highly predictive brain features but falls short of biomarker standards. *Neuroimage Clin.* 7, 359–366. doi: 10.1016/j.nicl.2014.12.013

Power, J. D., Cohen, A. L., Nelson, S. M., Wig, G. S., Barnes, K. A., Church, J. A., et al. (2011). Functional network organization of the human brain. *Neuron* 72, 665–678. doi: 10.1016/j.neuron.2011.09.006

Raschka, S., and Mirjalili, V. (2017). *Python Machine Learning*. Birmingham: Packt Publishing Ltd.

Sen, B., Borle, N. C., Greiner, R., and Brown, M. R. (2018). A general prediction model for the detection of ADHD and autism using structural and functional MRI. *PLoS ONE* 13:e0194856. doi: 10.1371/journal.pone.0194856

Subbaraju, V., Suresh, M. B., Sundaram, S., and Narasimhan, S. (2017). Identifying differences in brain activities and an accurate detection of autism spectrum disorder using resting state functional-magnetic resonance imaging: a spatial filtering approach. *Med. Image Anal.* 35, 375–389. doi: 10.1016/j.media.2016.08.003

Wong, S. C., Gatt, A., Stamatescu, V., and McDonnell, M. D. (2016). "Understanding data augmentation for classification: when to warp?" in *2016 International Conference on Digital Image Computing: Techniques and Applications (DICTA)* (Gold Coast, QLD: IEEE), 1–6. doi: 10.1109/DICTA.2016.7797091

Xu, Y., Jia, R., Mou, L., Li, G., Chen, Y., Lu, Y., et al. (2016). "Improved relation classification by deep recurrent neural networks with data augmentation," in *Proceedings of COLING 2016, the 26th International Conference on Computational Linguistics: Technical Papers* (Osaka: The COLING 2016 Organizing Committee), 1461–1470.

Yang, K., and Shahabi, C. (2004). "A PCA-based similarity measure for multivariate time series," in *Proceedings of the 2nd ACM International Workshop on Multimedia Databases* (Washington, DC: ACM), 65–74.

Yang, Z., Zhong, S., Carass, A., Ying, S. H., and Prince, J. L. (2014). "Deep learning for cerebellar ataxia classification and functional score regression," in *International Workshop on Machine Learning in Medical Imaging* (Springer), 68–76.

Zhang, Y., Zhang, H., Chen, X., Lee, S.-W., and Shen, D. (2017). Hybrid high-order functional connectivity networks using resting-state functional MRI for mild cognitive impairment diagnosis. *Sci. Rep.* 7:6530. doi: 10.1038/s41598-017-06509-0

Zunino, A., Morerio, P., Cavallo, A., Ansuini, C., Podda, J., Battaglia, F., et al. (2018). "Video gesture analysis for autism spectrum disorder detection," in *2018 24th International Conference on Pattern Recognition (ICPR)* (Beijing: IEEE), 3421–3426.

Conflict of Interest: The authors declare that the research was conducted in the absence of any commercial or financial relationships that could be construed as a potential conflict of interest.

Copyright © 2019 Eslami, Mirjalili, Fong, Laird and Saeed. This is an open-access article distributed under the terms of the Creative Commons Attribution License (CC BY). The use, distribution or reproduction in other forums is permitted, provided the original author(s) and the copyright owner(s) are credited and that the original publication in this journal is cited, in accordance with accepted academic practice. No use, distribution or reproduction is permitted which does not comply with these terms.

frontiers in Neuroinformatics

ORIGINAL RESEARCH
published: 04 February 2020
doi: 10.3389/fninf.2020.00003

Magia: Robust Automated Image Processing and Kinetic Modeling Toolbox for PET Neuroinformatics

Tomi Karjalainen[1], Jouni Tuisku[1], Severi Santavirta[1], Tatu Kantonen[1], Marco Bucci[1], Lauri Tuominen[2], Jussi Hirvonen[1,3], Jarmo Hietala[1,4], Juha O. Rinne[1,5] and Lauri Nummenmaa[1,6]*

[1]*Turku PET Centre, University of Turku and Turku University Hospital, Turku, Finland,* [2]*The Royal's Institute of Mental Health Research, University of Ottawa, Ottawa, ON, Canada,* [3]*Department of Radiology, University of Turku, Turku, Finland,* [4]*Department of Psychiatry, Faculty of Medicine, University of Turku and Turku University Hospital, Turku, Finland,* [5]*Division of Clinical Neurosciences, Turku University Hospital, Turku, Finland,* [6]*Department of Psychology, University of Turku, Turku, Finland*

Processing of positron emission tomography (PET) data typically involves manual work, causing inter-operator variance. Here we introduce the Magia toolbox that enables processing of brain PET data with minimal user intervention. We investigated the accuracy of Magia with four tracers: [^{11}C]carfentanil, [^{11}C]raclopride, [^{11}C]MADAM, and [^{11}C]PiB. We used data from 30 control subjects for each tracer. Five operators manually delineated reference regions for each subject. The data were processed using Magia using the manually and automatically generated reference regions. We first assessed inter-operator variance resulting from the manual delineation of reference regions. We then compared the differences between the manually and automatically produced reference regions and the subsequently obtained binding potentials and standardized-uptake-value-ratios. The results show that manually produced reference regions can be remarkably different from each other, leading to substantial differences also in outcome measures. While the Magia-derived reference regions were anatomically different from the manual ones, Magia produced outcome measures highly consistent with the average of the manually obtained estimates. For [^{11}C]carfentanil and [^{11}C]PiB there was no bias, while for [^{11}C]raclopride and [^{11}C]MADAM Magia produced 3–5% higher binding potentials. Based on these results and considering the high inter-operator variance of the manual method, we conclude that Magia can be reliably used to process brain PET data.

Keywords: PET, neuroinformatics, modeling, reference region, carfentanil, raclopride, madam, pib

OPEN ACCESS

Edited by:
Ludovico Minati,
Tokyo Institute of Technology, Japan

Reviewed by:
Harumasa Takano,
National Center of Neurology and Psychiatry, Japan
Frithjof Kruggel,
University of California, Irvine, United States

****Correspondence:***
Tomi Karjalainen
tomi.karjalainen@utu.fi

Received: *18 November 2019*
Accepted: *15 January 2020*
Published: *04 February 2020*

Citation:
Karjalainen T, Tuisku J, Santavirta S, Kantonen T, Bucci M, Tuominen L, Hirvonen J, Hietala J, Rinne JO and Nummenmaa L (2020) Magia: Robust Automated Image Processing and Kinetic Modeling Toolbox for PET Neuroinformatics. Front. Neuroinform. 14:3. doi: 10.3389/fninf.2020.00003

INTRODUCTION

The statistical power of neuroimaging studies has been widely questioned in recent years, leading to calls for significantly larger samples to avoid false-positive and negative findings (Yarkoni, 2009; Button et al., 2013; Cremers et al., 2017). Additionally, the role of researcher degrees of freedom, i.e., the subjective choices made during the process from data collection to its analysis, has been identified as an important reason for poor replicability of many findings (Simmons et al., 2011). Consequently, the focus in neuroimaging has shifted towards standardized,

large-scale neuroinformatics based approaches (Yarkoni et al., 2011; Poldrack and Yarkoni, 2016). Today, several standardized and highly automatized preprocessing pipelines are publicly available for processing functional magnetic resonance images (fMRI; Esteban et al., 2019). Such standardized methods are not, however, currently widely used for the analysis of positron emission tomography (PET) data, although recently some tools have become available (Gunn et al., 2016; Funck et al., 2018).

Compared to fMRI preprocessing, preprocessing of PET data is relatively straightforward because confounding temporal signals are rarely regressed out of the data, and the preprocessing thus only consists of spatial processes, such as frame-realignment and coregistration. Yet, any all-inclusive PET processing pipeline must be able to handle numerous kinetic models to support as many radiotracers as possible. Thus, unlike fMRI preprocessing tools, PET pipelines should handle both the preprocessing as well as the kinetic modeling for numerous tracers, making the development of a comprehensive PET pipeline a challenging task.

A particularly sensitive task in PET analysis is the requirement of the input function. Depending on tracer, the input function can be obtained either from blood samples or directly from the PET images, for example, if a reference region is available for the tracer. The blood samples require manual processing before the input function can be obtained from them. While population-based atlases (Fischl et al., 2002; Tzourio-Mazoyer et al., 2002; Eickhoff et al., 2005) provide an automatic way for defining reference regions (Yasuno et al., 2002; Schain et al., 2014; Tuszynski et al., 2016), they are suboptimal because the process requires warping of either the atlases or the PET images. Ideally, the reference region should be defined separately for each individual before spatial normalization. Consequently, manual delineation is still considered the gold standard for defining the reference regions, thus prohibiting a fully automatic analysis of PET data. Furthermore, manual reference region delineation is time-consuming and relies on numerous subjective choices. To minimize between-study variance resulting from operator-dependent choices (White et al., 1999), a single individual should delineate the reference regions for all studies within a project. Thus, manual delineation is not suited for large-scale projects where hundreds of scans are processed, or neuroinformatics approaches where an even significantly larger number of scans have to be processed.

To resolve these issues, we introduce Magia[1] that enables automatic modeling of brain PET data with minimal user intervention The major advantages of this approach involve:

1. Flexible, parallelizable environment suitable for large-scale standardized analysis.
2. Fully automated processing of brain PET data starting from raw images.
3. Visual quality control of the processing steps.
4. Centralized management and storage of study metadata, image processing methods and outputs for subsequent reanalysis and quality control.

[1]https://github.com/tkkarjal/magia

In this study, we compared Magia-derived input functions and the subsequent outcome measures against those obtained using conventional manual techniques with four tracers binding to different sites: [^{11}C]carfentanil, [^{11}C]raclopride, [^{11}C]MADAM, and [^{11}C]PiB. We also assessed inter-rater agreement in the reference region definition and uptake estimates, and regional and voxel-level outcome measures.

MATERIALS AND METHODS

Overview of Magia

Magia[1] is a freely available and fully automatic analysis pipeline for brain PET data. Running on MATLAB (The MathWorks, Inc., Natick, MA, USA), Magia combines methods from SPM12[2] and FreeSurfer[3]—two freely available and widely used tools–with in-house software developed for kinetic modeling. Magia has been developed alongside a centralized database[4] containing metadata about each study, facilitating data storage and neuroinformatics-type large-scale PET analyses. While the implementation of a similar database is highly recommended, Magia can also be installed and used without such database as long as the user can feed in the necessary information about the studies. Magia runs only on Linux/Mac. The Optimization Toolbox for MATLAB is required for fitting some of the models. Magia has been developed using MATLAB R2016b. Magia currently supports the simplified reference tissue model, Logan (Logan, 2000) with both plasma input and reference tissue input, Patlak (Patlak et al., 1983) with both plasma input and reference tissue input, SUV-ratio (Chen and Nasrallah, 2017; standardized uptake value), and fractional uptake ratio (FUR; Thie, 1995) analysis for late scans with plasma input. Also, the two-tissue compartmental model can be fitted to regional-level data.

A box-diagram describing the main steps in Magia processing is shown in **Figure 1**. Magia starts by preprocessing the PET images. The preprocessing consists of frame-alignment (motion-correction) and coregistration with the MRI. The MRI is processed with FreeSurfer to generate anatomical parcellations for defining regions of interest (Schain et al., 2014), and the reference region if one is required for the chosen kinetic model. FreeSurfer assigns an anatomical label to each brain voxel, and the regions of interest (ROIs) thus consist of all the voxels with the same anatomical label. Magia performs a two-step correction to the reference tissue mask (see below) before obtaining the input function for modeling; the corrections make the reference regions robust for many scanners and individuals. The MRI is also segmented into gray and white matter probability maps for spatial normalization (Ashburner and Friston, 2000). After modeling, the parametric images are spatially normalized and smoothed. In addition to the parametric images, Magia also calculates region-level parameter estimates for each study. Finally, the results are stored in a centralized archive in a standardized format along with visual quality control metrics, facilitating future population-level analyses.

[2]www.fil.ion.ucl.ac.uk/spm/
[3]https://surfer.nmr.mgh.harvard.edu/
[4]http://aivo.utu.fi

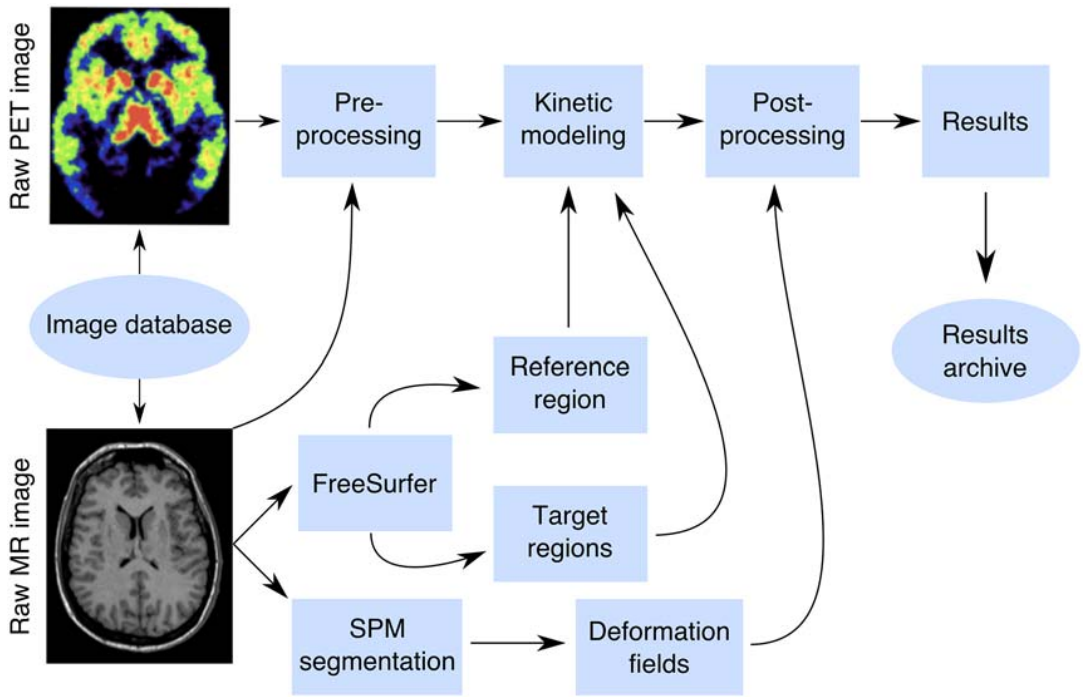


FIGURE 1 | The Magia pipeline combines FreeSurfer cortical mesh generation and parcellation, T1 MR image segmentation and normalization, automatic reference region and region of interest generation, and kinetic modeling.

The above-mentioned steps are only used when applicable. For example, for static PET-images, the frame alignment is skipped, and if there is no related MRI available, then a tracer-specific radioactivity template must be available to normalize the images. For all of the tracers included in this manuscript, such templates can be obtained from https://github.com/tkkarjal/magia/tree/master/templates. Magia also supports tracers that do not have a reference region. For such studies, the preprocessed (e.g., decay-corrected, metabolite-corrected, and possibly extrapolated) plasma input must be available. Magia has default settings for preprocessing, modeling, and post processing that have worked well during its development. However, Magia is also flexible in the sense that the user can override some of these options if needed.

Validation Data

To assess reliability of Magia we used historical control data using four radioligands with different targets and spatial distribution of binding sites: Dopamine D_2R receptor antagonist [^{11}C]raclopride, μ-opioid receptor agonist [^{11}C]carfentanil, serotonin transporter ligand [^{11}C]MADAM, and beta-amyloid ligand [^{11}C]PIB. For each radioligand we selected 30 studies (**Table 1**). We generated reference regions for all the tracers using traditional manual methods and the new automatic method and compared the results. The study was conducted as a part of a register-based study on brain imaging at Turku PET Centre. Per applicable legislation in Finland, fully anonymized medical register data (including PET and MRI scans) can be analyzed in the context of a register study without obtaining an active informed consent from the individuals included in the register, if information identifying the individuals is not obtained. The study protocol was approved by Turku University Hospital Research Board and the legislative team.

Manual Reference Region Delineation

Five researchers with good knowledge of human neuroanatomy delineated reference regions for every study according to written and visual instructions (**Figure 2A**). Cerebellar cortex was used as a reference region for [^{11}C]raclopride (Gunn et al., 1997), [^{11}C]MADAM (Lundberg et al., 2005) and [^{11}C]PiB (Lopresti et al., 2005). For [^{11}C]carfentanil, the occipital cortex was used (Endres et al., 2003). The regions were drawn using CARIMAS[5] on three consecutive transaxial slices of T1-weighted MR images, which is the current standard manual method at Turku PET Centre. Cerebellar reference was drawn in the cerebellar gray matter within a gray zone in the peripheral part of cerebellum, distal to the bright signal of white matter. The first cranial slice was placed below the occipital cortex to avoid spill-in of radioactivity. Typically, this is a slice where the temporal lobe is clearly separated from the cerebellum by the petrosal part of the temporal bone. The most caudal slice was typically located in the most caudal part of the cerebellum. Laterally, venous sinuses were avoided to avoid spill-in during the early phases of the scans. Posteriorly, there was about a 5 mm distance from the cerebellar surface to avoid spill-out effects. Anteriorly, the

[5]http://turkupetcentre.fi/carimas/

TABLE 1 | Summary of the studies.

	[^{11}C]carfentanil	[^{11}C]raclopride	[^{11}C]MADAM	[^{11}C]PiB
N (female)	30 (12)	30 (23)	30 (17)	30 (18)
Age (mean, range)	32 (20–51)	39 (20–60)	42 (25–57)	71 (66–80)
Scanners	HRRT PET/CT PET/MR	GE Advance PET/CT HRRT	HRRT	HRRT
Data range (years)	2007–2016	1998–2014	2008–2015	2014–2016

Scanners: HRRT (HRRT, Siemens Medical Solutions); PET/CT (Discovery 690 PET/CT, GE Healthcare); PET/MR (Ingenuity TF PET/MR, Philips Healthcare); GE Advance (GE Advance, GE Healthcare).

border of the reference region was drawn approximately 2 mm distal to the border of cerebellar white and gray matter, except in the most caudal slice, where the central white matter may no longer be visible.

The occipital reference region was defined on three consecutive transaxial slices, of which the most caudal slice was the second-most caudal slice before the cerebellum. The reference region was drawn J-shaped with medial and posterior parts. The reference region was drawn to roughly follow the shape of the cortical surface, but not individual gyri. The reference region was drawn approximately 1 cm wide with about 2 mm margin to the cortical surface to avoid spill-out effects. The anterior border of the reference region was placed approximately halfway between the posterior cortical surface and the splenium of the corpus callosum. The posterolateral border of the reference region approximated the medial-most part of the posterior horn of the lateral ventricle.

Automatic Reference Region Generation

Figure 2B shows an overview of the automated reference-region-generation process. First, T1-weighted MR images were fed into FreeSurfer to provide subject-specific anatomical masks for cerebellar and occipital cortices. Second, an anatomical correction was applied to the FreeSurfer-generated reference region mask to remove voxels that, based on their anatomical location alone, are likely to suffer from spill-over effects. For the cerebellar cortex, the most important sources of spill-over effects are occipital cortex and venous sinuses. Thus, the most outermost cerebellar voxels were excluded in the anatomical reference region correction. For the occipital cortex, voxels that were lateral to the lateral ventricles were excluded. This is because the most lateral parts of the FreeSurfer-generated occipital cortex extend to areas with specific binding for [^{11}C]carfentanil, and the lateral ventricles provide a reliable anatomical cut-off point for thresholding. Finally, the radioactivity concentration distribution within the anatomically corrected reference region was estimated, and the tails of the distribution were excluded. The lower and upper boundaries for the signal intensities were defined by calculating the full width at half maximum (FWHM) of the mean PET signal intensity distribution. This step ensures that the reference region will not contain voxels with atypically high or low radioactivity (e.g., signal from outside the brain). The automatic reference region generation process thus combines information from anatomical brain scans and the PET images to get a reliable estimate of nonspecific binding.

Quantifying Operator-Dependent Variability

We first investigated how subjective choices in manual reference-region delineation translate into differences in reference region masks, reference-region time-activity curves (TACs), and outcome measures. Anatomical differences in reference region masks were assessed in two ways: first, we calculated within-study spatial overlap between the manual reference regions. The spatial overlap was calculated in two stages: it was first calculated separately for all different manual reference region pairs, and those numbers were then averaged over to obtain a summary statistic for each study. Second, we investigated the differences in volumes of the manually delineated reference regions using the intra-class correlation coefficient (ICC). To estimate ICC, we first estimated a random-effects model $y \sim 1 + (1 \mid \text{operator}) + (1 \mid \text{study})$, where, y is the variable of interest, and then calculated the proportion of variance explained by the variance of the random-effect-components (Nakagawa et al., 2017). Calculated this way, ICC is restricted to between 0 and 1. The R package brms[6] was used to estimate the models, and the R package performance[7] was used to estimate ICC.

Differences in reference region TACs were assessed by calculating area under the curve (AUC) of them. Prior to the ICC analysis, we standardized all the AUCs with the mean radioactivity within the union of all manually delineated reference regions. This standardization removes between-study variance resulting from different scanners, body masses and injected doses.

The Volumetric Similarity of the Manual and Automatic Reference Regions

We compared the volumes of reference regions to assess whether the two techniques generate reference regions of systematically different sizes. For each study, we calculated the mean volume from all manually delineated reference regions and compared it to the volume of the Magia-derived reference region. We also quantified the anatomical overlap between the manually and the automatically derived reference regions. The overlap was defined as the ratio between the number of common voxels and the number of manual voxels. For each study, the overlap was first calculated separately for every manually delineated reference region after which the mean overlap was calculated.

[6]https://cran.r-project.org/package=brms
[7]https://easystats.github.io/performance/index.html

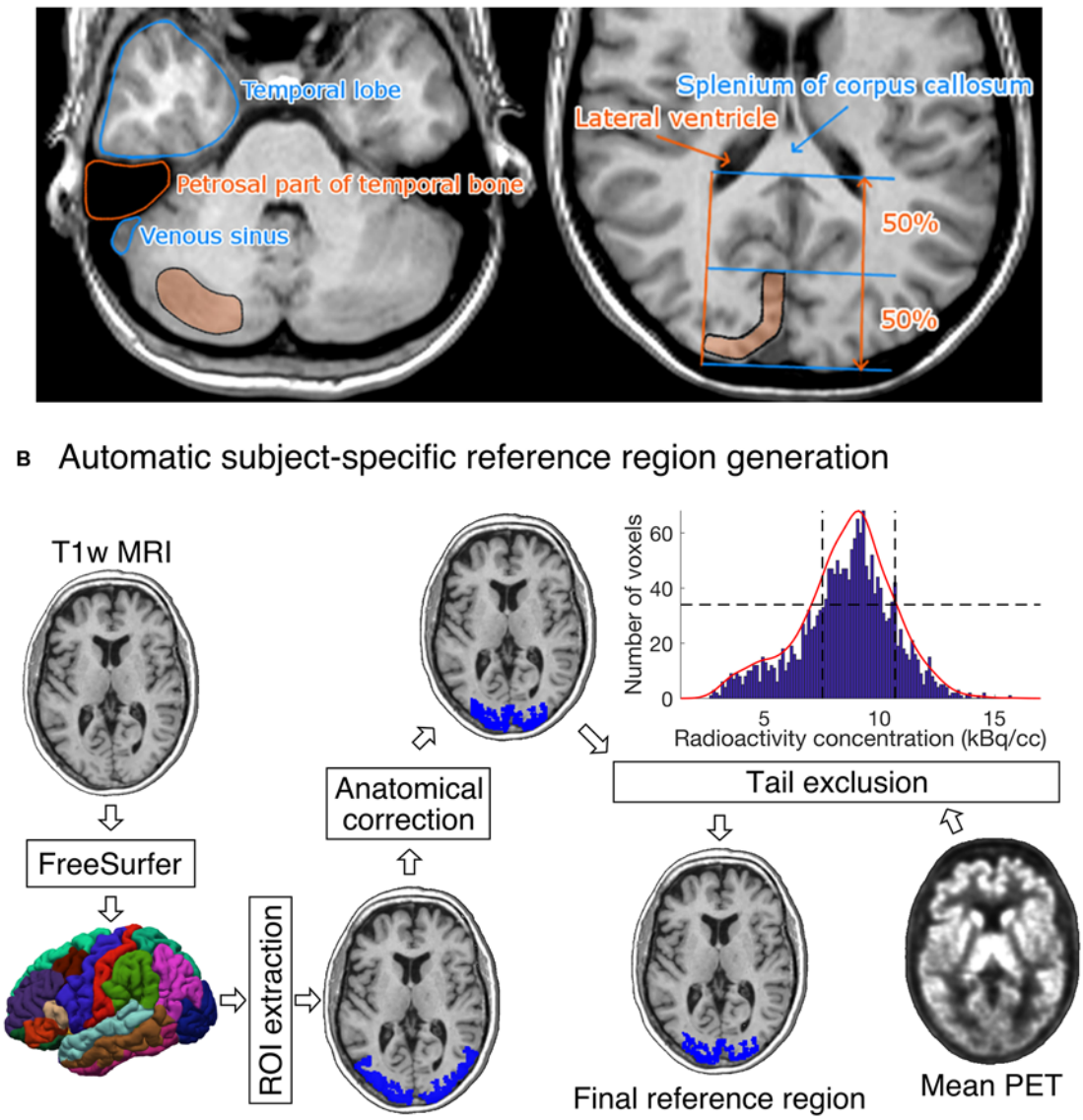


FIGURE 2 | (A) Visual instructions of the most cranial slice of manually delineated cerebellar (left) and occipital (right) reference regions. The reference regions were delineated on three consecutive transaxial T1-weighted MR images. Cerebellar reference region is shown on the left and occipital reference region on the right. **(B)** The diagram shows how a T1-weighted MR image of an individual's brain is processed to produce the final reference region. The shown example is from the [^{11}C]carfentanil data set. The rectangles represent processing steps between inputs and outputs. The FreeSurfer step assigns an anatomical label to each voxel of the subject's T1 weighted MR image. The ROI extraction step extracts a prespecified ROI from FreeSurfer's output. The anatomical correction removes voxels that are most likely to suffer from spillover effects; for [^{11}C]carfentanil data this means voxels lateral to the lateral ventricles. In the tail-exclusion step, radioactivity distribution within the anatomically corrected reference region is estimated, and the voxels whose intensities are on the tail-ends of the distribution are excluded.

Similarity of the Reference Region Radioactivity Concentrations

A functionally homogenous region should have approximately Gaussian distribution of radioactivity measured with PET (Teymurazyan et al., 2013). Functional homogeneousness was assessed using radioactivity distributions within the reference regions. The automatically and manually derived reference region masks were used to extract radioactivity concentration distribution within the reference regions. The study-specific manual distributions were averaged over the manual drawers to provide a single manual distribution for each study. The radioactivity concentrations were converted into SUV, after which the distributions were averaged over studies to provide tracer-specific distributions. Mean, standard deviations, mode, and skewness of the distributions were used to quantify the differences in the distributions.

Similarity of the Reference Region Time-Activity Curves

We compared the similarity of the automatically and manually delineated reference region TACs. For each study, the manual reference region TAC was defined as the average across the manual TACs to minimize the subjective bias in adhering to the instructions for manual reference region delineation. Activities were expressed as standardized uptake values (SUV, g/ml) which were obtained by normalizing tissue radioactivity concentration (kBq/ml) by total injected dose (MBq) and body mass (kg), thus making the different images comparable to each other. To assess the similarity of the shapes of reference region TACs, we calculated Pearson correlations between the manually and automatically delineated TACs for each tracer. Bias was assessed using the area under the curve (AUC).

Assessing the Similarity of the Outcome Measures

We used nondisplaceable binding potential (BP_{ND}) to quantify uptakes of [^{11}C]carfentanil, [^{11}C]raclopride and [^{11}C]MADAM. It reflects the ratio between specific and nondisplaceable binding in the brain. The binding potentials were calculated using a simplified reference tissue model whose use has been validated for these tracers (Gunn et al., 1997; Endres et al., 2003; Lundberg et al., 2005). SUV-ratio between 60 and 90 min was used to quantify [^{11}C]PiB uptake (Lopresti et al., 2005). All the studies were first processed using Magia. To obtain the outcome measures resulting from manually delineated reference regions the procedure was repeated with the only exception of replacing the automatically generated reference regions with a manually generated reference region. Thus, the only differences observed in the uptake estimates originate from differences in the reference regions. We estimated the outcome measures in one representative ROI for each tracer, and also calculated parametric images. The ROIs were extracted from the FreeSurfer parcellations.

RESULTS

Operator-Dependent Variation

The influence of different operators on reference region volumes, reference region time-activity AUCs, and outcome measures are presented for each tracer in **Table 2**. The spatial overlap between the manually delineated masks was modest, as the maximum overlap was 41% for [^{11}C]raclopride studies, while the overlap for the other tracers was 14–22%. The ICC for reference region volumes were moderate to good (0.74. . .0.83) for all tracers except [^{11}C]MADAM (ICC = 0.46). The reference region TAC AUCs varied substantially especially for [^{11}C]carfentanil and [^{11}C]MADAM, while for [^{11}C]PiB operator had little influence on the AUCs (ICC = 0.95). The operator had the most influence on outcome measures for [^{11}C]carfentanil and [^{11}C]MADAM. For [^{11}C]raclopride and [^{11}C]PiB operators had little influence on outcome measures (ICC $\geq$ 0.95).

Differences Between Manually and Automatically Produced Reference Regions

Differences in Reference Region Masks

We first compared the anatomical similarities between the automatically and manually delineated reference regions. For each tracer, automatic reference regions were consistently larger than manually derived reference regions (**Figure 3** and **Supplementary Figure S1**). In four [^{11}C]carfentanil studies at least one of the manually drawn reference regions was larger than the automatic occipital reference region. Magia-generated cerebellar reference regions were always larger than mean manual cerebellar reference regions. The automatically produced reference regions are naturally larger than the manually delineated ones because manual delineation requires mechanic work from highly trained individuals, thus providing a cost to the size of the regions.

Next, we determined whether the Magia-derived reference regions overlap with the manually drawn reference regions. The automatic occipital reference region for [^{11}C]carfentanil overlapped only 14% with a manual occipital reference region. The low overlap is explained by the substantial difference between the sizes of the manually and automatically generated occipital ROIs. Automatic cerebellar reference regions overlapped with manual reference regions by 55%, 59% and 61% for [^{11}C]raclopride, [^{11}C]MADAM and [^{11}C]PiB, respectively.

Differences in Reference Region SUV Distributions

The overlap between the manual and automatic radioactivity distributions was approximately 90% for all tracers (**Supplementary Figure S2**). All distributions were unimodal and highly symmetric for all tracers. The means of the distributions were practically equal (maximum difference of 0.07%). The standard deviations of the distributions differed

TABLE 2 | Operator-caused variation in basic characteristics derived from the reference region masks.

		Intra-class correlation coefficient		
Tracer	**Spatial overlap (%)**	**Reference region volume**	**Reference TAC AUC**	**Outcome measure**
[^{11}C]carfentanil	22	83	61	75
[^{11}C]raclopride	41	79	80	97
[^{11}C]MADAM	18	46	58	76
[^{11}C]PiB	14	74	95	95

TAC, time-activity curve; AUC, area under curve.

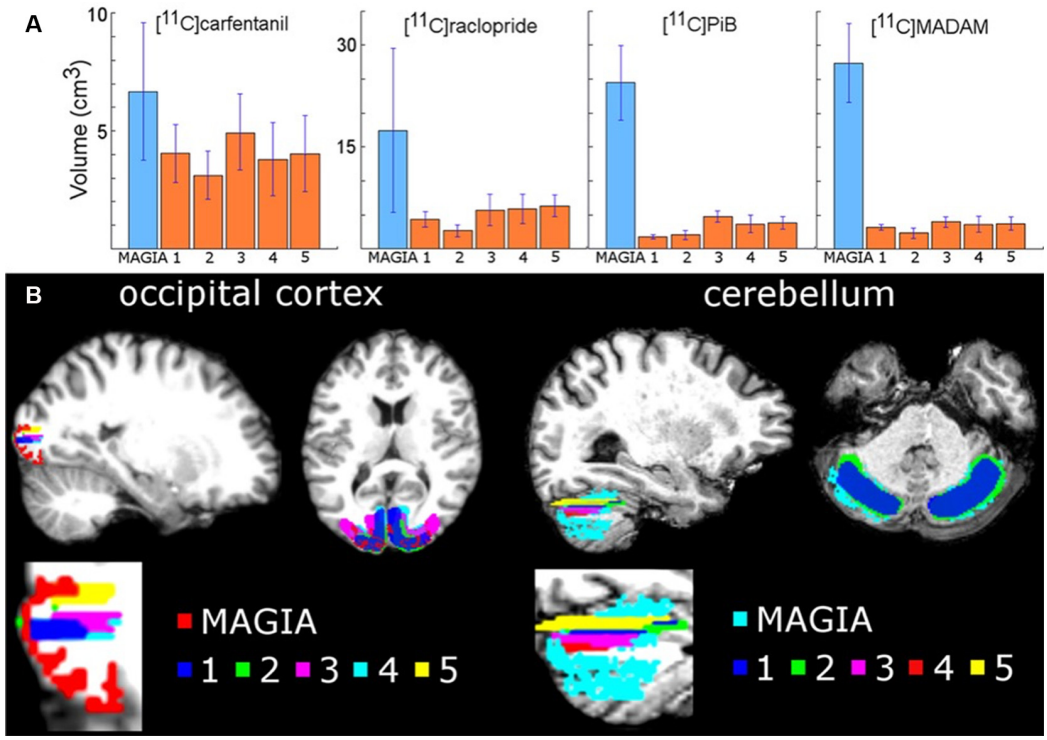


FIGURE 3 | (A) Mean volumes of Magia-generated reference regions compared to mean volumes of manually delineated reference regions. **(B)** Visual examples of Magia-generated and manual reference regions for one study.

by 14%, 11%, 12% and 18% for [^{11}C]carfentanil, [^{11}C]MADAM, [^{11}C]PIB and [^{11}C]raclopride, respectively. The modes of the automatically and manually derived distributions were 1.5 and 1.55 for [^{11}C]carfentanil, 1.95 and 2.05 for [^{11}C]MADAM, 1.65 and 1.70 for [^{11}C]PIB, and 1.35 and 1.35 for [^{11}C]raclopride. Thus, the maximum difference was less than 5%. The skewnesses of the Magia-derived and manually derived distributions were 1.2 and 0.9 for [^{11}C]carfentanil, 1.3 and 1.2 for [^{11}C]MADAM, 2.0 and 1.6 for [^{11}C]PIB, and 2.4 and 2.0 for [^{11}C]raclopride.

Differences in Reference Region Time-Activity Curves

The Magia-produced TACs were on average very similar to the average TACs calculated based on the manually delineated reference regions (**Figure 4**). The Pearson correlation coefficients were above 0.99 for all tracers. **Supplementary Figure S3** shows how the Magia-derived reference region time-activity curve AUCs compare against the manually obtained results. For [^{11}C]carfentanil, the between-study AUC means were practically identical (<1%). The Magia-produced reference regions had 2.6%, 1.1%, and 1.8% lower AUCs than the manual reference regions for [^{11}C]raclopride, [^{11}C]MADAM, and [^{11}C]PiB, respectively.

Differences in Outcome Measures

Pearson correlation coefficients between the mean of manual outcome measures and the Magia-derived outcome measures were 0.79, 0.98, 0.84, and 0.99 for [^{11}C]carfentanil, [^{11}C]raclopride, [^{11}C]MADAM, and [^{11}C]PiB, respectively. The outcome measures derived using automatic and manual methods are visualized in **Figure 5** in one representative ROI, the averaged outcome-measure-images are visualized in **Figure 6A** and the relative bias in the whole brain between them is visualized in **Figure 6B**. For [^{11}C]carfentanil and [^{11}C]PiB Magia produced basically no bias (less than 1%). For [^{11}C]MADAM, Magia produced up to 3–5% higher binding potential estimates in regions with high specific binding. In cortical regions with low specific binding, the bias was over 10%. For [^{11}C]raclopride, Magia produced approximately 4–5% higher binding potential estimates in striatum. In the thalamus, the bias was 8–10%. Elsewhere in the brain the bias varied considerably between 13–20%. For both [^{11}C]MADAM and [^{11}C]raclopride, the relative bias decreased significantly with increasing binding potential (**Figure 6C**).

DISCUSSION

We established that the automated Magia pipeline produces consistent estimates of radiotracer uptake for all the tested ligands, with very little or even no bias in the outcome measures. As expected, the manual delineation method suffered from significant operator-dependent variability, highlighting the importance of standardization of the process. The consistency coupled with significant gains in processing speed suggests that

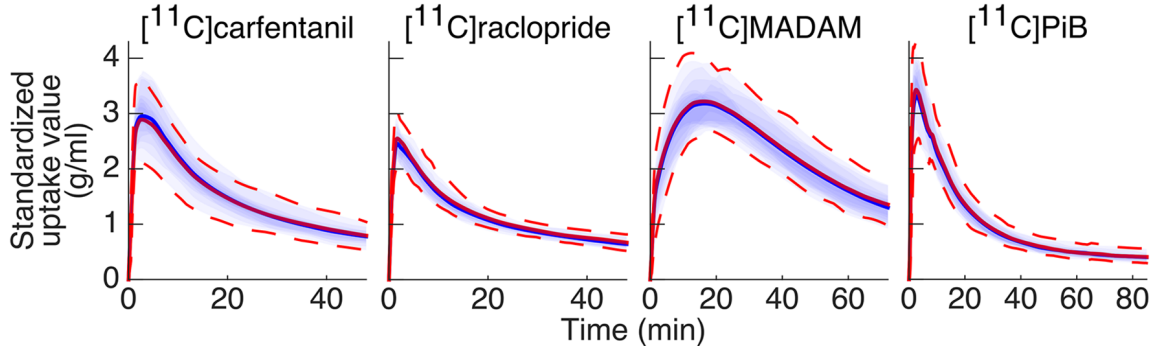


FIGURE 4 | Between-subject mean time-activity curves. Blue = Magia; red = manual.

Magia is well suited for automated analysis of brain-PET data for large-scale neuroimaging projects.

Outcome Measures Can Substantially Depend on Who Delineated the Reference Region

We estimated the amount of operator-dependent variation in outcome measures. Despite all operators drawing the ROIs using the same instructions (presented both verbally and as visual/written instructions available for reference while working) the ICC analyses show that for [^{11}C]carfentanil and [^{11}C]MADAM, the variation produced by different operators is significant, indicating that for these two tracers the subjective variation in manual ROI delineation (e.g., which transaxial slices to use, how to define ROI boundaries etc.) significantly influences the magnitude of binding potential estimates. Out of the tracers using the cerebellar cortex as the reference region, [^{11}C]MADAM had the lowest ICC with 76%. For [^{11}C]raclopride and [^{11}C]PiB the ICCs were over 95%, indicating that for these tracers manual delineation of reference regions may not be as crucial source of variation.

These differences between tracers likely reflect differences in the uniformity of the PET signal within the reference regions. If the reference region were perfectly homogenous with respect to the PET signal, it would not matter at all which voxels to choose. In reality, however, the PET signal is highly heterogenous. For example, the PET signal depends on the transaxial slices used. Presumably, these heterogeneities are substantial for [^{11}C]carfentanil and, to a lesser extent, for [^{11}C]MADAM, while the PET signal from cerebellar cortex using [^{11}C]raclopride and [^{11}C]PiB is significantly more homogenous. Indeed, the spatial overlap between the manually delineated reference region was higher for [^{11}C]carfentanil (22%) than for [^{11}C]PiB (14%), suggesting that even small differences in spatial overlap translate into substantial differences in binding potential for [^{11}C]carfentanil.

The influence of the operator on reference TAC AUCs was even larger. For all the tracers, the ICC of outcome measures was higher than the ICC for reference TAC AUCs. For example, while [^{11}C]raclopride BP_{ND} was barely influenced by the individual manually delineating the reference region, the ICC for [^{11}C]raclopride reference TAC AUC was only 80%, almost 20%-units less than for BP_{ND}. Thus, even the reference region TACs for [^{11}C]raclopride was not remarkably consistent between the operators, further highlighting the sensitivity of the delineation process despite detailed written and visual instructions. These results highlight the need for reference-region generation processes that do not suffer from subjectivity.

Reliability of Magia's Uptake Estimates

Importantly, Magia produced parameter estimates consistent with the *averaged* manual estimates (Pearson correlation coefficients >0.78 for all tracers). This suggests that: (i) even though individual operators yield different output metrics these are sampled from the same true parameter space; which (ii) is in turn accurately reflected by the Magia output. There was no systematic bias for [^{11}C]PiB SUVR and [^{11}C]carfentanil BP_{ND}. For [^{11}C]PiB, the difference between the manual and automatic SUVR estimates fluctuated randomly around zero. Because SUVR was used to quantify [^{11}C]PiB uptake, the random fluctuation was independent of the brain region. For [^{11}C]carfentanil, the random fluctuation was slightly greater in low-binding regions (but still within ±5%). In contrast to [^{11}C]PiB and [^{11}C]carfentanil, there were systematic differences between the manual and automatic binding potential estimates for [^{11}C]raclopride and [^{11}C]MADAM. For both tracers the bias decreased as a function of specific binding, and in high-binding regions (BP_{ND} > 1.5) the bias was less than 5%. Even if the bias increased sharply with decreasing binding potential, the problematic regions are not typically considered very interesting because of their poor signal-to-noise ratio.

The systematic bias for [^{11}C]MADAM and [^{11}C]raclopride is also reflected in the small differences in reference to tissue TACs. For the tracers using cerebellar reference region, Magia-derived reference tissue TACs had 2–3% lower AUCs. The peaks of the TACs were also slightly lower. For [^{11}C]PiB, the bias did not propagate into outcome measures because the SUV-ratio was calculated between 60 and 90 min when there was no bias in TACs. Because binding potential reflects the ratio

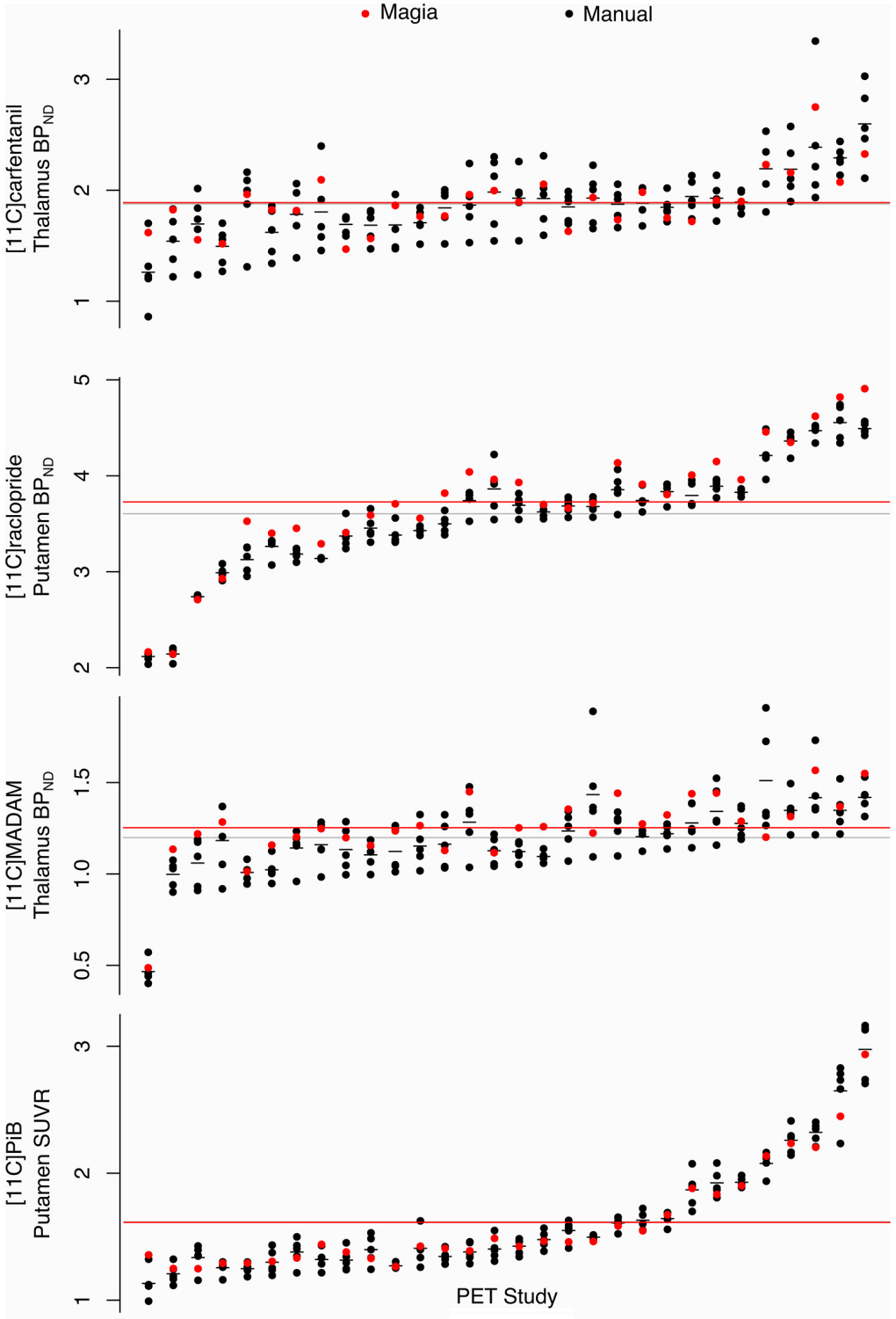


FIGURE 5 | Comparison of Magia-derived outcome measures against manually obtained ones.

between specific binding and unspecific binding (obtained from reference tissue), the reference TAC AUCs directly propagate into biases in binding potentials. Thus, these data indicate that Magia may produce slightly higher binding potential estimates than traditional methods at least if the cerebellar cortex is used as the reference region. These data do not,

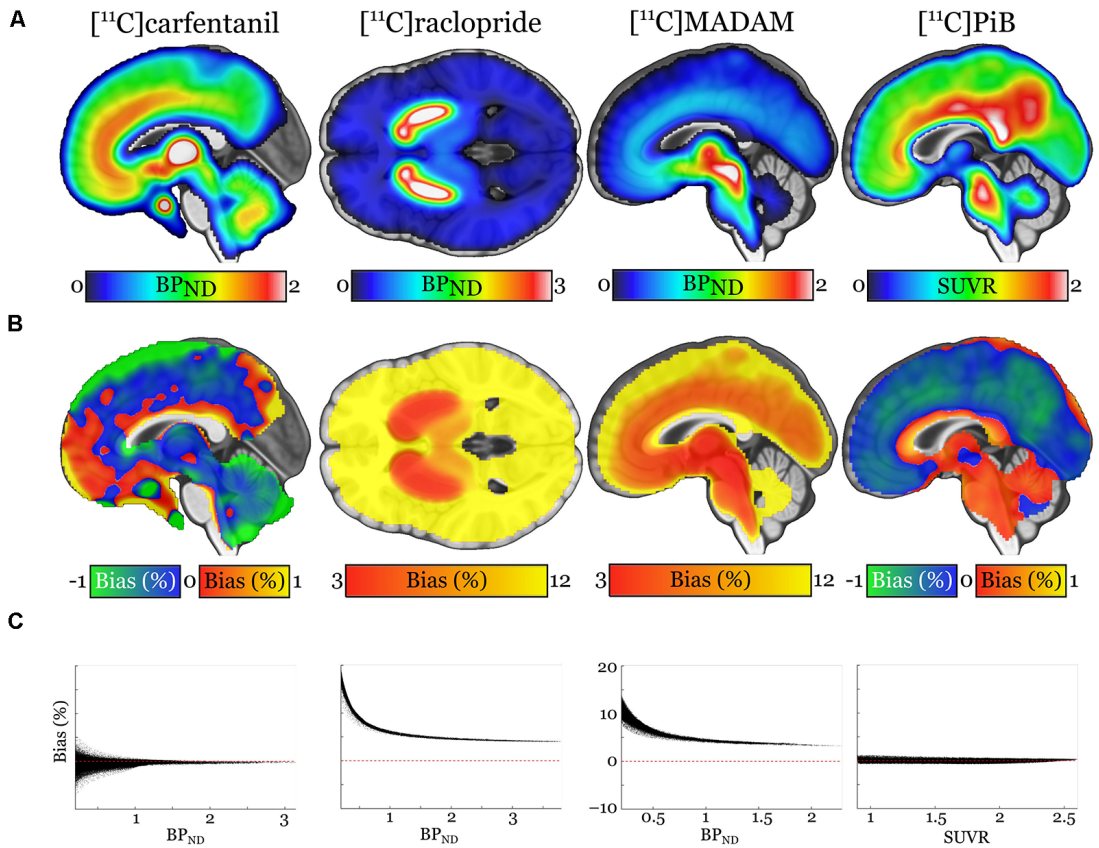


FIGURE 6 | (A) Visualization of the outcome measure distributions for each tracer. **(B)** Maps visualizing the relative biases of the Magia-derived outcome measures compared to the averages obtained by manual reference region delineation. The manual method is here presented as the ground truth, because the manual outcome for each scan is an average over five individual estimates, while the Magia result relies on a single estimate. **(C)** Associations between the outcome measure magnitude and relative bias.

however, imply that the bias should be regarded as error: in fact, Magia produces significantly larger reference regions, and consequently the reference tissue TACs are less noisy. This is desirable because the noise in the input function influences model fitting. However, the bias also means that Magia-produced estimates should not be combined with estimates produced with other methods.

Functional Homogeneity of the Reference Regions

We tested whether the assumption of homogenous binding within the reference regions holds for both automatic and manual reference regions. A homogenous source region should produce unimodal and approximately symmetric radioactivity distributions 21. Between-study average distributions were unimodal and symmetric for all tracers for both the manual and automatic methods. The distribution means were practically identical, but the modes were 1–2% higher for Magia. The manual distributions were slightly wider (the standard deviations were approximately 15% larger) because Magia cuts the distribution tails. The manual distributions were also slightly less skewed. Because averaging distributions tends to make them more Gaussian, this difference probably arises from the fact that the manual distributions that were used in the comparison were defined as an average over the five distributions delineated by the independent operators. The distribution overlaps were approximately 90% for all tracers. In sum, these results show that the Magia-generated reference region radioactivity distributions satisfy the requirement of functional uniformity.

Reference Tissue Time-Activity Curves

Despite their topographical differences, the automatically and manually produced reference regions yielded very similar TACs. For all tracers, the Pearson correlation coefficient between average automatic and manual reference tissue TACs was above 0.99. The TAC shapes were thus in excellent agreement. For [11C]carfentanil, also the AUC of reference region TACs were highly similar. The AUCs of cerebellar TACs were 2–3% lower for Magia, indicating that the cerebellar automatic TACs were slightly negatively biased compared to their manual counterparts. The source of this difference unknown but it could result e.g., from heterogenous nonspecific binding

within cerebellar cortex or from spill-in or spill-over effects. Whatever explains the small difference, these data do not directly indicate which method produced more realistic TACs. However, because the Magia-generated cerebellar reference regions were without exception substantially larger than their manual counterparts, the TACs of Magia presumably have a higher signal-to-noise ratio, suggesting that the Magia-derived metrics may compare favorably against the manually obtained metrics.

Solving Time Constraints in the Processing of PET Data

On average, drawing the reference region for a single subject took around 15 min, and without any automatization the modeling and spatial processing of the images standard tools (e.g., PMOD or Turku PET Centre modeling software) take on average 45 min. In contrast, it takes less than 5 min to set Magia running for a single study. Although the time advantage—roughly an hour per study—gained from automatization is still modest in small-scale studies (e.g., three 8-h working days for a study with 24 subjects) the effect scales up quickly, and manual modeling of a database of just 400 studies would take already 50 days. This is a significant investment of human resources, in particular, if the analyses have to be redone later with, for example, different modeling parameters requiring repeating of at least some parts of the process.

Comparison of Magia to Existing Tools

Several tools already exist for processing brain PET data. MIAKAT (Gunn et al., 2016) is another MATLAB-based tool that combines preprocessing and kinetic modeling. Compared to Magia, MIAKAT is missing support for the two-tissue compartmental model, SUV-ratio, as well as FUR-analyses. APPIAN (Funck et al., 2018) is another recent development that, unlike Magia, includes partial volume correction. However, APPIAN lacks motion-correction and also supports fewer kinetic models than Magia, and like MIAKAT, APPIAN also uses neuroanatomical atlases for ROI definition. Both of these tools, as well as all the other existing tools, are restricted in the sense that they require both MRI and PET data. Magia, in contrast, can also process brain PET data without MRI if a tracer-specific template is available. Magia also comes with default modeling options for several tracers. Accordingly, Magia is currently the most flexible open-source tool available for automated processing of brain PET data.

Limitations

SMagia is currently fully automatic only for tracers for which a reference region exists. However, even for blood-based inputs, Magia requires minimal user intervention, as Magia can read in the input function from the appropriate location. Magia was originally developed with the assumption that a T1-weighted MR image is available for each subject (for reference region delineation and spatial normalization). Because this assumption limited the applicability of the approach for reanalysis of some historical data, Magia can now also use neuroanatomical atlases for ROI definition and tracer-specific radioactivity templates for spatial normalization. Templates for each of the tracers used in this manuscript are available in https://github.com/tkkarjal/magia/tree/master/templates, and Magia can use whatever templates the user may have available. Thus, the availability of MRI is not necessary, but it is strongly recommended because most of the testing has been done with MRI-based processing, and because the ROIs as well as reference regions can then be generated in the native space. The drawback of FreeSurfer-based ROI-generation is that it is relatively slow ($\sim$ 10 h). Partial volume correction is not currently implemented in Magia, yet this feature will be added in future releases. Finally, Magia processes the studies independently of each other. Within-subject designs would benefit from consideration of multiple images per participant, but this is currently not possible.

CONCLUSION

Magia is a standardized and fully automatic analysis pipeline for processing brain PET data. By standardizing the reference region generation process, Magia eliminates operator-dependency in producing outcome-measures. For [^{11}C]carfentanil that uses the occipital cortex as the reference region, the reduced variance comes with no cost for bias in BP_{ND}. The SUVR estimates were also unbiased for [^{11}C]PiB. [^{11}C]raclopride and [^{11}C]MADAM BP_{ND} was slightly overestimated. However, compared to the variance resulting from operator dependency, this bias was negligible and may actually favor Magia. In any case, bias is meaningless in most population-level analyses. Magia enables standardized analysis of brain PET data, facilitating shift towards larger samples and more convenient data sharing across research sites.

DATA AVAILABILITY STATEMENT

The datasets generated for this study will not be made publicly available. The current data-sharing guidelines prohibit publishing the data. The Magia-pipeline itself, however, is freely available from https://github.com/tkkarjal/magia.

ETHICS STATEMENT

The study was conducted as a part of a register-based study on brain imaging at Turku PET Centre. Per applicable legislation in Finland, fully anonymized medical register data (including PET and MRI scans) can be analyzed in the context of a register study without obtaining an active informed consent from the individuals included in the register, if information identifying the individuals is not obtained. The study protocol was approved by Turku University Hospital Research Board and the legislative team.

AUTHOR CONTRIBUTIONS

TKar developed Magia, analyzed the data, and wrote the manuscript. JT contributed to the development of Magia and edited the manuscript. SS manually delineated reference

regions, contributed to data analysis and edited the manuscript. TKan contributed to data analysis and edited the manuscript. MB contributed to late development of Magia and edited the manuscript. LT contributed to the early development of Magia and edited the manuscript. JHir planned statistical analyses and edited the manuscript. JHie and JR provided data and edited the manuscript. LN provided data, contributed to the development of Magia and edited the manuscript.

FUNDING

This work was supported by the Academy of Finland grants #265915 and #294897 to LN. Sigrid Juselius Foundation separate grants to LN and JR. Päivikki and Sakari Sohlberg Foundation to TKar. Finnish Cultural Foundation Varsinais-Suomi Regional Fund to TKar. State Research Funding (VTR) for Turku University Hospital to TKar. State Research Funding (VTR) for Turku University Hospital to JR.

ACKNOWLEDGMENTS

This manuscript includes work in-part from a Thesis "Magia: Robust Automated Modeling And Image Processing Platform For Pet Neuroinformatics" by Santavirta (Santavirta, 2018). The manuscript has also been released as a preprint at biorXiv (Karjalainen et al., 2019).

SUPPLEMENTARY MATERIAL

The Supplementary Material for this article can be found online at: https://www.frontiersin.org/articles/10.3389/fninf.2020.00003/full#supplementary-material.

REFERENCES

Ashburner, J., and Friston, K. J. (2000). Voxel-based morphometry—the methods. *Neuroimage* 11, 805–821. doi: 10.1006/nimg.2000.0582

Button, K. S., Ioannidis, J. P. A., Mokrysz, C., Nosek, B. A., Flint, J., Robinson, E. S. J., et al. (2013). Power failure: why small sample size undermines the reliability of neuroscience. *Nat. Rev. Neurosci.* 14, 365–376. doi: 10.1038/nrn3475

Chen, Y. J., and Nasrallah, I. M. (2017). Brain amyloid PET interpretation approaches: from visual assessment in the clinic to quantitative pharmacokinetic modeling. *Clin. Transl. Imaging* 5, 561–573. doi: 10.1007/s40336-017-0257-4

Cremers, H. R., Wager, T. D., and Yarkoni, T. (2017). The relation between statistical power and inference in fMRI. *PLoS One* 12:e0184923. doi: 10.1371/journal.pone.0184923

Eickhoff, S. B., Stephan, K. E., Mohlberg, H., Grefkes, C., Fink, G. R., and Amunts, K. (2005). A new SPM toolbox for combining probabilistic cytoarchitectonic maps and functional imaging data. *NeuroImage* 25, 1325–1335. doi: 10.1016/j.neuroimage.2004.12.034

Endres, C. J., Bencherif, B., Hilton, J., Madar, I., and Frost, J. J. (2003). Quantification of brain mu-opioid receptors with [^{11}C]carfentanil: reference-tissue methods. *Nucl. Med. Biol.* 30, 177–186. doi: 10.1016/s0969-8051(02)00411-0

Esteban, O., Markiewicz, C. J., Blair, R. W., Moodie, C. A., Isik, A. I., Erramuzpe, A., et al. (2019). fMRIPrep: a robust preprocessing pipeline for functional MRI. *Nat. Methods* 16, 111–116. doi: 10.1038/s41592-018-0235-4

Fischl, B., Salat, D. H., Busa, E., Albert, M., Dieterich, M., Haselgrove, C., et al. (2002). Whole brain segmentation: automated labeling of neuroanatomical structures in the human brain. *Neuron* 33, 341–355. doi: 10.1016/s0896-6273(02)00569-x

Funck, T., Larcher, K., Toussaint, P.-J., Evans, A. C., and Thiel, A. (2018). APPIAN: automated pipeline for PET image analysis. *Front. Neuroinform.* 12:64. doi: 10.3389/fninf.2018.00064

Gunn, R., Coello, C., and Searle, G. (2016). Molecular imaging and kinetic analysis toolbox (MIAKAT)—a quantitative software package for the analysis of PET neuroimaging data. *J. Nucl. Med.* 57, 1928–1928.

Gunn, R. N., Lammertsma, A. A., Hume, S. P., and Cunningham, V. J. (1997). Parametric imaging of ligand-receptor binding in PET using a simplified reference region model. *NeuroImage* 6, 279–287. doi: 10.1006/nimg.1997.0303

Karjalainen, T., Santavirta, S., Kantonen, T., Tuisku, J., Tuominen, L., Hirvonen, J., et al. (2019). Magia: robust automated modeling and image processing toolbox for PET neuroinformatics. *bioRxiv* [Preprint]. doi: 10.1101/604835

Logan, J. (2000). Graphical analysis of PET data applied to reversible and irreversible tracers. *Nucl. Med. Biol.* 27, 661–670. doi: 10.1016/s0969-8051(00)00137-2

Lopresti, B. J., Klunk, W. E., Mathis, C. A., Hoge, J. A., Ziolko, S. K., Lu, X., et al. (2005). Simplified quantification of Pittsburgh Compound B amyloid imaging PET studies: a comparative analysis. *J. Nucl. Med.* 46, 1959–1972.

Lundberg, J., Odano, I., Olsson, H., Halldin, C., and Farde, L. (2005). Quantification of ^{11}C-MADAM binding to the serotonin transporter in the human brain. *J. Nucl. Med.* 46, 1505–1515.

Nakagawa, S., Johnson, P. C. D., and Schielzeth, H. (2017). The coefficient of determination R^2 and intra-class correlation coefficient from generalized linear mixed-effects models revisited and expanded. *J. R. Soc. Interface* 14:20170213. doi: 10.1098/rsif.2017.0213

Patlak, C. S., Blasberg, R. G., and Fenstermacher, J. D. (1983). Graphical evaluation of blood-to-brain transfer constants from multiple-time uptake data. *J. Cereb. Blood Flow Metab.* 3, 1–7. doi: 10.1038/jcbfm.1983.1

Poldrack, R. A., and Yarkoni, T. (2016). From brain maps to cognitive ontologies: informatics and the search for mental structure. *Annu. Rev. Psychol.* 67, 587–612. doi: 10.1146/annurev-psych-122414-033729

Santavirta, S. (2018). *Magia: Robust Automated Modeling and Image Processing Platform for PET Neuroinformatics.* Turku: University of Turku.

Schain, M., Varnäs, K., Cselényi, Z., Halldin, C., Farde, L., and Varrone, A. (2014). Evaluation of two automated methods for PET region of interest analysis. *Neuroinformatics* 12, 551–562. doi: 10.1007/s12021-014-9233-6

Simmons, J. P., Nelson, L. D., and Simonsohn, U. (2011). False-positive psychology: undisclosed flexibility in data collection and analysis allows presenting anything as significant. *Psychol. Sci.* 22, 1359–1366. doi: 10.1177/0956797611417632

Teymurazyan, A., Riauka, T., Jans, H. S., and Robinson, D. (2013). Properties of noise in positron emission tomography images reconstructed with filtered-backprojection and row-action maximum likelihood algorithm. *J. Digit. Imaging* 26, 447–456. doi: 10.1007/s10278-012-9511-5

Thie, J. A. (1995). Clarification of a fractional uptake concept. *J. Nucl. Med.* 36, 711–712.

Tuszynski, T., Rullmann, M., Luthardt, J., Butzke, D., Tiepolt, S., Gertz, H.-J., et al. (2016). Evaluation of software tools for automated identification of neuroanatomical structures in quantitative β-amyloid PET imaging to diagnose Alzheimer's disease. *Eur. J. Nucl. Med. Mol. Imaging* 43, 1077–1087. doi: 10.1007/s00259-015-3300-6

Tzourio-Mazoyer, N., Landeau, B., Papathanassiou, D., Crivello, F., Etard, O., and Delcroix, N. (2002). Automated anatomical labeling of activations in SPM using a macroscopic anatomical parcellation of the MNI MRI single-subject brain. *NeuroImage* 15, 273–289. doi: 10.1006/nimg.2001.0978

White, D. R. R., Houston, A. S., Sampson, W. F. D., and Wilkins, G. P. (1999). Intra- and interoperator variations in region-of-interest drawing and their effect on the measurement of glomerular filtration rates. *Clin. Nucl. Med.* 24, 177–181. doi: 10.1097/00003072-199903000-00008

Yarkoni, T. (2009). Big correlations in little studies: inflated fMRI correlations reflect low statistical power—commentary on Vul et al. (2009). *Perspectives on Psychological Science* 4, 294–298. doi: 10.1111/j.1745-6924.2009.01127.x

Yarkoni, T., Poldrack, R. A., Nichols, T. E., Van Essen, D. C., and Wager, T. D. (2011). Large-scale automated synthesis of human functional neuroimaging data. *Nat. Methods* 8, 665–670. doi: 10.1038/nmeth.1635

Yasuno, F., Hasnine, A. H., Suhara, T., Ichimiya, T., Sudo, Y., Inoue, M., et al. (2002). Template-based method for multiple volumes of interest of human brain PET images. *NeuroImage* 16, 577–586. doi: 10.1006/nimg.2002.1120

Conflict of Interest: The authors declare that the research was conducted in the absence of any commercial or financial relationships that could be construed as a potential conflict of interest.

Copyright © 2020 Karjalainen, Tuisku, Santavirta, Kantonen, Bucci, Tuominen, Hirvonen, Hietala, Rinne and Nummenmaa. This is an open-access article distributed under the terms of the Creative Commons Attribution License (CC BY). The use, distribution or reproduction in other forums is permitted, provided the original author(s) and the copyright owner(s) are credited and that the original publication in this journal is cited, in accordance with accepted academic practice. No use, distribution or reproduction is permitted which does not comply with these terms.

frontiers in Neuroinformatics

ORIGINAL RESEARCH
published: 14 February 2020
doi: 10.3389/fninf.2020.00006

Prediction of Pilot's Reaction Time Based on EEG Signals

Bartosz Binias[1]*, *Dariusz Myszor*[2], *Henryk Palus*[1] and *Krzysztof A. Cyran*[3]

[1] Department of Data Mining and Engineering, Faculty of Automatic Control, Electronics and Computer Science, Silesian University of Technology, Gliwice, Poland, [2] Department of Algorithmics and Software, Faculty of Automatic Control, Electronics and Computer Science, Silesian University of Technology, Gliwice, Poland, [3] Department of Computer Vision Graphics and Digital Systems, Faculty of Automatic Control, Electronics and Computer Science, Silesian University of Technology, Gliwice, Poland

The main hypothesis of this work is that the time of delay in reaction to an unexpected event can be predicted on the basis of the brain activity recorded prior to that event. Such mental activity can be represented by electroencephalographic data. To test this hypothesis, we conducted a novel experiment involving 19 participants that took part in a 2-h long session of simulated aircraft flights. An EEG signal processing pipeline is proposed that consists of signal preprocessing, extracting bandpass features, and using regression to predict the reaction times. The prediction algorithms that are used in this study are the Least Absolute Shrinkage Operator and its Least Angle Regression modification, as well as Kernel Ridge and Radial Basis Support Vector Machine regression. The average Mean Absolute Error obtained across the 19 subjects was 114 ms. The present study demonstrates, for the first time, that it is possible to predict reaction times on the basis of EEG data. The presented solution can serve as a foundation for a system that can, in the future, increase the safety of air traffic.

Keywords: aircraft control human factors, cognitive workload, data mining, electroencephalography, reaction time, safety, regression, prediction

OPEN ACCESS

Edited by:
Ludovico Minati,
Tokyo Institute of Technology, Japan

Reviewed by:
Elisa Visani,
Carlo Besta Neurological Institute (IRCCS), Italy
James Andrew O'Sullivan,
Columbia University, United States

***Correspondence:**
Bartosz Binias
bartbinias@gmail.com

Received: *17 June 2019*
Accepted: *24 January 2020*
Published: *14 February 2020*

Citation:
Binias B, Myszor D, Palus H and Cyran KA (2020) Prediction of Pilot's Reaction Time Based on EEG Signals. Front. Neuroinform. 14:6. doi: 10.3389/fninf.2020.00006

1. INTRODUCTION

Safety is an important consideration in the modern airline industry. Although many factors have an influence on the proper execution of flight processes, performance of the pilot is one of the most crucial factors. In particular, multiple sources point out that fatigue has a significant adverse impact on pilot performance (Lee and Kim, 2018; Bushmaker et al., 2019). The International Civil Aviation Organization (2016) defines fatigue as:

A physiological state of reduced mental or physical performance capability resulting from sleep loss or extended wakefulness, circadian phase, or workload (mental and/or physical activity) that can impair a crew member's alertness and ability to safely operate an aircraft or perform safety related duties.

Results of a survey published in 2002 demonstrate that fatigue is a significant issue among pilots, and may be responsible for 4–8% of aviation mishaps (Caldwell and Gilreath, 2002). Moreover, a survey conducted in a group of short-haul pilots points out that over 75% of pilots claimed that they have experienced significant fatigue (Jackson and Earl, 2006). In addition, over 70% of corporate pilots claimed that they have fallen into micro-sleep during various phases of the flight (Caldwell, 2005). Such micro-sleep states have been related to a reduced ability to respond to external stimuli (Ogilvie and Simons, 1992), as well as, degradation of performance on cognitive tasks (Belyavin and Wright, 1987).

Another large-scale study blames errors of the cockpit crew on 73% of the 456 aircraft crashes between the years 1959 and 1996 (National Research Council, 1998). Importantly, this trend does

not seem to decrease over time, as the same source suggests that 72% out of the 145 accidents between the years 1987 and 1996 can be attributed to the cockpit crew.

In 2003, the National Transportation Safety Board estimated that fatigue contributes to around 20–30% of transportation accidents (i.e., aircraft, marine, railway, road). Given that ∼70% of commercial aircraft accidents can be attributed to human errors, fatigue is thought to contribute to 15–20% of total aircraft accidents (Akerstedt et al., 2003).

Recent research study (Bennett, 2019) demonstrate that, on average, 7.3% of pilots who participated in this study and completed the inbound Top-of-Climb-Top-of-Descent scale were found to be either extremely tired or completely exhausted. In addition, 9.3% of pilots who completed the inbound Top-of-Descent-On-Blocks scale also claimed to be either extremely tired or completely exhausted. Of note, the Top-of-Climb-Top-of-Descent and Top-of-Descent-On-Blocks are phases of a flight. According to Bennet, these numbers could be even higher because there is a rule that pilots should not operate when fatigued; thus some pilots may under-report their fatigue level to avoid penalty. Exhaustion has been found to increase with the time of flight and Powell et al. estimated a linear relationship between tiredness and length of duty (Powell et al., 2007). It is worth mentioning that problems related to the workload and fatigue among pilots are important topics that have sparked recent changes in laws. For example, the European Aviation Safety Agency introduced new Flight Time Limitations (European Union Regulation 83/2014).

Considering the substantial impact of human factors on flight safety, there has been a rise of ideas and support for so-called, pilotless aircraft, in recent years (Ross, 2011; Stevenson, 2017). An approach that is most commonly postulated in this area is the idea of ground-based human or artificial intelligence support for a single pilot in an aircraft. However, a reduction in a number of on-board pilots might not necessarily be the best option, because the redundancy and support that two pilots provide to each other may be extremely valuable. Therefore, instead of removing pilots from cockpits, a more promising solution may be to support pilots with systems that can increase their capabilities and improve their performance during flights. The main hypothesis that will be tested in this work is that the electroencephalographic (EEG) signals recorded from a pilot's scalp during flight can be used in such performance-enhancing systems. In particular, we will test for associations between mental activity of pilots (as measured by EEG) and their ability to react quickly and make correct decisions in face of unexpected events. In this study, we also propose and test a basic pipeline that can be used for processing such signals and extracting information that can be used to predict a pilot's delay in response to unexpected events.

Use of EEG data in the context of prediction is most commonly associated with a seizure detection (Varsavsky et al., 2016). In a prospective study of antiepileptic drug withdrawal, a step-wise logistic regression analysis method was employed to predict an outcome of either antiepileptic drug withdrawal or seizure relapse (Overweg et al., 1987). However, an evaluation of the multivariate model showed that none of the variables that were related to the EEG signal contributed to the final score. A recent study presents a use of Deep Convolutional Neural Networks (CNN) for the automated detection and diagnosis of seizures using EEG signals (Acharya et al., 2018). Although CNN-based models are characterized by a high level of complexity, the additional preprocessing used in the work was limited to data standardization and normalization, and is thus fairly basic. Additionally, the aforementioned problem can be considered as more of a classification problem than a regression. EEG has already been utilized to predict a single-trial reaction time in a hand motor task (Meinel et al., 2015). The study by Meinel et al. used EEG band power features that were enhanced by a spatial filtering method called Source Power Comodulation. Alpha band power was found to comodulate with reaction time measured during an isometric hand force control task, which allowed for an average correlation of 0.19, with the best feature explaining up to 17% of the variation between single trials. Multiple studies have been performed to examine the impact of mental activity—as measured by EEG—on traffic safety. Most of these studies have been focused on car transport and driving. For instance, Deep Belief Networks (DBN) have been evaluated for their potential use in feature extraction and dimension reduction in predicting the cognitive state of drivers (Hajinoroozi et al., 2015). These studies show that DBN can predict around 85% of the variation in cognitive state. A subject-transfer framework for detecting drowsiness during simulated driving task based on EEG was also recently developed (Wei et al., 2018). In that study, response time was measured from the onset of a lane deviation to the onset of the response, which served as a behavioral assessment of drowsiness during the lane-keeping task. One interesting study associates periods of mind wandering during 20-min driving sessions with increased power in the alpha band of the EEG recording, as well as, a reduction in the magnitude of the P3a component of the event related potential in response to an auditory probe (Baldwin et al., 2017). Thus, these results suggest that, mind wandering can be detected on the basis of underlying brain physiology which has an impact on driving performance and the associated change in the driver's attentional state. Prior studies have documented changes in EEG activity that are present during the transition from normal drive to high mental workload and ultimately mental fatigue and drowsiness (Borghini et al., 2014). A review of the literature suggests that a high mental workload can be associated with increased EEG power in the theta band and a decreased power in alpha band. Additionally, increased EEG power in the theta, as well as, delta and alpha bands can be observed during the transition between mental workload and mental fatigue. Relatively fewer studies have explored the application of EEG data for the purpose of enhancing aircraft operations (Borghini et al., 2014). A recent study presented the idea of utilizing EEG signals in systems designed to monitor and enhance the performance of aircraft pilots (Binias et al., 2018). This work focuses on the problem of discriminating between states of brain activity related to idle but focused anticipation of a visual cue and the response to this cue. In this study, almost 78% average classification accuracy was obtained. This study can be regarded as a preamble to the work presented in the present article. Accordingly, to the best of our knowledge, no articles published to-date address the

problem of predicting the delay in response time based on EEG activity. Therefore, the ideas presented in this article can be considered to be innovative and novel. In addition, the present study used simulators of the Virtual Flight Laboratory; thus, the experimental design used in this study is air-craft oriented. This design is valuable, as it targets a very important, yet not sufficiently explored field.

The remainder of this article is organized as follows. First, we provide a description of the experimental set-up and experimental protocol in section 2.1. Then, a steps of the EEG data processing pipeline proposed in this research are described in detail in section 2.3. Section 2.3.1 provides an overview of the tuning procedure used to find the optimal settings of prediction algorithms, and contains details about the algorithm validation procedure. The obtained results are presented in section 3. A general discussion about the results and the implemented approach can be found in section 4. **Appendix A** presents a brief theoretical background to all machine learning and statistical methods used in this work.

2. MATERIALS AND METHODS

2.1. Study Population and Experiment Description

The goal of this experiment was to obtain the brain's bioelectrical activity prior to the occurrence of a visual cue. Additionally, we measured the time of delay in the participant's reaction time to that visual cue. To this end, we performed a series of experimental sessions. Each session consisted of a 2-h long simulated flight with activated auto pilot. Participants in this experiment were instructed to stay focused and maintain awareness while waiting for the appearance of the visual cue. Once the cue was observed, participants were instructed to press the button as quickly as possible. The location of the button was chosen to minimize the time required to react to the visual cue by restraining any additional movements of the pilots body, besides their fingers. Additionally, participants were asked to behave as pilots during regular flight, i.e., to observe cockpit instruments and scan the surroundings of the plane. The experiments took place in the Flight Navigational Procedure Training II class simulator and portrayed a *Cessna 172RG* airplane. To maintain consistency between successive experimental sessions, the simulated flight was on the route between Frankfurt and London. The same section of the flight was presented to each participant during the experiment. Flights took place at an average altitude of 6000 ft., and to simulate flight with auto pilot activated, the take off and landing were removed from the registered material. Moreover, the entire flight that was presented to participants took place over land. Importantly, sounds of engines were also generated in the cockpit.

Visual cues were displayed randomly with a normal distribution characterized by mean $\mu = 2.5$ min, standard deviation $\sigma = 1$ min. This variance was introduced to prevent habituation of the human brain to regular patterns. The visual cue was represented by a solid gray-colored box that overlapped 75% of the main simulator screen that was responsible for displaying the terrain. Participants were between the ages of 20 and 65 years. Before start of the session, participants were asked to complete a survey regarding the level of their fatigue. All participants claimed that they were well rested before the session and all provided consent to utilize the outcomes obtained of the experiment for scientific research. During the experimentation phase, 19 participants (3 females and 16 males) were examined. Every experimental session started at the same time of the day—around 12:00 (noon)—to minimize the potential effects of external factors on the experiment.

This experiment was approved by the The Jerzy Kukuczka Academy of Physical Education in Katowice Bioethical committee (protocol number 2/1/2017).

2.2. Hardware Description

This study analyzed EEG signals to examine bioelectrical activity of participants' brains during the experiments. EEG signals were recorded using the Emotiv EPOC+ Headset. This device provides a useful bandwidth in the range of 0.16–43 Hz, and is sequentially sampled at a frequency of 128 Hz. The resolution of the data is on the level of 14 bit ($1LSB = 0.51\ \mu V$). To avoid interference of the electrical network, a real-time, digital 5-th order Sinc filter and notch filters at 50 and 60 Hz were built into *EPOC+* (EMOTIV Systems, 2014). The placement of EPOC+ electrodes follows the $10 - 10$ configuration. Available channels are: AF3, F7, F3, FC5, T7, P7, O1, O2, P8, T8, FC6, F4, F8, AF4. with references in the P3/P4 locations. Emotiv headsets use active electrode placed in P3 location as an absolute voltage reference i.e., Common Mode Sense. The passive electrode located in P4 position serves as a feedback cancellation system to float the reference level on the common mode body potential i.e., Driven Right Leg (EMOTIV Systems, 2014). The position of electrodes is presented in **Figure 1** (Koessler et al., 2009).

Emotiv EPOC+ is a relatively inexpensive EEG recording device that was designed for scientific research and other non-medical applications. Due to it's many advantages, EPOC+ is regularly used in Brain-Computer Interface (BCI) and similar solutions (Alrajhi et al., 2017; Setiono et al., 2018; Borisov et al., 2019). EPOC+ has also proven to be useful in a study concerning the classification of brain activity of pilots (Binias et al., 2018). A study evaluating EPOC+ in tasks that measured alpha brain activity and the Visual Steady-State Response showed that EPOC+ is capable of performing at levels comparable to research-grade EEG systems (Grummett et al., 2015). Due to setup difficulties, however, the authors of that study were unable to provide evidence to support the use of Emotiv in paradigms that rely on time-locked events. However, some reports of Emotiv EEG systems use in such tasks are available (Tahmasebzadeh et al., 2013).

2.3. Data Processing and Analysis

2.3.1. Prediction of Response Delay

First, regression models were created to predict the delay in participant's response to the visual cue. The response delay is calculated as the offset between the moment in time when the cue was presented to the subject and the moment when subject's reaction to that cue was recorded. The prediction was made using

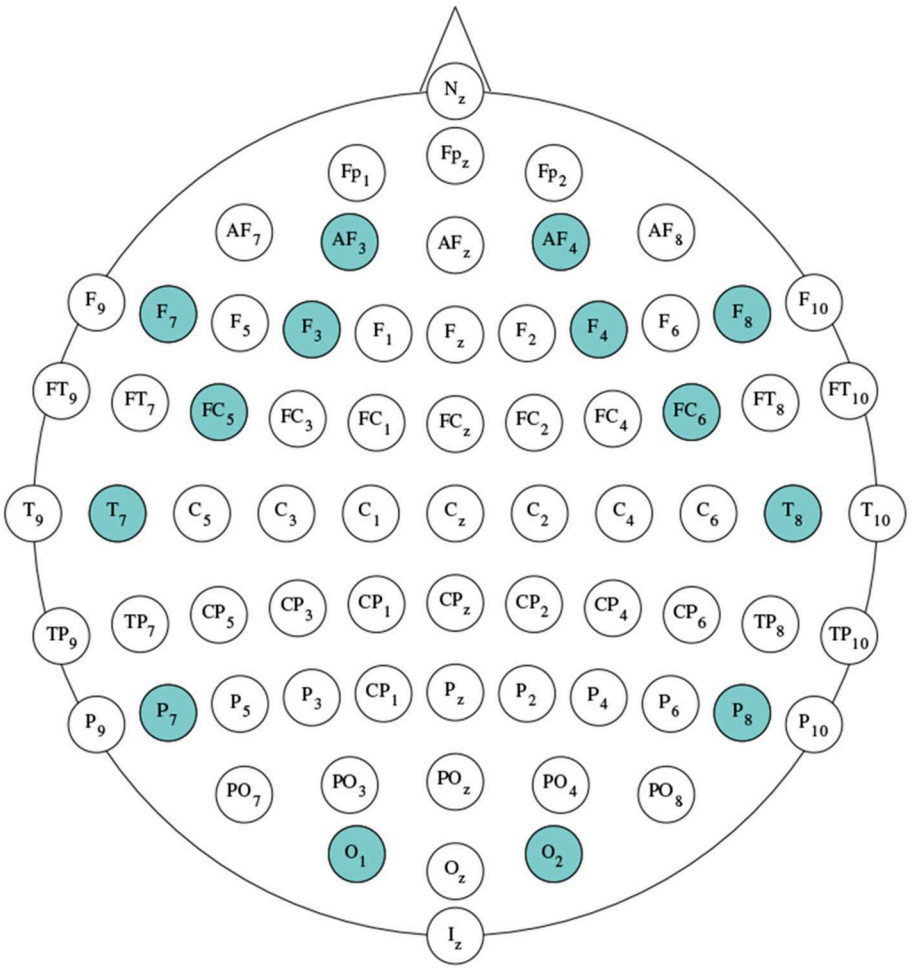


FIGURE 1 | Positions of electrodes in the standard 10-10 electrode montage system. Highlighted locations reflect positioning of the Emotiv Epoc+ electrode with respect to 10-10 system-based on Koessler et al. (2009).

only the segments of the recorded multichannel EEG signal that immediately preceded the onset of the cue. Such defined EEG segments will be referred to as the Temporal Segment of Interest (TSI). In particular, the length of the TSI is defined as the number of samples that will be considered when predicting the length of used time window. An illustrative representation of the concept of the TSI in the EEG signal and other defined names is presented in **Figure 2**.

Analysis of the raw, unprocessed signals in the TSI would not prove to be effective. Therefore, such data has to be appropriately preprocessed. First, the raw data were carefully examined to evaluate the significance of artifacts present in the recordings. A detailed description of this phase can be found in section 2.3.2. Next, the raw data from the TSI were divided into multiple signals on the basis of their frequency range, as described in section 2.3.3. From these signals, features were subsequently extracted according to procedure described in section 2.3.4. These features were used to train machine learning algorithms to predict the measured delay in a given subject's response to the occurrence of the visual cue. In the proposed approach, signal from each electrode is analyzed individually. A general flow of the EEG processing pipeline is presented in **Figure 3**.

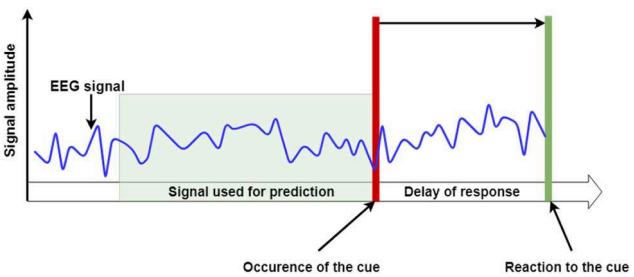


FIGURE 2 | An illustrative representation of the EEG signal's TSI. The delay of response is calculated as the offset between the moment in time when the cue was presented to the subject and the moment when the subject's reaction to that cue was recorded. The prediction was made using only the segments of recorded EEG signal that immediately preceded the cue onset- or the "Temporal Segment of Interest" (TSI).

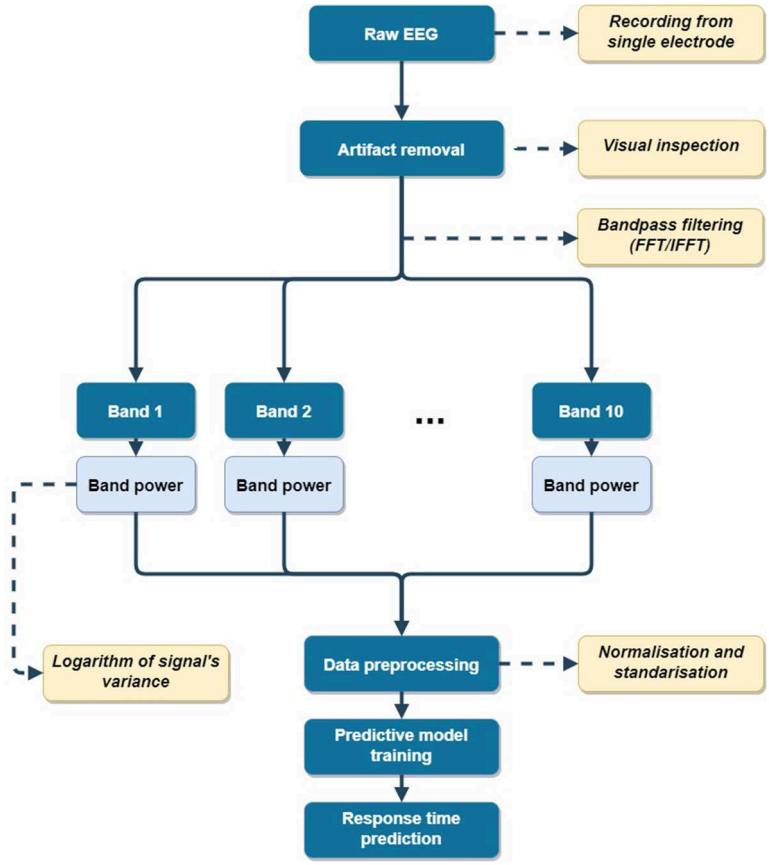


FIGURE 3 | EEG signal processing pipeline (for single electrode).

Performance of machine learning models is dependent on the values of the variables-or "hyperparameters." These hyperparameters differ based on different methods. The problem of choosing the optimal hyperparameters for a learning algorithm that minimizes a predefined loss function is called, hyperparameter optimization or tuning. For hyperparameter optimization, the present study used the Grid Search method (Bergstra et al., 2011). This approach involves an exhaustive searching through a manually specified subset of the hyperparameter space of a learning algorithm. Performance of various hyperparameter combinations was measured by 3-fold cross-validation on the training set with *Mean Absolute Error* (MAE) selected as the optimized performance metric.

For each subject, ∼48 events were obtained during the experimental stage. Samples were then randomly divided so that 75% of samples were used for the training and tuning of prediction algorithms. The remaining 25% of the samples served as an independent dataset on which the best model (i.e., selected after hyperparameter optimization) was tested for each compared algorithm. To reduce the impact of random data division on the final score, datasets for each individual participant were randomly split into train-test datasets 11 times. *MAE* values obtained for each random repetition were then averaged for each subject. Let us assume that y_m is the real time of response delay for sample m, and the predicted delay response time for that sample is $\hat{y}_m$. If M denotes the number of samples in the training set, then the final *MAE* value obtained from 11 cross-validations for subject s can be calculated with the following formula:

$$MAE_s = \frac{1}{11}\sum_{i=1}^{11}\left(\sum_{m=1}^{M}\frac{|\hat{y}_m - y_m|}{M}\right) \quad (1)$$

A brief description of regression algorithms selected for the comparison can be found in **Appendix A**. A list of used hyperparameters and the searched space of their values for each algorithm is presented in **Appendix B**. For a detailed description of all hyperparameters, please refer to the documentation for the Python-based machine learning library *scikit-learn* (Pedregosa et al., 2011).

2.3.2. Correction and Removal of Ocular Artifacts

Raw, multichannel time series data was obtained from EPOC+ devices during the experiment. Bioelectrical recordings from the brain are often contaminated with artifacts caused by muscle tensions, which are primarily related to eye movements and facial expressions. Given that these artifacts have a frequency spectrum that overlaps with part of the EEG spectra, the analysis of those signals is not only less effective, but in many cases, is impossible

in their presence (Binias et al., 2015). Many approaches for filtering out artifacts and retrieving the underlying neural information have been proposed. Most commonly, regression methods are performed either in time or frequency domains (Binias et al., 2015). These artifact regression methods have been found to be highly effective. However, a requirement of providing at least one signal with a noise reference is a downfall for solutions that favor a limited number of electrodes in the configuration. This is particularly problematic for solutions that are designed for use in aircraft, which is the case for the system developed for the present study. On the other hand, if artifact regression is applied in the time domain, methods based on Adaptive Noise Cancelling (ANC) can be implemented for real-time applications. Indeed, this is a benefit of ANC approaches. There are various other techniques that can be used for detecting and filtering muscle movement-related artifacts, including blind source separation based algorithms (Jung et al., 2000). These algorithms include Principal Component Analysis (PCA) and Independent Component Analysis (ICA), which rely on recorded EEG and noise signals for calibration (Makeig et al., 1996). PCA and ICA approaches are particularly effective when a large amount of data is recorded across many channels. Similar to ANC-based approaches, the high data dimensionality requirement forces an extended electrode set-up, which is an inconvenience for practical solutions. Additionally, it must be noted that these methods function best in semi-automatic approaches, where supervision of an experienced user (i.e., expert) is required (Makeig et al., 1996). Although there are many eye blink correction and filtering methods described in the literature, proper validation of these methods a very demanding matter. To address this would require an uncontaminated EEG signal that can be used to compare the obtained corrected data, to evaluate the quality of filtering. However, since EEG signals are recorded with disturbances already additively mixed, there is no precise way to extract an original, desired component. Thus, it is impossible to recover the exact morphology of the uncontaminated signal and consequently, no unambiguous way of evaluating the accuracy of the reconstruction of the filtered signal (Binias and Niezabitowski, 2017). In light of these limitations, we decided to simply remove highly contaminated TSIs from further analysis. This approach is commonly used in clinical practice. EEG segments were therefore visually inspected for the presence of artifacts that had an amplitude multiple times greater than that of the surrounding data. Based on this criteria, careful inspection of the data revealed that no EEG segments were removed due to their contamination. Since the main goal of this work was to provide an initial validation of the stated thesis rather than to propose a production ready solution, an automatic artifact removal method was not necessary. Additional motivation behind this approach was that the solution described in this work should serve as a baseline and reference for future improvements.

2.3.3. Frequency Analysis

As developments in neuroscience suggest, neural oscillations and their synchronization represent important mechanisms for inter-neuronal communication and the binding of information processed in distributed brain regions (Roach and Mathalon, 2008). Therefore, EEG signals are often analyzed based on their frequency characteristics. Indeed, time-frequency analysis of EEG signals can provide information on which frequencies have the most power at specific points in time and in certain location in the cortex. In the present study, the samples preceding the occurrence of the visual cue i.e., the TSI, will represent neural activity in the moment when performing of an action is required. The information about the spatial nature of observed processes will be obtained from the location of the EEG electrodes. In the proposed pipeline, EEG signals are analyzed in the following frequency bands, which correspond to specific brainwaves (Nunez and Srinivasan, 2006):

- Delta (1–4 Hz) (Landolt et al., 1996; Amzica and Steriade, 1998),
- Theta (4–8 Hz) (Strijkstra et al., 2003),
- Alpha (8–12 Hz) (Beatty, 1971; Strijkstra et al., 2003),
- Low Beta (12–16 Hz) (Beatty, 1971; Ang et al., 2012),
- Middle Beta (16–20 Hz) (Beatty, 1971; Ang et al., 2012),
- Middle-High Beta (20–24 Hz) (Beatty, 1971; Ang et al., 2012),
- High Beta (24–28 Hz) (Beatty, 1971; Ang et al., 2012),
- Gamma 1 (32–36 Hz) (Teplan, 2002; Ang et al., 2012),
- Gamma 2 (36–40 Hz) (Teplan, 2002; Ang et al., 2012),
- Broad band range (8–30 Hz) that is commonly related to the planning of motor movement (Blankertz et al., 2008).

Such bands have proven to be highly useful in a recent study that focused primarily on the problem of EEG-based discrimination between states of brain activity related to idle but focused anticipation of a visual cue and the response to that cue (Binias et al., 2018).

Since EEG is traditionally modeled as a series of sine waves of different frequencies that overlap in time and have different phase angles, the use of Fast Fourier Transform (FFT) for the frequency decomposition of such signal seems to be the most intuitive approach. To obtain bandpass filtered subsignals, each TSI was first decomposed into frequency components using FFT, for each channel separately. Then, the undesired frequencies were removed by changing their Fourier amplitudes to 0. Finally, the filtered signal was reconstructed using this modified Fourier representation using Inverse Fourier Transform algorithm. Although a detailed description of FFT is beyond the scope of this article, one important aspect of this approach warrants mention. That is, it is widely accepted that the larger the length of time window used for the FFT, the greater the frequency resolution of analysis. However, increasing the length of the TSI comes at the cost of decreasing the temporal resolution. This decrease in temporal resolution might cause a situation where the analyzed signal no longer represents the bioelectrical state of a subject's brain prior to the action requirement. As a result, these data might not be useful for predicting the delay in response. This problem is captured in the Heisenberg uncertainty principle (Folland and Sitaram, 1997). To address this problem, the present study utilized the, zero-padding, approach (Marple and Marple, 1987). In this method, the analyzed segment of a signal is extended by a sequence of zeros. This extended sequence is represented as a low frequency peak in the Fourier amplitude

spectrum. If such addition is correctly treated during the analysis (i.e., discarded), it won't negatively affect the outcome, but it will increase the frequency resolution. Given that frequency components lower than 1 Hz are not considered in the present study, the zero padding approach could be implemented. For the purpose of this research, 0.5 s time windows were used, which corresponds to 64 samples of TSI length. Analyzed segments were additionally padded with 192 zeros so that the total length of signal to be decomposed with FFT was 256 samples.

2.3.4. Feature Extraction

A common assumption is that changes in EEG power reflect changes in underlying neuronal activity (Roach and Mathalon, 2008). These power changes are typically referred to as Event-Related Synchronization and Event-Related Desynchronization, to describe the changes in EEG power that are related to the occurrence of a specific event (Pfurtscheller and Da Silva, 1999). Therefore, one of the most effective and widely used descriptors of EEG data is the power of the signal calculated in a specific frequency range (Blankertz et al., 2008). Since the mean value of the bandpass filtered signal tends to zero, the variance of such signal can be used to represent its bandpower. To improve the performance of chosen classification algorithm, the distribution of the extracted bandpower features is often normalized using a natural logarithm function (Binias et al., 2016a). The logarithm of variance feature, that will also be referred to as *logvar*, was chosen as the descriptive statistics in the described pipeline. Since the experimental set up consists of 14 electrodes and each signal is further decomposed into 10 frequency subbands, a total of 140 logvar features were obtained for each trial i.e., appearance of visual cue, in each experiment. Before tuning and training of the prediction algorithms, all features were subjected to the classical standardization and normalization procedures to obtain a zero mean value and unitary standard deviation. Section 2.3.1 contains a detailed description of the implemented approach to the problem of regression.

3. RESULTS

Summary statistics for delay times in response to the cue and a total number of epochs registered for each subject, are presented in **Table 1**. One of the initial hypotheses was that the delay in reaction time will increase with an increase in the duration of the experiment. To determine whether a relation between the time in experiment when the event happened and response delay, a Robust Linear Model (RLM) was fit to the data. The RLM is estimated via iteratively reweighted least squares (Huber, 1973). The robust criterion function used for downweighting the outliers was Hubers T for M estimation (Huber, 1973; Huber et al., 2013). A more detailed description of this approach lies beyond the scope of this article. The explanatory variable used for the modeling was the timestamp of the event i.e., cue appearance. The delay in response time was the explained variable. **Table 1** shows observed slope coefficients of fitted lines, as well as, *p*-values describing their statistical significance. Only for subjects 6, 7, 8, 9, 13, 14, 16, and 18, *p*-values of the slope coefficients were lower than 0.03 and can therefore be considered statistically significant. Slope coefficients for those subjects, as well as for other subjects, are very close to 0. Given these observations, it can be assumed that neither a linearly increasing nor decreasing trend can be attributed to the changes in response delay over time. Further analysis was conducted on the basic statistics of the data presented in **Table 1**, especially the standard deviation σ and the difference between minimal and maximal values for each subject with respect to the median. These additional analyses suggest high variability in response time values throughout each session.

TABLE 1 | Basic statistics of the response delay times summarized for each subject.

Subject	Min. [s]	Median [s]	Max. [s]	σ [s]	Slope [s/s]	*p*-value	No. epochs
1	0.408	0.553	1.616	0.305	1.82E-12	0.161	50
2	0.468	0.659	1.129	0.154	7.26E-13	0.527	44
3	0.402	0.592	1.124	0.163	–3.61E-12	0.120	46
4	0.450	0.627	0.934	0.130	–2.35E-12	0.393	45
5	0.386	0.495	0.784	0.097	1.01E-12	0.106	50
6	0.304	0.408	0.704	0.087	–1.14E-12	0.016	48
7	0.443	0.616	1.498	0.234	2.76E-12	0.027	49
8	0.323	0.544	2.113	0.426	7.43E-12	0.020	48
9	0.381	0.487	1.086	0.128	2.26E-12	<1E-5	50
10	0.658	1.199	3.279	0.613	6.57E-12	0.468	48
11	0.412	0.541	0.743	0.093	–8.59E-13	0.250	47
12	0.421	0.560	0.994	0.129	–7.99E-13	0.208	49
13	0.414	0.759	2.610	0.432	5.47E-12	<1E-5	51
14	0.379	0.664	1.982	0.238	–1.90E-12	0.025	49
15	0.278	0.421	0.665	0.091	3.90E-14	0.956	47
16	0.436	1.009	3.192	0.749	1.48E-11	<1E-5	43
17	0.390	0.555	1.660	0.229	–8.87E-13	0.301	50
18	0.375	0.547	1.296	0.181	1.59E-12	0.017	53
19	0.362	0.533	1.947	0.297	–1.99E-12	0.078	51

Average *MAE* scores obtained for different prediction algorithms are presented in **Table 2**. It can be observed that the best average results were obtained with the SVMRBF algorithm (114 ms). What is worth to notice is that MAE for subjects 10 and 16 is much higher than that of other subjects. However considering that the average reaction delay was around 600 ms, this is a relatively small error. Therefore, the obtained results can be considered satisfactory. Additionally, the standard deviations of absolute errors (AE) were taken into account and presented in **Table 3**. Again, the SVMRBF results were characterized by the lowest value of 68 ms. The maximal prediction AEs are shown in **Table 4**. Given that the presented solution is meant to be utilized for safety solutions in the future, this metric is especially important. Failing to predict a single decrease in performance (i.e., a drastic increase in response delay) might lead to more serious consequences than averaging a relatively higher mean error for all events. The average maximal prediction absolute error exceeded 200 ms for all algorithms, with SVMRBF outscoring other algorithms by at least 24 ms.

On average, all scores of both LASSO-based algorithms and Kernel Ridge regression were off by a few milliseconds

TABLE 2 | Comparison of prediction's Mean Absolute Errors obtained for each subject.

ID	LASSO [s]	LASSO-LARS [s]	KernelRidge [s]	SVMRBF [s]	Shuffled SVM [s]
1	0.140	0.140	0.144	0.125	0.230
2	0.077	0.077	0.082	0.082	0.144
3	0.076	0.070	0.062	0.077	0.138
4	0.081	0.081	0.103	0.092	0.164
5	0.062	0.062	0.059	0.073	0.091
6	0.046	0.046	0.044	0.050	0.066
7	0.121	0.121	0.138	0.121	0.196
8	0.264	0.264	0.210	0.231	0.317
9	0.067	0.066	0.066	0.065	0.086
10	0.292	0.292	0.380	0.265	0.425
11	0.063	0.063	0.063	0.064	0.079
12	0.058	0.058	0.053	0.061	0.088
13	0.190	0.190	0.199	0.132	0.233
14	0.085	0.086	0.094	0.069	0.104
15	0.058	0.058	0.050	0.059	0.069
16	0.411	0.409	0.406	0.340	0.684
17	0.105	0.105	0.138	0.087	0.146
18	0.074	0.074	0.076	0.073	0.127
19	0.105	0.105	0.106	0.108	0.167
AVG	0.125	0.125	0.130	0.114	0.187

TABLE 3 | Comparison of Absolute Errors Standard Deviations obtained for each subject.

ID	LASSO [s]	LASSO-LARS [s]	KernelRidge [s]	SVMRBF [s]	Shuffled SVM [s]
1	0.103	0.103	0.107	0.082	0.170
2	0.062	0.062	0.073	0.056	0.102
3	0.039	0.037	0.034	0.044	0.085
4	0.056	0.056	0.072	0.061	0.102
5	0.044	0.044	0.040	0.046	0.053
6	0.020	0.020	0.024	0.025	0.038
7	0.066	0.066	0.081	0.076	0.163
8	0.141	0.142	0.123	0.163	0.262
9	0.038	0.037	0.040	0.038	0.052
10	0.165	0.165	0.196	0.111	0.230
11	0.040	0.040	0.041	0.037	0.040
12	0.040	0.040	0.044	0.042	0.061
13	0.119	0.119	0.121	0.089	0.255
14	0.055	0.055	0.057	0.044	0.081
15	0.033	0.033	0.034	0.032	0.041
16	0.253	0.252	0.312	0.172	0.590
17	0.061	0.061	0.091	0.054	0.156
18	0.058	0.09	0.058	0.055	0.131
19	0.086	0.086	0.088	0.073	0.140
AVG	0.078	0.078	0.086	0.068	0.145

TABLE 4 | Comparison of Maximal Absolute Errors obtained for each subject.

ID	LASSO [s]	LASSO-LARS [s]	KernelRidge [s]	SVMRBF [s]	Shuffled SVM [s]
1	0.305	0.304	0.313	0.261	0.476
2	0.180	0.180	0.213	0.168	0.311
3	0.119	0.113	0.103	0.132	0.240
4	0.144	0.144	0.188	0.164	0.282
5	0.129	0.129	0.120	0.143	0.172
6	0.076	0.076	0.083	0.090	0.129
7	0.211	0.211	0.262	0.236	0.485
8	0.446	0.448	0.380	0.467	0.706
9	0.122	0.119	0.124	0.120	0.169
10	0.505	0.505	0.628	0.399	0.719
11	0.131	0.131	0.132	0.126	0.140
12	0.124	0.124	0.131	0.129	0.188
13	0.389	0.389	0.398	0.284	0.719
14	0.167	0.171	0.176	0.139	0.249
15	0.110	0.110	0.103	0.115	0.136
16	0.814	0.911	0.873	0.605	1.666
17	0.201	0.201	0.274	0.161	0.439
18	0.168	0.176	0.177	0.168	0.390
19	0.250	0.250	0.257	0.243	0.442
AVG	0.242	0.242	0.260	0.218	0.424

with respect to SVMRBF. In order to properly examine the performance differences between compared algorithms a one-way ANOVA test was performed, where all AEs of prediction were used as observations and each of the regression algorithms was representing an individual group. The computed F-value of one-way ANOVA test was 2.246. The associated p-value from the F-distribution was 0.081. Since the results of performed ANOVA tests indicate the existence of statistically significant, albeit subtle, differences between AE obtained within each group *post-hoc* t-tests were performed to investigate this furthermore. **Table 5** presents p-values obtained from performed t-tests. The results indicate that the SVMRBF algorithm allowed to obtain a significantly ($p < 0.05$) values of AE.

An additional analysis was carried out in order to validate the proposed solution further. For this purpose, the best performing algorithm—the SVMRBF—was trained with shuffled reaction times. The motivation behind that is to compare how well does the prediction work against simply learning to predict the average reaction time for each subject. Average MAEs obtained for each subject with this approach are presented in **Table 2** under *Shuffled SVM* column. Insignificant differences in MAE between properly trained algorithms and this would indicate that proposed approach is not using EEG information. F-value of performed one-way ANOVA (with *Shuffled SVM* included as one of the groups) was 20.901 (associated p-value is less than 10^{-16}). This indicates some statistical differences between groups and justifies performing additional *post-hoc* t-tests. Results presented in **Table 5** prove that all proposed algorithms perform significantly better than fitting average.

TABLE 5 | *p*-values of pairwise *t*-tests performed in order to compare absolute errors of prediction obtained with different regression algorithms.

p-value	LASSO	LASSO-LARS	KernelRidge	SVMRBF	Shuffled SVM
LASSO		0.991	0.627	0.043	<1E-7
LASSO-LARS	0.991		0.619	0.044	<1E-7
KernelRidge	0.627	0.619		0.014	<1E-6
SVMRBF	0.043	0.044	0.014		<1E-10
Shuffled SVM	<1E-7	<1E-7	<1E-6	<1E-10	

Since the best performing regression algorithm—SVMRBF—requires initial feature ranking and selection, analysis of the nature of top predictors could provide an interesting and valuable information. Presented in **Table 6** is a summary of most commonly selected features, across all 11 cross-validation, for each individual subject. **Figure 4** presents a histogram of top feature selections. It can be observed that optimal subset of features varies highly between subjects with most frequently selected features—Gamma 1 in AF3 electrode location and Gamma 1 in F8 electrode location—being common only for 5 subjects each. Further features—Gamma 2 (AF3 electrode), High Beta (AF3 electrode), Delta (T7 electrode) and Gamma 2 (AF4 electrode)—were common only for 4 subjects.

4. DISCUSSION

The present study provides a novel utilization of EEG to predict delays in response time. Indeed, we demonstrated that it is possible to obtain satisfactory results based solely on the processed EEG signals. The average MAE value for SVMRBF was 114 ms. This is a relatively small error, which indicates that the achieved results are very promising. This is particularly true given that this is the initial phase of this work and the first time that this problem has been approached. For all subjects, the MAE was at least a few times smaller than their lowest reaction delay. The other tested regression algorithms performed significantly worse than SVMRBF; however the gap between LASSO-LARS, LASSO, and Kernel Ridge regression was only couple seconds. With the lowest standard deviation of prediction's AE, SVMRBF was also the most precise algorithm. Additional tests proved that proposed solution performs significantly better than simple average fitting.

Errors obtained for 12 subjects did not exceed 100 ms. A higher score for some of the subjects emphasizes the complexity of the problem. Additionally, another important observation can be made—that none of the algorithms resulted in the lowest MAE for all subjects. Altogether, these findings might indicate that subject-specific algorithm selection might improve the performance of the proposed solution. However, the significantly higher errors for few subjects could be related to the phenomena known as BCI illiteracy (Allison and Neuper, 2010). Indeed, some studies suggest that there is a group of people not capable of using EEG-based BCI systems (Allison and Neuper, 2010; Vidaurre and Blankertz, 2010). While this possibility must be taken into consideration in future work this conclusion should not be drawn hastily to explain the poorer than expected performance of the proposed solution for some subjects.

The statistics presented in **Table 1** suggest no significant trend i.e., neither increasing nor decreasing in the lengths of delay in response times. Additionally, high values of standard deviations (compared to the median) might indicate that the times are

TABLE 6 | Summary of top features selected most commonly for individual subjects, as well as, for all subjects combined for SVMRBF algorithm.

ID	Top features
1	Delta (T7), Gamma 1 (FC5), Gamma 2 (F7), Gamma 2 (FC5),Gamma 2 (F7), High Beta (FC5), High Beta (T7), Low Beta (T7), Broad (T7), Mid Beta (T7)
2	Alpha (AF3), Alpha (F4), Alpha (F7), Alpha (T8), Delta (T8), Gamma 1 (P8), High Beta (T8), Broad (F7), Broad (T8), Mid Beta (P8)
3	Alpha (F3), Gamma 2 (AF3), Gamma 2 (F3), Low Beta (F3), Mid Beta (P8)
4	Alpha (O1), Alpha (T7), Delta (AF4), Delta (F3), Delta (F4), Delta (F7), Delta (FC6), Delta (P7), Delta (T7), Low Beta (F3)
5	Delta (P7), Gamma 2 (P7),Gamma 2 (P7), Mid Beta (P7)
6	Gamma 1 (AF3), Broad (AF4), Broad (F8), Raw (AF3), Raw (AF4)
7	Alpha (O1), Alpha (O2), Gamma 1 (F8), Gamma 2 (AF4), Gamma 2 (F8), Mid Beta (F3)
8	Gamma 1 (AF3), Gamma 1 (AF4), Gamma 1 (F7), Gamma 1 (F8), Gamma 1 (T8), Gamma 2 (AF3), Gamma 2 (AF4), Gamma 2 (O2),Gamma 2 (F8),Gamma 2 (FC5)
9	Alpha (T7), Delta (T7), Gamma 2 (T7),Gamma 2 (T7), High Beta (T7), Low Beta (T7), Mid Beta (T7), Theta (T7)
10	Alpha (AF3), Alpha (F3), Alpha (F4), Alpha (F7), Alpha (F8), Alpha (FC5), Alpha (FC6), Alpha (T8),Gamma 2 (F3),Gamma 2 (F7)
11	Gamma 1 (P8), Gamma 2 (F7),Gamma 2 (T7), High Beta (FC5), Low Beta (F4), Low Beta (P8)
12	Alpha (P7), Delta (F3), Gamma 2 (AF3),Gamma 2 (F4),Gamma 2 (FC6), High Beta (AF3), High Beta (O2), High Beta (T7), Broad (P7), Raw (F3)
13	Gamma 1 (F8),Gamma 2 (F8), High Beta (F7), High Beta (F8), High Beta (O2), Raw (F4)
14	Alpha (AF3), Gamma 1 (AF3), Gamma 2 (AF3),Gamma 2 (AF3), High Beta (AF3), Low Beta (F3)
15	Alpha (P8), Delta (F4), Gamma 1 (AF4), Gamma 1 (F8), Gamma 1 (O1), Gamma 1 (P8), Gamma 1 (T8), Gamma 2 (AF4), Gamma 2 (F8), Gamma 2 (T8)
16	Alpha (FC5), Alpha (O1), Alpha (O2), Alpha (P8), Delta (T7), Gamma 1 (T7), Gamma 2 (T7), Gamma 2 (T7), High Beta (AF3), High Beta (FC5)
17	Gamma 1 (AF3),Gamma 2 (AF3), High Beta (AF3), Low Beta (AF3)
18	Gamma 1 (AF3), Gamma 1 (AF4), Gamma 1 (F3), Gamma 1 (F4), Gamma 1 (F8), Gamma 1 (FC5), Gamma 1 (T7), Gamma 1 (T8), Gamma 2 (AF4), Gamma 2 (F3)
19	Alpha (O2), Gamma 1 (T7), Gamma 2 (T7), Low Beta (AF4), Broad (O2)
Overall	Gamma 1 (AF3), Gamma 1 (F8), Gamma 2 (AF3), High Beta (AF3), Delta (T7), Gamma 2 (AF4)

Frequency ranges correspond to those listed in section 2.3.3. Values in brackets correspond to electrode locations. Features are sorted alphabetically.

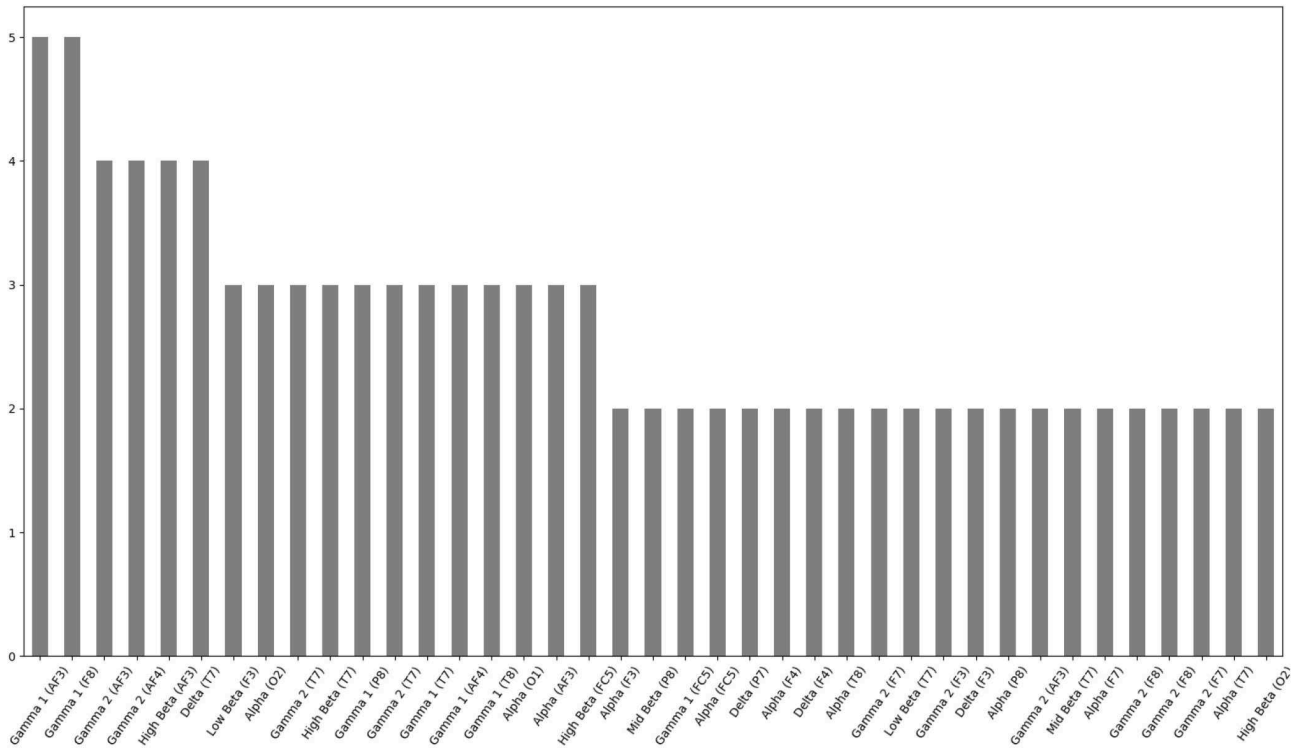


FIGURE 4 | Histogram of cumulative feature selections for all subjects for SVMRBF algorithms. Only features selected more than once were included.

random, or at least independent from obvious variables such as timestamp of experiment. Such high variability in the data is a good prognostic indicator of the experiment. In particular, when designing machine learning algorithms, great care needs to be taken to avoid tuning the model to strong correlations that have no actual relation to the explained or explanatory variables. If the data where instead aligned to any monotonic function that is dependent upon the timestamp, then relatively low regression errors could be obtained; however, EEG-related variables would have a negligible impact on that score. Since that is not a case, the obtained results can be considered satisfactory with a greater confidence.

The analysis of selected features for—the most effective—SVMRBF algorithm was additionally performed. A high variability between the optimal subsets of features selected for individual subjects was observed. In particular, the greatest number of subjects for whom same features were common (Gamma 1 in AF3 electrode location and Gamma 1 in F8 electrode location) was 5. This is merely over 25% of the total number of subjects. Therefore, no detailed conclusions about the mental processes underlying fast reaction related actions can be drawn at this stage of the experiment. Such differences can be explained by both, or either of individual characteristics of neural activity related to the presented task or overlapping of bioelectrical source activity caused by the effects of volume conduction. It is a common knowledge that due to this phenomena analysis of cortical activity may be less precise. Additionally, some important spatiotemporal features of the EEG signal might not be properly observed (Blankertz et al., 2008). Therefore, among the most important future additions to the pipeline is the implementation of a spatial filtering step (Blankertz et al., 2008). The use of a spatial filtering algorithm has proven to be highly beneficial in various EEG bandpower-based solutions (Binias et al., 2016b, 2018). Authors believe that such addition would no only allow to further decrease the prediction MAE, but also make the analysis of most relevant frequency bandwidths and cortical locations more accurate and exhaustive.

Another feature that should be tested, that may have an impact on prediction error is the removal and correction of short-time, high-amplitude artifacts such as eye movement, blinking, and muscle activity. Several approaches, including Artifact Subspace Reconstruction (ASR) or rejecting the subspace of ICA coefficients, may provide a potent solution to this problem (Le et al., 2011; Akhtar et al., 2012; Mullen et al., 2013). Due to its capability for real-time application, the ASR method, in particular, should be considered for addition to the pipeline.

The presented solution may serve as a starting point for future concepts and improvements. The idea of predicting the delay in response time to an unexpected event hides a much broader concept than the one reflected in the present experiment. The constant monitoring of predicted reaction time might shed new light on how pilot's capabilities change over the course

of a flight. These changes over time might then be used to trigger an alarm once a significant decrease in predicted reaction time is expected. Such an approach to addressing the problem would then provide an overview of the overall level of fatigue, rather than being a temporally-limited metric. A future follow-up experiment will be conducted that includes a larger sample size, and a measurement device that provides greater coverage of the brain's cortical areas. This followup experiment will validate the proposed approach and test the potential of the implemented solution.

DATA AVAILABILITY STATEMENT

The datasets generated for this study are available on request to the corresponding author.

ETHICS STATEMENT

The studies involving human participants were reviewed and approved by The Jerzy Kukuczka Academy of Physical Education in Katowice Bioethical Committee. The patients/participants provided their written informed consent to participate in this study.

AUTHOR CONTRIBUTIONS

BB designed and implemented the entire digital signal processing pipeline and data analysis methodology. Additionally, BB performed all of the described data analyses and prepared this manuscript. All data was obtained by DM, who additionally designed, created, and/or configured all software used for the purpose of the EEG recording. DM has also provided substantive consultation regarding the applied and designed methodology, and contributed to introduction, study population and experiment description, and discussion of this manuscript. The original research idea and plan of the conducted experiment was designed equally by BB and DM. HP provided substantive consultation throughout the course of the experiment, particularly (but not limited to) with respect to the applied statistical and machine learning methods. Additionally, HP assisted with the editorial organization of the article's content. KC provided substantive consultation regarding the aspects of the research that are related to aircraft.

FUNDING

This work was mainly supported by Silesian University of Technology grant—subsidy for maintaining and developing research potential. This work was partially supported by the research project (RAU-6, 2020) of the Silesian University of Technology, Department of Computer Graphics, Vision and Digital Systems (Gliwice, Poland). The research presented here was performed with the use of Emotiv EPOC+ Headset purchased with a Motorola Solutions Foundation grant from the Institute of Computer Science at Silesian University of Technology, no ZZD/1/Rau2/2015/507. The work was performed using a flight simulator purchased under POIG.02.03.01-24, Upper Silesian Center for Computational Science and Engineering. This work was additionally supported by the Silesian University of Technology Grant no. 02/020/BKM18/0155, 02/020/BK_19/0171 as well as 02/080/BK_20.

SUPPLEMENTARY MATERIAL

The Supplementary Material for this article can be found online at: https://www.frontiersin.org/articles/10.3389/fninf.2020.00006/full#supplementary-material

REFERENCES

Acharya, U. R., Oh, S. L., Hagiwara, Y., Tan, J. H., and Adeli, H. (2018). Deep convolutional neural network for the automated detection and diagnosis of seizure using EEG signals. *Comput. Biol. Med.* 100, 270–278. doi: 10.1016/j.compbiomed.2017.09.017

Akerstedt, T., Mollard, R., Samel, A., Simons, M., and Spencer, M. (2003). *Meeting to Discuss the Role of eu ftl Legislation in Reducing Cumulative Fatigue in Civil Aviation*. Brussels: European Transport Safety Council.

Akhtar, M. T., Jung, T.-P., Makeig, S., and Cauwenberghs, G. (2012). "Recursive independent component analysis for online blind source separation," in *2012 IEEE International Symposium on Circuits and Systems (ISCAS)* (Seoul: IEEE), 2813–2816.

Allison, B. Z., and Neuper, C. (2010). "Could anyone use a BCI?" in *Brain-Computer Interfaces* (London: Springer), 35–54.

Alrajhi, W., Alaloola, D., and Albarqawi, A. (2017). "Smart home: toward daily use of BCI-based systems," in *International Conference on Informatics, Health & Technology (ICIHT)* (Riyadh: IEEE), 1–5.

Amzica, F., and Steriade, M. (1998). Electrophysiological correlates of sleep delta waves. *Electroencephalogr. Clin. Neurophysiol.* 107, 69–83. doi: 10.1016/S0013-4694(98)00051-0

Ang, K. K., Chin, Z. Y., Wang, C., Guan, C., and Zhang, H. (2012). Filter bank common spatial pattern algorithm on BCI competition IV datasets 2a and 2b. *Front. Neurosci.* 6:39. doi: 10.3389/fnins.2012.00039

Baldwin, C. L., Roberts, D. M., Barragan, D., Lee, J. D., Lerner, N., and Higgins, J. S. (2017). Detecting and quantifying mind wandering during simulated driving. *Front. Hum. Neurosci.* 11:406. doi: 10.3389/fnhum.2017.00406

Beatty, J. (1971). Effects of initial alpha wave abundance and operant training procedures on occipital alpha and beta wave activity. *Psychonom. Sci.* 23, 197–199. doi: 10.3758/BF03336074

Belyavin, A., and Wright, N. A. (1987). Changes in electrical activity of the brain with vigilance. *Electroencephalogr. Clin. Neurophysiol.* 66, 137–144. doi: 10.1016/0013-4694(87)90183-0

Bennett, S. A. (2019). Pilot workload and fatigue on four intra-European routes: a 12-month mixed-methods evaluation. *J. Risk Res.* 22, 983–1003. doi: 10.1080/13669877.2018.1430704

Bergstra, J. S., Bardenet, R., Bengio, Y., and Kégl, B. (2011). "Algorithms for hyper-parameter optimization," in *Advances in Neural Information Processing Systems*, (Granada), 2546–2554.

Binias, B., Grzejszczak, T., and Niezabitowski, M. (2016a). "Normalization of feature distribution in motor imagery based Brain-Computer Interfaces," in *Control and Automation (MED), 2016 24th Mediterranean Conference on* (Athens: IEEE), 1337–1342.

Binias, B., Myszor, D., and Cyran, K. A. (2018). A machine learning approach to the detection of pilot"?s reaction to unexpected events based on EEG signals. *Comput. Intell. Neurosci.* 2018:2703513. doi: 10.1155/2018/2703513

Binias, B., Myszor, D., Niezabitowski, M., and Cyran, K. A. (2016b). "Evaluation of alertness and mental fatigue among participants of simulated flight sessions," in *Carpathian Control Conference (ICCC), 2016 17th International* (Tatranská Lomnica: IEEE), 76–81.

Binias, B., and Niezabitowski, M. (2017). "Adaptive nonlinear projective filtering - application to filtering of artifacts in EEG signals," in *Proceedings of the 14th International Conference on Informatics in Control, Automation and Robotics - Volume 1: ICINCO,* (Madrid: INSTICC; SciTePress), 440–448.

Binias, B., Palus, H., and Jaskot, K. (2015). "Real-time detection and filtering of eye movement and blink related artifacts in EEG," in *Methods and Models in Automation and Robotics (MMAR), 2015 20th International Conference on* (Miedzyzdroje: IEEE), 903–908.

Blankertz, B., Tomioka, R., Lemm, S., Kawanabe, M., and Muller, K.-R. (2008). Optimizing spatial filters for robust EEG single-trial analysis. *IEEE Signal Process. Magaz.* 25, 41–56. doi: 10.1109/MSP.2008.4408441

Borghini, G., Astolfi, L., Vecchiato, G., Mattia, D., and Babiloni, F. (2014). Measuring neurophysiological signals in aircraft pilots and car drivers for the assessment of mental workload, fatigue and drowsiness. *Neurosci. Biobehav. Rev.* 44, 58–75. doi: 10.1016/j.neubiorev.2012.10.003

Borisov, V., Syskov, A., and Kublanov, V. (2019). "Functional state assessment of an athlete by means of the Brain-Computer Interface multimodal metrics," in *World Congress on Medical Physics and Biomedical Engineering 2018* (Prague: Springer), 71–75.

Bushmaker, R., Corey, K., Dunn, J., Lalonde, T., and Estrada, S. (2019). Evaluation of a new helicopter crew transport fatigue assessment. *Air Med. J.* 38, 198–201. doi: 10.1016/j.amj.2018.11.006

Caldwell, J. A. (2005). Fatigue in aviation. *Travel Med. Infect. Dis.* 3, 85–96. doi: 10.1016/j.tmaid.2004.07.008

Caldwell, J. A., and Gilreath, S. R. (2002). A survey of aircrew fatigue in a sample of US Army aviation personnel. *Aviat. Space Environ. Med.* 73, 472–480. Available online at: https://psycnet.apa.org/record/2002-02983-006

EMOTIV Systems (2014). *EMOTIV EPOC Brain - Computer Interface and Scientific Contextual EEG. EMOTIV EPOC and Testbench^{TM} Specifications*. Technical report, EMOTIV Systems.

Folland, G. B., and Sitaram, A. (1997). The uncertainty principle: a mathematical survey. *J. Fourier Anal. Appl.* 3, 207–238. doi: 10.1007/BF02649110

Grummett, T., Leibbrandt, R., Lewis, T., DeLosAngeles, D., Powers, D., Willoughby, J., et al. (2015). Measurement of neural signals from inexpensive, wireless and dry EEG systems. *Physiol. Meas.* 36:1469. doi: 10.1088/0967-3334/36/7/1469

Hajinoroozi, M., Jung, T.-P., Lin, C.-T., and Huang, Y. (2015). "Feature extraction with deep belief networks for driver's cognitive states prediction from EEG data," in *2015 IEEE China Summit and International Conference on Signal and Information Processing (ChinaSIP)* (Chengdu: IEEE), 812–815.

Huber, M., Lechner, M., and Wunsch, C. (2013). The performance of estimators based on the propensity score. *J. Econometr.* 175, 1–21. doi: 10.1016/j.jeconom.2012.11.006

Huber, P. J. (1973). Robust regression: asymptotics, conjectures and Monte Carlo. *Ann. Stat.* 1, 799–821. doi: 10.1214/aos/1176342503

International Civil Aviation Organization (2016). *Manual for the Oversight of Fatigue Management Approaches (Doc 9966)*.

Jackson, C. A., and Earl, L. (2006). Prevalence of fatigue among commercial pilots. *Occup. Med.* 56, 263–268. doi: 10.1093/occmed/kql021

Jung, T.-P., Makeig, S., Humphries, C., Lee, T.-W., Mckeown, M. J., Iragui, V., et al. (2000). Removing electroencephalographic artifacts by blind source separation. *Psychophysiology* 37, 163–178. doi: 10.1111/1469-8986.3720163

Koessler, L., Maillard, L., Benhadid, A., Vignal, J. P., Felblinger, J., Vespignani, H., et al. (2009). Automated cortical projection of EEG sensors: anatomical correlation via the international 10–10 system. *Neuroimage* 46, 64–72. doi: 10.1016/j.neuroimage.2009.02.006

Landolt, H.-P., Dijk, D.-J., Achermann, P., and Borbely, A. A. (1996). Effect of age on the sleep EEG: slow-wave activity and spindle frequency activity in young and middle-aged men. *Brain Res.* 738, 205–212. doi: 10.1016/S0006-8993(96)00770-6

Le, Q. V., Karpenko, A., Ngiam, J., and Ng, A. Y. (2011). "ICA with reconstruction cost for efficient overcomplete feature learning," in *Advances in Neural Information Processing Systems*, (Granada), 1017–1025.

Lee, S., and Kim, J. K. (2018). Factors contributing to the risk of airline pilot fatigue. *J. Air Transp. Manage.* 67, 197–207. doi: 10.1016/j.jairtraman.2017.12.009

Makeig, S., Bell, A. J., Jung, T.-P., and Sejnowski, T. J. (1996). "Independent component analysis of electroencephalographic data," in *Advances in Neural Information Processing Systems*, (Denver, CO), 145–151.

Marple, S. L., and Marple, S. L. (1987). *Digital Spectral Analysis: With Applications*, Vol. 5. Englewood Cliffs, NJ: Prentice-Hall.

Meinel, A., Castaño-Candamil, J. S., Dähne, S., Reis, J., and Tangermann, M. (2015). "EEG band power predicts single-trial reaction time in a hand motor task," in *2015 7th International IEEE/EMBS Conference on Neural Engineering (NER)* (Montpellier: IEEE), 182–185.

Mullen, T., Kothe, C., Chi, Y. M., Ojeda, A., Kerth, T., Makeig, S., et al. (2013). "Real-time modeling and 3D visualization of source dynamics and connectivity using wearable EEG," in *2013 35th Annual International Conference of the IEEE Engineering in Medicine and Biology Society (EMBC)* (Osaka: IEEE), 2184–2187.

National Research Council (1998). *Improving the Continued Airworthiness of Civil Aircraft: A Strategy for the FAA's Aircraft Certification Service*. Washington, DC: National Academies Press.

Nunez, P. L., and Srinivasan, R. (2006). *Electric Fields of the Brain: the Neurophysics of EEG*. Oxford: Oxford University Press.

Ogilvie, R. D., and Simons, I. (1992). "Falling asleep and waking up: a comparison of EEG spectra," in *Sleep, Arousal and Performance*, eds J. B. Roger and D. O. Robert (Boston, MA; Basel; Berlin: Birkhäuser), 73–87.

Overweg, J., Binnie, C., Oosting, J., and Rowan, A. (1987). Clinical and EEG prediction of seizure recurrence following antiepileptic drug withdrawal. *Epilepsy Res.* 1, 272–283. doi: 10.1016/0920-1211(87)90002-7

Pedregosa, F., Varoquaux, G., Gramfort, A., Michel, V., Thirion, B., Grisel, O., et al. (2011). Scikit-learn: machine learning in Python. *J. Mach. Learn. Res.* 12, 2825–2830. Available online at: http://www.jmlr.org/papers/volume12/pedregosa11a/pedregosa11a.pdf

Pfurtscheller, G., and Da Silva, F. L. (1999). Event-related EEG/MEG synchronization and desynchronization: basic principles. *Clin. Neurophysiol.* 110, 1842–1857. doi: 10.1016/S1388-2457(99)00141-8

Powell, D., Spencer, M. B., Holland, D., Broadbent, E., and Petrie, K. J. (2007). Pilot fatigue in short-haul operations: effects of number of sectors, duty length, and time of day. *Aviat. Space Environ. Med.* 78, 698–701.

Roach, B. J., and Mathalon, D. H. (2008). Event-related EEG time-frequency analysis: an overview of measures and an analysis of early gamma band phase locking in schizophrenia. *Schizophr. Bull.* 34, 907–926. doi: 10.1093/schbul/sbn093

Ross, P. E. (2011). When will we have unmanned commercial airliners. *IEEE Spectr.* 48:38–43. Available online at: https://spectrum.ieee.org/aerospace/aviation/when-will-we-have-unmanned-commercial-airliners

Setiono, T., Handojo, A., Intan, R., Sutjiadi, R., and Lim, R. (2018). Brain Computer Interface for controlling RC-Car using Emotiv Epoc+. *J. Telecommun. Electr. Comput. Eng.* 10, 169–172.

Stevenson, B. (2017). *Unmanned Unlimited: With Small, Pilotless Aircraft Proving Their Worth in a Growing Range of Civil Applications, Regulators and Training Providers Find Themselves Scrambling to Keep Up With Technology*. Washington, DC: Flight International.

Strijkstra, A. M., Beersma, D. G., Drayer, B., Halbesma, N., and Daan, S. (2003). Subjective sleepiness correlates negatively with global alpha (8–12 Hz) and positively with central frontal theta (4–8 Hz) frequencies in the human resting awake electroencephalogram. *Neurosci. Lett.* 340, 17–20. doi: 10.1016/S0304-3940(03)00033-8

Tahmasebzadeh, A., Bahrani, M., and Setarehdan, S. K. (2013). "Development of a robust method for an online P300 Speller Brain Computer Interface," in *Neural Engineering (NER), 2013 6th International IEEE/EMBS Conference on* (IEEE), 1070–1075.

Teplan, M. (2002). Fundamentals of EEG measurement. *Meas. Sci. Rev.* (Karlova Ves), 2, 1–11.

Varsavsky, A., Mareels, I., and Cook, M. (2016). *Epileptic Seizures and the EEG: Measurement, Models, Detection and Prediction* (Boca Raton, FL: CRC Press), 1–370.

Vidaurre, C., and Blankertz, B. (2010). Towards a cure for BCI illiteracy. *Brain Topogr.* 23, 194–198. doi: 10.1007/s10548-009-0121-6

Wei, C.-S., Lin, Y.-P., Wang, Y.-T., Lin, C.-T., and Jung, T.-P. (2018). A subject-transfer framework for obviating inter- and intra-subject variability in EEG-based drowsiness detection. *Neuroimage* 174, 407–419. doi: 10.1016/j.neuroimage.2018.03.032

Conflict of Interest: The authors declare that the research was conducted in the absence of any commercial or financial relationships that could be construed as a potential conflict of interest.

Copyright © 2020 Binias, Myszor, Palus and Cyran. This is an open-access article distributed under the terms of the Creative Commons Attribution License (CC BY). The use, distribution or reproduction in other forums is permitted, provided the original author(s) and the copyright owner(s) are credited and that the original publication in this journal is cited, in accordance with accepted academic practice. No use, distribution or reproduction is permitted which does not comply with these terms.

frontiers in Neuroinformatics

METHODS
published: 28 February 2020
doi: 10.3389/fninf.2020.00007

A Standardized Protocol for Efficient and Reliable Quality Control of Brain Registration in Functional MRI Studies

Yassine Benhajali[1,2], AmanPreet Badhwar[2], Helen Spiers[3,4], Sebastian Urchs[2,5], Jonathan Armoza[2,6], Thomas Ong[7], Daniel Pérusse[1] and Pierre Bellec[2,8]*

[1] *Département d'Anthropologie, Université de Montréal, Montreal, QC, Canada,* [2] *Centre de Recherche de l'Institut Universitaire de Gériatrie de Montréal (CRIUGM), Montreal, QC, Canada,* [3] *The Zooniverse, Department of Physics, University of Oxford, Oxford, United Kingdom,* [4] *Electron Microscopy Science Technology Platform, The Francis Crick Institute, London, United Kingdom,* [5] *Integrated Program in Neuroscience, Montreal Neurological Institute, Montreal, QC, Canada,* [6] *English Department, New York University, New York, NY, United States,* [7] *Jewish General Hospital, Department of Radiology, McGill University, Montreal, QC, Canada,* [8] *Département de Psychologie, Université de Montréal, Montreal, QC, Canada*

Automatic alignment of brain anatomy in a standard space is a key step when processing magnetic resonance imaging for group analyses. Such brain registration is prone to failure, and the results are therefore typically reviewed visually to ensure quality. There is however no standard, validated protocol available to perform this visual quality control (QC). We propose here a standardized QC protocol for brain registration, with minimal training overhead and no required knowledge of brain anatomy. We validated the reliability of three-level QC ratings (OK, Maybe, Fail) across different raters. Nine experts each rated N = 100 validation images, and reached moderate to good agreement (kappa from 0.4 to 0.68, average of 0.54 ± 0.08), with the highest agreement for "Fail" images (Dice from 0.67 to 0.93, average of 0.8 ± 0.06). We then recruited volunteers through the Zooniverse crowdsourcing platform, and extracted a consensus panel rating for both the Zooniverse raters (N = 41) and the expert raters. The agreement between expert and Zooniverse panels was high (kappa = 0.76). Overall, our protocol achieved a good reliability when performing a two level assessment (Fail vs. OK/Maybe) by an individual rater, or aggregating multiple three-level ratings (OK, Maybe, Fail) from a panel of experts (3 minimum) or non-experts (15 minimum). Our brain registration QC protocol will help standardize QC practices across laboratories, improve the consistency of reporting of QC in publications, and will open the way for QC assessment of large datasets which could be used to train automated QC systems.

Keywords: quality control, fMRI, brain registration, crowdsourcing, visual inspection, inter-rater agreement

OPEN ACCESS

Edited by:
Pedro Antonio Valdes-Sosa, Clinical Hospital of Chengdu Brain Science Institute, China

Reviewed by:
Pierre Boulanger, University of Alberta, Canada
Olga V. Martynova, Institute of Higher Nervous Activity and Neurophysiology (RAS), Russia

****Correspondence:***
Yassine Benhajali
yassine.ben.haj.ali@umontreal.ca

Received: *18 July 2019*
Accepted: *12 February 2020*
Published: *28 February 2020*

Citation:
Benhajali Y, Badhwar A, Spiers H, Urchs S, Armoza J, Ong T, Pérusse D and Bellec P (2020) A Standardized Protocol for Efficient and Reliable Quality Control of Brain Registration in Functional MRI Studies. Front. Neuroinform. 14:7. doi: 10.3389/fninf.2020.00007

INTRODUCTION

Aligning individual anatomy across brains is a key step in the processing of structural magnetic resonance imaging (MRI) for functional MRI (fMRI) studies. This brain registration process allows for comparison of local brain measures and statistics across subjects. A visual quality control (QC) of brain registration is crucial to minimize incorrect data in downstream analyses of fMRI studies.

However, no standardized, validated protocol has yet been developed to streamline this QC. Here, we present a standardized procedure for visual QC of brain registration and describe the reliability of QC ratings from both expert raters and a large panel of non-experts recruited through an online citizen science platform[1].

Brain Registration

Magnetic resonance imaging is a non-invasive technique that can be applied to study brain structure (sMRI) and function (fMRI). Multiple steps are required to transform raw MRI data to processed images ready for downstream statistical analyses. One critical preprocessing step is brain registration; this involves aligning 3D brain images to a standard stereotaxic space, such as the MNI152/ICBM2009c template (Fonov et al., 2009). State-of-the-art registration procedures use non-linear optimization algorithms such as ANIMAL (Collins and Evans, 1997), DARTEL (Ashburner, 2007), or ANTS (Avants et al., 2009). Dadar et al. (2018) compared five publicly available, widely used brain registration algorithms in medical image analysis and found a failure rate of 16.8 ± 3.13% on their benchmarks. This lack of robustness is mainly due to differences in image quality, shape and cortical topology between individual brains. A visual QC of registered brain images is thus required to ensure good data quality for subsequent analyses.

Visual QC

The specific focus of the visual QC for sMRI registration depends on the intended use of the data. Voxel-based analysis of brain morphology typically calls for a highly accurate registration, as this step can impact brain tissue segmentation. In contrast, fMRI studies usually rely on larger voxel size and spatial blurring, and are less likely to be affected by small registration errors. To our knowledge, as of yet, there are no standardized criteria for tolerable errors in sMRI registration for fMRI processing pipelines. Many fMRI analytical software packages present users with images to assess the quality of T1 image registration. In one of the most recent packages developed by the community, fMRIprep (Esteban et al., 2019), the registered T1 image is presented across 21 brain slices, along with images for three other processing steps (skull stripping, tissue segmentation, and surface reconstruction), yielding a total of 84 brain slices for visual inspection. Established processing tools like FMRIB Software Library (Jenkinson et al., 2012) or the Statistical Parametric Mapping MATLAB package (Wellcome Centre for Human Neuroimaging, n.d.) also present users with reports that often include more than ten brain slices for visual inspection for each subject. This makes visual inspection tedious and time-consuming. Critically, none of these packages offer guidelines on how to assess the quality of structural brain registration for fMRI studies. Without such guidelines and with a large number of images to review, QC is likely to vary significantly across raters.

[1]www.zooniverse.org

Inter-Rater Agreement

Quality control studies of preprocessed images rarely report inter-rater reliability, and no such study examined brain registration to our knowledge. Pizarro et al. (2016) applied a support vector machine algorithm on visually rated (N = 1457 usable/unusable) sMRI data from 5 to 9 investigators who rated the same 630 images, but did not report agreement metrics. White et al. (2018) compared automated QC metrics and manual QC from 6662 sMRI data from 4 different cohorts/sites, merging visual inspection across sites, raters, protocols and scan quality but without presenting agreement statistics. Studies that do report inter-rater agreement mostly focus on issues related to raw MRI images (e.g. signal-to-noise ratio or susceptibility artifacts), head motion (e.g. ghosting or blurring), brain extraction, and tissue segmentation. Inter-rater agreement in these studies is found to vary considerably. For example, Backhausen et al. (2016) reported high agreement for two trained raters who visually inspected the same 88 sMRI, achieving an intra-class correlation of 0.931 for two categories of quality (pass-fail) on issues related to MRI acquisition and head motion. Esteban et al. (2017) reported a kappa of 0.39 between two raters for three quality categories (Exclude/Doubtful/Accept) on 100 images when ratings were based on the quality of the MRI acquisition, head motion, brain extraction and tissue segmentation. **Table 1** shows recent (2010 onward) studies reporting inter-rater agreements on visual QC of sMRI for a variety of issues. Only one study, Fonov et al. (2018), included brain registration for visual QC assessment. These authors reported a test-retest Dice similarity of 0.96% from one expert rater who evaluated as pass or fail 1000 images twice, but no inter-rater reliability estimate. Variability in reliability across studies may be due to two types of factors: user- and protocol-related factors. Protocol-related factors (e.g. clarity, levels of rating or training set) can be addressed by multiple iteration and refinement of the protocol. Factors related to the rater (e.g. level of expertise, fatigue, motivation, etc.) are more difficult to constrain or control. One solution to circumvent individual rater variability is to aggregate multiple ratings from a large pool of raters.

Crowdsourced QC

Crowdsourcing can be used to achieve multiple QC ratings on large collections of images rapidly. Crowdsourcing, as first defined by Howe in 2016, is " *the act of taking a job traditionally performed by a designated agent (usually an employee) and outsourcing it to an undefined, generally large group of people in the form of an open call*" (Howe, 2006). Crowdsourcing can be used in citizen science research projects where a large number of non-specialists take part in the scientific workflow to help researchers (Franzoni and Sauermann, 2014; Simpson et al., 2014). Crowdsourcing labor-intensive tasks across hundreds or thousands of individuals has proven to be effective in a number of citizen science research projects, such as modeling complex protein structures (Khatib et al., 2011), mapping the neural circuitry of the mammalian retina (Kim et al., 2014), and discovering new astronomical objects (Cardamone et al., 2009; Lintott et al., 2009).

TABLE 1 | Reported agreement in visual inspection of sMRI data on QC studies.

			Reported visual inspection issue related to				
Study	**QC agreement details**		**MRI Aquisition**	**Head motion**	**Brain extraction**	**Tissue segmentation**	**Brain registration**
Backhausen et al., 2016	Nb. Images	88	Image sharpness, ringing. Contrast to noise ratio (subcortical structures and gray/white matter) and susceptibility artifacts	Ghosting or blurring	N.R	N.R	N.R
	Nb. Raters	2					
	Rating scale	Include/Exclude					
	QC Manual	**Supplementary Material**					
	Agreement	ICC = 0.93					
Esteban et al., 2017	Nb. Images	100	signal-to-noise ratio. Image contrast and Ringing	Head motion artifacts	Gray/white matter and the pial delineation	Gray–white matter segmentation	N.R
	Nb Raters	2					
	Rating scale	Exclude/Doubtful/ Accept					
	QC Manual	N.R					
	Agreement	Cohen's Kappa = 0 39					
Rosen et al., 2018	Nb. Images	Phasel = l00, Phase2 = 100	N.R	N.R	N.R	N.R	N.R
	Nb. Raters	Phase1 = 2, Phase2 = 3					
	Rating scale	0/1/2					
	QC Manual	N.R					
	Agreement	Phasel = 100%, Phase2 = 85%					
Fonov et al., 2018 (preprint)	Nb. Images	9693 (1000 rated twice)	Effect of noise and image intensity non-uniformity	N.R	N.R	N.R	Incorrect estimates of, translation, scaling in all directions and rotation.
	Nb. Raters	1					
	Rating scale	Accept/Fail					
	QC Manual	Dadar et al., 2018 paper					
	Agreement	intra-rater Dice similarity = 0.96					
Klapwijk et al., 2019	Nb. Images	80	N.R	Ringing	Division between gray/white matter and pial surface	Gray–white matter segmentation	N.R
	Nb. Raters	5					
	Rating scale	Excellent/Good/ Doubtful/Failed					
	QC Manual	**Supplementary Material**					
	Agreement	Reliability = 0.53					

QC studies since 2010 that uses sMRI and reported their inter/intra-raters agreement (Pizarro et al., 2016; Esteban et al., 2017; Dadar et al., 2018; Fonov et al., 2018; Rosen et al., 2018; Klapwijk et al., 2019). N.R: Not reported.

In brain imaging, recent work by Keshavan et al. (2018) showed the advantages of using citizen science to rate brain images for issues related to head motion and scanner artifacts. These authors were able to gather 80,000 ratings on slices drawn from 722 brains using a simple web interface. A deep learning algorithm was then trained to predict data quality, based on the gathered rating from citizen science. The deep learning network performed as well as a the specialized algorithm MRIQC (Esteban et al., 2017) for quality control of T1-weighted images. QC of large open access databases like HCP (Glasser et al., 2016), UKbiobank (Alfaro-Almagro et al., 2018) or ABCD (Casey et al., 2018) is challenging and time consuming task if done manually. Using crowdsourced rating could be a key element to rate huge databases and eventually use these ratings to efficiently train a machine learning models to perform QC.

Here, we propose a novel, standardized visual QC protocol for the registration of T1 images by non-experts. We formally assessed protocol reliability, first with "expert" raters familiar with visual inspection of brain registration, and second with a large pool of "non-expert" raters with no specific background in brain imaging. These citizen scientists contributed via the world's largest online citizen science platform, called Zooniverse (Simpson et al., 2014). Zooniverse enabled the enrollment of more than 2000 volunteers from around the globe, thus enabling the evaluation of consensus between non-expert raters on a large scale. Specific aims and hypotheses of the study were as follows:

1. To establish a QC procedure for MRI brain registration that does not require extensive training or prior knowledge of brain anatomy. Our hypothesis was that such a procedure would help raters achieve more reliable visual QC.
2. To quantify the agreement between a consensus panel composed of non-expert raters and that of experts. Our hypothesis was that the consensus of non-experts would be consistent with experts' assessments, since the protocol requires no knowledge of brain anatomy.

METHOD

Quality Control Protocol Building

The QC protocol was developed iteratively over the past 5 years, with several rounds of feedback from users. Initially, the protocol was used internally in our laboratory (Yassine and Pierre, 2016), and required a visual comparison of T1 slices against a template using the Minctool *register* (Janke and Fonov, 2012). Although the protocol achieved good consistency of ratings between two expert users (kappa = 0.72), it was time consuming and hard to teach. We then switched from an interactive brain viewer to a static mosaic comprised of 9 different slices (3 axial, 3 sagittal, 3 coronal, see **Figure 1B**), and we highlighted anatomical landmarks using a precomputed mask. These landmarks were selected because we expected all of them to align well in the case of a successful registration, and the precomputed mask served as an objective measure to decide on the severity of a misalignment. We established guidelines on how to rate a registered image on a three-level scale ("OK," "Maybe," or "Fail") using these landmarks. The new protocol limited the need for extensive training for new users and potentially reduced the subjectivity of decision, notably for edge cases. The following sections describe the details and the validation of the final protocol (brain slices, landmarks and rating guidelines).

Brain Slices

A mosaic view of nine brain slices was extracted from each registered brain. The *x*, *y*, and *z* coordinates, corresponding to axial, coronal and sagittal views, were as follows:

x (sagitai)	*y* (coronal)	*z* (axial)
−50	−65	−6
−8	−20	13
30	54	58

Two images were generated: one using the individual T1 image of a subject, after brain registration, and one using the MNI2009c MRI T1 template averaged from 152 adults after iterative non-linear registration (Fonov et al., 2011), see **Figure 1A**.

Anatomical Landmarks

Notable anatomical landmarks included the central sulcus, cingulate sulcus, parieto-occipital fissure, calcarine fissure, tentorium cerebelli, lateral ventricles, bilateral hippocampal formation and the outline of the brain (see **Figure 1B**). To highlight these landmarks, we hand-drew a red transparent outline inside the brain with the MRIcron drawing tool (Rorden, 2014) using the MNI 2009 gray matter atlas as a reference. For the outline of the brain, we substracted a 4-mm eroded brain mask (MNI2009c release) from a 4-mm dilated brain mask. This process resulted in a roughly 8-mm thick mask centered on the outline of the brain in template space. The landmark boundaries served as the "confidence interval" of acceptable registration. The width of this confidence interval was somewhat arbitrary, but critically helped raters to consistently assess what amount of misregistration was acceptable. The scripts to generate the mosaic brain images with highlighted landmarks have been made available in the GitHub repository[2].

Rating Guidelines

We instructed raters to focus on the brain structures within the red anatomical landmarks, comparing the individual brain, after registration, with the MNI 2009c template. The two images were presented superimposed with each other, and raters were able to flip manually or automatically between the individual and the template brain. For a given anatomical landmark, raters were asked to tag any part of the brain structure that fell outside of the anatomical landmark for the individual brain. The template acted as a reference for what the structure looked like, and where it was supposed to be. **Figure 1C** provides examples of acceptable and unacceptable registration of brain structures within the

[2]https://github.com/SIMEXP/brain_match

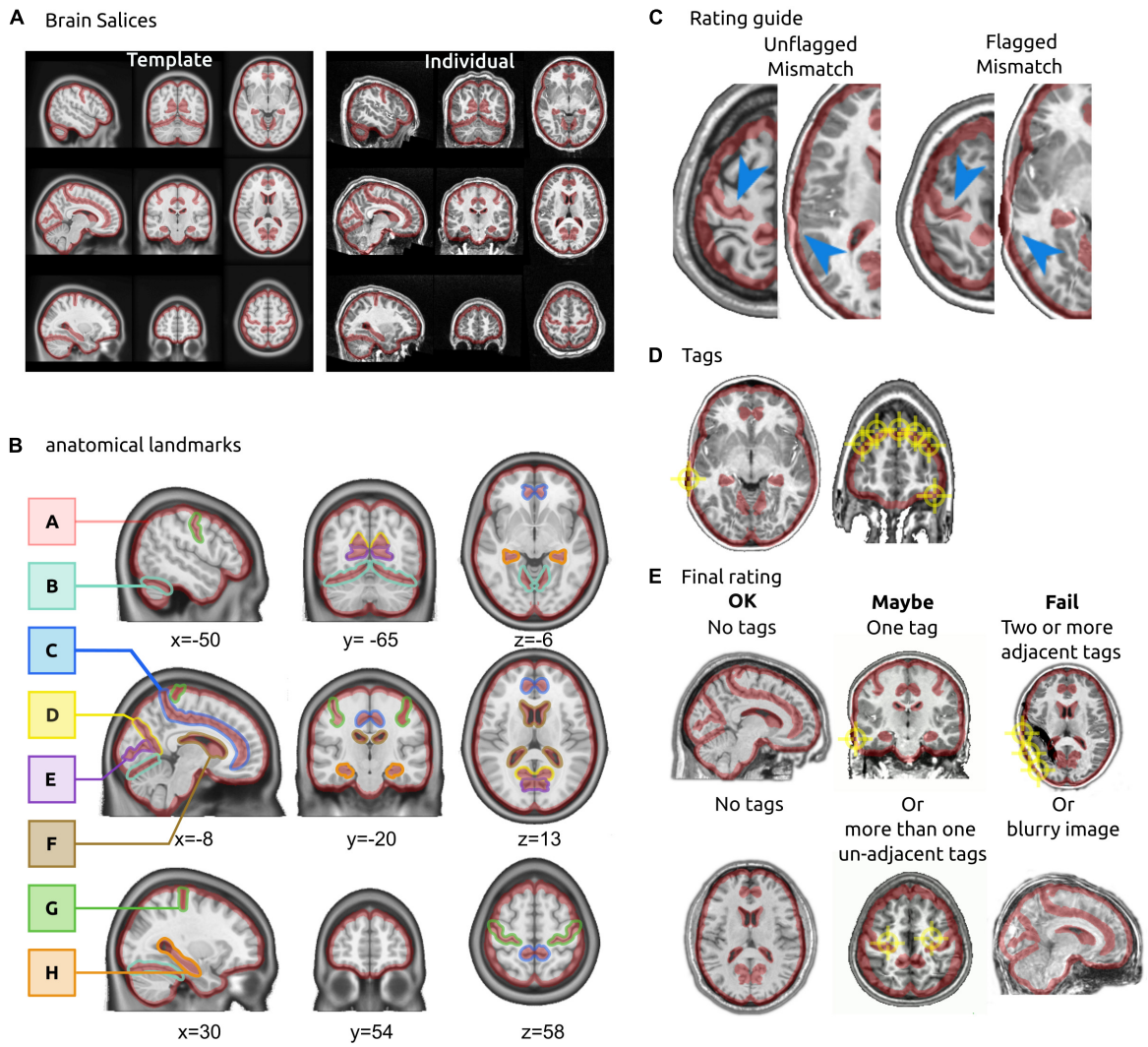


FIGURE 1 | QC protocol for brain registration. **(A)** Brain slices. The rater is presented with two sets of brain slices (3 axial, 3 sagittal and 3 coronal), one of them showing the template in stereotactic space and the other showing an individual T1 brain after registration. In the interface, the two images are superimposed and the rater can flip between them to visually assess the registration. **(B)** Anatomical landmarks. The landmarks for QC included: the outline of the brain (A), tentorium cerebelli (B), cingulate sulcus (C), parieto-cingulate sulcus occipital fissure (D), calcarine fissure (E), the lateral ventricles (F), central sulcus (G) and the hippocampal formation (H) bilaterally. The landmarks were outlined in stereotaxic space. **(C)** Rating guidelines. The boundaries of red landmarks act as "confidence interval" for registration: an area is tagged as a misregistration only if the target structure falls outside the boundaries. **(D)** Tags. Raters put tags on each misregistered brain structure. **(E)** Final rating. A final decision is reached on the quality of registration: an image with no tags is rated OK, one or more non-adjacent tags are rated Maybe, two or more adjacent tags are rated Fail. An image that is excessively blurry is also rated Fail.

landmarks. Raters were instructed to click all misregistered brain structures, which resulted in a series of tag spheres with 4 mm radius (**Figure 1D**). After an image was fully tagged, the overall registration quality was evaluated by the rater as follows:

- "OK" if no tag was reported,
- "Maybe" if one or several regions were tagged, yet no tag spheres overlapped (less than 8 mm apart),
- "Failed" if two tag spheres overlapped, meaning that an extensive brain area (>8 mm) was misregistered. Alternatively, a "Failed" rating was also issued if the entire image was of poor quality due to motion or a ringing artifact (**Figure 1E**).

Zooniverse Platform

We used the online citizen science platform Zooniverse (Simpson et al., 2014) as an interface to perform the validation of our QC protocol[3]. Zooniverse offers a web-based infrastructure for researchers to build citizen science projects that require a human visual inspection and possibly recruit a large number of zooniverse volunteers, who are not familiar with neuroimaging

[3]https://www.zooniverse.org/projects/simexp/brain-match

and have no formal requirements to participate (Franzoni and Sauermann, 2014; Simpson et al., 2014). Our project, called "Brain match" was developed with the support of the Zooniverse team, to ensure compliance with Zooniverse policies and appropriate task design for an online audience[4], and the project was also approved by our institutional review board. Note that the raters were considered part of the research team, and not participants of the research project, and thus they were not required to sign an informed consent form. The project underwent a "beta review" phase on zooniverse, where we collected feedback on the clarity and difficulty level of the task. Rating was performed by Zooniverse raters and expert raters. All ratings were performed on the zooniverse platform through the Brain Match dashboard[5]. The rating workflow was the same for the two types of types raters. Note that individuals participating in Zooniverse choose to voluntarily dedicate some of their time to science and thus do not constitute a representative sample of the general population.

Brain Images Validation and Training Sets

We used a combination of two publicly available datasets, COBRE (Mayer et al., 2013) and ADHD-200 (Bellec et al., 2017), for both the beta and the full launch of the project. These datasets have been made available after anonymization by consortia of research team, each of which received ethics approval at their local institutional review board, as well as informed consent from all participants. Each individual sMRI scan was first corrected for intensity non-uniformities (Sled et al., 1998) and the brain extracted using a region growing algorithm (Park and Lee, 2009). Individual scans were then linearly registered (9 parameters) with the T1 MNI symmetric template (Fonov et al., 2011). The sMRI scans were again corrected for intensity non-uniformities in stereotaxic space, this time restricted to the template brain mask. An individual brain mask was extracted a second time on this improved image (Park and Lee, 2009) and combined with template segmentation priors. An iterative non-linear registration was estimated between the linearly registered sMRI and the template space, restricted to the brain mask (Collins et al., 1994). The processed data were finally converted into mosaics and merged with a mask of anatomical landmarks using in-house scripts. Two expert raters (PB,YB) rated each 954 preprocessed images in ADHD-200, achieving a kappa of 0.72 (substantial agreement) from a random subset of 260 images. The COBRE dataset was rated by YB only.

On Zooniverse, raters were first invited to read a tutorial (**Supplementary Figure S2**) explaining the protocol, and then completed a QC training session, featuring 15 selected images (5 rated OK, 5 rated Maybe and 5 rated Fail, as rated by YB). Because the COBRE structural images were of higher quality, OK images were selected from COBRE while Maybe and Fail were selected from ADHD-200. For each training image, the rater was first asked to assess the image, and was then able to see the tags and the final ratings by an expert rater (YB).

After completing the training session, raters were presented a series of 100 "open label" cases, and were free to rate as many of these images as they wanted. We chose to present only 100 images in order to ensure we would have many ratings by different raters for each image, within a relatively short time frame. We arbitrary selected a subset of 100 images with a ratio of 35 Fail, 35 Maybe, and 30 OK images based on one expert rater (YB). Once again, the OK images were drawn from COBRE, while the Fail and Maybe were drawn from ADHD-200.

Raters

More than 2500 volunteers took part in our Brain Match project. They performed approximately 21,600 ratings of individual images over 2 beta-testing phases and two full workflows for a total of 260 registered brain images (see Brain images section). We used a retirement of 40 ratings, which means each image was rated by 40 different Zooniverse raters before being removed from the workflow. Only individuals who rated more than 15 images were kept in the final study. After data cleaning, 41 Zooniverse volunteer raters were kept. The distribution of rating per image showed a mean number of ratings of 21.76 ± 2.75 (see **Supplementary Figure S1**).

A group of 9 experts raters were also recruited for this study and each asked to rate all of the 100 validation images using the Brain Match interface. They were instructed to first start with the training session and to carefully read the tutorial before starting the main QC workflow. All raters had prior experience with QC of brain registration in the past. Each rater was free to perform the QC task at her pace without any specific direction on how to do it. The process was completed once all ratings were submitted.

Finally, a radiologist was also recruited for the study. He rated the same 100 images using Brain Match interface, also undergoing the training session before the rating process. Although the radiologist had no prior experience in QC of brain registration, that participant had very extensive experience in examining brain images following a standardized protocol, and served as a gold standard about what to expect from a fully compliant rater, trained on QC solely through available online documentation.

Agreement Statistics

We used Cohen's kappa (Cohen, 1960) to assess inter-rater reliability across all nine experts (ratings R1–R9). The kappa metric measures the agreement between two raters who rate the same amount of items into N mutually exclusives categories. The kappa is based on the difference between the observed agreement (p_o, i.e. the proportion of rated images for which both raters agreed on the category) and the probability of chance or expected agreement (p_e). Kappa (k) is computed as follows:

$$k = \frac{p_o - p_e}{1 - p_e}$$

In this work we used a weighted kappa metric, which assigns less weight to agreement as categories are further apart (Cohen, 1968). In our QC cases disagreements between OK and Maybe, and between Maybe and Fail count as partial

[4]https://www.zooniverse.org/lab-policies

[5]https://www.zooniverse.org/projects/simexp/brain-match

disagreements; disagreements between OK and Fail, however, count as complete disagreements. We used the R package irr (Gamer, 2012) to estimate the weighted kappa and Landis and Koch's (1977) interpretation of the strength of agreement for $\kappa \leq 0$ = poor, 0.01–0.20 = slight, 0.21–0.40 = fair, 0.41–0.60 = moderate, 0.61–0.80 = substantial, and 0.81–1 = almost perfect.

We also used the Sørensen–Dice coefficient (Dice) to assess the agreement within the rating categories of OK, Maybe and Fail (Sørensen et al., 1948), as follows:

$$DSC = \frac{2\left|X \bigcap Y\right|}{|X| + |Y|}$$

where X is the set of images rated "OK" by one rater and Y is the set of images rated "OK" by a second rater, $\bigcap$ is the intersection between two sets, and $|X|$ is the number of images. In plain English, the Dice between two raters for the OK category is the number of images that both raters rated "OK," divided by the average number of images rated "OK" across the two raters. The same Dice measure was generated as well for "Maybe" and "Fail" images. We interpreted Dice coefficients using the same range of strength of agreement as for the Kappa coefficient ($\leq$0 = poor, 0.01–0.20 = slight, 0.21–0.40 = fair, 0.41–0.60 = moderate, 0.61–0.80 = substantial, and 0.81–1 = almost perfect).

Consensus Panels

We also evaluated the reliability of QC ratings after pooling several raters into a consensus panel. The panel consensus was generated by counting the number of OK, Maybe and Fail attributed to an image from different raters (number of votes). The category with the highest vote count was selected as the consensus on that specific image for the panel. If there was a tie between 2 or 3 categories, the worst category was selected (Fail < Maybe < OK).

We tested different panel configurations, large and small, for expert and Zooniverse raters separately. Large panels were composed either by all 9 experts (panel Ec) or 41 Zooniverse users (panel Zc). We compared the agreement between Ec and Zc versus each individual expert rater (R1 to R9) as well as the ratings from the radiologist (Ra). For small panel, experts were arbitrarily split into three panels of three raters (panels Ec1, Ec2, and Ec3). The Zooniverse users were also arbitrarily split into two independent consensus panels of roughly equal size (Zc1 and Zc2). We quantified the agreement between small panels, as well as small vs. large panels.

RESULTS

Expert Raters Achieved Moderate Agreement, With "Fail" Rating Being the Most Reliable

Kappa agreement between expert raters across the three classes (OK, Maybe, Fail) was moderate to substantial (range 0.4–0.68, average of 0.54 $\pm$ 0.08), see **Figure 2**. However, there were marked differences in agreement across the three rating classes. The highest reliability was for "Fail," with between-rater Dice agreement ranging from substantial to almost perfect (0.67–0.93, average of 0.8 $\pm$ 0.06). The second class in terms of reliability was "OK," with Dice ranging from fair to strong (0.38–0.76), and the least reliable class was "Maybe," with Dice agreements ranging from slight to strong (0.23–0.72).

Large Panel of Experts or Zooniverse Raters Give Convergent, Reliable QC Ratings

We found that the kappa between Ec and individual expert raters was, as expected, improved over comparison between pairs of individual experts, with a range from moderate to strong (0.56–0.82), see **Figure 3**. As observed before, the Dice scores for Ec were highest in the "Fail" category (almost perfect agreement, range of 0.76–0.98), followed by the "OK" category (from substantial to almost perfect: range 0.66–0.85) and finally "Maybe" (fair to almost perfect, ranging from 0.38 to 0.8). These findings confirmed our previous expert inter-rater analysis, with "Fail" being a reliable rating, "Maybe" being a noisy rating, and "OK" being a moderately reliable rating. When comparing the individual experts with the Zooniverse panel Zc, we only observed a slight decrease in average Kappa compared with the Expert panel (0.61 for Zc vs. 0.7 for Ec), mostly driven by the "Fail" (0.82 for Zc vs. 0.88 for Ec) and "Maybe" (0.58 for Zc vs. 0.68 for Ec) ratings. When directly computing the agreement between the two consensus ranels Ec and Zc, the kappa was substantial (0.76), with almost perfect agreement for "Fail" (Dice 0.9) and "OK" (0.82), and substantial agreement for "Maybe" (0.77), see **Figure 3**. This comparison demonstrated that aggregating multiple ratings improved the overall quality, and that expert and zooniverse raters converged to similar ratings. The radiologist achieved a level of agreement with panels similar to what was observed with expert raters, and was substantially lower than the agreement between panels. This shows that the QC training material alone was enough for a radiologist to agree with QC experts, but a single user can likely not achieve high quality QC ratings by herself.

Small Consensus Panels of Expert (N = 3) or Zooniverse (N = 20) Raters Achieve Reliable QC Ratings

Once we established that large panels of raters lead to high levels of agreements, our next question was to determine whether small panels could also lead to reliable assessments. The small expert panels Ec1-3 reached lower agreement with Zc than the full Ec. Specifically, kappa was 0.64, 0.64, and 0.73 for Ec1 to Ec3 (with respect to Zc), compared to kappa of 0.76 for Ec vs. Zc. Similar observations were done when breaking down the comparison per category with Dice, with a decrease of 5% to 10% in this coefficient (see **Figure 4**). Comparing small zooniverse panels Zc1-2 with the full expert panel Ec, a slight decrease in reliability was observed, very similar in magnitude with comparisons between Ec1-3 and Zc. The agreements Ec1-3 vs. Zc, as well as Zc1-2 vs. Ec, remained substantial. This suggests that reliable three-level QC assessments can be performed by small panels of

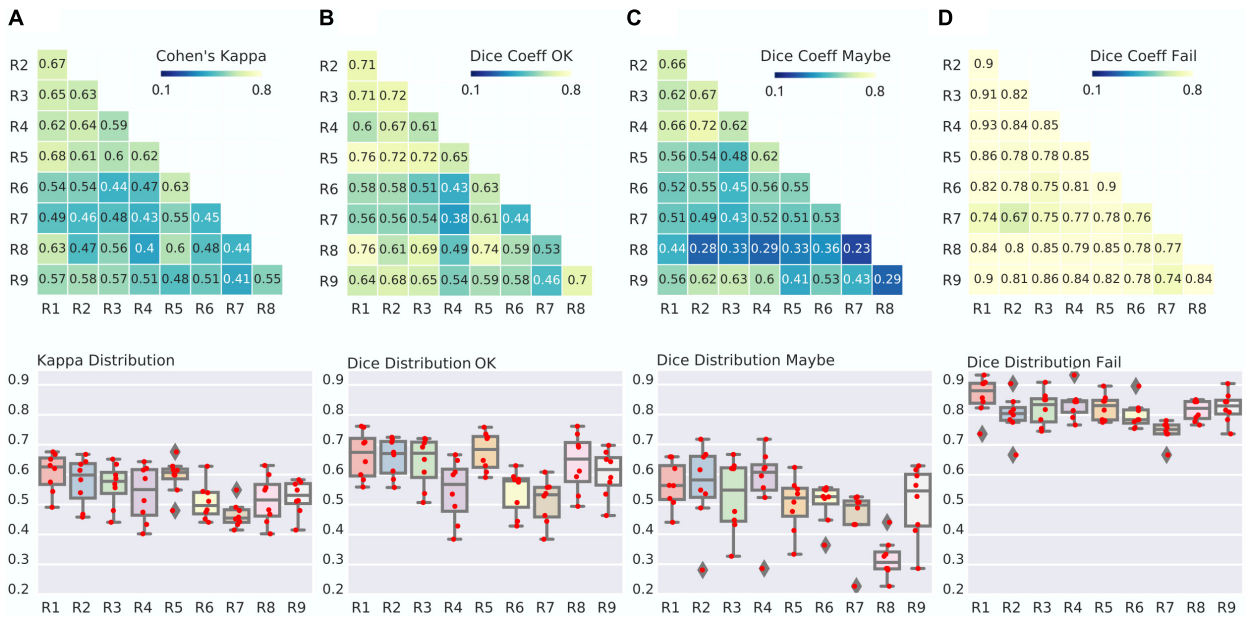


FIGURE 2 | Between-expert agreement. **(A)** Matrix of Kappa agreement between raters (top). Note that R1 to R9 are identification codes for the different expert raters. The distribution of agreement is also presented (bottom). For example, the boxplot for R1 shows the agreement between R1 and R2-R9. **(B–D)** Matrix and distribution for the Dice agreement between raters in the OK **(B)**, Maybe **(C)**, and Fail **(D)** categories.

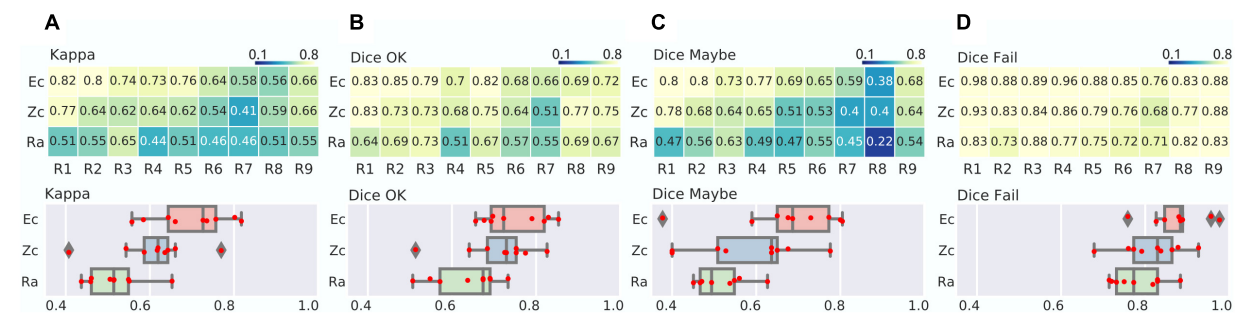


FIGURE 3 | Zooniverse, expert and radiologist agreements. **(A)** Matrix of Kappa agreement between consensus of experts (Ec), zooniverse users (Zc) and radiologist (Ra) raters, in rows, vs. individual experts (R1–R9), in column (top). The distribution of agreement is also presented (bottom). **(B–D)** Matrix and distribution for the Dice agreement in the OK **(B)**, Maybe **(C)**, and Fail **(D)** categories.

three experts ($n = 3$), or moderate panels of zooniverse users, with roughly 20 assessments by image (see **Supplementary Figure S1** for distribution).

DISCUSSION

This project proposes a standardized QC protocol with minimal training overhead and no required knowledge of brain anatomy. Our goal was to quantify the reliability of QC ratings between expert raters, as well as panels of expert or Zooniverse raters. Overall, our results demonstrated that our protocol leads to good reliability across individual expert raters, in particular for "Fail" images, and good reliability across panels of raters (both experts and Zooniverse), even for panels featuring only three experts. To our knowledge, this is the first quantitative assessment of between-rater agreement on QC of brain registration.

Visual QC

Our protocol was designed to be simple enough that even a rater without brain anatomy knowledge or prior QC experience could generate meaningful ratings. The mosaic view of 9 slices used in our protocol is similar to display images used in fMRI preprocessing tools like MRIQC (Esteban et al., 2017), fMRIPrep (Esteban et al., 2018) or CONN (Whitfield-Gabrieli and Nieto-Castanon, 2012). These QC tools also use an overlay that highlights brain borders or tissues segmentation. Differentiating aspects of our protocol are (1) fewer number of brain slices in the mosaic view, so that raters can more easily examine all presented images and (2) the overlay provides an objective

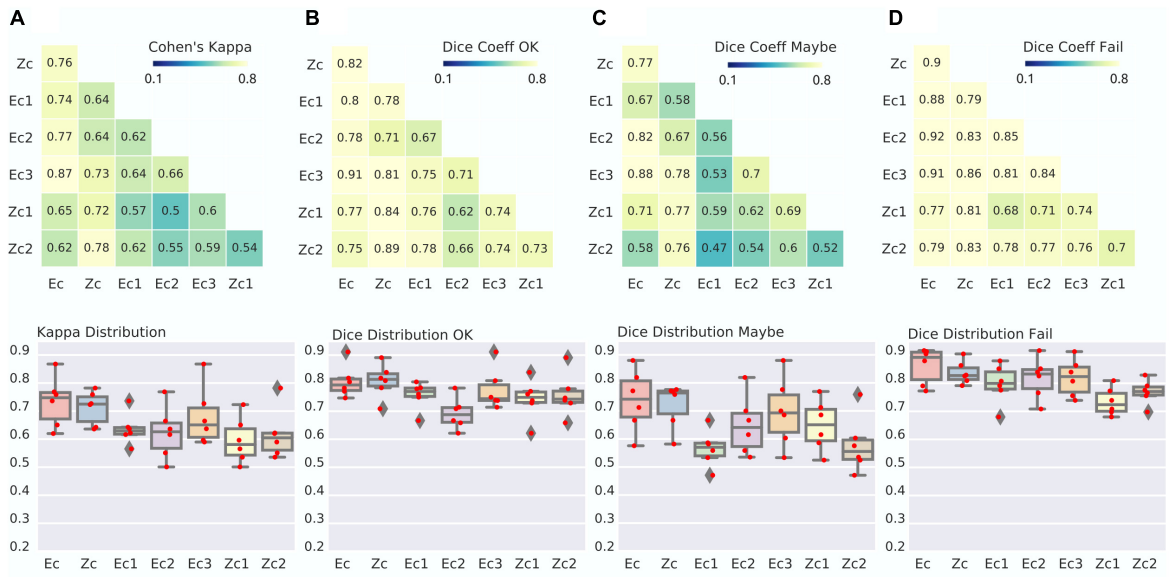


FIGURE 4 | Agreement between small panels of raters for both experts and Zooniverse panels. **(A)** Matrix of Kappa agreement between large panel consensus of experts (Ec), zooniverse users (Zc) and a small panel of expert (Ec1 = 3 rater, Ec2 = 3 rater, Ec3 = 3 rater) and small panel of Zooniverse raters (Zc1 = 20 rater, Zc2 = 21 rater) (top). The distribution of agreement is also presented (bottom). **(B–D)** Dice distribution between group consensus in the OK **(B)**, Maybe **(C)**, and Fail **(D)** categories.

confidence interval to assess the severity of misregistration in key anatomical landmarks. We believe that these two design principles helped reduce the subjectivity of brain registration QC, and increase between-rater agreement, although we did not formally test these hypotheses.

Inter-Rater Agreement

Table 1 shows that the visual QC agreement reported in recent studies ranged from 0.39 to 0.9. Interestingly, the studies which reached high levels of agreement (0.93–0.96) used ratings with only two levels (ex: pass, fail). Studies with three or more rating levels reported lower agreement scores (0.39–0.85), which were in line with our findings (average of 0.54 for experts). The most challenging rating in our protocol appeared to be the "Maybe" class, featuring mild, spatially limited registration errors. In contrast, good and failed registrations were easily detectable by expert raters. When working with three levels of ratings, the reliability of our protocol is not high enough to work with a single rater. We found that a consensus panel of three experts was sufficient to reach a good level of agreement (average of 0.64), which appears as a minimum panel size to generate high quality QC scores. Aggregating rating between expert or non-expert is a good solution to overcome the variability among human observers on the QC task.

Crowd Sourced QC

Crowdsourcing QC rating could be one solution to generate high quality QC ratings in big datasets like the UK biobank (Alfaro-Almagro et al., 2018). A recent work from Keshavan et al. (2018) showed that crowdsourced QC ratings on raw brain images can reach the performance of an automated state-of-the-art machine learning QC tool (Esteban et al., 2017). This work relied on a large pool (N = 261) of participants, many of whom had prior experience in neuroimaging. We recruited more than 2000 zooniverse non-expert raters, and found that a consensus panel of non-experts with adequate size (about 40 ratings per image) leads to QC ratings of similar quality to a panel of three experts.

Limitations of the Study

Our study has a number of limitations. First, our protocol is intended to be used with anatomical brain registration in the context of fMRI analyses in volumetric space, rather than surface. Structural brain imaging studies (i.e. cortical thickness) or surface-based fMRI analyses need other protocols that examine more closely fine anatomy and tissue segmentation. Also, our primary use case is large-scale research studies, and not clinical applications. Some clinical applications may require more stringent standards being applied on brain registration. Our protocol was validated with a specific brain registration tool, the CIVET pipeline, and may not be well suited for other algorithms.

Second, we did not control for screen size, screen resolution or fidelity of color representations in our validation, be it with experts or zooniverse individuals. The main use case for our protocol is the review of thousands of brain registration [e.g. in the ABCD sample (Casey et al., 2018)] in a relatively short span of time. The quality control procedure only examines coarse anatomical landmarks, and the required precision of the alignment is on the order of couple of millimeters. For that reason, we think that the characteristics of the screen will not affect significantly between-rater agreement. This is however a potential source of variations which may have decreased the observed agreement, both between experts and zooniverse raters.

Third, The success rate of our registration tool varies widely as a function of the imaging protocol. The Cobre dataset has almost only OK registration, while the ADHD has a lot of Maybe and some Fail. So we decided to mix two dataset, in order to assemble representative examples of the three classes. This may influence the results by increasing the potential agreement, if subjects learned to recognize which datasets the examples originated from.

Fourth, our choice on the number of rated images ($N = 100$) was selected arbitrarily. We checked the appropriateness of that choice by assessing the minimum number of rated cases with a three-choice decision using the R package "irr" (Gamer, 2012), that uses the minimum sample size estimation formula from Flack et al. (1988). We estimated the minimum sample size under the following scenario. The vector of marginal probability was given by rates for the 3 categories, OK = 0.3, Maybe = 0.35 and Fail = 0.35. These marginal probabilities were decided by our team when designing the dataset, based on an initial QC assessment performed by YB and PB. The value of kappa under the null hypothesis was set equal to 0.5 (k0 = 0.5) – i.e. we want to demonstrate an improvement over a baseline κ of 0.5. The true kappa statistic estimated between two expert was set equal to 0.72 (k1 = 0.72), as was observed in our sample. The type I error test was set equal to 0.05 ($\alpha = 0.05$). The desired power to detect the difference between the true kappa and the null kappa was investigated at 0.8 and 0.9, separately. The required number of ratings was estimated at $N = 54$ for a power of 0.8, and $N = 72$ for a power of 0.9. In our case, the number of images rated per expert was $N = 100$, which is more than required by the power analysis.

Fifth, We were unable to assess to what degree this protocol improves or not over current best practices in the fMRI community, in the absence of other standardized protocols available for comparison. We still produced preliminary evidence while developing the current protocol. During the beta phase of our project, we tested the agreement between consensus of Zooniverse raters and experts raters (on 29 images). The protocol used during that phase was different from the actual one. In particular, we did not instruct raters on how to take the final decision on the quality of registration (**Figures 1C–E**), and we did not offer a training set. The kappa measure between consensus Zooniverse raters and an expert during phase 1 was 0.34, by contrast with 0.61 using the current protocol. We regard these results as preliminary evidence that our protocol improves over our previous iteration. These results are to be interpreted with caution, as the number of images rated was low and we used only one expert rating. Note that the feedback received by beta testers helped us identify the importance of steps described in **Figures 1C–E**, and we suspect that protocols that do not include such detailed explanation have poor reliability. But we did not attempt to demonstrate this formally within the scope of the present study.

Finally, our protocol is missing an evaluation of another key registration step, i.e. alignment between functional images and the structural scan (Calhoun et al., 2017). We are currently working on an extension of our protocol for functional registration.

Future Work: Impact of QC on Downstream Analyses

Despite the ubiquity of visual brain registration QC in the neuroimaging research community, the impact of visual QC of brain registration on statistical analyses remains poorly characterized. Gilmore et al. (2019) used a multi-site dataset of structural MRI images with different age ranges to show how automated image quality metrics impacted regional gray matter volumes and their relationship with age. Ducharme et al. (2016) showed a significant impact of visual QC on the estimation of cortical trajectories. They demonstrated that, when omitting to discard subjects that did not pass QC, the developmental trajectory of cortical thickness followed a quadratic or cubic trend. By contrast, after filtering those subjects, the trajectory followed a linear trend. Standardizing the QC protocol will allow different laboratories to join their effort of rating and open up new opportunities to systematically investigate the impact of visual QC on the relationship between the brain and various phenotypes. This represents an important area of future work for brain registration.

CONCLUSION

Our QC protocol is the first reliable visual protocol for brain registration in fMRI studies. The protocol is easy to implement and requires minimum training effort. This protocol demonstrates a good reliability when performing a two level assessment (Fail vs. OK/Maybe) by an individual rater, or aggregating multiple three-level ratings (OK, Maybe, Fail) from a panel of experts (3 minimum) or non-experts (15 minimum). The images necessary to apply the protocol can be generated using an open-source tool, called dashQC_fmri (Urchs et al., 2018) and a live version can be tested on this link https://simexp.github.io/dashQC_BrainMatch/index.html. We hope this new protocol will help standardize the evaluation and reporting of brain registration in the fMRI community. This standardization effort will also enable the generation of high quality QC ratings on large amounts of data, which will in turn allow to train machine learning models to automatically perform brain registration QC, alleviating the need for visual review.

DATA AVAILABILITY STATEMENT

The datasets generated for this study are available on request to the corresponding author.

ETHICS STATEMENT

The studies involving human participants were reviewed and approved by the Comité d'éthique de la recherche vieillissement-neuroimagerie. Written informed consent for participation was not required for this study in accordance with the national legislation and the institutional requirements.

AUTHOR CONTRIBUTIONS

YB, AB, SU, HS, and PB contributed to the conception, revision, and design of the QC protocol. YB, SU, and PB generated and reviewed code for the study. YB, JA, and SU developed the QC interface. TO performed the rating as gold standard. All authors contributed to the manuscript revision, read, and approved the submitted version.

FUNDING

YB, AB, and PB are currently supported by the Canadian Consortium on Neurodegeneration in Aging (CCNA) and the Courtois NeuroMod Foundation. AB is currently supported by a CIHR Postdoctoral Fellowship (funding reference number #152548). At the start of the project AB was supported by the Alzheimer Society of Canada Postdoctoral Fellowship. PB is a Research Scholar from the Fonds de Recherche du Québec.

ACKNOWLEDGMENTS

We would like to acknowledge the following people for their contributions to the project. The nine expert raters: Perrine Ferre, Angela Tam, Jeni Chen, Cole Zweber, Carolina Makowski, Elizabeth DuPre, and Paule Joanne Toussaint. We also thank Andrew Doyle, Sara Dupont, Benjamin De Leener, and Maxime Pelland for their contribution on the beta testing phase. We would also like to thank the Zooniverse team, especially Laura Trouille, for their feedback and support along the process. Finally, we thank all the citizen-scientist on Zooniverse who participated in our project Brain Match. We are very grateful for your contributions.

SUPPLEMENTARY MATERIAL

The Supplementary Material for this article can be found online at: https://www.frontiersin.org/articles/10.3389/fninf.2020.00007/full#supplementary-material

REFERENCES

Alfaro-Almagro, F., Jenkinson, M., Bangerter, N. K., Andersson, J. L. R., Griffanti, L., Douaud, G., et al. (2018). Image processing and quality control for the first 10,000 brain imaging datasets from UK Biobank. *NeuroImage* 166, 400–424. doi: 10.1016/j.neuroimage.2017.10.034

Ashburner, J. (2007). A fast diffeomorphic image registration algorithm. *NeuroImage* 38, 95–113. doi: 10.1016/j.neuroimage.2007.07.007

Avants, B. B., Tustison, N., and Song, G. (2009). Advanced normalization tools (ANTS). *Insight J.* 2, 1–35.

Backhausen, L. L., Herting, M. M., Buse, J., Roessner, V., Smolka, M. N., and Vetter, N. C. (2016). Quality control of structural MRI images applied using FreeSurfer-a hands-on workflow to rate motion artifacts. *Front. Neurosci.* 10:558. doi: 10.3389/fnins.2016.00558

Bellec, P., Chu, C., Chouinard-Decorte, F., Benhajali, Y., Margulies, D. S., and Craddock, R. C. (2017). The neuro bureau ADHD-200 preprocessed repository. *NeuroImage* 144(Pt B), 275–286. doi: 10.1016/j.neuroimage.2016.06.034

Calhoun, V. D., Wager, T. D., Krishnan, A., Rosch, K. S., Seymour, K. E., Nebel, M. B., et al. (2017). The impact of T1 versus EPI spatial normalization templates for fMRI data analyses. *Hum. Brain Mapp.* 38, 5331–5342. doi: 10.1002/hbm.23737

Cardamone, C., Schawinski, K., Sarzi, M., Bamford, S. P., Bennert, N., Urry, C. M., et al. (2009). Galaxy zoo green peas: discovery of a class of compact extremely star-forming galaxies. *Mon. Not. R. Astron. Soc.* 399, 1191–1205. doi: 10.1111/j.1365-2966.2009.15383.x

Casey, B. J., Cannonier, T., Conley, M. I., Cohen, A. O., Barch, D. M., Heitzeg, M. M., et al. (2018). The adolescent brain cognitive development (ABCD) study: imaging acquisition across 21 sites. *Dev. Cogn. Neurosci.* 32, 43–54. doi: 10.1016/j.dcn.2018.03.001

Cohen, J. (1960). A coefficient of agreement for nominal scales. *Educ. Psychol. Meas.* 20, 37–46. doi: 10.1177/001316446002000104

Cohen, J. (1968). Weighted kappa: nominal scale agreement provision for scaled disagreement or partial credit. *Psychol. Bull.* 70, 213–220. doi: 10.1037/h0026256

Collins, D. L., and Evans, A. C. (1997). Animal: validation and applications of nonlinear registration-based segmentation. *Intern. J. Pattern Recognit. Artif. Intell.* 11, 1271–1294. doi: 10.1142/s0218001497000597

Collins, D. L., Neelin, P., Peters, T. M., and Evans, A. C. (1994). Automatic 3D intersubject registration of MR volumetric data in standardized Talairach space. *J. Comput. Assist. Tomogr.* 18, 192–205. doi: 10.1097/00004728-199403000-00005

Dadar, M., Fonov, V. S., Collins, D. L., and Alzheimer's Disease Neuroimaging Initiative, (2018). A comparison of publicly available linear MRI stereotaxic registration techniques. *NeuroImage* 174, 191–200. doi: 10.1016/j.neuroimage.2018.03.025

Ducharme, S., Albaugh, M. D., Nguyen, T.-V., Hudziak, J. J., Mateos-Pérez, J. M., Labbe, A., et al. (2016). Trajectories of cortical thickness maturation in normal brain development–the importance of quality control procedures. *NeuroImage* 125, 267–279. doi: 10.1016/j.neuroimage.2015.10.010

Esteban, O., Birman, D., Schaer, M., Koyejo, O. O., Poldrack, R. A., and Gorgolewski, K. J. (2017). MRIQC: advancing the automatic prediction of image quality in MRI from unseen sites. *PloS One* 12:e0184661. doi: 10.1371/journal.pone.0184661

Esteban, O., Blair, R., Markiewicz, C. J., Berleant, S. L., Moodie, C., Ma, F., et al. (2018). *Fmriprep*. doi: 10.5281/zenodo.1897231 (accessed December, 2018).

Esteban, O., Markiewicz, C. J., Blair, R. W., Moodie, C. A., Isik, A. I., Erramuzpe, A., et al. (2019). fMRIPrep: a robust preprocessing pipeline for functional MRI. *Nat. Methods* 16, 111–116. doi: 10.1038/s41592-018-0235-4

Flack, V. F., Afifi, A. A., Lachenbruch, P. A., and Schouten, H. J. A. (1988). Sample size determinations for the two rater kappa statistic. *Psychometrika* 53, 321–325. doi: 10.1007/bf02294215

Fonov, V., Dadar, M., The Prevent-Ad Research Group, and Louis Collins, D. (2018). Deep learning of quality control for stereotaxic registration of human brain MRI. *bioRxiv* [Preprint]. doi: 10.1101/303487

Fonov, V., Evans, A. C., Botteron, K., Almli, C. R., McKinstry, R. C., Collins, D. L., et al. (2011). Unbiased average age-appropriate atlases for pediatric studies. *NeuroImage* 54, 313–327. doi: 10.1016/j.neuroimage.2010.07.033

Fonov, V. S., Evans, A. C., McKinstry, R. C., Almli, C. R., and Collins, D. L. (2009). Unbiased nonlinear average age-appropriate brain templates from birth to adulthood. *NeuroImage* 47:S102. doi: 10.1016/j.neuroimage.2010.07.033

Franzoni, C., and Sauermann, H. (2014). Crowd science: the organization of scientific research in open collaborative projects. *Res. Policy* 43, 1–20. doi: 10.1016/j.respol.2013.07.005

Gamer, M. (2012). *Irr (Version 0.84.1) [Linux]*. Available online at: https://www.rdocumentation.org/packages/irr/versions/0.84.1(accessed September, 2016).

Gilmore, A., Buser, N., and Hanson, J. L. (2019). Variations in structural MRI quality impact measures of brain anatomy: relations with age and other sociodemographic variables. *bioRxiv* [Preprint]. doi: 10.1101/581876

Glasser, M. F., Smith, S. M., Marcus, D. S., Andersson, J. L. R., Auerbach, E. J., Behrens, T. E. J., et al. (2016). The human connectome project's neuroimaging approach. *Nat. Neurosci.* 19, 1175–1187. doi: 10.7554/eLife.38976

Howe, J. (2006). *The Rise of Crowdsourcing*. Available online at: https://sistemas-humano-computacionais.wdfiles.com/local--files/capitulo%3Aredes-sociais/Howe_The_Rise_of_Crowdsourcing.pdf (accessed May, 2019).

Janke, A., and Fonov, V. S. (2012). *Register (Version 1.4.00) [Linux]*. San Francisco, CA: Github.

Jenkinson, M., Beckmann, C. F., Behrens, T. E. J., Woolrich, M. W., and Smith, S. M. (2012). FSL. *NeuroImage* 62, 782–790. doi: 10.1016/j.neuroimage.2011.09.015

Keshavan, A., Yeatman, J. D., and Rokem, A. (2018). Combining citizen science and deep learning to amplify expertise in neuroimaging. *bioRxiv* [Preprint]. doi: 10.1101/363382

Khatib, F., DiMaio, F., Foldit Contenders Group, Foldit Void Crushers Group, Cooper, S., Kazmierczyk, M., et al. (2011). Crystal structure of a monomeric retroviral protease solved by protein folding game players. *Nat. Struct. Mol. Biol.* 18, 1175–1177. doi: 10.1038/nsmb.2119

Kim, J. S., Greene, M. J., Zlateski, A., Lee, K., Richardson, M., Turaga, S. C., et al. (2014). Space-time wiring specificity supports direction selectivity in the retina. *Nature* 509, 331–336. doi: 10.1038/nature13240

Klapwijk, E. T., van de Kamp, F., van der Meulen, M., Peters, S., and Wierenga, L. M. (2019). Qoala-T: a supervised-learning tool for quality control of FreeSurfer segmented MRI data. *NeuroImage* 189, 116–129. doi: 10.1016/j.neuroimage.2019.01.014

Landis, J. R., and Koch, G. G. (1977). The measurement of observer agreement for categorical data. *Biometrics* 33, 159–174.

Lintott, C. J., Schawinski, K., and Keel, W. (2009). Galaxy Zoo:'Hanny's Voorwerp', a quasar light echo? *Mon. Not. R. Astron. Soc.* 399, 129–140. doi: 10.1111/j.1365-2966.2009.15299.x

Mayer, A. R., Ruhl, D., Merideth, F., Ling, J., Hanlon, F. M., Bustillo, J., et al. (2013). Functional imaging of the hemodynamic sensory gating response in schizophrenia. *Hum. Brain Mapp.* 34, 2302–2312. doi: 10.1002/hbm.22065

Park, J. G., and Lee, C. (2009). Skull stripping based on region growing for magnetic resonance brain images. *NeuroImage* 47, 1394–1407. doi: 10.1016/j.neuroimage.2009.04.047

Pizarro, R. A., Cheng, X., Barnett, A., Lemaitre, H., Verchinski, B. A., Goldman, A. L., et al. (2016). Automated quality assessment of structural magnetic resonance brain images based on a supervised machine learning algorithm. *Front. Neuroinform.* 10:52. doi: 10.3389/fninf.2016.00052

Rorden, C. (2014). *MRIcron*. Available online at: https://www.nitrc.org/projects/mricron (accessed March, 2018).

Rosen, A. F. G., Roalf, D. R., Ruparel, K., Blake, J., Seelaus, K., Villa, L. P., et al. (2018). Quantitative assessment of structural image quality. *NeuroImage* 169, 407–418. doi: 10.1016/j.neuroimage.2017.12.059

Simpson, R., Page, K. R., and De Roure, D. (2014). "Zooniverse: observing the world's largest citizen science platform," in *Proceedings of the 23rd International Conference on World Wide Web*, New York, NY, 1049–1054.

Sled, J. G., Zijdenbos, A. P., and Evans, A. C. (1998). A nonparametric method for automatic correction of intensity nonuniformity in MRI data. *IEEE Trans. Med. Imaging* 17, 87–97. doi: 10.1109/42.668698

Sørensen, T. A., Sørensen, T., Sorensen, T., Sørensen, T. J., Sørensen, T. J., Biering-Sørensen, T., et al. (1948). *A Method of Establishing Groups of Equal Amplitude in Plant Sociology Based on Similarity of Species and its Application to Analyses of the Vegetation on Danish Commons*. Available online at: https://www.scienceopen.com/document?vid=fb7f6a95-4526-45b6-971d-e7b80e312998 (accessed March, 2017).

Urchs, S., Armoza, J., and Bellec, P. (2018). *dashQC: An Interactive Quality Control Dashboard — dashqc_fmri Alpha Documentation [Linux]*. Available online at: https://dashqc-fmri.readthedocs.io/en/latest/index.html (accessed December, 2019).

Wellcome Centre for Human Neuroimaging, (n.d.). *SPM12 – Statistical Parametric Mapping*. Available online at: https://www.fil.ion.ucl.ac.uk/spm/software/spm12/ (accessed April 19, 2019).

White, T., Jansen, P. R., Muetzel, R. L., Sudre, G., El Marroun, H., Tiemeier, H., et al. (2018). Automated quality assessment of structural magnetic resonance images in children: comparison with visual inspection and surface-based reconstruction. *Hum. Brain Mapp.* 39, 1218–1231. doi: 10.1002/hbm.23911

Whitfield-Gabrieli, S., and Nieto-Castanon, A. (2012). Conn: a functional connectivity toolbox for correlated and anticorrelated brain networks. *Brain Connect.* 2, 125–141. doi: 10.1089/brain.2012.0073

Yassine, B., and Pierre, B. (2016). *Quality Control and Assessment of the NIAK Functional MRI Preprocessing Pipeline*. London: Figshare. doi: 10.6084/m9.figshare.4204845.v1

Conflict of Interest: The authors declare that the research was conducted in the absence of any commercial or financial relationships that could be construed as a potential conflict of interest.

Copyright © 2020 Benhajali, Badhwar, Spiers, Urchs, Armoza, Ong, Pérusse and Bellec. This is an open-access article distributed under the terms of the Creative Commons Attribution License (CC BY). The use, distribution or reproduction in other forums is permitted, provided the original author(s) and the copyright owner(s) are credited and that the original publication in this journal is cited, in accordance with accepted academic practice. No use, distribution or reproduction is permitted which does not comply with these terms.

frontiers in Neuroinformatics

ORIGINAL RESEARCH
published: 10 March 2020
doi: 10.3389/fninf.2020.00008

Robust Monte-Carlo Simulations in Diffusion-MRI: Effect of the Substrate Complexity and Parameter Choice on the Reproducibility of Results

Jonathan Rafael-Patino[1]*, *David Romascano*[1], *Alonso Ramirez-Manzanares*[2], *Erick Jorge Canales-Rodríguez*[3,4,5], *Gabriel Girard*[1,3,6] and *Jean-Philippe Thiran*[1,3,6,7]

[1] Signal Processing Lab (LTS5), École Polytechnique Fédérale de Lausanne, Lausanne, Switzerland, [2] Computer Science Department, Centro de Investigación en Matemáticas, Guanajuato, Mexico, [3] Radiology Department, Centre Hospitalier Universitaire Vaudois, Lausanne, Switzerland, [4] FIDMAG Germanes Hospitalàries, Sant Boi de Llobregat, Barcelona, Spain, [5] Mental Health Research Networking Center (CIBERSAM), Madrid, Spain, [6] Centre d'Imagerie Biomédicale (CIBM), Lausanne, Switzerland, [7] University of Lausanne, Lausanne, Switzerland

Monte-Carlo Diffusion Simulations (MCDS) have been used extensively as a ground truth tool for the validation of microstructure models for Diffusion-Weighted MRI. However, methodological pitfalls in the design of the biomimicking geometrical configurations and the simulation parameters can lead to approximation biases. Such pitfalls affect the reliability of the estimated signal, as well as its validity and reproducibility as ground truth data. In this work, we first present a set of experiments in order to study three critical pitfalls encountered in the design of MCDS in the literature, namely, the number of simulated particles and time steps, simplifications in the intra-axonal substrate representation, and the impact of the substrate's size on the signal stemming from the extra-axonal space. The results obtained show important changes in the simulated signals and the recovered microstructure features when changes in those parameters are introduced. Thereupon, driven by our findings from the first studies, we outline a general framework able to generate complex substrates. We show the framework's capability to overcome the aforementioned simplifications by generating a complex crossing substrate, which preserves the volume in the crossing area and achieves a high packing density. The results presented in this work, along with the simulator developed, pave the way toward more realistic and reproducible Monte-Carlo simulations for Diffusion-Weighted MRI.

Keywords: diffusion, MRI, Monte-Carlo, simulations, microstructure, white matter

OPEN ACCESS

Edited by:
Alfred Anwander, Max Planck Institute for Human Cognitive and Brain Sciences, Germany

Reviewed by:
Pew-Thian Yap, University of North Carolina at Chapel Hill, United States
Michael Paquette, Max Planck Institute for Human Cognitive and Brain Sciences, Germany

***Correspondence:**
Jonathan Rafael-Patino
jonathan.patinolopez@epfl.ch

Received: *28 February 2019*
Accepted: *20 February 2020*
Published: *10 March 2020*

Citation:
Rafael-Patino J, Romascano D, Ramirez-Manzanares A, Canales-Rodríguez EJ, Girard G and Thiran J-P (2020) Robust Monte-Carlo Simulations in Diffusion-MRI: Effect of the Substrate Complexity and Parameter Choice on the Reproducibility of Results. Front. Neuroinform. 14:8. doi: 10.3389/fninf.2020.00008

1. INTRODUCTION

Diffusion-Weighted Magnetic Resonance Imaging (DW-MRI) is a non-invasive technique with enormous potential for the study of the brain's microstructure by measuring the diffusion properties of biological tissue. For instance, state-of-the-art methods can use these measurements to estimate tissue properties of the brain white matter, e.g., axonal diameter estimations (Assaf et al., 2008), orientation and volume fraction of the axonal bundles (Zhang et al., 2011; Daducci et al., 2015b) and neurite dispersion (Zhang et al., 2012). The previous information is valuable to understand the brain's maturation (Nilsson et al., 2012; Sexton et al., 2014) as well as the degeneration process associated with neuronal diseases like axonal degeneration (Lovas et al., 2000) and multiple sclerosis (Trapp et al., 1998).

In DW-MRI, an attenuated signal is usually recovered via a Pulsed Gradient Spin-Echo protocol (PGSE) (Stejskal and Tanner, 1965) sensitive to the displacement of the water molecules. Analytical solutions of the signal attenuation can be derived for simple geometrical shapes such as impermeable planes, cylinders, and spheres (Neuman, 1974). However, for applications where the signal attenuation of complex cellular structures or non-homogeneous media is needed, e.g., to generate ground truth data, an analytical solution is no longer feasible to pursue due to its inherent complexity. Because of this, simplifications of the diffusion media have been used as the backbone of most of the microstructure models in the literature (Bammer, 2003; Panagiotaki et al., 2012; Zhang et al., 2012; Ferizi et al., 2015).

Monte-Carlo Diffusion Simulations (MCDS) provide a fundamental approach to study the diffusion phenomena in scenarios where the analytical solutions cannot be computed due to their complexity. In contrast with other numerical methods, MCDS does not require an explicit model of the diffusion signal for a given geometry. Instead, MCDS require an accurate geometrical and physical representation of the diffusion media (called the substrate), a large number of samples, and an acquisition protocol like the classical Pulsed Gradient Spin-Echo (PGSE). In general, an accurate approximation of the diffusion signals, mimicking the ones obtained from the brain's white matter, can be computed if the substrate captures the relevant white matter microstructure features and the simulation parameters are tuned properly (number of samples and their step sizes). Despite this, many simplifications are usually used in order to decrease the computational burden. The most common ones include the use of substrates of small size, the use of a limited number of samples, the use of simple geometries, and the restriction of the 3D diffusion to the 2D case (Lipinski, 1990; Szafer et al., 1995; Fieremans et al., 2010; Dyrby et al., 2013).

Lipinski (1990) presented the first work, to the best of our knowledge, which employs MCDS to study the extracellular diffusion in brain tissue. In this work, 2D histological data was used to draw binary contours to be used as irregular intracellular barriers. From this study on, most studies simplified the representation of the extracellular space as a collection of restricted corridors in the orthogonal plane of the axonal direction and unrestricted parallel to them (Novikov et al., 2011; Dyrby et al., 2013; Sanguinetti and Deriche, 2014; Lin et al., 2016). In addition, the intracellular compartment is usually idealized as a collection of parallel hollow cylinders with constant radii or radii sampled from a distribution estimated from histological data (Fieremans et al., 2008; Hall and Alexander, 2009; Alexander et al., 2010; Raffelt et al., 2012). Recent studies have suggested that such simplification cannot capture the complexity of the axonal structures of white matter, and thus its diffusion characteristics (Nilsson et al., 2013; Ginsburger et al., 2018). For instance, changes in the diffusion signal and parameters derived from the diffusion tensor, such as the fractional anisotropy (FA) and mean diffusivity (MD), were obtained by introducing regular undulations in the intra-axonal compartment (Nilsson et al., 2012).

Because of the aforementioned problems, a number of works proposed experiments where non-trivial structures were used as intracellular substrates, e.g., dispersed axons (Ginsburger et al., 2018), the presence of abutting cylinders (Yeh et al., 2013) and arbitrarily generated meshes (Panagiotaki et al., 2010). However, to this day, such approaches have not been thoroughly adopted by the DW-MRI community because of the high computational burden they demand and the lack of available tools. Because of this, more realistic diffusion simulations remain virtually unexploited.

In this work, we study three important pitfalls encountered in the design of MCDS in the literature used to reduce the computational burden, namely the number of simulated particles and the number of time steps, the intracellular geometrical representation, and the generated extra-axonal space in terms of the substrate's size. Each experiment presented below illustrates a possible bias induced in the computed signal when such simplifications are not properly addressed, which affects its reproducibility. Finally, driven by the results from the previous experiments, we outline a general framework that can be used to generate complex substrates in order to overcome the limitations of previous studies.

2. THEORY

The obtained signal from a PGSE DW-MRI measurement, at a time t, is given by (Price, 1997)

$$S(t = TE) = S_0 \int P(\phi, t) e^{-i\phi} d\phi, \tag{1}$$

where S_0 denotes the signal obtained in the absence of a diffusion gradient magnetic field, TE is the echo time, $P(\phi, t)$ is the phase distribution function of the spin ensemble at time $t = TE$, and ϕ is the accumulated phase shift of the spin.

The amount of attenuation of a single diffusing spin on the measured PGSE signal is proportional to the dephasing due to the effect of the time-dependent magnetic field $G(t)$, and the spin's displacement. For a single spin and a given magnetic gradient vector, the phase shift due to the applied gradient over time can be numerically formulated as in Price (1997)

$$\phi(t) = a(t)\gamma G(t) \cdot x(t), \tag{2}$$

where γ is the gyromagnetic ratio, $G(t)$ is the applied magnetic diffusion gradient at time t, $x(t)$ is the spin's displacement from the starting position, and $a(t)$ is a function that shifts the sign of the gradient vector due to the refocusing Radio Frequency (RF) pulse. In a classic PGSE experiment: $a(t)$ is equal to $+1$ for all time t before the RF pulse and -1 after. The produced attenuated signal is then the result of the accumulated phase shift of the full assembly of spins at the TE, given by

$$S(t = TE)/S_0 = \left\langle e^{-i\int_0^{t=TE}\phi(t)dt'} \right\rangle. \tag{3}$$

2.1. Simulation Fundamentals

Equation (3) can be approximated using a finite number of spin samples N_s over a discrete time lapse, following an approach as in Szafer et al. (1995):

$$S/S_0 = \frac{1}{N_s}\sum^{N_s} e^{-i\sum_t^{Nt}\phi(t)dt}, \tag{4}$$

where dt is the step duration, defined as the total diffusion time divided by the number of steps taken (N_t). The value of dt can be fixed as in Hall and Alexander (2009) and Yeh et al. (2013) or normally distributed as in Balls and Frank (2009). In our exploration, we made use of fixed step sizes derived from Einstein's equation: $r = \sqrt{(6Ddt)}$, where D is the diffusion coefficient and r is the expected mean displacement. A fixed step size have been shown by Hall and Alexander (2009) to "reduce the fluctuation in the mean-square displacement of the spins and improve the convergence in the model." Moreover, Barlett et al. (2013) have shown the fixed step size to be better suited for non-homogeneous systems.

The idea behind a Monte-Carlo Diffusion Simulator is to compute Equation (4) by simulating the particles' Brownian motion and their interaction with respect to a defined substrate. At the beginning of the simulation, the particles are uniformly placed inside the defined substrate's voxel, or substrate's limits. This way, the number of particles in all compartments is proportional to the defined volume fractions. If necessary, the local position of each particle can be tracked to separate the signal contribution of each compartment by, for example, tracking if the particle is inside a given compartment. Over the duration of the simulation, the simulated particles collide and bounce with the substrate's barriers, depending on the barrier properties. Finally, the accumulated phase shift is tracked depending on the spin-echo protocol using Equation (4).

Overall, the formulation above presents an accurate numerical approximation of the diffusion signal based solely in the phase shift distribution. However, is worth noticing that many other effects such as noise levels or the magnetization relaxation should be considered in order to approximate a more realistic DWI-MRI signal.

3. MATERIALS AND METHODS

All the simulated signals presented below were computed using the sum of the accumulated phase shift approximation showed in Equation (4) implemented in an in-house Monte-Carlo simulator. The simulator employs a similar approach to compute the diffusion signal as the ones presented in Hall and Alexander (2009) and Yeh et al. (2013). The simulator uses a hybrid GPU/Multi-CPU framework, implemented in C++11. It includes routines to optimize the collision detection and the memory consumption based on the complexity analysis of **Appendix A**; making the software able to handle simulations of 3D meshed substrates with millions of triangles and particles. The simulator was initially validated by verifying that the generated signals from particles within impermeable planes, cylinders, and spheres were equal to those obtained from their corresponding analytical solutions. Moreover, results in more complex domains including the extra-axonal space of brain tissue, were comparable to those obtained from an alternative and independent Finite Element Method approach described in Rafael-Patino et al. (2017). The substrates' data, meshes, and the simulator are available from the corresponding author upon request on the paper's Git-Hub repository: (https://github.com/jonhrafe/Robust-Monte-Carlo-Simulations).

3.1. Confidence Level Estimation

In Monte-Carlo based methods, the number of samples is critical for the confidence level of the estimated results. However, the number of particles has the most significant impact on the computational burden. To highlight the importance of the number of simulated spins, an experiment was performed in order to quantify the variance of the estimated signal as a function of the number of particles sampled in a substrate. To do this, the errors of a set of simulated signals with different numbers of samples were measured. The measured errors were compared against the expected analytical solution in the intra-axonal space and for a gold-standard estimation of the extracellular space. A substrate with 10,000 parallel cylinders with diameters sampled from a Gamma distribution, $\Gamma(\kappa, \theta)$, with shape, $\kappa = 4.0$, and scale, $\theta = 4.5 \times 10^{-7}$, was used, resulting in a mean diameter $\mu = 1.8\,\mu$m with a standard deviation of $\sigma = 0.9\,\mu$m, using a packing algorithm as the one described in Hall and Alexander (2009), which results in a distribution of radii comparable to the ones found in the literature (Zhang et al., 2011; Dyrby et al., 2013; Benjamini et al., 2016).

This substrate was used since the analytical signal of the intra-axonal space can be computed using the volume-weighted sum of the individual signals:

$$S_i = \frac{v_1 Sc_{i,1} + \cdots + v_n Sc_{i,n}}{\sum v_j}, \tag{5}$$

where S_i is the *ith* acquisition, v_j is the volume of the *jth* cylinder and $Sc_{i,1}$ is the analytical signal of the cylinder obtained using the Gaussian Phase Distribution (GPD) approximation of the signal in cylinders for a given radius (Van Gelderen et al., 1994). **Figure 1** shows the resulting distribution of radii as well as the computed ground-truth intra-axonal signal. For the extracellular signal, as there is no analytical model, the gold-standard was estimated using a very high number of particles: 20×10^6 particles, and time-steps: 2×10^4 steps. These parameters were chosen based on previous results (Rafael-Patino et al., 2017) and by studying the convergence properties for higher numbers of particles and time-steps (Hall and Alexander, 2009). In fact, we verified that the signal converges for even less demanding simulation parameters (i.e., 1×10^6 particles, and 5×10^3 steps). In order to keep results as accurate as possible, however, we decided to use simulation parameters higher than the minimum required.

The estimated signals were computed varying the number of particles from 1×10^3 to 1×10^6 particles, and the time-steps from 1×10^2 to 2×10^4 steps. The diffusion coefficient

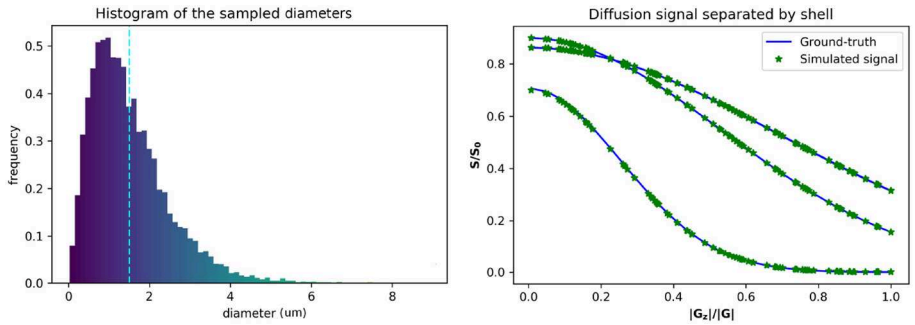


FIGURE 1 | Gamma distributed radii and corresponding intra-axonal diffusion signal. **(Left)** The distribution of the sampled diameters, the dotted line marks the sampled distribution mean. **(Right)** The computed ground-truth along with the simulated signal used for the intra-axonal space representation. A total of four curves are plotted corresponding to each *b*-value = 1925, 1932, 3093, and 13191 s/mm^2. The curves corresponding to a *b*-value = 1925 and 1932 s/mm^2 are completely overlapped and corresponds to the lowest decay. The signals of each shell are ordered by the normalized Z coefficient of the gradient direction.

was fixed to $D = 0.6 \times 10^{-3}\ mm^2/s$ (corresponding to an *ex-vivo* diffusivity), and TE = 0.054 s, for both, the simulations and the ground-truth data. The original optimized ActiveAx PGSE protocol (Alexander et al., 2010) was used, which consist of a four shell HARDI acquisition with 90 orientations per shell, each shell with the following parameters, respectively, (i) $b = 1,930\ s/mm^2$, $G = 140$ mT/m, $\delta = 0.010$ s, and $\Delta = 0.016$ s; (ii) $b = 1,930\ s/mm^2$, $G = 140$ mT/m, $\delta = 0.010$ s, and $\Delta = 0.016$ s; (iii) $b = 3,090\ s/mm^2$, $G = 131$ mT/m, $\delta = 0.007$ s, and $\Delta = 0.045$ s; (iv) $b = 13,190\ s/mm^2$, $G = 140$ mT/m, $\delta = 0.017$ s, and $\Delta = 0.035$ s. **Figure 1** shows the plot of a diffusion signal obtained with this protocol separated by shell and ordered with respect to the angle with the main fiber axis (Z-axis).

A bootstrapping analysis was performed to evaluate the variance of the error between the estimations with different samples sizes: 1×10^3, 2×10^3, 5×10^3, 1×10^4, 2×10^4, 5×10^4, 1×10^5, 2×10^5, 1×10^6, and 2×10^6 samples; and time-steps: 1×10^2, 5×10^2, 1×10^3, 5×10^3, 1×10^4, and 2×10^4. For each combination of the sample sized and time-steps, the signals from 50 repetitions were generated. The error between the ground-truth and each estimated signal was computed using the Relative Mean Absolute Error (RMAE), expressed as a percentage:

$$RMAE(S_{gt}, S_c) = \frac{100}{N_g} \sum_{i}^{N} \frac{|S_{gt}(i) - S_c(i)|}{|S_{gt}(i)|}, \tag{6}$$

where S_{gt} is the ground-truth signal, S_c is the estimated signal and N_g is the number of acquisitions. The result is a total of 50 estimated error points for each sample size.

3.2. Intra-Axonal Space Representation

In our second study, we look into the effect of using curved or angled geometries against straight cylinders as representations of the intra-axonal space. Such effect is of special interest on the computation of axonal diameter indexes when it is assumed that straight cylinders capture the diffusion properties of the intra-axonal compartment.

To understand this effect, an experiment extending the previous work from Nilsson et al. (2012) was performed, where the diffusion properties of undulating axonal substrates is studied. In our experiment, we quantified the difference on the diameter fitting estimation between parallel cylinders of constant radius and undulating cylindrical substrates.

To create curved cylindrical substrates for MCDS, a helical undulation parametrization along z was used

$$U(z) = \left(A_x cos(\frac{2\pi z}{L}), A_y sin(\frac{2\pi z}{L}), z \right), \tag{7}$$

where L is the wavelength and A_x, A_y denote the amplitude in the X and Y axis, respectively (Nilsson et al., 2012). The amplitudes Ax and Ay were set to be equal to obtain helical undulations. Using the formulation above, a set of substrates was created by deforming cylinders with diameters 1, 2, and 3 μm. The wavelength and amplitude of the undulations ranged from 4 to 32 μm and from 0.2 to 2.6 μm, respectively; which covers a range of values of interest in the literature (Haninec, 1986; Bain et al., 2004; Nilsson et al., 2012). The resulting undulating cylindrical shapes were triangulated to use them as mesh substrates suited for MCDS. **Figure 2** presents three different substrate examples.

To compute the diameter estimation error in the intra-axonal signal, a fitting procedure was performed using an exhaustive search approach. The exhaustive search computes the RMAE between the resulting simulated signal of each undulating substrate and the analytical signal of a range of cylinders with different diameters, sampled between 0.4 and 8 μm with a step size of 0.01 μm. The analytical signals were computed using the GPD approximation for the signal in cylinders (Van Gelderen et al., 1994). The fitting procedure returns the range of plausible diameters such that the computed error between them is below a given threshold. For each undulating substrate, the threshold was fixed to a 1% difference from the minimum fitting error, based on the results of the confidence study from section 4.1.

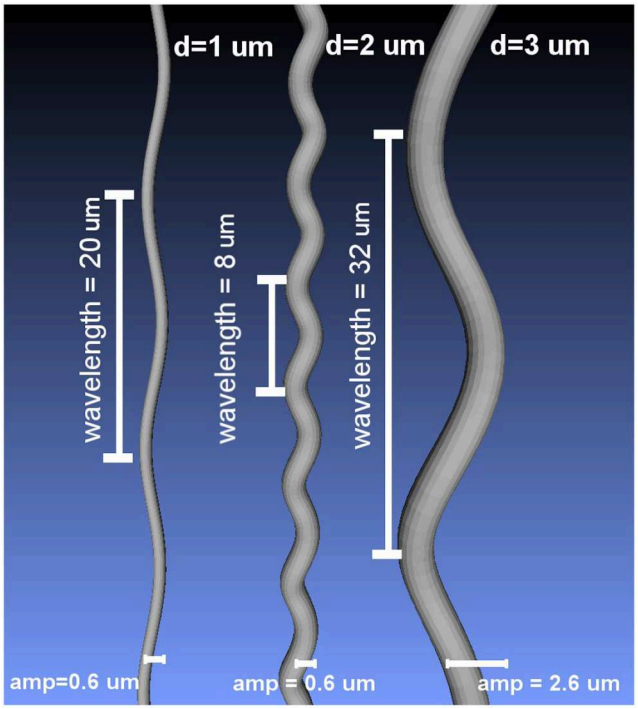


FIGURE 2 | Examples of the curved meshes used as intra-axonal substrates in this study, for three different diameters and different undulation parameters.

Two different acquisition protocols were used to perform the fitting procedure. First, the original *ex-vivo* ActiveAx PGSE protocol (Alexander et al., 2010) explained in section 3.1 was used. Second, we used an optimized PGSE protocol for *ex-vivo* axonal diameter estimation presented in Dyrby et al. (2013). The protocol consists of a three shell acquisition with 90 orientations per shell, and a $TE = 0.0359$ s. The relevant parameters of each shell are as follows, (i) $b = 2081\ s/mm^2$, $G = 300$ mT/m, $\delta = 0.0056$ s, and $\Delta = 0.0121$ s; (ii) $b = 3038\ s/mm^2$, $G = 219$ mT/m, $\delta = 0.007$ s, and $\Delta = 0.0204$ s; and (iii) $b = 9542\ s/mm^2$, $G = 300$ mT/m, $\delta = 0.0105$ s, and $\Delta = 0.0169$ s. Since the RMAE difference between cylinders of similar diameter depends on the protocol used an analysis of the sensitivity for each protocol was carried out.

Finally, the MC simulation parameters were chosen using a similar analysis as the one presented in section 3.1 (not shown). The confidence estimation was computed ranging the number of particles and time steps on the substrate with higher curvature (higher amplitude and smaller wavelength) and choosing a the parameters that shows almost no variance on the estimations. A total of 5×10^4 particles and 5×10^4 steps were chosen to compute the signal for each individual substrate separately.

3.3. Extra-Axonal Space Representation

In the case of macroscopically homogeneous substrates, e.g., with randomly packed cylinders and in absence of bundle dispersion, it has been shown that extra-axonal spins exhibit an effective diffusivity that can be described by an axi-symmetric tensor, if the volume size of the sample is high enough (Hrabe et al., 2004). Models to estimate white matter microstructure from DW-MRI therefore assume that the extra-axonal radial contribution does not change for any direction aligned to the bundle's perpendicular plane (Assaf et al., 2008; Alexander et al., 2010; Zhang et al., 2011, 2012; Panagiotaki et al., 2012; Daducci et al., 2015a; Benjamini et al., 2016).

Such an assumption seems to fit the validations. However, the importance of the design of the extra-axonal space has been underestimated in MCDS by assuming that substrates with any hindered configuration would match the model. To show the importance of the sample size, in terms of the number of cylinders used to construct a substrate, an analysis of the extra-axonal radial contribution in simulated signals was performed.

The radial extra-axonal DW-MRI signal was simulated for a selection of voxels with different numbers of cylinders, and a fixed distribution of diameters and intra-axonal volume fractions. To do so, N diameters ($N = 100, 1,000, 10,000, 50,000$ and $100,000$) were sampled from a gamma distribution with parameters $\Gamma(4.0, 4.5 \times 10^{-7})$, as in our first study. The corresponding cylinders were randomly positioned in substrates with voxel size adapted such that the intra-axonal volume fraction was 60% and ensuring periodicity at the voxel boundaries as is described in Hall and Alexander (2009). The extra-axonal signal was simulated with the following settings: 1×10^6 particles in the extra-axonal space with diffusivity of $0.6 \times 10^{-4}\ mm^2/s$, $TE = 0.075$ s, and 1×10^3 steps. This parameters where chooseng from the previous results showed in section 3.1. The diffusion protocol was set to highlight the radial contribution of the diffusion signal in different diffusion time regimes as follows: $G = 300$ mT/m, $\delta = 0.010$ s and Δ from 0.015 to 0.060 s, acquired in 180 directions evenly distributed over the xy-plane. The anisotropy of the simulated noiseless signal was quantified by computing the standard deviation of the signal divided by its mean, giving an estimate of how much the signal deviates from a perfectly radially isotropic signal.

3.4. Framework for Complex Substrates Generation

Driven by the results from the previous experiments, and based on a previously published algorithm to generate tractography phantoms (Close et al., 2009) the following section outlines a general framework in order to generate complex substrates. We show that such framework overcomes some of the simplifications presented in the previous sections. To illustrate such capabilities, a crossing of axons bundles was generated as a study case. A qualitative evaluation was performed over the representation of crossing fibers in terms of the resulting intra-axonal volume fraction and diffusion properties in different resolutions.

The framework is a tailored extension of the work presented in Close et al. (2009). The original framework is based in the optimization of a objective function that penalizes the overlap, curvature and length of a set of initial splines called as *strands*. Each strand has a constant radius used to ensure no overlapping. The optimization cost-function has the following form:

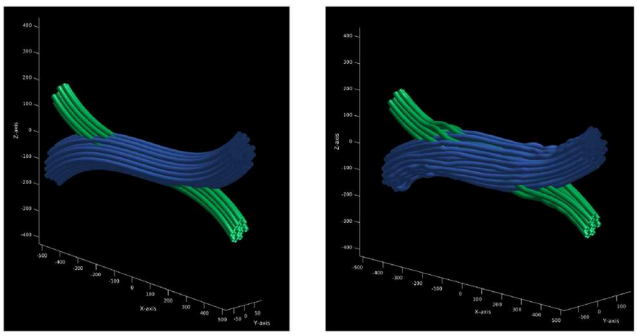


FIGURE 3 | Optimization procedure of initial trajectories. **(Left)** initial trajectories parametrized as a set of control points with constant radius. **(Right)** the resulting trajectories after the optimization procedure which ensures that there is no overlapping between the resulting strands.

$$E(\cup S) = \sum_{i}^{\#S} w_o J_o(S_i) + w_c J_c(S_i) + w_l J_l(S_i), \tag{8}$$

where the set $\cup S$ of size $\#S$, represents the set of all initialized strands. S_i represents the strand i for $i = 1, \cdots, \#S$. The functions $J_o(\cdot), J_c(\cdot), J_l(\cdot)$ are the overlap, curvature, and length penalization functions; and the coefficients w_o, w_c, and w_l are their, respectively, weights. Each strand S_i is parametrized using a discrete set of control points that define the backbone of the strand i and constant given radius; the transversal area associated with this radius is later subdivided to form sub-strands. Finally, the DW-MRI signal is then simulated by assigning a symmetric tensor along each sub-strand trajectory i.e., a simplistic local model of the micro-environment (Daducci et al., 2015b). The reader is referred to Close et al. (2009) for more details.

In our study, the aforementioned framework was modified and used to map a gamma distributed set of diameters inside the resulting strands' trajectories. The 3D-overlapping algorithm between strands implemented in the cost-function J_o, was also modified to make it more suitable for creating 3D meshes. This was done by computing the analytical intersection between two strands' control points, using the cylinder to cylinder collision detection described in Verth and Bishop (2008).

The result is a gamma distributed crossing configuration of deformed cylinders. The main advantage of this configuration is that the bundles inside a common area do not overlap or intersect, but interdigitate, which means that the volume is preserved in the crossing region. In addition, the curvature and length penalizations promotes a higher packing density. Finally, the proposed framework computes the DW-MRI signal by a Monte-Carlo simulation using a mesh substrate created from the configuration obtained above, instead of assigning a symmetric tensor along the sub-strands. **Figure 3** shows the crossing configuration before and after the optimization procedure.

In the presented study case, the diameters from a gamma distribution with parameters $\Gamma(1.2, 1.5 \times 10^{-6})$ were sampled, resulting in a mean diameter of $\mu = 1.8\,\mu$m and standard deviation $\sigma = 1.6\,\mu$m, which are in the range of anatomical interest (Alexander et al., 2010). The resulting values were truncated to avoid strands with diameters smaller than $0.2\,\mu$m. The dimensions of the resulting enclosing volume were $1{,}200 \times 240 \times 480\,\mu$m; the resulting 3D geometrical crossing is shown in **Figure 4**. The 3D mesh model consists of 1,698,328 triangular faces after a post-processing of decimation and smoothing to reduce the triangle density. The total length end-to-end of the most extended strand is 1.58 mm. The resulting diameter distribution of the overall structure is displayed in the bottom panel of **Figure 4**.

To compute the simulated MRI signal, the total volume was divided in three voxel resolutions: $80 \times 16 \times 32$, $40 \times 8 \times 16$, and $20 \times 4 \times 8$ voxels. A total of 105×10^6 particles, and 5,000 steps were used to compute the signal for the three resolutions. The original ActiveAx protocol (Alexander et al., 2010) from the first study was used with a diffusivity coefficient equal to 0.6×10^{-3} mm^2/s and a total diffusion time of 0.053 s.

To show qualitative results on the generated signals, the Diffusion Tensor (DT) estimation and the corresponding FA were computed using Dipy (Garyfallidis et al., 2014), as well as the ICVF maps for each of the three resolutions. Only the shell with $b = 3{,}080\ s/mm^2$ was used to compute the DT in each voxel. Given the lack of an analytic representation of the substrate, the ICVF was approximated by tracking the local position of the uniformly random located particles and labeling them as *inside* or *outside* the meshed substrate.

Finally, an evaluation of the axon diameter estimation within the crossing area was performed for the three different voxel resolutions. The axon diameter estimation was performed using the same exhaustive search method described in section 3.2. Only one single bundle orientation was used to compute the analytical GPD approximation; which was selected from the DT estimation at each voxel. The fitting procedure was performed using solely the intra-axonal signal and in voxels with FA greater than 0.25, in order to separate the effect of the extra-axonal space regarding the diameter mis-estimation.

4. RESULTS

4.1. Confidence Level Estimation

The overall results of the bootstrapping analysis are summarized in **Figures 5**, **6** for the intra- and extra-axonal space, and for both, the number of samples, and the number of time-steps. **Figure 5** shows the mean error of the 50 samples for each one of the possible combination of the selected parameters, color-coded in a heat-map. In **Figure 5**, we show the error of each repetition by (i) fixing the number of steps to the maximum value (2×10^4) and varying the number of particles (left column), and (ii) fixing the number of particles to the maximum value (2×10^6) and varying the number of steps (right column). Each data point represents one repetition of a given sample size. A total of 50 points are plotted in each row, and the mean error for each sample is highlighted with a red asterisk. The total simulation time for each repetition ranged from few seconds for the simulation with a total of 1×10^3 particles to 918 s for the simulation with 1×10^6

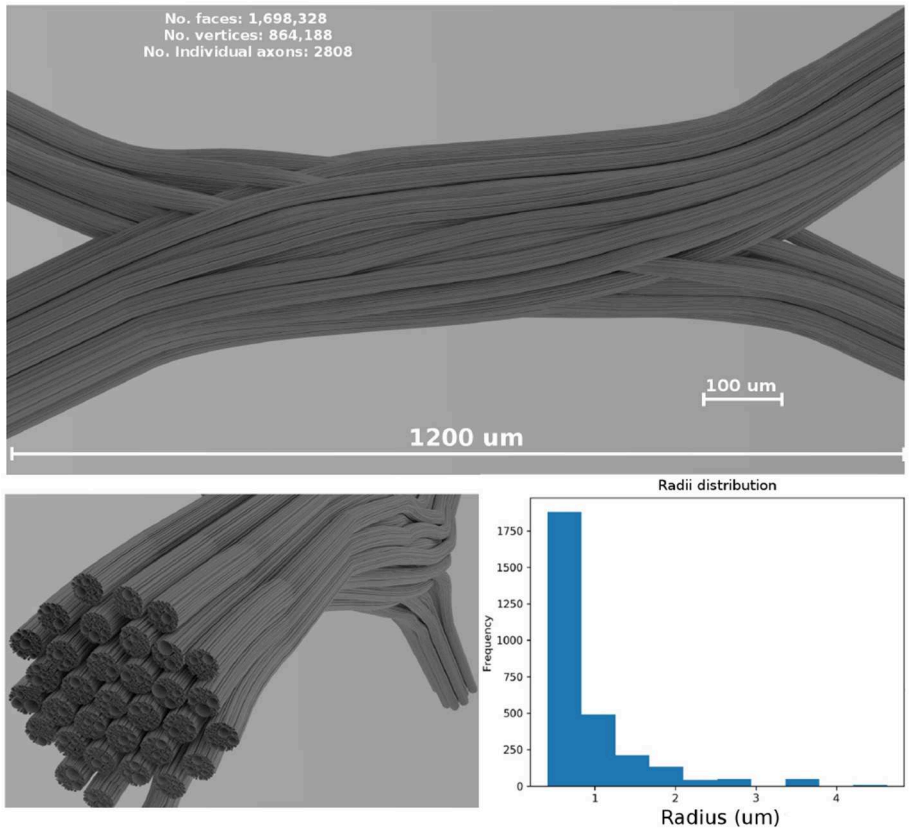


FIGURE 4 | (Top panel) Shows a visualization of the resulting fiber crossing substrate after the strand refinement and the smoothing and decimation of the triangular faces. **(Left-bottom panel)** Shows the resulting sub-strand configuration of one of the crossings bundles. **(Right-bottom panel)** Shows the overall diameter distribution of the displayed bundle on the **(left)**. A rendered video of the full crossing is included as **Supplementary Material**.

particles. Each simulation was performed in a single node of *Fidis* EPFL's cluster with 14 cores, 2.6 GHz, and 528 MB of RAM.

For the study regarding the number of particles in the intra-axonal space, the mean RMAE between the analytical ground truth and the set of repetitions with the biggest sample size of 2×10^6 particles was of 0.47%. For the extra-axonal space, the mean RMAE between the computed gold-standard with 20×10^6 and the set with 1×10^6 particles was equal to 0.71%. For the analysis varying the number of time-steps, the minimum mean RMAE achieved was of 0.44% for the intra-axonal space and 0.38% for the extra-axonal. The difference between the mean RMAE between 5×10^3 and 2×10^4 was less than 0.2% for both the intra- and extra-axonal space.

4.2. Intra-Axonal Space Representation

The range of diameters, computed from our fitting procedure on both protocols, are displayed in **Figure 7**. Each cell is colored according to its minimum RMAE. An amplitude (amp) of 0 μm corresponds to a straight cylinder which presented the minimum fitting error achievable for each diameter. Values with the highest amplitude and lowest wavelength (wl) corresponds to the axons with the highest undulation (amp = 2.6 μm, wl = 4 μm); on the other hand, values with the lowest amplitude and highest wavelength (amp = 0.2 μm, wl = 32 μm) corresponds to almost straight axons.

The protocols' sensitivity analysis is shown in **Figure 8** which presents a visualization of the RMAE between the analytical signal of straight cylinders with different diameters. Regions with homogeneous values are difficult to differentiate between each other, e.g., the region with diameters between 0 μm and 2.0 μm. The colored line shown in both plots marks the 1% level curve. In this plot, the protocols' contrast in function of the cylinder's diameter can be visualized, which correlates with the intervals showed in **Figure 7**.

4.3. Extra-Axonal Space Representation

Three different substrates (with 100, 1,000 and 10,000 cylinders, corresponding to voxel sizes of 23 × 23 μm, 71 × 71 μm, and 230 × 230 μm, respectively) and their corresponding radial DW-MRI signals, are shown in **Figure 9**. The shown voxel sizes were chosen to highlight the radial anisotropy in three representative sizes. The substrate with 10,000 cylinders, i.e., with the biggest voxel size, had the most isotropic radial DW-MRI signal. On the other hand, the most anisotropic signal was observed for the substrate with the smallest number of cylinders. **Figure 10** shows the mean and standard deviation

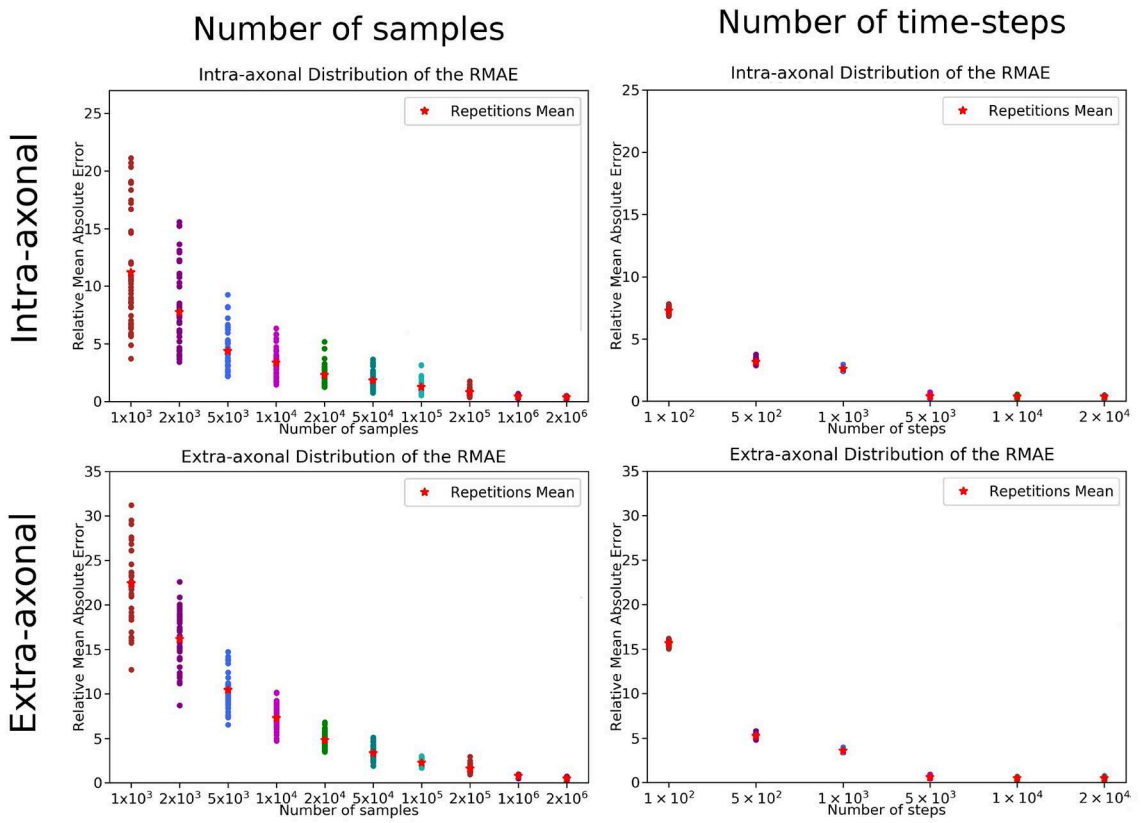


FIGURE 5 | RMAE for each repetition and sampled size for **(Left)** the number of samples and **(Right)** number of time-steps. The two panels on the top row correspond to the intra-axonal results, and the bottom row to the extra-axonal. The *X*-axis shows each sample size, and the Y-Axis shows the RMAE of all the repetition in same color. The mean RMAE of all the repetitions is depicted with a red marker.

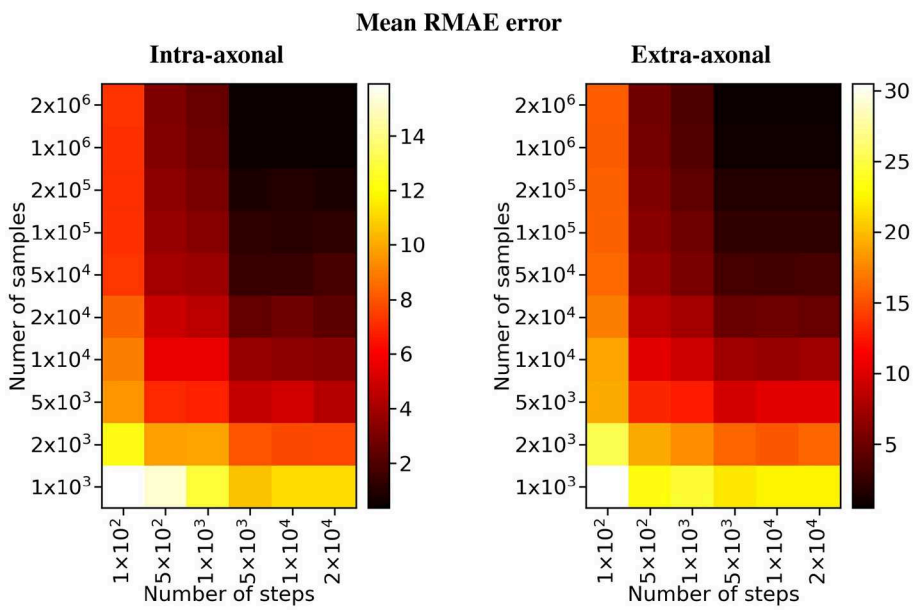


FIGURE 6 | Heat map of the mean RMAE for all the combinations between the number of steps and the number of samples. Each cell corresponds to the mean RMAE of the 50 repetitions.

Diameter = 1 um					
amp / wl	4 um	8 um	12 um	20 um	32 um
0 um	[0.4, 2.5]	[0.4, 2.5]	[0.4, 2.5]	[0.4, 2.5]	[0.4, 2.5]
0.2 um	[0.4, 1.6]	[0.4, 1.7]	[0.4, 1.9]	[0.4, 2.2]	[0.4, 2.0]
0.4 um	[0.4, 1.7]	[0.4, 1.9]	[0.4, 2.2]	[0.4, 2.3]	[0.4, 2.2]
0.6 um	[0.4, 1.8]	[0.4, 2.0]	[0.4, 2.4]	[0.4, 2.6]	[0.4, 2.4]
1.0 um	[0.4, 2.1]	[0.4, 2.5]	[0.4, 3.0]	[0.4, 3.3]	[0.4, 3.0]
1.6 um	[0.4, 3.8]	[0.4, 4.4]	[3.2, 4.5]	[3.2, 4.3]	[2.4, 3.8]
2.6 um	[6.6, 7.0]	[6.5, 6.9]	[6.2, 6.6]	[5.3, 5.9]	[4.3, 4.9]

Diameter = 2 um					
amp / wl	4 um	8 um	12 um	20 um	32 um
0 um	[1.1, 2.2]	[1.1, 2.2]	[1.1, 2.2]	[1.1, 2.2]	[1.1, 2.2]
0.2 um	[0.4, 1.9]	[0.4, 2.1]	[0.4, 2.3]	[1.6, 2.5]	[0.4, 2.3]
0.4 um	[0.4, 1.8]	[0.4, 2.1]	[0.4, 2.5]	[0.4, 2.5]	[0.4, 2.6]
0.6 um	[0.4, 1.9]	[0.4, 2.2]	[0.4, 2.7]	[0.4, 2.9]	[1.7, 2.9]
1.0 um	[0.4, 2.2]	[0.4, 2.8]	[0.4, 3.3]	[1.7, 3.4]	[1.9, 3.3]
1.6 um	[0.4, 4.2]	[2.6, 4.7]	[3.6, 4.7]	[3.5, 4.4]	[2.7, 3.9]
2.6 um	[6.9, 7.3]	[6.7, 7.1]	[6.4, 6.8]	[5.4, 6.0]	[4.4, 5.0]

Diameter = 3 um					
amp / wl	4 um	8 um	12 um	20 um	32 um
0 um	[2.9, 3.1]	[2.9, 3.1]	[2.9, 3.1]	[2.9, 3.1]	[2.9, 3.1]
0.2 um	[0.4, 2.9]	[1.8, 3.0]	[2.9, 3.1]	[2.6, 3.1]	[3.0, 3.2]
0.4 um	[0.4, 2.4]	[0.4, 3.0]	[2.0, 3.2]	[2.7, 3.2]	[2.5, 3.1]
0.6 um	[0.4, 2.4]	[0.4, 3.0]	[1.3, 3.4]	[2.5, 3.4]	[2.9, 3.4]
1.0 um	[0.4, 2.9]	[0.4, 3.6]	[2.6, 3.9]	[3.1, 3.9]	[2.7, 3.6]
1.6 um	[3.9, 4.9]	[3.9, 5.2]	[4.2, 5.1]	[3.9, 4.7]	[3.3, 4.2]
2.6 um	[7.3, 7.7]	[7.1, 7.5]	[6.7, 7.1]	[5.7, 6.2]	[4.7, 5.2]

Diameter = 1 um					
amp / wl	4 um	8 um	12 um	20 um	32 um
0 um	[0.4, 1.4]	[0.4, 1.4]	[0.4, 1.4]	[0.4, 1.4]	[0.4, 1.4]
0.2 um	[0.4, 1.3]	[0.4, 1.5]	[0.4, 1.6]	[0.4, 1.5]	[0.4, 1.7]
0.4 um	[0.4, 1.3]	[0.4, 1.7]	[0.4, 2.0]	[0.4, 1.9]	[0.4, 1.8]
0.6 um	[0.4, 1.5]	[0.4, 1.9]	[0.4, 2.2]	[0.4, 2.2]	[0.4, 2.1]
1.0 um	[0.4, 2.3]	[0.4, 2.6]	[1.6, 3.0]	[0.4, 2.7]	[0.4, 2.5]
1.6 um	[3.8, 4.6]	[3.9, 4.5]	[3.8, 4.3]	[3.2, 3.7]	[2.0, 3.1]
2.6 um	[6.3, 6.6]	[6.0, 6.3]	[5.6, 5.9]	[4.7, 5.0]	[3.6, 4.1]

Diameter = 2 um					
amp / wl	4 um	8 um	12 um	20 um	32 um
0 um	[1.9, 2.1]	[1.9, 2.1]	[1.9, 2.1]	[1.9, 2.1]	[1.9, 2.1]
0.2 um	[0.4, 1.8]	[1.4, 2.1]	[1.0, 2.1]	[1.3, 2.1]	[0.4, 2.1]
0.4 um	[0.4, 1.6]	[0.4, 2.0]	[0.4, 2.4]	[1.7, 2.4]	[1.5, 2.3]
0.6 um	[0.4, 1.8]	[0.4, 2.2]	[0.4, 2.6]	[0.4, 2.5]	[1.9, 2.5]
1.0 um	[0.4, 2.8]	[1.8, 3.1]	[2.4, 3.3]	[2.2, 3.0]	[1.4, 2.7]
1.6 um	[4.2, 4.9]	[4.2, 4.8]	[4.0, 4.5]	[3.3, 3.8]	[2.4, 3.2]
2.6 um	[6.6, 6.9]	[6.2, 6.5]	[5.8, 6.1]	[4.8, 5.2]	[3.8, 4.2]

Diameter = 3 um					
amp / wl	4 um	8 um	12 um	20 um	32 um
0 um	[2.9, 3.0]	[2.9, 3.0]	[2.9, 3.0]	[2.9, 3.0]	[2.9, 3.0]
0.2 um	[2.5, 2.9]	[2.8, 3.0]	[2.9, 3.0]	[3.0, 3.0]	[3.0, 3.0]
0.4 um	[0.4, 2.8]	[2.7, 3.1]	[2.9, 3.2]	[2.7, 3.1]	[3.0, 3.1]
0.6 um	[0.4, 2.8]	[2.6, 3.3]	[2.9, 3.3]	[2.9, 3.2]	[2.9, 3.1]
1.0 um	[2.6, 3.9]	[3.4, 3.9]	[3.4, 3.8]	[3.1, 3.5]	[2.9, 3.3]
1.6 um	[4.9, 5.5]	[4.8, 5.3]	[4.5, 4.9]	[3.8, 4.2]	[3.2, 3.7]
2.6 um	[7.1, 7.4]	[6.7, 7.0]	[6.2, 6.4]	[5.1, 5.5]	[4.2, 4.6]

RMAE
0.00%
1.42%
2.84%
4.26%
5.68%
7.10%
8.52%
9.94%
11.36%
12.78%
14.20%
15.62%
17.04%
18.46%
19.88%
21.30%
22.72%
24.14%
25.56%
26.98%
28.40%
29.82%
31.24%
32.66%
34.08%
35.50%
36.92%
38.34%

FIGURE 7 | Tables of the fitting results. Left column shows the fitted intervals of the original *ex-vivo* ActiveAx protocol (Alexander et al., 2010) and the right column of the optimized *ex-vivo* protocol from Dyrby et al. (2013), for the three simulated diameters. The min and max diameters (μm) of the fitted range are listed between the square brackets for each simulated amplitude and wavelength. The color of each cell is encoded with respect the minimum RMAE in the fitted range accordingly to the color-bar on the right.

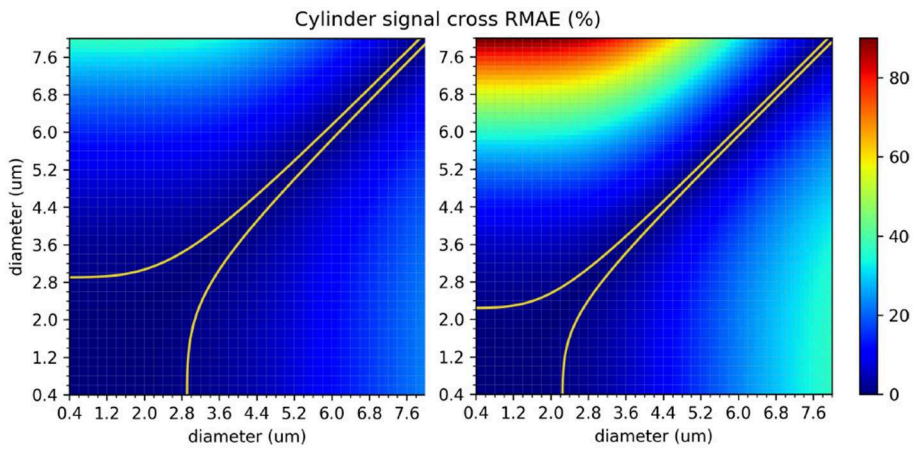


FIGURE 8 | The in-between RMAE of the analytical signal of a cylinder, obtained using the GPD approximation, for the range of diameters used in this study. The original *ex-vivo* ActiveAx acquisition protocol (Alexander et al., 2010) is displayed on the left panel, and the optimized *ex-vivo* acquisition protocol from Dyrby et al. (2013) on the right panel. Values of the diagonal correspond to the RMAE of two straight cylinders of the same diameter and therefore equals to 0. The colored line shown in both plots marks the 1% difference level curve.

of the radial extra-axonal signal as a function of the voxel size. The same experiment (not shown) was conducted using cylinders with higher diameter. Results indicated that the number of cylinders was the limiting factor. Indeed, the mean of the radial extra-axonal signal also converged for 10,000 cylinders, but this time a voxel size of approximately 400 $\times$ 400 μm was required to generate isotropic profiles instead of the 230 $\times$ 230 μm limit observed for a distribution with smaller cylinders.

4.4. Framework for Complex Substrates Generation

The resulting crossing with two fiber populations is outlined in **Figure 4**. The total optimization time to create the substrate

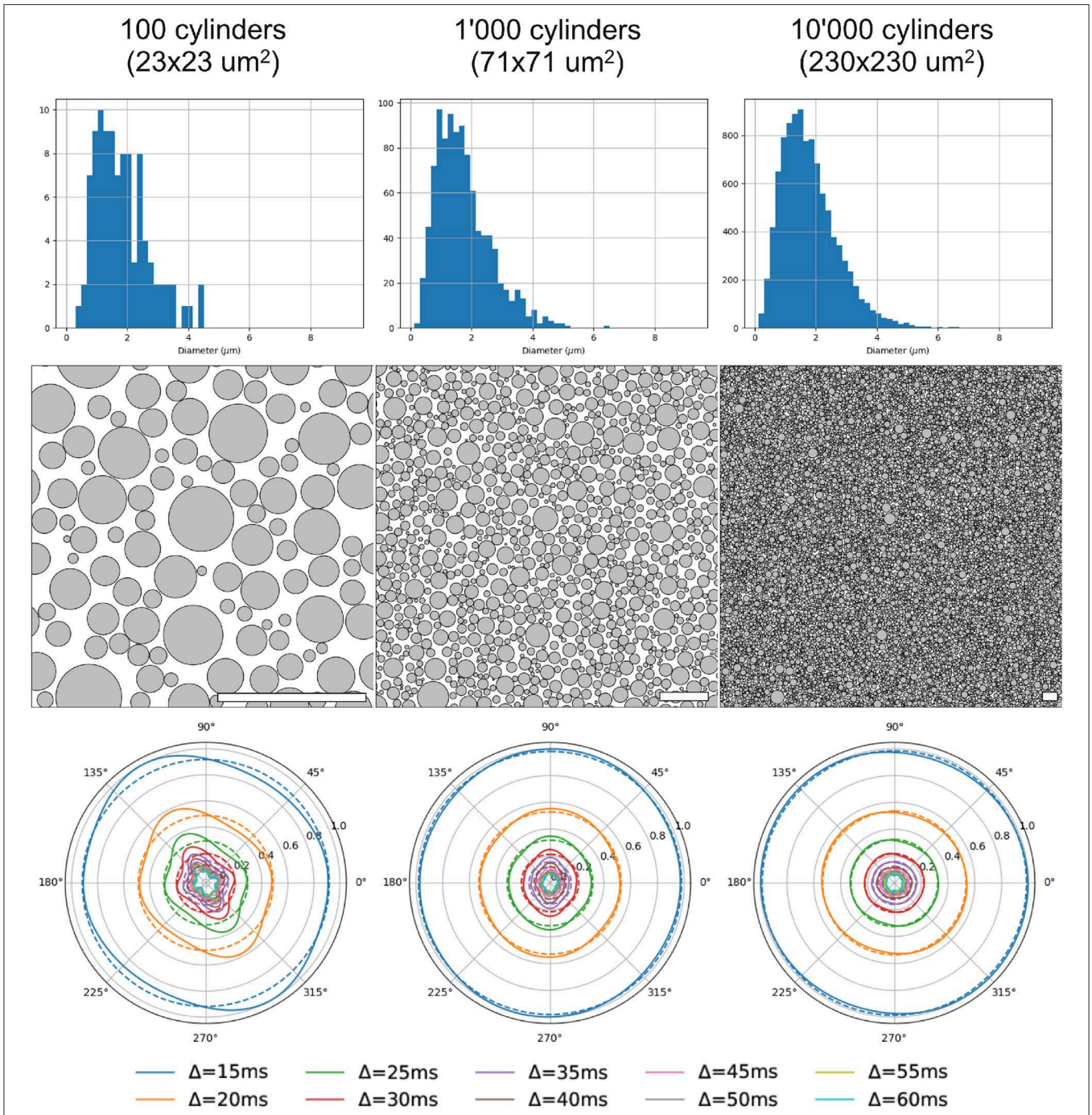


FIGURE 9 | Results for 3 substrates, with 100, 1,000, and 10,000 cylinders, respectively. First row: sampled diameter distributions for each voxel-size, getting closer to the desired distribution law as the voxel-size increases. Second row: cylinder positions in each substrate. White scale bar corresponds to 10 μm. Third row: radial DW-MRI signal simulated from the respective substrates. Each colored line corresponds to one different Δ duration. Dotted lines correspond to the mean radial signal for each diffusion time.

was around 42 h, where most of the optimization time (about 35 h) was needed in the second optimization iteration, after the subdivision on gamma distributed radii, that ensure that no small overlaps were introduced due to the subdivision and abrupt angular changes. The optimization was performed using a single core 2.8 GHz CPU. On the other hand, the total simulation time for the full geometry with 105×10^6 particles was less than 24 h using a total of 8 nodes with 28 cores on *fidis* EPFL's cluster with 6GB of RAM per node (48GB in total).

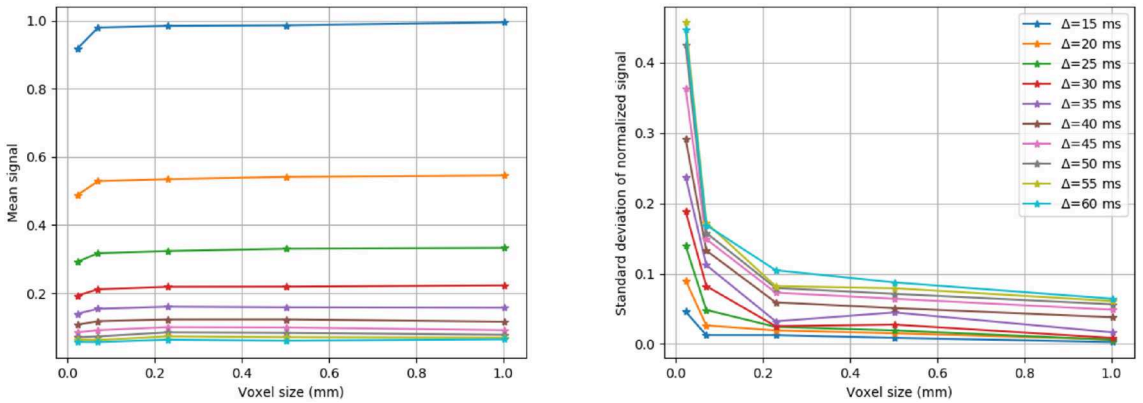


FIGURE 10 | Mean and standard deviation of the radial DW-MRI signal as a function of substrate size. The signal is shown for each of the different Δ.

The resulting diffusion tensor and FA maps are shown in **Figure 11** for the three different resolutions. Local diffusivity changes, as well as signal alterations related to the curvature of the individual axons, can be observed.

Figure 12 shows the intra-axonal volume fraction in all resolutions. In the highest resolution, small water compartments can be seen in the crossing sections; this is an effect of the optimization procedure which ensures no overlapping fibers. In the lowest resolution, such compartments are no longer visible, but they are reflected in the decrease of the intra-axonal volume fractions.

Figure 13 shows a visualization of one plane of the axon diameter estimation maps of the volumetric region highlighted in **Figure 12**, and the obtained diameter distribution for the three resolutions. The higher resolution (80 × 16 × 32) estimation includes a total of 2,848 voxels, while the lowest resolution contains a total of 112 voxels. **Figure 4** bottom-right panel shows the resulting sampled diameters inside the crossing configuration, which is noticeably skewed to smaller diameters; this is an effect of the packing algorithm inside individual circular strands which under-represent the tail of the distribution because of the difficulty of packing strands with big diameters. This effect will irremediably affect the effective apparent radius $r_{eff} \approx (\frac{<r^6>}{<r^2>})^{1/4}$ (Burcaw et al., 2015) given by the intra-axonal contribution of the signal. The resulting effective diameter of the conjoint assemble of strands was $2 * r_{eff} = 3.48\,\mu m$, which in average agrees with the estimated mean diameters shown in **Figure 13** on each resolution.

5. DISCUSSION

In the past two decades, the research community has used MCDS to generate and validate MR diffusion data and microstructure models (Lipinski, 1990; Hall and Alexander, 2009; Fieremans et al., 2010; Panagiotaki et al., 2010; Nilsson et al., 2012; Barlett et al., 2013; Baxter and Frank, 2013; Plante and Cucinotta, 2013). However, questions have been raised on the accuracy of the simplified geometries used to create the diffusion substrates (Balls and Frank, 2009; Panagiotaki et al., 2010; Nilsson et al., 2012, 2013), emphasizing the need of highly-validated and reproducible simulations. Such oversimplifications have been proven not to capture the complexity of the axonal structures of white matter, and thus its diffusion characteristics (Nilsson et al., 2013). Moreover, it can be argued that the use of such elementary geometries-used as backbone in the microstructure models-as a ground-truth, not only introduce a systematic bias that inherently supports the evaluated method, but also misapplies the very purpose of using Monte-Carlo simulations. In this work, we outlined pitfalls encountered in the design of such simulations. Our experiments showed how the design of each substrate compartment is likely to introduce an estimation bias if it is not addressed appropriately.

Our first study specifically shows the effect of an inappropriate selection of parameters on the reproducibility of a estimated signal, which could also skew an analysis toward inaccurate results. Differently to previous studies (Hall and Alexander, 2009), we compute the extra-axonal ground-truth from high-quality simulations, avoiding the use of tortuosity models that could introduce a bias because of their oversimplifications. The error in the estimation presented in **Figure 5** illustrates the great amount of possible estimation variability for a relatively simple substrate. We found that the signal on each compartment showed a high variability for simulations with less than 5×10^5 particles and 1×10^4 steps. We can extrapolate from this that any estimation from more complicated substrates, such as the ones with undulation or crossings, or even higher diffusivity, will likely entail even higher variability. In order to avoid such uncertainty on the estimations for more complicated substrates a similar analysis as the one presented should be procured.

In our second study, we explored the effect of breaking the assumption of straight cylinders as the intra-axonal representation in function of the apparent diameter estimation. The helical representation used in this study, while reported to appear in the nervous system, maybe not be an accurate representation of the axonal angular variations along the longitudinal direction in the brain white matter, specially in the micro-scale. However, it gives us a convenient starting point

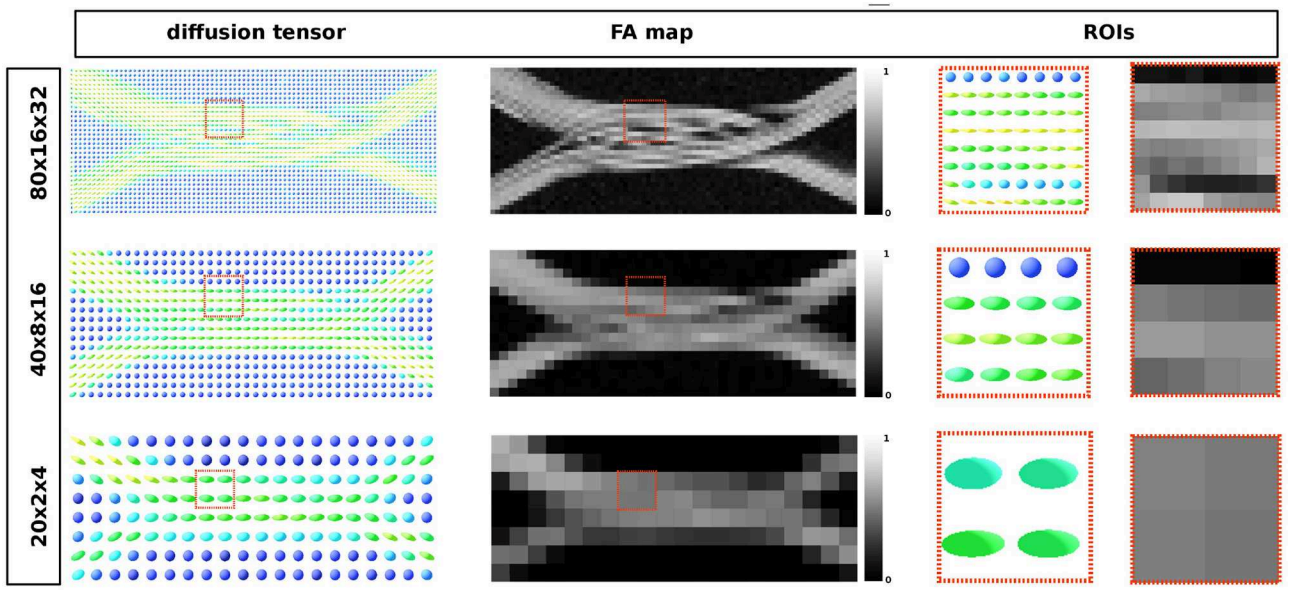


FIGURE 11 | From the leftmost to the right: diffusion tensor map, the resulting fractional anisotropy and the two highlighted ROIs in each map, respectively. Each image corresponds to the same volume slice in the *XZ*-plane. The ROI's highlights one area where different compartments result from the optimization procedure.

to study the effect of angular variations in the intra-axonal compartment over the diffusion signal, a theoretical analysis on this type of structures can be found as well in Brabec et al. (2019). From this study, we found a considerable mis-estimation in the presence of undulation for both protocols and in the three studied diameters. The relative fitting error for the smaller diameter (1 μm) was the higher among the three cases (more than 300% for some cases). Previously, Nilsson et al. (2017) proposed a formulation to compute the minimal diameter of a parallel cylinder able to produce a signal attenuation larger than that from a cylinder with a diameter of zero, using standard single-shell PGSE sequences. According to this formalism, the minimum differentiable diameter is $d_{min} = (768\sigma D/7\gamma^2\delta|G|^2)^{1/4}$, where σ is the significance level, defined as the minimum tolerated percentage of signal change. For a fixed value $\sigma = 1\%$ change, the resolution limit predicted for both protocols used in this study were $d_{min} = 2.29\,\mu m$ for $|G| = 140mT/m$, and $d_{min} = 1.76\,\mu m$ for $|G| = 300mT/m$. However, such estimates are based on a number of assumptions which does not hold in our experimental conditions. For example, the formulation is valid for parallel and straight cylinders and for acquisition protocols with a single shell with parameters $\delta = \Delta$. As in this experiment we are studying non-parallel and curved cylinders with multi-shell protocols with $\Delta >> \delta$, we performed a numerical sensitivity analysis to obtain more accurate resolution limits. From the resulting plots showed in **Figure 8**, it can be seen that the signal originated from cylinders with diameters below 2.5 μm for the first protocol, and 2.0 μm for the second, are virtually indistinguishable. On the other hand, diameters above 3.0 μm have more significant RMAE, which make them easier to differentiate. We also observed that the range of diameters from our fitting method did not follow a simple trend between protocols; that is to say, increments on the undulation parameters, which effect can be summarized in terms of the tortuosity factor (Nilsson et al., 2012) $\lambda = \sqrt{(2\pi A/L)^2 + 1}$, does not follow a simple relationship between protocols (horizontal axis of the results in **Figure 7**). This is likely to be an effect of the parameters of the acquisition protocol (δ, Δ, and the *TE*), which vary between shells and thus changing the effective diffusion time. From a comparison of both protocols, we corroborated that the optimized protocol showed better results in terms of the fitted diameter and range of similar diameters. However, there was still a considerable mis-estimation, especially for the undulation of 1 μm diameters. We consider this experiment to be of great interest for any future protocol optimization or diameter estimation framework, since it illustrates how sensible the estimation of the axon's diameter based on the cylindrical model are, even for regular and smooth angular deviations.

Our third experiment showed that a sufficiently rich sampling is required for the simulated signal to converge. Indeed, small substrates have a limited number of cylinders, limiting the variability of hindered micro-environments sampled by the spins during the M.C. simulation—yielding anisotropic patterns in the radial DW-MRI signal. The results also showed a bias in the mean amplitude, with small voxels having lower signal than bigger voxels. Our results suggest that, for a given diameter distribution, substrates with an area smaller than 200 × 200 μm will present biased extra-axonal signals. Such results are in accordance with previously results (Hall et al., 2017) in terms of the voxels' size. However, this lower bound probably depends on the distribution of diameters and cylinder packing on one side, as well as the typical diffusion length of the spins, given by their diffusivity and the diffusion time of the experiment.

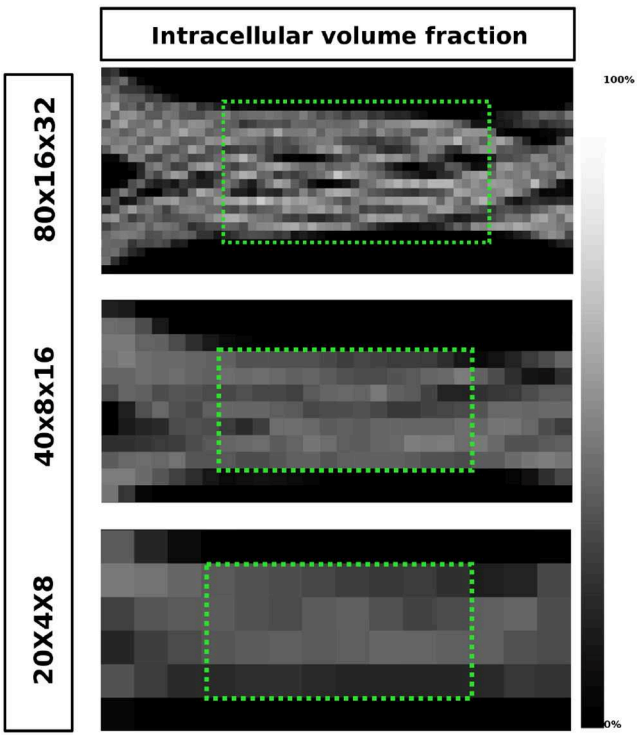


FIGURE 12 | The ICVF maps of one volume slice in the XZ-plane in three different resolutions. The highest achieved ICVF value for each resolution were: 0.8013, 0.5792, 0.4825, from top to bottom, respectively. The two green areas highlighted in the two lowest resolutions were used to evaluate the axon diameter estimation.

Finally, as part of our effort to create more realistic substrates, we outlined a framework to tackle the challenging problem of creating non-overlapping crossing configurations that preserves the volume fractions between the non-crossing and crossing area, while enforcing a high packing density. Configurations which mimic better real tissue (Shacklock, 2007), are important since they provide a more challenging environment to test and validate microstructure models and even tractography methods, in contrast with naive crossings which have been proven to be indistinguishable from a simple superposition of individual fascicles (Rensonnet et al., 2018). From the diffusion tensor and FA maps shown in **Figure 11** we can observe the presence of multiple compartments as an effect of the volume preservation condition. Also, **Figure 12** shows how the intra-axonal volume fraction changes as the resolution decreases. Such information can be used to study the microstructure information in the presence of several diffusion compartments and volume fractions in different resolutions without using an explicit interpolation. This decrease of the ICVF is an effect of the presence of dispersion and deformation of the fiber bundles. However, even in the lowest resolution, the intra-axonal volume fraction achieved was over 48%, which is considerably higher than the icvf (of 20%) of a previously presented framework for generating realistic numerical phantoms for crossing fascicles (Ginsburger et al., 2018). By optimizing the penalization term of the strands' curvature in our framework, we expect to be able to achieve even higher packing densities—closer to the expected ones from the brain's white matter tissue. On the other hand, the diameter estimations computed over the merging area of the two fiber populations, showed a overestimation in accordance with the results of section 3.2. Such mis-estimation can be explained by angular perturbations in the fiber trajectory in both the micro- and meso- scale of the simulated fibers. In previous studies, the axon diameters were overestimated by factors 3-5 in clinical scanners (Alexander et al., 2010; Zhang et al., 2011). This bias was attributed to the insensitivity of the measurement schemes to small axons (Dyrby et al., 2013), the noise, or the commonly neglected time-dependence of diffusion in the extra-axonal space (De Santis et al., 2016). The diameters reported in this study were estimated by using only the intra-axonal signals, thus the overestimation can be explained only by the dMRI signal insensitivity to the smaller axons and by the signal changes due to axon undulations and microscopic dispersion. This renders our estimations as a best case scenario.

5.1. Considerations and Future Work

The generalisability of the results presented above is subject to certain limitations. For instance, *in-vivo* diffusion and protocol settings, the use of non-regular deformations in the intra-axonal substrates, and the joint study of the intra- and extra- axonal space, may affect the results toward higher variability or mis-estimations of the axon diameters. In addition, a number of structural features present in white matter tissue -such as the axonal myelin sheath, Ranvier nodes, or diameter changes along the axons trajectory-are missing. Because of this, the results presented above should be taken as a type of lower bound in terms of the minimum parameters needed (for the number of samples and time-steps) and possible mis-estimations (in terms of our axon diameters estimates).

Notwithstanding these limitations, we consider that the aforementioned framework, complemented with the optimized simulator developed, are able to overcome the simulations pitfalls presented in this work. In addition, the parameter selection analysis presented in this work provides a way to ensure the reproducibly of the Monte-Carlo simulations. A thorough study of the properties of more complex substrates generated with the proposed framework is beyond the scope of this study. Future research should therefore concentrate on the generation and study of such configurations, which may help the DW-MRI research community to generate more reliable ground-truth data.

6. CONCLUSIONS

The main contribution of this work can be summarized in three main aspects. First, this paper outlines and investigates a set of pitfalls encountered on the parameter selection and substrates' design for Monte-Carlo simulations. Our results over the effect of the number of particles and time-steps, as well as our quantification over the effect of the substrate's size on the extra-axonal space can be immediately taken to evaluate the design of future experiments. In overall, we found that

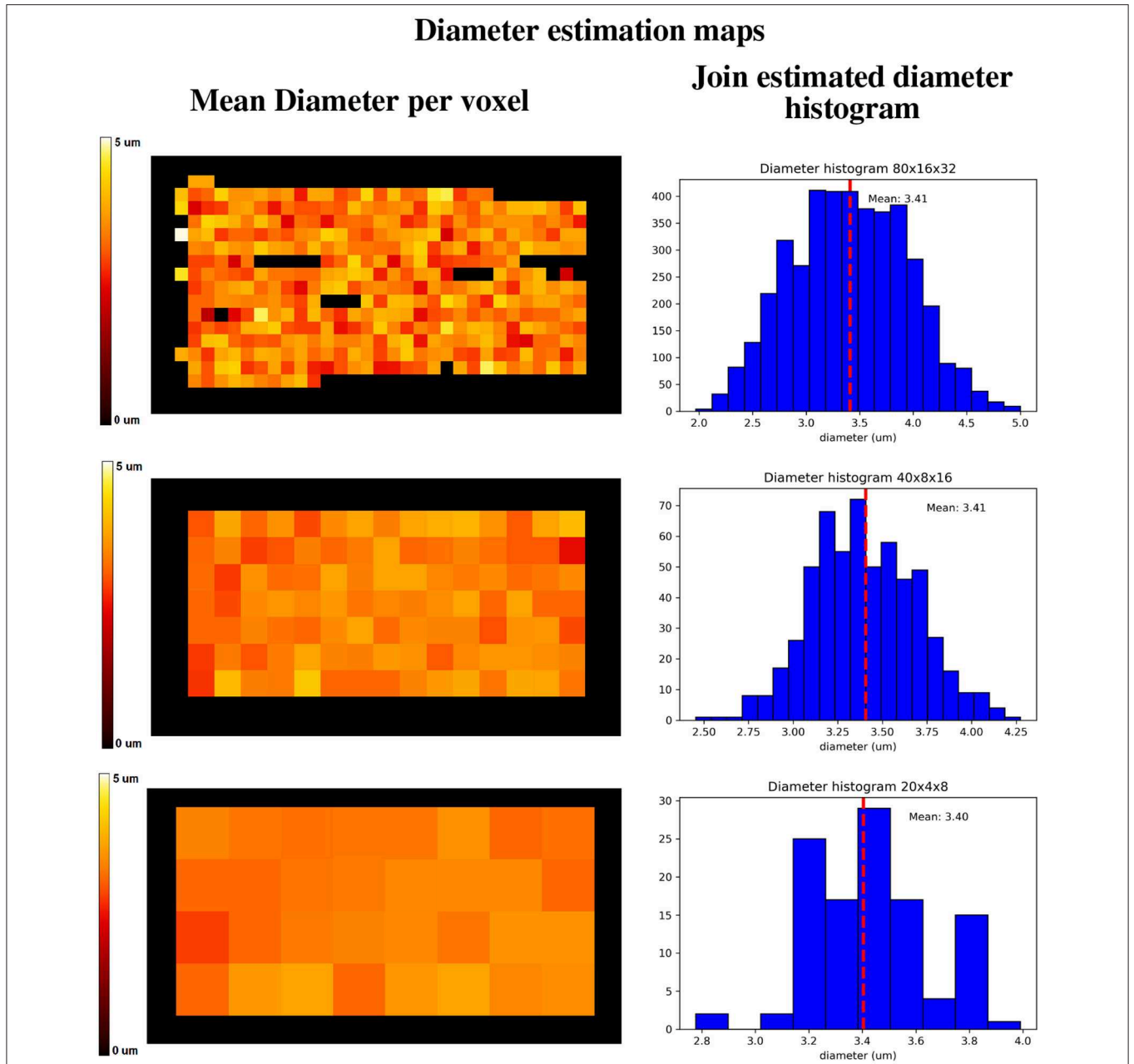


FIGURE 13 | Axon diameter estimation maps **(Left column)** of the regions highlighted in **Figure 12**, and diameter histograms **(Right column)** estimated on the full volume enclosed by the highlighted regions. Top row shows the axon diameter map and the diameter estimation histogram for the 80 × 16 × 32 nominal resolution; middle row shows the same maps for the 40 × 8 × 16 nominal resolution, and the bottom row shows the same maps for the 20 × 4 × 8 nominal resolution. The dotted line indicates the histograms' mean diameter within the regions, to be compared with the effective apparent diameter ($2 * r_{eff}$) of 3.48 um.

for experiments with parameters in the range used in this study—which are in the range of interest in the literature—simulations with less than 5×10^5 particles and 1×10^4 steps carried a significant variance between the computed signals for both, the intra- and extra-axonal compartments. In addition, we found that simulations substrates with less than 10,000 sampled cylinders induced an important bias on the directional symmetry of the diffusion signal in directions transversal to the main fiber direction. Such parameters are almost one order of magnitude bigger than previously used on the literature, which inherently affects the reproducibility of such results (Hall and Alexander, 2009; Alexander et al., 2010; Rensonnet et al., 2018, 2019). Second, our evaluation over the effect of introducing angular perturbations in the intra-axonal space representation—by means of the estimated axon diameter based on the cylindrical model—showed a considerable deviation

from the expected results. This results are somehow in agreement with previous findings and contributes additional evidence that suggests that performing whole brain axon diameter estimation is still far from being straightforward using simplified models, such as the straight cylindrical diffusion model. Finally, this paper presents a framework able to generate complex fiber configurations with desired microstructure information based on a previous algorithm used to create tractography phantoms. We showed the framework's capabilities to generate complex fibers configurations which, along with the simulator developed in this work, are able to generate more challenging and composite Monte-Carlo simulations.

We consider that the results presented in this work, along with the reported procedure to evaluate the estimations' variability, the substrate generation framework, and the simulator developed, pave the way toward more realistic and reproducible Monte-Carlo simulations for Diffusion-Weighted MRI.

DATA AVAILABILITY STATEMENT

The datasets generated for this study are available in: https://github.com/jonhrafe/Robust-Monte-Carlo-Simulations.

AUTHOR CONTRIBUTIONS

JR-P: original idea conception and experimental design, overall writing, plots and figures generation, and lead programmer of the simulator presented in this work. DR: section 3.3 experiment setup, generation of section 4.3 results and writing based on previously published work, and active contributions on the experimental setup and selected parameters. AR-M: contributed on sections 3.2 and 4.2 experiments design and writing, and overall review of the work and editing. EC-R: contributed on sections 4.1 and 3.1 experimental setup and parameters choice, overall review of the work and editing. GG: generation of the maps presented in section 4.4 coding and experimental setup, **Figures 10**, **11** generation based on previous work, and overall review of the work and editing. J-PT: supervised all the work done, contributed to the general writing, and editing of the work.

FUNDING

This project has received funding from the Swiss National Science Foundation under grant number 205320_175974. We gratefully acknowledge the support of NVIDIA Corporation with the donation of the Titan Xp GPU used for this research. This work was supported by EPFL through the use of the facilities of its Scientific IT and Application Support Center. This project has received funding from the European Union's Horizon 2020 Framework Programme for Research and Innovation under grant agreement 665667 (call 2015) and from the Natural Sciences and Engineering Research Council of Canada (NSERC).

ACKNOWLEDGMENTS

We would like to acknowledge Dr. Gary Zhang for his advice that highly contributed to the development of this work. We also thank Thomas Yu for his generous help proofreading this manuscript.

SUPPLEMENTARY MATERIAL

The Supplementary Material for this article can be found online at: https://www.frontiersin.org/articles/10.3389/fninf.2020.00008/full#supplementary-material

Supplementary Video 1 | 3d rendering of the resulting fiber-crossing substrate after refinement, and the smoothing and decimation of the triangular faces.

REFERENCES

Alexander, D. C., Hubbard, P. L., Hall, M. G., Moore, E. A., Ptito, M., Parker, G. J., et al. (2010). Orientationally invariant indices of axon diameter and density from diffusion MRI. *NeuroImage* 52:1374. doi: 10.1016/j.neuroimage.2010.05.043

Assaf, Y., Blumenfeld-Katzir, T., Yovel, Y., and Basser, P. J. (2008). Axcaliber: a method for measuring axon diameter distribution from diffusion MRI. *Magn. Reson. Med.* 59:15334406. doi: 10.1002/mrm.21577

Bain, A. C., Shreiber, D. I., Meaney, D. F. (2004). Modeling of microstructural kinematics during simple elongation of central nervous system tissue. *J. Biomech. Eng.* 125, 798–804. doi: 10.1115/1.1632627

Balls, G. T., and Frank, L. R. (2009). A simulation environment for diffusion weighted MR experiments in complex media. *Magn. Reson. Med.* 62:771. doi: 10.1002/mrm.22033

Bammer, R. (2003). Basic principles of diffusion-weighted imaging. *Eur. J. Radiol.* 45:169. doi: 10.1016/S0720-048X(02)00303-0

Barlett, V. R., Hoyuelos, M., and Martin, H. O. (2013). Monte carlo simulation with fixed steplength for diffusion processes in nonhomogeneous media. *J. Comput. Phys.* 239, 51–56. doi: 10.1016/j.jcp.2012.12.029

Baxter, G. T., and Frank, L. R. (2013). A computational model for diffusion weighted imaging of myelinated white matter. *NeuroImage* 75, 204–212. doi: 10.1016/j.neuroimage.2013.02.076

Benjamini, D., Komlosh, M. E., Holtzclaw, L. A., Nevo, U., and Basser, P. J. (2016). White matter microstructure from nonparametric axon diameter distribution mapping. *Neuroimage* 135, 333–344. doi: 10.1016/j.neuroimage.2016.04.052

Brabec, J., Lasic, S., and Nilsson, M. (2019). Time-dependent diffusion in undulating structures: impact on axon diameter estimation. *NMR Biomed.* 33:e4187. doi: 10.1002/nbm.4187

Burcaw, L. M., Fieremans, E., and Novikov, D. S. (2015). Mesoscopic structure of neuronal tracts from time-dependent diffusion. *NeuroImage* 114:15334406. doi: 10.1016/j.neuroimage.2015.03.061

Close, T. G., Tournier, J. D., Calamante, F., Johnston, L. A., Mareels, I., and Connelly, A. (2009). A software tool to generate simulated white matter structures for the assessment of fibre-tracking algorithms. *NeuroImage* 47:1288. doi: 10.1016/j.neuroimage.2009.03.077

Daducci, A., Canales-Rodríguez, E. J., Zhang, H., Dyrby, T. B., Alexander, D. C., and Thiran, J. P. (2015a). Accelerated microstructure imaging via convex optimization (amico) from diffusion MRI data. *NeuroImage* 105:32. doi: 10.1016/j.neuroimage.2014.10.026

Daducci, A., Palù, A. D., Lemkaddem, A., and Thiran, J. P. (2015b). Commit: convex optimization modeling for microstructure informed tractography. *IEEE Trans. Med. Imaging* 34:246. doi: 10.1109/TMI.2014.2352414

De Santis, S., Jones, D. K., and Roebroeck, A. (2016). Including diffusion time dependence in the extra-axonal space improves *in vivo* estimates of axonal diameter and density in human white matter. *NeuroImage* 130, 91–103. doi: 10.1016/j.neuroimage.2016.01.047

Dyrby, T. B., Sagaard, L. V., Hall, M. G., Ptito, M., and Alexander, D. C. (2013). Contrast and stability of the axon diameter index from microstructure imaging with diffusion MRI. *Magn. Reson. Med.* 70:711. doi: 10.1002/mrm.24501

Ferizi, U., Schneider, T., Witzel, T., Wald, L. L., Zhang, H., Wheeler-Kingshott, C. A., et al. (2015). White matter compartment models for *in vivo* diffusion MRI at 300 mt/m. *NeuroImage* 118, 468–483. doi: 10.1016/j.neuroimage.2015.06.027

Fieremans, E., Deene, Y. D., Delputte, S., Özdemir, M. S., D'Asseler, Y., Vlassenbroeck, J., et al. (2008). Simulation and experimental verification of the diffusion in an anisotropic fiber phantom. *J. Magn. Reson.* 190:189. doi: 10.1016/j.jmr.2007.10.014

Fieremans, E., Novikov, D. S., Jensen, J. H., and Helpern, J. A. (2010). Monte carlo study of a two-compartment exchange model of diffusion. *NMR Biomed.* 23:711. doi: 10.1002/nbm.1577

Garyfallidis, E., Brett, M., Amirbekian, B., Rokem, A., van der Walt, S., Descoteaux, M., et al. (2014). Dipy, a library for the analysis of diffusion MRI data. *Front. Neuroinform.* 8:8. doi: 10.3389/fninf.2014.00008

Ginsburger, K., Poupon, F., Beaujoin, J., Estournet, D., Matuschke, F., Mangin, J.-F., et al. (2018). Improving the realism of white matter numerical phantoms: a step toward a better understanding of the influence of structural disorders in diffusion MRI. *Front. Phys.* 6:12. doi: 10.3389/fphy.2018.00012

Hall, M. G., and Alexander, D. C. (2009). Convergence and parameter choice for monte-carlo simulations of diffusion MRI. *IEEE Trans. Med. Imaging* 28, 1354–1364. doi: 10.1109/TMI.2009.2015756

Hall, M. G., Nedjati-Gilani, G., and Alexander, D. C. (2017). Realistic voxel sizes and reduced signal variation in monte-carlo simulation for diffusion mr data synthesis. *arXiv: 1701.03634*.

Haninec, P. (1986). Undulating course of nerve fibres and bands of Fontana in peripheral nerves of the rat. *Anat. Embryol.* 174, 407–411. doi: 10.1007/BF00698791

Hrabe, J., Hrabetová, S., and Segeth, K. (2004). A model of effective diffusion and tortuosity in the extracellular space of the brain. *Biophys. J.* 87, 1606–1617. doi: 10.1529/biophysj.103.039495

Lin, M., He, H., Schifitto, G., and Zhong, J. (2016). Simulation of changes in diffusion related to different pathologies at cellular level after traumatic brain injury. *Magn. Reson. Med.* 76:290. doi: 10.1002/mrm.25816

Lipinski, H. G. (1990). Monte carlo simulation of extracellular diffusion in brain tissues. *Phys. Med. Biol.* 35:441. doi: 10.1088/0031-9155/35/3/012

Lovas, G., Szilágyi, N., Majtényi, K., Palkovits, M., and Komoly, S. (2000). Axonal changes in chronic demyelinated cervical spinal cord plaques. *Brain* 123:308. doi: 10.1093/brain/123.2.308

Neuman, C. H. (1974). Spin echo of spins diffusing in a bounded medium. *J. Chem. Phys.* 60:4508. doi: 10.1063/1.1680931

Nilsson, M., Lasič, S., Drobnjak, I., Topgaard, D., and Westin, C. F. (2017). Resolution limit of cylinder diameter estimation by diffusion MRI: the impact of gradient waveform and orientation dispersion. *NMR Biomed.* 30:e3711. doi: 10.1002/nbm.3711

Nilsson, M., Latt, J., Staahlberg, F., van Westen, D., and Hagslatt, H. (2012). The importance of axonal undulation in diffusion mr measurements: a monte carlo simulation study. *NMR Biomed.* 25:795. doi: 10.1002/nbm.1795

Nilsson, M., Westen, D. V., Staahlberg, F., Sundgren, P. C., and Latt, J. (2013). The role of tissue microstructure and water exchange in biophysical modelling of diffusion in white matter. *Magn. Reson. Mater. Phys. Biol. Med.* 26:345. doi: 10.1007/s10334-013-0371-x

Novikov, D. S., Fieremans, E., Jensen, J. H., and Helpern, J. A. (2011). Random walks with barriers. *Nat. Phys.* 7:1004.2701. doi: 10.1038/nphys1936

Panagiotaki, E., Hall, M. G., Zhang, H., Siow, B., Lythgoe, M. F., and Alexander, D. C. (2010). "High-fidelity meshes from tissue samples for diffusion mri simulations," in *Medical Image Computing and Computer-Assisted Intervention - MICCAI 2010* (Beijing), 404.

Panagiotaki, E., Schneider, T., Siow, B., Hall, M. G., Lythgoe, M. F., and Alexander, D. C. (2012). Compartment models of the diffusion mr signal in brain white matter: a taxonomy and comparison. *NeuroImage* 59:2241. doi: 10.1016/j.neuroimage.2011.09.081

Plante, I., and Cucinotta, F. A. (2013). "Monte-carlo simulation of particle diffusion in various geometries and application to chemistry and biology," in *Theory and Applications of Monte Carlo Simulations*, ed V. Chan, 193. doi: 10.5772/53203

Price, W. S. (1997). Pulsed-field gradient nuclear magnetic resonance as a tool for studying translational diffusion: part 1. Basic theory. *Concept. Magn. Reson.* 9:299.

Rafael-Patino, J., Ramirez-Manzanares, A., Peña Acevedo, J., and Zhang, H. (2017). "Validating particle dynamics in monte carlo diffusion simulation using the finite element method," in *Proceedings of the 25th Scientific Meeting of the International Society for Magnetic Resonance in Medicine* (Honolulu, HI), 1849.

Raffelt, D., Tournier, J.-D., Rose, S., Ridgway, G. R., Henderson, R., Crozier, S., et al. (2012). Apparent fibre density: a novel measure for the analysis of diffusion-weighted magnetic resonance images. *NeuroImage* 59, 3976–3994. doi: 10.1016/j.neuroimage.2011.10.045

Rensonnet, G., Scherrer, B., Girard, G., Jankovski, A., Warfield, S. K., Macq, B., et al. (2019). Towards microstructure fingerprinting: estimation of tissue properties from a dictionary of Monte Carlo diffusion MRI simulations. *NeuroImage* 184, 964–980. doi: 10.1016/j.neuroimage.2018.09.076

Rensonnet, G., Scherrer, B., Warfield, S. K., Macq, B., and Taquet, M. (2018). Assessing the validity of the approximation of diffusion-weighted-MRI signals from crossing fascicles by sums of signals from single fascicles. *Magn. Reson. Med.* 79, 2332–2345. doi: 10.1002/mrm.26832

Sanguinetti, G., and Deriche, R. (2014). "Mapping average axon diameters under long diffusion time," in *2014 IEEE 11th International Symposium on Biomedical Imaging (ISBI)* (Beijing), 242–245.

Sexton, C. E., Walhovd, K. B., Storsve, A. B., Tamnes, C. K., Westlye, L. T., Johansen-Berg, H., et al. (2014). Accelerated changes in white matter microstructure during aging: a longitudinal diffusion tensor imaging study. *J. Neurosci.* 46, 15425–15436. doi: 10.1523/JNEUROSCI.0203-14.2014

Shacklock, M. O. (2007). *Biomechanics of the Nervous System: Breig Revisited*. Adelaide, SA: Neurodynamic Solutions.

Stejskal, E. O., and Tanner, J. E. (1965). Spin diffusion measurements: spin echoes in the presence of a time-Dependent field gradient. *J. Chem. Phys.* 42, 288–292. doi: 10.1063/1.1695690

Szafer, A., Zhong, J., and Gore, J. C. (1995). Theoretical model for water diffusion in tissues. *Magn. Reson. Med.* 33:697. doi: 10.1002/mrm.1910330516

Trapp, B. D., Peterson, J., Ransohoff, R. M., Rudick, R., Mörk, S., and Bö, L. (1998). Axonal transection in the lesions of multiple sclerosis. *N. Engl. J. Med.* 338, 278–285. doi: 10.1056/NEJM199801293380502

Van Gelderen, P., Des Pres, D., Van Zijl, P. C., and Moonen, C. T. (1994). Evaluation of restricted diffusion in cylinders. Phosphocreatine in rabbit leg muscle. *J. Magn. Reson. Ser. B* 103, 255–260. doi: 10.1006/jmrb.1994.1038

Verth, J. M. V., and Bishop, L. M. (2008). "Chapter 12 - intersection testing," in *Essential Mathematics for Games and Interactive Applications, 2nd Edn.*, eds J. M. V. Verth and L. M. Bishop (Boston, MA: Morgan Kaufmann), 541–599.

Yeh, C.-H., Schmitt, B., Bihan, D. L., Li-Schlittgen, J.-R., Lin, C.-P., and Poupon, C. (2013). Diffusion microscopist simulator: a general monte carlo simulation system for diffusion magnetic resonance imaging. *PLoS ONE* 8:e76626. doi: 10.1371/journal.pone.0076626

Zhang, H., Hubbard, P. L., Parker, G. J. M., and Alexander, D. C. (2011). Axon diameter mapping in the presence of orientation dispersion with diffusion MRI. *Neuroimage* 56, 1301–1315. doi: 10.1016/j.neuroimage.2011.01.084

Zhang, H., Schneider, T., Wheeler-Kingshott, C. A., and Alexander, D. C. (2012). Noddi: practical *in vivo* neurite orientation dispersion and density imaging of the human brain. *NeuroImage* 61:1000. doi: 10.1016/j.neuroimage.2012.03.072

Conflict of Interest: The authors declare that the research was conducted in the absence of any commercial or financial relationships that could be construed as a potential conflict of interest.

Copyright © 2020 Rafael-Patino, Romascano, Ramirez-Manzanares, Canales-Rodríguez, Girard and Thiran. This is an open-access article distributed under the terms of the Creative Commons Attribution License (CC BY). The use, distribution or reproduction in other forums is permitted, provided the original author(s) and the copyright owner(s) are credited and that the original publication in this journal is cited, in accordance with accepted academic practice. No use, distribution or reproduction is permitted which does not comply with these terms.

frontiers in Neuroinformatics

ORIGINAL RESEARCH
published: 17 March 2020
doi: 10.3389/fninf.2020.00009

A Smart Region-Growing Algorithm for Single-Neuron Segmentation From Confocal and 2-Photon Datasets

Alejandro Luis Callara[1], Chiara Magliaro[1], Arti Ahluwalia[1,2]* and Nicola Vanello[1,2]*

[1] Research Center "E. Piaggio" - University of Pisa, Pisa, Italy, [2] Dipartimento di Ingegneria dell'Informazione, University of Pisa, Pisa, Italy

Accurately digitizing the brain at the micro-scale is crucial for investigating brain structure-function relationships and documenting morphological alterations due to neuropathies. Here we present a new Smart Region Growing algorithm (SmRG) for the segmentation of single neurons in their intricate 3D arrangement within the brain. Its Region Growing procedure is based on a homogeneity predicate determined by describing the pixel intensity statistics of confocal acquisitions with a mixture model, enabling an accurate reconstruction of complex 3D cellular structures from high-resolution images of neural tissue. The algorithm's outcome is a 3D matrix of logical values identifying the voxels belonging to the segmented structure, thus providing additional useful volumetric information on neurons. To highlight the algorithm's full potential, we compared its performance in terms of accuracy, reproducibility, precision and robustness of 3D neuron reconstructions based on microscopic data from different brain locations and imaging protocols against both manual and state-of-the-art reconstruction tools.

Keywords: neuron segmentation, confocal microscopy, 2 photon microscopy, expectation - maximization (EM) algorithm, mixture models, CLARITY

OPEN ACCESS

Edited by:
Sean L. Hill,
Centre for Addiction and Mental Health, Canada

Reviewed by:
Donglai Wei,
Harvard University, United States
Giulio Iannello,
Campus Bio-Medico University, Italy

****Correspondence:***
Alejandro Luis Callara
alejandrocallara@gmail.com
Arti Ahluwalia
arti.ahluwalia@unipi.it

Received: *19 July 2019*
Accepted: *26 February 2020*
Published: *17 March 2020*

Citation:
Callara AL, Magliaro C, Ahluwalia A and Vanello N (2020) A Smart Region-Growing Algorithm for Single-Neuron Segmentation From Confocal and 2-Photon Datasets. Front. Neuroinform. 14:9. doi: 10.3389/fninf.2020.00009

INTRODUCTION

Digitizing a high-fidelity map of the neurons populating the brain is a central endeavor for neuroscience research and a crucial step for the delineation of the full Connectome (Alivisatos et al., 2012). Moreover, single-neuron reconstruction from empirical data can be used to generate models and make predictions about higher-level brain organization, as well as to study the normal development of dendritic and axonal arbors or document neuro-(patho)physiological changes (Budd et al., 2015).

Confocal and two-photon microscopy are considered the best candidates to image defined cellular populations in three-dimensional (3D) biological specimens (Wilt et al., 2009; Ntziachristos, 2010). Their imaging depth, as well as the quality of the acquired datasets can be further improved thanks to recent tissue-clearing solutions, which render brain tissue transparent to photons by reducing the source of scattering, allowing confocal acquisitions with enhanced Signal to Noise Ratios and Contrast to Noise Ratios while maintaining low laser power (Chung and Deisseroth, 2013; Richardson and Lichtman, 2015; Magliaro et al., 2016). While these technologies

and protocols, combined with fluorescence-based labeling techniques, enable the imaging of the brain's intricacies at the microscale, single-cell segmentation algorithms able to deal with these datasets are still lacking (Magliaro et al., 2019), despite targeted initiatives such as the DIADEM (DIgital reconstructions of Axonal and DEndrite Morphology) challenge in 2009–2010 (Gillette et al., 2011) and the BigNeuron project in 2015 (Peng et al., 2015). In fact, different approaches have been implemented for reaching the goal of segmentation of single cells (Acciai et al., 2016). Most of these tools reconstruct the pathway of neurite or neural processes, i.e., neuron tracing (Quan et al., 2016; Kayasandik et al., 2018) using different approaches, ranging from active contour methods (Kass et al., 1988; Wang et al., 2009; Baswaraj et al., 2012) to hierarchical pruning (Peng et al., 2011a; Xiao and Peng, 2013), in an attempt to face the a number of key challenges: (i) noisy points causing over-tracing, (ii) gaps between continuous arbors causing under-tracing, and (iii) non-smooth surfaces of the arbors violating geometric assumptions (Liu et al., 2016). Among them, machine learning approaches are widely considered as robust for neural structure segmentation in image stacks (Januszewski et al., 2018; Sakkos et al., 2018). These methods mainly consist in building a classifier able to discern between foreground and background, thanks to prior information obtained through a training dataset of manually-segmented neuron structures. However, building the training dataset is very time consuming, in particular because it needs to be fleshed out when dealing with different images (e.g., neuron types with different morphology or stacks with different background/foreground features). Finally, many tools and algorithms for neuron segmentation primarily focus on sparsely labeled data, such that their application to images (or volumes) representing densely packed neurons, typical of mammalian brains, is limited (Chothani et al., 2011; Wang et al., 2011, 2017; Peng et al., 2014; Hernandez et al., 2018).

The outcomes of neuron reconstructions are traditionally stored in a.swc file format, where spatial (i.e., x, y, and z coordinates) and morphological (e.g., neurite thickness) information about specific points of interest (e.g., neuron nodes) are listed. This standard describes neuron morphology with a number of structurally connected compartments (e.g., cylinders or spheres representing neuron arborization or soma, respectively), thereby neglecting the morphological and volumetric information along the neuron's length (Magliaro et al., 2019).

Confocal and 2-photon datasets are characterized by on-plane and intra-plane pixel intensity heterogeneities, deriving from optical phenomena and the non-uniform distribution of fluorophores through the sample (Diaspro, 2001). Given these intrinsic features, a valid procedure for accurately digitizing the neural structures in the stack could be obtained by leveraging on local approaches and methods enforcing spatial constraints, such as region growing procedures (RG) (Brice and Fennema, 1970; Xiao and Peng, 2013; Acciai et al., 2016). RG is a pixel intensity-based segmentation method that identifies the foreground starting from a pixel, i.e., the seed, belonging to the foreground itself. The neighboring pixels of the seed are iteratively examined based on a predefined rule, usually a homogeneity predicate, which can be estimated locally to determine whether they should be added to the foreground or not. The performance of the procedure may be influenced by both the seed selection and the rule (Baswaraj et al., 2012). The choice of the rule may be non-trivial, in particular in view of delivering a general-purpose segmentation algorithm. Adaptive strategies based on mixture models have been successfully used in video foreground/background segmentation (Stauffer and Grimson, 1999; Barnich and Van Droogenbroeck, 2010). Here, we exploit a similar approach that takes into account the image formation process. Here we propose a novel RG strategy based on an estimation which considers the image formation process (Calapez and Rosa, 2010) to define intrinsic properties of signal distribution in the image in question.

Our rationale is that confocal and 2-photon microscopy are based on sampling successive points in a focal plane to reproduce the spatial distribution of fluorescent probes within a sample. Hence, each pixel contains a discrete measure of the detected fluorescence within a sample interval, represented by a photon count, and certain amount of noise, deriving from different sources (Pawley, 2006; Calapez and Rosa, 2010). Therefore, statistical methods represent a natural way of describing confocal or 2-photon datasets. Different models have been proposed to depict confocal image properties (Calapez et al., 2002; Pawley, 2006). Specifically, mixture models (MM) have been suggested as the best descriptor of the sharp peaks and the long tails typical of background and low fluorescence distributions (Calapez and Rosa, 2010).

Given these considerations, we have developed a new Smart Region Growing algorithm (SmRG), which couples the RG procedure with a MM describing the signal statistics, to calculate local homogeneity predicates (i.e., local thresholds) for iteratively growing the structure to be segmented. Here, we describe the SmRG workflow for single-neuron segmentation. Then, we evaluate its performance in segmenting different neuron types from confocal and 2-photon datasets, comparing the results with those obtained with a gold standard manual reconstruction. Furthermore, we compare our algorithm with state-of-the-art (SoA) tools widely used in the field of neuron reconstruction.

THE SMART REGION GROWING (SmRG) ALGORITHM

The Mixture Model

In its original version (Calapez and Rosa, 2010), the model is supposed to describe K different fluorescence levels or classes; the k-th class is described by the linear mixture model:

$$\psi_k\left(y\right) = \alpha_k \psi_B\left(y - K_0\right) + \left(1 - \alpha_k\right)\psi_{Sk}\left(y - K_0\right) \qquad (1)$$

where y, K_0 and α_k denote the pixel intensity level, the system offset and the mixture parameter respectively. ψ_B is the distribution for the background pixels and is modeled according to a discrete normal distribution, with variance v_B and mean K_0, and ψ_{Sk} is the intensity distribution of the k-th class pixels, described by a negative-binomial distribution with variance v_{Sk}

and mean μ_{Sk}. In accordance with (Calapez and Rosa, 2010) the negative-binomial distribution is re-parameterized in terms of

$$p_k = \frac{\mu_{Sk}}{v_{Sk}} \tag{2}$$

and

$$r_k = \frac{\mu_{Sk}^2}{v_{Sk} - \mu_{Sk}} \tag{3}$$

For region growing purposes, it is reasonable to assume the presence of a single class k of pixels, at least locally. In this case, the complete model for a pixel y_l is described by the 5-parameter distribution:

$$\psi\left(y_l; K_0, v_B, \alpha, r, p\right) = \alpha \frac{1}{Z\left(v_B\right)} \exp\left(-\frac{\left(y_l - K_0\right)^2}{2v_B}\right) + (1-\alpha)\frac{\Gamma\left(y_l - K_0 + r\right)}{\left(y_l - K_0\right)!\Gamma\left(r\right)} p^r \left(1-p\right)^{y_l - K_0} \tag{4}$$

where all the parameters are real values except for K_0 which is an integer and $\alpha \in [0, 1]$.

The model fitting is done by means of an Expectation-Maximization (EM) algorithm in which:

1. p and r are obtained by the method of moments (eqs. 2, 3)
2. K_0 and v_B are given by the maximization of the log-likelihood

$$L\left(\Theta | Y, X\right) = \sum_{y=\min Y}^{\max Y} \ln\left(\psi\right) \tag{5}$$

3. α is given by the posterior density

$$\alpha = \frac{\sum_{y=\min Y}^{\max Y} \alpha_y}{N} \tag{6}$$

The Algorithm Outlined

The SmRG is an open-source algorithm developed in Matlab (The Mathworks-Inc., United States). A package of the functions needed for running the algorithm are available at http://www.centropiaggio.unipi.it/smrg-algorithm-smart-region-growing-3d-neuron-segmentation.

The SmRG is driven by a homogeneity predicate for establishing a local threshold based on the intensity levels of confocal datasets. Specifically, it exploits the statistics of the background and the signal distributions of the confocal acquisitions and a linear MM to determine the probability with which a given pixel (voxel) can be considered as part of the foreground or not, as described in section "The Mixture Model." The rule to grow regions is then designed from these probabilities.

The workflow of the SmRG is sketched in **Figure 1**. It begins by selecting a seed, either manually or automatically (**Figure 1A**).

In the first case, the user is asked to identify the seed position by selecting a point on a focal plane (e.g., a pixel belonging to the soma), while in the latter the Hough transform (Nixon and Aguado, 2012) searches for spherical objects within the stack to identify the somata: the seed (or the seeds) is (or are) chosen as the center of the detected sphere (or spheres). Then, the homogeneity predicate is derived locally on an image volume centered on the seed. The volume dimension is a trade-off between the goodness-of-fit of the MM and the localness of the segmentation and by default is set to $\frac{N}{8} \times \frac{M}{8} \times 3$, where N and M are the on-plane size of the image stack. To ensure enough data points for MM fitting, the crop size is never smaller than 32×32×3. At this step a Hartigan's dip test (Hartigan and Hartigan, 1986) ($p < 0.01$) is performed on the pixel intensity distribution of the crop to test for unimodality against multimodality (**Figure 1B**). In the case of multimodality the segmentation proceeds with Otsu's method (Otsu, 1979), a well-known thresholding technique for multimodal distributions (Guo et al., 2012). Otherwise, a linear MM, considering the background as a normal distribution and the signal as a negative binomial, is fitted by means of an Expectation Maximization (EM) algorithm on the crop pixel intensity distribution. Indeed, mixture models combining normal and negative binomial distributions have been observed to fully characterize the signal associated with confocal images (Calapez and Rosa, 2010). The homogeneity predicate is derived from the posterior probability of the MM, α (or 1-α), denoting the probability at which a given pixel can be considered as part of the background (or the signal) distribution. The rule is thus obtained as a user defined threshold for α (e.g., with 1-$\alpha > 0.999$ all the seed's neighboring pixels whose probability of belonging to the signal exceeds 99.9% are segmented) (**Figure 1C**). Each

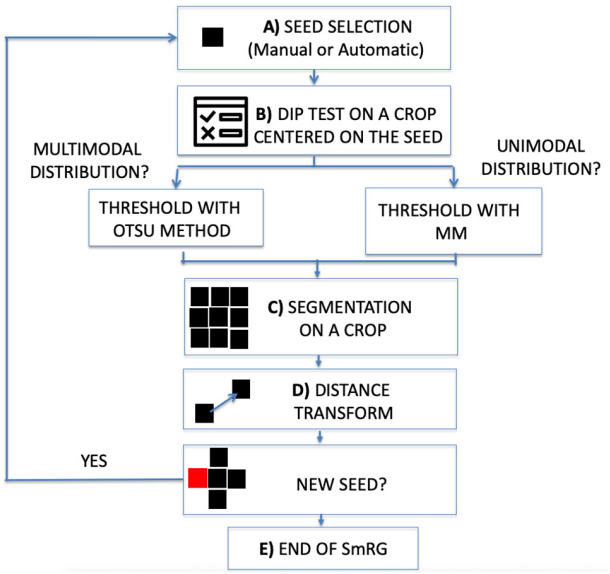


FIGURE 1 | Workflow of the SmRG. **(A)** Manual or automatic seed selection. **(B)** Dip test to test for unimodality against multimodality on a MxNx3 crop centered on the seed. The threshold is determined with Otsu's method or through the Mixture Model according to whether the distribution is multimodal or not. **(C)** 3D segmentation of a MxNx3 crop. **(D)** The regional maxima of the distance transform of the segmented MxNx3 crop are chosen as new seeds. **(E)** The procedure iterates until there are no more new seeds.

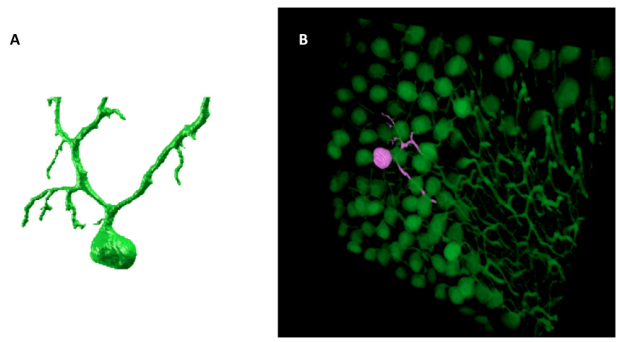


FIGURE 2 | An example of SmRG outcome: **(A)** a Purkinje cell from clarified murine cerebellum acquired using a Nikon A1 confocal microscope; **(B)** the same Purkinje cells identified within its confocal dataset.

pixel that satisfies this rule and is spatially connected to the seed within the crop is added to the object to be segmented. At this point, new seeds are chosen from the points just recognized as part of the neuron to be segmented. In particular, for each segmented plane the regional maxima of the distance transform (Maurer and Raghavan, 2003) are taken as new seeds (**Figure 1D**). The algorithm iterates for each detected seed and the process stops when there are no more pixels to add (**Figure 1E**).

The result of the SmRG is a 3D matrix of logical values, whose true values represent the voxels constituting an isolated neuron. **Figure 2** shows an example of a Purkinje cell segmented using the SmRG from a confocal dataset representing a 1 mm-thick slice from murine cerebellum, obtained after applying the CLARITY protocol described in Magliaro et al. (2016).

MATERIALS AND METHODS

To evaluate the SmRG's performance, we processed two different sets of data. First, confocal acquisitions of 1 mm-thick slices of clarified cerebellum from a L7GFP mouse were analyzed to isolate Purkinje Cells (PCs) expressing Green Fluorescent Protein (GFP). The aim was to demonstrate (i) the SmRG's accuracy with respect to a manual segmentation performed by experts, as it is still considered the gold standard for neuron segmentation (Al-Kofahi et al., 2003; Meijering, 2010), (ii) the SmRG's reproducibility, and (iii) its ability to handle 3D microscopic datasets representing dense-packed neurons compared with other tools available in literature.

Then, Olfactory Projection (OP) Fibers dataset from the DIADEM challenge was processed with the SmRG. The SmRG reconstructions were quantitatively compared to the manually-traced gold-standards provided by the DIADEM. Moreover, 3D neuron segmentation was performed using other SoA tools evaluating the outputs against the DIADEM gold standards through the metrics SD, SSD and SSD%. This allowed an assessment of the SmRG's ability to reconstruct 3D neuron morphology with the same precision and accuracy as SoA algorithms.

The tools used for both PC and OP datasets were the Vaa3D (version 3.200) app2 (Xiao and Peng, 2013), MST-tracing (Basu and Racoceanu, 2014), SIGEN (Ikeno et al., 2018) and MOST (Ming et al., 2013) plug-ins. They have been extensively validated in other reports and are widely used to compare reconstructions provided by new segmentation algorithms (Peng et al., 2014; Liu et al., 2016). A further quantitative comparative analysis with NeuroGPS (Quan et al., 2016) was performed was performed on the PC datasets.

Datasets Representing PCs

Accuracy Test: SmRG Algorithm Versus Manual Segmentation

The confocal datasets representing dense-packed PCs from 1 mm-thick slices from clarified L7GFP murine cerebellum were those already manually segmented in Magliaro et al. (2017). They are available for download at http://www.centropiaggio.unipi.it/mansegtool. Specifically, n = 3 Purkinje cells from three different datasets were segmented automatically with the SmRG algorithm and manually by 6 experts with the ManSegTool, a tool purposely developed for facilitating the manual segmentation of 3D stacks (Magliaro et al., 2017). The matrix and voxel sizes for the three datasets are: (i) Dataset 1: 512 × 512 × 143, x = 0.62 μm/pixel, y = 0.62 μm/pixel, z = 1.24 μm/pixel; (ii) Dataset 2: 1024 × 1024 × 389, x = 0.31 μm/pixel, y = 0.31 μm/pixel, z = 0.62 μm/pixel (iii) Datasets3: 512 × 512 × 139, x = 0.62 μm/pixel, y = 0.62 μm/pixel, z = 1.24 μm/pixel.

The SmRG's segmentation accuracy was evaluated by comparing morphometric features extracted from the two outputs. Briefly, we considered (i) the surface area, (ii) the volume, and (iii) the Sholl analysis (Sholl, 1955; Magliaro et al., 2017) of segmented structures. To compare Sholl profiles, we calculated the total area under the curve (AUC) using the trapezoidal rule thus obtaining a single measure for each profile (Binley et al., 2014). Statistical differences between the features in the manual segmented structures and those resulting from the SmRG were evaluated by means of the Friedman's test with replicates. Friedman's test allows testing treatments under study (i.e., columns) after adjusting for nuisance effects (i.e., rows). Replicates refer to more than one observation for each combination of factors. In our case, surface area, volume and the AUC of Sholl profiles were blocking factors (i.e., rows) with replicates represented by the three neurons, while users and SmRG represented treatments (i.e., columns). Thus, we are testing the null hypothesis of no difference between manual and SmRG-based segmentation.

SmRG Reproducibility

Reproducibility tests were performed by segmenting the same n = 3 PCs starting from different seeds. Specifically, we randomly chose 10 pixels picked from different regions of the neuron. Volume, surface area and AUC of Sholl profiles were obtained for each seed and the reproducibility was quantified for each neuron as the coefficient of variation of each measure (i.e., the standard deviation normalized by the mean).

SmRG vs. SoA Tools

In order to highlight the SmRG's ability to segment single-neurons from confocal datasets represented densely-packed cells, we processed a 3D image stack with the App2, MST, SIGEN, MOST Vaa3d plugins and with NeuroGPS.

The reconstructions provided by the Vaa3D plugins and by SmRG were visually compared. On the other hand, $n = 6$ neurons were segmented with SmRG and NeuroGPS and manually through ManSegTool. After translating the volumetric information obtained with SmRG and ManSegTool in swc format, the three reconstructions were quantitatively compared by means of the following metrics: (i) the spatial distance (SD), (ii) the substantial spatial distance (SSD), and (iii) the percentual substantial spatial distance (%SSD). The spatial distance is estimated as it follows:

$$SD = \frac{\sum_i d_{AB}(i)}{2|n_A|} + \frac{\sum_j d_{BA}(j)}{2|n_B|} \tag{7}$$

With

$$d_{AB(i)} = argmin_j \left| n_A(i) - n_B(j) \right|, \; j \in [1, |n_B|], \; i \in [1, |n_A|] \tag{8}$$

and

$$d_{BA(j)} = argmin_i \left| n_B(j) - n_A(i) \right|, i \in [1, |n_A|], j \in [1, |n_B|] \tag{9}$$

i.e., given two reconstructions, A and B, the spatial distance is obtained by averaging the Euclidean distance between the nodes of A and the nodes of B, i.e., d_{AB}, with the reciprocal measure, i.e., d_{BA}. Specifically, for each node belonging to A, d_{AB} is obtained by selecting the minimum distance between each node of B. d_{AB} is thus obtained by repeating this operation for every node of A and averaging the results. The same operation is performed with the nodes belonging to B, to obtain d_{BA}.

The SSD is obtained by selecting the node pairs in A and B with a minimal distance above a given threshold S and then performing their average. Specifically, given:

$$D_{AB} = \left\{ d_{AB}(i) \,|\, d_{AB}(i) > S \right\} \tag{10}$$

and

$$D_{BA} = \left\{ d_{BA}(j) \,|\, d_{BA}(j) > S \right\} \tag{11}$$

Then, the SSD is defined as follows:

$$SSD = \frac{\overline{D_{AB}}}{2} + \frac{\overline{D_{BA}}}{2} \tag{12}$$

Finally, the % SSD is obtained by estimating the ratio of nodes contributing to SSD. These metrics express the similarity of two different reconstructions (Peng et al., 2011b). Essentially, SD is a measure of how different two reconstructions are, while SSD and SSD% measure the extent of differences between two reconstructions considering only points above a tolerance threshold S. The tolerance threshold for the evaluation of the SSD metric was 2 (i.e., $S = 2$) voxels, as suggested in Peng et al. (2011a). Given that the SmRG's output is a 3D logical matrix constituting the whole neuron, while the DIADEM gold-standard is a set of points of interest (i.e., a *.swc file), a thinning procedure was necessary to reduce the volumetric information in SmRG to a skeleton. To this end, we calculated the 3D skeleton of the SmRG output via a 3-D Medial Surface Axis Thinning Algorithm (Lee et al., 1994). From the points constituting the skeleton we reconstructed the corresponding *.swc file, ensuring a fair mapping between the DIADEM reference points and the SmRG ones.

Moreover, the precision, recall and F-score of the SmRG reconstructions were determined with respect to the gold-standard, quantifying the spatial overlap between the closest corresponding nodes of the two reconstructions (Powers, 2011) and varying the tolerance threshold from 0.5 to 5 voxels, to evaluate the SmRG's sensitivity to this parameter (Radojeviæ and Meijering, 2018).

DIADEM Datasets Representing OP Fibers

The dataset representing OP Fibers is available at http://diademchallenge.org/olfactory_projection_fibers_readme.html. It contains 9 separate drosophila olfactory axonal projection image stacks acquired with a two-photon microscope and their respective gold standard reconstructions provided by the DIADEM (Evers et al., 2005; Jefferis et al., 2007). We segmented all the neurons except OP2, since it contains many irrelevant structures (Liu et al., 2016). The SmRG and SoA algorithm reconstructions were compared with the DIADEM gold-standards. Comparisons between automatic tools were made by means of the metrics described in section "SmRG vs. SoA Tools."

RESULTS

Purkinje Cell (PC) Segmentation

SmRG vs. Manual Segmentation

Figure 3 shows an example of the same PC segmented by an expert and by the SmRG. The SmRG's accuracy was assessed by comparing volume, surface area and AUC of Sholl profiles extracted from the segmented PCs with the results obtained by manually segmented ones (**Figure 4**). The single-neuron reconstructions provide quantitative information on the morphology of individual neurons in their native context where they are surrounded by neighboring cells. Clearly the algorithm developed is able to follow neurite arborization, segmenting smaller branches with similar performance to manual segmentation. Furthermore, the structure obtained with the SmRG is consistently characterized by a smooth volume, compared with the manual segmentation. A typical example is reported in **Figure 5**, showing a zoomed detail of manual and SmRG segmentation results.

The Friedman's test showed no significant differences between the SmRG and the ManSegTool segmentation in terms of surface area, volume and Sholl profiles of the segmented structures ($p = 0.8233$); a detailed ANOVA table of the Friedman's test is reported in **Table 1**. In summary, the results in the table demonstrate that the SmRG's performance is comparable to that obtained from manual segmentation performed by



FIGURE 3 | SmRG versus Manual Segmentation. **(A)** Gold-standard manual segmentation. **(B)** SmRG automatic segmentation. **(C)** Merge of manual (green) and automatic (red) segmentation, common voxels are reported in purple.

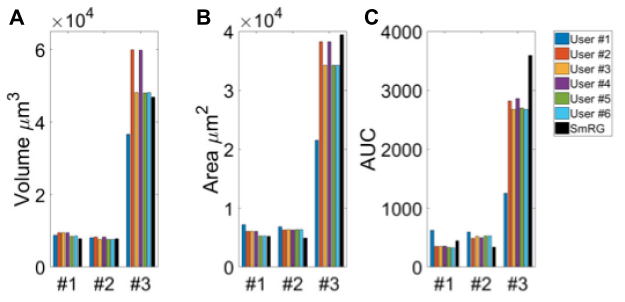


FIGURE 4 | Testing SmRG accuracy **(A)** Neuron volume. **(B)** Neuron surface. **(C)** AUC (area under the curve) of Sholl profiles. Friedman's test was performed with Volume, Area and AUC as blocking factors (rows, nuisance effects) with replicates (neurons #1, #2 and #3), and with users and SmRG as treatments (column). No statistical differences were observed (p-value = 0.8233).

experts in terms of the accuracy of the morphological parameters considered.

SmRG's Reproducibility

Table 2 reports the coefficients of variation of volume, surface area and AUC of Sholl profiles for each segmented PC. The maximum coefficient of variation was equal to 0.0258, demonstrating the robustness of the SmRG to changes in initial conditions (i.e., the position of a seed belonging to the structure of interest).

SmRG vs. Other Tools

Figure 6 shows an example of the outputs obtained segmenting the same confocal 3D stack with the App2, MST, SIGEN and MOST routines and with the SmRG. We were only able to assess the comparisons visually, since none of Vaa3D plugins was able to handle such dense datasets.

Figure 7 reports the same dense packed PCs segmented with both SmRG and NeuroGPS, showing that the performance of the two tools is comparable. This is also evident from the SD, SSD and SSD% metrics obtained with respect to the gold standard provided by the manual segmentation for all the neurons segmented except for PC2 (**Figure 8**). Moreover, the average precision, recall and F-score in **Figure 9** shows better precision and accuracy for our tool with respect to NeuroGPS for $S = 2$.

OP Fibers: SmRG vs. the DIADEM Gold-Standard

Olfactory Projection fibers segmented with the SmRG are reported in **Figure 10**, along with the manually-traced gold-standard provided by the DIADEM.

One of the distinctive characteristics of the SmRG is its ability to trace the axon topology of OP fibers while maintaining 3D volumetric information on neurons and their arbors. Indeed, the structure obtained with the SmRG is a smooth three-dimensional volume with voxel-resolution details on neuron morphology; a feature not available from swc structures. As a consequence, the SmRG reconstructions in **Figure 10** appear thicker than the 3D rendering of *.swc gold-standards.

As evident from the figure, some terminal branches of OP fibers are not comprised in the manually traced gold standard, since they have no effect on DIADEM metrics (Brown et al., 2011; Gillette et al., 2011). Nonetheless, the SD, SSD, and SSD% metrics used in this work are naturally biased by these missing branches. Thus, the comparison between automatic reconstructions and gold standard were limited to those branches included in by the DIADEM gold standard.

When evaluated against other SoA tools, the SmRG was observed to be comparable in terms of SD. On the other hand, our algorithm achieved the lowest values of SSD among all tools considered (with the exception of segmentation of OP5). It should be noted that the value of SSD% was higher for the SmRG with respect to other algorithms, since the estimation of the skeleton from the 3D output of SmRG produced a higher number of nodes compared to the other methods (**Figure 11**).

In **Figure 12** the average precision, recall and F-score across OP fibers are reported for SmRG and SoA tools as a function of the value of S. For $S = 5$, the SmRG outperforms other tools in terms of F-score which highlights its ability to segment OP fibers with high accuracy.

DISCUSSION

The SmRG for the automatic segmentation of microscopic data exploits the signal statistics typical of confocal and 2-photon images (Calapez and Rosa, 2010). Datasets representing neural tissues from different species, processed using different protocols (i.e., clarified murine cerebella and Drosophila brains fixed using classical procedures) and acquired with different imaging tools (i.e., confocal and two photon microscopy) were used to test the algorithm. The goodness of the SmRG reconstruction was compared with manually traced gold-standards as well as with algorithms available in the SoA.

A quantitative analysis of the SmRG's accuracy with PC datasets was performed for three different neurons, whose manually segmented counterpart was available in Magliaro et al. (2017). Although a limited set of neurons were analyzed, the reconstructions of the SmRG and the manually-segmented gold standards were comparable; moreover, the seeding and RG procedure was shown to be robust and independent of initial conditions. The analysis performed on PCs from clarified tissues highlighted the efficacy of the algorithm developed in isolating

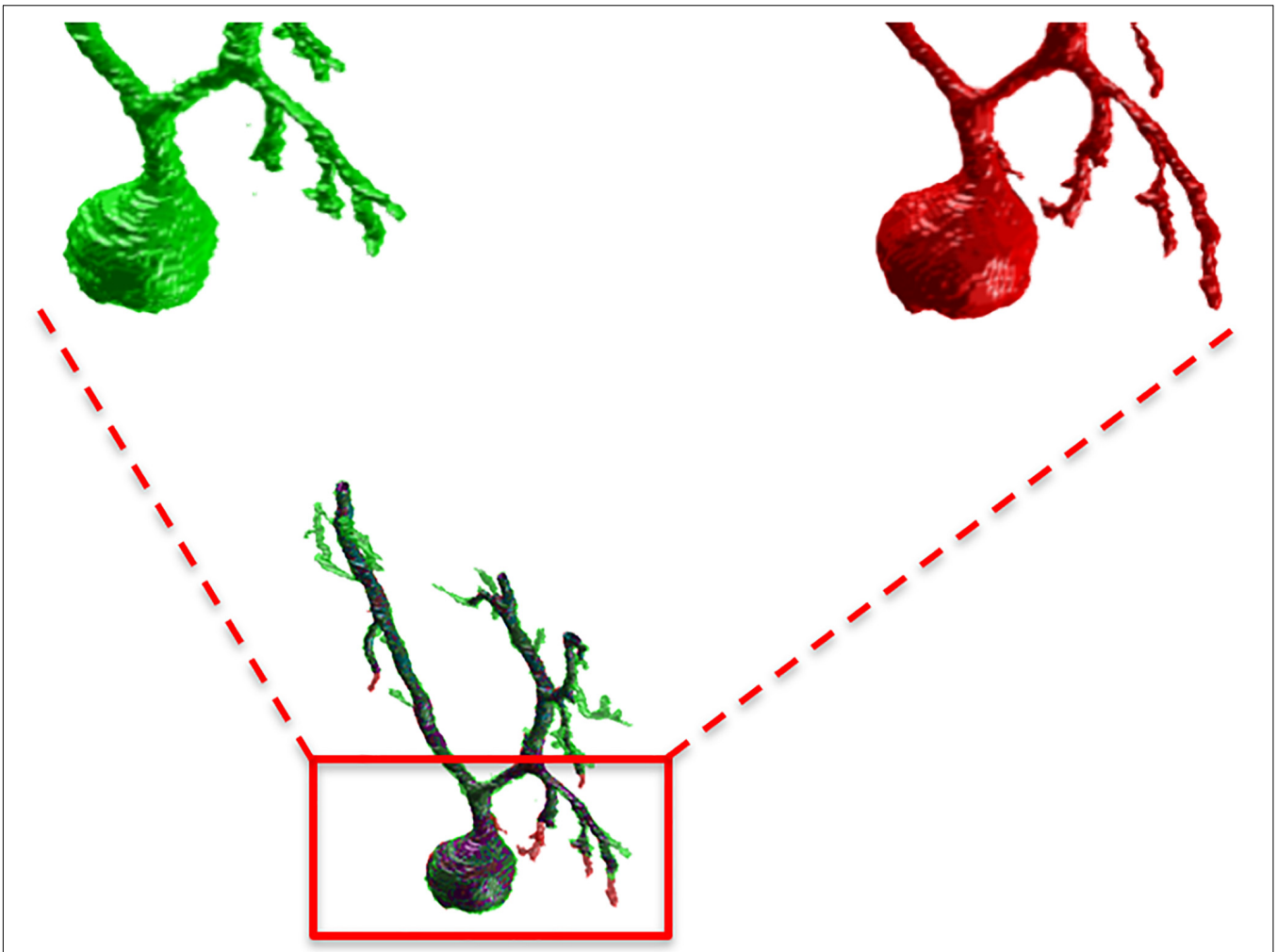


FIGURE 5 | A detail of the manual and SmRG neuron reconstruction. It is clear that the SmRG segmentation (red) leads to a smoother volume than the manual (green) one.

single neurons from densely-packed data with respect to some of the most widely used single neuron reconstruction tools available in the SoA (i.e., app2, MOST, MST-tracing, SIGEN) (Ming et al., 2013; Xiao and Peng, 2013; Basu and Racoceanu, 2014; Ikeno et al., 2018). In particular, none of the Vaa3D plug-ins allowed the reconstruction of 3D neuron morphology from the confocal stacks representing neurons in their native 3D context, limiting the evaluation of the SmRG's performance to a visual comparison. Indeed, many SoA algorithms perform extraordinarily well with low-quality images possessing noisy points, large gaps between neurites and non-smooth surfaces (Liu et al., 2016), since they were likely developed specifically for such purposes. On the contrary, they may perform modestly or even fail in reconstructing densely-packed neurons (Hernandez et al., 2018), such as PCs in the murine cerebella because the

TABLE 1 | Friedman's ANOVA table.

Source	SS	Df	MS	Chi-sq	p>Chi-sq
Columns	110.94	6	10.4907	2.08	0.8233
Interaction	64.89	12	5.4074		
Error	2132.67	42	50.7778		
Total	2308.5	62			

SS = Sum of Squares due to each sources; Df = Degree of freedom associated with each source; MS = Mean Squares, which is SS/Df; Chi-sq: Freedman Chi-square statistic; p: p-value for the Chi-square statistic.

TABLE 2 | Results of SmRG's reproducibility.

Neuron	Volume	Area	AUC
#1	0.0015	0.0025	7.8e−04
#2	0.0176	0.0258	0.0138
#3	0.0017	6.1e−04	0.0026

*Coefficients of variation for neuron volume, area and AUC for n different RG seeds. *The coefficient of variation corresponds to the standard deviation divided by the mean σ/μ.*

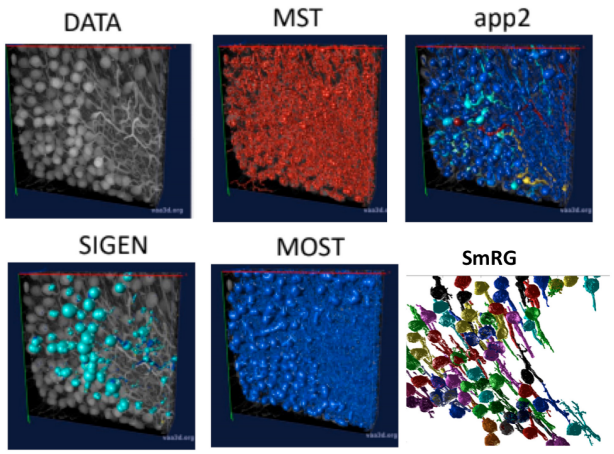


FIGURE 6 | An example of a confocal dataset representing PCs from a clarified L7GFP murine cerebellum, segmented with MST, app2, MOST, SIGEN, and SmRG. None of the SOA tools is able to deal with this dense dataset, while the SmRG is able to isolate the PCs within the dataset. Different colors refer to the different neurons recognized.

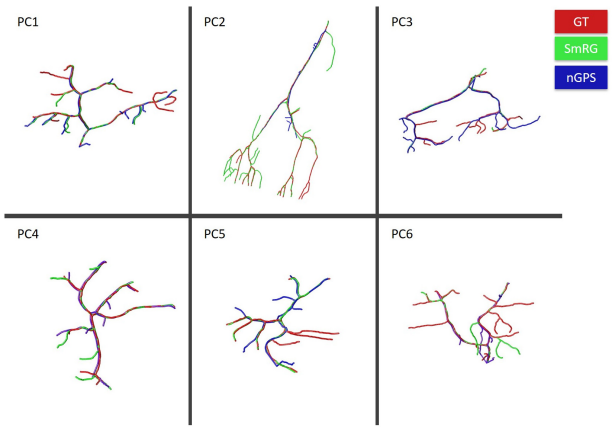


FIGURE 7 | PCs segmented with SmRG (green) and NeuronGPS (blue) and compared with the manually segmented gold-standard (red).

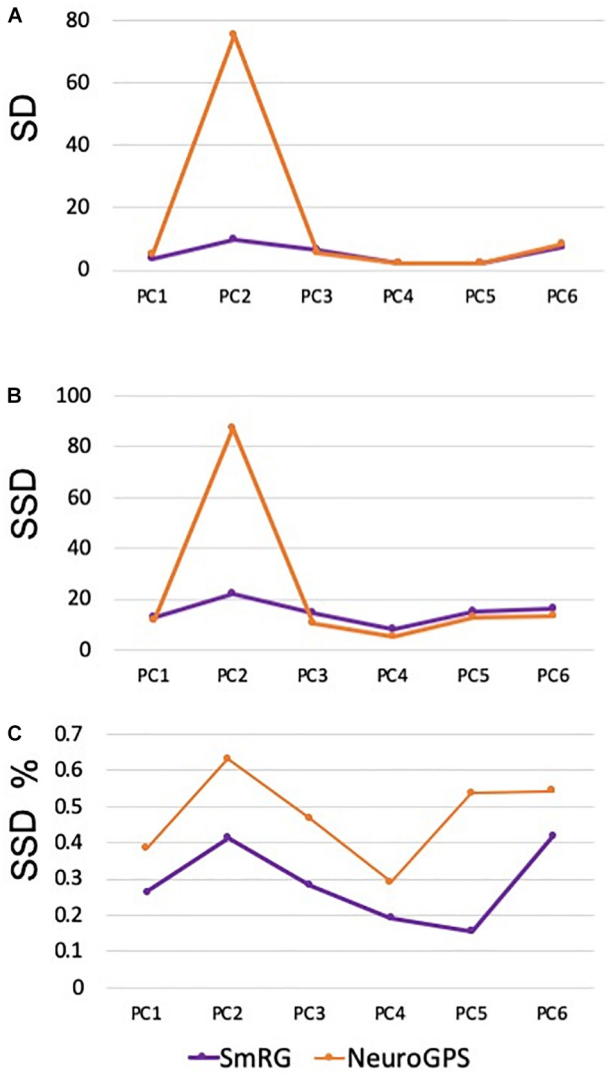


FIGURE 8 | Accuracy of SmRG and NeuronGPS against the manually segmented gold standard for different PCs. **(A)** SD **(B)** SSD, and **(C)** percentage SSD.

images have very different properties (i.e., a large number of pixels with high intensities). The quantitative analyses of SmRG and NeuronGPS' outcomes showed comparable performance of the two tools in terms of reconstructed arbors. In particular, SSD and SSD% values were similar for all PCs except for PC2, in which SmRG performs drastically better than NeuronGPS. Interestingly, SmRG reached a better precision (P) and accuracy (F-score) for all used thresholds with respect to NeuronGPS.

Reconstructions of OP fibers from the DIADEM challenge resulted in a comparable performance between the SmRG and well-established tools for neuron reconstruction in terms of SD, SSD, and SSD%. Specifically, the algorithm proposed here outperformed other tools in terms of SSD, which quantifies the discrepancy between two outcomes (Peng et al., 2011a), in almost all reconstructions. On the other hand, the SmRG exhibited higher values in the SSD% score. It should be noted that the gold-standard OP reconstructions are available in.swc format. Therefore, in order to compare the volumetric SmRG's outputs with the gold standards, firstly we were forced to reduce the information by means of a thinning algorithm. The thinning algorithm inevitably introduces mismatches, since it depends on the 3D morphology of the neuron, thus biasing the meaningfulness of the SSD% values when comparing SmrG and SoA tools (Liu et al., 2016). The precision and recall of SmRG outcomes with respect to the manually traced gold-standard provided by the DIADEM highlighted the performance of our tool with respect to SoA algorithms in the segmentation of OP fibers). In particular, for the highest values of the tolerance threshold considered, the SmRG's average values of precision,

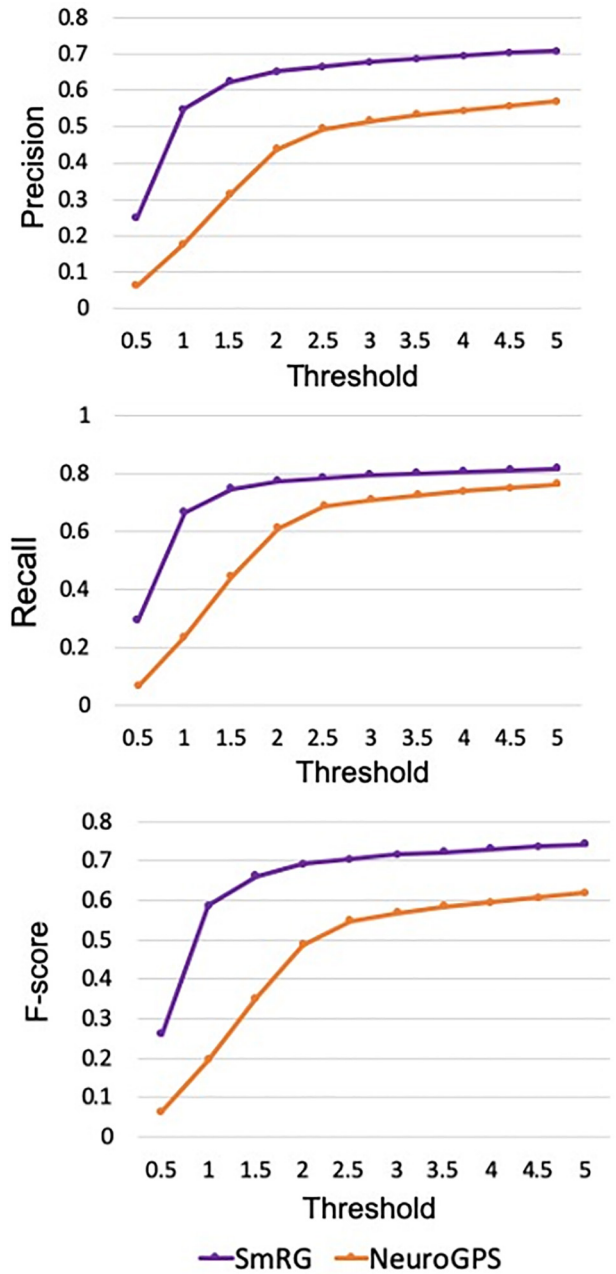


FIGURE 9 | Precision, Recall and F-Score for varying thresholds of SSD evaluation. SmRG has always better performance than NeuronGPS for increasing values of the threshold.

recall and f-score were all above 95%. This suggests that, although the algorithm was developed for segmenting neurons from clarified cerebral tissue, segmentation procedures based on local signal and noise statistics may be a successful strategy for "single-neuron" settings, and thus for delivering an adaptive and generalized algorithm, applicable to different contexts.

When two neurons naturally touch each other and the signal intensity is high, SmRG may reconstruct the

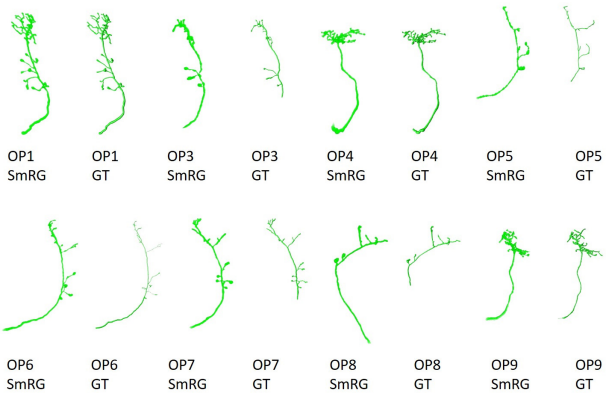


FIGURE 10 | OP fibers segmented with SmRG and compared with the DIADEM gold-standard (GS). Please note that for OP3, OP5, OP7, and OP8 the gold standard reconstruction misses some terminal branches (see DIADEM FAQ at http://diademchallenge.org/faq.html).

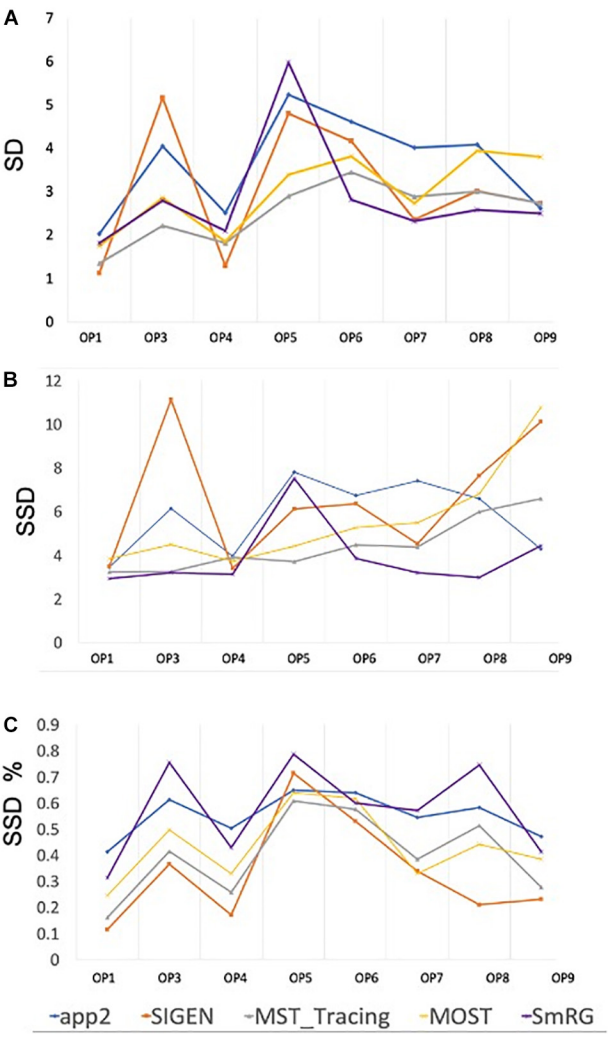


FIGURE 11 | Accuracy of SmRG and SoA tools against the DIADEM gold standard for different OP fibers. **(A)** SD **(B)** SSD, and **(C)** percentage SSD.

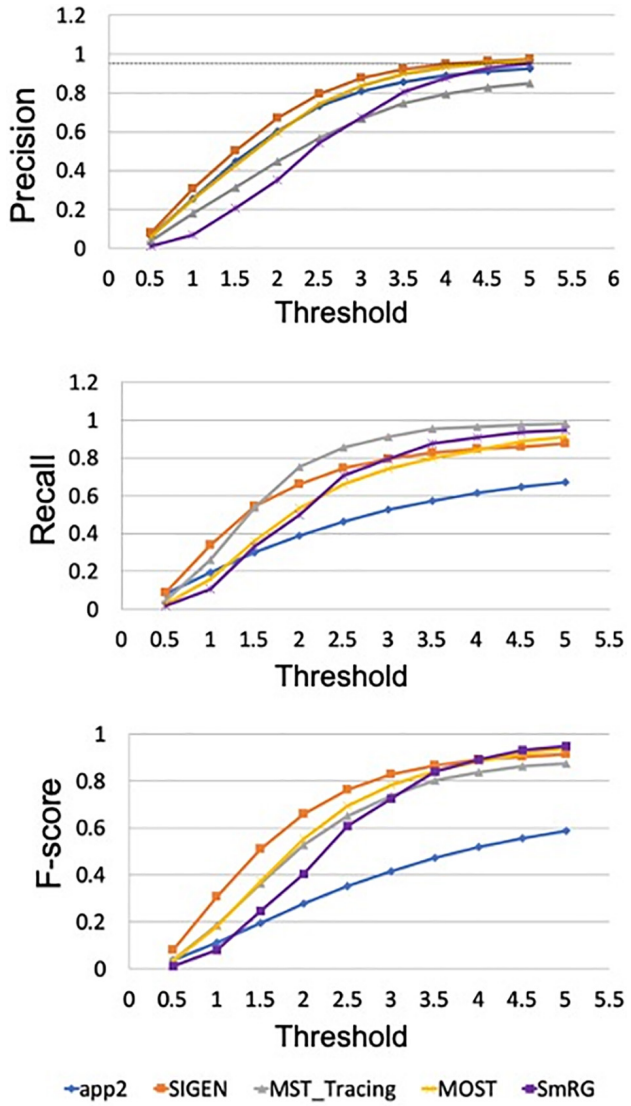


FIGURE 12 | Precision, Recall and F-Score for varying thresholds of SSD evaluation. SmRG and SoA tools have similar performance for increasing values of the threshold. For thresholds greater than four voxels, SmRG has the highest *F*-Score. For $S = 5$, we obtained $P = 0.9538 \pm 0.0350$, $R = 0.9770 \pm 0.0183$ and $F = 0.9651 \pm 0.0248$ (mean $\pm$ st. deviation) for the SmRG.

two objects as one, thus requiring their post-splitting. A watershed-based routine for separating neurons is provided at http://www.centropiaggio.unipi.it/smrg-algorithm-smart-region-growing-3d-neuron-segmentation. Nevertheless, we also take advantage of the lower intensity values of neuron boundaries with respect to neuron bodies. This heterogeneity in pixel intensity is exploited in SmRG and quantified by the mixture parameter. As a result, neuron boundaries with lower intensity values are not segmented, controlling for possible false merge errors.

We would like to highlight that SmRG was not compared with SoA segmentation approaches in terms of computational times. Indeed, tools such as app2, MST, SIGEN, MOST and NeuroGPS outperform our algorithm as they provide faster segmentations. However, while the Vaa3D plugins provide 3D neuron reconstructions with comparable accuracy and precision (**Figure 8**) for sparsely labeled data, they fail when performing segmentations of densely-packed neurons. As regards the tool described by Quan et al. (2016), the strength of SmRG lies in the amount of morphological information it provides with respect to the NeuroGPS neuron tracing.

CONCLUSION

Despite the numerous attempts addressed at 3D neuron reconstruction, little attention has been paid to delivering automatic and robust methods capable of dealing with the large variability of datasets representing densely-packed neurons, as well as for digitizing the morphology and volumetric characteristics of the segmented structures. As a result, the majority of algorithms are only able to handle with sparsely labeled data, compelling neuroscientists to manually segment images representing intricate neuronal arborisations and to reducing 3D space-filling neurons to skeletonized representations.

The SmRG, an open-source Matlab-based algorithm for the segmentation of complex structures in 3D confocal or 2-photon image stacks, overcome these setbacks. It provides an accurate reconstruction of 3D neuronal morphology acquired using confocal microscopy, which accounts for 80% of user needs in imaging facilities. The SmRG can potentially be extended to other imaging modalities (e.g., super-resolution microscopy) adopting the same statistical framework for identifying the signal and noise distribution from 3D images.

In addition, our tool allows the extraction of several useful morphological features from the segmented neurons. Preserving the volumetric information is an essential step for deciphering the Connectome. Besides structural mapping, from a biological perspective, digital 3D neuron reconstruction is crucial for the quantitative characterization of cell type by morphology and the correlation between morphometric features and genes (e.g., between wild-type and model animals) or patho-physiology (e.g., the detection of neuronal morphological anomalies in diseased individuals compared to healthy ones) (Acciai et al., 2016).

Future improvements could be obtained by coupling the NeuroGPS method (Quan et al., 2016) which rely on human strategies to separate individual neurons, with the SmRG's one, thus leveraging on both the geometric constraints of the former and the statistical properties of the latter, taking the best from both the approaches.

In conclusion, the SmRG can facilitate the identification of the different neural types populating the brain, providing

an unprecedented set of morphological information and new impetus toward connectomic mapping.

DATA AVAILABILITY STATEMENT

Publicly available datasets were analyzed in this study. This data can be found here: http://diademchallenge.org/data_set_downloads.html, http://www.centropiaggio.unipi.it/mansegtool.

AUTHOR CONTRIBUTIONS

AC, CM, and NV: conception and design of the segmentation tool. AC: implementation and testing of the algorithm. All authors interpretation of data and drafting of the manuscript.

FUNDING

This work was supported by the FLAG-ERA JTC 2019 project SENSEI (Partnering Project of the Human Brain Project).

ACKNOWLEDGMENTS

The authors would like to thank prof. Vincenzo Positano for the useful suggestions during the first steps of the algorithm design, as well as Gabriele Paolini and Gianluca Rho for their help during the first stages of SmRG implementation. The authors would also like to thank Michele Scipioni for useful suggestions during the development of the EM algorithm. CM was thankful to Fondazione Veronesi for her Post-Doctoral Fellowship.

REFERENCES

Acciai, L., Soda, P., and Iannello, G. (2016). Automated neuron tracing methods: an updated account. *Neuroinformatics* 14, 353–367. doi: 10.1007/s12021-016-9310-0

Alivisatos, A. P., Chun, M., Church, G. M., Greenspan, R. J., Roukes, M. L., and Yuste, R. (2012). The brain activity map project and the challenge of functional connectomics. *Neuron* 74, 970–974. doi: 10.1016/j.neuron.2012.06.006

Al-Kofahi, K. A., Can, A., Lasek, S., Szarowski, D. H., Dowell-Mesfin, N., Shain, W., et al. (2003). Median-based robust algorithms for tracing neurons from noisy confocal microscope images. *IEEE Trans. Inf. Technol. Biomed.* 7, 302–317. doi: 10.1109/TITB.2003.816564

Barnich, O., and Van Droogenbroeck, M. (2010). ViBe: a universal background subtraction algorithm for video sequences. *IEEE Trans. Image Process.* 20, 1709–1724. doi: 10.1109/TIP.2010.2101613

Basu, S., and Racoceanu, D. (2014). "Reconstructing neuronal morphology from microscopy stacks using fast marching," in *Proceedings of the 2014 IEEE international conference on image processing (ICIP)*, Piscataway, NJ.

Baswaraj, B. D., Govardhan, A., and Premchand, P. (2012). Active contours and image segmentation: the current state of the art. *Glob. J. Comput. Sci. Technol. Graph. Vis.* 12, 1–12. doi: 10.1002/mp.12593

Binley, K. E., Ng, W. S., Tribble, J. R., Song, B., and Morgan, J. E. (2014). Sholl analysis: a quantitative comparison of semi-automated methods. *J. Neurosci. Methods* 225, 65–70. doi: 10.1016/j.jneumeth.2014.01.017

Brice, C. R., and Fennema, C. L. (1970). Scene analysis using regions. *Artif. Intell.* 1, 205–226. doi: 10.1016/0004-3702(70)90008-1

Brown, K. M., Barrionuevo, G., Canty, A. J., De Paola, V., Hirsch, J. A., Jefferis, G. S., et al. (2011). The DIADEM data sets: representative light microscopy images of neuronal morphology to advance automation of digital reconstructions. *Neuroinformatics* 9, 143–157. doi: 10.1007/s12021-010-9095-5

Budd, J. M. L., Cuntz, H., Eglen, S. J., and Krieger, P. (2015). Editorial: quantitative analysis of neuroanatomy. *Front. Neuroanat.* 9:143. doi: 10.3389/fnana.2015.00143

Calapez, A., Pereira, H. M., Calado, A., Braga, J., Rino, J., Carvalho, C., et al. (2002). The intranuclear mobility of messenger RNA binding proteins is ATP dependent and temperature sensitive. *J. Cell Biol.* 159, 795–805. doi: 10.1083/jcb.200203046

Calapez, A., and Rosa, A. (2010). A statistical pixel intensity model for segmentation of confocal laser scanning microscopy images. *IEEE Trans. Image Process.* 19, 2408–2418. doi: 10.1109/TIP.2010.2047168

Chothani, P., Mehta, V., and Stepanyants, A. (2011). Automated tracing of neurites from light microscopy stacks of images. *Neuroinformatics* 9, 263–278. doi: 10.1007/s12021-011-9121-2

Chung, K., and Deisseroth, K. (2013). CLARITY for mapping the nervous system. *Nat. Methods* 10, 508–513. doi: 10.1038/nmeth.2481

Diaspro, A. (2001). *Confocal And Two-Photon Microscopy: Foundations, Applications and Advances. Confocal Two-Phot Microscopy Found Application Advanced by Alberto Diaspro*. Hoboken, NJ: Wiley.

Evers, J. F., Schmitt, S., Sibila, M., and Duch, C. (2005). Progress in functional neuroanatomy: precise automatic geometric reconstruction of neuronal morphology from confocal image stacks. *J. Neurophysiol.* 93, 2331–2342. doi: 10.1152/jn.00761.2004

Gillette, T. A., Brown, K. M., and Ascoli, G. A. (2011). The DIADEM metric: comparing multiple reconstructions of the same neuron. *Neuroinformatics* 9:233. doi: 10.1007/s12021-011-9117-y

Guo, X., Tang, C., Zhang, H., and Chang, Z. (2012). Automatic thresholding for defect detection. *ICIC Express. Lett.* 6, 159–164. doi: 10.1016/j.patrec.2006.03.009

Hartigan, J. A., and Hartigan, P. M. (1986). The dip test of unimodality. *Ann. Stat.* 14, 590–606.

Hernandez, M., Brewster, A., Thul, L., Telfer, B. A., Majumdar, A., Choi, H., et al. (2018). "Learning-based long-range axon tracing in dense scenes," in *Proceedings of the 2018 IEEE 15th International Symposium on Biomedical Imaging (ISBI 2018)*, Piscataway, NJ, 1578–1582.

Ikeno, H., Kumaraswamy, A., Kai, K., Wachtler, T., and Ai, H. (2018). A segmentation scheme for complex neuronal arbors and application to vibration sensitive neurons in the honeybee brain. *Front. Neuroinform.* 12:61. doi: 10.3389/fninf.2018.00061

Januszewski, M., Kornfeld, J., Li, P. H., Pope, A., Blakely, T., Lindsey, L., et al. (2018). High-precision automated reconstruction of neurons with flood-filling networks. *Nat. Methods* 15, 605–610. doi: 10.1038/s41592-018-0049-4

Jefferis, G. S., Potter, C. J., Chan, A. M., Marin, E. C., Rohlfing, T., Maurer, C. R. Jr., et al. (2007). Comprehensive maps of Drosophila higher olfactory centers: spatially segregated fruit and pheromone representation. *Cell* 128, 1187–1203. doi: 10.1016/j.cell.2007.01.040

Kass, M., Witkin, A., and Terzopoulos, D. (1988). Snakes: active contour models. *Int. J. Comput. Vis.* 1, 321–331. doi: 10.1007/bf00133570

Kayasandik, C., Negi, P., Laezza, F., Papadakis, M., and Labate, D. (2018). Automated sorting of neuronal trees in fluorescent images of neuronal networks using NeuroTreeTracer. *Sci. Rep.* 8, 1–12. doi: 10.1038/s41598-018-24753-w

Lee, T.-C., Kashyap, R. L., and Chu, C.-N. (1994). Building skeleton models via 3-D medial surface axis thinning algorithms. *CVGIP Graph. Model. Image Process.* 56, 462–478. doi: 10.1006/cgip.1994.1042

Liu, S., Zhang, D., Liu, S., Feng, D., Peng, H., and Cai, W. (2016). Rivulet: 3d neuron morphology tracing with iterative back-tracking. *Neuroinformatics* 14, 387–401. doi: 10.1007/s12021-016-9302-0

Magliaro, C., Callara, A. L., Mattei, G., Morcinelli, M., Viaggi, C., Vaglini, F., et al. (2016). Clarifying CLARITY: quantitative optimization of the diffusion based delipidation protocol for genetically labeled tissue. *Front. Neurosci.* 10:179. doi: 10.3389/fnins.2016.00179

Magliaro, C., Callara, A. L., Vanello, N., and Ahluwalia, A. (2017). A manual segmentation tool for three-dimensional neuron datasets. *Front. Neuroinform.* 11:36. doi: 10.3389/fninf.2017.00036

Magliaro, C., Callara, A. L., Vanello, N., and Ahluwalia, A. (2019). Gotta Trace 'em all: a mini-review on tools and procedures for segmenting single neurons towards deciphering the structural connectome. *Front. Bioeng. Biotechnol.* 7:202.

Maurer, C. R., and Raghavan, V. (2003). A linear time algorithm for computing exact euclidean distance transforms of binary images in arbitrary dimensions. *IEEE Trans. Pattern. Anal. Mach. Intell.* 25, 265–270. doi: 10.1109/TPAMI.2003.1177156

Meijering, E. (2010). Neuron tracing in perspective. *Cytom. Part A* 77, 693–704. doi: 10.1002/cyto.a.20895

Ming, X., Li, A., Wu, J., Yan, C., Ding, W., Gong, H., et al. (2013). Rapid reconstruction of 3D neuronal morphology from light microscopy images with augmented rayburst sampling. *PLoS One* 8:e84557. doi: 10.1371/journal.pone.0084557

Nixon, M., and Aguado, A. S. (2012). *Feature Extraction and Image Processing for Computer Vision*. Cambridge, MA: Academic Press.

Ntziachristos, V. (2010). Going deeper than microscopy: the optical imaging frontier in biology. *Nat. Methods* 7, 603–614. doi: 10.1038/nmeth.1483

Otsu, N. (1979). A threshold selection method from gray-level histograms. *IEEE Trans. Syst. Man. Cybern.* 9, 62–66. doi: 10.1109/TSMC.1979.4310076

Pawley, J. B. (2006). *Handbook Of Biological Confocal Microscopy*. Berlin: Springer, doi: 10.1007/978-0-387-45524-45522

Peng, H., Bria, A., Zhou, Z., Iannello, G., and Long, F. (2014). Extensible visualization and analysis for multidimensional images using Vaa3D. *Nat. Protoc.* 9:193. doi: 10.1038/nprot.2014.011

Peng, H., Long, F., and Myers, G. (2011a). Automatic 3D neuron tracing using all-path pruning. *Bioinformatics* 27, i239–i247. doi: 10.1093/bioinformatics/btr237

Peng, H., Long, F., Zhao, T., and Myers, E. (2011b). Proof-editing is the bottleneck of 3D neuron reconstruction: the problem and solutions. *Neuroinformatics* 9, 103–105. doi: 10.1007/s12021-010-9090-x

Peng, H., Meijering, E., and Ascoli, G. A. (2015). From diadem to bigneuron. *Neuroinformatics* 13:259. doi: 10.1007/s12021-015-9270-9

Powers, D. M. (2011). Evaluation: from precision, recall and F-measure to ROC, informedness, markedness and correlation. *J. Mach. Learn. Technol.* 2, 37–63.

Quan, T., Zhou, H., Li, J., Li, S., Li, A., Li, Y., et al. (2016). NeuroGPS-Tree: automatic reconstruction of large-scale neuronal populations with dense neurites. *Nat. Methods* 13, 51–54. doi: 10.1038/nmeth.3662

Radojeviæ, M., and Meijering, E. (2018). Automated neuron reconstruction from 3D fluorescence microscopy images using sequential monte carlo estimation. *Neuroinformatics* 17, 423–442. doi: 10.1007/s12021-018-9407-8

Richardson, D. S., and Lichtman, J. W. (2015). Clarifying tissue clearing. *Cell* 162, 246–257. doi: 10.1016/j.cell.2015.06.067

Sakkos, D., Liu, H., Han, J., and Shao, L. (2018). End-to-end video background subtraction with 3d convolutional neural networks. *Multimed. Tools Appl.* 77, 23023–23041. doi: 10.1007/s11042-017-5460-9

Sholl, D. A. (1955). The organization of the visual cortex in the cat. *J. Anat.* 89:33.

Stauffer, C., and Grimson, W. E. L. (1999). "Adaptive background mixture models for real-time tracking," in *Proceedings of the 1999 IEEE Computer Society Conference on Computer Vision and Pattern Recognition*, Cambridge, MA, 246–252.

Wang, C.-W., Lee, Y.-C., Pradana, H., Zhou, Z., and Peng, H. (2017). Ensemble neuron tracer for 3D neuron reconstruction. *Neuroinformatics* 15, 185–198. doi: 10.1007/s12021-017-9325-1

Wang, L., He, L., Mishra, A., and Li, C. (2009). Active contours driven by local Gaussian distribution fitting energy. *Signal. Process.* 89, 2435–2447. doi: 10.1016/j.sigpro.2009.03.014

Wang, Y., Narayanaswamy, A., Tsai, C.-L., and Roysam, B. (2011). A broadly applicable 3-D neuron tracing method based on open-curve snake. *Neuroinformatics* 9, 193–217. doi: 10.1007/s12021-011-9110-5

Wilt, B. A., Burns, L. D., Wei, Ho, E. T., Ghosh, K. K., Mukamel, E. A., et al. (2009). Advances in light microscopy for neuroscience. *Annu. Rev. Neurosci.* 32, 435–506.

Xiao, H., and Peng, H. (2013). APP2: automatic tracing of 3D neuron morphology based on hierarchical pruning of a gray-weighted image distance-tree. *Bioinformatics* 29, 1448–1454. doi: 10.1093/bioinformatics/btt170

Conflict of Interest: The authors declare that the research was conducted in the absence of any commercial or financial relationships that could be construed as a potential conflict of interest.

Copyright © 2020 Callara, Magliaro, Ahluwalia and Vanello. This is an open-access article distributed under the terms of the Creative Commons Attribution License (CC BY). The use, distribution or reproduction in other forums is permitted, provided the original author(s) and the copyright owner(s) are credited and that the original publication in this journal is cited, in accordance with accepted academic practice. No use, distribution or reproduction is permitted which does not comply with these terms.

frontiers in Neuroinformatics

ORIGINAL RESEARCH
published: 20 March 2020
doi: 10.3389/fninf.2020.00010

Predicting Body Mass Index From Structural MRI Brain Images Using a Deep Convolutional Neural Network

Pál Vakli[1], Regina J. Deák-Meszlényi[1], Tibor Auer[2] and Zoltán Vidnyánszky[1]*

[1] Brain Imaging Centre, Research Centre for Natural Sciences, Budapest, Hungary, [2] School of Psychology, Faculty of Health and Medical Sciences, University of Surrey, Guildford, United Kingdom

In recent years, deep learning (DL) has become more widespread in the fields of cognitive and clinical neuroimaging. Using deep neural network models to process neuroimaging data is an efficient method to classify brain disorders and identify individuals who are at increased risk of age-related cognitive decline and neurodegenerative disease. Here we investigated, for the first time, whether structural brain imaging and DL can be used for predicting a physical trait that is of significant clinical relevance—the body mass index (BMI) of the individual. We show that individual BMI can be accurately predicted using a deep convolutional neural network (CNN) and a single structural magnetic resonance imaging (MRI) brain scan along with information about age and sex. Localization maps computed for the CNN highlighted several brain structures that strongly contributed to BMI prediction, including the caudate nucleus and the amygdala. Comparison to the results obtained via a standard automatic brain segmentation method revealed that the CNN-based visualization approach yielded complementary evidence regarding the relationship between brain structure and BMI. Taken together, our results imply that predicting BMI from structural brain scans using DL represents a promising approach to investigate the relationship between brain morphological variability and individual differences in body weight and provide a new scope for future investigations regarding the potential clinical utility of brain-predicted BMI.

Keywords: deep learning, convolutional neural networks, magnetic resonance imaging, body mass index, caudate nucleus, amygdala

OPEN ACCESS

Edited by:
Ludovico Minati,
Tokyo Institute of Technology, Japan

Reviewed by:
M. Justin Kim,
University of Hawai'i at Mānoa, United States
Guido van Wingen,
University of Amsterdam, Netherlands
Ahmed El-Gazzar,
University of Amsterdam, Netherlands, in collaboration with reviewer GW

****Correspondence:***
Pál Vakli
vakli.pal@ttk.mta.hu

Received: *20 November 2019*
Accepted: *02 March 2020*
Published: *20 March 2020*

Citation:
Vakli P, Deák-Meszlényi RJ, Auer T and Vidnyánszky Z (2020) Predicting Body Mass Index From Structural MRI Brain Images Using a Deep Convolutional Neural Network. Front. Neuroinform. 14:10. doi: 10.3389/fninf.2020.00010

INTRODUCTION

Over the last few years, the use of deep learning (DL) has become increasingly widespread in the analysis of neuroimaging data in several different application domains (Arbabshirani et al., 2017; Litjens et al., 2017; Shen et al., 2017; Zaharchuk et al., 2018; Davatzikos, 2019). DL is a branch of machine learning that allows the construction of computational models that learn to represent data at increasing levels of abstraction to solve specific tasks (LeCun et al., 2015; Goodfellow et al., 2016). Among DL methods, deep convolutional neural networks (CNNs) (LeCun et al., 1990;

Lecun et al., 1998), which are widely adopted in the computer vision community due to their capability to achieve outstanding object detection performance (Krizhevsky et al., 2012), represent a promising approach to analyzing brain imaging data in studies of psychiatric and neurological disorders (Vieira et al., 2017; Durstewitz et al., 2019). The majority of studies employing CNNs used structural and/or functional magnetic resonance imaging (MRI) data to examine patients with Alzheimer's disease and mild cognitive impairment (Gupta et al., 2013; Payan and Montana, 2015; Sarraf and Tofighi, 2016; Farooq et al., 2017; Meszlényi et al., 2017; Hosseini-Asl et al., 2018; Islam and Zhang, 2018; Basaia et al., 2019); although there are examples of studies classifying other mental disorders as well, such as attention-deficit hyperactivity disorder (Zou et al., 2017) and alcoholism (Wang et al., 2017).

The potential of these methods lies partly in that—in contrast to conventional mass univariate analytical methods—machine learning in general and DL in particular allow statistical inferences at the individual level (Vieira et al., 2017). Besides the diagnosis of brain disorders, machine learning can also be used to identify individual differences in the brain aging process (Cole and Franke, 2017; Cole et al., 2019). DL methods are increasingly prevalent in this application area as well, as CNNs can be used to predict the chronological age of individual subjects based on structural brain MRI scans with a mean absolute error (MAE) of 4.16 years (Cole et al., 2017). Comparable results can be obtained with CNNs using whole-brain functional connectivity patterns, derived from resting-state fMRI data, as input (Li et al., 2018; Vakli et al., 2018). These findings bear significance for two main reasons. First, they provide proof of concept that a single MRI scan contains information that is strongly related to chronological age (Cole and Franke, 2017). Second, they provide a means to quantify the individual risk of age-related cognitive decline and disease. In fact, several studies have shown that an increase in brain-predicted age relative to chronological age is associated with various neurological and psychiatric disorders, poorer physical fitness, and increased risk of mortality (Franke and Gaser, 2012; Koutsouleris et al., 2014; Cole et al., 2015, 2018; Habes et al., 2016; Löwe et al., 2016; Pardoe et al., 2017).

The above findings demonstrate how computational models aimed at predicting a certain biometric trait have potential clinical applicability. Here we investigated whether structural brain imaging and machine learning can be used for predicting a physical trait that is of significant clinical relevance—the body mass index (BMI) of the individual. The prevalence and disease burden of excessive body weight is on the rise globally (The GBD 2015 Obesity Collaborators, 2017), and there is extensive evidence showing a relationship between obesity—defined as a BMI greater than 30 kg/m^2—and brain health. In particular, a number of studies have shown that obesity and associated cardiovascular disease and metabolic disorders in midlife are related to cognitive impairment and dementia in later life (Pedditizi et al., 2016; Dye et al., 2017; Alford et al., 2018; Singh-Manoux et al., 2018). To date, a large number of studies using conventional neuroimaging methods have investigated the differences in brain structure and function between obese/overweight and lean individuals. Increased BMI has been associated with reduced gray matter volume (Pannacciulli et al., 2006; Taki et al., 2008; Raji et al., 2010; Brooks et al., 2013) and white matter integrity (Stanek et al., 2011; Kullmann et al., 2015). Altered resting-state functional connectivity (Avery et al., 2017) and activation to visual food cues in brain regions involved in reward processing and inhibitory control (Carnell et al., 2012; Pursey et al., 2014; Val-Laillet et al., 2015) have also been described in obese individuals. A recent study has investigated the associations between obesity, regional gray matter volumes, and white matter microstructure, as assessed by MRI, in a large sample of 12,087 participants (Dekkers et al., 2019). The authors have found sex differences in the relationship between total body fat percentage and the volume of several subcortical regions of the brain reward system, and contrary to previous findings, a positive association between total body fat percentage and white matter microstructural coherence.

Training a machine learning algorithm to predict individual BMI based on brain imaging data has several potential applications. On the one hand, once sufficiently accurate prediction performance is achieved, it is possible to investigate which features (e.g., structural properties of the brain) contribute significantly to the predicted value. This has the potential to provide complementary information regarding the relationship between brain structure and body weight, besides conventional neuroimaging approaches. On the other hand, it can pave the way for potential clinical applications, inasmuch as the discrepancy between the true and the predicted BMI might be related to individual differences in food intake regulation and associated propensity for future weight gain. This would be analogous to that how the difference between brain-predicted and chronological age is used to quantify health risks.

Here we apply, for the first time to our knowledge, DL to predict individual BMI based on brain imaging data. In particular, we employ a CNN for BMI prediction based on T1-weighted structural MR images, as well as information about the participants' age and sex. This approach has the advantage of being able to use minimally preprocessed neuroimaging data as input and automatically learn a hierarchical set of representations suitable for solving the task at hand (LeCun et al., 2015), as opposed to conventional neuroimaging and machine learning methods that rely on *a priori* manual extraction of features from raw data (Vieira et al., 2017). Based on the findings discussed above, we hypothesized that BMI could be accurately predicted based on a single MRI bran scan, and hence a CNN can be trained to effectively perform this task on novel scans as well.

Once a well-performing model has been obtained and tested on new data, a logical next step is to try to make sense of why the model predicts what it predicts. While deep neural networks are usually regarded as "black boxes," it is possible to give reasonable explanations for their predictions without elucidating the underlying mechanisms (Lipton, 2016). Common approaches include projecting hidden layer activations back to input space to find patterns that excite feature maps the most (Zeiler and Fergus, 2014), examining the effect of occluding different parts of the input image on model performance (e.g., Vakli et al., 2018), or identifying those pixels in the input image that have the greatest impact on the model's predictions (e.g., Simonyan et al., 2013).

With regard to the latter approach, a particular method that has been used extensively in recent years to provide "visual explanations" for CNNs' decisions is Gradient-weighted Class Activation Mapping (Grad-CAM) (Selvaraju et al., 2017). This technique uses the gradient information flowing into the last convolutional layer of the CNN to highlight image regions that played an important role in predicting a certain target concept. Here we adapted this method to the context of regression based on 3D images to localize brain regions that made a significant contribution to BMI prediction.

Since the present study represents one of the first attempts to apply Grad-CAM for analyzing neuroimaging data, we also intended to investigate the neural underpinnings of individual differences in body weight using a more conventional neuroimaging approach and compare the obtained results. To this end, we performed automatic anatomical processing using the FreeSurfer software and general linear modeling to examine the relationship between brain morphology and BMI. FreeSurfer implements the automatic reconstruction of the cortical surface as well as subcortical structure segmentation using a probabilistic atlas (Dale et al., 1999; Fischl et al., 1999). The simultaneous application of the DL and automatic segmentation methods was motivated by the possibility that, as compared to this more conventional latter approach, using minimally preprocessed anatomical images and representation learning paired with gradient-based visualization would yield complementary evidence regarding the relationship between brain structure and body weight.

MATERIALS AND METHODS

Dataset

All analyses reported in this article include participants from the UK Biobank population cohort[1]. UK Biobank is a large prospective study comprising around 500,000 individuals recruited between 2006 and 2010 from across Great Britain who underwent physical and cognitive assessment, provided biological samples and completed questionnaires examining health and lifestyle (Allen et al., 2012). A subset of the participants (N = 22,392) underwent additional MRI from May 2014 until the data release in October 2018. Participants with a self-reported history of cancer, stroke, heart attack, deep-vein thrombosis, or pulmonary embolism diagnosed by a medical doctor (based on data-fields 2453, 6150, and 6152) were omitted from the current study. Additionally, only participants whose body mass indices were reported at the time of the imaging visit (data-field 21,001 instance 2) were included in the analyses. Finally, participants with a raw T1-weighted structural image deemed "unusable" by the UK Biobank team were also excluded. Image quality control on behalf of UK Biobank consisted of the rough manual review of T1 images supplemented by a beta-version automated quality control pipeline (Alfaro-Almagro et al., 2018). Eventually, 9518 females, aged between 45 and 80 years (mean ± SD = 62.11 ± 7.30 years), and 8420 males, aged between 44 and 80 years (mean ± SD = 63.21 ± 7.59 years), were included in the present study. For females, BMI ranged between 13.39 and 58.70 kg/m^2 (mean ± SD = 26.15 ± 4.72 kg/m^2), while for males, it ranged between 16.67 and 58.04 kg/m^2 (mean ± SD = 27.03 ± 3.99 kg/m^2).

All participants provided informed consent to participate in the UK Biobank study. The UK Biobank Research Ethics Committee (REC) approval number is 11/NW/0382. Detailed information on the consent procedure of UK Biobank are available at the following URL: http://biobank.ctsu.ox.ac.uk/crystal/field.cgi?id=200.

Data Acquisition and Preprocessing

Neuroimaging

Data were acquired on Siemens Skyra 3T MRI scanners (Siemens Healthcare, Erlangen, Germany) at the UK Biobank imaging centers in Cheadle, Newcastle, and Reading. A standard Siemens 32-channel RF receive head coil was applied. The brain imaging protocol included a T1-weighted 3D magnetization-prepared rapid gradient echo (MPRAGE) sequence for structural imaging, using in-plane acceleration (iPAT = 2) and a field-of-view (FOV) of 208 × 256 × 256 with isotropic 1 mm spatial resolution.

Raw T1-weighted images were preprocessed by the UK Biobank team using an automated processing pipeline based on FSL tools (Jenkinson et al., 2012). The preprocessing pipeline included gradient distortion correction, cutting down the FOV, skull stripping, and non-linear transformation to MNI152 space (Alfaro-Almagro et al., 2018). In-house preprocessing was limited to reducing the size of the images to ease the computational burden of processing large 3D volumes. In particular, the "zoom" function of the multi-dimensional image processing package (scipy.ndimage) of the SciPy ecosystem[2] was used to resample each image by a factor of 0.5 using spline interpolation, resulting in images of shape 91 × 109 × 91 with isotropic 2 mm spatial resolution.

Body Mass Index

Data on weight were collected using a Tanita BC418MA body composition analyzer (Tanita Corporation of America, Inc., Arlington Heights, IL, United States). A Seca 240 cm height measure (Seca Deutschland, Hamburg, Germany) was used to obtain standing height measurement from participants. Body mass index was calculated as follows:

$$\text{BMI} = \text{weight in kilograms/height in meters}^2$$

Further details on the anthropometric measurements can be obtained from the following URL: http://biobank.ndph.ox.ac.uk/showcase/refer.cgi?id=146620.

Age and Sex

The age of each participant was derived from the date of birth (data-fields 34, 52) and the date of the imaging visit (data-field 21,003 instance 2) and was given in years with precision to the month. Sex was self-reported (data-field 31) and coded as 0 for female and 1 for male.

[1]https://www.ukbiobank.ac.uk/

[2]https://scipy.org/

Prediction of Body Mass Index

Neural Network Architecture

We used a CNN to predict BMI. The prediction of the model is based on three inputs from each subject:

1. T1-weighted brain image in MNI152 space, encoded in a Numpy[3] array of shape 91 × 109 × 91.
2. Chronological age of the participant in years with precision to the month.
3. Sex of the participant (0 for female and or 1 for male).

[3]https://numpy.org/

The output of the network is a single scalar corresponding to the predicted BMI of the subject.

A schematic illustration of the network architecture is given in **Figure 1**. The network comprises repeated blocks of 3D spatially separable convolutional layers followed by batch normalization (Ioffe and Szegedy, 2015) and rectified linear unit (ReLU) activation function (Nair and Hinton, 2010). In 3D spatially separable convolutional layers, instead of convolving the input

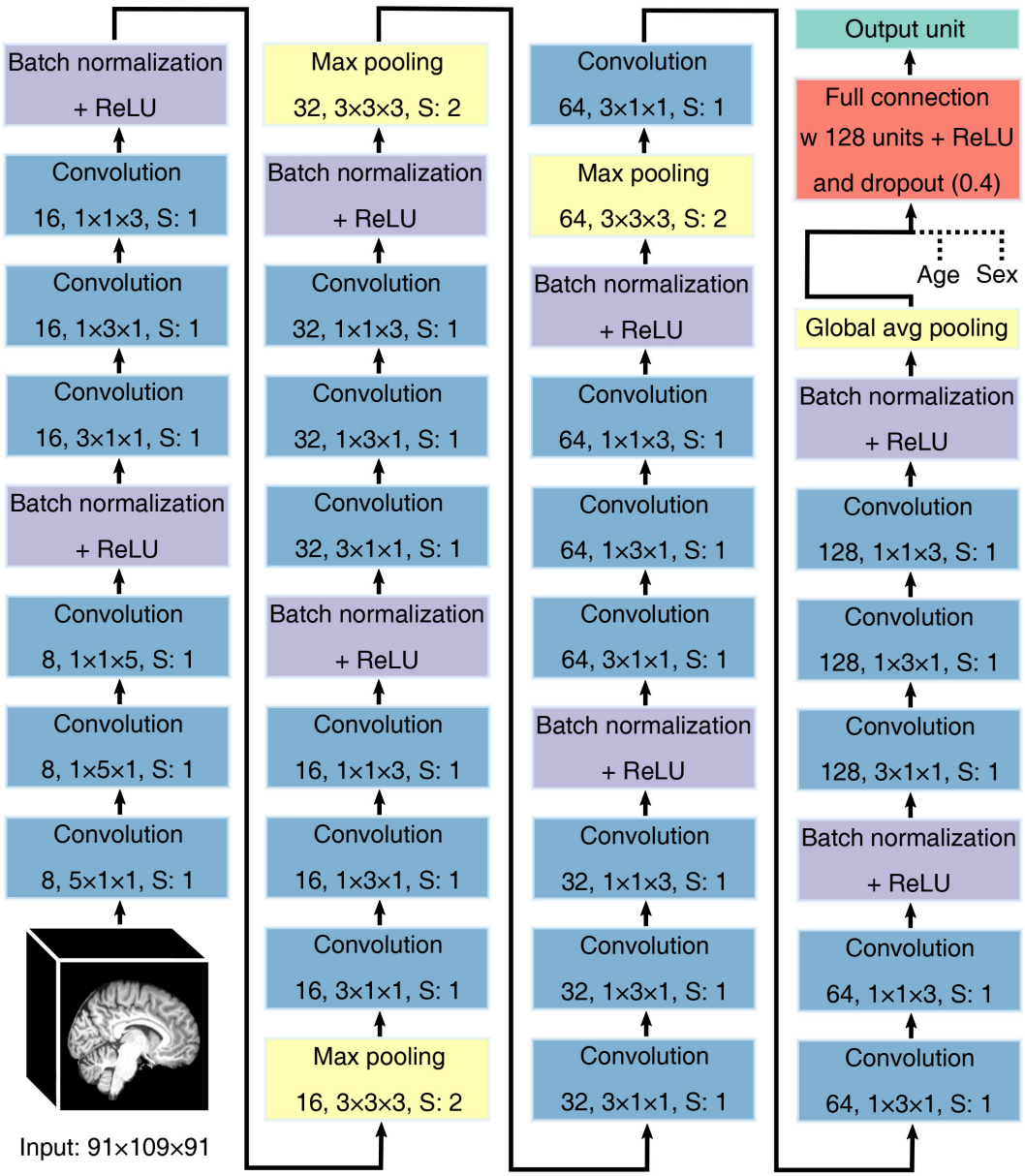


FIGURE 1 | Schematic illustration of the architecture of the convolutional neural network used for predicting body mass index. The network comprises repeated blocks of 3D spatially separable convolutional layers followed by batch normalization and ReLU, with every other block followed by a pooling layer to subsample the input. Global average pooling is used to map the feature maps of the last block to a vector (with a single scalar for each feature map) that is fed into a fully connected hidden layer followed by a single output unit for BMI prediction. Dashed lines denote concatenation, S denotes stride.

with filters of shape $N \times N \times N$, a cascade of three asymmetric filters of shapes $N \times 1 \times 1$, $1 \times N \times 1$, and $1 \times 1 \times N$ is used. Such a factorization of convolution operations reduces the computational cost by reducing the number of parameters (Szegedy et al., 2016) and has been used effectively in 3D medical image processing (Silva et al., 2018). Filter size is $N = 5$ (with a stride of 1) for the first set of convolution operations and $N = 3$ afterward. The number of filters is eight in the first convolutional layer and is doubled at regular intervals to enable the learning of a rich set of feature representations of the input brain image. All convolutional layers used SAME padding.

Every other batch normalization layer is followed by max pooling (filter shape $3 \times 3 \times 3$, stride = 2) to subsample the input images, and global average pooling is implemented after the last batch normalization layer to calculate the average intensity value of each feature map computed by the last convolutional layer. The output of this operation, along with the values representing age and sex, is fed into a fully connected hidden layer with 128 units and ReLU activation function. This hidden layer is connected to a single output unit, the activation of which corresponds to the predicted BMI value.

The CNN has 231,681 parameters overall, out of which 230,961 parameters are trainable. The model was implemented in Python using TensorFlow 1.13.[4] and the source code of the model along with the learnt parameters is available on GitHub: https://github.com/vaklip/cnn_3d_regression.

To examine whether information about age and sex was crucial for BMI prediction we also trained a network that was identical to the one described above, except that the values representing age and sex were not concatenated to the output of the global average pooling operation nor were they fed to the network in any other way.

Model Training

The weights of the convolutional and fully connected layers were initialized using Xavier initialization (Glorot and Bengio, 2010). The shifting and scaling parameters of the batch normalization layers were initialized to zeros and ones, respectively. The bias terms of the fully connected layers were initialized to 0.01. To train the network, we used mean squared error as the loss function, Adam optimizer (Kingma and Ba, 2014) with a learning rate of 0.0005 (momentum decay hyperparameter $\beta1 = 0.9$, scaling decay hyperparameter $\beta2 = 0.999$) and a batch size of eight. Dropout regularization (Wager et al., 2013; Srivastava et al., 2014) with a dropout rate of 0.4 was applied to the fully connected hidden layer during training.

The brain images of all participants were randomly assigned to disjoint training ($N = 13938$), validation ($N = 2000$), and test ($N = 2000$) sets. Only data in the training and validation sets were used for training and hyperparameter selection. The model was trained on the training set for a total of 50 epochs, and its performance was evaluated on the validation set after each epoch. A snapshot of the model parameters leading to the best validation set performance was restored and the final model was evaluated on the test set. Model performance is characterized by the MAE, standard deviation of the absolute error (STDAE), coefficient of determination (R^2), root mean square error (RMSE), and Pearson's correlation coefficient (r) between the true and predicted BMI values.

A single NVIDIA Quadro M4000 GPU was used to train the CNN, with a runtime of about 1 h per epoch.

Transfer Learning

We used transfer learning to investigate the generalizability of our approach. Transfer learning refers to the method of training a neural network on one dataset (the source domain) and then adapting the model to a different dataset and/or task (the target domain) by transfer and fine-tuning of the previously learned model weights. In our case, the UK Biobank dataset constituted the source domain and the Information eXtraction from Images (IXI) dataset[5] including brain MR images from multiple sites in London constituted the target domain. We included the T1-weighted MR images of 269 subjects from the IXI dataset who fell into the age range corresponding to the UK Biobank sample: 177 females aged between 44 and 78 years (mean $\pm$ SD = 60.50 $\pm$ 8.32 years) and 115 males aged between 44 and 79 years (mean $\pm$ SD = 59.48 $\pm$ 9.05 years). These images were recorded using Philips Intera 3T ($N = 96$; Hammersmith Hospital) and Philips Gyroscan Intera 1.5T ($N = 173$; Guy's Hospital) scanners and a FOV of $150 \times 256 \times 256$ and spatial resolution of 1.2 mm $\times$ 0.938 mm $\times$ 0.938 mm. Images recorded at a third location (Institute of Psychiatry using a GE 1.5T system) were omitted from the current analysis due to the very low number of participants that matched the given age range ($N = 23$). In-house image preprocessing was limited to spatial normalization to MNI152 space and skull-stripping using the SPM12 toolbox[6] and custom-made scripts running on MATLAB 2015a (MathWorks Inc., Natick, MA, United States).

Images were randomly divided into disjoint training ($N = 197$), validation ($N = 36$), and test sets ($N = 36$). The weights of the network were initialized to those learnt on the UK Biobank dataset and then trained on the IXI dataset for 50 epochs, using data augmentation (random rotations of maximum 5 degrees and translations of 10 voxels). The neural network architecture and training hyperparameters were the same as those used for training on UK Biobank data. A snapshot of the model parameters leading to the best validation set performance (evaluated at the end of each epoch) was restored and the final model was evaluated on the test set.

Localizing Brain Regions Relevant for BMI Prediction

In order to obtain localization maps highlighting brain regions that are important for BMI prediction, we used a modified version of the Grad-CAM (Selvaraju et al., 2017). The Grad-CAM method aims to provide visual explanations for the decisions made by a wide variety of CNNs. It uses the gradients of a given target concept flowing into the final convolutional layer

[4]https://www.tensorflow.org

[5]https://brain-development.org/ixi-dataset/

[6]http://www.fil.ion.ucl.ac.uk/spm/software/spm12/

to produce a coarse localization map that highlights regions in the input image that are important for predicting that concept. We applied two modifications to the original method. First, we adapted it for processing 3D images, similarly to (Wang et al., 2019). We computed the gradient of the predicted BMI-score y with respect to the feature maps A^n of the last convolutional layer, and performed global average pooling on these gradients to obtain an importance weight α_n for each feature map:

$$\alpha_n = \frac{1}{Z} \sum_i \sum_j \sum_k \frac{\partial y}{\partial A^n_{ijk}} \quad (1)$$

where Z is the number of units in a feature map. Then, the weighted combination of the features maps was calculated to obtain the localization map $L \in \mathbb{R}^{u \times v \times w}$:

$$L = \sum_n \alpha_n A^n \quad (2)$$

In the original formulation of Grad-CAM, which was developed to provide class-discriminative visualizations, a ReLU was applied to L in order to highlight features that have a positive influence on the class of interest, as negative values would likely belong to other classes (Selvaraju et al., 2017). Here, since our CNN performed a regression task with a single output unit, and hence we were interested in features that have either positive or negative influence on predicted BMI, we omitted this step.

Localization maps were computed for each individual in the UK Biobank test set. They were upsampled to match the size of the input images using spline interpolation (for details, see section "Neuroimaging"). Intensity values were standardized to have zero mean and unit variance. As all brain images were registered to MNI152 space, a voxelwise grand average localization map across all test subjects could be computed. The resulting map was thresholded at two standard deviations from the mean and superimposed on the ch2bet MRIcron[7] template to visualize regions in the brain that made a strong contribution to BMI prediction. To investigate the robustness of the results, a grand average localization map was also computed for the training set. This localization map was visually indistinguishable from the one obtained for the test set.

Examining the Relationship Between BMI and Brain Volumetric and Morphometric Variability

Based on the visualization provided by the modified Grad-CAM method, we performed further exploratory analyses to investigate the association between BMI and morphological variability in the human brain using the UK Biobank data. To this end, we randomly selected a subset of 200 participants from the test set, with the only constraint being that the male–female ratio and the distribution of chronological age and BMI remain similar to those in the overall test set. We used FreeSurfer 6.0[8] to automatically parcellate the cortical surface and segment the subcortical structures in the anatomical images of these subjects (Dale et al., 1999; Fischl et al., 1999). Then we investigated the relationship between different measures of cortical and subcortical anatomy—estimated by FreeSurfer—and the true BMI of participants, as detailed below.

Subcortical Segmentation

The volume-based stream of FreeSurfer (Fischl et al., 2002, 2004) was used to quantify the volumes of left and right hemisphere subcortical structures. Subcortical structures were selected for volumetric analysis based on the regions highlighted in the localization map produced by the modified Grad-CAM method. We computed partial correlations to examine the relationship between subcortical structure volume and BMI while controlling for chronological age, sex, and overall subcortical gray matter volume. We controlled for the former two variables since they were added as covariates to the CNN model which was therefore able to adjust for structural differences between individuals of different age and sex. Partial correlations were calculated using Statistica 13.4. (TIBCO Software Inc., Palo Alto, CA, United States).

Cortical Parcellation

The surface-based stream of FreeSurfer (Dale et al., 1999; Fischl et al., 1999) was used to construct models of the boundaries between white matter and cortical gray matter (the white surface), and between gray matter and the cerebrospinal fluid (the pial surface). The triangular tessellation of these surfaces allows for the calculation of several morphometric measures at each location (vertex) of the cortex, including cortical thickness, area, and curvature. We investigated the relationship between these three measures and BMI using FreeSurfer's Query, Design, Estimate, Contrast (QDEC) tool. Specifically, after smoothing individual subject data to the average surface with a 10-mm full-width at half maximum Gaussian kernel, a general linear model (GLM) with one of the morphometric measures as dependent variable was applied at each vertex, accounting for the effects of age, sex, and total cortical gray matter volume. False discovery rate (FDR) correction (threshold at 0.05) was applied to reduce Type I. errors associated with multiple comparisons.

Based on the grand average localization map, we directly investigated the association between the morphology of the right middle temporal gyrus and BMI. In particular, we computed partial correlations to examine the relationship between BMI and surface area, mean thickness and curvature while controlling for age, sex, and total cortical gray matter volume.

RESULTS

BMI Prediction

Overall, results showed that our CNN model can be used to predict BMI with high accuracy. Prediction error on the validation set reached a minimum after 32 epochs (MAE = 2.41 kg/m^2, STDAE = 1.93 kg/m^2). The model generalized well to the brain images in the test set

[7] https://people.cas.sc.edu/rorden/mricron/index.html
[8] http://surfer.nmr.mgh.harvard.edu

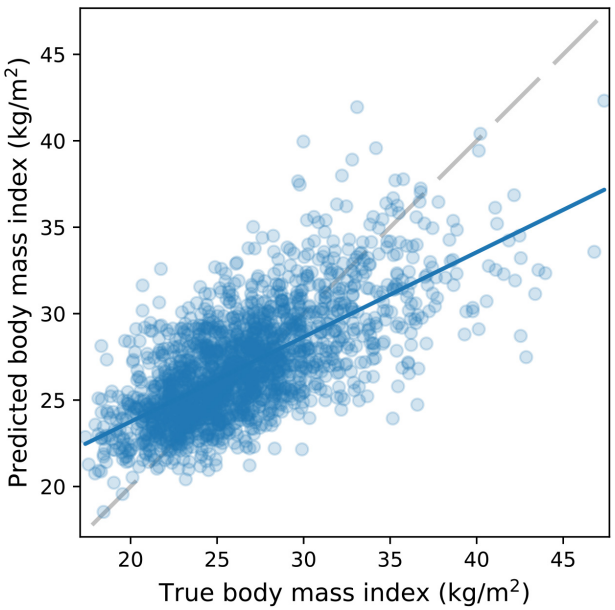


FIGURE 2 | BMI prediction accuracy on the UK Biobank dataset. The scatterplot depicts the true (horizontal axis) and the CNN-predicted BMI (vertical axis) on the test set (*N* = 2000). A least squares regression line (continuous blue) is superimposed on the scatterplot.

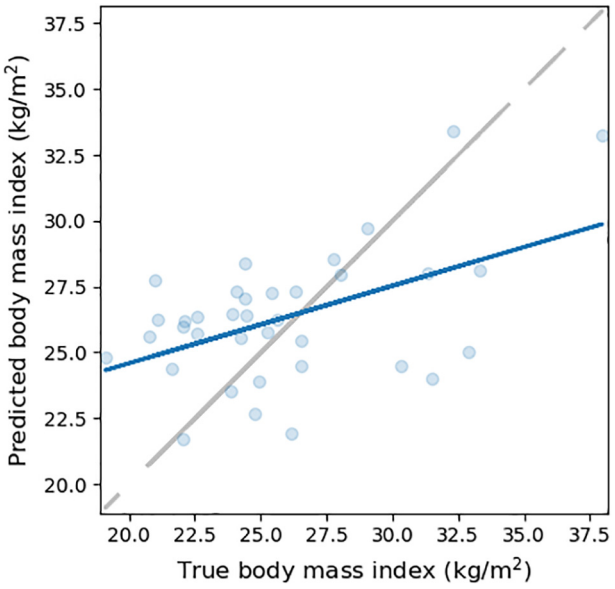


FIGURE 3 | BMI prediction accuracy on the IXI dataset. The scatterplot depicts the true (horizontal axis) and the CNN-predicted BMI (vertical axis) on the test set (*N* = 36). A least squares regression line (continuous blue) is superimposed on the scatterplot.

(**Figure 2**): MAE = 2.48 kg/m^2; STDAE = 2.09 kg/m^2; RMSE = 3.24 kg/m^2; Pearson $r = 0.68$; $R^2 = 0.44$.

When training the network without feeding information about age and sex to it, it took longer to reach a minimum of prediction error on the validation set (after 41 epochs, MAE = 2.36 kg/m^2, STDAE = 2.09 kg/m^2). Nevertheless, the model generalized well to the test set images: MAE = 2.41 kg/m^2; STDAE = 2.11 kg/m^2; RMSE = 3.20 kg/m^2; Pearson $r = 0.7$; $R^2 = 0.46$.

When fine-tuning learned weights on the IXI dataset, validation error reached a minimum after 44 epochs (MAE = 2.53 kg/m^2; STDAE = 2.00 kg/m^2).We obtained reasonable BMI prediction on the IXI test set (**Figure 3**; MAE = 3.00 kg/m^2; STDAE = 2.12 kg/m^2; RMSE = 3.67 kg/m^2; Pearson $r = 0.49$; $R^2 = 0.21$), albeit it was below the performance obtained in the case of the UK Biobank dataset.

Localization Map

The grand average localization map across all the 2000 subjects' images in the test set is depicted in **Figure 4**. The map highlights several regions that, on average, have a strong influence on predicted BMI. These regions include the left caudate, the left medial temporal lobe in the vicinity of the amygdala, and the lateral surface of the right temporal cortex, encompassing the middle temporal gyrus.

Brain Volumetric and Morphometric Analyses

Based on the localization map, two subcortical regions, the left caudate and amygdala, were selected for volumetric analysis in a subset of the test subjects (**Figure 5**). On the one hand, there was no significant partial correlation between the volume of the caudate and the true BMI of the subjects when controlling for chronological age, sex, and overall subcortical gray matter volume ($r = 0.028$, $p = 0.7$). This may be accounted for by sex differences in the relationship between caudate volume and BMI (**Figure 5**, left panel). On the other hand, a significant partial correlation between the volume of the amygdala and BMI was observed ($r = 0.19$, $p = 0.008$), showing that increased BMI is associated with increased amygdalar volume.

Regarding the analysis of cortical morphometry, no significant association between BMI and cortical thickness or curvature was observed after correcting for multiple comparisons (FDR threshold at 0.05). However, a positive relationship was observed between BMI and the area of the isthmus cingulate in the right hemisphere (**Figure 6**). The direct tests (partial correlations) of the association between BMI and morphological measures of the right middle temporal gyrus yielded no significant results.

DISCUSSION

In this proof-of-concept study, we established that a deep CNN can be used to predict individual BMI with high accuracy, based on a single structural MRI brain scan and information about age and sex. This finding is in line with the results of several previous studies showing gray and white matter structural alterations in obese individuals (Brooks et al., 2013; Kullmann et al., 2015; Dekkers et al., 2019). We also demonstrated that gradient-based visualization can be used effectively to highlight brain regions that play an important role in BMI prediction.

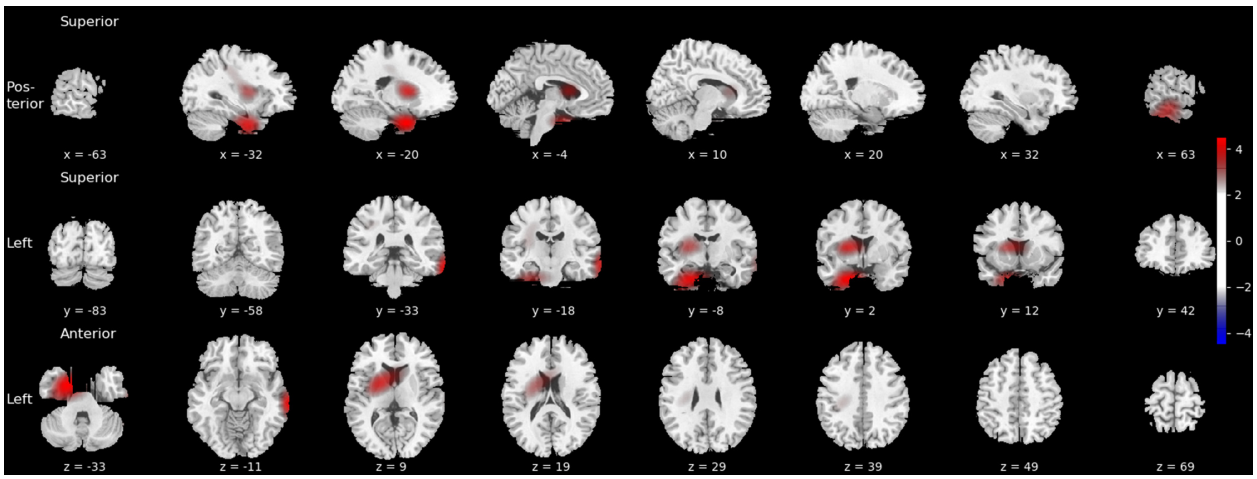


FIGURE 4 | Grand average localization map highlighting brain regions that strongly contribute to predicted BMI. Activation values are *z*-scored and thresholded at $|Z| > 2$. The localization map is superimposed on the ch2bet MRIcron template with MNI coordinates displayed below each slice.

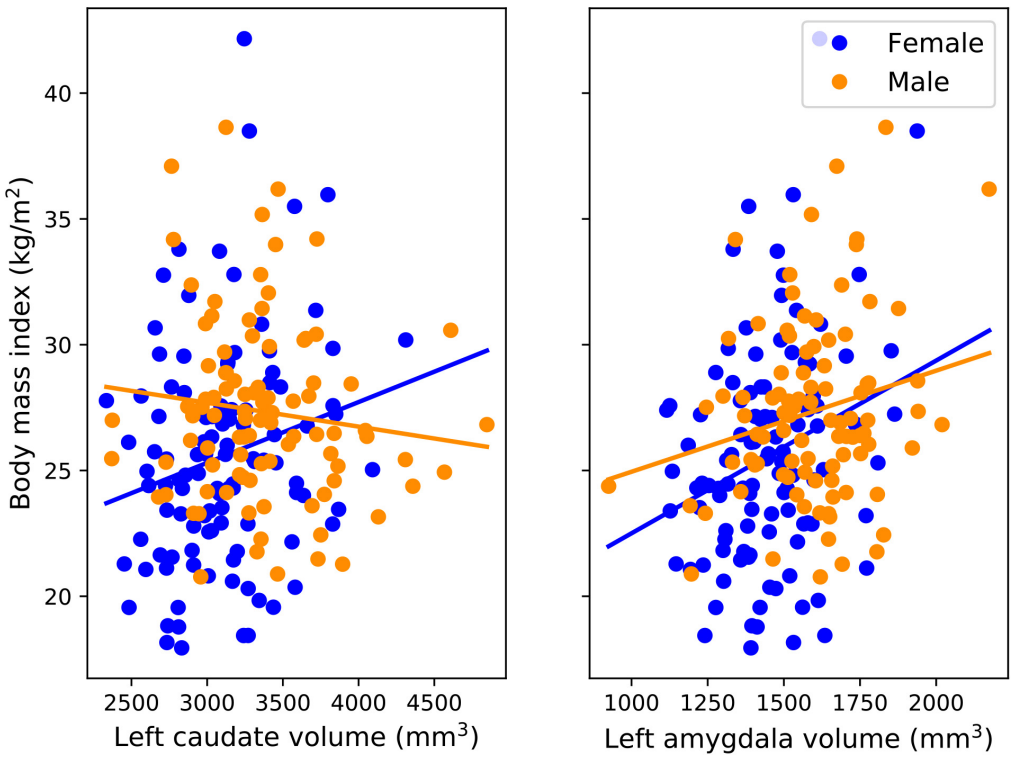


FIGURE 5 | BMI and subcortical volumes. Scatterplots depict the volumes of the caudate **(left panel)** and amygdala **(right panel)** in the left hemisphere and the true BMI values of male ($N = 93$) and female ($N = 107$) subjects in the test set.

More specifically, we used the Grad-CAM method, based on the gradient information flowing into the last convolutional layer of the CNN (Selvaraju et al., 2017), and adapted it to the context of regression using 3D images to identify brain regions that, on average, made a strong contribution to predicted BMI values. Our results suggest that, in addition to conventional neuroimaging methods and analytical techniques, the use of DL along with visual explanations for model predictions is a suitable approach for identifying the brain structural correlates of individual variability in body weight.

In particular, the localization map produced by the Grad-CAM method highlighted a set of brain regions including a portion of the left medial temporal lobe in the vicinity of the amygdala. The relationship between amygdalar volume and

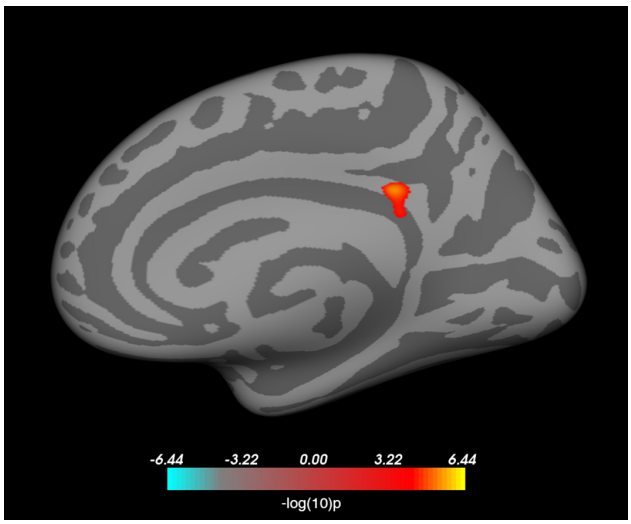


FIGURE 6 | Vertex-wise analysis of surface area using FreeSurfer. BMI is significantly associated with surface area in a right hemisphere cluster encompassing the isthmus cingulate cortex (when age, sex, and total cortical gray matter volume are controlled for). The cluster survived false discovery rate correction at threshold $p < 0.05$.

BMI was also confirmed by using FreeSurfer-based subcortical segmentation and partial correlation correcting for age and sex, which showed that higher BMI was associated with larger amygdalar volume. Previous studies using voxel-based (Taki et al., 2008) and tensor-based morphometry (Raji et al., 2010) found a relationship between BMI and the volume of gray and white matter in the medial temporal lobe. With regard to the amygdala, a positive relationship between BMI and amygdalar volume was already found in children and adolescents (Perlaki et al., 2018), young adults (Orsi et al., 2011), and elderly subjects (Widya et al., 2011); although a negative association has also been described (Kharabian Masouleh et al., 2016). Taken together, these results show that the DL approach paired with gradient-based visualization and more conventional neuroimaging methods provide converging evidence regarding the link between body weight and amygdalar structure. This is in accordance with the results of functional neuroimaging studies providing evidence for the involvement of the amygdala in processing visual food cues (van der Laan et al., 2011; Tang et al., 2012; van Bloemendaal et al., 2014).

Besides the commonalities, several discrepancies have been observed between the results of the Grad-CAM-based localization and the vertex-wise analysis using FreeSurfer. On the one hand, the vertex-wise analysis yielded a significant association between BMI and the surface area in a region corresponding to the isthmus cingulate in the right hemisphere. While at least one previous study reported a relationship between BMI and the morphology of the posterior cingulate cortex (Kharabian Masouleh et al., 2016), this region did not light up in the Grad-CAM-based localization map. On the other hand, several other brain structures were deemed important based on the localization map, in the case of which the conventional automatic brain segmentation approach failed to confirm an association with BMI, namely the lateral surface of the right temporal cortex and a region encompassing the left caudate nucleus. With regard to the latter, a previous study has shown that the volume of the caudate heads bilaterally show a positive association with BMI in men, after adjusting for age, lifetime alcohol intake, history of hypertension, and diabetes mellitus (Taki et al., 2008). Sex differences have also been shown to be manifest regarding the relationship between total body fat and caudate volume (Dekkers et al., 2019). Our results regarding the association with BMI are also indicative of such differences (**Figure 5**, left panel). In addition, the discrepancy between our observations with DL and conventional approaches is likely to stem from the differences in the applied methodologies as well. In our study, we used FreeSurfer for the automated segmentation of predefined subcortical structures and examined the linear relationship between BMI and a single scalar estimate of the volume of the caudate. FreeSurfer segmentation includes a series of pre-processing steps applied to the MRI volumes, followed by labeling the volumes based on a probabilistic atlas built from a set of hand-labeled images, as well as subject-specific measurements (Fischl et al., 2002, 2004). In contrast, the CNN is fed with minimally preprocessed images and learns a series of transformations to map those images to the corresponding BMI values. Each of these transformations map the representation of the input at one level into a representation at a slightly more abstract level (LeCun et al., 2015). Compared to the conventional automated brain segmentation methods, visualizations based on these more abstract representations may provide additional information with regard to the relationship between brain architecture and body weight. Similarly, several recent studies applied the Grad-CAM method to highlight brain regions that made an important contribution to predicting depression and epilepsy (Pominova et al., 2018), brain age (Bermudez et al., 2019), and Alzheimer's disease (Feng et al., 2018) based on structural MRI data.

Besides being a promising tool for neuroscientific investigation, brain-predicted BMI may also have practical utility. We managed to adapt the CNN model to a novel dataset, suggesting that our method is more generally applicable to a variety of different MR scanner types. Coming back to the relationship between the amygdala and body weight, this brain structure has been shown to be involved in the evaluation of food cues (Siep et al., 2009) and to constitute a part of a neural circuitry involved in the regulation of food craving (Dietrich et al., 2016). In a recent review, it has been argued that structures of the medial temporal lobe, in particular the amygdala and the hippocampus, may play an important role in the regulation of body weight, and that the amygdala is crucial for the regulation of feeding behavior based on environmental cues (Coppin, 2016). Based on the localization map produced by the Grad-CAM method, it is reasonable to hypothesize that brain-predicted BMI may be related to individual differences in the processing of food stimuli and cue-induced feeding. On this basis, one intriguing possibility is that increased brain-predicted BMI relative to the actual BMI might reflect a greater propensity to weight gain. This mode of application is similar to how the

difference between brain-predicted and chronological age might have clinical utility (Cole and Franke, 2017). However, it is important to note that brain structural alterations might not be the cause but the consequence of obesity. In fact, obesity-driven neuroinflammation has been shown to affect several brain regions including the hippocampus and the amygdala (Guillemot-Legris and Muccioli, 2017). Further research is necessary to examine whether and how brain-predicted BMI is related to pathophysiological processes and eating behavior.

CONCLUSION

Our findings provide proof of concept that individual BMI can be predicted with high accuracy from a single MRI scan using DL methods and suggest a relationship between the morphology of subcortical structures and body weight.

DATA AVAILABILITY STATEMENT

Publicly available datasets were analyzed in this study. This data can be found here: this research has been conducted using the UK Biobank Resource under Application Number 27236. All analyses reported in this paper include participants from the UK Biobank population cohort (https://www.ukbiobank.ac.uk/). The source code of the presented model along with the learnt parameters is available on GitHub: https://github.com/vaklip/cnn_3d_regression.

ETHICS STATEMENT

The studies involving human participants were reviewed and approved by UK Biobank Research Ethics Committee (REC; approval number: 11/NW/0382). The participants provided their written informed consent to participate in this study.

AUTHOR CONTRIBUTIONS

All authors listed have made a substantial, direct and intellectual contribution to the work, and approved it for publication.

FUNDING

ZV was supported by a grant from the Hungarian Brain Research Program 2.0 (NAP 2.0 4001-17919).

ACKNOWLEDGMENTS

This research has been conducted using the UK Biobank Resource under Application Number 27236.

REFERENCES

Alfaro-Almagro, F., Jenkinson, M., Bangerter, N. K., Andersson, J. L. R., Griffanti, L., Douaud, G., et al. (2018). Image processing and quality control for the first 10,000 brain imaging datasets from UK Biobank. *Neuroimage* 166, 400–424. doi: 10.1016/j.neuroimage.2017.10.034

Alford, S., Patel, D., Perakakis, N., and Mantzoros, C. S. (2018). Obesity as a risk factor for Alzheimer's disease: weighing the evidence. *Obes. Rev.* 19, 269–280. doi: 10.1111/obr.12629

Allen, N., Sudlow, C., Downey, P., Peakman, T., Danesh, J., Elliott, P., et al. (2012). UK Biobank: current status and what it means for epidemiology. *Health Policy Technol.* 1, 123–126. doi: 10.1016/j.hlpt.2012.07.003

Arbabshirani, M. R., Plis, S., Sui, J., and Calhoun, V. D. (2017). Single subject prediction of brain disorders in neuroimaging: promises and pitfalls. *Neuroimage* 145, 137–165. doi: 10.1016/j.neuroimage.2016.02.079

Avery, J. A., Powell, J. N., Breslin, F. J., Lepping, R. J., Martin, L. E., Patrician, T. M., et al. (2017). Obesity is associated with altered mid-insula functional connectivity to limbic regions underlying appetitive responses to foods. *J. Psychopharmacol.* 31, 1475–1484. doi: 10.1177/0269881117728429

Basaia, S., Agosta, F., Wagner, L., Canu, E., Magnani, G., Santangelo, R., et al. (2019). Automated classification of Alzheimer's disease and mild cognitive impairment using a single MRI and deep neural networks. *Neuroimage Clin.* 21:101645. doi: 10.1016/j.nicl.2018.101645

Bermudez, C., Plassard, A. J., Chaganti, S., Huo, Y., Aboud, K. S., Cutting, L. E., et al. (2019). Anatomical context improves deep learning on the brain age estimation task. *Magn. Reson. Imaging* 62, 70–77. doi: 10.1016/j.mri.2019.06.018

Brooks, S. J., Benedict, C., Burgos, J., Kempton, M. J., Kullberg, J., Nordenskjöld, R., et al. (2013). Late-life obesity is associated with smaller global and regional gray matter volumes: a voxel-based morphometric study. *Int. J. Obes.* 37, 230–236. doi: 10.1038/ijo.2012.13

Carnell, S., Gibson, C., Benson, L., Ochner, C. N., and Geliebter, A. (2012). Neuroimaging and obesity: current knowledge and future directions. *Obes. Rev.* 13, 43–56. doi: 10.1111/j.1467-789X.2011.00927.x

Cole, J. H., and Franke, K. (2017). Predicting age using neuroimaging: innovative brain ageing biomarkers. *Trends Neurosci.* 40, 681–690. doi: 10.1016/j.tins.2017.10.001

Cole, J. H., Leech, R., and Sharp, D. J. (2015). Prediction of brain age suggests accelerated atrophy after traumatic brain injury. *Ann. Neurol.* 77, 571–581. doi: 10.1002/ana.24367

Cole, J. H., Marioni, R. E., Harris, S. E., and Deary, I. J. (2019). Brain age and other bodily 'ages': implications for neuropsychiatry. *Mol. Psychiatry* 24, 266–281. doi: 10.1038/s41380-018-0098-1

Cole, J. H., Poudel, R. P. K., Tsagkrasoulis, D., Caan, M. W. A., Steves, C., Spector, T. D., et al. (2017). Predicting brain age with deep learning from raw imaging data results in a reliable and heritable biomarker. *Neuroimage* 163, 115–124. doi: 10.1016/j.neuroimage.2017.07.059

Cole, J. H., Ritchie, S. J., Bastin, M. E., Hernández, M. C. V., Maniega, S. M., Royle, N., et al. (2018). Brain age predicts mortality. *Mol. Psychiatry* 23, 1385–1392. doi: 10.1038/mp.2017.62

Coppin, G. (2016). The anterior medial temporal lobes: their role in food intake and body weight regulation. *Physiol. Behav.* 167, 60–70. doi: 10.1016/j.physbeh.2016.08.028

Dale, A. M., Fischl, B., and Sereno, M. I. (1999). Cortical surface-based analysis: I. Segmentation and surface reconstruction. *Neuroimage* 9, 179–194. doi: 10.1006/nimg.1998.0395

Davatzikos, C. (2019). Machine learning in neuroimaging: progress and challenges. *Neuroimage* 197, 652–656. doi: 10.1016/j.neuroimage.2018.10.003

Dekkers, I. A., Jansen, P. R., and Lamb, H. J. (2019). Obesity, brain volume, and white matter microstructure at MRI: a cross-sectional UK Biobank study. *Radiology* 291, 763–771. doi: 10.1148/radiol.2019181012

Dietrich, A., Hollmann, M., Mathar, D., Villringer, A., and Horstmann, A. (2016). Brain regulation of food craving: relationships with weight status and eating behavior. *Int. J. Obes.* 40, 982–989. doi: 10.1038/ijo.2016.28

Durstewitz, D., Koppe, G., and Meyer-Lindenberg, A. (2019). Deep neural networks in psychiatry. *Mol. Psychiatry* 24, 1583–1598. doi: 10.1038/s41380-019-0365-9

Dye, L., Boyle, N. B., Champ, C., and Lawton, C. (2017). The relationship between obesity and cognitive health and decline. *Proc. Nutr. Soc.* 76, 443–454. doi: 10.1017/S0029665117002014

Farooq, A., Anwar, S., Awais, M., and Rehman, S. (2017). "A deep CNN based multi-class classification of Alzheimer's disease using MRI," in *Proceedings of the 2017 IEEE International Conference on Imaging Systems and Techniques (IST)*, Beijing, 1–6. doi: 10.1109/IST.2017.8261460

Feng, X., Yang, J., Lipton, Z. C., Small, S. A., Provenzano, F. A., and Initiative, A. D. N. (2018). Deep learning on MRI affirms the prominence of the hippocampal formation in Alzheimer's disease classification. *bioRxiv* [Pripriint]. doi: 10.1101/456277

Fischl, B., Salat, D. H., Busa, E., Albert, M., Dieterich, M., Haselgrove, C., et al. (2002). Whole brain segmentation: automated labeling of neuroanatomical structures in the human brain. *Neuron* 33, 341–355. doi: 10.1016/S0896-6273(02)00569-X

Fischl, B., Sereno, M. I., and Dale, A. M. (1999). Cortical surface-based analysis: II: inflation, flattening, and a surface-based coordinate system. *Neuroimage* 9, 195–207. doi: 10.1006/nimg.1998.0396

Fischl, B., van der Kouwe, A., Destrieux, C., Halgren, E., Ségonne, F., Salat, D. H., et al. (2004). Automatically parcellating the human cerebral cortex. *Cereb. Cortex* 14, 11–22. doi: 10.1093/cercor/bhg087

Franke, K., and Gaser, C. (2012). Longitudinal changes in individual BrainAGE in healthy aging, mild cognitive impairment, and Alzheimer's disease. *GeroPsych* 25, 235–245. doi: 10.1024/1662-9647/a000074

Glorot, X., and Bengio, Y. (2010). "Understanding the difficulty of training deep feedforward neural networks," in *Proceedings of the Thirteenth International Conference on Artificial Intelligence and Statistics*, eds Y. W. Teh, and M. Titterington (Sardinia: PMLR), 249–256.

Goodfellow, I., Bengio, Y., and Courville, A. (2016). *Deep Learning*. Cambridge MA: MIT press.

Guillemot-Legris, O., and Muccioli, G. G. (2017). Obesity-induced neuroinflammation: beyond the hypothalamus. *Trends Neurosci.* 40, 237–253. doi: 10.1016/j.tins.2017.02.005

Gupta, A., Ayhan, M. S., and Maida, A. S. (2013). "Natural image bases to represent neuroimaging data," in *Proceedings of the 30th International Conference on International Conference on Machine Learning - Volume 28 ICML'13, (JMLR.org)*, Atlanta.

Habes, M., Janowitz, D., Erus, G., Toledo, J. B., Resnick, S. M., Doshi, J., et al. (2016). Advanced brain aging: relationship with epidemiologic and genetic risk factors, and overlap with Alzheimer disease atrophy patterns. *Transl. Psychiatry* 6:e775. doi: 10.1038/tp.2016.39

Hosseini-Asl, E., Ghazal, M., Mahmoud, A., Aslantas, A., Shalaby, A. M., Casanova, M. F., et al. (2018). Alzheimer's disease diagnostics by a 3D deeply supervised adaptable convolutional network. *Front. Biosci. Landmark Ed.* 23:584–596. doi: 10.2741/4606

Ioffe, S., and Szegedy, C. (2015). Batch normalization: accelerating deep network training by reducing internal covariate shift. *arXiv* [Preprint]. Available at: http://arxiv.org/abs/1502.03167 [accessed July 29, 2019].

Islam, J., and Zhang, Y. (2018). Brain MRI analysis for Alzheimer's disease diagnosis using an ensemble system of deep convolutional neural networks. *Brain Inf.* 5:2. doi: 10.1186/s40708-018-0080-3

Jenkinson, M., Beckmann, C. F., Behrens, T. E. J., Woolrich, M. W., and Smith, S. M. (2012). FSL. *Neuroimage* 62, 782–790. doi: 10.1016/j.neuroimage.2011.09.015

Kharabian Masouleh, S., Arélin, K., Horstmann, A., Lampe, L., Kipping, J. A., Luck, T., et al. (2016). Higher body mass index in older adults is associated with lower gray matter volume: implications for memory performance. *Neurobiol. Aging* 40, 1–10. doi: 10.1016/j.neurobiolaging.2015.12.020

Kingma, D. P., and Ba, J. (2014). Adam: a method for stochastic optimization. *arXiv* [Preprint]. Available at: http://arxiv.org/abs/1412.6980 [accessed January 22, 2018].

Koutsouleris, N., Davatzikos, C., Borgwardt, S., Gaser, C., Bottlender, R., Frodl, T., et al. (2014). Accelerated brain aging in schizophrenia and beyond: a neuroanatomical marker of psychiatric disorders. *Schizophr. Bull.* 40, 1140–1153. doi: 10.1093/schbul/sbt142

Krizhevsky, A., Sutskever, I., and Hinton, G. E. (2012). "ImageNet classification with deep convolutional neural networks," in *Advances in Neural Information Processing Systems 25*, eds F. Pereira, C. J. C. Burges, L. Bottou, and K. Q. Weinberger (Red Hook, NY: Curran Associates, Inc.), 1097–1105.

Kullmann, S., Schweizer, F., Veit, R., Fritsche, A., and Preissl, H. (2015). Compromised white matter integrity in obesity. *Obes. Rev.* 16, 273–281. doi: 10.1111/obr.12248

LeCun, Y., Bengio, Y., and Hinton, G. (2015). Deep learning. *Nature* 521:nature14539. doi: 10.1038/nature14539

LeCun, Y., Boser, B. E., Denker, J. S., Henderson, D., Howard, R. E., Hubbard, W. E., et al. (1990). "Handwritten digit recognition with a back-propagation network," in *Advances in Neural Information Processing Systems 2*, ed. D. S. Touretzky (Burlington, MA: Morgan-Kaufmann), 396–404.

Lecun, Y., Bottou, L., Bengio, Y., and Haffner, P. (1998). Gradient-based learning applied to document recognition. *Proc. IEEE* 86, 2278–2324. doi: 10.1109/5.726791

Li, H., Satterthwaite, T. D., and Fan, Y. (2018). "Brain age prediction based on resting-state functional connectivity patterns using convolutional neural networks," in *Proceedings of the 2018 IEEE 15th International Symposium on Biomedical Imaging (ISBI 2018)* (Washington, DC: IEEE), 101–104. doi: 10.1109/ISBI.2018.8363532

Lipton, Z. C. (2016). The mythos of model interpretability. *arXiv* [Preprint]. Available at: https://arxiv.org/abs/1606.03490v3 [accessed October 3, 2019].

Litjens, G., Kooi, T., Bejnordi, B. E., Setio, A. A. A., Ciompi, F., Ghafoorian, M., et al. (2017). A survey on deep learning in medical image analysis. *Med. Image Anal.* 42, 60–88. doi: 10.1016/j.media.2017.07.005

Löwe, L. C., Gaser, C., Franke, K., and The Alzheimer's Disease Neuroimaging Initiative, (2016). The effect of the APOE genotype on individual *BrainAGE* in normal aging, mild cognitive impairment, and Alzheimer's disease. *PLoS One* 11:e0157514. doi: 10.1371/journal.pone.0157514

Meszlényi, R. J., Buza, K., and Vidnyánszky, Z. (2017). Resting State fMRI functional connectivity-based classification using a convolutional neural network architecture. *Front. Neuroinformatics* 11:61. doi: 10.3389/fninf.2017.00061

Nair, V., and Hinton, G. E. (2010). "Rectified linear units improve restricted Boltzmann machines," in *Proceedings of the 27th International Conference on International Conference on Machine Learning ICML'10*, Haifa, 807–814.

Orsi, G., Perlaki, G., Kovacs, N., Aradi, M., Papp, Z., Karadi, K., et al. (2011). Body weight and the reward system: the volume of the right amygdala may be associated with body mass index in young overweight men. *Brain Imaging Behav.* 5, 149–157. doi: 10.1007/s11682-011-9119-2

Pannacciulli, N., Del Parigi, A., Chen, K., Le, D. S. N. T., Reiman, E. M., and Tataranni, P. A. (2006). Brain abnormalities in human obesity: a voxel-based morphometric study. *Neuroimage* 31, 1419–1425. doi: 10.1016/j.neuroimage.2006.01.047

Pardoe, H. R., Cole, J. H., Blackmon, K., Thesen, T., and Kuzniecky, R. (2017). Structural brain changes in medically refractory focal epilepsy resemble premature brain aging. *Epilepsy Res.* 133, 28–32. doi: 10.1016/j.eplepsyres.2017.03.007

Payan, A., and Montana, G. (2015). Predicting Alzheimer's disease: a neuroimaging study with 3D convolutional neural networks. *arXiv* [Preprint]. Available at: https://arxiv.org/abs/1502.02506v1 [accessed September 26, 2019].

Pedditizi, E., Peters, R., and Beckett, N. (2016). The risk of overweight/obesity in mid-life and late life for the development of dementia: a systematic review and meta-analysis of longitudinal studies. *Age Ageing* 45, 14–21. doi: 10.1093/ageing/afv151

Perlaki, G., Molnar, D., Smeets, P. A. M., Ahrens, W., Wolters, M., Eiben, G., et al. (2018). Volumetric gray matter measures of amygdala and accumbens in childhood overweight/obesity. *PLoS One* 13:e0205331. doi: 10.1371/journal.pone.0205331

Pominova, M., Artemov, A., Sharaev, M., Kondrateva, E., Bernstein, A., and Burnaev, E. (2018). "Voxelwise 3D convolutional and recurrent neural networks for epilepsy and depression diagnostics from structural and functional MRI data," in *Proceedings of the 2018 IEEE International Conference on Data Mining Workshops (ICDMW)*, Singapore, 299–307. doi: 10.1109/ICDMW.2018.00050

Pursey, K. M., Stanwell, P., Callister, R. J., Brain, K., Collins, C. E., and Burrows, T. L. (2014). Neural responses to visual food cues according to weight status:

a systematic review of functional magnetic resonance imaging studies. *Front. Nutr.* 1:7. doi: 10.3389/fnut.2014.00007

Raji, C. A., Ho, A. J., Parikshak, N. N., Becker, J. T., Lopez, O. L., Kuller, L. H., et al. (2010). Brain structure and obesity. *Hum. Brain Mapp.* 31, 353–364. doi: 10.1002/hbm.20870

Sarraf, S., and Tofighi, G. (2016). Classification of Alzheimer's disease using fMRI data and deep learning convolutional neural networks. *arXiv* [Preprint]. Available at: https://arxiv.org/abs/1603.08631v1 [accessed September 26, 2019].

Selvaraju, R. R., Cogswell, M., Das, A., Vedantam, R., Parikh, D., and Batra, D. (2017). Grad-CAM: visual explanations from deep networks via gradient-based localization. *arXiv* [Preprint]. Available at: http://openaccess.thecvf.com/content_iccv_2017/html/Selvaraju_Grad-CAM_Visual_Explanations_ICCV_2017_paper.html [accessed July 31, 2019].

Shen, D., Wu, G., and Suk, H.-I. (2017). Deep learning in medical image analysis. *Annu. Rev. Biomed. Eng.* 19, 221–248. doi: 10.1146/annurev-bioeng-071516-044442

Siep, N., Roefs, A., Roebroeck, A., Havermans, R., Bonte, M. L., and Jansen, A. (2009). Hunger is the best spice: an fMRI study of the effects of attention, hunger and calorie content on food reward processing in the amygdala and orbitofrontal cortex. *Behav. Brain Res.* 198, 149–158. doi: 10.1016/j.bbr.2008.10.035

Silva, J. F., Silva, J. M., Guerra, A., Matos, S., and Costa, C. (2018). "Ejection fraction classification in transthoracic echocardiography using a deep learning approach," in *Proceedings of the 2018 IEEE 31st International Symposium on Computer-Based Medical Systems (CBMS)*, Karlstad, 123–128. doi: 10.1109/CBMS.2018.00029

Simonyan, K., Vedaldi, A., and Zisserman, A. (2013). Deep inside convolutional networks: visualising image classification models and saliency maps. *arXiv* [Preprint]. Available at: https://arxiv.org/abs/1312.6034v2 [accessed October 4, 2019].

Singh-Manoux, A., Dugravot, A., Shipley, M., Brunner, E. J., Elbaz, A., Sabia, S., et al. (2018). Obesity trajectories and risk of dementia: 28 years of follow-up in the Whitehall II Study. *Alzheimers Dement.* 14, 178–186. doi: 10.1016/j.jalz.2017.06.2637

Srivastava, N., Hinton, G., Krizhevsky, A., Sutskever, I., and Salakhutdinov, R. (2014). Dropout: a simple way to prevent neural networks from overfitting. *J. Mach. Learn. Res.* 15, 1929–1958.

Stanek, K. M., Grieve, S. M., Brickman, A. M., Korgaonkar, M. S., Paul, R. H., Cohen, R. A., et al. (2011). Obesity is associated with reduced white matter integrity in otherwise healthy adults*. *Obesity* 19, 500–504. doi: 10.1038/oby.2010.312

Szegedy, C., Vanhoucke, V., Ioffe, S., Shlens, J., and Wojna, Z. (2016). *Rethinking the Inception Architecture for Computer Vision*. Available at: https://www.cv-foundation.org/openaccess/content_cvpr_2016/html/Szegedy_Rethinking_the_Inception_CVPR_2016_paper.html [accessed July 29, 2019].

Taki, Y., Kinomura, S., Sato, K., Inoue, K., Goto, R., Okada, K., et al. (2008). Relationship between body mass index and gray matter volume in 1,428 healthy individuals. *Obesity* 16, 119–124. doi: 10.1038/oby.2007.4

Tang, D. W., Fellows, L. K., Small, D. M., and Dagher, A. (2012). Food and drug cues activate similar brain regions: a meta-analysis of functional MRI studies. *Physiol. Behav.* 106, 317–324. doi: 10.1016/j.physbeh.2012.03.009

The GBD 2015 Obesity Collaborators, (2017). Health effects of overweight and obesity in 195 countries over 25 years. *N. Engl. J. Med.* 377, 13–27. doi: 10.1056/NEJMoa1614362

Vakli, P., Deák-Meszlényi, R. J., Hermann, P., and Vidnyánszky, Z. (2018). Transfer learning improves resting-state functional connectivity pattern analysis using convolutional neural networks. *Gigascience* 7:giy130. doi: 10.1093/gigascience/giy130

Val-Laillet, D., Aarts, E., Weber, B., Ferrari, M., Quaresima, V., Stoeckel, L. E., et al. (2015). Neuroimaging and neuromodulation approaches to study eating behavior and prevent and treat eating disorders and obesity. *Neuroimage Clin.* 8, 1–31. doi: 10.1016/j.nicl.2015.03.016

van Bloemendaal, L., Jzerman, R. G. I, ten Kulve, J. S., Barkhof, F., Konrad, R. J., Drent, M. L., et al. (2014). GLP-1 receptor activation modulates appetite- and reward-related brain areas in humans. *Diabetes* 63, 4186–4196. doi: 10.2337/db14-0849

van der Laan, L. N., de Ridder, D. T. D., Viergever, M. A., and Smeets, P. A. M. (2011). The first taste is always with the eyes: a meta-analysis on the neural correlates of processing visual food cues. *Neuroimage* 55, 296–303. doi: 10.1016/j.neuroimage.2010.11.055

Vieira, S., Pinaya, W. H. L., and Mechelli, A. (2017). Using deep learning to investigate the neuroimaging correlates of psychiatric and neurological disorders: methods and applications. *Neurosci. Biobehav. Rev.* 74, 58–75. doi: 10.1016/j.neubiorev.2017.01.002

Wager, S., Wang, S., and Liang, P. S. (2013). "Dropout Training as Adaptive Regularization," in *Advances in Neural Information Processing Systems 26*, eds C. J. C. Burges, L. Bottou, M. Welling, Z. Ghahramani, and K. Q. Weinberger (Red Hook, NY: Curran Associates, Inc), 351–359.

Wang, J., Knol, M., Tiulpin, A., Dubost, F., De, M. B., Vernooij, M., et al. (2019). Grey matter age prediction as a biomarker for risk of dementia: a population-based study. *bioRxiv* [Preprint]. doi: 10.1101/518506

Wang, S.-H., Lv, Y.-D., Sui, Y., Liu, S., Wang, S.-J., and Zhang, Y.-D. (2017). Alcoholism detection by data augmentation and convolutional neural network with stochastic pooling. *J. Med. Syst.* 42:2. doi: 10.1007/s10916-017-0845-x

Widya, R. L., de Roos, A., Trompet, S., de Craen, A. J., Westendorp, R. G., Smit, J. W., et al. (2011). Increased amygdalar and hippocampal volumes in elderly obese individuals with or at risk of cardiovascular disease. *Am. J. Clin. Nutr.* 93, 1190–1195. doi: 10.3945/ajcn.110.006304

Zaharchuk, G., Gong, E., Wintermark, M., Rubin, D., and Langlotz, C. P. (2018). Deep learning in neuroradiology. *Am. J. Neuroradiol.* 39, 1776–1784. doi: 10.3174/ajnr.A5543

Zeiler, M. D., and Fergus, R. (2014). "Visualizing and understanding convolutional networks," in *Computer Vision – ECCV 2014*, eds D. Fleet, T. Pajdla, B. Schiele, and T. Tuytelaars (Cham: Springer), 818–833. doi: 10.1007/978-3-319-10590-1_53

Zou, L., Zheng, J., Miao, C., Mckeown, M. J., and Wang, Z. J. (2017). 3D CNN based automatic diagnosis of attention deficit hyperactivity disorder using functional and structural MRI. *IEEE Access* 5, 23626–23636. doi: 10.1109/ACCESS.2017.2762703

Conflict of Interest: The authors declare that the research was conducted in the absence of any commercial or financial relationships that could be construed as a potential conflict of interest.

Copyright © 2020 Vakli, Deák-Meszlényi, Auer and Vidnyánszky. This is an open-access article distributed under the terms of the Creative Commons Attribution License (CC BY). The use, distribution or reproduction in other forums is permitted, provided the original author(s) and the copyright owner(s) are credited and that the original publication in this journal is cited, in accordance with accepted academic practice. No use, distribution or reproduction is permitted which does not comply with these terms.

frontiers in Neuroinformatics

ORIGINAL RESEARCH
published: 30 April 2020
doi: 10.3389/fninf.2020.00015

EEG Signal Reconstruction Using a Generative Adversarial Network With Wasserstein Distance and Temporal-Spatial-Frequency Loss

Tian-jian Luo[1,2,3*†], *Yachao Fan*[2†], *Lifei Chen*[1,3], *Gongde Guo*[1,3] *and Changle Zhou*[2]

[1] College of Mathematics and Informatics, Fujian Normal University, Fuzhou, China, [2] School of Informatics, Xiamen University, Xiamen, China, [3] Digital Fujian Internet-of-Thing Laboratory of Environmental Monitoring, Fujian Normal University, Fuzhou, China

Applications based on electroencephalography (EEG) signals suffer from the mutual contradiction of high classification performance vs. low cost. The nature of this contradiction makes EEG signal reconstruction with high sampling rates and sensitivity challenging. Conventional reconstruction algorithms lead to loss of the representative details of brain activity and suffer from remaining artifacts because such algorithms only aim to minimize the temporal mean-squared-error (MSE) under generic penalties. Instead of using temporal MSE according to conventional mathematical models, this paper introduces a novel reconstruction algorithm based on generative adversarial networks with the Wasserstein distance (WGAN) and a temporal-spatial-frequency (TSF-MSE) loss function. The carefully designed TSF-MSE-based loss function reconstructs signals by computing the MSE from time-series features, common spatial pattern features, and power spectral density features. Promising reconstruction and classification results are obtained from three motor-related EEG signal datasets with different sampling rates and sensitivities. Our proposed method significantly improves classification performances of EEG signals reconstructions with the same sensitivity and the average classification accuracy improvements of EEG signals reconstruction with different sensitivities. By introducing the WGAN reconstruction model with TSF-MSE loss function, the proposed method is beneficial for the requirements of high classification performance and low cost and is convenient for the design of high-performance brain computer interface systems.

Keywords: EEG signals reconstruction, generative adversarial network, Wasserstein distance, sampling rate, sensitivity

OPEN ACCESS

Edited by:
Gaute T. Einevoll, Norwegian University of Life Sciences, Norway

Reviewed by:
Gautam Agarwal, University of California, Berkeley, United States
Alexander J. Stasik, University of Oslo, Norway

***Correspondence:**
Tian-jian Luo
createopenbci@fjnu.edu.cn

†These authors have contributed equally to this work

Received: *19 September 2019*
Accepted: *16 March 2020*
Published: *30 April 2020*

Citation:
Luo T, Fan Y, Chen L, Guo G and Zhou C (2020) EEG Signal Reconstruction Using a Generative Adversarial Network With Wasserstein Distance and Temporal-Spatial-Frequency Loss. Front. Neuroinform. 14:15. doi: 10.3389/fninf.2020.00015

1. INTRODUCTION

Electroencephalography (EEG) (Cecotti and Graser, 2011; Narizzano et al., 2017; Freche et al., 2018) is one of the most important non-invasive neuroimaging modalities used in cognitive neuroscience research (Mullen et al., 2015; Mete et al., 2016; Luo et al., 2018b) and brain-computer interface (BCI) development (Ahn and Jun, 2015; Arnulfo et al., 2015; Sargolzaei et al., 2015; Kumar et al., 2017). However, EEG-based cognitive neuroscience and BCI fields currently face a bottleneck in that high sampling rate and high-sensitivity EEG amplifier hardware are extremely expensive and generally complicated to operate for collecting signals (Jiang et al., 2017). Ideally, EEG amplifiers with high sampling rates and sensitivities are preferred to record high-resolution

brain activities underlying different stimuli. Lowering the sampling rate and sensitivity may influence the utility of acquired signals (Wu et al., 2015). Therefore, extensive efforts have been dedicated to reconstructing high-sampling-sensitivity EEG (HSS-EEG) signals from low-sampling-sensitivity EEG (LSS-EEG) signals to improve performance. The up-sampling operation is one of the conventional time-series reconstruction methods. By using an up-sampling operation, the reconstructed signals are up-sampled and with different sensitivity. The reconstruction methods can be divided into three categories:

1. Reconstruction by interpolation (Erkorkmaz, 2015).
2. Reconstruction by mathematical modeling (Naldi et al., 2017).
3. Reconstruction by deep neural networks (Jin et al., 2017).

Among the methods for reconstructing EEG signals by interpolation algorithms, such as bilinear interpolation, nearest neighbor interpolation, and spline interpolation, several are based on the successive assumption of signal values (Marques et al., 2016). Such an assumption does not consider the complexity of signals, and, therefore, it is difficult to represent brain activity from reconstructed signals. Reconstruction based on mathematical models, such as compressive sensing, subspace projection, and frequency transformation, optimizes an objective function that incorporates mathematical models and prior information in the different domains of the signals. These algorithms greatly improve signal performance and quality; however, they may still lose the details representing brain activity and suffer from artifacts. In addition, reconstruction by a single mathematical model and a single domain has simplified the range of applications of reconstructed EEG signals. These algorithms greatly improve signal performance and quality (Choudhary et al., 2016); however, they may still lose the details representing brain activity and suffer from artifacts. Additionally, the high computational cost of constructing mathematical models remains another potential risk in practical applications.

In contrast to interpolation and mathematical models, the recent explosive development of deep neural networks (DNNs) has shed light on novel opinions and promised potential in the field of signal reconstruction. In recent years, most DNNs studies have focused on image signal reconstruction from the perspective of noise, super-resolution, and denoising (LeCun et al., 2015). A state-of-the-art image reconstruction performance was obtained by the new game theoretic generative model of generative adversarial networks (GANs) (Goodfellow et al., 2014). GANs are used to generate images from artificial data, construct high-resolution (HR) images from low-resolution (LR) copies (Ledig et al., 2017), and denoise CT images from noisy images (Yang et al., 2018), and such models achieve the best performance in reconstruction tasks. Inspired by the applications of GANs in the image reconstruction field, researchers have focused on reconstructing EEG signals using GANs. Research on "GANs conditioned by brain signals" (Kavasidis et al., 2017) has used GANs to generate images seen by subjects from recorded EEG signals. Another deep EEG super-resolution study used GANs to produce HR EEG data from LR samples by generating channel-wise up-sampled data to effectively interpolate numerous missing channels (Hartmann et al., 2018). Such an algorithm produced higher spatial resolution EEG signals to improve performance.

Although GANs have been used to reconstruct images from EEG signals with a visualized spatial feature space, the sampling rate and sensitivity resolution in the temporal feature space are still two key limitations of EEG signals. To counterbalance the performance of EEG signals and the cost of EEG amplifiers, we propose using a GAN with the Wasserstein distance (WGAN) model as the discrepancy measure between different sampling rates and sensitivities and a spatial-temporal-frequency loss function that computes the difference between EEG signals in an established feature space. The GAN/WGAN architecture is used to encourage the reconstructed LSS-EEG signals to share the same distribution as the HSS-EEG signals. Because EEG signals are multi-channels time-series data, instead of using the mean square error by temporal features as the loss function, we propose a novel spatial-temporal-frequency loss function, which is robust enough for the EEG signals, to extract the spatial-temporal-frequency features for reconstruction. By using the GAN/WGAN architecture and the carefully designed loss function to reconstruct HSS-EEG signals from LSS-EEG signals, this study has made two contributions:

1. The GAN/WGAN architectures are trained by EEG signals of different sampling rates and different sensitivities to compare the classification performances of the reconstructed EEG signals.
2. The spatial-temporal-frequency loss is applied to maintain robustness of GAN/WGAN architectures training, and the loss function helps reconstruction signals to obtain more discriminant patterns.

2. METHODS

2.1. EEG Signal Reconstruction Model

For the reconstruction of EEG signals, let $z \in R^{N\times T_1\times S}$ denote the LSS-EEG signals from distribution P_L, and $x \in R^{N\times T_2\times S}$ denote the HSS-EEG signals from the real distribution P_H. In the definition, N denotes the number of channels, and T_1 and T_2 denote the samples of one trial for LSS-EEG signals and HSS-EEG signals during recordings, respectively. S denotes the number of trials for the motor-based tasks. The reconstruction goal is to formulate a function $f(z)$ that projects LSS-EEG signals z to HSS-EEG signals x:

$$f(z): z \rightarrow x \tag{1}$$

In fact, the reconstruction function maps the LSS-EEG samples from P_L into a certain distribution P_C, and our goal is to adjust a

Abbreviations: EEG, electroencephalography; HSS-EEG, high sampling rate and sensitivity EEG; LSS-EEG, low sam-pling rate and sensitivity EEG; DNNs, deep neural networks; GAN, generative adversarial network; WGAN, GAN with Wasserstein distance; HR, high resolution; LR, low resolution; FBCSP, filter bank common spatial pattern; PSD, power spectral density; TSF-MSE, temporal-spatial-frequency mean square error; AO, action observation; GAL, grasp and lift; MI, motor imagery; ReLU, rectified linear unit; BN, batch normalization; SVM, support vector machine; SVD, singular value decomposition; ERD/ERS, event-related desynchronization/event-related synchronization.

certain distribution P_C to make it close to the real distribution P_H by varying the function $f(z)$. The reconstruction has two procedures with GAN. In the generation procedure, the object is to adjust EEG samples from distribution P_L to distribution P_C. In the discriminator procedure, the object is to adjust EEG samples from distribution P_C to distribution P_H. The reconstruction procedure can ultimately be treated as a procedure to adjust EEG samples from one distribution to another.

Typically, since EEG signals are nonlinear and non-stationary, the noise model in such signals is complicated, and the reconstruction mapping relationship is non-uniformly distributed across the signals. Thus, there is no clear indication of how the distributions of LSS-EEG and HSS-EEG signals are related to each other. It is difficult to reconstruct LSS-EEG signals using conventional methods. However, the uncertainties in the noise model and the reconstruction mapping relationship can be ignored by using deep neural networks (DNNs), as the DNNs can efficiently learn high-level features from nonlinear and non-stationary signals and reconstruct a representation of the data distribution from modest-sized signal patches. Therefore, the GAN framework based on DNN is suitable for EEG signal reconstruction. In summary, a modified GAN framework with the Wasserstein distance and temporal-spatial-frequency (TSF) loss is introduced to reconstruct HSS-EEG signals from LSS-EEG signals.

2.2. GAN With Wasserstein Distance

The GAN framework consists of two opposing neural networks, a generator G, and a discriminator D, that are optimized to minimize a two-player min-max problem (Goodfellow et al., 2014). The discriminator is trained to distinguish the generated samples from the real samples, while the generator is trained to generate fake samples that are not determined as fake by the discriminator. For the reconstruction of EEG signals, we further defined the discriminator D_{θ_D} and the generator G_{θ_G} to solve the min-max problem:

$$\min_{\theta_G}\max_{\theta_D} L_{GAN}(D_{\theta_D}, G_{\theta_G}) = E_{x\sim P_H}\left[logD_{\theta_D}(x)\right] + E_{z\sim P_L}\left[log\left(1 - D_{\theta_D}\left(G_{\theta_G}(z)\right)\right)\right] \tag{2}$$

where $E(\cdot)$ denotes the expectation operator. When the discriminator meets the real data, it will satisfy $D_{\theta_D}(x) = 1$ to discriminate the real data. Here, $D_{\theta_D}(x) = 1$ reaches the expectation for $logD_{\theta_D}(x)$. When the discriminator meets the generated data, it will satisfy $D_{\theta_D}\left(G_{\theta_G}(z)\right) = 0$ to discriminate the generated data. Here, $D_{\theta_D}\left(G_{\theta_G}(z)\right) = 0$ reaches the expectation for $log\left(1 - D_{\theta_D}\left(G_{\theta_G}(z)\right)\right)$. Therefore, the minimax optimal function is designed by the expectation operator. The general reconstruction idea is to train a generator for the purpose of fooling a differentiable discriminator that is trained to distinguish reconstructed HSS-EEG signals from real HSS-EEG signals. In constructing EEG signals, GANs suffer from remarkable training difficulty due to the nonlinear and non-stationary characteristics of EEG signals. To overcome the training problem of the original GAN framework, instead of using Jensen–Shannon divergence, the WGAN framework uses the Wasserstein distance to compare sample distributions (Gulrajani et al., 2017). From the definition of WGAN, the min-max problem optimized by D_{θ_D} and G_{θ_G} can be written:

$$\min_{\theta_G}\max_{\theta_D} L_{WGAN}(D_{\theta_D}, G_{\theta_G}) = -E_{x\sim P_H}\left[D_{\theta_D}(x)\right] + E_{z\sim P_L}\left[D_{\theta_D}\left(G_{\theta_G}(z)\right)\right] + \lambda E_{\tilde{x}\sim P_R}\left[\left(\left\|\nabla_{\tilde{x}}(D(\tilde{x}))\right\|_2 - 1\right)^2\right] \tag{3}$$

In the min–max problem, the Wasserstein distance is estimated by the first two terms. The last term is the gradient penalty for network regularization. In the penalty term, P_R denotes the distribution of uniform samples $\tilde{x}$ along straight lines connecting pairs of generated and real samples. $\nabla_{\tilde{x}}(\cdot)$ is the gradient calculator, and the parameter λ is a constant weighting parameter for the penalty term. In fact, the WGAN framework removes the log function and drops the last sigmoid layer to keep the gradient while training the min-max problem. The discriminator D_{θ_D} and the generator G_{θ_G} are trained alternatively by optimizing one and updating the other.

2.3. TSF-MSE Loss Function

To allow the generator to transform the data distribution from a low sampling rate and sensitivity to a high sampling rate and sensitivity, another part of the loss function needs to be added to the GAN/WGAN architecture to retain the detail and information content of the EEG signals. A widely used loss function for signal details and information contents is the mean square error (MSE) loss function (Yang et al., 2018). Typically, as the common MSE is computed by minimizing the point-wise error in image processing, the temporal MSE is computed by minimizing the time sampling point-wise error between a LSS-EEG patch and a HSS-EEG patch by the time step:

$$L_{T-MSE}(G_{\theta_G}) = E_{(x,z)}\left[\frac{1}{T^2}\left\|G(z(t)) - x(t)\right\|_F^2\right] \tag{4}$$

where $\|\cdot\|_F$ denotes the Frobenius norm, L_{T-MSE} denotes the temporal MSE for the generator G_{θ_G}, t is the time step of real EEG signals and generated EEG signals, and T is the number of time steps for each batch. In contrast to images, EEG signals are multi-channel time-series data, and the spatial and frequency features must be considered for reconstruction. Therefore, in addition to the temporal MSE L_{T-MSE} between time steps, the spatial MSE L_{S-MSE} between channels and the frequency MSE L_{F-MSE} between signal batches also need to be considered for encouraging the GAN/WGAN architecture to construct more accurate HSS-EEG signals. Recently, common spatial patterns (CSP) have been widely used to extract spatial features from EEG signals (Luo et al., 2018a), and power spectral density (PSD) features are widely used to extract frequency features from EEG signals (Petroff et al., 2016). The CSP algorithm is used to compute the optimal projection vectors to project the original EEG signal to a new space to obtain good spatial resolution and discrimination between different classes of EEG signals. The PSD algorithm is used to compute the power values on specific

frequencies to compose a spectra. Using these two algorithms, the spatial MSE L_{S-MSE} and the frequency MSE L_{F-MSE} are defined for the generator:

$$L_{S-MSE}(G_{\theta_G}) = E_{(x,z)}\left[\frac{1}{C^2}\left\|G(CSP(z(c))) - CSP(x(c))\right\|_F^2\right] \quad (5)$$

$$L_{F-MSE}(G_{\theta_G}) = E_{(x,z)}\left[\frac{1}{N^2}\left\|G(PSD(z(n))) - PSD(x(n))\right\|_F^2\right] \quad (6)$$

where $CSP(\cdot)$ and $PSD(\cdot)$ are the CSP feature and PSD feature extractor, respectively. c is the channel of real EEG signals and the same of the generated EEG signals, C is the number of channels, n is the batch of real EEG signals and the same as that of the generated EEG signals, and N is the number of batches. For convenience, the TSF loss is computed by weighting three such MSE losses:

$$\begin{aligned} L_{TSF-MSE}(G_{\theta_G}) &= \lambda_T \cdot L_{T-MSE}(G_{\theta_G}) + \lambda_S \cdot L_{S-MSE}(G_{\theta_G}) \\ &\quad + \lambda_F \cdot L_{F-MSE}(G_{\theta_G}), \end{aligned} \quad (7)$$

where $\lambda_T, \lambda_S, \lambda_F$ are the weights of three such different MSE losses, respectively. Datasets with different sampling rates and sensitivities will obtain different weights, and, thus, the values of the weights will be determined by experiments.

In addition, to confirm that the EEG signals are temporally and spatially coherent, a regularization loss $L_{TV}(G_{\theta_G})$ based on total variation is used in the generator:

$$L_{TV}(G_{\theta_G}) = \frac{1}{CT}\sum_{c=1}^{C}\sum_{t=1}^{T}\left\|\nabla_z G_{\theta_G}(z)_{c,t}\right\| \quad (8)$$

where $\nabla_z(\cdot)$ is the gradient calculator; the gradient regularization loss will encourage temporal and spatial coherence of the reconstruction. Combining Equations (3), (7), and (8), the overall joint reconstruction loss function is expressed as

$$\min_{\theta_G}\max_{\theta_D} L_{TSF-MSE}(G_{\theta_G}) + \lambda_1 L_{WGAN}(D_{\theta_D}, G_{\theta_G}) + \lambda_2 L_{TV}(G_{\theta_G}) \quad (9)$$

where λ_1 and λ_2 are the weights for controlling the trade-off among the WGAN adversarial loss, the TSF-MSE loss and the TV loss.

2.4. Network Structures

The proposed WGAN-EEG reconstruction framework is illustrated in **Figure 1**. The WGAN-EEG framework consists of three parts to reconstruct HSS-EEG signals from LSS-EEG signals. For the first part of the deep generator G_{θ_G}, "B residual blocks" with an identical layout that was proposed by "Kaiming He" (He et al., 2016) are employed in the generator network. To facilitate the high sensitivity of EEG signals, 16 "B residual blocks" are applied to LSS-EEG signals to extract deep features for the generator. In each "B residual block," following the common usage of the deep learning community, two convolutional layers with small 3*3 kernels, 1 stride, and 64 feature maps (k3n64s1) are followed by a batch-normalization layer (BN) and the ReLU activation function (Ioffe and Szegedy, 2015). To increase the sampling rate of the input EEG signals, the trained deconvolutional layer (stride = 0.5) is followed by "B residual blocks" to increase the sampling rate. In real-world application, the WGAN-EEG architecture is trained well to fit HSS-EEG signals before usage. In the usage scenario, the recorded LSS-EEG

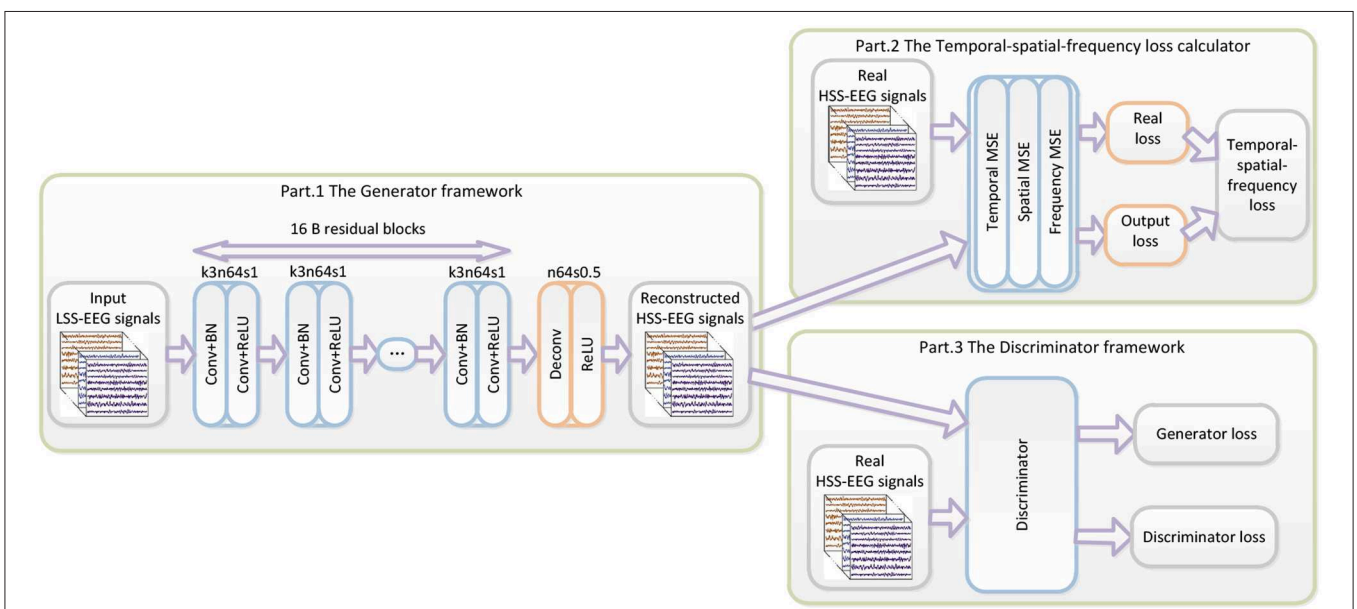


FIGURE 1 | The architecture of the WGAN-EEG. The WGAN-EEG framework consists of three parts to reconstruct HSS-EEG signals from LSS-EEG signals. For the first part of the deep generator, "B residual blocks" with an identical layout are employed in the generator network. The second part of the WGAN-EEG framework is the TSF-MSE loss calculator. The third part of the WGAN-EEG is used to discriminate real HSS-EEG signals from generated HSS-EEG samples.

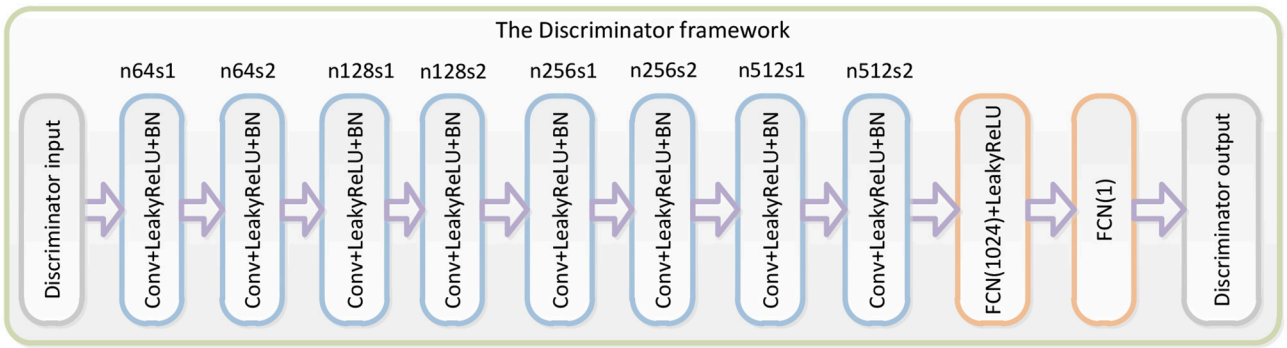


FIGURE 2 | Details of the discriminator in the WGAN-EEG. We followed the architectural guidelines for the discriminator to use the LeakyReLU activation function and avoid max-pooling along the network. The discriminator network contains eight convolutional layers with an increasing number of filter kernels by a factor of 2. After eight convolutional layers, there are two FCN layers, of which the first layer has 1,024 outputs with the LeakyReLU activation function, and the second layer has a single output. Following the instructions of the WGAN, the discriminator of the WGAN-EEG has no sigmoid cross entropy layer.

signals are incorporated into the well-trained architecture to reconstruct HSS-EEG signals to improve the sensitivity.

The second part of the WGAN-EEG framework is the TSF-MSE loss calculator, which is realized in **Figure 1**. The reconstructed output HSS-EEG signals $G_{\theta_G}(z)$ from the generator G_{θ_G} and the ground truth HSS-EEG signals x are fed into the calculator to extract the CSP features and the PSD features. Then, using the extracted features, the TSF-MSE loss is computed by Equations (4), (5), (6). The reconstruction error computed by the loss function is then back-propagated to update the generator network's weights.

The third part of the WGAN-EEG used to discriminate real HSS-EEG signals from generated HSS-EEG samples, the discriminator network D_{θ_D}, is shown in **Figure 2**. Here, we followed the architectural guidelines for the discriminator to use the LeakyReLU activation function and avoid max-pooling along the network (Zhang et al., 2017). The discriminator network contains eight convolutional layers with an increasing number of filter kernels by a factor of 2. In fact, the convolutional kernels are increased from 64 to 512 kernels, and the stride is alternatively increased from 1 to 2 to reduce the EEG signal sampling rate when the number of features is doubled. In the discriminator, each convolutional layer is followed by a LeakyReLU activation function and a batch-normalization layer. After eight convolutional layers, there are two FCN layers, of which the first layer has 1,024 outputs with the LeakyReLU activation function, and the second layer has a single output. Following the instructions of the WGAN (Gulrajani et al., 2017), the discriminator of the WGAN-EEG has no sigmoid cross entropy layer.

The WGAN-EEG framework is trained by using EEG signal batches and applied on the entity of each signal trial. The details of training the WGAN have been described in the experiments.

3. RESULTS

3.1. Experimental Datasets

To explore the feasibility and performance of the proposed algorithm, three EEG signal datasets with different sampling rates and sensitivities are applied to train and evaluate the proposed networks. **Table 1** illustrates the details of these three different EEG datasets.

TABLE 1 | Details of the three different EEG datasets.

Datasets	Action observation	Grasp and lift	Motor imagery
Sampling rate/s	250	500	250
Sensitivity/bit	0.024 μV/bit	0.1 μV/bit	100 μV/bit
Channels	64	32	22
Classification categories	2	6	4
Subject number	6	12	9
Trials/Subject	384	576	1,560
Trial duration/s	5 s	0.5 s	4 s
Device	NeuroScan SymAmp2	BrainAmp	Unknown

(1) Action Observation (AO) dataset (Luo et al., 2018b): The AO dataset[1] was collected from our previous research on different speed modes during AO. The EEG signals were acquired from the "NeuroScan SymAmp2" device with 64 channels, and the sampling rate and sensitivity were 250 Hz and 0.024 μV/bit, respectively. In this dataset, six subjects were invited to observe a robot's actions at four different speeds. Thus, the dataset had 24 subsets for each subject in each AO speed mode. Each subset contained 384 trials with 192 trials of left leg movements and 192 trials of right leg movements for a binary classification, and each trial lasted 5 s. To train the GAN/WGAN, a "leave-one-rest" strategy is used for training. In our pre-training experiments, more signals caused a problem of over-fitting and a large time complexity for GAN/WGAN training. Since 13 subsets containing 4,992 trials were enough to obtain the best performance, we left one subset and randomly selected 13 subsets from the remaining 23 subsets for training; the left subset was reconstructed after obtaining the well-trained

[1]https://pan.baidu.com/s/4gap5N4.

GAN/WGAN. Therefore, all 24 subsets were reconstructed through 24 rounds of the above procedure. Because the AO dataset was acquired at a sampling rate of 250 Hz, we down-sampled all trials of EEG samples to the sampling rate of 125 Hz for the sake of sampling rate reconstruction.

(2) Grasp and Lift (GAL) dataset (Luciw et al., 2014): The GAL dataset[2] recorded EEG signals while the subjects grasped and lifted an object. The EEG signals were acquired using the "BrainAmp" device with 32 channels, and the sampling rate and sensitivity were 500 Hz and 0.1 μV/bit, respectively. In this dataset, 12 subjects executed six movements for 1,560 trials, and each trial lasted 0.5 s; thus, the classification of EEG signals contained six categories. To train the GAN/WGAN, a "leave-one-rest" strategy is used for training. The 9,360 trials carried out by six subjects were enough to train the GAN/WGAN, and we thus left one subject's signals and randomly selected six subjects' signals from the remaining 11 subjects' signals for training; the left subjects' signals were reconstructed after obtaining the well-trained GAN/WGAN. Therefore, all 12 subjects' signals were reconstructed through 12 rounds of the above procedure. In the experiment, to validate the reconstruction of the sampling rate, all signals were down-sampled to a sampling rate of 250 Hz.

(3) Motor Imagery (MI) dataset (Tangermann et al., 2012): The MI dataset[3] was from the "BCI competition IV dataset 2a." Nine subjects participated in the MI experiment during which EEG signals were recorded while the subject imagined his/her own leg, foot, and tongue movements, and each trial lasted for 4 s. There were 22 channels, and the sampling rate and sensitivity were 250 Hz and 100 μV/bit, respectively. In this dataset, nine subjects executed four motor imagery tasks, and each subject had 576 trials of EEG signals for a four categories for classification.To train the GAN/WGAN, a "leave-one-rest" strategy is used for training. The 4,032 trials carried out by seven subjects were enough to train the GAN/WGAN, and we thus left one subject's signals and randomly selected seven subjects' signals from the remaining eight subjects' signals for training; the left subjects' signals were reconstructed after obtaining the well-trained GAN/WGAN. Therefore, all nine subsets were reconstructed through nine rounds of the above procedure. For the same purpose, all trials of EEG signals were down-sampled at a sampling rate of 125 Hz.

3.2. Training Details

In the training procedure, we trained six models using the GAN/WGAN framework within three different datasets. All down-sampled training EEG samples were fed into the generator, and the real training EEG samples were fed into the discriminator. The generated EEG samples and the real EEG samples were discriminated by the TSF-MSE loss function to update the generator and the discriminator for solving the min-max problem. Because the AO dataset and the GAL dataset have high sampling rates and a high number of channels, models for these two datasets were trained over 30 epochs. However, the MI dataset has a lower sampling rate and fewer channels, and, therefore, this dataset was trained over 20 epochs. Each epoch traverses all the data in the corresponding dataset. According to the different devices used to record EEG signals, the generators of the GAN/WGAN frameworks were specified by different scopes of generation for different datasets. We specified the generation scopes of [−40, 40 μV], [−50, 50 μV], and [−100, 100 μV] for the AO dataset, the GAL dataset, and the MI dataset, respectively.

In our experiments, we randomly extracted pairs of signal patches from down-sampled EEG signals and real EEG signals as our training inputs and labels. The patch size is $N * \tau$, where N is the channel number for different datasets, and τ is the EEG samples from the temporal domain. Since the limited trials of EEG signals (<500 trials for one subject) and smaller values of τ will construct more accurate sequential relationships for the EEG signals, following our previous research (Luo et al., 2018a), we cropped a minimal length for the training of the deep neural network. According to the pre-experiment, we set $\tau = 12$ to satisfy the minimal length for the convolution in the GAN/WGAN architecture. In the optimization of the generator and the discriminator, according to current research (Basu et al., 2018), the GAN models were optimized by the Adam algorithm (Basu et al., 2018), and the WGAN models were optimized by the RMSprop algorithm (Mukkamala and Hein, 2017). The optimization procedure for the GAN/WGAN architectures is shown in **Figure 3**. The mini-batch size was set to 32. Following the instructions of the GAN/WGAN frameworks (Goodfellow et al., 2014; Gulrajani et al., 2017), the Adam optimizer's hyperparameters were set as $\alpha = 10^{-5}, \beta_1 = 0.5, \beta_2 = 0.9$, and the RMSprop optimizer's hyperparameters were set as $\alpha = 10^{-5}, \beta = 0.9$. The hyperparameter for the gradient penalty of WGAN framework was set as $\lambda = 10$ according to the suggestion in the reference (Gulrajani et al., 2017). The hyperparameters for the SRGAN/SRGAN frameworks in Equation (9) were set as $\lambda_1 = 10^{-3}$ and $\lambda_2 = 2 * 10^{-8}$ by the suggestions of reference (Ledig et al., 2017). The hyperparameters in the TSF-MSE loss function of Equation (7) and the joint reconstruction were set of different values according to the experimental experience of each reconstruction round, and the average values with standard deviations of all parameters in three datasets are given in **Table 2**. The optimization processes for the GAN framework and the WGAN framework are similar; however, some places are changed to the corresponding optimizer and the loss functions (see **Figure 3**).

The GAN/WGAN frameworks were implemented in Python 2.7 with the Tensorflow 1.8 library. Two NVIDIA 1080Ti GPUs were used in this study.

3.3. Network Convergence

To visualize the convergence of the GAN/WGAN frameworks, the conventional temporal MSE, frequency MSE, spatial MSE, the proposed TSF-MSE losses, and the Wasserstein distance for validation of three different datasets were computed according to Equations (2), (3), (4), and (5). **Figure 4** shows the averaged temporal MSE, frequency MSE, spatial MSE, and TSF-MSE

[2]https://www.kaggle.com/c/grasp-and-lift-eeg-detection/data.
[3]http://www.bbci.de/competition/iv/#datasets.

Require: Set hyper-parameters, $\lambda = 10$ for penalty weight, $\alpha = 1e-5, \beta_1 = 0.5, \beta_2 = 0.9$ for Adam, $\alpha = 1e-5, \beta = 0.9$ for RMSprop, $\lambda_T = 0.5, \lambda_S = 0.25, \lambda_F = 0.25, \lambda_1 = 0.1, \lambda_2 = 0.1$ for TSF-MSE weights.

Require: Set the number of total epochs, $N_{epoch} = 30$ for AO and GAL, $N_{epoch} = 20$ for MI, the number of iteration for discriminator training $N_D = 4$, the batch size $m = 32$, and EEG signal patch size $N \times \tau = 64/32/22 \times 12$.

Require: Initial generator network parameters G_{θ_G}, and discriminator parameters D_{θ_D}.

Require: Calculate CSP features and PSD features to construct TSF-MSE loss function

for $epoch = 0, \ldots, N_{epoch}$ **do**

  for $t = 1, \ldots, N_D$ **do**

    Sample a batch of HSS-EEG signal patches $\{x^{(i)}\}_{i=1}^{m}$, latent LSS-EEG signal patches $\{z^{(i)}\}_{i=1}^{m}$, and random numbers $\{\varepsilon^{(i)}\}_{i=1}^{m} \sim Uniform[0,1]$.

    for $i = 1, \ldots, m$ **do**

      $\tilde{x}^{(i)} \leftarrow \varepsilon^{(i)} x^{(i)} + (1 - \varepsilon^{(i)}) G(z^{(i)})$

      GAN: $L^{(i)}(D) \leftarrow log(D(G(z^{(i)}))) + log(D(x^{(i)}))$

      WGAN: $L^{(i)}(D) \leftarrow D(G(z^{(i)})) - D(x^{(i)}) + \lambda(\left\|\nabla D(\tilde{x}^{(i)}\right\|_2 - 1)^2)$

    end for

  end for

  Update Discriminator:

  GAN: $w \leftarrow Adam(\nabla_w 1/m \sum_{i=1}^{m} L^{(i)}(D), w, \alpha, \beta_1, \beta_2)$

  WGAN: $w \leftarrow RMSprop(\nabla_w 1/m \sum_{i=1}^{m} L^{(i)}(D), w, \alpha, \beta)$

  Sample a batch of LSS-EEG signal patches $\{z^{(i)}\}_{i=1}^{m}$ and corresponding HSS-EEG signal patches $\{x^{(i)}\}_{i=1}^{m}$,

  for $i = 1, \ldots, m$ **do**

    $L^{(i)}(G) \leftarrow \lambda_1 L_{TSF-MSE}(z^{(i)}, x^{(i)}) + \lambda_2 L_{TV}(z^{(i)}) - D(G(z^{(i)}))$

  end for

  Update Discriminator:

  GAN: $\theta \leftarrow Adam(\nabla_\theta 1/m \sum_{i=1}^{m} L^{(i)}(G), w, \alpha, \beta_1, \beta_2)$

  WGAN: $\theta \leftarrow RMSprop(\nabla_\theta 1/m \sum_{i=1}^{m} L^{(i)}(D), w, \alpha, \beta)$

end for

FIGURE 3 | The optimization procedure for the GAN/WGAN. Following the instructions of the GAN/WGAN frameworks, the Adam optimizer's hyperparameters are set as $\alpha = 1e-5, \beta_1 = 0.5, \beta_2 = 0.9$, and the RMSprop optimizer's hyperparameters are set as $\alpha = 1e-5, \beta = 0.9$. The hyperparameter for the gradient penalty is set as $\lambda = 10$ according to the suggestion in the reference. The hyperparameters in the TSF-MSE loss function and the joint reconstruction are set as $\lambda_T = 0.5, \lambda_S = 0.25, \lambda_F = 0.25, \lambda_1 = 0.1, \lambda_2 = 0.1$ according to our experimental experience. The optimization processes for the GAN and the WGAN are similar, except some places are changed to the corresponding optimizer and the loss functions.

losses vs. the number of epochs for different datasets within the GAN/WGAN frameworks.

From **Figures 4A–D**, for a given framework and dataset, we have compared the variations and differences between the conventional temporal MSE, frequency MSE, spatial MSE, and our proposed TSF-MSE. In the four figures, all of the iterative curves are shown to have decreased rapidly within the first 10 epochs (each epoch contains 10 error recordings), and the

TABLE 2 | The hyperparamter λ_T, λ_S, λ_F tuning of the novel TSF-MSE loss function for all experiments.

Reconstruction	λ_T	λ_S	λ_F
AO− > AO	0.46 ± 0.12	0.23 ± 0.06	0.30 ± 0.09
GAL− > GAL	0.44 ± 0.13	0.21 ± 0.08	0.35 ± 0.06
MI− > MI	0.53 ± 0.16	0.20 ± 0.11	0.27 ± 0.03
GAL− > AO	0.47 ± 0.12	0.18 ± 0.09	0.31 ± 0.07
MI− > AO	0.41 ± 0.13	0.31 ± 0.08	0.27 ± 0.09
AO− > GAL	0.50 ± 0.14	0.22 ± 0.09	0.33 ± 0.06
MI− > GAL	0.52 ± 0.12	0.22 ± 0.08	0.25 ± 0.08
AO− > MI	0.60 ± 0.18	0.31 ± 0.09	0.07 ± 0.01
GAL− > MI	0.58 ± 0.17	0.33 ± 0.08	0.06 ± 0.01

initial decreases indicated that these two metrics are positively correlated for the EEG signal reconstruction. However, for each dataset or when using GAN/WGAN frameworks, the loss results of TSF-MSE were lower than the loss results of conventional temporal MSE, frequency MSE, and spatial MSE. In addition, of these four losses, the WGAN frameworks oscillated in the convergence process, while the GAN frameworks smoothed in the convergence process. Comparing the oscillation of losses, the TSF loss exhibited varied smoothing for the WGAN framework compared to the GAN framework for each dataset. These observations of network convergence suggested that the conventional MSE losses and our proposed TSF-MSE loss have different focuses within the GAN/WGAN frameworks. By applying the generators, the difference between conventional MSE losses and our proposed TSF-MSE loss will be further revealed in the reconstructed EEG signals.

Figure 5 illustrates the Wasserstein distance estimation vs. the number of epochs for three different datasets. The plotted Wasserstein values were estimated by the definition of $-E_{x\sim P_H}\left[D_{\theta_D}(x)\right]+E_{z\sim P_L}\left[D_{\theta_D}\left(G_{\theta_G}(z)\right)\right]$ in Equation (3). From the figure, we have found a reduction in the Wasserstein distances as the number of epochs increased, but different datasets have different decay rates of the reducing Wasserstein distance. For the curves of the three datasets, we noted that the Wasserstein distance we computed is a surrogate that has not been normalized by the total number of EEG signal samplings, and, therefore, the curves would have decreased to close to zero after 100 epochs by using the normalization for the EEG signals.

3.4. Reconstruction Results

To show the reconstruction effects of the GAN/WGAN frameworks with our proposed TSF-MSE loss function, we considered two different aspects of the reconstruction results. The first one was the sampling rate reconstruction by the same sensitivity signals' GAN/WGAN frameworks, which is shown in **Figure 6**. The second one was the sensitivity rate reconstruction by the different sensitivity signals' GAN/WGAN frameworks, which is shown in **Figure 7**. Since the proposed reconstruction method used a novel TSF-MSE loss function for the training of GAN/WGAN architectures, the statistical temporal, frequency, and spatial results were also compared between the original signals and the reconstructed signals. **Figures 8–10** illustrated the mean temporal error, mean spectra difference, and brain electrical activity mapping on 12 Hz of a single trial compared with the original EEG signals and all reconstructed EEG signals.

To plot the reconstruction results of different models and situations, we chose the same trial from each dataset for the comparison experiments. Because the number of channels differs for each dataset, we choose the "*FPz*" channel for the experiments to plot the figures. In addition, as one trial over a long period of time will hide some details of the reconstruction signals, we chose the 50 ms range of (500 and 550 ms) for the AO and MI datasets and the 50 ms range of (100 and 150 ms) for the GAL dataset to plot the details of the reconstruction results. From the reconstruction results by the same details shown in **Figure 6**, we have found that the signals' proximity between the reconstructed data and the original data decreased in the following order for the three datasets: AO > GAL > MI. The difference between the GAN framework and the WGAN framework cannot be realized at the signal level. In the figures shown in **Figure 7**, the high sensitivity EEG signals' GAN/WGAN frameworks reconstructed the low sensitivity EEG signals well, such as the AO and GAL data reconstructed by the MI GAN/WGAN frameworks. However, the low sensitivity EEG signals' GAN/WGAN models cannot reconstruct accurate high sensitivity EEG signals, such as MI data reconstructed by the AO and GAL GAN/WGAN frameworks.

For the statistical results in **Figures 8–10**, we have found that excepting for the temporal errors, reconstructed EEG signals show the same regulations on frequency and spatial features. For the reconstructions of the same sensitivity, the mean spectra results have shown that WGAN architectures outperform than GAN architectures, so do the brain electrical activity mapping (BEAM) results for reconstructions of the same sensitivity. As for the reconstructions of different sensitivity, we have found that higher sensitivity models bring lower spectra difference and more distinct ERS/ERD phenomenon on BEAMs, while lower sensitivity models bring higher spectra difference and less distinct ERS/ERD phenomenon on BEAMs.

3.5. Classification Results

In fact, the qualitative analysis could not yield promising insight regarding HSS-EEG signals reconstructed by LSS-EEG signals. Hence, a quantitative analysis was applied to explore the performance of reconstructed EEG signals. In this paper, because the AO dataset corresponded to action observation, the GAL dataset corresponded to action execution, and the MI dataset corresponded to motor imagery, these three datasets caused the same event-related desynchronization/event-related synchronization (ERD/ERS) phenomenon, which can be classified by filter bank common spatial patterns (FBCSP) and a support vector machine (SVM) (Luo et al., 2018a,b). The ERS/ERD phenomenon from EEG signals is common on three motor-related datasets, and such phenomena are usually used for the motor-based BCI. Therefore, the ERS/ERD phenomenon will be the key index with which to measure the performance of BCI system by EEG signals. This study thus selected the ERS/ERD phenomenon from EEG signals as a quantitative measure, and FBCSP features with an SVM classifier were applied to explore

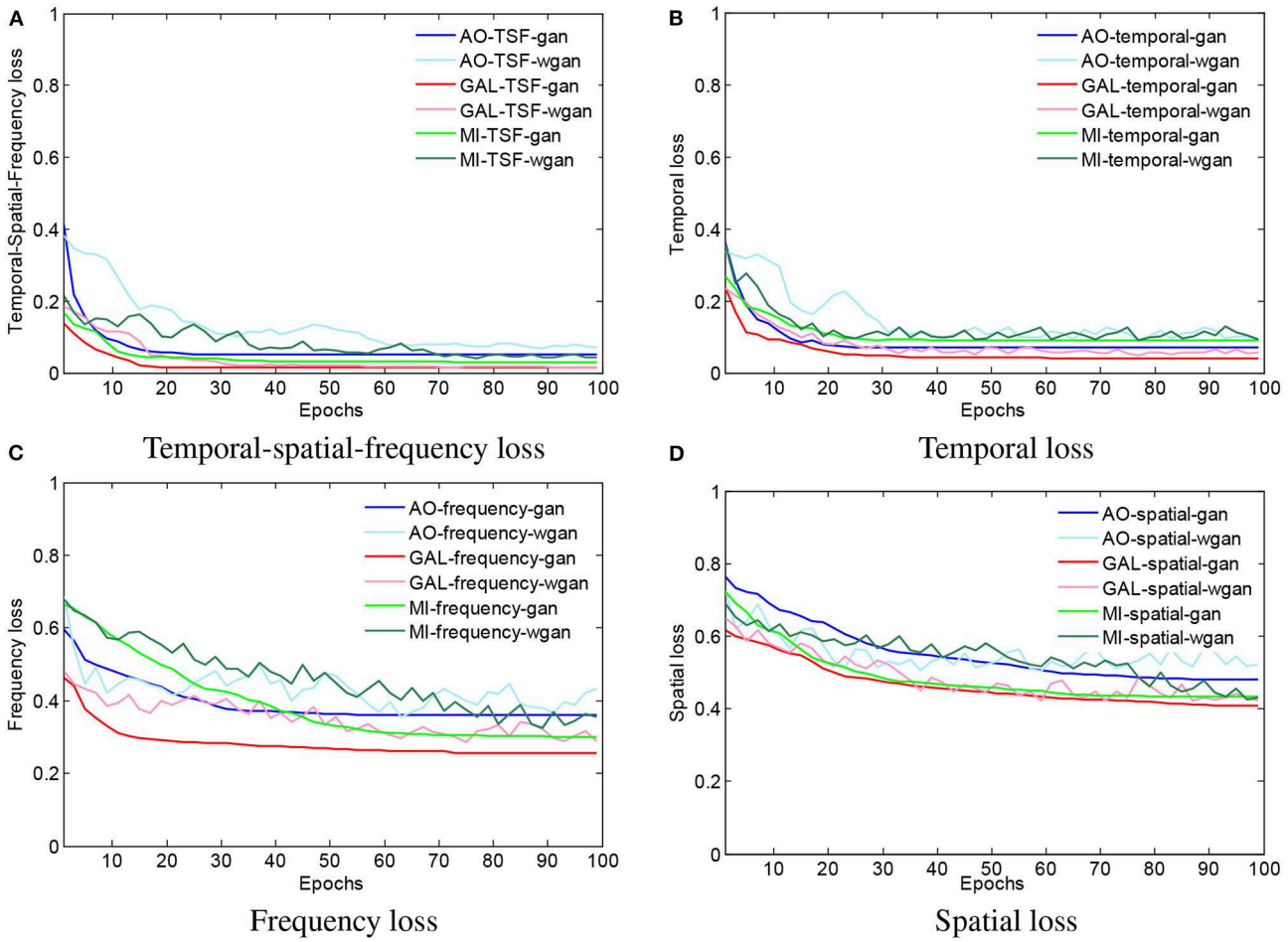


FIGURE 4 | The averaged MSE and Wasserstein distance estimations for training the GAN/WGAN. In the four figures, all of the iterative curves decreased rapidly within the first 10 epochs (each epoch contains 10 errors recording), and the initial decreases indicated that these two metrics are positively correlated for the EEG signal reconstruction. However, for each dataset or using GAN/WGAN frameworks, the loss results of TSF-MSE are lower than the loss results of conventional temporal, frequency, and spatial MSE. In addition, of these four losses, the WGAN frameworks oscillate in the convergence process, while the GAN frameworks are smoothed in the convergence process. **(A)** Temporal-spatial-frequency loss, **(B)** Temporal loss, **(C)** Frequency loss, **(D)** Spatial loss.

the performances of the original signals and the reconstructed signals. For comparison with different models and different sensitivities, there were several hyperparameters for the FBCSP features, SVM classifier, and deep learning classifier:

(1) Because all three datasets contain the ERD/ERS phenomenon, which is detected on the band of [8, 30 Hz], the filter bank strategy is used to divide the whole band to obtain universality for different subjects. In this study, the width and overlapping ratio were set to 4 and 2 Hz for the filter bank dividing, as shown in **Table 3**. After the EEG signals are filtered by the optimal filter bank, the CSP algorithm was included to extract FBCSP features (Ang et al., 2012).

(2) The CSP algorithm (Ang et al., 2012) is presented to every filter result to extract the optimal spatial features by computing a problem of maximizing the power ratio for different AO/AE/MI tasks. Then, the maximizing power ratio is computed by the singular value decomposition (SVD) algorithm to obtain eigenvalues and eigenvectors. Because different datasets have EEG signals from different channels, the number of eigenvalues used for constructing the CSP spatial vector were set to $m = 8, m = 4$, and $m = 4$ for the AO dataset, the GAL dataset, and the MI dataset, respectively.

(3) In the classification, the SVM classifier was issued to classify the extracted FBCSP features from three different datasets. To overcome the non-stationary and nonlinear characteristics of EEG signals, the linear kernel with hyperparameters was set to $c = 0.01$ and $g = 2$ for the classifiers for all datasets. To compare the classification performance for both the original data and the reconstructed data, an 8*8 cross-validation strategy was applied to each dataset, and the average classification results were recorded.

(4) In order to validate the performance improvement of reconstructed signals, a convolutional neural networks

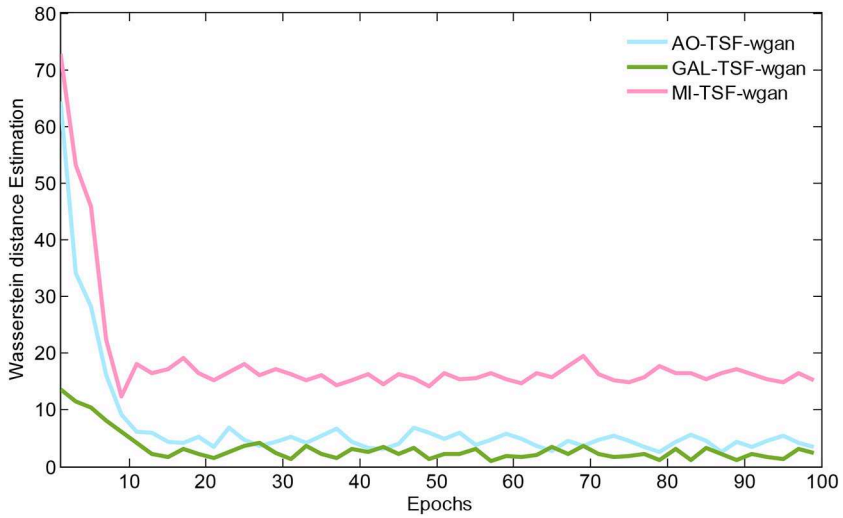


FIGURE 5 | The Wasserstein distance estimation vs. the number of epochs for three different datasets. The plotted Wasserstein values are estimated by the definition of $-E_{x\sim P_H}\left[D_{\theta_D}(x)\right]+E_{z\sim P_L}\left[D_{\theta_D}\left(G_{\theta_G}(z)\right)\right]$ in Equation (3). For the curves of these three datasets, we note that the Wasserstein distance we computed is a surrogate that has not been normalized by the total number of EEG signal samplings, and, therefore, the curves would have decreased to close to zero after 100 epochs by using the normalization for the EEG signals.

based deep learning model "FBCSPNet" from reference (Schirrmeister et al., 2017) was introduced to compare the classification performance between original signals and reconstructed signals. Experimental parameters were set as the same from the reference for AO/GAL/MI datasets.

Classification results for the sampling rate reconstruction by the same sensitivity signals' GAN/WGAN frameworks are shown in **Tables 4–6** for AO dataset, GAL dataset, and MI dataset, respectively. In addition, classification results for the sensitivity rate reconstruction by the different sensitivity signals' GAN/WGAN frameworks are shown in **Tables 7–9** for AO datset, GAL dataset, and MI dataset, respectively. In all tables, the results are presented by classification accuracy forms, and a paired t-test statistical technique was used to detect whether the reconstructed EEG signals significantly outperform than the original EEG signals. P-value of the t-test statistics are provided in the tables, and $^{*}p < 0.05$ and $^{**}p < 0.01$ represent the results compared among two columns are significantly different and extremely significantly different.

Tables 4–6 illustrate the up-sampling classification results compared with the original data, the spline reconstructed data, the GAN reconstructed data, and the WGAN reconstructed data. Among the three datasets, we have found that the WGAN reconstructed data achieved the best classification performance. In the AO dataset, the WGAN reconstructed signals achieved the best classification accuracy (67.67%), which was higher than those of the original data (63.57%), the spline reconstructed data (60.91%), and the GAN reconstructed data (65.41%). In the GAL dataset, the WGAN reconstructed signals achieved the best classification accuracy (73.89%), which was higher than those of the original data (69.78%), the spline reconstructed data (68.25%), and the GAN reconstructed data (73.63%). In the MI dataset, the WGAN reconstructed signals achieved the best classification accuracy (64.01%), which was higher than those of the original data (61.98%), the spline reconstructed data (60.41%), and the GAN reconstructed data (63.61%).

From the t-test statistical results that computed compared signals, the reconstructed GAN/WGAN model signals exhibited significant improvement of classification, producing a better performance than the original signals, while spline reconstructed signals exhibited significant reduction of classification performance, lower that of the original signals. The significant improvement and reduction are presented for all AO/GAL/MI datasets ($^{*}p < 0.05$). Specifically for the WGAN model in AO dataset and GAN/WGAN model in MI dataset, the classification performances presented were extremely significant ($^{**}p < 0.01$). Therefore, we have concluded that the GAN/WGAN models with proposed TSF-MSE loss function showed a significant improvement for reconstructing EEG signals with the same sensitivity.

Tables 7–9 give the classification results compared with the GAN/WGAN models trained with different sensitivities. **Table 7** gives the classification results of the AO data reconstructed by the GAL/MI trained GAN/WGAN models. **Table 8** gives the classification results of the GAL data reconstructed by the AO/MI trained GAN/WGAN models. **Table 9** gives the classification results of the MI data reconstructed by the AO/GAL trained GAN/WGAN models. For the AO dataset, signals reconstructed by the GAL-GAN model achieve the best average classification accuracy (64.55%), which was higher than those of the original data (63.51%) and the data reconstructed by the GAL-WGAN (64.40%), the MI-WGAN (62.07%), and the MI-GAN (62/08%). For the GAL dataset, signals reconstructed by the AO-GAN model achieve the best average classification accuracy (70.60%),

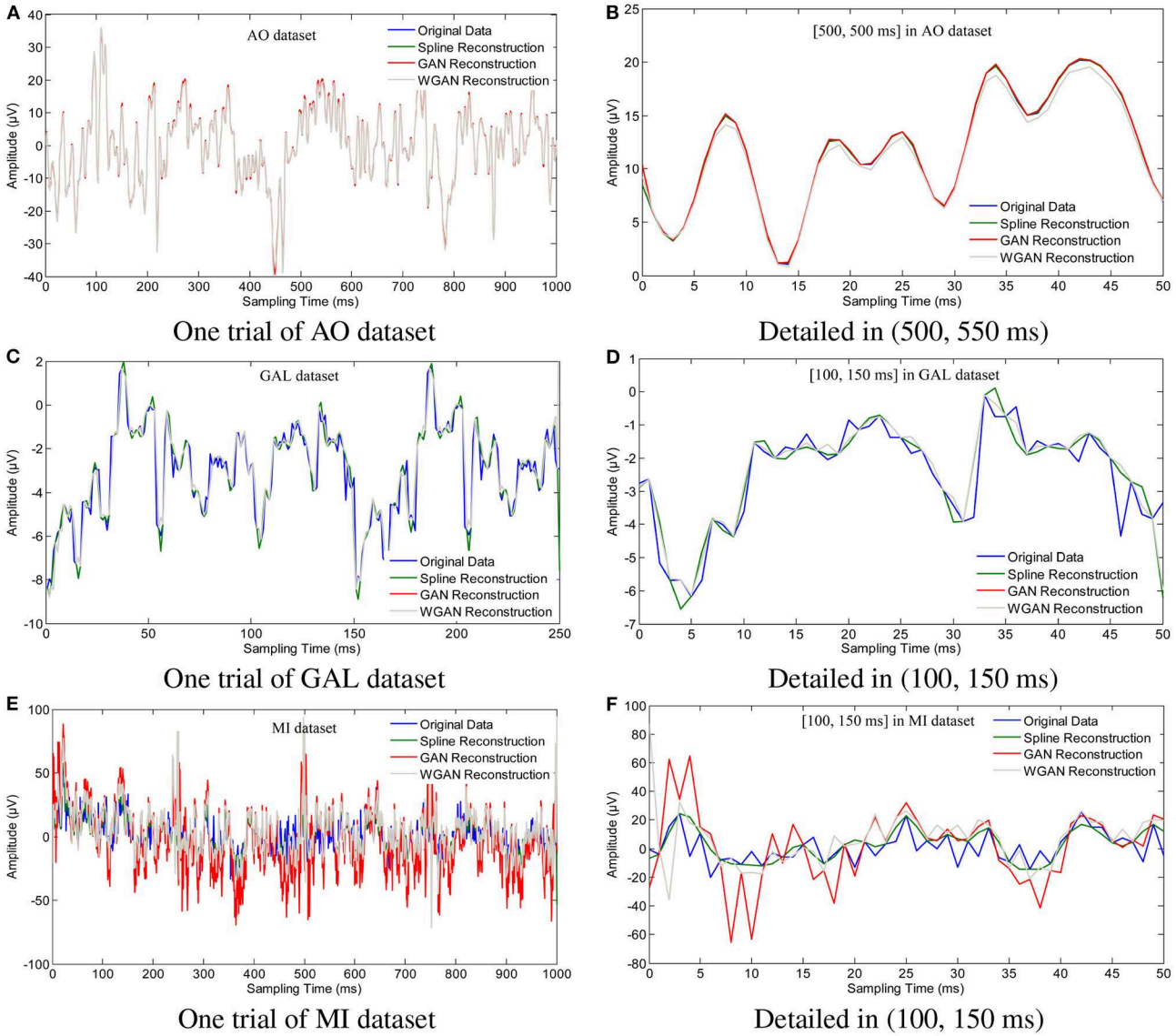


FIGURE 6 | Sampling rate reconstruction by the same sensitivity GAN/WGAN frameworks. Sampling rate and sensitivity reconstruction by the same sensitivity GAN/WGAN frameworks. The reconstruction results of one trial for AO dataset, GAL dataset, and MI dataset. Meanwhile, the detailed reconstruction results in (500, 550 ms) of AO datasets and (100, 150 ms) of GAL and MI datasets are also given. **(A)** One trial of AO dataset, **(B)** Detailed in (500, 550 ms), **(C)** One trial of GAL dataset, **(D)** Detailed in (100, 150 ms), **(E)** One trial of MI dataset, **(F)** Detailed in (100, 150 ms).

which is higher than those of the original data (69.78%) and the data reconstructed by the AO-WGAN (70.34%), the MI-WGAN (69.57%), and the MI-GAN (70.21%). For the MI dataset, signals reconstructed by the AO-GAN model achieved the best average classification accuracy (64.93%), which was higher than those of the original data (61.98%) and the data reconstructed by the AO-WGAN (63.29%), the MI-WGAN (63.66%), and the MI-GAN (63.39%). The GAN model performed better than the WGAN model for reconstructing EEG signals by different sensitivities, and LSS-EEG signals reconstructed by HSS-EEG models will increase the sampling rate and sensitivity of signals, which will increase the classification performance.

From the *t*-test statistical results that computed between compared signals, the AO dataset reconstructed signals by GAL-WGAN and GAL-GAN, showing significant improvement of classification performance than the original signals ($^*p < 0.05$), while other datasets reconstructed signals showed no significant performance compared to the original signals($^*p > 0.05$). In addition, AO dataset reconstructed signals by MI-GAN a classification performance that was significantly worse than the original signals ($^*p < 0.05$). Therefore, we have concluded that the GAN/WGAN models with proposed TSF-MSE loss function showed significant performance improvement with enough data and no significant performance improvement without enough

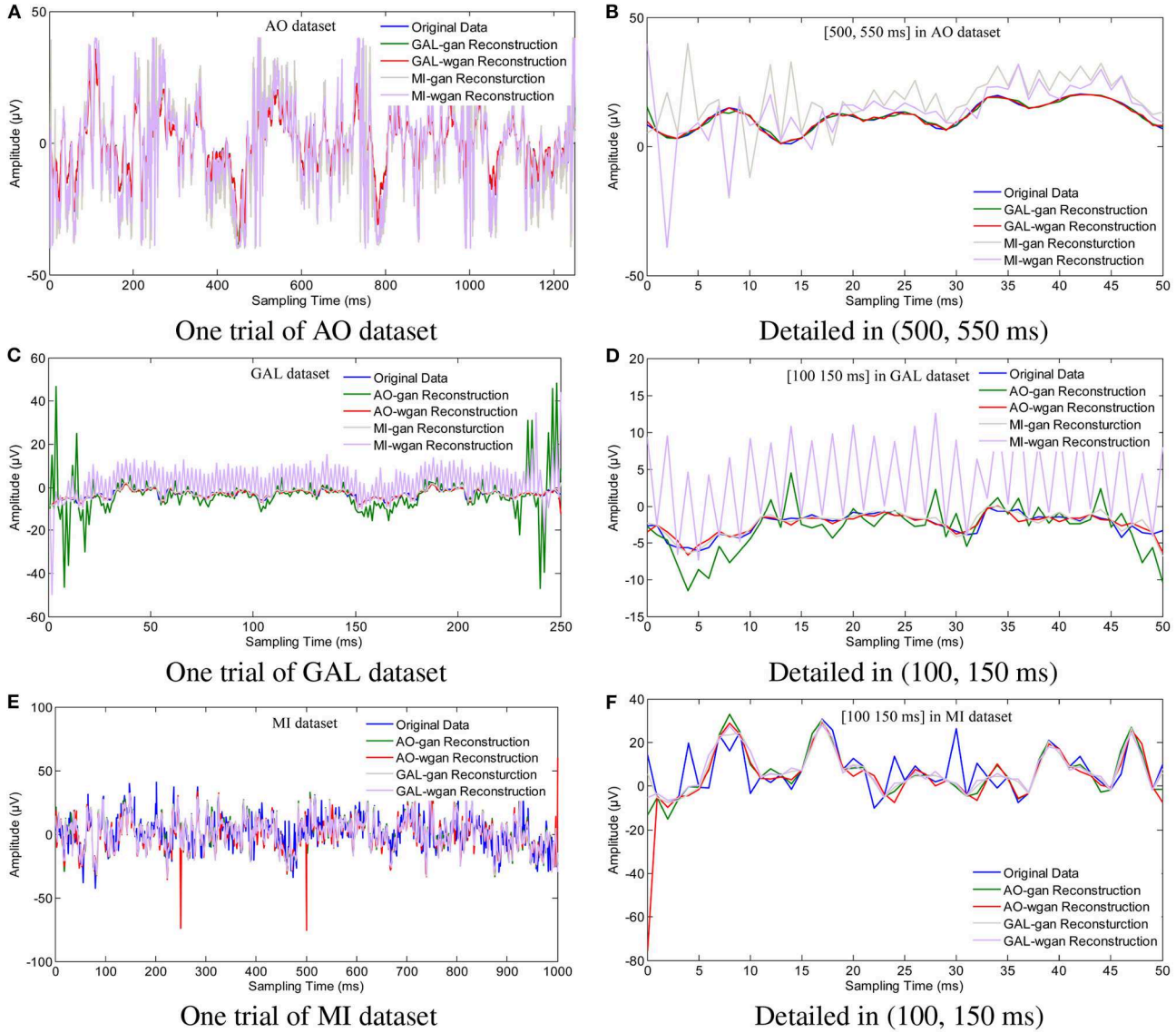


FIGURE 7 | Sampling rate reconstruction by different sensitivity GAN/WGAN frameworks. Sampling rate and sensitivity reconstruction by different sensitivity GAN/WGAN frameworks. The reconstruction results of one trial for AO dataset, GAL dataset, and MI dataset. Meanwhile, the detailed reconstruction results in (500, 550 ms) of AO datasets and (100, 150 ms) of GAL and MI datasets are also given. **(A)** One trial of AO dataset, **(B)** Detailed in (500, 550 ms), **(C)** One trial of GAL dataset, **(D)** Detailed in (100, 150 ms), **(E)** One trial of MI dataset, **(F)** Detailed in (100, 150 ms).

data for reconstructing EEG signals with the same sensitivity. Besides, if there is a large gap of sensitivity between two EEG signals datasets, the lower sensitivity based GAN model will cause significant worse performance of reconstructing high sensitivity signals to low sensitivity signals (such as MI-GAN applied to AO dataset).

Since this study has proposed a novel loss function to build the GAN/WGAN architectures for reconstructions, we have also compared the mean classification accuracy between temporal-MSE based GAN/WGAN architectures and TSF-MSE based GAN/WGAN architectures. Due to the single spatial-MSE and frequency-MSE cannot reconstruct signals, these two losses were not included in the comparison. **Table 10** illustrates the comparison results for all reconstructions and datasets. We have also used a paired t-test statistical technique to detect whether the TSF-MSE based GAN/WGAN architectures significantly outperform than the temporal-MSE based GAN/WGAN architectures. In **Table 10**, $AO- > AO$ means AO dataset reconstructed by the same sensitivity AO dataset, $GAL- > AO/MI- > AO$ represents AO dataset reconstructed by the different sensitivity GAL/MI datasets, and so forth. Experimental results have shown that no matter GAN architecture or WGAN architecture, TSF-MSE loss function outperformed the conventional temporal-MSE loss function (*p

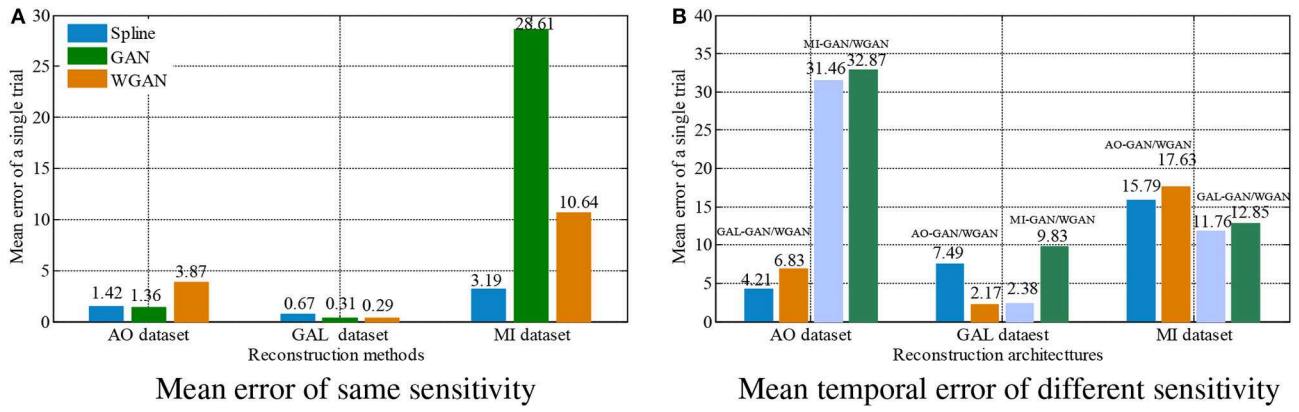


FIGURE 8 | Statistical mean temporal error comparison between the same and different sensitivity GAN/WGAN frameworks.The high-sensitivity EEG signals' GAN/WGAN frameworks reconstruct the low sensitivity EEG signals well, such as the AO and GAL data reconstructed by the MI GAN/WGAN frameworks. However, the low sensitivity EEG signals' GAN/WGAN models cannot reconstruct accurate high-sensitivity EEG signals, such as MI data reconstructed by the AO and GAL GAN/WGAN frameworks. **(A)** Mean error of same sensitivity, **(B)** Mean temporal error of different sensitivity.

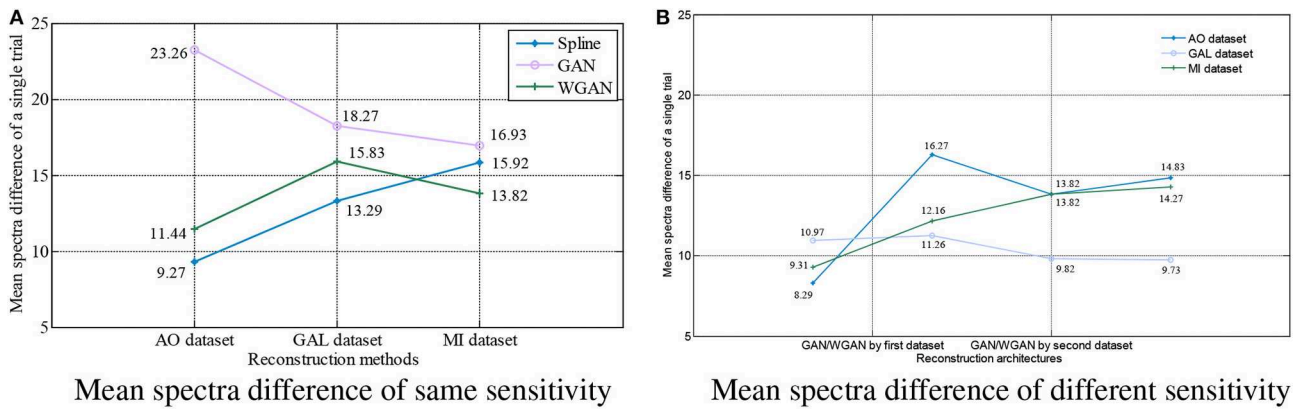


FIGURE 9 | Statistical mean spectra difference comparison between the same and different sensitivity GAN/WGAN frameworks. For the reconstructions of the same sensitivity, the mean spectra results have shown that WGAN architectures outperform than GAN architectures. As for the reconstructions of different sensitivity, we found that higher sensitivity models brought lower spectra difference, while lower sensitivity models brought higher spectra difference. **(A)** Mean spectra difference of same sensitivity, **(B)** Mean spectra difference of different sensitivity.

< 0.05). Therefore, the novel loss function proposed by us will significantly improve the performance of the reconstructed EEG signals.

Classification of reconstructed signals between the "FBCSP+SVM" classifier and "FBCSPNet" classifier Schirrmeister et al. (2017) are illustrated in **Table 11**. The results have shown average classification results of "FBCSP+SVM" and "FBCSPNet" for both GAN and WGAN models on three datasets. The improved ratios have shown that the GAN model and WGAN model bring 3.75 and 5.25% improvement on the average, respectively, to all three datasets for the "FBCSP+SVM" classifier. In addition, the GAN model and WGAN model bring 1.68 and 2.21% improvement on average, respectively, for all three datasets for "FBCSPNet" classifier. Therefore, we have concluded that EEG signals reconstructions by GAN/WGAN model are advantageous to the classification performance for different classifiers. If the classifier exhibits the a better performance, it has the ability to obtain more discriminant ERD patterns, so the improvement of the deep learning classifier is less than the conventional classifier.

In order to intuitively represent the differences between EEG signals reconstruction by the same sensitivities or different sensitivities of EEG signals, **Figure 11** illustrates the average results of these comparisons. In **Figure 11**, the **Figure 11A** shows the average results of **Tables 4–6** and **Figure 11B** shows the average results of **Tables 7–9**. From the average figures, the disciplines of EEG signals reconstruction by the GAN/WGAN models analyzed above can be found.

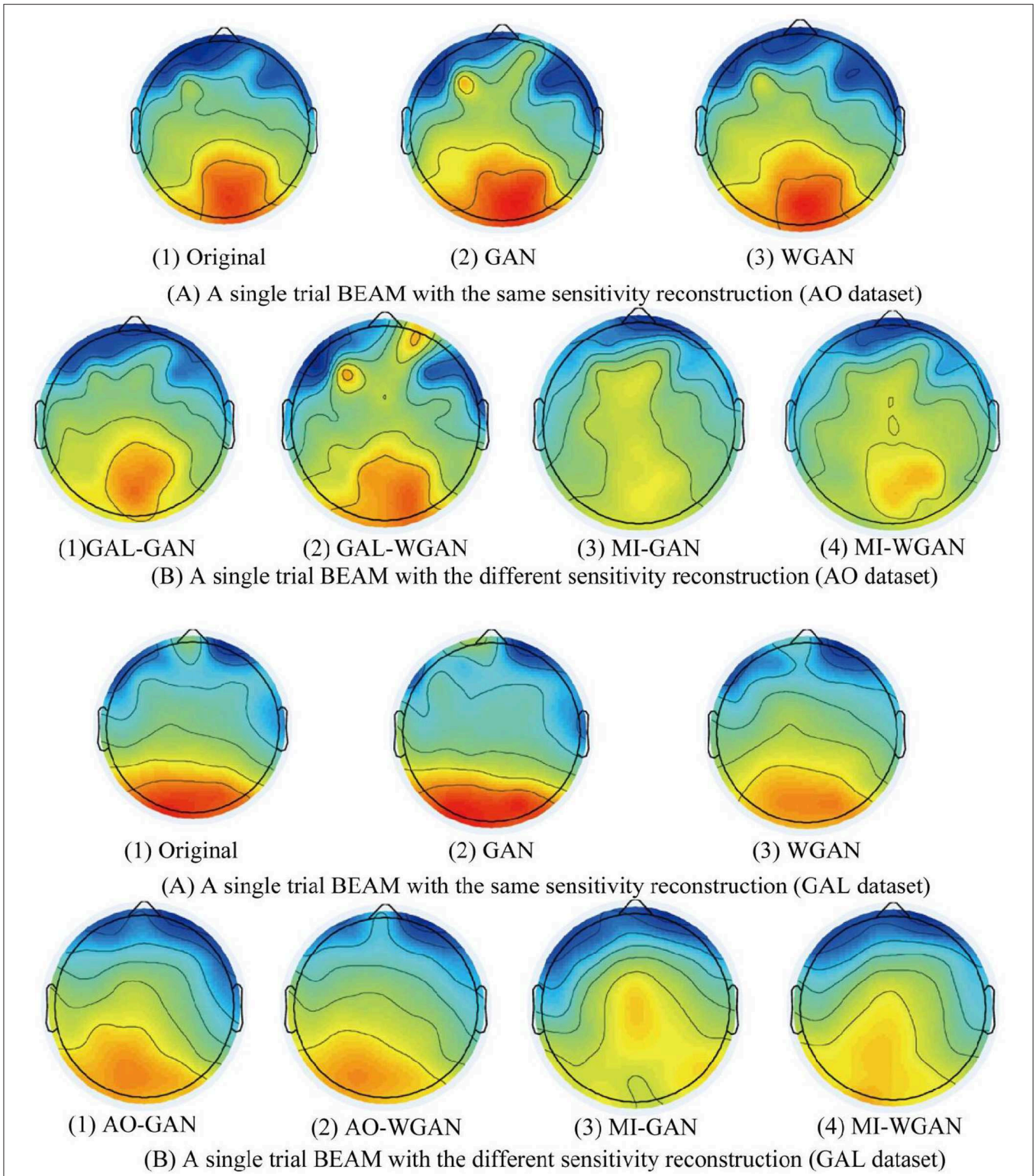


FIGURE 10 | A single reconstruction trial BEAM on 12 Hz comparison between the same and different sensitivity GAN/WGAN frameworks. For the reconstructions of the same sensitivity, the BEAM results have shown that WGAN architectures outperform GAN architectures. As for the reconstructions of different sensitivity, we have found that high-sensitivity models bring more distinct ERS/ERD phenomenon on brain electrical activity mappings (BEAMs), while low-sensitivity models bring less distinct ERS/ERD phenomenon on BEAMs. **(A)** BEAMs of AO datasets with same and different sensitivity reconstruction. **(B)** BEAMs of GAL datasets with same and different sensitivity reconstruction.

TABLE 3 | The optimal division of bandpass filters.

Sub-bands	fb_1	fb_2	fb_3	fb_4	fb_5
Frequency (Hz)	[8, 12]	[10, 14]	[12, 16]	[14, 18]	[16, 20]
Sub-bands	fb_6	fb_7	fb_8	fb_9	fb_{10}
Frequency (Hz)	[18, 22]	[20, 24]	[22, 26]	[24, 28]	[26, 30]

TABLE 4 | Classification results of GAN/WGAN frameworks for the sampling rate reconstruction of the same sensitivity signals in AO dataset.

Subjects	Original data (a)	Spline data (b)	GAN up-sampling (c)	WGAN up-sampling (d)
AO-1	62.83	58.72	64.51	**69.52**
AO-2	53.12	51.67	52.83	**55.61**
AO-3	70.31	68.92	**73.96**	72.66
AO-4	75.26	71.78	73.96	**80.99**
AO-5	59.12	58.27	61.28	**64.22**
AO-6	74.22	70.30	73.96	**76.82**
AO-7	55.43	54.28	**60.72**	59.83
AO-8	58.27	55.42	**59.82**	59.73
AO-9	77.08	76.07	83.85	**84.37**
AO-10	68.49	68.78	**75.26**	70.57
AO-11	79.17	74.64	87.76	**89.85**
AO-12	73.44	66.15	66.67	**75.53**
AO-13	55.83	59.42	61.42	**63.49**
AO-14	61.82	55.23	63.83	**65.72**
AO-15	55.49	53.82	56.29	**58.73**
AO-16	62.42	57.59	63.86	**65.82**
AO-17	64.58	57.81	58.59	**67.44**
AO-18	53.28	53.28	55.87	**57.89**
AO-19	52.82	51.87	55.89	**57.63**
AO-20	63.83	62.57	**68.59**	67.83
AO-21	70.31	61.98	61.98	**72.91**
AO-22	57.55	55.73	57.29	**59.37**
AO-23	61.83	58.89	**63.82**	63.58
AO-24	59.27	58.73	62.82	**63.93**
AVG	63.57	60.91	65.41	67.67
T-test	–	a vs. b	c vs. a	d vs. a
p-value	–	$^{**}p < 0.01$	$^{*}p < 0.05$	$^{**}p < 0.01$

The bold text is the best performance.

TABLE 5 | Classification results of GAN/WGAN frameworks for the sampling rate reconstruction of the same sensitivity signals in GAL dataset.

Subjects	Original data (a)	Spline data (b)	GAN up-sampling (c)	WGAN up-sampling (d)
GAL-1	69.23	68.71	72.81	**75.63**
GAL-2	65.06	65.42	**68.93**	68.72
GAL-3	74.04	71.69	79.83	**80.54**
GAL-4	59.17	58.66	**62.82**	61.93
GAL-5	79.94	74.48	**83.61**	82.83
GAL-6	69.04	69.76	74.63	**75.59**
GAL-7	74.33	68.79	**68.67**	68.27
GAL-8	79.81	77.62	79.82	**80.42**
GAL-9	64.04	63.48	72.24	**72.68**
GAL-10	65.38	65.48	74.81	**75.61**
GAL-11	63.21	62.52	**72.60**	72.07
GAL-12	74.10	72.42	**72.85**	72.36
AVG	69.78	68.25	73.63	73.89
T-test	–	a vs. b	c vs. a	d vs. a
p-value	–	$^{*}p < 0.05$	$^{*}p < 0.05$	$^{*}p < 0.05$

The bold text is the best performance.

TABLE 6 | Classification results of GAN/WGAN frameworks for the sampling rate reconstruction of the same sensitivity signals in the MI dataset.

Subjects	Original data (a)	Spline data (b)	GAN up-sampling (c)	WGAN up-sampling (d)
MI-1	60.59	57.82	61.62	**62.81**
MI-2	70.31	68.58	71.18	**73.35**
MI-3	53.47	53.82	54.93	**56.81**
MI-4	59.38	56.71	**61.83**	60.62
MI-5	72.22	70.49	73.88	**76.57**
MI-6	67.36	65.73	68.72	**68.81**
MI-7	56.25	55.41	**58.83**	57.61
MI-8	57.81	56.43	**58.81**	57.69
MI-9	60.42	58.67	**62.73**	61.85
AVG	61.98	60.41	63.61	64.01
T-test	–	a vs. b	c vs. a	d vs. a
p-value	–	$^{**}p < 0.01$	$^{**}p < 0.01$	$^{**}p < 0.01$

The bold text is the best performance.

4. DISCUSSION

4.1. Reconstruction by Using GAN/WGAN Frameworks and TFS-MSE Loss

The purpose of this paper is to reconstruct HSS-EEG signals from LSS-EEG signals by using GAN/WGAN frameworks with a carefully designed loss function. In this paper, among the experiments of three different EEG datasets, we have compared the performance of GAN/WGAN frameworks for up-sampling with the same sensitivity and reconstruction with different sensitivities. The classification performances show significant improvement in terms of reconstructions of the same sensitivity. For AO dataset, the classification performances also show significant improvement by reconstructions of GAL-WGAN and GAL-GAN. However, other datasets reconstruction signals with different sensitivity have no significant improvement than original signals. There are two possible reasons for the statistical results. One possible reason is that the AO dataset has enough subsets (a total of 24) to compute the *t*-test index. However, datasets GAL and MI with 12 subsets and nine subsets, respectively, are not sufficient to compute the *t*-test index. Another possible reason may be due to the signal amplitude range for the GAN/WGAN reconstruction. In our experiments, the reconstructed signals amplitude range was set as the same as the original signals, and the amplitude range may have prevented the variations of reconstructed signals brought by

TABLE 7 | Classification results for the sensitivity rate reconstruction of AO dataset by the different sensitivity signals' GAN/WGAN frameworks.

Subjects	Original data (a)	GAL-WGAN (b)	GAL-GAN (c)	MI-WGAN (d)	MI-GAN (e)
AO dataset reconstructed by the gal and mi models					
AO-1	62.83	**64.81**	64.57	60.73	61.82
AO-2	53.12	55.82	**56.18**	53.27	52.63
AO-3	70.31	72.13	**73.18**	69.53	70.83
AO-4	75.26	73.44	**75.78**	67.71	69.53
AO-5	59.12	61.73	**62.16**	58.83	56.76
AO-6	74.22	76.56	**77.87**	76.82	75.26
AO-7	55.43	**57.61**	56.89	55.43	54.68
AO-8	58.27	**59.46**	58.83	56.27	56.29
AO-9	77.08	76.56	**77.34**	72.14	73.44
AO-10	68.49	72.66	70.57	**75.26**	71.09
AO-11	79.17	83.07	**83.85**	78.91	81.51
AO-12	**73.44**	71.62	72.57	70.57	66.93
AO-13	55.83	56.73	**56.94**	54.87	55.16
AO-14	61.82	62.73	**63.81**	60.57	60.81
AO-15	55.49	**56.81**	56.43	55.36	55.61
AO-16	62.42	63.55	**64.31**	61.28	61.37
AO-17	**64.58**	61.72	60.03	55.47	56.25
AO-18	53.28	53.89	**53.61**	52.13	52.28
AO-19	52.82	53.61	**54.18**	52.36	53.17
AO-20	63.83	**64.81**	63.76	62.67	62.89
AO-21	**68.72**	63.59	62.18	57.62	58.73
AO-22	57.55	59.11	59.55	60.42	**61.46**
AO-23	61.83	62.81	**63.75**	62.19	61.68
AO-24	59.27	60.73	**60.81**	59.36	59.81
AVG	63.51	64.40	64.55	62.07	62.08
T-test	–	b vs. a	c vs. a	d vs. a	e vs. a
p-value	–	$^*p < 0.05$	$^*p < 0.05$	$p = 0.0738$	$^*p < 0.05$

The bold text is the best performance.

TABLE 8 | Classification results for the sensitivity rate reconstruction of GAL dataset by the different sensitivity signals' GAN/WGAN frameworks.

Subjects	Original data (a)	AO-WGAN (b)	AO-GAN (c)	MI-WGAN (d)	MI-GAN (e)
GAL dataset reconstructed by the ao and mi models					
GAL-1	69.23	**73.53**	72.76	72.56	70.19
GAL-2	**65.06**	63.21	62.88	61.86	61.03
GAL-3	**74.04**	59.74	66.03	61.99	58.59
GAL-4	59.17	59.74	**66.03**	61.99	58.59
GAL-5	79.94	76.28	**80.96**	76.15	77.18
GAL-6	69.04	**73.33**	72.56	73.21	76.35
GAL-7	**74.33**	69.77	66.25	64.82	66.91
GAL-8	79.81	78.53	74.17	**81.92**	79.49
GAL-9	64.04	65.58	65.58	64.30	**67.63**
GAL-10	65.38	62.76	62.24	60.64	**67.50**
GAL-11	63.21	85.13	85.00	**85.51**	85.38
GAL-12	74.10	**76.47**	72.76	69.94	73.72
AVG	69.78	70.34	**70.60**	69.57	70.21
T-test	–	b vs. a	c vs. a	d vs. a	e vs. a
p-value	–	$p = 0.821$	$p = 0.731$	$p = 0.937$	$p = 0.870$

The bold text is the best performance.

TABLE 9 | Classification results for the sensitivity rate reconstruction of MI dataset by the different sensitivity signals' GAN/WGAN frameworks.

Subjects	Original data (a)	AO-WGAN (b)	AO-GAN (c)	GAL-WGAN (d)	GAL-GAN (e)
MI dataset reconstructed by the gal and ao GAN/wgan models					
MI-1	60.59	61.63	59.90	58.33	**67.53**
MI-2	70.31	71.70	69.10	**75.00**	73.26
MI-3	53.47	**58.16**	54.17	53.99	55.03
MI-4	59.38	**68.58**	68.58	64.41	66.67
MI-5	72.22	68.92	**76.22**	73.09	66.67
MI-6	67.36	**70.49**	70.49	69.62	68.75
MI-7	56.25	58.68	**73.44**	58.85	60.07
MI-8	57.81	54.34	54.51	**63.54**	56.60
MI-9	**60.42**	57.12	57.99	56.08	55.90
AVG	61.98	63.29	**64.93**	63.66	63.39
T-test	–	b vs. a	c vs. a	d vs. a	e vs. a
p-value	–	$p = 0.380$	$p = 0.215$	$p = 0.175$	$p = 0.215$

The bold text is the best performance.

the signals with different sensitivity. Therefore, in future works, more experiments for different ranges are also needed for a same dataset to confirm the relationship between signal amplitude range and patterns classification performance. For the average classification accuracy for all experiments, the up-sampled EEG signals performed better than the original data, and we think this might be due to the fact that the reconstruction procedure obtains more discriminant signals. In addition, the original temporal-MSE and the proposed TSF-MSE as loss functions were also compared.

The up-sampling reconstruction with the same sensitivity results have demonstrated that using the WGAN helps to improve signal qualities and statistical properties. Comparing the reconstruction HSS-EEG signals and the original real HSS-EEG signals in **Figures 6**, **8A**, **9A**, **10A**, we can see that the WGAN framework helps to solve the problem of the over-smoothing effect suffered by the conventional temporal-MSE signal generators (Aydin et al., 2015). Although the reconstructed HSS-EEG signals shared a similar result, as in **Figures 6**, **8A**, **9A**, and **10A,B**, the quantitative analysis of classifying signals by a machine learning model, as given in **Tables 4–6**, **Figure 11A**, have shown that the WGAN framework yields a higher classification accuracy and obtains more reliable statistical properties due to more discriminant patterns. However, if we use GAN/WGAN frameworks alone, the critical ERD/ERS of brain activity characteristics in the EEG signals will be reduced along with the single temporal loss. Theoretically, the GAN/WGAN frameworks are based on generative models, and such models generate naturally appearing HSS-EEG signals but

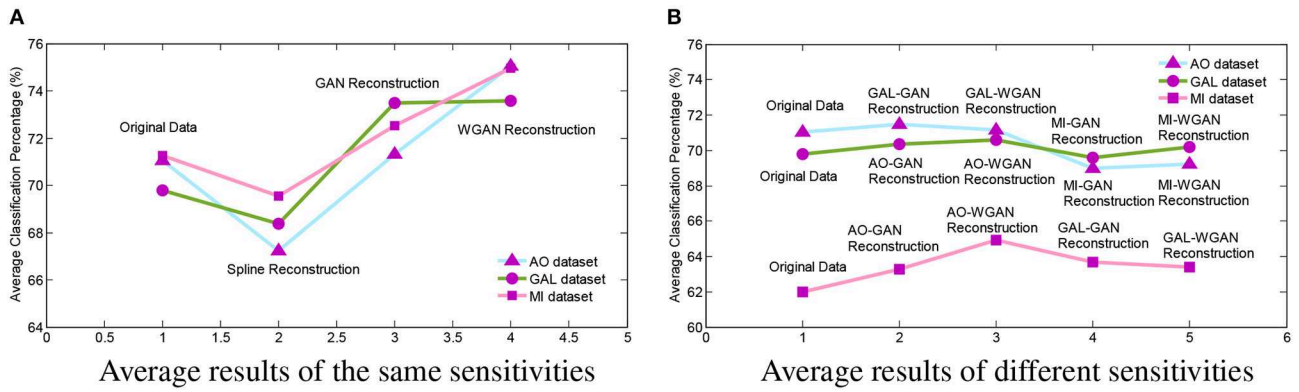


FIGURE 11 | Reconstruction results comparison between the same and different sensitivity GAN/WGAN frameworks. In order to intuitively represent the differences between EEG signals reconstruction by the same sensitivities or different sensitivities of EEG signals, the average results of such compared experiments are illustrated to show the disciplines of EEG signals reconstruction by the GAN/WGAN models analyzed above. **(A)** Average results of the same sensitivities, **(B)** Average results of different sensitivities.

TABLE 10 | The comparison results between Temporal-MSE and TSF-MSE of constructing GAN/WGAN architectures for reconstruction.

Reconstruction	Temporal-GAN (a)	TSF-GAN (b)	Temporal-WGAN (c)	TSF-WGAN (d)
AO− > AO	64.86	65.41	64.32	**67.67**
GAL− > GAL	71.43	**74.64**	72.68	73.89
MI− > MI	62.43	63.61	63.83	**64.01**
GAL− > AO	64.16	**64.55**	63.85	64.40
MI− > AO	**62.31**	62.07	61.84	62.08
AO− > GAL	68.84	**70.60**	68.73	70.34
MI− > GAL	68.93	**70.21**	69.29	69.57
AO− > MI	62.35	**64.93**	62.86	63.29
GAL− > MI	62.19	63.39	62.28	**63.66**
T-test	–	b vs. a	–	d vs. c
p-value	–	$^{**}p < 0.01$	–	$^{*}p < 0.05$

The bold text is the best performance.

TABLE 11 | The comparison average results of three datasets between FBCSP+SVM classifier and FBCSPNet classifier.

Datasets	FBCSP+SVM			FBCSPNet		
	Original data	TSF-GAN	TSF-WGAN	Original data	TSF-GAN	TSF-WGAN
AO dataset	63.57	65.41	67.67	67.29	68.41	68.84
GAL dataset	69.78	73.63	73.89	73.61	74.82	75.23
MI dataset	61.98	63.61	64.01	65.47	66.64	66.86
Average	65.11	67.55	68.52	68.79	69.95	70.31
Improved Ratio	–	3.75%	5.25%	–	1.68%	2.21%

cause severe distortion of the ERD/ERS characteristics in the EEG signals (Choi et al., 2017). Therefore, an additive loss function should be included to guarantee that the ERD/ERS characteristics remain the same for the reconstruction.

Beyond the above analysis, the TSF-MSE loss function was introduced to guarantee the ERD/ERS characteristics during the training of the GAN/WGAN frameworks, and the classification performance of ERD/ERS characteristics can be found in the compared results in **Table 10**. As is well known, the temporal-MSE loss was the basis of the time-series data, and such loss will guarantee the reconstructed shape of the temporal domain. However, EEG signals are multi-channel time-series data, and the spatial domain is thus also important in the reconstruction. In addition, most ERD/ERS characteristics are reflected in the frequency domain, making the frequency domain also important in the reconstruction. Therefore, the TSF-MSE constructed by the original signals from the temporal domain, the FB-CSP features from the spatial domain, and the PSD features from the frequency domain have been introduced in this paper to guarantee the EEG signals temporal characteristics, spatial characteristics, and ERD/ERS characteristics (Strohmeier et al., 2016). Additionally, the TSF-MSE-based GAN/WGAN models cause lower losses than the temporal MSE, frequency MSE, and spatial MSE-based GAN/WGAN models (see **Figure 4**). Our proposed TSF-MSE-based WGAN framework outperformed the other models in reconstructing up-sampled EEG signals with the same sensitivity. These results demonstrate that we can use this method to increase the sampling rate of EEG signals to achieve higher performance in brain-computer interfaces (BCIs) or EEG-based rehabilitation treatments.

4.2. EEG Signal Reconstruction With Different Sensitivities

In this paper, in addition to reconstructing HSS-EEG signals from the same sensitivity, we also reconstructed HSS-EEG signals from different sensitivities. In fact, if EEG signals with low sensitivity can be reconstructed into high-sensitivity signals, the reconstructed HSS-EEG signals will contain more details of the ERD/ERS characteristics, which will improve the classification performance for many applications. Among the

experimental results shown in **Tables 4–9**, we can conclude that the average classification accuracies of WGAN framework are higher than GAN framework for reconstruction with the same sensitivity on all datasets, while the GAN framework obtained better average classification accuracies for reconstruction with different sensitivities on all datasets. In addition, a larger gap in the sensitivity will significantly increase the average classification accuracies of all datasets, while a smaller gap in the sensitivity will result in a smaller difference in the average classification accuracies of all datasets (see the comparison results in **Tables 7–9**, **Figure 11B**). We can also find indicators for different sensitivity gaps in **Figure 7**. For example, considering the AO data reconstructed by the MI-GAN and MI-WGAN models (see **Figure 7B**), a high-sensitivity signal reconstructed by the low-sensitivity GAN/WGAN models caused the signals to be overfitted and exceed the original data range. Hence, the reconstructed results contained fewer ERD/ERS characteristics to classify the EEG signals, and the classification accuracy was lower than the results using the original data. Conversely, for the MI data reconstructed by the AO-GAN and AO-WGAN models (see **Figure 7F**), we can see that the low-sensitivity MI data reconstructed by the high sensitivity models presented more variations in the temporal domain. Because the variations in the time-series represented detailed characteristics of ERD/ERS, the reconstructed high sensitivity EEG signals performed better in the classification of ERD/ERS characteristics. Therefore, in practical applications, we can train a high-sensitivity GAN model for EEG signal reconstruction. By applying the GAN/WGAN models, the ERD/ERS characteristics extracted from low sensitivity devices can be enhanced for use in real-time and real-application BCI or rehabilitation treatment.

In contrast to the results of reconstructing HSS-EEG signals with the same sensitivity, the GAN framework performed better than the WGAN framework for reconstructing HSS-EEG signals with different sensitivities. An approaching value range caused a smaller difference between the GAN framework and the WGAN framework (the AO dataset and the GAL dataset), but a separated value range caused a large difference between the GAN framework and the WGAN framework. Therefore, the difference in the classification performance was caused by the different value ranges of different sensitivities. We suggest two reasons for this difference: first, the WGAN framework contained a gradient penalty, and such a penalty would be out of the value ranges for different value ranges. The penalty then influenced the convergence of the WGAN framework (Mescheder et al., 2018), and, thus, the results of the WGAN framework were lower than the results of the GAN framework. Second, the WGAN framework used an RMSprop optimizer to train deep neural networks, but the GAN framework used an Adam optimizer (Basu et al., 2018). In fact, the Adam optimizer has a momentum gradient procedure, which will be fitted for regressing different value ranges. Hence, the different value ranges can be reconstructed by the Adam optimizer (Zou et al., 2018). In all of these, if we have recorded the highest sensitivity EEG signals, we must also record low-sensitivity EEG signals. We can use the highest sensitivity EEG signals to train a GAN/WGAN model to reconstruct the low sensitivity EEG signals, and the reconstructed EEG signals can be used to improve classification performance for the construction of real-time and real-application BCIs or rehabilitation treatment.

4.3. The Application of Reconstructed EEG Signals by GAN/WGAN Frameworks

Over the past decade, most EEG-based studies have been focused on constructing BCIs or developing rehabilitation treatments (Ang et al., 2015). However, there are two main limitations to the application of EEG signals when constructing such systems, namely, the cost and portability of EEG recording devices. In fact, HSS-EEG signals will yield the best performance in BCIs and rehabilitation treatments, although HSS-EEG signals are usually recorded by expensive devices, posing an inconvenience. For example, in the "NeuroScan SymAmp2" device (Chu et al., 2016), the recording system consists of two computers and one device to link them together. One computer is used to present a stimulus for the BCI or rehabilitation treatment, and the other computer is used to record and store the EEG signals for computing the BCI or rehabilitation results. Subjects must sit in a room to wear a "NeuroScan Quik Cap" to collect data. The collection procedure is complex, and the resistance must be maintained under 5 kΩ by using conductive paste on each electrode (Agnew et al., 2012). Because the resistance is kept low and the device has a high sensitivity, the recorded EEG signals will have the ERD/ERS characteristics required for classification in BCI and rehabilitation treatment.

In general, the "NeuroScan SymAmp2" device is expensive, and the EEG signals must be recorded indoors in a limited environment (e.g., a dimly lit, sound-attenuated room). Hence, it is difficult to implement the results of the "NeuroScan SymAmp2" device (the same sensitivity as signals in AO dataset) in applications such as BCI and rehabilitation treatment. Nevertheless, low-cost and portable devices, such as "Emotiv" (the same sensitivity as signals in MI dataset), have high electrode resistance and a low sampling rate and sensitivity for recording EEG signals. The device only provides poor ERD/ERS characteristics for classification in BCI and rehabilitation treatment applications. The "Emotiv" device can be worn at any time via a simple process without requiring the resistance to be kept level (Neale et al., 2017). The energy supply for the device is a battery, and the device uses WiFi or Bluetooth communication. These advantages allow the device to be inexpensive, portable, and convenient for constructing BCIs and developing rehabilitation treatment. These mutual contradictions for signal precision and signal cost and portability inspire us to train a model to reconstruct HSS-EEG signals from LSS-EEG signals. The trained model meets the requirements of high precision and portability with low cost and can be used to improve EEG-based applications.

In fact, signal reconstruction is a difficult problem in digital signal processing, but an effective and feasible reconstruction method could significantly promote the application of signals. In this study, by using a GAN framework with Wasserstein distance and the carefully designed TSF-MSE loss function, well-trained reconstruction models have been shown to be able to reconstruct HSS-EEG signals from LSS-EEG signals. Experimental results reveal that LSS-EEG signals (just like those recorded by "Emotiv") reconstructed by the HSS-EEG

signals (just like those recorded by "NeuroScan SymAmp2") trained models and enhanced the average classification accuracies of ERD/ERS characteristics for action observation, action execution, and motor imagery. These results inspire new ways to construct BCIs or develop novel rehabilitation treatments, but more researches need to be done to explore significant enhancement reconstruction methods across EEG signals with different sensitivities.

Based on the method of this paper, the improvement of sampling rate and sensitivity will improve the specific ERD/ERS phenomenon of MI, AO, and AE, so as to improve the performance of the BCI system. Although the CNN- based GAN/WGAN architectures will take a significant amount of time to build an available GAN/WGAN architecture, once the reconstruction model is built, the use of such a model will not take long, and the reconstructed EEG time series can be obtained within a specific time (<1 s for a trial). In future works, we can either reduce the complex of GAN architecture or improve the computational efficiency to reduce the usage time for reconstructing GAN/WGAN architecture. Then, the GAN/WGAN architectures will be used for real-time inference. In general, we used a low-cost, portable device to collect LSS-EEG signals for use in BCI or rehabilitation treatment. Before analyzing the collected data, the GAN/WGAN reconstruction models were applied to reconstruct HSS-EEG signals. The reconstructed HSS-EEG signals can significantly improve the classification performance and information transfer rate for use in BCIs or rehabilitation treatments.

5. CONCLUSION

In this paper, we have proposed a contemporary deep neural network that uses a GAN/WGAN framework with a TSF-MSE-based loss function for LSS-EEG signal reconstruction. Instead of designing a complex GAN framework, this work has been dedicated to designing a precise loss function that guides the reconstruction process so that the reconstructed HSS-EEG signals are as close to the ground truth as possible. Our experimental results suggest that the GAN/WGAN frameworks give a significant improvement on the classification performance of EEG signals reconstruction with the same sensitivity, but the classification performance improvements of EEG signal reconstructions with different sensitivity were not significant, which further exploration. The carefully designed TSF-MSE-based loss function solves the well-known over-smoothing problem and seems to result in more discriminant patterns than the original EEG signals; this will improve the classification performance of EEG signals. The reconstructed HSS-EEG signals will be beneficial for use in BCI and rehabilitation treatment applications. Future studies will focus on the reconstruction signal amplitude ranges of EEG signals with different sensitivity and selection of datasets to confirm the required number of signals and to explore the significant performance improvement of EEG signal reconstruction with different sensitivity. In addition, the efficiency of EEG signal reconstruction by the GAN/WGAN frameworks will be studied further in the future.

DATA AVAILABILITY STATEMENT

The datasets generated for this study can be found in:

1. https://pan.baidu.com/s/1NC4-ywOssfX2nUMaEeGlRw please use the extract code "g8ip" in the dialog box to access the Datasets.
2. https://www.kaggle.com/c/grasp-and-lift-eeg-detection
3. BCI Competition IV "Dataset 2b": http://www.bbci.de/competition/iv/#datasets.

AUTHOR CONTRIBUTIONS

TL and YF designed the experiments. YF and LC completed the experiments. TL and GG analyzed the EEG data. CZ, LC, GG, and TL wrote the paper.

FUNDING

This work was supported by the National Natural Science Foundation of China under Grant (Nos. U1805263, 61672157, 61976053, and 61673322). The funding body played a role in supporting the experiments.

ACKNOWLEDGMENTS

The authors want to thank the members of the digital Fujian internet-of-thing laboratory of environmental monitoring at the Fujian Normal University and the brain-like robotic research group of Xiamen University for their proofreading comments. The authors are very grateful to the reviewers for their constructive comments, which have helped significantly in revising this work.

REFERENCES

Agnew, Z. K., Wise, R. J., and Leech, R. (2012). Dissociating object directed and non-object directed action in the human mirror system; implications for theories of motor simulation. *PLoS ONE* 7:e32517. doi: 10.1371/journal.pone.0032517

Ahn, M., and Jun, S. C. (2015). Performance variation in motor imagery brain-computer interface: a brief review. *J. Neurosci. Methods* 243, 103–110. doi: 10.1016/j.jneumeth.2015.01.033

Ang, K. K., Chin, Z. Y., Wang, C., Guan, C., and Zhang, H. (2012). Filter bank common spatial pattern algorithm on BCI competition IV datasets 2a and 2b. *Front. Neurosci.* 6:39. doi: 10.3389/fnins.2012.00039

Ang, K. K., Chua, K. S. G., Phua, K. S., Wang, C., Chin, Z. Y., Kuah, C. W. K., et al. (2015). A randomized controlled trial of EEG-based motor imagery brain-computer interface robotic rehabilitation for stroke. *Clin. EEG Neurosci.* 46, 310–320. doi: 10.1177/1550059414522229

Arnulfo, G., Narizzano, M., Cardinale, F., Fato, M. M., and Palva, J. M. (2015). Automatic segmentation of deep intracerebral electrodes in computed tomography scans. *BMC Bioinformatics* 16:99. doi: 10.1186/s12859-015-0511-6

Aydin, Ü., Vorwerk, J., Dümpelmann, M., Küpper, P., Kugel, H., Heers, M., et al. (2015). Combined EEG/MEG can outperform single modality EEG or MEG source reconstruction in presurgical epilepsy diagnosis. *PLoS ONE* 10:e0118753. doi: 10.1371/journal.pone.0118753

Basu, A., De, S., Mukherjee, A., and Ullah, E. (2018). Convergence guarantees for RMSProp and ADAM in non-convex optimization and their comparison to Nesterov acceleration on autoencoders. *arXiv [preprint]*. arXiv:1807.06766.

Cecotti, H., and Graser, A. (2011). Convolutional neural networks for P300 detection with application to brain-computer interfaces. *IEEE Trans. Pattern Anal. Mach. Intell.* 33, 433–445. doi: 10.1109/TPAMI.2010.125

Choi, M.-H., Kim, B., Kim, H.-S., Gim, S.-Y., Kim, W.-R., and Chung, S.-C. (2017). Perceptual threshold level for the tactile stimulation and response features of ERD/ERS-based specific indices upon changes in high-frequency vibrations. *Front. Hum. Neurosci.* 11:207. doi: 10.3389/fnhum.2017.00207

Choudhary, K. S., Rohatgi, N., Halldorsson, S., Briem, E., Gudjonsson, T., Gudmundsson, S., et al. (2016). EGFR signal-network reconstruction demonstrates metabolic crosstalk in EMT. *PLoS Comput. Biol.* 12:e1004924. doi: 10.1371/journal.pcbi.1004924

Chu, C.-H., Yang, K.-T., Song, T.-F., Liu, J.-H., Hung, T.-M., and Chang, Y.-K. (2016). Cardiorespiratory fitness is associated with executive control in late-middle-aged adults: an event-related (de) synchronization (ERD/ERS) study. *Front. Psychol.* 7:1135. doi: 10.3389/fpsyg.2016.01135

Erkorkmaz, K. (2015). Efficient fitting of the feed correction polynomial for real-time spline interpolation. *J. Manufact. Sci. Eng.* 137:044501. doi: 10.1115/1.4030300

Freche, D., Naim-Feil, J., Peled, A., Levit-Binnun, N., and Moses, E. (2018). A quantitative physical model of the TMS-induced discharge artifacts in EEG. *PLoS Comput. Biol.* 14:e1006177. doi: 10.1371/journal.pcbi.1006177

Goodfellow, I., Pouget-Abadie, J., Mirza, M., Xu, B., Warde-Farley, D., Ozair, S., et al. (2014). "Generative adversarial nets," in *Advances in Neural Information Processing Systems* (Montreal, QC), 2672–2680.

Gulrajani, I., Ahmed, F., Arjovsky, M., Dumoulin, V., and Courville, A. C. (2017). "Improved training of wasserstein gans," in *Advances in Neural Information Processing Systems* (Long Beach, CA), 5767–5777.

Hartmann, K. G., Schirrmeister, R. T., and Ball, T. (2018). EEG-GAN: Generative adversarial networks for electroencephalograhic (EEG) brain signals. *arXiv [preprint]*. arXiv:1806.01875.

He, K., Zhang, X., Ren, S., and Sun, J. (2016). "Deep residual learning for image recognition," in *Proceedings of the IEEE Conference on Computer Vision and Pattern Recognition*, 770–778. doi: 10.1109/CVPR.2016.90

Ioffe, S., and Szegedy, C. (2015). Batch normalization: accelerating deep network training by reducing internal covariate shift. *arXiv [preprint]*. arXiv:1502.03167.

Jiang, Y., Deng, Z., Chung, F.-L., Wang, G., Qian, P., Choi, K.-S., et al. (2017). Recognition of epileptic EEG signals using a novel multiview TSK fuzzy system. *IEEE Trans. Fuzzy Syst.* 25, 3–20. doi: 10.1109/TFUZZ.2016.2637405

Jin, K. H., McCann, M. T., Froustey, E., and Unser, M. (2017). Deep convolutional neural network for inverse problems in imaging. *IEEE Trans. Image Process.* 26, 4509–4522. doi: 10.1109/TIP.2017.2713099

Kavasidis, I., Palazzo, S., Spampinato, C., Giordano, D., and Shah, M. (2017). "Brain2image: converting brain signals into images," in *Proceedings of the 2017 ACM on Multimedia Conference* (ACM), 1809–1817. doi: 10.1145/3123266.3127907

Kumar, S., Sharma, A., and Tsunoda, T. (2017). An improved discriminative filter bank selection approach for motor imagery EEG signal classification using mutual information. *BMC Bioinformatics* 18:545. doi: 10.1186/s12859-017-1964-6

LeCun, Y., Bengio, Y., and Hinton, G. (2015). Deep learning. *Nature* 521:436. doi: 10.1038/nature14539

Ledig, C., Theis, L., Huszár, F., Caballero, J., Cunningham, A., Acosta, A., et al. (2017). "Photo-realistic single image super-resolution using a generative adversarial network," in *CVPR, Vol. 2* (Honolulu, HI), 4. doi: 10.1109/CVPR.2017.19

Luciw, M. D., Jarocka, E., and Edin, B. B. (2014). Multi-channel EEG recordings during 3,936 grasp and lift trials with varying weight and friction. *Sci. Data* 1:140047. doi: 10.1038/sdata.2014.47

Luo, T.-J., Lv, J., Chao, F., and Zhou, C. (2018b). Effect of different movement speed modes on human action observation: an EEG study. *Front. Neurosci.* 12:219. doi: 10.3389/fnins.2018.00219

Luo, T.-J., Zhou, C., and Chao, F. (2018a). Exploring spatial-frequency-sequential relationships for motor imagery classification with recurrent neural network. *BMC Bioinformatics* 19:344. doi: 10.1186/s12859-018-2365-1

Marques, A. G., Segarra, S., Leus, G., and Ribeiro, A. (2016). Sampling of graph signals with successive local aggregations. *IEEE Trans. Signal Process.* 64, 1832–1843. doi: 10.1109/TSP.2015.2507546

Mescheder, L., Geiger, A., and Nowozin, S. (2018). "Which training methods for GANs do actually converge?" in *International Conference on Machine Learning* (Stockholm), 3478–3487.

Mete, M., Sakoglu, U., Spence, J. S., Devous, M. D., Harris, T. S., and Adinoff, B. (2016). Successful classification of cocaine dependence using brain imaging: a generalizable machine learning approach. *BMC Bioinformatics* 17:357. doi: 10.1186/s12859-016-1218-z

Mukkamala, M. C., and Hein, M. (2017). "Variants of RMSProp and Adagrad with logarithmic regret bounds," in *Proceedings of the 34th International Conference on Machine Learning, Vol. 70* (Sydney, NSW), 2545–2553.

Mullen, T. R., Kothe, C. A., Chi, Y. M., Ojeda, A., Kerth, T., Makeig, S., et al. (2015). Real-time neuroimaging and cognitive monitoring using wearable dry EEG. *IEEE Trans. Biomed. Eng.* 62, 2553–2567. doi: 10.1109/TBME.2015.2481482

Naldi, A., Larive, R. M., Czerwinska, U., Urbach, S., Montcourrier, P., Roy, C., et al. (2017). Reconstruction and signal propagation analysis of the Syk signaling network in breast cancer cells. *PLoS Comput. Biol.* 13:e1005432. doi: 10.1371/journal.pcbi.1005432

Narizzano, M., Arnulfo, G., Ricci, S., Toselli, B., Tisdall, M., Canessa, A., et al. (2017). SEEG assistant: a 3Dslicer extension to support epilepsy surgery. *BMC Bioinformatics* 18:124. doi: 10.1186/s12859-017-1545-8

Neale, C., Aspinall, P., Roe, J., Tilley, S., Mavros, P., Cinderby, S., et al. (2017). The aging urban brain: analyzing outdoor physical activity using the emotiv affectiv suite in older people. *J. Urban Health* 94, 869–880. doi: 10.1007/s11524-017-0191-9

Petroff, O. A., Spencer, D. D., Goncharova, I. I., and Zaveri, H. P. (2016). A comparison of the power spectral density of scalp EEG and subjacent electrocorticograms. *Clin. Neurophysiol.* 127, 1108–1112. doi: 10.1016/j.clinph.2015.08.004

Sargolzaei, S., Cabrerizo, M., Sargolzaei, A., Noei, S., Eddin, A. S., Rajaei, H., et al. (2015). A probabilistic approach for pediatric epilepsy diagnosis using brain functional connectivity networks. *BMC Bioinformatics* 16:S9. doi: 10.1186/1471-2105-16-S7-S9

Schirrmeister, R. T., Springenberg, J. T., Fiederer, L. D. J., Glasstetter, M., Eggensperger, K., Tangermann, M., et al. (2017). Deep learning with convolutional neural networks for EEG decoding and visualization. *Hum. Brain Mapp.* 38, 5391–5420. doi: 10.1002/hbm.23730

Strohmeier, D., Bekhti, Y., Haueisen, J., and Gramfort, A. (2016). The iterative reweighted mixed-norm estimate for spatio-temporal MEG/EEG source reconstruction. *IEEE Trans. Med. Imaging* 35, 2218–2228. doi: 10.1109/TMI.2016.2553445

Tangermann, M., Müller, K.-R., Aertsen, A., Birbaumer, N., Braun, C., Brunner, C., et al. (2012). Review of the BCI competition IV. *Front. Neurosci.* 6:55. doi: 10.3389/fnins.2012.00055

Wu, W., Chen, Z., Gao, X., Li, Y., Brown, E. N., and Gao, S. (2015). Probabilistic common spatial patterns for multichannel EEG analysis. *IEEE Trans. Pattern Anal. Mach. Intell.* 37, 639–653. doi: 10.1109/TPAMI.2014.2330598

Yang, Q., Yan, P., Zhang, Y., Yu, H., Shi, Y., Mou, X., et al. (2018). Low dose CT image denoising using a generative adversarial network with wasserstein distance and perceptual loss. *IEEE Trans. Med. Imaging* 37, 1348–1357. doi: 10.1109/TMI.2018.2827462

Zhang, X., Zou, Y., and Shi, W. (2017). "Dilated convolution neural network with leakyrelu for environmental sound classification," in *2017 22nd International Conference on Digital Signal Processing (DSP)*, 1–5. doi: 10.1109/ICDSP.2017.8096153

Zou, F., Shen, L., Jie, Z., Zhang, W., and Liu, W. (2018). A sufficient condition for convergences of Adam and RMSProp. *arXiv [preprint]. arXiv:1811.09358*. doi: 10.1109/CVPR.2019.01138

Conflict of Interest: The authors declare that the research was conducted in the absence of any commercial or financial relationships that could be construed as a potential conflict of interest.

Copyright © 2020 Luo, Fan, Chen, Guo and Zhou. This is an open-access article distributed under the terms of the Creative Commons Attribution License (CC BY). The use, distribution or reproduction in other forums is permitted, provided the original author(s) and the copyright owner(s) are credited and that the original publication in this journal is cited, in accordance with accepted academic practice. No use, distribution or reproduction is permitted which does not comply with these terms.

frontiers in Neuroinformatics

TECHNOLOGY AND CODE
published: 07 August 2020
doi: 10.3389/fninf.2020.00033

A Quantitative EEG Toolbox for the MNI Neuroinformatics Ecosystem: Normative SPM of EEG Source Spectra

Jorge Bosch-Bayard[1,2,3], *Eduardo Aubert-Vazquez*[3], *Shawn T. Brown*[2], *Christine Rogers*[2], *Gregory Kiar*[2], *Tristan Glatard*[2], *Lalet Scaria*[2], *Lidice Galan-Garcia*[3], *Maria L. Bringas-Vega*[2,3], *Trinidad Virues-Alba*[3], *Armin Taheri*[2], *Samir Das*[2], *Cecile Madjar*[2], *Zia Mohaddes*[2], *Leigh MacIntyre*[2], *CHBMP*[3], *Alan C. Evans*[2]* and *Pedro A. Valdes-Sosa*[1,2,3]*

[1] The Clinical Hospital of Chengdu Brain Sciences Institute, University of Electronic Science and Technology of China UESTC, Chengdu, China, [2] McGill Centre for Integrative Neuroscience (MCIN), Ludmer Centre for Neuroinformatics and Mental Health, Montreal Neurological Institute (MNI), McGill University, Montreal, QC, Canada, [3] Cuban Neuroscience Centre, Havana, Cuba

OPEN ACCESS

Edited by:
Jan G. Bjaalie,
University of Oslo, Norway

Reviewed by:
Cyril R. Pernet,
University of Edinburgh, United Kingdom
Faranak Farzan,
Simon Fraser University, Canada

***Correspondence:**
Alan C. Evans
alan@bic.mni.mcgill.ca
Pedro A. Valdes-Sosa
pedro.valdes@neuroinformatics-collaboratory.org

Received: 13 May 2019
Accepted: 26 June 2020
Published: 07 August 2020

Citation:
Bosch-Bayard J, Aubert-Vazquez E, Brown ST, Rogers C, Kiar G, Glatard T, Scaria L, Galan-Garcia L, Bringas-Vega ML, Virues-Alba T, Taheri A, Das S, Madjar C, Mohaddes Z, MacIntyre L, CHBMP, Evans AC and Valdes-Sosa PA (2020) A Quantitative EEG Toolbox for the MNI Neuroinformatics Ecosystem: Normative SPM of EEG Source Spectra. Front. Neuroinform. 14:33. doi: 10.3389/fninf.2020.00033

The Tomographic Quantitative Electroencephalography (qEEGt) toolbox is integrated with the Montreal Neurological Institute (MNI) Neuroinformatics Ecosystem as a docker into the Canadian Brain Imaging Research Platform (CBRAIN). qEEGt produces age-corrected normative Statistical Parametric Maps of EEG log source spectra testing compliance to a normative database. This toolbox was developed at the Cuban Neuroscience Center as part of the first wave of the Cuban Human Brain Mapping Project (CHBMP) and has been validated and used in different health systems for several decades. Incorporation into the MNI ecosystem now provides CBRAIN registered users access to its full functionality and is accompanied by a public release of the source code on GitHub and Zenodo repositories. Among other features are the calculation of EEG scalp spectra, and the estimation of their source spectra using the Variable Resolution Electrical Tomography (VARETA) source imaging. Crucially, this is completed by the evaluation of z spectra by means of the built-in age regression equations obtained from the CHBMP database (ages 5–87) to provide normative Statistical Parametric Mapping of EEG log source spectra. Different scalp and source visualization tools are also provided for evaluation of individual subjects prior to further post-processing. Openly releasing this software in the CBRAIN platform will facilitate the use of standardized qEEGt methods in different research and clinical settings. An updated precis of the methods is provided in **Appendix I** as a reference for the toolbox. qEEGt/CBRAIN is the first installment of instruments developed by the neuroinformatic platform of the Cuba-Canada-China (CCC) project.

Keywords: Statistical Parametric Mapping, qEEGt, CBRAIN, EEG tomography, quantitative EEG, open science

INTRODUCTION

Electroencephalography (EEG) is one of the oldest, most useful, and widely deployable methods to study normal and pathological brain function. It is characterized by its sensitivity and exquisite temporal resolution (Niedermeyer et al., 2010). Unfortunately, this type of physiological measurement fell out of favor in research and clinical applications a few decades ago, "eclipsed" by the new neuroimaging techniques (Single Photon Emission Tomography—SPECT, Positron Emission Tomography—PET, and Functional Magnetic Resonance Imaging—fMRI) that were deemed to have true 3D spatial resolution. In fact, it was affirmed that EEG was not even an imaging modality, or in any case, was one with a very poor spatial resolution. This neglect of EEG has been detrimental to translational Neurotechnology.

The negative perception of electrophysiology is now being reversed. Fundamental to this is the development of EEG Source Imaging (ESI) that has achieved considerable maturity (Michel et al., 2004) by leveraging Bayesian estimation prior information about source localizations and connectivity (Wang et al., 2019). As recently reviewed in Babiloni et al. (2019b) ESI is currently an active area of clinical research.

A convergent, but separate, strand of EEG clinical research has been known as "quantitative analysis of EEG" (qEEG) (John et al., 1977; Pardoux, 2008). For a detailed history see Hernandez-Gonzalez et al. (2011). In its most widely used form, the Tomographic Quantitative Electroencephalography (qEEGt) technique extracts frequency specific information about normal and abnormal brain states via the EEG frequency spectrum at scalp electrodes. It then tests for compliance of each electrode and frequency bin (or band) to a normative, most commonly by transformation of each log spectral value to a z transform with respect to an age specific mean and standard deviation. This has been shown to be a useful preprocessing step for either visual inspection or to use multivariate methods to detect and classify brain pathology (Fernández-Bouzas et al., 1995; Hernandez-Gonzalez et al., 2011; Nunez et al., 2019). z values are displayed as topographic maps on the scalp as statistical tests for deviations from normative data. This "significance probability mapping" (spm) inspired developments in Neuroimaging. In fact, SPM (acronym in capitals, Statistical Parametric Mapping) (Friston et al., 1995) owes its acronym to this type of spatial display of statistical tests, but for 3D neuroimages from other imaging modalities (PET, MRI, fMRI). The transition from EEG spm to SPM required to provide a 3D extension of qEEG by means of ESI.

This transformation of qEEG spm to SPM was originally achieved in 2001 (Bosch-Bayard et al., 2001). In this work:

a) The Variable Resolution Electrical Tomography (VARETA) electrophysiological source imaging method was used to obtain source spectra and their log transforms over a defined grid of voxels with high frequency resolution (Szava et al., 1994).
b) Statistical Parametric maps of z-sores for the log source spectra were obtained for each voxel and each frequency bin. Each z score is obtained by subtracting an age-dependent mean and dividing by the age-dependent standard deviation.
c) These age dependent means and standard deviations are embodied in a set of age regression equations for each voxel and each frequency bin.

This "normative SPM of EEG source spectra" is what we have termed "quantitative EEG tomography" or qEEGt. It is essential to note that the current qEEGt toolbox was based on the first wave (1988–2003) of the Cuban Human Brain Mapping Project (CHBMP) (Hernandez-Gonzalez et al., 2011), which acquired the EEG of 211 subjects aged 5–87, randomly selected from the general population. Due to the lack of an individual Magnetic Resonance Image (iMRI) for each subject, an "average head model" was used (Evans et al., 1993). The validity and accuracy of this approach to calculate an approximate lead field has been described elsewhere (Valdés-Hernández et al., 2009). Rather than being a drawback, this use of an approximate head model for ESI has proven to be a valuable instrument in settings which preclude the use of iMRIs (Bosch-Bayard et al., 2012). qEEGt has thus been acknowledged as the first application of Statistical Parametric Mapping to electrophysiology (Friston, 2007, p. 8: "The MEG-EEG years"). The full formal specification for qEEGt is provided in **Appendix I**.

In view of these developments it is surprising that most of the major brain initiatives such as the UK Biobank (www.ukbiobank.ac.uk), ADNI (adni.loni.usc.edu), ABCD (https://abcdstudy.org) have no electrophysiological component. Fortunately the Human Connectome Project (http://www.humanconnectomeproject.org/) and the CAMCAN (www.cam-can.org) project have at least included MEG data collections, thus providing temporal resolution equivalent to EEG. In Canada, the Brain-Code project (https://braininstitute.ca/research-data-sharing/brain-code) has been launched, which is an informatics platform that hosts several biological EEG/MEG data across a growing list of brain pathologies that is shared by over 20 institutions in Ontario, and around 120 researchers. This initiative supports the EEG working group of the Canadian Biomarker Integration Network in Depression (CAN-BIND) that elaborates guidelines for EEG recording and processing standardization (Farzan et al., 2017).

We believe that this situation is partly due to the lack of open-access, structured pipelines, embedded in a major neuroimaging Neuroinformatics platform. While there exist now many different source imaging methods (Vega-Hernández et al., 2008), current packages for this purpose do not provide SPM for the comparison of spectral parameters against validated, population based normative data. Those few packages which in effect provide this functionality, do not make their high dimensional set of regression equations publicly available but rather keep them proprietary.

In this paper we provide an open-access pipeline integrating the qEEGt analysis toolbox developed at the Cuban Neuroscience Center (CNEURO) with a major processing portal for deployment of advanced neuroimaging pipelines: the Canadian Brain Imaging Research Platform (CBRAIN) (Sherif et al., 2014) and the Longitudinal Online Research and Imaging System (LORIS) (Das et al., 2012). Not only can this pipeline be accessed

via CBRAIN but the exact version of the qEEGT toolbox, which includes the VARETA source imaging method, the full set of regression equations with regard to age, as well as the procedures for calculation of z-spectra are also publicly available in Github: https://github.com/CCC-members/QEEGT-Toolbox (doi: https://doi.org/10.5281/zenodo.3745563). Making the code available also facilitates its use by users who may want to merge the qEEGT with their own tools or want to integrate it with other tools like EEGLAB via plugins. This last choice may be attractive for EEGLAB users since EEGLAB can read many different EEG formats. In the future it would be possible creating text files from different EEG formats loaded by EEGLAB to be used by the qEEGT toolbox widening the scope of the present contribution.

For those interested in comparing the formulation described in **Appendix I** for the frequency domain VARETA (FD-VARETA), with the code provided in the github and Zenodo repositories, the major part of its implementation can be found among lines 1090–1230 and then from lines 1719–1804 of the github/Zenodo code. In this version we only implemented part of the FD-VARETA methodology. Some quantities were pre-calculated and assumed constant since their calculation is time-consuming. It is explained in **Appendix I**. A modern full implementation of FD-VARETA, that fulfills the formulation described in **Appendix I** can be found in https://github.com/CCC-members/BC-VARETA_Toolbox. In that toolbox, the equivalent version to the formulation of the present paper is the ridge penalty. A more advanced methodology also included in that toolbox is based on the graphical lasso penalty.

NORMATIVE DATABASE

A feature of this toolbox is that it includes normative data which allows the calculation of univariate measurement of deviation from normality of the log EEG spectra both at the scalp and at the sources. To our knowledge, this is the first qeeg toolbox that makes freely available this type of information.

The normative data provided with this toolbox were obtained from the first wave Cuban Human Brain Mapping project (CHBMP) (Hernandez-Gonzalez et al., 2011). They comprise age regression coefficients for all scalp channels and sources in the frequency range of 0.39–19.11 Hz, with a sampling resolution of 0.39 Hz. The age range goes from 5 to 87 years old of a sample of 211 normal subjects obtained from the normal Havana population.

Age dependent regressions were calculated for the Eyes Closed, Eyes Open, and Hyperventilation states. The sample was selected from Havana population using a quasi-random algorithm, to guarantee a balanced age representation. Strict clinical criteria were followed to eliminate from the sample subjects who were not functionally healthy.

The subjects were recorded during the morning to guarantee the state of wakefulness. The following instructions were given prior to the EEG recording and checked for just before the session: (a) to go to bed before 11 pm the night before and sleep for at least 8 h; (b) to abstain from alcohol, coffee, black tea, chocolate or soda the day before; (c) to and to have abnormal breakfast in the morning. Additionally, before starting the recording at the clinic they were offered a snack to avoid prolonged fasting period.

CBRAIN OVERVIEW

CBRAIN is a Montreal Neurological Institute (MNI) initiative developed to address the storage and processing needs driven by the unprecedented growth of neuroimaging data and distributed computing infrastructure. It has been developed as a collaborative high-performance computing (HPC) portal enabling efficient processing of high volumes of data across national networks such as the Compute Canada clusters. The platform allows researchers to perform computationally intensive analyses by connecting to a national or international network of HPC facilities via a user-friendly web-based interface.

The CBRAIN platform provides many Neuroinformatics tools and methods including those developed by the MNI-based McGill Center for Integrative Neuroscience (MCIN) headed by Dr. Alan Evans for the study of the different types of anatomical and functional MRI techniques such as CIVET image processing (http://www.bic.mni.mcgill.ca/ServicesSoftware/CIVET-2-1-0-Introduction, MacDonald et al., 2000) and the MINC toolkit (https://github.com/BIC-MNI/minc-toolkit-v2). The platform also provides other neuroimaging pipelines from third parties such as Freesurfer (https://surfer.nmr.mgh.harvard.edu/), FSL (Smith et al., 2004; https://www.fmrib.ox.ac.uk/fsl), SPM (https://www.fil.ion.ucl.ac.uk/spm/; Friston, 2007), and others. Deployment of pipelines throughout the CBRAIN computational ecosystem automated through the use of the Boutiques JSON standard and Singularity containers that allow for machine-independent execution with no additional software development (Glatard et al., 2018). Once deployed, any user from any geographical region may benefit of the remote resources offered within the CBRAIN ecosystem. The CBRAIN computational ecosystem is comprised of multiple compute and storage resources located in Canada and around the world. At the time of writing this report, CBRAIN has a current user base of over 600 users over 191 sites in 29 countries and provides over 50 preconfigured tools for neuroscience and other research domains. This platform has let to over 60 peer-reviewed publications and has served over 100 million CPU hours of computing and 100 TBs of data creating a collaborative research network spanning the globe.

Traditionally, researchers are left to work with laborious scripting and command line interfaces to run advanced analyses on HPC resources, requiring extensive training and expertise to accomplish science. Additionally, creating large sets of experiments and aggregation and visualizing results are usually done by hand or by customized software packages. CBRAIN solves this problem by giving researchers a central location and an easy-to-use interface for submitting complicated software packages on computational resources, handling the logistics of such large-scale work behind the scenes so that scientists can concentrate on getting science done. After logging into the platform, users can utilize CBRAIN's web-based portal to upload

and move data, set up and execute computational tasks, and visualize and download results on any of the high-performance computing and cloud resources registered in CBRAIN. An open-source codebase and extensive documentation for administrators enable new cloud resources or data centers to be connected to CBRAIN in a clearly documented and secure manner.

Users can have fine-grained permission control over all resources, data and tools, enabling relevant and secure sharing, and collaboration across geographically distant groups. New toolkits are provided through containerized pipelines (i.e., software installed on a light-weight virtual machine) so that they are highly portable and reproducible. Leveraging this platform for deployment enables wide access to an easily executable and live environment for the of the qEEGt toolbox, with security and cloud connectivity for user-specific datasets.

The pipelines mounted on CBRAIN for data processing and analysis facilitate the reproducibility of research and support the transparency of provenance, i.e., documenting steps to reach the same results in future and how to process other datasets. All these concepts are in line with the goals of open science.

CBRAIN is linked to the Longitudinal Online Research and Imaging System (LORIS), which is an open-source, web-based, data, and project management software aimed at storing behavioral, clinical, neuroimaging, and genetics data. LORIS is designed to gather longitudinal data from patients and to facilitate its curation and further processing. It also offers visualization tools and allows users to leverage external tools. Features include project management and study design; data collection supporting multiple modalities; workflows for data management and quality control; 3D visualization tools; and data querying and sharing tools. LORIS currently has over 400 international projects and partner sites (Das et al., 2016).

At present, CBRAIN and LORIS have developed the capability to accommodate EEG data in a standardized format in LORIS for further processing in CBRAIN. Additionally, our new pipeline has been added to CBRAIN to perform Tomographic Quantitative EEG analysis (qEEGt) of data stored either in LORIS or loaded directly via CBRAIN-connected servers. The EEG data is stored in LORIS in the newly defined BIDS-EEG format (Madjar et al., 2018; Pernet et al., 2018) to address the challenges of data exchange across projects.

THE qEEGt PLUGIN FOR CBRAIN

User Options

We provide tools in CBRAIN capable of running quantitative analysis of EEG both at the sensors space (qEEG) and the sources level (qEEGt).

The qEEGt tool assumes that the analysis windows (epochs) have been previously selected by an expert neurophysiologist using some other system and any necessary preprocessing steps have already been performed. The selected EEG epochs are passed to the plugin and the following options are available:

a. Changing the EEG reference to any of the leads included in the recording montage or re-referencing the data to the average reference;
b. Correcting the EEG by the Global Scale Factor (GSF) (Hernández et al., 1994), which is a factor to account for a high percent of variability present in the EEG related to technical details and not to neurophysiological variability, thus, this factor makes the recordings from different devices and different persons more comparable;
c. Transforming the EEG signal to the frequency domain by means of the FFT;
d. Calculating the cross-spectral matrices for the set of leads recorded at the scalp, including the power spectra for the leads for two models: the narrow band and the broad band models;
e. Calculating the coherence[1] and phase differences between all leads in the whole frequency range;
f. Estimating the power spectra at the sources by means of solving the EEG inverse problem, using the VARETA methodology;
g. Calculating the Z-probabilistic measurements for the spectra of the currents at the sources, using the norms of the Cuban population, in a range from 5 to 87 years old; and
h. Selecting different visualization tools.
i. A step by step guide of how to proceed to run the qEEGT pipeline in CBRAIN is provided in **Appendix II**.

qEEGt Visualization

Once the qEEGT has been run (following the steps shown in **Appendix II**), the user can select the option to visualize the results. In that case, all the different measurements calculated are loaded in a tabbed display for showing the results in the best possible way, either as 2D topographic maps or 3D tomographic images depending on the data type.

The CBRAIN visualization tool opens a graphical user interface, in which all qEEGt results can be visualized: either raw or Z spectra at the sensors space at each frequency, synchronized with the corresponding 3D tomographic maps at the sources, for the narrow band model (high resolution spectral model) (see **Figure 1**).

A compact visualization of the Broad Band Model, both for the raw spectra as well as for the normative data is also provided, as topographical maps, for the calculated frequency bands (see **Figure 2**). A bipolar color palette has been created for the Z-scores, which allows to highlight the negative values (decrement) in blue and positive values (excess) in red. In the case of the raw

[1]The coherence matrix has been included in this toolbox because of historical reasons, although this is not a connectivity toolbox. The coherence is a basic measurement that is included in most of the quantitative analysis. This measurement is widely used in EEG research to assess electrical symmetry between pairs of homologues channels (right-left hemispheres same position channels) rather than for connectivity. This use is important to assess normal brain functioning and it is of clinical importance. It is not intended to be a measurement of connectivity. It is a well-known fact that any connectivity measurement at the scalp is affected by the volume conduction effect. Therefore, none of the recently defined methods to estimate brain coupling in the frequency domain can provide a real estimation of the functional connections among the brain regions. Additionally, Nolte et al. (2019) have shown that most of the phase coupling measurement are in fact a function of the complex coherency.

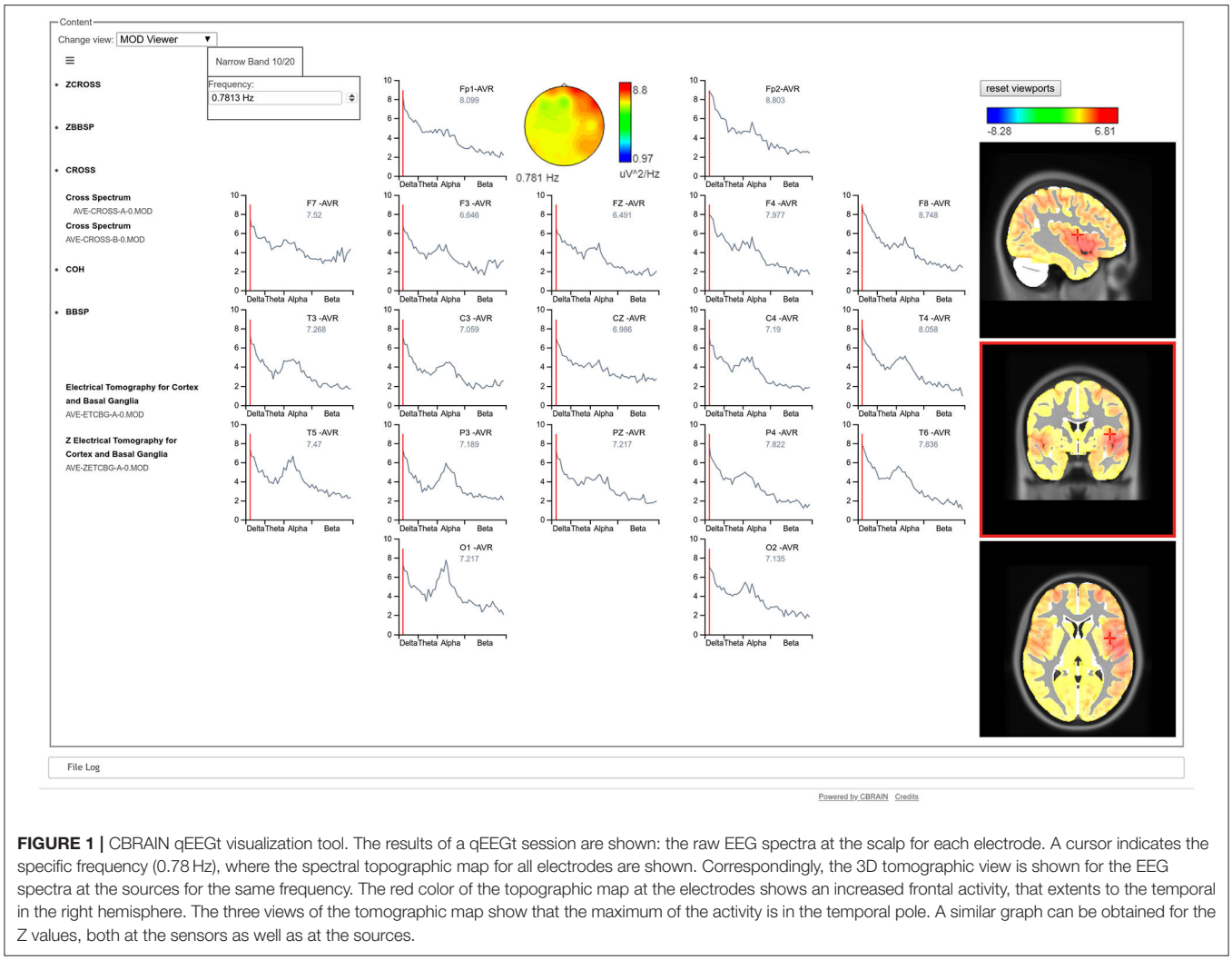


FIGURE 1 | CBRAIN qEEGt visualization tool. The results of a qEEGt session are shown: the raw EEG spectra at the scalp for each electrode. A cursor indicates the specific frequency (0.78 Hz), where the spectral topographic map for all electrodes are shown. Correspondingly, the 3D tomographic view is shown for the EEG spectra at the sources for the same frequency. The red color of the topographic map at the electrodes shows an increased frontal activity, that extents to the temporal in the right hemisphere. The three views of the tomographic map show that the maximum of the activity is in the temporal pole. A similar graph can be obtained for the Z values, both at the sensors as well as at the sources.

values, the same color palette is used for simplicity. Otherwise specified, the traditional bands are calculated: Delta, Theta, Beta, Alpha, Beta, and Total for the Absolute Power (AP) and the Mean Frequency (MF). Meanwhile, the Relative Power (RP) does not include the Total band.

It is also possible to visualize topographic maps of coherence, frequency by frequency, showing the coherences between one channel vs. the rest of the head, as it is shown in **Figure 3**.

Example of Use: A Case Presentation

To illustrate the use of the qEEGt plugin in CBRAIN, we present the processing of an EEG study of a male patient, 71 years old, who suffered thrombotic brain stroke in the middle cerebral artery of the right hemisphere, 3 days before the EEG study. The accident produced a facial paralysis and dysarthria, visual impairment, and motor deficit in the left side of the body.

The EEG was recorded with a MEDICID IV System, sampled every 5 ms, and was edited offline. The patient was seated in a comfortable chair in a dimly lit room, with the eyes closed. The EEG was recorded from 19 leads of the 10–20 International System, using linked earlobes as a reference. A1–A2 reference was used so that the measurements were taken under the same conditions as the Cuban normative database, distributed with the qEEGt software. The amplifier bandwidth was set from 0.5 and 30 Hz. An expert electroencephalographer, visually edited the recording, selecting 24 artifact-free epochs of 2.56 s each, for the quantitative analysis.

With the qEEGt software, we first calculated the EEG spectra at the 19 electrodes of the 10/20 system, for the Eyes Closed (EC) condition. The Log of the spectra was compared against the normative EEG database of the Cuban Neuroscience Center and the probabilistic Z values were obtained for each lead and frequency.

Figure 4 shows the results of the analysis for some selected frequencies: 1.5 Hz for Delta band; 3.5 and 5.85 Hz for Theta band; and 15 Hz for Beta band. The significance thresholds have been corrected for multiple comparisons using the Z maximum statistic criterion (Galan et al., 1994) for a p value of 0.05.

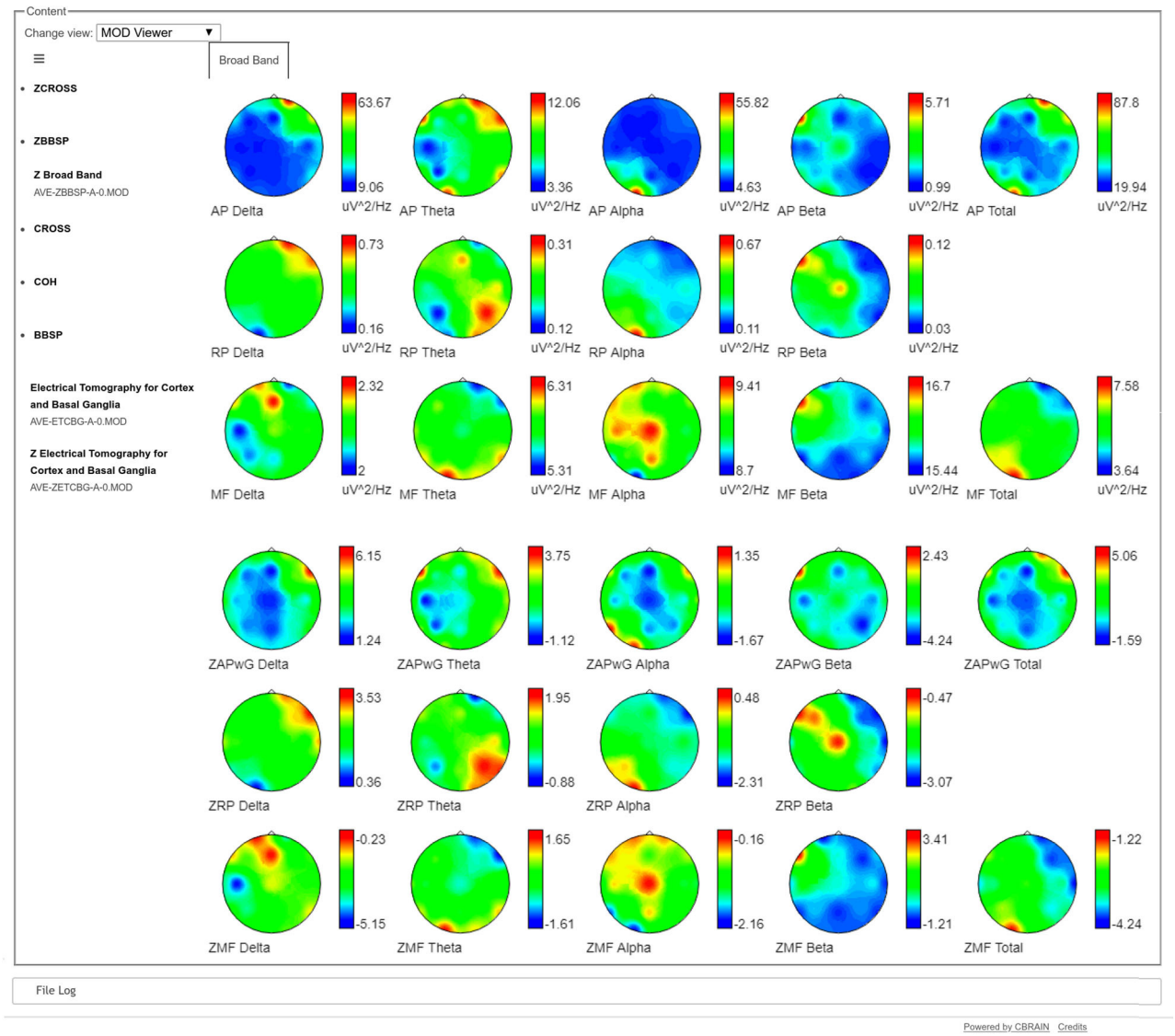


FIGURE 2 | Broad Band Model visualization of raw and Z spectra. The three upper rows show the raw Absolute Power (AP), Relative Power (RP), and Mean Frequency (MF) of the individual's spectra respectively. The three bottom lines show the corresponding Z scores, calculated against the Cuban Normative Database. The red color in the raw Absolute Power maps (first row) show the same frontal and temporal higher slow activity (Delta and Theta) that was observed in **Figure 1** in the right hemisphere, while the Alpha activity is concentrated in the contrary part of the contrary hemisphere (O1). The blue colors show the leads where the amplitude of the raw activity is smaller. In the case of the Z maps, the red colors indicate areas of excess of activity regarding the values of the normative database and blue colors indicate decrements of activity compared to the normative database. For example, the red colors of the Delta Z Absolute Power in the 4th row show values which are more than 6 standard deviations above the normative values. Meanwhile, in the same row, blue colors show values which are 4 standard deviations below the normative values in the parietal leads of the right hemisphere.

However, in Theta band we show the significant areas also for $p = 0.01$ (corrected by multiple comparisons) to better highlight the more pathological areas.

Figures 4A,B show a pathological excess of Delta activity at 1.5 Hz in the right hemisphere, with a location coincident with the lesion. **Figure 4B** shows the pathological areas at a threshold of $p = 0.01$. The area is limited to the territory of the middle cerebral artery. At the same time, **Figure 4F** shows a defect of Beta activity in the same area as **Figure 4A**, except that it extends to the occipital area of the contrary hemisphere too.

At the limit between Delta and Theta (**Figures 4C,D**), the excess of pathological activity is extended to almost the whole right hemisphere and to the frontal part of the left hemisphere. The threshold at $p = 0.01$ shown in **Figure 4D** is to stress the point that at this frequency the most pathological areas does not coincide with the exact location of the lesion but with the surrounding area. This result is consistent with previous

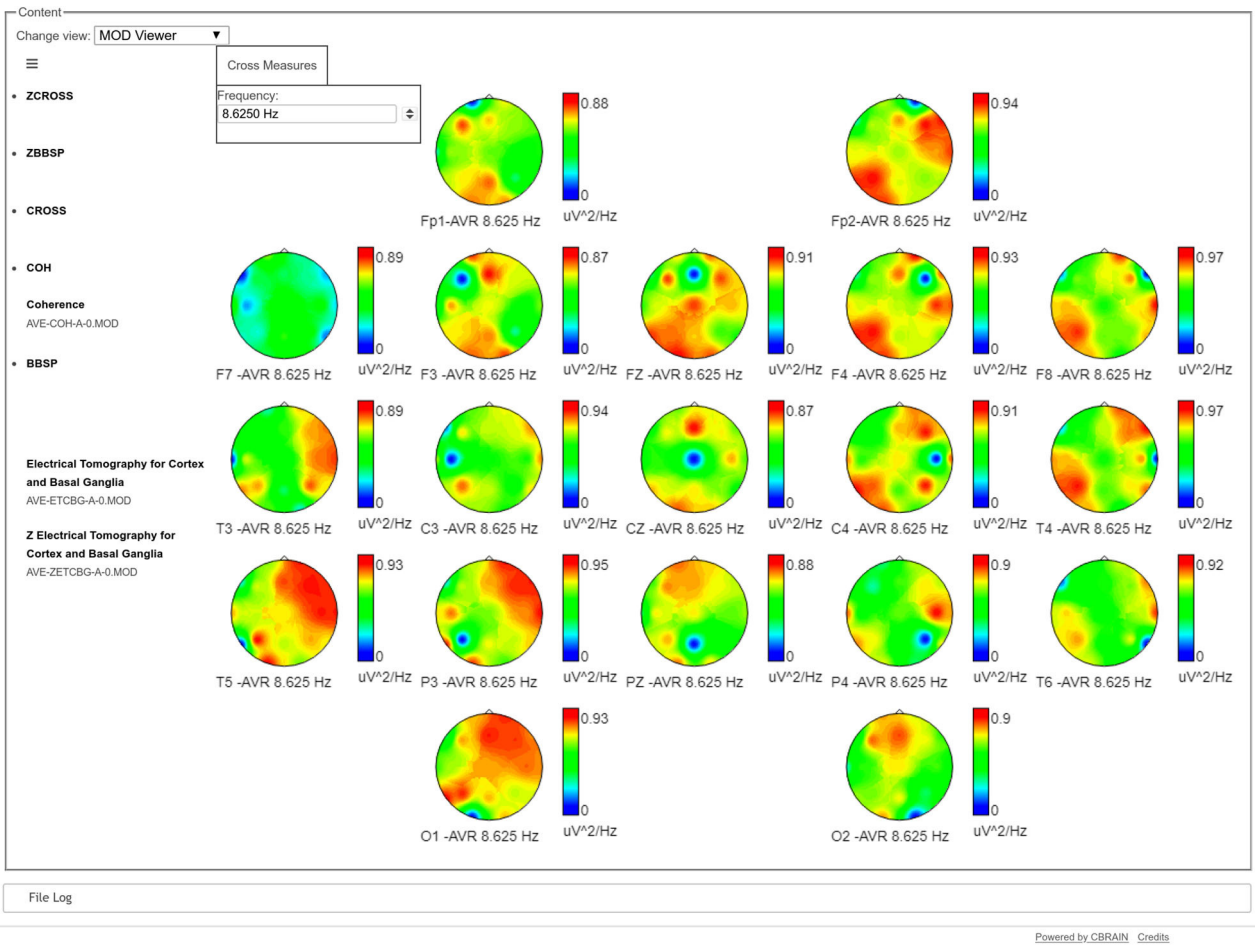


FIGURE 3 | Topographical maps of the coherences of one electrode against the rest, at a specific frequency (8.6 Hz in the example). In each map, the blue dot refers to the position of the target electrode, showing its coherence regarding the rest of the head. Values in these maps go from 0 (blue) to red (1). For example, the maps of T5, P3, and O1 show a very high coherence between the parieto-occipital leads of the left hemisphere with the frontal and temporal leads of the contrary hemisphere. In the case of Fp2, it has high coherence values both with the frontal and temporal leads of its same hemisphere and the parietal and occipital leads of the contrary hemisphere.

results by Fernández-Bouzas et al. (2002) in a qEEGt study of persons who suffered brain infarcts they found two major areas of pathological excess of slow activity: one coincident with the localization at the slower frequencies (Delta) and a second one coincident with the localization of the ischemic penumbra, which surrounds the lesion.

Note that from **Figures 4A–F**, the threshold value for the Z activity is decreasing with the frequency ($Z = 3.75$ at 1.5 Hz; $Z = 2.3$ at 5.85 Hz). It means that the slower the frequency the more significant pathological values. This is also consistent with the Gloor's hypothesis (Gloor et al., 1977) about the origin of the Delta waves in the brain produced by the neuronal deafferentation in the brain cortex directly below the lesion. Finally, in **Figure 4E**, at 5.85 Hz the pathological activity was only significant at the threshold of $p = 0.05$ but not for $p = 0.01$ after correction for multiple comparisons. In the same way, there was no significant pathological activity in Alpha band.

As an independent confirmation we show a morphometric analysis of the T1 MRI of the same person (**Figure 5**). The statistical parametric map was performed using the plugin IBASPM (https://www.fil.ion.ucl.ac.uk/spm/ext/#IBASPM) based on the regional volume of the MRI. The subject's values were compared with the normative values obtained from the Cuban Normative database (Z values). The yellow color identified the regions with brain damage: occipital damage responsible of visual impairment; and the lesion in Broca's area may explain the language impairment, not detected by MRI. These two abnormality patterns are in consonance with the qEEGt findings shown in **Figures 4C,F**.

This case presentation of a clinical patient is only to illustrate the use of the toolbox and its possibilities. This section is not intended as a validation of the VARETA methodology, which has been widely used and validated for many years in different clinical and experimental settings. A non-exhaustive list of about 200 citations retrieved from Google Scholar in September 2019 (excluding auto citations) is provided as a supplemental material (53 of them belong to the period 2013–2019).

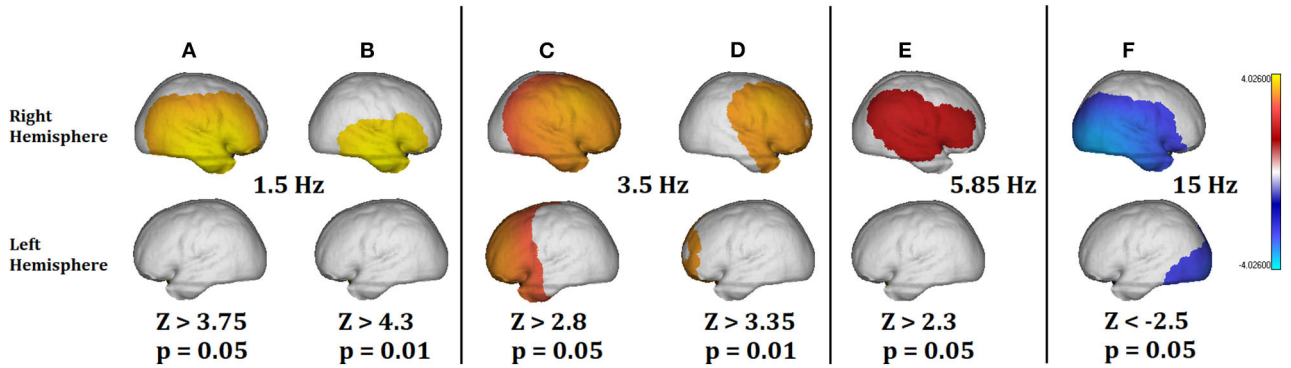


FIGURE 4 | Summary of the qEEGt analysis of the 71 years old patient. The more significant results are shown for bands Delta, Theta, and Gamma at two thresholds ($p = 0.05$ and $p = 0.01$). **(A)** (p =0.05) and **(B)** ($p = 0.01$) show a pathological excess of Delta activity in the right hemisphere. **(C)** ($p = 0.05$) and **(D)** ($p = 0.01$) show the excess of pathological activity in the right hemisphere and frontal part of the left hemisphere. **(D)** Shows that the most pathological areas in Theta coincide with the exact location of the surrounding area of the lesion. **(E)** Shows that no pathological activity was significant at 5.85 Hz for $p = 0.01$. **(F)** Shows a pathological decrease of activity in the Beta band, related to the location of the lesion and the edema area. No significant differences were found in the Alpha band. The implications of these results are discussed in the text.

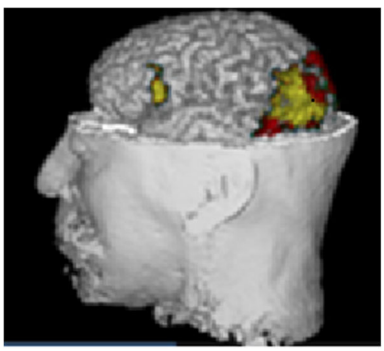


FIGURE 5 | Morphometric analysis of the T1 MRI of the same case. Statistical parametric mapping using the plugin IBASPM based on the regional volume of the MRI in comparison with the normative data (Z values). The yellow area identified the regions with brain damage, occipital damage responsible of visual impairment, and lesion in Broca's area which explained the language impairment, not detected by MRI. The correspondence with **Figure 4** is striking.

It is also important to emphasize that in this toolbox we do not include statistical tools for group analysis of neuroimages. The z score is only an intermediate step, useful for visualization purposes and classification. The true multivariate nature of the data must be considered in further applications. Tools for group statistics of neuroimages developed at the Cuban Neuroscience Center will be added as CBRAIN plugins in the future, for example, Mahalanobis maps (Galan et al., 1994) for visualization, or stable biomarker identification (Bosch-Bayard et al., 2018) among others.

IMPLEMENTATION DETAILS AND CHALLENGES

The Matlab code of the qEEGt procedure was modified to condense it in a single procedure, which performs all the analysis and produces all the necessary outputs. This procedure was compiled and use as the input for the CBRAIN plugin.

A Boutique JSON descriptor for qEEG (doi: 10.5281/zenodo.1451003) was created to define the format of the command line execution and the various options that can be set. Then a Singularity container was created to provide a machine independent installation of the qEEG tool. Finally, CBRAIN can automatically import the Boutique descriptor to create the tool and deploy it for users.

The highly interactive qEEGt visualization capability is built in the highly modular ReactJS framework (which makes it independent of the computer platforms) with any modern internet browser. The application is designed as an SDI (Single Document Interface) with a graphical user interface oriented to provide the maximum amount of information with the minimum amount of user input.

Note that there are facilities for the creation of data structures for storing EEG information in the LORIS data platform as well as the implementation within the CBRAIN high-performance computing platform of a core of tools developed at CNEURO.

DISCUSSION AND CONCLUSIONS

The present qEEGt plugin is the first step to introduce EEG functionalities in CBRAIN, one of the most widely used ecosystems for brain imaging analysis. Will facilitate the extended use the qEEGt method and toolbox, which has proven to be a useful tool for the quantitative EEG analysis, both at the electrode and at the sources level.

This method introduced the concept of "normative SPM of EEG source spectra" based on the use of EEG normative databases. The resulting SPM "z maps" that compare individuals to age appropriate norms is an essential pre-processing tool which facilitates assessment of pathological states (or at least deviation from normality). It is to be noted that the normative

data encoded in the regression equations of the current qEEGt toolbox are the first open source information of this type. Importantly, they are not only for the usual brain states available in most databases namely Eyes Closed and/or Eyes Open, but also include other states that are clinically relevant such as Hyperventilation. Although these tools are still mainly used for research, they have a clinical usefulness, specifically the assessment of deviation from normality (Nuwer et al., 1994, 1999; Babiloni et al., 2019a).

The plugin resulted easy to operate for totally naive users in a reasonable time for a single task. Familiarity with the tool and batch processing of several EEG recordings will increase productivity with the toolbox. Nevertheless we continue to evaluate both the CBRAIN interface as well as the toolbox to increase its user friendliness.

As mentioned in the introduction, our development of qEEG was based on the Cuban Human Brain Mapping Project (CHBMP), which was carried out in three waves: the first one (1988–2003) acquired the EEG of 211 subjects aged 5–87, randomly selected from the general population. At that time, only EEG was recorded since there were no MRI systems available. While useful in setting for which MRI is not feasible or costly, future work must extend the methods to individualized brain morphology. This is the more necessary since though there has been work with EEG SPM in individualized source space (Park et al., 2002), it yet has to be extended to age corrected normative measures.

Fortunately two subsequent waves (2004–2014) and (since 2018) of the CHBMP have been launched since then, which now included individualized MRI, DWI as well as high resolution EEG (more details in Hernandez-Gonzalez et al., 2011). These projects have generated normative data that has been used in different Public Health Systems (Hernandez-Gonzalez et al., 2011; Valdés-Sosa et al., 2018) which will lead to successive versions of qEEGt in CBRAIN, and whose results will be described in further publications and will certainly address individualized head models.

Among the additional facilities to be included to qEEGt soon are:

d) Individualized head geometry for Human Connectome compatible pipelines
e) Improved approximate head models (Valdés-Hernández et al., 2009) for situations in which MRI is difficult to acquire.
f) Extension of EEG sources features to non-stationary and nonlinear phenomena.
g) Inclusion of third generation methods for joint estimation of EEG source activation and connectivity (Paz-Linares et al., 2017, 2018).
h) A toolbox for biomarker selection from EEG source features (Bosch-Bayard et al., 2018).

This step, of making our toolbox available in CBRAIN (as well as the methods in Github) will allow us to place in the public scrutiny the procedures and, we hope, to increase the contributions and interactions with other similar efforts.

DATA AVAILABILITY STATEMENT

All datasets generated for this study are included in the article/**Supplementary Material**.

AUTHOR CONTRIBUTIONS

PV-S contributed key concepts of the qEEG, the mathematical definition of VARETA and qEEGt VARETA, wrote and revised the paper, and directed and organized the three waves of the Cuban Human Brain Mapping projects (CHBMP). JB-B programmed all the algorithms, created the Norms, methods testing, wrote the paper, and participated in dockerization in CBRAIN. EA-V created all visualization tools and the user-friendly version of the qEEGT software. SB organized and directed the qEEGt dockerization in CBRAIN and throughout paper revision. CR participated in qEEGt integration with LORIS and throughout paper revision. GK, TG, and LS carried out the qEEGt dockerization in CBRAIN and wrote the qEEGT web interface for CBRAIN. LG-G developed all the statistical methods of qEEGT as well as permutations methods for high dimensional datasets. MB-V and TV-A participated in the clinical evaluation of qEEGt. AT wrote the web visualization for the qEEGT in CBRAIN. SD, CM, ZM, and LM participated in qEEGt integration in LORIS, discussions, and paper revision. Evans organized, facilitated, supervised, and provided the environment and resources for qEEGt integration in CBRAIN, as well as paper revision. JB-B, EA-V, LG-G, and TV-A participated and carried out in the three waves of CHBMP and have worked in the topic for more than 25 years. All authors contributed to the article and approved the submitted version.

ACKNOWLEDGMENTS

We want to acknowledge the effort of a group of persons that have been carrying out the qEEGt project at the Cuban neuroscience Center since the early 90's. The CHBMP corporate author is all the personnel who made possible the Cuban Human Brain Mapping project, starting in 1988: Pedro Valdes-Sosa, Mitchell Valdes-Sosa, Susana Szava, Lidice Galan-Garcia, Jorge Bosch-Bayard, Trinidad Virues-Alba, Eduardo Aubert-Vazquez, Maria C. Perez-Avalos, Alfredo Alvarez-Amador, Guido Diaz, Maria Esther de Quesada, Jose Aquino, Calixto Machado, Pedro Figueredo, Roberto Pascual-Marqui, Jorge Riera-Diaz, Rolando Biscay-Lirio, Jose Carballo, Juan Carlos Jimenez, Octavio Baez, Gerardo Ruiz-Parodis, Manuel Sanchez, Juan Almira, Celso Rodriguez, Carlos Suarez-Murias, Eduardo Eimil, Clara Castro, Bertha Castellanos, Nelsa Echevarría, Jorge Rojas, Francisco Valdes, Mario Salcedo, and the group of neurophysiologists, technicians, and nurses who made the project possible.

SUPPLEMENTARY MATERIAL

The Supplementary Material for this article can be found online at: https://www.frontiersin.org/articles/10.3389/fninf.2020.00033/full#supplementary-material

REFERENCES

Babiloni, C., Barry, R. J., Başar, E., Blinowska, K. J., Cichocki, A., Drinkenburg, W. H. I. M., et al. (2019a). International Federation of Clinical Neurophysiology (IFCN)—EEG research workgroup: recommendations on frequency and topographic analysis of resting state EEG rhythms. Part 1: applications in clinical research studies. *Clin. Neurophysiol.* 131, 285–307. doi: 10.1016/j.clinph.2019.06.234

Babiloni, C., Del Percio, C., Pascarelli, M. T., Lizio, R., Noce, G., Lopez, S., et al. (2019b). Abnormalities of functional cortical source connectivity of resting-state electroencephalographic alpha rhythms are similar in patients with mild cognitive impairment due to Alzheimer's and Lewy body diseases. *Neurobiol. Aging* 77, 112–127. doi: 10.1016/j.neurobiolaging.2019.01.013

Bosch-Bayard, J, Valdés-Sosa, P., Virues-Alba, T., Aubert-Vázquez, E., John, E. R., Harmony, T., et al. (2001). 3D statistical parametric mapping of EEG source spectra by means of variable resolution electromagnetic tomography (VARETA). *Clin. EEG* 32, 47–61. doi: 10.1177/155005940103200203

Bosch-Bayard, J., Galán-García, L., Fernandez, T., Lirio, R. B., Bringas-Vega, M. L., Roca-Stappung, M., et al. (2018). Stable sparse classifiers identify qEEG signatures that predict learning disabilities (NOS) severity. *Front. Neurosci.* 11:749. doi: 10.3389/fnins.2017.00749

Bosch-Bayard, J., Valdés-Sosa, P. A., Fernandez, T., Otero, G., Pliego, B., Ricardo-Garcell, J., et al. (2012). NeuroImage 3D statistical parametric mapping of quiet sleep EEG in the first year of life. *NeuroImage* 59, 3297–3308. doi: 10.1016/j.neuroimage.2011.11.001

Das, S., Glatard, T., MacIntyre, L. C., Madjar, C., Rogers, C., Rousseau, M.-E., et al. (2016). The MNI data-sharing and processing ecosystem. *NeuroImage* 124(Pt B), 1188–1195. doi: 10.1016/j.neuroimage.2015.08.076

Das, S., Zijdenbos, A. P., Harlap, J., Vins, D., and Evans, A. C. (2012). LORIS: a web-based data management system for multi-center studies. *Front. Neuroinf.* 5:37. doi: 10.3389/fninf.2011.00037

Evans, A., Collins, D., Millst, S., Brown, E., Kelly, R., and Peters, T. (1993). "3D statistical neuroanatomical models from 305 MRI volumes," in *Proceedings of IEEE—Nuclear Science Symposium and Medical Imaging Conference* (San Francisco, CA), 1813–1817. doi: 10.1109/NSSMIC.1993.373602

Farzan, F., Atluri, S., Frehlich, M., Dhami, P., Kleffner, K., Price, R., et al. (2017). Standardization of electroencephalography for multi-site, multi-platform and multi-investigator studies: insights from the canadian biomarker integration network in depression. *Sci. Rep.* 7:7473. doi: 10.1038/s41598-017-07613-x

Fernández-Bouzas, A., Harmony, T., Fernández, T., Aubert, E., Ricardo-Garcell, J., Valdés, P., et al. (2002). Sources of abnormal EEG activity in spontaneous intracerebral hemorrhage. *Clin. EEG* 33, 70–76. doi: 10.1177/155005940203300205

Fernández-Bouzas, A., Harmony, T., Galán, L., Marosi, E., Fernández, T., Reyes, A., et al. (1995). Comparison of Z and multivariate statistical brain electromagnetic maps for the localization of brain lesions. *Electroencephal. Clin. Neurophys.* 95, 372–380. doi: 10.1016/0013-4694(95)00111-B

Friston, K. (2007). "Statistical parametric mapping" in *Statistical Parametric Mapping: The Analysis of Funtional Brain Images*, *1st Edn*, eds W. Penny, K. Friston, J. Ashburner, S. Kiebel, and T. Nichol (Amsterdam; Boston, MA: Elsevier/Academic Press).

Friston, K. J., Holmes, A. P., Worsley, K. J., Poline, J. B., Frith, C. D., Frackowiak, R. S. J. (1995). Statistical parametric maps in functional imaging: a general linear approach. *Hum. Brain Mapp.* 2, 189–210. doi: 10.1002/hbm.460020402

Galan, L., Biscay, R., Valdes, P., Neira, L., and Virues, T. (1994). Multivariate statistical brain electromagnetic mapping. *Brain Topogr.* 7, 17–28. doi: 10.1007/BF01184834

Glatard, T., Kiar, G., Aumentado-Armstrong, T., Beck, N., Bellec, P., Bernard, R., et al. (2018). Boutiques: a flexible framework to integrate command-line applications in computing platforms. *GigaScience* 7:giy016. doi: 10.1093/gigascience/giy016

Gloor, P., Ball, G., and Schaul, N. (1977). Brain lesions that produce delta waves in the EEG. *Neurology* 27, 326–333. doi: 10.1212/WNL.27.4.326

Hernández, J. L., Valdés, P., Biscay, R., Virues, T., Szava, S., Bosch, J., et al. (1994). A global scale factor in brain topography. *Int. J. Neurosci.* 76, 267–278. doi: 10.3109/00207459408986009

Hernandez-Gonzalez, G., Bringas-Vega, M. L., Galán-García, L., Bosch-Bayard, J., Melie-Garcia, Y. L. L., Valdes-Urrutia, L., et al. (2011). Multimodal quantitative neuroimaging databases and methods: the cuban human brain mapping project. *Clin. EEG Neurosci.* 42, 149–159. doi: 10.1177/155005941104200303

John, E., Karmel, B., Corning, W., Easton, P., Brown, D., Ahn, H., et al. (1977). Neurometrics. *Science* 196, 1393–1410. doi: 10.1126/science.867036

MacDonald, D., Kabani, N., Avis, D., and Evans, A. C. (2000). Automated 3-D extraction of inner and outer surfaces of cerebral cortex from MRI. *NeuroImage* 12, 340–356. doi: 10.1006/nimg.1999.0534

Madjar, C., Rogers, C., Desjardins, J., Lo, D., Safi-Harab, M., Legault, M., et al. (2018). "Electrophysiology data sharing: inserting standardized EEG data into the LORIS framework using BIDS," in *INCF Congress: Neuroinformatics 2018*, ed G. Node (Montreal, QC), 90.

Michel, C. M., Murray, M. M., Lantz, G., Gonzalez, S., Spinelli, L., and Grave De Peralta, R. (2004). EEG source imaging. *Clin. Neurophysiol.* 115, 2195–2222. doi: 10.1016/j.clinph.2004.06.001

Niedermeyer, E., Schomer, D. L., and Lopes da Silva, F. H. (2010). *Niedermeyer's Electroencephalography leBasic Principles, Clinical Applications, and Related Fields*. Philadelphia, PA; Baltimore, MD: Wolters Kluwer Health. doi: 10.1093/med/9780190228484.001.0001

Nolte, G., Galindo-Leon, E., Li, Z., Liu, X., and Engel, A. K. (2019). Mathematical relations between measures of brain connectivity estimated from electrophysiological recordings for Gaussian distributed data. *bioRxiv* 680678. doi: 10.1101/680678

Nunez, P. L., Nunez, M. D., and Srinivasan, R. (2019). Multi-scale neural sources of EEG: genuine, equivalent, and representative. A tutorial review. *Brain Topogr.* 32, 193–214. doi: 10.1007/s10548-019-00701-3

Nuwer, M. R, Lehmann, D., da Silva, F. L., Matsuoka, S., Sutherling, W., and Vibert, J. F. (1999). IFCN guidelines for topographic and frequency analysis of EEGs and EPs. The International Federation of Clinical Neurophysiology. *Electroencephalogr. Clin. Neurophysiol. Suppl.* 52, 15–20.

Nuwer, M. R., Lehmann, D., Lopes da Silva, F., Matsuoka, S., Sutherling, W., and Vibert, J.-F. (1994). IFCN guidelines for topographic and frequency analysis of EEGs and EPs. Report of an IFCN committee. *Electroencephalogr. Clin. Neurophysiol.* 91, 1–5. doi: 10.1016/0013-4694(94)90011-6

Pardoux, E. (2008). *Markov Processes and Applications: Algorithms, Networks, Genome and Finance*. West Sussex: Wiley. doi: 10.1002/9780470721872

Park, H.-J., Kwon, J. S., Youn, T., Pae, J. S., Kim, J.-J., Kim, M.-S., et al. (2002). Statistical parametric mapping of LORETA using high density EEG and individual MRI: application to mismatch negativities in Schizophrenia. *Hum. Brain Mapp.* 17, 168–178. doi: 10.1002/hbm.10059

Paz-Linares, D., Gonzalez-Moreira, E., Bosch-Bayard, J., Areces-Gonzalez, A., Bringas-Vega, M. L., and Valdes-Sosa, P. A. (2018). Neural connectivity with hidden gaussian graphical state-model. arXiv[Preprint]. *arXiv:1810.01174*. Available online at: https://arxiv.org/abs/1810.01174v3

Paz-Linares, D., Vega-Hernández, M., Rojas-López, P. A., Valdés-Hernández, P. A., Martínez-Montes, E., and Valdés-Sosa, P. A. (2017). Spatio temporal EEG source imaging with the hierarchical Bayesian elastic net and elitist lasso Models. *Front. Neurosci.* 11:635. doi: 10.3389/fnins.2017.00635

Pernet, D. C., Appelhoff, S., Flandin, G., Phillips, C., Delorme, A., and Oostenveld, R. (2018). BIDS-EEG: an extension to the brain imaging data structure (BIDS) specification for electroencephalography. *PsyArxiv*. doi: 10.31234/osf.io/63a4y

Sherif, T., Rioux, P., Rousseau, M.-E., Kassis, N., Beck, N., Adalat, R., et al. (2014). CBRAIN: a web-based, distributed computing platform for collaborative neuroimaging research. *Front. Neuroinf.* 8:54. doi: 10.3389/fninf.2014.00054

Smith, S. M., Jenkinson, M., Woolrich, M. W., Beckmann, C. F., Behrens, T. E. J., Johansen-Berg, H., et al. (2004). Advances in functional and structural MR image analysis and implementation as FSL. *NeuroImage* 23, S208–S219. doi: 10.1016/j.neuroimage.2004.07.051

Szava, S., Valdes, P., Biscay, R., Galan, L., Bosch, J., and Jimenez, J. C. (1994). High resolution quantitative EEG analysis. *Brain* 6, 211–219. doi: 10.1007/BF01187711

Valdés-Hernández, P. A., von Ellenrieder, N., Ojeda-Gonzalez, A., Kochen, S., Alemán-Gómez, Y., Muravchik, C., and Valdés-Sosa, P. A. (2009). Approximate

average head models for EEG source imaging. *J. Neurosci. Methods* 185, 125–132. doi: 10.1016/j.jneumeth.2009.09.005

Valdés-Sosa, P. A., Galler, J. R., Bryce, C. P., Rabinowitz, A. G., Bringas-Vega, M. L., Hernández-Mesa, N., et al. (2018). Seeking biomarkers of early childhood malnutrition's long-term Effects. *MEDICC Rev.* 20, 43–48. doi: 10.37757/mr2018.v20.n2.10

Vega-Hernández, M., Martínez-Montes, E., Sánchez-Bornot, J. M., Lage-Castellanos, A., and Valdés-Sosa, P. A. (2008). Penalized least squares methods for solving the EEG inverse problem. *Stat. Sin.* 18, 1535–1551. Available online at: https://www.jstor.org/stable/24308568

Wang, Y., Van de Moortele, P.-F., and He, B. (2019). Automated gradient-based electrical properties tomography in the human brain using 7 Tesla MRI. *Magn. Reson. Imaging* 63, 258–266. doi: 10.1016/j.mri.2019.08.003

Conflict of Interest: The authors declare that the research was conducted in the absence of any commercial or financial relationships that could be construed as a potential conflict of interest.

Copyright © 2020 Bosch-Bayard, Aubert-Vazquez, Brown, Rogers, Kiar, Glatard, Scaria, Galan-Garcia, Bringas-Vega, Virues-Alba, Taheri, Das, Madjar, Mohaddes, MacIntyre, CHBMP, Evans and Valdes-Sosa. This is an open-access article distributed under the terms of the Creative Commons Attribution License (CC BY). The use, distribution or reproduction in other forums is permitted, provided the original author(s) and the copyright owner(s) are credited and that the original publication in this journal is cited, in accordance with accepted academic practice. No use, distribution or reproduction is permitted which does not comply with these terms.

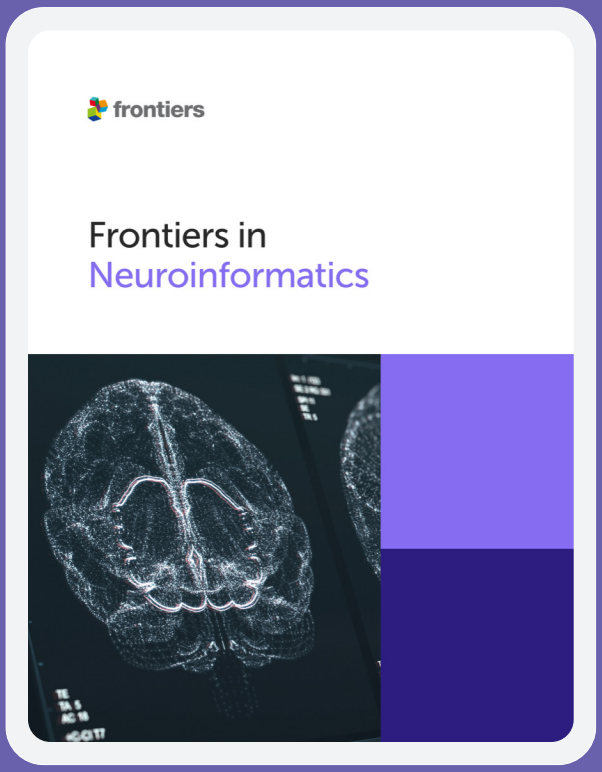
Frontiers in Neuroinformatics

Leading journal supporting neuroscience in the information age

Part of the most cited neuroscience journal series, developing computational models and analytical tools used to share, integrate and analyze experimental data about the nervous system functions.

Discover the latest Research Topics

See more →



Frontiers

Avenue du Tribunal-Fédéral 34
1005 Lausanne, Switzerland
frontiersin.org

Contact us

+41 (0)21 510 17 00
frontiersin.org/about/contact